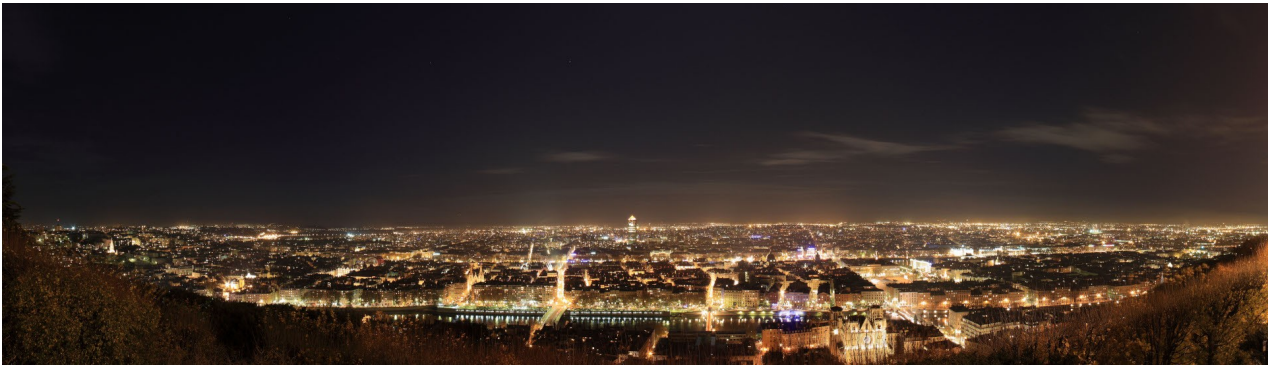


enerstock

**Proceedings of the 16th IEA ES TCP
International Conference on Energy Storage**

ENERSTOCK 2024



**Lyon, France
June 5–7, 2024**

**Proceedings of the 16th IEA ES TCP
International Conference on Energy Storage (ENERSTOCK 2024)**

Chair: Kévyne Johannes, INSA Lyon, France

Website: www.enerstock2024.org

Editor: Frédéric Kuznik, INSA Lyon, France

DOI: 10.5281/zenodo.13790499

Published: 18 September 2024

ISBN 978-2-9595978-0-0

Copyright © 2024 INSAVALOR, Villeurbanne, France

Cover picture copyright © 2008 Mickaël Melzani licensed under CC BY-SA 3.0

This document is licensed under CC BY-NC-ND 4.0



Foreword

Dear Participants,

On behalf of the Organizing Committee, we would like to extend our heartfelt gratitude to all of you who attended the Enerstock 2024 conference in Lyon, France. Your contributions made this event a resounding success, enriching the experience for everyone involved.

The presentations delivered during the conference were of an exceptionally high scientific level, showcasing latest research and innovative solutions across a wide range of topics in energy storage. From advancements in thermal energy storage to new perspectives on electrical storage and power-to-gas technologies, the breadth and quality of the knowledge shared were truly inspiring.

We are particularly grateful for the fruitful discussions that emerged from these sessions. The active exchange of ideas and the collaborative spirit among participants fostered a dynamic environment, which is crucial for driving the field forward.

A special thank you goes to the Scientific Committee, whose expertise and guidance were crucial in shaping the program. We are also thankful to the reviewers, who worked diligently to ensure the high standards of the conference, and to the session chairpersons for their leadership in steering the discussions.

Your engagement and dedication are what made Enerstock 2024 an outstanding event. We look forward to continuing this dialogue and working together to advance our shared goals.

Thank you once again for your invaluable participation, and we hope to see you at future events!

Warm regards,

Prof. Kévyn JOHANNES, *Chairman of the Organizing Committee*
Prof. Frédéric KUZNIK, *Chairman of the Scientific Committee*
Enerstock 2024 Conference
Lyon, France, 11 July 2024

Acknowledgements

The Organising Committee is deeply appreciative of the sponsorship generously provided by the following industry sponsors:

Gold sponsors



Silver sponsor



Scientific Committee

Chair: Prof. Frédéric KUZNIK, INSA Lyon, France
Dr Liang AN, Hong Kong Polytechnic University, China
Prof. Umberto BERARDI, Toronto Metropolitan University, Canada
Prof. Luisa CABEZA, University of Lleida, Spain
Prof. Michel DE PAEPE, Ghent University, Belgium
Dr Stefania DOPPIU, CIC energiGUNE, Spain
Dr Enrico FABRIZIO, Politecnico di Torino, Italy
Prof. Mohammed FARID, University of Auckland, New Zealand
Prof. Gilles FRAISSE, USMB Chambéry, France
Dr Andreas HAUER, ZAE Bayern, Germany
Prof. Kévyne JOHANNES, INSA Lyon, France
Dr Ana LÁZARO, Universidad de Zaragoza, Spain
Dr Alexandre MALLEY-ERNEWEIN, Université Lyon 1, France
Dr Kokouvi Edem N'TSOUKPOE, 2iE Ouagadougou, Burkina Faso
Dr Christian OBRECHT, INSA Lyon, France
Prof. Halime PAKSOY, Çukurova University, Turkey
Prof. Elena PALOMO DEL BARRIO, CIC energiGUNE, Spain
Prof. Marco PERINO, Politecnico di Torino, Italy
Dr Alenka RISTIĆ, National Institute of Chemistry, Slovenia
Prof. Dirk Uwe SAUER, RWTH Aachen, Germany
Dr Uroš STRITIH, University of Ljubljana, Slovenia
Dr Wim VAN HELDEN, AAE – INTEC, Austria
Prof. Annelies VANDERSICKEL, DLR Stuttgart, Germany
Prof. Laurent ZALEWSKI, Université d'Artois, France
Prof. Herbert A. ZONDAG, Eindhoven University of Technology, Netherlands

Organizing Committee

Chair: Prof. Kévyne JOHANNES, INSA Lyon, France
Co-chair: Prof. Frédéric KUZNIK, INSA Lyon, France
Dr Christian OBRECHT, INSA Lyon, France
Dr Alexandre MALLEY-ERNEWEIN, Université Lyon 1, France

Plenary speakers



Carnot Battery Development – State of the art & prospects,
Annelies Vandersickel - DLR, Germany



Share of storage in the electricity mix of prospective scenarios in France, **Pierre Sacher** - ADEME, France



Energy storage for supporting Renewable businesses,
Lionel Nadau - ENGIE, France

Extended Abstracts

4-Dimensional monitoring of the temperature and energy performance of borehole heat exchanger systems: the Hoogezand pilot (Groningen, Netherlands), Daniel Bakker <i>et al.</i>	1
A critical Outlook to commercial high-temperature Thermal Energy Storage, Ammann Sebastian <i>et al.</i>	6
A novel process for the generation of ice slurry based on a dispersible two-substance system, Matthes Manuel <i>et al.</i>	9
A novel synthesis and characterization of α -Fe ₂ O ₃ @Ppy photoanode for photoelectrochemical water splitting, Emir Sedat <i>et al.</i>	13
A Review of Pilot-scale and Application-scale Latent Thermal Energy Storage Heat Exchanger Configurations, Suswal Aditya Singh <i>et al.</i>	17
Advanced controllers for electrically heated floors in residential buildings to shift peak load, Sun Ying <i>et al.</i>	21
Advanced numerical model to analyze the thermal response of macroencapsulated PCMs for building applications, Alvarez-Rodriguez Matias <i>et al.</i>	25
An analysis of energy storage policy in the UK (2000-2023): capturing key insights and lessons learned, Harrison Chris <i>et al.</i>	29
An innovative, modular sorption storage system for residential applications, Hengel Franz <i>et al.</i>	37
Assessing Zeolite Imidazolate Frameworks as Thermal Energy Storage Materials, Byrne Ciara <i>et al.</i>	41
Bench-scale long-term phase change material analysis for thermal energy storage design, Gunasekara Saman Nimali <i>et al.</i>	45
Binder-free K ₂ CO ₃ granules for thermochemical heat storage, Salehzadeh Delaram <i>et al.</i>	49
Bio-based shape-stabilized phase change materials for hot water storage, Marske Felix <i>et al.</i>	54
Biomimicry-inspired design optimization of a latent thermal energy storage system using phase change materials, Mehraj Nadiya <i>et al.</i>	58
Carbon Capture and Heating – Can we combine long-term energy storage with Direct Air Capture?, Klockow Eva <i>et al.</i>	63

Ceramic coatings for containment of aluminium silicon metallic phase change material in thermal storage applications, Villada Carolina <i>et al.</i>	65
Characterization of coated silica sand by Mn diffusion into crystal cell., Cerutti-Cristaldo Leonel Mario <i>et al.</i>	67
Characterizing Na ₂ S kinetics for thermochemical energy storage applications through algorithmic optimization, Kieskamp Bram <i>et al.</i>	71
Comparative Simulations for the Verification of Simulation Models for Large Thermal Energy Storages, Schmidt Thomas <i>et al.</i>	75
Comparison between a conventional TES system and an EAF slag-based thermocline configuration for CSP plants using the LCA methodology., Majó Marc <i>et al.</i>	79
Compatibility of demolition wastes with solar salt for high temperature packed-bed thermal energy storage applications, Koçak Burcu <i>et al.</i>	84
Conceptual Development and Upscaling Considerations of a Radial Flow Packed Bed Thermal Energy Storage with Multiple Coaxial Particle Layers, Apostolopoulos - Kalkavouras Konstantinos <i>et al.</i>	87
Continuous synthesis of 9,10-dihydroxystearic acid from bio-based resources for sustainable PCM production, Escribà-Gelonch Marc <i>et al.</i>	92
Cool-Data: PCM cold storage development for server room cooling, Englmaier Gerald <i>et al.</i>	95
Corrosion control of a Fe-based alloy (DMV 310 N) in molten MgCl ₂ -KCl-NaCl for heat storage and transfer at very high temperatures, Ding Dr. Wenjin <i>et al.</i>	99
Corrosion test on nitrate salts for building heating applications, Palacios Anabel <i>et al.</i>	100
Critical review on the environmental assessment of xylitol as phase change material, Santos Humberto <i>et al.</i>	103
Degradation of Erythritol after ageing at elevated temperature and cycling under real application conditions, Klünder Franziska <i>et al.</i>	107
Demonstration of cold thermal energy storage for air conditioning in a CO ₂ supermarket refrigeration system, Selvnes Håkon <i>et al.</i>	111
Design and commissioning of the worldwide first nitrate molten salt test rig for component testing at 620°C, Klasing Freerk <i>et al.</i>	115
Design of borehole heat exchangers combined with a permanent dewatering system in series, Park Seung-Hoon <i>et al.</i>	118
Design, implementation and monitoring results from the 70,000 m ³ pit thermal energy storage (PTES) in Høje Taastrup, Copenhagen, Sørensen Per Alex <i>et al.</i>	122
Design Optimization of Synthetic Methane Production Sites Incorporating Direct Air Capture Technology, Humbert Gabriele <i>et al.</i>	126

Development and characterization of a new bio-sourced composite material based on phase change material and hemp shives, Toifane Hachmi <i>et al.</i>	130
Development and multiscale characterization of a sensible/sorption bimodal heat storage for cooling tower application, Arnaud Bruch <i>et al.</i>	134
Development and performance evaluation of a K ₂ CO ₃ -based closed-cycle sorption heat storage system, Jain Kartik <i>et al.</i>	138
Development of a lifetime assessment approach for polyolefinic insulation materials in pit thermal energy storages, Peham Lukas <i>et al.</i>	143
Development of ceramic protective coatings for solid-solid Phase Change Materials, Crocomo Paola <i>et al.</i>	147
Development of microencapsulated phase change material with Zn-10 mass% Al alloy core for heat utilization around 400 °C, Kawaguchi Takahiro <i>et al.</i>	151
Electrical tortuosities of honeycomb and triply periodic minimal surface (TPMS)-based porous structures for Power-to-Heat applications, Ott Thorsten <i>et al.</i>	153
Electrified cascade PCM concept for Thermal Energy Storage in a CSP plant, Lopez-Roman Anton <i>et al.</i>	155
Energy Storage Systems and Renewable Integration: Pathways to Carbon Neutral Buildings, Han Gwangwoo <i>et al.</i>	159
Enhance the productivity of solar still by using combined reflectors and latent thermal energy storage, Al-Saaidi Hussein Alawai Ibrahim <i>et al.</i>	163
Enhancing energy flexibility in buildings: A design-phase approach to couple Latent Heat Thermal Energy Storage (LHTES) and Heat Pumps, Perino Marco <i>et al.</i>	167
Enhancing grid integration of renewable energy with seasonal thermal energy storage using molten salt tanks, Prieto Cristina <i>et al.</i>	171
Erosion of a tube immersed in a bubbling fluidized bed at high temperature: a numerical study, Domínguez-Coy Pedro <i>et al.</i>	175
Evaluation of the life cycle energy and greenhouse gas emissions of a space heating systems using ettringite as an adsorbent material, Bonnin Salomé <i>et al.</i>	179
Evaluation of thermal energy storage performance of composite binary salt hydrates with MgCl ₂ /2CaCl ₂ in a packed bed reactor, Liu Hongzhi <i>et al.</i>	183
Evaluation of volcanic ash as TES material: Case of study of a CSP plant, Barreneche Camila <i>et al.</i>	187
Experimental analysis of partial charge and discharge operation of a Latent Heat Thermal Energy Storage device, Safaee Raman <i>et al.</i>	192
Experimental assessment of inorganic salts impregnated silica gel matrix for thermal energy storage applications., Fotia Antonio <i>et al.</i>	196

Experimental characterisation and numerical modelling of a novel heat exchanger for latent heat thermal energy storage composed with open-cells metallic lattice structure cast around tubes, Vesin Sébastien <i>et al.</i>	201
Experimental Characterization of a High-Temperature Thermal Energy Storage System Based on Nitrate Salt as Phase-Change-Material for Steam Generation, Fluri Thomas <i>et al.</i>	205
Experimental Evaluation of a Phase-change Thermal Storage, Harrison Stephen <i>et al.</i>	209
Experimental Study of a Bench Scale Packed-bed Latent Heat Storage Unit with Al-Si based PCM pellets, Nakamura Tomokazu <i>et al.</i>	213
Experimental Study of Thermochemical Heat Storage with Zeolite 13X for Utilization of Industrial Wasted Heat, Hong Sungkook <i>et al.</i>	216
Experimental Study on Thermal Storage System with Sand and Al-Si Alloy for Coal-fired Plant Retrofit Carnot Battery, Junhyun Cho <i>et al.</i>	219
Experimental investigation of a façade-integrated adsorption system for solar cooling, Boeckmann Olaf <i>et al.</i>	222
Experimental study of heat transfer enhancement in a latent heat thermal energy storage using metal wool, Ribezzo Alessandro <i>et al.</i>	224
From Heat Storage to Heat Sink: The Role of Phase Change Materials in Battery Thermal Management, Balwani Apoorva <i>et al.</i>	228
Genetic Algorithm Based Optimization of a closed sorption heat storage system using COMSOL Multiphysics and MATLAB, Abohamzeh Elham <i>et al.</i>	231
GeoBOOST: Pioneering Efficient Geothermal Solutions through Barrier Mitigation in Europe, Witte Henk	235
GIS-Based GSHP Sizing and Estimation Tool: Facilitating Non-Expert User Engagement and Technology Dissemination, Badenes Borja <i>et al.</i>	239
Graphite Based Encapsulation Concept for a High Temperature Metallic Latent Thermal Energy Storage System, Badenes Borja <i>et al.</i>	243
High Temperature PCMs for industrial steam systems, Zondag Herbert <i>et al.</i>	247
High Temperature Thermal Energy Storage with Phase Change Materials in Concentrated Solar Power System: A Case Study, Shan Lianying <i>et al.</i>	251
Highly Accurate Simulation of the Flow Effects during Loading with Swirl, Oestreich Felix <i>et al.</i>	256
Improved Thermophysical and Mechanical Properties in LiNaSO ₄ Composites for Thermal Energy Storage, Taeño Maria <i>et al.</i>	260
Impact of thermocouple position on the supercooling of distilled water, Rabbi Jawad <i>et al.</i>	265

Impact of Using Different Phase Change Materials on a PCM-HX's Performance, Callaghan Ryan L. <i>et al.</i>	269
Influence of host matrices on the thermochemical energy storage capacity of novel organic salt hydrate, Previti Emanuele <i>et al.</i>	273
Influence of operating conditions on the melting front movement in tube-in-tube latent thermal energy storage heat exchangers, Van Zele Julie <i>et al.</i>	277
Innovative transient modelling of concrete-based solid medium for thermal energy storage systems, Tagle-Salazar Pablo D. <i>et al.</i>	281
Integrated High Temperature Heat Pump and Thermal Energy Storage Laboratory Rig – Engineering Considerations and Preliminary Design, Sanclemente Lozano Mateo <i>et al.</i>	285
Interpretable Reinforcement Learning Control for Battery Storage in Grid-Interactive Communities, Takahashi Ken <i>et al.</i>	289
Inventory data generation for prospective lifecycle design thorough full-year simulation of Carnot Battery with Al-Si based PCM, Fujii Shoma <i>et al.</i>	294
Investigating the relation between the crystallisation velocity and the hysteresis of phase change materials with two polyethylene glycols, Hiebler Stefan <i>et al.</i>	298
Investigation of a thermochemical storage system for the use of solar energy in domestic applications, Niederkofler Tobias	302
Large Scale Testing of Refractory Bricks for Molten Salt Thermal Energy Storage, Odenthal Christian <i>et al.</i>	307
LargeTESmtk: A comprehensive modeling toolkit for large-scale thermal energy storage systems, Reisenbichler-Sommerhofer Michael <i>et al.</i>	311
Layered manganese dioxide as a versatile heat-storage material utilizing environmental water vapor, Okamoto Norihiko L. <i>et al.</i>	315
Lignin modified ecological coating as thermal barrier in container materials for sorption heat pumps., Amini Sara <i>et al.</i>	319
Liquid metals – efficient heat transfer fluids for high-temperature heat storage, Niedermeier Klarissa <i>et al.</i>	323
Long-term stability investigation of capric acid as potential phase change material, Ayaz Hamza <i>et al.</i>	326
Long term thermal function of the HT BTES plant at Xylem in Emmaboda, Sweden, Andersson Olof <i>et al.</i>	330
Malta's Pumped Heat Energy Storage Technology: a Clean Combined Heat and Power Plant, Hippler-Nettlau Janina <i>et al.</i>	334
Manufacturing Composites for High-Temperature Thermal Energy Storage applications From lab to pilot scale, Navarro Helena <i>et al.</i>	338

Mechanochemical synthesis of layered hybrid organic-inorganic perovskites for thermal energy storage materials, Salgado-Pizarro Rebeca <i>et al.</i>	342
Membrane-Encapsulated Salt Hydrate: An Anti-agglomeration Approach to Enhance Cyclability, Elahi Behrooz	345
Metallic phase change material (PCM) for high temperature applications, selection, synthesis and characterisation., Williamson Kyran <i>et al.</i>	350
Methodology for integrating renewable energy and thermal storage systems in the electricity market, Pavón-Moreno M.carmen <i>et al.</i>	354
Modeling multi-basin water-gravel thermal energy storages with STORE, Bott Christoph <i>et al.</i>	358
Modelling of heat and moisture transfer through the lid of Pit Thermal Energy Storages, Brand Tom <i>et al.</i>	362
Modelling of thermal storage systems using artificial intelligence, Rojas Cala Edgar Felipe <i>et al.</i>	366
Molecular Dynamics Simulation of the Polyvinyl Alcohol Template Effect in n-Octadecane Phase Change Slurry Crystallization, Kick Moritz <i>et al.</i>	370
Monitoring results of energy-efficient demonstration buildings with thermal activated building mass as energy storage, Rohringer Christoph <i>et al.</i>	374
Multi-scale experimental characterization and management of the supercooling of Isosorbide as Phase Change Material for thermal energy storage, Bruch Arnaud <i>et al.</i>	377
Nanofabrication of Multi-Shells Hollow CuO Microspheres for an Enhanced Cyclic Redox Reaction in High-Temperature Thermochemical Heat Storage Applications, Agalit Hassan <i>et al.</i>	381
Numerical analysis of an off-grid positive temperature cold room coupled with latent thermal energy storage for food preservation, Slaviero Gianluca <i>et al.</i>	385
Numerical and dynamic energy modeling for performance analysis of an integrated photovoltaic/thermal-heat pump system, Chae Soowon <i>et al.</i>	389
Numerical investigation about the electrical heating of a molten salt mixture for thermal energy storage applications, Cagnoli Mattia <i>et al.</i>	393
Numerical investigation of porous media layers for improved stratification within cold storage, Gamisch Sebastian <i>et al.</i>	397
Numerical modelling of a Pit Thermal Energy Storage used for performance guarantee., Fournier Nathan <i>et al.</i>	401
Numerical simulations for improvements of the experimental system for testing adsorption heat storage materials, Mlakar Urška <i>et al.</i>	405
Optimizing the size of a heat storage tank for a district heating system, Champel Bénédicte <i>et al.</i>	409

Performance enhancement of a Latent Heat Thermal Energy Storage for Domestic Hot Water production, Champel Bénédicte <i>et al.</i>	413
Performance of high-temperature thermochemical systems based on carbonates and mixed oxides in fluidized bed reactors., Liberatore Raffaele <i>et al.</i>	417
Phase change material integrated underground thermal energy storage in heating and cooling applications: A review, Dong Haoyang <i>et al.</i>	421
Prediction and experimental characterization of a peritectic mixture of sodium acetate trihydrate and sodium nitrate to be used as phase change material, Rathgeber Christoph <i>et al.</i>	425
Proposal of advanced electrochemical techniques for improved monitoring control in sorption materials for TES systems, Fernández Ángel G. <i>et al.</i>	429
Protic dialkylammonium-based ionic liquids as promising solid-solid phase change materials for thermal energy storage: synthesis and thermo-physical characterization, Lopez-Morales Jorge L. <i>et al.</i>	432
Recent advance on metal/alloy based micro-encapsulated phase change materials for middle-high temperature applications, Nomura Takahiro	437
Reduction of the Winter Gap Problem - Energy Efficiency vs. Energy Flexibility, Ochs Fabian <i>et al.</i>	440
Renewal planning method of air-conditioning heat source system with diurnal water thermal storage for demand response in an existing building, Imaida Mio <i>et al.</i>	444
Rheological study on xylitol crystallization by seeding and shearing for its use as PCM: Influence of shear rate, temperature and seed size, Navarro Miguel <i>et al.</i>	448
Selection of suitable inorganic materials to be applied as PCMs in high temperatures thermal energy storage system, Martinez Alcocer Franklin R. <i>et al.</i>	453
Selection of the storage system for industrial steam supply with heat pumps, Nefodov Dimitri <i>et al.</i>	457
Sensible/latent hybrid heat storage using molten nitrate and Al alloy-based phase-change material, Shimizu Yuto <i>et al.</i>	460
Small-scale field demonstration of zeolite based mobile thermochemical energy storage, Fujii Shoma <i>et al.</i>	463
Solar heating and cooling with latent heat storage for temporary shelters, Paksoy Halime <i>et al.</i>	467
Solid-Solid Phase Change Materials for the Thermal Management of Li-Ion Batteries, Saad Ali <i>et al.</i>	471
Solidification enhancement by changing fin structures using Straight and Y-shaped fins for M-TES applications, Demirkiran İsmail <i>et al.</i>	474
Specific heat capacity variability analysis of Chilean copper slag for packed-bed thermal energy storage applications, Segovia Valentina <i>et al.</i>	478

Stability Evaluation of Cation-exchanged Zeolites through Repeated Experiment of Heat Charging and Discharging, Seongeun Kim <i>et al.</i>	482
Stability test of three different phase change material emulsions, Gschwander Stefan	485
Study of solid-state transition kinetics of supercooled neopentyl glycol by infrared thermography, Dauvergne Jean Luc <i>et al.</i>	489
Study on Estimation of Time-Specific CO ₂ Emission Factors and New Operation of Thermal Energy Storage System., Yamanashi Haruki <i>et al.</i>	493
Supercooling suppression of Al-Si phase change material for efficient thermal energy storage and practical applications, Mba Joshua Chidiebere <i>et al.</i>	497
Surface engineering for TES application enhancement., Betancor Lorena <i>et al.</i>	500
Swedish State-of-the-Art on Ground-source De-Icing and Snow Melting Systems, Gehlin Signhild <i>et al.</i>	504
Synergistic Approaches to Modulate Transition Temperatures in Enhanced Organic Plastic Crystals, Serrano Ángel <i>et al.</i>	508
Synergistic effect of textile-reinforced mortar and phase change materials in buildings, Ayed Rabeb <i>et al.</i>	511
System and Component Model Development of a Secondary Loop System with Buried Thermal Energy Storage Tank, Moghimi Pouria <i>et al.</i>	515
Test rig for investigating the optimisation of operating strategies for steam supply with passive Latent Heat – Thermal Energy Storages, Dietz Larissa <i>et al.</i>	519
Testing and Analysis of a Dual-Tube Latent Heat Storage System, Moghimi Pouria <i>et al.</i>	522
The IN-Campus: A lighthouse site for re-used infrastructures as seasonal thermal energy storage, Bott Christoph <i>et al.</i>	526
Thermal discharge performance of a composite foam in an indirect fixed-bed reactor for thermochemical energy storage, Funayama Shigehiko <i>et al.</i>	530
Thermal Energy Storage as a Service Business Model for Food Supply Chain Decarbonisation, Wang Xinfang	532
Thermal energy storage in energy communities: a perspective overview through a bibliometric analysis, Brunelli Luca <i>et al.</i>	534
Thermal Energy Storage with Molten Salts: Predictive Models for thermo-physical properties., Liberatore Raffaele <i>et al.</i>	538
Thermal modelling of the discharge of a 180kW.h latent thermal energy storage demonstrator, Da Col Amandine <i>et al.</i>	542
Thermal response of layered hybrid organic-inorganic perovskites as solid-solid phase change materials, Salgado-Pizarro Rebeca <i>et al.</i>	547

Thermo-mechanical assessment of steels under service conditions in hot tanks used in CPS., Ardila Sergio <i>et al.</i>	551
Thermochemical energy storage in a CSA-based cementitious material, Beaupere Noé <i>et al.</i>	554
Thermochemical energy storage properties of $\text{Ca}_2\text{AlMnO}_5+\delta$, Tanahashi Keita <i>et al.</i>	559
Thermocline thermal storage material based on reclaimed and low-cost materials., Devise Charles <i>et al.</i>	563
Thermochemical Energy Storage Unit for H ₂ Based Systems, Bürger Inga	567
Understanding and overcoming the challenges for the integration of large-scale Thermal Energy Storage, Tosatto Alice <i>et al.</i>	569
Unexplored synthetic approaches for CaCl_2 impregnation for thermal energy storage, Fotia Antonio <i>et al.</i>	573
Unlocking feasibility: Role of insulation distribution in large-scale seasonal thermal energy storage applications, Dahash Abdulrahman	577
Use of bibliometric analysis to evaluate the influence of cement and concrete on carbon capture, utilization, and storage over the years, Santini Carolina <i>et al.</i>	582
Use of plastic waste to formulate new microencapsulated phase change materials (MPCM) with thermal, mechanical and chemical resistance, Giro-Paloma Jessica <i>et al.</i>	586
Utilization of UTES with solar energy in de-icing and snow melting - IEA ES TASK 38, Adl-Zarrabi Bijan <i>et al.</i>	590
Author Index	594



4-Dimensional monitoring of the temperature and energy performance of borehole heat exchanger systems: the Hoogezand pilot (Groningen, Netherlands)

Henk Witte¹, Daniel Bakker^{1*}, Manos Pefkos², Pieter Doornenbal², Henk Kooi²
1 Groenholland Geo-Energysystems BV, Valscherkade 26B, 1059CD Amsterdam, Netherlands
2 Deltares, Daltonlaan 600, 3584 BK Utrecht, the Netherlands

*Corresponding author e-mail: daniel.bakker@groenholland.nl

Keywords: borehole heat exchangers, building energy use, monitoring, distributed temperature sensing, flow modelling

Introduction

The OPTIGBES project aims to optimize design and operation of closed-loop ground source energy systems through detailed monitoring of the systems temperatures, heating and cooling demands on the user and source side coupled with detailed monitoring of the borehole heat exchanger temperature response with Distributed Temperature Sensing (DTS). A unique feature of the project is that the DTS is not only installed in the borehole heat exchangers, but also in additional observation wells at different (small) distances from the boreholes.

Goals of the project are to: 1) assess the heat flow and temperature response of the ground 2) validate and improve current state-of-art design methods; 3) obtain a better understanding of the energy profile data (and variations therein) used for the design; 4) assess the use of design methods based on collective borehole heat exchangers for fields of individual systems and 5) analyse and optimize the operation of the ground source heat pump systems in-situ.

Methodology

The Hoogezand pilot project is an apartment building of 45 apartments, each apartment has an individual heat pump and is connected to an individual borehole heat exchanger (BHE). The BHE (See Table 1 for info on construction parameters) field was drilled in parking areas next to the building. Three borehole heat exchangers were selected for detailed monitoring (See Figure 2¹). Around these BHE additional boreholes were drilled (to different depths, depending on distance to the BHE) as observation points.



Figure 1: The Hoogezand pilot site apartment building, borehole heat exchanger field area in the foreground. (Location of Hoogezand within Netherlands indicated on map).

To monitor the temperature evolution in time and space, a distributed temperature sensing (DTS) system based on fibre-optic (FO) temperature monitoring was installed in the selected boreholes. In these BHE both up- and downgoing pipes are monitored. The FO-cables are taped to the outside of the exchanger tubes. For the observation boreholes the fibre optic cables were lowered in, after which the boreholes were backfilled with grout

The site subsurface was characterized in detail by performing a Type II thermal response test (Witte et al 2002, van Gelder et al 1999), geophysical logging of the boreholes and deviation measurements to measure the deviation from the vertical for the monitored BHE.

¹ Note: one borehole could not achieve the intended end-depth, therefore a second borehole was drilled (35a and b, see Figure 2)

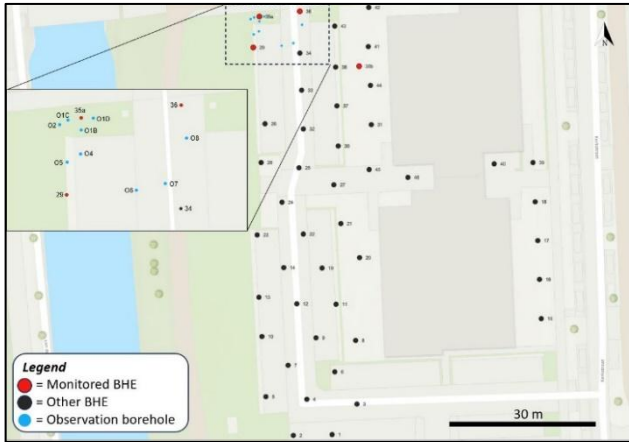
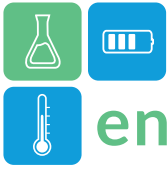


Figure 2. Borehole heat exchanger and observation points field topology.

Borehole depth (m)	130
Borehole diameter (m)	0.168
Backfilling thermal conductivity (W/mK)	2.0
U-pipe outer diameter (m)	0.032
U-pipe inner diameter (m)	0.026
Pipe hart-to-hart distance (m)	0.07

Table 1. Borehole heat exchanger construction parameters.

The heat pump, provided by the project partner Nathan Projects, is the Alpha-Innotec WZSV 62H3 (Table 2).

Parameter	Min	max
Heating capacity (kW) B0W35	1.25	5.95
COP B0W35 (EN 14511)	4.86	
Heating capacity (kW) B0W55	1.0	5.17
COP B0W55 (EN 14511)	3.13	
Passive cooling (kW)		5.8
Flow rate heat source (l/hr)	1450	
Flow rate user (l/hr)	1050	

Table 2. Heat pump (Alpha Innotec HP WZSV 62H3) data.

Data collection and analysis apartment data

In the three apartments selected calibrated energy meters (Kamstrup Multical 403) were installed in the source side, user side and domestic hot water circuit. Also, two electrical kWh meters were installed in the heat pump (one for the pumps and auxiliary power, one for the compressor). Data is collected in a purpose built low-cost (BeagleBone™) computer that collects data from the meters and from the installed heat pump using the Modbus protocol. Data is stored on a local SD card and automatically uploaded to a data-server daily.

Data processing is implemented in Python using Pandas. The daily datafiles are filtered for missing observations and other potential errors and, depending

on the parameter of interest, sums (energy) or averages (temperature) are calculated for selected time intervals (hourly/daily or monthly).

Data collection and analysis DTS data

DTS-measured temperature in all boreholes was calibrated, to obtain the true temperature profile in each channel. Using PT100 temperature transducers which are placed, together with the FO cables, in constant-temperature warm and ambient-temperature cold baths at the surface, the calibration process corrects for optical loss with distance in the FO cables. Each DTS channel covers multiple boreholes, location in the three dimensional space is obtained from the distance on the FO. The up- and down-going FO cable directions of the observation wells were averaged. The clocks of the DTS and apartment data were synchronized. Unfortunately, there is a mismatch between the boreholes with DTS and the apartments with energy-meter monitoring. A broader monitoring dataset of the heat pump management system was therefore studied. Only one apartment could be matched to a FO-monitored BHE (nr 29) by comparing the DTS data with the apartment monitoring data for several heating and cooling requests. For this match, various graphical representations are made to study the relationship between heat pump - DTS response, and the apartment sided fluid temperatures in the tubing.

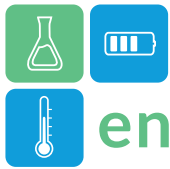
3D Feflow modelling is performed on two different timescales: 1. Short term responses in fluid temperatures and borehole wall temperatures using isolated requests for the matched BHE29 to evaluate the lowest BHE-fluid temperatures to be expected during a design peak heating demand. 2. Long term temperature responses at the observation points when accounting for all monitored BHE.

Results

Site characterisation

Based on stratigraphic data from the national database, the estimated soil thermal conductivity of the profile up to a depth of 140 meters was 2,27 W/mK. The TRT results on the three boreholes show a significantly higher soil thermal conductivity ranging between 2.83 and 3.43 W/mK and a borehole thermal resistance between 0.08 and 0.12 K/(W/m). The high thermal conductivity may indicate that the sandy deposits have been over-compacted due to glacial cover during the Saale glacial cycle.

Apartment monitoring and design evaluation



After an initial testing phase data collection started 15/7/2021. For the purpose of this paper the data period considered is two years, from 1/1/2022 to 31/12/2023.

Figure 3 shows the design heating, domestic hot water and cooling loads as well as the measured values for the three apartments. In this extended abstract only summary data are presented.

Design load calculations are usually based on calculation of heat-loss (thermal capacity required) for a specific (conservative) climate year combined with empirically derived full-load hours of the heat pump. Original design loads were 3780 kWh space heating, 1030 kWh domestic hot water production and 1310 kWh space cooling. Measured total energy for the three apartments for 2022 and 2023 are presented in figure 3.

Overall yearly seasonal efficiencies for total heating (space heating and domestic hot water) range between 4.7 and 4.9. Cooling is supplied as passive cooling with an SPF of 15 or higher.

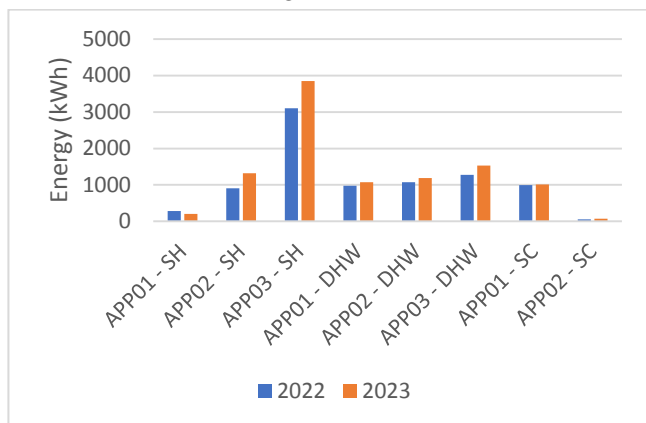


Figure 3. Measured space heating (SH), domestic hot water (DHW) and cooling(SC) energy for three apartments 2022 and 2023. All energy values in kWh.

Space heating energy show a very high variation between the three apartments. Difference between lowest and highest value is 2815 kWh in 2022 and 3646 kWh in 2023. The apartment with the highest load is located on the top floor, whereas Apartment 1 and 2 are located more centrally. Not only does this affect insulation but also the neighbouring apartments are already heated and limit the heat demand. Domestic hot water demand is more equally distributed.

DTS monitoring, modelling

Figure 4 provides an example of the DTS response in BHE29 for a cooling demand. The borehole warming is apparent from the measurements. Temperatures

remain low relative to the fluid temperatures inside the tube of the BHE (highest temperatures correspond to where the FO-cable is taped to the tube). DTS temperatures do not approach the apartment's outlet temperatures during the request, and they remain closer to the background temperature. There seems to be a large gradient over the tube wall, which decreases longer into the loading event. Figure 5 shows the long-term (2.5 year) temperature development averaged over 20-130 m depth for observation wells (a) and monitored BHE (b). A clear net ground cooling trend can be seen at the observation points between the BHE. For the BHE themselves this trend not (yet) as distinct within this period.

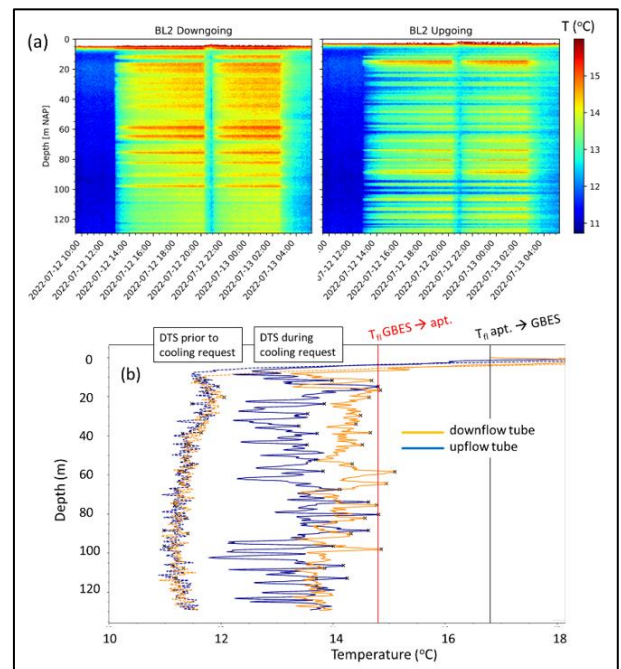


Figure 4. Example of the DTS-response to cooling demand on BHE29. (a) T-depth-time plots for the downflow and upflow legs of the BHE. (b) T-depth response at 2022-07-12 19:05. x-symbols indicate where the FO-cable is taped to the tube. The apartment-side fluid temperatures to and from the BHE are shown. The 'background' DTS temperatures prior the cooling demand are shown for reference.

Figure 6 shows an example of modelled temperature response around the monitored BHE using Feflow. Figure 7 shows a comparison across the entire monitoring period of the temperatures for the deeper observation wells, between the DTS data and the modelled temperatures from that Feflow scenario. This scenario only regards the influence of the monitored boreholes on the observation wells. From Figure 7 it is clear that the measured DTS temperatures are much lower than what the prediction if the Feflow scenario with only the 4 monitored BHE.

Conclusions

This paper shows the first results of a detailed monitoring system installed in and between several borehole heat exchangers. In spite of a number of problems with the monitoring system, specifically the fact that the monitoring boreholes were not correctly connected to the apartments that are monitored, several conclusions can be drawn:

- There is a large variation in heating, cooling and DHW demand between the different apartments. Partly this can be explained by the relative location of the apartment in the building (number of outside walls and number of neighbouring apartments).

- There is a net cooling trend visible in the temperature development of the deep observation wells. This is indicative of net overall heat extraction and may partly be explained by thermal interactions due to other (not monitored) boreholes.
- Unmonitored boreholes further away from the observation wells also contribute to temperature decrease at observation wells.
- A portion of the other BHE in the rest of the field may contribute significantly to the temperature decreases measured at the observation wells

Figure 6. 2D slice across Feflow model containing all monitored BHE and observation wells. .

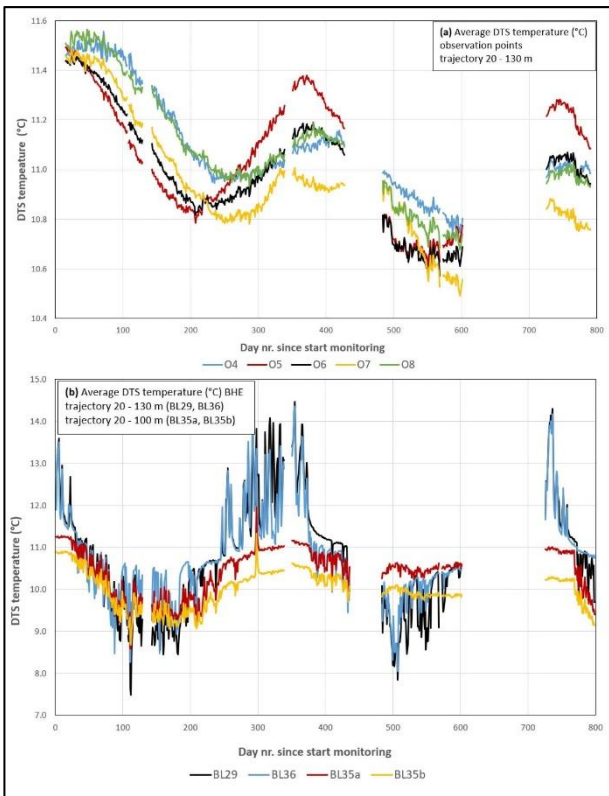


Figure 54. Long-term development of temperatures as measured with DTS for (a) deep observation wells. (b) monitored BHE.

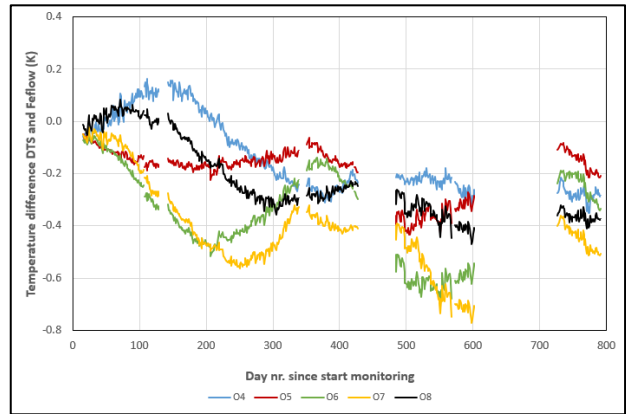


Figure 7. Difference in long-term temperature development between results from Feflow and the collected DTS measurements.

Further analysis will be carried out to evaluate the implications for design of borehole heat exchanger systems based on the measured energy demand and recorded borehole fluid flow and return temperatures.

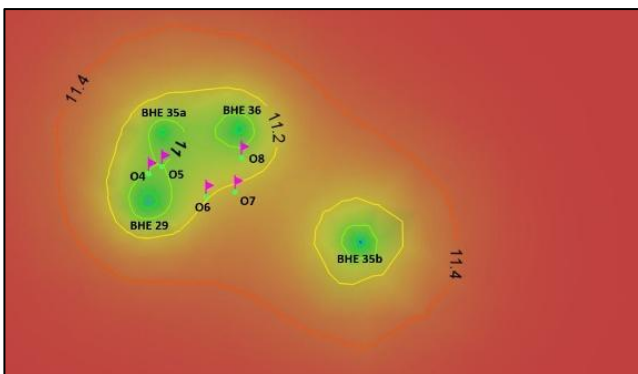
Temperature development in the ground, including thermal effects on the surrounding monitoring boreholes, will be carried out by numerical modelling where the matched apartment data is used for validation. Inverse modelling of the other borehole heat exchangers (matching load to temperature response) will be used to subsequently study the temperature effect on the surrounding boreholes. In spite of the shortcomings of the monitoring system this will allow evaluation of thermal interactions between neighbouring borehole heat exchanger systems.

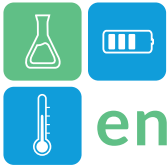
Acknowledgements

This study has been financially supported by the Netherlands Enterprise Agency (RVO), project TEUE219012 and Branchevereniging Bodemenergie.

References

Van Gelder, A.J., Witte, H.J.L., Kalma, S., Snijders, A. and R.G.A. Wennekes 1999. In-situ Messungen

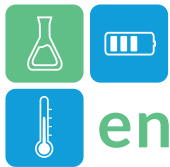




ENERSTOCK 2024
The 16th IEA ES TCP International Conference on Energy Storage
June 5–7, 2024
Lyon, France

der thermische Eigenschaften des Untergrunds durch Wärmeentzug. IN: T. Hitziger (Ed): OPET Seminar "Erdgekoppelte Wärmepumpen zum heizen und Klimatisieren von Gebäuden. 109 pp.

Witte, H.J.L., A.J. van Gelder, J.D. Spitler. 2002. In Situ Measurement of Ground Thermal Conductivity: The Dutch Perspective. ASHRAE Transactions, Vol. 108., No. 1.



A critical Outlook to commercial high-temperature Thermal Energy Storage

Anabel Palacios¹, Sebastian Amman^{1*}, Ludger Fischer, Jörg Worlitschek

¹ Lucerne School of Engineering and Architecture, Technikumstrasse 21, 6048 Horw, Switzerland

*Corresponding author: sebastian.ammann@hslu.ch

Abstract

This work presents a critical review on the commercially available high temperature thermal energy storage technologies. The demand for renewable energy is growing as the focus on decarbonisation of industry increases. However, renewables do not provide a constant supply of energy. Thermal Energy Storage (TES) is therefore needed to smooth out peaks in renewable energy production and to balance day and night and seasonal fluctuations. TES is a growing market, expected to reach 8 billion by 2030. The market currently offers several options for high-temperature energy storage, most of which use low-cost storage media such as stones, rocks, metals or bricks. This paper evaluates and compares different methods for high-temperature TES using Key Performance Indicators (KPIs).

Keywords: High temperature, commercial, industrial, TES, sensible.

Introduction

In striving for an energy future that is both sustainable and resilient, the role of effective energy storage methods has become increasingly evident over recent years. Thermal Energy Storage (TES) in particular, as it provides a flexible approach to overcoming the associated challenges with the fluctuating supply of renewable energy sources and the growing need for power systems.

Over the past decade, one of the main focuses has been the implementation of TES systems in industrial processes to reduce dependence on fossil fuels e.g. natural gas, oil, etc. Steel, cement, and chemicals are the top three emitting industries and are among the most difficult to decarbonize due to the need of continuous energy input at high temperatures and include economic factors such as low profit margins, capital intensity, etc.

The thermal energy storage market offers various options to decarbonise intensive energy industries, providing modular and stacked storage options from 300-1'500°C. This paper provides an overview of the main players in the high-temperature TES market by analysing and comparing the technology attributes.

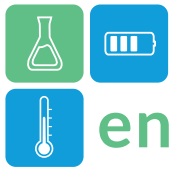
Market overview of high temperature TES systems

The Thermal Energy Storage market has experienced significant growth and evolution in recent years. The global thermal energy storage market was estimated at 4.4 billion U.S. dollars in 2022. It was forecast to grow at a compound annual growth rate (CAGR) of 7.2 per cent until 2030, reaching eight billion dollars that year (Statista TES market n.d.).

One approach to TES at high-temperature involves a molten salt system. The liquid salt retains thermal energy ranging from 250°C to 560°C. This system typically requires dual-tank arrangement, with one tank serving as the cold storage and the other as the hot storage. The molten salt circulates between these tanks during charging and discharging.

Alternatively, commercial solid-state storage media are readily available, environmentally friendly, and functional across a broader spectrum of temperatures compared to their liquid counterparts. These materials exhibit superior thermal stability, allowing operational temperatures to exceed 1'000°C. Additionally, the absence of fluid leakage and corrosion concerns potentially reduces both material and maintenance expenses, compared to liquid-based storage solutions.

TES systems are differentiated based on the use of an additional heat transfer fluid (HTF). In systems that do not use a HTF for charging, electrical heaters are integrated directly into the storage material, facilitating



heat transfer via conduction and radiation. In contrast, in systems with a HTF, air or steam is heated by electrical heaters through convection, circulated through the storage material, and then recirculated through both the heaters and the TES.

Commercial TES options were pinpointed through online and literature reviews. Table 1 lists all the companies that were evaluated. The options can be classified into solid-state storage and molten salts.

Critical outlook

This section compares the key KPIs that can be found in each technology's specification sheet or on the suppliers' websites. Only the solid-state options are considered in Figure 1 only considers solid-state option as solely they offer a modular approach; all the molten salt options are implemented in a two-tank configuration, one cold and one hot (Stekli, Irwin, and Pitchumani 2013), which can be constructed and designed to meet the charge/discharge profiles. Of these, Abengoa and HYME are the most promising as Abengoa is a mature company in the renewable energy market and HYME offers an option that overcomes the current limitations of molten salt technologies. HYME's technology is based on the fact that its storage

media (sodium hydroxide) can reach higher temperatures than ordinary solar salt (Jonemann 2013).

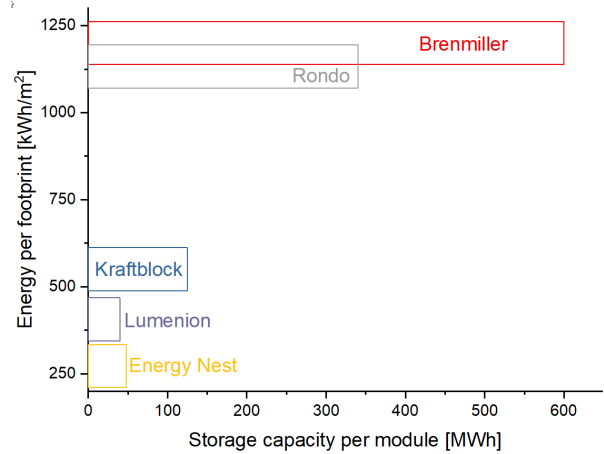
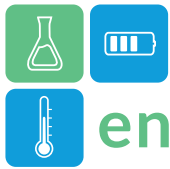


Figure 1. Energy per Footprint vs. Storage capacity per module of the different solid-state TES

The stored energy per area of a system is primarily determined by the maximum height. Brenmiller's B-cells can be stacked up to 25m, providing the highest energy per footprint and the highest storage capacity per module. Rondo also achieves high energy per footprint due to the height of 10m. Rondo offers two different storage sizes, the RHB100 with a storage capacity of 130MWh and the RHB300 with a storage capacity of 340MWh. The difference between

Table 2. Summary of TES technology providers, all data has been collected from their official websites.

Company	Storage Media	HFT	Temperature	Biggest installation
Antora	Solid state (Carbon blocks)	Without HTF	Up to 1'500°C	30 MWh
Rondo	Solid state (concrete bricks)	With HTF (air)	Up to 1'200°C	2 MWh
Abengoa	Liquid (Molten salt)	Without additional HTF (Molten salt)	Up to 400°C	1.9 GWh (Cerro Dominador)
HYME	Liquid (Molten salt)	Without additional HTF (Molten salt)	Up to 900°C	1 MWh
Brenmiller	Solid state (Vulcanic rocks blocks)	Without HTF.	Up to 750°C	24 MWh
Kraftblock	Solid state (Own oxide formulation)	With HTF (air).	Up to 1'500°C	70 MWh
Polar night	Solid state (Sand)	With HTF (air)	Up to 600°C	8 MWh
Magaldi	Solid state (fluidized sand)	With HTF (air).	Up to 400°C	N/A
Siemens Gamesa	Solid state (Vulcanic rocks blocks)	With HTF (air).	Up to 1000°C	130 MWh
MAN Energy	Liquid (Molten salts)	Molten salts as HTF	Up to 500°C	N/A
Energy Nest	Solid state (concrete blocks)	Without HTF.	Up to 400°C	6 GWh
Lumenion	Solid state (steel elements)	With HTF (air).	Up to 600°C	20 MWh



Kraftblock, Lumenion and Energy Nest lies in the different temperature levels, which can be seen more clearly in Figure 2.

The comparison of the operational temperature range and the energy storage density shows a direct correlation, as all storage materials have a similar specific heat capacity. The two molten salt storages (Abengoa and HYME), together with energy Nest and Lumenion, have a maximal temperature range of 450°C to 650°C and therefore the lowest energy density (Fig. 2). Brenmiller, with its slightly higher maximal temperature, also has a slightly higher energy storage density. Kraftblock and Rondo, with a maximal temperature of 1'500°C, have the highest energy storage density (Fig. 2).

There were significant differences among the different

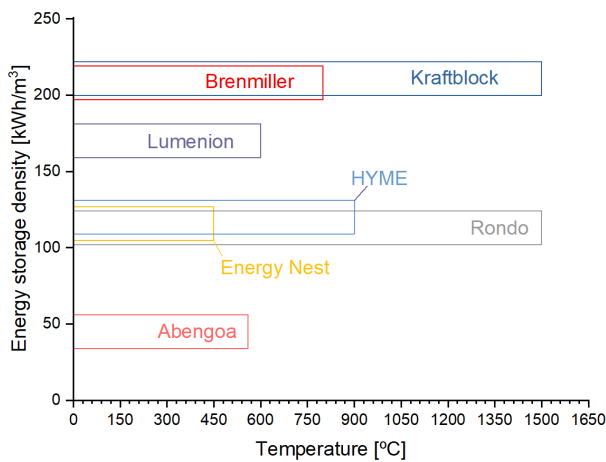


Figure 2: Energy storage density vs Operational temperature.

systems/technologies. The energy storage density as well as the energy per footprint were calculated solely for the storage, all auxiliary installations such as blowers, pumps, steam boilers, pipes and electric cabinets were not considered.

These auxiliary installations differ depending on the specific project and whether the storage is charged with electricity or heat, and if the discharged heat is used as steam or directly as hot gas.

Conclusions

Sensible heat storage is the most mature TES technology and has been used since ancient times to store heat for domestic use. Inexpensive and accessible storage media such as stones, rocks or bricks have been developed achieving relatively compact units with high efficiencies (97%) and storage capabilities up to 600 MWh per module. Although there have been significant improvements in the field of system design and operation, a lack of progress has been reported in enhancing materials that are commercially adopted in the TES provider's systems.

References

- Jonemann, Matthieu. 2013. "Advanced Thermal Storage System with Novel Molten Salt." *Contract* (May). <http://www.nrel.gov/docs/fy13osti/58595.pdf>.
- "Statista TES Market." <https://www.statista.com/statistics/1304464/global-thermal-energy-storage-market-value/>.
- Stekli, Joseph, Levi Irwin, and Ranga Pitchumani. 2013. "Technical Challenges and Opportunities for Concentrating Solar Power With Thermal Energy Storage." *Journal of Thermal Science and Engineering Applications* 5(2): 021011.



A novel process for the generation of ice slurry based on a dispersible two-substance system

Manuel Matthes, Jonathan Rausendorf, Markus Richter, Thorsten Urbaneck*
Chemnitz University of Technology, Professorship of Applied Thermodynamics,
Reichenhainer Str. 70, 09126 Chemnitz, Germany

*Corresponding author e-mail: thorsten.urbaneck@mb.tu-chemnitz.de

Abstract

A novel process for the generation of ice slurry based on a dispersible two-substance system of water (cold carrier) and a gas/gas mixture (refrigerant, e.g. carbon dioxide) has been developed (Urbaneck and Richter, 2022a). The process is based on the combination of the two substances under high pressure and subsequent expansion. Depending on the process conditions, various refrigeration effects can occur and be used for ice slurry generation. The article describes the closed process and the basic design of the system.

Keywords: Ice Slurry, Slush Ice, Generation, Dispersion, Storage, Natural Refrigerant

Introduction

The energy transition and climate policy goals require the optimisation of existing techniques and the development of new processes. This also applies to refrigeration and cold storage. Ice slurry is an environmentally friendly and pumpable secondary refrigerant with high latent heat capacity. Various approaches to ice slurry production exist (Kauffeld, 2005; Rausendorf and Urbaneck, 2023). However, established methods have various drawbacks, such as wear on mechanically moving components, the need for a separate refrigeration machine, the use of disadvantageous refrigerants, inefficient operation of refrigeration machines, limited ice production rates, or scalability issues for very large cooling capacities.

As part of the *Forschungsplattform für Kälte- und Energietechnik KETEC* research project (Urbaneck et al., 2023) funded by the German Federal Ministry of Education and Research an approach to ice slurry production was developed in subproject 9 with the goal of overcoming the limitations of conventional systems. The novel method (Urbaneck and Richter, 2022a) based on a dispersible two-substance system aims to produce ice slurry continuously, on a scalable and efficient basis, using natural refrigerants or coolants. The theoretical approach is explained below.

Process Description

The basic approach of the method resp. methods by Urbaneck and Richter (2022a; 2022b) involves creating a dispersion of the refrigerant and a cold carrier at high pressure. The process does not

necessarily require the use of additives, so preferably pure water is used as the cold carrier. However, a combination with additives that lower the freezing point or promote phase transition is generally possible. Various gases, such as carbon dioxide (R744), are suitable as refrigerants. Subsequently, the dispersed substances (refrigerant and cold carrier) are expanded, and depending on the process parameters, various cooling effects can occur, leading to the production of ice, ice slurry, snow, cold water or a combination of these. This work considers only the closed process without the discharge of ice slurry from the system (Urbaneck and Richter, 2022a). An open process is also possible (Urbaneck and Richter, 2022b) and subject to separate publications. Furthermore, this article only deals with the production of ice slurry.

There are already various approaches to the production of ice slurry by the direct contact of an evaporating re-frigerant with water as the cold carrier¹, where the at high pressure liquified refrigerant is expanded into the cold carrier in a low-pressure vessel (Kauffeld, Kawaji and Egolf, 2005). To avoid the entrainment of the refrigerant into the ice slurry-consuming system and associated health or environmental risks, preferably insoluble refrigerants are used (ibid.). The pressure drop-induced

¹ The IIR Handbook on Ice Slurries by Kauffeld, Kawaji, and Egolf (2005) refers to works by Wobst and Vollmer (1999), Knodel and Costenero (1986), Hansen et al. (2001) and Chuard and Fortuin (1999) on this matter.

evaporation of the refrigerant can cause the injection nozzles to freeze in many cases. This adverse effect is described for example by Zhang et al. (2019), Wijesundera et al. (2004) and Hayder, Danook and Sultan (2020). Other approaches attempt to bypass this problem through additives in the cold carrier or flow mechanical adjustments to the refrigerant injection, see Wijesundera et al. (2004), Hayder, Danook and Sultan (2020), Zhang et al. (2019), Kiatsiriroat, Thalang and Dabbhasuta (2000), and Thongwik et al. (2008). The new method presented here differs, especially through the joint expansion of the refrigerant with the cold carrier, allowing ice formation in the flow process without the risk of freezing the refrigerant nozzle. Furthermore, the process parameters (e.g., pressure) can be varied and controlled over a wider range.

The simplest version of the closed process is shown in Figure 1. The method allows for various modifications and extensions. The cold carrier water (dark blue) and the gaseous and/or liquid refrigerant (green) are brought together and dispersed at high pressure in the so-called apparatus, where, depending on the thermodynamic conditions, flow characteristics, residence time and other factors, various contact or mixing effects may occur. The apparatus has properties of a nozzle and serves as the expansion device for the dispersion flow (turquoise). As a result of the pressure reduction, cooling occurs, leading to the formation of ice particles. The process utilizes the degassing of the dissolved refrigerant in water, the evaporation of the refrigerant, and the Joule-Thomson effect depending on the process parameters as cooling effects.

In addition to the mentioned cooling effects, the dissociation of gas hydrate particles can be used. Gas hydrates are an ice-like solid phase formed from water and certain gases generally at relatively low temperatures and high pressures², usually enclosing one gas molecule in a water molecule cage (Sloan and Koh, 2007). Due to their comparatively high enthalpy of fusion, gas hydrates represent a promising storage medium for refrigeration (Fournaison, Delahaye and

Chatti, 2004). In the presented method, however, the dissociation of gas hydrates represents a possible cooling effect. In this process, the apparatus must be adapted to generate gas hydrate particles and relax the material flow containing the solid phase.

The combined ice slurry-bearing material flow (light blue & green) then enters a vessel (loading), which serves as a storage for the ice slurry and in which the separation of the refrigerant from the cold carrier takes place. In contrast to other substance systems (e.g., oil-water [Gschwander, 2022]) a very good and technically simple separation of the refrigerant and the cold carrier can be achieved according to initial considerations. The gaseous refrigerant is extracted from the upper part of the storage and, if necessary, dried before being compressed and cooled flowing back into the apparatus.

The storage contains water without ice in the lower part due to the density differences between ice or ice slurry and water. A pump conveys the water from the lower storage area, achieving a significant increase in pressure.

In the discharge circuit, the ice slurry (light blue) is taken from the storage and directed to a heat exchanger. The release of cooling capacity (supply task) occurs through the melting of the ice particles and the warming of the substance flow. Alternatively, the return of the discharge circuit (dark blue) can also be directly fed into the cold carrier circuit and the loading pump (dotted line).

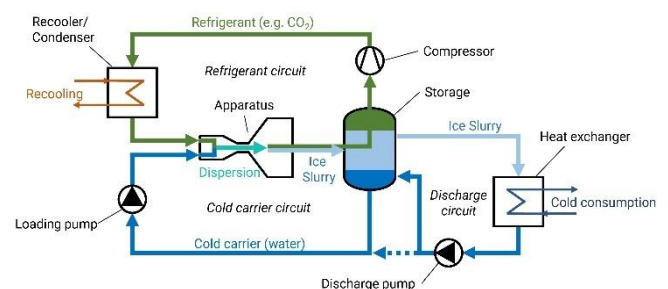
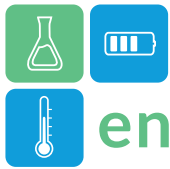


Figure 1: Schematic illustration of the closed process according to Urbaneck and Richter (2022a; 2022b).

The apparatus is the component of this process where ice formation occurs, presenting crucial differences and advantages compared to conventional ice slurry generation methods such as scraped surface, falling-film, super-cooling and vacuum techniques. The process exhibits characteristics of the injector technology, particularly the direct heat transfer between the cold carrier water and the refrigerant, as well as the convergence of both sub-stance flows in a nozzle-like component. However, a significant

² Generally, gas hydrates tend to be stable below ambient temperature and above atmospheric pressure; however, this is not a universally applicable statement. On the one hand, stability conditions vary significantly depending on the encapsulated gas. On the other hand, the hydrate formation temperature increases with increasing pressure and vice versa (Sloan and Koh, 2007).



difference lies in the fact that the ice-producing refrigeration effects occur due to a pressure reduction in the flow process of both substance streams together resp. the merged dispersion substance stream. In this way, ice formation takes place after the refrigerant outlet, preventing clogging of the refrigerant injector by ice. As mentioned earlier, the generation of ice particles is possible by utilising various refrigeration effects, and the apparatus must be designed according to the chosen process to achieve optimal ice particle formation in the flow. Depending on the refrigeration effects used, there is also the option to additionally heat or cool the interior walls of the component. The resulting non-equilibrium multiphase flow in the component and the structural design of the apparatus are the subject of current investigations. The concept of the apparatus and the presented process can, in principle, be scaled from the lower kilowatt to the megawatt range through appropriate dimensioning and, if necessary, parallelisation. The apparatus has no moving parts and is thus not subject to associated mechanical wear.

In the closed system, the storage vessel has at least the function of separating the gaseous refrigerant from the water, although heat transfer between gas bubbles and liquid may still occur. Depending on the application, in cases of discontinuous refrigeration demand, it also functions to store the ice slurry. Stirring devices and/or appropriately designed flow conditions prevent clumping of the ice, ensuring the maintenance of homogeneity and phase composition of the ice slurry (Kauffeld, Kawaji and Egolf, 2005). Additionally, the upper part of the storage vessel may contain a sufficiently large refrigerant gas reservoir, serving as a pressure maintenance system during non-operation or in case of a failure. This helps avoid the pressure increase issues known during system downtime, e.g. at R744 chillers (Sawalha, 2008).

The refrigerant circuit in the process involves at least a single or multi-stage compression of the refrigerant and an inter-/recooling, serving as the heat sink of the process. Due to the direct contact between the refrigerant and the cold carrier (water), the presence of moisture in the refrigerant circuit must be considered. On one hand, water droplets can be entrained in the gas stream, requiring the use of a droplet separator and possibly drying components to protect the compressor. On the other hand, many suitable refrigerants in the gas phase exhibit solubility of water. This can react with compressor oil, leading to damage of the system (Goswami et al., 1996;

Cartlidge and Schellhase, 2003). In such cases, oil-free compressors should be employed. Furthermore, it is essential to assess whether there is a risk of unintended gas hydrate formation due to moisture in the refrigerant. The refrigerant circuit, influenced significantly by compression, has a substantial impact on the overall efficiency of the process. Therefore, modifications and circuit extensions, especially in this aspect, offer opportunities for optimisation.

Vice versa, there might be a solubility of the refrigerant in water as well. In this case, particular attention must be paid to associated changes in water chemistry and unintended outgassing in the conduits due to pressure- and/or temperature-induced changes in solubility. The use of oil-lubricated pumps in the cold carrier/ discharge circuit must also be carefully examined for potential interactions between the lubricant and the working media.

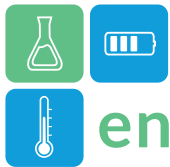
Summary and Outlook

The presented method by Urbaneck and Richter (2022a; 2022b) offers the possibility to produce ice, ice slurry, snow, cold water or a combination, with various advantages over conventional ice slurry production methods. Notably, the use of natural and pure substances allows compliance with the highest hygiene standards. The approach integrates the ice generator, refrigeration machine, and storage into one system, enabling highly efficient heat transfer through direct contact between the refrigerant and the cold carrier. Given numerous potential extensions and modifications, the process can be adapted to cooling needs in various applications. The scalability of the method allows for deployment in both small and large power ranges. The integrated storage allows for flexibility in refrigeration, addressing the requirements of the energy transition. As part of process optimisation, the use of waste heat from refrigerant compression is also a viable option.

A laboratory experiment with the refrigerant CO₂ confirmed the theoretical approach. The details of the experimental setup and results are presented in a separate work.

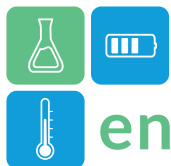
Acknowledgment

The underlying joint project is funded by the German Federal Ministry of Education and Research (BMBF) under the codes 03SF0623A/B/C, based on a decision by the German Bundestag. Project management is undertaken by the Project Management Jülich (PtJ).



References

- Cartlidge, D.; Schellhase, H. (2003): Using acid number as a leading indicator of refrigeration and air conditioning system performance. *Air-Conditioning and Refrigeration Technology Institute (US)*, 2003.
- Chuard, M.; Fortuin, J. P. (1999): COLDECO – A New Technology System for Production and Storage of Ice. *Proceedings of the First IIR Workshop on Ice Slurries, Yverdon-les-Bains, 1999, conference proceedings*, p. 140-146, as cited in Kauffeld, Kawaji and Egolf (2005).
- Fournaison, L.; Delahaye, A.; Chatti, I. (2004): CO₂ Hydrates in Refrigeration Processes. *Ind. Eng. Chem. Res.*, 43. Vol. (2004), p. 6521-6526.
- Goswami, D. Y.; Mathur, G. D.; Gupta, S.; Stoff, L.; Colacino, F. (1996): An experimental investigation of the effect of moisture on the performance of an air-conditioning system. In: *IECEC 96. Proceedings of the 31st Intersociety Energy Conversion Engineering Conference. IEEE*, 1996, p. 2021-2026.
- Gschwander, S. (2022), internal reference, Project Forschungsplattform für Kälte- und Energietechnik KETEC (04.02.2022).
- Hansen, T.; Kauffeld, M.; Sari, O.; Egolf, P. W.; Pasche, F. (2001): Research, Development and Applications of Ice Slurry in Europe. *Fourth IIR Work-shop on Ice Slurries, Osaka, 2001*, as cited in Kauffeld, Kawaji and Egolf (2005).
- Hayder, S. H.; Danook, S. H.; Sultan, H. S. (2020): Direct-Contact Evaporation Using Different Refrigerants: A Review. *Basrah Journal for Engineering Sciences*, 20. Vol. (2020) Nr. 2, p. 34-47.
- Kauffeld, M.; Kawaji, M.; Egolf, P. W. (2005): *Handbook on ice slurries: fundamentals and engineering*. Paris: International Institute of Refrigeration, 2005. — ISBN 2-913149-44-8
- Kiatsiriroat, T.; Thalang, K. N.; Dabhasuta, S. (2000): Ice Formation Around a Jet Stream of Refrigerant. *Energy Conversion & Management*, 41. Vol. (2000), p. 213-221.
- Knodel, B. D.; Costenero, J. A. (1986): Apparatus and Method of Ice Production by Direct Refrigerant Contact with Aqueous Liquid. US 4754610, patent application of 17.04.1986.
- Rausendorf, J.; Urbaneck, T. (2023): Herstellungsverfahren von Eisbrei - Stand der Technik und Forschung. *HLH Lüftung/Klima Heizung/Sanitär Gebäudetechnik VDI Fachmedien 74. Vol.* (2023) Issue 03 p. 56-60. – ISSN 1436-5103
- Sawalha, S. (2008): Safety of CO₂ in Large Refrigeration Systems. *Stockholm: Royal Institute of Technology*, 2008, p. 81-93.
- Sloan Jr, E. D.; Koh, C. A. (2007): *Clathrate hydrates of natural gases*. CRC press, 2007.
- Thongwik, S.; Vorayos, N.; Kiatsiriroat, T.; Nuntaphan, A. (2008): Thermal Analysis of Slurry Ice Production System Using Direct Contact Heat Transfer of Carbon Dioxide and Water Mixture. *International Communications in Heat and Mass Transfer*, 35. Vol. (2008), p. 756-761.
- Urbaneck, T.; Richter, M. (2022a): Verfahren und Anlage zur Erzeugung von Eis, Eisbrei/Eispartikeln, Schnee, Hydraten, Kaltwasser oder deren Kombinationen bzw. Mischung/Suspension in einem geschlossenen Prozess. DE102022134153.4, patent application of 20.12.2022; DE202022107104, utility model application of 20.12.2022, granted at 01.03.2023.
- Urbaneck, T.; Richter, M. (2022b): Verfahren zur Abkühlung mindestens eines Kältemittels und/oder mindestens eines Kälte-trägers in einem offenen Prozess. DE102022134154.2, patent application of 20.12.2022; DE202022107105, utility model application of 20.12.2022, granted at 08.03.2023.
- Urbaneck, T.; Richter, M.; Hempel, O.; Safarik, M.; Müller, M.; Henninger, S.; Schossig, P.; Henninger, H.-M. (2023): KETEC Forschungsplattform Kälte- und Energietechnik - Entwicklung, Ziele und fachliche Ausrichtung. *ki – Kälte-, Luft- und Klimatechnik Hüthig 58. Vol.* (2023) Issue 1-2, p. 38-41. – ISSN 1865-5432
- Wijesundera, N. E.; Hawlader, M. N. A.; Andy, C. W. B.; Hossain, M. K. (2004): Ice-slurry production using direct contact heat transfer. *International Journal of Refrigeration*, 27. Vol. (2004), Nr. 5, p. 511-519.
- Wobst, E.; Vollmer, D. (1999): Ice Slurry Generation by Direct Evaporating of Refrigerant. *Proceedings of the First IIR Workshop on Ice Slurries, Yverdon-les-Bains, 1999, conference proceeding*, p. 126-132, as cited in Kauffeld, Kawaji and Egolf (2005).
- Zhang, Y.; Su, L.; Dong, K.; Liu, T. (2019): Experimental study of ice slurry production system using direct contact heat transfer of RC318 and water in a horizontal pipe. *Energy Procedia*, 158. Vol. (2019) p. 4495-4501.



A novel synthesis and characterization of α -Fe₂O₃@Ppy photoanode for photoelectrochemical water splitting

Sedat Emir^{1,2}, Fatih Tezcan², Gülfeza Kardaş^{1*}, Halime Ömür Paksoy¹

¹Cukurova University, Faculty of Arts and Sciences, Chemistry Department, Adana, Turkey

²Tarsus University, Vocational School of Technical Sciences at Mersin Tarsus Organized Industrial Zone, Department of Chemistry and Chemical Process Technology, Mersin, Turkey

*Corresponding author e-mail: gulfeza@cu.edu.tr

Abstract

In this study, α -Fe₂O₃/Ppy photoanode is synthesized and applied to photoelectrochemical hydrogen production. α -Fe₂O₃ and Ppy are fabricated in powder form with hydrothermal deposition and chemical methods, respectively. The slurry form of α -Fe₂O₃ and α -Fe₂O₃/Ppy is conducted over the FTO by the doctor blade. The applied procedure enabled further loading of α -Fe₂O₃ and α -Fe₂O₃/Ppy on the substrate, promising advantage utmost photoresponse under solar light in water splitting. The photoelectrodes are characterized by scanning electron microscopy (SEM), X-ray diffraction (XRD), Raman spectroscopy, and UV-vis spectroscopy. The XRD pattern confirms the hexagonal crystal phase of α -Fe₂O₃, leading to further photocatalytic performance on photoelectrochemical hydrogen production. SEM images indicated that α -Fe₂O₃ morphology resembles nanorods and coatings of α -Fe₂O₃ and α -Fe₂O₃/Ppy on FTO substrates measuring about 125 mm and 250 mm, respectively. The linear sweep voltammetry (LSV) shows that the photocatalytic response of Fe₂O₃/Ppy is about 5-fold further (1.032 mA cm⁻²) compared to α -Fe₂O₃ (0.232 mA cm⁻²) at 1.229 V vs. Ag/AgCl.

Keywords: Hematite, Ppy, photoanode, doctor blade, water splitting,

Introduction

Oil derivatives are used as the primary energy source worldwide, and they cause global warming by emitting CO₂. Especially in the last decade, global warming has caused a severe climate crisis all over the world. Taking this into account, many countries and the European Union (Green Deal) have announced their short-term and long-term targets for energy production from environmentally friendly renewable energy sources instead of petroleum products. Among the decarbonization targets, hydrogen is stated to play a key role in reducing global warming due to its high energy capacity and the fact that it only turns into water with oxidation. It is necessary to switch to low-cost hydrogen production processes with solar energy, which is a renewable energy source. Photoelectrochemical systems are one of the most preferred methods due to their high hydrogen gas yield and the use of photon energy. Photoelectrochemical hydrogen production using solar energy was first investigated by Fujishima and al. (1972). In the literature, there are many studies on hydrogen production such as TiO₂ Zhang and al. (2022), ZnO

Guo and al. (2022), WO₃ Li and al. (2021) semiconductors by photoelectrochemical water splitting using solar energy. However, these semiconductors have disadvantages because they only absorb in the UV-vis spectrum. Therefore, scientists have focused their efforts on semiconductors that absorb in the visible region, such as Cu₂O Jeong and al. (2022), CuO Siavash and al. (2021), BiVO₄ Majumder and al. (2022) and α -Fe₂O₃ Li and al. (2020). Among these semiconductors, advantages of Fe₂O₃, such as its natural abundance, non-toxicity, and favorable valence band position for water oxidation, enable it to stand out. However, the photocatalytic activity of α -Fe₂O₃ is undesired due to the lower reaction kinetics of the oxygen evolution reaction (OER), recombination of the electron-hole pairs. These drawbacks can be overcome by forming heterostructures with Fe₂O₃ semiconductor. The heterostructure can be obtained with various semiconductors and polymer-based material Behera and al. (2022), Tian and al. (2022). Although heterostructure of α -Fe₂O₃ has been available with suitable band gap energy of semiconductors, the heterostructure structure combination papers of α -Fe₂O

with polymer is limited in the literature. Therefore, in this research, the synthesis of α -Fe₂O₃/Ppy on FTO substrate by the doctor blade and the application of the doctor blade to loading photocatalytic material have created a novelty of phptpcatalyst for photoelectrochemical hydrogen production.

Methodology

α -Fe₂O₃ powder was fabricated by the hydrothermal approach. A deposition bath included 0.12 M FeCl₃ and 0.12 M CO(NH₂)₂. The deposition bath was poured into a hydrothermal reactor and heated at 100 °C for 12 hours. After the procedure, a yellowish powder was gathered, which was cleaned numerous times with distilled water and ethanol, respectively. The yellowish powder was furnace at 550 °C for 5 hours to achieve α -Fe₂O₃ powder.

0.61 M FeCl₃ in a two-necked vessel and add 100 mL 0.01 M HCl. Then 3 mL of pyrrole was added slowly at room temperature, and the reaction was continued for 1 hour with a magnetic stirrer. The resulting polymer solid is rubbery and black in color. The polypyrrole solid was washed with distilled water and then with ethyl alcohol until the filtrate became clear. It was dried for 24 hours at 65 °C in an oven.

The FTO prepared by applying washing and cleaning procedures and cut into 0.8 × 1.25 cm² was made suitable for coating. Then, α -Fe₂O₃ and Ppy were prepared in the form of slurry colloidal α -Fe₂O₃ and Ppy in separate containers. The slurry α -Fe₂O₃ was coated on FTO using the Doctor Blade technique and apparatus. Then, Ppy, which was a slurry in a separate container, was coated on FTO/ α -Fe₂O₃ with the same technique and method. The resulting coated materials are FTO/ α -Fe₂O₃ and FTO/ α -Fe₂O₃/Ppy. The obtained FTO/Fe₂O₃ and FTO/ α -Fe₂O₃/Ppy were dried in a 100 °C oven for 2 hours and then made ready for characterization and electrochemical experiments.

The photocatalytic performance was carried out in 0.1 M Na₂SO₃-0.1 M phosphate buffer under 100 mW cm⁻² solar irradiance.

Results and Discussion

The α -Fe₂O₃ and α -Fe₂O₃/Ppy are characterized by scanning electron microscopy (SEM), X-ray diffraction (XRD), Raman spectroscopy, and Uv-vis spectrometers. Figure 1 shows the XRD pattern of the photoelectrode between 20 and 80 of 2 θ values. It indicates that the obtained peaks of α -Fe₂O₃ and α -Fe₂O₃/Ppy at the 2 θ of 24.14°, 33.15°, 35.62°, 40.85°, 49.45°, 54.05°, 62.42°, 63.99° and 71.92° correspond to the hkl planes of (012), (104), (110), (113), (024),

(116), (214), (030) and (1010) (pdf card no: 98-015-4190). The relatively intensity of 2 θ peaks of 33.15° and 35.62° confirm the hexagonal phase of α -Fe₂O₃ (hematite phase) for α -Fe₂O₃ and α -Fe₂O₃/Ppy photoelectrodes Kyesmen and al. (2021), Wannapop and al. (2021). In addition, the intensity of the 2 θ peaks of α -Fe₂O₃/Ppy photoelectrode is decreased with Ppy polymer loading on the α -Fe₂O₃. It can be suggested that an amount of Ppy is adequate to obtain heterostructure of Fe₂O₃/Ppy by the doctor blade.

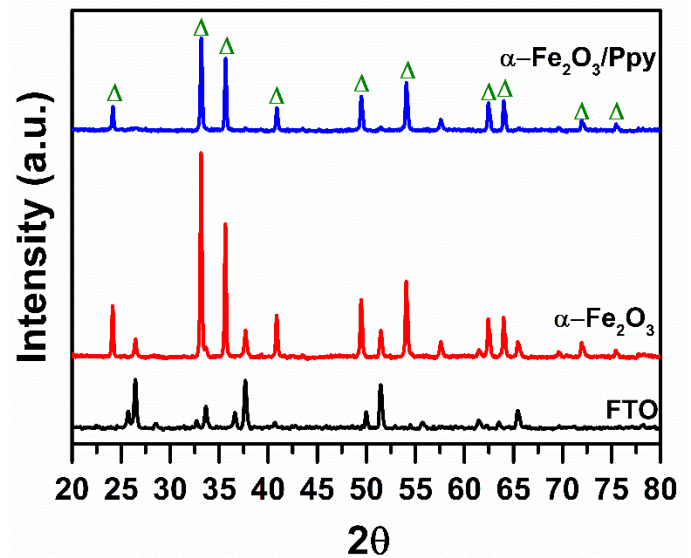


Figure 1: XRD pattern of α -Fe₂O₃ and α -Fe₂O₃/Ppy.

Raman shift of photoelectrodes was performed in the range of 200 to 800 cm⁻¹ of wavenumber, as given in Figure 2. α -Fe₂O₃ and α -Fe₂O₃/Ppy photoelectrodes give two peaks at 225 and 447 cm⁻¹ correspond to A_{1g} and E_g mode, respectively. It indicates the synthesis of α -Fe₂O₃.

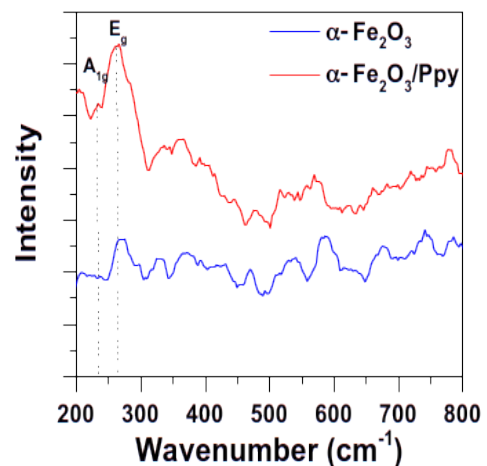


Figure 2: Raman shift of α -Fe₂O₃ and α -Fe₂O₃/Ppy.

The surface analysis of $\alpha\text{-Fe}_2\text{O}_3$ and $\alpha\text{-Fe}_2\text{O}_3/\text{Ppy}$ photoelectrodes was performed cross-section and upper-section by SEM images to demonstrate the loading of materials on the FTO surface with the doctor blade method. Figure 3 shows the SEM images of $\alpha\text{-Fe}_2\text{O}_3$ (a,b) and $\alpha\text{-Fe}_2\text{O}_3/\text{Ppy}$ (c,d). It indicates that $\alpha\text{-Fe}_2\text{O}_3$ is obtained at nanoparticle dimensions, and $\alpha\text{-Fe}_2\text{O}_3$ deposition achieves a thickness of approximately 125 μm on FTO by the doctor blade method. Therefore, it can be enabled by enhancing the excitation of electrons by photon energy, resulting in further performance on OER. Furthermore, deposition thickness is increased with the loading of Ppy on the FTO/ $\alpha\text{-Fe}_2\text{O}_3$ by the doctor blade method. The $\alpha\text{-Fe}_2\text{O}_3/\text{Ppy}$ deposition thickness achieves about 250 μm , leading electron transfer pathways through Ppy and $\alpha\text{-Fe}_2\text{O}_3$ and it can improve photocatalytic performance in the OER process.

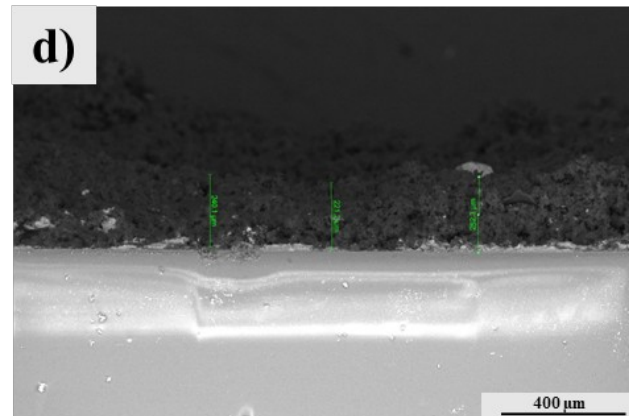
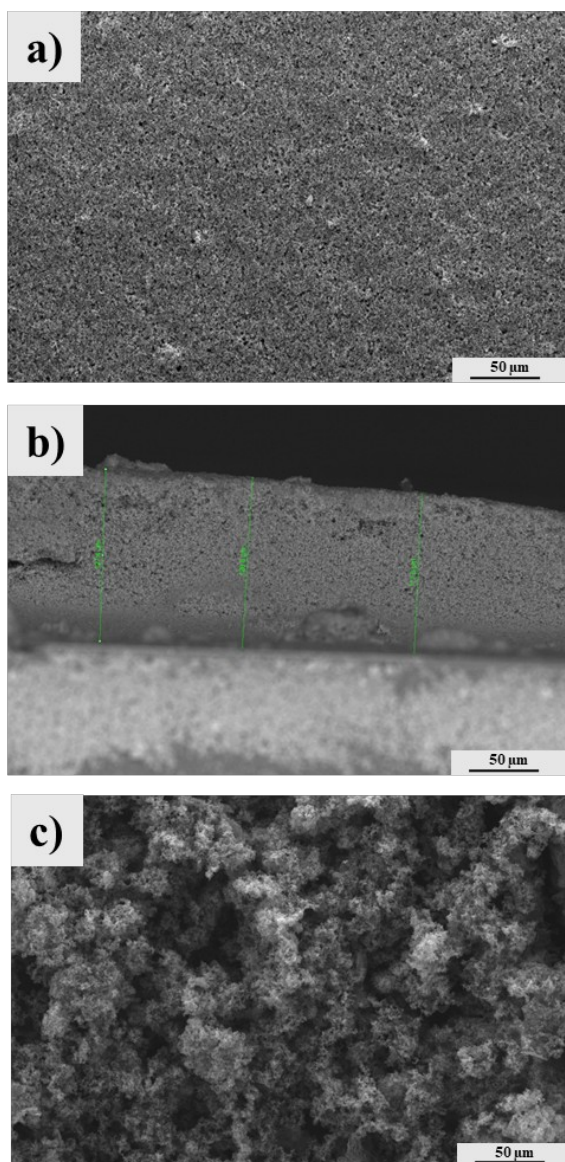


Figure 3: SEM images of $\alpha\text{-Fe}_2\text{O}_3$ (a,b) and $\alpha\text{-Fe}_2\text{O}_3/\text{Ppy}$ (c,d)

A solar light absorption behavior of photoelectrodes was analysed by Uv-vis spectrometer. Figure 4 shows absorption spectra ranging from 450 to 800 nm, indicating $\alpha\text{-Fe}_2\text{O}_3$ and $\alpha\text{-Fe}_2\text{O}_3/\text{Ppy}$ light absorption performs about 600 nm. It confirms that $\alpha\text{-Fe}_2\text{O}_3$ material undergoes deposition on the FTO substrate by doctor blade method. Furthermore, Ppy material commonly enhances light absorption of heterostructure. The absorption of $\alpha\text{-Fe}_2\text{O}_3/\text{Ppy}$ indicates that Ppy enables improvement of absorption across the broad spectrum. Therefore, it suggests increasing the photocatalytic response of photoelectrode on the OER process.

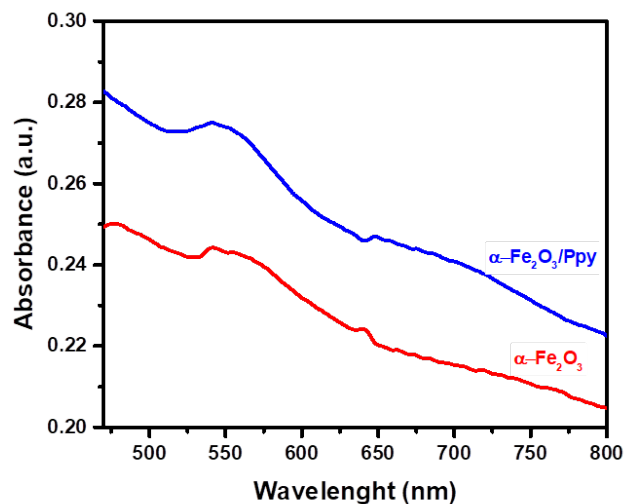
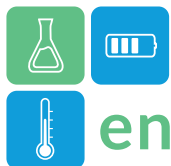


Figure 4: Uv-vis spectrum of $\alpha\text{-Fe}_2\text{O}_3$ and $\alpha\text{-Fe}_2\text{O}_3/\text{Ppy}$

LSV measurement was conducted to define photocatalytic performance of samples for photoelectrochemical water splitting under solar light irradiation. Figure 5 shows the photocatalytic response of $\alpha\text{-Fe}_2\text{O}_3/\text{Ppy}$ is about 5-fold further (1.032 mA cm^{-2}) compared to $\alpha\text{-Fe}_2\text{O}_3$ (0.232 mA cm^{-2}). It could be concluded that Ppy deposition on the $\alpha\text{-Fe}_2\text{O}_3$ leads to



enhance catalytic performance on OER process for photoelectrochemical water splitting.

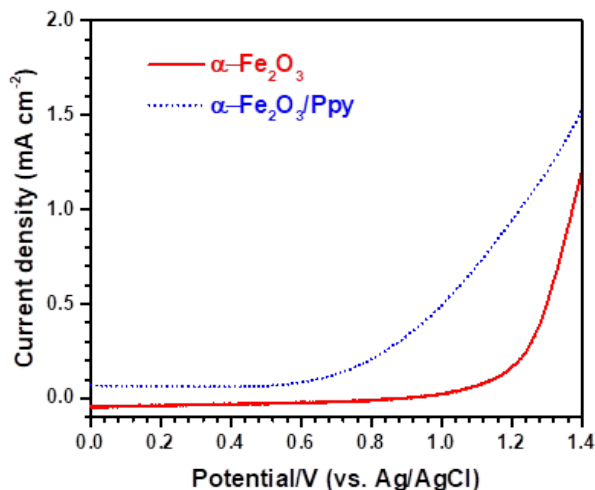


Figure 5: LSV measurement of α -Fe₂O₃ and α -Fe₂O₃/PPy into 0.1 M Na₂SO₃-0.1 M phosphate buffer under 100 mW cm⁻² solar irradiance.

Conclusions

In summary, the synthesis of α -Fe₂O₃ and Ppy are accomplished with hydrothermal deposition and chemical method, respectively. The XRD results confirmed that the hexagonal phase of α -Fe₂O₃ (hematite phase) is obtained and the deposition of Ppy on FTO/ α -Fe₂O₃ leads to a decreasing main peak intensity of α -Fe₂O₃. SEM images show that deposition thickness of α -Fe₂O₃ and α -Fe₂O₃/Ppy are 125 and 250 μ m on the FTO surface by doctor blade method and α -Fe₂O₃ dimension is in the nanoscale. Consequently, Ppy deposition on the α -Fe₂O₃ enables improved higher photocurrent density on OER process for photoelectrochemical hydrogen production with solar irradiation.

Acknowledgment

This document has been prepared within the framework of Research and International Networking on Emerging Inorganic Chalcogenides for Photovoltaics COST: CA21148.

References

Behera, G.C., and al. (2022) WS₂ nanosheets functionalized Fe₂O₃ nanorod arrays as a type II heterojunction for photoelectrochemical water splitting. *Applied Surface Science Advances*. doi.org/10.1016/j.apsadv.2022.100293

Fujishima, A. and al. (1972) Electrochemical photolysis of water at a semiconductor electrode. *Nature*. doi.org/10.1038/238037a0

Guo, X., and al. (2022) Heteroepitaxial growth of core-shell ZnO/CdS heterostructure for efficient and stable photocatalytic hydrogen generation. *Int J Hydrogen Energy*. doi.org/10.1016/j.ijhydene.2022.08.032

Jeong, D. and al. (2022) Characterization of Cu₂O/CuO heterostructure photocathode by tailoring CuO thickness for photoelectrochemical water splitting. *RSC Advance*. doi.org/10.1039/d1ra08863g

Kyesmen, P.I., and al. (2021) Heterojunction of nanostructured α -Fe₂O₃/CuO for enhancement of photoelectrochemical water splitting. *J Alloys Compd*. doi.org/10.1016/j.jallcom.2021.158724

Li, J. and al. (2021) Synthesis of vertical WO₃ nanoarrays with different morphologies using the same protocol for enhanced photocatalytic and photoelectrocatalytic performances. *RSC Adv*. doi.org/10.1039/d1ra03149j

Li, Y. and al. (2020) Synthesis of α -Fe₂O₃/g-C₃N₄ photocatalyst for high-efficiency water splitting under full light. *Mater Des*. doi.org/10.1016/j.matdes.2020.109191

Majumder, S. and al. (2022) Facile fabrication of BiVO₄/Bi₂S₃/NiCoO₂ for significant photoelectrochemical water splitting. *Appl Surf Sci*. doi.org/10.1016/j.apsusc.2021.151562

Moakhar, R., and al. (2021) Photoelectrochemical Water-Splitting Using CuO-Based Electrodes for Hydrogen Production: A Review. *Advanced Materials*. doi.org/10.1002/adma.202007285

Tian, Z. and al. (2022) Enhanced efficiency of organic solar cells by using a ZnO-Fe₂O₃ electron transport layer. *J Solgel Sci Technol*. doi.org/10.1007/s10971-022-05877-y

Wannapop, S., and al. (2021) Experimental study of thin film Fe₂O₃/TiO₂ for photocatalytic Rhodamine B degradation. *Inorganic Chemistry Communication*. doi.org/10.1016/j.inoche.2021.108585

Zhang, X., and al. (2022) Recent Advances in TiO₂-based Photoanodes for Photoelectrochemical Water Splitting. *Chemistry Asian Journal*. doi.org/10.1002/asia.202200668



A Review of Pilot-scale and Application-scale Latent Thermal Energy Storage Heat Exchanger Configurations

Aditya Singh Suswal^{1,*}, Saman Nimali Gunasekara¹, Justin Ningwei Chiu¹, Samer Sawalha¹
1 KTH Royal Institute of Technology, Department of Energy Technology, Brinellvägen 68, Stockholm, Sweden

*Corresponding author e-mail: adityass@kth.se

Abstract

Thermal energy storage (TES) systems using phase change materials (PCMs) with solid-liquid transitions can provide highly effective latent heat storage and release. Yet the commercial feasibility of latent heat thermal energy storage (LHTES) systems depends notably on efficient and economical heat exchanger designs connecting PCM tanks and the surrounding fluid. This review discusses LTES heat exchanger configurations studied at the pilot and application scales. Although pilot-scale studies have achieved excellent efficiencies through high surface area-to-volume ratios, challenges remain in large-scale performance. Some persistent challenges arise with certain PCMs, including phase separation and hysteresis effects. Application-scale testing shows trade-offs in complexity and cost. Of the many LHTES system configurations analyzed, only shell and tube exchangers have achieved application-scale deployment leveraging direct contact between PCM and tubes. While encapsulated designs and advanced direct contact prototypes demonstrate potential in pilot studies, broader translation success remains confined largely to simplified cylindrical vessels and tubing.

Keywords: Phase change material, Phase separation, Pilot and application scales

Introduction

With global energy demand continuously rising with significant climate impacts, there is an urgent need to scale up renewable energy penetration to transition away from fossil fuels (IEA, 2022). However, the variable nature of most renewables creates a mismatch between energy supply and demand. In this context, thermal energy storage (TES) is poised to play an indispensable role in connecting renewable energy generation to end-use loads (Wang et al., 2022). Latent heat thermal energy storage (LHTES) has attracted particular interest given its higher energy storage density than sensible heat alternatives and a nearly isothermal phase change process. Using phase change materials (PCMs) to store and release large amounts of latent heat during phase transitions can enhance efficiency relative to the broader temperature swing of sensible storage media.

Among TES approaches, LHTES using PCMs thus offers extremely compact systems and excellent thermodynamic performance. However, multiple inherent issues with PCMs pose barriers to effective heat transfer and cycling stability. Many candidate PCMs, like salt hydrates and paraffin waxes (i.e. mixtures), face problems, including segregation into

higher and lower melting temperature domains during phase separation requiring emulsification (Jouhara et al., 2020). Mechanical stability over thousands of freeze-thaw cycles without degradation presents long-term operation challenges.

The practical efficiency of LHTES devices strongly depends on storage configurations mainly of PCM containment and heat exchanger design. Diverse enclosure geometries have been studied, from cylinders (shell-and-tube, triplex tubes, concentric annuli) to spheres, rectangles, squares, elliptical casings, cones, and more (Elarem et al., 2021). Attempts at addressing inherent PCM limitations prompt growing interest in configuring design modifications beyond basic shapes such as cylinders and spheres. Interventions directly in the PCM include the addition of thermal conductivity enhancers like fins, foam matrices, and nanoscale particles, as well as nucleating agents to trigger crystallization (Elarem et al., 2021). Cascading multiple complementary PCMs broadens usable temperature ranges. New exchanger types include rotating designs for transporting the PCM versus circulating a heat transfer fluid. Figure 1 demonstrates the available configurations of LHTES in the pilot and application stages.

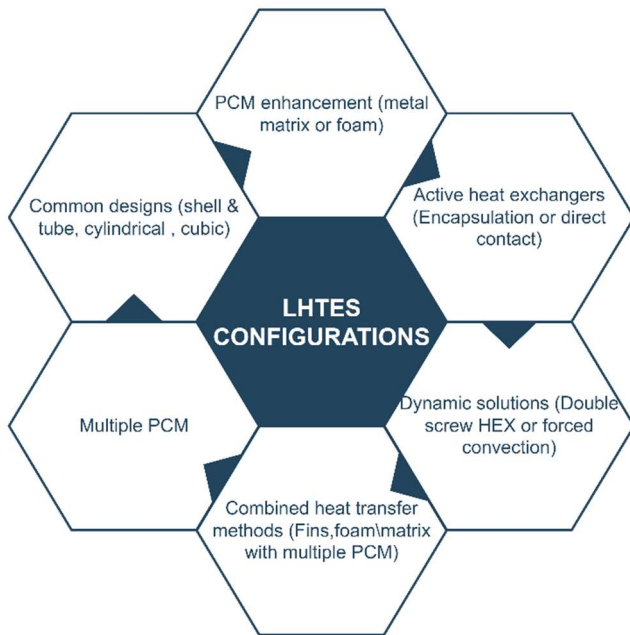


Figure 1: Illustration of different LHTES configurations

Even with a spectrum of containment structures and augmentations analysed, from small laboratory prototypes to simulated scaled-up systems, real-world testing of complete LHTES devices at application scales is rarely addressed in the literature. Thus, knowledge gaps remain in translating success at the pilot scale into commercially viable configurations whose performance matches models and pilot-scale demos.

Therefore, this work aims to provide an overview of different types of LHTES configurations employed in application and/or at pilot-scale TES projects. Therein, it is also aimed to review the heat transfer characteristics across implemented LHTES systems, to obtain vital insight into configuration decisions balancing storage density, cyclic lifetime, and scalability, which are essential for linking renewables to demand via thermal networks.

Methodology

A structured literature search on published scientific journal articles was conducted to identify studies of LHTES heat exchangers. Studies that tested an LHTES heat exchanger design at the pilot scale or application scale were prioritized. Both experimental studies assessing thermal performance metrics and considering review articles and purely theoretical/simulation-based studies were included.

Data extraction and analysis of key information was done considering the most relevant studies identified, including heat exchanger configurations and materials,

PCM properties, experiment scale, thermal capacity, and efficiency metrics. Heat exchangers were categorized by scale, and their designs were compared.

Configurations of LHTES and their heat exchangers

Containment designs

LHTES using PCMs requires carefully engineered configurations matching storage containment and heat transfer components. Basic shapes include cylinders, spheres, rectangular prisms, and stacked tube arrays with PCM filled in the gaps, as summarized in Figure 2 from A to E, respectively. Shell-and-tube remains common given straightforward material pairings: salts or paraffin contained inside or outside metal pipes conducting heat transfer fluid (HTF). Concentric tube-in-tube exploits the annulus for PCM storage using a centered carrier tube. Triplex tube configurations utilize triangular conduits in a larger external shell (Kumar et al., 2023).

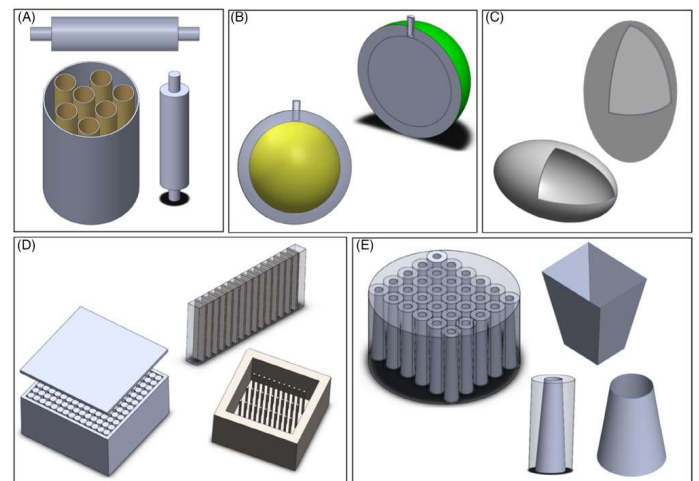


Figure 2 : Different LHTES shapes (Elarem et al., 2021)
 Copyright © 2019 John Wiley and Sons- [CC BY-SA 3.0](https://creativecommons.org/licenses/by-sa/3.0/)

Advanced containment designs leverage multiple smaller PCM volumes, which enhance heat transfer surface area, like plates, tubes, and spheres packed into larger units. Oval cassette arrangements allow volume expansion during phase change without stress accumulation. Some novel methods directly leverage the PCM as an active heat exchange surface rather than passive material in static vessels. For instance, rotating designs transport low-viscosity PCMs like oils across hot and cold ducts, while stationary cassettes pump heat transfer fluid instead. In-addition, thin rotating disks can sandwich PCM for rapid charging and discharging across large areas (Kumar et al., 2023).

Active Heat exchangers

The immobility of PCM can cause unintended solidification, which can cause thermal resistance during discharging or charging. Thus, the main idea behind an active heat exchanger is to keep the PCM moving or apply similar techniques that can cause forced convection so as to improve the heat exchange rate at fusion (Elarem et al., 2021). In active heat exchanger systems, two main containment approaches exist: bulk PCM storage in conventional heat exchangers (e.g direct contact or PCM slurries) and macro encapsulation of PCM inside larger storage containments (like packed beds). Encapsulation strategies often prove more favourable for addressing certain PCM challenges and boosting surface area in contact with heat transfer fluids.

The challenges in low thermal conductivity of PCMs prompt growing interest in matrix structures and encapsulation. Metal foams and honeycombs conduct heat through internal pores filled with PCM, though issues like material compatibility persist (Elarem et al., 2021). Different types of macroencapsulation techniques can be observed in Figure 3, from spherical, to plate, or tube encapsulation

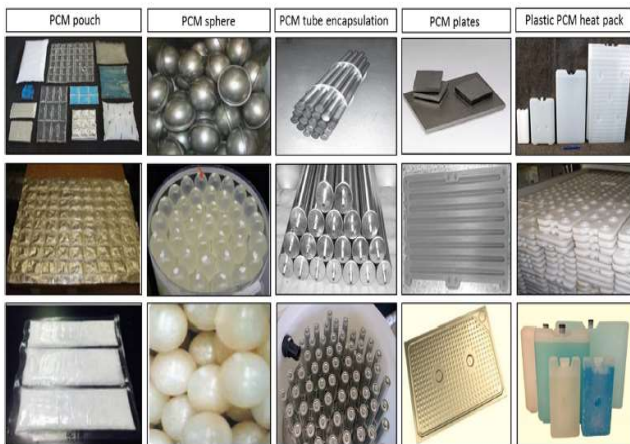


Figure 3 : Illustration of different PCM encapsulation (Elarem et al., 2021) Copyright © 2019 John Wiley and Sons- [CC BY-SA 3.0](https://creativecommons.org/licenses/by-sa/3.0/))

Micro and macro encapsulation techniques contain PCMs in, e.g., polymer shells or larger reservoirs, guarding against leakage while boosting heat transfer via increased surface area and composite conductance. Microcapsules also limit volume expansion compared to bulk PCM as microencapsulation is a technique of surrounding tiny particles of a core material with a coating or embedding them within a matrix, e.g. as seen in Figure 4. The core material is encapsulated to create a capsule with a distinct inner section (the core) separated from the outer section (the coating or matrix) by a layer of air. This air space can accommodate any

expansion or contraction occurring in the core material during a phase change (Wang et al., 2022).

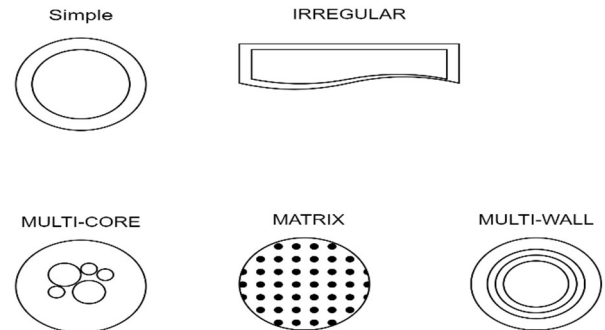
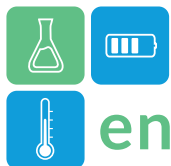


Figure 4 : Different Microencapsulation Techniques, Redrawn based on (Jouhara et al., 2020)

Pilot and experimental studies

Encapsulation allows tailoring shells to match desired temperature ranges and prevents reactions between certain PCMs and metals. Although the idea of encapsulation is better in terms of increasing the surface area and heat transfer characteristics, the research conducted by (Lv et al., 2023) shows that using a spiral-finned pilot scale LHTES unit with 5675 kg of PCM shows the best heat transfer performance in a shell and tube heat exchanger. It also gives insights into charging direction being an essential factor as it determines which part of the TES starts dropping temperature first, and there is a more significant temperature difference vertically than horizontally. However, orientation impacts performance. For instance, a study by (Xu et al., 2019) found that vertical encapsulated shells fared better in charge-discharge cycling times but showed lower effective thermal conductivity versus horizontal alignments due to phase separation influences. Theoretical work has also proposed ellipse, ribbed, spheroidal, and other shell geometries for potentially improved heat transfer characteristics (Jouhara et al., 2020). Though some encapsulated products are commercially manufactured, few large-scale validations have reproduced modeling gains, representing an area needing further analysis.

Pilot scale experimental studies are crucial for understanding the behavioral patterns of TES. It was demonstrated by (Besagni & Croci, 2019) in a study that used a fin and tube heat exchanger immersed in a tank containing phase change material (PCM) to investigate how different boundary conditions such as flow rate and inlet/outlet temperatures influence power supplied and stored thermal energy. As (Saini et al., 2023) contends in a analysis, LHTES technology breakthroughs enabling lower levelized costs at system level could catalyse displacement of predominant



sensible heat storage methods across heating and cooling networks in the context of steam generation. This substantially decreased levelized cost of energy (LCOE) for LHTES represents the field's largest outstanding goal given the vast scalability potential of effectively designed and integrated LHTES configurations. The upcoming design of a pilot LHTES system in this project [HYSTORE](#) will explore the implementation of the various configurations discussed above such as bulk or macro-encapsulated design in full-scale implementation.

Conclusion

In summary, LHTES continues to confront inherent PCM limitations like low thermal conductivity alongside the need to identify storage configurations, cost-effectiveness, and manufacturability at scale. In summary, the HEX geometries summarized in Table 1 are found to be successfully used in the pilot and application scales.

Table 1

LHTES type (Type of scale)	Geometries	Storage sizes (PCM), (kg)	Source
Encapsulation (Pilot)	Cylindrical macro-encapsulation	154	(Xu et al., 2019)
Direct Contact (Pilot)	Cubic Shell and tube	5675	(Lv et al., 2023)
Direct contact (Application)	Fin and tube HEX in a insulated tank	58	(Besagni & Croci, 2019)

Although inserts like thermal conductivity enhancers and matrix materials have enhanced heat transfer with novel active exchange designs exploiting direct PCM contact through encapsulation, true commercial translation remains lacking. Moreover, most analysis concentrates on small prototypes, rather than validation in fully-sized containment units and exchangers facing real-world ambient temperatures, extended cycling, and long-term material compatibility challenges. While advances are being made in materials, encapsulation strategies, and heat exchanger approaches, a more holistic assessment is necessary, likely by hybridizing multiple promising concepts. Broader testing under fully representative pilot programs linked to renewable heating/cooling networks could drive systems optimized around storage density, capacity over thousands of cycles, and scalability.

Acknowledgement

The Hystore project receives funding from the European Union's Horizon 2020 research and innovation program, under grant agreement number 1010967.

References

- Besagni, G., & Croci, L. (2019). Experimental study of a pilot-scale fin-and-tube phase change material storage. *Applied Thermal Engineering*, 160, 114089. <https://doi.org/10.1016/j.applthermaleng.2019.114089>
- Elarem, R., Alqahtani, T., Mellouli, S., Askri, F., Edacherian, A., Vineet, T., Badruddin, I. A., & Abdelmajid, J. (2021). A comprehensive review of heat transfer intensification methods for latent heat storage units. *Energy Storage*, 3(1), e127. <https://doi.org/10.1002/est2.127>
- IEA. (2022). *World Energy Outlook*. IEA. <https://iea.blob.core.windows.net/assets/830fe099-5530-48f2-a7c1-11f35d510983/WorldEnergyOutlook2022.pdf>
- Jouhara, H., Żabnieńska-Góra, A., Khordehghah, N., Ahmad, D., & Lipinski, T. (2020). Latent thermal energy storage technologies and applications: A review. *International Journal of Thermofluids*, 5–6, 100039. <https://doi.org/10.1016/j.ijft.2020.100039>
- Kumar, A., Maurya, A., Siddiqui, M., Alnaser, I., & Ashraf, I. (2023). Transient analysis of PCM discharging in a rotary triplex tube with wave-shaped fins. *Journal of Energy Storage*, 110178. <https://doi.org/10.1016/j.est.2023.110178>
- Lv, L., Zou, Y., Huang, S., Wang, X., Shao, R., Xue, X., Rong, Y., & Zhou, H. (2023). Experimental study on a pilot-scale medium-temperature latent heat storage system with various fins. *Renewable Energy*, 205, 499–508. <https://doi.org/10.1016/j.renene.2023.01.089>
- Saini, P., Ghasemi, M., Arpagaus, C., Bless, F., Bertsch, S., & Zhang, X. (2023). Techno-economic comparative analysis of solar thermal collectors and high-temperature heat pumps for industrial steam generation. *Energy Conversion and Management*, 277, 116623. <https://doi.org/10.1016/j.enconman.2022.116623>
- Wang, S., Lei, K., Wang, Z., Wang, H., & Zou, D. (2022). Metal-based phase change material (PCM) microcapsules/nanocapsules: Fabrication, thermophysical characterization and application. *Chemical Engineering Journal*, 438, 135559. <https://doi.org/10.1016/j.cej.2022.135559>
- Xu, T., Chiu, J. N., Palm, B., & Sawalha, S. (2019). Experimental investigation on cylindrically macro-encapsulated latent heat storage for space heating applications. *Energy Conversion and Management*, 182, 166–177. <https://doi.org/10.1016/j.enconman.2018.12.056>



Advanced controllers for electrically heated floors in residential buildings to shift peak load

Ying Sun^{1*}, Fariborz Haghighat²

1 School of Environmental and Municipal Engineering, Qingdao University of Technology, Qingdao, China

2 Energy and Environment Group, Department of Building, Civil and Environmental Engineering
Concordia University, Montreal, Canada

*Corresponding author e-mail: sun_ying@qut.edu.cn

Abstract

Effective control strategies play a vital role in enlarging the peak shifting ability of thermal energy storage systems. This study presents two advanced controllers, i.e., the self-learning predictive control and the data-driven based model predictive control (DDMPC). The proposed controllers are used to control the electrically heated floors (EHF) in residential buildings to shift the peak load. Simulation results show that these two controllers could effectively shift the peak load, reduce the heating cost, and maintain the thermal comfort.

Keywords: Thermal energy storage, Control, Data-driven

Introduction

Building energy demand is not static, but changes over time. Due to occupants' living habits, daily peak load may occur during early morning or late afternoon (*Rate Flex D | Hydro-Québec*, n.d.). This phenomenon further results in increased stress on the electricity grid during peak periods. An effective solution to pave the grid stress resulting from peak load is the usage of an energy storage system by taking advantage of its ability to store energy during the off-peak periods and release it for later use.

In recent years, thermal energy storage (TES) systems have been widely used in buildings for peak shifting or renewable energy storage. High thermal mass materials in building envelopes may provide sufficient thermal energy storage capacity for peak shifting. For instance, appropriate system configurations of an electrically heated floor (EHF) system in a residential building could shift both morning peaks and evening peaks (Olsthoorn et al., 2019). Furthermore, in Canada, electrically heated floors (EHF) in which electric wires are buried in concrete slabs have been used as the thermal energy storage system in residential buildings. (Thieblemont et al., 2018)

Effective control strategies are crucial to take advantage of the full capacity of TES systems in buildings to enlarge the peak shifting and energy cost-saving potential (Tarragona et al., 2020). For instance, Thieblemont et al. (Thieblemont et al., 2018) developed a self-learning predictive controller for the

operation of electrically heated floor (EHF) in a residential building. At the same time, in recent years, data-driven-based MPCs have drawn increasing attention to control TES systems (Lee et al., 2022).

In this study, two advanced controllers are introduced to enlarge the peak shifting ability of the EHF. The proposed controllers will be implemented into two experimental buildings to control the set-point temperature for heating.

Methodology

In this section, two advanced controllers are introduced.

Self-learning predictive controller

The schematic of the self-learning predictive controller is presented in Figure 1. It contains two parts: high-level controller and low-level controller. In the high-level controller, the next day's hourly outdoor ambient temperature and solar radiation are categorized into the corresponding half-day temperature and solar radiation class, i.e., [Ti, Si], by the weather forecast model. Based on this weather class, the energy consumption prediction model would predict the half-day energy consumption (E_Com). Then, E_Com is distributed to peak periods by the scheduling model. Note that the energy consumption prediction model is trained by the building response analysis module that analyses feedback data from the experimental building.

The low-level controller is used to set the thermal comfort bound by setting threshold for the indoor air temperature.

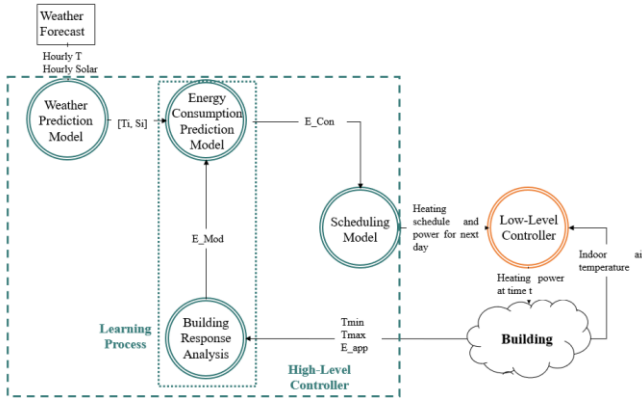


Figure 1: Schematic of the self-learning predictive control (Thieblemont et al., 2018)

Data-driven based model predictive controller (DDMPC)

The general schematic for DDMPC is given in Figure 2. Firstly, data-driven based predictive models should be trained and validated. The procedure for the predictive model development includes: data collection, data preparation, feature engineering, model training, and model validation. Details for feature engineering, data-driven algorithms, and multi-step prediction procedure could be found in (Sun et al., 2020). The second step in the DDMPC is to construct the objective function based on the predicted values. The control objective could be to minimize the heating cost or minimize energy consumed during the peak periods by optimal set-point temperature. In the optimization process module, the optimization problem could be solved by various optimization algorithms, such as genetic algorithm, differential evolution, particle swarm optimization, etc.

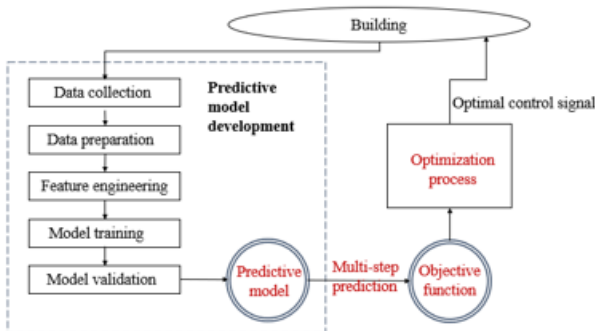


Figure 2: Schematic of the DDMPC

Case Studies

The developed controllers are implemented into two residential buildings which are heated by electrically heated floor (EHF). The experimental buildings show similar characteristics to around 1.6 million typical

detached houses in Quebec, Canada. The studies are based on numerical simulation on the validated TRNSYS model of these two experimental buildings. The validation of the developed TRNSYS model could be found in previous research works (Sun et al., 2018, 2021; Thieblemont et al., 2016). In this section, the configuration of thermal energy storage components (i.e., electrically heated floors) in the experimental houses is first introduced. Then, the detailed description of the experimental houses is presented. Note that the experimental building No.1 is used to investigate the applicability of the self-learning predictive controller, while the experimental building No.2 is used to verify the implementation of DDMPC.

Electrically heated floors (EHFs)

The two experimental houses are both equipped with EHF, whose schematic is presented in Figure 3. The electrical heating wires are buried in the middle of a 152 mm-thick concrete slab. Due to the high thermal mass offered by the concrete slab, the EHF could act as the sensible thermal storage system.

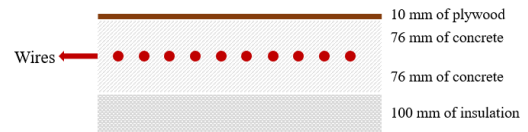


Figure 3: Schematic of the EHF(Sun et al., 2021)

Table 1 : Thermos-physical properties of the EHF(Sun et al., 2021)

	Conductivity (W/m*k)	Specific Heat (kJ/kg*K)	Density (kg/m ³)
Concrete	2.25	0.99	2200
Insulation	0.04	1.5	35
Plywood	0.164	1.63	670

Experimental house No.1-Two storey building

The two-storey building is located in Quebec, Canada, and its building area is 144 m² per floor. Its front view is shown in Figure 4. EHF are installed in the basement, while the second floor is heated by traditional baseboard heaters and the ground floor is

heated by surface EHF's which do not have considerable energy storage capacity.



Figure 4: Front view of the experimental house No.1

Critical peak pricing (CPP, as shown in Table 2) is implemented to encourage consumers to shift their electricity demand and ease the pressure on the electrical grid. The peak period and off-peak period are presented as white and black portions, respectively, in Figure 5.

Table 2: CPP in Quebec

	Condition	Periods	
		Peak period	Off-peak period
Electricity price (¢/kWh)	< 40 kWh/per day	50	3.98
Electricity price (¢/kWh)	> 40 kWh/per day	50	7.03
Subscription fee (¢/day)	-	40.64	

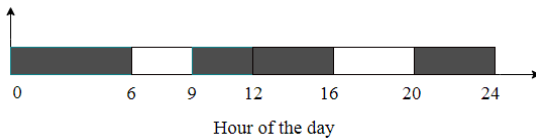


Figure 5: Peak period (white blocks) and off-peak period (black blocks) of the place where experimental building No.1 located

Experimental house No.2-Bungalow building

The second experimental building, as shown in Figure 6, is a traditional residential building located in Montreal, Quebec, Canada, which was built in 1960, with a building area of 104 m². In its TRNSYS model, the building was simulated as one-zone, heated by EHF's. CPP is also implemented to this building, while

duration of peak periods and off-peak periods for this district is presented in Figure 7.



Figure 6: Front view of the experimental house No.2

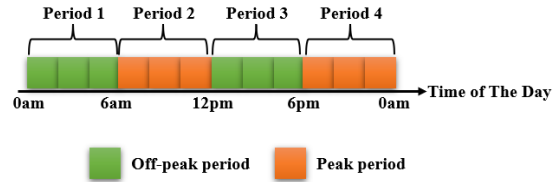


Figure 7: Peak period and off-peak period of the place where experimental building No.2 located

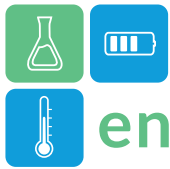
Results and Discussion

Results for self-learning predictive controller

The simulation results found that the self-learning predictive controller could effectively shift the energy consumed for heating to the off-peak period during night. Its peak shifting potential in the basement compared with the reference case (setting 21.5 °C as the set-point temperature) is 97.57%. Besides, implementing self-learning predictive controller to control the EHF's in the basement could save 22.89% heating cost for the entire building compared to the reference case. However, it shows a slightly negative effect on the thermal comfort, as the indoor air temperature may drop below the thermal comfort threshold, i.e., 21 °C.

Results for DDMPC

In the case study, a support vector machine (SVM) model is developed to predict the building energy consumed during each peak period or off-peak period, and another SVM model is constructed to predict whether or not the indoor air temperature is lower than the thermal comfort threshold. Then, the predicted energy consumption is integrated into the objective function to enlarge energy consumed during the off-peak periods and reduce the energy consumed during peak periods. The predicted value from the indoor temperature prediction model is used to construct the constraints.



The numerical study results show that ~65% peak load could be shifted to peak periods when using DDMPC, see Figure 8. Besides, the daily heating cost could be decreased from 27.57 CAD when setting the set-point temperature at 21 °C to 14.25 CAD when using DDMPC. Furthermore, the DDMPC could reduce the duration with uncomfortable thermal environment from 958 hours during the winter to 431 hours.

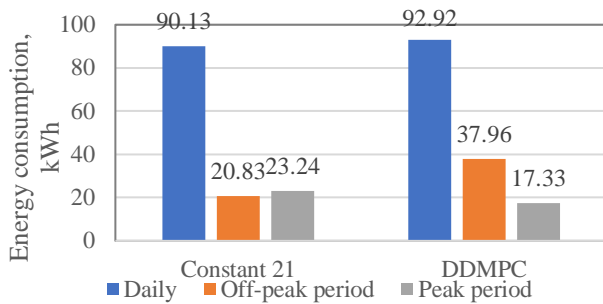


Figure 8: Average energy consumption of different controllers during different periods

Discussion

Although the applicability of the self-learning predictive controller and the DDMPC is investigated separately in this study, comparison between these two control strategies still needs further investigation. Besides, field test is needed to pave the way for implementing these two controllers in the real world.

Conclusions

This study presented two advanced controllers to control the thermal energy storage system in residential buildings to achieve peak shifting. Two case studies were conducted to investigate their ability on heating cost saving, peak shifting, and thermal comfort maintenance. Simulation results showed that these control strategies could effectively shift the peak load to the off-peak periods. However, future study should be done to compare the applicability between these two controllers.

References

Lee, D., Ooka, R., Matsuda, Y., Ikeda, S., & Choi, W. (2022). Experimental analysis of artificial intelligence-based model predictive control for thermal energy storage under different cooling load conditions. *Sustainable Cities and Society*,

79, 103700.
<https://doi.org/10.1016/j.scs.2022.103700>

Olsthoorn, D., Haghigat, F., Moreau, A., Joybari, M. M., & Robichaud, M. (2019). Integration of electrically activated concrete slab for peak shifting in a light-weight residential building—Determining key parameters. *Journal of Energy Storage*, 23, 329–343.
<https://doi.org/10.1016/j.est.2019.03.023>

Rate Flex D | Hydro-Québec. (n.d.). Retrieved 13 March 2020, from <http://www.hydroquebec.com/residentiel/espace-clients/tarifs/tarif-flex-d.html>

Sun, Y., Haghigat, F., & Fung, B. C. (2020). A review of the-state-of-the-art in data-driven approaches for building energy prediction. *Energy and Buildings*, 221, 110022.

Sun, Y., Panchabikesan, K., Haghigat, F., Luo, J. T., Moreau, A., & Robichaud, M. (2021). Development of advanced controllers to extend the peak shifting possibilities in the residential buildings. *Journal of Building Engineering*, 43, 103026.

Sun, Y., Panchabikesan, K., Joybari, M. M., Olsthoorn, D., Moreau, A., Robichaud, M., & Haghigat, F. (2018). Enhancement in peak shifting and shaving potential of electrically heated floor residential buildings using heat extraction system. *Journal of Energy Storage*, 18, 435–446.

Tarragona, J., de Gracia, A., & Cabeza, L. F. (2020). Bibliometric analysis of smart control applications in thermal energy storage systems. A model predictive control approach. *Journal of Energy Storage*, 32, 101704.
<https://doi.org/10.1016/j.est.2020.101704>

Thieblemont, H., Haghigat, F., & Moreau, A. (2016). Thermal Energy Storage for Building Load Management: Application to Electrically Heated Floor. *Applied Sciences*, 6(7), Article 7.
<https://doi.org/10.3390/app6070194>

Thieblemont, H., Haghigat, F., Moreau, A., & Lacroix, G. (2018). Control of electrically heated floor for building load management: A simplified self-learning predictive control approach. *Energy and Buildings*, 172, 442–458.
<https://doi.org/10.1016/j.enbuild.2018.04.042>



Advanced numerical model to analyze the thermal response of macroencapsulated PCMs for building applications

Matias Alvarez-Rodriguez^{1,*}, Mar Alonso-Martinez¹, Ines Suarez-Ramon¹, Dana Rodriguez-Garcia¹
1 University of Oviedo, GICONSIME Research Group, Pedro Puig Adam Street (West Department Building EDO-7), 33204 Gijón, Spain

*Corresponding author e-mail: alvarezrmatias@uniovi.es

Mathematical modeling of phase change materials (PCMs) incorporated in building envelopes is a key factor for the deployment of this technology. This work presents a finite difference numerical model of a PCM macrocapsule and compares numerical and experimental results. Melting and solidification of a PCM panel were assessed with a temperature variation rate of 1 °C/h, typical of building envelope applications. The effective heat capacity method was used for the phase change modeling. PCM thermal response was analyzed in two cases: using the effective heat capacity obtained with traditional characterization methods and using the effective heat capacity determined through the inverse method for the whole macrocapsule. Small-scale characterization leads to inaccurate results, overestimating the latent heat. Inverse-method-determined properties yield accurate results, demonstrating that PCM must be characterized in conditions as close as possible to their real application.

Keywords: Phase Change Materials, Latent Heat Thermal Energy Storage, Numerical Model, Thermal characterization, Effective Heat Capacity

Introduction

Nowadays, the building sector is responsible for 35% of final energy consumption and 38% of total CO₂ emissions (United Nations Environment Programme, 2022). Incorporating phase change materials (PCMs) in building envelopes tackles this: it reduces energy demand in buildings and improves the performance of heating and cooling systems (Jin et al., 2018).

PCMs macroencapsulated in metallic panels are widely studied. They are easily incorporated, avoid direct contact between PCMs and other construction materials, improve heat transfer, prevent leakage and are convenient for transportation (Rathore & Shukla, 2019). However, the wide variety of PCMs, wall designs, climatic conditions and desired interior conditions complicate the selection of the most adequate PCM and wall typology (Izquierdo-Barrientos et al., 2012). Mathematical modeling addresses this complex optimization problem, reducing costs and time of study.

Thermophysical properties of PCMs must be adequately determined to ensure accurate models. Traditional PCM characterization methods analyze smaller samples than the PCMs used in building envelopes, and with high heating rates. Numerical results are inaccurate when building envelopes with

PCMs are modeled using the PCMs properties obtained with these methods (Kuznik et al., 2016).

This work presents a numerical model of a macroencapsulated PCM panel and studies its transient thermal response in two cases: using the thermophysical properties determined by traditional methods, which analyze small quantities of PCM, and using the effective heat capacity of the whole macrocapsule determined through the inverse method.

Methodology / Materials and Methods

This work analyzes a PCM macroencapsulated in an aluminum panel, in this case, the commercial paraffin mixture RT21-HC (Rubitherm Technologies GmbH, n.d.) (Figure 1).

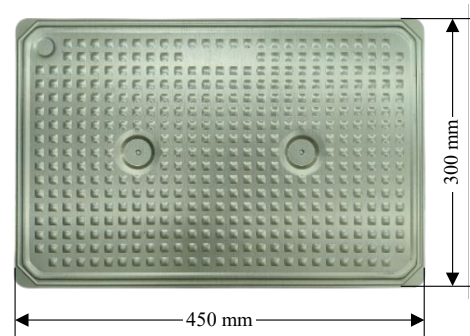


Figure 1: Studied macrocapsule

Since the PCM is a mixture, phase change occurs throughout a temperature range, bounded by the lower and higher limits of phase change. The total thickness of the panel is 10 mm and the thickness of the aluminum is 0.5 mm. The panel contains 0.5 kg of paraffin and its total weight is 0.85 kg.

The PCM panel was suspended in a thermally insulated hotbox connected to a climatic module which modifies temperature and relative humidity of air in a closed loop. The temperature of the air in the hotbox was varied at a constant rate of 1 °C/h, typically experienced in building envelopes. The temperature variation curve defined in the experiment consists of four stages:

1. Solidification: temperature was decreased from 28 °C to 8 °C at a constant rate of 1 °C/h.
2. Thermal stabilization in the solid phase: constant temperature for 3 hours to ensure that the PCM is completely solidified.
3. Melting: temperature was increased to 28 °C at a constant rate of 1 °C/h.
4. Thermal stabilization in the liquid phase: constant temperature for 3 hours to ensure that the PCM is completely melted.

The test was repeated three times.

Heat flux, \dot{q}^{exp} , and temperature, T_o^{exp} , were measured on the surface of the panel. A flat surface on which to place the sensors was ensured by adding a thin layer of mortar of 6 mm on each side.

The finite difference method was used to simulate the transient thermal behavior of the PCM panel. The simulation domain is divided in cells and the heat diffusion equation is solved in each of them.

The effective heat capacity method was used to model the phase change process. The method consists of integrating the latent heat and the sensible heat into a temperature-dependent property: the effective heat capacity, Cp_{eff} .

The effective heat capacity is constant and equal to the specific heat when the PCM is outside the phase change range. However, it varies when the PCM is within the phase change range, with values always higher than the specific heat, representing the latent heat exchange (Thonon et al., 2020).

The following assumptions were made:

- Contact thermal resistances are negligible.
- Density (ρ), thermal conductivity (k), and specific heat (Cp) are constant for all materials (Table 1). The effective heat capacity of the PCM depends on the temperature.
- Heat transfer is one-dimensional, due to the reduced thickness of the mortar-capsule assembly, compared to the heat exchange surface.

- Temperature distribution in the capsule is symmetric. The uniform air temperature in the insulated hotbox ensures the validity of this assumption. Under this hypothesis, only half of the capsule is modeled.

Table 1: Thermophysical properties of the materials

Material	ρ (kg/m ³)	k (W/m·K)	Cp (J/kgK)
Mortar	2194	1.4	780
Aluminum	2770	150	875
PCM	630	0.2	Cp_{eff} (T)

The boundary conditions are adiabatic walls for the top and bottom walls, symmetry condition for the symmetry axis and temperature boundary condition in the mortar surface. For this temperature boundary condition, the temperature measured in the tests is used.

The initial condition is that temperature of all cells in the domain equals T_o^{exp} at the beginning of the experiment. Uniform temperature distribution in the whole panel is ensured since thermal stabilization periods are performed prior to the solidification and the melting processes.

The output of the model is the surface heat flux \dot{q}^{num} . Figure 2 illustrates the simulation domain and the boundary conditions.

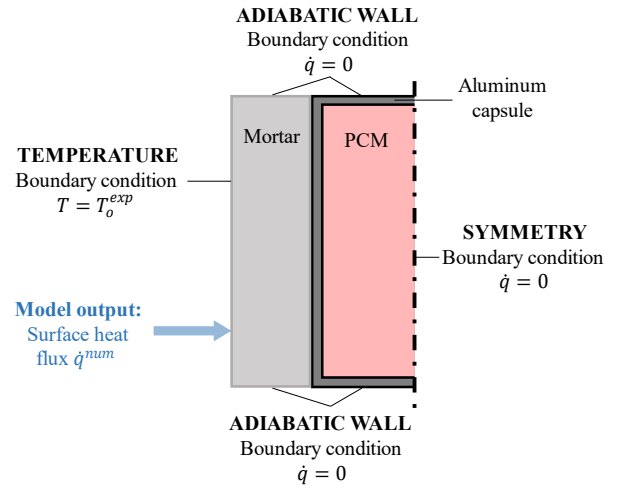


Figure 2: Simulation domain and boundary conditions

The PCM panel is modelled under two scenarios: using the effective heat capacity specified by technical datasheet, $Cp_{eff,dat}$, and using the effective heat capacity determined through the inverse method, $Cp_{eff,inv}$. Both are temperature dependent and have different values for solidification (S) and melting (M). This yields four effective heat capacity curves: $Cp_{eff,dat}^S$, $Cp_{eff,dat}^M$, $Cp_{eff,inv}^S$ and $Cp_{eff,inv}^M$. Figure 3 shows the different effective heat capacities, where it is observed that datasheet values are much greater than those determined through the inverse method.

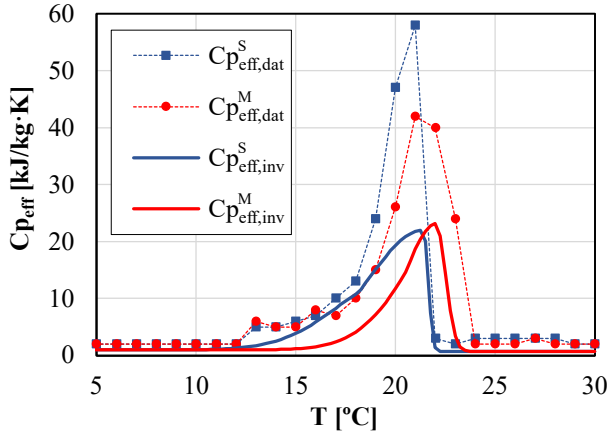


Figure 3: Effective heat capacity of RT21-HC

Results and Discussion

The analysis of the transient thermal behavior of the PCM panel is performed on the melting and solidification stages.

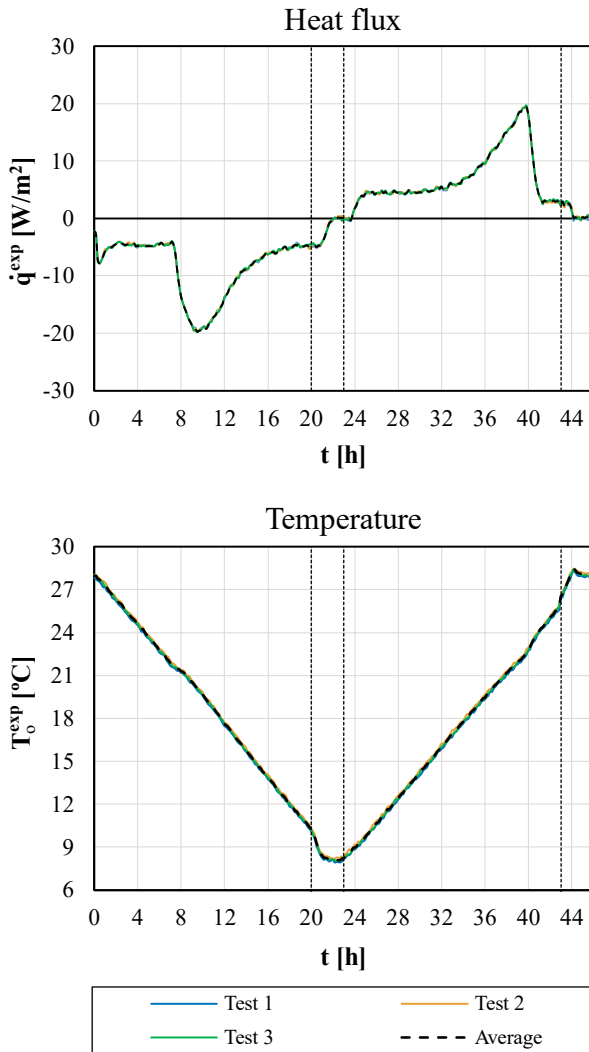


Figure 4: Experimental results: surface heat flux and temperature

Figure 4 presents the experimental results. Variability between the three tests is negligible. As such, the average T_o^{exp} and \dot{q}^{exp} are calculated as the mean value between the three tests at each time. The average T_o^{exp} is used as the input boundary condition in the model and the average \dot{q}^{exp} is used for comparing the experimental and the numerical results. Time intervals enclosed in the dashed lines correspond to the thermal stabilization periods.

Phase change periods are clearly identified in the heat flux curve. Constant values of \dot{q}^{exp} indicate sensible heat exchange, whereas the bell-shaped intervals with increased heat flux imply latent heat exchange. Negative heat flux means that the PCM solidifies, and positive heat flux represents the melting process.

Phase change is also observed in the temperature output. Sensible heat exchange is characterized by constant temperature variation rates (constant slope lines). The phase change occurs in the intervals where the temperature does not follow a linear tendency and subtle curves are observed.

Figure 5 shows the numerical results and compares them to the experimental results. The numerical heat flux calculated with the inverse method results, \dot{q}_{inv}^{num} , fits the experimental heat flux, both in sensible heat exchange and phase change periods. However, modeling the PCM with the datasheet properties leads to overestimating the heat flux, \dot{q}_{dat}^{num} . This is especially relevant during the phase change process, where the numerical heat flux is twice as much the experimental heat flux. During the sensible heat exchange periods, the error is also relevant: on average, \dot{q}_{dat}^{num} is 25 % higher than \dot{q}^{exp} . This means that if the datasheet properties were used to model the PCM panel properties on a building simulation software, relevant errors would be made on the estimation of the thermal attenuation achieved by the PCM.

The relative error of the numerical results based on the inverse method characterization, ϵ_{inv} , is lower than 10% both in melting and solidification. In contrast, the relative error of the numerical results using the technical datasheet, ϵ_{dat} , is approximately 50% in solidification and 80% in melting process (Table 2). Such high values indicate the lack of fitness of the numerical results if the effective heat capacity determined through traditional methods is employed.

Table 2: Relative error of the numerical results

Process	ϵ_{dat} (%)	ϵ_{inv} (%)
Solidification	49.14	6.12
Melting	80.57	8.91

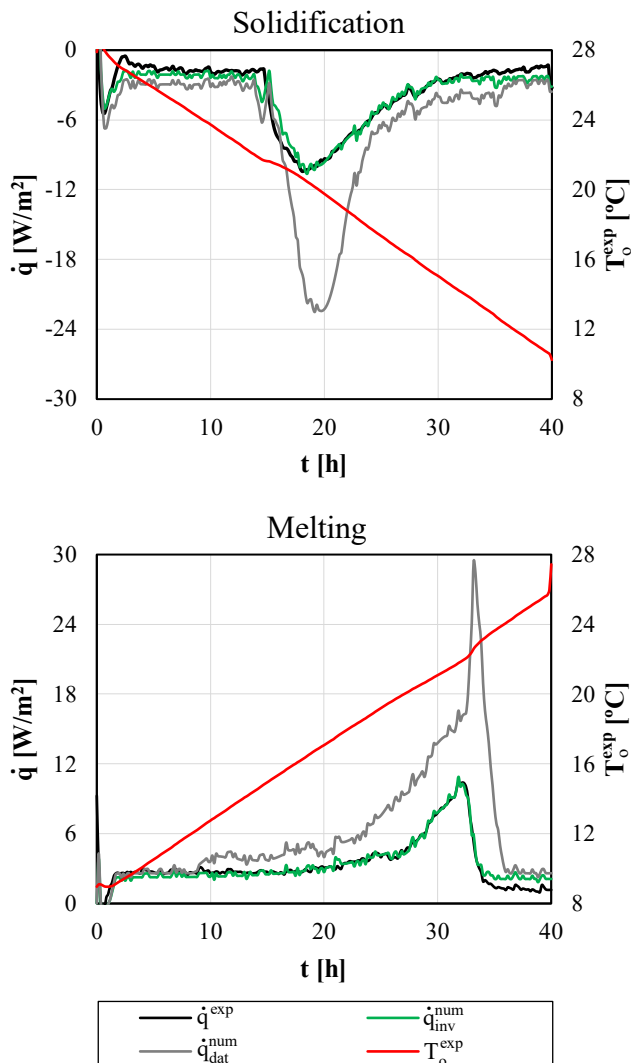
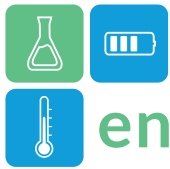


Figure 5: Numerical results of the model

Conclusions

This work demonstrates that PCM characterization must be performed with PCM quantities and temperature variation rates similar to their application. The model proves that when traditional characterization results are used, based on the analysis of small quantities, numerical results are inaccurate.

Mathematical models of building envelopes with macroencapsulated PCMs tend to overestimate the efficiency of the phase change mechanism if the datasheet properties are considered for the model.

The deployment of latent heat thermal energy storage in the building sector requires more specific PCM characterization methods. Although experimental studies of macroencapsulated PCMs in building envelopes endorse the potential of this technology, accurate mathematical models are a key factor to facilitate its implementation.

Acknowledgements

This work was supported by the Spain Ministry of Universities (FPU21/05062); the Spain Ministry of Science and Innovation (PID2021-128056OA-I00 and RED2022-134219-T); and FICYT (SV-PA-21-AYUD 2021 51328).

References

- Izquierdo-Barrientos, M. A., Belmonte, J. F., Rodríguez-Sánchez, D., Molina, A. E., & Almendros-Ibáñez, J. A. (2012). A numerical study of external building walls containing phase change materials (PCM). *Applied Thermal Engineering*, 47, 73–85. <https://doi.org/10.1016/j.applthermaleng.2012.02.038>.
- Jin, X., Hu, H., Shi, X., Zhou, X., Yang, L., Yin, Y., & Zhang, X. (2018). A new heat transfer model of phase change material based on energy asymmetry. *Applied Energy*, 212, 1409–1416. <https://doi.org/10.1016/J.APENERGY.2017.12.103>.
- Kuznik, F., Johannes, K., Franquet, E., Zalewski, L., Gibout, S., Tittlein, P., Dumas, J. P., David, D., Bédécarrats, J. P., & Lassue, S. (2016). Impact of the enthalpy function on the simulation of a building with phase change material wall. *Energy and Buildings*, 126, 220–229. <https://doi.org/10.1016/J.ENBUILD.2016.05.046>.
- Rathore, P. K. S., & Shukla, S. K. (2019). Potential of macroencapsulated PCM for thermal energy storage in buildings: A comprehensive review. *Construction and Building Materials*, 225, 723–744. <https://doi.org/10.1016/J.CONBUILDMAT.2019.07.221>.
- Rubitherm Technologies GmbH. (n.d.). Rubitherm - PCM RT-Line. Retrieved May 27, 2021, from <https://www.rubitherm.eu/en/index.php/productcategory/organische-pcm-rt>.
- Thonon, M., Fraisse, G., Zalewski, L., & Pailha, M. (2020). Towards a better analytical modelling of the thermodynamic behaviour of phase change materials. *Journal of Energy Storage*, 32, 101826. <https://doi.org/10.1016/J.EST.2020.101826>
- United Nations Environment Programme. (2022). 2022 Global Status Report for Buildings and Construction: Towards a Zero emission, Efficient and Resilient Buildings and Construction Sector. <https://www.unep.org/resources/publication/2022-global-status-report-buildings-and-construction>.



An analysis of energy storage policy in the UK (2000-2023): capturing key insights and lessons learned

Chris Harrison¹, Andrew Hutchinson², Arman Alahyari³, Tanuj Rawat³, Thomas Bryden⁴, Hui Yan⁵,
Andrew Forsyth⁵, Daniel J. Rogers⁴, Charalampos Patsios³, Dan Gladwin², Jonathan Radcliffe^{1,*}

1 University of Birmingham, Edgbaston, Birmingham, UK

2 University of Sheffield, Sheffield, UK

3 Newcastle University, Newcastle upon Tyne, UK

4 University of Oxford, Oxford, UK

5 University of Manchester, Manchester, UK

*Corresponding author e-mail: j.radcliffe@bham.ac.uk

Abstract

Energy storage has emerged as an important component of the UK's pathway to net zero, with a rapid increase in the deployment of electrical energy storage (EES) systems over the last decade. Through a systematic and wide-ranging review of energy policy, this article outlines the key policy developments that have enabled this and their impacts. We find an increasing emphasis placed on EES in the development of energy policy in the UK. However, the market dominance of batteries indicates the need to provide more support for alternative storage technologies that can provide further benefits. This work, conducted as part of the Energy Storage Integration for Net Zero (ESI4NZ) project, is intended to provide lessons for policy makers in other markets undertaking similar programmes of reform.

Keywords: Storage, Policy, Markets, UK, Great Britain

Introduction

For over a decade, and supported by government policy, private investments in renewable energy have driven an increase in generation from renewable sources in Great Britain (GB) (Figure 1). The need for flexibility technologies to support the deployment of renewable energy at scale has been recognised for over 20 years, e.g. (Royal Commission on Environmental Pollution, 2000). This includes the introduction of Demand Side Response (DSR) measures, increased interconnectivity with Europe and the deployment of Electrical Energy Storage (EES). However, policy support for such flexibility has come more recently.

Since 2015, there has been a growing increase in the amount of EES capacity on the British electricity grid (Figure 2). In addition to the reducing costs of storage, this increase in capacity has been partly enabled by an increasingly favourable policy and market framework. In this paper, an assessment of the policy landscape for EES in the UK is explored, to identify the key successes as well as considering the remaining policy challenges and opportunities. The article is of interest

for those seeking a summary of the developments in the UK and to policy makers in other markets considering similar reforms.

Methodology

To identify UK energy policies relating to EES technology, a systematic search of public sector websites has been conducted searching on the term "energy storage". Although the UK government retains responsibility for energy policy in GB, aspects of other policy areas that can impact deployment of EES have been devolved to constituent nations. The websites of the following organisations have therefore been searched:

- UK government
- Ofgem, the energy regulator
- National Grid Electricity System Operator (ESO)
- Distribution Network Operators (DNOs)
- Energy Networks Association (ENA)
- Devolved Governments (Welsh, Scottish)
- European Union



Search results were reviewed for their relevance and significance to electrical energy storage. Where policies were deemed to be of relevance, they have been recorded and assessed against a set of key criteria relating to energy storage (e.g. demonstration of technical feasibility, new markets). Based on publication dates, a comprehensive timeline of UK policies has been developed and will be published as part of future work for the ESI4NZ project. It is important to note that many of the policies that impact on storage are not necessarily *specific* to storage. The economic viability of EES to operate in any given electricity market can be impacted by the presence and viability of other technologies. Most evidently, policies for renewable energy (e.g. solar PV) can have implications on the need for and economic plausibility of storage. This can be extended to policies for (a) emissions reduction, (b) other flexibility technologies, (c) network infrastructure and (d) energy market structures. Such ‘indirect’ policies, which impact on EES, have been captured and analysed.

Results and Analysis

The ‘policy search’ conducted for this article identified over 650 different policy outputs. A review of these items found policies with varying degrees of relevance to storage (see Figure 3). Numerous types of policy have been identified (e.g. UK legislation, EU legislation, strategy documentation, market incentives etc). From analysis of the search results, storage policy in this article has been divided into three distinct periods; (a) 2000-2008, relative inaction on energy storage but a growing consensus on the need to act on climate change; (b) 2009-2017, an increasing recognition of the need for storage, with some fundamental changes to the market; (c) 2018-2023, accelerating storage policy development. These time periods are described in further detail below.

2000-2009: Building momentum for climate action

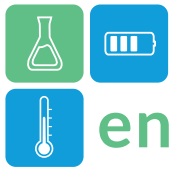
In this decade, UK (and EU) energy policy had only limited action or discussion around the role of EES in Britain. The absence of EES in policy discussion at this time is understandable; many of the issues that could be resolved by EES, such as managing generation from variable renewables, had yet to emerge. However, policies introduced in this period would have future implications for storage. This period was used to build the case for acting on climate change and creating a legislative framework that

could support this. Generally, an emphasis was placed on the need to (a) increase end-use efficiency and (b) deploy renewable energy systems. This is evidenced by pieces of key legislation that were introduced during this time. This included the EU Directive on Renewable Electricity (European Union, 2001) which (at that point in time) required the UK to meet 10% of its 2020 electricity consumption with renewables. In the UK, the Renewables Obligation (HM Government, 2002) was introduced to mandate the procurement of renewable electricity. The 2003 publication of the ‘*Energy White Paper*’ (HM Government, 2003) was a moment of key significance, targeting a 60% reduction in emissions by 2050. Around the same time, the electricity market in England & Wales was under-going a series of major reforms via the ‘NETA’ (New Electricity Trading Arrangements) programme (Ofgem, 2001). This included the introduction of the ‘Balancing Mechanism’ which remains a key market by which demand-supply parity is maintained (and, thus, one which energy storage assets may generate revenue). These changes would additionally be introduced into Scotland in 2005 (Ofgem, 2005), alongside further reforms, via the British Electricity Trading and Transmission Arrangements (BETTA). Interest specifically in EES from policy makers during this time was limited to consumer electronics (e.g. EU Battery Directive 2006/66/EC, EU's Waste Batteries and Accumulators Directive).

2009-2017: A shifting narrative on EES

The new coalition government formed in 2010 brought a further programme of market reforms to incentivise renewables. This included the introduction of the Contracts for Difference (CfD) and Capacity Market (CM) schemes via the Energy Act (2013) (HM Government, 2013b). These competitive auctions, which remain in operation, provide guaranteed revenue to successfully tendered generation projects. The CM has supported both pumped storage and batteries (National Grid ESO, 2023b).

The growth in renewables during the 2010s complemented by an increased discussion around the role of energy storage. In comparison with the prior decade, documentation and analysis from (HM Government, 2010) and (Scottish Government, 2010) began to note the importance of storage to the future electricity grid. This is significant when considering



its relative absence in government literature in the 2000s. In 2012, energy storage was included by the UK government as one of its identified ‘Eight Great Technologies’ and, as a direct result, was subject to an increased level of research funding support (HM Government, 2013a). As the decade progressed, the UK’s devolved governments were also increasingly noting the importance of storage (Scottish Government, 2016; National Assembly for Wales, 2016). The apparent changing view on the role of storage in the future electricity grid during this period is also suggested in consideration of the ESO’s ‘Future Energy Scenario’ analysis (Figure 4).

With increasing importance being placed on energy storage during the 2010’s, the UK’s energy policy actors moved towards the development of more targeted action. Part of this activity has included an exploration of grid-scale demonstration projects (UK Power Networks, 2014; UK Power Networks, 2017). Meanwhile, the Smart Grid Forum, created by the Department for Energy and Climate Change (DECC) and the energy regulator Ofgem, was introduced to advise the government on how to support the development of a more flexible electricity grid (Smart Grid Forum, 2014). This was followed by a series of reports considering the opportunities and challenges of flexibility in more detail (Ofgem, 2015; Department of Energy & Climate Change, 2015), and culminated in the ‘Smart Systems and Flexibility Plan’ (SSFP) (HM Government and Ofgem, 2017). The SSFP represents an important milestone for the UK energy storage sector, identifying key challenges and policy actions to overcome the barriers to market entry for storage. Indeed, 2017 can be considered a major turning point for EES in Britain. The launch of a consultation (Ofgem, 2017) to address regulatory issues associated with storage would seek to resolve previously raised concerns relating to ‘double charging’ and asset ownership; changes would subsequently be introduced to provide clarity on these issues. In R&D terms, meanwhile, the proposal (Walport, 2017) and launch (HM Government, 2017) of the Faraday Initiative has created a major source of financial support for driving UK research and industrialisation of battery storage.

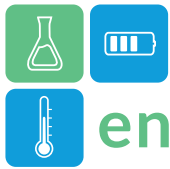
2018-2023: Improving fortunes for EES in the UK

The SSFP targeted improvements in the regulatory and market framework which would attract private

investment in storage and consequently lead to increases in EES capacity. Indeed, the late 2010’s to early 2020’s has seen a growth in storage projects (Figure 5). This has partly been enabled by the reduction in battery costs observed in the 2010s (Schmidt et al., 2017). However, this has additionally been supported by policy, such as reducing the burden of planning applications for larger storage projects (HM Government, 2020) and the creation of new market services (National Grid ESO, 2023c). These markets have been introduced partly to account for the changing grid requirements (and to capture the benefits of storage technologies; e.g. rapid response times). The new frequency regulation services in particular have enabled battery systems to generate revenue (Figure 6). However, auctions for these services have shown signs of saturation (e.g. falling auction clearing prices). Separately, the DNOs (in their transition to taking a more active role in the electricity market as Distribution System Operators) have been developing new markets to reduce local network constraints (Flexible Power, n.d.). Such new revenue opportunities are intended to support new forms of generation (e.g. storage) whilst overcoming emerging constraint issues. Meanwhile, the introduction of dynamic time of use (ToU) tariffs by some electricity suppliers (e.g. Octopus Energy, n.d.) have helped to improve the opportunities for residential storage although there is relatively poor visibility of this to the wider public (Ofgem, 2020). It is worth commenting, however, that academic studies have indicated that domestic battery systems remain unattractive from an investment perspective in GB (Gardiner et al., 2020; Zakeri et al., 2021). It is notable that, unlike in other nations (e.g. Germany, Italy), residential battery systems are not financially incentivised by the UK government.

Whilst there has been progress in bringing battery energy storage to the market, the need to develop solutions for ‘Long Duration Energy Storage’ (e.g. seasonal reserves) has been widely commented on (e.g. (The Royal Society, 2023)). The launch of the *Longer Duration Energy Storage Competition* (HM Government, 2021) is intended to support domestic innovation in this area but additional revenue opportunities will be necessary to create the economic case for the operation of such storage technologies.

Discussion



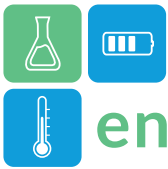
The UK has been successful in developing markets in which storage can operate. However, there remain some key issues for the future UK electricity system that storage can help resolve. As is apparent from the UK government's renewable energy planning database (Department for Energy Security and Net Zero, 2023), the vast majority (~99%) of new storage projects are in the form of electrochemical battery storage (Table 1). Other technologies which are known to provide different benefits have, as yet, struggled to achieve the same levels of interest from private investors. Perhaps the most well documented issue here relates to the need for seasonal storage reserves. It is widely acknowledged that current UK market conditions are insufficient to enable the levels of investment to store energy beyond relatively short periods of time (e.g. a day). The Scottish government have supported calls for the introduction of a funding mechanism for long duration storage for many years (Scottish Government, 2016; Scottish Government, 2023). Central UK government have more recently been consulting on appropriate approaches to support storage as part of its consultation for the Review of Electricity Market Arrangements (REMA), with cap-and-floor mechanisms identified as a plausible means for supporting long-duration flexibility options (HM Government, 2022). This is likely, therefore, to be the next major development in UK energy storage policy.

A less well discussed issue in policy literature is around the role that (very) short and medium-storage duration technologies can play. In the case of the former, it appears that technologies associated with very short-duration charge and discharge cycles (e.g. flywheels) will struggle to compete in the UK electricity market (Hutchinson and Gladwin, 2021). The economic favourability of batteries (and their ability to compete across multiple time-frames) may lock such technologies out of the market. In some sense, this may not represent a significant concern with the market arguably having found the 'best solution'. However, there are many 'externalities' that are not captured by the current market framework (e.g. access to critical minerals and their environmental impacts) which may be alleviated by the introduction of alternative technologies. Our policy analysis has highlighted a general absence of such considerations and the need for policy to capture such factors (and thus regulate or monetize the potential benefits of technologies that can provide short-duration market services).

Perhaps the most critical challenge for EES that has emerged in recent terms relates to grid connections. As a result of grid infrastructure constraints, some projects have connection delays of over a decade (Department for Energy Security & Net Zero and Ofgem, 2023), creating a major bottle-neck for the deployment of low-carbon generation and flexibility. The acceleration of grid reinforcements to overcome this issue in the long-term will be vital but, in the short-to-medium term alternative solutions must, and have, been sought. To enable faster connections, there have been efforts to provide novel solutions, including the introduction of non-firm connection agreements and so-called Active Network Management schemes (Energy Networks Association, 2015). Meanwhile, the on-going reform of the connections queue system is aimed at progressing the most viable projects in the connections queue (Department for Energy Security & Net Zero and Ofgem, 2023). The success of these reforms will be pivotal in further progressing the decarbonisation of the grid in the coming years.

In developing its energy policy framework, the market-based focus of the UK government has driven some success in driving the deployment of grid-scale battery storage. However, there are risks that such an approach may lead to undesirable consequences. The actions of private asset owners will inevitably place priority on revenue optimisation; in the current framework, this will revolve around taking part in multiple services (i.e. revenue stacking). Firstly, academic literature indicates that economic-based operation could lead to an increase in grid emissions (Pimm et al., 2021; A. Alahyari et al., 2023). This is a plausible eventuality without regulation to control charge-discharge timings (as is an approach introduced in other nations (Center for Sustainable Energy, 2023)). Further, the lack of incentive for storing energy beyond small time intervals (i.e. to take advantage of price differentials) and the lack of incentives for a harmonised charge-discharge scheduling may inevitably lead to shortages and sub-optimal storage deployment. To reduce the likelihood of this scenario, some commentators have proposed the need for a central authority to control the dispatch of storage assets to overcome this (i.e. to guide the charge-discharge process).

Conclusions



The introduction of climate targets and fundamental changes to the energy market since the 2000s has created opportunities for renewable energy. The resulting increase in solar and wind generation has naturally created more favourable conditions for storage. In recent years, and in an apparent acknowledgement of its importance to the UK, storage has received an increasing level of focus in policy debate. Central government (aided by other actors in the sector) have sought to remove many of the barriers to market entry. Whilst these interventions have helped to support the deployment of BESS, other EES technologies have struggled to benefit. More activity is anticipated, in particular for the development of long-duration energy storage but further consideration may be required to also support short-duration storage technology.

Figures and Tables

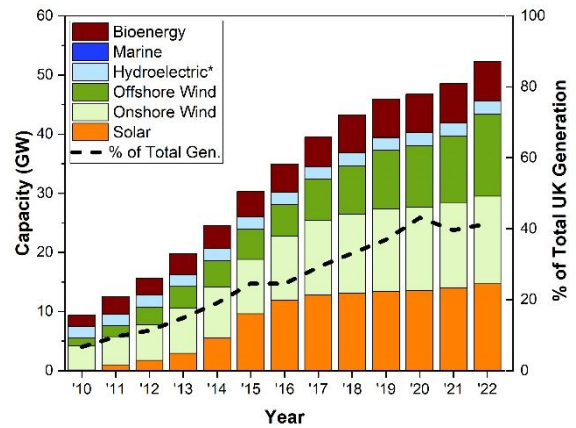


Figure 1 – Change in renewable energy capacity in the UK (2010–2022) (IRENA, 2024). *Hydroelectric capacity excludes pumped storage

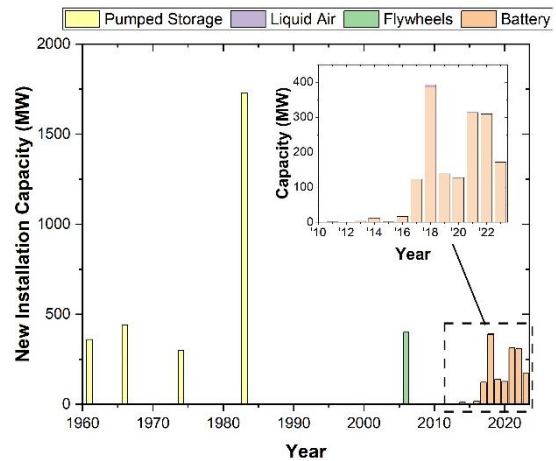


Figure 2 – New operational energy storage installations in the UK by capacity (1960–2023) - data to October 2023 (Department for Energy Security and Net Zero, 2023)

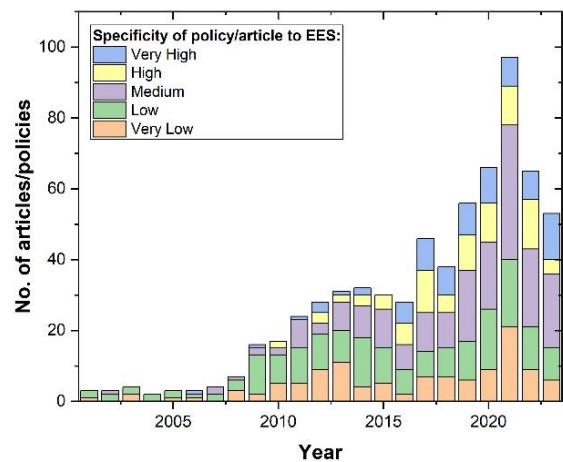


Figure 3 - Overview of policies studied for this article by year and specificity to EES (2000–2023)

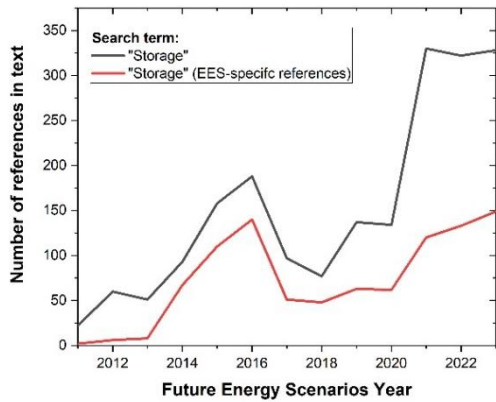
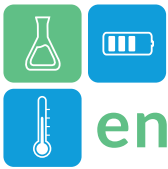


Figure 4 – Number of references to the word “storage” in the ESO’s Future Energy Scenarios publications by year (and the number of those references which are specific to EES rather than, for example, ‘carbon capture and storage’)

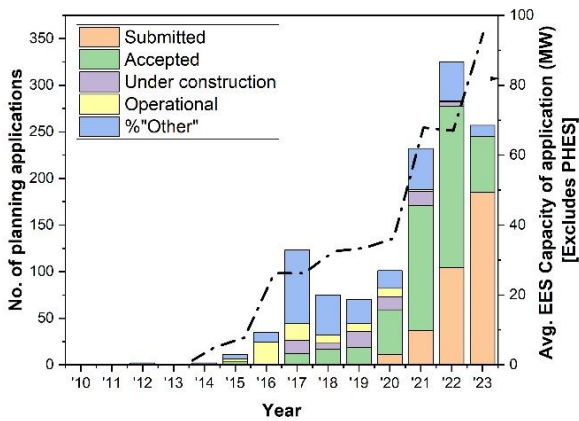


Figure 5 – Energy storage projects (2010-2023) by application date and status and average capacity of planned asset – data to October 2023 (Department for Energy Security and Net Zero, 2023)

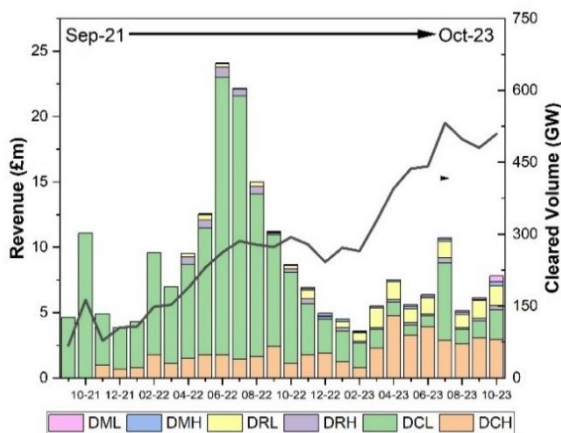


Figure 6 – Market data from UK frequency services Dynamic Containment Low & High (DCL, DCH), Dynamic Regulation Low & High (DRL, DRH) and Dynamic Moderation Low & High (DML, DMH) - data to October 2023 (National Grid ESO, 2023a)

Table 1 – Summary of EES projects in the Renewable Energy Database (Department for Energy Security and Net Zero, 2023). (BESS=Battery Energy Storage System, LAES=Liquid Air Energy Storage, CAES=Compressed Air Energy Storage, FESS=Flywheel Energy Storage System, PHEs=Pumped Hydroelectric Storage).

	No. of assets in operation (Capacity)	No. of projects ‘under construction’ (Capacity)
BESS	105 (1600 MW)	71 (2739 MW)
LAES	2 (5.4 MW)	0 (49.9 MW)
CAES	1 (Not specified)	1 (5 MW)
FESS	1 (400 MW)	0 (-)
PHEs	4 (2828 MW)	5 (3049.9 MW)

Acknowledgment

The work has been conducted as part of the UK Engineering and Physical Sciences Research Council (EPSRC)-funded Energy Storage Integration for a Net Zero Grid (ESI4NZ) project, grant reference EP/W02764X/1.

References

A. ALAHYARI et al. (2023) Assessing the impact of distributed energy storage in future distribution grids. In: *Energy Storage Conference 2023 (ESC 2023)*. pp. 112–118.

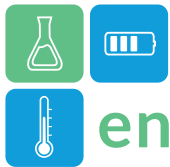
CENTER FOR SUSTAINABLE ENERGY, S.C.E.P.G. AND E.C.S.S. (2023) *Self-Generation Incentive Program handbook*.

DEPARTMENT FOR ENERGY SECURITY & NET ZERO and OFGEM (2023) *Connections Action Plan*.

DEPARTMENT FOR ENERGY SECURITY AND NET ZERO (2023) *Renewable Energy Planning Database: quarterly extract*. Available from : <https://www.gov.uk/government/publicatio>



- ns/renewable-energy-planning-database-monthly-extract [Accessed 12/01/24].
- DEPARTMENT OF ENERGY & CLIMATE CHANGE (2015) *Towards a Smart Energy System*.
- ENERGY NETWORKS ASSOCIATION (2015) *Good Practice Guide Active Network Management*.
- EUROPEAN UNION (2001) *Directive 2001/77/EC of the European Parliament and of the Council of 27 September 2001 on the promotion of electricity produced from renewable energy sources in the internal electricity market*.
- FLEXIBLE POWER *About Flexibility Services*. Available from : <https://www.flexiblepower.co.uk/about-flexibility-services> [Accessed 04/01/24].
- GARDINER, D. et al. (2020) Quantifying the impact of policy on the investment case for residential electricity storage in the UK. *Journal of Energy Storage*, 27, p. 101140.
- HM GOVERNMENT (2010) *2050 Pathways Analysis*.
- HM GOVERNMENT (2017) *Business Secretary to establish UK as world leader in battery technology as part of modern Industrial Strategy*. Available from : <https://www.gov.uk/government/news/business-secretary-to-establish-uk-as-world-leader-in-battery-technology-as-part-of-modern-industrial-strategy> [Accessed 04/01/24].
- HM GOVERNMENT (2013a) *Eight great technologies*. Available from : <https://www.gov.uk/government/publications/eight-great-technologies-infographics> [Accessed 03/01/24].
- HM GOVERNMENT (2013b) *Energy Act 2013*.
- HM GOVERNMENT (2003) *Energy White Paper*.
- HM GOVERNMENT (2021) *Longer Duration Energy Storage Demonstration (LODES) competition*. Available from : <https://www.gov.uk/government/collections/longer-duration-energy-storage-demonstration-lodes-competition> [Accessed 04/01/24].
- HM GOVERNMENT (2022) *Review of Electricity Market Arrangements Consultation Document*.
- HM GOVERNMENT (2020) *The Electricity Storage Facilities (Exemption) (England and Wales) Order 2020*.
- HM GOVERNMENT (2002) *The Renewables Obligation Order 2002*. London: UK Parliament.
- HM GOVERNMENT and OFGEM (2017) *Upgrading our energy system: smart systems and flexibility plan*.
- HUTCHINSON, A.J. and GLADWIN, D.T. (2021) Techno-Economic Analysis of a Flywheel Energy Storage System performing a Dynamic Frequency Response Service. *IEEE International Symposium on Industrial Electronics*, 2021-June, pp. 3–8.
- IRENA (2024) *IRENASTAT Online Data Query Tool*. Available from : <https://www.irena.org/Data/Downloads/IRENASTAT> [Accessed 12/01/24].
- NATIONAL ASSEMBLY FOR WALES (2016) *A Smarter Energy Future for Wales*.
- NATIONAL GRID ESO (2023a) *Dynamic Containment, Regulation and Moderation auction results*. Available from : <https://www.nationalgrideso.com/data-portal/dynamic-containment-data> [Accessed 12/01/24].
- NATIONAL GRID ESO (2023b) *Final Auction Report 2022 Four Year ahead Capacity Auction (T-4)*.
- NATIONAL GRID ESO (2023c) *Markets Roadmap*.
- OCTOPUS ENERGY *The 100% green electricity tariff with Plunge Pricing*. Available from : <https://octopus.energy/smart/agile/> [Accessed 04/01/24].
- OFGEM (2005) *BETTA User Guide*.
- OFGEM (2017) *Clarifying the regulatory framework for electricity storage: licensing*.
- OFGEM (2020) *Energy consumers' experiences and perceptions of smart 'Time of Use' tariffs*.
- OFGEM (2015) *Making the electricity system more flexible and delivering the benefits for consumers*.
- OFGEM (2001) *New Electricity Trading Arrangements (NETA) Programme*



enerstock

ENERSTOCK 2024
The 16th IEA ES TCP International Conference on Energy Storage
June 5–7, 2024
Lyon, France

- Implementation Phase Overview of Programme Progress.*
- PIMM, A.J. et al. (2021) Using electricity storage to reduce greenhouse gas emissions. *Applied Energy*, 282(PA), p. 116199.
- ROYAL COMMISSION ON ENVIRONMENTAL POLLUTION (2000) *Energy - The Changing Climate.*
- SCHMIDT, O. et al. (2017) The future cost of electrical energy storage based on experience rates. *Nature Energy*, 2(8), pp. 1–8.
- SCOTTISH GOVERNMENT (2023) *Call for UK Government to support pumped hydro storage through a market mechanism: letter to Prime Minister.* Available from : <https://www.gov.scot/publications/call-for-uk-government-to-support-pumped-hydro-storage-through-a-market-mechanism-letter-to-prime-minister/#:~:text=Pumped%20hydro%20storage%20is%20currently,of%20pumped%20hydro%20storage%20projects.> [Accessed 05/01/24].
- SCOTTISH GOVERNMENT (2010) *Energy Storage and Management Study.*
- SCOTTISH GOVERNMENT (2016) *Future of hydropower.* Available from : <https://www.gov.scot/news/future-of-hydropower/> [Accessed 03/01/24].
- SMART GRID FORUM (2014) *Smart Grid Vision and Routemap Smart Grid Forum.*
- THE ROYAL SOCIETY (2023) *Large-scale electricity storage.*
- UK POWER NETWORKS (2014) *Demonstrating the benefits of short-term discharge energy storage on an 11kV distribution network UK Power Networks.*
- UK POWER NETWORKS (2017) *Smarter Network Storage Close-Down Report.*
- WALPORT, M. (2017) *Reviewing the case for a new research institution to act as a focal point for work on battery technology, energy storage and grid technology.*
- ZAKERI, B. et al. (2021) Policy options for enhancing economic profitability of residential solar photovoltaic with battery energy storage. *Applied Energy*, 290, p. 116697.



An innovative, modular sorption storage system for residential applications

Franz Hengel^{1,*}, Roland Kerschenbauer¹, Waldemar Wagner¹

1AEE – INSTITUTE FOR SUSTAINABLE TECHNOLOGIES (research institute), Feldgasse 19,
Gleisdorf, Austria

*Corresponding author e-mail: f.hengel@aee.at

Abstract

In future energy systems volatile production will be dominant. Heating uses a major share of energy in energy systems. Therefore, the deployment of thermal energy storage is key to successful energy management. Sorption heat storage is a promising technology for long-term storage application.

The FlexModul project examines the potential to store heat in a closed fixed-bed sorption heat storage system on a long-term basis for application on household scale from a technical standpoint of view in the field or in field-realistic conditions. Therefore, extensive measurement equipment's to get knowledge of the system and components, e.g. distribution of heat in the sorption storage system during discharging and charging, heat transfer rates, etc. are installed in the demonstrator in the laboratory. A second demonstrator is installed in the field to get knowledge of a dynamic real system. With the collected data and the defined KPI's optimizations based on the system layout, operation strategies, component design, etc. are derived and reported to push the compact storage system toward market.

Keywords: zeolite 13X, sorption storage system, residential buildings, decentralized, peak-shaving

Introduction

In recent years, many countries have changed and adapted their energy policies according to the Paris Agreement in 2015. Germany, Austria, and Switzerland all have dedicated plans to phase out coal, nuclear power, and eventually even natural gas. Additionally, they heavily invest in renewable energy resources while needing to ensure a high level of stability and security. Germany's phase out of coal has just been confirmed, committing to gas-powered plants, which are ready to run on hydrogen. Switzerland has recently committed to a 2050 net-carbon-zero strategy, while Austria is targeting 2040 net-zero emissions. (OECD, 2021 & OECD, 2022 & Seitz et al., 2022)

To give a contribution to the above described strategies the overall aim of the project FlexModul is to develop and demonstrate an innovative, modular and compact sorption storage system which is i) easy to scale due to its modular design and ii) easy to adapt to different applications in the heating as well as electricity sector and therefore shows the potential of thermal storages as a cross-section technology that significantly enhances the flexibility of the complete energy system and substantially decrease CO₂ emissions. The versatile range of applications of sorption storages will be investigated and two use cases will be demonstrated a) seasonal storage of solar energy for a single-family

house, b) Power-to-Heat (P2H) storage for daily storage of fluctuating PV or CHP electricity integrated in a building.

Based on the goals of the project the present publication focuses on the highlight of the innovative and flexible part of the system, the design of the components, the optimized operation of the storage system, and reports the challenges of the compact storage technology for the demonstrations.

Methodology/System description

The innovative sorption storage system was designed, dimensioned, constructed and initially set up and commissioned in the laboratory as part of the national project FlexModul. The core component is the sorption storage tank that is used for domestic application based on the adsorption / desorption principle.

Based on Yu et al. (2013) the general equation of the sorption process can be written as formula (1). There the participants of the sorption process are displayed, where A is the sorbent, B is the sorbate, the combination of A/B is called working pair, m and n are the mole numbers and ΔH (J) is the enthalpy, or the energy available to the user.

$$A \times (m + n) + \Delta H \Leftrightarrow A \times mB + nB \quad (1)$$

Using this principle long-term storages can be used nearly heat loss free, as for the system.

Figure 1 shows the FlexModul system with a high temperature storage (HT-S) including an electric heater, two sorption storage tanks (S1 and S2), the evaporator and condenser with the water reservoir (C/E) and the heat pump system for the low temperature source (HP/LT). The C/E is connected via a steam line to transfer the sorbat in case of the adsorption process to the sorption storage tanks, S1 or S2. The C/E is also connected via the hydronic pipes to transfer heat to another component in case of condensing during the charging process. However, during the adsorption process water is adsorbed at the sorbents, zeolite 13 X and release heat to the hydronic system via a heat exchanger HX 3 that is used to supply for space heating (SH) or domestic hot water (DHW). Either S1 can be discharged for SH or DHW or S2 depending on the needed energy and system control strategy. The system can be easily extended by adding additional sorption storage tanks (S3, S4, etc.). The heat pump as source supplies the C/E to evaporate the water in the system and drive the adsorption process.

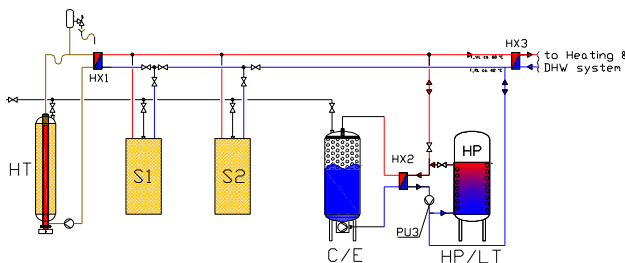


Figure 1: Hydronic scheme of the whole FlexModul system

On the other hand, during the charging process the HT-S is used and dried out with the electrical heater (EH) driven e.g. by renewable energy source like a PV system, hydro power plant, etc. During the charging process the EH heats up the zeolite in the HT-S up to 250 °C. During and after the end of the charging process the HT-S releases sensible heat that is used for S1 or S2 or stored in C/E or HP/LT depending on the control logic. Or can be used directly for SH or DHW. In case of charging of S1 or S2 the heat from the HT-S is transferred to the according sorption storage for preconditioning, and begins with the charging process by opening the vacuum valves e.g. between HT-S and S1 for the transition process driven by the pressure as force. This is done until equilibrium is reached. The charging process of the HT-S starts from new on until it is fully charged (dried out of zeolite). This cycle is

done until S1 or S2 is fully charged again or until renewable energy sources are not available anymore. The storage is designed for a storage capacity of around 180 kWh (1000 kg of zeolite 13X material as sorbent) but can be extended by using additional sorption storage tanks (S3, S4, etc.).

Figure 2 shows a picture of the real system in a reversed arrangement, i.e. the HT-S is on the right-hand side and the heat pump system behind the C/E and S1 and S2 on the left-hand side. To work with low evaporation temperatures the system is evacuated and tested to be tight for the application. Therefore, the vacuum evacuation pump is connected to the system to the right-hand side.



Figure 2: Real demonstrator in the laboratory at AEE INTEC (high temperature Storage to the right followed by sorption storage S1 and S2 and condenser/evaporator to the left and the heat pump behind the C/E

The sorption storage system was assembled in the laboratory at AEE INTEC and equipped with measurement equipment to get knowledge of the system's performance. Figure 3 shows the temperature sensors in the sorption storage tanks where in total 8 sensors in different heights in vacuum were installed. Additional to the temperature sensors in the vacuum two pressure transmitters are installed in the steam pipe to determine the condition in the system for each storage by using temperature and pressure at steady-state conditions. Also, with the measurement equipment the state of charge of each sorption storage tank can be calculated. Besides the mentioned sensors further sensors are installed to determine the behaviour as well as the performance of the total FlexModul system. These are:

- 8x temperature sensors in vacuum in S1 and S2 type Pt100 class A
- 2x pressure transmitter in the steam line Endress+Hauser from 0-10 mbar and 0-300 mbar
- 4x temperature sensors at the surface of HT-S and S1 and S2 under insulation to calculate the heat losses of the storages with a Pt100, class A
- 3x Heat meters $q_p = 1,5 \text{ m}^3/\text{h}$ from Techem. at SH/DHW, source and sensible heat during charging process to measure temperature, volume flow rate, heating energy and power
- 4x temperature sensors in the hydronic system of S1 and S2 to measure supply and return temperature
- 2x temperature sensors in the source circuit for evaporation in the C/E
- pressure meters for safety reason

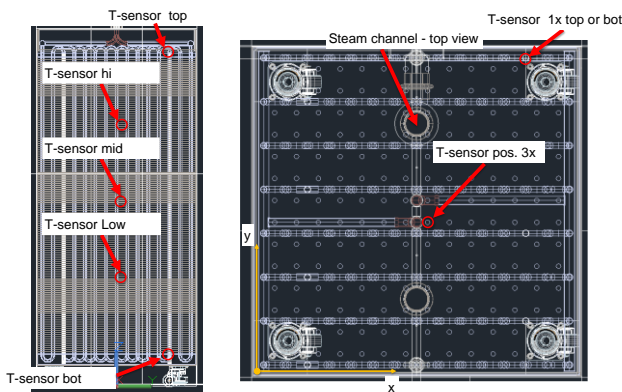


Figure 3: Temperature sensor positions in S1 and S2 to determine the dynamics of diffusion in the tank, side view to the left and top view to the right

Figure 4 and Figure 5 summarizes the mentioned process in a process flow chart, where Figure 4 indicates the operation process for charging of the total system, by using e.g. solar energy or Power-to-Heat (P2H) from a PV system especially during availability and increase the share of renewable energy. As to maximize the efficiency of the system also the sensible heat is stored and can be used for further purposes. On the other hand, Figure 5 shows on the right-hand side the process for adsorption of the system and release the heat for domestic hot water or space heating on demand.

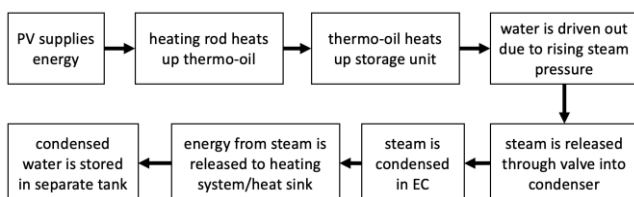


Figure 4: Charging process flow diagram of the FlexModul system

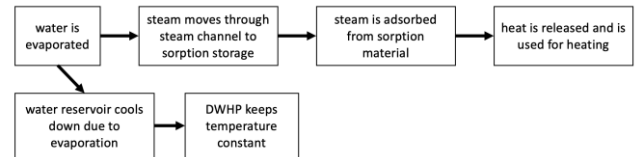


Figure 5: Charging process flow diagram of the FlexModul system

The obtained findings from the laboratory tests will be transferred to the demo sites and will be tested in real field conditions in the year 2024 that is at the moment on-going. Also, the integration strategy in the field is documented and will be optimized.

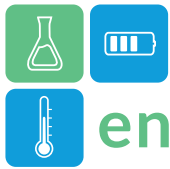
Results and Discussions

The results are derived from the measurements in the two demonstrators at the laboratory with an extensive test strategy and in the field on realistic conditions. It will give answers to the following questions, which are worked out in the next few months until May 2024 to present it on the ENERSTOCK 2024 conference:

- What is the heating capacity of one sorption storage system during SH applications?
- What energy can be withdrawn for one Sorption storage module under different pre-/conditions?
- What is the dynamic of S1 or S2 during the discharging process as well as for the charging process?
- What is the performance of the system by using the sensible heat too?
- What is the performance at different temperature lifts (evaporation temperature to supply temperature for SH/DHW)?
- Assessment of the techno-economic view for the whole FlexModul system?
- Which market can be addressed by the innovative FlexModul system?

Conclusion

Finally, the conclusions of the project are derived from the measurements of the FlexModul system in the field or in field-realistic operation, and assessed with the defined KPI's or questions especially for techno-economic evaluation. The focus is to push the innovative, modular, decentralized seasonal storage system toward market and to also give useful hints for the design, commissioning and field operation of such a system.

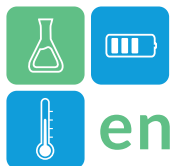


Acknowledgment

The RTI initiative Energy Model Region by the Climate and Energy Fund is carried out with research and environmental funding made available by the Austrian Research Promotion Agency (FFG) and Kommunalkredit Public Consulting (KPC) under the FFG project number 880777 in cooperation with the Green Energy Lab (GEL).

References

- Maresch B. F. (2023): Techno-economic assessment of the application of sorption heat storage in single-family houses; Master thesis during the project FlexModul, Montan Universität Leoben, Chair of Economic- and Business Management, Austria
- OECD (2021): Regional Outlook 2021 - Country notes, Austria, Progress in the net zero transition. oecd.org. URL: <https://www.oecd.org/regional/RO2021%20Austria.pdf> (Retrieved: 03.01.2024)
- OECD (2022): Nuclear Energy Agency (NEA) - Achieving Net Zero Carbon Emissions in Switzerland in 2050: Low Carbon Scenarios and their System Costs. oecd.org. URL: https://www.oecd-nea.org/jcms/pl_74877/achieving-net-zero-carbon-emissions-in-switzerland-in-2050-low-carbon-scenarios-and-their-system-costs (Retrieved: 03.01.2024).
- Seitz, C.; Carrel, P.; Eckert, V. Germany's biggest power producer RWE to phase out coal by 2030 | Reuters. Reuters. URL: <https://www.reuters.com/business/sustainable-business/rwe-aims-phase-out-coal-by-2030-2022-10-04/> (Retrieved: 03.01.2024).
- Yu, N.; Wang, R. Z.; Wang, L. W. (2013): Sorption thermal storage for solar energy. In: Progress in Energy and Combustion Science, Vol. 39, No. 5, pp. 489–514.



Assessing Zeolite Imidazolate Frameworks as Thermal Energy Storage Materials

Ciara Byrne^{1,2,*}, Katja Vodlan³, Connor Hewson⁴, Paul Iacomi⁴, Amalija Golobič³, Nataša Zabukovec Logar^{1,2}

1 National Institute of Chemistry, 1000 Ljubljana, Slovenia.

2 University of Nova Gorica, 5000 Nova Gorica, Slovenia.

3 University of Ljubljana, 1000 Ljubljana, Slovenia.

4 Surface Measurement Systems, London, HA0 4PE, United Kingdom

*Corresponding author e-mail: ciara.byrne@ki.si

Abstract

Zeolitic imidazolate frameworks (ZIFs) are comprised of transition metal ions (Zn) and imidazolate linkers. Due to their properties (large surface areas, suitable pore size distribution and structure stability), ZIFs have great potential for adsorptive separation and storage applications. Two ZIF structures (ZIF-71 and ZIF-93) with similar porosity but different functional groups on the framework have been investigated for thermal energy storage application, with water as the adsorbate. The ZIF-71 and ZIF-93 samples were successfully prepared by conventional solvothermal synthesis as well as greener mechanochemical approaches. The research shows that one of the two studied materials, ZIF-93, exhibits a high energy storage potential, due to its high water uptake capacity, high sorption enthalpies and high hydrothermal stability.

Keywords: ZIF-93; ZIF-71; water uptake; desorption enthalpy; green synthesis

Introduction

The increasing demand of heating/cooling is of grave concern due to the ever increasing population. Since energy for heating and cooling represents up to 50% of world final energy consumption, there has been an increased interest in finding environmentally friendly methods for the optimization of heat supply/demand. One method that addresses this issue and uses renewable energy is Thermal Energy Storage (TES), which uses the reversible chemical reactions and/or sorption processes of gases in solids or liquids. One major benefit of using this method is that it only shows an insignificant amount of heat loss while reaching a considerably higher energy storage density.

Sorption-based thermal energy storage can be examined using traditional adsorbents (*e.g.* zeolites) or innovative adsorbents (*e.g.* metal-organic frameworks (MOFs)).(Henninger *et al.*, 2017; Ristić and Logar, 2019) One of the subgroups of MOFs is Zeolitic imidazolate frameworks (ZIFs), which are comprised of transition metal ions (Zn, Co, etc.) and imidazolate linkers.(Ban *et al.*, 2016) ZIFs are structured similarly to zeolites, where the metal ion replacing the Si/Al and the imidazolate linker replacing the O atoms. ZIFs are considered to be highly stable. Due to their properties, including ordered porous structures and possibility to shape them in glass-like monoliths, ZIFs also have

been proposed as supports for adsorptive separation applications.(Zhou *et al.*, 2018) In spite of a great potential, the reports on the optimization of ZIF for heat storage and allocations applications are still scarce. Furthermore, their large-scale application is limited by the absence of low-cost mass production, as well as the lack of sustainable synthesis routes, that would lower the environmental impact of the ZIF preparation.(Li *et al.*, 2022) Most of the stable ZIFs are synthesized via solvothermal synthesis, which requires higher temperatures and can take up to 72 h or more. Large amounts of *N,N*-dimethylformamide (DMF) are often used as well, as it is decomposed during the synthesis in a way to stimulate the ZIF formation. As DMF is known to be toxic and carcinogenic, a great effort has been made to implement greener solvents to the ZIF synthesis process and lower its impact on the environment.(Škrjanc, Byrne and Zabukovec Logar, 2021) Additionally, the search for a DMF replacement has gained greater interest as a result of the EU heavily restricting or in some cases completely banning the use of DMF as of this year (2023).

The ZIFs studied were selected based on their reported pore sizes and pore capacities.(Phan, Christian J. Doonan, *et al.*, 2010) ZIF-71 and ZIF-93 were selected as they have large pore entrances and pore/cage capacities (Table 1). (Banerjee *et al.*, 2008; Morris *et*

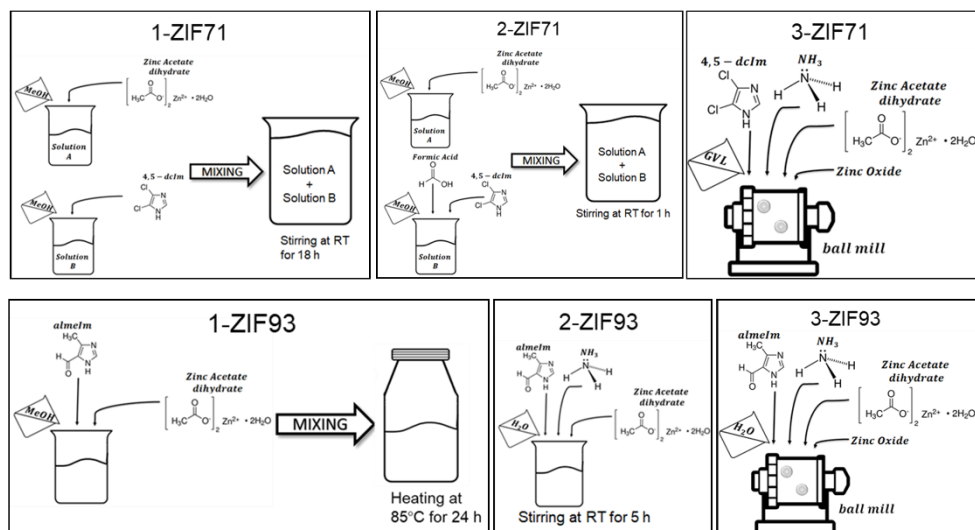
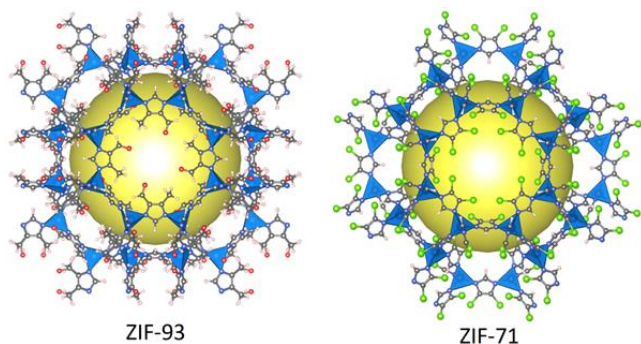


Figure 1: Synthesis methods for ZIF-71 and ZIF-93

al., 2010; Phan, Christian J Doonan, *et al.*, 2010) Both ZIFs have a RHO topology (Figure 1). DMF was successfully replaced with methanol in the synthesis of ZIF-71 and ZIF-93. (Ramos-Fernandez *et al.*, 2018; Liu and Yuan, 2019) However to the best of our knowledge ZIF-71 and ZIF-93 have not been successfully synthesized via mechanochemical synthesis, which is also considered a green synthesis approach, since we can exclude solvents from the synthesis.

Table 1. Pore entrance size, the pore/cage capacity and topology for the two ZIFs examined.

ZIF	Pore entrance [Å]	Pore capacity [Å]
ZIF-71	4.2	16.5
ZIF-93	3.6	17.9



The RHO topology of ZIF-93 and ZIF-71. ZnN₄ tetrahedra are shown in blue, while the yellow spheres indicate empty space in the cage. Linkers are shown in ball and stick representation (H in pink, C in grey, N in blue, O in red and Cl in green).

Therefore, this presentation will discuss the green synthesis of ZIF-71 and ZIF-93 and the impact that this has on the structural properties and their heat storage potential.

Methodology

ZIF-71 and ZIF-93 were synthesised using three different methods: as per literature, using an optimised precipitation method and *via* ball milling (see Figure 2). Both ZIFs used Zinc acetate dihydrate as the zinc precursor. The linkers used were 4,5-dichloroimidazole for ZIF-71 and 4-methyl-5-imidazolecarboxaldehyde for ZIF-93. Methanol, water or γ -valerolactone (GVL) were used as the solvent depending on the synthesis method (see Figure 2). Additionally, the optimised precipitation method and the ball milling synthesis used formic acid or ammonia in small quantities to act as a catalyst. The samples that required activation were heated in a vacuum oven at 150°C overnight. The structural properties of the ZIF samples were determined using PXRD, TGA and N₂ physisorption. The water uptake (mmol) was examined using a DVS (Surface Measurement Systems). The isotherms were collected at 25°C in the relative pressure range from 0 – 0.9. Finally, the ZIFs were analysed with DSC to determine the desorption enthalpy. The ZIFs were placed in a desiccator with water-saturated solution of NaCl (rh = 75%) for 1-5 days prior to DSC analysis.

Results and Discussion

Figure 3 shows the PXRD for all 6 samples synthesised, the calculated ZIF-71 and the calculated ZIF-93 patterns. The formation of ZIF-71 and ZIF-93 in the synthesised samples was confirmed by comparing them with the calculated patterns. As there were no additional peaks in any of the samples they were shown to be phase pure. PXRD was performed after activation to show the structure remained intact after the process.

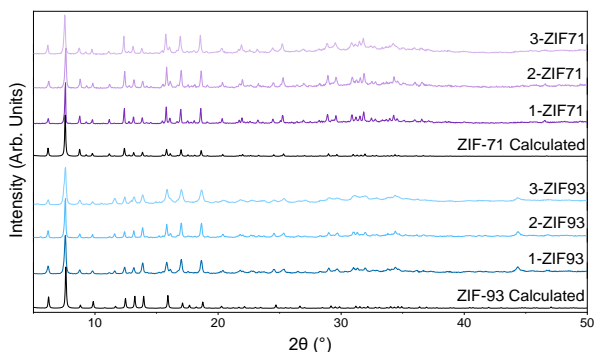


Figure 3: XRD of the calculated patterns and all as-synthesised samples for ZIF-71 and ZIF-93

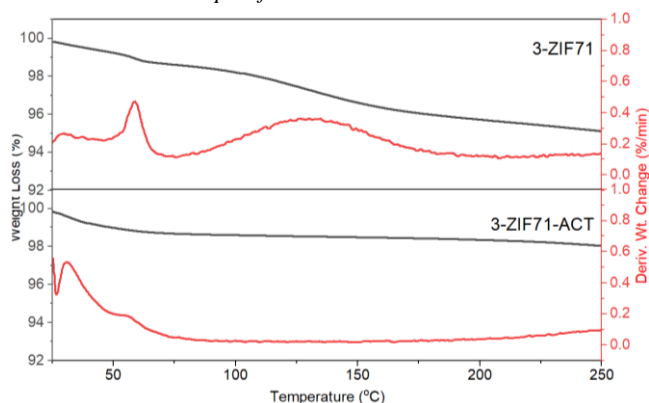


Figure 4: TGA of 3-ZIF71 before and after activation.

TGA was primarily used to determine if the ZIF samples required activation, though what temperature the structure collapsed at was also of interest. 1-ZIF71 and 2-ZIF71 were the only samples that did not require activation based on the TGA. All other samples needed activation. As an example, Figure 4 shows the TGA for 3-ZIF71 before and after activation. Any peaks or mass loss before 100°C are generally assigned to vapours/solvent that is on the surface of the sample. The peak/mass loss that can be seen in Figure 3 at temperatures between 100–200°C (top TGA) is a result of solvent in the pores and therefore the sample needed to be activated.

Nitrogen physisorption was completed to determine the specific surface area. This ranged from 789–1008 m²/g for ZIF-71 and 615–1239 m²/g for ZIF-93 (see Figure 5). Most of these values exceed results from previously published studies, with past studies showing 604 m²/g – 864 m²/g for ZIF-93 and 652 m²/g – 782 m²/g for ZIF-71. (Morris *et al.*, 2010; Japip *et al.*, 2014; Li *et al.*, 2014; Gao *et al.*, 2018; Ramos-Fernandez *et al.*, 2018; Ding *et al.*, 2023; Luque-Alled *et al.*, 2023) It is worth noting that the two samples that are in the previously published range for both ZIFs are the ball-milled samples.

Figure 5 also shows the water uptake for all samples. The water uptake for all ZIF-71 samples ranged between 0.2–0.4 mmol/g (0.3–0.65%). Surprisingly, 3-ZIF71, which is the ball mill sample and had the lowest specific surface area, had the highest water uptake. For ZIF-93, the water uptake ranged from 8.2–15.3 mmol/g (14.7–27.5%). The modified precipitation method showed the highest uptake and specific surface area.

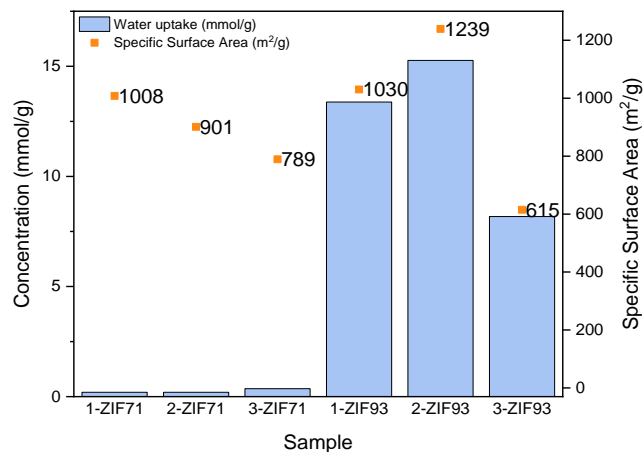


Figure 5: Water uptake at 0.8 P/P₀ with the specific surface area for all samples

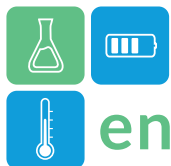
Finally, DSC was used to determine the heat storage potential of all samples. In all cases, it was not possible to get any readings for ZIF-71. On the other hand, the best performing ZIF-93 sample showed a desorption enthalpy that reached 503 J/g. This is slightly lower than the currently best performing ZIF (ZIF-90) by ~40 J/g, but has been proven to be more hydrothermally stable than ZIF-90. (Byrne *et al.*, 2021) This was confirmed by XRD measurements of ZIF-93 samples after water sorption studies.

Conclusions

In this study, ZIF-71 and ZIF-93 were first synthesised using solvothermal and mechanochemical method. Our study showed the successful preparation of ZIF-93 samples at room temperature, by using water as a solvent or by following the mechanochemical route. The thermal energy storage potential was assessed by using DCS based desorption enthalpy measurements, which revealed ZIF-93 to have good heat storage potential over a longer period of time, also when prepared by greener mechanochemical approaches.

Acknowledgment

This research was funded by Slovenian Research Agency Research program P1-0021. The authors would like to thank Aljaž Škrjanc for assistance with the ball mill synthesis and Edi Kranjc for PXRD measurements.



References

- Ban, Y. *et al.* (2016) ‘Dual-ligand zeolitic imidazolate framework crystals and oriented films derived from metastable mono-ligand ZIF-108’, *Microporous and Mesoporous Materials*, 219, pp. 190–198. doi: 10.1016/j.micromeso.2015.08.013.
- Banerjee, R. *et al.* (2008) ‘High-throughput synthesis of zeolitic imidazolate frameworks and application to CO₂ capture’, *Science*, 319(5865), pp. 939–943. doi: 10.1126/science.1152516.
- Byrne, C. *et al.* (2021) ‘Evaluation of ZIF-8 and ZIF-90 as heat storage materials by using water, methanol and ethanol as working fluids’, *crystals*, 11(11), p. 1422. doi: 10.3390/cryst11111422.
- Ding, Y. *et al.* (2023) ‘Amine group graft ZIF-93 to create gas storage space to improve the gas separation performance of Pebax-1657 MMMs’, *Separation and Purification Technology*, 309(December 2022), p. 122949. doi: 10.1016/j.seppur.2022.122949.
- Gao, M. *et al.* (2018) ‘A combined experimental-computational investigation on water adsorption in various ZIFs with the SOD and RHO topologies’, *RSC Advances*, 8(69), pp. 39627–39634. doi: 10.1039/c8ra08460b.
- Henninger, S. K. *et al.* (2017) ‘New materials for adsorption heat transformation and storage’, *Renewable Energy*, 110, pp. 59–68. doi: 10.1016/j.renene.2016.08.041.
- Japip, S. *et al.* (2014) ‘Highly permeable zeolitic imidazolate framework (ZIF)-71 nano-particles enhanced polyimide membranes for gas separation’, *Journal of Membrane Science*, 467, pp. 162–174. doi: 10.1016/j.memsci.2014.05.025.
- Li, H. *et al.* (2022) ‘Green Synthesis of Zeolitic Imidazolate Frameworks: A Review of Their Characterization and Industrial and Medical Applications’, *Materials*, 8(2), pp. 775–784. doi: 10.1016/j.gee.2021.09.003.
- Li, Y. *et al.* (2014) ‘ZIF-71 as a potential filler to prepare pervaporation membranes for bio-alcohol recovery’, *Journal of Materials Chemistry A*, 2(26), pp. 10034–10040. doi: 10.1039/c4ta00316k.
- Liu, X. and Yuan, J. (2019) ‘Molecular Simulation of bioalcohol purification in ZIF-1, -3, -7 and -9 frameworks’, *IOP Conference Series: Earth and Environmental Science*, 358(5). doi: 10.1088/1755-1315/358/5/052069.
- Luque-Alled, J. M. *et al.* (2023) ‘Organic solvent-free fabrication of thin film polyamide/zeolitic imidazolate framework membranes for removal of dyes from water’, *Chemical Engineering Journal*, 470(June). doi: 10.1016/j.cej.2023.144233.
- Morris, W. *et al.* (2010) ‘A combined experimental-computational investigation of carbon dioxide capture in a series of isorecticular zeolitic imidazolate frameworks’, *Journal of the American Chemical Society*, 132(32), pp. 11006–11008. doi: 10.1021/ja104035j.
- Phan, A., Doonan, Christian J., *et al.* (2010) ‘Capture Properties of Zeolitic Imidazolate Frameworks’, *Accounts of Chemical Research*, 43(1), pp. 58–67. Available at: <http://www.ncbi.nlm.nih.gov/pubmed/19877580>.
- Phan, A., Doonan, Christian J., *et al.* (2010) ‘Synthesis, structure, and carbon dioxide capture properties of zeolitic imidazolate frameworks’, *Accounts of Chemical Research*, 43(1), pp. 58–67. doi: 10.1021/ar900116g.
- Ramos-Fernandez, E. V. *et al.* (2018) ‘A water-based room temperature synthesis of ZIF-93 for CO₂ adsorption’, *Journal of Materials Chemistry A*, 6(14), pp. 5598–5602. doi: 10.1039/c7ta09807c.
- Ristić, A. and Logar, N. Z. (2019) ‘New composite water sorbents CaCl₂-PHTS for low-temperature sorption heat storage: Determination of structural properties’, *Nanomaterials*, 9(1). doi: 10.3390/nano9010027.
- Škrjanc, A., Byrne, C. and Zabukovec Logar, N. (2021) ‘Green Solvents as an Alternative to DMF in ZIF-90 Synthesis’, *Molecules (Basel, Switzerland)*, 26(6). doi: 10.3390/molecules26061573.
- Zhou, C. *et al.* (2018) ‘Metal-organic framework glasses with permanent accessible porosity’, *Nature Communications*, 9(1), pp. 1–9. doi: 10.1038/s41467-018-07532-z.



Bench-scale long-term phase change material analysis for thermal energy storage design

Saman Nimali Gunasekara^{1,*}, Landry Cogrel², Oxana Samoteeva¹, Ana Maria Correa Bernal¹, Marcel Glomba³, Esther Kieseritzky³, Tilman Barz⁴, Fabrizia Giordano⁴, Samer Sawalha¹, Justin Ningwei Chiu¹
1 KTH Royal Institute of Technology, Energy Technology, Brinellvägen 68, 100 44, Stockholm, Sweden
2 École Nationale Supérieure d'Ingénieurs de Poitiers, Ingenieur Energetique et Environnement 2, Poitiers, France

3 Rubitherm Technologies GmbH, Imhoffweg 6, D-12307 Berlin, Germany

4 AIT Austrian Institute of Technology GmbH, Giefinggasse 2, 1210 Vienna, Austria

*Corresponding author e-mail: saman.gunasekara@energy.kth.se

Abstract

Thermal energy storage is indispensable to realize carbon neutral energy systems, enabling flexible coupling of thermal and power sectors with e.g. heat pumps. Phase change materials (PCMs) are an attractive compact thermal energy storage (TES) counterpart, to move beyond the state-of-the-art in sensible TES. Although many PCM intrinsic property data exist, their thermal cycling data at application-representative volumes are scarce. To address this gap, here, two bio-based PCMs: RT57HC and RT60HC were analysed in a bench-scale (~44 l) shell-and-tube PCM-TES system respectively for 27 and 53 complete cycles, between 35-80 °C. The results show quite consistent TES capacity. Where, the maximum difference between the average storage capacity and each cycle for heating and cooling was only 0.5% and 0.5% for RT57HC and 0.8% and 0.3% for RT60HC. Both PCMs show no supercooling, and only 6-8 °C maximum hysteresis, making them ideal candidates for the considered PCM-TES applications.

Keywords: Phase change material (PCM), Bench-scale, Thermal energy storage (TES), Long-term cycling

Introduction

With around 50% of global final energy use resolving into heating and cooling (REN21, 2019), thermal energy storage (TES) is indispensable in realizing carbon-neutral energy systems. Phase change materials (PCMs) are a compact TES alternative with competitive advantages over the less compact sensible TES materials and the less developed thermochemical TES materials (TCMs) (Gunasekara, et al., 2021).

The project [HYSTORE](#) (Hybrid services from advanced TES systems) works on developing and operating PCM and TCM-based TES installations coupled with heat pumps in real demonstration sites, for flexible sector coupling (FSC) of thermal and electrical systems.

Decades of numerous material-level (i.e., intrinsic) property characterizations of a myriad of PCMs exist, as discussed in e.g. (Gunasekara, et al., 2021), (Gunasekara, Phase Equilibrium-aided Design of Phase Change Materials from Blends - for Thermal Energy Storage, 2017). However, their long-term cycling properties at application-representative volumes, e.g. bench- and pilot-scales, are scarce (Gunasekara, et al., 2021). This is mainly due to practical and resource limitations in running such

large-scale TES systems for long-term primarily for material analyses.

To address this knowledge gap, in HYSTORE, KTH Royal Institute of Technology (KTH), together with partners Rubitherm Technologies GmbH (RUBI) and AIT Austrian Institute of Technology GmbH aimed to characterize two short-listed PCMs in bench-scale for their long-term cycling characteristics. These include: TES capacity, hysteresis, supercooling, and long-term stability. This paper presents the key results of this analysis.

Materials and Methods

This section concisely presents the key details of the materials and methods employed in this work.

Materials

Through a comprehensive scrutiny of many PCM candidates, two bio-based alternatives were chosen from RUBI's product portfolio for this bench-scale analysis campaign at KTH. These are namely RT57HC and RT60HC. These are intended to cater to space heating TES applications, within the operating range of ~25- 65 °C (with preferably: freezing \geq 40-45 °C and melting \leq 55-60 °C), for successful coupling with heat pumps to enable FSC.

These two PCMs were selected for the bench-scale long-term cycling characterization based on their superior properties versus other alternatives. These mainly concern phase change temperatures, enthalpies as well as compatibility with stainless steel (SS) and aluminium, which are the intended heat exchanger (HEX) materials of the project partners. Their main intrinsic thermal properties are summarized in Table 1.

Table 1: Phase change properties of RT57HC and RT60HC

PCM	Phase change enthalpy (kJ/kg)	Phase change temperature range (°C)
RT57HC	230	53-59
RT60HC	210	58-61

These properties are obtained using a “heat flow optimized temperature curve analysis” (WOTKA) in a 3-layer calorimeter (Laube, 2023). The resultant enthalpy change with temperature respectively for RT57HC and RT60HC for heating and cooling are depicted in Figure 1 and Figure 2.

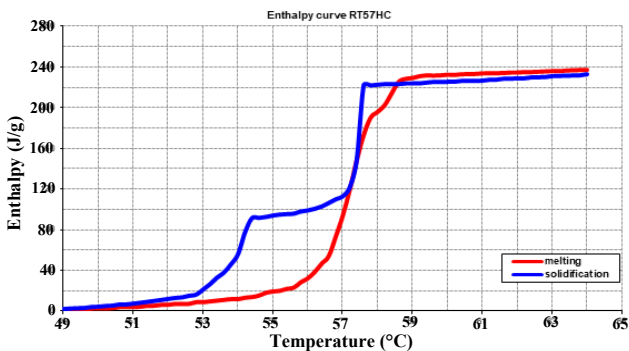


Figure 1. Enthalpy (H) versus temperature (T) curve of RT57HC. Copyright © 2023 RUBI - [CC BY-SA 3.0](#)

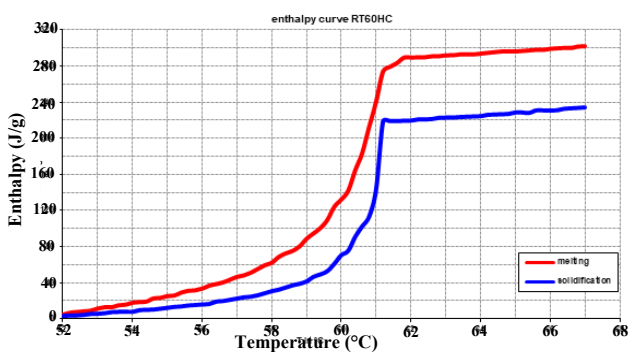


Figure 2. Enthalpy (H) versus temperature (T) curve of RT60HC. Copyright © 2023 RUBI - [CC BY-SA 3.0](#)

Methods: Bench-scale PCM cycling testing

A bench-scale PCM-TES unit of ~44 l volume with a shell-and-tube HEX (PCM in shell), with its layout and photo in Figure 3 and Figure 4, was used. Its main components are presented in Table 2. The heat transfer fluid (HTF) (in HEX tubes) was Renolin Therm 300 X (Fuchs Lubricants Sweden AB, 2023).

Eight PT100 sensors measure the temperature inside this PCM-TES unit. Each PCM was molten in an oven at 85 °C, and then poured into the PCM-TES unit. In total 39.93 kg of RT57HC and 38.92 kg of RT60HC respectively, was cycled between 35 °C and 85 °C (per the HTF in buffer tank). The thermostat baths were here maintained at isothermal conditions at 30 °C (for cooling) and 95 °C (for heating). Each heating/cooling cycle in the thermostat bath was maintained for 16 hours, thus allowing sufficient time for all the eight PT100s to reach isothermal end points (~80 °C and 35 °C respectively).

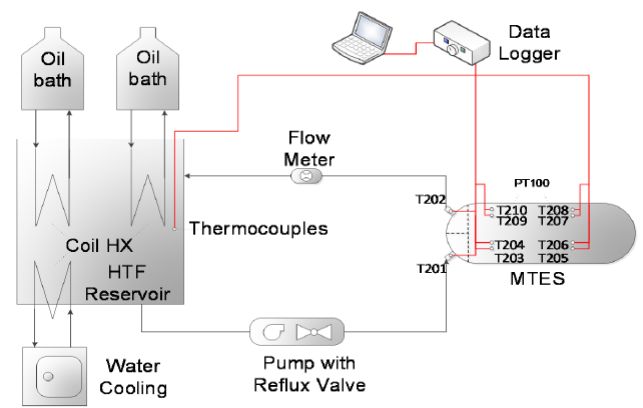


Figure 3. Bench-scale PCM-TES set-up layout sketch (Adapted from (Laestander, Melander, Bromander, & Sjöberg, 2015), (Chiu J., 2022). Copyright © 2015,2022 KTH - [CC BY-SA 3.0](#))

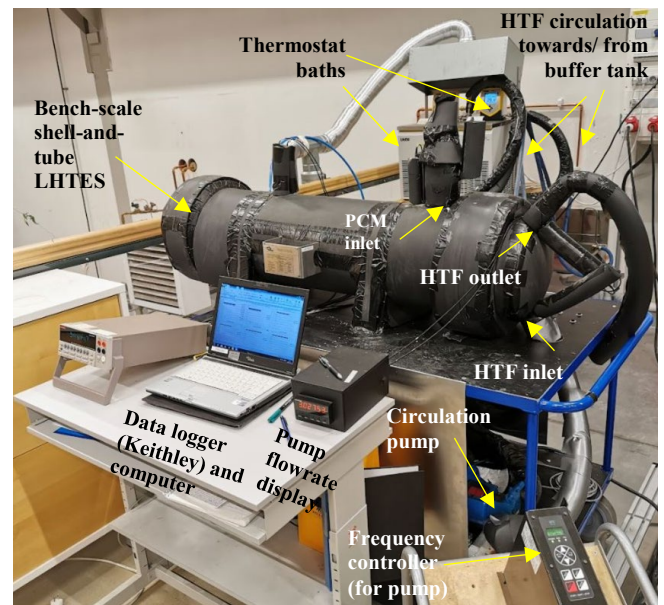
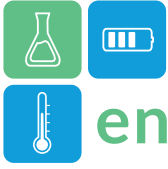


Figure 4: The LHTES system at KTH. (HTF: Heat transfer fluid)

Table 2: Bench-scale PCM-TES system components details (Laestander, Melander, Bromander, & Sjöberg, 2015)

Component	Description
Oil reservoir	Container for the heat transfer fluid (i.e., a thermal oil)
Cycloidal gear pump with reflux valve	Pumps heat transfer fluid from the oil reservoir to the tank



LHTES tank	Shell and tube heat exchanger which holds the PCM on the shell side, while letting it being heated up by the oil running on the tube side
Positive displacement flow meter	Measures the flow of oil which the pump is delivering
PT100s & thermocouples	Temperature measuring equipment
Temperature converter	Device converting the information given by the PT100s to a temperature input data into computer
Thermostat oil baths	Heats up the oil to an appropriate temperature
Coil Heat Exchanger (HEX)	A closed loop which leads the heating/cooling fluids through the oil reservoir
Water sink	Provides water to cool down the oil
Insulation	Reduce heat losses and protects users

The HTF flow rate was maintained at 3 l/min, and its inlet and outlet temperatures were measured, and adjusted based on density data from (Fuchs Lubricants Sweden AB, 2023).

RT57HC and RT60HC respectively underwent 27 and 53 complete heating/cooling cycles (per time available). Their key thermal properties in bench-scale cycling were analysed based on the temperature and HTF flow measurements, for the latent heat as well as sensible heat storage within the temperature range 35–79 °C. The detailed calculation method is explained in (Laestander, Melander, Bromander, & Sjöberg, 2015) and (Gunasekara, et al., 2024), with the phase change enthalpy curve adapted by a Dirac delta (Heaviside) function D (Chiu & Martin, 2012).

In summary, the TES capacity was calculated considering the properties of respectively the HTF (per Eq. 1) and the PCM (per Eq. 2 and Eq. 3). The HEX was made of SS (~150 kg) and the heat absorbed by this was also calculated (per Eq. 4) to be 3300 kJ. The final energy balance for charging (i.e. heat absorption) and discharging (i.e. heat release) of the PCM relative to the heat in HTF and SS HEX can thus be expressed, including heat losses (Q_{Losses} , kJ) as in Eq. 5 and Eq. 6 respectively. The detailed calculation methodology is explained in (Gunasekara, et al., 2024).

$$Q_{HTF} = \sum_{i=A}^B \int_{t_i}^{t_{i+1}} \rho_{T_{mean,HTF}} \times \dot{v} \times c_{p_{mean,HTF}} \times (T_{in,i} - T_{out,i}) dt \quad Eq. 1$$

$$Q_{PCM} = \sum_{i=A}^B \dot{Q}_{PCM_i} \times 2 \quad Eq. 2$$

$$\dot{Q}_{PCM_i} = \sum_{s=203}^{s=210} \{m_s \times [c_{p_{T_{mean,i,PCM,s}}} + D(T_{mean(i,i+1),s}) \times \Delta h_{PC}] \times (T_{i+1,s} - T_{i,s})\} \quad Eq. 3$$

$$Q_{SS_{HEX}} = m_{SS_{HEX}} \times c_{p_{SS_{HEX}}} \times \Delta T \quad Eq. 4$$

$$Q_{HTF} = Q_{PCM} + Q_{SS_{HEX}} + Q_{Losses} \quad Eq. 5$$

$$Q_{PCM} = Q_{HTF} + Q_{SS_{HEX}} + Q_{Losses} \quad Eq. 6$$

Here, Q_{HTF} : Energy capacity in HTF (kJ); A and B : The end time points of the energy capacity calculation time period (for a heating/ cooling cycle), \dot{v} : Volumetric flowrate of the HTF (m^3/s); $\rho_{T_{mean,HTF}}$: At time i , HTF density at the mean of HTF inlet and outlet temperatures (kg/m^3); $c_{p_{T_{mean,HTF}}}$: At time i , HTF specific heat capacity at mean of inlet and outlet temperatures ($kJ/(kg \cdot K)$); $T_{in,i}$ and $T_{out,i}$: At time i , HTF inlet and outlet temperatures ($^{\circ}C$); S : Sensor, 203, 204, 205, 206, 207, 208, 209 or 210; m_s : Final PCM mass per sensor (kg); $T_{i+1,s}$ and $T_{i,s}$: At two successive time steps i and $i+1$, PCM temperature around a respective sensor ($^{\circ}C$); $T_{mean(i,i+1),s}$: Mean temperature of a sensor between successive time steps i and $i+1$ ($^{\circ}C$); $c_{p_{T_{mean,i,PCM,s}}}$: At time i , the specific heat capacity for $T_{mean(i,i+1),s}$ of PCM around a respective sensor ($kJ/(kg \cdot K)$); Δh_{PC} : Enthalpy ($kJ/(kg)$) of phase change; $Q_{SS_{HEX}}$: Heat absorbed by the SS HEX (kJ); $m_{SS_{HEX}}$: Total weight of the TES HEX (empty) made of stainless steel (150 kg); and $c_{p_{SS_{HEX}}}$: Specific heat capacity of SS ($kJ/(kg \cdot K)$).

Results and Discussion

The 27 cycles of RT57HC and 53 cycles of RT60HC showed no noticeable phase change temperature variations, as shown (using sensor 203 e.g.) in Figure 5 and Figure 6.

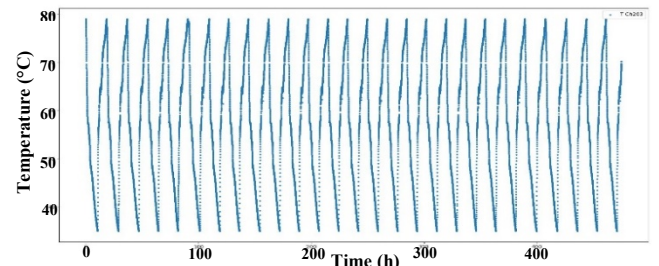


Figure 5. Thermal cycling of RT57HC for 27 cycles (Sensor 203)

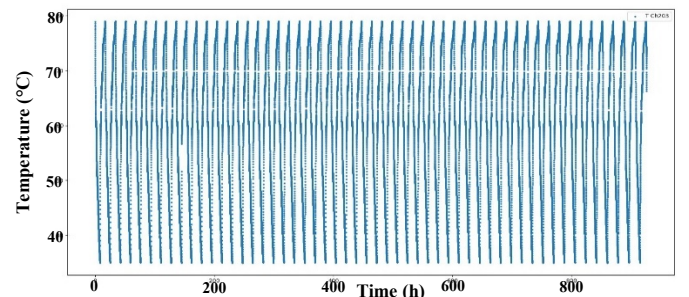
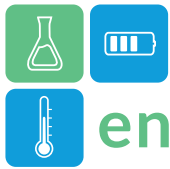


Figure 6. Thermal cycling of RT60HC for 53 cycles (Sensor 203)



Their TES capacities also show no significant variations from the initial to final analysed cycle, as shown with a few representative cycles e.g. in Table 3 and Table 4. These also displayed no discernible supercooling. Hysteresis was observed with its maximum incidence within the complete melting range, at 8 °C (55.0–63.1 °C) for RT57HC and 6 °C (56.1–62.2 °C) for RT60HC.

Table 3. RT57HC TES capacity, energy from/to HTF, energy to SS HEX and heat losses through 27 heating and cooling cycles.

Cycle nr.	TES capacity from PCM [kJ]	%difference of each cycle Vs. average	HTF capacity [kJ]	Heat losses (kJ)	Heat losses %
Heating					
1	19135	0.51%	-15516	6919	-45%
5	19296	0.33%	-15941	6654	-42%
10	19212	0.11%	-15428	7084	-46%
15	19297	0.34%	-15731	6866	-44%
20	19314	0.42%	-15136	7478	-49%
26	19298	0.34%	-15230	7368	-48%
Average [kJ]	19232		-15534	6998	-45%
Cooling					
1	-15767	0.49%	11630	-837	5%
5	-15865	0.02%	11391	-1174	7%
10	-15851	0.05%	11574	-977	6%
15	-15861	0.00%	11357	-1204	8%
20	-15865	0.02%	11278	-1287	8%
26	-15853	0.04%	11671	-882	6%
Average [kJ]	-15861		11476	-1085	7%

Table 4. RT60HC TES capacity, energy from/to HTF, energy to SS HEX and heat losses through 53 heating and cooling cycles.

Cycle nr.	TES capacity from PCM [kJ]	%difference of each cycle Vs. average	HTF capacity [kJ]	Heat losses (kJ)	Heat losses %
Heating					
2	15257	0.20%	-14743	3814	-26%
9	15343	0.76%	-13266	5377	-41%
20	15233	0.04%	-14187	4346	-31%
30	15242	0.10%	-14758	3784	-26%
40	15250	0.15%	-15162	3388	-22%
53	15240	0.09%	-15748	2792	-25%
Average [kJ]	15226		-14791	3736	-25%

Cooling					
2	-13527	0.02%	11621	1394	-10%
8	-13562	0.27%	11196	934	-7%
20	-13544	0.14%	11003	759	-6%
30	-13515	0.07%	11272	1057	-8%
40	-13529	0.03%	10899	670	-5%
53	-13525	0.00%	10612	387	-3%
Average [kJ]	-13525		11044	819	-6%

Conclusions

Bench-scale long-term thermal cycling of the bio-based PCMs RT57HC and RT60HC show in this work satisfactory thermal stability with no supercooling and reasonable hysteresis, verifying their suitability in TES applications of this project.

Acknowledgments

This project HYSTORE is funded by the European Union's Horizon 2020 research and innovation programme under grant agreement N° 1010967.

References

- Chiu, J. (2022). Laboratory Handout Latent Heat Thermal Energy Storage Performance Analysis (MJ2386 Energy Storage Technologies). Stockholm, Sweden: KTH Royal Institute of Technology, Heat and Power Technology. Retrieved December 12, 2023
- Chiu, J. N., & Martin, V. (2012). Submerged finned heat exchanger latent heat storage design and its experimental verification. *Applied Energy*, 93, 507–516. doi:https://10.1016/j.apenergy.2011.12.019
- Fuchs Lubricants Sweden AB. (2023). *RENOLIN THERM 300 X*. (FUCHS LUBRICANTS SWEDEN AB) Retrieved December 13, 2023, from https://fuchs.azureedge.net/fileadmin/se/product-data/renolin-therm-300-x%3Bpds%3Bse-en%3B121504.pdf
- Gunasekara, S. N. (2017). *Phase Equilibrium-aided Design of Phase Change Materials from Blends - for Thermal Energy Storage*. Industrial Engineering and Management, Energy Technology. Stockholm: KTH Royal Institute of Technology. Retrieved 01 13, 2024, from http://urn.kb.se/resolve?
- Gunasekara, S. N., Barreneche, C., Fernández, A. I., Calderón, A., Ravotti, R., Ristić, A., . . . Stamiatiou, A. (2021). Thermal Energy Storage Materials (TESMs)—What Does It Take to Make Them Fly? *Crystals*, 11, 1276. doi:https://doi.org/10.3390/cryst11111276
- Gunasekara, S. N., Samoteeva, O., Glomba, M., Kieseritzky, E., Tilman, B., & Palomba, V. (2024). *HYSTORE- D2.2 Report on the characterization of the pre-selected materials for HYSTORE solutions I-III*. Stockholm: HYSTORE (through the European Commission).
- Laestander, S., Melander, J., Bromander, K. N., & Sjöberg, G. (2015). *Thermal Energy Storage Testing - An applied energy project*. School of Industrial Engineering and Management, Energy Technology. Stockholm: KTH Royal Institute of Technology. Retrieved 11 15, 2023
- Laube, A. (2023, 12 04). *Wärme- und anwendungstechnische Prüfungen Andreas Laube*. Retrieved 12 04, 2023, from http://wunda.tech/3-Schicht-Kalorimeter/
- REN21. (2019). *Renewables 2019 Global Status Report*. Paris: REN21 Secretariat.



Binder-free K_2CO_3 granules for thermochemical heat storage

Delaram Salehzadeh^{1,*}, Johan E. ten Elshof², Mohammad Mehrali¹

¹University of Twente, Faculty of Engineering Technology, Department of Thermal and Fluid Engineering, Enschede, 7500 AE, The Netherlands

²University of Twente, MESA+ Institute for Nanotechnology, Enschede, 7500 AE, The Netherlands

*Corresponding author e-mail: d.salehzadeh@utwente.nl

Abstract

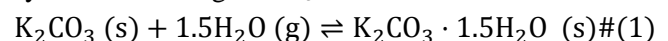
Thermochemical heat storage systems encounter challenges such as agglomeration within the reactor bed, which limits gas molecule movement and diminishes overall efficiency. This study proposes an approach to mitigate this issue by producing millimeter-sized potassium carbonate (K_2CO_3) granules without binders using the wet granulation technique. Through 10 cycles, initial hydration loading started at 0.19 mol_{H₂O}/mol_{K₂CO₃} in the first cycle and increased steadily to 1.42 mol_{H₂O}/mol_{K₂CO₃} by the 10th cycle. During 6-hour hydration periods, the released heat from the granules significantly increased from 57 J/g to 535 J/g after 10 cycles, attributed to changes in pore volume and granule structure throughout cycling. Despite pore enlargement, the granules maintained structural integrity, highlighting their stability across repeated cycles. This study underscores the potential of binder-free potassium carbonate granules to enhance heat storage efficiency, providing valuable insights for optimizing thermochemical heat storage systems, particularly in terms of scalability for mass production of these granules.

Keywords: Thermochemical heat storage, Salt hydrates, Potassium carbonate (K_2CO_3), Granulation

Introduction

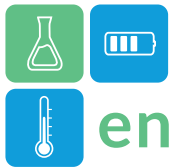
Thermal energy accounts for a substantial share of a country's overall energy consumption. Therefore, by using household heat storage to meet the demand for thermal energy, it is possible to significantly contribute to the energy transition [1, 2]. The utilization of renewable energy sources such as solar or wind power is dependent on certain times and locations [3]. Thermochemical energy storage (TCES) is a very efficient technique for storing heat with negligible energy loss. Thermochemical energy storage relies on the reversible chemical processes that take place between sorbates and sorbents. Salt hydrates are a type of thermochemical storage material (TCM) that exhibit potential due to their advantageous characteristics [4]. Potassium carbonate (K_2CO_3) possesses favourable characteristics for household heat storage, including non-toxicity, chemical stability, high energy density, and a suitable temperature range for space heating and hot water production. Furthermore, it is compatible with built-in heat sources for charging, as long as the

temperature remains below 160 °C [5]. Eq. 1 represents the equilibrium reaction for the gas-solid system containing K_2CO_3 :



In the hydration or discharging step (left-to-right reaction), water vapor is absorbed by the potassium carbonate, which results in the formation of potassium carbonate sesquihydrate and the release of heat [6].

An issue that arises with using powdered salt hydrates is the occurrence of caking, which is the agglomeration of powdered salt hydrate particles [7]. The process of agglomeration creates obstacles that hinder the movement of water vapor molecules in the reactor. Hence, an additional manufacturing process is necessary in order to convert powdered materials into precisely specified millimeter-sized particles. Neglecting this might result in a significant pressure drop inside the thermochemical reactor bed, mostly due to inadequate diffusion and bed flowability. As a result, the reactor bed experiences a reduced power output [8]. This work presents a detailed analysis of



the performance and characteristics of binder-free K_2CO_3 granules, aiming to contribute valuable insights into optimizing thermochemical heat storage systems. The granulation approach represents a promising pathway for scaling up the production of granules, thereby enhancing the sustainability and effectiveness of thermal energy storage technologies.

Materials and method

Potassium carbonate (K_2CO_3) was supplied from Thermo Fisher Scientific. The process of granulation was conducted with a high-shear rate laboratory mixer (Eirich EL1). Then 300 g of powder were added to the mixing pan at a speed of 5 m/s for 2 min during the premixing phase. The granulation process involved the use of deionized water at various concentrations (20, 23, or 25 wt% of the total batch mass). The water was added slowly to the mixture over a period of 1 min, while the mixing speed was maintained at 5 m/s and the granulator angle was set at 20°. Following this, the rotor speed was increased to 10 m/s, and the process was completed in 2 min. After granulation, the granules were dried in a hot air oven at 100 °C for 5 hours, followed by sieving to select granules within the size range of 1-5 mm.

Microstructural investigations were carried out utilizing a field emission scanning electron microscope (FESEM) (LJSM-7200F, Jeol) operating at an accelerating voltage of 5 kV. The granule's 3D pore structure was examined by ZEISS Xradia Context micro-CT imaging. 5 W of power and 60 kV of acceleration voltage were employed during the scanning procedure. The system LE3 filter was used to filter the polychromatic beam. To achieve the optimal signal-to-noise ratio, 4016 projections with a pixel size of 1.5 μm and camera binning of 1 were taken around 360° with an exposure period of 4 s. Pore analysis was conducted using Dragonfly software from Object Research Systems. A Volume of Interest (VOI) was defined within the granule structure, shaped as a spherical region with a diameter of 2 mm. This VOI excluded superficial regions of the specimen affected by treatment. The analysis distinguished between open pores accessible from the surface and closed pores located within the inaccessible interior. This was achieved by creating a shell-like region along the VOI edges, isolating inaccessible interior pores within it. Pores touching the surface shell were analyzed separately, and

volume percentages for each category were computed accordingly.

The K_2CO_3 granule was subjected to simultaneous thermal analysis (STA) using Netzsch STA 449 F3 Jupiter equipment linked to the ProUmid humidifier. In order to examine the cyclic hydration behaviour, a granule with an approximate weight of 15 mg was initially dried at 160 °C with a continuous flow rate of 300 mL/min for 90 min. The hydration was carried out for 6 hours under a water vapor pressure of 13 mbar and a temperature of 30 °C, and the dehydration was conducted at 100 °C for 6 hours with zero water vapor pressure. Finally, the granule was subjected to 10 hydration and dehydration cycles using TGA and DSC measurements. The loading quantity was determined by calculating the ratio of the increase in moles during hydration to the moles of the dried sample.

Results and Discussion

The moisture content has a substantial impact on the binding characteristics of the powder particles during the process of granulation, thereby impacting the formation of granules. First, the ideal water amount for achieving successful granulation was determined by testing water proportions of 20, 23, and 25% of the total batch. The addition of 20% water caused the formation of granules smaller than 1 mm. Increasing the water content to 23% reduced the amount of fine granules, and formed 26.6% of granules within the size range of 2–3 mm. Nevertheless, the use of 25% water resulted in the creation of a substantial chunk without forming any granules. Therefore, a water content of 23% was determined to be the ideal level for achieving successful granulation. The histogram depicted in Fig. 1a illustrates that granules within the size range of 2-3 mm exhibited the highest yield, and consequently, they were chosen for subsequent analysis, as shown in Fig. 1b.

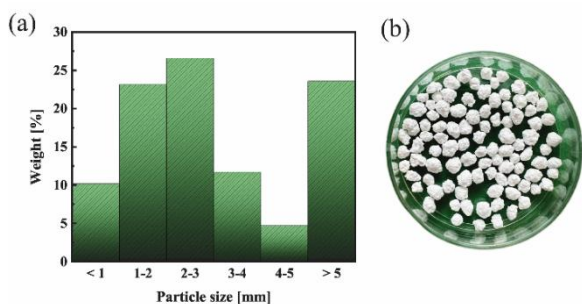


Fig. 1. (a) Histogram of granule size determined by sieve analysis. (b) K_2CO_3 granules within the size range of 2-3 mm.

In Fig. 2, the cross-sectional FESEM image of the K_2CO_3 granule illustrates the presence of macropores within the structure of the granule. The interior of the granule exhibited a higher porosity towards its center, whereas the outer regions appeared denser.

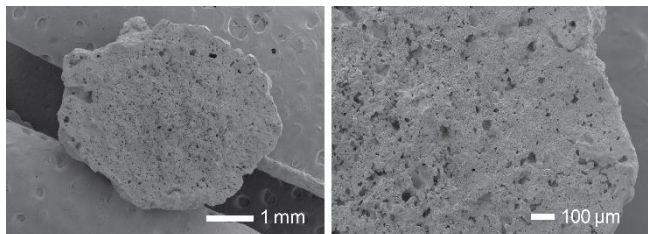


Fig. 2. Cross-sectional FESEM image of a dry K_2CO_3 granule with an acceleration voltage of 5 kV.

Pore analysis using Dragonfly software involved defining a spherical Volume of Interest (VOI) with a 2 mm diameter within the granule, excluding superficial regions potentially affected by sample treatment. Open pores accessible from the surface were represented in blue, while closed pores located in the inaccessible interior were shown in red. Analysis of the porosity of the K_2CO_3 granule in Fig. 3 revealed an open porosity of 19.8% and a closed porosity of 4.6%.

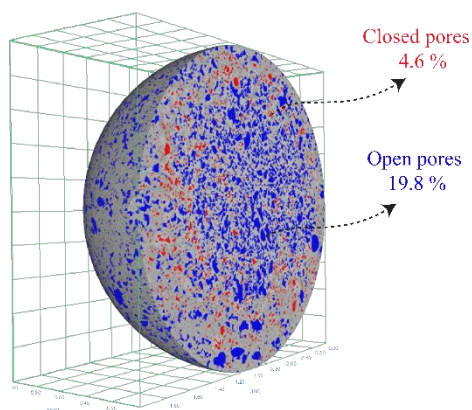


Fig. 3. Pore analysis in a 2 mm diameter spherical VOI within the K_2CO_3 granule using micro-CT analysis. Open and closed pores are depicted in blue and red colors, respectively.

The investigation of the K_2CO_3 granule before and after the cycling test using micro-CT provided important insights into its structural characteristics, porosity, and density. Fig. 3 shows that after undergoing 10 cycles of hydration and dehydration, although the granule developed larger pores, it managed to maintain its structural integrity. This suggests that despite the changes in pore size, the overall cohesion and stability of the granule were maintained throughout the cycling process. The total porosity and density of the granule can be also determined by dividing the granule's weight by its total volume using micro-CT and Dragonfly software. Relative density is computed using Eq. 2 by dividing the measured density by the 2.43 g/cm^3 theoretical crystal density of anhydrous K_2CO_3 :

$$\rho_{\text{rel}} = \frac{\rho_{\text{measured}}}{\rho_{\text{theoretical}}} = 1 - \varepsilon$$

(2)

where ρ_{rel} is relative density, ρ_{measured} is measured density, $\rho_{\text{theoretical}}$ is theoretical crystal density, and ε is porosity. Therefore, the relative density of the K_2CO_3 granule was found to be 1.79 g/cm^3 , indicating a total porosity of 26%. The porosity value obtained from the pore analysis within the spherical VOI is slightly lower compared to that calculated using Eq. 2. This discrepancy can be attributed to the approach of employing a spherical volume of interest with a 2 mm diameter, which aims to mitigate edge effects by focusing on a defined region rather than considering the entire granule. Additionally, the difference may also stem from the voxel size used during scanning, which was $1.5 \mu\text{m}$. This size limitation means that pores smaller than the voxel size cannot be detected, potentially leading to an underestimation of porosity by the software analysis. Despite these factors, both methods yielded reasonable estimates of total porosity.

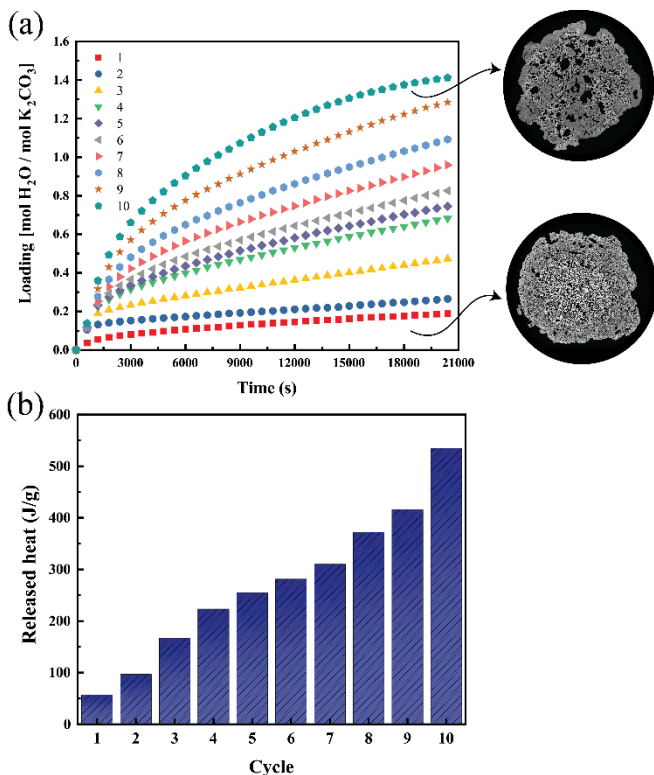


Fig 4. (a) Cyclic hydration loading with micro-CT images of the K_2CO_3 granule before and after cycling. (b) Cyclic released heat during 6 h hydration over 10 cycles.

To examine the cyclic performances, TGA and DSC analyses were conducted on K_2CO_3 granule through 10 hydration cycles. The degree of hydration is illustrated in Fig. 4a. The initial cycle demonstrated a small hydration loading of approximately 0.19 $\text{mol}_{\text{H}_2\text{O}}/\text{mol}_{\text{K}_2\text{CO}_3}$. However, this loading progressively increased with each subsequent cycle, reaching a hydration loading of 1.42 $\text{mol}_{\text{H}_2\text{O}}/\text{mol}_{\text{K}_2\text{CO}_3}$ by the 10th cycle. Table 1 displays the hydration loadings of the K_2CO_3 granule across 10 cycles. Micro-CT image of the granule before cycling demonstrates the presence of distributed pores in the central region and a less porous outer layer, which is consistent with the findings in the SEM image. Following 10 cycles, the granule maintained its structural integrity, demonstrating consistent stability throughout the cyclic process. The porosity percentage increased from 26% before the cycling test to 38% after 10 cycles. Additionally, the granule density increased from 1.79 g/cm^3 to 1.50 g/cm^3 .

Table 1: Cyclic hydration loading and released heat during 6 h hydration of K_2CO_3 granule over 10 hydration cycles.

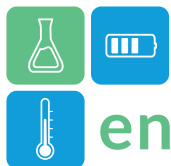
Cycle	Loading	Released
-------	---------	----------

	($\text{mol}_{\text{H}_2\text{O}}/\text{mol}_{\text{K}_2\text{CO}_3}$)	heat (J/g)
1	0.19	57
2	0.27	96
3	0.49	167
4	0.70	223
5	0.76	254
6	0.85	281
7	0.98	310
8	1.12	372
9	1.31	416
10	1.42	535

Fig. 4b presents the corresponding DSC findings for these processes. Using Netzsch software, the heat released during hydration was calculated by integrating the area under each DSC peak, and specific values are detailed in Table 1, which shows an enhancement in the released heat by the granule during 6 hours of hydration from 57 J/g to 535 J/g by the 10th cycle. The improved performance of granules after repeated loading is due to the pores and granule volume changes over cycles. Nonetheless, the hydration of K_2CO_3 granules did not reach completion throughout the 10 hydration cycles. This is attributed to the existence of dense areas in the granules and insufficient porosity, which hinder the easy transport of water vapor.

Conclusions

To sum up, this study has successfully employed the wet granulation process to develop binder-free granular potassium carbonate granules. The optimal water content for successful granulation was determined to be 23% of the total batch mass. The K_2CO_3 granules' interior had more pores toward the center, while the edges looked denser, giving the granules an overall porosity percentage of 26% and a relative density of 1.79 g/cm^3 . Throughout 10 cycles of hydration, it was observed that the initial cycle exhibited a low hydration loading of around 0.19 $\text{mol}_{\text{H}_2\text{O}}/\text{mol}_{\text{K}_2\text{CO}_3}$. Subsequently, with each cycle, this loading steadily rose, culminating in a hydration loading of 1.42 $\text{mol}_{\text{H}_2\text{O}}/\text{mol}_{\text{K}_2\text{CO}_3}$ by the 10th cycle. Additionally, the released heat of the granule during 6 hours of hydration increased from 57 J/g to 535 J/g by the 10th cycle due to the pores and granule volume changes throughout the cycles. Despite the expansion of pores within the granule following the cycling process, its structural integrity remained intact,



indicating that the granule retained its overall stability throughout the cyclic procedure. It should be noted that complete hydration of K_2CO_3 granules was not achieved within the 10 hydration cycles. This is attributed to the presence of dense areas within the granules and insufficient porosity, which hinders the easy transport of water vapor.

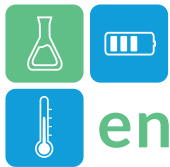
Despite limitations, this research breakthrough not only facilitated the production of salt hydrate granules but also holds great promise for significantly enhancing the efficiency of thermochemical heat storage applications. The findings underscore the potential of binder-free potassium carbonate granules in improving heat storage efficiency over multiple cycles. These insights provide valuable information for optimizing material design to achieve enhanced heat storage performance across various industrial and renewable energy applications. This study represents a crucial step toward scaling up granule production, advancing sustainable energy solutions.

Acknowledgment

The authors appreciate the financial support provided by the sectorplan techniek and TKI Urban Energy (SALTECH project - TKITOE2021402).

References

- [1] Uchino, T., & Fushimi, C. (2021). Fluidized bed reactor for thermochemical heat storage using Ca (OH) 2/CaO to absorb the fluctuations of electric power supplied by variable renewable energy sources: A dynamic model. *Chemical Engineering Journal*, 419, 129571.
- [2] Li, W., Klemeš, J. J., Wang, Q., & Zeng, M. (2021). Characterisation and sorption behaviour of LiOHLiCl@ EG composite sorbents for thermochemical energy storage with controllable thermal upgradeability. *Chemical Engineering Journal*, 421, 129586.
- [3] Yan, T., Li, T. X., & Wang, R. Z. (2016). Thermochemical heat storage for solar heating and cooling systems. In *Advances in Solar Heating and Cooling* (pp. 491-522). Woodhead Publishing.
- [4] Kousksou, T., Bruel, P., Jamil, A., El Rhafiki, T., & Zeraouli, Y. (2014). Energy storage: Applications and challenges. *Solar Energy Materials and Solar Cells*, 120, 59-80.
- [5] Mazur, N., Blijlevens, M. A., Ruliaman, R., Fischer, H., Donkers, P., Meekes, H., ... & Huinink, H. (2023). Revisiting salt hydrate selection for domestic heat storage applications. *Renewable Energy*, 218, 119331.
- [6] Houben, J., Sögütoglu, L., Donkers, P., Huinink, H., & Adan, O. (2020). K_2CO_3 in closed heat storage systems. *Renewable Energy*, 166, 35-44.
- [7] Chen, M., Wu, S., Xu, S., Yu, B., Shilbayeh, M., Liu, Y., ... & Gong, J. (2018). Caking of crystals: Characterization, mechanisms and prevention. *Powder Technology*, 337, 51-67.
- [8] Aarts, J., van Ravensteijn, B., Fischer, H., Adan, O., & Huinink, H. (2023). Polymeric stabilization of salt hydrates for thermochemical energy storage. *Applied Energy*, 341, 121068.



Bio-based shape-stabilized phase change materials for hot water storage

Felix Marske,* Eric Matthes

Technical University of Berlin, Institute of Chemistry, Department of Technical Chemistry, Berlin, DE

*Corresponding author e-mail: marske@tu-berlin.de

Abstract

Shape-stabilized phase change materials (ss-PCMs) enhance heat storage capacity in applications like hot water storage tanks and construction materials and have the potential to extend the lifespan of batteries and photovoltaic cells by passively cooling them. Commercial ss-PCMs often suffer from low latent heat and mechanical stability issues. Recently, we addressed these concerns through an innovative silica sol-gel synthesis, resulting in monolithic ss-PCMs with exceptional compressive strength (~2 MPa) compared to typical values (~10 kPa). However, achieving high latent heat required the use of paraffinic mixtures derived from oil. In this study, we explore the shaping of bio-based PCMs to create more sustainable products, with our ss-PCMs offering latent heats of 167 J/g and compressive strengths of 1.2 MPa. The addition of 15 wt% ss-PCMs increases hot water storage tank capacity by 64 %. Nevertheless, these ss-PCMs have stability issues in water environments and require additional coatings for protection.

Keywords: Phase Change Material, Shape Stabilization, Thermal Energy Storage, Hot Water Storage, Silica

1 Introduction

The intermittency of renewable energies like solar thermal (ST) or photovoltaic modules (PV), unfolds the necessity of energy storage in present and future energy systems. Hot water storage tanks (HWST) are promising thermal energy storage devices for building applications and are up to 62 % less expensive than electrical battery modules per energy capacity. calculation) The function of HWST is simple: They can store surplus heat from ST applications or excess PV electricity as heat, either directly or via electrical water heating.

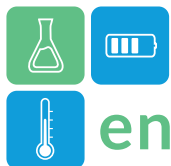
Water is one of the best specific heat storage (SHS) materials, but it has significant drawbacks, including the large volume required and the wide temperature intervals necessary for sufficient energy storage in HWST. (Seddegh and al., 2015) This restricts its application to smaller buildings with adequate space for HWST. Furthermore, modern heating systems employ a narrower temperature range between initial and final water temperatures due to higher heating surfaces, potentially reducing stored heat in HWST.

To construct smaller and more efficient HWST, phase change materials (PCMs) are promising alternatives to replace water as heat storage material. PCMs can store heat by melting and release the stored heat by freezing. (Wang and al., 2022) The heat storage capacity per unit

volume is 5 to 9 times greater for PCMs than for water in a temperature range of 10 °C around the melting point of PCM. Typical organic PCMs include paraffins, glycols, alcohols, esters, and acids with latent heat ranging from 100 to 250 J/g and low thermal conductivities around 0.2 W/mK. Their minimal supercooling and high long-term performance (~15,000 heating/freezing cycles) currently make them superior to salt hydrates. (Wang and al., 2022) However, the market penetration of organic PCMs remains low due to the challenge of integrating them into existing applications.

To address this challenge, liquid PCM is transformed into shape-stabilized solid boards with no leakage through blending methods, vacuum impregnation or polymerization reactions. (Aftab and al., 2018) However, shape-stabilized PCMs (ss-PCMs) available in the market typically exhibit either low mechanical stability (e.g., 5 kPa for PCM/graphite blends) (Yang and al., 2016) or low PCM mass fractions (e.g., 15 wt% PCM in gypsum boards) (Liu and al., 2019) hindering their usage and integration in applications.

In recent years, we have successfully developed ss-PCMs with high mechanical stability (1-2 MPa), comparable to that of gypsum boards, and high latent heat (120 J/g). (Marske and al., 2020; Marske and al., 2022a), using silica as a porous carrier and butyl stearate (BS) as the PCM through a novel progen-



assisted sol-gel process. Moreover, we were able to further increase the latent heat of our ss-PCMs to 160 J/g by blending BS with paraffins derived from crude oil. (Marske and al., 2022b)

To address the 12 principles of green chemistry, we replaced the paraffin mixtures with the bio-based PCM Crodatherm 21 (~200 J/g) and prepared bio-based ss-PCMs in this study. After ss-PCM analysis, we utilized cylindrical ss-PCM monoliths as filler material in a prototype HWST to evaluate the increase in heat storage capacities.

2 Experimental

2.1 Materials

The stabilized silica sol Köstrosol 0730 was procured from *Chemiewerk Bad Köstritz*, Germany. Sodium dodecyl sulfate (SDS, ≥ 99.0 % GC) and poly(vinyl alcohol) (PVA, 88 % hydrolyzed, average molecular weight 22000) were acquired from *Sigma-Aldrich* and *ACROS Organics*, respectively. The PCM Crodatherm 21 was sourced from *Croda International*.

2.2 Synthesis

A total of 11 g Crodatherm 21, 3.71 g water, 0.33 g PVA, 0.44 g SDS, and 4.95 g Köstrosol 0730 were transferred in 60 ml polypropylene beakers and shape-stabilized using our porogen-assisted sol-gel process (Marske and al., 2022b).

2.3 Characterization and experimental methods

The porous structure of silica in ss-PCMs was assessed using mercury (Hg) intrusion measurements under assuming a cylindrical pore structure (Pascal40 at 400 kPa and Pascal440 at 400 MPa, *Porotec*). The microstructure of ss-PCMs was visualized using high-resolution scanning electron microscopy (HRSEM, Merlin microscope, *Zeiss*) with secondary electron acceleration set at 3 – 5 kV. Samples were mounted on conductive carbon tape for measurement.

Thermal conductivity was assessed using a TPS 1500 thermal analyzer from *Hot Disk AB*, employing a transient plane source (TPS) method in a sandwich configuration (5 °C). The ss-PCM monoliths were halved and placed on the sensor and heater unit during measurement (uncertainty: ± 0.76 %). The phase change behavior was analyzed with an 822e calorimeter by *METTLER TOLEDO* using DSC with a heating rate of 1 °C/min, ranging from -20 to 60 °C and back (average uncertainty for latent heats: ± 2.9 %, constant sample mass: 15 mg, on-set temperature: melting and freezing point). Long-term performance tests were carried out via DSC between 5 to 60 °C (heating rate: 10 °C/min) until the ss-PCMs were 3000

times melted and frozen (heating rate of 1 °C/min for the 3000. cycle).

The PCM leakage of the ss-PCMs was determined by calculating the mass percentage difference before and after heating the sample at 100 °C for 1 week (uncertainty: ± 5.0 %). The average compressive strength of ss-PCMs (uncertainty: ± 2.0 %) was measured in five tests using a TBH355 hardness tester from *ERWEKA* at 5 °C (solid PCM).

The ss-PCMs were used as filler material in a cylindrical flow through HWST with water as heat transfer fluid (HTF). The HWST was 16cm high and 10.2 cm in inner diameter (maximum ss-PCM loading: 14.9 wt%). The HWST was heated and cooled from 15 °C to 30 °C at five different HTF volume streams (0.25 to 1.8 l/min). The inlet and outlet temperatures were used to calculate the heat storage capacity factor.

3 Results and Discussion

To create more sustainable products by replacing paraffinic PCMs, we shape-stabilized the bio-based PCM Crodatherm 21 using our recently developed sol-gel synthesis (Figure 1). (Marske and al., 2022a) The products were monolithic and cylindrical with a diameter of 3.0 cm, a height of 2.2 cm, and a density of ~ 0.88 g/cm³, comparable to ss-PCMs based on BS. Moreover, they were slightly translucent and had PCM mass fractions of 83 wt% with gelation times of 24 h.

3.1 Mechanical and structural properties of ss-PCMs

To evaluate shape-stability, the bio-based ss-PCM samples were placed on a thin sheet of paper and heated to 100 °C for one week to test for PCM leakage. No wet spots were observed on the paper, and there was no significant weight loss of the sample after one week of heating, demonstrating 100 % shape-stability and no PCM leakage. Next, we shape-stabilize Crodatherm 21 with a PCM content exceeding 83 wt% to determine the upper limit for shape-stabilization. Beyond 88 wt% PCM content, the samples started to fracture and at 94 wt% PCM the shape-stability was completely lost, similar to our paraffinic and BS-based ss-PCMs. (Marske and al., 2022b)

To further characterize the mechanical properties, we evaluated the compressive strength of the bio-based ss-



Figure 1 Pictures of ss-PCMs synthesized with Crodatherm 21.

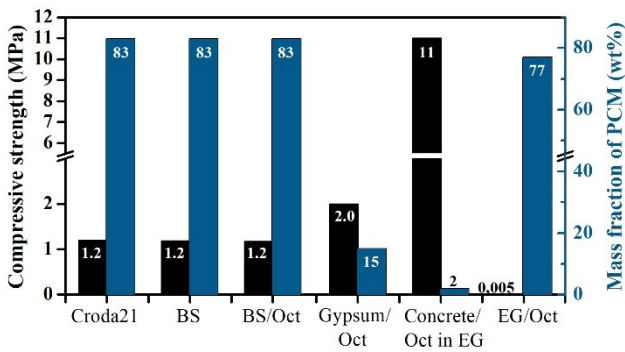


Figure 2 Comparison of the compressive strength of our ss-PCMs based on Crodatherm 21 (Croda21), BS (BS), and BS/Octadecane (BS/Oct) (Marske and al., 2022b) with literature-reported ss-PCMs based on gypsum and Oct (Liu and al., 2019), concrete blended with Oct encapsulated in graphite (EG) (Zhang and al., 2013), and Oct confined in a graphite foam (Yang and al., 2016). PCMs and compared these values with those from literature studies (Figure 2). Our bio-based ss-PCMs exhibit compressive strengths nearly identical to our previous paraffinic and BS-based ss-PCMs (Marske and al., 2022b), making them excellent candidates for energy-saving construction materials requiring high mechanical stability. These compressive strengths are also similar to those of solid ss-PCMs composed of PCM/gypsum (Liu and al., 2019), which have 5 to 6 times lower PCM mass fraction than our ss-PCMs.

To understand the exceptional mechanical properties of our ss-PCMs, we conducted pore structure analysis via scanning electron microscopy (SEM) and assessed silica pore structure and porosity using Hg intrusion porosimetry after calcination of ss-PCMs for 6 h at 600 °C (Figure 3). The silica pore structure in ss-PCMs is spherical and interconnected with pores ranging from 0.1 to 5 μm and mean macropore diameter of 429 nm. The porosity and macropore volumes of the calcined ss-PCM are 95 % and 8.2 cm³/g, similar to paraffinic and BS-based ss-PCMs. Therefore, shape-stabilized Crodatherm 21 should exhibit the same high mechanical stability as our previously reported ss-PCMs (Figure 2). (Marske and al., 2020)

3.2 Thermal properties of ss-PCMs

To characterize the amount of immobilized PCM undergoing a phase change in a specific time period,

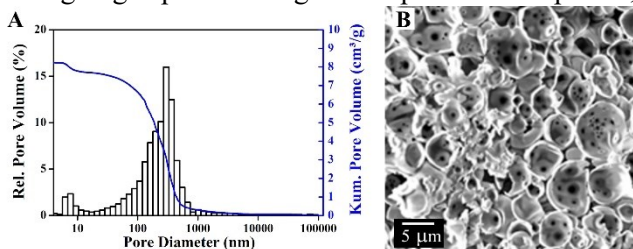


Figure 3 Mercury intrusion measurement (A) and SEM image (B) of ss-PCM based on Crodatherm 21 after calcination at 600 °C.

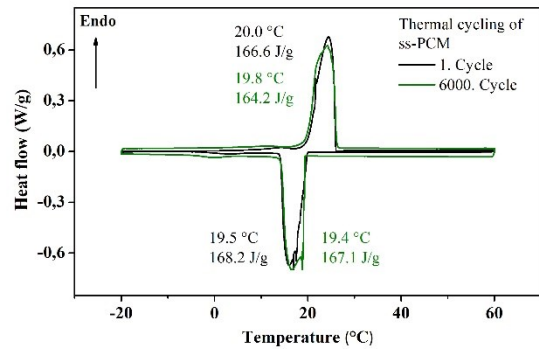


Figure 4 DSC curves of ss-PCMs based on Crodatherm 21 after 1 and 6000 melting and freezing cycles.

we conducted thermal conductivity and differential scanning calorimetry (DSC) measurements.

Our ss-PCMs exhibit a thermal conductivity of 0.4 W/mK (5 °C), similar to our previously synthesized ss-PCMs. (Marske and al., 2020; Marske and al., 2022b) When compared to literature-reported ss-PCMs based on gypsum and Oct, (Liu and al., 2019) our ss-PCMs have thermal conductivities of 0.1 W/mK higher, making them a promising and energy-saving alternative to gypsum boards.

The latent heat of our ss-PCMs is 167 J/g, with a melting point of 20.0 °C and a freezing point of 19.4 °C (Figure 4). In comparison, pure Crodatherm 21 has a latent heat of 205 J/g, a lower melting point of 19.7 °C, and the same freezing point at 19.4 °C. The lower melting point of the PCM is attributed to interactions with the silica surface. (Marske and al., 2020) The effective mass fraction of PCM is calculated as the quotient of latent heat of ss-PCMs and pure PCM, multiplied by 100, resulting in a value of 83 %. This equivalence to the PCM mass fraction of 83 wt% ensures that the entire immobilized PCM of the ss-PCM undergoes a phase change. Therefore, the PCM phase can be fully exploited in possible applications.

The difference between the melting and freezing points defines the supercooling. Our ss-PCMs exhibit low supercooling effects of 0.5 °C. After 6000 cycles of melting and freezing, the latent heat and supercooling remain nearly constant, indicating high long-term performance. Consequently, the ss-PCM should last for at least 16 years in building applications, assuming one melting/freezing cycle per day in building applications.

3.3 Hot water storage tank filled with ss-PCMs

The high latent heat, high durability, and high mechanical stability of our ss-PCMs make them ideal for domestic HWST. Therefore, we sealed the water-soluble ss-PCMs with alumina foil and filled them as a stacked configuration in prototype HWST (Figure 5b).

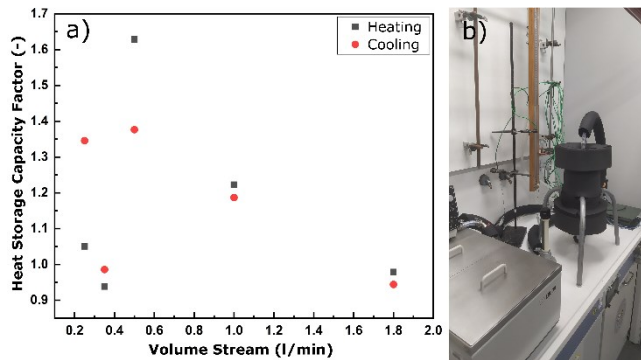


Figure 5 Heat storage capacity factor related to the applied volume stream (a). The experiments were performed from 1.8 to 0.25 l/min. Picture of measurement setup (b).

Compared to HWST filled solely with water, the heat storage capacity factor (HSCF) of our HWST filled with 14.9 wt% ss-PCMs and water increases by 64%, twice higher than the HSCF of similar studies (Cabeza and al, 2005) and possibly because of the high thermal conductivity and high silica surface area of our ss-PCM. The HSCF of the prototype HWST is calculated as follows:

$$HSCF = \frac{Q_{SL}}{Q_L} = \frac{\int (T_{I,SL} - T_{O,SL}) dt}{\int (T_{I,S} - T_{O,S}) dt} \quad (1)$$

with Q as the stored heat in the hybrid sensible-latent (SL) or sensible (S) HWST and T as the temperature measured in the inlet (I) or in the outlet (O) of HWST. When the HTF volume stream decreases, HSCF should increase. (Castell and al., 2011) Therefore, the HSCF should reach theoretically a maximum of 0.25 l/min for our HWST. Here, the HSCF (Figure 5a) peaks at 0.5 l/min and declines at lower HTF volume streams, indicating ss-PCM decomposition by hydrolysis after a few cycles. (Hüsing and Schubert, 1998) Additionally, the compressive strength of ss-PCMs decreases from 1.2 MPa to 0.1 MPa after a few thermal cycles in HWST. For future studies, a proper sealing or coating of our ss-PCMs must be developed as hydrolysis protection against hot water in HWST.

4 Conclusions

We substituted paraffinic PCMs derived from crude oil with the bio-based PCM Crodatherm 21 to produce environmentally friendly ss-PCMs through our porogen-assisted silica sol-gel process. The bio-based ss-PCMs exhibit no leakage effects and, consequently, have high latent heats of 167 °C, with a melting point of 20 °C and minimal supercooling effects of 0.5 °C. Since the latent heat aligns with the PCM mass fraction, the entire PCM phase remains shape-stabilized and undergoes a phase change.

The silica phase in the bio-based ss-PCMs is spherical and interconnected with a mean macropore diameter of 429 nm, making it stable enough (1.2 MPa) to be used as an energy-saving alternative to gypsum boards or as filler material in HWST.

Integrated into a prototype HWST, the bio-based ss-PCMs increase the heat storage capacity by 64% at 14.9 wt% ss-PCM loading compared to a water-based HWST but decompose in hot water after a few cycles.

After hot water protection through coating, these ss-PCMs should be integrated into larger HWST systems within buildings to realistically evaluate their potential in future studies

5 Acknowledgment

Special thanks to EXIST-Forschungstransfer funding program of the German Federal Ministry for Economic Affairs and Climate Action, and the European Social Fund (Project Nanolope, grant no. 03EFVBE143).

6 References

- Aftab, W. and al. Energy Environ. Sci. 2018, Vol. 11, pp. 1424. DOI: 10.1039/C7EE03587J
- Cabeza, L.F. and al. Solar Energy Materials and Solar Cells, 2006, Vol. 90, pp. 1273-1282. DOI: 10.1016/j.solmat.2005.08.002
- Castell, A. and al. Applied Energy, 2011, Vol. 88, pp. 4120-4127. DOI: 10.1016/j.apenergy.2011.03.046
- Hüsing, N. and Schubert, U. Angewandte Chemie International Edition 1998, Vol. 37, 1-2, pp. 45. ISSN 14337851.
- Liu, Z. and al. J. Hazard. Mater. 2019, Vol. 364, pp. 620. DOI: 10.1016/j.jhazmat.2018.10.061
- Marske, F. and al. RSC Adv. 2020, Vol. 10, pp. 3083. DOI: 10.1039/C9RA10631F
- Marske, F. and al. J. Energy Storage 2022, Vol. 49, pp. 104127. DOI: 10.1016/j.est.2022.104127
- Marske, F. and al. J. Build. Eng. 2022, Vol. 60, pp. 105198. DOI: 10.1016/j.job.2022.105198
- Mongird, K. and al. Energies 2020, Vol. 13, pp. 3307. DOI: 10.3390/en13133307
- Seddegh, S. and al. Renew. Sust. Energ. Rev. 2015, Vol. 49, pp. 533. DOI: 10.1016/j.rser.2015.04.147
- Wang, X. and al. Energy Build. 2022, Vol. 260, pp. 111923. DOI: 10.1016/j.enbuild.2022.111923
- Yang, J. and al. J. Mater. Chem. A 2016, Vol. 4, pp. 18851. DOI: 10.1039/C6TA08454K
- Zhang, Z. and al. Renew. Energy 2013, Vol. 50, pp. 675. DOI: 10.1016/j.renene.2012.08.024



Biomimicry-inspired design optimization of a latent thermal energy storage system using phase change materials

Nadiya Mehraj, Carles Mateu, Gabriel Zsembinszki, Saranprabhu Mani Kala, Sara Risco, Luisa F. Cabeza

GREiA Research Group, Universitat de Lleida, Pere de Cabrera s/n, 25001 Lleida, Spain

*Corresponding author e-mail: luisaf.cabeza@udl.cat

Abstract

This study aims at designing a new thermal energy storage (TES) tank biomimicry inspired. This paper presents a first experimental evaluation of the concept and the first steps towards optimization using genetic algorithm (GA) techniques. The concept is based on an innovative pipe branching geometry within a shell-and-tube tank configuration that can maximize heat transfer while meeting pressure drop constraints and effectively managing the temperature gradient. Promising designs will be carefully chosen for prototyping and their charging and discharging rates will be measured through experimental testing. The simulation results showed superior performance compared to the initial biomimicry-inspired prototype that did not undergo GA optimization. Therefore, it is anticipated that the optimized designs will confirm the effectiveness of GA optimization and offer valuable insights into enhancing thermal energy storage (TES) performance.

Keywords: Latent thermal energy storage (LTES), phase change material (PCM), biomimicry, design optimization, genetic algorithm (GA)

Introduction

Latent thermal energy storage (LTES) systems require effective heat transfer to efficiently charge and discharge thermal energy (Cabeza et al., 2021). However, the low thermal conductivity nature of the storage media used, phase change materials (PCMs), pose thermal transfer challenges (Cabeza et al., 2011). Nature provides examples of highly optimized branching vascular networks that maximize surface area for fluid transport within physical constraints, which can be an inspiration for heat exchanger geometry optimization (Fan & Khodadadi, 2011).

Branched structures resembling tree-like networks are found extensively in biology facilitating circulatory, respiratory, and nutrient distribution functions (Wang et al., 2022). Features such as recursive dichotomous branching and tapering vessel diameters enable tremendous surface area enhancement over simple parallel designs. Studies showed that biomimetic models of angiosperm leaf venation and lung airways outperform conventional designs for heat and mass exchange applications (Capata & Gagliardi, 2019).

By applying principles of biomimicry, compact yet extensively branched internal configurations could boost heat exchanger performance (Olabi et al., 2023). Natural architectures self-assemble to achieve multifunctional efficiencies - transporting fluids while conserving space and material. Biologically inspired

designs may therefore offer inherently optimized multifaceted solutions (Calamas & Baker, 2013).

This work generates novel branching pipe geometries within the design variables of a shell-and-tube heat exchanger using evolutionary computation techniques allow increasingly complex biological abstraction. Experimental validation assesses if computationally optimized biomimetic designs confer thermal benefits as inspired by nature's vascular fluid distribution networks (Lin et al., 2023). Outcomes provide insight regarding leverage of biomimicry for enhance heat transfer applications in TES technologies (Huang et al., 2023).

Material and methods

TES concept

The TES concept proposed in this study utilizes a biomimicry-inspired internal pipe branching design within a shell-and-tube heat exchanger configuration. As shown in Figure 1a, the piping network mimics the hierarchical structure of vascular networks found in nature. Similar to how the branching patterns of veins in leaves or lungs serve to efficiently distribute fluids over complex surfaces, the internal pipe geometry follows a recursively branching dendritic structure. This fractal-like arrangement, with tapering pipe diameters mimicking the narrowing of vessels, aims to maximize the heat exchange surface area between the pipe walls and surrounding phase change material

(Figure 1b). By self-assembling a highly branched yet compact piping design inspired by natural fluid distribution systems, we expect that this biomimetic approach can enhance charging and discharging performance for effective thermal energy storage compared to conventional parallel piping arrangements with limited surface contact.

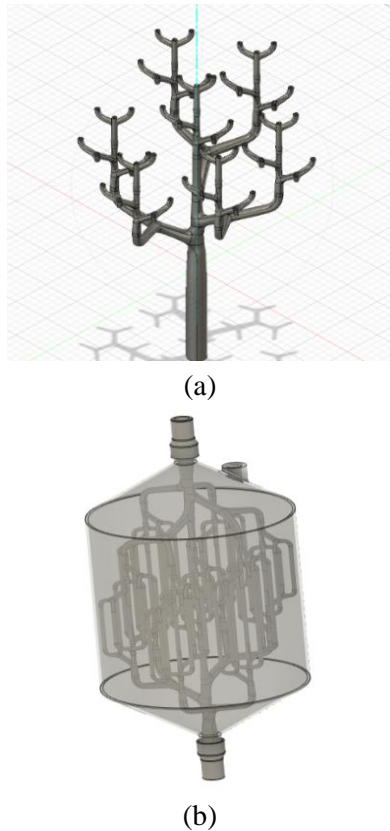


Figure 1. Schematic of the design of the TES prototype. (a) Fractal like arrangement (b) TES tank concept based on biomimetic design

Experimental methodology

By conducting charging and discharging procedures for the heat transfer fluid (HTF) at a constant flow rate of 3 L/min, the performance of the LTES prototype was assessed. The PCM was first cooled during the charging procedure until the temperature sensor registered at 15 ± 1 °C. The temperature of the HTF inlet was then adjusted to 45 °C. Upon reaching a temperature of 45 ± 1 °C, the PCM was deemed fully charged. The PCM was heated to 45 ± 1 °C on the temperature sensor before the HTF inlet temperature was adjusted to 14 °C for the discharging procedure. The PCM temperature was deemed to have reached 15 ± 1 °C, marking the end of the discharging

operation. There were three iterations of the charging and discharging procedures.

The heat transfer rate during the charging and discharging processes, also known as the charging and discharging power, respectively, was calculated using an energy balance applied to the HTF between the inlet and outlet of the LHS prototype, as described by Equation (1):

$$\dot{Q} = \rho \cdot c_p \cdot \dot{V} \cdot \Delta T_{HTF} \quad (1)$$

In Equation 1, \dot{Q} (in W) represents the heat transfer rate, ρ (in kg/m^3) is the density of the HTF, c_p (in $\text{J}/\text{kg} \cdot \text{K}$) is the specific heat capacity of the HTF, \dot{V} (in m^3/s) is the flow rate of the HTF, and ΔT_{HTF} (in K) is the absolute value of the difference between the temperatures of the HTF at the inlet and outlet of the LHS prototype.

Problem formulation and GA optimization

The objective of this study is to optimize the pipe branching geometry of a preliminary prototype of biomimetic heat exchanger which must maximize heat transfer rate while minimizing charging/discharging time using GA following the steps listed below:

1. Genetic representation

Potential designs are encoded as genome in the GA. Genes encode parent pipe length, children pipe length, internal pipe diameter, pipe thickness, bifurcation angles, branching locations, and levels of bifurcation.

An initial random population of designs will be generated within the defined bounds of each gene.

2. Evaluation function

It includes various calculations depending upon the chosen variants to be optimized, here the fitness function involves the following calculations:

- Heat transfer surface area
- Limiting pressure drop
- Amount of PCM (storage capacity)

3. Genetic operations

Standard genetic operators like crossover and mutation are applied over generations to evolve new populations.

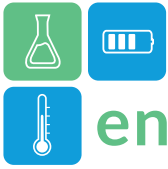
4. Selection

Designs with the highest fitness scores, maximizing \dot{Q} within pressure limits and minimizing charging and discharging time, will be selected.

5. Prototyping and testing

Promising designs will be fabricated, and their thermal performance will be experimentally validated.

Results and discussions



Within the enforced pressure drop limit of 5 kPa, the top designs found by the GA (Table 1), which will be evaluated in a lab shortly, demonstrated a significant increase in heat transfer surface area as compared to a preliminary prototype (Figure 1c). Many of the optimized branching patterns resemble fractal-like structures observed in vascular networks, with recursive dichotomous branching and tapering diameters.

Figures 2 and 3 show the results of preliminary biomimetic inspired TES prototype design through temperature and power profiles during charging and discharging without GA optimization. To validate the improvements in the overall performance of TES design resulting from GA optimization, future work will evaluate a prototype that has been optimized using GA. The comparison between the dimensions of tested prototype and GA optimized design are provided in table 1.

Table 1. Comparison between design parameters of preliminary prototype and simulated prototype

Parameters	Prototype dimensions	GA simulated dimensions
Inlet pipe diameter	11 mm	12.99 mm
Inlet pipe thickness	0.64 mm	0.77 mm
Inlet pipe diameter after tapering at level 0	8 mm	9.22 mm
Inlet pipe diameter after tapering at level 1	6 mm	6.15 mm
Angle between main pipe and level 0 branches	59°	54.32°
Angle between main pipe and level 1 branches	59°	46.92°
Total heat transfer area	$9.6 \times 10^4 \text{ mm}^2$	$1.2 \times 10^5 \text{ mm}^2$
Total number of branches at level 0	7	8
Total number of branches at level 1	7	8

Hence, Table 1 shows that the GA optimized heat exchanger significantly improves upon the preliminary prototype, particularly in total heat transfer area, which has increased by approximately 30%. This enhancement suggests greater efficiency and superior heat exchange performance in the optimized model which improves the future scope of obtaining the better performing LHS system.

The temperature and power progression for the design that was experimentally evaluated as a preliminary design produced utilizing the biomimicry concept without GA optimization during the charging process is shown in Figure 2. The effect of the phase change can be observed in the first 10 minutes and after which the PCM temperature increases at very high rates. The charging was complete in 1.8 hrs. After the initial peak at 700 W due to transients, the heat transfer rate was almost constant around 150 W during phase change and then it decreased with the progression of experiment.

The discharging process is shown in Figure 3. In this case, the temperature of the PCM remains almost constant during phase change, which lasts around 1 hr. The heat transfer rate is also lower than in charging, with values around 100 W during phase change. This indicates that the discharging (i.e., PCM solidification) process was slower than the charging, also reflected by the duration of the discharging process, which lasted for about 2.7 hrs.

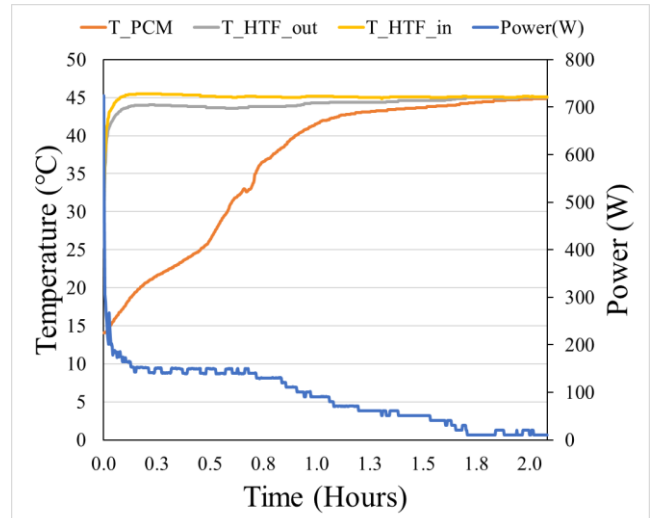


Figure 2. Temperature and power evolution during charging process

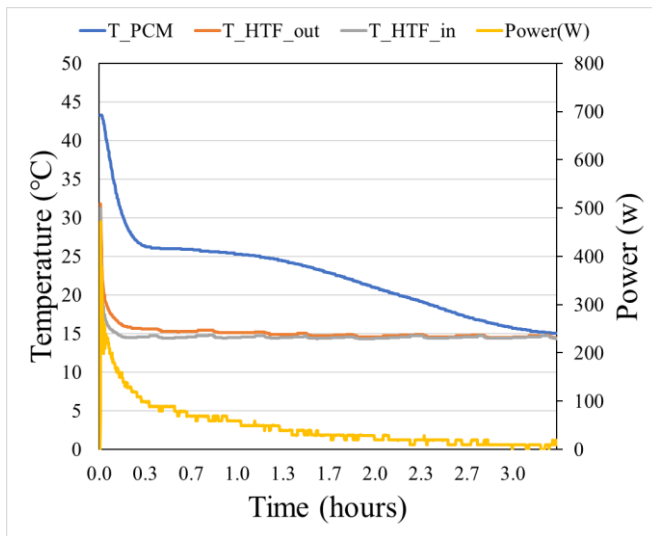


Figure 3. Temperature and power evolution during discharging process

This confirms the efficacy of biomimicry-inspired branching pipe geometries that maximize heat exchange surface area within constraints, outperforming conventional arrangements. The enhancements are attributed to the fractal-like optimized networks achieving multi-fold surface area increases over simple parallel designs.

Conclusions

This study laid the foundation for optimizing the biomimetic design of an LTES system using GA techniques. The preliminary results showed the potential of biomimetic-inspired branching pipe geometries in enhancing heat transfer performance compared to conventional designs. The next step in this research will focus on further refining and optimizing the biomimetic designs through the application of GA. This iterative process aims to maximize heat transfer rates and minimize charging and discharging times, ultimately improving the TES performance. The findings from this study provide a promising direction for future research in developing advanced LHS systems based on biomimicry and GA optimization.

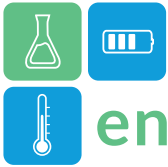
Acknowledgment

This study received funding from the European Union's Horizon Europe Research and Innovation Programme under grant agreement No. 101103552 (SUSHEAT). Views and opinions expressed are however those of the author(s) only and do not necessarily reflect those of the European Union or CINEA. Neither the European Union nor the granting authority can be held responsible for them.

The authors also thank the Generalitat de Catalunya for the quality accreditation granted to their research group (2021 SGR 01615). GREiA is certified agent TECNIO in the category of technology developers of the Government of Catalonia. This work is partially supported by ICREA under the ICREA Academia programme.

References

- Cabeza, L. F., Castell, A., Barreneche, C., de Gracia, A., & Fernández, A. I. (2011). Materials used as PCM in thermal energy storage in buildings: A review. *Renewable and Sustainable Energy Reviews*, *15*(3), 1675–1695. <https://doi.org/https://doi.org/10.1016/j.rser.2010.11.018>
- Cabeza, L. F., de Gracia, A., Zsembinszki, G., & Borri, E. (2021). Perspectives on thermal energy storage research. *Energy*, *231*, 120943. <https://doi.org/10.1016/j.energy.2021.120943>
- Calamas, D., & Baker, J. (2013). Performance of a biologically inspired heat exchanger with hierarchical bifurcating flow passages. *Journal of Thermophysics and Heat Transfer*, *27*(1), 80–90. <https://doi.org/10.2514/1.T3950>
- Capata, R., & Gagliardi, L. (2019). Experimental investigation on the Reynolds dependence of the performance of branched heat exchangers working with organic fluids. *International Journal of Heat and Mass Transfer*, *140*, 129–138. <https://doi.org/https://doi.org/10.1016/j.ijheatmasstransfer.2019.05.114>
- Fan, L., & Khodadadi, J. M. (2011). Thermal conductivity enhancement of phase change materials for thermal energy storage: A review. *Renewable and Sustainable Energy Reviews*, *15*(1), 24–46. <https://doi.org/https://doi.org/10.1016/j.rser.2010.08.007>
- Huang, Y., Deng, Z., Chen, Y., & Zhang, C. (2023). Performance investigation of a biomimetic latent heat thermal energy storage device for waste heat recovery in data centers. *Applied Energy*, *335*. <https://doi.org/10.1016/j.apenergy.2023.120745>
- Lin, X., Qiu, C., Wang, K., Zhang, Y., Wan, C., Fan, M., Wu, Y., Sun, W., & Guo, X. (2023). Biomimetic bone tissue structure: An ultrastrong thermal energy storage wood. *Chemical*



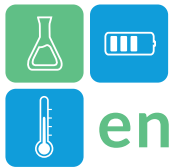
ENERSTOCK 2024
The 16th IEA ES TCP International Conference on Energy Storage
June 5–7, 2024
Lyon, France

Engineering Journal, 457, 141351.
<https://doi.org/https://doi.org/10.1016/j.cej.2023.141351>

Olabi, A. G., Abdelghafar, A. A., Maghrabie, H. M., Sayed, E. T., Rezk, H., Radi, M. Al, Obaideen, K., & Abdelkareem, M. A. (2023). Application of artificial intelligence for prediction, optimization, and control of thermal energy storage systems. *Thermal Science and*

Engineering Progress, 39, 101730.
<https://doi.org/10.1016/J.TSEP.2023.101730>

Wang, S., Hou, X., Yin, J., Xing, Y., & Wang, Z. (2022). Comparative Study of the Thermal Enhancement for Spacecraft PCM Thermal Energy Storage Units. In *Aerospace* (Vol. 9, Issue 11).
<https://doi.org/10.3390/aerospace9110705>



Carbon Capture and Heating – Can we combine long-term energy storage with Direct Air Capture?

Eva Klockow¹, Matthias Schmidt², Venizelos Sourmelis², Viktor Kühl², Marie Gollsch¹, Marc Linder^{1,*}

¹ German Aerospace Center (DLR e.V.), Institute of Engineering Thermodynamics, Pfaffenwaldring 38-40, 70569 Stuttgart, Germany

² German Aerospace Center (DLR e.V.), Institute of Engineering Thermodynamics, Linder Höhe, 51147 Cologne, Germany

*Corresponding author e-mail: marc.linder@dlr.de

Abstract

This contribution describes the current status of a thermochemical long-term energy storage based on quicklime and water. The prototype offers the possibility to transport the material from inexpensive storage volumes to the reaction chamber – and further. This possibility could form the starting point for a combination of long-term energy storage with Direct Air Capture of CO₂ based on the abundantly available material limestone.

Keywords: Thermochemical, Energy Storage, Quick Lime, Technical Lime Cycle, Direct Air Capture

Introduction

About 2/3 of the final energy demand in German households is required for heat supply, with currently less than 20 % provided from renewable energies. As a result, heating accounts for a large share of CO₂ emissions in Germany and the world.

At DLR, an energy storage technology was developed that can collect renewable energy during periods of high availability, store it as chemical potential with minimum losses and release it in periods of high demand as renewable thermal energy, e.g. for household heating in winter [M. Schmidt et al.]. The laboratory prototype is shown in Figure 1. One of its main features is the independent scalability of the storage capacity which only requires potentially inexpensive volumes at ambient temperature and pressure.



Figure 1: Laboratory Prototype of Thermochemical Long-Term Storage based on Quick Lime and Water

This thermochemical energy storage concept is based on the reversible, exothermic reaction from CaO to

Ca(OH)₂, with limestone and water as abundant and globally available raw materials. Currently, a slightly modified version of the thermochemical store is being integrated into a research high-rise building at the university of Stuttgart in the framework of the collaborative research project CRC 1244 [CRC 1244].

However, as in all long-term energy storage options, the storage material is most of the time passively waiting for its use, we are trying to activate this passive period by combining long-term energy storage with Direct Air Capture of CO₂.

Carbon Capture and Heating

The concept of carbon capture and heating (CCH) is based on the well-known “technical lime cycle”, as shown in Figure 2. It starts with the natural mineral CaCO₃ (limestone). During a calcination process CO₂ is released, captured on site and energy is stored as chemical potential.

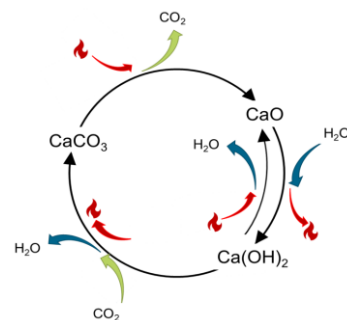
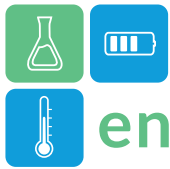


Figure 2: Schematics of the Technical Lime Cycle



As shown in Figure 2, two successive exothermic reactions (hydration and carbonatation) follow which ultimately close the cycle: The above described thermochemical storage utilizes the first one, namely the reversible hydration of quick lime (CaO , cf. indicated charging and discharging on the right). In this case the successive carbonatation reaction should be avoided since its product, the original CaCO_3 is technically inert, at least at the intended charging conditions.

The main concept of CCH is now to actually allow the second reaction and try to take advantage of it. Therefore, after heat has been provided on demand, the passive storage phase of $\text{Ca}(\text{OH})_2$ is used to bind atmospheric CO_2 through carbonatation.

Figure 3 shows a schematic of this concept: on the left, limestone is calcined thereby releasing CO_2 as point source. The upper arrow represents the transport of the stored energy to decentralized consumers. There, tap water can be used to discharge thermal energy on demand – and hydrated quick lime is stored under atmospheric conditions for carbonatation. The lower arrow represents therefore the transport of chemically stored CO_2 back to the original calcination site where the directly captured CO_2 is released again but can now be captured from a point source.

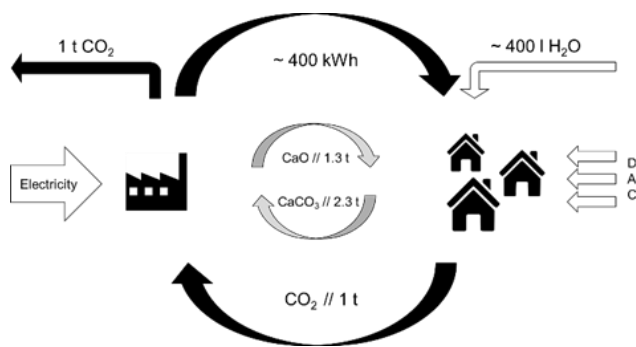


Figure 3: Carbon Capture and Heating – the closed material cycle delivers heat and collects CO_2 . The numbers are related to 1 t of captured CO_2 , ideally calculated [M. Linder].

The numbers given in Figure 3 are calculated assuming ideal conditions and full conversions. The inner circle shows that 1.3 t of CaO is necessary to deliver around 400 kWh of heat and 2.3 t of CaCO_3 have to be moved in order to transport 1 t of captured CO_2 . In order to release the chemically stored thermal energy of 400 kWh, around 400 l of water (e.g. from the tap or

collected) have to be added. The required energy to burn the limestone and drive the whole cycle depends highly on the technology used for the calcination. The minimal required energy to release 1t of CO_2 from limestone is around 1,140 kWh.

Conclusions

We investigate a concept that could combine long-term energy storage, renewable heating on demand and Direct Air Capture of CO_2 – based on the worldwide abundantly available raw material limestone. The backbone for such a concept would be a district-based transport system that transfers the different lime-based compounds between the central charging and decentral discharging sites. An analogy, yet not circular, could be the collection of decentral waste to burn it centrally for energy supply. However, since the rate at which the different lime compounds can pass through the system primarily depends on the kinetically slow carbonatation, the contribution will describe the concept in detail, present the current status of the technology and add experimental results that show how the reaction is influenced by surface and atmospheric conditions as relative humidity and temperature.

Acknowledgment

This work was partially funded by the Vector Stiftung (Project ID: P2022-0320) and the Deutsche Forschungsgemeinschaft (DFG, German Research Foundation)—Project-ID 279064222—in the frame of the SFB 1244.

References

- M. Schmidt and M. Linder. A Novel Thermochemical Long Term Storage Concept: Balance of Renewable Electricity and Heat Demand in Buildings (2020), Frontiers in Energy Research; <https://doi.org/10.3389/fenrg.2020.00137>
- CRC 1244: Collaborative Research Centre 1244 at the University of Stuttgart, Germany; [CRC1244 | University of Stuttgart \(uni-stuttgart.de\)](https://www.crc1244.uni-stuttgart.de/), (Dec. 1st 2023)
- M. Linder. Carbon Capture and Heating – could we rethink the lime cycle? Zenodo (2023). <https://doi.org/10.5281/zenodo.8034159>

Ceramic coatings for containment of aluminium silicon metallic phase change material in thermal storage applications

Carolina Villada^{1,*}, Nuria Navarrete¹, Matthias Kolbe¹, Veronika Stahl², Werner Kraft², Florian Kargl¹
1 Institute of Materials Physics in Space, German Aerospace Center (DLR), Linder Höhe, Cologne, Germany

2 Institute of Vehicle Concepts, German Aerospace Center (DLR), Pfaffenwaldring 38-40, Stuttgart, Germany

*Corresponding author e-mail: carolina.villadavargas@dlr.de

Abstract

Metallic phase change materials (mPCM) have been investigated due to their high thermal conductivity suitable for latent heat thermal storage. The compatibility of mPCM with container materials is a key parameter for ensuring long service life of a thermal storage system for electric bus heating applications. In this work, the performance of Al_2O_3 , multi-coated $\text{Al}_2\text{O}_3/\text{Ni-Ti}$, and $\text{Al}_2\text{O}_3/\text{ZrO}_2$ plasma sprayed coatings are investigated for their ability to prevent attack of stainless steel by the eutectic Al-12.5 wt. % Si at 650 °C. The solid-liquid interface as well as the coating thickness and potential interactions were characterised with optical and scanning electron microscopy. Results showed that Al_2O_3 and multi-coated $\text{Al}_2\text{O}_3/\text{Ni-Ti}$ coatings resisted in the liquid aluminium alloy during 2 weeks static experiments and no evidence of reaction was observed, while the $\text{Al}_2\text{O}_3/\text{ZrO}_2$ coating showed cracks.

Keywords: Ceramic coating, Liquid metal, Phase change material, Latent heat

Introduction

Battery electric vehicles operating in cold weather conditions must maintain appropriate air temperatures where people or electric components are located. Using the electric battery for these purposes reduces the driving range of the vehicle. Storage of heat in a thermal storage unit during charging and release of this heat during driving helps mitigate this problem. This application is well suited to metal and metal alloys due to the volume constrictions and charge/discharge rate requirements. The eutectic aluminium silicon (Al-12.5 wt.% Si) has gained special attention due to its high heat of fusion of ~505 kJ/kg and energy density of ~340 kWh/m³ (Villada, 2023). Reaction tests are used to further develop container materials that show potential compatibility for longer lifetimes and high temperature resistant (Withey, 2016). Previous experiments have shown dissolution and intermetallic phases with conventional 304 and 309 steels at 650 °C from 8 h up to 336 h. Therefore, this study is focused on the investigation of the compatibility of aluminium silicon eutectic (Al-12.5 wt.% Si) with different ceramic coated steel housing materials. Our recent projects have targeted the development of a thermal storage concept for electric bus heating with a preliminary material selection and experimental validation. Figure 1 shows the schematics of a storage concept design using mPCM (Kraft, 2021).

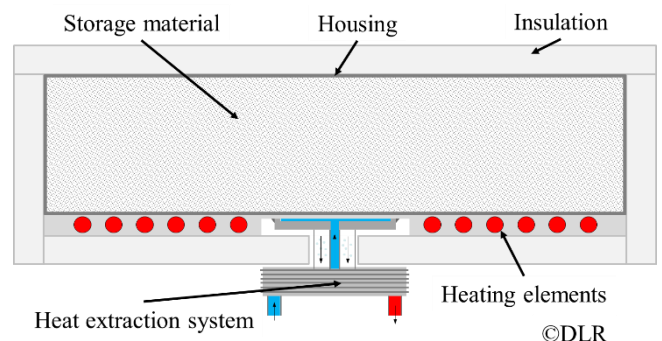


Figure 1: Schematics of storage concept for a battery electric bus.

The main attention regarding ceramic coating compatibility is focused on the characterisation of the interface between the liquid material and the coating layer, which have shown their effectiveness for limiting the corrosivity of the liquid aluminium alloy. An important outcome is that the Al-12.5 wt.% Si is a promising mPCM together with ceramic coated steel containers.

Materials and methods

To investigate the operational compatibility of Al-12.5 wt.% Si, static reaction experiments were undertaken. Here, mPCM pellets were placed inside different crucibles of stainless steel coated with Al_2O_3 , multi-coated $\text{Al}_2\text{O}_3/\text{Ni-Ti}$ and $\text{Al}_2\text{O}_3/\text{ZrO}_2$, and held at approximately 650 °C under inert atmosphere.

Following the reaction experiment, the crucible and sample pairs were examined in terms of mass change and chemical interactions. The crucible and sample pairs were cross-sectioned for Scanning Electron Microscopy (SEM), Energy-dispersive X-ray spectroscopy (EDX) and Electron backscatter diffraction (EBSD) on representative points and areas.

Coating materials selection

Table 1 shows the coating material selection in this investigation including the coating thickness at the bottom zone. Two different ceramic coatings were applied on a 304 steel. The Al_2O_3 was produced by atmospheric plasma spray (APS) and the $\text{Al}_2\text{O}_3/\text{ZrO}_2$ by high velocity oxy-fuel (HVOF) spray technique. The 309 steel multi-coated with Al_2O_3 had an intermediate layer of Ni-Ti. This intermediate layer was used to avoid stresses between the steel and alumina due to their thermal expansion coefficients.

Table 1: Material selection for static reaction experiments with Al-12.5 wt.% Si alloy.

Coating sprayed technique	Crucible material	Coating thickness [μm]
APS	Multi-coated ($\text{Al}_2\text{O}_3/\text{Ni-Ti}$) 309 steel	268.4 \pm 19.6
APS	Al_2O_3 coated 304 steel	162.7 \pm 6.4
HVOF	$\text{Al}_2\text{O}_3/\text{ZrO}_2$ coated 304 steel	126.6 \pm 2.4

Results and Discussion

The coating parameters are an important aspect since a deficient coating can let the liquid metal get into contact with the steel. Although 3 different coatings have been selected, all 3 performed similarly during 336 h at 650 °C. After our reaction experiments, the Al_2O_3 and multi-coated $\text{Al}_2\text{O}_3/\text{Ni-Ti}$ coatings were compatible chemically, no dissolution, cracking or damage was observed, preventing a reaction between the steel and the Al-12.5 wt.% Si alloy. The $\text{Al}_2\text{O}_3/\text{ZrO}_2$ coating showed some localised cracks but no evidence of attack on the steel was observed. Figure 2 shows the interface between the mPCM and the $\text{Al}_2\text{O}_3/\text{ZrO}_2$ coated 304 steel crucible material.

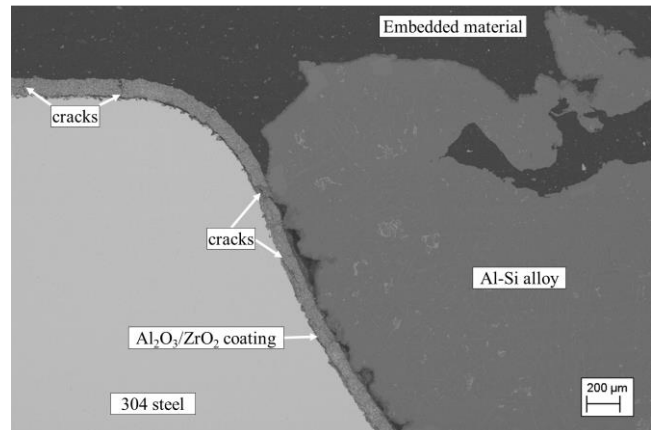


Figure 2: SEM image after static reaction experiment at 650 °C of Al-12.5 wt.% Si with $\text{Al}_2\text{O}_3/\text{ZrO}_2$ coated 304 steel crucible material.

Conclusions

The eutectic composition was shown to be compatible with Al_2O_3 , multicoating $\text{Al}_2\text{O}_3/\text{Ni-Ti}$ and $\text{Al}_2\text{O}_3/\text{ZrO}_2$ ceramic coatings during long term reaction experiments up to 336 h. Although the $\text{Al}_2\text{O}_3/\text{ZrO}_2$ coating showed a more even distributed coating thickness, some cracks were observed after the experiment. From this study, ceramic coatings could serve as a barrier and could be recommended as housing materials for mPCM used in thermal heat storage applications. Further research is being considered regarding thermal cycling, thermal contact resistance and the effect of thermomechanical stresses, which are relevant during the TES system operation.

Acknowledgment

This research was funded within the project FFAE: Fokusanwendungen, Fahrzeugstruktur, Antriebsstrang, Energiemanagement. The authors would like to thank Christian Semmler from the Universität Stuttgart for the Al_2O_3 and $\text{Al}_2\text{O}_3/\text{ZrO}_2$ coating processing.

References

- Kraft W., Stahl V., Vetter P., Nees F. (2021) Thermal High Performance Storages for electric bus heating. Enerstock Online Conference, 8-11 June 2021.
- Villada, C. and al. (2023). Recycling of aluminium scrap into phase change materials for high-temperature storage applications: Thermophysical properties and microstructural characterisation. Journal of Energy Storage. doi.org/10.1016/j.est.2023.108822.
- Withey, E. and al. (2016). Plasma sprayed coatings for containment of Cu-Mg-Si metallic phase change material. Surface and coatings technology. doi.org/10.1016/j.surfcoat.2016.06.063



Characterization of coated silica sand by Mn diffusion into crystal cell.

L.M. Cerutti-Cristaldo^{1,*}, M. Díaz-Heras^{1,2}, J.C. Pérez-Flores^{1,2},
J. Canales-Vázquez^{1,2}, J.A. Almendros-Ibáñez^{1,2}

1-Universidad de Castilla-La Mancha, Renewable Energy Research Institute, Albacete, Spain

2-Universidad de Castilla-La Mancha, E.T.S. de Ingeniería Industrial, Albacete, Spain

*Corresponding author e-mail: leonelmario.cerutti@uclm.es

Abstract

Nowadays, the global energy crisis and concerns about pollution affect most countries around the world. As a result, many renewable alternatives to traditional energy sources have been developed in the last few decades. Among these alternatives, concentrated solar power plants (CSP) are particularly advantageous due to the possibility of integrating both thermal energy generation and storage systems into a single solution. Additionally, the introduction of solid particles in solar receivers will greatly enhance the performance of CSP plants, increasing the operative temperature conditions over 1000 °C, with the consequent energy conversion efficiency increase and reduction of the levelized cost of electricity (LCOE), which are some of the main disadvantages of current CSP technology.

Therefore, the characterization and development of new solid particles are critical aspects for improving the CSP performance. Previous studies have explored a novel coating process involving the diffusion of manganese ions into silica structure, aiming to enhance their optical properties by darkening. In this work, the effect of the thermal treatment is evaluated by X-Ray Diffraction, Scanning-Electron Microscope and morphological parameters. The results observed clearly indicate a diffusion of manganese in the sand, which will increase its absorptivity and the efficiency of a potential CSP system.

Keywords: Fluidized bed, CSP, Thermal energy storage, Solid particles, Solar receiver

Introduction

Currently, there is a growing concern regarding the increase in pollution levels and the emerging global energy crisis. As a solution to this situation, numerous global initiatives for energy transition aiming at reducing pollution levels are being implemented, such as the Net Zero Emission (NZE) by 2050. According to the International Energy Agency (IEA), renewable energy sources, particularly solar and wind technologies, will play a significant role in achieving the necessary CO₂ reductions for the NZE Scenario (IEA, 2023).

Within solar technology, the most widespread is solar photovoltaic (PV) due to the continuing decrease in the cost of PV arrays and the increase in their power conversion efficiency, in addition to their easy power input scaling (Singh, 2013). Despite this, concentrated solar power (CSP) has significant advantages, such as the capability to integrate energy generation and storage. This integration can balance supply and demand instabilities created by solar energy intermittency (Achkari and al., 2020).

The main limitation of current CSP is the high levelized cost of electricity (LCOE), although it has fallen by 68% from 2010 to 2021 (IRENA, 2023). This decrease could be also powered by the introduction of solid particles in solar receivers technology to the next-gen of CSP plants, achieving operational temperatures over 1000 °C, much higher than the current limitation at 565 °C with molten salts solar receivers. In combination with the sCO₂ Brayton cycle, it achieves greater power conversion efficiency (Nie and al., 2022).

Consequently, considering all these facts, the selection of the material for solid particles is a crucial aspect in CSP efficiency. Therefore, many works have focused on the characterization of solid particles for this application. Among the more promising materials (Palacios and al., 2019; Díaz-Heras and al., 2020), SiC is highly suitable due to its good mechanical properties, such as high wear resistance, thermal shock resistance, high strength at elevated temperatures, high thermal conductivity, and a natural black color with high absorptivity (0.9). However, it is an expensive material as it must be synthesized.

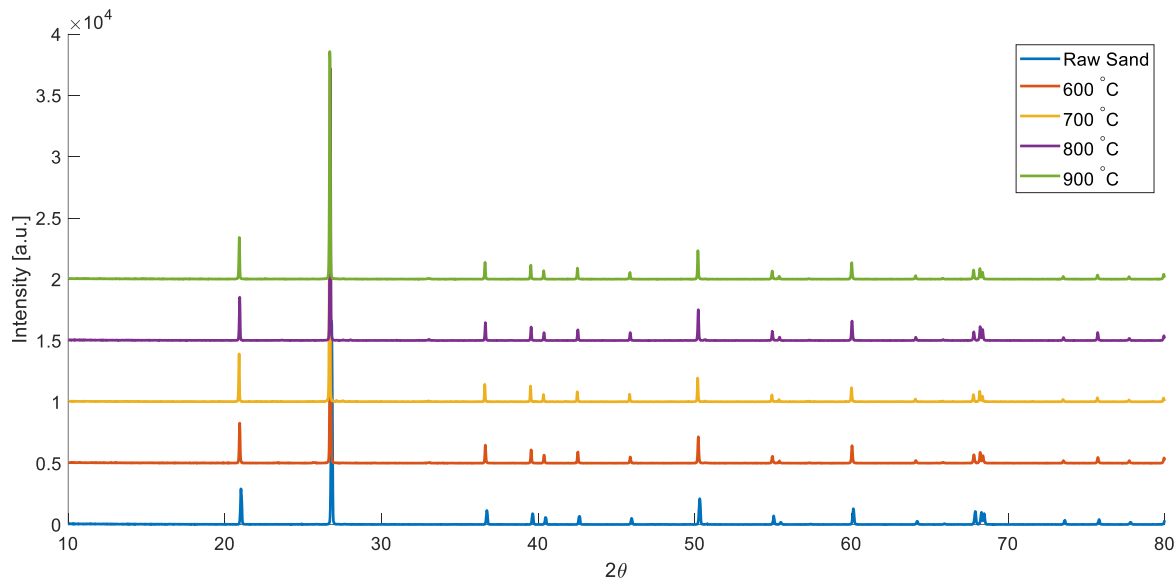


Figure 1: X-Ray Diffraction patterns.

On the other hand, silica sand has a high durability, a high melting-point, it is resistant to heat and chemical attack, worldwide available and inexpensive material. The main disadvantage is its white color with low absorptivity (Palacios and al., 2019). This issue can be minimized through coating processes on the particles to darken them and consequently enhance their optical properties.

There are many studies on coating processes using nanoparticles (Chung and al., 2023; Farchado and al., 2024), such as black spinel oxide nanoparticles, to achieve high absorptivity values, thermal stability, and low degradation with temperature. The main challenges are to reduce the cost of the nanoparticles and extend its durability under high abrasion conditions.

Therefore, this work presents a new coating method based on ion diffusion through the silica sand structure. The aim is to promote a permanent color change, increase the absorption rate of the sample, ensure long-term durability, and maintain a low cost.

Methodology

For the sample preparation, $MnCO_3$ and silica sand are mixed in an agate mortar, maintaining a weight ratio of 1:50, respectively. The samples are then heated in a muffle furnace at four different temperatures (600, 700, 800, and 900 °C) for 6 hours.

To assess the penetration of Mn ions into silica, X-ray diffraction (XRD) patterns have been collected and analyzed. Additionally, the samples have been observed using a scanning electron microscope (SEM)

and morphologically characterized with a particle morphological microscope.

Results and Discussion

The morphological parameters evaluated include the equivalent particle diameter, measured as the diameter that produces a circle with the same area as the particle projection. Circularity is defined as the ratio between the actual particle perimeter and the perimeter of the equivalent area circle. Convexity represents the ratio between the full convex hull perimeter and the actual particle perimeter. Aspect ratio is measured as the relationship between the length and width of the particle. These parameters are relevant for the design of the fluidized bed solar central receiver.

Table 1 compiles the mean values of the morphological parameters, demonstrating significant variations in particle shape. One of the most notable observations is the clear reduction in the mean particle diameter (dp), from the initial 183 μm value to less than half after the coating process. This reduction is attributed to two factors. Firstly, the introduction of fine particles of $MnCO_3$ to the original sample. Secondly, and more relevant, during the mixing process in the mortar, the samples suffer grinding, leading to an increase in the number of small particles and a reduction in the overall mean value.

Table 1: Mean values of morphological parameter.

Sample	dp [μm]	Circularity [-]	Convexity [-]	Asp. Ratio [-]
Raw	183.0	0.23	0.95	0.16
600 °C	62.1	0.75	0.96	0.56
700 °C	81.6	0.73	0.97	0.55
800 °C	73.8	0.76	0.96	0.57
900 °C	81.5	0.63	0.97	0.47

The mean diameter is expected to increase again after undergoing a fluidization process, during which the small particles are carried out of the bed by the air stream. The increase in circularity and aspect ratio can also be attributed to the polishing process experienced by the samples, resulting in a more regular shape that is closer to a sphere.

The diffraction patterns, as shown in Figure 1, provide information about the chemical composition and crystal structure of the samples. From bottom to top, the patterns represent raw silica sand and the coated samples heated at 600, 700, 800, and 900 °C. The general pattern corresponds to the main diffraction peaks of silica sand, and the emergence of new peaks can be explained by the presence of secondary phases from the MnCO₃ decomposition at high temperatures.

The critical aspect is the horizontal shift experienced by the diffraction peaks as the temperature increases, as shown in Figure 2. Initially, the shift is towards lower 2θ until it reaches 700 °C, attributed to the introduction of Mn²⁺ ions into the silica structure.

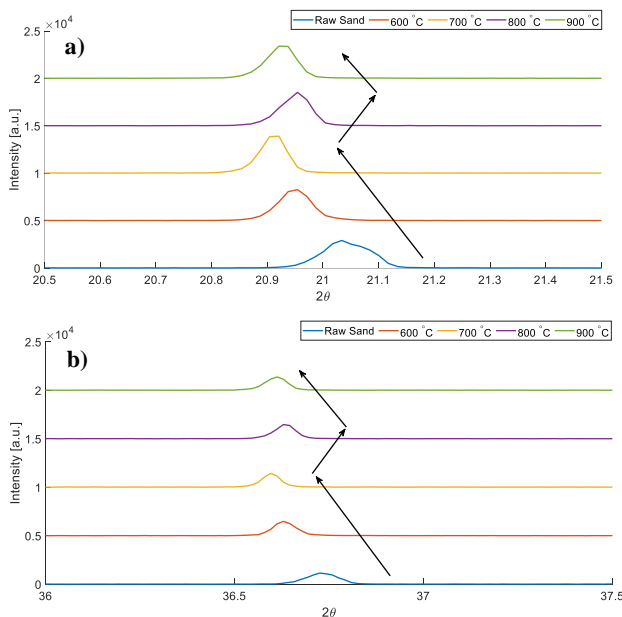


Figure 2: Main diffraction peaks zoom, (a) 2θ between [20.5°, 21.5°], (b) 2θ between [36°, 36.5°].

Beyond 700 °C, the shift changes its tendency toward higher 2θ angles, and it decrease again at 900 °C. As silica undergoes a phase transformation in this temperature range (Ratnawulan and al., 2018) and the solubility of Mn²⁺ drops. However, as this is a solid diffusion process, higher temperatures lead to a gradual increase in the Mn content in the silica structure.

Figure 3 shows the surface of a grain of raw sand at x1000 magnification, to provide a comparison with the

coated samples in Figure 4. The presence of residual MnCO₃ particles in the coated samples is evident. Moreover, their adherence to the sand grain increases with increasing the temperature, resulting in a more homogeneous particle surface.

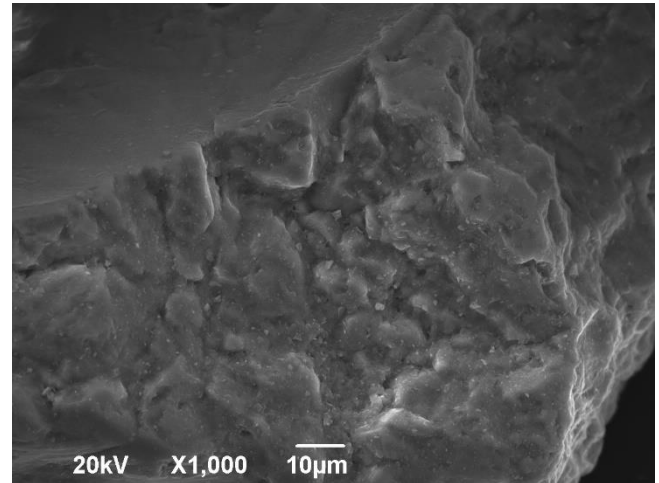


Figure 3: Raw sand SEM image.

Additionally, the emergence of new small particles created by the cracking of the material during the mixing process is noteworthy. While the promoted color change is rather clear in all samples, there is no notable difference between them.

Conclusions

The manganese diffusion into silica has been proved, hence it is expected that it will have a longer durability under fluidization conditions. Nevertheless, it is still necessary to quantify the impact of such change. Besides, the influence of different weight ratios should be evaluated in order to optimize it.

In future works the samples performance for CSP application will be analyzed in an experimental facility, using a beam-down fluidized bed solid particles solar receiver. Moreover, the color change will be quantitatively measured by using a spectrometer.

Acknowledgment

This work was funded by grants PID2021-127322OB-I00, TED2021-131046B-I00 and RED2022-134219-funded by MCIN/AEI/ 10.13039/501100011033 and by "ERDF A way of making Europe" and "European Union NextGenerationEU/PRTR"; grant SBPLY/21/180501/000017 funded by the regional government of Castilla-La Mancha and grant 2022-GRIN-34343 funded by Universidad de Castilla-La Mancha.

References

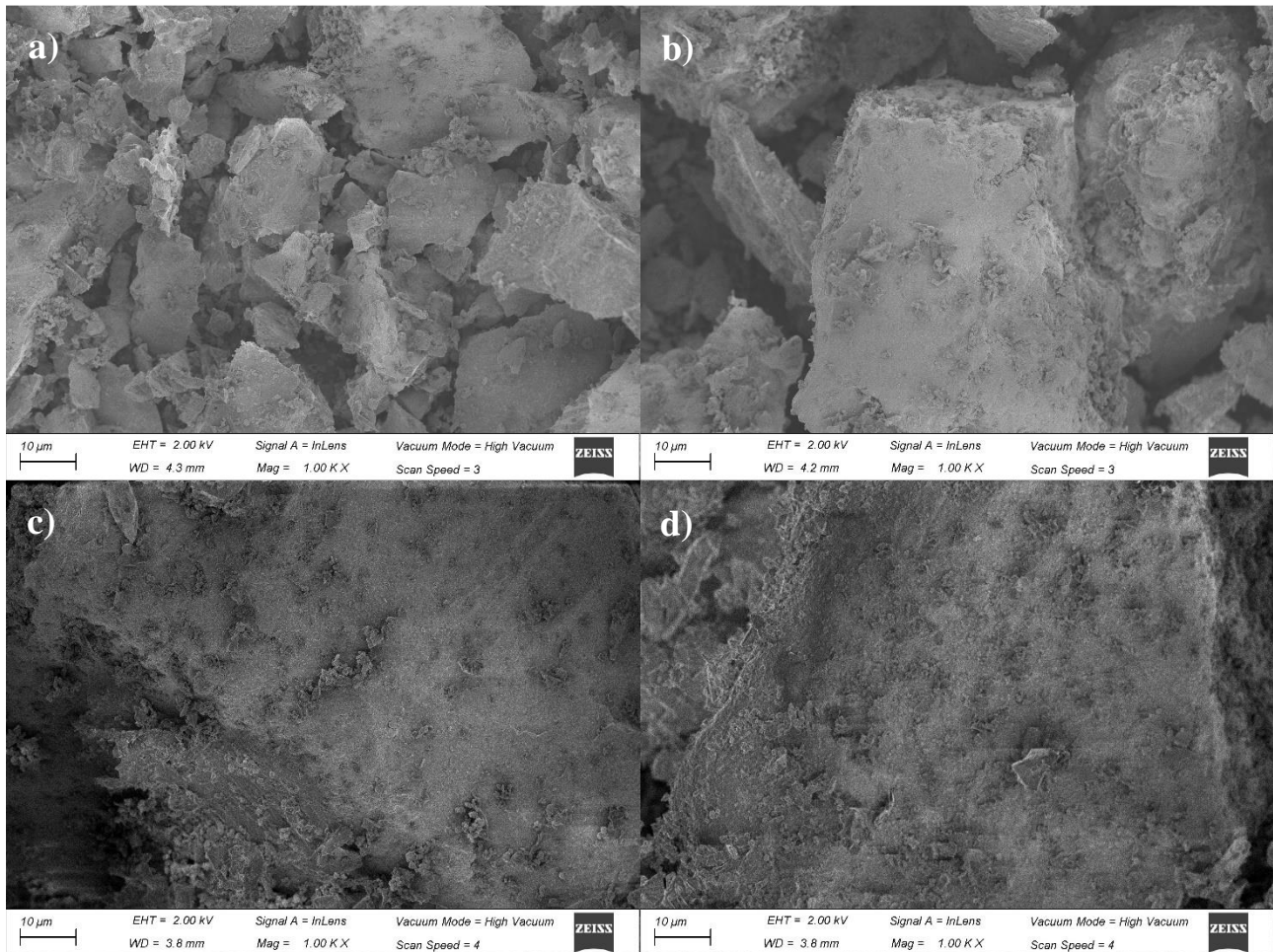


Figure 2: Sem images (a) 600 °C, (b) 700 °C, (c) 800 °C and (d) 900 °C

IEA (2023), Tracking Clean Energy Progress 2023, IEA, Paris <https://www.iea.org/reports/tracking-clean-energy-progress-2023>, License: CC BY 4.0

SINGH, Girish Kumar. Solar power generation by PV (photovoltaic) technology: A review. *Energy*, 2013, vol. 53, p. 1-13.

ACHKARI, O.; EL FADAR, A. Latest developments on TES and CSP technologies—Energy and environmental issues, applications and research trends. *Applied Thermal Engineering*, 2020, vol. 167, p. 114806.

IRENA (2023), World Energy Transitions Outlook 2023: 1.5°C Pathway, Volume 1, International Renewable Energy Agency, Abu Dhabi.

NIE, Fuliang, et al. Solid particle solar receivers in the next-generation concentrated solar power plant. *EcoMat*, 2022, vol. 4, no 5, p. e12 207.

PALACIOS, Anabel, et al. Study on solar absorptance and thermal stability of solid particles materials used as TES at high temperature on different aging

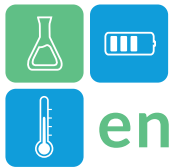
stages for CSP applications. *Solar Energy Materials and Solar Cells*, 2019, vol. 201, p. 110088.

DÍAZ-HERAS, M., et al. Experimental study of different materials in fluidized beds with a beam-down solar reflector for CSP applications. *Solar Energy*, 2020, vol. 211, p. 683-699.

CHUNG, Ka Man; CHEN, Renkun. Black coating of quartz sand towards low-cost solar-absorbing and thermal energy storage material for concentrating solar power. *Solar Energy*, 2023, vol. 249, p. 98 106.

FARCHADO, Meryem, et al. Performance improvement of CSP particle receivers by Materials and Solar Cells, 2024, vol. 266, p. 112681.

RATNAWULAN, R.; FAUZI, A.; HAYATI, A. E. S. Characterization of silica sand due to the influence of calcination temperature. *En IOP Conference Series: Materials Science and Engineering*. IOP Publishing, 2018. p. 012008.



Characterizing Na₂S kinetics for thermochemical energy storage applications through algorithmic optimization

Bram Kieskamp^{1,*}, Amirhoushang Mahmoudi¹, Mina Shahi^{1,*}

¹ University of Twente, Department of Thermal and Fluid Engineering, Enschede, The Netherlands

*Corresponding author e-mails: b.m.kieskamp@utwente.nl, m.shahi@utwente.nl

In this study, the application of the Shuffled Complex Evolution (SCE) method for algorithmic optimization has demonstrated its effectiveness in calibrating the reaction model for sodium sulfide (Na₂S) for use in thermochemical energy storage (TCES) systems. The research revealed that both two-step and three-step reaction models for Na₂S align well with experimental data. This method significantly streamlines the data requirements, as it relies primarily on time-series data of conversion, temperature, and pressure, which are readily accessible from Thermogravimetric (TG) measurements. However, despite these advancements, thorough validation of these models is essential, especially under diverse operating conditions beyond the initial test environments. This study highlights the potential of advanced algorithmic techniques for material characterization for TCES applications.

Keywords: Thermochemical Energy Storage, Na₂S, Shuffled Complex Evolution

Introduction

Thermochemical energy storage (TCES) is emerging as a key player in the field of energy storage, exhibiting high energy densities and the capability to store heat for prolonged periods. This makes it particularly useful for offsetting the irregularities in renewable energy generation. TCES systems utilize reversible chemical reactions, making them highly efficient in managing the energy supply-demand balance.

Sodium Sulfide (Na₂S) is a particularly promising material for TCES due to its high energy storage density, setting it apart from other salt hydrates. The practical application of Na₂S, however, relies on a comprehensive understanding of its kinetic behavior during hydration and dehydration cycles. This aspect is critical, yet underexplored, posing a challenge for its effective integration into TCES systems.

Foundational research by Andersson et al. (1986) and De Boer et al. (2002) established the equilibrium states and conditions of Na₂S. Sögütöglu et al. (2018) investigated its cyclic behavior, revealing strong cyclic stability in a CO₂ free environment and noting the presence of reaction hysteresis. However, the quantification of this hysteresis and its impact on the efficiency and reliability of TCES systems remains uninvestigated.

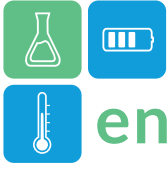
Three primary methods for kinetic analysis can be identified (Purnomo et al., 2020):

1. Isoconversional approaches like the Kissinger and Ozawa-Flynn-Wall methods (Vyazovkin et al., 2011)
2. Purely data-driven techniques employing statistical and machine learning tools.
3. Algorithmic methods combining computational models with experimental data.

Algorithmic methods are of specific interest here, due to their ability to calibrate well defined and widely used kinetic equations with minimal requirements for data and analysis.

Shuffled Complex Evolution (SCE), one such algorithmic method, is particularly noteworthy for analyzing complex, multi-step reactions with numerous parameters. It's a preferred method in thermal decomposition studies due to its effective exploration of parameter spaces and finding optimal solutions at minimal computational cost. SCE's adaptability makes it ideal for the kinetic analysis of Na₂S.

This study applies SCE to explore the reaction kinetics of Na₂S in hydration-dehydration processes. Our aim is to provide detailed and precise kinetic data, crucial for optimizing Na₂S-based TCES systems. The insights gained from this study could significantly impact TCES efficiency, promoting more effective use of renewable energy sources.



Methodology

STA analysis

The methodology for investigating the thermal properties of Sodium sulfide nonahydrate ($\text{Na}_2\text{S} \cdot 9 \text{H}_2\text{O}$) involved Simultaneous Thermal Analysis (STA). The $\text{Na}_2\text{S} \cdot 9 \text{H}_2\text{O}$, sourced from Fisher Scientific, was used in its crystalline form, without undergoing sieving or any preprocessing steps.

A Netzsch STA 449 F3 Jupiter system was employed for the STA experiments, utilizing nitrogen as the purge gas at a flow rate of 200 mL/min, connected through an MHG humidifier. We analyzed samples with weights in the range of 2 to 10 mg, each placed in an Alumina crucible of 85 μL capacity to maintain uniform thermal properties and reaction conditions. The choice of small sample sizes was deliberate to reduce thermal gradients and promote homogenous reaction conditions. To avert the melting of nonahydrate, which typically occurs at 49°C (de Boer et al., 2002), the samples were first dehydrated to the pentahydrate state at 45°C, maintaining 0% relative humidity for 3 hours. Afterwards, operating conditions were varied to facilitate hydration and dehydration reactions between the pentahydrate and hemihydrate states.

Data recording during STA was set at an interval of 3 seconds. The mass change was observed using thermogravimetric (TG) analysis. For the conversion rate analysis, the TG data was refined using a Savitzky-Golay smoothing filter, with a window size of 201 and a polynomial of second order.

Reaction model

Hydration and dehydration reactions occur in several, distinct, steps (de Boer et al., 2002). Four distinct stable hydration states have been found previously; the hemihydrate ($\text{Na}_2\text{S} \cdot 0.5 \text{H}_2\text{O}$), dihydrate ($\text{Na}_2\text{S} \cdot 2 \text{H}_2\text{O}$), pentahydrate ($\text{Na}_2\text{S} \cdot 5 \text{H}_2\text{O}$) and nonahydrate ($\text{Na}_2\text{S} \cdot 9 \text{H}_2\text{O}$). The exact water contents of these hydrates is different from these values, but for the sake of consistency with the literature this terminology is kept. The equilibrium diagram of these phases is given in Figure 1.

For TCES applications, the 0.5-5 reaction is of specific interest, with the 5-9 reaction being excluded due to unfavorable reaction conditions (Donkers et al., 2017). This is a multi-step reaction going through the stable dihydrate state. Furthermore, based on observed reaction behavior, the 0.5-2 reaction seems to go through a volatile intermediate step, which would make it a three step reaction. Both the reaction kinetics

of a one and two step reaction are investigated in this study.

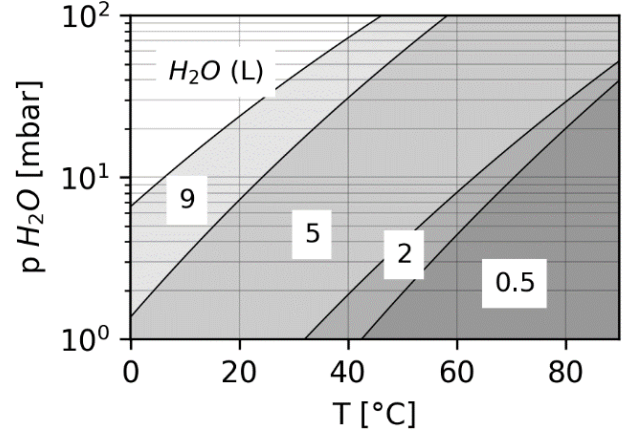


Figure 1: Na_2S equilibrium diagram, based on equilibrium data from de Boer et al. (2002). Numbers indicate the approximate numbers of the stable hydration states

The individual reaction steps are modelled through Equation 1 for the hydration reactions and Equation 2 for the dehydration reactions:

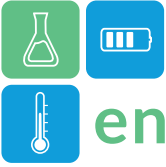
$$\frac{d\alpha_p}{dt} = k_r \cdot (\alpha_r)^q \cdot e^{-\frac{E_A}{RT}} \cdot \left(\frac{p_{\text{H}_2\text{O}}}{p^*} - 1 \right)^n \quad (1)$$

$$\frac{d\alpha_p}{dt} = k_r \cdot (\alpha_r)^q \cdot e^{-\frac{E_A}{RT}} \cdot \left(\frac{p^*}{p_{\text{H}_2\text{O}}} - 1 \right)^n \quad (2)$$

With α_p and α_r being the molar fractions of the product and the reactant, respectively, k_r a rate constant in 1/min, q the conversion model exponent, E_A the activation energy in J/mol, R the ideal gas constant in J/mol K, T the temperature in K, $p_{\text{H}_2\text{O}}$ the water vapor pressure, p^* the reaction onset pressure, and n the pressure model exponent. The reaction onset pressure is used instead of the equilibrium pressure, as it was previously found to be an effective way of accounting for reaction hysteresis (Kieskamp et al., 2023).

Optimization algorithm

The calibration of the parameters of the reaction models given in Equation 1 and Equation 2 is done through the Shuffled Complex Evolution method developed at the University of Arizona (SCE-UA, Duan et al., 1993). In this implementation, the multi-step reaction models are numerically integrated over the pressure and temperature conditions used in the STA measurements. Afterwards, the mean squared error (MSE) of the model and the experiment is calculated through a weighted sum of the conversion and conversion rate:



$$MSE = \frac{1}{N} \sum_{i=1}^N (\phi_{exp,i} - \phi_{model,i})^2 + 100 \cdot \frac{1}{N} \sum_{i=1}^N \left(\frac{d\phi_{exp,i}}{dt} - \frac{d\phi_{model,i}}{dt} \right)^2 \quad (3)$$

With N the number of sampled points and ϕ the hydrate number at the time of sampling. In the model this is calculated as:

$$\phi_{model} = \sum_n M_n \alpha_n \quad (4)$$

With M_n the molar mass of the hydrate. As this is unknown for the intermediate reaction states, this introduces 1 or 2 additional unknown parameters, depending on a 2 or 3 step reaction process, for a total of 17 parameters for the 2 step reaction and 26 parameters for the 3 step reaction. Optimization of these parameters with SCE is done using one million repetitions and 130 complexes.

Results and Discussion

To get a diverse dataset, STA measurements are performed over a range of pressure and temperature conditions. Time series data of this is given in Figure 2. Through the TG and DTG data the hydration and hydration rate of the sample is obtained, shown in Figure 3. A diverse range of conversion rates is obtained, suitable for model calibration.

In the numerical model Equation 1 and Equation 2 are integrated over time with the temperature and pressure again given by Figure 2. Through the SCE optimization the free parameters are optimized to

minimize the MSE between the model and the measurements. The free parameters are bounded by the values given in Table 1.

Table 1: Parameter bounds for the SCE calibration.

Parameter	Lower bound	Upper bound
k_r	400	800
E_A	15000	30000
q	0.1	0.9
n	0.1	2
M	1	4.5

The results for the SCE calibration of the two and three step reaction models are overlaid in Figure 3. A good fit of the conversion is observed for both models, with only a slight deviation of the three step model around $t = 3100s$ and of the two step model around $t = 4500s$. More deviations can be observed in the conversion rate fit, with the dehydration rate peaks specifically showing significant deviations. This behaviour could be caused by a suboptimal selection of the dehydration model or insufficient repetitions of the SCE calibration.

The MSE (Equation 3) of the two and three step model is $1.17 \cdot 10^{-3}$ and $0.95 \cdot 10^{-3}$, respectively, indicating that both models represent the data well, with the three step model being slightly superior. This could be caused by the three step model more accurately representing the underlying physics of the system, but might also be the model overfitting the data. In future study, this should be investigated through thorough model validation.

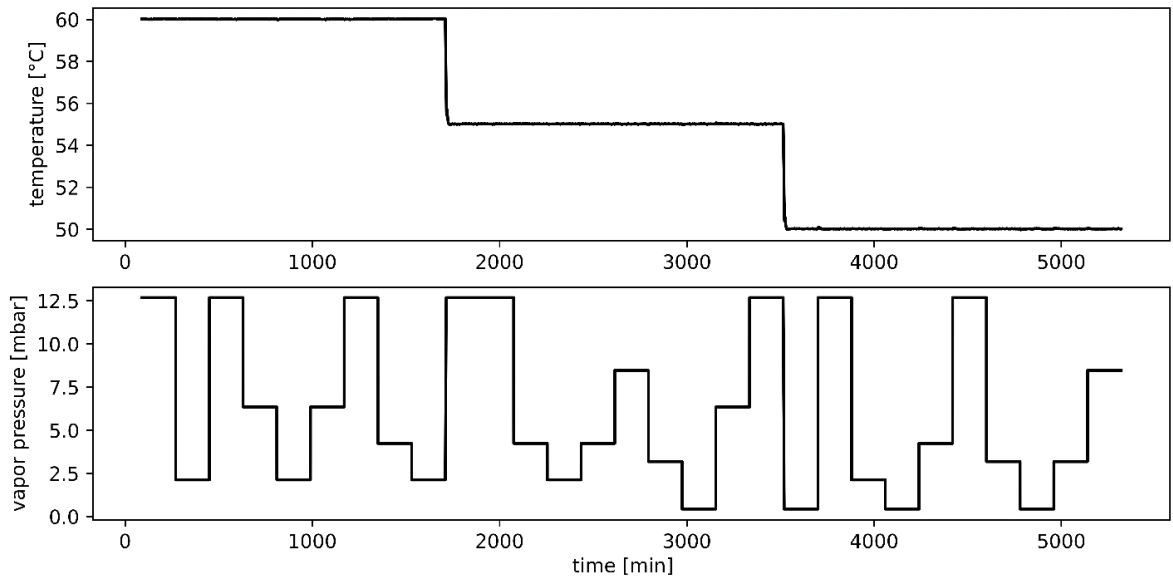


Figure 2: Temperature and pressure time series as used in the STA measurement and the corresponding numerical model



Conclusions

In this study, algorithmic optimization through SCE was shown to be an effective method for calibrating reaction models. Both the two and three step reaction models were able to achieve a good fit with measurement data. Furthermore, this approach reduced the requirements on the data and analysis, as only time series data of the conversion, temperature and pressure is required, which can easily be acquired from TG measurements. However, careful validation is still required to ensure model accuracy and to ascertain the accuracy outside of test conditions.

Acknowledgment

This work was co-financed by TKI- Energy through the allowance scheme of the Top Sector Alliance for Knowledge and Innovation (TKI) of the Ministry of Economic Affairs and Climate Policy. Ares B.V. and its employees are gratefully acknowledged for valuable discussions on experimental methods.

References

- Andersson, J. Y., & Azoulay, M. (1986). Mechanisms and kinetics of the thermal decomposition of sodium sulphide pentahydrate under controlled water vapour pressure. *Journal of the Chemical Society, Dalton Transactions*, 3, 469–475. <https://doi.org/10.1039/DT9860000469>
- De Boer, R., Haije, W. G., & Veldhuis, J. B. J. (2002). Determination of structural, thermodynamic and phase properties in the Na₂S-H₂O system for application in a chemical heat pump. [https://doi.org/10.1016/S0040-6031\(02\)00158-2](https://doi.org/10.1016/S0040-6031(02)00158-2)

- Purnomo, D. M. J., Richter, F., Bonner, M., Vaidyanathan, R., & Rein, G. (2020). Role of optimisation method on kinetic inverse modelling of biomass pyrolysis at the microscale. *Fuel*, 262(September 2019), 116251. <https://doi.org/10.1016/j.fuel.2019.116251>
- Vyazovkin, S., Burnham, A. K., Criado, J. M., Pérez-Maqueda, L. A., Popescu, C., & Sbirrazzuoli, N. (2011). ICTAC Kinetics Committee recommendations for performing kinetic computations on thermal analysis data. *Thermochimica Acta*, 520(1–2), 1–19. <https://doi.org/10.1016/J.TCA.2011.03.034>
- Donkers, P. A. J., Sögütöglü, L. C., Huinink, H. P., Fischer, H. R., & Adan, O. C. G. (2017). A review of salt hydrates for seasonal heat storage in domestic applications. *Applied Energy*, 199, 45–68. <https://doi.org/10.1016/j.apenergy.2017.04.080>
- Kieskamp, B., Mahmoudi, A., & Shahi, M. (2024). A novel multi-reactor system for thermochemical heat storage through detailed modeling of K₂CO₃ particles. *Journal of Energy Storage*, 78(October 2023), 110028. <https://doi.org/10.1016/j.est.2023.110028>
- Duan, Q. Y., Gupta, V. K., & Sorooshian, S. (1986). Shuffled complex evolution approach for effective and efficient global minimization. *Journal of Optimization Theory and Applications*, 2(3), 28–31.

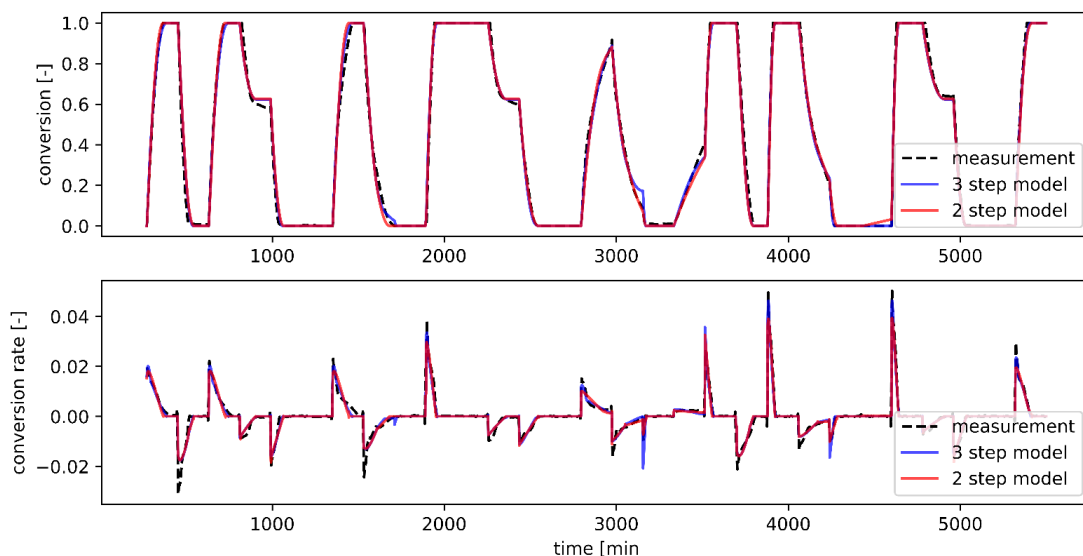


Figure 3: conversion and conversion rate results of the STA measurement. Overlaid are the 3 and 2 step reaction models.

Comparative Simulations for the Verification of Simulation Models for Large Thermal Energy Storages

Thomas Schmidt^{1*}, Michael Reisenbichler-S.², Abdulrahman Dahash³, Ioannis Sifnaios⁴, Steven van der Wilk⁵, Geoffroy Gauthier⁶, Jeff Thornton⁷, Alice Tosatto⁸, Fabian Ochs⁸, Julian Formhals⁹

1 Solites – Steinbeis Research Institute for Solar and Sustainable Thermal Energy Systems, Meitnerstr. 8, 70563 Stuttgart, Germany

2 AEE - Institute for Sustainable Technologies, Feldgasse 19, 8200 Gleisdorf, Austria

3 AIT Austrian Institute of Technology GmbH, Center for Energy, Sustainable Thermal Energy Systems, Giefinggasse 2, 1210 Vienna, Austria

4 Department of Civil and Mechanical Engineering, Technical University of Denmark, Koppels Allé, 2800 Kgs. Lyngby, Denmark

5 IF Technology, Velperweg 37, 6824 BE Arnhem, Netherlands

6 PlanEnergi, Nørregade 13, 1165 København K, Denmark

7 Thermal Energy System Specialists (TESS), 3 N. Pinckney Street, Madison WI 53703USA

8 Energy Efficient Building Unit, University of Innsbruck, Technikerstraße 13, 6020 Innsbruck, Austria

9 Vattenfall Wärme Berlin AG, Hildegard-Knef-Platz 2, Berlin 10829, Germany

*Corresponding author e-mail: schmidt@solites.de

Abstract

This paper describes the work of Task 39 of the IEA Energy Storage Technology Collaboration Program, Subtask C: Large Thermal Energy Storages for District Heating – Round Robin Simulations. The aim of the work was to verify and compare numerical simulation models for Large Thermal Energy Storages (LTES) by means of comparative simulations. Models for the following storage concepts were considered: Aquifer Thermal Energy Storage (ATES), Borehole Thermal Energy Storage (BTES), Pit Thermal Energy Storage (PTES), and Tank Thermal Energy Storage (TTES). In total, eleven partner institutions contributed 37 simulation models for six specified test cases to the comparative simulations. Results for the single test cases show, in general, good agreements for annual heat values for TES charging and discharging and acceptable deviations in short-term evolutions of storage temperatures.

Keywords: Comparative simulation, verification of simulation models, LTES, ATES, BTES, PTES, TTES

Introduction

For the proper design and system integration of large thermal energy storages (LTES), suitable, accurate and verified simulation models are essential. Various models were developed in the past for different LTES concepts (see Figure 1), simulation platforms and application purposes. Important aspects in an LTES project development are, e.g., the LTES dimensioning that can only be carried out considering the LTES system integration. Suitable models for this must take into account the short-term interaction with the system's energy producers and sources as well as energy consumers. Models for this purpose have been mostly developed for system simulation platforms like TRNSYS or Modelica/Dymola.

Another important aspect is the detailed component-level design and optimisation of an LTES. For this task,

models in more detailed and flexible simulation tools like COMSOL Multiphysics are used.

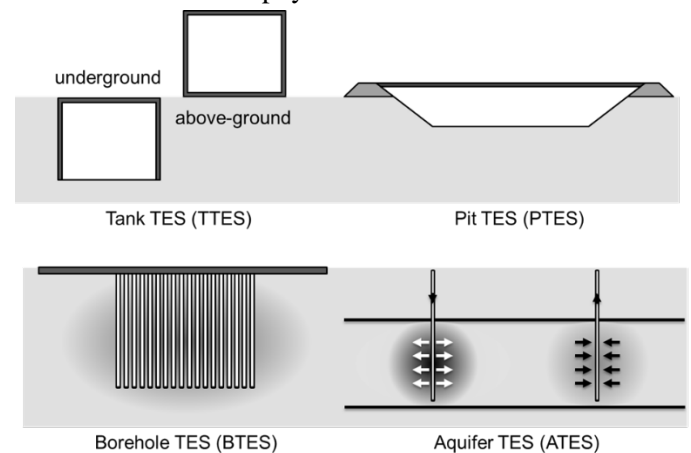
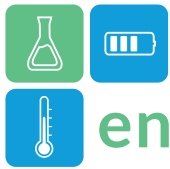


Figure 1: Overview of LTES concepts considered in the comparative simulations.



The aim of the presented work is to develop and apply a verification method for LTES simulation models.

Methodology

Verification of simulation models can be done in different ways. Commonly used approaches include comparing simulation results with measurement data or analytical solutions, or comparing simulation results between different, ideally partially already validated simulation models. Because of the high complexity and dynamic operation conditions, analytical solutions are only available for very simplified heat transfer aspects. Also, high-quality measurement data is difficult to find for LTES, as real-scale laboratory experiments are not available and monitoring systems of realised projects are designed for operational and not scientific purposes. Completeness and quality of measurement data can, therefore, not satisfy scientific requirements in most cases. For these reasons, a verification procedure based on pre-defined and representative test cases and comparative simulations was developed. More specifically, (1) test cases for the LTES concepts shown in Figure 1 have been defined, (2) simulation models for the test cases were created and applied by the authors, and (3) the simulation results of the models were compared. As some of the models have been validated before, a comparison of model results can be a valid way for verification, if deviations between the concerned model results are acceptable.

Table 1 gives an overview of the test cases defined for the comparative simulations. For each test case, a detailed description of the specific storage configuration and the required simulation outputs was developed. These test case descriptions will be available from the beginning of 2024 on the Task 39 website (IEA ES Task 39 (2024)).

Table 1: Overview of test cases defined for the verification of LTES simulation models.

Test case	Description	TES volume
ATES-1	2-well ATES	375 000 m ³ (soil)
BTES-1	Cylindrical BTES	80 000 m ³ (soil)
PTES-1-C	Truncated and inverted cone PTES	100 000 m ³ (water)
PTES-1-P	Truncated and inverted pyramid PTES	100 000 m ³ (water)
TTES-1-AG	Above-ground TTES	50 000 m ³ (water)
TTES-1-UG	Ground-buried TTES	100 000 m ³ (water)

Simple yearly operation profiles for the test cases were defined at this stage. A charging period of four months was assumed with constant mass flow and constant inlet temperatures, followed by a one-month idle phase. After this, a four-month discharging period (again with constant mass flows and inlet temperatures), followed by a three-month idle phase. The simulation period for the test cases was five years. However, for the ATES-1 test case, ten years were used. The multi-year simulation periods were used to also consider the heat-up phase of the surrounding ground, which mainly takes place in the first years of operation.

Besides the LTES configurations and the operation profiles, a set of model outputs was defined for each test case to enable a clear and efficient assessment of simulation outputs. The pre-defined outputs comprise the most important energy flows, temperatures and mass flows of the hydraulic circuits for charging and discharging of the LTES, as well as temperature developments in the storage volumes and in specific locations of the surrounding ground. For the pre-defined model outputs an evaluation template is also available.

Results and Discussion

Table 2 gives an overview of the participation in the different test cases.

Table 2: Overview of the participation in the different test cases.

Test case	No. of participations	No. of participating institutions	No. of different LTES models
ATES-1	4	3	4
BTES-1	6	4	4
PTES-1-C	12	9	6
PTES-1-P	2	2	2
TTES-1-AG	4	3	4
TTES-1-UG	9	7	7

Exemplarily, two selected results are presented here for the test case PTES-1-C. In Figure 2, results for the main heat flows are presented for the 5th year of operation. Differences compared to the corresponding mean values between the nine contributions shown here are $\pm 2\%$ for charged heat, $\pm 3\%$ for discharged heat, $\pm 1\%$ for overall thermal losses and -33% to $+12\%$ for internal energy change in the considered period. The relative deviations for the internal energy change seem high; the absolute values and deviation are, however, small, as can be seen in Figure 2.



Figure 3 shows the temperature stratification in the water volume of the PTES after two months of charging at the beginning of the fifth year. All presented models show a similar temperature level and stratification. However, a closer look identifies two groups of models with one group tending to a slightly higher pronounced temperature stratification compared to the other group. The group that shows slightly higher stratification comprises two COMSOL models and a Dymola model (Dis PlaTES). These models have a different approach for the calculation of the heat balance in the water volume compared to the other models. The work carried out so far does not allow any statement to be made as to which of the results of the two groups is more correct than the other. Further investigations will be done in the follow-up IEA ES Task 45.

Conclusions and Outlook

In general, the results for all test cases show good agreement between the participating models for the major energy values, such as the charged and discharged amounts of heat on a yearly or monthly basis. The short-term (hourly) temperature development in the storage volume and the TES outlet temperature towards the system also show satisfactory agreement but with somewhat higher deviations in some cases. Temperature results for the defined locations in the surrounding ground also show somewhat higher deviations in some cases; however, post-processing of model outputs, e.g., interpolation between single cells of the numerical grid, can be both time-consuming and error prone.

The discussions between the task members during the development and definition of the test cases and during the simulation phase showed that, even though all members are experts in the field of LTES, there were still some misunderstandings and misinterpretations of specific details in the early stages, which led to differences in simulation results that could be eliminated after some clarifications. This emphasizes the crucial need for detailed and clear definitions for

comparative simulations to make sure that differences in results are actually caused by the investigated models and not by user behaviour.

The presented work was conducted within the concluded IEA ES Task 39. A collection of model fact sheets, the definition of the test cases, the template for the evaluation of the simulation results, and a summary report and reference book for the results of the comparative simulation for all the test cases will be available from the beginning of 2024 at (IEA ES Task 39 (2024)). These documents and files allow other interested users to apply the presented test cases for their models and verify or compare their results with the results from this work.

In the follow-up IEA ES Task 45, the work will be continued with additional and more advanced test cases that will consider more dynamic and realistic operational profiles as well as sensitivity studies for the most important design parameters.

Acknowledgment

The work described here has been done within the framework of IEA ES Task 39 and was financially supported by several national support projects from participating countries. The authors gratefully acknowledge this support. The authors themselves carry the responsibility for the content of this paper.

References

- IEA ES Task 39 (2024) Large Thermal Energy Storages for District Heating, Website: <https://iea-es.org/task-39/>
- Ochs, F., Dahash, A., Tosatto, A., Reisenbichler, M., O'Donovan, K., Gauthier, G., Skov, C.K. and Schmidt, T. (2022), Comprehensive comparison of different models for large-scale thermal energy storage. In International Renewable Energy Storage Conference 2021 (IRES 2021) (pp. 36-51). Atlantis Press.

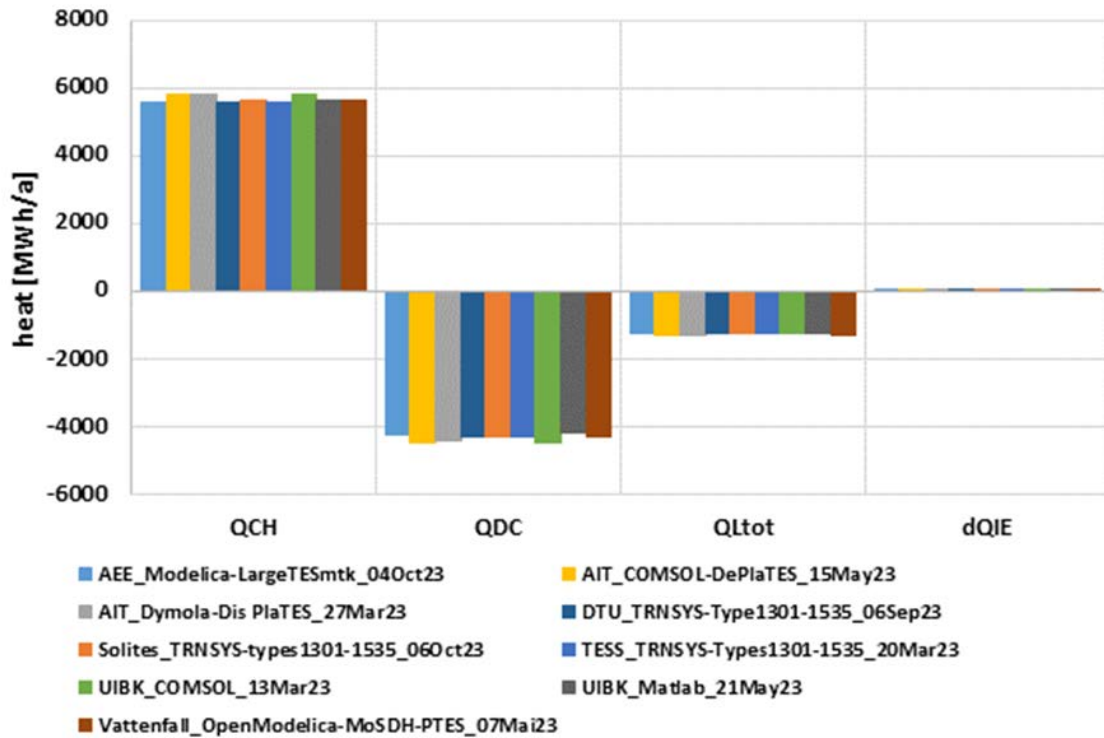
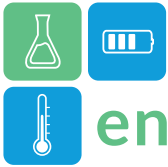


Figure 2: Results for charged (Q_{CH}) and discharged (Q_{DC}) heat, overall thermal losses (Q_{Ltot}) and change in internal energy content (dQ_{IE}) in the 5th year of operation for nine participations in the conical PTES test case.

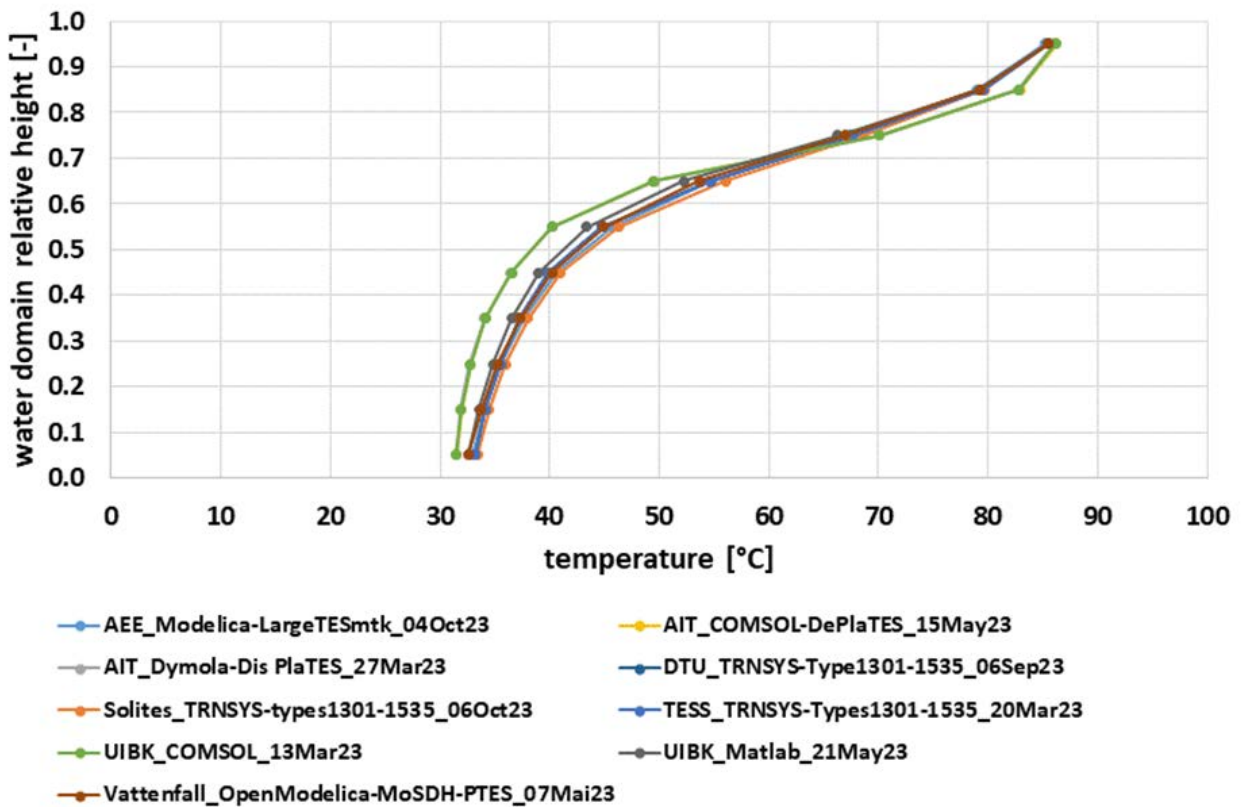
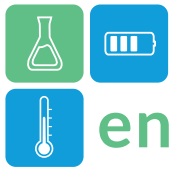


Figure 3: Results for the temperature distribution inside the water volume after two months of charging in the 5th year of operation for the conical PTES test case.



Comparison between a conventional TES system and an EAF slag-based thermocline configuration for CSP plants using the LCA methodology.

Marc Majó*, Carlos A. Vielma, Alejandro Calderón, Adela Svobodova, Ana Inés Fernández, Camila Barreneche, University of Barcelona, Faculty of Chemistry, Department of Materials Science and Physical Chemistry, Martí i Franqués, 1, floor 7, Barcelona, Spain.

*Corresponding author e-mail: marc.majo@ub.edu

Abstract

The global energy crisis, driven by fossil fuel dependence, demands sustainable models. Solar thermal power, especially Concentrated Solar Power (CSP), is a promising technology with significant potential in energy storage. Thermal Energy Storage (TES) systems, often using molten salts, help improve CSP efficiency. This research compares these systems through Life Cycle Assessments (LCAs), exploring alternative materials like EAF steel slag to boost sustainability in CSP plants and reduce environmental impact.

Keywords: Thermal Energy Storage, Concentrating Solar Power, Life Cycle Assessment

Introduction

The International Energy Agency (IEA) highlights a global energy crisis affecting societies due to surging resource demand, driven by population growth and emerging markets (International energy agency, 2022). This heightened demand, primarily reliant on fossil fuels, exacerbates environmental issues like greenhouse gas emissions (Ellabban et al., 2014). To counter this, a shift to sustainable energy models is crucial.

Solar thermal power emerges as a promising renewable energy source, notably for its minimal environmental impact compared to conventional methods (Abokersh et al., 2021; Sueyoshi & Goto, 2019). Concentrated Solar Power (CSP) plants, utilizing sunlight to generate heat energy, are gaining traction worldwide (ELSihiy et al., 2021; Grosu et al., 2018; Peiró et al., 2018). However, harnessing solar energy faces challenges due to its intermittency and storage inefficiencies (Alnaimat & Rashid, 2019).

Thermal Energy Storage (TES) systems play an important role in improving CSP plant efficiency (Cabeza et al., 2021; Peiró et al., 2018). These systems, categorized into sensible heat, latent heat, and thermochemical storage, aim to store excess thermal energy for later use (Gil et al., 2010). Incorporating TES enhances grid stability, reducing reliance on fossil fuels during solar radiation fluctuations (Le Roux et al., 2021; Zhao et al., 2017).

Molten salts are the predominant TES technology in commercial CSP systems (Prieto & Cabeza, 2019), despite their environmental drawbacks and cost (El Alami et al., 2020; Oró et al., 2012). Optimizing TES systems is crucial, prompting exploration of

alternatives like passive thermocline configurations using materials such as EAF steel slag (Ferrer et al., 2017; Jacob et al., 2022).

Using Life Cycle Assessments (LCAs), we can compare the environmental impacts of various TES systems, showing the potential of waste-based materials to reduce environmental footprints (Whitaker et al., 2013). Based on these insights, this research aims to employ the LCA methodology to compare the environmental impact between a CSP plant utilizing EAF steel slag in a passive storage thermocline setup and a traditional two-tanks CSP plant. This comparison seeks to identify material enhancements, emphasizing the valorisation of industrial waste to increase the sustainability of TES technology and minimize environmental impacts.

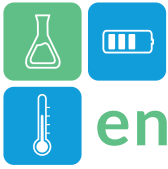
Materials and methodology

Description of the CSP plant and the TES system

In this study, a power tower configuration was selected for CSP generation, designed to operate 24 hours per day, following a baseload configuration during a lifetime of 30 years. The thermocline storage system of the plant consists of the following elements:

- Nitrate salt inventory: molten solar salt (60 wt% NaNO_3 , 40 wt% KNO_3) as heat transfer fluid (HTF) and thermal storage material (TESM)
- Thermocline tank: filled with EAF steel slag as TSM (packed-bed)
- The molten salt circulation pumps

The potential utilization of EAF steel slag as a filler material in a TES system in direct contact with the solar salt was analysed and, as a result, a production process which involves fine milling, compression, and sintering of the raw slag was considered to improve its



mechanical and chemical resistance to thermal cycling of the final slag pebbles to be used in the tank (Cabello Núñez et al., 2019; López Sanz et al., 2019).

LCA Methodology

The LCA of a process or product is regulated by the ISO 14040 (ISO, 2006b) and ISO 14044 (ISO, 2006a) Standards, which are designated to facilitate comparison between competitive solutions. The impact evaluation methods selected are ReCiPe and IPCC2013, extracted from the Ecoinvent database (Wernet et al., 2016) using the software GaBi (Thinkstep, 2017).

The functional unit chosen was "1 kWh of net electricity fed to the grid". The scope of this study encompasses the "cradle-to-grave" perimeter, which covers the entire life cycle of CSP tower plant components. This includes assessing the impact in its construction, operation, and end-of-life phases. However, the EAF steel slag is aborbed in a cradle-to-gate perimeter, which involves its study until the manufacturing phase.

Regarding to the slag allocation, the subdivision method is applied to consider only the steel slag subprocess functions (Lalau et al., 2016). The EAF steel fabrication is considered a primary process, and shaping the slag to make pebbles is defined as a secondary process. To determine the environmental load of the by-product, the mass and economic allocation methods were contemplated following the approach of Eq. (1) (Chen et al., 2010):

$$\vec{F}_i = c \cdot \vec{F}_{prim} + m_i \cdot \vec{F}_{secon} - m_j \cdot \vec{F}_{avoid} \quad (1)$$

Where:

\vec{F}_i : Environmental flow inventories for the by-product

\vec{F}_{prim} : Primary process

\vec{F}_{secon} : Secondary process

\vec{F}_{avoid} : Avoided process

m_i : By-product mass

m_j : Avoided product mass

c : Allocation coefficient, varies based on the method
Data inventory, assumptions and scenarios

The inputs and outputs inventory of the two-tanks CSP tower plant was extracted from Gasa et al. (Gasa et al., 2021) 2021 and it was utilized as a basis for constructing the inventory of the single-tank CSP tower plant by scaling volumetrically the materials needed in the TES and HTF systems. To make this possible, the following were considered as starting points: the

thermal storage capacity of the plant (5.330 MWh_{th}), the reduction of the molten salts inventory, and the physical/thermal properties of the TESMs at 400 °C.

The inventory of materials for the CSP tower plant is assumed to be the same as the conventional storage configuration, with the exception of TES and HTF system. Both systems must provide the same thermal storage capacity. The consumptions of water and energy in the operational phase are assuming the same as the conventional CSP plant, as either the consumption of energy in the end-of-life phase.

Two depletion scenarios of the molten salt inventory were defined:

- First scenario: 67% reduction (common case (Lalau et al., 2016; Price et al., 2002))
- Second scenario: 80% reduction (optimistic case (Hoffmann et al., 2016; Xu et al., 2012))

Thus, comparative results emulating the conditions of using the typical filler materials in thermocline TES systems were obtained.

Results and Discussion

Life cycle inventory analysis

The material demand of the TES and HTF systems for each configuration is illustrated in Table 1.

Table 1: Materials inventory of the TES and HTF systems.

Component	Conventional TES & HTF (Gasa et al., 2021)	Thermocline TES & HTF		Unit
		First Scenario	Second scenario	
Nitrate salts	5.60x10 ⁴	1.84x10 ⁴	1.12x10 ⁴	t
Slag pebbles	--	4.97x10 ⁴	5.93x10 ⁴	t
Chromium steel 18/8	1.20x10 ³	1.08x10 ³	1.06x10 ³	t
Reinforcing steel	1.40x10 ³	1.26x10 ³	1.24x10 ³	t
Stone wool	5.80x10 ²	5.25x10 ²	5.14x10 ²	t

Even when the mass of the slag experiences a significant increment in the second scenario, the inventory of the other components continues reducing. This is due to the volumetric scaling where the density of the slag is superior (2,850 kg/m³ (Cabello Núñez et al., 2019; López Sanz et al., 2019)) in relation to the salts (1,848 kg/m³ (Awad et al., 2018)). As a result of it, the slag pebbles inside the thermocline tank provide the same storage capacity of the conventional plant while reducing the materials intensity. This is important since size reduction of the TES and HTF system can entail a diminution of the environmental impact and affects positively the economic evaluation of the plant (Cabello Núñez et al., 2019).

Life cycle impact assessment



Regarding to the portioning of the by-product environmental impact, when the allocation was made by mass coefficient, slag receives 13% of the steel production impact, while doing it by cost, it receives 3%. The diminution in the molten salt inventory, the fewer requirement of materials to construct the tank, and the slag utilization entail to a reduction of the ReCiPe indicator of environmental impact for the thermocline configurations. Figure 1 allows to analyse the global impact of the CSP plant in the studied scenarios.

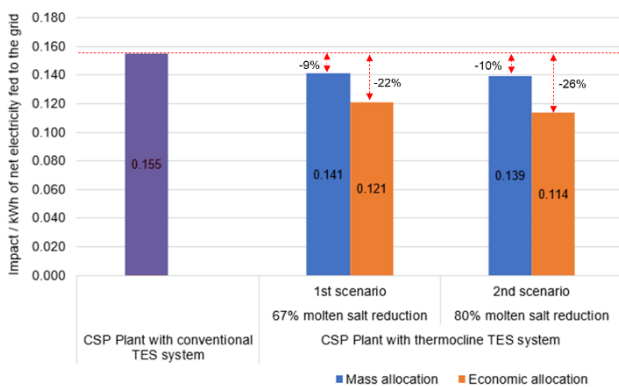


Figure 1: ReCiPe. Impact comparison in the studied scenarios.

On the other hand, the IPCC2013 method indicates an increment of greenhouse gas emissions when utilizing allocation by mass. However, when including a weighting by the slag price (economic allocation) the emissions accounted in the thermocline scenarios decrease by up to 9% (Figure 2).

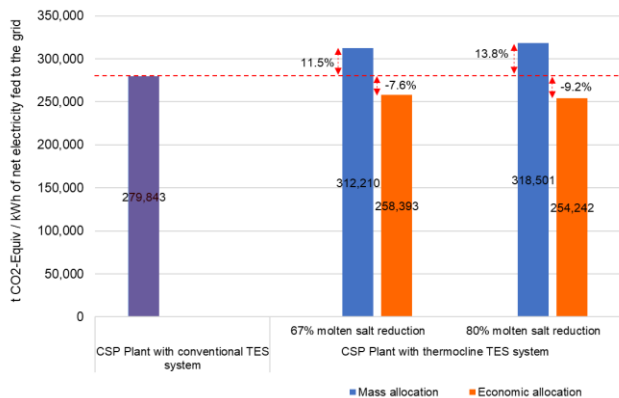


Figure 2: IPCC2013. Emissions of GWG in t CO₂-Equiv.

It is recognized that when a by-product replaces another material, it takes on its own environmental impact but also gets credit for avoiding the original impact (Esther et al., 2020). Thus, the price weighted allocation method seems to be appealing to companies that want to use the by-product for TES purposes.

Conclusions

The economic allocation method has proven to be more accurate than other studied allocation methodologies for the steel slag by-product. This approach has demonstrated usefulness in evaluating alternative wastes and by-products. The assessment indicates a potential reduction in the environmental impacts of a conventional CSP plant when compared to the thermocline alternative system. This reduction is achieved by replacing a significant portion of the molten salts inventory while revaluing a high-energy-density by-product like EAF steel slag.

Acknowledgment

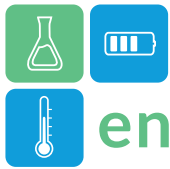
The authors would like to thank the Catalan Government for the quality accreditation given to their research group DIOPMA (2017 SGR 0118, 2021 SGR 00708). DIOPMA is a certified agent TECNIO in the category of technology developers from the Government of Catalonia. This work is part of PCI2020-120695-2 and PCI2020-120682-2 projects funded by Ministerio de Ciencia e Innovación - Agencia Estatal de Investigación (MCIN/AEI/10.13039/501100011033) and by the European Union “NextGenerationEU”/PRTR”, Development and evaluation of novel concepts for LHTES funded by CSO - Israeli Ministry of Energy, 120N663 project funded by TÜBITAK— Scientific and Technological Research Council of Turkey, and 121N737 project funded by TÜBITAK. This work has been partially funded by the Spanish government PID2021-123511OB-C32 (MINECO/FEDER, UE).

References

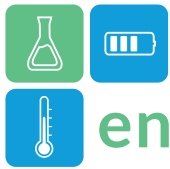
- Abokersh, M. H., Norouzi, M., Boer, D., Cabeza, L. F., Casa, G., Prieto, C., Jiménez, L., & Vallès, M. (2021). A framework for sustainable evaluation of thermal energy storage in circular economy. *Renewable Energy*, 175, 686–701. <https://doi.org/10.1016/j.renene.2021.04.136>
- Alnaimat, F., & Rashid, Y. (2019). Thermal energy storage in solar power plants: A review of the materials, associated limitations, and proposed solutions. In *Energies* (Vol. 12, Issue 21). MDPI AG. <https://doi.org/10.3390/en12214164>
- Awad, A., Navarro, H., Ding, Y., & Wen, D. (2018). Thermal-physical properties of nanoparticle-seeded nitrate molten salts. *Renewable Energy*, 120, 275–288. <https://doi.org/10.1016/j.renene.2017.12.026>
- Cabello Núñez, F., López Sanz, J., & Zaversky, F. (2019). Analysis of steel making slag pebbles as filler material for thermocline tanks in a hybrid thermal energy storage system. *Solar Energy*,



- 188, 1221–1231.
<https://doi.org/10.1016/j.solener.2019.07.036>
- Cabeza, L. F., de Gracia, A., Zsembinszki, G., & Borri, E. (2021). Perspectives on thermal energy storage research. *Energy*, 231.
<https://doi.org/10.1016/j.energy.2021.120943>
- Chen, C., Habert, G., Bouzidi, Y., Jullien, A., & Ventura, A. (2010). LCA allocation procedure used as an incitative method for waste recycling: An application to mineral additions in concrete. *Resources, Conservation and Recycling*, 54(12), 1231–1240.
<https://doi.org/10.1016/j.resconrec.2010.04.001>
- El Alami, K., Asbik, M., & Agalit, H. (2020). Identification of natural rocks as storage materials in thermal energy storage (TES) system of concentrated solar power (CSP) plants – A review. *Solar Energy Materials and Solar Cells*, 217.
<https://doi.org/10.1016/j.solmat.2020.110599>
- Ellabban, O., Abu-Rub, H., & Blaabjerg, F. (2014). Renewable energy resources: Current status, future prospects and their enabling technology. In *Renewable and Sustainable Energy Reviews* (Vol. 39, pp. 748–764). Elsevier Ltd.
<https://doi.org/10.1016/j.rser.2014.07.113>
- ELSihiy, Els. S., Liao, Z., Xu, C., & Du, X. (2021). Dynamic characteristics of solid packed-bed thermocline tank using molten-salt as a heat transfer fluid. *International Journal of Heat and Mass Transfer*, 165.
<https://doi.org/10.1016/j.ijheatmasstransfer.2020.120677>
- Esther, L. A., Pedro, L. G., Irune, I. V., & Gerardo, F. (2020). Comprehensive analysis of the environmental impact of electric arc furnace steel slag on asphalt mixtures. *Journal of Cleaner Production*, 275.
<https://doi.org/10.1016/j.jclepro.2020.123121>
- Ferrer, G., Barreneche, C., Solé, A., Martorell, I., & Cabeza, L. F. (2017). New proposed methodology for specific heat capacity determination of materials for thermal energy storage (TES) by DSC. *Journal of Energy Storage*, 11, 1–6.
<https://doi.org/10.1016/j.est.2017.02.002>
- Gasa, G., Lopez-roman, A., Prieto, C., & Cabeza, L. F. (2021). Life cycle assessment (Lca) of a concentrating solar power (csp) plant in tower configuration with and without thermal energy storage (tes). *Sustainability (Switzerland)*, 13(7).
<https://doi.org/10.3390/su13073672>
- Gil, A., Medrano, M., Martorell, I., Lázaro, A., Dolado, P., Zalba, B., & Cabeza, L. F. (2010). State of the art on high temperature thermal energy storage for power generation. Part 1-Concepts, materials and modellization. In *Renewable and Sustainable Energy Reviews* (Vol. 14, Issue 1, pp. 31–55).
<https://doi.org/10.1016/j.rser.2009.07.035>
- Grosu, Y., Ortega-Fernández, I., González-Fernández, L., Nithiyantham, U., Baba, Y. F., Al Mers, A., & Faik, A. (2018). Natural and by-product materials for thermocline-based thermal energy storage system at CSP plant: Structural and thermophysical properties. *Applied Thermal Engineering*, 136, 185–193.
<https://doi.org/10.1016/j.applthermaleng.2018.02.087>
- Hoffmann, J. F., Fasquelle, T., Goetz, V., & Py, X. (2016). A thermocline thermal energy storage system with filler materials for concentrated solar power plants: Experimental data and numerical model sensitivity to different experimental tank scales. *Applied Thermal Engineering*, 100, 753–761.
<https://doi.org/10.1016/j.applthermaleng.2016.01.110>
- International energy agency. (2022). *World Energy Outlook 2022*. www.iea.org/t&c/
- ISO. (2006a). International Organization for Standardization. (2006). Environmental management: life cycle assessment; requirements and guidelines (Vol. 14044). Geneva, Switzerland: ISO. *International Organization for Standardization, 2006*.
- ISO. (2006b). ISO 14040 International Standard. Environmental management — Life cycle assessment — Principles and framework. *International Organization for Standardization (ISO), Geneva, Switzerland*.
- Jacob, R., Sergeev, D., & Müller, M. (2022). Valorisation of waste materials for high temperature thermal storage: a review. In *Journal of Energy Storage* (Vol. 47). Elsevier Ltd.
<https://doi.org/10.1016/j.est.2021.103645>
- Lalau, Y., Py, X., Meffre, A., & Olives, R. (2016). Comparative LCA Between Current and Alternative Waste-Based TES for CSP. *Waste and Biomass Valorization*, 7(6), 1509–1519.
<https://doi.org/10.1007/s12649-016-9549-6>



- Le Roux, D., Lalau, Y., Rebouillat, B., Neveu, P., & Olivès, R. (2021). Thermocline thermal energy storage optimisation combining exergy and life cycle assessment. *Energy Conversion and Management*, 248. <https://doi.org/10.1016/j.enconman.2021.114787>
- López Sanz, J., Cabello Nuñez, F., & Zaversky, F. (2019). Benchmarking analysis of a novel thermocline hybrid thermal energy storage system using steelmaking slag pebbles as packed-bed filler material for central receiver applications. *Solar Energy*, 188, 644–654. <https://doi.org/10.1016/j.solener.2019.06.028>
- Oró, E., Gil, A., de Gracia, A., Boer, D., & Cabeza, L. F. (2012). Comparative life cycle assessment of thermal energy storage systems for solar power plants. *Renewable Energy*, 44, 166–173. <https://doi.org/10.1016/j.renene.2012.01.008>
- Peiró, G., Prieto, C., Gasia, J., Jové, A., Miró, L., & Cabeza, L. F. (2018). Two-tank molten salts thermal energy storage system for solar power plants at pilot plant scale: Lessons learnt and recommendations for its design, start-up and operation. *Renewable Energy*, 121, 236–248. <https://doi.org/10.1016/j.renene.2018.01.026>
- Price, H., Lüpfert, E., Kearney, D., Zarza, E., Cohen, G., Gee, R., & Mahoney, R. (2002). Advances in parabolic trough solar power technology. *Journal of Solar Energy Engineering, Transactions of the ASME*, 124(2), 109–125. <https://doi.org/10.1115/1.1467922>
- Prieto, C., & Cabeza, L. F. (2019). Thermal energy storage (TES) with phase change materials (PCM) in solar power plants (CSP). Concept and plant performance. *Applied Energy*, 254. <https://doi.org/10.1016/j.apenergy.2019.113646>
- Sueyoshi, T., & Goto, M. (2019). Comparison among three groups of solar thermal power stations by data envelopment analysis. *Energies*, 12(13). <https://doi.org/10.3390/en12132454>
- Thinkstep. (2017). *GaBi Databases*. GaBi Databases Upgrades & Improvements 2017 Edition.
- Wernet, G., C., B., Steubing, B., Reinhard, J., Moreno-Ruiz, E., & Weidema, B. (2016). Ecoinvent Version 3. *The International Journal of Life Cycle Assessment*, 21(9).
- Whitaker, M. B., Heath, G. A., Burkhardt, J. J., & Turchi, C. S. (2013). Life cycle assessment of a power tower concentrating solar plant and the impacts of key design alternatives. *Environmental Science and Technology*, 47(11), 5896–5903. <https://doi.org/10.1021/es400821x>
- Xu, C., Wang, Z., He, Y., Li, X., & Bai, F. (2012). Parametric study and standby behavior of a packed-bed molten salt thermocline thermal storage system. *Renewable Energy*, 48, 1–9. <https://doi.org/10.1016/j.renene.2012.04.017>
- Zhao, B., Cheng, M., Liu, C., & Dai, Z. (2017). An efficient tank size estimation strategy for packed-bed thermocline thermal energy storage systems for concentrated solar power. *Solar Energy*, 153, 104–114. <https://doi.org/10.1016/j.solener.2017.05.057>



Compatibility of demolition wastes with solar salt for high temperature packed-bed thermal energy storage applications

Burcu Koçak*, Gülfeza Kardeş, Halime Paksoy

Çukurova University, Faculty of Art and Sciences, Chemistry Department, Balcali Mahallesi, Sarıçam, Adana, Türkiye

*Corresponding author e-mail: kocakburcu@gmail.com

Abstract

Packed-bed thermal energy storage using demolition wastes as sensible thermal energy storage material is a sustainable system to eliminate the gap between the energy supply-demand in concentrated solar power plants. Although demolition wastes are superior to many natural and waste materials with their good thermal and mechanical properties, their compatibilities with heat transfer fluid should be investigated due to their direct contact in packed-bed. In this study, compatibility of packing materials developed from demolition waste with solar salt has been investigated up to 500 °C for 500 hours. Results showed that packing materials are thermally stable up to 600 °C but surface cracks seen may increase at longer cycle times. Compatibility of packing with solar salt is recommended to be evaluated beyond 500 hours of cycling.

Keywords: Demolition waste, solar salt, concentrated solar power plant, thermal cycling, packed-bed

Introduction

Thermal energy storage (TES) system stores considerable amount of excess energy from concentrated solar power (CSP) plant to minimize the natural interruptions of solar energy. 2-tank TES system using molten salt is the most common technology integrated in CSP plants to increase electricity generation capacity. However, tons of molten salt used in 2-tank TES causes higher investment cost and environmental impacts in the process from the manufacturing phase to their disposal (Lalau and al. 2026).

Valorising of waste materials as heat storage material in packed-bed TES system is a sustainable way to decrease tons of heat transfer fluid (HTF) amount. But, waste based storage material has to show long-term durability in direct contact with solar salt.

There are a few studies in literature that investigated compatibility of waste materials with solar salt and other HTFs. Ortega-Fernández and al. (2018) conducted corrosion studies between steel slag and ceramic by-product with solar salt. Salt degradation has been detected due to the formation of nitrites in the salt. In the study of Grosu and al. (2018), compatibilities of BOF slag, magnetite ore and river rock with Delcoterm Solar E15 thermal paraffinic oil and HitecXL salt were investigated for packed-bed TES applications. Results showed that three materials were not compatible in direct contact with solar salt while magnetite ore and

river rock showed good compatibility with paraffinic oil.

In our previous study (Koçak and al, 2021), demolition waste based packing materials showed good thermal and mechanical stability in direct contact with Therminol 66 synthetic oil at 180 °C after 500 thermal cycling. In this study, compatibility of demolition waste based packing materials in direct contact with solar salt was investigated up to 500 °C for 500 h to evaluate the feasibility of using demolition waste in a packed-bed TES system.

Materials and Method

Novel packing materials used in this study were produced from demolition waste samples taken from an urban regeneration project in Adana, Turkey. Demolition waste samples were crushed, dried and sieved to obtain homogeneous dry powders. Demolition waste powders were mixed with 10% (by wt) Portland white cement and tap water. Then, the mixture was moulded and dried to produce spherical packing materials with a diameter of 10 mm.

Selected heat transfer fluid is solar salt that contains 60% Sodium Nitrate and 40% Potassium Nitrate. Packing materials developed from demolition waste were immersed in a ceramic container filled with solar salt. Repeated heating and cooling cycles were applied in an oven up to 500 °C for 500 h. The oven was heated to maximum temperature of 500 °C at a heating rate of 10 °C/min and stayed at 500 °C for 8 hours to simulate

CSP plants operation. Then it was cooled down to room temperature with a cooling rate of 2 °C/min.

In order to evaluate packing's thermal and mechanical compatibility with solar salt, TGA, SEM EDS analysis were done before and after 500 h test.

Thermogravimetric analysis (TGA) was carried out by Mettler Toledo TGA 3+ device to evaluate the thermal stability of packing materials. Internal structural analysis was performed by Quanta 650 Field Emission SEM device. Energy Dispersive Spectroscopy (EDS) analysis was used to investigate the effect of thermal cycling on chemical composition of packing material.

Results and Discussion

Figure 1 a and b show the demolition waste based packing materials before and after 500 h of thermal cycling. Major colour change was observed after 500 h of thermal cycling. Also, substantial surface changes are observed due to the formation of cracks on the packing surface.



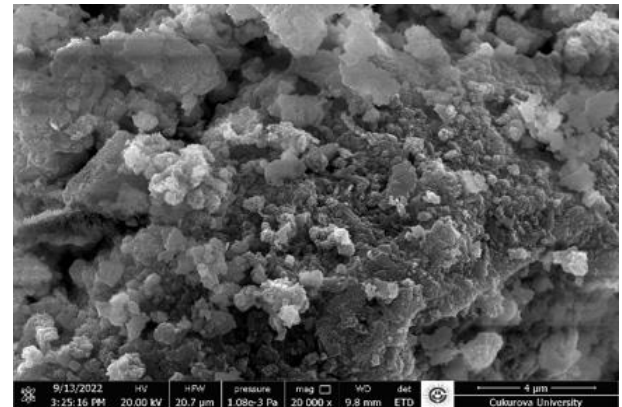
(a)



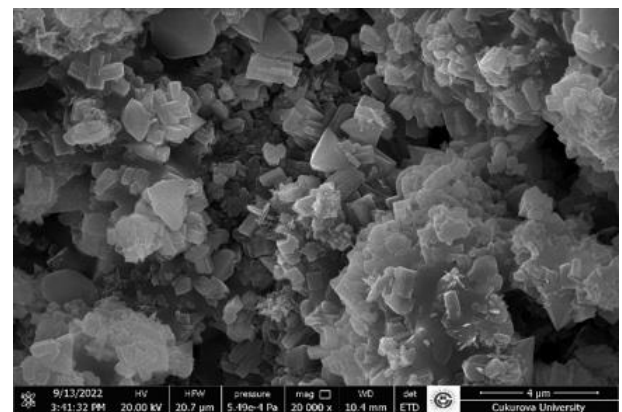
(b)

Figure 1: Demolition waste based packing materials a) before cycling; b) after 500 h

In Figure 2, the SEM images of demolition waste based packing materials before test (a) and after 500 h test (b) are presented. In the packings before the test (Figure 2a), non-uniform grain structure is observed due to the heterogeneous structure coming from construction materials such as calcium, silicon and iron. In Figure 2b, the crystal structure of solar salt that has penetrated into packing material can be seen.



(a)



(b)

Figure 2: 2000X SEM images of test samples a) before cycling; b) after 500 h

EDS analysis was performed by the SEM device with the EDS detector. The chemical change in the samples after the test is shown in Table 1. As expected in the EDS analysis, high levels of sodium and potassium elements originating from solar salt were detected in the samples after the 500 h test. Other changes identified after 500h thermal cycling were in Carbon (C) and Sulfur (S) elements. C with 6.25% and S with 2.99% before cycling were not detected after 500h test. S with a boiling point of 446.6 °C may have evaporated in the thermal cycling test performed at 500 °C. According to the study by Bilgin et al. (2022), the reason why carbon cannot be detected in EDS analysis can be explained by C being hidden in interstitial spaces in the crystal lattice due to its very small radius.



Table 1: EDS analysis of test samples.

Elements	Before thermal cycling (%wt)	After 500 h (%wt)
C	6.25	-
O	4.22	39.85
Mg	1.18	1.86
Al	2.26	2.98
Si	7.74	7.86
S	2.99	-
K	0.37	3.14
Ca	29.27	33.15
Fe	1.73	2.63
Na	-	8.38

Figure 3 shows TGA test results. Before thermal cycling test sample, 8% mass loss has been observed up to 700 °C. The first mass loss observed between 100 and 200°C corresponds to the evaporation of water resulting from the moisture in the samples. Decomposition starts after 700 °C. It can be seen from green line in the figure, demolition waste based packing materials after 500 h thermal cycling test have good thermal stability up to 600 °C. 10% mass loss between 600-800 °C comes from decomposition of solar salt penetrated into packing material.

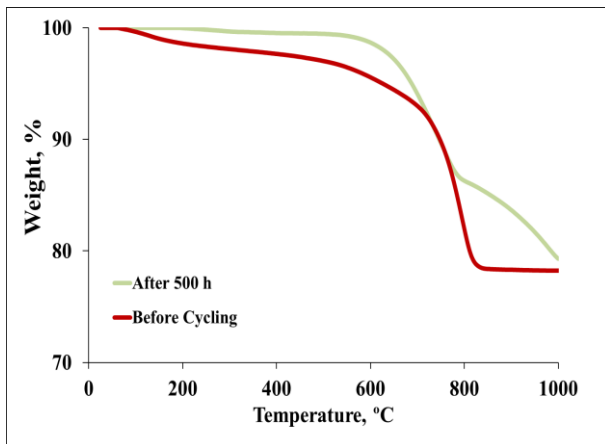


Figure 3: TGA Analysis, before cycling and after 500 h

Conclusions

In this study, thermal stability of demolition waste based packing materials were assessed using repeated heating cooling cycles up to 500 °C for 500h in solar salt. Although, TGA analysis showed that packings are durable up to 600 °C, crack formations on the packing surface, that have been observed after thermal cycling can cause problems upon further cycling. These cracks may be caused by molten salt penetration into packing materials and crystallization in the cooling cycle. So, compatibility of packing with solar salt should be evaluated at longer term of cycling test.

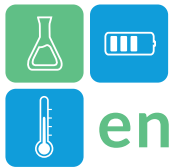
Further improvement durability of demolition waste based packing in solar salt can be investigated using different formulations and additives.

Acknowledgment

The authors thanks BAP Projects (no: FDK-2018-9602 and no: FBA-2022-13205) and Horizon 2020 research and innovation project INPATH TES (Grant agreement ID:657466). And this study was partially funded by CSP-ERA-Net 1st Cofund Joint Call by AEI - Spanish Ministry of Science, Innovation and Universities, TÜBITAK - Scientific and Technological Research Council of Turkey (Project No:120N663), and CSO - Israeli Ministry of Energy. CSP-ERA-Net is supported by the European Commission within the EU Framework Program for Research and Innovation HORIZON 2020 (Cofund ERA-NET Action, N° 838311).

References

- Bilgin T., Altunbaş O., Güral A., (2022) Nikel İlaveli Toz Metalurjisi Çeliklerin Darbe Tokluk Özelliklerine Farklı Karbon Oranı ve Sıcaklık Etkilerinin İncelenmesi, *Politeknik Dergisi*, 25(3): 1281-1285
- Grosu Y., Ortega-Fernández I., López del Amo J. M., Faik A., (2018) Natural and by-product materials for thermocline-based thermal energy storage system at CSP plant: Compatibility with mineral oil and molten nitrate salt, *Applied Thermal Engineering*, 136, 657-665, <https://doi.org/10.1016/j.applthermaleng.2018.03.034>.
- Koçak B., Fernandez A. I., Paksoy H., (2021). Long-term stability of sensible thermal energy storage materials developed from demolition wastes interacting with hot heat transfer fluid, *Int J Energy Res.*, 1–13. <https://doi.org/10.1002/er.7193>
- Lalau Y., Py X., Meffre A., Olives R., 2016. Comparative LCA Between Current and Alternative Waste-Based TES for CSP, *Waste Biomass Valor* (2016) 7:1509–1519 <https://doi.org/10.1007/s12649-016-9549-6>
- Ortega-Fernández I., Grosu Y., Ocio A., Arias P. L., Rodríguez-Aseguinolaza J., Faik A., (2018) New insights into the corrosion mechanism between molten nitrate salts and ceramic materials for packed bed thermocline systems: A case study for steel slag and Solar salt, *Solar Energy*, 173, 152-159, <https://doi.org/10.1016/j.solener.2018.07.040>



Conceptual Development and Upscaling Considerations of a Radial Flow Packed Bed Thermal Energy Storage with Multiple Coaxial Particle Layers

Konstantinos Apostolopoulos-Kalkavouras, Silvia Trevisan, Rafael Eduardo Guedez Mata
Department of Energy Technology, KTH Royal Institute of Technology, 100 44 Stockholm, Sweden
E-mail: koak@kth.se

Abstract

Industrial heat decarbonization is one of the main challenges in the ongoing global energy transition and thermal energy storage (TES) is seen as one of the vital technologies that could contribute to this effort. Packed bed TES systems have the potential to provide heat storage in high temperatures using natural rocks or industrial waste materials and can unlock new opportunities for the power generation sector as well as for the hard-to-abate industries [1]. In the context of this work, an innovative high-temperature radial flow packed bed TES system is considered and will be prototyped in the KTH Solar lab. The initial conceptualization of the storage is presented and is complemented by modeling results and relevant literature review. Some radial TES designs are proposed and compared based on their upscaling potential and the flexibility they can provide for the experimental campaign in the lab. Preliminary results show that a flat-top radial flow dual-layer design shows low pressure drop, good upscaling potential and high flexibility in lab-scale that can provide a wide range of data which are expected to be representative of a larger scale TES operation.

Keywords: Thermal Energy Storage, Packed bed, Radial flow, High temperature heat, Concentrated Solar Power

Introduction

Air driven packed bed thermal energy storage is believed to offer several advantages when compared to other kinds of high-temperature TES, such as: utilization of natural rocks or waste materials which are cheap and abundant, high operating temperatures only depending on the melting point of the solid filler used, low safety concerns, direct heat transfer between heat transfer fluid (HTF) and solid filler, minimal degradation and corrosion and no chemical instability [2]. Several packed bed designs have been proposed and tested, of which most have a cylindrical or conical shape, horizontal or vertical orientation and axial flow profile. The main disadvantages of such designs are related to thermal losses, high pressure drop, thermal ratcheting and thermo-mechanical stresses [3], [4]. However, radial flow packed bed storage designs have also been proposed and show promising results in decreasing the pressure drop while maintaining relatively low thermal losses and thermal stresses [5]. The aim of the present paper is to propose such a radial flow design, suitable for high-temperature applications in the range of 200 – 800 °C, utilizing industrial by-products such as copper slags, which generally show exceptional thermodynamic properties suitable for heat storage applications. Therefore, design options are

explored and compared based on a conceptual framework as well as modeling.

Methodology

Some conceptual design aspects are illustrated in Table 1. In all potential designs the hot HTF is entering through the top of the TES tank, flows into a central inner perforated pipe and comes to contact with the solid filler, it flows radially outward through the bed and it leaves from the outlets located on the sides, either at the top or at the bottom of the tank, depending on the specific design. During discharge the flow is reverted, meaning that the cold HTF is entering from the outlets and leaving from the inlet opening at the top, so that the thermocline developed along the tank's radius is sustained. One of the main aspects of the TES conceptualization is the upscaling potential of the system, from a performance as well as practical perspective related to construction, operation, and maintenance. The design process begins with ideation around the different options presented in that aim to deal with issues related to the lab scale operation and flexibility. However, it is also considered crucial to assess the scalability of these designs from a practical point of view. After the initial conceptualization some options are discarded and the work is complemented with relevant modeling campaign, aiming at selecting one final configuration for the development of the

prototype. One main design aspect considered in this stage is the option of using 2 coaxial layers of particles with different diameters for the solid packing. Preliminary analysis of the expected pressure drop profile is performed by using the Ergun equation and benchmarking against similarly sized axial flow packed beds:

$$\Delta P = \frac{150 \mu L (1 - \varepsilon)^2}{D_p^2 \varepsilon^3} u_s + \frac{1.75 L \rho (1 - \varepsilon)}{D_p \varepsilon^3} u_s |u_s| \quad (1)$$

Additionally, to assess the scalability of the designed PBs, the area required for different sizes of cylindrically shaped radial flow PBs is calculated based on the thermodynamic properties of the solid packing (copper slags) and the geometric characteristics of the storage tank, for varying aspect ratios of the PB. For comparison with molten salts, the are occupied by the cold and the hot tank of a typical MS system is considered. All above calculations are aiming at finding an “optimum” aspect ratio for the PB that would induce limited pressure drop, increased thermal efficiency, high energy density and thus low area requirements.

Results and Discussion

Figure 1 illustrates two proposed designs as well as some selected design parameters considered for the prototype TES. From a conceptual perspective an upscaled radial TES could potentially be similar to design a, with flange openings on top for material loading and unloading and outlets located near the top so that tank can be buried in the ground. In comparison, design b is similar and has the same available volume, but the top of the tank is a full flange. Such design could simplify laboratory processes and improve the accessibility to the interior of the tank for loading/unloading of solid particles, while accommodating also a fully removable inlet and minimizing any chance for leaving space with loosely packed material near the top of the TES, leading in uneven flow profiles. Meanwhile, the thermal and flow profiles are expected to be similar for both designs and a potential upscaled version. Another concept investigated and visualized in Figure 2 is the use of two layers of particles with different diameters. Preliminary results suggest that the existence of larger particles near the center of the tank could locally reduce the pressure drop and the smaller particles in the outer layer could

Table 1: Conceptual design consideration for the innovative radial flow high temperature packed bed TES

Main structure	Top flange(s)	Inlet type	Outlets position	Wall type	Alternative ideas
<p>Flat bottom</p>	<p>Multiple circular</p>	<p>Removable inlet</p>	<p>Bottom outlets fixed on the side</p>	<p>Vertical walls</p>	<p>Tilted tank</p>
<p>Inclined bottom</p>	<p>Rectangular</p>	<p>Fixed inlet</p>	<p>Top outlets fixed on the top</p>	<p>Inclined walls inwards</p>	<p>Horizontal plug flow design</p>
<p>All flat</p>	<p>One circular/conical</p>	<p>Fixed venturi inlet</p>	<p>Top outlets fixed on the side</p>	<p>Inclined walls outwards</p>	<p>Modified horizontal-radial plug flow design</p>
		<p>Fixed narrowed inlet</p>			<p>Modified horizontal-radial tilted plug flow design</p>

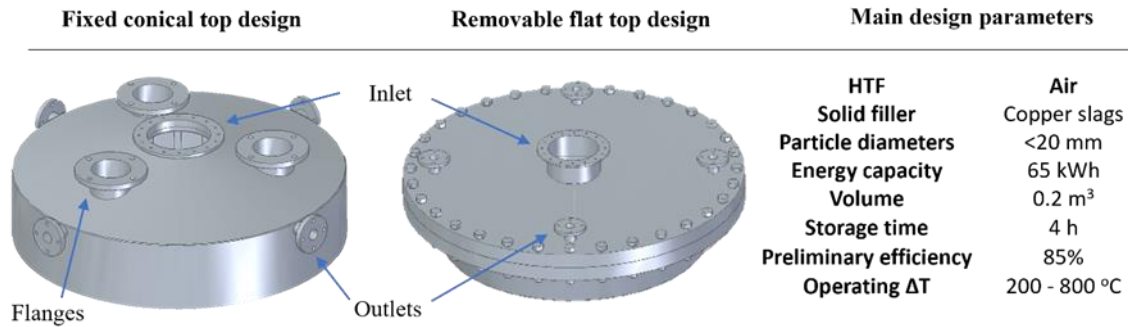


Figure 1: LAB scale designs: Left: CAD drawing of a fixed conical top packed bed design with vertical walls. Middle: CAD drawing of a removable flat top radial flow packed bed design with inclined walls. Right: Main design parameters

compensate for potential reduction in the convective heat transfer in the inner layer due to the lower available heat exchange area.

As shown in the figure, the local pressure drops near the axis of the radial flow bed are much higher than in the outer layers due to the increase of the available area for the flow, along the radius. Both the relative contribution of the different layers on the pressure drop and the pressure drop profile depend on the aspect ratio of the radial flow packed bed, and it's a decisive factor for the selection of an appropriate layer size. A radially movable mesh separator for the layers is also considered in designs a and b so that different radii for the layers could be experimentally tested.

Figure 3 is illustrating the total pressure drop distribution for several potential lab-scale configurations of radial flow cylindrical packed beds and their comparison with corresponding axial flow systems. The preliminary results suggest that the radial systems show a high pressure drop reduction when compared with similar axial systems, keeping the aspect ratio (R/H in radial systems is translated into H/D in axial systems for a reasonable comparison with respect to the flow direction) and the particle diameters unchanged. Another notable aspect of these results is that by increasing the radius of the inner particle layer, the total pressure drop decreases even further, as expected. On the same time, the useful TES duration is minimally decreased (3–6 %) in the radial systems compared to the corresponding axial ones which indicates a similar pattern for the thermal efficiency. The addition of larger particles in the inner layer in the radial TES cases, also results in minor decrease of the useful duration values due to a slightly decreased heat exchange area between the air and the larger particles.

Finally, the scalability of this such a cylindrical radial low TES concept is also investigated by examining different potential upscaled configurations for up to 6

GWh of total heat storage capacity in the temperature range 200 -800 °C. Such a system could be either modular by using several PB tanks in series, or one-tank system, depending on the application. Space availability can be limited and thus the space requirement is considered an important factor for potential upscaled systems. The most space-saving configuration would be a vertically stacked TES concept which could be applicable to industries with

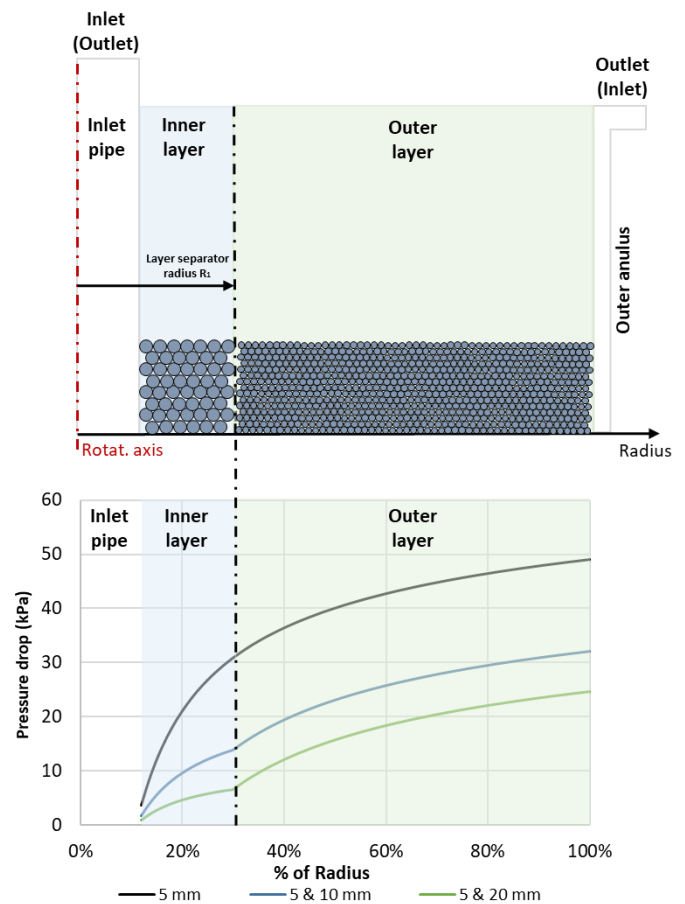


Figure 2: Visualization of the layered radial TES concept. Pressure drop profile in an upscaled radial flow packed bed.

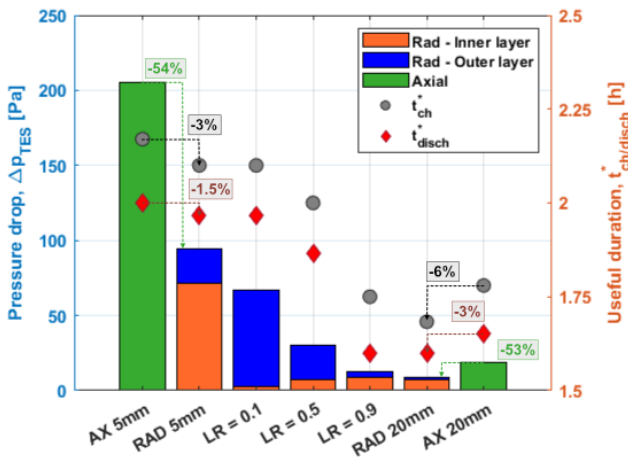


Figure 3: Pressure drop and useful duration estimation for different particle diameters and different layer sizes. Comparison with axial flow PB. LR is defined as the layer radius ratio $L1/L2$.

low space availability. However, a large-scale packed bed system could be ground mounted to reduce complexity and mechanical stresses or even buried in the ground to reduce heat losses to the environment.

In Figure 4, the energy capacity per area required is presented for several one-tank radial flow PBs, one-tank axial flow PBs, as well as one modular system that consists of several ground mounted tanks in a staggered configuration, for different systems sizes (0.1 to 6 GWh) and aspect ratios for the PBs (0.5 to 6). As expected, the space savings are much higher for higher system capacities, and they asymptotically decrease for higher aspect ratios in the radial case. When compared to a large scale (6 GWh) typical two-tank MS system [6], the corresponding radial flow PB storage seems to

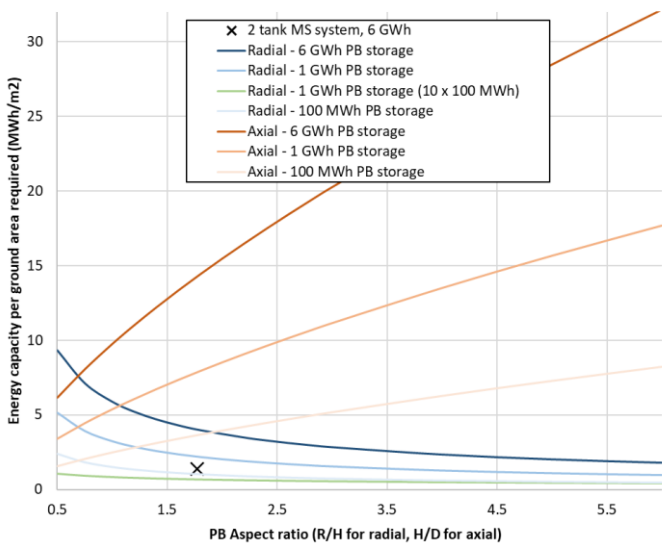


Figure 4: Energy capacity per area required for different sizes of packed bed TES and typical two-tank molten salt systems in CSP industry [6]

require half the area for most aspect ratios. However, this comparison also depends on the operating temperatures of the system since in the scenario presented, the MS system operates between 245 and 560 °C while the PB systems operate between 200 and 800 °C. The axial flow PBs can store more energy using the same ground area, for the aspect ratios investigated, which is expected since they expand more on the height dimension than in the radial one that faces the ground. However, as shown previously, the axial flow PBs are characterized by considerably higher pressure drops, especially in high aspect ratios, where the bed's radius is much smaller and subsequently the energy stored per area required is greatly increased. Therefore, even though the radial flow PBs may require more area than the axial ones, given the same nominal energy capacity, the overall upscaled system is expected to be more compact than the 2-tank molten salt storage system that is currently popular in CSP applications. Moreover, the highly reduced pressure drops and the expected minimal reduction in thermal efficiency for the radial flow systems, are indicative of the potential of radial flow packed beds in high temperature TES applications.

Conclusions

This work introduces an innovative layered radial flow packed-bed TES concept that aims to improve the thermal performance, reduce the pressure drop and focus on the upscaling potential of such TES. From the presented results the following conclusions can be drawn:

- Practical design considerations related to the PB tank design and its potential upscaled version, have a strong impact on the flexibility and operation of the lab prototype.
- A layered radial flow TES configuration with larger particles on the inner layer can lead to a great reduction in the total pressure drop of the system.
- The size of the layers has a strong influence over the pressure drop profile along the radius of the PB.

An upscaled radial PB system with aspect ratio of around 1.5-3 can offer a more space optimized solution compared to a typical two-tank molten salt system.

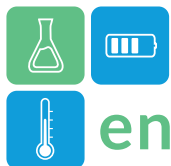
Acknowledgment

This project has received funding from the European Union's Horizon Europe research and innovation programme under grant agreement No 10108389.



References

- [1] G. Zanganeh, A. Pedretti, A. Haselbacher, and A. Steinfeld, “Design of packed bed thermal energy storage systems for high-temperature industrial process heat,” *Appl. Energy*, vol. 137, pp. 812–822, Jan. 2015, doi: 10.1016/J.APENERGY.2014.07.110.
- [2] M. Hänchen, S. Brückner, and A. Steinfeld, “High-temperature thermal storage using a packed bed of rocks – Heat transfer analysis and experimental validation,” *Appl. Therm. Eng.*, vol. 31, no. 10, pp. 1798–1806, Jul. 2011, doi: 10.1016/J.APPLTHERMALENG.2010.10.034 .
- [3] B. Cárdenas *et al.*, “Techno-economic optimization of a packed-bed for utility-scale energy storage,” *Appl. Therm. Eng.*, vol. 153, pp. 206–220, May 2019, doi: 10.1016/J.APPLTHERMALENG.2019.02.134 .
- [4] L. Geissbühler, A. Mathur, A. Mularczyk, and A. Haselbacher, “An assessment of thermocline-control methods for packed-bed thermal-energy storage in CSP plants, Part 1: Method descriptions,” *Sol. Energy*, vol. 178, pp. 341–350, Jan. 2019, doi: 10.1016/J.SOLENER.2018.12.015.
- [5] S. Trevisan, W. Wang, R. Guedez, and B. Laumert, “Experimental evaluation of an innovative radial-flow high-temperature packed bed thermal energy storage,” *Appl. Energy*, vol. 311, p. 118672, Apr. 2022, doi: 10.1016/J.APENERGY.2022.118672.
- [6] Thomas Bauer *et al.*, “Blueprint for Molten Salt CSP Power Plant, Cologne, Germany. Final report of the research project ‘CSP-Reference Power Plant’ No 0324253,” 2021. [Online]. Available: <https://elib.dlr.de/141315/>
<https://blog-tractebel.lahmeyer.de/publications/>



Continuous synthesis of 9,10-dihydroxystearic acid from bio-based resources for sustainable PCM production

Marc Escribà-Gelonch^{1,2*}, Daylen Y. Font-Prieur^{1,3}, Ramon Canela-Garayoa², Emiliano Borri¹,
Luisa F. Cabeza^{1,*}

¹ GREiA research group, University of Lleida, Pere de Cabrera s/n, 25001 Lleida, Spain

² University of Lleida-Agrotecnio. Department of Environment, Soil Sciences and Chemistry – DBA Center, Av. Rovira Roure 191, 25198, Lleida, Spain.

³ Universidad de Cienfuegos “Carlos Rafael Rodríguez”, Carretera a Rodas km 3 ½ Cuatro Caminos, 59430 Cienfuegos, Cuba.

*Corresponding author e-mail: marc.escriba@udl.cat; luisaf.cabeza@udl.cat

Abstract

Flow chemistry allows the production of 9,10-dihydroxystearic acid as building block for the production of phase change material (PCM) composites. Using bio-based fat from agro-food industry as raw materials, an efficient and selective extraction of unsaturated fatty acids is enabled. All advantages of flow chemistry, including process intensification, are available and valued for this fully continuous process. 9,10-dihydroxystearic acid is a precursor of PCMs suitable to be used for thermal energy storage.

Keywords: Phase change materials, flow chemistry, 9,10-dihydroxystearic acid, building block.

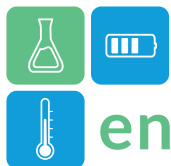
Introduction

Heating/cooling energy expenses account for around 45% of the whole energy consumption. Most of the source of this energy production is based on non-renewable fossil fuels which, in addition to promoting high CO₂ emissions, generate the consequent environmental impacts (Nijs *et al.* 2021). Within this framework, electrification becomes a key factor for mitigating the effects of emissions to achieve the transition towards renewable energy sources (RES) and sustainable green energy. Yet, besides strict energy generation, its sustainable storage has become a central point for energy management needs, especially in buildings. A proper integration of energy storage generates benefits, i.e., short-duration peak shifting, long-duration storage of RES, flexible operation of multiple RES sources and coupling of buildings with the wider electricity grid. One alternative to this aim is the use of phase change materials (PCM) suitable to be produced under sustainable conditions from bio-based materials, as PCMs such as paraffins or salt products do not fully fulfil environmental requirements.

Food industry, in addition to producing delicious and necessary goods, is a vast source of processing co-products which are difficult to manage and valorise (Adamczak *et al.* 2004; Ramani *et al.* 2010). Among

others, animal fat (triacylglycerols) is one of the main components suitable to be valorised given the content on saturated and the appreciated unsaturated fatty acids. Endowed by high thermal and chemical stability as well as high heat capacity, FA are much suitable to be used for thermal energy storage (TES) applications, playing as PCM (Zhang *et al.* 2014), additionally coming from bio-based renewable sources. Previous studies about bio-based organic PCMs have suggested saturated fatty acids as a main source of PCM, as they can remain stable during phase change cycles with no risk of oxidation (Yu *et al.* 2014; Jeong *et al.* 2013; Jeong *et al.* 2014). Nevertheless, fatty acids hydrogenation involves the loss of value of unsaturated fatty acids.

Recently we developed a methodology for production of 9,10-dihydroxystearic (DHSA) acid based on oleic acid directly recovered from fat acylglycerols previous hydrolysis (Gallart-Sirvent *et al.* 2016). DHSA is a valuable building block with good melting enthalpy and phase change temperature higher than common fatty acids, which gives DHSA a prominent potential for producing derivatives with high PCM capacity. Yet, the DHSA synthesis involves a number of hazardous materials (including hydrogen peroxide and formic acid) and process safety risks (including thermal



stability and exothermic reaction), leading to scalability issues (Clay *et al.* 2019).

Differently, flow chemistry allows the continuous processing of small volume streams, resulting in an inherent increased safety and full process control, which ease improved product quality, cost efficiency, and overall production flexibility. These features are key drivers which have contributed to the growth of continuous flow chemistry, especially regarding problematic reactions too dangerous to be handled on larger scale by batch reactions such as oxidations. In this report, a continuous processing for the synthesis of DHSAs from oleic acid extracted from animal or vegetal biomass is presented as a previous step for PCMs continuous production using DHSAs as building block.

Methodology

A tentative setup is designed according to a previous kinetic study of the reaction in batch (Figure 1). Each section of the multi-step process is immediately set according to process conditions due to high mass and heat transfer rates obtained within flow systems. Eventually, every sub-step can be easily isolated to be assessed individually. Such process control allows to precisely optimize process parameters such as temperature, pressure and residence time while operating with high concentrations or even solvent free. By this approach, process intensification is accessible beyond conventional conditions allowed in batch, making possible to operate in explosive regimes, with highly exothermic reactions (Hessel *et al.* 2009). Whilst unstable or hazardous reagents can be rapidly generated in situ and consumed within flow reactors, in batch their accumulation can be very dangerous for the integrity of the reactor making the process unfeasible (Dallinger *et al.* 2020).

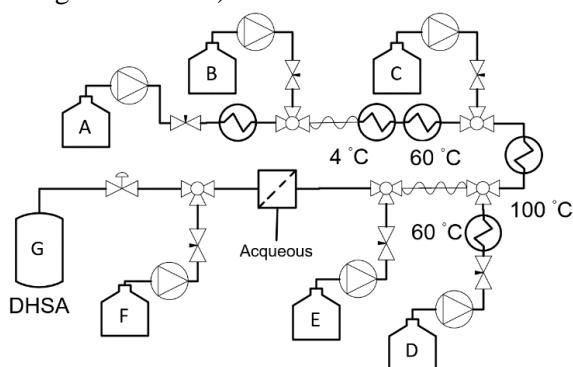


Figure 1. Continuous flow processing setup. (A = oleic acid in formic acid solution; B = hydrogen peroxide; C = ethanol; D = H_2SO_4 solution; E = $NaOH$ solution; F = $NaCl$ solution; G = DHSAs solution)

Because of the O/W biphasic operation, mass transfer is enhanced by the use of Kenics® micro-static mixers after every reactant addition to increase turbulences and ensure a proper mixing. In the last step, an in-line L/L separator allows aqueous phase to be separated prior purification.

Expected Results

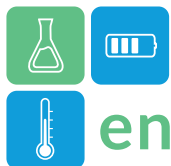
By using flow chemistry, the performance of the DHSAs synthesis is intended to be assessed. The small volume of reactants required allows to perform a simple and time- and cost-efficient screening of the reaction conditions, obtaining rapid and effective process optimization. Small volumes also contribute to overcome safety issues derived of handling of potentially hazardous reagents of reactions. The high process control implies also the opportunity of process automation, bringing under this light to process simplification.

The possibility to work at high pressure-temperature conditions allows process intensification through a drastic reduction of reaction times, which in a last term increases productivity. Reactions become usually more selective under intensive conditions. Due to the short residence time in the microreactor, it is possible to perform reactions that involve transient and reactive intermediates that could not be otherwise handled or stored in traditional batch mode. Additionally, operating in closed capillaries also avoids undesired interactions with external agents, i.e., oxygen.

Once with the optimized conditions in hand, the scaling-up challenge can be faced, as different strategies can be used in scaling up flow chemistry (Escribà-Gelonch *et al.* 2019). Process optimization implies also the optimal use of resources with lower energy expenses, contribution to the reduction of environmental impacts associated to the production process.

Acknowledgments

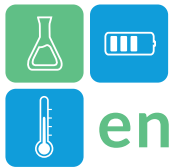
This document has been prepared within the framework of IEA ES TCP. This project was funded by the European Union's Horizon Europe Research and Innovation Programme under grant agreement No. 101096921 (THUMBS UP). Views and opinions expressed are however those of the author(s) only and do not necessarily reflect those of the European Union or CINEA. Neither the European Union nor the granting authority can be held responsible for them.



This work is partially supported by ICREA under the ICREA Academia programme. The authors would like to thank the Departament de Recerca i Universitats of the Catalan Government for the quality accreditation given to their research group (2021 SGR 01615). GREiA is certified agent TECNIO in the category of technology developers from the Government of Catalonia.

References

- Adamczak, M., Bednarski, W., et al. (2004) Enhanced activity of intracellular lipases from *Rhizomucor miehei* and *Yarrowia lipolytica* by immobilization on biomass support particles. *Process Biochem.* 39, 1347–1361. Doi: 10.1016/S0032-9592(03)00266-8.
- Clay, M., Kidd, M. B., et al. (2019). Symposium Series no. 166 Avoiding Engineering Catastrophe: New Insights from Data.
- Dallinger, D., Gutmann, B., et al. (2020) The Concept of Chemical Generators: On-Site On-Demand Production of Hazardous Reagents in Continuous Flow. *Acc. Chem. Res.* 53, 1330–1341. Doi: 10.1021/acs.accounts.0c00199.
- Escribà-Gelonch, M., et al. (2019) Multistep Solvent-Free 3 m² Footprint Pilot Miniplant for the Synthesis of Annual Half-Ton Rufinamide Precursor. *ACS Sustain. Chem. Eng.* 7, 20, 17237–17251. Doi: 10.1021/acssuschemeng.9b03931.
- Gallart-Sirvent, P., Yara, E., et al (2016) Recycling *Rhizopus oryzae* resting cells as biocatalyst to prepare near eutectic palmitic-stearic acid mixtures from non-edible fat. *J. Mol. Catal. B: Enzym.* 134, 172–177. Doi: 10.1016/j.molcatb.2016.11.015.
- Hessel, V. (2009), Novel Process Windows – Gate to Maximizing Process Intensification via Flow Chemistry. *Chem. Eng. Technol.*, 32: 1655-1681. <https://doi.org/10.1002/ceat.200900474>.
- Jeong, S. G., Chung, O., et al. (2013) Improvement of the thermal properties of Bio-based PCM using exfoliated graphite nanoplatelets. *Energy Mater. Sol. Cells* 117, 87–92. Doi: 10.1016/j.solmat.2013.05.038.
- Jeong, S. G., Lee, J. H., et al. (2014) Thermal performance evaluation of Bio-based shape stabilized PCM with boron nitride for energy saving. *Int. J. Heat Mass Transf.* 71, 245-250. Doi: 10.1016/j.ijheatmasstransfer.2013.12.017.
- Nijs W., et al (2021) EU challenges of reducing fossil fuel use in buildings, EUR 30922 EN, Publications Office of the European Union.
- Ramani, K. Kennedy, L.J., et al. (2010) Purification, characterization and application of acidic lipase from *Pseudomonas gessardii* using beef tallow as a substrate for fats and oil hydrolysis. *Process Biochem.*, 2010, 45, 1683–1691. Doi: 10.1016/j.procbio.2010.06.023.
- Yu, S., Jeong, S. G., et al. (2014) Bio-based PCM/carbon nanomaterials composites with enhanced thermal conductivity. *Sol. Energy Mater Sol. Cells* 120, 549–554. Doi: 10.1016/j.solmat.2013.09.037.
- Zhang, N., Yuan, Y., et al. (2014) Preparation and properties of palmitic-stearic acid eutectic mixture/expanded graphite composite as phase change material for energy storage. *Energy* 78, 950–956. Doi: 10.1016/j.energy.2014.10.092.



Cool-Data: PCM cold storage development for server room cooling

Gerald Englmaier^{1,*}, Janne Dragsted¹, Charlotte Jensen¹, Konstantin Filonenko², Dominik Franjo Dominkovic²

¹Department of Civil Engineering and Mechanical Engineering, Technical University of Denmark, Koppels Allé, Building 404, 2800 Kgs. Lyngby, Denmark

²Department of Applied Mathematics and Computer Science, Technical University of Denmark, Richard Petersens Plads, Building 324, 2800 Kgs. Lyngby, Denmark

*Corresponding author e-mail: gereng@dtu.dk

Abstract

Solutions for flexible, secure, and reliable integrated cooling energy system for data centres have been investigated in the framework of the Danish research project “Cool-Data”. To increase the operation flexibility of chillers for server room cooling via water to air heat exchangers, the first cold storage prototype was developed: It contained an immersed fin heat exchanger and 152 kg salt hydrate as Phase Change Material (PCM) with a melting temperature of 15 °C. Tested with constant inlet temperatures at the heat exchanger in the temperature range of 10–23 °C, a cold capacity of 7.5 kWh was measured – a proof of concept was achieved. Next, a numerical model was developed in Ansys Fluent, which was then used to investigate improved heat exchanger geometries. Findings from experimental testing and numerical modelling were applied in a second cold storage prototype with improved geometry. It contained 230 l of PCM and was tested first with the originally used salt hydrate and then with paraffin with a melting temperature of 18 °C. In conclusion, both configurations were successfully tested under laboratory conditions. Higher energy storage densities in small temperature range were obtained with salt hydrate (>50 kWh/m³), while the use of paraffin resulted in more stable thermal power during PCM solidification.

Keywords: Cold storage, server room, data center, phase change material, prototype testing.

Introduction

The International Energy Agency has estimated that data centres used between 220 and 320 TWh of electricity in 2021, i.e., 0.9%–1.3% of the global final electricity demand 2018 (IEA, 2023). From 2010–2020 data center workloads rose approximately 10-fold, but energy use remained almost stable (IEA, 2022), thanks to energy efficiency improvements of equipment. Geographic clusters of data centres are established in locations with favourable conditions in terms of climate and electric supply quality. For example, the Danish Energy Agency estimates that electricity demand from data centers in Denmark will raise 7-fold from 2021 to 2030 (Monsalves et al., 2023).

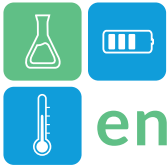
Thermal energy storage (TES) is an important technology to enable increased utilization of renewable energy by bridging the time gap between demand and supply. The main advantage of phase change materials (PCMs) is the high storage density in small temperature intervals. Ice water storage tanks have been efficiently applied as constant low-

temperature heat source (0 °C) in heat pump systems, leading to a higher performance for building applications (IEA SHC, 2015). To increase the flexibility of chillers operating above 8 °C – for room cooling via water to air heat exchanger – utilization of PCM with melting temperatures of 12–18 °C is aimed.

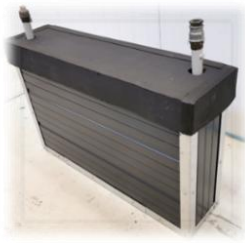
For cold storage application, two groups of materials are considered: a) Inorganic PCM (water, salt hydrates, eutectic mixtures); b) Organic PCM (paraffin and fatty acids). While inorganic materials typically provide the higher energy storage density and thermal conductivity, organic PCMs provide low or no subcooling and have a lower density than water. (Cabeza et al., 2011)

Methodology

Application-orientated storage development was conducted in collaboration with industrial partners under the framework of the Danish Grand Solution project “Cool-Data” – with the following goal: Cold storage for server room cooling (small and medium-sized data centers) to provide operation flexibility of compressor-driven chillers.

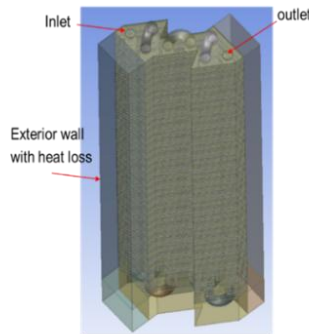


1st prototype:



P1: 115 l salt hydrate (152 kg)

Validated CFD model



2nd prototype:



P2: 230 l salt hydrate (304 kg)

P3: 230 l paraffin (170 kg)

Figure 1: Storage development within the Cool-Data project – illustration of storage configurations P1-3 as well as of a CFD mesh used during numerical investigations.

By utilizing several storage units it will be possible to cover a constant cooling demand for 2–3 hours in order to maximize the utilization of solar and wind electricity from the grid while increasing cold supply security.

As first step, material screening was conducted based on literature study and information obtained from PCM producers. It was concluded that salt hydrates with nucleating agents are beneficial properties in terms of energy storage density and costs.

Fig. 1 shows the two types of storage prototypes which have been built in accordance with application requirements in collaboration with the Danish manufacturer Energy-Cool ApS. The first prototype (P1) contained a metal fin heat exchanger. The storage was first filled up with 115 liter water (determination PCM volume) and then with 152 kg of salt hydrate composite SP15 gel with an onset melting temperature of 15 °C. The PCM volume of second prototype was also determined by initial water filling (230 liter) – then 304 kg of SP15 gel was applied (P2). Finally, the second prototype was tested with paraffin RT 18HC with an onset melting temperature of 18 °C (P3).

A variable laboratory heat/cold source (operated via a LabView control program) was used for cyclic testing of storages. Heat flow at storage inlet/outlet and internal PCM temperatures were monitored to track heat transfer rates as well as PCM solidification and melting behaviour.

Two CFD models – the enthalpy method and the effective heat capacity method - were developed in

ANSYS Fluent environment. Model validation was obtained by comparison with experimentally obtained heat transfer rates for the charging and discharging process of prototype 1. Lab measurements with two different heat transfer fluid flow rates (5 l/min and 10 l/min) were utilized. This work was published by Zhu et al. (2023).

The main purpose was to identify the most accurate numerical approach to model salt hydrate behaviour in interaction with a finned heat exchanger – addressing the challenges of undercooling of the liquid phase prior solidification as well as changing crystallization speed. The “enthalpy method” was found superior and therefore applied for design optimizations in terms of geometry of the cold storage and its immersed heat exchanger. This knowledge was applied when designing P2 and P3 – besides practical manufacturing aspects.

Selected Results

Fig. 2 shows the development of transferred energy obtained during selected tests of storage configurations P1, P2 (both utilizing salt hydrate composite) and P3 (utilizing paraffin). For comparison, the inlet temperatures of the heat transfer fluid during melting and solidification were set in relation to the onset melting temperatures of the used PCM. The measured cold capacities were approximately 7.5 kWh for P1, 14 kWh for P2 and 11.6 kWh for P3 respectively. The resulting energy storage density potential was >50 kWh per m³ PCM (liquid phase) when applying salt hydrate composite.

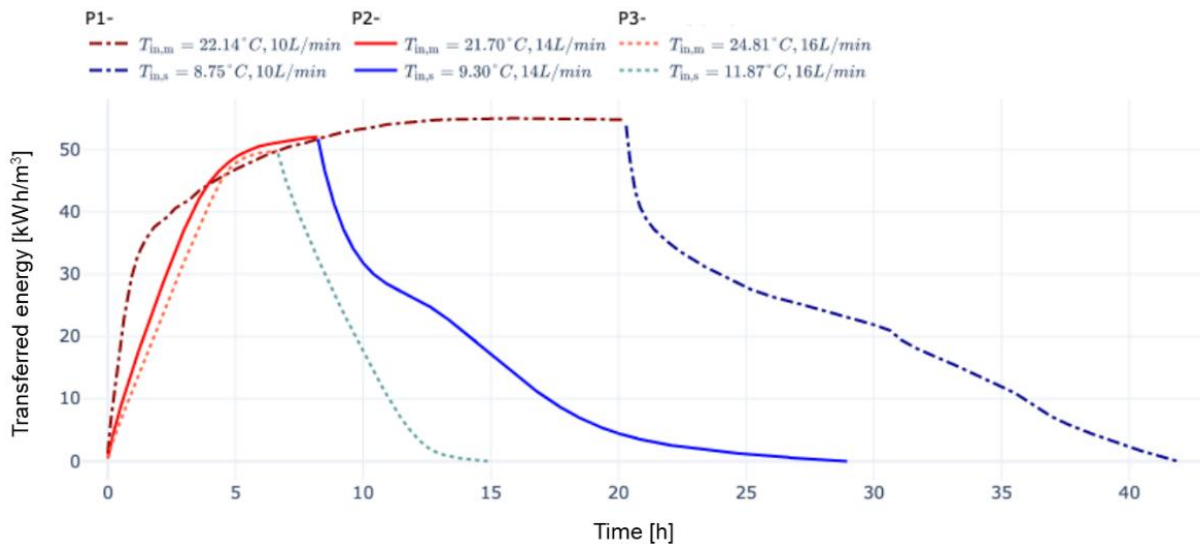
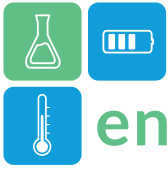


Figure 2: Heat transfer during selected test runs with P1 (dash-dotted line), P2 (solid line) and P3 (dotted line); test sequence: PCM melting (red lines) followed by PCM solidification (blue lines). The transferred energy is displayed normalized per cubic meter PCM.

Fig. 3 shows the development of obtained U/A values during PCM melting and solidification with P1. With salt hydrate (P1, P2), heat transfer rates were generally higher during melting than during solidification. This effect is related to the solidification kinetics of salt hydrate: subcooling of the melted phase and crystallization speed. Test cycles with incomplete melting resulted in slight improvement of the kinetics. When applying paraffin (P3), thermal power during melting and solidification differed only slightly.

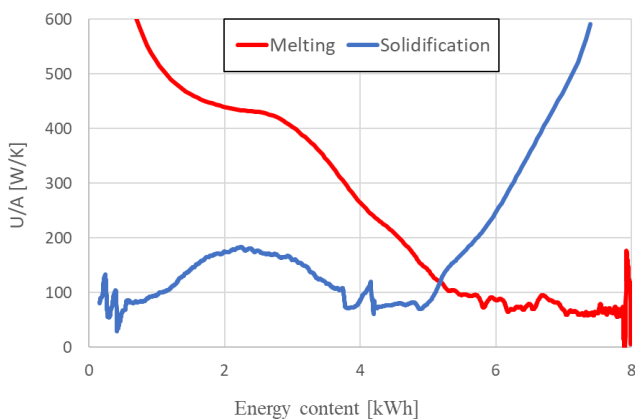


Figure 3: Obtained U/A values during test of P1 with an initial PCM temperature of 10 °C – followed by heating to 25 °C and cooling to 10 °C with a fluid flow rate of 5 l/min.

Conclusions and Outlook

A big application potential for PCM cold storage for server room cooling in the temperature range of 12–18 °C was identified. Two storage prototype geometries were developed, and their applicability was successfully tested in the laboratory. The applied salt

hydrate was attractive regarding storage density and price, but crystallization kinetics were slower in comparison to paraffin. Thus, with prototype 3 (containing 230 l paraffin) higher thermal power was measured during PCM solidification.

The numerical model in ANSYS Fluent can be utilized for further design optimizations. It is validated with experimental data from prototype 1 utilizing salt hydrate SP15 gel – the authors propose investigations with different geometries and PCM in future research.

Heat transfer fluid rates during laboratory tests were limited. For future research higher flow rates should be applied to fully elucidate the application potential of the developed cold storage prototypes. For system implementation, configuration of multiple storage units is aimed to provide constant power for server room cooling. This challenge is currently addressed within the Cool-Data project: A system model was developed in Modelica environment able to utilize model predictive control algorithms for optimal storage operation. The layout of the model and its functionality were already presented by Filonenko et al. (2023).

Acknowledgement

This work was financed by the Innovation Fund Denmark in the framework of the project titled ‘Cool-Data Flexible Cooling of Data Centers’ (no. 0177-00066B). We would like to thank our partners at Energy-Cool ApS for their excellent collaboration.

References



Cabeza, L., et. al, (2011), Material used as PCM in thermal energy storage in buildings: A review, *Renewable and Sustainable Energy Reviews*, vol, 15, pp. 1675-1695.

Filonenko, K., Dominkovic, D. F., Jensen, A. U., & Englmaier, G. (2023). Investigation of cold storage integration in a Danish data center. In *Building Simulation Conference Proceedings (Vol. 18, pp. 2875 - 2878)*. International Building Performance Simulation Association.
<https://doi.org/10.26868/25222708.2023.1560>

International Energy Agency (2023). Data centres and data transmission networks. International Energy Agency.

International Energy Agency (2022). Global trends in internet traffic, data centres workloads and data centre energy use, 2010-2020.
<https://www.iea.org/data-and-statistics/charts/global-trends-in-internet-traffic-data-centres-workloads-and-data-centre-energy-use-2010-2020>.

IEA Solar Heating and Cooling Programme (SHC) Task 42 (2015), Compact Thermal Energy Storage, Position paper. Available: <http://task42.iea-shc.org/publications>

Jerez Monsalves, J., Bergaentzlé, C., & Keles, D. (2023). Impacts of flexible-cooling and waste-heat recovery from data centres on energy systems: A Danish case study. *Energy*, 281, Article 128112.
<https://doi.org/10.1016/j.energy.2023.128112>

Zhu, Y., Kong, W., Fan, J., Englmaier, G., & Yuan, Y. (2023). Numerical investigation on radiative heat loss of a direct absorption solar collector using the discrete ordinates method. *Applied Thermal Engineering*, 236, Article 121560.
<https://doi.org/10.1016/j.applthermaleng.2023.121560>



Corrosion control of a Fe-based alloy (DMV 310 N) in molten $\text{MgCl}_2\text{-KCl-NaCl}$ for heat storage and transfer at very high temperatures

Dr. Wenjin Ding^{1,*}, Hem Barot¹, Ralf Hoffmann¹, Dr. Thomas Bauer²

1 Institute of Engineering Thermodynamics, German Aerospace Center (DLR). Pfaffenwaldring 38, 70569 Stuttgart, Germany.

2 Institute of Engineering Thermodynamics, DLR. Linder Höhe, 51147 Cologne, Germany.

*Corresponding author e-mail: wenjin.ding@dlr.de

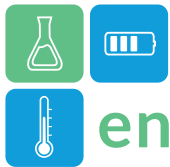
Abstract

Next-generation concentrating solar power (CSP) plant with operating temperatures higher than 700°C needs an advanced high-temperature thermal energy storage (TES) system and advanced power cycle (e.g., supercritical CO₂ Brayton) for a higher energy conversion efficiency and lower levelized cost of electricity (LCOE). $\text{MgCl}_2\text{-KCl-NaCl}$ is a promising candidate of such very high-temperature heat storage and transfer due to its low cost (<0.35 USD/kg) and excellent thermophysical properties (e.g., high thermal stability >1000°C). Using Fe-based (Fe: ≥50 wt.%) alloys as the main structural material for the chloride-based TES system is the key to ensuring its cost competitiveness. However, it is universally believed that Fe-based alloys have unacceptably high corrosion rates in unpurified molten $\text{MgCl}_2\text{-KCl-NaCl}$ at such high temperatures. Theoretically, purification with Mg metal can reduce the corrosion rates of Fe-based alloys to acceptable low levels (<30 μm/year) at very high temperatures (≥800°C). In this work, to experimentally verify a commercial highly creep-resistant austenitic stainless steel DMV 310 N (Fe-based, ASME code listed) as the high-temperature structural material for the chloride-based TES at very high temperatures, it was immersed in the Mg-purified molten $\text{MgCl}_2\text{-KCl-NaCl}$ at 800°C for 500 hours. The SEM and EDX results show that after immersion, the typical Cr-depleted corrosion layers on the samples are negligibly thin (only several μm). Based on mass loss and microstructural analysis results, the corrosion rate of DMV 310 N is below 30 μm/year. Therefore, from the perspective of corrosion, the cost-effective Fe-based alloys possess good compatibility with the Mg-purified molten $\text{MgCl}_2\text{-KCl-NaCl}$ even at 800°C. According to preliminary calculation, the cost of TES using chlorides at >700°C could be potentially reduced close to that using commercial nitrates/nitrites at ≤565°C, leading to a significant reduction of the LCOE of CSP with higher operating temperatures.

Keywords: Concentrating solar power (CSP), Thermal energy storage (TES), Fe-based alloy, Corrosion control, Mg corrosion inhibitor.

Acknowledgment

The work is performed under the DLR basic funding from German Federal Ministry for Economic Affairs and Climate Action (Bundesministerium für Wirtschaft und Klimaschutz, BMWK).



Corrosion test on nitrate salts for building heating applications

Maria Clara Silva Silveira², Anabel Palacios*², Christoph Rathgeber¹, Henri Schmit¹, Poppy O'Neill³, Anastasia Stamatidou²

¹ Bavarian Center for Applied Energy Research (ZAE Bayern), Walther-Meissner-Str. 6, 85748 Garching, Germany

² Lucerne School of Engineering and Architecture, Technikumstrasse 21, 6048 Horw, Switzerland

³ Cowa Thermal Solutions AG, Platz 4, Technopark Luzern, Root CH-6048, Luzern, Switzerland

*Corresponding author: anabel.palacios@hslu.ch

Abstract

In this work, the corrosivity of two salts identified as potential materials for storing heat for space-heating and in domestic hot water systems have been studied after 1 month of static immersion in contact with relevant construction material used in piping and heating systems. To simulate different breakage scenarios of the capsules in the system, ranging concentrations have been considered (from 1 to 20 capsule breakage) as immersion media. The outcomes of the study are that most of the materials are within the limits for safety after a month and that aluminium and copper are the metals that show higher corrosion rates even after some days of immersion.

Keywords: Phase change materials, building applications, Corrosion test, nitrate salts.

Introduction

Corrosion poses a significant threat to the longevity and performance of thermal energy storage systems. Specifically, when storage media are integrated into these systems, the risk of corrosion is heightened due to potential interactions with metallic components, such as pipes and heat exchangers (Farrell et al., 2006). Corrosion can lead to system inefficiencies, reduced lifespan, and increased maintenance costs. Therefore, it becomes imperative to thoroughly assess the corrosive effects of PCM within the Thermal energy Storage (TES) infrastructure (Mohamed et al., 2017).

In the framework of the *Euteq* project, different phase change materials mixtures have been identified for the potential of heat storage in the temperature range from 35-60°C, which is suitable to be used for space-heating and domestic hot water storage systems. In this extended abstract, we show the main outcomes of a corrosion study performed on relevant metals used as construction materials in piping, heat exchangers and vessels immersed in different concentrations of the potential PCM mixtures after 35 days of steady corrosion test at 65°C.

Methodology

Two PCM were identified as potential compositions for storage between 35-60 °C, $\text{CaNO}_3 \cdot 4 \text{H}_2\text{O}$ and a peritectic composition of SAT- NaNO_3 . These PCMs are envisioned to be integrated into macrocapsules that will be immersed in water in the HEX. For this reason, assuming that leakage or breakage of the capsules can be a danger to the system by leading to corrosion and pitting in the containment structures. The corrosion tests used different PCM concentrations diluted in water to aim to replicate various leakage scenarios that may occur within a TES system. By diluting the PCM in water, we simulate the potential for PCM leakage into the heating system water at different percentages, ranging from minor leaks to more substantial integral breaches.

To comprehensively evaluate the corrosion potential of PCMs, our study employed corrosion tests of five metals: aluminium, stainless steel, steel, copper, and brass, the most found metals in heating systems and piping networks.

The corrosion tests were conducted by static submersion of the metal sheets into the diluted PCM solutions for 35 days at 65°C. The initial weight (before the corrosion experiment), and the final weight (after

the cleaning procedure) are then measured, and the weight loss (Eq. 1) is converted into specific weight loss (in $\text{mg}\cdot\text{cm}^{-2}$) by dividing the weight loss by the exposed surface of the sample. The procedure to determine the final weight is explained in the standard ISO 8407. The corrosion rate (CR) is then calculated using Eq. 2.

$$\Delta W = (W_f - W_i) \quad (1)$$

Where W_i is the initial weight of the sample before the corrosion experiment, W_f is the final weight determined after the cleaning procedure, and ΔW is the weight loss in mg. CR is the corrosion rate expressed in $\mu\text{m}/\text{year}$, 8760 is the number of hours in one year, S is the surface of the sample (in cm^2), ρ_{alloy} is the density the alloy e.g. of stainless steel 316L ($7.98 \text{ g}\cdot\text{cm}^{-3}$) and t is the exposure duration of the corrosion experiment in hours (840 h in this study).

$$\text{CR} = [8760 \cdot (\Delta W / S) \cdot 0.001] / (\rho_{\text{alloy}} \cdot 0.0001 \cdot t) \quad (2)$$

Results and discussion

The corrosion tests revealed that 4 metal specimens fall below the generally accepted limit of 0.1 mm/year recommended for the thickness of typical metal specimens in the average heating system (Groysman, 2009) (see Fig.1). Within the acceptable range aluminium and copper show the highest corrosion out of all metal specimens and should be closely monitored is installed in heating systems as it is close to the corrosion limit.

Steel is the metal that shows the highest corrosion rate, which is distant from the acceptable value. Given that these salt mixtures have been tailored to the needs of the project it is difficult to compare the results to the literature, however, steel was found to be a highly corrosive metal when in contact with CaNO_3 as reported by (Danielik et al., 2017). A correlation between the PCM concentration and the corrosion rate cannot be concluded, as higher PCM concentration does not lead to higher corrosion rates in all cases.

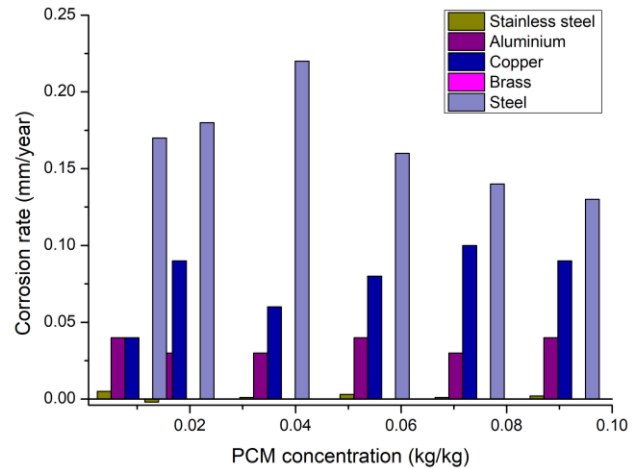


Fig. 1 Corrosion rates (mm/year) versus PCM (CaNO_3) dilution for each metal specimen.

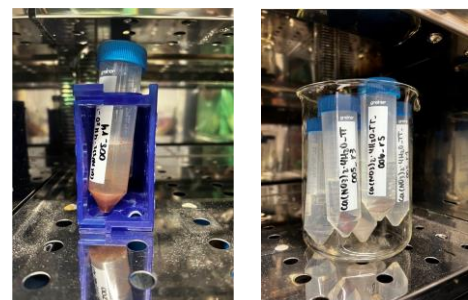
Regarding the differences between calcium nitrate and SAT, the corrosion rates when immersed in SAT are 10 times higher than the ones for CaNO_3 . For instance, when immersed in SAT mixture the corrosion of copper started immediately after the samples were put in the oven while it took some days to visibly observe corrosion when immersed in CaNO_3 , see Fig. 2 and Fig. 3.



Copper

Aluminium

Fig. 2 Visual inspection of specimens immersed in salts after 35 days SAT- NaNO_3 mixture.



Copper

Aluminium



Fig. 3 Visual inspection of specimens immersed in salts after 35 days CaNO_3 mixture.

Conclusions

In conclusion, the corrosion tests conducted on various metal specimens demonstrate that stainless steel, aluminium, copper and brass exhibit corrosion rates below the standard threshold. Notably, steel and copper exhibited the highest levels of corrosion among the tested metals. While brass showed the best results, given the proximity of copper and aluminium to the established corrosion limit, it is imperative to closely monitor these materials, especially when utilized in heating systems, to ensure their longevity and reliability. Further tests such as X-Ray Diffraction and microscope imaging will be carried out on the corroded samples to assess the oxides formed and the type of corrosion.

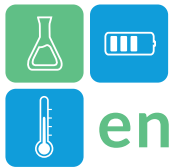
References

- Danielik, V., Šoška, P., Felgerová, K., & Zemanová, M. (2017). The corrosion of carbon steel in nitrate hydrates used as phase change materials. *Materials and Corrosion*, 68(4), 416–422. <https://doi.org/10.1002/maco.201609160>
- Farrell, A. J., Norton, B., & Kennedy, D. M. (2006).

Corrosive effects of salt hydrate phase change materials used with aluminium and copper. *Journal of Materials Processing Technology*, 175(1–3), 198–205. <https://doi.org/10.1016/j.jmatprotec.2005.04.058>

Groysman, A. (2009). Corrosion Monitoring. In A. Groysman, *Corrosion for Everybody* (pp. 205–343). Springer Dordrecht.

Mohamed, S. A., Al-Sulaiman, F. A., Ibrahim, N. I., Zahir, M. H., Al-Ahmed, A., Saidur, R., Yılbaş, B. S., & Sahin, A. Z. (2017). A review on current status and challenges of inorganic phase change materials for thermal energy storage systems. *Renewable and Sustainable Energy Reviews*, 70(June 2015), 1072–1089. <https://doi.org/10.1016/j.rser.2016.12.012>



Critical review on the environmental assessment of xylitol as phase change material

Humberto Santos^{1,*}, Silvia Guillen-Lambea¹

¹ Aragón Institute for Engineering Research (I3A), Thermal Engineering and Energy Systems Group, University of Zaragoza, Agustín de Betancourt Building, C/María de Luna 3, 50018, Zaragoza, Spain

*Corresponding author e-mail: hdasilva@unizar.es

Abstract

Recently, xylitol has been investigated as phase change material for thermal energy storage system. Due to the lack of studies regarding the life cycle assessment of xylitol as phase change material, the objective of this work is to provide an overview of the production methods and market along with a critical review of the environmental impacts associated to its production. Based on the literature investigated, the market seems to be well established and distributed globally, which is a positive aspect for the use of xylitol as phase change material. Regarding the environmental assessment, the comparisons among the selected studies show that the global warming potential varies from 1.81 kg CO₂ eq. to 17.29 kg CO₂ eq.kg⁻¹ xylitol produced. Additionally, life cycle assessment carried out in this work show that the main contributors of environmental impacts are the farming, energy and sulfuric acid during the production phase.

Keywords: xylitol, life cycle assessment, phase change material, thermal energy storage

Introduction

Biomass contains mainly three components; cellulose, hemicellulose and lignin, from which hemicellulose is the source of xylose, subsequently turned in xylitol (Venkateswar Rao et al. 2016). Although xylitol is well known in the food and pharmaceutical industries, it also has applications as Phase change material (PCM) for Thermal energy storage (TES) systems (Anish et al. 2020). PCMs store or release considerable amounts of energy during their melting and solidification due to their heat of fusion (Kylili and Fokaides 2016).

Xylitol production can be either chemical or biotechnological: in the chemical production xylitol is mainly produced by catalytic synthesis, which requires high temperature, higher pressures and short reaction time compared to the biotechnological production. For instance, the temperature and pressure demand in the chemical process are in the range of 140-200°C and 50-60 bar, respectively (Dasgupta et al. 2017).

In a scenario where xylitol is proposed as PCM, it is important to understand the life cycle impacts associated to its production, use and disposal. Life cycle assessment (LCA) has become one of the most used tools to investigate a life cycle impact of a product or service.

As will be shown along the study, it has been observed a scarcity of scientific works related to environmental performance of xylitol as PCM for TES. The first step to consider in accomplishing a cradle-to-grave (production, use and disposal) LCA of xylitol, is to have a comprehensive overview of the market and its

production environmental impacts in a perspective cradle-to-gate.

Therefore, the main objective of this work is to discuss xylitol production and market, and critically investigate the environmental impacts associated to its production, i.e., in a cradle-to-gate perspective. For this purpose, a critical review has been conducted. Thus, providing information on xylitol production process, market trends, and environmental impacts during production is a significant step to ensure future successful cradle-to-grave assessment of its potential as PCM in thermal energy storage system.

Methodology

To have a comprehensive cradle-to-grave study of xylitol as PCM for TES, it is necessary to understand and have reliable data for three different stages of the whole life cycle, i.e., production, application in the energy storage system as PCM, and its final disposal. This paper covers the first part, which is associated with the life cycle impacts of xylitol production, or the cradle-to-gate stage. The methodology adopted is depicted in Figure 1. The production process along with the market information is gathered from literature. Subsequently, a systematic review is conducted with the LCA studies available. Finally, life cycle assessment is conducted based on the available inventories.

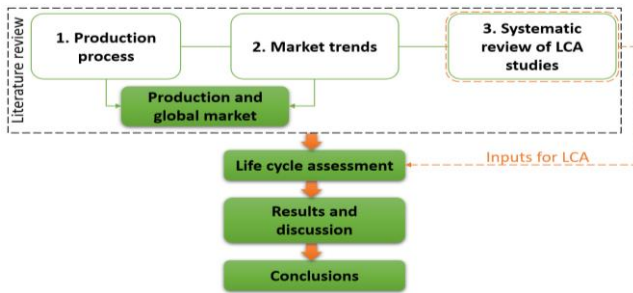
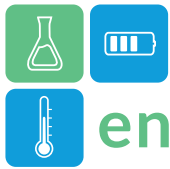


Figure 1: Methodology approach followed

It is important to know how the PCM is manufactured as each production process has its steps and technical particularities. In this respect, the two main processes utilized worldwide are briefly compared. Additionally, a review focusing on the distribution of the global market is also carried out.

A systematic review was conducted on the current LCA studies on the production of xylitol. Scopus was the main source, but when necessary other databases were used to refine the search of papers, such as Google Scholar and Science Direct. Although xylitol has been studied for decades, a limited number of papers is available about its life cycle impacts, especially for the commercial chemical process, in which data are very confidential. The scripts used to find the papers were:

1. {XYLITOL} AND {LCA} – 9 papers;
2. {XYLITOL} AND {LIFE CYCLE ANALYSIS} – 3 papers;
3. {XYLITOL} AND {LIFE CYCLE ASSESSMENT} – 9 papers.

The screening process was subdivided into 3 parts. The search gives a total of 21 papers. The first screening found 5 papers repeated in the three searches, leaving a total of 16 papers. The second screening showed that 6 papers were not specifically on LCA of xylitol, although mentioned it in the text, therefore a total of 10 papers is left. After a thorough screening looking for details, only 4 references from Scopus were relevant for this specific review, out of which only one is about the chemical production of xylitol, and none of them mentioned the possibility of using xylitol as PCM, corroborating the scarcity of scientific work related to LCA of xylitol as PCM. In addition to these, a reference regarding the production of xylitol through chemical process for TES applications is found in another database.

From the selected papers in the systematic review, two of them which were based on the same life cycle impact assessment (LCIA) method, Recipe (H) Midpoint, were chosen for further investigation. New life cycle assessment was conducted including their inventory inputs and outputs with Recipe (H) Midpoint.

Results and Discussion

Although it can be found in small quantities in fruits and vegetables, the routes to obtain xylitol are based on chemical or biotechnological processes. In both processes, xylitol is derived from biomass. The biotechnological process differs from the chemical in respect to the step of obtaining the xylose, in which microorganisms are in charge of producing it through fermentation. Thus, biotechnological process uses lower pressure and temperature, simpler fermentative approach instead of catalytic hydrogenation (chemical process), less energy, has no risk of metal catalysts contamination in the final product and is claimed to be cheaper when compared to the chemical process (Umaí et al. 2022).

A statistical study for the year of 2020 shows that the global market of xylitol in dollars is comprised of 42.2% - Pacific Asia, 23% - Europe, 19.2% North America, 9.2% - Latin America and 6.4% - Africa and Middle East (Zhou 2021). From 2006 to 2022 the production increased from 80 to 200 tones. It is expected to grow 5% annually from 2023 to 2030 as reported by (Mathew et al. 2018).

The papers selected according to the criteria presented in the methodology are described as follows based on the life cycle environmental assessment.

1. Biotechnological process I: uses sugarcane as biomass in a cradle-to-gate approach in OpenLCA, with EcoInvent as database and ReCiPe (H) Midpoint (Shaji et al. 2022).
2. Biotechnological process II: uses corncobs in a cradle-to-gate perspective in SimaPro with EcoInvent as database and CML-IA baseline as method. (Dasgupta et al. 2021).
3. Biotechnological process III: uses wheat straw as feedstock in a cradle-to-gate approach with mainly EcoInvent as dataset and ReCiPe (H) Midpoint as method (Vollmer et al. 2023).
4. Chemical process I: the feedstock is Empty fruit bunch (EFB) from palm oil processing and uses a cradle-to-grave perspective (Johansson and Norrman, n.d.).
5. Chemical process II: EFB as feedstock in a cradle-to-gate perspective in SimpaPro with CML-IA Baseline as impact method (Hafyan et al. 2019).

Figure 2 presents the results of GWP by production process according to the reviewed papers following the methodology proposed. Regarding the chemical process I, the GWP is nearly 7.00 kg CO₂ eq. per kg of xylitol, while the chemical process II is nearly 55% less. Biotechnological process II is almost 10 times that amount of biotechnological process I. Comparing the



inventory of both processes, it was confirmed that the electricity consumption in the fermentation process was 3.39 kWh and 35.43 kWh for the biochemical process I and II, respectively. Biotechnological process I GWP was lower than both chemical processes. It corresponded to 25.8% and 47.2% of the GWP of the chemical process I and II, respectively. However, biotechnological process III shows a GWP of 12.3 kg CO₂ eq., even higher than both chemical processes.

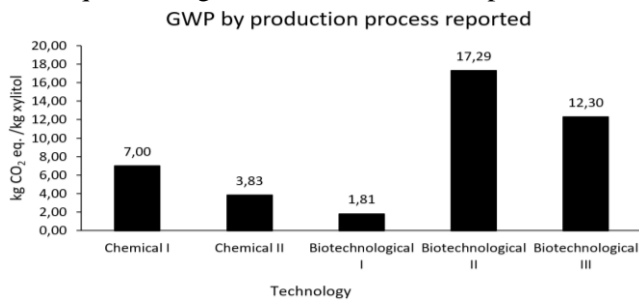


Figure 2. GWP of chemical and biotechnological production of xylitol.

For the comparison of the cumulative energy demand (CED) some assumptions are needed. Since the chemical process does not report further information on the energy used for the cultivation of the feedstock, the analysis of the CED has been limited to the production within the factory, that is a gate-to-gate analysis, from the moment the raw material enters the gates of the manufacturing plant until it is finally ready for distribution and consumption. The analysis of the inventory of the biochemical process I shows that the electricity expenditure to produce one kg of xylitol is 5.15 kWh, while the value reported for the chemical process I is 5.55 kWh, which represents a consumption

process, while the highest part of energy consumption in the biotechnological process occurs during the fermentation and filtration stages.

The life cycle assessment conducted is discussed as follows. The LCA results of biotechnological processes I and III are shown in Figure 3. Note that energy in this context, can be either thermal or electrical. For biotechnological process I, only electricity has been reported, while for process III electricity and steam are sources of energy. In biotechnological process I, the biggest contributors are farming, energy, sulfuric acid and quick lime. Among those, electricity plays a major role in the impacts, e.g., it represents more than 80% of the impacts in marine eutrophication (MEP) and land use (LOP). Sulfuric acid used for the hydrolysis impacts directly in terrestrial ecotoxicity (TE). The farming stage was responsible for more than 50% of the impacts in the water consumption. Sulfuric acid showed an expressive to the impacts in terrestrial ecotoxicity.

In biotechnological process III, steam, wheat straw (farming), electricity, sulfuric acid and brine waste are the biggest contributors of environmental impact. Steam plays a major role in the impact categories, being responsible for nearly 85% of GWP and 90% of fossil resources scarcity (FFP). Additionally, it is evident that the feedstock farming process influences in all impact categories for both processes, however, in the case of biotech I the farming stage highlights although it is not higher in all impact categories. Unlike the biotechnological process I, electricity contribution is extremely low, and that could be attributed to the fact that the electricity considered by the authors has an

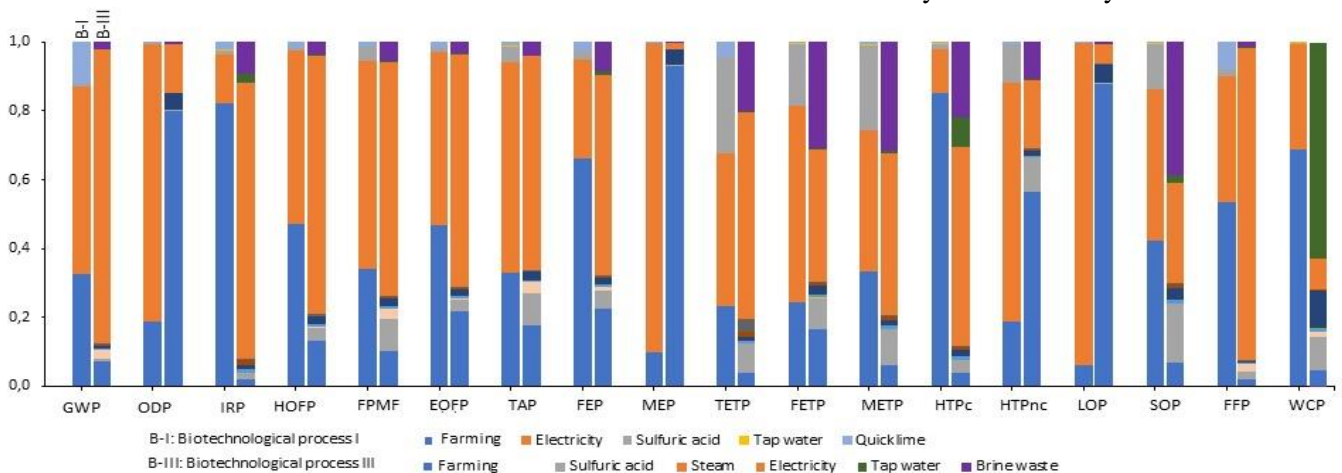


Figure 3. Environmental impacts for biotechnological processes I and III.

of nearly 9% higher than the biotechnological process. Additionally, for the chemical process, the 94% of the CED is thermal energy needed as heating for the

emission factor of 0.0206 kg CO₂ eq.kWh⁻¹, while for the biotech I the same factor has an impact of 0.27 kg CO₂ eq.kWh⁻¹, more than 10 times higher.



Both production processes have different inputs in the environmental assessment, but it can be concluded that in the cradle-to-gate stage, the overall impacting input is the energy necessary during its production.

Conclusions

1. Xylitol market is globally distributed and this could be a positive aspect in the scenario for application of xylitol as PCM;
2. Few publications on xylitol as PCM, and the one available, usually have different LCA methodology, making it difficult to compare distinct processes;
3. Based on the life cycle assessment studies available in literature it is possible to see that the biotechnological process I has less environmental impacts compared to the other processes in terms of GWP and CED. Lower pressure and temperature required for the biotechnological process could be one of the explanations.
4. Energy use for xylitol production is the major contributor on environmental impacts;

Acknowledgment

This work has been partially financed by the State Research Agency (SRA) and European Regional Development Fund (ERDF), project TED2021-131061B-C31 and Silvia Guillén acknowledges the funding from grant RYC2021-034265-I funded by MCIN/AEI/10.13039/501100011033 and “European Union Next Generation EU/PRTR”

References

Anish, R., V. Mariappan, Mahmood Mastani Joybari, and Ammar M. Abdulateef. 2020. “Performance Comparison of the Thermal Behavior of Xylitol and Erythritol in a Double Spiral Coil Latent Heat Storage System.” *Thermal Science and Engineering Progress* 15 (March). <https://doi.org/10.1016/j.tsep.2019.100441>.

Dasgupta, Diptarka, Sheetal Bandhu, Dilip K. Adhikari, and Debashish Ghosh. 2017. “Challenges and Prospects of Xylitol Production with Whole Cell Bio-Catalysis: A Review.” *Microbiological Research*. Elsevier GmbH. <https://doi.org/10.1016/j.micres.2016.12.012>.

Dasgupta, Diptarka, Arushdeep Sidana, Prasenjit Ghosh, Tripti Sharma, Jasvinder Singh, Asmita Prabhune, Snehal More, Thallada Bhaskar, and Debashish Ghosh. 2021. “Energy and Life Cycle Impact Assessment for Xylitol Production from Corncob.” *Journal of Cleaner Production* 278 (January). <https://doi.org/10.1016/j.jclepro.2020.123217>.

Hafyan, Rendra, Lupete Bhullar, Zulfan Putra, MR Bilad, MDH Wirzal, and NAHM Nordin. 2019. “Sustainability Assessment of Xylitol Production from Empty Fruit Bunch.” *MATEC Web of Conferences* 268: 06018. <https://doi.org/10.1051/matecconf/201926806018>.

Johansson, Elin, and Filip Norrman. n.d. “Life Cycle Analysis on Phase Change Materials for Thermal Energy Storage.”

Kylili, Angeliki, and Paris A. Fokaidis. 2016. “Life Cycle Assessment (LCA) of Phase Change Materials (PCMs) for Building Applications: A Review.” *Journal of Building Engineering*. Elsevier Ltd. <https://doi.org/10.1016/j.jobe.2016.02.008>.

Mathew, Anil K., Amith Abraham, Kiran Kumar Mallapureddy, and Rajeev K. Sukumaran. 2018. “Lignocellulosic Biorefinery Wastes, or Resources?” In *Waste Biorefinery*, 267–97. Elsevier. <https://doi.org/10.1016/B978-0-444-63992-9.00009-4>.

Shaji, Arun, Yogendra Shastri, Vinod Kumar, Vivek V. Ranade, and Neil Hindle. 2022. “Sugarcane Bagasse Valorization to Xylitol: Techno-Economic and Life Cycle Assessment.” *Biofuels, Bioproducts and Biorefining* 16 (5): 1214–26. <https://doi.org/10.1002/bbb.2368>.

Umai, Devasena, Ramalingam Kayalvizhi, Vinod Kumar, and Samuel Jacob. 2022. “Xylitol: Bioproduction and Applications-A Review.” *Frontiers in Sustainability*. Frontiers Media S.A. <https://doi.org/10.3389/frsus.2022.826190>.

Venkateswar Rao, Linga, Jyosthna Khanna Goli, Jahnvi Gentela, and Sravanthi Koti. 2016. “Bioconversion of Lignocellulosic Biomass to Xylitol: An Overview.” *Bioresource Technology*. Elsevier Ltd. <https://doi.org/10.1016/j.biortech.2016.04.092>.

Vollmer, Nikolaus I., Carina L. Gargalo, Krist V. Gernaey, Stig I. Olsen, and Gürkan Sin. 2023. “Life Cycle Assessment of an Integrated Xylitol Biorefinery with Value-Added Co-Products.” *International Journal of Life Cycle Assessment*. <https://doi.org/10.1007/s11367-023-02194-6>.

Zhou, Quan. 2021. “2021年全球木糖醇行业现状及中国木糖醇进出口现状分析，我国是全球重要出口国。” <https://www.huaon.com/channel/trend/768983.html>. December 10, 2021.



Degradation of Erythritol after ageing at elevated temperature and cycling under real application conditions

Franziska Klünder^{1*}, Thomas Haussmann¹

¹ Fraunhofer Institute for Solar Energy Systems, Heidenhofstraße 2, Freiburg, Germany

*Corresponding author e-mail: franziska.kluender@ise.fraunhofer.de

Abstract

Latent heat storage systems can be used to store thermal energy. It is necessary that the phase change materials (PCMs) used, have stable thermal properties. The aim of the study is to find out whether aging under real application conditions can be accelerated by thermal aging at elevated temperature. The sugar alcohol Erythritol was investigated for its degradation. Two different approaches are followed and will be compared. First, Erythritol is investigated in a finned tube heat exchanger under real application conditions and second, Erythritol is aged in closed 100 ml laboratory bottles at constant temperature. The aging is carried out at three different temperatures, all above the melting temperature. To compare the degradation in both experiments, Erythritol is examined after the experiments using differential scanning calorimetry (DSC) and attenuated total reflection (ATR).

Keywords: PCM, Degradation, Erythritol

Introduction

For the use of latent heat storage, it is important that the thermal properties of the phase change material (PCM) remain constant over the service life. It is therefore important to investigate the degradation of PCMs. A wide variety of methods is used for this in the literature, including ageing at elevated temperatures and cycling of the materials. In addition, the sample sizes, geometries and parameters selected for the experiments differ, which makes it almost impossible to compare different studies. However, the ageing tests often lack a comparison with real aged samples in order to use the laboratory tests to extrapolate the service life. (Bayón and Rojas 2019)

In this study, the PCM Erythritol is aged under real application conditions. The results are compared with laboratory experiments at elevated temperatures.

Erythritol is a sugar alcohol in which two polymorphic phases can occur. According to Lopes et al. (Lopes Jesus et al. 2010) the occurrence of polymorphic phase depends on the cooling rate. When the stable crystal structure is formed, Erythritol melts at 117 °C whereas for the metastable crystal structure the subsequent melting takes place at 104 °C (Lopes Jesus et al. 2010). In the study of Alferez Luna et al. (Alferez Luna et al. 2021), the material was examined in small samples with and without antioxidants and in different atmospheres. For this purpose, the respective samples were aged at different constant temperatures above the melting temperature. The subsequent results show that ageing is influenced both purely by temperature and by

the atmosphere. (Alferez Luna et al. 2021) This is also known from an aging hypothesis of Kakiuchi et al. (Kakiuchi et al. 1998), which declares that Erythritane is formed by the influence of temperature and that this Erythritane reacts in combination with oxygen to form an acid, which in turn catalyzes the further formation of Erythritane. (Kakiuchi et al. 1998) Other sugar alcohols, such as D-Mannitol, have also been investigated by means of aging at elevated temperatures. (Neumann et al. 2019; Bayón and Rojas 2017; Taftanazi et al. 2017) Here too, the atmosphere has a significant influence on the deterioration. What has not been done in these experiments is a comparison of the level of degradation with samples that were aged under real application conditions. This study is intended to close the gap.

Materials and methods

The experiments were carried out with Erythritol from Cargill® as PCM. DSC measurements with a heating/cooling rate of 0.5 K/min in a temperature range from 0 °C to 130 °C shows the occurrence of different polymorphic phases. For the stable phase an onset melting temperature of 119.3 °C and a melting enthalpy of 343.8 kJ/kg is determined. The metastable phase shows a melting onset temperature of 107.3 °C and a melting enthalpy of 312.1 kJ/kg. (Gamisch et al. 2023)

Ageing experiments at elevated temperature were performed in closed 100 ml laboratory bottles. Erythritol was filled in solid with an approx. mass of 91.79 g ± 0.93 g and afterwards closed with a lid. No

inert gas was used in the bottles, so the remaining volume in the bottles contains air. The laboratory bottles were exposed to a constant temperature environment. Three different sets of experiments were performed, the first 10 K above the melting temperature at 130 °C, the second at 140 °C and the third at 150 °C. After a defined time of 5, 25, 50, 250, 500 and 1000 h, samples were taken out of the experiments. For each time and temperature, five samples were prepared.

Aging at real application conditions was performed in a fin/tube heat exchanger (Figure 1) with a PCM mass of 34.2 kg. The aluminium fins have a 4 mm distance. Three tubes (stainless steel) meander through the heat exchanger shell (stainless steel) at different levels. After filling the material into the heat exchanger, a stainless-steel lid was used to close the shell. The atmosphere in the heat exchanger is air. The temperature profile was adapted from a storage for a geothermal power plant from (Alp Sahiller and Rougé, 2021). The temperature was cycled between 90 °C and 150 °C. Each cycle took 24 h, 12 h for heating and cooling each. After defined cycles, samples were taken out of the heat exchanger at different locations (next to T1, T2 and T7 in Figure 1). A glass tube is inserted between the fins up to the bottom of the heat exchanger to take the samples.

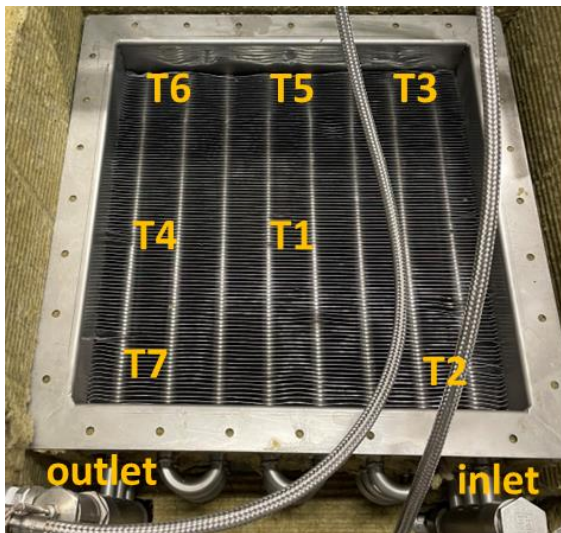


Figure 1: Heat exchanger (fin/tube) for measurements at real application conditions with the position of the temperature sensors. DSC measurements were performed using the Q200 from TA Instruments. Three cycles were carried out with a heating/cooling rate of 0.5 K/min. Only the third cycle is used for the evaluation in this study. The temperature limits were set at 0 °C and 130 °C. Isothermal phases of 5 min were set for the upper and lower temperature limits.

A Spectrum Two™ spectrometer from PerkinElmer was used for ATR measurements. For the analysis the samples were grinded. A resolution of 16 and four scans were used.

Results and Discussion

Aging at elevated temperature

Aging at elevated temperature showed the following degradation phenomena: Color change, increased polymorphism, enthalpy change and new bands in the ATR spectrum.

The first thing to notice about the samples is the change in color from white to brown (Figure 2). Higher temperatures and longer aging time lead to darker samples.

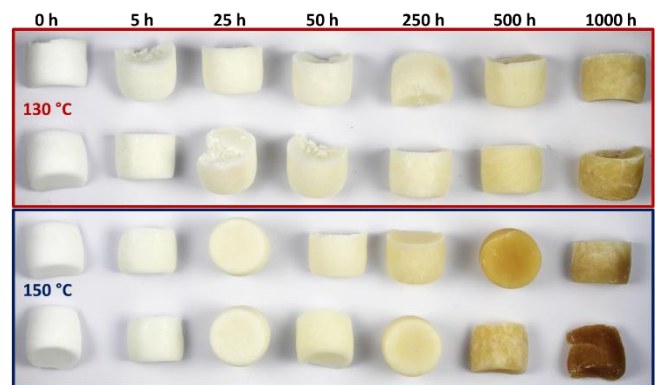


Figure 2: Optical changes of Erythritol after aging at elevated temperature at 130 °C (upper half) and 150 °C (lower half)

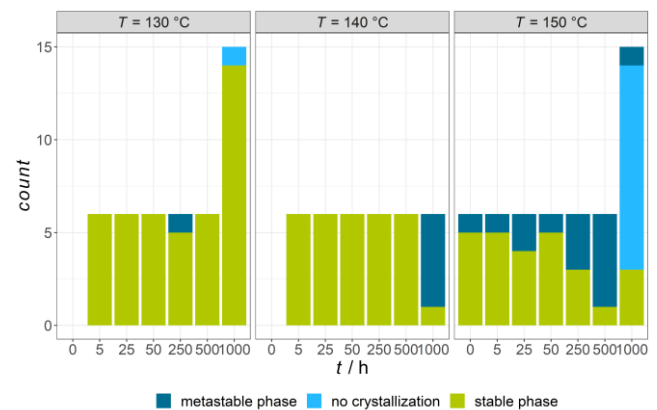


Figure 3: Phases of Erythritol after treatment at elevated temperature in the last DSC cycle (Gamisch et al. 2023)

Figure 3 gives an overview of the frequency of occurrence of stable and metastable phases during the third melting of the samples in the DSC. At each time step (5 h to 500 h), two laboratory bottles were examined (the lightest and the darkest). Three samples were taken from each bottle, making a total of six measurements. At 130 °C and 150 °C after 1000, all five bottles were analyzed with three samples each (15 measurements). The samples after 1000 h and 150 °C

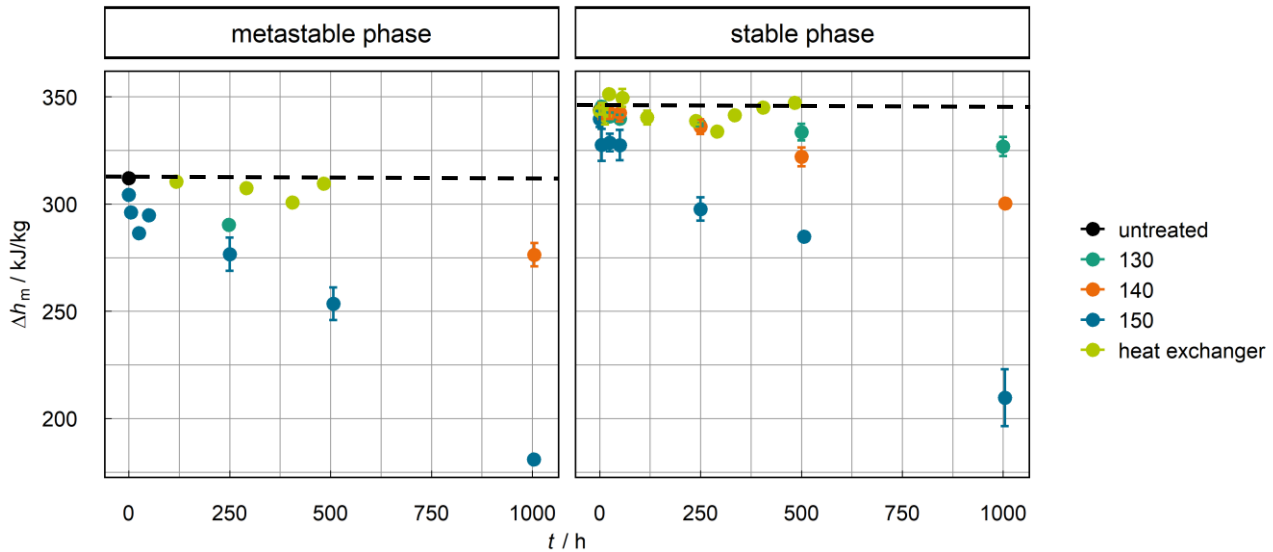


Figure 4: Melting enthalpy of Erythritol before and after experiments at elevated temperature

showed that most of the samples (11 in total) no longer crystallized in the DSC. In addition, Figure 3 shows that the occurrence of the metastable phase increases with increasing aging temperature and time. (Gamisch et al. 2023)

The change in the enthalpy of fusion as a function of temperature and time is shown in Figure 4, where the dashed line raises the enthalpy of the untreated sample. The measurements of the metastable phase are shown on the left-hand side and the stable phase on the right-hand side. If more than one value was measured for one of the respective times, the mean value was calculated and the error bars represent the standard deviation of the values. The enthalpy of fusion of the samples decreases with increasing temperature and time. Erythritol shows a decrease in melting enthalpy of $39.02\% \pm 3.87\%$ after 1000 h at 150 °C for the stable phase and 42.03 % for the metastable phase. In relative terms, the decreases in enthalpy also barely differ at all times.

Figure 5 shows the ATR spectra of untreated Erythritol, Erythritane and the aged samples of all temperature levels after 1000 h. For all aged samples, an overlapped peak at 3363 cm^{-1} is detected (purple line), which fits to the spectrum of Erythritane. Another indication for the presence of Erythritane in the aged samples are the newly formed peaks at 1124 cm^{-1} (orange line). This fits to the aging theory of Kakiuchi (Kakiuchi et al. 1998).

Aging in heat exchanger under real application conditions

The experiments in the heat exchanger are still ongoing. So far, 65 cycles have been examined and there has been no change in the enthalpy of fusion

higher than the error of the DSC. An additional sample was also taken from the top of the heat exchanger to examine whether the sample has a higher degradation on the surface only. There is no difference between the surface sample and the sample representing the whole height of the heat exchanger. The results of the DSC measurements of the heat exchanger are also displayed in Figure 4 (light green dots). The time refers to temperatures of the PCM above 148 °C. Figure 6 shows the change in color of the Erythritol during the experiment.

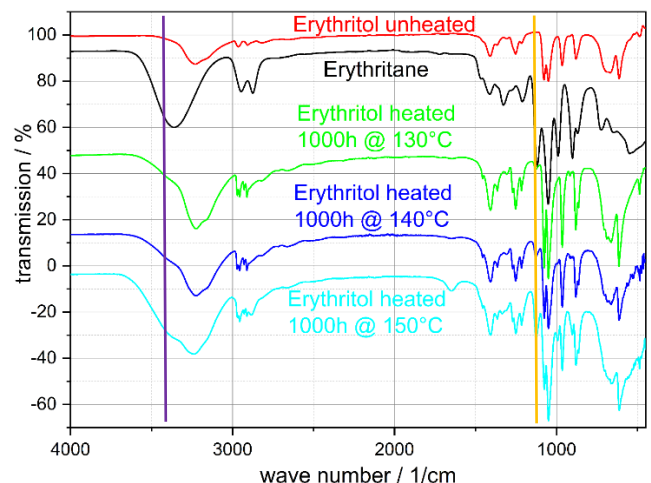
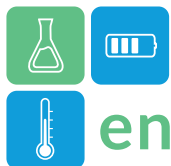


Figure 5: ATR results of untreated Erythritol, Erythritane and the samples which were aged 1000 h at elevated temperature

In Figure 7 an example of one complete cycle is shown. During the heating cycle, the temperature sensor (T2), which is positioned near the inlet, shows the fastest heating of the PCM. As expected, however, sensor T4 (center right Figure 1) shows the most constant PCM temperature during the phase transition. During cooling, the temperature sensors in the PCM exhibit a



similar behavior. However, the PCM shows supercooling before crystallization starts and nucleation is triggered between 100 °C and 105 °C.



Figure 6: Change of color of Erythritol before cycling and after 65 cycles

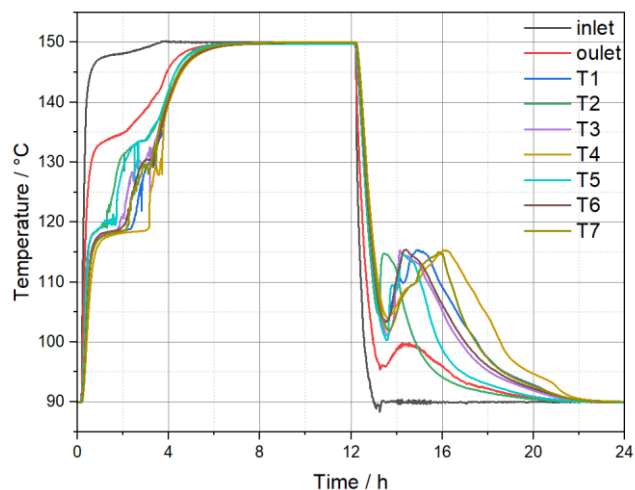


Figure 7: Example of one cycle performed with the heat exchanger

Conclusion

The samples, which were treated at elevated temperature, show an increasing coloration with increasing temperature and duration of the experiment, while the samples from the heat exchanger already had a slight coloration at the beginning of the experiment, which did not increase further during the experiment.

As expected, the DSC results of the samples aged at elevated temperature show a higher decrease in enthalpy over time at higher temperatures. However, only the samples after 1000 h at 140 °C and the samples after 250 h at 150 °C show a decrease in enthalpy of more than 10 %. Erythritol in the heat exchanger shows no change (beyond the uncertainty of the DSC) after the first 65 cycles.

In the ATR measurements of the samples aged at elevated temperature, the occurrence of Erythritane could be detected, which is more clearly visible with increasing degree of aging.

Acknowledgment

The authors acknowledge financial support from the German Federal Ministry for Economic Affairs and Climate Action (BMWK) for the project PCM Metro II (FKZ 03ET1584B).

References

- Alferez Luna, M.P.; Neumann, H.; Gschwander, S. (2021). Stability Study of Erythritol as Phase Change Material for Medium Temperature Thermal Applications. *Applied Sciences*. DOI: 10.3390/app11125448.
- Alp Sahiller, H.; Rougé, S. Enhancing the flexibility of electricity generation and heating for Kızıldere II geothermal power plant by demonstrating heat storage systems. In: *9th Eur. Conf. Ren. Energy Sys. 21-23 April 2021, Istanbul, Turkey*.
- Bayón, R.; Rojas, E. (2017). Feasibility study of D-mannitol as phase change material for thermal storage. *AIMS Energy*. DOI: 10.3934/energy.2017.3.404.
- Bayón, R.; Rojas, E. (2019). Development of a new methodology for validating thermal storage media: Application to phase change materials. *Int J Energy Res*. DOI: 10.1002/er.4589.
- Gamisch, S.; Kick, M.; Klünder, F.; Weiss, J.; Laurenz, E.; Haussmann, T. (2023). Thermal Storage: From Low-to-High-Temperature Systems. *Energy Tech*. DOI: 10.1002/ente.202300544.
- Kakiuchi, H.; Yamazaki, M.; Yabe, M.; Chihara, S.; Terunuma, Y.; Sakata, Y.; Usami, T. (1998). A Study of Erythritol as Phase Change Material. 2nd Workshop. Sofia, Bulgaria, 11.11.1998.
- Lopes Jesus, A.J.; Nunes, S.C.C.; Ramos Silva, M.; Matos Beja, A.; Redinha, J.S. (2010). Erythritol: crystal growth from the melt. *International journal of pharmaceutics*. DOI: 10.1016/j.ijpharm.2009.12.043.
- Neumann, H.; Burger, D.; Taftanazi, Y.; Alferez Luna, M.P.; Haussmann, T.; Hagelstein, G.; Gschwander, S. (2019). Thermal stability enhancement of d-mannitol for latent heat storage applications. *Solar Energy Materials and Solar Cells*. DOI: 10.1016/j.solmat.2019.109913.
- Taftanazi, Y.; Neumann, H.; Burger, D.; Hagelstein, G.; Abu El-Rub, Z.; Gschwander, S. (2017). Stability study of Phase change Material between 100°C and 200°C. *The Eighth Jordan International Chemical Engineering Conference (JICChEC 2017)*.

Demonstration of cold thermal energy storage for air conditioning in a CO₂ supermarket refrigeration system

Håkon Selvnes^{1,*}, Alexis Sevault¹, Hagar Elarga², Armin Hafner³

¹ Cartesian AS, Tempevegen 22, Trondheim, Norway

² SINTEF Energy Research, Sem Sælands vei 11, Trondheim, Norway

³ Norwegian University of Science and Technology, Department of Energy and Process Engineering, Kolbjørn Hejes veg 1B, Trondheim, Norway

*Corresponding author e-mail: hakon.selvnes@cartesian.no

Abstract

The refrigeration systems are among the major contributors of electrical energy use in modern supermarkets. Due to the high efficiency of CO₂ (R744) refrigeration systems and the simultaneous concern of using high global warming potential (GWP) refrigerants and refrigerants forming TFA as breakdown products, supermarkets worldwide are transitioning to CO₂ systems. These integrated systems maintain the temperature of chilled and frozen goods in the supermarket, in addition to heating and air conditioning (AC) of the ventilation air in the air handling unit (AHU) for the shop. The design capacity of the refrigeration system must handle the peak refrigeration load and AC demand occurring typically on the warmest summer day. This results in a large overcapacity and operation of the refrigeration unit on inefficient part load for most of the year. This paper describes the approach taken in an ongoing demonstration project proposing to integrate a cold thermal energy storage (CTES) using the innovative pillow-plate technology from Cartesian AS, into the CO₂ refrigeration system to supply the AC load during high-demand hours. The standard glycol circuit to the AHU is replaced with a CO₂ circuit from the refrigeration system and connected to the CTES unit, which uses water/ice as the storage medium. The indicated impact on equipment sizing, peak power use and energy savings is presented.

Keywords: Cold thermal energy storage, Refrigeration, Energy efficiency

Introduction

The refrigeration and heat pump sector has started a transition away from the high global warming potential (GWP) HFC refrigerants following the F-gas regulation imposed by the European Union. Carbon dioxide (CO₂, R744) refrigeration systems are the preferred selection for commercial refrigeration and supermarket applications in many countries in Europe, including Norway. The market penetration reached close to 23% in Europe by the end of 2023, according to Atmosphere¹. CO₂ is regarded as a safe, environmentally friendly and future-proof choice for refrigeration and heat pumps systems. Cold thermal energy storage (CTES) with phase change materials (PCMs) utilising the latent storage principle has attracted a lot of attention in the research community the latest years, with high interest in the refrigeration field (Selvnes et al., 2021). The match between the near isothermal phase transition of PCMs and evaporation/condensation of refrigerants is particularly attractive from an efficiency perspective. This paper

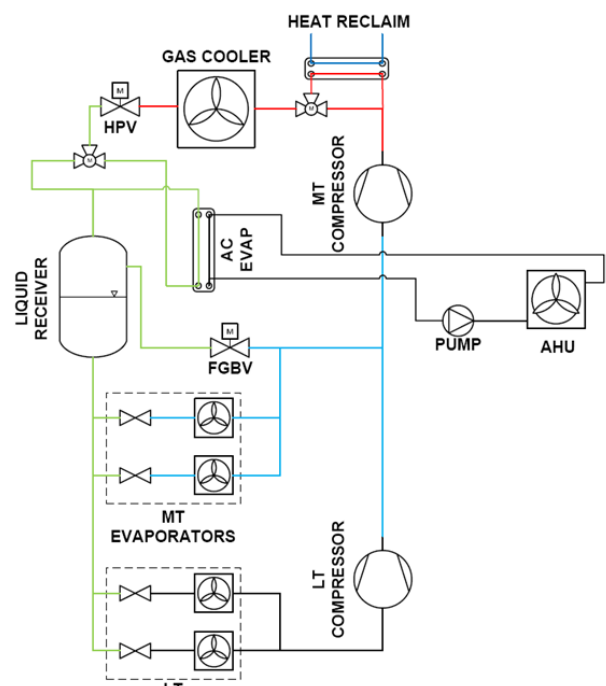


Figure 1: Reference CO₂ system for the demonstration project

¹ <https://atmosphere.cool/product/natural-refrigerants-state-of-the-industry-2023-edition-free/>

presents the ongoing demonstration project aiming to deliver proof-of-concept of integrating a CTES system in a commercial refrigeration unit using CO₂ as the refrigerant.

Methodology

This section describes the concept of integrating the CTES system into the standard CO₂ refrigeration system considered in the demonstration project. The most common refrigeration system installed in Northern Europe today is a transcritical CO₂ booster system. The reference installation of this study is one of these systems installed by a leading supermarket chain in Northern Europe. The shop where the demonstration CTES system will be placed is in the southern part of Norway to ensure utilisation of the proposed CTES system. A schematic diagram of the system architecture is presented in Figure 1. The colours refer to the pressure level of the respective parts of the system: High pressure (red), intermediate pressure (green), MT evaporator pressure (blue) and LT evaporator pressure (black). In addition, the glycol system from the AC evaporator to the AHU is shown in black. The reference system is a standard transcritical booster system, including integration of AC and heat reclaim for heating of shop. The schematic represents the low temperature (LT) and medium temperature (MT) evaporators providing the cooling of the frozen and chilled goods, respectively. The corresponding MT and LT compressors are arranged in a booster configuration, referring to the LT compressor

discharge line being connected directly to the MT compressor suction line. Furthermore, the heat reclaim heat exchanger downstream of the MT compressor discharge can deliver heating of the shop during cold periods. If no heating is required, the heat is rejected to the ambient air in the gas cooler. The optimal high pressure according to ambient conditions is managed by the high-pressure valve (HPV), located downstream of the gas cooler. The AC system of the reference system includes a heat exchanger with a 3-way valve downstream of the HPV on the CO₂ side, and a pumped loop of glycol delivering cooling to the heat exchanger in the AHU. The cooling of the glycol circuit is carried out by evaporating the two-phase mixture of refrigerant downstream of the HPV the receiver (intermediate pressure). The heat absorbed by the refrigerant from cooling the glycol circuit results in an increased amount of refrigerant vapour sent to the receiver, which is further throttled by the flash gas bypass valve (FGBV) to the MT compressor suction level.

These units may not be the most efficient under those very specific warm conditions and for large share of AC demand but are simple and robust. For shops with significant AC demand for longer periods, a parallel compression or ejector system will be significantly more effective (Gullo et al., 2018; Sarkar & Agrawal, 2010). This system is delivered to all the new grocery stores in this food retail company, although the ambient conditions vary greatly across the country. The design capacity for the LT compressors, MT compressors and

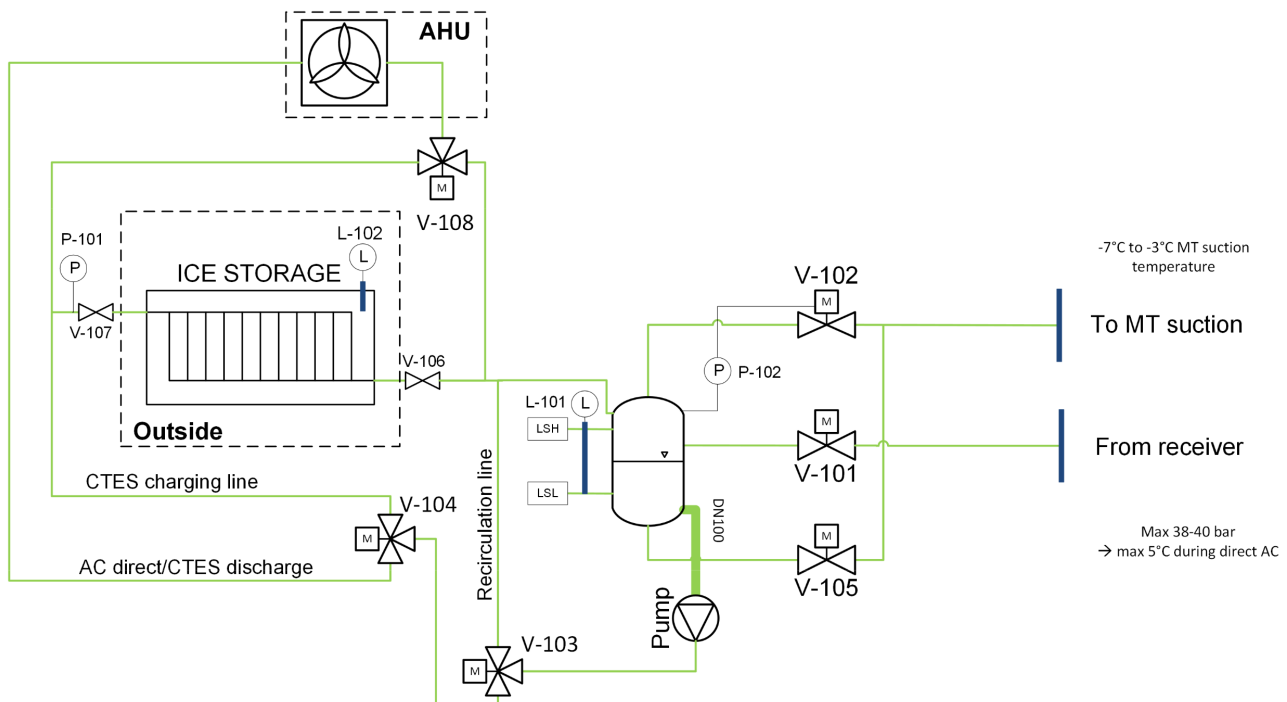


Figure 2: Simplified piping and instrumentation diagram of the CTES system installed in the demonstration unit



the AC load are 10 kW, 80 kW and 25 kW, respectively. Since this refrigeration system is in a booster configuration, the MT compressor capacity must be sufficient to handle the combined refrigeration load from the LT, MT and AC level and compress it to the gas cooler pressure for heat rejection. The cooling of the glycol circuit is handled at the intermediate pressure level (receiver pressure) but is throttled to the MT suction pressure from the receiver. From the MT compressor perspective, the load from AC therefore occurs at the same temperature as the MT evaporator load.

The AC load is mostly dependent on the ambient temperature and have a distinct peak during the warm days and is normally low during the night. For the demonstration project the glycol circuit for the AC, including the glycol/CO₂ plate heat exchanger (denoted “AC EVAP” in Figure 1), is replaced by a CO₂ circuit connected to the main system. A simplified piping and instrumentation diagram of the CTES system and its connection points to the main CO₂ system is shown in Figure 2. The CTES unit is Cartesian’s Thermal Box unit (www.cartesian.no), utilizing pillow plates as method of heat transfer between the PCM and the CO₂ (see Figure 3). Due to suitable temperature of phase transition, low cost and excellent thermal properties, water/ice is chosen as the PCM.

The major difference to the reference system is that the cooling of ventilation air in the AHU now is carried out by circulating CO₂ directly in the ventilation heat exchanger. A separate liquid receiver and a refrigerant pump ensures the delivery of refrigerant to the AHU and CTES unit in the various modes of operation. The CTES system can be operated in four different modes:

1. **Standby mode.** When no need for AC and the storage is fully charged.
2. **Charging mode.** The main CO₂ refrigeration system is used to freeze the ice in the storage. Typically operated during the night when there is no need for AC and excess refrigeration capacity.
3. **Discharging mode.** There is AC demand in the shop, typically during mid-day to evening. CO₂ is circulated between the CTES unit and the AHU to cool the air to the shop.
4. **Direct AC mode.** CO₂ is pumped directly to the AHU to cool the air. The resulting refrigeration load is taken directly by the main CO₂ refrigeration system (bypassing storage).

The pressure is regulated by valve V-102 on the CTES liquid receiver, functioning as a flash gas by-pass valve

during standby and discharging mode. The valve is fully open during the charging mode, equalizing the pressure in the CTES system to the MT suction pressure of the main CO₂ system.

Expected results

The motivation of installing a CTES system into an integrated CO₂ refrigeration system for a supermarket are summarized in the following four points:

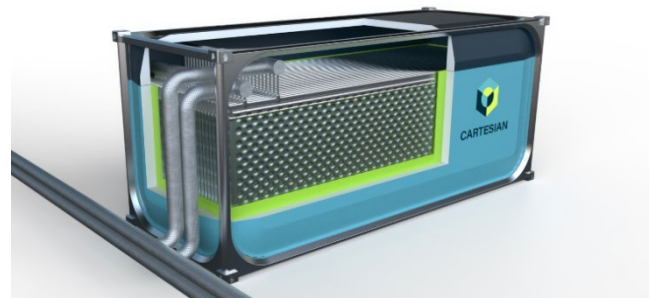


Figure 3: Illustration of Cartesian’s Thermal Box with pillow plates

1. **Reduced need for refrigeration capacity.** The dimensioning refrigeration load for an integrated supermarket refrigeration system occurs during the warmest day of the year. The AC load can contribute to a significant share of the total refrigeration load, hence increasing the required capacity of the refrigeration system. Installing a CTES system that can accumulate in advance the cold capacity needed to cover the AC load of the following day will therefore significantly reduce the load on the main refrigeration system. Hence the refrigeration system can be designed with a much lower capacity, saving on the capital costs of the refrigeration plant.
2. **Improvement in Coefficient of Performance (COP).** Since the cold capacity for AC is accumulated by running the refrigeration system during the night, the ambient temperature is normally lower than during the peak hours of the day when the AC load is high. The accumulation of the cold capacity is then carried out with a lower temperature difference to overcome for the refrigeration plant, increasing the COP of the unit. This results in energy savings since the accumulation is accomplished using the MT pressure level, which is identical to the reference installation. Furthermore, adding refrigeration load during the night due to accumulation will help reduce the number of start-stop cycles of the



compressors. This is a common issue when the AHU air rates are reduced to a minimum and the shop is closed. Reducing the stop-start cycles can contribute to prolong the lifetime of the compressors.

3. **Load shifting.** By running the refrigeration system to accumulate cold capacity for AC during the night, a share of the electricity consumption of the refrigeration plant is shifted to low-cost hours. This will contribute to reducing the energy cost of the supermarket. The impact of load shifting can be further exploited by integrating predictive control algorithms to optimize the accumulation of cold in the CTES unit according to weather prediction and electricity prices.
4. **Peak shaving.** By shifting the AC load to low-demand hours, the maximum power requirement of the refrigeration system is reduced, referred to as peak shaving. In many locations, grid companies impose peak power fees based on the maximum power draw for the previous period (month, quarter, or year). Reducing the maximum power draw by utilizing CTES technology can reduce the grid fees significantly. A previous simulation study has shown up to 13-19% peak power reduction during a summer week in various Norwegian cities (Selvnes et al., 2023).

The data on energy use and operation of the CTES system from the demonstration will be analyzed and compared with an identical reference shop nearby. The two shops are equal in shop area, refrigeration plant and air handling unit.

Conclusions

This paper has presented the ongoing demonstration project TES-AC: Monitoring and analysis of a pilot thermal energy storage (TES) unit to supply Air Conditioning (AC) in commercial refrigeration systems. The project aims to deliver proof-of-concept of using cold thermal energy storage (CTES) technology to achieve load shifting, peak shaving and

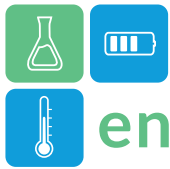
improved energy efficiency in a Norwegian supermarket. The project will pave the way for market penetration of CTES technology in the refrigeration sector and showcase the benefits of the technology.

Acknowledgment

The work is part of HighEFF - Centre for an Energy Efficient and Competitive Industry for the Future, an 8-year Research Centre under the FME-scheme (Centre for Environment-friendly Energy Research, 257632). The authors gratefully acknowledge the financial support from the Research Council of Norway and user partners of HighEFF. The work has been carried out within the scope of the HighEFF-supported Novel and Innovative Emerging Concept (NEIC) project TES-AC: Monitoring and analysis of a pilot thermal energy storage (TES) unit to supply Air Conditioning (AC) in commercial refrigeration systems.

References

- Gullo, P., Hafner, A., & Banasiak, K. (2018). Transcritical R744 refrigeration systems for supermarket applications: Current status and future perspectives. *International Journal of Refrigeration*, 93, 269–310. <https://doi.org/10.1016/j.ijrefrig.2018.07.001>
- Sarkar, J., & Agrawal, N. (2010). Performance optimization of transcritical CO₂ cycle with parallel compression economization. *International Journal of Thermal Sciences*, 49(5), 838–843. <https://doi.org/10.1016/j.ijthermalsci.2009.12.001>
- Selvnes, H., Allouche, Y., Manescu, R. I., & Hafner, A. (2021). Review on cold thermal energy storage applied to refrigeration systems using phase change materials. *Thermal Science and Engineering Progress*, 22, 100807. <https://doi.org/10.1016/j.tsep.2020.100807>
- Selvnes, H., Pardiñas, Á. Á., & Hafner, A. (2023, April 27). *Cold thermal energy storage for air conditioning in a supermarket CO₂ booster refrigeration system*. 10th IIR Conference: Ammonia and CO₂ Refrigeration Technologies, Ohrid, North Macedonia. <https://doi.org/10.18462/IIR.NH3-CO2.2023.0021>



Design and commissioning of the worldwide first nitrate molten salt test rig for component testing at 620°C

Freerk Klasing^{1,*}, Thomas Bauer¹

1 German Aerospace Center, Institute of Engineering Thermodynamics, Linder Hoehe, Cologne, Germany

*Corresponding author e-mail: freerk.klasing@dlr.de

Abstract

Energy storage is crucial for the on-demand generation of electricity from renewable sources like wind and photovoltaics. Thermal energy storage can be particularly useful, especially when repurposing existing fossil-fired power plants, as it provides a cost-effective solution for implementing large-scale grid energy storage (Trieb et al., 2022). State-of-the-art molten salt storage systems operate at a maximum temperature of 565°C (Mehos et al., 2020). However, utilities aim for a higher temperature of at least 620°C to accommodate supercritical steam cycles. These higher temperatures are crucial to obtain maximum efficiencies. Research has shown that this temperature increase is generally feasible from a material compatibility perspective (Bonk et al., 2020). So far, there are no commercial components, such as pumps, valves, and instrumentation, available on the market for 620°C nitrate salt. For this purpose, a test rig for up to 400 kg nitrate molten salt was developed and built at DLR. The aim of the experiments is to demonstrate the functionality of pump and valve prototypes as well as measurement equipment at a temperature of 620°C. First hydraulic pre-tests demonstrated the general operability of all components with water before hot commissioning with molten salt at 620°C.

Keywords: Thermal energy storage, Molten salt, Pump, Valve

Introduction

The transition to renewable energy sources, such as wind and photovoltaics, presents challenges to grid stability. To ensure on-demand electricity generation, energy storage is crucial. Thermal storage is a promising solution, particularly in the repurposing of fossil-fired plants. Molten salt systems are an efficient means of storing and releasing thermal energy, with current systems operating at 565°C. However, there is a growing demand for temperatures exceeding 620°C to maximize efficiencies. The research indicates that 620°C systems lack commercial components. However, efforts are underway to develop and validate high-temperature components for molten salt storage systems. Testing is currently being conducted at the German Aerospace Center.

The purpose of the component test rig established at DLR (see figure 1) is to conduct a series of experiments to test and certify a recently developed submersible pump and two on-off valves, as well as flow and pressure measurement technology for molten salt at elevated operating temperatures of 620°C.

In addition to measuring the pump characteristic curve for the pump discharge head, an NPSH (net positive

suction head) measurement must also be carried out before subjecting all components to an endurance test lasting several months. A new approach for pressure and flow measurement is introduced and will be evaluated for its reliability and accuracy. The On-Off-Valve will be repeatedly opened and closed.

Methodology

The test rig consists of a 700mm diameter vessel that can be heated up to 700°C. It is filled with nitrate molten salt (60% NaNO₃ and 40% KNO₃) and purged with reactive gases to suppress salt decomposition. A pump with an 18kW motor and level and temperature instrumentation are submerged from the top. Trace heated pipes route the salt flow from the pump through two On-Off-Valves in parallel back to the oven (figure 2).



Figure 1: 400kg nitrate molten salt test rig for component testing at DLR

For pressure measurement a newly developed approach is introduced: the piezoresistive strain gauge pressure transducers are shielded from the high temperatures either by a gas cushion or sodium-potassium filled capillary tubes with diaphragm seals.

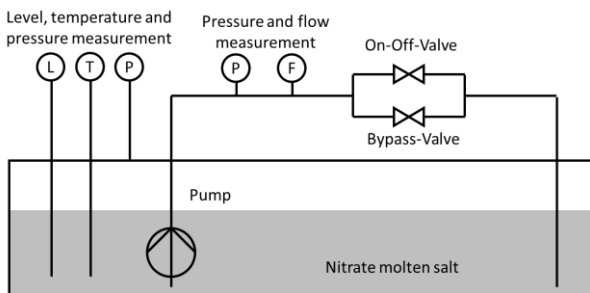


Figure 2: Simplified piping and instrumentation diagram

For the flow measurement an orifice plate with a differential pressure measurement with gas cushion is used.

For the pump characteristic curve measurement, the following methodology was used:

- Adjust the flow by opening or closing one of the two valves
- Measurement of pressure, liquid level and flow to calculate pump discharge head

The valves and all other components are equipped with thermocouples to monitor the temperature distribution during the 5-minute open-close cycle of the valves.

During hot commissioning, the nitrous gases and oxygen content of the gas atmosphere above the molten salt are monitored and assessed. Salt samples are taken to measure its stability.

Results and Discussion

First hydraulic pre-tests with water were carried out to measure the pump characteristic curve and compare it with the pump curve according to the manufacturers prototype. Figure 3 shows the pump discharge head over the volume flow rate.

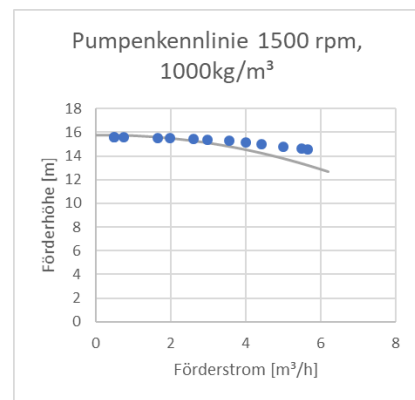


Figure 3: Measured pump head over volume flow (blue dots) compared to pump curve according to manufacturers prototype (grey line) at 1500 rpm with water

The measured data from the pump test indicates that all instrumentation is functioning properly and is in good agreement with the manufacturer's data.

Further results on the hot commissioning with molten salt, NPSH-measurements and experimental data from the gas atmosphere and salt sampling monitoring and valve and instrumentation testing will be presented.

Conclusions

At DLR, a component test rig was established to conduct experiments on a newly developed submersible pump, two on-off valves, and advanced flow and pressure measurement technology for molten salt at elevated operating temperatures of 620°C. The first hydraulic pre-tests confirmed the general operability of all components with water before hot commissioning with molten salt at 620°C.

Qualifying components such as pumps, valves, and instrumentation for higher operating temperatures is crucial for the further implementation of advanced thermal energy storage systems in real applications, such as supercritical steam cycles in power plants.



Acknowledgment

This research was funded by the German Federal Ministry for Economic Affairs and Climate Action (BMWK) in the LIMELISA project (Contract No. 03EE5050).

References

- Bonk, A., Braun, M., Sötz, V. A., & Bauer, T. (2020). Solar Salt – Pushing an old material for energy storage to a new limit. *Applied Energy*, 262, 114535.
<https://doi.org/https://doi.org/10.1016/j.apenergy.2020.114535>
- Mehos, M., Price, H., Cable, R., Kearney, D., Kelly, B., Kolb, G., & Morse, F. (2020). *Concentrating Solar Power Best Practices Study*.
- Trieb, F., Liu, P., & Koll, G. (2022). Thermal Storage Power Plants (TSPP) - Operation modes for flexible renewable power supply. *Journal of Energy Storage*, 50, 104282.
<https://doi.org/https://doi.org/10.1016/j.est.2022.104282>



Design of borehole heat exchangers combined with a permanent dewatering system in series

Seung-Hoon, Park¹, Eui-Jong Kim^{2,*}

¹ Korea Conformity Laboratories, 7, Nambusunhwan-ro 319-gil, Seocho-Gu, Seoul, Republic of Korea

² Inha University, Department of Architectural Engineering, 100 Inha-ro, Michuhol-Gu, Incheon, Republic of Korea

*Corresponding author e-mail: ejkim@inha.ac.kr

Abstract

The ground source heat pump (GSHP) system can stably supply heating and cooling energy to buildings with high efficiency. Most buildings exhibit a thermal load imbalance between cooling and heating. The ground thermal imbalance results in long-term ground heat accumulation and causes long-term variations in the ground temperature. In this study, a novel hybrid GSHP (HyGSHP) system was proposed using an hourly simulation-based analysis method. In this study, a small-scale unused groundwater resource corresponding to 10% of the building peak load and capable of supplying both cooling and heating as a supplemental hybrid heat source was installed in series. Based on the hourly simulation and optimization technique, the proposed system is effective in reducing the required length of borehole heat exchangers (BHE) by half compared with the common GSHP.

Keywords: hybrid ground source heat pump, borehole, permanent dewatering system

Introduction

GSHP systems comprise BHE loops on the source side of the heat pumps and load-side building loops. In principle, GSHP systems supply heat by extracting heat energy from the ground through BHEs and injecting it into the building zone through load-side loops. Conversely, during the cooling operation, heat energy is extracted from the building zone through the load-side loop and injected into the ground via the BHEs. In the case of a dominant heating or cooling load of the building, the ground temperature continuously decreases or increases owing to the thermal imbalance between the ground heat injection and extraction, and the large thermal capacity of the ground. This may cause long-term degradation of the coefficient of performance (COP) of the heat pump, and the required length of the BHEs must be larger than that of the balanced ground load cases.

In recent years, a hybrid heat source coupled with GSHP (HyGSHP) system is gathering considerable attention as a promising solution to the conventional GSHP problems (Bayer et al., 2012). Relevant studies have employed various strategies on HyGSHP systems to restrain the long-term ground temperature variations and discussed their potential economic benefits from multiple aspects. In practice, HyGSHP systems can be configured with various sources, connection and operating strategies. Particular sizing and analysis methods have been proposed for such HyGSHP (Park et al., 2017).

In this study, an extremely small amount of unused groundwater, corresponding to 10% of the peak building load, was used to suppress the long-term ground temperature variations and demonstrate the benefits of the proposed HyGSHP system.

Methodology

The permanent dewatering (PD) system is a construction method for draining groundwater that responds to the buoyancy of the bottom of the building foundation owing to earth pressure and groundwater pressure (Cashman et al., 2020). In principle, PD is a drainage system installed at the bottom of the foundation to drain the groundwater introduced by the forcible infiltration of groundwater pressure, as depicted in Figure 1.

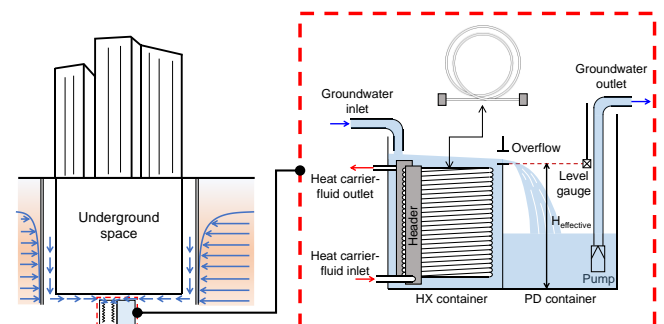


Figure 1: Permanent Dewatering system

PD systems operate throughout the life cycle of a building. Therefore, it is an unused energy source that can be used for heating and cooling facilities if the amount and temperature of the inflowing groundwater are stable. However, it is regarded as a cost expenditure for structural stability. Throughout the year, this groundwater maintains a stable temperature of around 15–20°C and can be used as a heat source for heat pumps. However, its majority forms an unused energy resource that is discharged into sewage or rivers.

Park et al. (2021) proposed a method to use the waste groundwater as a heat source for heat pumps. Accordingly, the proposed hybrid system uses a PD module to use groundwater heat as a hybrid heat source.

The PD based inflow water amount varies depending on the target sites. Although this study does not describe a method for stably securing groundwater resources, PD modules of various capacities (kW) corresponding to the level of groundwater inflow were investigated in the previous work, and a small capacity of PD is used as a hybrid source.

As the HyGSHP system derives energy using the supplemental hybrid heat source and BHEs, system engineers must determine the procedure for arranging and utilizing the hybrid heat sources and BHEs. In particular, this study used two distinct heat sources: the PD module used groundwater as its heat source and the BHE used the ground temperature. Serial configurations are investigated for installing the PD module and BHE on the heat pump source side, and serial configurations can be classified into "PD modules to BHEs (P2B)" configuration and "BHE to PD module (B2P)" configuration based on the circulation order of the heat carrier fluid as shown in Figure 2.

The sizing results of the proposed HyGSHP were evaluated using an optimization-based sizing method. These comparative simulation tests were carried out for a typical cooling-dominant building case, and the reference case was set to the common GSHP system, as shown in Figure 2.

In this research, the cooling dominant sample building load is used in BHE sizing and operation optimization. The hourly profile and the scale (kW) of the sample building load is presented in Figure 3, where the time of the year in hours is plotted in the x-axis, and the cooling and heating loads are present in the (+) and (-) y-axis, respectively. As observed, the annual peak load of 500 kW occurred in Jun, and the maximum heating load of 259 kW occurred in December. The total annual

cooling and heating loads were 323 and 43 MWh, respectively.

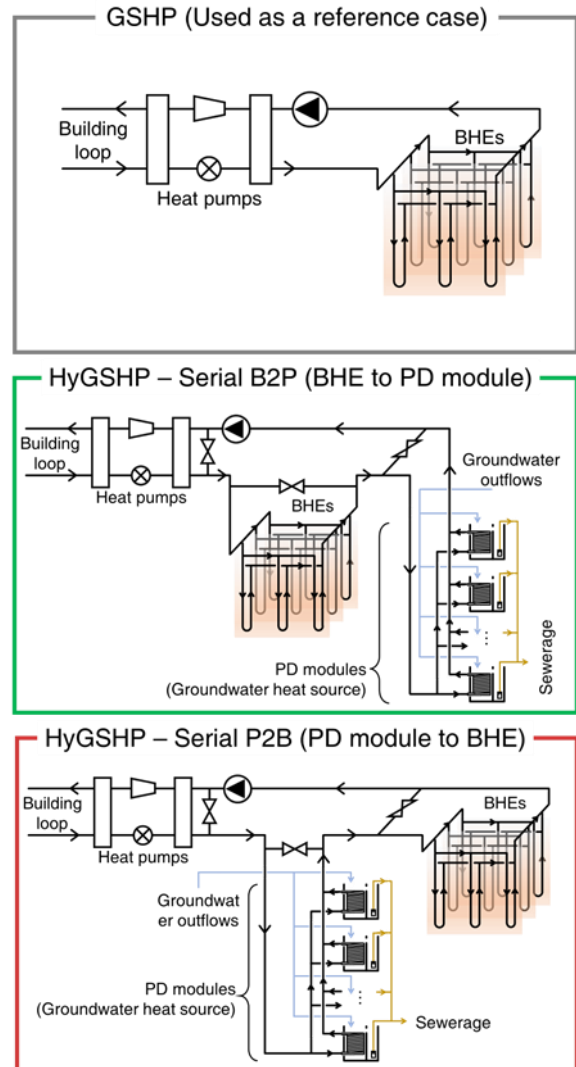


Figure 2: Proposed HyGSHP and piping configuration

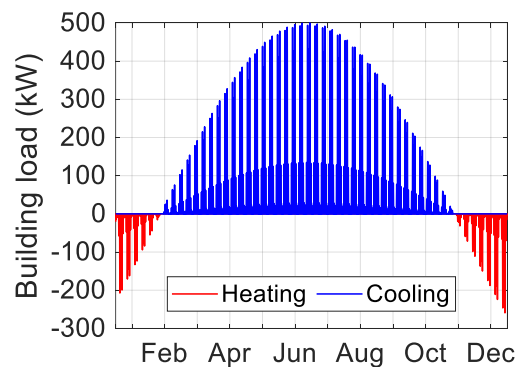
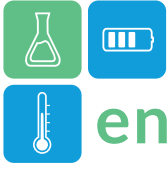


Figure 0. Annual building load



For sizing, an optimization must be run where the control variable is the number of BHEs and the desired EWT was set at 30°C, and the temperature gradient ($\Delta T = |LWT - EWT|$) on the heat pump source side was set at a maximum of 5°C. Thereafter, the total length of the BHE that can be reduced to the greatest possible extent under the same conditions was derived through Coordinate search algorithm. The optimization problem for BHE sizing is defined in Equation 1. Table 1 presents other parameters used for this optimization simulation.

$$\min F_{\text{obj}}(\mathbf{X}) = \text{abs}(EWT_{\text{set}} - EWT^t) + \mu, \quad \forall t = \{1, 2, \dots, 262800\}$$

$$\mu = \begin{cases} 10^9 & (EWT^t \geq 30^\circ\text{C}) \text{ or } \text{abs}(LWT - EWT)^t \geq 5^\circ\text{C} \\ 0 & (EWT^t < 30^\circ\text{C}) \text{ or } \text{abs}(LWT - EWT)^t < 5^\circ\text{C} \end{cases} \quad (1)$$

Table 1: Parameters for evaluating the long-term ground temperature variation

Parameters	Values	Units
Bore field configuration	Cylindrical	–
Number of BHEs	To be calculated	–
PD module entire capacity	50	kW
Initial ground temperature	15	°C

Results and Discussion

Under the same conditions, the long-term ground temperature variations of the HyGSHP systems with 50-kW-capacity PD modules are displayed in Figure 4.

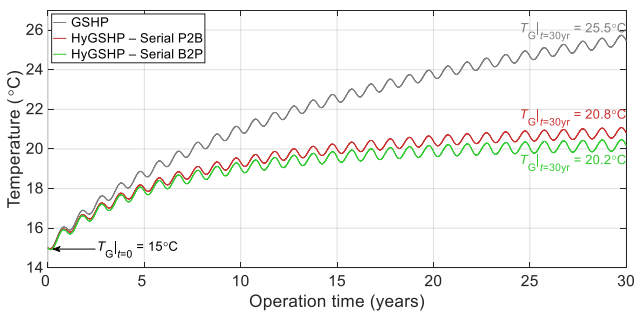


Figure 4. The long-term ground temperature (T_g) evolutions over 30 years of simulation

A conventional GSHP system requires 155 BHEs to supply the required heating and cooling energy for a given building load. After 30 years, the final T_g of an appropriately designed GSHP was 25.5°C, which increased by 10.5°C from the initial 15°C. In contrast, the final T_g of the HyGSHPs with the same BHE lengths but using a PD module of 50 kW capacity—equivalent to 10% of the building load—as a hybrid

heat source, increased to a lesser extent with a higher EWT compared to the GSHP case.

Consequently, the total length of the BHEs required for each case is depicted in Figure 5. As shown in the figure, the less increased EWT under same simulation conditions can in other words reduce the required length of BHEs. In this test case, the reduction rate is high enough to employ the proposed HyGSHP.

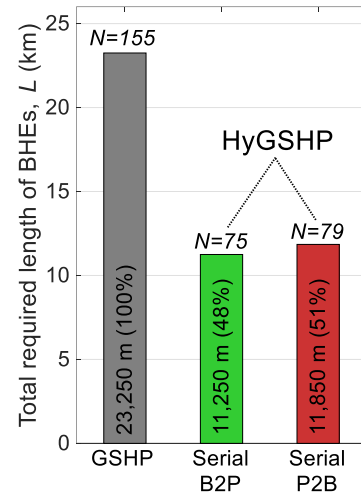


Figure 5. The total required length of BHEs and the number of BHEs for the GSHP, HyGSHP cases

These results can be explained by the energy flows of the PD and BHEs. The total thermal energy supplied by the PD modules to the buildings were 2.8 GWh in the serial B2P case and 4.2 GWh in the serial P2B case, with 1.6 and 1.5 GWh for heat carrier fluid cooling, respectively. Notably, a significant amount of cooling energy supplied by the PD modules is used for underground cooling. This is considered a unique synergistic effect if a groundwater hybrid heat source capable of both cooling and heating is connected to the serial HyGSHP system configuration.

Table 2. Total heat energy transferred through PD modules over 30 years

HyGSHP systems	Total heat transferred (GWh)	To the building (GWh)	To the ground (GWh)
Serial B2P	4.4	2.8	1.6
Serial P2B	5.7	4.2	1.5

Conclusions

The large thermal capacity of the ground can be used as an economically efficient heat-storage medium when ground heat exchangers are used. However, such



enerstock

ENERSTOCK 2024

The 16th IEA ES TCP International Conference on Energy Storage

June 5–7, 2024

Lyon, France

a large capacity causes long-term degradation of heat pumps for thermally imbalanced building loads.

In this study, the groundwater flow was exploited as a hybrid heat source that can be used for both heating and cooling. A small capacity of the PD that can feed heat within stable ranges of water temperature was effective in reducing ground heat build-up and reducing the required lengths of the BHEs.

Acknowledgment

This work was supported by a National Research Foundation of Korea (NRF) grant that was funded by the Korean government (MSIP) (No. 2021R1A2C4002936).

In addition, most of the results presented in this study were extracted from the first author's PhD dissertation.

References

- Bayer, P., Saner, D., Bolay, S., Rybach, L., and Blum, P. (2012) Greenhouse gas emission savings of ground source heat pump systems in Europe: A review, *Renewable and Sustainable Energy Reviews*, 16(2), 1256-1267.
- Park, S. H., Kim, J.Y., Jang, Y.S., Kim, E.J. (2017) Development of a Multi-Objective Sizing Method for Borehole Heat Exchangers during the Early Design Phase, *Sustainability*, 9, 1876
- Cashman, P. M., and Preene, M. (2020) *Groundwater lowering in construction: a practical guide to dewatering*, CRC Press
- Park, S. H., Jang, Y. S., and Kim, E. J. (2021). Design and Performance Evaluation of a Heat Pump System Utilizing a Permanent Dewatering System, *Energies*, 14(8), 2273.



Design, implementation, and monitoring results from the 70,000 m³ pit thermal energy storage (PTES) in Høje Taastrup, Copenhagen

Per Alex Sørensen*¹, Niels From¹, Hendrik Wetzel¹, Ioannis Sifnaios², Adam R. Jensen²

¹ PlanEnergi, Jyllandsgade 1, 9520 Skørping, Denmark

² Technical University of Denmark, Department of Civil and Mechanical Engineering, Koppels Allé 404, 2800 Kgs. Lyngby, Denmark

*pas@planenergi.dk

Abstract

In the last decade, pit thermal energy storages (PTES) have been implemented in connection with large-scale solar thermal plants in Denmark. Typically, a large-scale solar thermal plant charges the PTES in the summer, and the stored heat is then discharged to a district heating network in the fall and winter. In February 2023, a new 70,000 m³ PTES was set into operation in Høje Taastrup near Copenhagen. The storage provides increased flexibility to Copenhagen's district heating network, which is supplied by three waste incineration plants, four biomass CHP plants, and several heat pumps and backup boilers. The CHP plants are required to produce heat when needed, but plant operation can be optimized by decoupling heat supply and demand using a PTES. The PTES is expected to operate as a short-term storage with several charge/discharge cycles per year, leading to an almost constant water temperature of 90°C under the PTES lid. This has required the implementation of new materials and construction processes compared to existing PTES, especially regarding the polymer membranes used for water-tightening of the storage.

Keywords: pit thermal energy storage, sector coupling, implementation, lid construction, monitoring results

Introduction

In Heat Plan Greater Copenhagen 3 from 2014, which was prepared by the transmission companies CTR, HOFOR, and VEKS, the following is stated about heat storage:

"[There is] a large economic potential for investing in heat storage in the metropolitan area. The next step is to find suitable locations for the establishment of heat storages in relation to grid connection and space for thermal plants and to assess when the heat storage is best established over the next 20 years."

Subsequent analyses showed that a 70,000 m³ heat storage could be profitable with the existing heat production system. Subsequently, Høje Taastrup Fjernvarme (HTF) found a suitable site, and VEKS and HTF decided to begin the process before the Final Investment Decision (FID).

The preliminary budget showed a total investment of 10.0 million € and an expected annual income (operational benefit) of 0.85 million € in 2025. The economic benefit came from 1) optimisation of heat production in relation to the electricity market (higher income from electricity sales), 2) reduced production from gas boilers in demand peaks, and 3) increased production from waste incineration plants in the

summer. Out of the total budget, 6.3 million € were used for connecting the storage to the transmission and distribution systems (for pipes, heat exchangers, etc.). The PTES is charged from VEKS' transmission system and discharged to HTF's distribution system.

In addition, the project involved the development of the storage technology, as it would be the first short-term operating PTES, meaning that the stored water under the lid would be almost constantly at 90 °C. Since this had never been tested before, it required improvements of the available polymer membranes in order to withstand the higher temperatures.

The project was granted a total funding of almost 1.8 million €, with the following deliverables:

- Operational strategy for the pit heat storage
- Design and construction of the pit heat storage
- Monitoring results after 1 and 2 years of operation

Methods

This section gives information regarding the design and construction of the pit heat storage in Høje Taastrup.

Inlet and outlet

From the beginning, the size of the heat storage was set at 70,000 m³. The site where the heat storage is located is bordered by a highway on the south side and a drinking water pipeline on the north side, which led to

an unconventional design. For this reason, the final design was an elongated heat storage, where the inlet and outlet are located at the eastern end of the 170-meter-long storage.

Compared to previously established pit heat storages, the diffuser system was changed so that both the top and bottom diffusers are "half" (i.e., single-plate) diffusers, where the lid and bottom liner act as the upper and lower diffuser halves, respectively (see Figure 1).



Figure 1: Diffuser installation.

Choice of polymer membrane

The top of the storage would be almost constantly exposed to 90 °C if the storage was to operate with a two-week storage duration. This presented a challenge for the supplier of the HDPE liner, who proposed a double-liner solution with two liners on top of each other. This solution was expensive, slow to set up, and untested.



Figure 2: Liner installation.

The giga_TES research project in Austria recommended looking at a Polypropylene High Temperature Resistant (PP-HTR) liner instead. This liner was newly developed and not in production, but laboratory tests showed a long technical lifetime (i.e., 33 years at 95°C). Thereby, the project developers had a choice between two unproven solutions and ended up

choosing the PP liner for sealing the bottom and sides. A floating PP liner was also placed to separate the lid construction from the storage water. Moreover, a leakage detection system was installed under the bottom liner in the storage in order to detect possible leakages to the ground through the liner.

Lid construction

The tendered design of the lid of the pit storage was a revised version of the Dronninglund PTES lid design from 2013, but new experiences from Dronninglund showed problems with the durability of the insulation, water accumulation on the lid, and moisture and oxygen diffusion through the floating liner that separates the lid structure from the storage water. To address these issues, the tendered design was modified. At the same time, a new lid solution was developed by Aalborg CSP and implemented in the pit storage in Marstal (Figure 3). The project steering committee decided on Aalborg CSP's solution. The installed lid had different layers of insulation (with different temperature resistance) and was divided into multiple modules for more efficient rain handling. A slope was created towards the centre of each module using varying levels of pebbles, and a pump was located at the centre to remove the rainwater.

Testing at JKU Linz of the polymer mats, used as lid insulation in Dronninglund, which are also used by Aalborg CSP and in the revised lid solution, resulted in a completely new generation of insulation mats with a significantly longer technical lifetime being delivered to the project in Høje Taastrup.

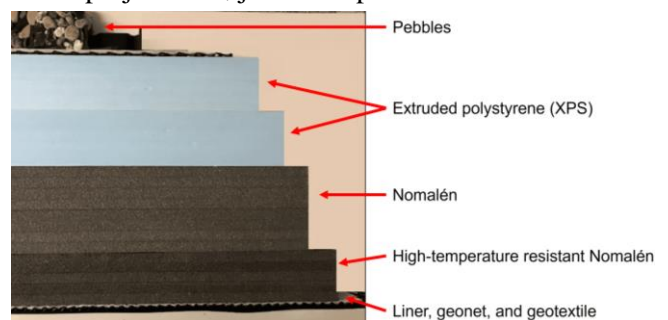
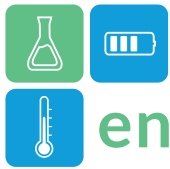


Figure 3: A crosscut of the installed lid (Sifnaios, 2023).

Implementation experiences

Construction of the pit heat storage began in the spring of 2020. Excavation, construction of the inlet and outlet arrangement, installation of the leakage detection system, PP liner, and a thin protective PE liner (to limit UV exposure and soiling of the water during filling) proceeded as planned. The water-filling stage started in November 2020, using water from the VEKS transmission system.



At the end of January 2021, there was an alarm from the leak detection system. It turned out that the liner had cracked from the embankment to the storage bottom on one side. The triggering factor was probably that the protective liner was mounted using wooden pegs that had been pierced through the PP liner. Additionally, sub-freezing conditions had caused the PP liner to become brittle due to contraction.

The damage spread and proved so extensive that the entire liner ended up requiring replacement. Thus, a new liner was installed that included a plasticizer additive that enabled the liner to maintain some plasticity even down to $-5\text{ }^{\circ}\text{C}$.

At the end of October 2022, water heating, commissioning, and testing of control functions started. The storage was completely charged by New Year 2022-23 and was handed over for commercial operation on February 15, 2023.

The monitoring program

In order to monitor the operation and performance of the PTES in Høje Taastrup, a number of sensors were installed (see Figure 4). The monitoring program included the following parameters:

- The storage temperature is measured using four temperature strings, each having 14 PT100 sensors. Two strings are placed at the east end of the PTES and two at the west end.
- Several sensors have been placed between the insulation layers in the lid measuring temperature, humidity, and heat flux.
- The ground temperature is measured using a temperature string having 10 PT100 sensors. The temperature is measured until a depth of 15 m from the top of the embankment.

- The moisture and thermal conductivity of the ground is measured at a depth of 1 m from the top of the embankment.
- A weather station is used to measure the ambient air temperature, humidity, and wind speed.
- The storage water level is measured in a small well adjacent to the PTES using a guided radar and a hydrostatic sensor.

Results

The storage has been in operation since mid-February 2023. However, the first year of operation has mainly been used to develop and test a forecasting-based control strategy. Thus, the presented results should be considered preliminary and may not be indicative of long-term performance.

Figure 5 presents the storage temperatures, weekly charged/discharged energy, and energy content since March 2023. It can be observed that the storage temperature ranged between 45 and $90\text{ }^{\circ}\text{C}$. In order to evaluate the PTES energy content, it should be noted that the storage max capacity is estimated at approximately $3,300\text{ MWh}$. Consequently, it may be observed that the storage was almost fully charged for the first time in April 2023, while approximately $500\text{--}1000\text{ MWh}$ were charged or discharged most weeks, demonstrating the short-term operation of the storage.

Despite the lack of an appropriate control strategy, the storage has been in operation for approximately one year by the time of writing, with a yearly energy efficiency of approximately 90% . However, the efficiency is expected to increase due to the increase in the ground temperature that will reduce the heat losses toward the ground and due to the additional storage cycles. For short-term operating PTES, this is expected to happen after approximately eight years of operation (Sifnaios et al., 2023). In general, the storage efficiency

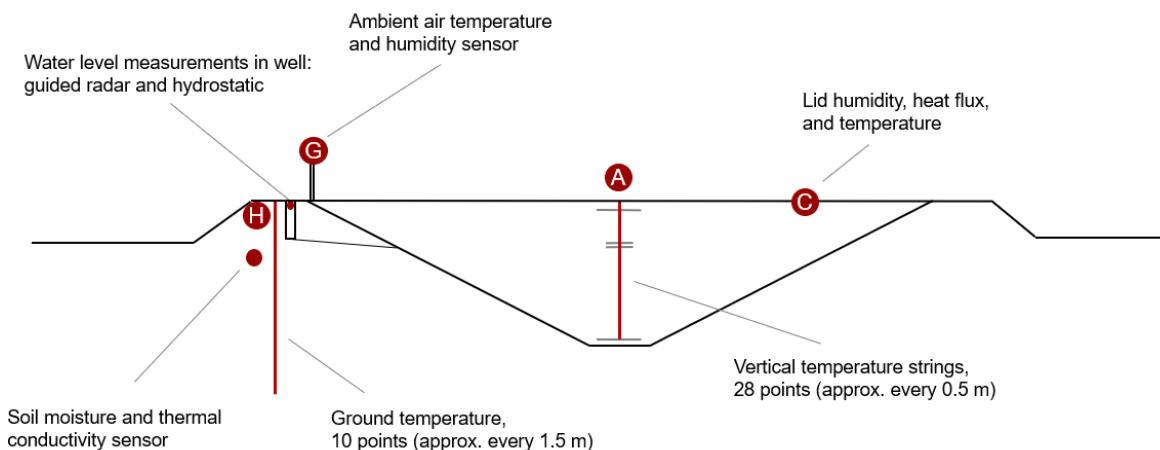


Figure 4: Schematic of the storage monitoring equipment and measurement points.

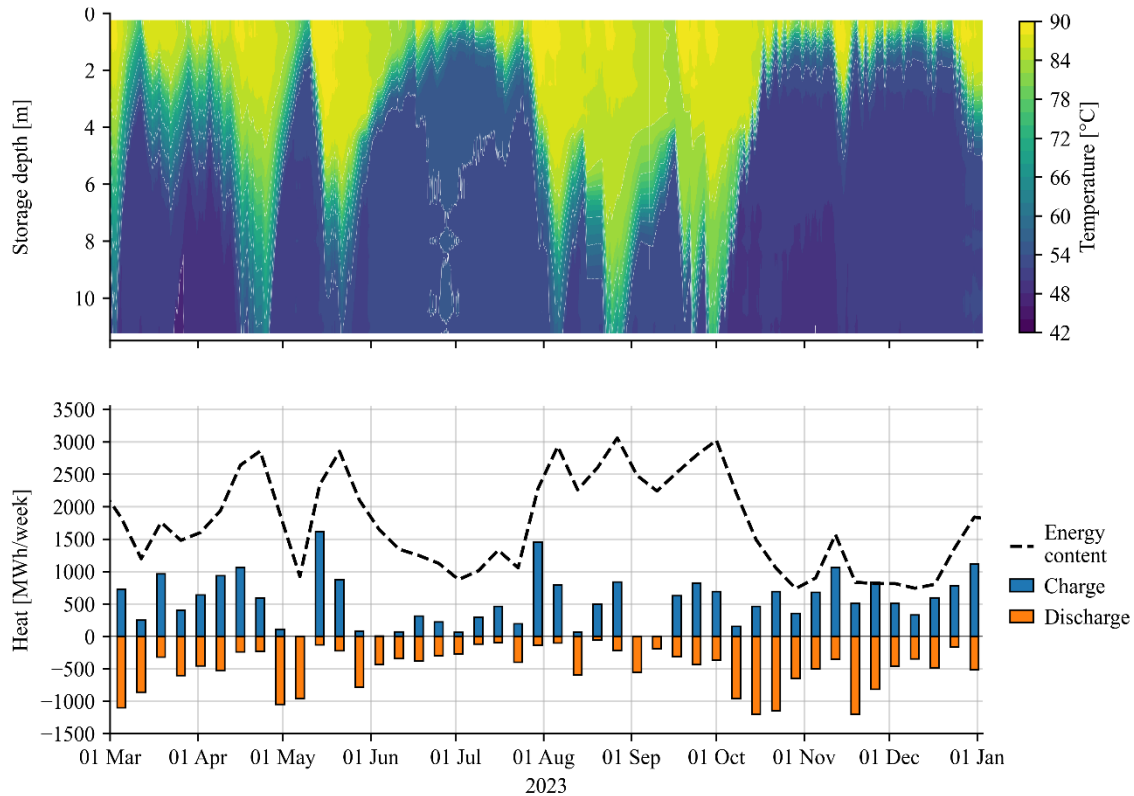
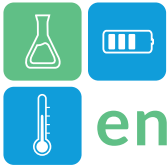


Figure 5: Storage temperatures (top) and weekly charged/discharged energy and energy content (bottom).

is expected to be closer to 95% after the stabilization of heat losses.

Since the PTES in Høje Taastrup was the first to have the diffusers installed at one end of the storage (instead of the middle), the investigation of stratification was of significant interest. Measurements have shown that there was a deviation smaller than 1 K between the two ends of the storage, indicating a horizontal uniformity of temperatures. However, the PTES has not yet operated at the designed flow rates (approx. 600 m³/hr) for long periods of time; thus, a proper evaluation of stratification has not been performed yet.

Conclusions

This paper presented an overview of the design, implementation, and preliminary results of the first PTES operating as a short-term heat storage. Since the storage has operated for less than a year and does not operate exactly as intended yet, it was not possible to draw many conclusions. Nevertheless, this study proves that the PTES operates as expected, indicating

that PTES can be used not only as seasonal heat storage systems but also as short-term.

Acknowledgment

This study was financed by the Energy Technology Development and Demonstration Programme (EUDP) through grant no. 64020-2025 (Integrate 2) and 64018-0134 (FLEX-TES).

References

- Sørensen P.A. et al. (2023) Design and construction of pit thermal energy storage in Høje Taastrup.
- Sifnaios, I., 2023. Investigations of pit thermal energy storages in district heating systems. Technical University of Denmark. <https://doi.org/10.11581/DTU.00000291>
- Sifnaios, I., Jensen, A.R., Furbo, S., Fan, J., 2023. Heat losses in water pit thermal energy storage systems in the presence of groundwater. Appl. Therm. Eng. 235, 121382. <https://doi.org/10.1016/j.applthermaleng.2023.121382>



Design Optimization of Synthetic Methane Production Sites Incorporating Direct Air Capture Technology

Gabriele Humbert^{1,*}, Binod Prasad Koirala¹, Philipp Heer¹

¹ Urban Energy Systems Laboratory, Empa - Swiss Federal Laboratories for Materials Science and Technology, 8600 Dübendorf, Switzerland

*Corresponding author e-mail: gabriele.humbert@empa.ch

Abstract

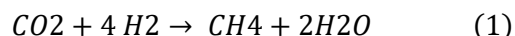
This study introduces a mixed integer linear programming (MILP) methodology to optimize the design and operation of synthetic methane production facilities, integrating Direct Air Capture (DAC) technology. The approach uniquely addresses both the sizing and operational aspects, reducing the levelized cost of methane by 29.0% compared to investment-focused strategies. The research highlights cost-driving factors and provides comprehensive insights for efficiently designing synthetic methane production sites.

Keywords: MILP, power to gas, optimization, synthetic methane, modelling

Introduction

New sustainable ways to store and use energy from renewable energy sources (RES) are imperative to meet climate targets (Koirala et al. 2021). Furthermore, the current levels of atmospheric carbon dioxide are alarmingly high, necessitating effective strategies for CO₂ removal.

Synthetic methane production emerges as a promising solution addressing both the need for sustainable energy and atmospheric CO₂ reduction. This process involves the reaction of carbon dioxide with hydrogen steam, as shown in Eq. (1):



Electrolyzers powered by RES can be used to produce the necessary H₂, while carbon capture technologies can generate the necessary CO₂ (Tregambi et al. 2023). In particular, direct air capture (DAC) technologies can employ materials and local renewable energy to absorb CO₂ from the ambient air, providing a local source of CO₂ without geographical constraints and contributing to carbon reduction in the environment (Wiegner et al. 2022).

Compared to directly using H₂ as an energy carrier, CH₄ has a higher energy density and allows the use of current network and storage infrastructures. However, the synthetic methane production process is complex and not yet cost-effective. It requires careful consideration of multiple energy vectors and their optimal integration to minimize costs (Jülch 2016).

This study focuses on the design of a synthetic methane production site, utilizing a Proton Exchange Membrane (PEM) electrolyzer and a DAC unit with solid sorbent. The design aims to achieve a predetermined daily

production target. Diverging from existing literature, this research employs a mixed integer linear programming (MILP) framework which enables the simultaneous determination of optimal component sizes and operational strategies. The findings are benchmarked against optimization approaches targeting investment cost minimization solely, providing insightful guidelines for the effective design of synthetic methane production sites incorporating DAC technology.

The synthetic methane production site

The energy system considered in the analysis is depicted in Figure 1. The synthetic methane is generated in a Sabatier reactor fed by CO₂ and H₂ flows exiting, respectively, a DAC unit with solid sorbent and a PEM electrolyzer. The heat necessary to drive the endothermic adsorption of CO₂ is retrieved from a district heating network (DHN), while a heat pump (HP) is considered to elevate the temperature of the retrieved heat, T_{DHN} = 65 °C, to the desired temperature value, T_{DAC} = 100 °C. The electricity required to power all components is obtained from PV panels or the grid, and, during periods of excess, electricity can be sold to the grid. No buffers are considered for the chemical compounds necessary to run the Sabatier reaction.

Methodology

A MILP approach was used to determine the optimal size and operation of the system depicted in Figure 1. The next sections illustrate the design variables, constraints and objective functions that characterize the optimization problem.

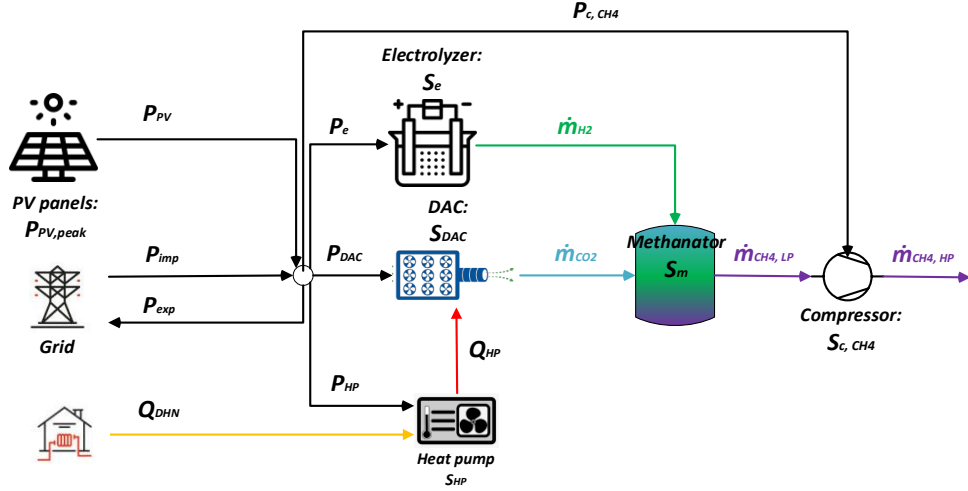


Figure 1: Schematic of the synthetic methane production site.

Design variables

Design variables considering both the sizing and operational problems were adopted in the design optimization problem:

- (i) *Continuous sizing design variables*: the PV system peak power, S_{PV} , the heat pump nominal power, S_{HP} , and the methanation reactor nominal power output, S_m ;
- (ii) *Discrete sizing design variables*: the PEM electrolyzer nominal size, S_{PEM} , and the number of DAC modules, S_{DAC} ;
- (iii) *Continuous operational design variables*: the heat retrieved from the DHN, Q_{DHN} , the electricity imported from the grid, P_{imp} , the electricity exported to the grid, P_{exp} , the CO_2 mass flow rate, \dot{m}_{CO_2} , and the CH_4 mass flow rate, $\dot{m}_{CH_4,LP}$;
- (iv) *Discrete operational design variables*: the electrolyzer status, $Flag_{PEM}$, and a startup variable for the electrolyzer, $Startup_{PEM}$;

Constraints

The amount of synthetic gas generated was constrained to 100 kg/day, while the molar flow balance at every time step, k , was constrained in agreement with the stoichiometric coefficients of the Sabatier reaction. The mass flow rate of CO_2 was constrained by the productivity, γ_{DAC} , of a DAC module multiplied by the number of DAC modules:

$$\dot{m}_{CO_2}(k) \leq S_{DAC} \gamma_{DAC} \quad (2)$$

Solid sorption capture was considered, in which the CO_2 is adsorbed on the surface of a solid material and desorbed upon low-temperature heat provision (100 °C) (Wiegner et al. 2022).

The mass flow rate of CH_4 was constrained by the size of the methanation reactor:

$$\dot{m}_{CH_4}(k) HHV_{CH_4} \leq S_m \quad (3)$$

Where HHV_{CH_4} is the higher heating value of methane. The power balance for the energy system was ensured through the following constraints:

$$P_{imp}(k) + P_{PV}(k) = P_{exp}(k) + P_{PEM}(k) + P_{DAC}(k) + \frac{Q_{HP}(k)}{COP} + P_c(k) \quad (4)$$

Where COP is the heat pump coefficient of performance, estimated as 50% of its theoretical limit. The heat balance was ensured by imposing:

$$Q_{HP}(k) \geq Q_{DAC}(k) \quad (5)$$

Finally, the components' power and heat flows were set lower or equal to their maximum sizes, in analogy Eq. (2). The upper boundary for the sizing design variables, necessary to perform the MILP optimization, were defined by considering the desired synthetic methane production to be achieved in a single time step.

Objective function

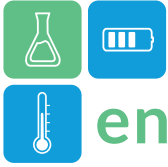
The analysis aims at minimizing the total cost, C_{tot} , linked to the production of synthetic gas. The total cost was calculated as the sum of the annualized investment cost, $C_{inv,a}$, maintenance costs, C_{maint} , and operational costs, C_{op} .

As an additional figure of merits, the Value-Adjusted Levelised Cost of Methane was defined as follows:

$$VALCOM = \frac{C_{tot}}{m_{CH_4,y} HHV_{CH_4}} \quad (6)$$

Input data

The optimization problem considered a 1-hour resolution with a 1-year horizon. The boundary conditions considered, specifically irradiance, cost to import electricity, cost to export electricity and cost to import DHN were assumed for the city of Dubendorf and the year 2022. The techno-economic parameters



adopted were assumed in agreement to (Minutillo et al. 2021) for the PEM electrolyzers, (Tregambi et al. 2023) and (Jülch 2016) for the methanation reactor and (Wiegner et al. 2022) for the DAC unit. For the latter, the single module was considered in this work as one fourth of the one reported in (Wiegner et al. 2022), resulting thus with a productivity of 2.75 kgCO₂/module/h and a unit price of 50.0 k€/module.

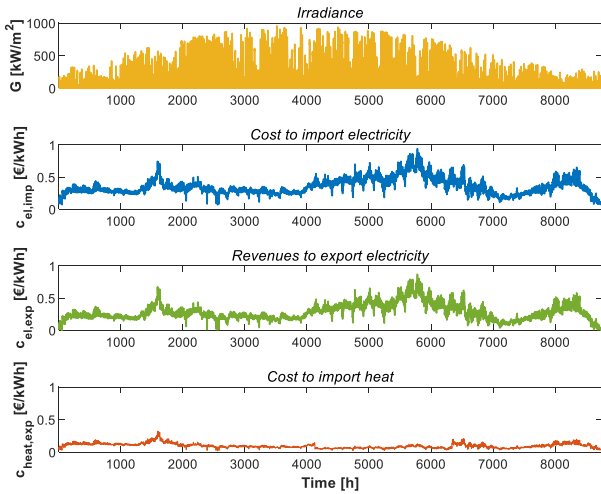


Figure 2: Input data for the selected case study.

Results and discussion

The results obtained through the optimization approach illustrated in the previous section are compared for the total cost minimization scenario and for the annualized investment cost minimization scenario. The latter serves as a benchmark scenario where the operational costs are disregarded during the design process.

The sizes of the key components deriving from the two optimization scenarios are reported in Table 1. No investments are made in the PV field for the investment cost minimization scenarios, as no benefits are captured by the optimization problem if such an objective function is selected. The sizes obtained for the other key components for the second optimization scenario considered are the minimum ones that allow to achieve the imposed synthetic methane generation constraint of 100 kg/day. Interestingly, such sizes are similar to the ones emerging from the total cost minimization. Previous studies exhibited larger sizes to improve operational flexibility and limit the impact of operational cost on the total cost (Humbert et al. 2023). However, for the synthetic methane production site under consideration, investment cost present a high weight on the total cost and, therefore, the optimal sizes of the key components result small also for optimization scenario 1. Nonetheless, the installation

and exploitation of PV implies reduced operational costs, which in turn reduces the VALCOM by 29.0%.

Table 1: Optimal sizes for the two optimization scenarios.

	Opt. scenario 1 min (C_{tot})	Opt. scenario 2 min ($C_{inv,a}$)
S_{PV} [kW _{peak}]	284.4	0.0
S_{DAC} [n° modules]	5	5
S_{PEM} [kW]	120.0	120.0
S_m [kW]	74.5	64.4
S_{HP} [kW]	15.9	13.8
S_c [kW]	0.5	0.4
VALCOM [€/MWh]	514.3	724.9

The key components operation is depicted for a typical summer week in Figure 3 in the instance of the optimization scenario 1. The largest electricity consumption is dictated by the PEM electrolyzer, which accounts for more than 90% of the site's annual energy consumption. The PEM electrolyzer is switched off during the evening, when the electricity prices are typically higher.

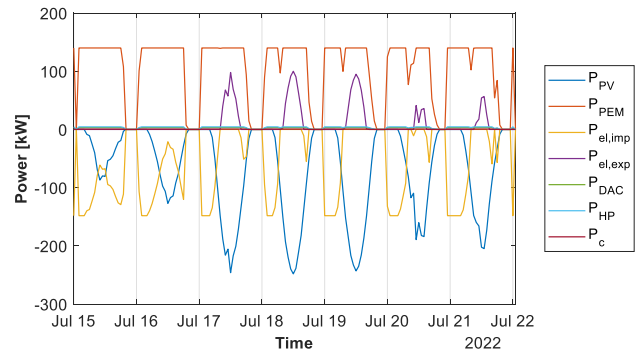


Figure 3: Key components operation during a summer week for the min (C_{tot}) scenario.

From the results reported in Figure 3, the energy consumption related to DAC appears to play a negligible role in the operational cost minimization of the site. While these results appear to be consistent with the ones reported in the literature (Tregambi et al. 2023), this might be dictated by the assumptions made for the DAC system consumption, for which constant parameters were selected based on the average temperature and relative humidity of Dubendorf. However, as reported by (Wiegner et al. 2022), DAC energy consumption strongly varies with the weather conditions and increases during hot and dry days.

The shares for the annualized investment cost for the two optimization scenarios considered are depicted in Figure 4. A large discrepancy is found, mainly dictated by the investments related to the PV field. In both scenarios, a large share of the investment cost is linked to the DAC unit, indicating that a large reduction in the technology cost is necessary to abate the cost of synthetic methane production.

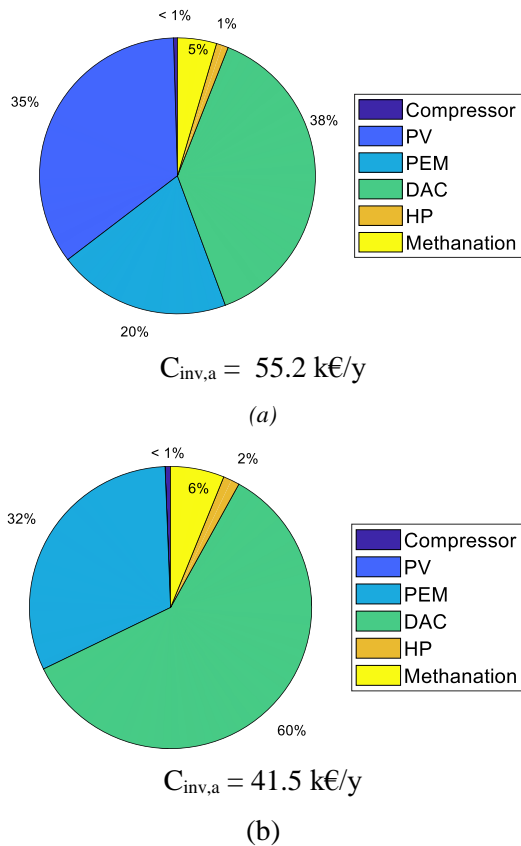


Figure 4: Comparison of the shares for the investment costs for (a) total cost minimization scenario and (b) total investment cost minimization scenario.

The operational costs accounted for 85.6% of the VALCOM in optimization scenario 2. Such a share reduces to 71.8% in scenario 1, leading to the VALCOM reduction reported in Table 1. The large share is dictated by the large electricity price characterizing the considered year, 2022. Numerical tests conducted in previous years, e.g. 2018, showed this share to reduce to 49.4%.

Conclusions

Overall, the results reported in this work demonstrate the importance of considering operational cost minimization during the design of a synthetic methane production site. A 29.0% reduction in the VALCOM was estimated, which was mainly dictated by the operational freedom allowed by the use of larger component sizes compared to an optimization design problem addressing investment cost minimization solely. However, The VALCOM calculated in this research surpasses the existing methane market price, indicating that additional advancements or financial incentives are necessary to enhance the viability of this

system. Besides, reducing the investment costs for DAC technology is crucial.

In future works, the optimization tool will be extended to account for the influence of weather conditions and workload on the key components and on the use of stochastic forecasts for the sensitive input data. Besides, the thermal integration of the heat produced during electrolysis and methanation will be considered, as well as the use of buffers to allow for a smart use of the required compounds.

Acknowledgment

The authors would like to acknowledge the financial support from the Swiss Federal Office of Energy (SFOE) for the project **Sweet PATHFNDR**, grant agreement no. SI/502259-01.

References

- Humbert, Gabriele, Hanmin Cai, Binod Prasad Koirala, and Philipp Heer. 2023. "Cost-Effective Hydrogen Generation: Concurrent Optimization of Component Sizes and System Operation." In *ICAE 2023 Proceedings*, , 1–6.
- Jülch, Verena. 2016. "Comparison of Electricity Storage Options Using Levelized Cost of Storage (LCOS) Method." *Applied Energy* 183: 1594–1606.
- Koirala, Binod et al. 2021. "Integrated Electricity, Hydrogen and Methane System Modelling Framework: Application to the Dutch Infrastructure Outlook 2050." *Applied Energy* 289: 116713.
- Minutillo, M. et al. 2021. "Analyzing the Levelized Cost of Hydrogen in Refueling Stations with On-Site Hydrogen Production via Water Electrolysis in the Italian Scenario." *International Journal of Hydrogen Energy* 46(26): 13667–77. <https://doi.org/10.1016/j.ijhydene.2020.11.110>.
- Tregambi, Claudio et al. 2023. "Techno-Economic Assessment of a Synthetic Methane Production Process by Hydrogenation of Carbon Dioxide from Direct Air Capture." *International Journal of Hydrogen Energy* (xxxx). <https://doi.org/10.1016/j.ijhydene.2023.06.289>.
- Wiegner, Jan F., Alexa Grimm, Lukas Weimann, and Matteo Gazzani. 2022. "Optimal Design and Operation of Solid Sorbent Direct Air Capture Processes at Varying Ambient Conditions." *Industrial and Engineering Chemistry Research*.



Development and characterization of a new bio-sourced composite material based on phase change material and hemp shives

Hachmi TOIFANE^{1*}, Pierre TITTELEIN¹, Anh Dung TRAN LE², Laurent ZALEWSKI¹, Thierry CHARTIER¹

¹ Univ. Artois, IMT Nord Europe, Junia, Univ. Lille, ULR 4515, Laboratoire de Génie Civil et géo-Environnement (LGCgE), F-62400 Béthune, France.

² Laboratory of Technologies Innovative (LTI), University of Picardie Jules Verne-IUT of Amiens, Le Bailly 80025 Amiens Cedex, France

* Corresponding author e-mail : hachmi.toifane@univ-artois.fr

Abstract:

This study introduces an innovative composite material composed of bio-sourced phase-change material (PCM) of plant origin combined with hemp shives, developed in response to environmental challenges in the construction sector. The state of the art emphasizes the low thermal storage capacity of bio-based materials and highlights increasing need for developing sustainable materials that offer optimal thermal, and mechanical performances. The PCM's thermal properties and the ones of hemp shives results in a material that combines lightness, strength, and thermal regulation. Various formulations have been assessed and compared to conventional hemp concrete. Thermal characterization that includes the measurements of thermal conductivity and numerical simulations to evaluate the thermal storage capacity has been carried out. The results indicate that the addition of PCM significantly enhances the material's thermal storage capacity, positioning this one as a promising, eco-friendly solution for sustainable construction and for improving the thermal comfort and energy efficiency of buildings.

Keywords: Hemp composite, Bio-sourced Phase Change Material (PCM), Thermal storage, Hemp shives

1. Introduction

This study is part of the energy transition and aims to design an innovative hemp concrete incorporating phase-change materials (PCM) to improve thermal comfort in buildings and reduce energy consumption. Hemp concrete is particularly interesting as an ecological and insulating building material, obtained from renewable and recyclable resources. It is combined with a biosourced solid/liquid phase-change material to enhance its thermal performance. This PCM, as its name suggests, has the ability to change phase reversibly by storing/releasing latent heat energy, giving it an interesting advantage over conventional building materials. The PCM used in this study is Inertek 26. These are 5-25 μm polymer capsules containing a mixture of methyl palmitate and methyl stearate, two fatty acid-based vegetable oils, which are themselves embedded in a plaster coating (Thermoconfort_26 named after ThC_26). Previous studies have shown that this type of PCM improves the thermal performance of building materials, such as concrete (Liston et al. 2016), thus offering promising solutions for energy storage in construction. This paper presents work carried out by the LGCgE laboratory of

the Université d'Artois and the LTI laboratory of the Université Picardie Jules Vernes, aimed at designing and characterizing this hemp concrete containing a mixture of PCMs.

2. Methodology

2.1 Formulation

The initial formulation of hemp concrete without PCM contains 55% water, 22,5% hemp shives and 22,5% Calcia NHL5 pure natural white hydraulic lime binder. It serves as a starting point for two other formulations containing respectively 50% and 60% of coating integrating PCM (ThC_26) in relation to the total dry mass (hemp shives, binder, ThC_26). A summary of the formulations studied is presented in Table 1. Both the water/binder ratio (W/B) and the water/granulate ratio (W/G) are around 2,4, offering good workability in the fresh state. In addition, a Sika ViscoCrete®-850 plant-based superplasticizer, based on cane sugar, is used to fluidize the mixes. The mixtures were poured into the molds and compacted by hand with a wooden cleat. Demolding took place after 3 days for all samples (Figure 1), which were then stored at room temperature (20°C) and 50% relative humidity.

Table 1 : formulations studied

Component	ρ [kg.m ⁻³]	0% ThC_26	50% ThC_26	60% ThC_26
ThC_26	723	-	30,8	40
Hemp shives	133	22,3	15,5	13,4
Binder NHL5	830	22,3	15,5	13,4
Water	1000	55,4	38,2	33,2



Figure 1 : samples used for testing

2.2 Thermophysical characterization

To characterize the thermophysical parameters of samples, heat capacities (solid/liquid), thermal conductivities (solid/liquid) and latent heat, the device available in LGCgE was used (Figure 2). This is a fluxmetric bench experimental set-up similar to the hot plate method, which has been presented in numerous works such as (Zalewski et al. 2019) and (Thonon et al. 2020). The 25x25x5 cm³ samples are positioned between two heat exchanger plates thermoregulated by thermostatic baths in order to impose thermal stresses (T) on samples. The heat flux variations (ϕ) are measured by heat fluxmeters (Figure 3). The thermal stresses used are dynamic, in the form of steps. Heat flux response make it possible to calculate, for formulations without PCM, the specific heat capacity (C), according to Eq. (1), based on the quantity of energy exchanged (Q) from the initial temperature ($T_{initial}$) to the final temperature (T_{final}).

$$C = \frac{Q}{\Delta T} \quad [\text{J} \cdot \text{kg}^{-1} \cdot \text{°C}^{-1}] \quad (1)$$

$$\text{With } Q = \int_{t_{initial}}^{t_{final}} \Delta\phi \, dt \quad [\text{J}]$$

$$\text{and } \Delta T = T_{final} - T_{initial} \quad [°\text{C}]$$

For samples containing PCM, these steps vary between 10 and 20°C (solid PCM) or between 30 and 40°C (liquid PCM – Figure 3). These allow thermal conductivities (λ_S , λ_L), heat capacity and thermal resistances to be determined by the inverse method.

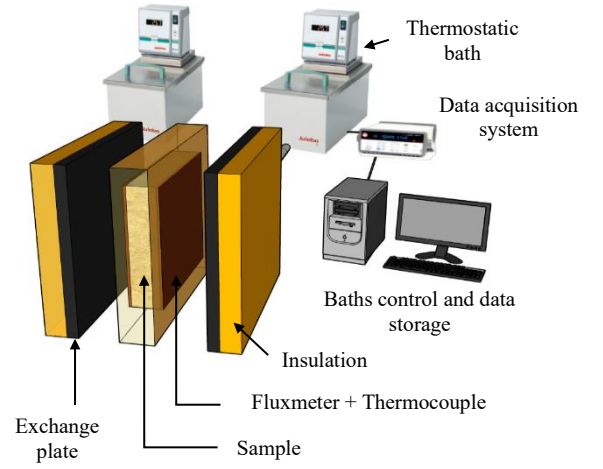


Figure 2 : Experimental apparatus

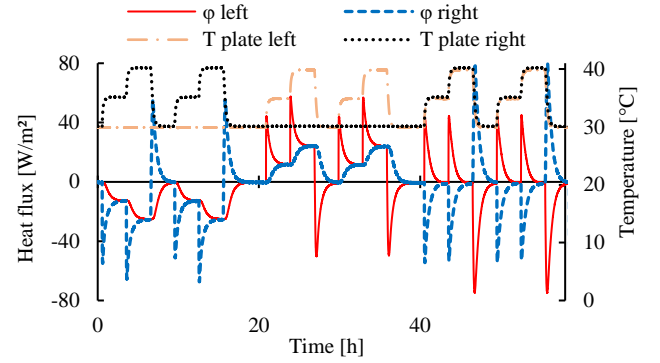


Figure 3 : Evolution of the heat flux for thermal stress in the shape of steps (30-40°C)

Other thermal stresses in the form of ramps ranging from 10 to 45°C, for durations varying between 4h and 24h, are also applied to the samples to determine their latent heat (L_A) and melting temperatures (T_A , T_M). These types of cycle enable the PCM to store/release energy by alternating between solid and liquid phases. The temperature and heat flux data collected during these test campaigns are used as input parameters for a numerical model to simulate the thermal behavior of the material, for subsequent characterization by inverse method. This inverse characterization is achieved by using genetic algorithms to reduce an objective function defined as the quadratic difference between the experimentally measured heat fluxes (ϕ_{exp}) and the numerically simulated (ϕ_{num}) heat fluxes to the left (L) and right (R) of the sample, Eq. (2).

$$f_{obj} = \sum \left(\left(\phi_{L_{exp}}(t) - \phi_{L_{num}}(t) \right)^2 + \left(\phi_{R_{exp}}(t) - \phi_{R_{num}}(t) \right)^2 \right) \quad (2)$$

The numerical model used, coded in the python language, was developed and detailed in previous work carried out at LGCgE (Toifane et al. 2022) and successfully characterized a similar composite.

2.3 Mechanical characterization

In order to evaluate the mechanical strength of the various hemp concrete formulations, they are tested in simple bending on 3 supports, using 4x4x16 cm³ specimens and following the EN 1015-11 standard. The press used is the Autograph AG-X plus model (Shimadzu) with a capacity of 200 KN, coupled with Trapezium X software for machine control and data acquisition. The loading speed is set at 2 mm/min. For each formulation, the test is performed on 3 specimens and the final flexural strength is the average of the 3 values obtained. The two pieces of each specimen, obtained after flexural fracture, are then used to perform simple compression tests. The experimental set-up for the mechanical tests is shown in Figure 4.



Figure 4 : experimental apparatus for bending (left) and compression (right) tests

3. Results and Discussion

3.1 Thermal properties

Figure 5 shows the evolution of the sum of the heat flux measured on a sample without ThC₂₆, over time, when subjected to thermal loading in the shape of a ramp. During temperature rise, the flux increases to around 15 W/m² before dropping to zero when the temperature stabilizes at 45 °C. This is due to the fact that hemp concrete exchanges energy by sensible heat. A similar phenomenon is observed when the material is cooled. In the case of samples including biosourced PCM, the latent heat involved. This phenomenon can be seen in Figure 6, highlighted by the flux peaks that appear when the materials reach 28,6 °C in the melting phase and around 25,8 °C in the solidification phase. This is due to the fact that the PCM changes phase (solid-liquid), exchanging energy via latent heat. Unlike conventional materials, PCM have the ability to store energy during phase change, and release it later. It can also be seen that as the concentration of PCM in the sample increases, so does this latent heat and the heat capacity, highlighting the effect of adding PCM to hemp concrete.

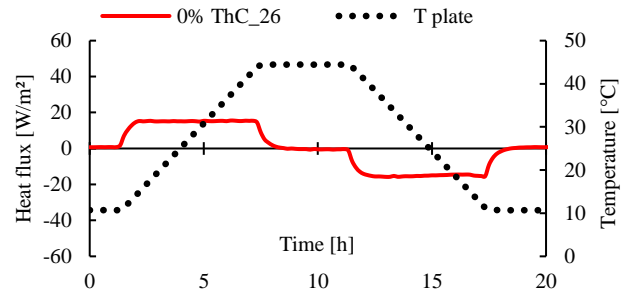


Figure 5 : Evolution of the heat flux: 0% ThC₂₆

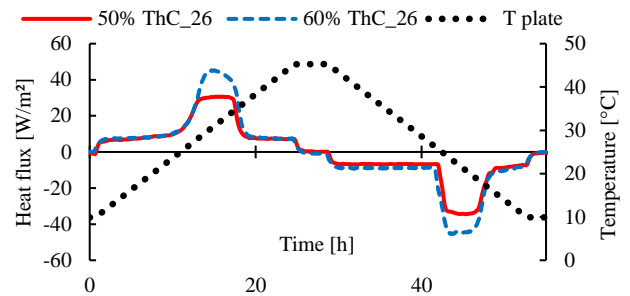


Figure 6 : Evolution of the heat flux: 50% and 60% ThC₂₆

From the heat flux and temperature measurements, the thermal conductivity (solid/liquid), heat capacity (solid/solid) and latent heat can be determined by inverse methods as preview works (Zalewski et al. 2019) (Table 2). PCM's change-of-state temperatures, i.e. T_A (pure solvent melting) and T_M (end of melting), are also determined in the same way. The values obtained are as follows:

- Melting phase T_A: 29,9 °C and T_M: 28,6 °C
- Solidification phase T_A: 27,4 °C and T_M: 25,8 °C

Table 2 : comparaison of formulations

Formulation	ρ [kg/m ³]	λ [W/(m.°C)]	C [J/(kg.°C)]	L _A [J/kg]
0% ThC ₂₆	296	0,11	1 361	-
Evrard	440	0,10	1 530	-
50% ThC ₂₆	434	λ_S : 0,11	C _S : 1 342	48 256
		λ_L : 0,12	C _L : 1 541	
60% ThC ₂₆	459	λ_S : 0,13	C _S : 1 476	63 600
		λ_L : 0,12	C _L : 1 759	

The conductivities and thermal capacities obtained are in line with several works carried out on hemp concrete, such as (Evrard 2008). These parameters can be used to numerically simulate the thermal behavior of the various formulations as 50% ThC₂₆ (figure 7) and considering the PCM as binary solution. It can be seen that by increasing the percentage of ThC₂₆, the thermal conductivities and capacities are almost equivalent, the density and latent heat increase, and therefore the storage capacity significantly.

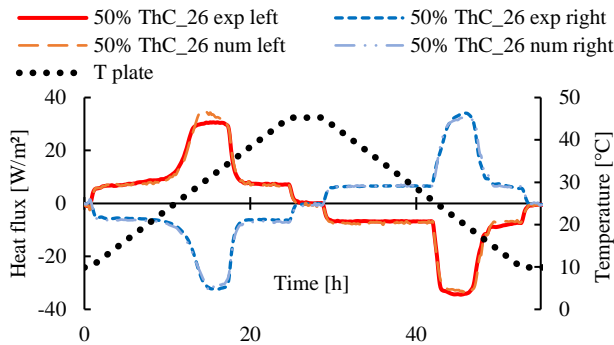


Figure 7 : comparison of experimental and numerical heat flux

3.2 Mechanical properties

The results of the mechanical strength tests on the materials tested are shown in Table 3 and in Figures 8 and 9. Maximum stresses are considered at 20% deformation of the 4x4x16 cm samples, i.e. 8mm.

Table 3 : mechanical strength of formulations studied

Formulation	σ_b (MPa)	σ_c (MPa)
0% ThC_26	0,13	0,32
50% ThC_26	1,21	2,14
60% ThC_26	1,34	2,83

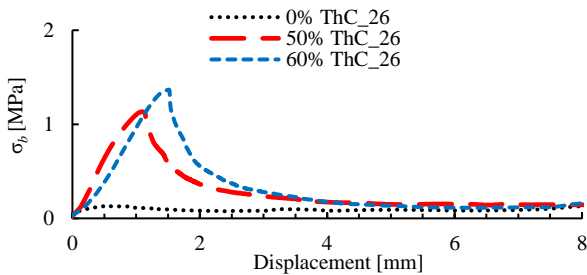


Figure 8 : bending stress as a function of displacement

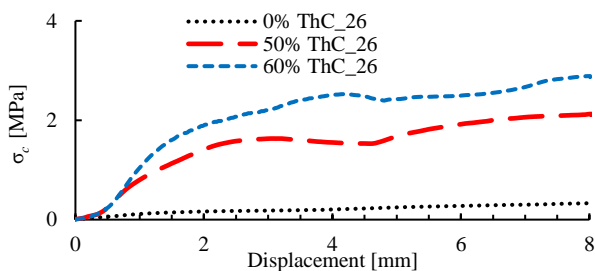


Figure 9 : compressive stress as a function of displacement

According to these analyses, the addition of PCM to hemp concrete increases its flexural (σ_b) and compressive strength (σ_c), compared to the 0% ThC_26, which has similar values to the literature. This is because the PCM microcapsules are embedded in a gypsum plaster before being mixed into the hemp concrete. The mechanical strength of these PCM-containing samples exceeds, in most cases, the strength values reported in the literature for conventional hemp concrete, namely: $\sigma_c > 2$ MPa (Cérézo 2005) and $\sigma_b > 0,8$ MPa (Elfordy et al. 2008).

4. Conclusion

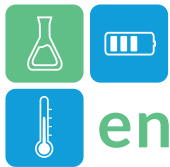
These initial investigations, carried out on this new hemp concrete incorporating bio-based PCM, clearly show the advantages of combining these two materials. The presence of coating integrating PCM has improved the mechanical properties and in particular the thermal storage of hemp concrete, which contributes to improving the thermal comfort of buildings. Although this approach is very promising, it requires hygric analysis and further studies under real conditions to assess the impact of PCM.

Acknowledgment

Researchers from the LGCgE laboratory of the University of Artois and the LTI laboratory of the University of Picardie Jules Verne would like to thank the Hauts-De-France region which has funded the project "MABIOMCP" through the MANIFEST State (France)/Region Plan Contract. The authors are indebted to WINCO/MCI company for the provision of Thermoconfort_26.

References

- Cérézo, Véronique. 2005. "Propriétés Mécaniques, Thermiques et Acoustiques d'un Matériau à Base de Particules Végétales" These, Lyon, INSA.
- Elfordy, S., F. Lucas, F. Tancret, Y. Scudeller, and L. Goudet. 2008. "Mechanical and Thermal Properties of Lime and Hemp Concrete ('Hempcrete') Manufactured by a Projection Process." *Construction and Building Materials* 22 (10): 2116–23.
- Evrard, Arnaud. 2008. "Transient Hygrothermal Behavior of Lime-Hemp Materials."
- Liston, Leah Christine, Yaghoob Farnam, Matthew Krafcik, Jason Weiss, Kendra Erk, and Bernard Y. Tao. 2016. "Binary Mixtures of Fatty Acid Methyl Esters as Phase Change Materials for Low Temperature Applications." March 5, 2016.
- Thonon, Maxime, Gilles Fraisse, Laurent Zalewski, and Mickael Pailha. 2020. "Towards a Better Analytical Modelling of the Thermodynamic Behaviour of Phase Change Materials." *Journal of Energy Storage* 32 (December): 101826.
- Toifane, Hachmi, Pierre Tittlein, Yassine Cherif, Laurent Zalewski, and Hervé Leuck. 2022. "Thermophysical Characterization of a Thermoregulating Interior Coating Containing a Bio-Sourced Phase Change Material." *Applied Sciences* 12 (8): 3827.
- Zalewski, Laurent, Erwin Franquet, Stéphane Gibout, Pierre Tittlein, and Didier Defer. 2019. "Efficient Characterization of Macroscopic Composite Cement Mortars with Various Contents of Phase Change Material." *Applied Sciences* 9 (March): 1104.



Development and multiscale characterization of a sensible/sorption bimodal heat storage for cooling tower application

Arnaud Bruch^{1,*}, Igor Rangel Correa Ferreira¹, Sylvie Rougé¹, Grégory Largiller¹, Kevyn Johannes², Frédéric Kuznik²

¹ Univ Grenoble Alpes, CEA, LITEN, DTCH, LCST, F-38000 Grenoble, France

² INSA-Lyon, CETHIL, F-69621 Villeurbanne, France

*Corresponding author e-mail: arnaud.bruch@cea.fr

Abstract

This study presents experimental results on so-called cTES (for cold Thermal Energy Storage), in the specific configuration of coupled heat and moisture storage. An effective improvement of coupled sensible/sorption energy storage is presented, by the development of a new sensible/sorbant material made of glass sphere coated with a mixture of AQSOA Z05 zeolith and PDMS Sylgard 184. The process of manufacturing and the characterization of the equilibrium isotherms of the coating are first presented. Main result show that the new coating is highly effective with more than 95% of the sorbant material being active. The experimental characterization of the thermal behaviour at prototype scale (>approximately 440 kg of coated spheres and 270 kg of uncoated spheres) is then presented. The results highlight effective operation of the cTES, i.e. water storage during adsorption and flattening of the ambient air temperature during desorption.

Keywords: sorption, cold Thermal Energy Storage, coupled storage, wet cooling alternative

Introduction

Wet cooling towers are the most efficient choice for condenser cooling in thermal based power plants but are less and less compatible with the growing water-scarcity in numerous regions (Turchi et al. 2014). On the other end of the spectrum, the use of air-cooled systems reduces up to 80% of water consumption (Carter and Campbell 2009), but the efficiency of the turbine decreases significantly if the temperature of ambient air exceeds 20°C (Balogh and Szabo 2008).

Different hybrid or alternative cooling solutions with lower water consumption without prohibitive performance losses have been proposed as illustrated by the A.R.I.D. US program (ARID 2015). The use of thermal energy storage has also been proposed and already studied, with storage of the power block heat during the day and its evacuation during the night, when ambient temperatures are colder (Manglik and Jog 2016, WASCOP 2019, Bruch et al. 2021). An enhancement of such concept has been proposed by Rougé et al. 2021 with a coupled storage of heat and moisture from ambient air. Their experimental results have proven the effectiveness of the concept, with flattening of the air temperature during daytime near

night temperatures. However, the bi-granulometry used by the authors leads to significant of inactive adsorbent.

This paper presents an effective improvement of the concept of coupled sensible/sorption energy storage by the development of a composite storage material made of glass spheres coated with a mixture of adsorbent AQSOA Z05 zeolite and polymer binder. The material is first characterized at small scale, with experimental equilibrium curves. Then results obtained at prototype scale are presented and analyzed.

Fabrication and characterization of the composite material

The composite material used for the coupled sensible-sorption storage has been obtained from the aluminophosphate FAM-Z05 sorbant combined with silicone binder PDMS, named Sylgard-184. The adsorbent FAM-Z05 has been chosen since it fulfils most of the study's requirements and notably the complete desorption at temperature around 40°C and the concentration of most adsorbed/desorbed water in a small temperature range. The procedure used for the fabrication of the SyZ05 material and the Gl-SylZ05 composite is schematically presented in Figure 1. It mainly consists in a dip coating procedure of adsorbent coating on a glass sphere substrate

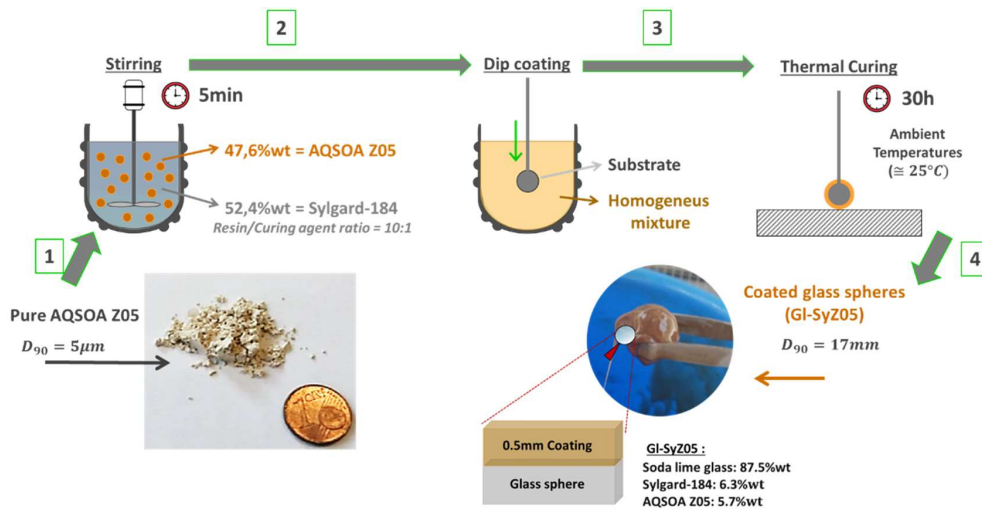


Figure 1: Scheme representation of the composite fabrication procedure

Figure 2 presents typical results obtained during adsorption of water vapor at 25°C and 60°C, with water vapor pressure up to 160mbar. The results highlight that the binder Sylgard-184 has little effect on the sorption reaction, since the composite maintains the same shape of the equilibrium isotherms. In addition, the AQSOA Z05 remains 95 to 100% active when embedded in the novel composite, with around 95% of the maximum uptakes when compared to its pure form. The authors believe that the 5% difference in uptake may be due to a proportion of inactive adsorbent, but there may be also some uncertainties in the material proportions during fabrication. A good agreement with literature data (Goldworthy 2014, Shimooka et al. 2007, Teo et al. 2017) is also observed.

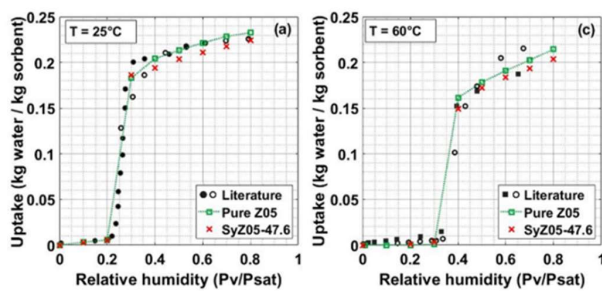


Figure 2: Typical equilibrium isotherms of pure Z05 and SyZ05 material, comparison with literature data.

Experimental facility for reactor scale characterization

The experimental facility used for the characterization at reactor scale is schematically presented in Figure 3.

It consists mainly in an open air-loop, with controlled mass flow rate, temperature and relative humidity. It was designed to provide air at a maximal superficial and interstitial velocities of 0.3 m/s and 0.8 m/s respectively, temperature between 15 and 50°C and specific humidity between 2 and 20 g of vapour per kg of dry air at the inlet of the sensible-sorption module. More detailed description of the experimental facility is given in Rougé et al. 2021. The reactor tank is a cylindrical stainless steel tank surrounded by domed ends, with inner diameter of 0.61 m and total height of 1.7 m. A metallic honeycomb and a diffusor are installed at the two inlets of the reactor tank with the aim to smooth the air profile during the experiments and ensure transverse homogeneity.

The reactor was filled with a mixture of 17 mm spheres of glass and composite material GI-SyZ05. To ensure proper mix, the reactor height was divided into 30 equally thick layers, each layer being filled with homogeneous distribution of sphere glass and GI-SyZ05. At the end of the process, the tank is filled with approximately 440 kg of coated spheres and 270 kg of uncoated spheres.

The tank is finely instrumented with inlet/outlet Pt100 temperature and about 90 embedded thermocouples (type T, 1 mm diameter) to check the thermal behaviour (see Figure 4). Special attention has been paid to the inlet and outlet humidity sensors (with dedicated calibration sessions to highlight the influence of operating parameters of the humid air flow) to assess the relevancy and accuracy of the measurements.

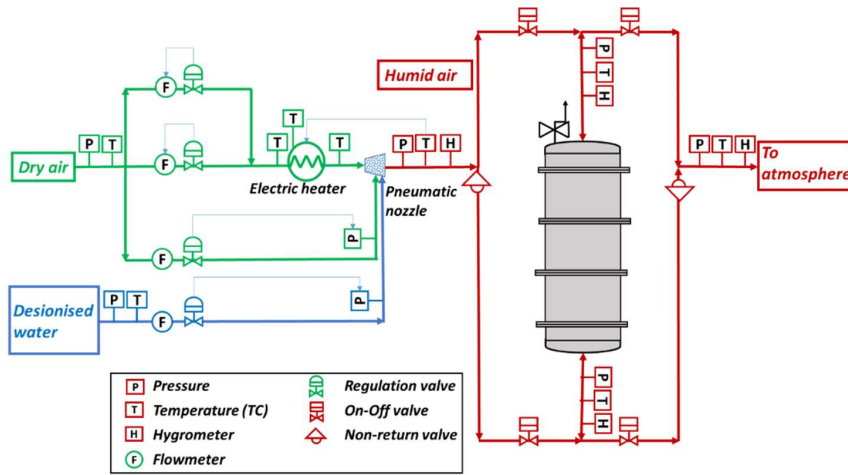


Figure 3: Scheme of the experimental set-up

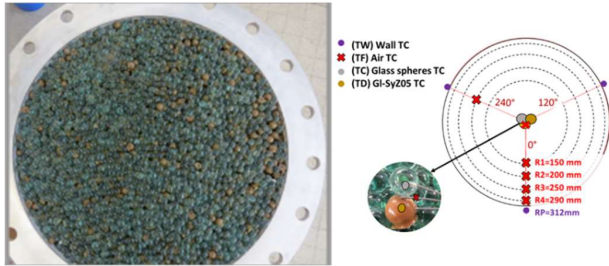


Figure 4: Left: Mixture of coated (orange) and uncoated (green) solid filler; Right: transverse distribution of thermocouples.

Experimental characterization at reactor scale

Some simplified tests conditions have been first defined, to evaluate and characterize the thermal behaviour and try to highlight the contributions of sensible heat and sorption to the coupled phenomenon. Figure 5 presents typical results obtained in successive cycles with constant inlet air temperature (Type II tests) and constant inlet vapour pressure (Type III tests).

Type II tests allow to focus on the sorption effect since initial bed and inlet temperatures are constant. From Figure 5, the effect of the sorption is quantitatively limited but clearly observable: due to adsorption in charge, the outlet temperature is temporarily increased, which is linked to decrease of pressure vapour and increase of the stored water mass. A maximum of about 2 kg of water if adsorbed/desorbed from cycle to cycle. The opposite is observed in discharge (i.e. desorption). In all cases, an “established behaviour” is observed after 1 to 2 cycles only, i.e. the first cycle highlights a specific thermal behaviour due to initial conditions and next cycles exhibit behaviour independent of the cycle number. It should be noted that the difference on the inlet air temperature between charge and discharge can be attributed to regulation issues.

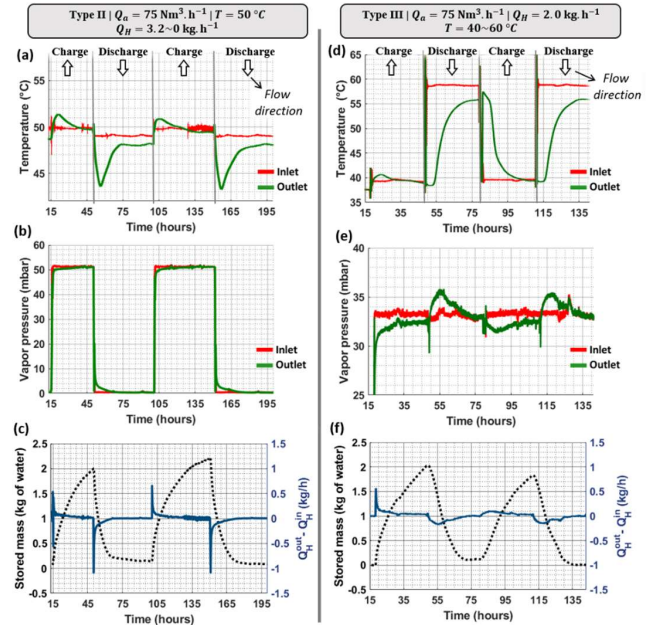


Figure 5: Typical results obtained in tests at constant inlet temperature (left) and constant inlet vapour pressure (left). Evolutions of inlet/outlet air temperatures (top), vapour pressure (middle) and water stored mass (bottom).

Considering constant inlet vapour pressure and varying inlet temperature, i.e. varying inlet relative humidity, is closer to the reality (Rougé et al. 2021) and leads to similar observations even if the results are more complicated to interpret due to sensible and sorption coupling.

Figure 6 depicts the influence of the air/water mass flow rate, considering similar conditions of temperature and relative humidity. The results highlight that the lower the air/water flowrate, the greater the thermal effects observed. Neglecting potential effects of thermal losses with varying mass



flow rate and cycle duration, this may be explained by the reaction kinetics which seems to be only slightly impacted by the air/water flow rate. Thus, the sorption thermal power is slightly affected by the flow rate and the observed thermal effects are proportional to the flow rate.

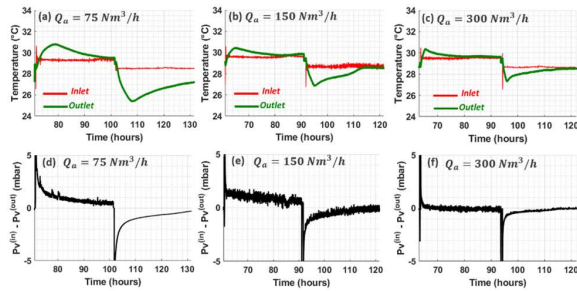


Figure 6: Influence of air/water mass flow rate, Type II tests.

It should be noted that the observed effects presented in Figure 5 and Figure 6 are quantitatively rather small, with temperature variations due to sorption of only few degrees. The authors explain this by the behaviour of the PDMS binder used during the fabrication of the composite material, whose permeability seems to be much lower than expected. As a consequence, the sorption process is lowered, cycle durations are increased and thermal effects are being diluted over time.

Conclusion

The preparation and the characterization of an innovative composite material made of glass spheres coated with AQSOA Z05 zeolite mixed with polymer binder has been presented. It appears that the addition of AQSOA Z05 powder into the polymer matrix demonstrates to be a favourable approach since the AQSOA Z05 remains 95 to 100% active.

At reactor scale, the composite material highlights the expected behaviour, i.e. water storage during adsorption and flattening of the air temperature during desorption.

However, even if additional experimental campaign are needed to properly characterized the material and the storage set-up, the observed thermal effects are quite lower than expected, typically about few °C only. This has been explained by the permeability of the polymer binder which seems to be quite lower than expected.

Next steps include the characterization of the kinetics of the composite material and the search for more efficient polymer matrix.

References

- Rougé S., Soriano O., Bruch A., Largiller G., Bentivoglio J., Experimental characterization of coupled sensible heat and moisture storage for dry cooling enhancement, *Applied Thermal Engineering* 192, (2021), 116922.
- Balogh A. and Szabó Z., “HELLER System: The Economical Substitute for Wet Cooling - to avoid casting a shadow upon the sky,” *Therm. Eng.*, p. 45, 2008
- Turchi C.S. Wagner M.J., and Kutscher C.F., “Water Use in Parabolic Trough Power Plants: Summary Results from WorleyParsons’ Analyses,” NREL/TP-5500-49468, 1001357, Dec. 2010. doi: 10.2172/1001357.
- Carter N.T. and Campbell R.J., “Water Issues of Concentrating Solar Power (CSP) Electricity in the U.S. Southwest,” p. 20, 2009.
- ARID, https://arpa-e.energy.gov/sites/default/files/documents/files/ARID_ProgramOverview.pdf, 2015
- Manglik R.M. and Jog M.A., “Resolving the energy–water nexus in large thermoelectric power plants: a case for application of enhanced heat transfer and high-performance thermal energy storage.,” *J. Enhanc. Heat Transf.*, vol. 23, no. 4, 2016, doi: 10.1615/JEnhHeatTransf.2017024681.
- WASCOP project, 2016-2019, Grant Agreement 654479.
- Bruch A., Bourdon D., Dumas C., Blaise A., Chouvel-Saye A., Experimental characterization of a water/rock thermocline cold thermal energy storage for optimization of condenser cooling, *Journal of energy storage* 44, 2021, 103426.
- Goldsworthy M.J. 2014. “Measurements of Water Vapour Sorption Isotherms for RD Silica Gel, FAM-Z01, FAM-Z02, FAM-Z05 and CECA Zeolite 3A.” *Microporous and Mesoporous Materials* 196, 2014.
- Shimooka S., Kazunori O., Hideto H., Takahiko T., Hiroyuki K., Akio K., Mitsuhiro K., and Hitoki M. 2007. “The Evaluation of Direct Cooling and Heating Desiccant Device Coated with FAM.” *JOURNAL OF CHEMICAL ENGINEERING OF JAPAN* 40 (13): 1330–34.
- Teo W.B., Chakraborty A., and Fan W. 2017. “Improved Adsorption Characteristics Data for FAM Types Zeolites and Water Systems under Static and Dynamic Conditions.” *Microporous and Mesoporous Materials* 242 (April): 109–17.



Development and performance evaluation of a K_2CO_3 -based closed-cycle sorption heat storage system

Kartik Jain^{1,*}, Akshay Chate¹, Amrit Ambirajan¹, Susmita Dash¹, and Pradip Dutta^{1,2}

¹Department of Mechanical Engineering, Indian Institute of Science, Bangalore, 560012

²Interdisciplinary Centre for Energy Research, Indian Institute of Science, Bangalore, 560012

*Corresponding author e-mail: kartikjain@iisc.ac.in

Abstract

A laboratory-scale sorption heat storage system with a capacity of 3 MJ has been developed, utilizing potassium carbonate (K_2CO_3) salt hydrate, chosen for its high energy storage capacity and cost-effectiveness. The system employs a shell and tube-type heat exchanger configuration for the energy storage reactor, with the tube pitch and vapour flow path length determined based on scaling analysis [1]. Results from heat storage (charging or dehydration) as well as heat release (discharging or hydration) processes are presented, emphasizing the significant impact of varying vapour pressures on hydration reaction rates and subsequent heat release rates. It has been observed that the vapour pressure on the evaporator-condenser side during the charging and discharging processes is the primary factor determining the state of the reactive salt and thus plays a vital role in influencing the performance of the closed cycle sorption heat storage system.

Keywords: Sorption heat storage, salt hydrate, hydration, dehydration, closed system.

Introduction

According to the International Energy Agency (IEA), heating accounted for nearly half of global energy consumption in 2021, exceeding electricity (20%) and transportation (30%) [2]. Building heating, including space heating in cold regions and domestic hot water production, comprised about 46% of global heat consumption [3,4]. Prioritising renewable energy sources can reduce fossil fuel dependence and lower greenhouse gas emissions, although solar energy's intermittent nature presents challenges. Efficient high-density thermal energy storage systems with minimal losses are needed to fill this gap.

Sorption heat storage (SHS) systems, or sorption thermal batteries, offer alternatives to conventional heat pumps for space heating and hot water production [3,5]. These systems operate by an endothermic reaction in a selected sorption material's solid-gas pair (AB) during the *charging process*, storing surplus heat (e.g., solar energy or waste heat). The stored heat is later retrieved through a reversible exothermic reaction during the *discharging process*, making it available for heating applications. Among the various available sorption materials, salt hydrates stand out as suitable candidates for low and medium-temperature applications due to their high energy storage density ($>2\text{GJ/m}^3$) and their charge and discharge temperatures aligning well with the requirements of the built environment. Additionally, salt hydrates are cost-effective compared to pure adsorbents and employ

water vapour as a sorbate, which is a safe and readily available resource [6].

SHS systems have open or closed cycle operating modes [7]. Compared to an open system, a closed system can deliver higher output temperature for heating applications, and a small amount of energy is required for vapour transport [8]. The proposed SHS system operates in a closed cycle, as shown in *Figure 1*. During charging, surplus heat (Q_{ch}) from solar or industrial waste heat is added to the energy storage reactor through a suitable heat transfer fluid (HTF), causing water vapour to be released from the hydrous salt through an endothermic dehydration reaction (*Figure 1a*). The released water vapour is then stored separately in an evaporator/condenser unit. Whenever the stored heat is required again, it can be retrieved by sending the water vapour back to the reactor, facilitating the exothermic hydration reaction. The released heat (Q_{dis}) can be utilised for heating applications by employing a suitable HTF circulating through the reactor.

For the proposed sorption system, the design of the reactor is crucial since it facilitates hydration (exothermic) and dehydration (endothermic) reactions, both involving heat exchange with the HTF. These processes involve interconnected heat and mass transfer, directly influencing the system's performance metrics, such as specific power and energy storage capacity. However, reactor design presents significant challenges due to the low thermal conductivity and low permeability of the salt hydrates [9].

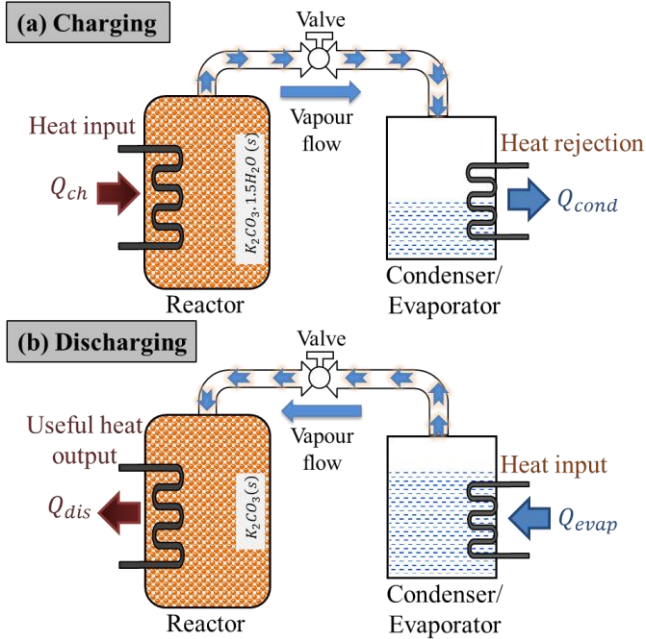


Figure 1: Schematic representation of the proposed SHS system in closed operating mode.

In a recent study by the present authors [1], a generalised scaling procedure was established for estimating the critical length scales for optimal bed design. Results show that there exist critical regions in the porous reactor bed where the reaction doesn't occur due to limited thermal diffusion and vapor transport rates. In the present work, a laboratory-scale experimental setup is designed and developed for conducting experimental studies on the salt hydrate of choice ($K_2CO_3 \cdot 1.5H_2O$) for its implementation in a closed-cycle SHS system. The main objective of this study is to investigate the performance of the developed system.

Design of SHS System

This section highlights the design features and constructional details of the developed system, designed to store approximately 3.0 MJ (0.833 kWh) of energy.

System Layout

Figure 2a illustrates the schematic of the developed laboratory-scale SHS system. The primary components include a reactor or energy storage bed (ESB) and an evaporator/condenser (E/C), interconnected by a pipe for vapour passage. A manually operated vapour valve controls the flow of water vapour during charging and discharging reactions. Both the reactor and E/C unit are linked to individual temperature control baths, ensuring constant temperature through the circulation of HTF, specifically a 50:50 v mixture of Ethylene Glycol/Water. This HTF is selected for its suitability

for the required charging ($\geq 100^\circ C$) and discharging ($\geq 5^\circ C$) temperatures. The system comprises three circuits: vapour, water, and reactor and E/C HTF. Pressure sensors at the reactor and E/C unit, along with eight thermocouples at various locations, facilitate measurement. The individual components are detailed in the following subsections.

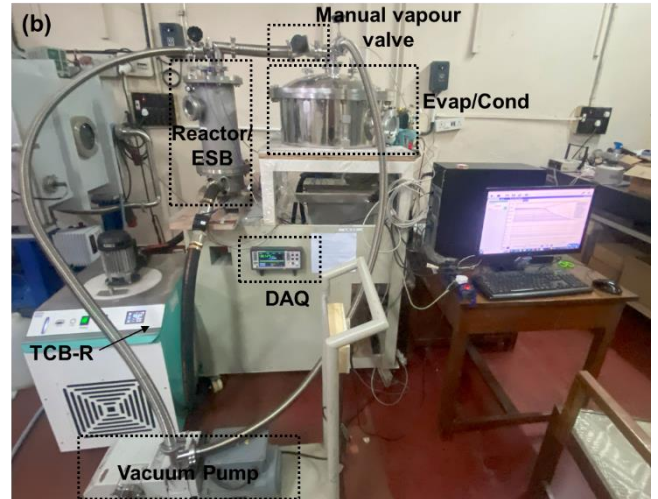
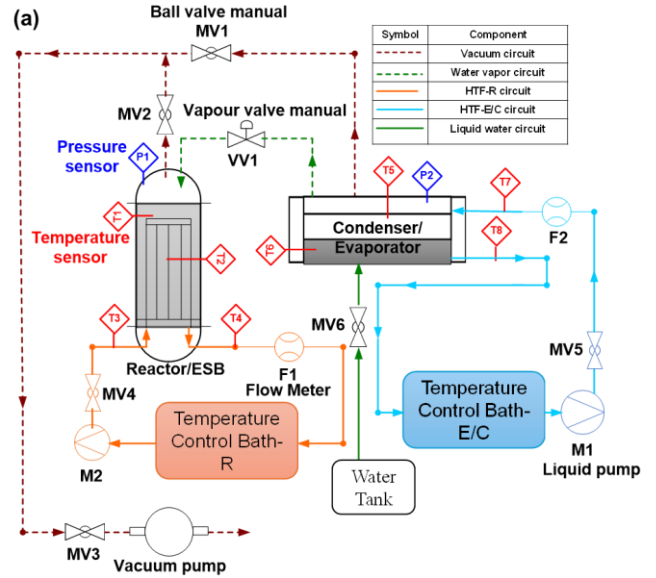
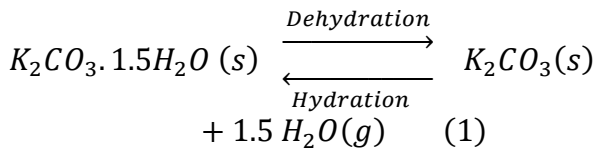


Figure 2: Laboratory-scale experimental setup: (a) Schematic representation, and (b) Photograph of the setup without thermal insulation.

Energy Storage Reactor

An energy storage reactor is designed to accommodate the reactive salt ($K_2CO_3 \cdot 1.5H_2O$) during charging as well as and discharging processes. Salt stores energy based on reversible thermochemical reaction given by Equation (1):



Calculations, concerning 3 MJ of heat release during the discharging (hydration) process led to a mass of 4.5 kg reactive salt. The storage reactor is constructed as a shell and tube-type heat exchanger, with reactive salt particles located on the shell side and HTF flowing through tubes. The shell and tube configuration is chosen to facilitate easier vapour flow through the bed, albeit at the expense of available heat transfer area, owing to the absence of fins. Additionally, the absence of fins allows for straightforward packing of reactant salt particles into the reactor from the top. Tube pitch and height are determined based on insights gained from scaling analysis [1] and numerical results. A thin annular mesh, as depicted in *Figure 3* (sectional view), is inserted between the shell and copper tube assembly. This mesh serves two purposes: holding the potassium carbonate salt particles and creating a small annular vapour passage, facilitating predominant vapour transport across the diameter of the bed. Thermowells with a 3 mm inner diameter are welded to the reactor's top, providing guidance for thermocouples (TC) within the bed and enabling easy insertion and extraction of TC without compromising the vacuum.

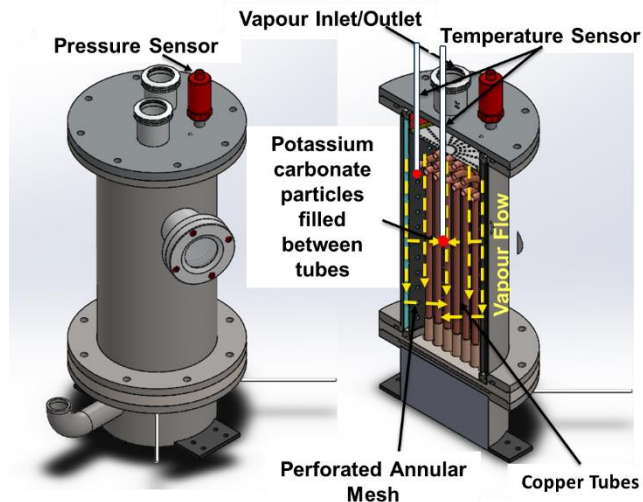


Figure 3: CAD model of energy storage reactor with annular mesh; arrows depict vapour flow direction.

Evaporator/Condenser Unit

The reactor bed is connected to an evaporator/condenser unit, as illustrated in *Figure 2*. This unit must be meticulously designed to ensure it supplies adequate water vapour to the energy storage reactor during the hydration reaction and effectively condenses the vapour at an appropriate rate during the

dehydration reaction. The timing and rate of evaporation and condensation should align with those of the hydration and dehydration reactions to prevent limitations on the reactor's performance due to insufficient vapour supply or removal. To meet these criteria, the length and pitch of the heat-exchanging coil are carefully chosen to ensure sufficient heat supply/removal during evaporation and condensation while minimising temperature differences at the coil's inlet and outlet. *Figure 4* provides a sectional view (CAD model) detailing both the external and internal aspects of the evaporator/condenser unit.

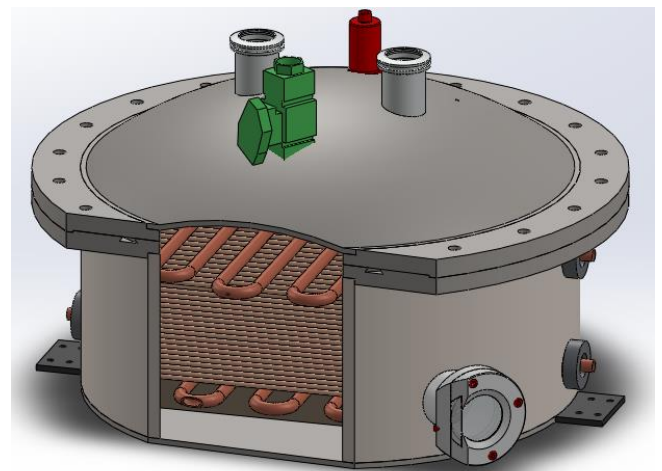


Figure 4: CAD model of the evaporator/condenser unit.

Experimental procedure

Potassium carbonate salt is inherently hygroscopic, meaning it can absorb moisture during packing and handling. Therefore, it's advisable to commence the cycle with a dehydration process. Following the dehydration reaction, only K_2CO_3 remains in the storage reactor at the start of a hydration cycle. The reaction gas side is evacuated to remove inert gases, and the steam pressure in the evaporator is adjusted accordingly.

To initiate the hydration reaction, the valve between the evaporator and the reactor is opened, allowing water vapour to enter the reaction chamber. The exothermic reaction commences, indicated by an increase in bed temperatures. Throughout the procedure, the HTF mass flow and inlet temperature remain constant. The vapour pressure is maintained until the complete reaction, indicated by a steady water level in the evaporator. The change in the evaporator's water level can be measured to estimate the percentage of salt reacted.

Results and Discussion

Experimental results of the charging and discharging processes are discussed in this section.

Charging (Dehydration) Process

Figure 5 illustrates temporal variation of the reactor bed temperatures and vapour pressure inside the reactor and condenser during the charging process. The condenser pressure is maintained at close to 1.2 kPa by supplying the HTF at 10°C. On the reactor side, the HTF is supplied at 90°C, leading to an increase in the bed temperature. The HTF supplies endothermic reaction heat to the salt bed, initiating the dehydration reaction, which releases water vapour. Since the vapour valve is initially closed, Figure 5 demonstrates that the vapour pressure inside the reactor bed increases (indicated by the black dotted line) with an increase in bed temperature. After approximately 15 minutes, the rate of increase in vapour pressure slows down due to a decrease in the dehydration reaction rate with increased vapour pressure. After 25 minutes, when the valve is opened, the vapour starts flowing towards the condenser, leading to a decrease in pressure inside the reactor bed. It is interesting to observe that the temperature also drops as soon as the vapour pressure drops inside the reactor bed. This may be due to an increase in the dehydration reaction rate with a decrease in vapour pressure, resulting in more absorption of heat.

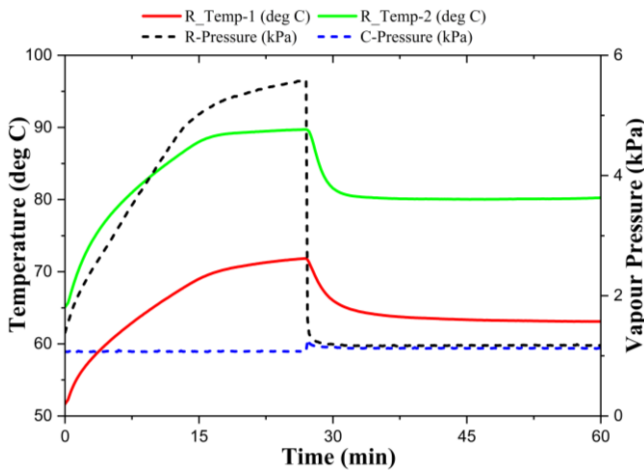


Figure 5: Temporal variation of reactor bed temperatures and vapour pressure during the charging process.

Discharging (Hydration) Process

Figure 6 illustrates the results of the discharging process when the evaporator pressure is maintained at 1.2 kPa by supplying HTF at 10°C. It can be seen from the graph that the reactor bed temperature increases instantaneously after opening the vapour valve, allowing vapour flow from the evaporator to the reactor bed. The maximum heat discharging temperature in this case is close to 50°C. The graph shows that initially, the temperature rise is faster, which slows down eventually after some time due to a decrease in

the rate of hydration reaction. The maximum temperature lift inside the reactor bed is 35°C at the bottom thermocouple (red line).

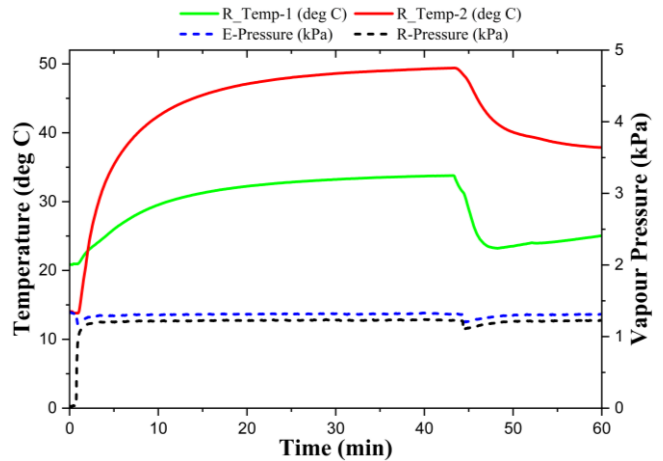


Figure 6: Temporal variation of reactor bed temperatures and vapour pressure during the discharging process at an evaporator pressure of 1.2 kPa.

Additionally, the vapour pressure was changed to 5 kPa in another experiment to observe the influence on the reachable temperature in the reactor bed. Figure 7 illustrates that the heat discharging temperature increases to 70°C in this case. Additionally, the slope of the bed temperature curve also increases because the rate of hydration reaction increases with an increase in vapour pressure, leading to more heat release. However, at high supply vapour pressure, the reactive salt may form an aqueous solution (deliquescence), thereby affecting the cyclability of the salt. The measured change in water level inside the evaporator indicates that 2.69 kg salt participated in the reaction resulting in the total estimated heat recovery of 1.77 MJ.

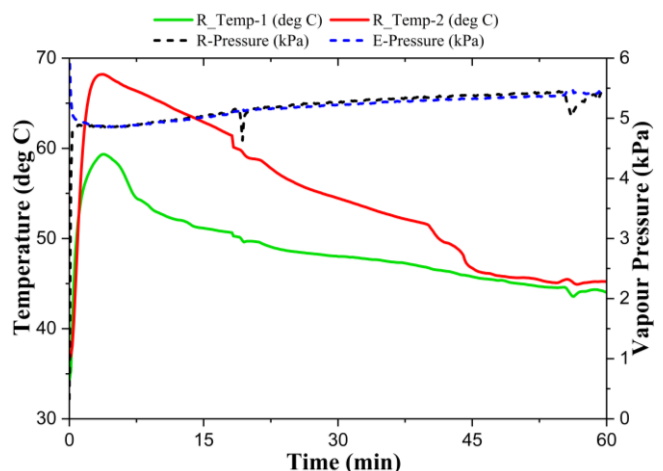


Figure 7: Temporal variation of reactor bed temperature and vapour pressure during the discharging process at evaporator pressure of 5 kPa.



Conclusions

A laboratory-scale experimental setup with 4.5 kg potassium carbonate salt is successfully developed and tested. Based on the measured water level in the evaporator, an estimated 1.77 MJ of heat is recovered during the discharging process. During the discharging process, low vapour pressure results in a decreased hydration rate and, hence, a decreased rate of release of the stored heat, leading to a decrease in maximum heat discharging temperature. However, for the very high vapour pressure, the release rate of the stored heat increases, but the reactive salt may form an aqueous solution (deliquescence), further affecting the reactive salt's cyclability.

Acknowledgment

Authors thank the Science and Engineering Research Board (SERB), Department of Science and Technology (DST), Government of India for funding support (Grant No. SPR/2021/000432-G) to carry out this work.

References

- [1] K. Jain, S. Dash, P. Dutta, A scaling procedure for designing thermochemical energy storage system, *Int J Heat Mass Transf* 220 (2024) 124981. <https://doi.org/10.1016/J.IJHEATMASSTRANSFER.2023.124981>.
- [2] IEA (2021), *Renewables 2021 – Analysis*, IEA, Paris, (n.d.). <https://www.iea.org/reports/renewables-2021> (accessed May 17, 2023).
- [3] H. Lund, S. Werner, R. Wiltshire, S. Svendsen, J.E. Thorsen, F. Hvelplund, B.V. Mathiesen, 4th Generation District Heating (4GDH): Integrating smart thermal grids into future sustainable energy systems, *Energy* 68 (2014) 1–11. <https://doi.org/10.1016/J.ENERGY.2014.02.089>.
- [4] X.S. Jiang, Z.X. Jing, Y.Z. Li, Q.H. Wu, W.H. Tang, Modelling and operation optimization of an integrated energy based direct district water-heating system, *Energy* 64 (2014) 375–388. <https://doi.org/10.1016/J.ENERGY.2013.10.067>.
- [5] L. Gao, J. Zhao, Z. Tang, A Review on Borehole Seasonal Solar Thermal Energy Storage, *Energy Procedia* 70 (2015) 209–218. <https://doi.org/10.1016/J.EGYPRO.2015.02.117>.
- [6] P.A.J. Donkers, L.C. Sögütoglu, H.P. Huinink, H.R. Fischer, O.C.G. Adan, A review of salt hydrates for seasonal heat storage in domestic applications, *Appl Energy* 199 (2017) 45–68. <https://doi.org/10.1016/J.APENERGY.2017.04.080>.
- [7] H. Deshmukh, M.P. Maiya, S. Srinivasa Murthy, Study of sorption based energy storage system with silica gel for heating application, *Appl Therm Eng* 111 (2017) 1640–1646. <https://doi.org/10.1016/J.APPLTHERMALENG.2016.07.069>.
- [8] B. Fumey, R. Weber, L. Baldini, Sorption based long-term thermal energy storage – Process classification and analysis of performance limitations: A review, *Renewable and Sustainable Energy Reviews* 111 (2019) 57–74. <https://doi.org/10.1016/J.RSER.2019.05.006>.
- [9] W. Li, J.J. Klemeš, Q. Wang, M. Zeng, Salt hydrate-based gas-solid thermochemical energy storage: Current progress, challenges, and perspectives, *Renewable and Sustainable Energy Reviews* 154 (2022) 111846. <https://doi.org/10.1016/J.RSER.2021.111846>.

Development of a lifetime assessment approach for polyolefinic insulation materials in pit thermal energy storages

Lukas Peham*¹, Gernot M. Wallner¹, Per Alex Sørensen²
 1 Institute of Polymeric Materials and Testing - University of Linz,
 Altenbergerstraße 69, 4040 Linz, Austria
 2 PlanEnergi, Jyllandsgade 1, 9520 Skørping, Denmark
lukas.peham@jku.at

Abstract

Polyolefinic (PO) foams are used for the insulation of pit thermal energy storages (PTES). The main objective was to develop a lifetime assessment approach based on experimental ageing data, temperature loading profiles of PTES close to the lid and cumulative damages. PO foams of varying density and stabilizer content were exposed to dry and damp heat conditions. Accelerated ageing was performed at temperatures ranging from 75 to 105°C. Failure and endurance times were determined by tensile testing and evaluation of strain-at-break values. An Arrhenius model was applied to describe the temperature-dependent material ageing. Endurance times were extrapolated from elevated to service-relevant temperatures. For lifetime assessment a cumulative damage model was implemented considering the geometry of the foam insulation, temperature loading profiles and moisture- and temperature-dependent thermal conductivity values. For the seasonal storage in Dronninglund and the buffer storage in Høje-Taastrup lifetime values of 38 and 14 years were deduced, respectively. The investigations revealed a high potential for improvement of the long-term durability by adequate stabilization of the PO foam material.

Keywords: thermal energy storage, lid construction, foam insulation, lifetime model

Introduction

Heating and cooling, encompassing domestic hot water and space heating, constitute half of Europe's energy demand. While 66% of the thermal energy is still generated by fossil fuels, only 13% are generated by renewable energy sources (Mathiesen, 2017). To compensate fluctuating renewable energy sources and heat demand, large thermal energy storages are of utmost importance in district heating networks. Several PTES have been installed in Danish districts such as Dronninglund (60,000 m³), Høje-Taastrup (75,000 m³), Marstal (75,000 m³), Toftlund (85,000 m³) or Vojens (203,000 m³).

In pit thermal energy storages (PTES) hot water is stored in large, excavated basins. The side walls and the bottom is sealed against water loss with a liner made from either polyethylene (PE) or polypropylene (PP). The top of the PTES is covered with a thermally insulated floating lid (see Figure 1).

A high temperature resistant polyolefin liner is commonly used as water barrier layer. On top, several layers of polyolefin (PO) foam are protecting the energy storage from heat loss, followed by an extruded polystyrene (XPS) foam for structural

reasons. To control moisture transport in the lid structure the top insulation is covered by a semipermeable liner. For proper drainage gravel is placed on top with a higher amount towards the centre, where a rainwater pump is installed.

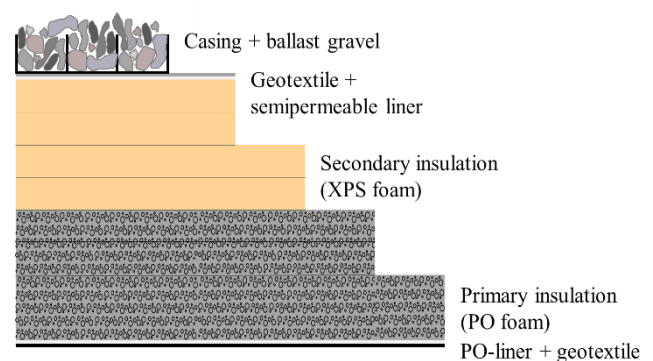
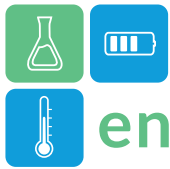


Figure 1: Structure of a floating lid implemented in the PTES of the Danish cities Dronninglund and Høje-Taastrup

The PO foam is situated closest to the top temperature of the PTES of up to 95°C. Therefore, an excellent temperature stability is required. The primary focus of this paper was to systematically investigate the long-term behaviour of various polyolefin foams under dry and damp heat conditions. To assess the lifetime of



PO foams in floating lid structures a semiempirical model was developed, based on temperature loading profiles of the PTES in the Danish cities Dronninglund and Høje-Taastrup.

Methodology

Materials, specimen and ageing conditions

Polyolefin (PO) foams were provided by NMC Termonova (Inkoo, Finland) with a thickness of 3 mm and a density of 28 or 30 kg/m³. The designation of the grades is reflecting the density (28 and 30). Furthermore, stabilized versions 30/1 and 30/2 were also investigated. Compared to grade 30/1 a factor 2 higher amount of the stabilizer package was added to formulation 30/2. Details on the PO materials and the stabilizer package are non-disclosed by the supplier.

10 mm wide stripes were cut and positioned in open frames for dry heat or in autoclaves for damp heat exposure, respectively (Figure 2). The autoclaves were partly filled with deionized water. Accelerated ageing was carried out at temperatures of 75, 85, 95 and 105°C in FED 53 heating chambers (Binder, Tuttlingen, Germany). After defined time intervals, specimen are removed, and degradation indicators are evaluated. So far, a maximum exposure time of 21,000 hours was achieved.

To evaluate ultimate failure, tensile testing was performed. Stabilizer- and polymer ageing was monitored by Differential Scanning Calorimetry (DSC). As ageing indicators strain-at-break and oxidation onset temperature were evaluated.

Tensile testing was carried out at ambient conditions (23°C, 50%rh) at a testing rate of 50 mm/min and a clamping length of 50 mm. Ultimate mechanical failure was classified, when strain-at-break dropped below strain-at-yield ($\epsilon_b < \epsilon_y$). For thermal analysis, samples of 2 mg were placed in a perforated 3 μ L aluminum pans. Thermograms were recorded from ambient to 250°C at a heating rate of 10°C/min. The cell was purged with synthetic air at a constant flow of

20 mL/min.

Moisture is significantly reducing the insulation performance. Therefore, water uptake was investigated by exposure of foam sheets to damp heat environment of 95°C and 100%rh. The mass was measured in the reference state and after specific time intervals until a plateau was reached. The moisture content was deduced normalizing the mass of the exposed to the reference samples.

Lifetime assessment modelling

The implemented lifetime estimation approach is based on a cumulative damage model considering the geometry of the foam insulation, extrapolation of endurance times, temperature loading profiles, moisture- and temperature-dependent thermal conductivity values and two failure criteria. The endurance time of exposed foam specimen was extrapolated to service-relevant temperatures using an Arrhenius relationship.

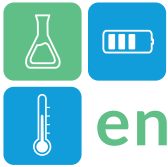
Based on the temperature distribution in the lid, the heat flow to the ambient is calculated. As first failure criterion a maximum heat loss by 20% increase is defined. The maximum operating temperature of XPS is limited by the onset of the glass transition temperature at 65°C. Hence, the second failure criterion is reached when the temperature limit is exceeded at the PO – XPS interface.

Degradation of the polyolefinic foam closest to the hot water surface, is associated with full embrittlement and failure of the first PO foam layer with a thickness of 3mm. As a consequence the temperature distribution across the lid structure is recalculated affecting the remaining endurance time of the subsequent PO foam layers. The thickness reduction resulting in a change of the temperature profile of the overall lid structure is taken into account. Temperature dependent damages of each layer are accumulated.

Results and discussion



Figure 1: Methodological approach for accelerated ageing testing of PO foams



Long-term behaviour of PO foam materials

Strain-at-break values of the investigated foam materials are shown in Figure 3 as a function of dry heat exposure time at 75, 85, 95 and 105°C. Open symbols indicate full embrittlement of the specimen. Initial strain-at-break values were 78% for grade 28 and 150% for grade 30. Tensile testing revealed a strain-at-yield of 10% for both base grades. Additional stabilization did not affect the mechanical properties in the reference state.

So far, full embrittlement was reached at 105°C after 2,400 hours for grade 28, after 4,100 hours for grade 30 and after 15000 hours for the stabilized grades 30/1 and 30/2. At lower exposure temperatures full

embrittlement was not reach after 21,000 hours. However, the end of the endurance time at lower temperatures is expected within the next few month. Based on the endurance time at 105°C and the current maximum exposure time at 95°C, a first extrapolation from elevated to service relevant temperatures was performed.

In order to get further insight on the effect of the stabilizer concentration, thermal analysis was conducted. The evaluation of the oxidation onset temperature did not show any significant differences between the formulations. It is assumed, that for both grades the maximum stabilizer content was exceeded. Previous ageing experiments revealed that stabilizer is

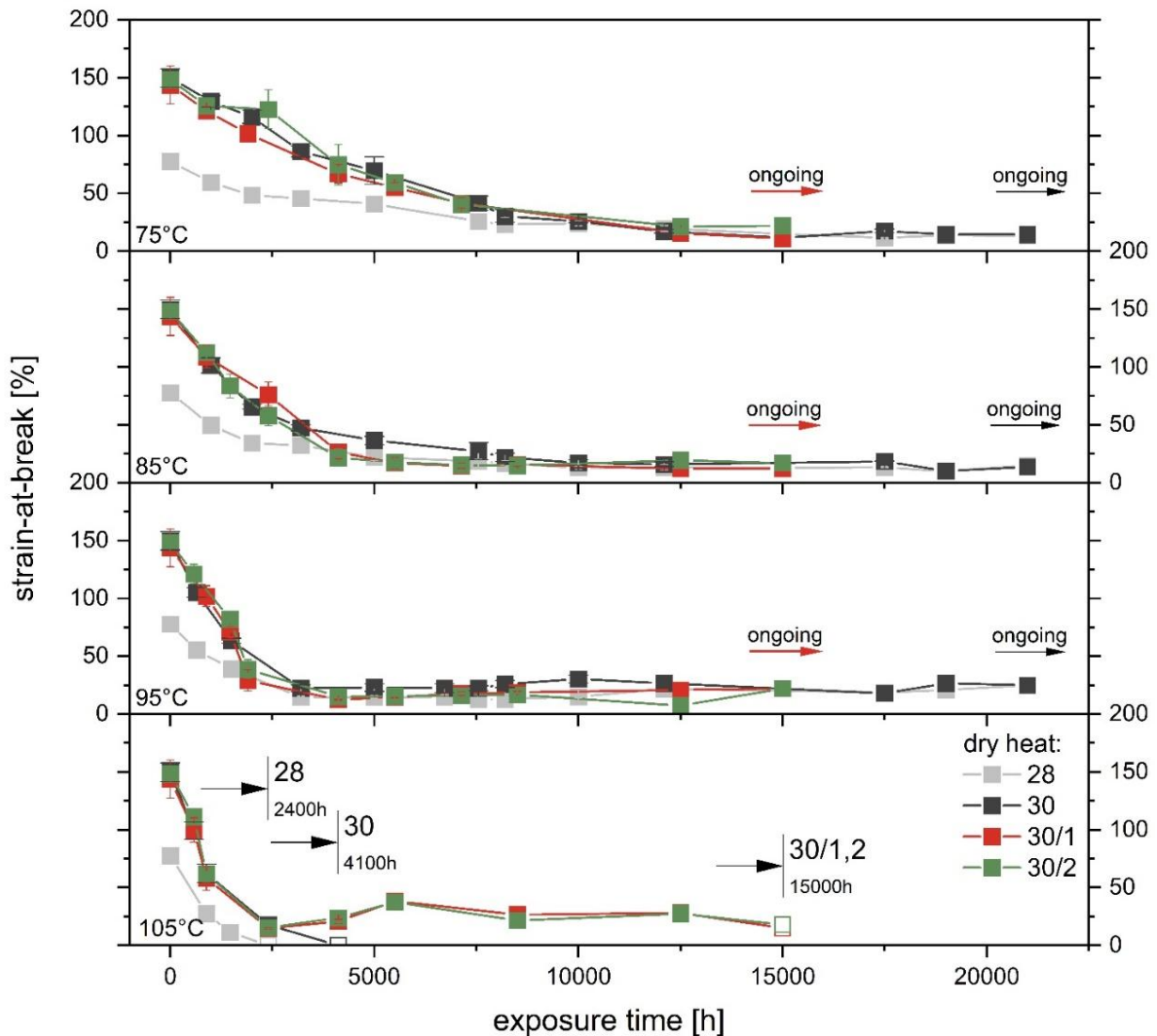


Figure 3: Strain-at-break values of unstabilized and stabilized, crosslinked PO foam specimen exposed to dry heat at temperatures ranging from 75 to 105°C



migrating and evaporating from the material (Peham et al. 2023).

Temperature profiles and environmental condition

Lifetime estimates calculated in this paper are based on the PTES in the cities of Dronninglund and Høje-Taastrup. While the PTES in Dronninglund is operating as a seasonal storage with estimated temperatures ranging from 44 to 85°C, the PTES in Høje-Taastrup is a buffer storage with a constant temperature on the top of 90°C (Figure 4). The average ambient temperature in the city of Copenhagen in 2022 is ranging from 2 to 24°C.

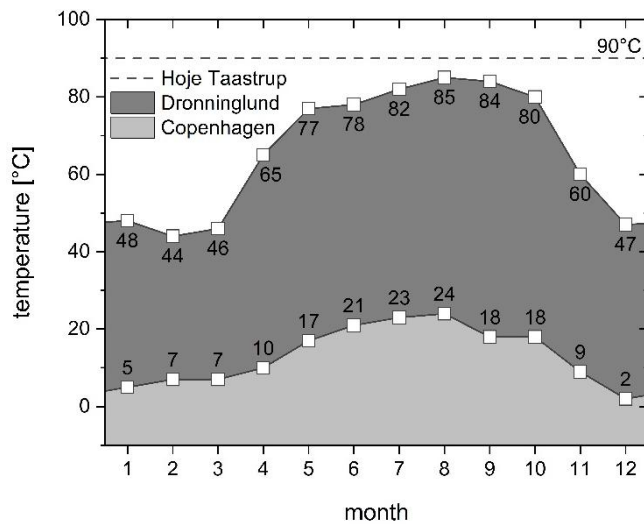


Figure 4: Temperature profiles of the pit thermal energy storages of Dronninglund and Høje-Taastrup and the monthly ambient temperature in Copenhagen in 2022

Extended water absorption tests indicated, that most of the moisture is taken up within the first 10 to 30 days. A plateau in water uptake at 2% was measured for PO foams. 10% was reported for XPS (Dechow & Epstein, 1978). It was assumed, that water is replacing the gases in the polymer foams, resulting in an increase of the thermal conductivity by 6% for PO and 40% for XPS (Dechow & Epstein, 1978).

Lifetime estimates

Although in the PTES of the Danish cities of Dronninglund and Høje-Taastrup the PO foam 30/1 is installed, lifetime estimates are based on grade 30. So far, not-sufficient long-term ageing data are available for stabilized grade.

The lid structure is made from 125 mm PO and 150 mm of XPS foam. In a first step, the endurance times for every temperature pair (monthly PTES top- and ambient- temperature) was calculated. The ultimate lifetime estimation was deduced based on the accumulation and weighing of damages at different interrelated temperature pairs by the frequency distribution. Lifetime values of 38 and 14 years were deduced for the PTES of Dronninglund and Høje-Taastrup, respectively. The investigations clearly revealed a high potential for improvement of the lifetime by adequate stabilization of the PO foam.

Conclusions

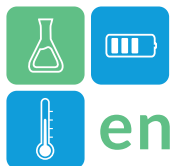
In order to estimate the lifetime of insulated lid structures for pit thermal energy storages (PTES) a calculation model based on extrapolation of long-term material behaviour, geometry, temperature conditions, moisture- and temperature- dependent thermal conductivity values and failure criteria was implemented. Considering a non-stabilized reference PO foam, lifetime values of 14 and 38 years was estimated for the lid structures of the PTES in the Danish cities of Dronninglund and Høje-Taastrup.

Acknowledgment

This research work was performed as part of the collaborative project Integrate 2. The financial support by the Energy Technology Development and Demonstration Program (EUDP) is gratefully acknowledged.

References

- Mathiesen, B.V. (2017) Heating and cooling: facts and figures, 2017. <https://heatroadmap.eu/heating-and-cooling-energy-demand-profiles> (accessed: 09.2023).
- Peham L. et al. (2023) Temperature dependent degradation of phenolic stabilizers and ageing behaviour of PP-R micro-specimen. Polymer Degradation and Stability. doi: 10.1016/j.polymdegradstab.2023.110311
- Dechow F.J. and Epstein K.A. (1978) Laboratory and Field Investigations of Moisture Absorption and Its Effect on Thermal Performance of Various Insulations. ASTM International. doi: 10.1520/STP35747S



Development of ceramic protective coatings for solid-solid Phase Change Materials

Paola Crocomo,^{1*} María Taeño,¹ Cristina Luengo,¹ Angel Serrano,¹ Stefania Doppiu,¹ Elena Palomo.^{1,2}

¹ Center for Cooperative Research on Alternative Energies (CIC energiGUNE), Basque Research and Technology Alliance (BRTA), Alava Technology Park, Albert Einstein 48, 01510 Vitoria-Gasteiz, Spain

² Ikerbasque, Basque Foundation for Science, 48013 Bilbao, Spain

*Corresponding author e-mail: pcrocomo@cicenergigune.com

Abstract

In a world experiencing transition toward renewable energy systems, thermal energy storage is of utmost importance. Phase change materials (PCMs) stand out as versatile solutions, using the storage and release of thermal energy through reversible phase transitions at almost constant temperature. PCMs which undergo solid-solid transitions lead to many advantages when compared to solid-liquid transitions. Within the scope of this study, ceramic mixtures were optimized to be used as protective coatings for an inorganic solid-solid PCM named LNS (LiNaSO₄), against mixture of molten salts in high temperature storage systems. Through XRD and STA analysis, the optimized ceramic mixtures were tested to evaluate their compatibility with the LNS material, whilst also working as a protection against the molten salts. Dip-coating techniques were chosen as the coating method, and its parameters were optimized to produce most efficient coatings. Final ceramic coatings were characterized by SEM, EDX and XRD analysis.

Keywords: Phase Change Materials, Ceramics, Protective coating

Introduction

Phase Change Materials (PCMs) offer compact solutions for Thermal Energy Storage (TES) systems. While many are familiar with the most traditional PCMs that shift between solid and liquid states, the solid-solid PCMs offer distinct advantages such as increased stability, easy handling and do not carry the risk of undergoing leakage, which translate into less CAPEX of the storage systems.

In a world experiencing transition toward renewable energy systems, the importance of TES rises. This paper addresses TES for Concentrated Solar Power (CSP) plants with molten salts, usually a mixture of sodium nitrate (NaNO₃) and potassium nitrate (KNO₃) (Piemonte and al., 2011), as heat transfer fluid (Prieto and Cabeza, 2021).

Latent heat storage based on solid-solid PCMs for CSP is being developed at CIC energiGUNE as an appealing alternative to double-tank molten salt technology. As established by Doppiu and al. (2019) and Taeño et al. (2024), the inorganic salt produced by the peritectoid reaction between a stoichiometric proportion of Li₂SO₄ and Na₂SO₄ (referred as to LNS in this paper) undergoes solid-solid phase transitions with high enthalpy values, which makes it a promising candidate to be applied as a TES system at high temperatures. Although, due to the novelty of this inorganic PCM, its

incompatibility with the nitrate-based molten salts has not yet been addressed.

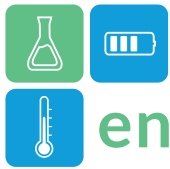
Ceramics are well known stable inorganic materials, having good mechanical strength, high hardness, and high temperature resistance (Belmonte, 2006). Therefore, within this study a ceramic coating is investigated, with the aim of protecting the solid-solid PCM material against commercial molten salts.

Materials and Methods

All reagents of analytical grade were purchased from Sigma-Aldrich and used without any previous purification.

The study and development of the ceramic coatings consists of:

- Development and optimization of ceramic mixtures: Various ceramic suspensions were prepared through the variations in solid content, solvent base, filler, dispersant, presence (or not) of other solids, type of clay and addition of film formers. The preparation of such suspensions was done through the blend of all the components by hand, followed by an activation of the ceramic component using an ultrasonic stirrer.
- Study of the compatibility between LNS and the ceramic materials: The compatibility tests were performed through the dip-coating of LNS pellets with ceramic mixtures. The LNS samples were analysed before and after the coating, through DTA and XRD, to



evaluate if there were any changes in structure or thermal properties.

- Study of the compatibility between different compositions of ceramic materials and commercial molten salts: The compatibility of different produced ceramic materials was tested against the presence of molten salts, in a muffle furnace, under 500°C for 100 hours. The compatibility was evaluated through Scanning Electron Microscopy (SEM) and energy-dispersive X-ray spectroscopy (EDX).
- Optimization of dip-coating parameters, such as: withdraw speed, immersion time, drying temperature, calcination rate, dip-coating cycles, etc.
- Characterization of the developed coatings and final coated PCMs (thickness, morphology, thermal properties, chemical composition) using X-ray diffraction (XRD), SEM, EDX and Simultaneous Thermal Analysis (STA), Differential Scanning Calorimetry (DSC) and Hot Disk.

Results and Discussion

Development and optimization of ceramic mixtures

The presence of different additives leads to mixtures with completely different properties, such as viscosity, drying time and contraction, cracks formation, etc. All these distinct properties influence and the formation of the coating layer.

The optimized ceramic mixture was the one that presented a fast-drying stage, good adhesion to the PCM material, absence of cracking during the drying/calcination process and homogeneous coating formation. The mixture which exhibits these characteristics is composed of 15wt% silica (SiO_2), 5wt% calcium carbonate (CaCO_3), 78wt% bentonite, 2% sodium silicate and 45% water.

Compatibility test between LNS and ceramic materials

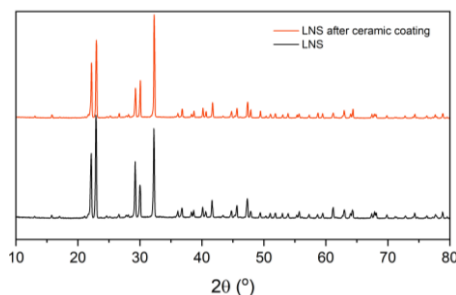


Figure 1. XRD analysis of LNS samples before (black line) and after (red line) ceramic coating.

No drastic changes were observed between the XRD analysis of LNS samples before and after ceramic coating, as it can be seen in Figure 1. Meaning that

ceramic coating does not affect the crystallographic structure, chemical composition, and physical properties of the PCM material.

Through STA measurements it is possible to observe Differential thermal analysis (DTA) at the same time as Thermogravimetric analysis (TGA). The DTA method allows to identify phase transitions which a sample undergoes by changes in temperature.

Figure 2 shows the DTA comparison between LNS samples before and after ceramic coating, where the sample afterwards (red line) presents only one solid-solid phase transition around 500°C. The enthalpy values observed at such phase transitions during the heating of the PCM material were 155.07 and 155.54 J/g for the samples before and after the ceramic coating, respectively. Proving that the coating does not affect the TES properties of the material.

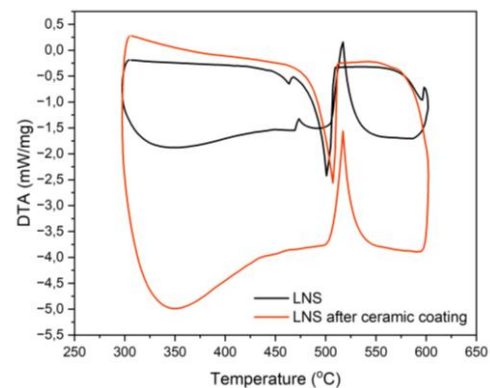


Figure 2. DTA of LNS samples before (black line) and after (red line) ceramic coating

The TGA comparison exhibited in Figure 3 establishes the high thermal stabilities of LNS material even after (red line) ceramic coating, displaying only 0.5% mass loss up to 100°C, which can be attributed to absorbed water, and no more considerable mass loss up to 600°C.

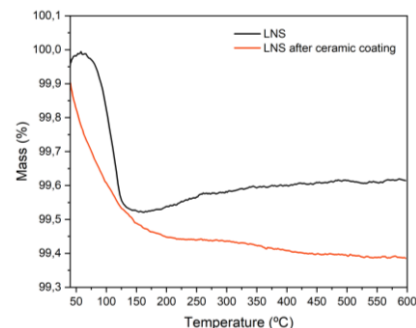


Figure 3. TGA of LNS samples before (black line) and after (red line) of ceramic coating.

Compatibility test between ceramics and molten salts

The compatibility was evaluated through SEM analysis with the help of an EDX detector. The ceramic mixtures were considered compatible in cases where no absorption of the molten salts was observed into the ceramic materials. Figure 4 shows the SEM images of samples of ceramic materials after compatibility test with molten salts under 500°C for 100h.

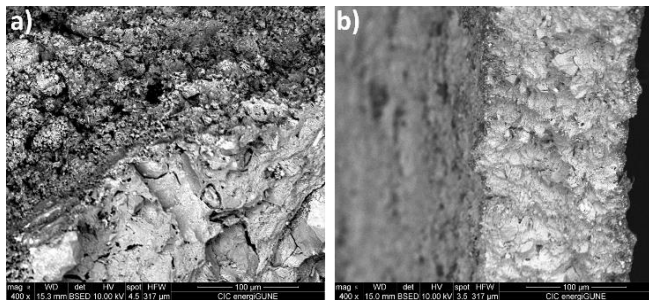


Figure 4. SEM images of samples a) 1 and b) 2 of ceramic coatings after compatibility test against molten salts.

Table 2 depicts the elements detected (through the EDX analysis) in the ceramic samples after compatibility test against molten salts. As mentioned before, molten salts are a mixture of nitrate (NO_3^{2-}) compounds. Therefore, the lack of detected Nitrogen (N) confirms in both cases (samples 1 and 2) that no molten salt was found absorbed in the ceramic coatings. All the other elements are found into the ceramic materials.

Table 1. Elements detected through EDX analysis in samples 1 and 2 after compatibility test against molten salts.

Element	Sample 1 (wt%)	Sample 2 (wt%)
Oxygen (O)	9.79	24.52
Sodium (Na)	1.88	1.75
Magnesium (Mg)	0.65	1.21
Aluminium (Al)	6.68	11.79
Silicon (Si)	45.38	35.35
Potassium (K)	14.29	17.16
Calcium (Ca)	21.35	8.21

Characterization of the developed coatings

The first LNS pellet was dip-coated using the suspension of the optimized ceramic mixture, with $10 \text{ mm}\cdot\text{s}^{-1}$ withdraw speed, 10 seconds immersion time, 24h drying at room-temperature (RT), 1h calcination at 565°C and second drying stage at 550°C for 10h. Figure 5 displays the SEM images of the surface of such ceramic coated LNS pellet, where it can be seen the roughness of the formed coating.

Through the SEM images of the cross-section of the coated LNS pellet, shown in Figure 6, the lack of homogeneity in the coating thickness was noticed. With thickness values varying between 130 and

$750 \mu\text{m}$. Nevertheless, as it can be seen in Figure 6a, the high adhesion of the coating layer to the PCM pellet seems very promising.

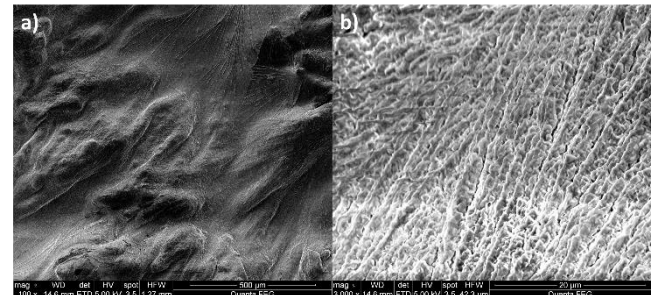


Figure 5. SEM images of surface of ceramic coated LNS pellet.

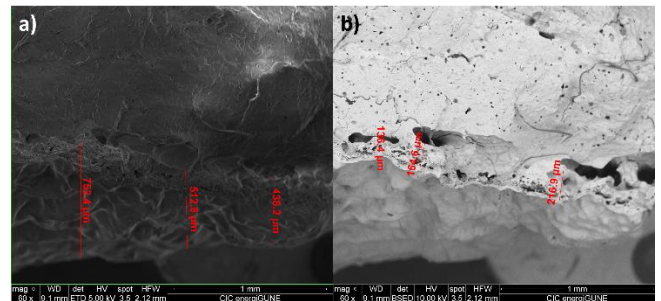


Figure 6. SEM images of cross-section of ceramic coated LNS pellet.

Future perspectives

The optimization of dip-coating parameters is necessary to evaluate how the different parameters will influence on the formation of the coating layer. Such study will be carried out in the near future, followed by the full structural and thermal characterization of the final coated materials.

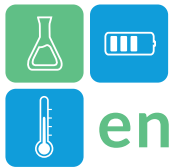
Conclusions

Ceramics are well known stable inorganic materials, having good mechanical strength, high hardness, wear resistance, high temperature resistance and relatively low density. In this work ceramic mixtures were used successfully as protective coatings of PCM materials, against reaction/degradation in contact with molten salts. The physicochemical characteristics of the developed coatings were established. Additionally, soon, the optimized dip-coating parameters will be determined, followed by the full characterization of the developed coating and final coated materials. The final materials (coated LNS) will be thoroughly studied to evaluate the effect of ceramic coating in the thermal properties of the PCM material, through the characterization of heat capacity and thermal conductivity after coated.



References

- Belmonte (2006). Advanced Ceramic Materials for High Temperature Applications. *Advanced Engineering Materials* 2006, 8, 693.
- Doppiu, S. and al. (2019) The $\text{Li}_2\text{SO}_4\text{--Na}_2\text{SO}_4$ System for Thermal Energy Storage. *Materials* 2019, 12, 3658.
- Guillot, S. et al. (2012) Corrosion effects between molten salts and thermal storage material for concentrated solar power plants. *Applied Energy* 2012, 94, 174.
- Piemonte, V. et al. (2011) Life Cycle Assessment of a high temperature molten salt concentrated solar power plant. *Solar Energy* 2011, 85, 1101.
- Prieto, C. and Cabeza, L. F. (2021). Thermal energy storage with phase change materials in solar power plants. Economic analysis. *Journal of Energy Storage* 2021, 43, 103184.
- Taeño, M. and al. (2024) Improved Thermophysical and Mechanical Properties in LiNaSO_4 Composites for Thermal Energy Storage. *Nanomaterials* 2024, 14, 78.



Development of microencapsulated phase change material with Zn-10 mass% Al alloy core for heat utilization around 400 °C

Takahiro Kawaguchi^{1,2 *}, Melbert Jeem², Takahiro Nomura²

1 Division of Materials Science and Engineering, Graduate School of Engineering, Hokkaido University, Kita13 Nishi8, Kita-ku, Sapporo, Japan

2 Center for Advanced Research of Energy and Materials, Faculty of Engineering, Hokkaido University, Kita13 Nishi8, Kita-ku, Sapporo, Japan

*Corresponding author e-mail: kawataka@eng.hokudai.ac.jp

Abstract

Latent heat storage (LHS) by alloy phase change material (PCM) is promising for heat utilization at medium-to-high temperatures ranging from 300-500 °C. Microencapsulated PCM (MEPCM) consisted of an alloy core and oxide coating have many advantages such as enhanced resistance between the liquid alloy and structure material, as well as the ability to integrate with particle materials. In this study, MEPCMs with Zn-10 mass% Al alloy core were fabricated via a dry synthesis approach. The prepared MEPCMs had a latent heat capacity of 81.06 J g⁻¹ and cyclic durability over 300 cycles. The Zn-10 mass% Al MEPCM is expected to be suitable for heat applications in medium-to-high temperature range.

Keywords: Latent heat storage, Microcapsule, Alloy phase change material

Introduction

In recent years, the significance of thermal energy storage (TES) has escalated, primarily due to its capacity to store heat, which is crucial in stabilizing the fluctuating heat outputs originating from industrial processes and renewable energy sources. Currently, the dominant method for such heat utilization involves sensible heat storage (SHS) technology, which relies on specific heat of materials. However, the development of TES materials with superior heat storage capacity offers a viable pathway for system space reduction. This potential benefit arises from the comparatively lower heat storage capability of current SHS technologies (Nomura. and al., 2010).

Latent heat storage (LHS) using solid-liquid phase change of phase change material (PCM) is recognized for its capacity to store heat at constant temperature alongside a superior heat storage capacity. At temperatures below 300 °C, organic PCMs have been predominantly utilized. On the other hand, molten salts and alloys were mainly proposed as suitable PCM for medium-to-high temperature ranges (300-500 °C). In particular, alloys have garnered attention in this domain due to their higher thermal conductivity compared to molten salts (Fernández and al., 2017). However, melting alloy PCMs exhibit low corrosion resistance, hence necessitating careful consideration of their reactive interactions with structural materials.

Microencapsulated PCM (MEPCM) comprising an alloy core and oxide coating can prevent corrosion reaction. Furthermore, MEPCM offers the versatility to combine with other materials. This includes the use of sintering aids to make composite materials and the incorporation of catalyst particles, which are instrumental in managing the thermal aspects of catalytic reaction. Therefore, MEPCM represents an innovative material with the potential to facilitate novel heat applications, particularly in the medium-to-high temperature range.

In this study, we attempted to fabricate MEPCM with a Zn-10 mass% Al core. This process involved a dry synthesis approach—the high-speed impact blending method (HIB) method to mechanically adhere a precursor coating to the alloy particles, followed by a high-temperature heat-oxidation treatment to achieve a stable oxide coating.

Materials and method

Raw materials

Zn-10 mass% Al alloy spherical particles (Median diameter:35.2 μm, density:6.09 g cm⁻³, latent heat capacity:121 J g⁻¹, solid-liquid phase change temperature:382-431 °C, Hikari Material Industry Co. Ltd.) were used as raw core material of the MEPCM. AlOOH particles (Median diameter:0.6 μm, density:3.07 g cm⁻³, Taimei Chemicals Co., Ltd.) were purchased for the coating material of the MEPCM.

High-speed Impact Blending (HIB) method

Firstly, Zn-10 mass% Al alloy particles were adequately mixed with 20 vol.% of AlOOH for 10 min. This ensures a weak attachment of the AlOOH particles to the surface of the alloy particles. Following, 20 g of the mixed particles were inserted to a hybridization system (Nara Hybridization System, Nara Machinery Co., Ltd.), where high-speed rotating blades attached to a rotor enabled collision of those particles, giving rise to the High-speed Impact Blending (HIB). During HIB, the rotor speed was 80 m s^{-1} and sustained for 3 min.

Heat oxidation treatment

In order to obtain a stable oxide coating, 150 mg of the HIB-treated MEPCM were oxidized at $800 \text{ }^\circ\text{C}$ for 3 h in O_2 flow by thermogravimetric analysis and differential scanning calorimetry (TGA-DSC).

Observation and analysis

Observation and analysis of the prepared MEPCM precursors and MEPCM were conducted by field-emission scanning electron microscopy (FE-SEM), X-ray diffraction (XRD), and TGA-DSC. Then, the cyclic durability of the PCM, encompassing 300 cycles of liquid and solid phases was assessed using TGA-DSC. The cyclic test was conducted over a temperature range of $300\text{-}500 \text{ }^\circ\text{C}$ at $50 \text{ }^\circ\text{C min}^{-1}$, and in an air flow.

Results and Discussion

Figure 1 shows the SEM image of the MEPCM after the heat-oxidation treatment. Notably, the MEPCMs retained their spherical shape, enduring both mechanical impact of the HIB process and elevated temperature surpassing the melting point of Zn-10 mass% Al alloy by the heat-oxidation treatment. In addition, strong aggregation or fusion between particles were not observed after each treatment. From the XRD measurement, the peaks derived from the Zn-10 mass% Al PCM core were confirmed. In addition, ZnO and $\alpha\text{-Al}_2\text{O}_3$ were detected from the XRD pattern. Moreover, the encapsulated structure, comprising the alloy core and oxide coating was proved by the cross-sectional observation of the MEPCM. This analysis confirmed that the alloy core within the MEPCM remained intact even after the heat-oxidation treatment.

Figure 2 shows the DSC curves of the as-prepared and 300 cyclic-tested MEPCM during heating. Endothermic peaks were observed at $276 \text{ }^\circ\text{C}$ and $378\text{-}420 \text{ }^\circ\text{C}$. According to the Zn-Al phase diagram, these peaks correspond to solid-solid and solid-liquid phase change of the alloy, respectively. In particular, the latent heat capacity calculated from the peak at $378\text{-}420 \text{ }^\circ\text{C}$ was 81.06 J g^{-1} . After the 300 cyclic tests, the

shape of the MEPCMs retained. In addition, the latent heat capacities and peak temperatures of the cyclic tested MEPCM in Figure 2 were preserved from as-prepared MEPCM.

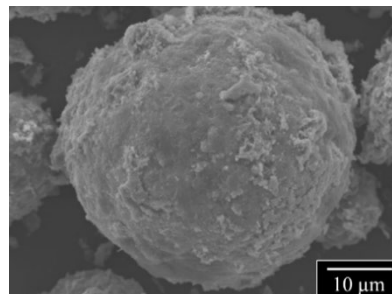


Figure 1: SEM image of MEPCM after heat-oxidation treatment.

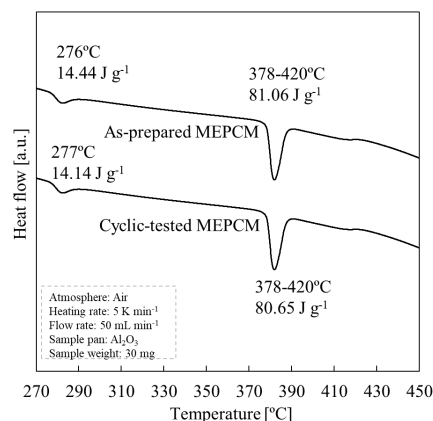


Figure 2: DSC curves of as-prepared and cyclic-tested MEPCM.

Conclusions

In summary, the MEPCM with the Zn-10 mass% Al core and oxide coating was fabricated by the HIB treatment and heat-oxidation treatment. The MEPCM had the latent heat capacity of 81.06 J g^{-1} and heat storage performance was retained after 300 cyclic tests. These results suggest the potential application of Zn-10 mass% Al MEPCM in heat utilization around $400 \text{ }^\circ\text{C}$.

Acknowledgment

This work was partially supported by JSPS KAKENHI and Grant-in-Aid for JSPS Fellows, Grant Numbers JP22K18993 and JP23KJ0032

References

- Fernández, A. I. and al. (2017) Considerations for the use of metal alloys as phase change materials for high temperature applications. *Solar Energy Materials and Solar Cells*. doi.org/10.1016/j.solmat.2017.06.054.
- Nomura, T. and al. (2010) Technology of latent heat storage for high temperature application: a review. *ISIJ International*. doi.org/10.2355/isijinternational.50.1229



Electrical tortuosities of honeycomb and triply periodic minimal surface (TPMS)-based porous structures for Power-to-Heat applications

Thorsten Ott^{1,*}, Volker Dreißigacker¹, Stefan Zunft¹

¹German Aerospace Center, Institute of Engineering Thermodynamics, Stuttgart, Germany

*Corresponding author e-mail: thorsten.ott@dlr.de

Introduction

In today's Power-to-Heat systems for heating gaseous heat transfer media using heaters and solid media thermal energy storage systems, indirect heating through metallic heating wires is common. These wires are embedded in a surrounding structure or supported by a structural framework. The generated Joule heat is transferred to the structures through thermal radiation and conduction, and to the heat transfer media through convection. Hence, such options are limited in terms of temperature, operating life and heat transport resistance. In contrast, directly-heated structures offer advantages in terms of power density and heat transport efficiency through the immediate heating of the solid storage and heater structures. The challenge now is to identify, in addition to suitable materials capable of operating at high temperatures, geometric structures that exhibit an appropriate/adjustable electrical resistance depending on the application while simultaneously achieving high specific surfaces for high convective heat transport efficiency at moderate pressure losses, requiring certain void fractions. The goal is, therefore, to capture geometric influences on the effective electrical resistance of porous structures and derive efficiently directly-heatable geometric structures from them. Due to their high specific surfaces and geometric variability, conventional honeycomb and TPMS structures are thus favored options being investigated for this purpose.

Method

Due to the multitude of possible geometric options, a dimensionless parameter for the purpose of comparison, the electrical tortuosity, is used to identify efficiently directly-heated structures. The electrical tortuosity is the ratio of the resulting effective ohmic resistance of a porous structure to the resistance of the appropriate solid body having identical external dimensions. It serves to capture the geometry-dependent electrical resistance. This geometric and material-independent parameter allows for computationally efficient investigation of large-scale structures without depicting the entire structure in detail. Therefore, the effective electrical resistance is determined using finite element analysis (FEA) by depicting representative elementary cells (the smallest repeating structure) of various TPMS (see Figure 1) and honeycomb structures in ANSYS and setting appropriate electrical boundary conditions.

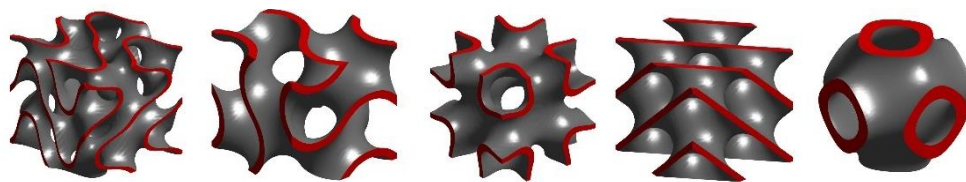
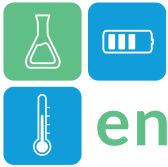


Figure 1: Within the scope of this work investigated types of TPMS structures (from left to right: Fischer-Koch-S, Gyroid, Schoen-IWP, Schwarz-D and Schwarz-P)

From these results, the electrical tortuosity is derived and parametrized as a function of central geometric parameters, such as void fraction and aspect ratio, which is new to the literature.

Results

Within the scope of this work, five different TPMS along with squared and circular honeycomb structures were examined. It has been found that the electrical tortuosity of both honeycomb and TPMS structures is unaffected by the area to volume ratio. In general, the results show that the electrical tortuosity rises with increased porosity with the values for the honeycomb structures slightly higher than those of the TPMS structures, which are very close to each other. For cubic TPMS structures with a porosity of 50 %, electrical tortuosities in the range of 2.6-2.8 can be achieved, meaning that the electric resistance compared to the solid body can be increased by the same factor. Furthermore, the results show that electrical tortuosities can be increased by varying the aspect ratio (non-cubic

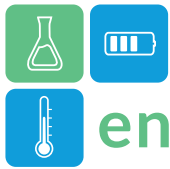


ENERSTOCK 2024
The 16th IEA ES TCP International Conference on Energy Storage
June 5–7, 2024
Lyon, France

designs) leading to anisotropic electrical tortuosities. Analyses of the current density distribution additionally allow for the selection of structures with nearly homogeneous heating.

Conclusions

Within the scope of the work, it was demonstrated that the electrical resistance can be adjusted through various geometric structures. The electrical tortuosity is used as a benchmark for evaluating the effective electrical resistance of porous structures. This contribution will present favored selected structures that exhibit not only high electrical tortuosities but also a homogeneous current density distribution, while offering high specific heat transport surfaces and a certain void fraction for moderate pressure losses. The deduced and parametrized equations for electrical tortuosity depending on central geometric parameters can be used as a computationally efficient tool for the design of Power-to-Heat-systems, both for use as heaters and as directly-heated thermal energy storage systems.



Electrified cascade PCM concept for Thermal Energy Storage in a CSP plant

Anton Lopez-Roman^{1,*}, M. Carmen Pavón-Moreno¹, Paolo De Giorgi², Luisa F. Cabeza³, Cristina Prieto^{1,*}

¹University of Seville, Camino de los Descubrimientos s/n, Seville, Spain

²Build to Zero, S.L., Gonzalo Jiménez de Quesada 2, Seville, Spain,

³GREiA Research Group, University of Lleida, Pere de Cabrera s/n, Lleida, Spain

*Corresponding author e-mail: antonlopez@us.es cprieto@us.es

Abstract

Non-dispatchable renewable technologies cannot completely decarbonize the electricity generation sector, while dispatchable technologies such as Concentrated Solar Power are too expensive for a wide commercial deployment. Aiming to reduce the cost of this technology, this document presents an electrified PCM thermal energy storage in cascade configuration with hybridization capabilities. This configuration can store energy at temperatures up to 610 °C using state-of-the-art CSP technology, which enables the use of advanced power cycles such as supercritical CO₂ cycles. A cascade configuration of the PCM is described to reduce the hysteresis effect generated due to the charge/discharge of the latent TES using a sensible current, and a final electrified step is proposed to ensure a maximum temperature output of the TES.

Keywords: Phase Change Material ; Thermal Energy Storage ; Concentrated Solar Power

Introduction

Renewable energy technologies have become a major topic due to global warming with expected cumulative investments between 13 and 38 USD trillion between 2016 and 2050 [1]. The growth among these renewable technologies has been led by solar photovoltaic (PV) and wind, with a final share of more than 57% of the total renewable installed capacity worldwide [2].

However, these technologies are non-dispatchable and as such their growth is limited in order to ensure proper management of the electricity grid [3]. Concentrated Solar Power (CSP), on the other hand, can be fully dispatchable once a Thermal Energy Storage (TES) system is installed. The cost of this technology is still too high to compete with other renewable technologies if the dispatchability of the generated energy is not taken into consideration [4], but the potential for cost reductions is also high.

Advanced thermal cycles such as supercritical CO₂ cycles can further increase the efficiency of this technology and reduce its costs, but to do so, temperatures up to 600 °C are required. The state-of-the-art TES technology, solar salt storage in direct configuration in two tanks for CSP plants in tower configuration, can store energy up to 565-580 °C, not enough for the supercritical CO₂ power cycles to be cost-effective.

In this work, an innovative thermal energy storage based on Phase Change Material (PCM) is presented,

able to reach operating temperatures up to 610 °C and enabling the use of supercritical CO₂ power cycles. This TES addresses the low thermal conductivity of PCM by using metal wools [5], and include internal electric heaters to work as a power-to-heat reservoir, further increasing the capacity factor of the plant while improving grid stability services at the same time. These electric heaters grant the CSP plant the ability to hybridise with other collocated renewable technologies, typically photovoltaic, or even from the grid with PPAs.

Plant concept

The proposed power plant has the same configuration as the typical CSP plant: i) a solar field, ii) a thermal storage system, iii) a heat exchanger and iv) a power cycle. In the solar field (i), the energy from the sun is concentrated using mirrors called heliostats into a receiver, where the energy is transferred to a heat transfer fluid (HTF). The HTF transfers the heat to the storage system (ii) or to the power block (iv) through the heat exchanger (iii). Thanks to the use of electric heaters embedded in the TES, this plant can easily hybridize with a collocated photovoltaic plant or take advantage of excess renewable energy from the grid (Figure 1).

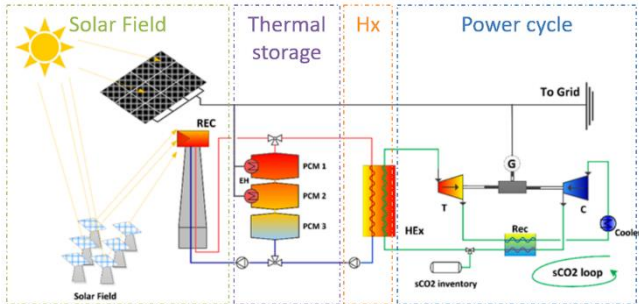
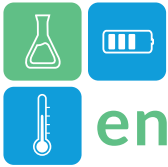


Figure 1 CSP plant configuration

The HTF selected for the proposed plant is the same as most CSP plants in tower configuration use worldwide, solar salt (40/60 wt% $\text{KNO}_3/\text{NaNO}_3$). This binary salt has excellent properties and is economically viable, but its maximum operating temperature is limited to a degradation phenomenon that occurs when the salts are kept at high temperatures for a prolonged period of time. This degradation mechanism is time-related, as described by Bell et Al. [6] and McConohy et Al. [7] and thus, the authors propose to only use the solar salts as HTF and store the energy in an indirect system based on PCM. This configuration allows to increase the maximum operative temperature of the salts up to 610°C for small periods of time without degradation.

TES

The proposed TES configuration is based on latent heat storage using phase change materials. The advantage of the high energy density of latent heat storage and the typical affordable cost of the materials is challenged by their low thermal conductivity, which poses a threat to the commercial viability of the solution. Several researchers have been actively working on this topic and have proposed different solutions such as the use of nano-additives, fins, or graphite foams [8], [9], [10]. All these options have their advantages, but they have an important impact on the final cost of the solution. Metal wools, on the other hand, are cheap, do not impose a large volume increase and can strongly increase the thermal conductivity [5]. This thermal conductivity enhancement is anisotropic, allowing the horizontal direction in vertical tanks to be favoured and thus promoting a thermocline behaviour.

One of the advantages of using latent heat energy is its capability of providing energy at constant temperature. This is very useful for certain purposes but becomes a liability when the HTF works only in the sensible phase. When a PCM is charged with a sensible current, the temperature of the HTF has to always be higher than the temperature of the PCM and the opposite when

discharging. As it can be seen in Figure 2, this creates a thermal hysteresis between the charge and discharge stages, reducing the maximum output temperature of the tank, reducing the tank efficiency, and hindering cyclic operations. The solar salt used as HTF has very strict temperature limits of operation: 280°C as lower limit due to freezing issues and 610°C as upper limit due to degradation phenomena. The thermal hysteresis between charge and discharge becomes, in this way, a major drawback for the use of PCM storage in the CSP industry. In addition to this issue, the high temperature difference of up to 300°C at the start of the charge or discharge phases between the PCM and the HTF poses a mechanical problem with a difficult engineering solution. This can be partially mitigated by using only the latent regime of the PCM, at the cost of reducing the energy density and increasing the mass of PCM for the same energy output.

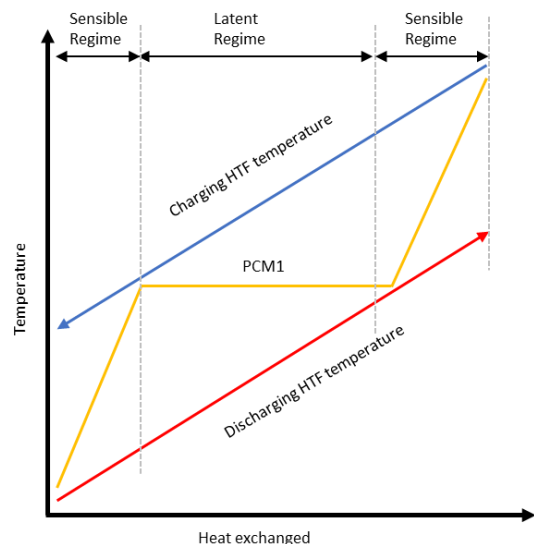


Figure 2 Heat distribution in a PCM during charge and discharge

Cascade configuration

To address both issues, the authors propose to use a cascade configuration made of several PCM that melts at different temperatures between the lower and upper HTF limits, as displayed in Figure 3. In this configuration, the thermal hysteresis is greatly reduced, as is the temperature difference among each step of the cascade, built in independent tanks called modules.

To reduce the hysteresis, each step should have a similar melting energy, which implies that each module will have a different amount of PCM to cover for the different melting enthalpies of the selected materials. Also, the temperature ranges should be evenly distributed. This also helps to reduce the mechanical stress due to temperature differences.

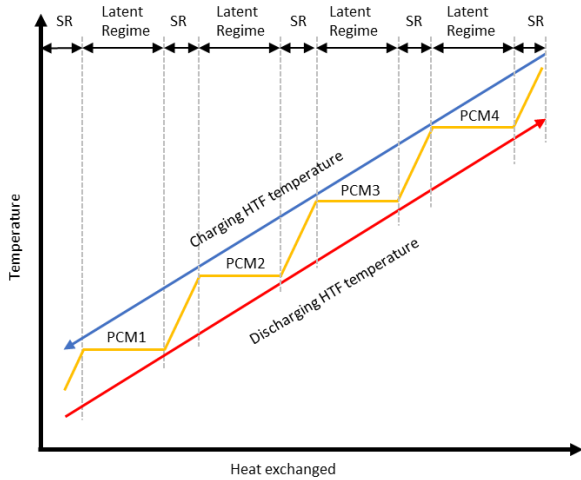


Figure 3 Heat distribution of a cascade PCM during charge and discharge

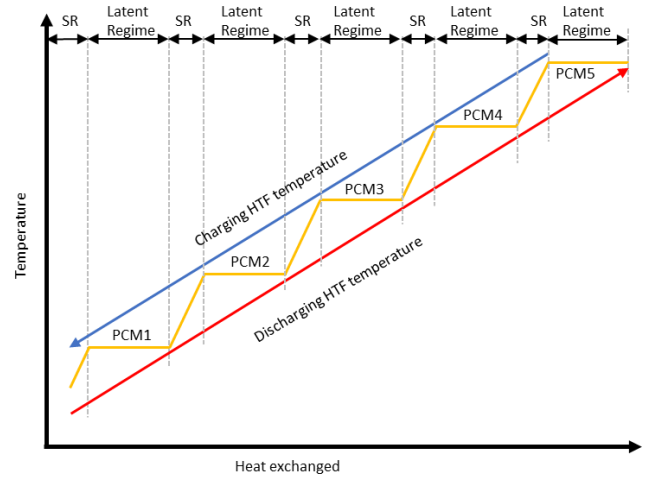


Figure 4 Heat distribution of an electrified cascade PCM during charge and discharge

When considering the availability of PCM in the required range, during the preliminary investigations of the HYBRIDplus project from which this investigation has been carried out, 67 PCM candidates have been identified. Studies performed up to date have discarded some of these materials due to hygroscopy, corrosiveness with metal wools, poor performance, or cost [11], but there are still several candidates under study.

Electrified cascade configuration

Each module is internally electrified, and as such the energy can be provided partially or totally by excess electricity from the collocated PV plant or from the grid. This hybridization does not affect the normal operation of the plant, but just increases its operative hours and thus its capacity factor. To further reduce the thermal hysteresis and guarantee the maximum temperature output from the TES, another PCM step is included in the cascade with a melting temperature above the maximum operating temperature of the salts (Figure 4).

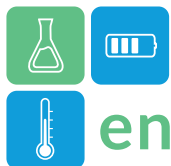
This PCM is not expected to be charged thermally, but only electrically, with thermal discharge. Using this configuration, the plant can operate at its maximum temperature defined by the degradation of the solar salt, maximizing the efficiency of the power cycle and ensuring constant temperature on the TES discharge.

Concept demonstration

The cascade concept proposed in this document is going to be demonstrated in a pilot plant under construction in the premises of the University of Seville. This pilot plant will test three PCM modules with different melting temperatures in cascade configuration using solar salts as HTF and with embedded electric heaters to move the technology up to a TRL5-6. For this pilot plant, the PCM modules will have a shell and tube configuration with the PCM on the shell and the HTF flowing through the tubes. All modules will use metal wools as heat enhancement method, favouring the horizontal plane in order to generate a thermocline inside the tank.

The electric heater capabilities will be emulated with three different configurations, one for each module: immersed heater, ohmic heating and magnetic charge [12]. To simulate the solar field, an inline electric heater for the solar salts used as HTF for the thermal charge will be installed, and the discharge energy will be dissipated to the atmosphere.

With the aim of learning from the experience, the installation of the PCM modules will be sequential. The low temperature module will be installed first, with an immersion heater for electrification. With the lessons learnt during the first tests, a second module will be installed, and then a third. For the second and third modules, different electrification methods will be studied. At the end of the experimentation campaign, it is expected to have the three modules working in cascade.



Conclusions

This document presents the electrified cascade concept used for the PCM-TES of the HYBRIDplus project. The cascade configuration reduces thermal hysteresis effect of charging/discharging a latent heat storage with a sensible current, reducing the temperature difference between charge and discharge. At the same time, the thermal stress is greatly reduced thanks to this configuration.

A proposal of improvement with the addition of a final electric stage for maximum output temperature is presented, ensuring temperatures up to 610 °C in the discharge and enabling the coupling with advanced supercritical CO₂ power cycles.

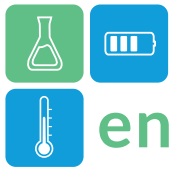
In order to obtain the optimum number of steps for the cascade configuration, a techno-economic analysis should be performed, since increasing the number of steps reduces the thermal hysteresis and increases performance but increases the complexity and the final cost. There is a minimum number of steps based on the maximum thermal gradient of the module for mechanical considerations.

Acknowledgment

This project has received funding from the European Union's Horizon Europe research and innovation programme under grant agreement No 101084182.

References

- [1] IRENA, *Global Renewables Outlook: Energy Transformation 2050*. Abu Dhabi: International Renewable Energy Agency, 2020.
- [2] IRENA, *Renewable capacity statistics 2023*. Abu Dhabi: International Renewable Energy Agency, 2023.
- [3] IRENA, *Electricity storage valuation framework: Assessing system value and ensuring project viability*. 2020.
- [4] I. Renewable Energy Agency, *Renewable power generation costs in 2021*. 2022. [Online]. Available: www.irena.org
- [5] C. Prieto, A. Lopez-Roman, N. Martínez, J. M. Morera, and L. F. Cabeza, 'Improvement of Phase Change Materials (PCM) Used for Solar Process Heat Applications', *Molecules*, vol. 26, no. 5, p. 1260, Feb. 2021, doi: 10.3390/molecules26051260.
- [6] S. Bell, T. Steinberg, and G. Will, 'Corrosion mechanisms in molten salt thermal energy storage for concentrating solar power', *Renewable and Sustainable Energy Reviews*, vol. 114, p. 109328, Oct. 2019, doi: 10.1016/j.rser.2019.109328.
- [7] G. McConohy and A. Kruiženga, 'Molten nitrate salts at 600 and 680°C: Thermophysical property changes and corrosion of high-temperature nickel alloys', *Solar Energy*, vol. 103, pp. 242–252, May 2014, doi: 10.1016/j.solener.2014.01.028.
- [8] C. Xu, H. Zhang, and G. Fang, 'Review on thermal conductivity improvement of phase change materials with enhanced additives for thermal energy storage', *J Energy Storage*, vol. 51, p. 104568, Jul. 2022, doi: 10.1016/j.est.2022.104568.
- [9] S. Tan and X. Zhang, 'Progress of research on phase change energy storage materials in their thermal conductivity', *J Energy Storage*, vol. 61, p. 106772, May 2023, doi: 10.1016/j.est.2023.106772.
- [10] C. Prieto, C. Rubio, and L. F. Cabeza, 'New phase change material storage concept including metal wool as heat transfer enhancement method for solar heat use in industry', *J Energy Storage*, vol. 33, p. 101926, Jan. 2021, doi: 10.1016/j.est.2020.101926.
- [11] F. R. Martinez Alcocer, E. Borri, S. Ushak, C. Prieto, and C. Luisa F., 'Corrosion effect analysis of inorganic compounds at high temperature for latent heat thermal energy storage application', in *13th National and 4th International Conference in Engineering Thermodynamics*, Castellon, Dec. 2023, pp. 743–745.
- [12] A. Lopez-Roman, P. De Giorgi, L. F. Cabeza, and C. Prieto, 'Electrically charged PCM thermal storage solution for CSP plants', in *13th National and 4th International Conference in Engineering Thermodynamics (CNIT)*, Castellon, Dec. 2023, pp. 25–28. doi: 10.5281/zenodo.10351777.



Energy Storage Systems and Renewable Integration: Pathways to Carbon Neutral Buildings

Gwangwoo Han^{1,*}, Min-Hwi Kim², Jong-Kyu Kim²

1 Korea Institute of Energy Research, Energy ICT Research Department, 152, Gajeong-ro, Daejeon, South Korea

2 Korea Institute of Energy Research, Renewable Energy System Laboratory, 152, Gajeong-ro, Daejeon, South Korea

*Corresponding author e-mail: gwhan@kier.re.kr

To achieve carbon neutrality in the building sector, this research explores the role of Energy Storage Systems (ESS), focusing on renewable energy integration, electrification, and balancing energy production with consumption. This study, conducted at the Korea Institute of Energy Research, analyses 2022 year-round data from a community of buildings post-transition to enhanced solar power and improved HVAC systems. Findings reveal that enhanced ESS capacity in South Korea's electricity tariff framework can unintentionally increase operational costs. This occurs as excess electricity, often more profitable when sold during on-peak hours, is instead stored in ESS, reducing potential peak grid sale revenues. However, in settings with no feed-in tariffs ($X_{\text{tariff}} = 0$), expanding ESS capacity is financially advantageous, substantially lowering costs through improved self-consumption. The research highlights a significant threshold for electricity cost savings as X_{tariff} decreases below 0.4. The study underlines the importance of well-considered policy measures to promote ESS adoption and renewable energy, which is essential for advancing carbon neutrality in the building sector.

Keywords: Building sector, Energy storage system, Renewable energy integration, Self-consumption

Introduction

Achieving carbon neutrality in the building sector is critical to responding to climate change (IRENA, 2023). Central to this challenge are three major strategies: firstly, increasing the share of renewable energy sources and integrating them into the existing power grid; secondly, transitioning from fossil fuel-based heating, ventilation, and air conditioning (HVAC) systems to electrical systems; and thirdly, resolving the mismatch between energy production and consumption to improve self-consumption rates, which in turn stabilizes the power grid's operation (IEA, 2023; IRENA, 2023).

This study concentrates on analyzing the third strategy, particularly examining the effects of energy storage systems (ESS) as a solution to the production-consumption mismatch. However, in countries like South Korea, the lack of financial penalties for sending electricity back to the grid, coupled with the absence of a profitable policy for arbitrage, has hindered the economic viability of ESS.

Our study addresses this challenge by focusing on a community comprising several types of buildings that

share energy, for which a year's worth of empirical data has been collected. Utilizing this data, we analyze the operational costs with the increased capacity of ESS and the varying rates for electricity fed back into the grid, offering insights into the economic and practical feasibility of such systems in a real-world context.

Methodology

The empirical study was conducted in an urban electrified energy community at the Korea Institute of Energy Research, comprising two residential buildings, one office building, and one experimental building. As of September 2021, this community underwent remodeling to transition from zero-energy to plus-energy buildings (An, 2023). This involved enhancing the proportion of solar power generation, strengthening building insulation, and improving HVAC facilities.

Figure 1 illustrates the actual energy community and its digital twin counterpart. The digital twin effectively visualizes the electricity produced and consumed in individual buildings, the charging and

discharging of the ESS, and the power inflow and outflow between the community as a whole and the grid. Figure 2 depicts the energy flow diagram among the facilities within the community. Electricity and heat generated from renewable sources are converted to the ESS or HVAC systems within the community and are then supplied to various electrical loads, as well as heating, cooling, and hot water demands.



(a)



(b)

Figure 1: Electrified energy community (a) Real-image (b) digital-twin environment

Data measured through an advanced metering infrastructure (AMI) is transmitted via various communication and programmable logic controller (PLC) modules and then minutely stored in a database within a data server. This study focuses on analyzing the effects of ESS based on one-minute interval operational data collected over the year 2022.

For the analysis of annual electricity costs, the tariff structure of South Korea referred to is outlined in Table 1 (KEPCO, 2023). The electricity rates of general type in South Korea vary seasonally and hourly, including on-peak, mid-peak, and off-peak power rates. Additionally, electricity generated from renewable sources enjoys cost-effectiveness without any penalty. In contrast, countries like those in Europe already have a feed-in penalty in place for sending electricity back to the grid and are progressively increasing this ratio (Stelt, 2018).

Therefore, this study compares how the annual electricity cost changes when the feed-in ratio increases from 0 to 1 and when the proportion of ESS increases, allowing for self-consumption of the produced electricity. For brevity in this research, the calculation of demand charge based on power output has been omitted.

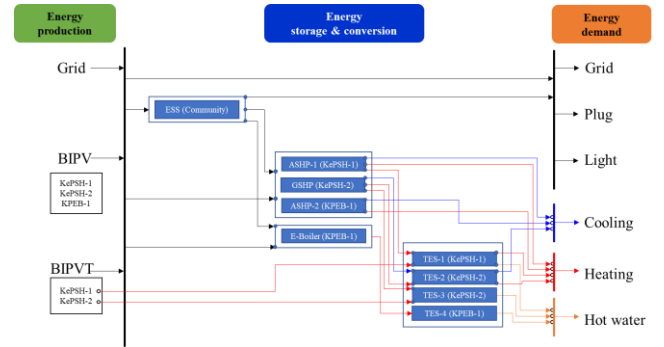


Figure 2: Energy flows between facilities

Table 1: Electricity tariff of South Korea (The date of application: 2023-11-09) (a) Energy charge [KRW/kWh] (b) Seasonal time zone breakdown (KEPCO, 2023)

Periods	Jun-Aug	Mar-May Sep-Oct	Nov-Feb
Off-peak	84.1	84.1	92.8
Mid-peak	135.3	91.5	123.2
On-peak	157.8	102.8	138.0

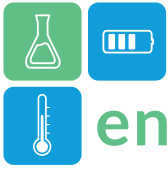
(a)

Periods	Jun-Aug	Mar-May Sep-Oct	Nov-Feb
Off-peak	22:00~08:00		22:00~08:00
Mid-peak	08:00~11:00		08:00~09:00
	12:00~13:00 18:00~22:00		12:00~16:00 19:00~22:00
On-peak	11:00~12:00		09:00~12:00
	13:00~18:00		16:00~19:00

(b)

Results and Discussion

The electric power mismatch (difference between demand and production) in the energy-sharing community, depicted in Figure 3, highlights the seasonal variance. As part of the case study, the community incorporated a 14 kWh capacity Li-ion battery-based ESS, strategically discharging during high-demand periods in the mornings and late afternoons and charging during peak solar hours around midday. The annual self-consumption rate, a key metric in our study calculated using Equation 1 (Salom, 2014), was 57.74%.



$$\gamma_{self,cons} = \frac{\min[\sum_{t=0}^t E_{self}, \sum_{t=0}^t E_{cons}]}{\sum_{t=0}^t (E_{prod} - (E_{ess,cha} - E_{ess,dis}))} \quad (1)$$

Where, $E_{self} = \sum_{t=0}^t (E_{prod} - (E_{ess,cha} - E_{ess,dis}) - E_{toGrid})$

This figure is significant as it represents how much the community relies on its own produced energy, utilizing it directly or storing it via ESS rather than exporting surplus to the grid. The higher the self-consumption rate, the more effectively the community utilizes its produced energy internally, reducing its dependency on external power sources.

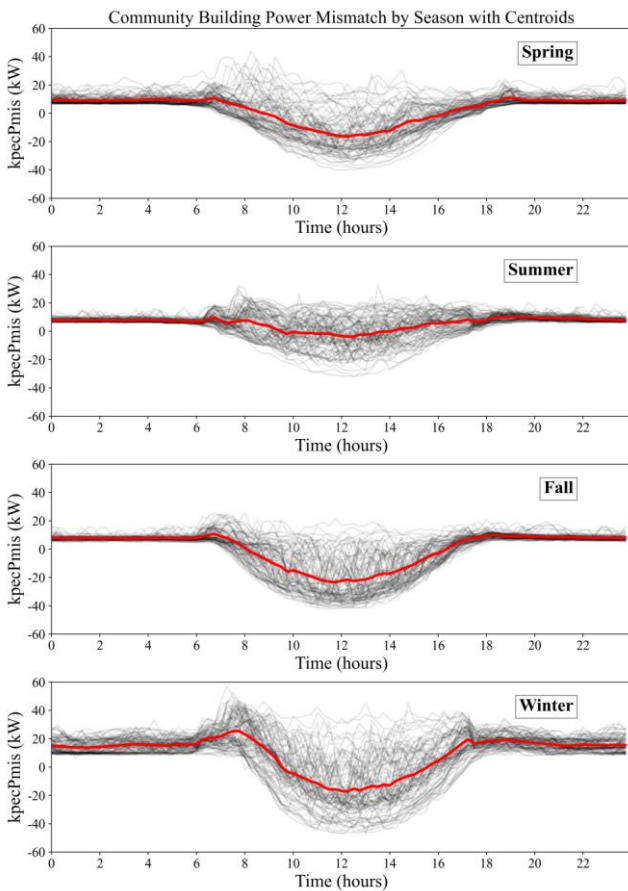


Figure 3: Power mismatch pattern by seasons (Redline: Centroid)

Figure 4 presents a case study analyzing the impact of varying the electricity feed-in tariff rate (X_{tariff}) and increasing ESS capacity. In the current scenario in South Korea, where X_{tariff} equals 1, increasing the ESS capacity from its current level (as in Case 1 to Case 3) paradoxically leads to higher operational costs. This is because the peak solar generation times (between 10 AM and 2 PM), which coincide with the on-peak periods in Korea, make it more cost-efficient to sell electricity to the grid than to store it in the ESS.

In an alternate scenario with X_{tariff} at 0, the dynamics shift dramatically. The inability to gain revenue from

grid exports means that the community's electricity costs could nearly double without an increase in ESS capacity. This scenario underscores the cost-effectiveness of using ESS to manage and utilize excess daytime energy. The result indicates that an ESS expansion to 100 kWh (as seen in Case 3) can increase the community's self-consumption rate by 14.52 percentage points, translating to a 14.3% annual electricity cost savings.

A comprehensive analysis of the impact of X_{tariff} changes and ESS capacity expansion on electricity cost savings reveals that until X_{tariff} drops to 0.8, increasing ESS capacity yields minimal economic benefits for the community. However, a significant difference (over 5%) starts to manifest when X_{tariff} falls below 0.4.

This study also acknowledges the current downward trend in Li-battery costs due to mass production. However, our analysis indicates that in certain countries, the economic feasibility of ESS deployment for the building sector remains constrained. One approach to artificially enhance ESS profitability is through the policy-driven reduction in X_{tariff} . However, this could counterintuitively impede the adoption rate of renewable energy in nations with a low renewable energy ratio, which could suppress carbon neutrality. Therefore, it is imperative that policies be implemented in tandem with the reduction in ESS prices and the proliferation of renewable energy.

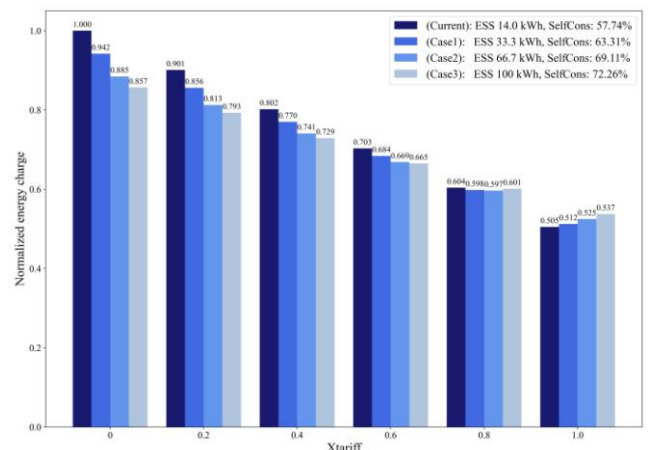


Figure 4: Community energy charge with feed-in-tariff rates and ESS capacities

Conclusions

In pursuing carbon neutrality, the building sector must focus on enhancing renewable energy integration, advancing electrification, and improving self-



consumption rates by addressing the mismatch between energy production and consumption for grid stability. Our study delves into the third aspect, examining the impact of ESS in achieving this goal. The empirical analysis, based on a year's worth of data from an energy-sharing community, reveals that increasing ESS capacity under the current South Korean electricity tariff system paradoxically increases operational costs due to more cost-effective grid sales during peak solar generation times. However, in scenarios without feed-in tariffs ($X_{\text{tariff}} = 0$), enhancing ESS capacity substantially reduces electricity costs by boosting self-consumption rates. This finding underlines the potential of ESS in achieving energy efficiency and cost-effectiveness, particularly in settings with no feed-in tariff incentives. The study thus advocates for balanced policy measures that encourage ESS adoption while promoting renewable energy use, which is essential for progress toward carbon neutrality in the building sector.

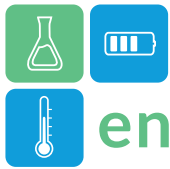
Acknowledgment

This research was funded by the Korea Institute of Energy Research's (KIER's) basic project, grant number C4-2421 and C4-2432.

References

- An, Y. and al, A. (2023). Retrofit of renewable energy systems in existing community for positive energy community. *Energy Reports*. doi.org/10.1016/j.egy.2023.02.055.
- An, Y. and al. (2023). Experimental performance analysis of photovoltaic systems applied to an positive energy community based on building renovation, *Renewable Energy*. doi.org/10.1016/j.renene.2023.119369.
- IEA. (2023). *Energy Technology Perspectives 2023*
- IRENA. (2023). *Innovation landscape for smart electrification: Decarbonising end-use*
- IRENA. (2023). *World Energy Transitions Outlook 2023: 1.5°C Pathway*
- Korea Electric Power Corporation (KEPCO). (2023), *Electric Rates Table*. Available from, https://home.kepco.co.kr/kepco/EN/F/htmlView/E_NFBHP00102.do?menuCd=EN060201
- Salom, J. and al, (2014). Analysis of load match and grid interaction indicators in net zero energy

- buildings with simulated and monitored data. *Applied Energy*. doi.org/10.1016/j.apenergy.2014.09.018
- Stelt, S. and al, (2018). Techno-economic analysis of household and community energy storage for residential prosumers with smart appliances. *Applied Energy*. doi.org/10.1016/j.apenergy.2017.10.09



Enhance the productivity of solar still by using combined reflectors and latent thermal energy storage

Hussein Alawai Ibrahim Al-Saaidi^{1,*}, Cristina Prieto^{1,*}

^{1,*} (University of Seville, Department of Energy Engineering), Camino de los Descubrimientos s/n, 41092 Sevilla, Spain

*Corresponding author e-mail: cprieto@us.es

Abstract

Basin-type solar is still a simple design construction with low operating and maintenance costs and a long life, but the low productivity offsets these advantages. The present work examines the combined effect of added internal and inclined from vertical external reflectors with different angles and thermal energy storage phase change material (paraffin wax) on the of the productivity enhancement the basin types solar still. From experimental investigations, it was found that reflectors can significantly increase the amount of solar radiation absorbed on the basin liner and daily productivity in May. On the other hand, an inclined external reflector can improve the productivity up to a certain angle ($\theta_m = 15^\circ$) and decline as θ_m increases after the peak. Paraffin wax has increased overall productivity and worked well as PCM to provide energy for continuous water production during the night. The daily productivity of the still with the inclined external reflector set at 15° was about 18% higher than that of the vertical external reflector and about 2.3 times more than that of the productivity of still without reflectors or PCM.

Keywords: Reflectors, Solar still, Finned absorber, Phase change materials (PCM), Paraffin wax

Introduction

The supply of drinking water is a main problem in the world. Drinking water is a necessity for humans along with air and food. Pollution of lakes and rivers by sewage and industrial effluents have caused a scarcity of fresh water in many places. Deserts and arid regions, which have inhospitable climatic conditions, have only brackish water sources (underground water) and freshwater rarely found in these places. Surveys show that about 97% of the water available on earth is salty, only 1% is fresh, and the rest, that is, 2% is brackish.

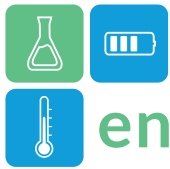
One of the inherent benefits of solar distillation is its low energy consumption. Moreover, it is simpler and more economical than other methods. It is also economical and much simpler to use than previous methods. It requires easy maintenance and simple technology. hence, it can be used in any place without much problem (Malik and al., 1983).

A passive solar still technique is one where evaporation and condensation processes occur

naturally. Single-slope-basin solar still can be considered as the basic type of passive solar still. To achieve higher distillate productivity of single slope, many researchers have used different techniques like fins, nanoparticles, cover cooling, latent heat storage materials, wick materials, evacuated tube collectors, integrated water heaters, condensing covers, photovoltaic thermal collectors, heat pumps (Omara and al., 2019).

One approach to enhance the productivity of solar still is to increase the amount of solar radiation received. Internal and inclined external reflectors are used to increase the concentration of solar radiation received by the solar still (Selvaraj and el., 2018).

(Kalifa, 2009) experimentally presented the effect of using internal and inclined external reflectors at different inclined angles from vertical 0° , 10° , 20° , and 30° on the productivity of single-basin solar still for seven months. The results reported that productivity enhanced by about 34% by keeping the inclined angle of the external reflector at 20° .



Adding fins in the base enhances the productivity of solar still by increasing the rate of heat transfer between the base and water. Fins were worked to extend the exposure area leading to the absorbing of more solar energy.

(Omara and al., 2011) investigated the increasing the absorber surface area. Three solar stills were designed as conventional, corrugated and finned, solar stills. The results showed improved productivity of corrugated and finned solar stills by 21% and 40%, respectively, compared to conventional solar still.

(Bataineh and Abbas 2020) studied experimentally and numerically the effect of utilizing both fins and internal reflectors together on the productivity of solar still. The results revealed an increase in efficiency and an average monthly productivity of 29% and 3.014 L/day.m².

Thermal energy storage materials PCM were used to increase solar still performance by absorbing the energy during the daytime and releasing this energy during nighttime (Kateshia and al., 2022).

(Algua and al., 2020) explored experimentally used phase change material paraffin wax and 1% nanofluids graphene oxide on the productivity of single-basin solar still. The results showed an increase in productivity by 47% when using PCM and 196% when using PCM and nanofluids compared with traditional solar still.

(Suraparaju and al., 2021) investigated the enhancement of productivity of basin type solar still with phase change material paraffin wax inserted into a solid staggered pin-finned absorber with different water depths. The results showed an improvement in productivity by 24% compared to the conventional still. It was also observed that there was an increase in thermal efficiency of developed still by 12.23, 22.66 and 24.26% compared with traditional ones for water depths 4, 3 and 2 cm, respectively.

(Abdullah and al., 2020) studied the impact of a mixture of copper oxide nanoparticles (CuO) with black paint, internal reflector, and phase change materials on the performance of the tray distiller. The results revealed that productivity improved by 14, 57, 70 and 108% when utilizing CuO nanoparticles,

internal reflectors, CuO nanoparticles and reflectors, and collection nanoparticles, reflectors, and paraffin wax, respectively, compared to traditional solar still.

With respect to the existing literature and the expertise of the authors, there has been no prior investigation into the combined impact of employing phase change material within a longitudinal fins absorber in a basin-type solar still, along with the incorporation of internal and external reflectors extending from the back wall, on the performance of the solar still.

The aim of this study is to improve the productivity of distilled water in solar stills by incorporating both internal and external reflectors with varying inclined angles, along with phase change materials (PCMs) serving as a thermal storage medium. The outcomes are then compared to those of a conventional solar still to assess advancements in distilled water productivity and daily efficiency when utilizing PCMs in the specific environmental conditions of Iraq.

Methodology

The experimental prototypes are single-slope basin-type solar stills with a tilted cover angle fixed at 30°. The experiments are carried out at Baghdad 33.3° N latitude in May 2022 for three different configurations.

The conventional solar still, solar still with internal and external reflectors and solar still with reflectors and PCM inside storage tank have longitudinal fins are shown in Figure 1. The experimental prototypes manufactured from galvanised iron sheets of 1mm thickness and 0.25 m² base areas are tucked and welded to construct the distiller body. All inner faces of the galvanised body are covered by an internal reflector mirror of 4 mm thickness. The 1 cm thick wooden box is fabricated to contain the galvanised body and 6 cm thick polystyrene sheets. The external reflector extends from the still back wall. Its thickness is 4 mm with an area of 0.25 m². Paraffin wax is utilized as a phase change material (PCM) due to its wide availability, low cost, and melting and solidification temperature (52-62 °C). The Paraffin wax thermophysical properties are shown in Table 1.

The PCM container is manufactured using galvanised 1 mm thickness and dimensions 495×495 ×30 mm

length width and height, respectively. The container has longitudinal fins welded to it, fabricated from galvanised 1mm thickness and dimensions 495×30 mm length and width, respectively, as shown in Figure 2. A solarimeter in the range 0–5000 W/m² range, K-type thermocouples, and a calibrated flask of 2 L capacity are used to measure solar radiation, different temperatures, and distillate yield.

Table 1: Thermophysical properties of PCM.

Properties	PCM
Type	Paraffin wax (52-62 °C)
Thermal conductivity [W/mK]	0.2
Specific heat [kJ/kg K]	2000
Density [kg/m ³]	820
Heat of fusion [kJ/kg]	168000
Thermal expansion coefficient of paraffin [1/K]	0.0006
Dynamic viscosity of liquid paraffin [kg/m s]	0.004

The solar still is kept facing south to receive the maximum possible solar radiation. The water used in the experiments is tap water with depth maintained at 5 cm in the basin and all the inner surfaces of the galvanised basin were cleaned from salt deposits and repainted with mat black dye every week to maintain the absorptivity of the still and to avoid corrosion of the galvanised body.

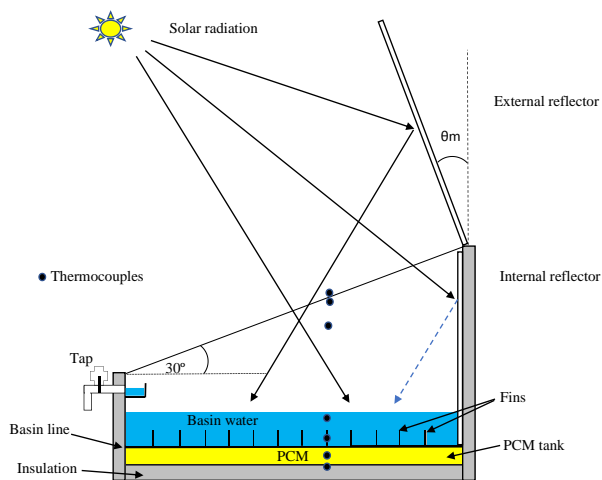


Figure 1: schematic diagram of the experimental prototype solar still with PCM, longitudinal fins and reflectors

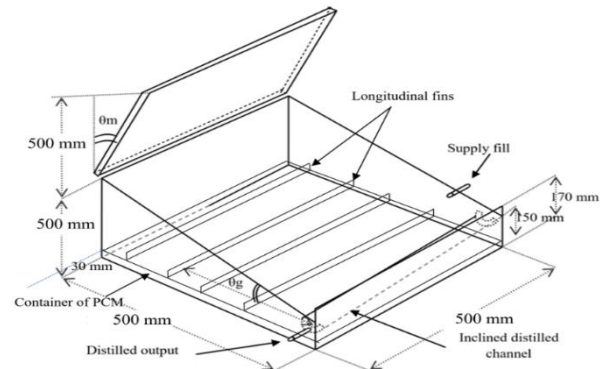


Figure 2: dimensions and configuration of basin solar still with fins, reflectors and PCM

Results

Experimental investigations are carried out for three modes, which include: still without reflector, still with internal and external reflectors, still with PCM and internal and inclined external reflector for reflector angles of 0°, 15°, 30° and 45° from vertical. All of these experiments are carried out in Baghdad on sunny and clear days with a 30° tilt angle of the glass cover.

The use of internal and external reflector with inclined angle ($\theta_m = 0^\circ$) is more effective than that of the solar still without using reflectors on spring equinox day of May, the daily productivity of vertical IES (680 ml/0.25 m² day) is about 18% higher than that of without reflectors (570 ml/0.25 m² day). This happens because the location of the Sun moves from the north side toward the south from winter to spring seasons. In May (spring equinox day), the vertical external reflector reflects maximum solar radiation on the basin liner due to the solar altitude angle becomes inclined around noon. Paraffin wax worked well as PCM to absorb the energy reflected from the reflectors during the daytime and supply the energy during nighttime for continuous distillate water production and has enhanced the overall productivity as shown in Figure 3.

The solar radiation reflected from the external reflector rises with increasing angle θ_m , but peaks at about ($\theta_m = 15^\circ$) and declines with the increase of θ_m after the peak. This is due to inclined external reflector would lead to increase the ratio of the reflected solar radiation that can be absorbed on the basin liner to the total amount of reflected radiation

from the external reflector, however on the other hand, the total amount of reflected radiation from the inclined external reflector would decrease with increasing inclination angle of the external reflector as shown in Figure 4.

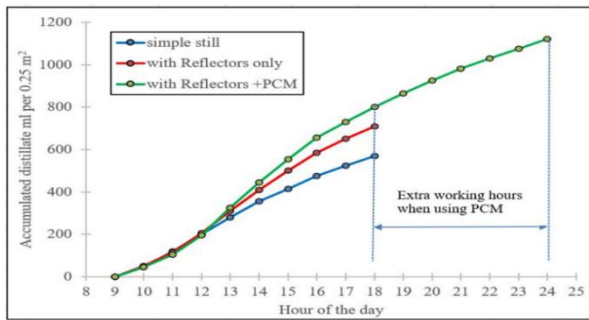


Figure 3: A comparison between the working hours productivity of the three modes investigated in May.

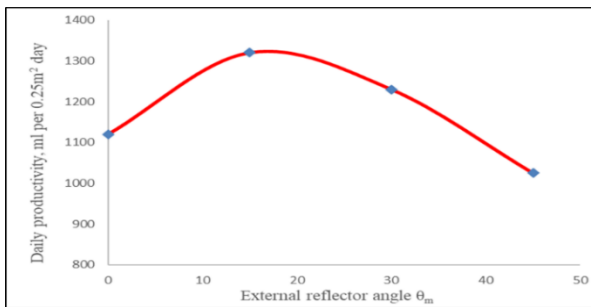


Figure 4: The productivity for IES with different reflector angle θ_m in May.

Conclusion

The conclusions of this work are summarised as follows:

1. Both internal and vertical external reflectors significantly increase the solar radiation reflected and absorbed by the phase change material (PCM) during the spring season, leading to enhanced productivity of the solar still.
2. The tilting of the external reflector proves to be effective in increasing the productivity of the single basin type solar still, particularly during the spring months.
3. The utilization of PCM is effective in providing energy during nighttime, ensuring continuous distillate water production, and contributing to an overall improvement in productivity.

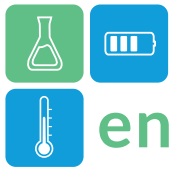
4. The daily productivity of a solar still with internal and inclined external reflectors ($\theta_m=15^\circ$) incorporating PCM is estimated to be approximately 18% higher than that of a solar still with internal and vertical external reflectors ($\theta_m=0^\circ$), and roughly 2.3 times higher than that of a still without reflectors and PCM.

Acknowledgment

This work was partially funded by European Union's HORIZON MSCA Doctoral Network program under grant agreement 101072537 TOPCSP.

References

- Kateshia J and Lakhera V. (2022). A comparative study of various fatty acids as phase change material to, Elsevier, doi.org/10.1016/j.est.2021.103947.
- Selvaraj K and Natarajan A. (2018). Factors influencing the performance and productivity of solar stills—A review. Elsevier, doi.org/10.1016/j.desal.2017.09.031.
- Omara M. el. (2019) Phase change materials (PCMs) for improving solar still productivity: a review, Springer, doi.org/10.1007/s10973-019-08645-3.
- Suraparaju S. K. and Natarajan S. K. (2021). Experimental investigation of single-basin solar still using solid staggered fins inserted in paraffin wax PCM bed for enhancing productivity, Springer Nature, doi.org/10.1007/s11356-020-11980-w.
- Alagua K. and al. (2020) Solar Desalination Using Solar Still Enhanced by PCM and Nano Fluid, AIP Conf. Proc, doi.org/10.1063/5.0034238.
- Omara Z.M. el. (2011) Performance of finned and corrugated absorbers solar stills under Egyptian conditions, Elsevier, doi:10.1016/j.desal.2011.04.042.
- Abdullaha A.S. el. (2020) Improving the trays solar still performance using reflectors and phase change material with nanoparticles, Elsevier, doi.org/10.1016/j.est.2020.101744
- Khalifa N. el (2009) Effect of inclination of the external reflector on the performance of a basin type solar still at various seasons, Elsevier, doi:10.1016/j.esd.2009.09.001
- Bataineh M. el (2020) Performance analysis of solar still integrated with internal reflectors and fins, Elsevier, doi.org/10.1016/j.solener.2020.04.059.



Enhancing energy flexibility in buildings: A design-phase approach to couple Latent Heat Thermal Energy Storage (LHTES) and Heat Pumps

Marco Perino¹, Matteo Bilardo¹, Enrico Fabrizio^{1,*}

¹TEBE Research Group, Department of Energy, Politecnico di Torino, Corso Duca degli Abruzzi 24, 10129 Torino, Italy

*Corresponding author e-mail: enrico.fabrizio@polito.it

Abstract

This paper explores the feasibility of utilizing Latent Heat Thermal Energy Storages (LHTES) coupled with Heat Pumps for efficient summer and winter energy generation in buildings. The study introduces the design phase of a case study promoted by the Italian National Recovery and Resilience Plan aimed at creating a full-scale experimental facility. This facility, designed within the framework of the NEST (Network 4 Energy Sustainable Transition) action, focuses on testing, developing, and optimizing measures to enhance energy flexibility in buildings. The prototype includes small heat pumps and sets of LHTES to meet the variable and challenging energy needs of a university laboratories. The case study aims to demonstrate the practical application of designing a LHTES coupled with heat pumps, leveraging innovative control strategies for effective Demand Side Management (DSM), dynamic pricing policies, and improved utilization of on-site renewable energy sources (RES). Transitioning from research to implementation reveals barriers such as a lack of engineering knowledge, manufacturer-centric approaches, and Building Energy Management Systems (BEMS) rigidity. Challenges also persist in the considerable size of Thermal Energy Storage (TES). Overcoming these challenges is crucial for realizing the full potential of LHTES and advancing energy-efficient solutions in building energy systems.

Keywords: LHTES, Heat Pump storage, PCM Storages.

Introduction

Reducing energy demand, switching to cleaner energy sources, and making the most of renewable energy are crucial steps for global energy transition and decarbonization. Achieving these goals largely depends on advancements in technology, the development of new materials, and the implementation of advanced control systems.

The building sector, constituting approximately 40% of the total energy demand in developed countries and the EU, represents a key area for the implementation of energy-efficient solutions. Alarming, 75% of this energy is currently derived from fossil fuels (European Commission 2016). Within this sector, the residential domain accounts for 54% of heating and cooling consumption, with electric heating and cooling contributing 13.4% to the final electricity consumption in the EU28 (Mantzou et al. 2017, Nijs et al. 2017).

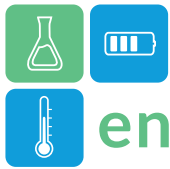
Considering the scenario where all fossil-fueled heat generation technologies are instantaneously replaced by reversible heat pumps, a potential reduction of about 16% in combined emissions from the heat and power sector can be achieved. However, this transition poses challenges, with heat pumps expected to contribute

26% to total electricity demand, necessitating a strategic balance between summer and winter seasons.

The anticipated widespread adoption of heat pumps for residential heating and cooling by 2030 is projected to elevate electricity's share to 40%, reaching 50-70% by 2050 (Bruxelles, 8.7.2020 COM- 2020 - 299 final). However, this transformation encounters infrastructural challenges, demanding careful consideration of sustainability and resilience in the energy supply chain.

As the current power system's capacity is exceeded at rates above 32%, the necessity for additional "clean" capacity becomes increasingly evident.

To meet electrification thresholds, a shift towards renewable energy sources (classifiable as VRES: Variable Renewable Energy Source) is essential, with projections suggesting a share of 55-60% by 2030 and around 84% by 2050. However, challenges such as intermittent energy availability and excess energy production must be addressed. Increased energy flexibility, facilitated by a consistent link between the electric and heating/cooling sectors, can mitigate these challenges. For instance, leveraging excess electric energy for heating needs during low demand periods and storing thermal energy can significantly reduce



energy waste. This requires addressing two primary challenges:

- Ensuring a consistent availability of resources at all times. The intermittent nature of energy sources may result in imbalanced residual loads, requiring coverage with expensive and/or environmentally polluting power systems.
- Managing the potential surplus of energy production compared to simultaneous demand, leading to curtailed energy, such as losses in energy production by Variable Renewable Energy Sources (VRES).

In extreme future scenarios of electrification, without specific interventions, the unserved energy may result in an average loss of load around 2%, with some countries experiencing lost load values of up to 7% (Kavvadias et Al. 2019).

A solution to enhance energy flexibility involves a closer integration of the electric and heating/cooling sectors. The adoption of multifunctional Heat Pumps (HP) coupled with Latent Heat Thermal Energy Storage (LHTES) emerges as a promising strategy. By simultaneously producing heat and cold and incorporating thermal energy storage, these technologies can alleviate issues related to energy imbalance, excess production, and waste energy.

This paper introduces a full-scale experimental facility aimed at exploring techniques and technologies to enhance energy flexibility. The focus lies on optimizing control strategies and integrating components and subsystems of multifunctional Heat Pumps and Latent Heat Thermal Energy Storage systems. The research aims to contribute valuable insights for addressing the challenges associated with the future electrification of buildings.

The case study of the HP_FlexLab

Within the framework of the research activities under the PNRR action (PE 2 – Scenari energetici del futuro – NEST – Network 4 Energy Sustainable Transition – Spoke 8 “Final use optimization, sustainability & resilience in energy supply chain” – Task 8.3.4) and the “Dipartimento di Eccellenza: I-Sinergys” – DENERG, a project has been initiated to establish a comprehensive experimental facility. This facility aims to test, develop, and optimize measures that enhance energy flexibility in buildings. The system consists of a prototype integrating small-scale heat pumps capable of producing hot water at relatively high temperatures and two sets of Latent Heat Thermal Storages

(LHTES), one operating at high and the other at low temperatures. The facility will cater to the energy demands of laboratories “Codegone ed Anglesio” at the Department of Energy – DENERG – Politecnico di Torino, chosen due to the laboratories' variable and challenging energy demands, making them an ideal setting to develop and implement innovative control strategies for energy flexibility.

Through the combined use of Heat Pumps (HP) and LHTES, several benefits can be achieved:

- 1- Effective Demand Side Management (DSM), enabling the shifting of higher energy demand to off-peak hours.
- 2- Improved utilization of “dynamic pricing” policies for energy, expected to be prevalent in future energy scenarios.
- 3- Enhanced use of on-site Renewable Energy Sources (RES).

Figure 1 depicts the time profiles of chilled and hot water demands, emphasizing the worst-case design conditions. These profiles, focused on separate hot/chilled water production, do not consider potential “waste heat” utilization, where chilled water is produced during heating mode and hot water during cooling mode. The exploitation of these “by-products” can be flexible and beneficial for laboratories through hot/cold heat storages.

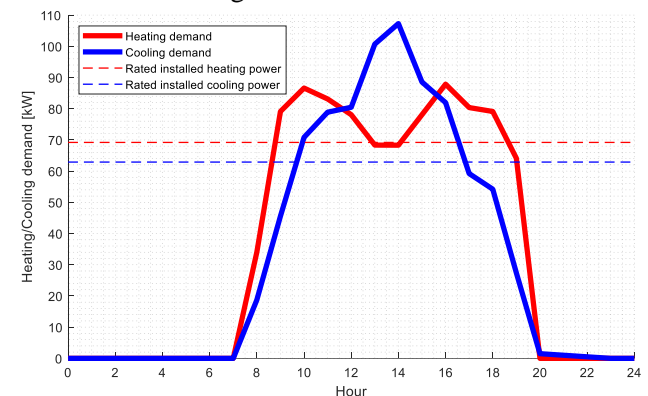


Figure 1: Hourly demand profile for heating and cooling.

A detailed analysis based on hourly energy demand profiles explored various scenarios to determine the optimal system architecture, LHTES size, and HP installed power. Three typical approaches for sizing LHTES were considered: load shifting, load leveling, and demand limiting. The choice of HP for this study is the Innova - eHPoca GEO WW 9M, featuring a nominal heating power of 8.65 kW and a nominal cooling power of 7.86 kW¹. The results, summarized in

¹ The design of the prototypal installation is being done in cooperation with Innova Srl and the University of Padova. The final design will make use of innovative propane-based HP (for achieving a higher temperature of the hot

water) whose development is, at present, under way. Their features (in terms of size and nominal power) will be, however, similar to those of the eHPoca GEO WW 9M.

Table 1, highlight the advantages of employing Thermal Energy Storage (TES). Notably, the “load shifting” architecture requires the maximum installed power and storage size but reduces the number of HP required. The “load levelling” strategy minimizes both installed power and TES size, while the “demand limiting” configuration lies between the other two, providing flexibility and opportunities for Demand Side Management (DSM), VRES management, and energy price exploitation.

Table 1: Results of the three possible configurations of the system for heating (H) and cooling (C) conditions.

Scenario	H (#HP, Capacity [kW])	C (#HP, Capacity [kW])	H storage [kWh]	C storage [kWh]
1.Load shifting	8 (69.2)	8 (62.9)	852	795
2.Load levelling	5 (43.3)	5 (39.3)	447	428
3.Demand limiting	6 (51.9)	6 (47.2)	543	523
4.No storages	11 (95.2)	14 (110.0)	-	-

Table 2 illustrates the impact of the storages in terms of volume and PCM mass, with LHTES offering a theoretically higher energy density. However, due to space constraints in the laboratory, the size of LHTES for all scenarios in Table 2 is incompatible. To address this, the final configuration adopted a Demand Limiting approach with increased heating/cooling power and reduced LHTES size, allowing flexibility in operation and a switch to a “Load Shifting” concept during periods of low energy demand.

Table 2: TES and LHTES size in relation to the various scenarios (first row: thermal storage medium stored in puffers)².

	TES ($\Delta T=40^{\circ}\text{C}$)			LHTES ³					Scenario	
	H20	H20	sp 58*	RT 54 HC	RT62 HC	RT64 HC	RT69 HC	SP 5 gel		RT 5 HC
	H	C	H	C	H	C	H	C		C
V [m ³]	366.9	341.9	9.51	19.04	15.87	15.63	15.87	14.22	14.94	Load Shifting
# puffer	184	171	7	14	12	12	12	11	11	
PCM [kg]	-	-	12364	15234	13330	12188	13330	18489	11357	
V [m ³]	96	92	4.98	9.97	8.31	8.18	8.31	7.66	8.04	Load Levelling
# puffer	48	47	4	8	6	6	6	6	6	
PCM [kg]	-	-	6471	7973	6977	6379	6977	9952	6113	
V [m ³]	116.7	112.5	6.05	12.11	10.09	9.94	10.09	9.36	9.83	Demand Limiting
# puffer	59	57	5	9	8	8	8	7	8	
PCM [kg]	-	-	7864	9690	8478	7752	8478	12164	7472	

² Innova Srl Puffer 2000 liters — size (@ x h): 1300 x 2408 mm.

Table 3 summarizes the features of the final system architecture, and Figure 2 represents the conceptual scheme of the laboratory layout. A dynamic simulation model in TRNSYS was developed to evaluate the preliminary performance of the system. Heating and cooling design load was simulated, using thermal levels of the storages consistent with the PCM phase melting range. Figure 3a and 3b depict typical thermal profiles over 24 hours, illustrating direct heating/cooling and the charging and discharging phases of the LHTES. The control strategy, although preliminary, proposes a hybrid version between the “Demand limiting” and “Load shifting” scenario, ensuring a limited installed power at the expense of WSHP operation during off-load hours.

Table 3: Preliminary configuration of the HP_FlexLab system.

	#HP	Capacity [kW]	PCM [kg]	Storage [kWh]	Volume [m ³]	# Puffer
H	8	69.2	1431 (SP58*)	98.8	2.2	2
C	5	62.9	2407 (RT 5 HC)	1686.5	6.3	3

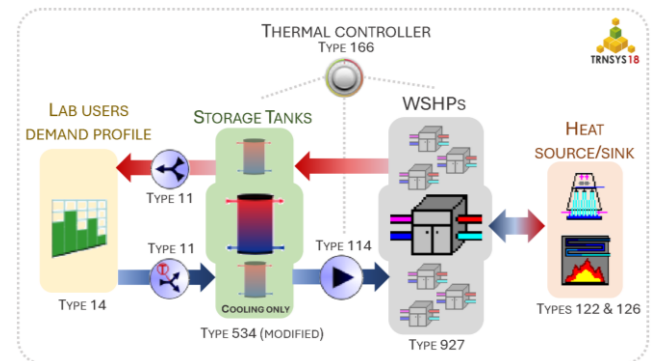


Figure 2: Conceptual scheme of the HP_FlexLab prototype (with TRNSYS types modelled).

Conclusions

In conclusion, the feasibility of employing latent heat thermal energy storages (LHTES) coupled with heat pumps for year-round air conditioning in buildings is well-supported by existing technological tools and theoretical foundations. The potential for advancing this concept lies not only in the innovative prediction and control strategies available today, such as Model Predictive Control (MPC) and Artificial Intelligence (AI), but also in the need to overcome practical barriers for real-world implementation.

While aggressive policies for electrification in the heating/cooling sector show promise, transitioning from research to practical application reveals significant hurdles. A notable challenge is the existing

³ For technical details of the PCMs used, please refer to the data sheets provided by the manufacturer Rubitherm Technologies GmbH (<https://www.rubitherm.eu/en/productCategories.html>)



gap in engineering knowledge and confidence in novel approaches and systems. Manufacturers often operate in isolation, concentrating on individual components or subsystems without prioritizing their adaptable integration into comprehensive systems. This

compartmentalized approach results in rigid specifications and operation modes, primarily focused on ensuring the safe and reliable operation of individual components, with limited consideration for the overall ensemble's efficiency.

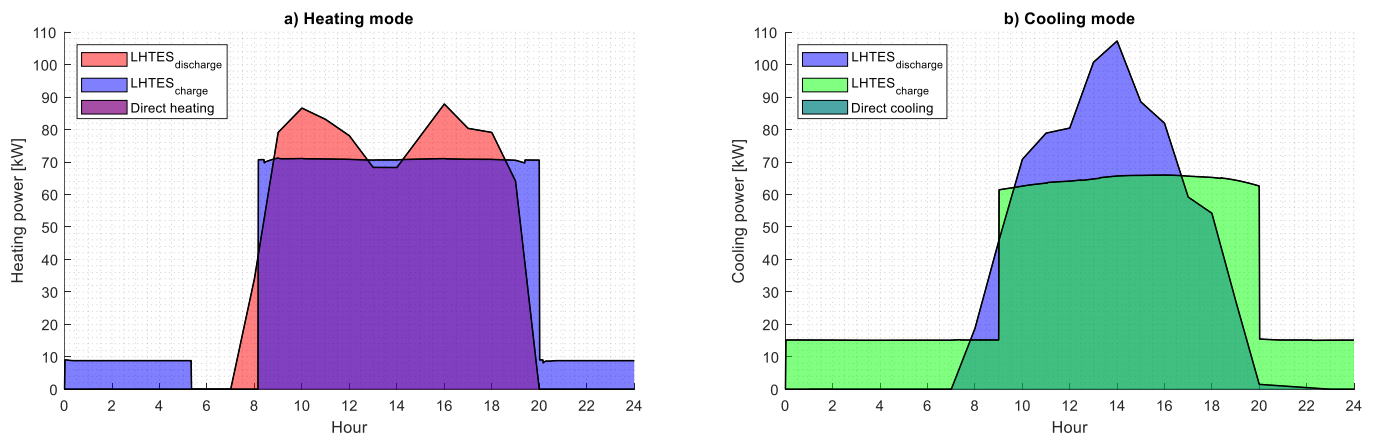


Figure 3: Typical profiles for the operation of the system (3a — Heating mode, 3b — Cooling mode).

Furthermore, Building Energy Management Systems (BEMS) exhibit rigidity and reliance on proprietary know-how, which poses challenges for seamless integration with advanced control methods such as AI and MPC. These factors collectively hinder the practical implementation of innovative and flexible strategies in real-world scenarios.

Notably, Thermal Energy Storage (TES) plays a pivotal role in achieving effective Demand Side Management (DMS). However, challenges persist, particularly in the considerable size of TES, even with the adoption of LHTES, limiting their widespread adoption. Bridging the gap between theoretical advancements and practical implementation requires collaborative efforts among manufacturers, researchers, and policymakers to foster a holistic approach that prioritizes system-wide efficiency over isolated components. Overcoming these barriers will be crucial for realizing the full potential of LHTES coupled with heat pumps in advancing sustainable and flexible air conditioning solutions for buildings.

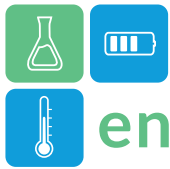
Acknowledgements

The research activity presented in this paper is done in a project funded under the National Recovery and Resilience Plan (NRRP), Mission 4 Component 2 Investment 1.3 - Call for tender No. 1561 of 11.10.2022 of Ministero dell'Università e della Ricerca (MUR); funded by the European Union – NextGenerationEU. Award Number: Project code PE00000021,

Concession Decree No. 1561 of 11.10.2022 adopted by Ministero dell'Università e della Ricerca (MUR), CUP E13C22001890001, according to attachment E of Decree No. 1561/2022, Project title “Network 4 Energy Sustainable Transition - NEST”. The development of the prototype is done in cooperation with INNOVA S.r.l. industry and the University of Padova - prof. Caludio Zilio.

References

European Commission. 2016a. “An EU Strategy on Heating and Cooling. COM (2016) 51 Final.”
 Bruxelles, 8.7.2020 COM (2020) 299 Final. Communication from the commission to the European Parliament, the council, the European economic and social committee and the committee of the regions - Powering a climate-neutral economy: An EU Strategy for Energy System Integration
 Kavvadias, K., Jimenez Navarro, J. e Thomassen, G., Decarbonising the EU heating sector: Integration of the power and heating sector, Publications Office of the European Union, Luxembourg, 2019.
 Mantzos, L., T. Wiesenthal, N. A. Matei, S. Tchung-Ming, and M. Rozsai. 2017. “JRC-IDEES: Integrated Database of the European Energy Sector.”
 Nijs, Wouter, Pablo Ruiz Castillo, and Ignacio Hidalgo Gonzalez. 2017. Baseline Scenario of the Total Energy System up to 2050 - Business-as-Usual Reference Scenarios.



Enhancing grid integration of renewable energy with seasonal thermal energy storage using molten salt tanks

Cristina Prieto¹, Pablo D. Tagle-Salazar^{1,2}, David Patiño³, Julieta Schallenberg-Rodríguez⁴, Padraig Lyons⁵, Luisa F. Cabeza²

1 University of Seville, Department of Energy Engineering, Camino de los Descubrimientos s/n, 41092, Seville, Spain

2 GREiA Research Group, Universitat de Lleida, Pere de Cabrera s/n, 25001, Lleida, Spain

3 Department of Economics and Economic History, University of Seville, Avda. Ramón y Cajal s/n, 41018, Seville, Spain

4 Group for the Research in Renewable Energy Systems, Universidad de Las Palmas de Gran Canaria.

5 Tyndall National Institute, International Energy Research Centre, T12 R5CP, Cork, Ireland

*Corresponding author e-mail: cprieto@us.es

Abstract

In the context of the ongoing global energy transition, addressing the challenges necessitates a profound focus on energy storage technologies. This work presents a novel approach to addressing the challenges of seasonal energy storage within the context of the ongoing global energy transition. While conventional literature has predominantly focused on pumped hydroelectricity, this research introduces an alternative solution utilizing two-tank molten salts systems. These systems, already established in commercial Concentrating Solar Power (CSP) plants, offer a promising avenue for large-scale seasonal energy storage applications. To substantiate this claim, a rigorously validated model specific to molten salt technology was employed to assess heat loss estimation from storage tanks throughout the year. The findings demonstrate the remarkable thermal performance of well-insulated molten salt tanks, with minimal heat losses sustained over extended periods, exhibiting a marginal decrease of approximately 1 K per day. This exceptional thermal retention capability ensures the sustained economic viability of the power block for an impressive span of 3–4 months. This study not only extends the application of molten salt systems beyond their traditional use but also offers practical insights into their feasibility and economic viability for seasonal storage. By proposing an innovative solution, leveraging existing technology, and conducting thorough assessments, this research contributes to advancing the discourse on energy storage technologies in the context of the global energy transition.

Keywords: seasonal energy storage, two-tanks molten salts system, performance, heat losses.

Introduction

The global energy system transformation is a profound structural shift in both energy supply and consumption, characterized by a transition from fossil-based to zero-carbon alternative sources. According to data from (IRENA, 2019), the success of this ongoing energy transition hinges on transforming the global energy sector to zero-carbon sources by the latter half of this century. The goal is to reduce 36.9 Gt energy-related CO₂ emissions for mitigating climate change and restricting global temperature rise to within 1.5 °C of pre-industrial levels. According to (International Energy Agency, 2013), the total renewable electricity generation surged from 6213 TWh in 2010 to 9506 TWh in 2020, with significant contributions from solar PV (+96.18%), wind (+78.70%), and other renewable sources (+46.49%). This remarkable growth

underscores the momentum and importance of renewable energy sources in the global energy landscape.

The most widespread thermal energy storage (TES) system within commercial Concentrating Solar Power (CSP) applications is the two-tank configuration with molten salt as storage medium. This preference is primarily attributed to its favourable thermal characteristics and cost-effectiveness (González-Roubaud et al., 2017). Presently, molten salts serve as a TES solution for the two most well-established solar concentrating technologies available in the market, namely parabolic trough and tower systems. According to data from (IRENA, 2020), there is currently a total installed capacity of 491 GWh for molten salts systems,

with projections indicating a potential increase to 631 GWh by 2030.

While molten salt storage in CSP facilities has effectively managed daily solar generation intermittency, it has traditionally been overlooked for seasonal storage. Perceived constraints include concerns about space requirements, long-term thermal efficiency, maintenance expenses, and limited charge-discharge cycles. As the need for seasonal energy storage solutions continues to grow, research and development efforts are now exploring more suitable alternatives to tackle this vital challenge in the transition toward a sustainable energy landscape (IRENA, 2020; LDES Council & McKinsey & Company, 2022). Notably, molten salts represent a viable and promising candidate for seasonal energy storage due to their exceptional storage capacity, thermal efficiency, adaptable design, wealth of accumulated expertise, and successful track record in various applications. The primary innovation of this paper lies in demonstrating the feasibility of utilizing molten salts for seasonal energy storage within the grid.

Methodology

In order to assess the feasibility of employing molten salts technology for long-term energy storage, a comprehensive investigation was undertaken, focusing on the evaluation of heat losses within the storage tanks throughout the year. This study was conducted in the context of Seville, Spain. The investigation further involved a sensitivity analysis, wherein variations in mineral wool insulation thickness were considered. These heat losses are instrumental in determining the temperature declines during the designated storage periods, based on specific insulation thickness, and prevailing climatic factors, distinguishing between winter and summer conditions (as expressed through the coefficient slope denoted as 'S' in K/day, Figure 1a). The assessment of accuracy was performed using Equation (1), with the objective of quantifying any disparities in outcomes concerning different seasons. This parameter was devised to quantify the extent of deviation in results pertaining to distinct seasonal variations.

$$Error = \frac{S_{winter} - S_{summer}}{S_{summer}} \cdot 100\% \quad (1)$$

It is well-established that as insulation thickness increases, heat losses experience a diminishing trend, conforming to an anticipated asymptotic profile shown in Figure 1b. Furthermore, the slope associated with the temperature drop is also expected to demonstrate

analogous asymptotic behaviour concerning insulation thickness

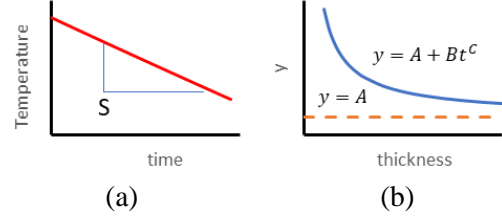


Figure 1: Description of the methodology considered. (a) Calculation of the slope (temperature drop with time) and (b) Estimation of the asymptote at $y=A$.

This investigation aims to ascertain the coefficients A, B, and C characterizing the asymptotic profile in relation to both heat flow and the temperature drop slope. To attain this determination, a regression methodology was employed, relating heat flow and slope to insulation thickness. The computation of coefficients A, B, and C was executed to maximize the coefficient of determination (R^2) within the context of the regression analysis. This approach facilitates a precise delineation of asymptotic characteristics pertinent to the heat losses flow and temperature drop slope as insulation thickness increases. The derived asymptotic value of the slope 'S' is subsequently utilized to calculate the temperature drop of the salt inventory, an essential parameter for estimating the duration for which the tanks can retain energy, considering assumed thermal losses. This critical assessment is integral for ensuring the economic performance of the entire solar power plant.

Storage tank

Figure 2 shows a schematic diagram of the molten salt tank. Stainless steel was used on the metal jacket, with a thickness of 0.6 cm, 3.3 cm and 0.7 cm for the bottom, walls, and top roof respectively. The insulation layer was modelled as mineral wool, whose thickness is the variable of the sensitivity analysis. The insulation in the bottom is fixed, modelled as a three-layer insulation (2 fine layers of refractory sand, one thick layer of refractory brick). The initial temperature of the salt inventory is 565 °C.

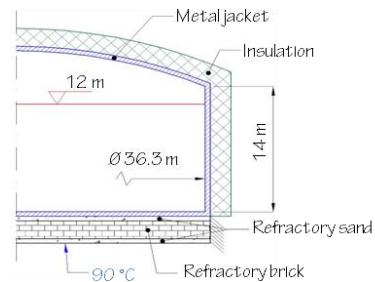
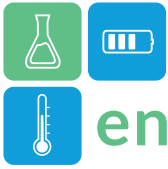


Figure 2: Section of the molten salt tank.



Weather conditions

The simulation encompasses an analysis of the storage tank over two distinct climatic scenarios, representing the contrasting months of July (characterizing summer conditions) and January (representing winter conditions). In the context of solar irradiation, data for direct normal irradiance exceeding 400 W/m^2 , results in daily averages of 8.25 kWh/m^2 for summer and 3.4 kWh/m^2 for winter. The summertime ambient temperature exhibits a prevailing range of 22 to $38 \text{ }^\circ\text{C}$, while wintertime temperatures predominantly fluctuate within the range of 9 to $17 \text{ }^\circ\text{C}$. Wind speed remains relatively low throughout both scenarios, with speeds consistently below 2.5 m/s .

Description of the transient model for heat loss estimation

The methodology employed for thermal performance assessment centres around a one-dimensional and transient analysis of heat transfer, a comprehensive framework with its formulation, limitations, validation, and foundational assumptions extensively addressed in previous research by (Tagle-Salazar et al., 2023).

This analytical model accounts for the full dynamics of heat transfer within and surrounding the tank, incorporating heat transfer mechanisms of conduction, convection, and radiation. Notably, this model introduces an innovative approach to estimating local heat loss attributed to assembly defects, a parameter of significant consequence as it exerts a substantial influence on the cumulative heat loss of the system (Prieto et al., 2016; Tagle-Salazar et al., 2023). This multifaceted analysis represents a critical component in understanding and optimizing the thermal performance of the system under scrutiny.

Governing equation of cooling down of the salt inventory is shown in Equation (2). Heat flow $\dot{Q}_{TES,loss}$ considers the convective and radiative heat losses in the surface of the salt inventory inside the tank plus the local heat loss due to assembly defects.

$$m \frac{d(h)}{dt} = -\dot{Q}_{TES,loss} \quad (2)$$

Results

Figure 3 offers an illustration of the projected heat loss trends concerning insulation thickness for both the walls and the top of the thermal storage system. Notably, both profiles exhibit the anticipated asymptotic behaviour as delineated in the methodological framework. It is noteworthy that the observed heat losses exhibit remarkable consistency between the summer and winter seasons, despite the

notable divergence in weather conditions. The heat loss through the walls experiences a significant reduction, declining from approximately 275 W/m^2 with a 15 cm insulation thickness to a mere 47 W/m^2 with 1 m of insulation. A parallel trend is observed for heat loss through the top, with values decreasing from 193 W/m^2 to 34 W/m^2 within the same spectrum of insulation thickness.

In Figure 4, the temperature drop over time for various insulation thicknesses is depicted. For tanks with 15 cm of insulation, losses are 2.3 K/day . Using 45 cm insulation, these losses reduce to 1.23 K/day . An asymptote is reached around 1 m of insulation, resulting in a reduction of 75.47% in temperature drop from 15 cm to 1 m insulation. Additionally, with errors consistently below 2% , seasonal weather fluctuations have a negligible impact.

The results of the calculated coefficients A, B, C of thermal losses and the slope of temperature drop are presented in Table 1. Notice that the cooling rate exhibits an asymptote at 0.53 K/day . This value represents the minimal achievable rate of temperature decline when dealing with either infinite thickness of insulation ($t \rightarrow \infty$) or ideal insulation ($k \rightarrow 0$). This temperature drop constitutes a crucial parameter for subsequent analyses concerning the thermal characteristics of analogous molten salt storage tanks. Furthermore, the heat flux at the walls and top exhibits a significantly low asymptotic value ($A \rightarrow 0$). These outcomes validate the assumption of a zero-value asymptote for heat loss through walls and the roof as the insulation thickness increases.

Table 1: Results of the calculated thermal losses and the temperature drop

Parameter	Heat loss (W/m^2)		Slope S (K/day)
	Walls	Top	
A	-9.95	-5.84	0.53
B	59.16	41.78	0.36
C	-0.83	-0.82	-0.84
$R^2 (A \neq 0)$	0.9987	0.998	1.0000
$R^2 (A = 0)$	0.9991	0.9994	0.9843

In the 1.5m -insulation scenario, the temperature of the salt inventory drops around $24 \text{ }^\circ\text{C}$. Considering an effective operational range of $260\text{--}565 \text{ }^\circ\text{C}$ for seasonal TES, this temperature drop leads to round-trip efficiency reduction ranging from 8% to 5% . In electricity generation, a temperature loss of $24 \text{ }^\circ\text{C}$ impacts discharge efficiency. Rankine cycle efficiency drops when heat sink temperature decreases ($565 \text{ }^\circ\text{C}$ to $530 \text{ }^\circ\text{C}$) due to reduced temperature difference. This results in a 2% cycle efficiency loss (Zhai et al., 2020).

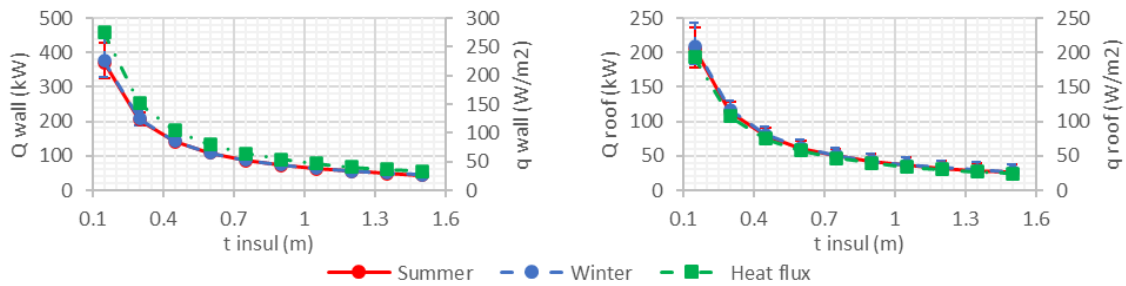


Figure 3: Calculated heat losses in the molten salt tank. Left: losses through the walls. Right: losses through the tank top.

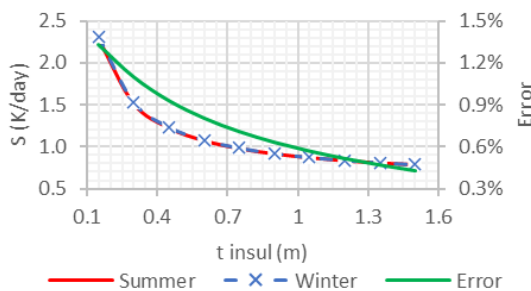


Figure 4: Temperature drop with time (S) vs. insulation thickness.

Conclusions

The study highlights the strong potential of molten salt thermal storage for seasonal use, emphasizing the importance of insulation system design and construction processes for economic viability. Commercial tanks exhibit asymptotic heat loss behaviour, with monthly losses ranging from 5% to 8% for insulation thicknesses over 1.25 m. These findings validate their suitability for seasonal storage while emphasizing the role of construction process in enhancing viability. The impact on the thermal power cycle is minimal, remaining under 2% in the worst-case scenario.

Acknowledgment

This work was partially funded by the Ministerio de Ciencia e Innovación de España TED2021-132216A-I00 funded by MCIN/AEI/ 10.13039/501100011033 and the European Union by NextGenerationEU/PRTR. Partially funded by the Ministerio de Ciencia e Innovación de España (PID2021-123511OB-C31 - MCIU/AEI/FEDER, UE; RED2022-134219-T). The authors at University of Lleida would like to thank the Catalan Government for the quality accreditation given to their research group GREiA (2017 SGR 1537). GREiA is a certified agent TECNIO in the category of technology developers from the Government of Catalonia.

References

González-Roubaud, E., Pérez-Osorio, D., & Prieto, C. (2017). Review of commercial thermal energy storage in concentrated solar power plants: Steam vs. molten salts. *Renewable and Sustainable Energy*

Reviews, 80, 133–148.
<https://doi.org/https://doi.org/10.1016/j.rser.2017.05.084>

International Energy Agency. (2013). *Transition to sustainable buildings: Strategies and opportunities to 2050*. <https://www.iea.org/etp/buildings/>

IRENA. (2019). *Global Energy Transformation: A Roadmap to 2050*. In *Global Energy Transformation. A Roadmap to 2050*. <https://www.irena.org/publications/2019/Apr/Global-energy-transformation-A-roadmap-to-2050-2019Edition>

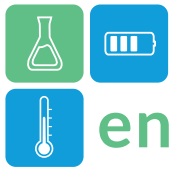
IRENA. (2020). *Innovation Outlook: Thermal Energy Storage*. https://www.irena.org/media/Files/IRENA/Agency/Publication/2020/Nov/IRENA_Innovation_Outlook_TES_2020.pdf?rev=6950b7b9792344b5ab28d58e18209926

LDES Council, & McKinsey & Company. (2022). *Net-zero heat: Long Duration Energy Storage to accelerate energy system decarbonization*.

Prieto, C., Osuna, R., Fernández, A. I., & Cabeza, L. F. (2016). Molten salt facilities, lessons learnt at pilot plant scale to guarantee commercial plants; heat losses evaluation and correction. *Renewable Energy*, 94, 175–185.
<https://doi.org/10.1016/j.renene.2016.03.039>

Tagle-Salazar, P. D., Prieto, C., López-Román, A., & Cabeza, L. F. (2023). A transient heat losses model for two-tank storage systems with molten salts. *Renewable Energy*, 219, 119371.
<https://doi.org/10.1016/j.renene.2023.119371>

Zhai, H., Wang, S., An, B., & Dai, X. (2020). Performance and parameter sensitivity comparison of CSP power cycles under wide solar energy temperature ranges and multiple working conditions. *Energy Conversion and Management*, 218, 112996.
<https://doi.org/10.1016/j.enconman.2020.112996>



Erosion of a tube immersed in a bubbling fluidized bed at high temperature: a numerical study

Pedro Domínguez-Coy^{1,*}, Juan Ignacio Córcoles^{1,2}, José Antonio Almendros-Ibáñez^{1,2}

1 Universidad de Castilla-La Mancha, Renewable Energy Research Institute, Section of Solar Energy and Energy Efficiency, C/ de la Investigación s/n 02006, Albacete, Spain

2 Universidad de Castilla-La Mancha, Escuela Técnica Superior de Ingeniería Industrial de Albacete, Dpto. de Mecánica Aplicada e Ingeniería de Proyectos, Campus Universitario s/n 02071, Albacete, Spain

*Corresponding author e-mail: Pedro.Dominguez@uclm.es

Abstract

Fluidization processes of particles are common in industry. In fluidized beds, impacts of particles may lead to the accelerated erosion of internals, increasing the operation costs. Due to the complexity of the analysis of the multiphase flow and the erosion process itself, modelling erosion at industrial scale remains unsolved. To the day of this study, computational fluid dynamics-discrete element method (CFD-DEM) has been successfully applied to erosion predictions, but its large computational cost limits its application to lab-scale calculations.

Multiphase-Particle In Cell (MP-PIC) simulations have proven their accuracy in predicting the hydrodynamic behaviour of a fluidized bed, but quantitative erosion models are not usually coupled with this type of numerical simulations. This study uses the hydrodynamic data obtained with MP-PIC simulations and different erosion models to predict erosion rates on the surface of a tube immersed in a lab-scale fluidized bed under different fluidization velocity and temperature conditions.

Keywords: Erosion, Wear, Fluidized bed, MP-PIC, Multi-phase flow

Introduction

Some solid particles, like sand, can withstand very high temperatures (over 1,000 °C), and their high density makes them suitable for thermal energy storage material in storage tanks or directly integrated in solar receivers. As heat exchange between an immersed tube and fluidized particles is efficient, it is possible to store thermal energy as sensible heat in particles, and then fluidize those particles to extract that energy (Córcoles *et al.*, 2023).

The use of fluidization techniques has interesting features because of the high mixture and surface per volume ratios within the emulsion phase. However, continuous impingement of particles on immersed surfaces can erode the lasts.

Despite erosion is a well-known phenomenon, it involves complex particle-surface interactions. Thus, scientists have been using empirical correlations to predict when a part will fail or need to be replaced. Although empirical correlations are useful, their applicability is strongly constrained by the similarity to the experimental conditions of their obtention.

Another approach to predict erosion are numerical simulations. CFD-DEM techniques have proven their accuracy (Dong *et al.*, 2022), but as a high computational effort is required, their use is limited to

lab-scale applications. MP-PIC is a less computational cost simulation method whose accuracy on hydrodynamic predictions has been assessed for industrial-scale simulations. Nonetheless, there are few MP-PIC studies focused on erosion in the literature. In addition, since some interesting applications of fluidized beds are at high temperature, it is important to be able to predict erosion under those conditions.

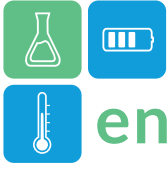
The purpose of this study is to couple erosion models and MP-PIC simulations, and to study the evolution of erosion varying temperature and fluidization velocity with three erosion models to discuss their behaviour.

Methodology

A 300x60x40 mm (height, wide, depth) bubbling fluidized bed was simulated for 30 s with MP-PIC commercial software Barracuda Virtual Reactor (v.22.1), and the time-averaged erosion rate was calculated using MATLAB (R2023a) on a 15-mm-diameter tube whose longitudinal axis is located 30 mm above the distributor. The first five seconds were not considered to calculate erosion as the bed fluidization start-up time lasts a few seconds.

Materials

The hydrodynamic calculations were carried out with a computer equipped with an Intel® Xeon® E-2620 v4, 2.10 GHz dual processor CPU, and 64 GB RAM.



Methods

Three erosion models were implemented in MATLAB: Finnie (Finnie, 1960), Oka (Oka *et al.*, 1997), and SCFMED (Lyczkowski and Bouillard, 2002).

The erosion model of Finnie predicts erosion on ductile surfaces assuming that erosion resembles a cutting machine tool. Equation (1) is the erosion model of Finnie.

$$\begin{cases} E_{Finnie} = \frac{\dot{m}_p u_p^2 (\sin 2\alpha - 3 \sin^2 \alpha)}{8 \sigma_f A_t}, & \alpha < 18.5^\circ \\ E_{Finnie} = \frac{\dot{m}_p u_p^2 \cos^2 \alpha}{24 \sigma_f A_t}, & \alpha \geq 18.5^\circ \end{cases} \quad (1)$$

Where E_{Finnie} is the erosion rate, expressed in units of length eroded by unit of time, \dot{m}_p is the flow rate of particles impinging on the target surface, u_p is the particle velocity, α is the impingement angle, σ_f is the yield stress of the target and A_t is the area of the finite element.

Similarly, Oka *et al.* (1997) developed an erosion model, but this one was developed for both ductile and brittle materials.

$$E_{Oka} = \frac{\dot{m}_p}{A_t} K H_t^{k_1} \left(\frac{u_p}{u'}\right)^{k_2} \left(\frac{d_p}{d'_p}\right)^{k_3} \sin^{n_1} \alpha (1 + H_t (1 - \sin \alpha))^{n_2} \quad (2)$$

Where H_t is the hardness of the target surface expressed as a pressure, K , k_1 , k_2 , k_3 , n_1 , and n_2 are model coefficients.

Lyczkowski and Bouillard (2002) modelled erosion as a function of the dissipated kinetic energy, stating that:

$$E_{SCFMED} = E_0 \frac{(1-\varepsilon)(\varepsilon - \varepsilon_{gd})}{\varepsilon^2} (1 + 0.01167 Re_{LB}) \quad (3)$$

Where ε is the void fraction, ε_{gd} is the void fraction in the densest region of the bed, and E_0 and Re_{LB} are determined using equations (4) and (5).

$$E_0 = \frac{(1 - e^2)(75 \mu_f g x_d)}{\varphi_p d_p H_t} \quad (4)$$

$$Re_{LB} = \frac{\varphi_p d_p \rho_f u_f}{\mu_f} \quad (5)$$

Where e is the momentum conservation coefficient, μ_f is the viscosity of the fluid, g is the acceleration of the gravity, x_d is a characteristic acceleration distance (in the order of magnitude of the distance between the tubes of a bundle), φ_p is the shape factor of the particles, d_p is the particles' diameter, ρ_f is the fluid's density and u_f is the fluid's velocity.

Results and Discussions

Grid analysis

To validate the numerical model, a grid independence analysis was performed. Up to six different grids were tested. Table 1 shows the number of elements of the grids, ranging from 4,389 to 47,232. Figure 4 shows the results when Finnie model was applied. Similar results were obtained for Oka and SCFMED.

The results showed that the results are not independent of the grid, but a similar order of magnitude was obtained. Grid D (23,959 elements) was the one which follows better the averaged values. Therefore, Grid D will be the used for the rest of simulations.

Table 1: Number of elements of the grids.

Grid	A	B	C	D	E	F
Elem.	4,389	9,072	14,432	23,959	32,046	47,232

Parametric study

A parametric study was also conducted to quantify the influence of several simulation parameters on erosion. The Maximum Momentum Redirection Coefficient (MMRC) was tested for three values (20%, 40% and 60%), the normal and tangent-to-wall coefficients were tested for 0.3, 0.5 and 0.85, the diffuse bounce was tested for 1, 3 and 5, and Wen-Yu-Ergun, EMMS-Yang 2004, Turton-Levenspiel and Ganser drag models were implemented. Table 2 summarize the results of the influence of the drag model on erosion. Values marked with "Ref." were taken as reference values for the baseline simulation.

In the literature, Wen-Yu-Ergun drag model is accepted as the most accurate model for bubbling fluidization. EMMS-Yang 2004 was developed for more diluted flows, such as circulating fluidized beds. Turton-Levenspiel drag model calculates drag force assuming single spherical particles, while Ganser model calculates drag forces for single non-spherical particles.

The results show that the drag model was the parameter with the greatest influence, followed by the tangent-to-wall retention coefficient and the normal-to-wall retention coefficient. These retention coefficients model the amount of momentum that the particle retains after a collision. No consistent result of the influence of the retention coefficients was found.

Table 2: Influence of the drag model on the time-averaged circumferential erosion.

Drag model	Finnie (μm/h)	Oka (μm/h)	SCFMED (μm/h)
Wen-Yu-Ergun (Ref)	$2.42 \cdot 10^{-2}$	$7.60 \cdot 10^{-4}$	$1.98 \cdot 10^{-2}$

Drag model	Finnie ($\mu\text{m/h}$)	Oka ($\mu\text{m/h}$)	SCFMED ($\mu\text{m/h}$)
EMMS-Yang 2004	$4.69 \cdot 10^{-2}$	$1.61 \cdot 10^{-3}$	$2.28 \cdot 10^{-2}$
Turton-Levenspiel	$3.50 \cdot 10^{-2}$	$1.15 \cdot 10^{-3}$	$1.53 \cdot 10^{-2}$
Ganser	$3.73 \cdot 10^{-2}$	$1.25 \cdot 10^{-3}$	$2.01 \cdot 10^{-2}$

The other parameters have a smaller influence on erosion than the chosen grid. Further simulations were carried out using the reference values.

Evolution of erosion with fluidization velocity and temperature

The influence of fluidization velocity was assessed simulating four velocities. Similarly, fluidization at four temperatures (300, 600, 900 and 1200 K) were tested and compared. Figure 2 shows the evolution of the time-averaged void fraction with height along a vertical line (reference line) located in the intersection of planes $x = 1 \text{ cm}$ and $z = 0.02 \text{ cm}$. The bed expansion increases with both fluidization velocity and temperature, although sensibility with temperature is lower. This is a measure of bubbling activity. The results of averaged erosion rates are shown in Figure 3. Finnie and Oka erosion models show an increase on erosion with fluidization velocity. That is coherent with previous results (Wiman and Almstedt, 1997), which observed how erosion increases with fluid velocity until the point when the transition towards a turbulent fluidization regime begins. Nonetheless, SCFMED does not reflect this trend, showing a decrease on erosion. This may be related with the mathematical expression of the model, where velocity is only accounted indirectly, by using the Reynolds number. In addition, as void fraction (ϵ) decreases with increasing fluidization velocity because of the bed expansion, seems to be reasonable this dissimilar evolution of SCFMED.

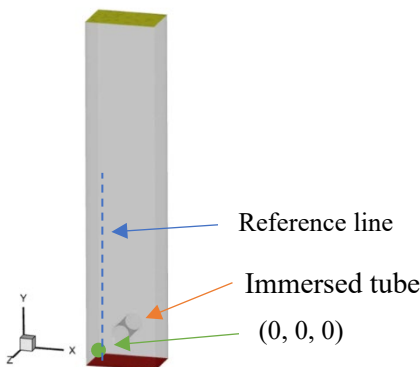


Figure 1: 3D model.

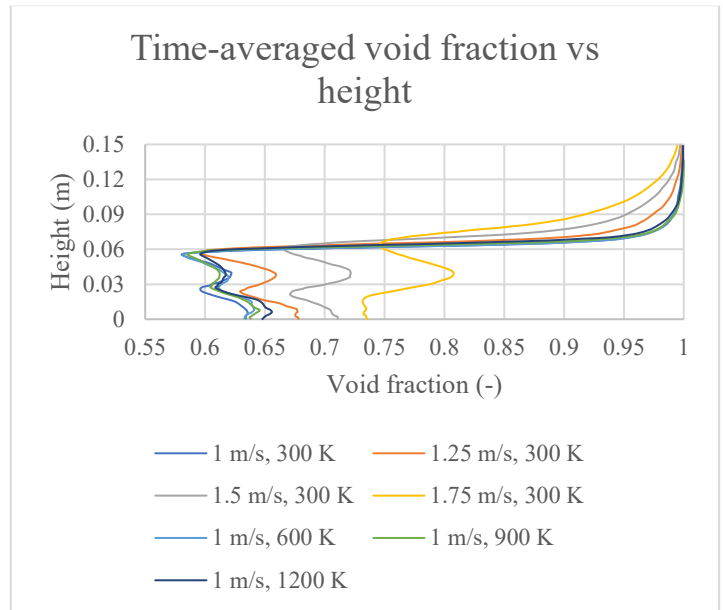


Figure 2: Evolution of time-averaged void fraction with height.

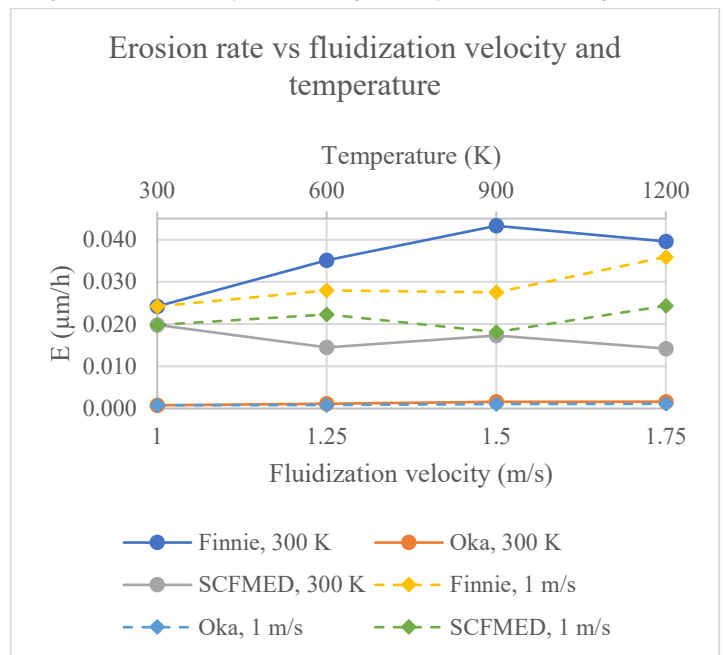


Figure 3: Influence of fluidization velocity and temperature on erosion.

Averaged erosion rates tend to increase with temperature when Finnie and Oka erosion models are implemented. Nonetheless, this trend cannot be observed when SCFMED model is used. Again, SCFMED seems not to reflect the hydrodynamic changes.

The mechanical properties of the materials have been considered to remain constant with temperature since no data of mechanical resistance or hardness at high temperature were available in the literature. Consequently, these preliminary results on temperature



must be adjusted varying those mechanical parameters. Nonetheless, it allowed to detect changes in bed hydrodynamics at high temperature, which were also reported by previous studies (Wiman and Almstedt, 1997).

Conclusions

Although the accuracy of the results on erosion rates have not been compared with experimental data, they follow the expected trend with fluidization velocity and temperature when Finnie and Oka erosion models is implemented. Due to the absence of data on hardness or yield stress at high temperature (out of the scope of this study), the values of these properties at ambient temperature have been used. Therefore, results are influenced by the fluidization dynamics and not by the possible variations of these properties.

Grids were found to have some influence on erosion results, but all grids gave similar results (within the same order of magnitude). All simulation parameters showed some influence on erosion predictions, but the drag model is the most influential one.

Three erosion models were tested. Finnie and Oka erosion model reproduced the typical Type A erosion profile (MacAdam and Stringer, 1995), apart from SCFMED. Finnie and SCFMED gave similar quantitative results. The quantitative results obtained applying Oka model were about two orders of magnitude smaller.

Erosion is strongly related to bubbling activity. Both, erosion, and bubbling, grow up with fluidization velocity and temperature.

Acknowledgments

This work was funded by grants PID2021-127322OB-I00, TED2021-131046B-I00 and RED2022-134219-T funded by MCIN/AEI/ 10.13039/501100011033 and by "ERDF A way of making Europe" and "European

Union NextGenerationEU/PRTR"; grant SBPLY/21/180501/000017 funded by the Regional Government of Castilla-La Mancha and grant 2022-GRIN-34343 funded by Universidad de Castilla-La Mancha.

References

- Córcoles, J.I. *et al.* (2023) 'Flow and heat transfer analysis of a gas-particle fluidized dense suspension in a tube for CSP applications', *Renewable Energy*, 206, pp. 1–12. Available at: <https://doi.org/10.1016/j.renene.2023.02.004>.
- Dong, Y. *et al.* (2022) 'Hybrid high-temperature fouling and erosion characteristics of gas-particle flow around heating tube via CFD-DEM', *Advanced Powder Technology*, 33(12). Available at: <https://doi.org/10.1016/j.appt.2022.103850>.
- Finnie, I. (1960) 'Erosion of surfaces by solid particles', *Wear* [Preprint].
- Lyczkowski, R.W. and Bouillard, J.X. (2002) 'Scaling and guidelines for erosion in fluidized beds', *Powder Technology*, 125, pp. 217–225. Available at: www.elsevier.com/locate/powtec.
- MacAdam, S.S. and Stringer, J. (1995) 'The circumferential distribution of wastage on in-bed tubes in fluidized bed combustors', *Wear*, pp. 325–331.
- Oka, Y.I. *et al.* (1997) 'The impact angle dependence of erosion damage caused by solid particle impact', *Wear*, pp. 573–579.
- Wiman, J. and Almstedt, A.E. (1997) 'Hydrodynamics, erosion and heat transfer in a pressurized fluidized bed: influence of pressure, fluidization velocity, particle size and tube bank geometry', *Chemical Engineering Science*, 52(16).

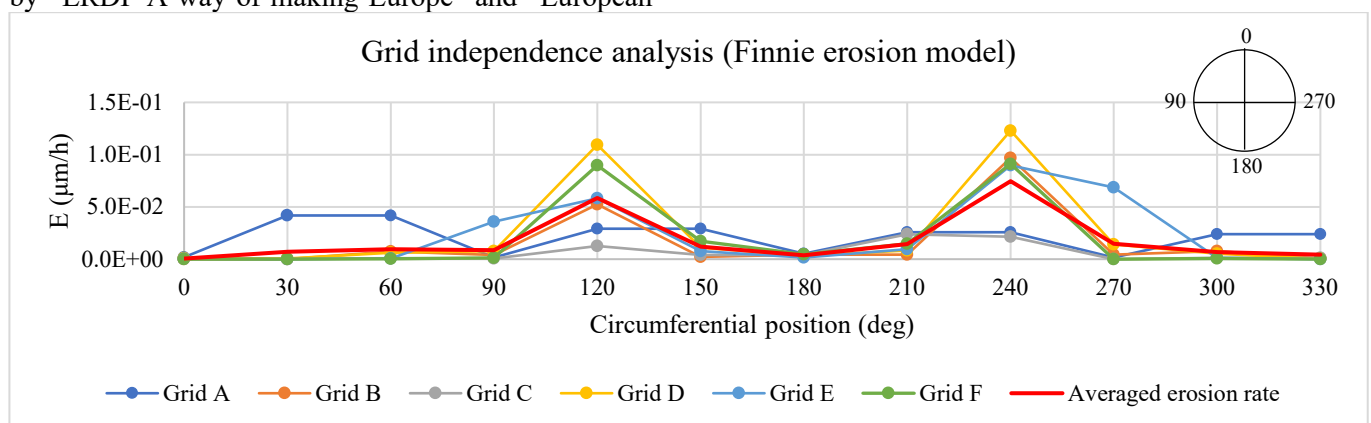


Figure 4. Grid analysis. Finnie erosion model.



Evaluation of the life cycle energy and greenhouse gas emissions of a space heating systems using ettringite as an adsorbent material

S. Bonnin^{*1}, E. Gengembre¹, K. Johannes², F. Kuznik², A. Malley-Ernewein³

¹ Holcim Innovation Center, 95 rue du Montmurier, 38291 Saint Quentin Fallavier, France

² Institut National des Sciences Appliquées de Lyon, CETHIL, (UMR 5008), F-69621, Villeurbanne, France

³ Université Claude Bernard Lyon 1, 71 rue Peter Fink, Bourg-en-Bresse / Bâtiment Sadi-Carnot, 9 rue de la Physique, Campus LyonTech La Doua

Corresponding author: Fax: +33 474821594 Email: salome.bonnin@holcim.com

Decarbonisation in urban heat leads to the use of intermittent energy sources which requires energy storage solutions. Nowadays, various thermal energy storage solutions exist, the most promising being thermochemical energy storage because it's offered a relatively higher theoretical energy density and a long shelf life without heat dissipation during storage compared to latent heat energy storage for example. Microporous silica gel, SrBr₂ hydrate and zeolite are good examples of materials that can be incorporated into thermal energy storage systems.

However, these promising materials have a significant limit: the cost. This is one of main obstacles for the development of thermochemical energy storage in real application scales (individual house, apartment, district and even city). A more affordable cement-based solution, ettringite, had demonstrated equivalent thermal storage capacity and could be applied in a large-scale application.

In this study, two thermo-chemical storage methods for residential application are reviewed according to a life cycle assessment (LCA) approach focusing on the life cycle greenhouse gas (GHG) footprint. The production of an ettringite-based material was found to emit 11x less CO₂ than zeolite 13x, while having a higher energy density.

Keywords: Long term energy storage, Thermochemical energy storage, Life cycle assessment, Greenhouse gas emission, Ettringite

1. Introduction

Heat and electricity storage systems have an important role in the decarbonization of the energy system as they help increase the shares of renewable energy sources in electricity generation. Integrating thermal energy storage (TES) with renewable energy provides a viable solution to the intermittent nature of solar and wind energy systems by storing excess energy when there is an abundance and discharging when the renewable source is not available [17] as shown schematically in Figure 1.

Following this observation, many reviews and articles on the use of different heat systems and their environmental impact were studied to note the potential of TES in current heat systems [16, 18, 9, 15].

TES materials could be divided into sensible heat, latent heat, and sorption storage materials. Among them, chemical sorption materials are very promising thanks to their high energy storage densities and little

heat losses during storage, especially if the storage duration is long [2].

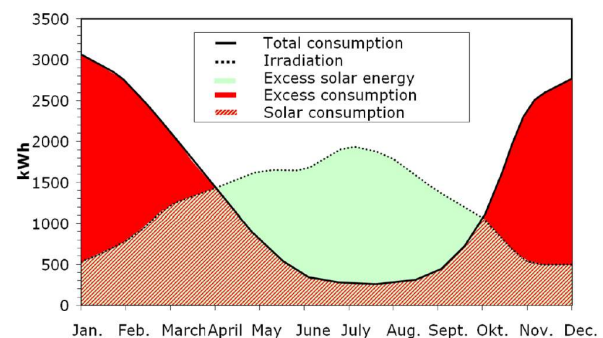
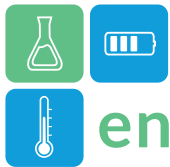


Figure 1 : The seasonal mismatch of between accessible solar energy and heating demand for a family (Zondag, A H, 2020) [20]

Compounds like micro-porous silica gel, SrBr₂ hydrate and MgSO₄-Zeolithe are reported to be of interest for integration into TES systems. However, the cost of materials could be one of main obstacles for the



development of thermochemical energy storage in real application scales (individual house, apartment, district and even city). Fortunately, a mineral named ettringite can easily overcome this limit thanks to its large resource from cementitious materials [3].

Ettringite has been widely studied its properties in building materials but in 1982, a new application for ettringite as a TES material has been proposed due to its reversible and exothermic reaction with water [11], giving it a sorption enthalpy of -1316 kJ/mol [1].

The aim of this article is to study an LCA model to estimate the greenhouse gas of an ettringite-based thermal storage system compared to a zeolite material storage system by using the same design model.

2. Methodology

This study is focus on the comparison between two adsorbent materials for thermal energy storage.

The methodology used to carry out this study is based on the T.V. Tran et al. (2023) study [17] which details the heat system design for the zeolite material, key components, the workflow and system boundaries. GHG emissions are based on the LCA concept.

2.1. System review

2.1.1. Existing model

After studying several thermochemical storage systems, zeolite appeared to be the material most similar to ettringite in terms of operation for thermal energy storage. Starting from this basis, the scientific article of T.V. Tran et al. (2023) [17] was found and is the LCA reference of this study. It's evaluated the energy and emission performances of a zeolite 13x-based heating system charged by a solar air collector.

2.1.2. Adaptation to an ettringite-based material

The model used as the heat system is either designed for another material (zeolite 13x) that has different properties to ettringite. Some parameters need to be adjusted to suit our material.

For example, the area of the solar collector system required is calculated using the maximum energy that can be stored in the adsorbent. This value makes it possible to average the minimum energy required to fully load the storage system daily.

Table 1 : Adsorbents properties

Adsorbent material	Material diameter (mm)	Volumic mass (kg/m ³)	Energy density (kWh/m ³)	Reference
Zeolite 13x pellet	10	704	154	[17, 7]
Ettringite-based particule	1-2	1070	176	[4]

According to the Table 1, ettringite and zeolite-based materials have a significative diameter difference that will increase the flow resistance and the fan capacity which can impact the overall energy efficiency [19].

The ettringite-based material of this study is a formulation taking from the study of Chen et al. (2021) [4] which is a mixture of two cements with a W/C = 1.1 showing an ettringite rate of 80 wt% in the material.

2.2. Life cycle assessment of the system

LCA, according to the International Organization for Standardization (ISO) guidelines and framework, is used to evaluate life cycle GHG emissions [12, 13]. LCA has four phases: goal and scope definition, inventory analysis, impact assessment, and interpretation [2].

2.2.1. Goal and scope definition

The overall objective of this study's LCA is to develop to understand the GHG emissions of an ettringite-based thermal storage in a residential space heating application and compare it with the zeolite 13x solution. Such an assessment will provide insights into the use of solar-integrated adsorbent as an environmentally sustainable alternative to the conventional heating systems available in the market. 1 kWh of heat generated from ettringite-based material storage is considered as the functional unit and GHG emissions is the environmental indicators. The functional unit is the reference unit to which all input and output requirements are normalized. It is used as a base to have a meaningful comparison among different technologies with the same function.

A classic system boundary considered for the life cycle assessment, includes material extraction, manufacturing, transportation, operation, and end-of-life (recycling).

Since we were unable to find the emissions of a large - scale recycling plant for our ettringite-based material, the recycling scenario has not been studied. Analyses of uncertainty and sensitivity have not yet been studied. We also assumed that the emissions of the assembly of this heating system in a residential house are negligible and, therefore, they are not included in the calculation.

2.2.2. Inventory analysis

Inventory analysis involves input and output data compilation and calculation at each stage of the life cycle of a product system. This study is focus on the comparison of two adsorbent materials, ettringite-based and zeolite-based material related to the heat system can be found on the T.V Tran et al. (2023) article [17].

The life of the system is considered to be 20 years because of the recommendation that a regular gas furnace be changed after about that length of time [17].

3. Results and discussion

3.1. Materials emissions

Table 2 shows the CO₂ emissions associated with the production of one kilogram of each of the two adsorbent materials selected for this study. The uncertainty value linked to the CO₂ impact of zeolite is a calculation of the standard deviation of CO₂ values found in the literature. For ettringite-based material, a sensitivity analysis was carried out considering a pessimistic impact on cement (1 kg CO₂ eq/kg of cement).

The impact of ettringite-based material is calculated by using the impact of the cement mix by considering the dilution of water, neglecting the impact of the transport and the manufacturing process. These initial results, show that ettringite-based material has a significantly lower GHG impact for a higher energy density.

Table 2 : Emissions from adsorbent materials

Adsorbent material	CO ₂ impact		Notes
	g CO ₂ eq/kg	kg CO ₂ eq/m ³	
Zeolite 13x pellet	4930 ± 150	3473 ± 108	[8, 10, 14]
Ettringite-based cementitious particule	357 ± 120	382 ± 127	Cement impacts are recovered from EPDs [5, 6]

As reported in the T.V. Tran et al. (2023) article [17], the material production of the all heating system represent 25% of the life cycle GHG emissions of which 5% is the zeolite impact. The study of a new material with a lower GHG impact opens the doors to a life cycle GHG heating system potential that is also lower.

3.2. Heat systems emissions

Figure 2 shows that the use of a domestic heating system using zeolite as an adsorbent material is 5 times more interesting than others electrical heating solutions by applying Alberta grid emissions to all the space heating systems studied.

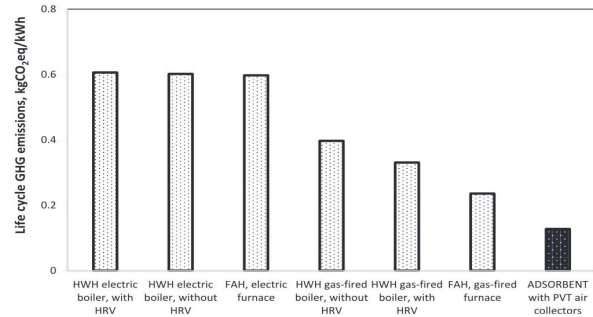


Figure 2 : GHG emissions comparison among different heating systems in Alberta (Tran, Tien Viet and al., 2023) [17]

The recalculation of a heating system using ettringite has not yet been carried out, but it is assumed to be similar to that of zeolite. Therefore, assuming that the only major change is in the production of the adsorbent material, ettringite-based material appears to be a good material as a thermal energy storage solution in a domestic heating system.

Furthermore, the heating system under consideration in this study is designed for a single-house application. It is relatively straightforward to envisage that on an industrial scale, the contribution of the adsorbent material to the CO₂ impact of the system will be greater.

More studies need to be done to understand the lifetime, charging/discharging properties, and recyclable characteristics of the zeolite material and the ettringite material.

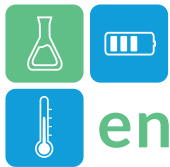
Conclusions

After studying several scientific articles, it is clear that the production of materials and the operating phase account for the majority of the environmental impact of a heating system. It is therefore not surprising that several adsorbent materials are being studied as thermal energy storage solutions.

By studying the ettringite-based material compared to zeolite 13x in a thermal system, it appeared to be more interesting in terms of energy performance, greenhouse gas emissions and cost. Which makes ettringite a promising material for thermal energy storage in a residential house application.

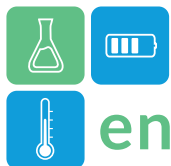
Acronyms

TES	Thermal Energy Storage
LCA	Life Cycle Assessment
GHG	GreenHouse Gas
CO ₂	Carbon dioxide
EPD	Environmental Product Declaration
W/C	Water/cement mass ratio



References

- [1] Baquerizo, Luis G., Thomas Matschei, et Karen L. Scrivener. « Impact of Water Activity on the Stability of Ettringite ». *Cement and Concrete Research* 79 (janvier 2016): 31-44. <https://doi.org/10.1016/j.cemconres.2015.07.008>.
- [2] Chen, B. and al. (2021) Investigation on Ettringite as a Low-Cost High-Density Thermochemical Heat Storage Material: Thermodynamics and Kinetics. *Solar Energy Materials and Solar Cells* 221: 110877. <https://doi.org/10.1016/j.solmat.2020.110877>.
- [3] Chen, B. and al. (2019) Physicochemical Properties of Ettringite/Meta-Ettringite for Thermal Energy Storage: Review. *Solar Energy Materials and Solar Cells* 193: 320-34. <https://doi.org/10.1016/j.solmat.2018.12.013>
- [4] Chen, B. (2020). Study of an ettringite-based thermochemical energy storage for buildings. INSA-Lyon, France.
- [5] CSA cement EPD <https://api.environdec.com/api/v1/EPDLibrary/File/s/99c83b8d-d46f-4237-f61d-08dbfcbc4c1b/Data>
- [6] CEM I cement average EPDs in France https://www.infociments.fr/sites/default/files/articles/pdf/2024_15_01_ICV_FRANCE%20CIMENT_CEM%20I_v3.1_0.pdf
- [7] D. Dicaire and F.H. Tezel, (2013). Use of adsorbents for thermal energy storage of solar or excess heat: improvement of energy density, *Int. J. Energy Res.* 37 (9) 1059–1068.
- [8]ecoinvent 3.9.1 Dataset Documentation 'zeolite production, powder - RER - zeolite, powder'
- [9] Fujii, Shoma, and al. (2022). Prospective Life Cycle Assessment for Designing Mobile Thermal Energy Storage System Utilizing Zeolite ». *Journal of Cleaner Production* 365: 132592. <https://doi.org/10.1016/j.jclepro.2022.132592>.
- [10] Horn and al., « Life Cycle Assessment of Innovative Materials for Thermal Energy Storage in Buildings ». *Procedia CIRP* 69 (2018): 206-11.
- [11] Ings, J.B., and Brown, P.W. (1982), An evaluation of hydrated calcium aluminate compounds as energy storage media, NASA STI/Recon Technical Report N, pp. 83.
- [12] International Organization for Standardization, ISO 14040 International Standard-Environmental Management-Life Cycle Assessment-Principles and Framework, 2006. Geneva, Switzerland.
- [13] International Organization for Standardization, ISO 14044 International Standard-Environmental Management: Life Cycle Assessment; Requirements and Guidelines, 2006. Geneva, Switzerland.
- [14] Nienborg and al., « Closed Adsorption Heat Storage—A Life Cycle Assessment on Material and Component Levels ». *Energies* 11, n° 12 (6 décembre 2018): 3421.
- [15] Raluy, R. Gemma, and Ana Cláudia Dias. (2020) Life Cycle Assessment of a Domestic Gas-Fired Water Heater: Influence of Fuel Used and Its Origin ». *Journal of Environmental Management* 254 : 109786. <https://doi.org/10.1016/j.jenvman.2019.109786>.
- [16] Saoud, Assaad, Hassan Harajli, and Rima Manneh. (2021) Cradle-to-Grave Life Cycle Assessment of an Air to Water Heat Pump: Case Study for the Lebanese Context and Comparison with Solar and Conventional Electric Water Heaters for Residential Application. *Journal of Building Engineering* 44: 103253. <https://doi.org/10.1016/j.jobeb.2021.103253>.
- [17] Tran, Tien Viet and al. (2023) Developing a Framework to Evaluate the Life Cycle Energy and Greenhouse Gas Emissions of Space Heating Systems Using Zeolite 13× as an Adsorbent Material ». *Journal of Energy Storage* 74 : 109443. <https://doi.org/10.1016/j.est.2023.109443>.
- [18] Yang, Lijun, Radu Zmeureanu, and Hugues Rivard. (2008) Comparison of Environmental Impacts of Two Residential Heating Systems. *Building and Environment* 43, n° 6 : 1072-81. <https://doi.org/10.1016/j.buildenv.2007.02.007>.
- [19] Zhengzhou Gold Mountain Science and Technique Co. Ltd, Molecular Sieve Zeolite 13X [cited 2020 April 24]; Available from: <http://www.adsorbentcn.com/13x.htm>, 2019.
- [20] Zondag, A H. (2020). Seasonal and daily heat storage for heating & cooling of buildings. <http://www.concreteheat.com/downloads/>



Evaluation of thermal energy storage performance of composite binary salt hydrates with $\text{MgCl}_2/2\text{CaCl}_2$ in a packed bed reactor

Hongzhi Liu^{1,*}, Fang He¹, Katsunori Nagano¹

1 Hokkaido University, Faculty of Engineering, Environmental System Research Laboratory, N13-W8, 060-8628, Sapporo, Japan

*Corresponding author e-mail: liuhz@eng.hokudai.ac.jp

Abstract

The energy storage performance of composite binary salt hydrates of mesoporous Wakkanai Siliceous Shale (WSS) + $\text{MgCl}_2/2\text{CaCl}_2$ and microporous 13X + $\text{MgCl}_2/2\text{CaCl}_2$ in packed bed reactors were evaluated experimentally and numerically. The proposed numerical model can predict the experimental results well; thus, the effects of the porous matrix, particle size, and the height of the packed bed were discussed. The packed bed reactor with WSS composite salt hydrates can supply a higher outlet air temperature than the one with 13X composites. Moreover, a packed bed with a smaller particle size exhibits higher energy storage density, and a particle size of 2 mm is recommended by considering both the storage density and the pressure drop. Though the high-temperature outlet air prolongs with the increase of the height, the height of the packed bed still needs to be determined according to the actual demand of requirements of temperature and energy storage density.

Keywords: Thermochemical energy storage (TCES), Composite salt hydrates, MgCl_2 and CaCl_2

Introduction

Salt hydrate as one type of TCES material is suitable for storing thermal energy below 150°C with the advantages of high energy storage density (ESD), non-pollution, mild reaction, and dehydration temperature consistent with the temperature provided by the solar collector. Though pure salt hydrates have high theoretical ESD, they suffer from defects such as easy deliquescence and poor heat and mass transfer properties (Jarimi and al., 2019). Thereby composite salt hydrates were proposed by impregnating pure salt hydrates into a porous matrix (Zhang and Wang, 2020). Moreover, binary salt hydrates are obtained by mixing two pure salt hydrates to improve kinetics and cycle stabilities (Rammelberg and al., 2016). In this study, the storage performances of two composite binary salt hydrates of WSS+ $\text{MgCl}_2/2\text{CaCl}_2$ and zeolite 13X $\text{MgCl}_2/2\text{CaCl}_2$ in packed bed reactors were evaluated numerically.

Materials and TES reactor study

Synthesis of composite $\text{MgCl}_2/2\text{CaCl}_2$

Composite binary salt hydrates were fabricated by the vacuum impregnation method. The mixture of MgCl_2 and CaCl_2 with a molar ratio of 1:2 ($\text{MgCl}_2/2\text{CaCl}_2$) was used to fabricate the composite binary salt hydrates, which was proved to have high thermal energy storage

density and fast kinetics (Rammelberg and al., 2016). Wakkanai Siliceous Shale (WSS) is a natural mesoporous material distributed in the northern part of Hokkaido in Japan, and the pellet diameter is within 1.5-2.5 mm. Zeolite 13X with a diameter of 1.6-2.5 mm was selected. Three samples with different mass fractions were synthesized for each porous material as shown in Table 1. The average pore diameter of the WSS composites is about 8 nm, denoted as mesoporous material. While the 13X composites are denoted as microporous material with an average pore diameter smaller than 2 nm.

Table 1: Fabricated composite $\text{MgCl}_2/2\text{CaCl}_2$.

Matrix	WSS			13X		
x (wt.%)	7.37	13.65	20.38	7.24	13.50	17.90
Sample	WSS 7	WSS 13	WSS 20	13X 7	13X 13	13X 17

Figure 1 shows the sorption isotherm of composite binary salt hydrates at 25°C with a saturation pressure of 3.1684 kPa. The impregnation of $\text{MgCl}_2/2\text{CaCl}_2$ has a significant impact on the water uptake of the composites. Compared with the pure porous materials, there is a large promotion in water uptake of the composite $\text{MgCl}_2/2\text{CaCl}_2$. A first quick mass lift of WSS composite $\text{MgCl}_2/2\text{CaCl}_2$ can be observed when the relative pressure P/P_0 is lower than 30%, considered as the hydration of salt. A followed stable growth between RH 30%-70% is thought to be caused by the chemical sorption of the previously formed salt hydrate.

When the relative humidity is larger than 70%, a high slope increase in water uptake is the contribution of capillarity condensation. The equilibrium water uptake of microporous 13X is quite larger than that of mesoporous WSS with homogeneous micropore distribution. For the 13X composite $MgCl_2/2CaCl_2$, the first mass lift when the relative pressure P/P_0 is lower than 40% is related to the monolayer sorption in the micropores.

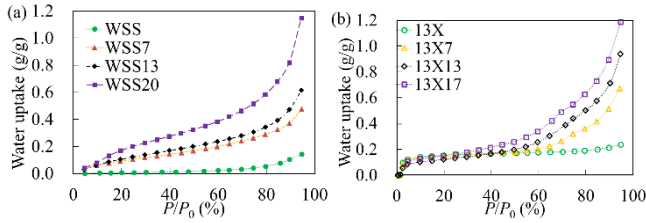


Figure 1: Sorption isotherm of (a) WSS+ $MgCl_2/2CaCl_2$ and (b) 13X+ $MgCl_2/2CaCl_2$.

Experimental setup of packed bed reactor

An open TCES system was developed, in which a packed reaction bed with an inner diameter of 36 mm and a height of 50 mm was installed as shown in Figure 2. In the heat release process, humid air enters from the bottom and reacts with the inside composite binary salt hydrates in the bed. In the heat storage process, hot air regenerates the composite binary salt hydrates.

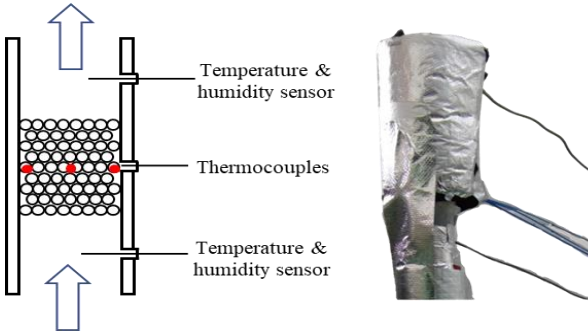


Figure 2: Packed bed reactor filled with composites.

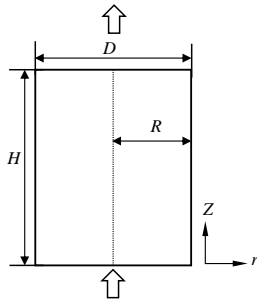


Figure 3: Physical model of the packed bed.

Numerical simulation of packed bed reactor

A two-dimensional model is illustrated in Figure 3 based on the following assumptions. The air flowing through the packed bed is regarded as an ideal gas. The

specific heat capacity, density, and thermal conductivity of particles are consistent in radial direction. The radiation heat transfer is not considered. The gas phase and the solid phase are in local thermal equilibrium. The heat loss through the outside of the reactor is ignored with sufficient thermal insulation.

1. Governing equations

(1) Mass conservation equation of water vapor

$$\varepsilon(r) \frac{\partial C}{\partial \tau} - \nabla \cdot (D_{md} \nabla C) + \varepsilon(r) u \frac{\partial^2 C}{\partial z^2} = \pm (1 - \varepsilon(r)) \rho_p \frac{dw}{d\tau} \quad (1)$$

C is the molar concentration of water vapor in air, mol/m^3 ; ρ_p is the particle density, kg/m^3 ; D_{md} is the molecular diffusion coefficient (Majumdar, 1998), m^2/s ; w is the instantaneous water uptake, mol/kg ; $\varepsilon(r) = 0.4 + 0.544 \exp(-5(r_{bed} - r)/d_p)$ is the void fraction of the packed bed (Winterberg and al., 2000).

(2) The flow of air in a packed bed follows Darcy's law and permeability equation (Ergun, 1952).

$$-\frac{\partial p}{\partial z} = \alpha \frac{(1 - \varepsilon)^2}{\varepsilon^3} \frac{\eta}{d_p^2} u + \beta \frac{(1 - \varepsilon)}{\varepsilon^3} \frac{\rho}{d_p} u^2 \quad (2)$$

(3) Energy conservation equation

$$\frac{\partial T}{\partial \tau} - \nabla \cdot (\lambda \nabla T) + \varepsilon(r) u C_{p,g} \frac{\partial T}{\partial z} = \mp (1 - \varepsilon(r)) \rho_p \frac{dw}{d\tau} \cdot \Delta H \quad (3)$$

$$\overline{\rho C_p} = \varepsilon \rho_g C_{p,g} + (1 - \varepsilon) \varepsilon_p \rho_g C_{p,g} + (1 - \varepsilon) \rho_g C_{p,s} + (1 - \varepsilon) \rho_p w C_{p,water} M_{water} \quad (4)$$

(4) The LDF model is used to represent the reaction kinetics, where the effective diffusion coefficient D_{eff} is shown in Equation (6).

$$\frac{dq}{d\tau} = \frac{15 D_{eff}}{r_p^2} (w_{eq} - w) \quad (5)$$

$$D_{eff} = \frac{\varepsilon_s D_{pd}}{\tau_p} + \frac{\rho_s}{\rho_g} \frac{D_{sd}}{\tau_s} \frac{\partial w_{eq}}{\partial x_s} M_{water} \quad (6)$$

2. Initial and boundary conditions

(1) Initial condition in heat release process: $T_0 = 25^\circ\text{C}$, $C_0 = C(25^\circ\text{C}, 4\% \text{RH})$, $w_0 = w(25^\circ\text{C}, 4\% \text{RH})$.

(2) Initial conditions in the heat storage process: the initial temperature, water vapor concentration, and water uptake are the final corresponding parameters at the end of the heat release process.

(3) Inlet condition: $u = u_{g,in}$, $T = T_{g,in}$, $C = C_{g,in}$.

(4) The inner wall of the reactor is set as non-slip and adiabatic boundary conditions.

$$(5) \text{ Outlet condition: } \frac{\partial u}{\partial z} = 0, \frac{\partial u}{\partial r} = 0, \frac{dT}{dz} = 0.$$

Results and discussion

Model validation

Mesh number 9804 was chosen after the mesh check because it could achieve sufficient calculation accuracy. The adaptive time step was adopted with an initial time step of 0.001 s. In the experiment, the inlet air flow rate was 0.18 m/s, and the desorption temperature was 60°C. The numerical simulation results are compared with the experimental results in both heat release and storage processes (WSS7) as shown in Figure 4. Though there is some discrepancy (10-30 min) in the heat storage process, the relative error in the subsequent period is less than 10%.

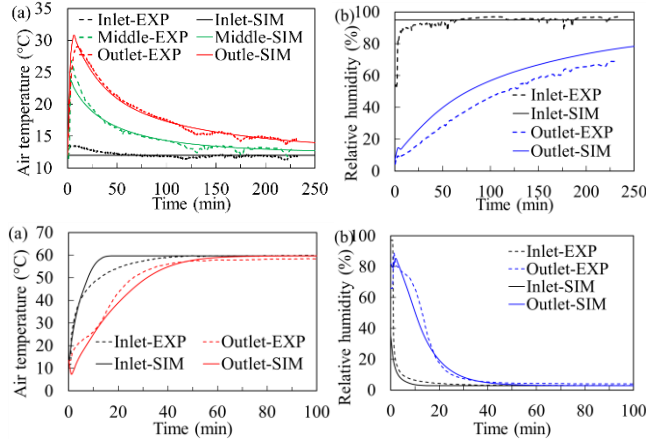


Figure 4: (a) Air temperature and (b) outlet air humidity of WSS7 (up) heat release process; (down) heat storage process.

Effect of porous matrix and salt content

The outlet air temperature of the packed bed reactor with different samples is shown in Figure 5. The salt content has a small impact on the maximum outlet air temperature of the reactor with WSS composites. It has a significant effect on the releasing duration of high-temperature outlet air because the increase in the salt content of the composite binary salt hydrates can accelerate the total sorbed water amount. The outlet air temperature of the packed bed reactor with 13X composites is lower than that of the packed bed reactor with WSS composite with the same salt content because the desorption temperature of 60°C is not enough to desorb the strong monolayer sorption on 13X. The cumulative thermal energy in the heat storage/release processes is calculated by Equation (7) and (8), respectively. The volumetric ESD and the average volumetric heat power are calculated. The ESD of WSS20 of 1 GJ/m³ with a temperature lift of as high as 40°C is the highest among tested samples. The increase in salt content is conducive to improving the

sorption capacity, which is conducive to releasing sorption heat as a result.

$$Q_{\text{TES}} = \rho_g C_{p,g} G \int_0^{t_{\text{TES}}} (T_{g,\text{in}} - T_{g,\text{out}}) dt \quad (7)$$

$$Q_{\text{TER}} = \rho_g C_{p,g} G \int_0^{t_{\text{TER}}} (T_{g,\text{out}} - T_{g,\text{in}}) dt \quad (8)$$

$$\text{ESD} = \frac{Q_{\text{TER}}}{V} \quad (9)$$

$$P = \frac{c_{p,g} \rho_g f_g \int_0^{\tau} (T_{g,\text{out}} - T_{g,\text{in}}) d\tau}{V \cdot \tau} \quad (10)$$

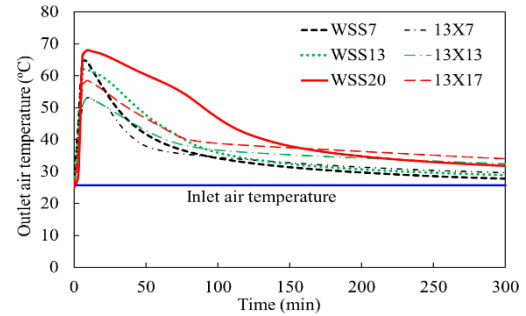


Figure 5: Outlet air temperature of packed bed reactors.

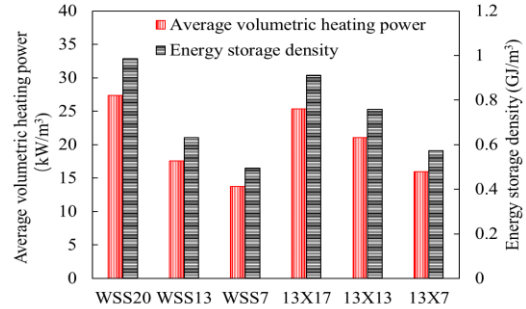


Figure 6: Volumetric power and ESD of composites.

Effect of the particle size

The outlet air temperature of packed beds with different particle sizes at the same inlet air flow rate is shown in Figure 7. Because of the increased specific surface area of particles, the maximum outlet air temperature increases with the decrease in particle size.

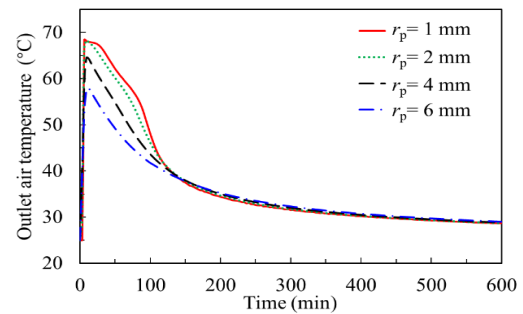


Figure 7: Outlet air temperatures (particle sizes).

The pressure drop and ESD are illustrated in Figure 8. Considering both the ESD and the pressure drop, composite binary salt hydrates with a particle size of 2 mm are proper.

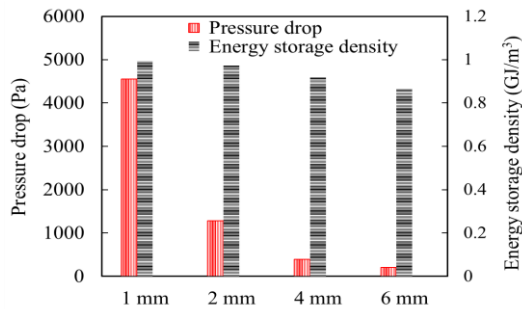


Figure 8: Pressure drops and ESDs of packed beds (particle sizes).

Effect of the height of the packed bed

The outlet air temperature of the packed bed with different heights is shown in Figure 9. The height of the packed bed has nearly no influence on the maximum outlet air temperature of the packed bed. With the increase of the height, more composites can be utilized to sorb water vapor, release heat, and prolong the heat release duration. The material level ESD has been calculated based on the total sorbed water amount within 600 min, which is illustrated in Figure 10 as well as the reactor level ESD calculated according to Equation (9). 60 % of the material level ESD can be realized through the packed bed reactor. The decrease of ESD with the height is considered to be caused by the same inlet air flow rate. A reasonable height of the packed bed should be decided by considering the needed air temperature and duration.

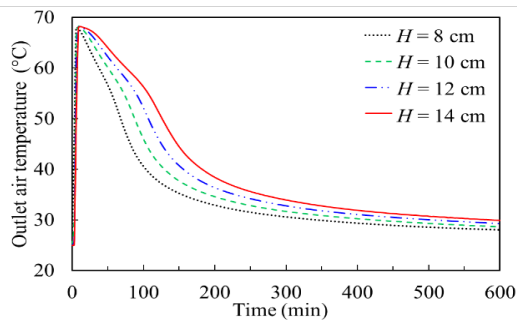


Figure 9: Outlet air temperature (heights).

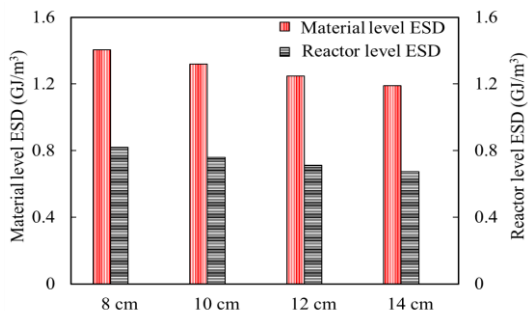


Figure 10: Material and reactor level's volumetric ESDs (heights).

Conclusions

The storage performance of packed bed reactors with composite binary salt hydrates was studied experimentally and numerically.

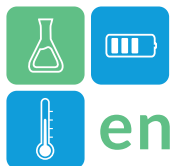
- (1) The proposed numerical model can predict the experimental results well.
- (2) The packed bed reactor with WSS composite salt hydrates can supply a higher outlet air temperature than the one with 13X composites.
- (3) The WSS20 showed the highest thermal energy storage density. Reducing the particle size can improve the energy storage density of the packed bed, and a particle size of 2 mm is recommended by considering both the pressure drop and the energy storage density.
- (4) Though the high-temperature outlet air prolongs with the increase of the height, the height still needs to be calculated according to the actual demand of the outlet air temperature and duration.

Acknowledgment

The authors would like to thank Mr. Zhendong Ye for helping to conduct the experiments.

References

- Ergun, S. (1952). Fluid Flow Through Packed Columns. Chemical Engineering Progress
- Jarimi, H. and al. (2019). Review on the recent progress of thermochemical materials and processes for solar thermal energy storage and industrial waste heat recovery. International Journal of Low-Carbon Technologies. <https://doi.org/10.1093/ijlct/cty052>
- Majumdar, P. (1998). Heat and mass transfer in composite desiccant pore structure for dehumidification. Solar Energy. [https://doi.org/10.1016/S0038-092X\(97\)00080-7](https://doi.org/10.1016/S0038-092X(97)00080-7)
- Rammelberg, H.U. and al. (2016). Thermochemical heat storage materials – Performance of mixed salt hydrates. Solar Energy. <https://doi.org/10.1016/j.solener.2016.07.016>
- Winterberg, M. and al. (2000). A simple and coherent set of coefficients for modeling of heat and mass transport with and without chemical reaction in tubes filled with spheres. Chemical Engineering Science. [https://doi.org/10.1016/S0009-2509\(99\)00379-6](https://doi.org/10.1016/S0009-2509(99)00379-6)
- Zhang, Y. and Wang, R. (2020). Sorption thermal energy storage: Concept, process, applications and perspectives. Energy Storage Materials. <https://doi.org/10.1016/j.ensm.2020.02.024>



Evaluation of volcanic ash as TES material: Case of study of a CSP plant.

Camila Barreneche*, Marc Majó, Alejandro Calderón, Adela Svobodova, Ana Inés Fernández
University of Barcelona, Faculty of Chemistry, Department of Materials Science and Physical Chemistry, Martí i
Franqués, 1, floor 7, Barcelona, Spain.

*Corresponding author e-mail: c.barreneche@ub.edu

Abstract

Energy storage strategies are needed today more than ever. Improving these technologies and implementing new ones, will help us to make a better use of the renewable energies. Thermal storage using sustainable solids, is a strategy under study for the new generation of concentrating solar power (CSP) plants. The use of low-cost ceramic materials such as natural materials or wastes, will help in a levelized cost of electricity (LCOE) reduction. This will make CSP plants significantly more competitive, bringing them up to the level of conventional energy plants. The objective of this study is to characterize and evaluate the properties of volcanic ash as an alternative thermal energy storage material. Thermal, chemical, physical and mechanical properties have been analysed, along with its high temperature stability. This complete evaluation will provide insight into the potential use of volcanic ash as a TES material in CSP plants, which will contribute to the increased adoption of renewable energy sources.

Keywords: CSP, TES, Volcanic ash

Introduction

With the increasing demand for clean energy, concentrating solar power (CSP) technology has become a promising option for electricity generation. However, the success of CSP plants largely depends on the availability and cost-effectiveness of the thermal energy storage (TES) materials used in the power plant. Although molten salts are the predominant TES technology in commercial CSP projects (Prieto & Cabeza, 2019), alternative sustainable materials are being studied for its implementation as TES media (Jacob et al., 2022). The use of an alternative material as TES could reduce the costs of the production of electricity used and will help in operational and production of electricity costs reduction (Navarro et al., 2012). With the use of high-temperature particles, the maximum storage temperature can also be increased, and the thermal-to-electric efficiency of the power cycles improved. Also, it enables the use of other HTF for a higher cycle efficiency at elevated temperatures such as supercritical CO₂ (Turchi et al., 2013). Also, particle solar receivers, to capture the solar radiation from the heliostat field, are currently being investigated and tested. Unlike conventional receivers, particle receivers use solid particles that are heated as they fall through a beam of concentrated sunlight (Ho, 2016). When searching for natural rocks capable of withstanding high temperatures for multiple cycles or having good contact with different HTFs, numerous

rock types have been investigated (El Alami et al., 2020). Volcanic ash is an abundant, inexpensive and extreme heat-resistant material with potential for use as TES medium. The objective of this study is to characterize and evaluate the properties of volcanic ash as an alternative thermal energy storage material. Chemical, thermal, physical and mechanical properties have been analysed, along with its high temperature stability with a cycling test between 250 °C to 750 °C.

Materials and methodology

Materials

The volcanic ash for this research was collected near El Paso village on the western flank of La Palma island's Cumbre Vieja rift zone in the Canary Islands, Spain, by members of the Institute for Environmental Studies and Natural Resources (I-UNAT) at the University of Las Palmas de Gran Canaria. The collected sample was then dried and sieved for subsequent evaluation and testing.

Thermal cycling test

To conduct the thermal cycling test in this experiment, a specialized Carbolite-gero equipment designed for the Birmingham Centre for Energy Storage (BCES) was used. The automated cycling mechanism transfers a volcanic ash sample into a high-temperature zone for a specified duration and then relocates it to a low-temperature area for cooling. This cycle is repeated as needed. A small round tablet made of volcanic ash, measuring 3.81 mm in thickness and 12.7 mm in

diameter, was fabricated for the test using an automated press and a specific mold. The tablet underwent 1000 cycles, alternating between temperatures of 250 °C and 750 °C in an air atmosphere. Each complete cycle lasted 22 minutes, with 10 minutes of heating inside the furnace and 12 minutes in the lower-temperature zone using a fan for controlled cooling.

Characterization techniques

Real density was determined using a helium pycnometer (Accu-Pyc 1330), and particle size distribution (PSD) was analyzed with a laser diffraction particle size analyzer (Beckman Coulter LSTM 13 320) using the Fraunhofer mathematical model. SEM images obtained from a Hitachi TM3030 scanning electron microscope were used to evaluate particle surfaces before and after thermal exposure. Major compound evaluation was conducted through X-Ray Fluorescence (XRF) using a Panalytical Philips PW 2400. Then, the crystalline phase determination was accomplished with X-Ray diffraction (XRD) equipment (Bruker D8), and a comparison of XRD patterns was made before and after the thermal cycle.

Additionally, thermogravimetric analysis (TGA) up to 750 °C in an air atmosphere assessed changes in solid particles. Differential scanning calorimetry (DSC) was carried out through simultaneous thermal analysis (STA 449 F3 Jupiter Netzsch) at the University of Birmingham, calculating specific heat capacity at 300 °C and 750 °C under air atmosphere. Thermal conductivity was determined using a Laser Flash (LFA 427 Netzsch) at the University of Birmingham, and thermal diffusivity was determined based on sample thickness and time at 50% temperature increase, as expressed in eq. 1. The thermal conductivity of the sample was then calculated using the obtained thermal diffusivity, heat capacity (C_p), and bulk density (ρ) through the relation expressed in eq 2.

$$a = 0.1388 \frac{l^2}{t_{0.5}}$$

$$\lambda = a \cdot C_p \cdot \rho$$

Where l is the sample thickness, t is the time, λ is the thermal conductivity, a is the thermal diffusivity, C_p is specific heat capacity and ρ is the bulk density of the sample.

A Thermo-Mechanical Analyzer (TMA 450, TA Instruments) measured the coefficient of thermal expansion (CTE) for different temperature ranges, extending from 50 to 750 °C with a heating rate of 5 °C/min. The selected temperature intervals for CTE

determination were 50 °C to 275 °C, 275 °C to 500 °C, and 500 °C to 725 °C.

Results and Discussion

The real density of the volcanic ash sample, received in dust form, was assessed using a helium pycnometer, yielding a value of $2.41 \pm 0.01 \text{ g/cm}^3$. Additionally, a tablet with dimensions of 3.81 mm thickness, 12.7 mm diameter, and a mass of 0.99 g was created for thermal cycling evaluation and the bulk density calculated before and after the thermal cycling are $2.06 \pm 0.02 \text{ g/cm}^3$ and $2.02 \pm 0.02 \text{ g/cm}^3$ respectively.

The PSD evaluation indicated a normal distribution in volume percentage (vol. %) of the particles and with a d_{90} of 250 μm . Conversely, a significant quantity of fine particles was identified.

The SEM images in figure 1 illustrate the shape and roughness of volcanic ash particles after an initial sieving to remove excess fines. Particle surfaces were examined both before and after thermal cycling. SEM images of volcanic ash as received at 100x (figure 1(a)) and at 500x (figure 1(b)) can be observed. Figure 1(b) and (c), shows the same magnitudes of resolution after the thermal cycling. SEM images after 1000 cycles between 250 °C and 750 °C reveal noticeable cracks on the surfaces of many particles, detailed in the same figure. Additionally, agglomerations of particles are observed around larger particles, potentially attributed to crystallographic changes and sintering at high temperatures.

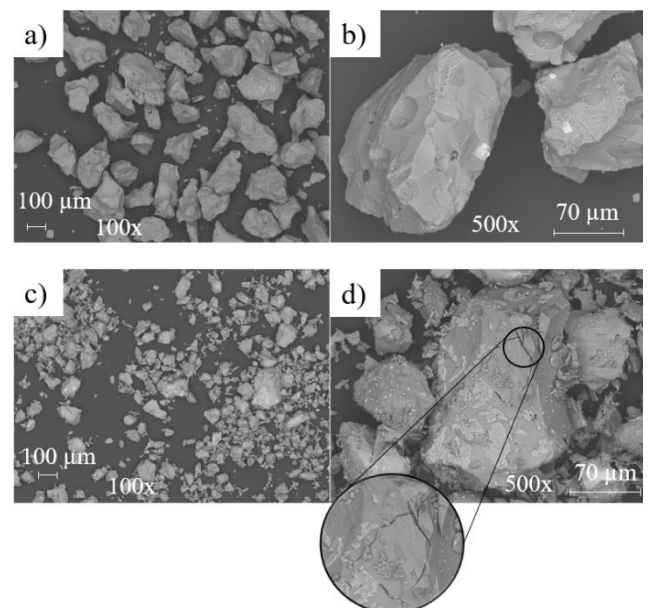


Figure 1: SEM images of: a) volcanic ash as received at 100x and b) 500x and, c) volcanic ash after thermal cycling test at 100x and d) 500x.

The XRF evaluation, reveals the percentage of major compounds in a volcanic ash sample. The analysis shows a

notable presence of SiO₂ (43.7 wt.%), along with significant percentages of Fe₂O₃ (13.6 wt.%), Al₂O₃ (13.2 wt.%), and CaO (11.6 wt.%). In smaller percentages, MgO (8.5 wt.%), TiO₂ (3.7 wt.%), Na₂O (3.3 wt.%), K₂O (1.4 wt.%), P₂O₅ (0.8 wt.%), and MnO (0.2 wt.%) were also detected.

Figure 2 displays XRD diffractograms depicting the volcanic ash before and after thermal cycling. The major crystalline phases in the sample prior to cycling (Figure 2a) include diopside, anorthite, and olivine. Minor phases such as metallic oxides like magnetite and titanomagnetite are also identified. After the cycling test (Figure 2b), a second crystallographic determination reveals the transformation of magnetite peaks into hematite. A slight increase in mass is anticipated due to the oxidation of iron compounds, as validated further on by TGA analysis in table 1, indicating noticeable mass gain during initial thermal exposure.

However, peaks associated with the titanomagnetite phase remain unchanged, suggesting a lack of observable modifications in our sample. Despite the potential transformation of titanomagnetite documented in the literature (Gorbatova et al., 2021), progressing from titanomagnetite to ilmenite and further to rutile at temperatures below 850 °C, specific alterations related to these transitions are not prominently evident in our findings. While our testing methodology's temperature range might initiate these reactions, our results have not detected such transformations.

Table 1 provides thermal stability metrics, including mass variation (%), specific heat capacity (C_p), thermal conductivity (λ), and thermal diffusivity (a) of volcanic ash. The thermal evaluation, conducted at 300 °C and 750 °C, aimed to assess stability within this temperature range. Values were recorded for the first and second temperature cycles and after the thermal cycling test. An initial mass increase, attributed to the oxidation of iron compounds, occurred after the first cycle, accompanied by a reddish coloration in the sample. This mass variation remained constant throughout subsequent thermal cycles. The specific heat capacity exhibited a slight reduction after the cycles, aligning with its expected increase with temperature. Similarly, thermal conductivity increased with temperature compared to values before thermal exposure, correlating with specific heat capacity changes. The calculated thermal diffusivity also showed an increase from values before to after the treatment, dependent on temperature.

Table 1: Thermal characterization of volcanic ash during its thermal cycling test.

Volcanic ash	1 st cycle	2 nd cycle	1000 cycles
Mass variation (%)	0.57	0.03	0.03
C _p at 300 °C (J/g·°C)	0.95±0.02	0.94±0.03	0.90±0.01
C _p at 750 °C (J/g·°C)	1.13±0.04	1.20±0.05	1.01±0.04
λ at 300 °C (W/m·°C)	0.36±0.01	-	0.58±0.01

λ at 750 °C (W/m·°C)	0.43±0.01	-	0.61±0.02
a at 300 °C (mm ² /s)	0.18±0.01	-	0.31±0.01
a at 750 °C (mm ² /s)	0.17±0.01	-	0.29±0.02

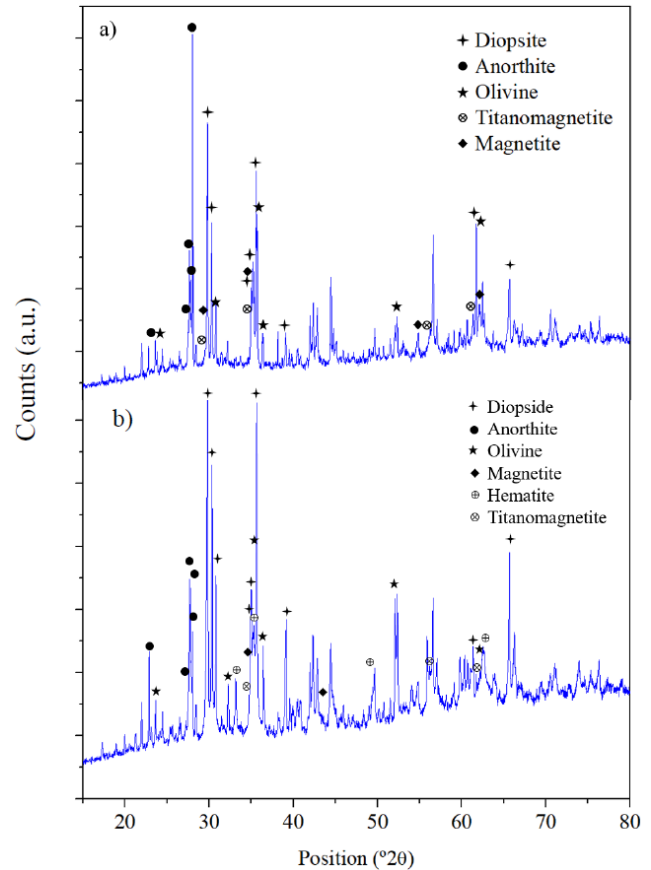
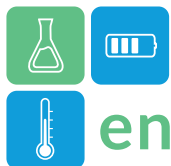


Figure 2: XRD peak identification and comparison of volcanic ash a) after thermal cycling and b) before thermal cycling.

The CTE values for volcanic ash can be observed in table 2. A comparison with various materials commonly found in TES tank components is also presented. The temperature variation in all intervals was 225 °C, and the percentage of change and CTE increase with temperature. The CTE of volcanic ash closely aligns with that of Inconel 600, especially at high temperatures, but differs significantly from the values of AISI 347 stainless steel. To prevent potential structural issues in the tank over multiple cycles, the CTE values of the metal components should closely match those of the ceramic particles. Considering these findings, the utilization of Inconel 600 appears more suitable for applications involving solid particle materials.



Volcanic ash	CTE (10 ⁻⁶ .°C)	CTE (10 ⁻⁶ .°C) of AISI 347 (Desai & Ho, 1978)	CTE (10 ⁻⁶ .°C) of Inconel 600 (Raju et al., 2004)
50 °C to 275 °C	8.99±0.90	17.27	13.30
275 °C to 500 °C	12.59±0.19	19.40	13.95
500 °C to 725 °C	15.24±2.95	20.76	15.65

Conclusions

The study thoroughly examined volcanic ashes from La Palma Island's 2021 eruption for high-temperature thermal storage up to 750°C. XRD evaluation revealed silicate families like diopside, anorthite, and olivine. Thermal cycling maintained the structure but oxidized metallic oxides, resulting in a 0.54% mass gain. Their thermal expansion resembled metallic alloys in thermal energy storage tanks. SEM images showed particle cracking and surface formations post-thermal cycling.

La Palma Island's volcanic ash shows significant potential as an alternative and sustainable material for TES applications. In conclusion, the evaluated volcanic ash demonstrates promising properties for high-temperature TES applications, offering cost-effective solutions and potential energy storage savings.

Acknowledgment

This work is part of PCI2020-120695-2 and PCI2020-120682-2 projects funded by Ministerio de Ciencia e Innovación - Agencia Estatal de Investigación (MCIN/AEI/10.13039/501100011033) and by the European Union “NextGenerationEU”/PRTR”, Development and evaluation of novel concepts for LHTES funded by CSO - Israeli Ministry of Energy, 120N663 project funded by TÜBITAK— Scientific and Technological Research Council of Turkey, and 121N737 project funded by TÜBITAK. The authors would like to thank the Spanish Government and the Ministry of Economy and Competitiveness for the grant PID2021-123511OB-C32 funded by MCIN/AEI/10.13039/501100011033 and the Catalan Government for the quality accreditation given to their research group DIOPMA (2021 SGR 00708). DIOPMA is a certified agent TECNIO in the category of technology developers from the Government of Catalonia.

References

Desai, P. D., & Ho, C. Y. (1978). Thermal Linear Expansion of Nine Selected AISI Stainless Steels.

American Iron and Steel Institute, 51. <https://apps.dtic.mil/sti/citations/ADA129159>

El Alami, K., Asbik, M., & Agalit, H. (2020). Identification of natural rocks as storage materials in thermal energy storage (TES) system of concentrated solar power (CSP) plants – A review. *Solar Energy Materials and Solar Cells*, 217(April), 110599. <https://doi.org/10.1016/j.solmat.2020.110599>

Gorbatova, E. A., Kholodnov, V. V., Pirogov, B. I., Kolkova, M. S., & Shagalov, E. S. (2021). Solid-Phase Transformations of Titanomagnetite and Ilmenite during Oxidizing Roasting of Disseminated Titanomagnetite–Ilmenite Ore at the Medvedevskoe Deposit and Certain Geological Events (Southern Urals). *Geology of Ore Deposits*, 63(5), 431–453. <https://doi.org/10.1134/S1075701521040036>

Ho, C. K. (2016). A review of high-temperature particle receivers for concentrating solar power. *Applied Thermal Engineering*, 109, 958–969. <https://doi.org/10.1016/j.applthermaleng.2016.04.103>

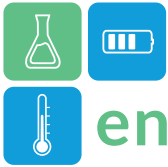
Jacob, R., Sergeev, D., & Müller, M. (2022). Valorisation of waste materials for high temperature thermal storage: a review. *Journal of Energy Storage*, 47, 103645. <https://doi.org/10.1016/j.est.2021.103645>

Navarro, M. E., Martínez, M., Gil, A., Fernández, A. I., Cabeza, L. F., Olives, R., & Py, X. (2012). Selection and characterization of recycled materials for sensible thermal energy storage. *Solar Energy Materials and Solar Cells*, 107, 131–135. <https://doi.org/10.1016/j.solmat.2012.07.032>

Prieto, C., & Cabeza, L. F. (2019). Thermal energy storage (TES) with phase change materials (PCM) in solar power plants (CSP). Concept and plant performance. *Applied Energy*, 254(January), 113646. <https://doi.org/10.1016/j.apenergy.2019.113646>

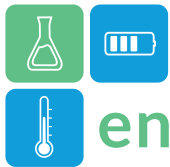
Raju, S., Sivasubramanian, K., Divakar, R., Panneerselvam, G., Banerjee, A., Mohandas, E., & Antony, M. P. (2004). Thermal expansion studies on Inconel-600® by high temperature X-ray diffraction. *Journal of Nuclear Materials*, 325(1), 18–25. <https://doi.org/10.1016/j.jnucmat.2003.10.007>

Turchi, C. S., Ma, Z., Neises, T. W., & Wagner, M. J. (2013). Thermodynamic study of advanced supercritical carbon dioxide power cycles for



ENERSTOCK 2024
The 16th IEA ES TCP International Conference on Energy Storage
June 5–7, 2024
Lyon, France

concentrating solar power systems. *Journal of Solar Energy Engineering, Transactions of the ASME*, 135(4), 1–7.
<https://doi.org/10.1115/1.4024030>



Experimental analysis of partial charge and discharge operation of a Latent Heat Thermal Energy Storage device

Raman Safaee¹, Phil Ward², Yulong Ding¹, Adriano Sciacovelli^{1*}

1 University of Birmingham, School of Chemical Engineering, Birmingham Centre for Energy Storage, B15 2TT, Birmingham, United Kingdom

2 Eskimo Products Limited, 133 Cumberland Road, BS1 6UX, Bristol, United Kingdom

*Corresponding author e-mail: a.sciacovelli@bham.ac.uk

Abstract

The attractiveness of integrating Thermal Energy Storage (TES) units to space heating systems, and the sporadic nature of buildings heating and cooling demands, highlight the importance of partial charge and discharge behaviour of TES systems. Present paper is dedicated to enriching current limited knowledge on TES systems behaviour over various partial operations. The experimental analysis in the paper contains test results on a PCM-incorporated finned tube heat exchanger under full and partial charge and discharge conditions. Results indicate that performance deviation in partial operation with respect to full operation is negligible, which suggests TES units can effectively work at various partial operations. However, observations show that most stable behaviours occur in the SoC range 20% – 80%. In spite of positive findings with the adopted heat exchanger, more extensive studies with different geometries are suggested.

Keywords: PCM, Thermal Energy Storage, State-of-Charge, Partial operation

Introduction

Latent Heat Thermal Energy Storage (LHTES) technology is an interesting field of science that has recently attracted considerable attention. The heightened attention can be attributed to affordability and the high energy density which makes LHTES products interesting candidates for energy management applications across a variety of sectors, including domestic space heating which can substantially benefit from electricity tariff variations using energy storage technologies. Thermal Energy Storage for domestic heating applications have been studied significantly in the recent decade and various case studies have been investigated (Nair et al., 2022). However, very few studies have investigated the performance of TES devices over partial charge and discharge operation, which can be a very common operation in domestic heating systems in buildings.

Specific analysis of partial charge and discharge operation in TES systems appear in a few titles in the literature, which are mostly tailored for higher temperature ranges than domestic space heating. A study is carried out by Georg Scharinger-Urschitz et al. (Scharinger-Urschitz et al., 2020) analysing a vertical finned shell and tube heat exchanger filled with Sodium Nitrate as the PCM with a melting point of 306 °C. The

study tracks the state of charge and power curves for various partial load cycles and provides data on the Exchanged power for each case. Another study by Gasia et al. (Gasia et al., 2019) considers a TES heat exchanger filled with HDPE as the PCM with a melting temperature at around 130 °C and investigates the influence of charge level and storage time between charge and discharge on the performance of the system in full discharge condition. A numerical study by Arena et al. (Arena et al., 2018) uses D-Mannitol (melting point 167 °C) and investigates the exchanged power curve and the residual stored energy in discharge. Mentioned studies and other available data in the literature suggest that partial charge/discharge studies about TES-integrated space heating systems are scarce and there is room for analytical and experimental analysis on the matter.

Scope and aims

The paper studies the feasibility and performance of the system in subsequent partial charge and discharge of a PCM-incorporated heat exchanger. The performance is assessed through device temperature, power and SoC curves extracted from experimental data. The partial operation is defined through different time and temperature intervals, and the aim will be to provide an accurate understanding of the performance under

various conditions including heat input/output, charge/discharge patterns, and storage time.

Methodology

An experimental set-up together with a 1-kWh TES device are realised for proper performance testing in various conditions. The test piece is composed of a finned tube heat exchanger with 24 mm tube pitch and 5mm fin pitch, placed in a casing and submerged in 13kg of PCM. The employed PCM is OM42 developed and produced by Pluss Advanced Technologies, which is an organic PCM characterised with suitable thermophysical properties. The properties of OM42 are provided in Table 1.

Table 1: OM42 thermo-physical properties

Phase transition temperature	43 – 44 °C
Latent heat of fusion	195 kJ/kg
Average specific heat	2.75 kJ/kg/K

The experimental set-up illustrated in Figure 1, is a water recirculating cycle particularly designed and produced for TES performance testing. The test rig can produce warm water in the range 20 – 80 °C, and flow rates in the range 2 – 25 l/min, which will allow us to emulate a variety of applications in the realm of domestic space heating.

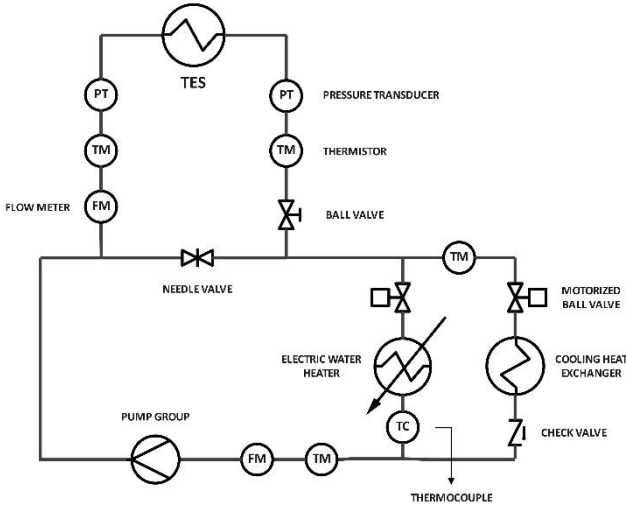


Figure 1: Experimental set-up P&ID

The TES charge operation is performed thanks to the 3-kW immersion heating element in an unvented water tank (since the systems is pressurized), which ensures a steady temperature over the charging period. The cooling heat exchanger is a fan assisted liquid air heat exchanger with a nominal capacity of 3 kW. It is utilised for the heat discharge operation of the device. The realised 1-kWh test piece device (as illustrated in Figure 2) is equipped with various thermocouples for

real-time temperature measurements of the PCM during each operation.



Figure 2: Realised TES test piece

Performance assessment methodology

The pivotal input data for post-processing and eventual performance assessments are the flow rate and temperature measurements. Important performance indicators derived from these data are the exchanged power curve, and the state of charge (SoC).

The exchanged power rate between the TES device and the input water stream is calculated through Eq. (1):

$$P = mC_p(T_{out} - T_{in}) \quad (1)$$

Where P , m , C_p , T_{out} , and T_{in} stand for exchanged power, water mass flow rate, water specific heat, water inlet temperature to the TES and water outlet temperature out of the TES respectively.

Having the power curve in real time, the device state of charge is calculated based on Eq. (2):

$$SoC [\%] = \frac{\int_0^{T_1} P dt}{C} \times 100 \quad (2)$$

Where t and C stand for elapsed time and the total effective heat capacity of the device in kJ. The effective heat capacity is the total actual capacity of the system extracted from experiments, and it is compared to the theoretical storage capacity calculated using the PCM thermophysical properties calculated by Eq. (3):

$$C = m_{PCM}C_{p,s}(T_{melt} - T_{initial}) + \Delta h + m_{PCM}C_{p,l}(T_{final} - T_{melt}) \quad (3)$$

Where the m_{PCM} , Δh , $C_{p,s}$, and $C_{p,l}$ stand for the PCM mass, latent heat of fusion, solid and liquid specific heat respectively. And the melt, initial and final subscripts show the melting point, initial and final temperature of the PCM respectively.

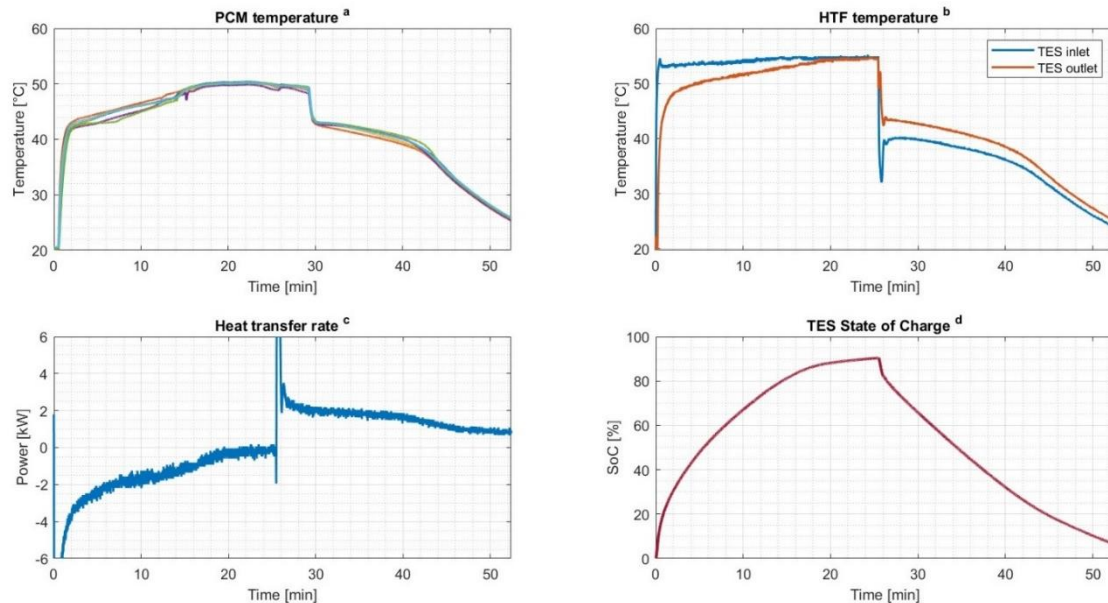


Figure 3: Experimental performance data over full charge and discharge operation

Results and discussion

The charging operation is carried out with a constant flow rate at 55 °C, a temperature very close to the maximum possible supply temperature of the majority of heat pumps in the market (Kwon et al., 2023). The discharge operation is done through the cooling heat exchanger; therefore, a variable temperature and variable power is expected due to the decrement of the flow temperature. The water flow rate in both charge and discharge operations are kept at 10 l/min to emulate real heat pump operation.

The PCM temperature, the inlet and outlet flow temperatures, the power curve and the estimated SoC are depicted in Figure 3 in real time. First important and interesting finding of the figures is that the period in charge and discharge are almost similar although the heat transfer rates are dissimilar. The heat transfer rate in the charging phase is very higher at the beginning of the process due to the high temperature difference between the flow and the PCM, but it drops dramatically when entering the phase transition region. The discharge operation instead, maintains an almost constant temperature and power for a considerable portion of the discharge phase. It can be inferred that high heat input in charge or discharge phase will deplete most of the SoC in the first 10% of the operation and the remaining heat is exchanged at much lower rates during the rest of the period.

Moderate heat transfer rates, on the other hand, produce an almost constant output temperature and heat transfer rate for a substantial part of the process, which is a desirable operation in domestic environments where

constant heat is required to ensure thermal comfort in the zone.

Results on the discharge phase suggest that a moderate heat exchange rate (power) in discharge, will provide a fairly constant output temperature, which a desirable feature in heating applications. The definition of the moderate discharge power is highly case-dependant, and it depends on the characteristics of the heat exchangers.

Another interesting aspect of Figure 3, is the SoC graph in real time, which shows the SoC slope variations are much lower in the discharge phase for mentioned reasons. It can also be noticed that considering 30°C as the minimum meaningful discharge temperature of the device, a SoC equal to 18% is the minimum SoC at which the device can operate, lower than which the produced flow temperature would not be satisfactory for heating applications. Although the heat can still be utilised for preheating and return-line connections.

Further analysis has been done on subsequent partial charge and discharge operation of the device with the same conditions. The results are provided in Figure 4.

The results suggest that intermittent charge and discharge operation on the device does not incur significant perturbations on the device performance.

An observation in the graphs b and c, and d of Figure 4, is that the exchanged power is almost constant in the discharge phase for SoC above 20%, which shows that imposing a decent discharge power to the TES device, will always result in very smooth and quasi-constant heat transfer rate either in full or partial charge and discharge operation.

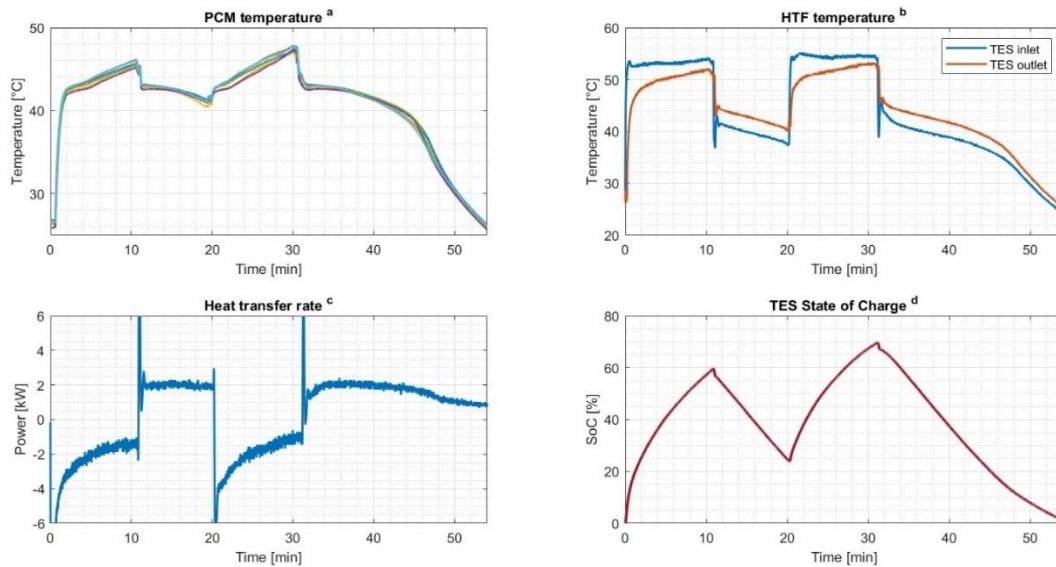


Figure 4: Experimental performance data over partial charge and discharge operation

Another observation on the discharge curve is about the minimum SoC at which the device operates at a reasonable power. Considering minimum temperature to be 30°C, the minimum feasible SoC seem to be about 10%, which is lower than the previous case. This suggests that the minimum operable state of charge depends on the initial condition and discharge heat rate.

It is also to be noted that the water flow rate can have a considerable impact on the discharge phase as it can alter the discharge power which has direct influence on the SoC and the discharge time. It has been observed that higher flow rates up to 20 LPM will decrease the discharge time by up to 15%.

Conclusions

The viability of subsequent partial charge/discharge operations of a 1-kWh TES test piece have been investigated through experimental performance assessments. Results, indicate that the performance deviation of the device in partial operation with respect to full operation is negligible, which attests the feasibility of adopting partial patterns in actual LHTES-integrated space heating systems.

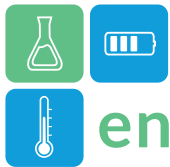
The actual performance of the TES device proves to be steady and acceptably predictable in the SoC range between 20% and 80%, with unsteady heat rate above 80% and not sufficient heat below 20%.

Acknowledgements

Present work has been funded by Innovate UK and Eskimo Products Ltd. (EP) As part of a KTP program between EP and University of Birmingham.

References

- Arena, S., Casti, E., Gasia, J., Cabeza, L. F., & Cau, G. (2018). Numerical analysis of a latent heat thermal energy storage system under partial load operating conditions. *Renewable Energy*, *128*, 350–361. <https://doi.org/10.1016/j.renene.2018.05.072>
- Gasia, J., de Gracia, A., Zsembinszki, G., & Cabeza, L. F. (2019). Influence of the storage period between charge and discharge in a latent heat thermal energy storage system working under partial load operating conditions. *Applied Energy*, *235*, 1389–1399. <https://doi.org/10.1016/j.apenergy.2018.11.041>
- Kwon, Y., Bae, S., Chae, H., & Nam, Y. (2023). Economic and performance analysis of ground source heat pump system for high-rise residential buildings considering practical applications. *Energy Reports*, *10*, 4359–4373. <https://doi.org/10.1016/j.egy.2023.10.086>
- Nair, A. M., Wilson, C., Huang, M. J., Griffiths, P., & Hewitt, N. (2022). Phase change materials in building integrated space heating and domestic hot water applications: A review. In *Journal of Energy Storage* (Vol. 54). Elsevier Ltd. <https://doi.org/10.1016/j.est.2022.105227>
- Scharinger-Urschitz, G., Schwarzmayr, P., Walter, H., & Haider, M. (2020). Partial cycle operation of latent heat storage with finned tubes. *Applied Energy*, *280*. <https://doi.org/10.1016/j.apenergy.2020.115893>



Experimental assessment of inorganic salts impregnated silica gel matrix for thermal energy storage applications.

A. Fotia^{1,*}, E. Mastronardo¹, V. Brancato², C. Milone¹, A. Frazzica², L. Calabrese¹,

¹ University of Messina, Department of Engineering, Contrada di Dio, 98165 Messina, Italy

² CNR - Istituto di Tecnologie Avanzate per l'Energia "Nicola Giordano", Via Salita S. Lucia sopra Contesse 5, 98126 Messina, Italy

*Corresponding author e-mail: antonio.fotia@unime.it

The state of the art in thermal energy storage has seen significant advancements with the incorporation of inorganic salts impregnated in different matrices. These matrices have shown promise in addressing the limitations of this kind of material, particularly in terms of reducing deliquescence. In this study, silica gel was examined as a matrix that was impregnated with three different inorganic salts: calcium chloride, magnesium chloride and magnesium sulphate. Deliquescence observations were carried out via optical microscopy. Thermogravimetric analyses in static and dynamic vapor conditions, were performed in order to extrapolate the water uptake and enthalpy values of the different samples. The results obtained show that the CaCl₂30SG sample appears to be the best performing in terms of enthalpy and water uptake.

Unfortunately, the sample containing calcium chloride exhibited a significantly greater degree of deliquescence than the other two samples analysed. Hence, a promising candidate could be considered MgSO₄30SG which enables lower deliquescence with still a high storage capacity.

Keywords: silica gel, salt hydrates, impregnation, thermal storage capacity

Introduction

Thermal energy storage (TES) systems have gained significant attention in order to efficiently store and utilize thermal energy for various applications, including solar power plants, electronic devices, photovoltaic modules, and Li-ion battery systems (Arshad et al., 2020). These systems rely on the use of heat storage materials, such as inorganic salts, to store and release thermal energy. In particular, inorganic salt have garnered significant attention due to their high latent heat of fusion, cost-effectiveness, and high volumetric energy storage density (Xie et al., 2017). The solid-state hydration of salts, such as salt hydrates, has been particularly emphasized in the context of TES (Sögütöglü et al., 2019). Furthermore, salt hydrates, have attracted attention due to their reasonable price, wide sources, good thermal conductivity, and high volumetric energy storage density (Jing et al., 2023). In fact, inorganic salt hydrates, such as calcium chloride hexahydrate (CaCl₂•6H₂O), have been utilized in solar energy heating and building materials owing to their suitable phase-change temperature and high thermal storage capacity (Zhang et al., 2018). However, inorganic salts have certain drawbacks, such as phase separation

and supercooling, which limit their applicability in thermal energy storage systems (Tao et al., 2020). To overcome these challenges, researchers have turned to impregnating inorganic salts into various matrices to enhance their chemical and thermal stability.

Materials and Method

Silica gel in the shape of spheres (average grain size 0.779 mm), magnesium chloride anhydrous, calcium chloride dihydrate, magnesium sulphate heptahydrate and water for analysis were purchased from Sigma-Aldrich. All the materials used were at first dehydrated in oven at 120°C overnight.

The three analyzed samples were obtained by impregnating silica gel with an aqueous solution containing dissolved salt. The composites thus obtained are composed of 30% salt and 70% silica gel.

Table 1 - Batches prepared.

Sample Code	Salt	Matrix	%Salt
CaCl ₂ 30SG	CaCl ₂	Silica gel	30.0
MgCl ₂ 30SG	MgCl ₂	Silica gel	30.0
MgSO ₄ 30SG	MgSO ₄	Silica gel	30.0

The morphology and deliquescence of the materials were evaluated by a digital optical microscope. The images obtained (Figure 1) show the samples, dry and after one hour of exposure to a relative humidity of 60% and a temperature of 26.5°C.

The DVS Vacuum a thermogravimetric dynamic vapour system (manufactured by Surface Measurements Systems, Ltd., Alperton, UK), was employed to evaluate the composite materials' hydration and dehydration capabilities. The apparatus configuration comprises a 0.1 µg precise microbalance and a control system that regulates the flow of water vapour pressure within the sample holder's chamber. The water vapour pressures used for the experiments are 8.65, 12.24, and 17 mbar.

A specialized thermogravimetric static apparatus (Themys One, Setaram) equipped with an evaporator and a vacuum system conducted the assessment of thermal storage capacity. The procedure began with vacuum dehydration of the sample at a temperature of 120°C for a duration of 3 hours (under a vacuum pressure of 10^{-2} mbar). Subsequently, the thermal storage capacity was measured under isobaric conditions at 17 mbar (evaporation temperature of 15°C). This evaluation was performed during the cooling process, ranging from 120°C to 25°C, with a scanning rate of 5°C/min.

Results and Discussion

The images obtained (Figure 1) through the optical microscope highlight a marked deliquescence in the silica gel impregnated with calcium chloride (visually identifiable by the acquired transparency in the particles) after one hour exposed in a controlled atmosphere (r.h.=60%, T=26.5°C). The other two batches, impregnated with magnesium chloride and magnesium sulphate, prove to be more stable and do not show deliquescence after exposure in the humid environment.

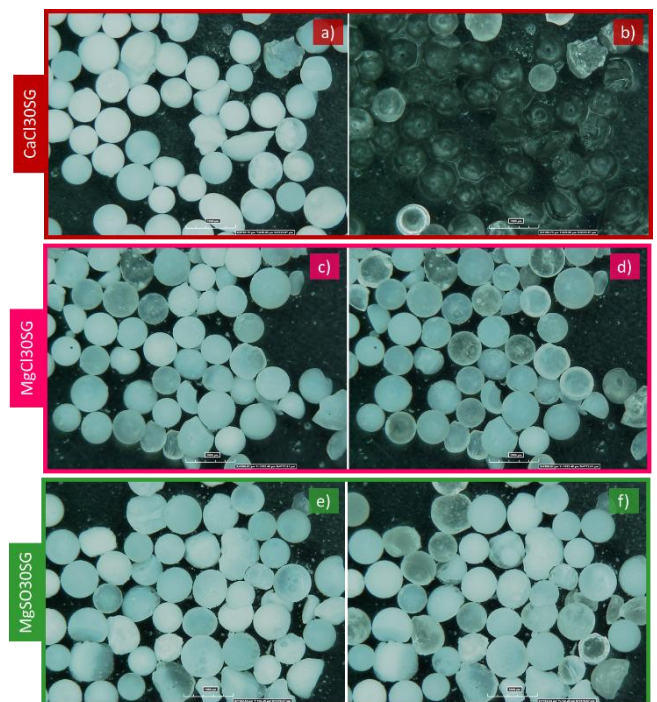
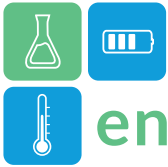


Figure 1 - Comparison of optical microscope images of dried samples a), c) and e), and after one hour exposed in a controlled atmosphere b), d), and f).



Further information can be argued evaluating the trend of water vapour sorption isobars in the range of temperature 30-150°C (

MgSO₃0SG samples, the curves present an exponential-type trend. While analysing the shape of the curve relating to the CaCl₃0SG sample, we can notice two steps corresponding to the temperatures of 50°C and 75°C. These two steps are due to phases in which the calcium chloride is stable at a certain level of hydration (Van Essen et al., 2009). For all three samples, the hysteresis phenomenon decreases as the water vapour pressure increases.

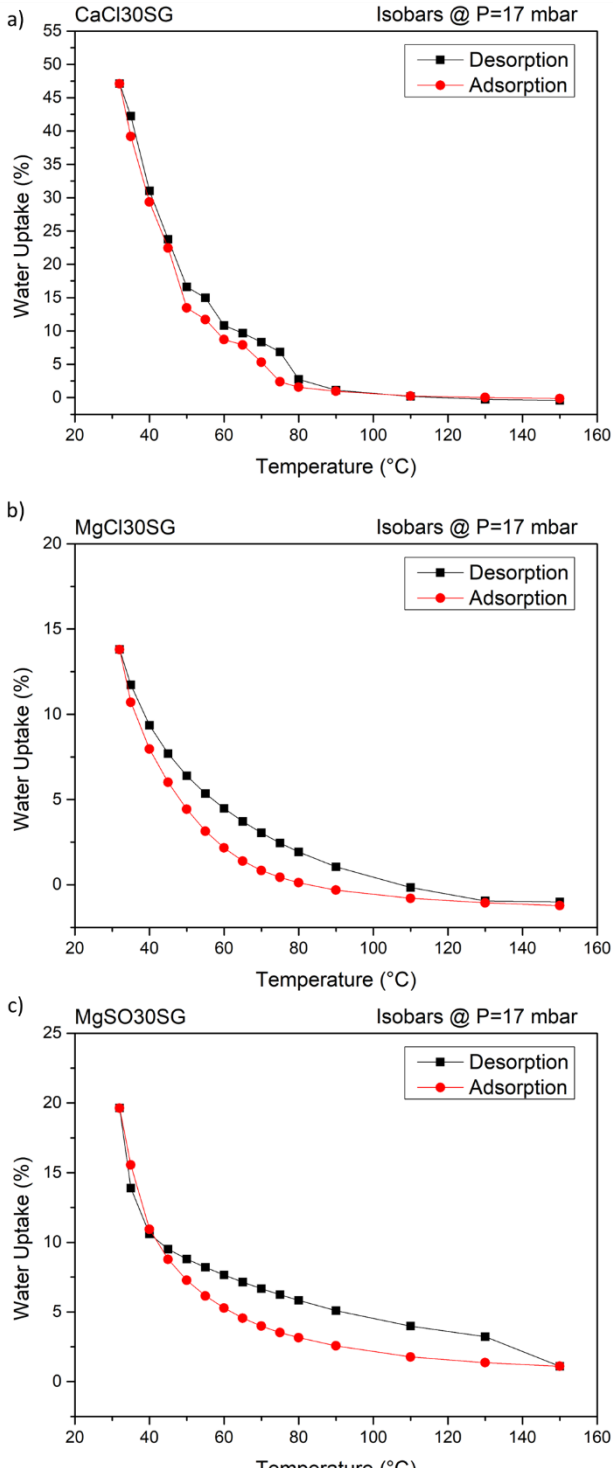


Figure 2).

The different shapes of the isobars obtained from the DVS analysis depend on the salts used for impregnation. For brevity, only the curves relating to a vapour pressure equal to 17mbar have been represented. In the case of the MgCl₃0SG and

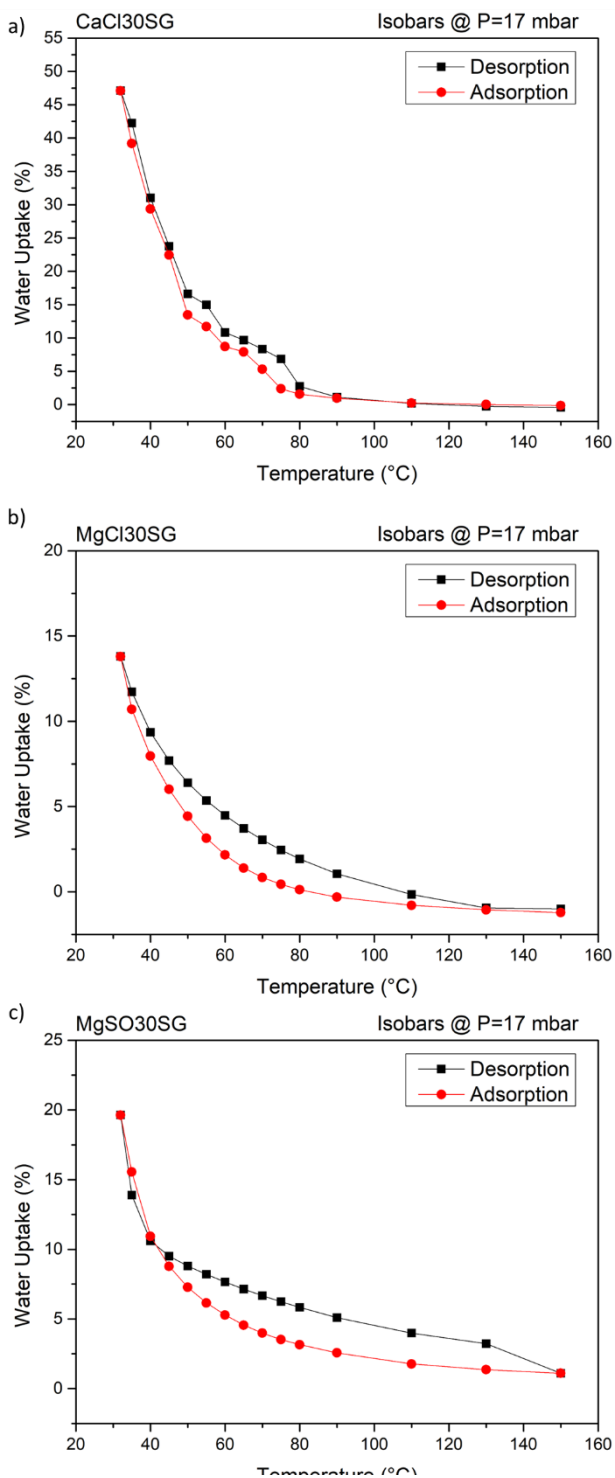
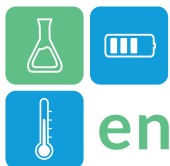


Figure 2 – Water vapor sorption isobars of a) CaCl30SG, b) MgCl30SG and c) MgSO30SG.

Figure 4 shows the water uptake and enthalpy values. These values were extrapolated from thermogravimetric analyses (Figure 3), identifying the maximum water uptake for each batch (occurring at the lowest applied temperature equal to 30°C). Both

values relative to the sample impregnated with calcium chloride are greater than those of the other two samples. In fact, for the CaCl30SG sample it has a water uptake of 47.77% compared to 23.93% and 26.72% for the MgCl30SG and MgSO30SG. Consequently, the sample containing calcium chloride possesses an enthalpy of 1374.63 J/g, whereas the samples containing magnesium chloride and magnesium sulphate have enthalpy values 44.50% (763.04 J/g) and 30.13% (960.51 J/g) lower than CaCl30SG batch, respectively. The enthalpy values were calculated through the time-dependent integration of the heat flow curve.

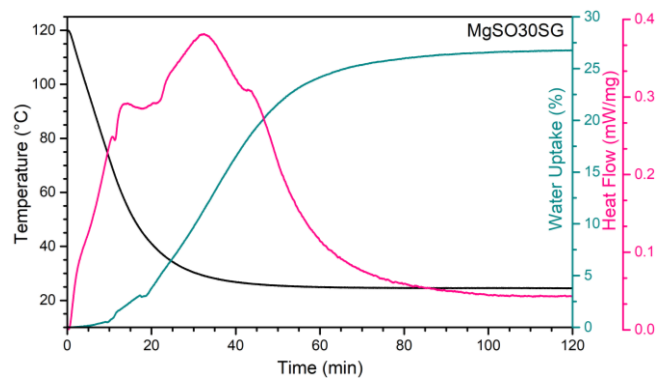


Figure 3 - Results of static thermogravimetric analysis relative of MgSO30SG.

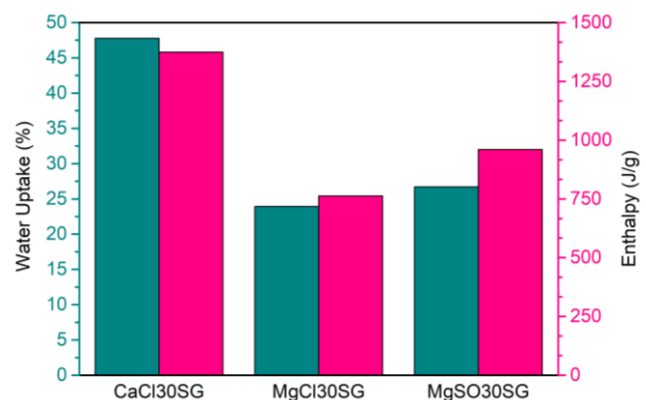
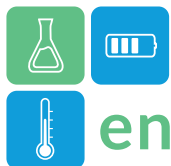


Figure 4 - Comparison between the water uptake and enthalpy values of the different samples.

Conclusion

In conclusion, from the study of the results obtained, the CaCl30SG sample appears to be the best performing in terms of enthalpy and water uptake. Unfortunately, the sample containing calcium chloride exhibited a significantly greater degree of deliquescence than the other two samples analysed.



enerstock

ENERSTOCK 2024

The 16th IEA ES TCP International Conference on Energy Storage

June 5–7, 2024

Lyon, France

Acknowledgment

This project has received funding from ThumbsUp (Thermal energy storage solUtions to optimally Manage BuildingS and Unlock their grid balancing and

flexibility Potential). ThumbsUP is a Horizon Europe Project supported by the European Commission under contract No. 101096921.

References

- Arshad, A., Jabbar, M., & Yan, Y. (2020). Thermophysical characteristics and application of metallic-oxide based mono and hybrid nanocomposite phase change materials for thermal management systems. *Applied Thermal Engineering*, 181, 115999. <https://doi.org/10.1016/J.APPLTHERMALENG.2020.115999>
- Jing, Y., Dixit, K., Schiffres, S. N., & Liu, H. (2023). Carbon Foam/CaCl₂·6H₂O Composite as a Phase-Change Material for Thermal Energy Storage. *Energy and Fuels*, 37(16), 12381–12390. <https://doi.org/10.1021/acs.energyfuels.3c01275>
- Sögütöglu, L. C., Steiger, M., Houben, J., Biemans, D., Fischer, H. R., Donkers, P., Huinink, H., & Adan, O. C. G. (2019). Understanding the Hydration Process of Salts: The Impact of a Nucleation Barrier. *Crystal Growth and Design*, 19(4), 2279–2288. <https://doi.org/10.1021/acs.cgd.8b01908>
- Tao, W., Kong, X., Bao, A., Fan, C., & Zhang, Y. (2020). Preparation and phase change performance of graphene oxide and silica composite Na₂SO₄·10H₂O phase change materials (PCMs) as thermal energy storage materials. *Materials*, 13(22), 1–12. <https://doi.org/10.3390/ma13225186>
- Van Essen, V., Cot Gores, J., Bleijendaal, L., Zondag, H., Schuitema, R., Bakker, M., & van Helden, W. (2009). Characterization of Salt Hydrates for Compact Seasonal Thermochemical Storage. *Proceedings of the ASME 2009 3rd International Conference on Energy Sustainability Collocated with the Heat Transfer*

and InterPACK09 Conferences. *ASME 2009 3rd International Conference on Energy Sustainability*, 825–830.

- Xie, N., Huang, Z., Luo, Z., Gao, X., Fang, Y., & Zhang, Z. (2017). Inorganic salt hydrate for thermal energy storage. In *Applied Sciences (Switzerland)* (Vol. 7, Issue 12). MDPI AG. <https://doi.org/10.3390/app7121317>
- Zhang, X., Li, X., Zhou, Y., Hai, C., Shen, Y., Ren, X., & Zeng, J. (2018). Calcium Chloride Hexahydrate/Diatomite/Paraffin as Composite Shape-Stabilized Phase-Change Material for Thermal Energy Storage. *Energy and Fuels*, 32(1), 916–921. <https://doi.org/10.1021/acs.energyfuels.7b02866>



Experimental characterisation and numerical modelling of a novel heat exchanger for latent heat thermal energy storage composed with open-cells metallic lattice structure cast around tubes

Sébastien Vesin*, Léa Yvernault, Jérôme Pouvreau
CEA Grenoble, 17 Avenue des Martyrs, 38000 Grenoble
*Corresponding author e-mail: sebastien.vesin@cea.fr

Abstract

This study numerically and experimentally investigates a novel design of heat exchanger for Latent Heat Thermal Energy Storage. This novel heat exchanger is composed with an open-cells aluminium alloy (AlSiG03) lattice structure block (0.25 m^3) cast around 16 heat transfer tubes, made of steel. This design of LHTES shows several advantages in terms of modularity, reduction of manufacturing operations and integration (stackable, joinable). A first Proof of Concept of this LHTES designed, manufactured and tested with different hydraulic configurations. The experimental data from these tests allowed validating results of a dynamic model of this LHTES developed on Dymola software, and used to simulate its behaviour.

Keywords: Phase change material, multi-pass, Dymola, Kelvin open-cells

Introduction

Latent Heat Thermal Energy Storage (LHTES) is particularly advantageous to increase flexibility of recent district heating network (DHN) (Guelpa, E. and al, 2019; Martinez, S. and al, 2022) with a low operating temperature range (i.e. between supply and return), and expanded in cities where there are high land pressures. In these cases, the volumetric energy density of storage, which represents the compactness of the Thermal Energy Storage (TES), is a key parameter. For low operating temperatures range, such as $20 \text{ }^\circ\text{C}$ between the supply and the return of DHN, LHTES can reach a volumetric energy density between 50 kWh/m^3 and 100 kWh/m^3 , while water sensible heat storage can reach in maximum $\approx 22 \text{ kWh/m}^3$ (Sadeghi, G., 2022). The volumetric energy density of LHTES mainly depends on PCM physical properties (latent heat and density) and the volume fraction in the storage between the PCM and the heat exchanger needed to transfer heat between heat transfer fluid (HTF) and PCM. Indeed, the design of LHTES heat exchanger is an important parameter because it directly affects the heat transfer during charge and discharge phases. This heat exchanger has to be designed to get a high heat convective coefficient on HTF side and a high exchange surface in PCM volume for efficient heat conduction, due to the low thermal conductivity of most of PCM (Khademi et al, 2022; Xu et al, 2022). Most of full-scale LHTES demonstrators are based on finned tubes & shell heat exchanger, using standards components from industry. The standard dimensions of industrial finned tubes, such as fins height and pitch,

tubes diameter, require deploying a large amount of tubes in the LHTES to be able to conduct heat in the whole volume occupied by PCM. This consideration has many drawbacks. A large amount of tube involves a large amount of welds on tubes sheets, increasing the manufacturing cost of LHTES. Furthermore, in terms of performances, more tubes there are, lower is the flow velocity and consequently, lower is the convective heat coefficient of HTF. To overcome this limitation, studies on LHTES designs suggest adding insert inside each tube to reduce hydraulic section, in order to increase flow velocity (Bentivoglio, F. et al., 2021). However, this LHTES design option can add a significant extra factoring cost and lead to fouling issue. A last criterion concerns the shape of TES, which can be a distinct parameter, especially when the storage is deployed in a restricted space with a low ceiling height, such as most of DHC substations. On this point, most of TES are cylinder shapes and need a high height (to be efficient), which is the case of temperature-stratified water TES or LHTES with a cylinder shell. For the same square surface and height occupied, a cylinder has a volume 17 % lower than a parallelepiped shape.

Due to their thermal properties, lattice structure are attractive for application in TES (Uzair, S. et al., 2022; Qureshi, Z.A. and al, 2021). Lattice structures offer a wide range of possibilities for the design and the shape of LHTES, without being dependent on industrial standards. For example, these possibilities allow to design parallelepiped LHTES with a high extended

exchange surface and a low PCM free volume, while having few tubes with a small diameter.

The first objective of this development was to design and to realize a large-scale ($\approx 0.25 \text{ m}^3$) proof-of-concept (POC) of a modular LHTES, which is composed with metallic lattice structure & tubes heat exchanger. In a second time, the objective was to develop a numerical model for metallic lattice structure & tubes heat exchanger PCM storage, validated with experimental data from tests performed on this POC.

Use case and operating conditions

The operating conditions considered for the design and for the experimental characterization of this POC are those of a low temperature DHN (e.g. heat pump-powered heating, with operating temperature range between $85 \text{ }^\circ\text{C}$ and $65 \text{ }^\circ\text{C}$).

Conception

For measuring performance of this novel LHTES design, a first POC was designed, built and experimentally characterized on CEA's thermal hydraulic bench test. The heat exchanger of this LHTES POC is composed with an open-cells aluminum alloy (AlSiG03) lattice structure block cast around 16 heat transfer tubes, made of steel (see Figure 1 and details in Table 1). The metallic lattice structure & tubes heat exchange is produced in a single operation, significantly reducing manufacturing costs. Hydraulic distribution of HTF (cf. Table 1) can be easily configured for the tests thanks to connections at tube ends and adding manifolds. The lattice structure heat exchanger is coupled with a parallelepiped shell, composed with sidewalls and flange walls. To compensate thermal expansion of PCM during its solid-liquid phase change, a free volume, which can contain inert gas, is kept above the cast lattice structure heat exchanger in the shell. This free volume is accessible by removing the lid, to fill up the shell with PCM or to put the instrumentation (see Figure 2). According to operating temperature range considered

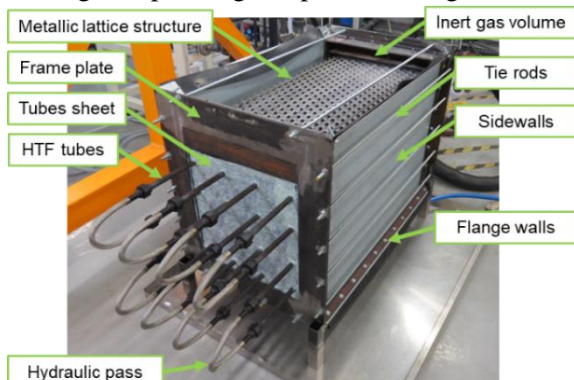


Figure 1: Details on main components of the first POC

for design and for tests, Crodatherm 74, which is a bio based PCM with a melting temperature around $72 \text{ }^\circ\text{C}$ was used.

Table 1: Features of the LHTES composed with lattice structure heat exchanger

Features of the LHTES (POC)	
Heat exchanger design of LHTES	Parallelepiped shell containing an open-cell metallic cast lattice structure around heat transfer tubes <ul style="list-style-type: none"> PCM is contained in the shell and in contact with metallic lattice structure HTF goes through tubes
Lattice structure type	Kelvin open-cells
Cell diameter of lattice structure	40 mm
Porosity of lattice structure	$\approx 85 \%$
Lattice structure material	AlSiG03
Cast lattice structure dimension (L x W x H)	1 x 0.5 x 0.5 m (parallelepiped block)
Number of HTF tubes	16
Heat transfer tubes material, diameter	S235GH, DN10 sch. 10S
Volume fractions	78.7 % PCM, 14.9 % AlSiG03 cast lattice structure 4.8 % Shell (S235GH), 0.7 % Tubes (S235GH) 0.9 % HTF
Modifiable hydraulic configuration	2 passes of 8 tubes 4 passes of 4 tubes 16 passes of 1 tube

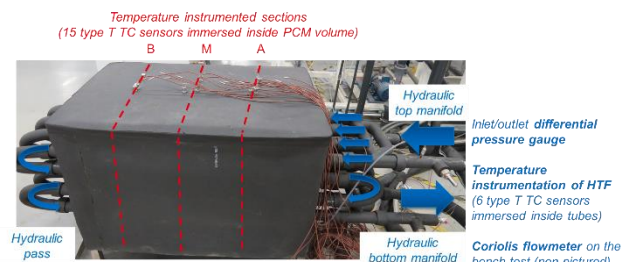


Figure 2: Details on thermal and hydraulic instrumentation of the first POC (hydraulic configuration: 4 tubes on 4 passes)

Numerical modelling

A dynamic, simplified model of the LHTES has been developed using Dymola software, in order to meet a sizing objective (Da Col and al., 2023).

A cylinder containing several thicknesses describes the part where the heat exchange between the HTF and the materials takes place (see Figure 3). The HTF (water) is discretised according to its path through the tubes in the axial direction, the material thicknesses are discretised in the radial direction (a layer of steel (tube), a layer of aluminium (coating) and then a layer of a material considered homogeneous (PCM and lattice structure)). For the last zone, equivalent material properties are used. Only the apparent thermal conductivity is defined by fitting the experimental data. Differential scanning calorimetry (DSC), using curves following Kahwaji’s recommendations (Kahwaji and al., 2021) was used to determine the thermal properties of PCM.

In the axial direction, to determine the temperature evolution of the HFT, mass and energy balances are solved. The fluid is in turbulent regime and mixed or forced convection. The Metais and Hausen correlations for horizontal tubes (Metais and al., 1964) describe the evolution of the associated heat transfer coefficient. In the radial direction, only radial conduction is considered.

The numerical model does not take into account conduction between adjacent tubes or their position in the storage. It considers tubes of the total length of the hydraulic fluid path and accounts for the mixed zone in cylindrical form (normally parallelepipedic). For its initialization and for the evaluation of the heat losses, the model considers experimental data.

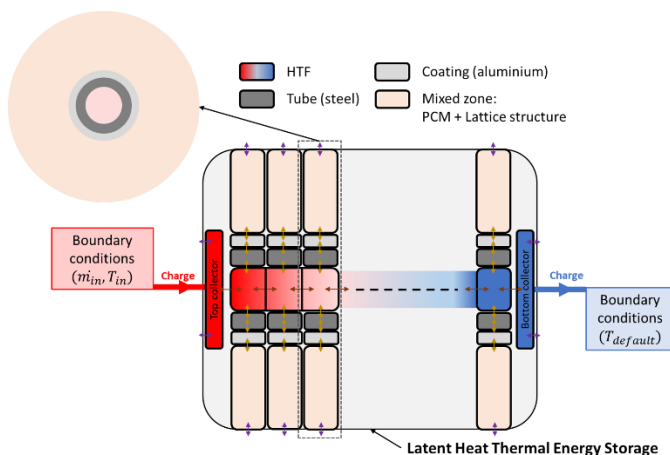


Figure 3: Representation of the LHTES discretisation in modelling, in the case of a storage charge

Results and discussion

The results of LHTES operation under specific operating conditions (Table 2), when the storage is discharged, are shown in the following figures.

Table 2: Operating conditions of the reported result

LHTES operation	Charge	Discharge
HTF mass flow rate	532 kg/h	266 kg/h
HTF inlet temperature	85 °C	65 °C
LHTES initial temperature	40.6 °C	83.5 °C

When charging, the storage enables 80 % of its energy to be charged in 2.7 h and 100 % in 4.2 h, with a power of between 5 kW and 3 kW when the PCM changes state.

When discharging, 80 % of its energy is restored in 4.8 h. The power output is between 3 kW and 2 kW.

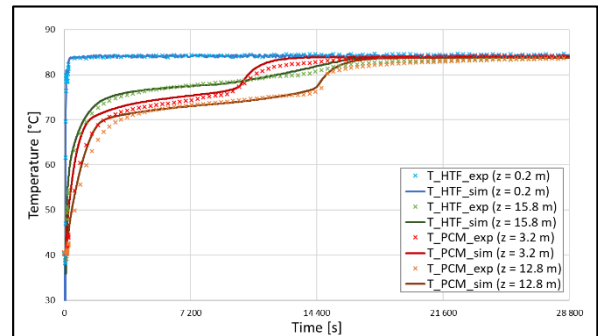


Figure 4: Temperatures evolution of HTF and PCM (Charge with 16 hydraulic passes, $\dot{m} = 532 \text{ kg/h}$, $T_{in} = 85 \text{ °C}$)

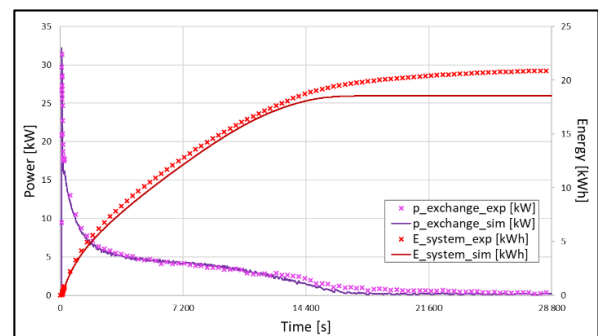


Figure 5: Heat exchanged and LHTES energy (Charge with 16 hydraulic passes, $\dot{m} = 532 \text{ kg/h}$, $T_{in} = 85 \text{ °C}$)

Comparison of the numerical model results (sim) with the experimental results (exp) shows good agreement in terms of LHTES outlet temperatures. The temperature variations observed in the PCM may be due to inaccurate positioning of the thermocouples, in addition to the assumptions of the numerical model

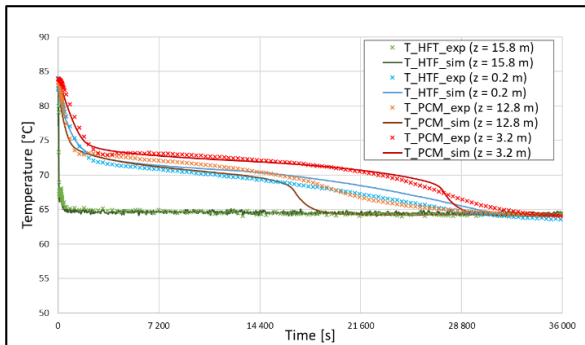


Figure 6: Temperatures evolution of HTF and PCM (Discharge with 16 hydraulic passes, $\dot{m} = 266 \text{ kg/h}$, $T_{in} = 65 \text{ °C}$)

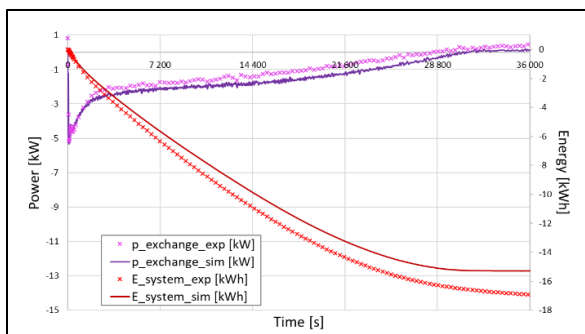


Figure 7: Heat exchanged and LHTES energy (Discharge with 16 hydraulic passes, $\dot{m} = 266 \text{ kg/h}$, $T_{in} = 65 \text{ °C}$)

Conclusions

A parallelepiped LHTES incorporating a lattice metal structure was designed and manufactured to overcome the constraints of space requirements and manufacturing standards for heat storage. This proof of concept was characterised during an experimental campaign. The results demonstrated and confirmed its performances.

These results also allowed a first comparison with a numerical system model developed in parallel. Although the results obtained by the model are satisfactory, there is still inaccuracy regarding the fixed value of the conductivity of the mixed zone, which may depend on various factors (e.g. phase of the PCM or presence of voids).

A further experimental campaign will be carried out soon to confirm the behaviour of this LHTES under different operating conditions and depending on the applicability of the heat transfer correlations.

A first full-scale demonstrator of this novel LHTES has been deployed on a district heating network, integrating three modules in parallel.

Acknowledgments

The Region Auvergne-Rhône-Alpes, as part of EasyPOC program, funded this project.

The heat exchanger composed with open-cells metallic Lattice structure was manufactured by Grims Energies company (<https://grimsenergies.com>).

References

- Bentivoglio, F. et al (2021), Design and operation of a 180 kWh PCM heat storage at the Flaubert substation of the Grenoble urban heating network, Applied Thermal Engineering, doi: 10.1016/j.applthermaleng.2020.116402.
- Da Col, A. et al (2023), Modelling a latent heat thermal storage demonstrator and identification of the model key-parameters, Journal of Energy Storage, doi:10.1016/j.est.2023.109239
- Guelpa, E. and al (2019), Thermal energy storage in district heating and cooling systems: A review, Applied Energy, doi: 10.1016/j.apenergy.2019.113474.
- Kahwaji, S and al (2021), Thermal property determination for phase change materials, The Journal of Chemical Thermodynamics, doi: 10.1016/j.jct.2021.106439
- Khademi, A. and al. (2022), A brief review on different hybrid methods of enhancement within latent heat storage systems, Journal of Energy Storage, doi: 10.1016/j.est.2022.105362.
- Martinez, S. and al (2022), Demand-side flexibility in a residential district: What are the main sources of uncertainty?, Energy & Buildings, doi: 10.1016/j.enbuild.2021.111595.
- Metais, B. and al (1964), Forced, Mixed and Free Convection Regimes, Journal of Heat Transfer, doi: 10.1115/1.3687128
- Qureshi, Z.A. and al (2021), Thermal characterization of 3D-Printed lattices based on triply periodic minimal surfaces embedded with organic phase change material, Case Studies in Thermal Engineering, doi: 10.1016/j.csite.2021.101315.
- Sadeghi, G. (2022), Energy storage on demand: Thermal energy storage development, materials, design, and integration challenges, Energy Storage Materials, doi: 10.1016/j.ensm.2022.01.0
- Uzair, S. et al. (2022) Manufacturing and potential applications of lattice structures in thermal systems: A comprehensive review of recent advances, International Journal of Heat and Mass Transfer, doi: 10.1016/j.ijheatmasstransfer.2022.123352
- Xu, C. et al (2022), Review on thermal conductivity improvement of phase change materials with enhanced additives for thermal energy storage, Journal of Energy Storage, doi: 10.1016/j.est.2022.104568.

Experimental Characterization of a High-Temperature Thermal Energy Storage System Based on Nitrate Salt as Phase-Change-Material for Steam Generation

Thomas Fluri^{1,*}, Ralf Müller¹, Martin Karl¹, Fanny Hübner¹, Julius Weiss¹, Subrata Sarkar², Partha Mukherjee², Prabakaran S², Ankit Gupta²

¹ Fraunhofer Institute for Solar Energy Systems ISE, Heidenhofstr. 2, 79110 Freiburg, Germany

² NTPC Energy Technology Research Alliance, NTPC Ltd, E-3, ECOTECH-II, Greater NOIDA, Gautam Buddh Nagar, U.P. 201306, INDIA

*Corresponding author e-mail: thomas.fluri@ise.fraunhofer.de

Abstract

The decarbonization of the industrial sector has emerged as an important issue in addressing climate change. To support this objective, a thermal energy storage system based on the latent heat of solid-to-liquid phase change using a nitrate salt mixture as phase change material with a storage capacity of 250 kWh has been developed and experimentally characterized at Fraunhofer ISE. The storage was then shipped to NTPC, Greater Noida, India to be integrated with a solar dish system as steam source and an absorption chiller as steam sink. The present paper focusses on the experimental discharge characterization during laboratory testing before shipping.

Keywords: Thermal Energy Storage, Phase Change Material, Steam Generation, Industrial Process Heat

Introduction



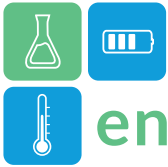
Figure 1: Side view of PCM-TES module before thermal insulation, showing threaded fittings for thermo-couple integration

Thermal energy storage plays an important role in enhancing the efficiency and reliability of renewable energy sources by addressing the intermittency and fluctuation in energy production. Salt-based PCMs, with their high heat storage capacity and good long-term stability, have emerged as promising candidates for TES applications for steam generation [1,2]. A challenge with solid-liquid phase PCM storage is the low conductivity of the storage material in solid state. Several conductivity enhancement techniques are however known [3]. For salts as PCM mostly finned tube arrangements have been investigated [1]. Using metal foam for conductivity has been investigated in lab scale [4]. There is little experience with actual integration in an industrial process or a power plant. A storage with NaNO_3 as PCM and longitudinal finned pipes has been successfully integrated with a cogeneration plant [5].

In the present paper the discharge characterization of a thermal energy storage system with an NaNO_3 - KNO_3 eutectic mixture as PCM and radially finned tubes is presented (see Figure 1).

Methodology

The storage module was designed to finally be integrated with a solar dish as steam source and to provide steam to an absorption chiller with the following operating parameters:



- Maximum steam mass flow during discharge: 210 kg/h
- Minimum steam mass flow during discharge: 70 kg/h
- Maximum input steam parameters: 34 bar/240°C
- Nominal output steam parameters: 8.9 bar/175°C
- Target storage capacity: 250 kWh

For testing in the lab, the solar dish was emulated by a gas-fired thermal oil heater connected to an evaporator for charging. During the charging process steam enters the storage from the top. During the discharging process feedwater at a temperature of approx. 50 °C is fed through the bottom connection of the storage. The steam produced by the storage module is sent back to the condenser (see **Figure 2**). The steam flow is measured by an orifice plate flow meter. For plausibility checking the feedwater flow is also measured by a clamp-on ultrasonic flow meter. Temperatures at the inlet and outlet of the storage are measured with PT100 temperature sensors. The discharge power is evaluated from

$$\dot{Q}(t) = \dot{m}(t) \times (h_{out}(t, p, T) - h_{in}(t, p, T))$$

and integrated over the defined discharge time period to give the discharge energy. To identify the period for the thermal capacity evaluation a minimum steam mass flow threshold of 70 kg/h was set. The periods at the beginning and at the end of the discharge test with lower steam mass flows are neglected and only the period during which this minimum steam mass flow requirement is met is considered for the evaluation.

Results and Discussion

Several charging/discharging operations of the storage module have been performed at different mass flows (fast discharge at 210 kg/h, normal discharge at 100 kg/h and slow discharge at 70 kg/h). Figure 3 displays the results of the normal speed discharging operation of September 24 (total duration: 3 hrs and 39 min) in detail. The graph shows that the steam mass flow could be kept above 100 kg/h between 07:30 and 10:30. After that, during the last 40 minutes of operation, the steam output had to be gradually

reduced to maintain a system pressure above 8.6 bar. When the steam flow dropped below the threshold of 70 kg/h, the discharging process was considered as complete, i.e., the storage as fully discharged and the feed water pump was switched off. Over this time period the discharged thermal energy amounts to 259.9 kWh, i.e. well above the target storage capacity of 250 kWh. Also the required minimum and maximum steam mass flow rates (70 – 210 kg/h, respectively) could be met. Maximum steam mass flow rate during “fast discharging” could be maintained for approx. 1 hour, with subsequent reduction of steam mass flow down to 70 kg/h within another hour.

Steam at the design pressure of the absorption chiller to be used in the final application of approx. 9 bar could be produced, while maintaining the pressure nearly constant throughout the entire discharging process, until the steam output amount dropped below the required level of 70 kg/h.

The experimental investigations presented here demonstrate the viability and effectiveness of this high-temperature thermal energy storage system. We observed efficient steam generation using the stored energy, showcasing the potential for industrial applications. Preliminary tests indicate thermal stability and reliability of the system.

Conclusions

A thermal energy storage module using nitrate salt as PCM was manufactured, integrated in an existing lab steam facility, and successfully tested. The promising results obtained demonstrate the feasibility of using such a system for steam generation, facilitating the integration of renewable energy sources into industrial processes. The storage module has been shipped to India in the meantime for integration with the solar collector and to be used as a continuous heat source for an existing absorption chiller.

Acknowledgment

Support for this work by KfW is gratefully acknowledged.

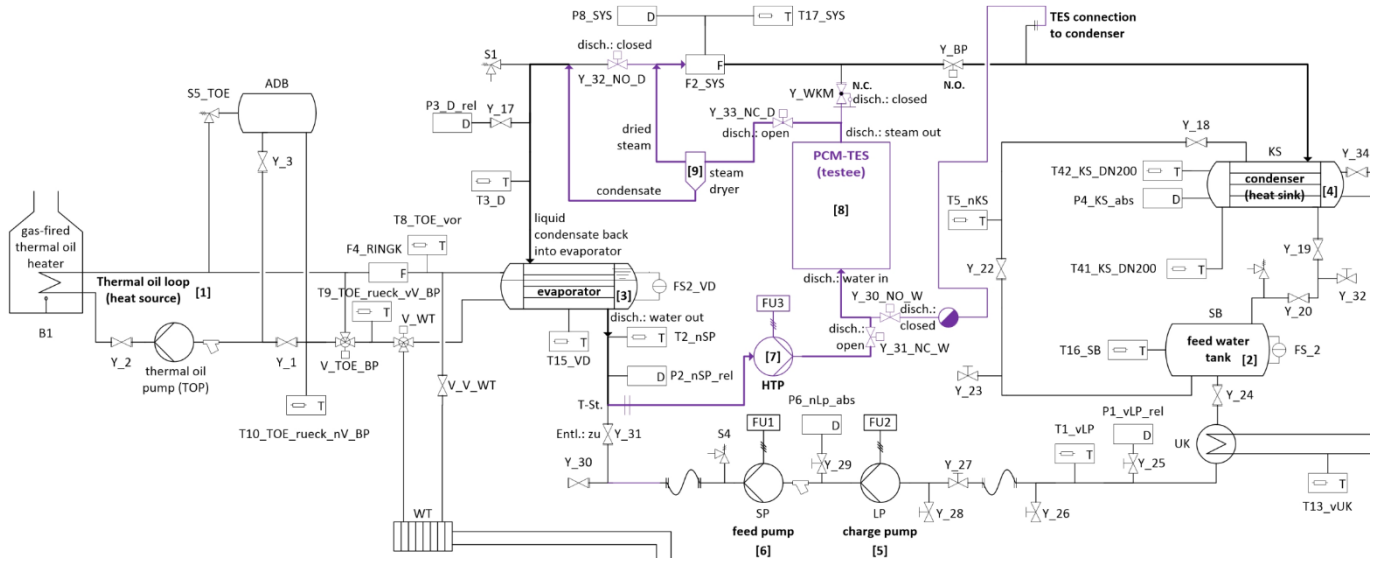


Figure 2: Process flow diagram of the steam facility with interconnected PCM-TES in Fraunhofer ISE's lab, displaying the operational mode "discharging of TES"

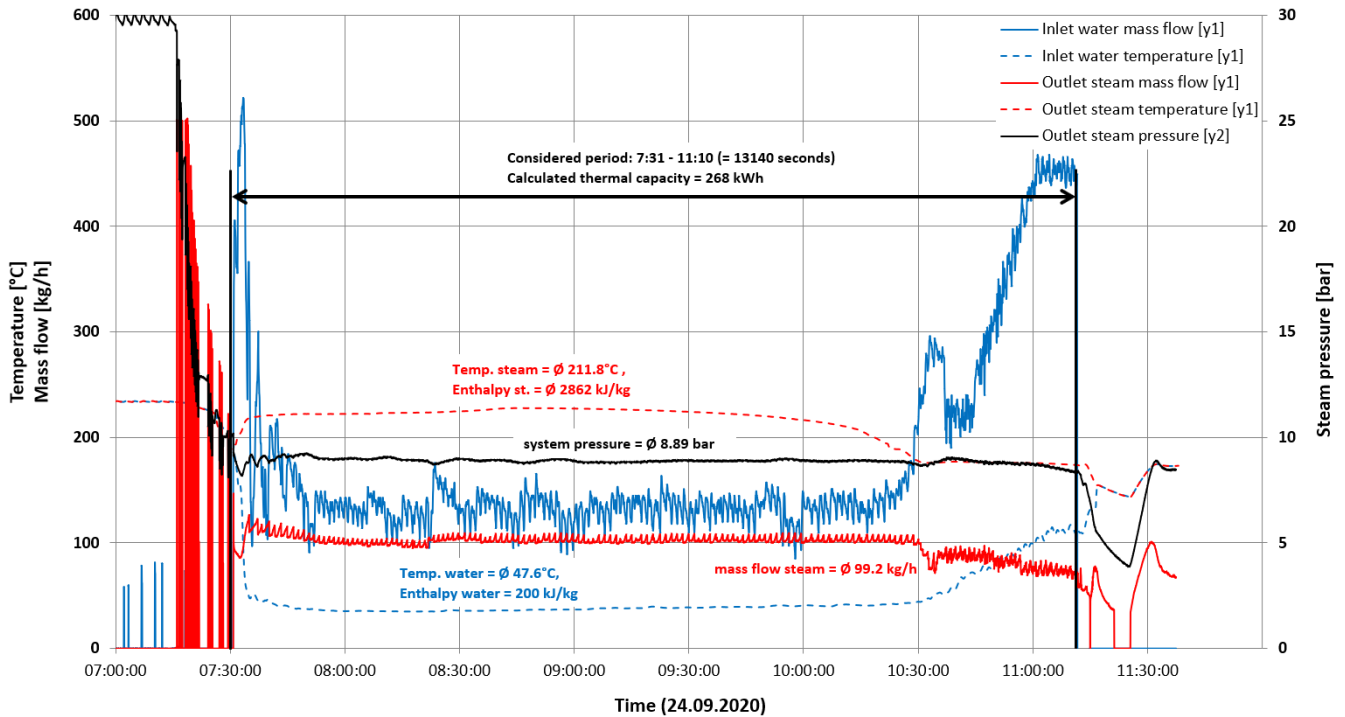
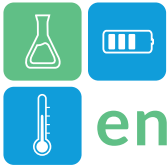


Figure 3: Plot of experimental data from discharging test

References

- [1] Garcia P, Largiller G. Performances and control aspects of steam storage systems with PCM: Key learnings from a pilot-scale prototype. *Appl Energy* 2022;325:119817.
- [2] Prieto C, Cabeza LF. Thermal energy storage (TES) with phase change materials (PCM) in solar power plants (CSP). Concept and plant performance. *Appl Energy* 2019;254:113646.
- [3] Gasia J, Miró L, Cabeza LF. Materials and system requirements of high temperature thermal energy storage systems: A review. Part 2: Thermal conductivity enhancement techniques. *Renew Sust Energ Rev* 2016;60:1584–601.



ENERSTOCK 2024
The 16th IEA ES TCP International Conference on Energy Storage
June 5–7, 2024
Lyon, France

- [4] Prieto C, Rubio C, Cabeza LF. New phase change material storage concept including metal wool as heat transfer enhancement method for solar heat use in industry. *Journal of Energy Storage* 2021;33:101926.
- [5] Johnson M, Fiss M. Superheated steam production from a large-scale latent heat storage system within a cogeneration plant. *Commun Eng* 2023;2(1).



Experimental Evaluation of a Phase-change Thermal Storage

Stephen Harrison^{1,*}, Roy Indranil², Anh Kiet Nguyen²

1 Queen's University, Dept. of Mechanical and Materials Engineering, Kingston ON, Canada

2 QSBR Innovations, 192 Hickson Ave, Kingston ON, Canada

*Corresponding author e-mail: stephen.harrison@queensu.ca

Abstract

Thermal energy storage has been used in domestic hot water systems for many years. Virtually all these systems have been based on sensible heating of potable water that is available on demand to meet the needs of consumers. The use of phase-change materials for thermal storage has been investigated by many researchers in the past. They have the potential to provide a high energy density storage of thermal energy that can be delivered at a nearly constant temperature. Many studies have also identified the challenges associated with using phase-change energy storage materials and their integration into practical components that have consistent performance. The recent advent of commercial products using phase-change materials has incentivized the development and refinement of test methods and standard procedures for evaluating the performance of these devices under repeatable conditions. In this study, a commercially available, latent heat storage was tested according to a pre-existing test method, designed to evaluate similar products.

Keywords: Latent heat thermal storage, Phase-Change, Thermal Performance

Introduction

In support of the development of a standardized test and rating method for latent-heat storage systems, a commercially available, phase-change thermal storage (Waser *et al.*, 2018) was tested in a laboratory environment according to ASHRAE 94.1-2010 (ASHRAE, 2010). The unit consisted of a leak proof container, filled with a salt hydrate with a nominal phase-change temperature of 58°C. It is charged by circulating a hot fluid through its integral tube and sheet heat exchanger and discharged by circulating a cool liquid through a separate discharge flow loop. The unit was 0.183 m³ in volume and weighed 176 kg.

Thermal energy is stored in the phase-change material primarily as latent-heat and depends on the storage material's latent heat of fusion. The storage system requires hot water between 65-80°C to achieve a full charge. Charging the storage causes the transition from the solid-phase to the liquid-phase, while discharging reverses the process releasing heat through a heat exchanger to a cooler liquid, water in this case.

In this way the storage makes use of the latent heat of fusion to increase the energy density of the storage. Depending on the phase-change material used, energy storage can be significantly greater than that associated with sensible heat storage, e.g., the heating of water. The unit tested is primarily used for heating domestic

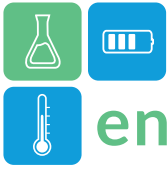
water for sanitary use. When hot water is required, "mains" water is circulated through the unit removing stored heat from the storage, while reversing the charge phase-change process. If the system is unable to meet hot water demand, a backup internal heater (2.8 kW) is available to provide auxiliary heat input.

Test Procedure

Tests were conducted according to the general requirements of ASHRAE Standard 94.1-2010 for phase-change storages. The thermal storage system was installed and commissioned as recommended in the user manual. The unit was situated/installed in a temperature-controlled room. The room temperature was monitored and recorded while testing the storage according to the ASHRAE standard.

An instrumented calorimeter rig was used to function as a controlled heat source for the storage. The calorimeter rig comprised of two temperature-controlled heaters (total capacity ~ 7 kW), speed controlled positive displacement pumps that can pump up to 12 LPM, an expansion tank, a pressure relief valve, air eliminators, a magnetic flowmeter and temperature sensors.

The calorimeter rig was connected to the thermal storage using high temperature heater hose and quick disconnect fittings. The quick disconnect fittings were used to switch between charge flow loop and discharge



flow loops. A 4-junction differential thermopile was installed at the inlet and the outlet of the storage in addition to individual thermocouples for measuring the temperature change of fluid moving into and out of the storage. The sections of pipe between the storage and thermocouples were insulated. These temperature sensors were calibrated to an error of less than $\pm 1\%$ using a temperature bath and reference thermometers. The flowmeter was calibrated with a bucket, stopwatch, and weigh scale arrangement. The sensors in this experimental setup were wired and interfaced to a Rockwell data system for recording, visualizing, and reporting data.



Figure 1: Phase-change thermal storage under test

The phase-change material in the thermal storage was cycled through its solid and liquid phases several times before testing began on the system as per requirements in the operation manual.

The thermal storage was charged at constant power by running hot water from the calorimeter through the charge loop of the storage. The power input to the charge loop was provided by electric heaters of nominal 3.5 kW or 7 kW capacity.

The thermal storage was discharged by running 20°C water from the calorimeter through the discharge loop to the drain.

Due to the nature of phase-change material, supercooling was observed in all discharge tests. Actual power input or output from the storage was calculated from the product of the water mass flowrate, specific heat and the temperature difference across the inlets and outlets of the storage.

A computer data acquisition system was used to record test data at a 2-minute interval. Data was output to a text file that was used for further analysis. A summary of the tests conducted is shown in Table 1.

Table 1: Summary of tests conducted.

Test	Charge Power	Charge Flowrate	Discharge Flowrate	Charge Duration	Discharge Duration
	kW	Lpm	Lpm	hh:mm	hh:mm
1	6	5	5	2:16	1:00
2	6	10	10	2:04	0:44
3	3.5	10	10	5:02	0:42
4	3.5	5	5	5:00	1:10

Results and Discussion

During the charge and discharge periods, the fluid mass flow rate, and the difference in temperature of the heat transfer fluid entering and leaving the storage device, ($t_{in} - t_{out}$), was recorded. For each test, the heat input Q_c , heat output, Q_d , were determined and the storage efficiency η , calculated as:

$$\eta = \frac{Q_d}{Q_c} \quad (1)$$

In addition, standby heat loss was measured. A summary of the results of the charge, discharge and standby loss tests are listed in Table 2.

Table 2: Summary of charge, discharge, and standby tests

Test	Q_c	Q_d	Standby Time	Q-loss	η
	kWh	kWh	hh:mm:ss	kWh	-
1	12.26	11.54	0:40:00	0.72	0.94
2	11.49	10.91	1:54:47	0.58	0.95
3	12.60	8.77	66:38:08	3.83	0.67
4	12.27	10.87	17:30:26	1.40	0.89

Representative plots of inlet and outlet fluid temperatures, and calculated thermal power, during the charge and discharge periods, are shown in Figures 2 to 5. Standby losses were determined by measuring the difference in the energy stored during the charge tests and the energy extracted during the corresponding discharge test. Both long and short standby periods were evaluated. From the long standby test, the average standby heat loss rate was estimated to be 0.08 kW. No appreciable heat loss was detected for the short test.

The ASHRAE test procedure requires charge and discharge tests to be conducted at constant power. It was observed during the test sequences, that our recirculating flow calorimeter apparatus did not have sufficient heater capacity to test the very high charge rates as specified, (e.g., 4 times the design charge rate). Based on the capacity of the unit's electric heater, testing would also be required at input power over 11 kW. The heater capacity of the test calorimeter has subsequently been increased to allow future testing at the higher input power.

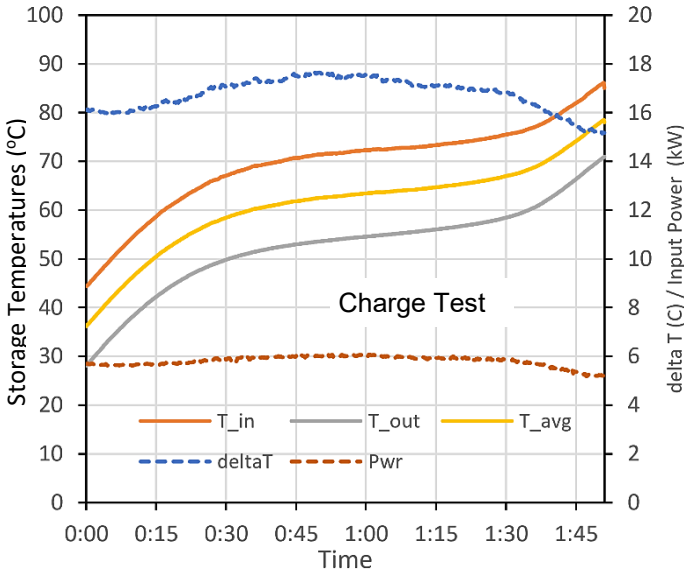
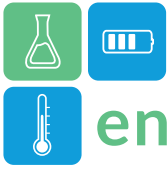


Figure 2: Input power and fluid temperatures for test 1; 6 kW heat input, 5 Lpm water flowrate

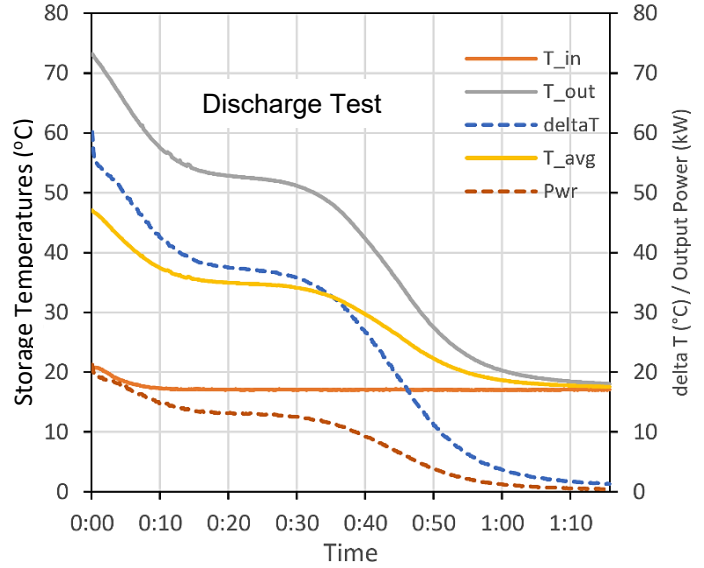


Figure 3: Power output and fluid temperatures for test 1; 5 Lpm water flowrate

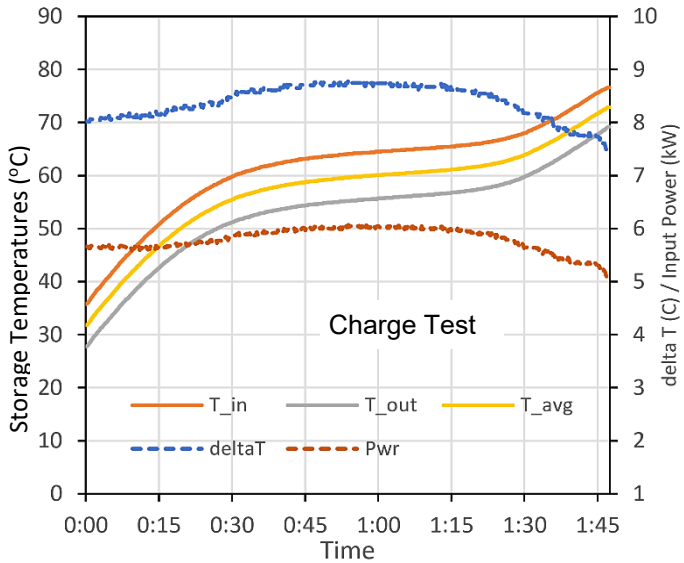


Figure 4: Input Power and fluid temperatures for test 2; 6 kW heat input, 10 Lpm water flowrate

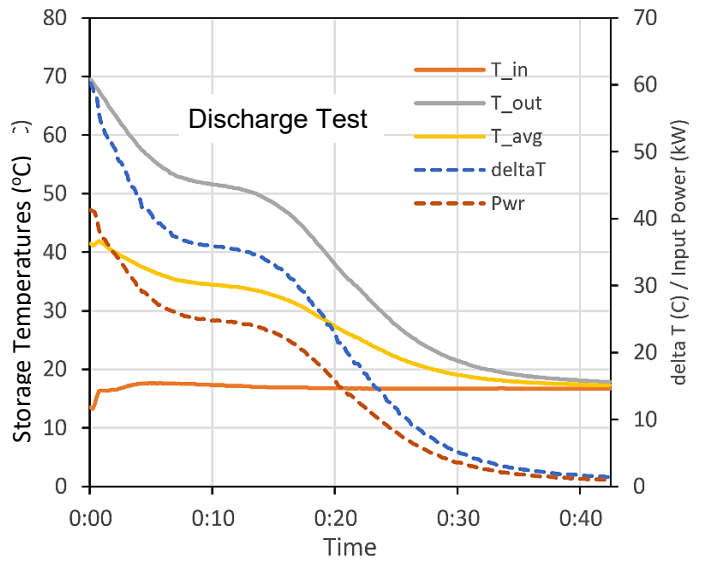


Figure 5: Power output and fluid temperatures for test 2; 10 Lpm water flowrate

When charging the storage at constant power through the recirculating hydraulic loop, rather than from the integral electric heater, it was observed that the inlet temperature to the storage varied significantly over the test period.

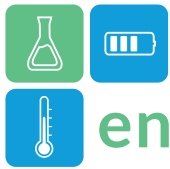
It was also observed that it was difficult to maintain a constant power discharge rate when the inlet fluid temperature and flow through the discharge loop were held constant. During these discharge test sequences, the outlet fluid temperature and discharge power, decreased over time. This would seem to be an issue to be addressed in future revisions of the standard.

Another limitation of the ASHRAE standard is if

product ratings and detailed design data are required at other charge and discharge conditions (e.g., flowrates and temperatures), the full test sequences will have to be repeated numerous times. The standard does allow storage efficiency and thermal capacities to be determined, but a more comprehensive test procedure and performance characteristic is required for system design and simulation.

It is anticipated that in many field installations, the storage will be charged at a constant temperature rather than at constant power input. For example, from a central boiler or community district energy supply.

To illustrate this, charge tests were conducted at 3 L/m



and three different supply temperatures (i.e., 57, 66 and 77°C). Figure 6 shows energy stored vs average storage temperature. The yellow line shows a regression curve fit to the experimental charge data and the blue, orange and green lines indicate the temperature of the inlet fluid during charging. The intersection of these lines with the regression line indicates the level of charge reached and the limit to the available energy. At the charge temperatures indicated, the energy storage equals 4.8, 10.3 and 12 kWh, respectively.

This is an important result as it stresses the importance of charging the storage at a temperature above the phase-change temperature if the full capacity is required. Small deviations below the phase-change temperature may have large effects on storage capacity. This result also indicates that a similar but reverse effect may result when discharging the storage. Small deviations in discharge temperature may have large effects on the delivered energy.

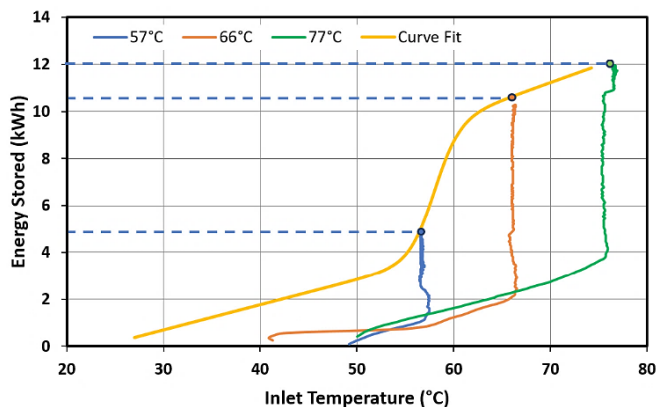


Figure 6: Energy stored vs the fluid charge temperature

Conclusions

The characteristics of phase-change materials have been widely studied in the past (Sharma *et al.*, 2009), but only recently have commercially available units entered the marketplace. Although, rating standards for phase-change storage units have been developed, their ability to characterize operation in “real world” installations has been questioned.

This preliminary study illustrates the need to not only determine “rated” overall charge and discharge efficiency of a phase-change storage, but the need to characterize the energy capacity versus effective storage temperature as a function of fluid flowrates and temperatures. This information is particularly important for the integration of a phase-change storage into a larger system or the prediction of system performance.

It is apparent that many factors affect the performance

of a full-scale phase-change thermal storage, e.g., charge and discharge temperatures, fluid flow rates and standby thermal losses. Additionally, the choice of phase-change material depends on specific features such as heat exchanger design, material packaging, and cycle life. It is expected that a full-scale unit’s performance will differ from laboratory tests conducted on small PCM samples.

Manufacturers’ products often contain proprietary features or material compositions that they are unwilling to divulge. As more commercial units enter the market there is a need for a practical and comprehensive component test procedure that accounts for all these factors.

This study has shown that meaningful performance data can be obtained for phase-change thermal storages using the test apparatus and general test procedures described in ASHRAE 94.1-2010. This standard provides a consistent method and determination of storage capacity, standby losses, and storage efficiency under specified conditions.

However, it does not produce sufficient data to fully characterize the performance of a phase-change storage without repeated tests being conducted at a full range of operational conditions.

Further work should be undertaken to streamline and refine the test procedure, and analysis, such that these thermal storage units can be fully characterized through an efficient and practical test sequence. This would allow the performance of these system to be predicted within current system simulation tools.

Acknowledgment

Support for this study was provided by CanmetENERGY-Ottawa / Energy Efficiency and Technology Sector / Natural Resources Canada. In particular, the contribution and guidance of Dr. Reda Djebbar throughout is study, is appreciated.

References

- Waser, R. *et al.* (2018). Fast and experimentally validated model of a latent thermal energy storage device for system level simulations, *Applied Energy*, 231.
- ANSI/ASHRAE Standard 94.1-2010. (2010) Method of Testing Active Latent-Heat Storage Devices Based on Thermal Performance, ISSN 1041-2336, ASHRAE, 1791 Tullie Circle, NE, Atlanta, GA
- Sharma, A. *et al.* (2009). Review on thermal energy storage with phase change materials and applications. *Renewable and Sustainable Energy Reviews*, 13(2), 318-345.



Experimental Study of a Bench Scale Packed-bed Latent Heat Storage Unit with Al-Si based PCM pellets

Tomokazu Nakamura^{1,*}, Yusuke Sato¹, Lianying Shan², Justin Ningwei Chiu², Shoma Fujii³, Takahiro Nomura¹

¹ Faculty of Engineering, Hokkaido University, Kita 13 Nishi 8, Kita-ku, Sapporo 060-8628, Japan

² Department of Energy Technology, KTH Royal Institute of Technology, Brinellvägen 68, SE-10044 Stockholm, Sweden

³ Institute for Future Initiatives, The University of Tokyo, 7-3-1 Hongo, Bunkyo-ku, Tokyo, 113-8654, Japan

*Corresponding author e-mail: tomonakamura@eng.hokudai.ac.jp

Abstract

The global push for decarbonization has accelerated the integration of renewable energy sources, with the International Energy Agency (IEA) projecting a substantial 89% share of renewables by 2050. Energy storage technology is essential to ensure a stable renewable energy supply as output fluctuates. This study investigates the heat storage and discharge performance of a bench-scale packed-bed latent heat storage system with Al-Si based PCM pellets with melting temperature of 577 °C. Heated air flows through the packed bed for direct contact heat exchange. Results reveal a notable heat storage density of 0.23 MW_{th} h m⁻³ ($\Delta T = 350\text{K}$). This study identifies the heat exchange fluid and not the pellet thermal conductivity, as the rate-limiting factor in heat transfer mechanism. The dependency of the heat coefficient on the Reynolds number underlines the system sensitivity to operating conditions.

Keywords: Thermal energy storage, Latent heat storage, High temperature application

Introduction

The introduction of renewable energy is rapidly expanding as part of efforts to promote decarbonization. According to International Energy Agency (IEA) statistics, the share of renewable energy sources is expected to reach 89% by 2050 (IEA, 2023). A stable supply of renewable energy is required to develop energy storage technology to control fluctuating output. Thermal energy storage is one of the methods in that, The Carnot Battery is an energy storage technology that converts surplus electricity into heat, stores it in a thermal storage system, and uses the stored heat to generate electricity (Power-to-heat-to-power), when supply is required (Eggers and al., 2022). It has also been reported that heat previously obtained from fossil fuels can be obtained from renewable energy sources (power-to-heat), thereby contributing to carbon neutrality in industry (Madeddu and al., 2020). In such cases, the storage of excess renewable energy as thermal energy is also considered promising.

Latent heat storage using metallic PCM with high heat storage density and thermal conductivity attracts attention for high-temperature TES. Our team is developing Al-Si alloy based microencapsulated phase

change material (MEPCM) with melting temperature at 577 °C and a PCM composite pellet with matrix of the MEPCM. The MEPCM pellet can be used for direct contact heat exchange in the same way as sensible heat storage (Koide and al., 2023). In this study, we evaluated the heat storage and release performance of a bench-scale packed bed latent heat storage system filled with the Al-Si based MEPCM pellet.

Methodology

Cylindrical pellets with a diameter of about 10 mm were prepared from Al-25mass%Si@ α -Al₂O₃ (melting point T_m : 577 °C) MEPCM and a shell of α -Al₂O₃. Figure 1 shows an image of high-temperature latent heat storage pellets. The pellets were produced by mixing and sintering MEPCM powder and inorganic binders. Table 1 lists the properties of the MEPCM pellet. These thermophysical properties, density, and volume fraction in packed bed are measured values. The heat storage density per packed bed volume (Q_v) was obtained from the sensible heat in the pellet liquid phase (c_{pl}), latent heat of solidification (L_s), sensible heat in the pellet solid phase (c_{ps}), pellet density (ρ), and the pellet volume fraction in the packed bed (ϕ) using the following Eq. (1).

$$Q_v = \left(\int_{300}^{T_m} c_{ps} \cdot dT + \int_{T_m}^{650} c_{pl} \cdot dT + L_s \right) \cdot \rho \cdot \varphi \quad (1)$$

Table 1: Properties of MEPCM pellet.

Properties	Unit	Value
Specific heat (Typical value for solid phase)	J g ⁻¹ K ⁻¹	1.15
Specific heat (Typical value for liquid phase)	J g ⁻¹ K ⁻¹	2.36
Thermal conductivity (Typical value for solid phase)	W m ⁻¹ K ⁻¹	1.67
Thermal conductivity (Typical value for liquid phase)	W m ⁻¹ K ⁻¹	2.36
Latent heat of solidification	J g ⁻¹	254
Melting point	°C	577
Pellet diameter	mm	9.72
Pellet width	mm	9.87
Pellet density	kg m ⁻³	1.85×10 ³
Volume fraction of packed bed	-	0.60

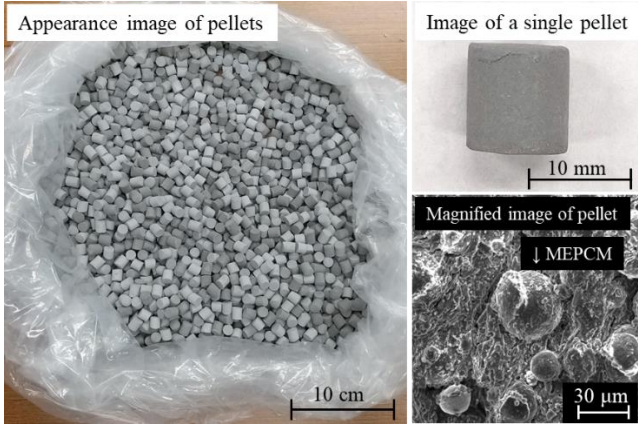


Figure 1: Image of high-temperature latent heat storage pellets.

Figure 2 shows the thermal energy storage (TES) apparatus used in this study. It consists of an 18 cm wide square duct at 56 cm height and is filled with 19.7 kg of the pellets. Air heated by an air heater flows through the packed bed for direct contact heat exchange. Thermocouples are placed in the packed bed at every 10 cm height starting at 6 cm from the bottom and it indicates T_0 , T_{10} , T_{20} , T_{30} , and T_{40} . The initial temperature of the packed bed is set at 300 °C and the inflow air temperature at 650 °C for heat storage; the initial temperature of the packed bed is at 650 °C and the inflow air temperature at 300 °C for heat discharge. The effect on heat exchange rate is investigated at three air flow rates of 0.25, 0.5, and 0.75 N m³ min⁻¹.

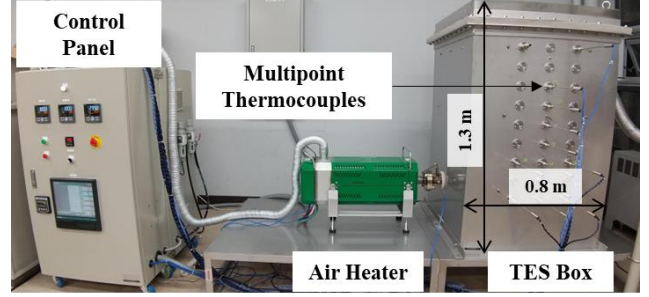


Figure 2: Thermal energy storage (TES) apparatus.

Results and Discussion

Q_v is calculated with Eq. (1) from the physical properties of the pellets and the volume fraction ratio into the packed bed, at a temperature difference of 350 K (300°C-650°C). In this case, Q_v is 0.23 MW_{th} h m⁻³ (0.83×10⁶ kJ m⁻³).

Figure 3 shows the temperature history in the packed bed during heat release at an air flow rate of 0.5 N m³ min⁻¹. The straight line in the figure indicates the fluid temperature. This temperature history shows a temperature stagnation region near the melting point between 580 °C and 530 °C, which is a characteristic of latent heat storage.

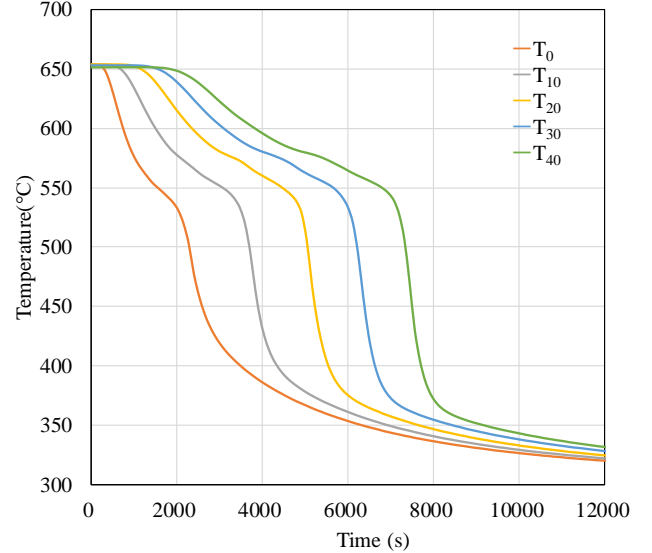
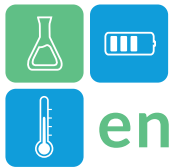


Figure 3: The temperature history in the packed bed during heat release at an air flow rate of 0.5 N m³ min⁻¹.

The average heat exchange rate per internal volume of thermal energy storage (q_{Ave}) was obtained from the inlet temperature (T_{in}), the outlet temperature (T_{out}), mass flow rate (m), specific heat of air (c_p), end time of heat release (t_f), and internal volume of thermal energy storage (V_{tes}) using the following Eq. (2).

$$q_{Ave} = \frac{\int_0^{t_f} \int_{T_{in}}^{T_{out}} m \cdot c_p \cdot dT \cdot dt}{t_f} \times \frac{1}{V_{TES}} \quad (2)$$



t_f is the time from the start of heat release until T_{out} reaches 350°C.

Figure 4 shows the relationship between q_{Ave} and Reynolds number (Re) during heat release at each air flow rate. The heat exchange rate increased in proportion to the Re in the transition flow region, which is the operating condition of this experiment. The trend of increase in heat exchange rate was similar to previous studies (Koide and al., 2023), and the heat exchange rate per unit thermal energy storage (0.05 $\text{kW}_{th} \text{L}^{-1}$) required for the Carnot battery operation was achieved.

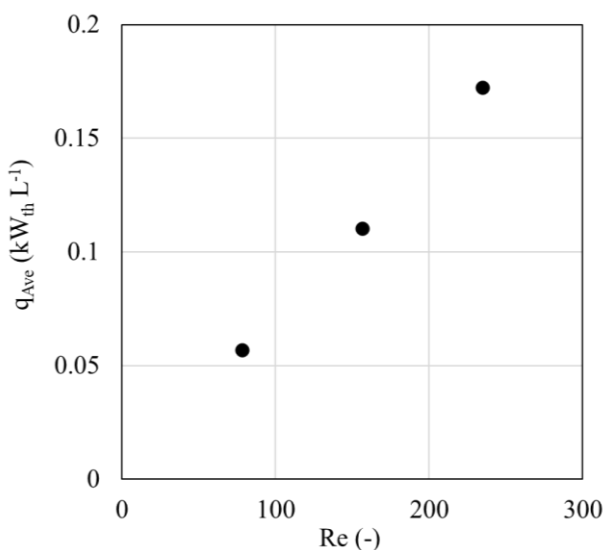


Figure 4: Relationship between the Average heat exchange rate per internal volume of thermal energy storage (q_{ave}) and the Reynolds number during heat release at each air flow rate.

Conclusions

In this study, 19.7 kg pellets of microcapsule particles with an Al-Si alloy core and $\alpha\text{-Al}_2\text{O}_3$ shell were used as the main latent heat storage material. We evaluated the heat storage and discharge performance of a direct contact heat exchange system in a bench-scale packed bed filled with high-temperature latent heat storage pellets using this MEPCM as the main component.

From the physical properties of the pellets and the volume fraction ratio in the packed bed, the heat storage density per packed bed volume (Q_v) at a

temperature difference of 350 K (300°C-650°C) achieved is $0.23 \text{ MW}_{th} \text{h m}^{-3}$ ($0.83 \times 10^6 \text{ kJ m}^{-3}$).

Temperature history showed a temperature stagnation region near the melting point, which is a characteristic of latent heat storage.

The temperature history inside the pellets showed almost the same values as the packed bed temperature profile. This indicates that the rate-limiting factor of heat transfer is not the thermal conductivity of the pellets, but the rate of heat exchange by the heat transfer fluid.

The heat exchange rate increases proportionally to the Re in the transition flow region, this indicates direct dependency of the heat storage performance to the flow operating condition of the flow.

Acknowledgment

This paper is based on results obtained from a project, JPNP20005, subsidized by the New Energy and Industrial Technology Development Organization (NEDO).

References

- Eggers, J.R., and al. (2022), Design and performance of a long duration electric thermal energy storage demonstration plant at megawatt-scale. *Journal of Energy Storage*. doi.org/10.1016/j.est.2022.105780
- IEA, (2023) World Energy Outlook 2023. P.279. IEA. <https://www.iea.org/reports/world-energy-outlook-2023>, License: CC BY 4.0 (report); CC BY NC SA 4.0 (Annex A)
- Koide, H. and al. (2023) Performance analysis of packed bed latent heat storage system for high-temperature thermal energy storage using pellets composed of micro-encapsulated phase change material. *Energy*. doi.org /10.1016/j.energy.2021.121746
- Madeddu, S. and al. (2020) The CO₂ reduction potential for the European industry via direct electrification of heat supply (power-to-heat). *Environmental Research Letters*. doi.org/10.1088/1748-9326/abbd02

Experimental Study of Thermochemical Heat Storage with Zeolite 13X for Utilization of Industrial Wasted Heat

Sung-Kook Hong*, Hyun-Hee Lee, Si-Won Yoon, Seong-Eun Kim, Duck-Jae Wei
 Korea Institute of Energy Research, Energy Convergence System Research Dept., 152, Gajeong-ro, Yuseong-gu, Daejeon, Korea
[*sungkookhong@kier.re.kr](mailto:sungkookhong@kier.re.kr)

Abstract

The experimental study of thermochemical heat storage (THS) has been performed to obtain an insight into the design and operation of THS system for utilization of industrial wasted heat. The heat storage system consists of a lab-scale chamber with 3kWh capacity stacked by zeolite 13X. Experiments were conducted depending on the variation of operating parameters, such as charging temperature, absolute humidity, and stage of charge. As the input water vapour increased, the heat power increased, and the maximum output was obtained more than 2 kW. In addition, it was confirmed that the temperature deviation was maintained within ± 3 degrees while maintaining the temperature of 70-130°C to respond to the amount of input water vapour. Based on the experimental data for various operating conditions, we intend to design, manufacture, and evaluate about 200 kWh THS heat storage modules in the near future.

Keywords: Thermochemical Heat Storage (THS), Zeolite 13X, Industrial Wasted Heat

Introduction

The amount of industrial wasted heat energy, which is more than 10% of the heat energy used in the industrial field, is discarded. In order to effectively use these discarded thermal energy, it is of paramount importance to match the imbalance of time and space between consumers and suppliers (industrial wasted heat). Therefore, if high-density heat storage technology is applied and actively utilized, as shown in Fig. 1, energy saving and greenhouse gas reduction can be greatly contributed (Cabeza, 2016; Wang, 2020).

Thermochemical heat storage is one of the most promising storage methods because it offers high heat storage density and stores energy for a long period with negligible loss compared to conventional heat storage technologies that utilize sensible or phase change heat (Rindt, 2018; Kuznik, 2021; Shuli, 2022). A high-density heat storage system using thermochemical material that can store such industrial wasted heat and supply it to desired heat and temperatures of various consumers. So far, there is a lack of related studies applying the THS system. Hence, an experiment has been performed to obtain an insight into the design and operation of THS system for utilization of industrial wasted heat. Experiments were conducted depending on the variation of

operating parameters, such as charging temperature, absolute humidity, and stage of charge. Especially, water vapour control is considered for heat output and temperature control. Through this study, we intend to design a 200kWh THS module in the near future.

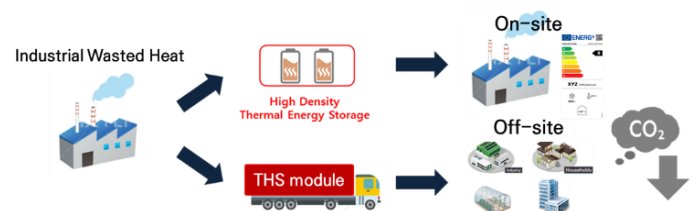


Figure 1: Conceptual diagram of industrial wasted heat utilization using THS system

Methodology

Fig. 2 shows the test apparatus used in this experiment. It consists of a storage chamber (reactor), heat exchanger, controller, and data acquisition system. A more detailed schematic of the test rig is shown in Fig. 2. An electric heater and a humidifier (water vapour generation) are installed to simulate the heat storage and heat release processes, respectively. For the heat storage process, the electric heater is



operated and for the heat release process, the humidifier is utilized.

In this study, zeolite 13X with stable characteristics was used as the thermochemical storage material. It is spherical in shape with a diameter of 3 – 5 mm (Sungkook, 2022).

absolute humidity was in the range of 10 – 50 g/kg. Detailed experimental conditions are listed in Table 1.

Table 1: Experimental conditions.

	Charging process	Discharging process
Temperature (°C)	160~220	20~25
Absolute Humidity (g/kg)	Ambient Condition	10~50

Results and Discussion

Fig. 3 illustrates the temperature distribution across the storage chamber during the heat storage and release process, which occurs at a charging temperature of 220 °C. Owing to the hot air intake, the chamber was heated to 220 °C in a very short duration and remained constant during the entire heat charging process. In the case of the heat dissipation process to obtain the stored heat, wet air is supplied to the chamber. The discharging time is extended to 10,000 sec. As shown in Fig. 3 of discharging process, the temperature of air at the outlet rises quickly up to 100 °C owing to the fast adsorption reaction characteristics of zeolite. After 2,000 sec, the temperature difference between the inlet and outlet is maintained at over 70 °C to boost the air passing through the chamber. After 8000 sec, the temperature decreases to the inlet temperature indicating the end of the adsorption reaction in most of the zeolite in the chamber.

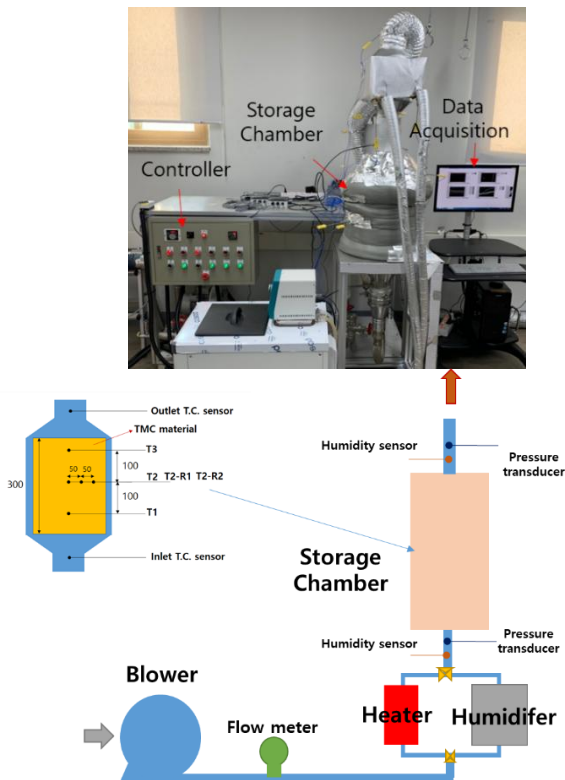


Figure 2: Picture and schematics of experimental apparatus

For data acquisition of parameters, namely temperature, humidity, and pressure, each sensor is installed as illustrated in Fig. 2. The humidity sensors are installed at the inlet and outlet of the chamber to measure the variation in humidity during the heat release process. Five K-type thermocouples are installed inside the chamber as shown in Fig. 2, where T1, T2, and T3 are positioned at the center of the chamber. Additional K-type thermocouples are placed at the inlet and outlet of the chamber. To measure the pressure drop across the chamber, pressure transducers are installed at the inlet and outlet of the chamber. The flow rate of the air passing into the chamber is measured using an orifice-type flow meter and it is controlled by an inverter connected to the blower. The absolute humidity of the supplied air was controlled by the humidifier. In this study, the value of

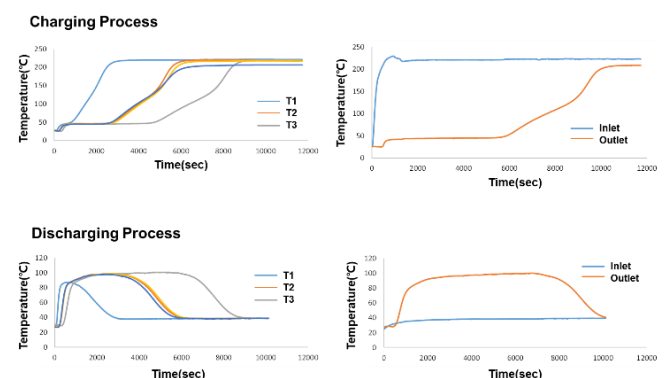


Figure 3: Temperature distribution during the heat charging & discharging process under charging temperature of 220 °C

Fig. 4 depicts the average value of the available heat power depending on the variation of humidity in all the tested cases. The average heat power has a linear



relationship with absolute humidity. It shows a minimum output of 0.4kW to a maximum output of 2kW depending on the amount of input water vapour.

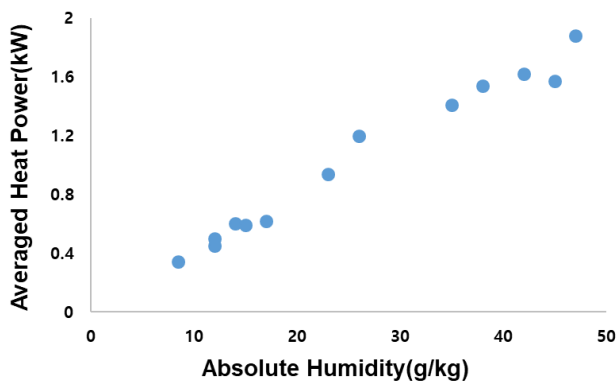


Figure 4: Averaged heat power at different values of absolute humidity

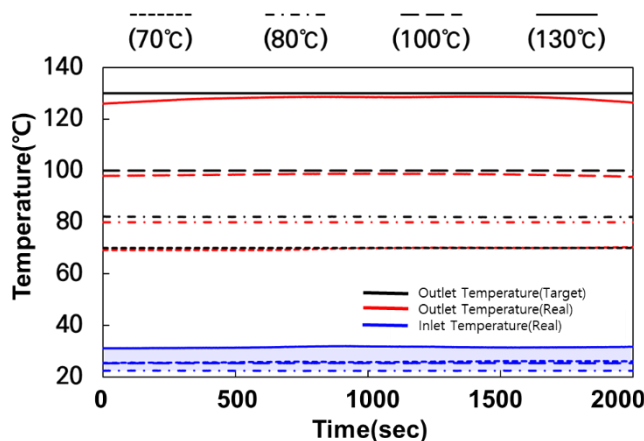


Figure 5: Comparison of outlet temperature and target temperature depending on water vapour control

Fig. 5 shows the change in outlet temperature obtained through water vapour control to respond to the consumer side. As shown in Fig. 5, by adjusting the water vapour, it was possible to keep the desired temperature deviation within ± 3 degrees.

Conclusions

In this study, an experiment on high-density thermochemical heat storage was conducted to utilize the industrial wasted heat. The results show that

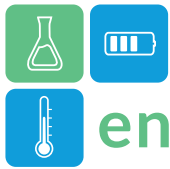
increasing the input humidity to induce increased power, and an averaged heat power of 2 kW was obtained. In addition, it was confirmed that the temperature deviation was maintained within ± 3 degrees while maintaining the temperature of 70–130°C to respond to the amount of input water vapour. Through this study, we intend to design a 200kWh THS module in the near future.

Acknowledgment

This material is based upon work supported by the research funding from Korea Institute of Energy Research (KIER) (Project No. GP2021-0020).

References

- Cabeza, L. F. and al. (2016). Thermal energy storage (TES) for industrial waste heat (IWH) recovery: A review. *Applied Energy*, doi.org/10.1016/j.apenergy.2016.06.147
- Wang, R.Z. and al. (2020). Thermal energy storage using absorption cycle and system: A comprehensive review. *Energy Conversion and Management*, doi.org/10.1016/j.enconman.2020.112482
- Rindt, C.C.M. And al. (2018). Investigation of a household-scale open sorption energy storage system based on the zeolite 13X/water reacting pair. *Applied Thermal Engineering*, doi.org/10.1016/j.applthermaleng.2018.04.092
- Kuznik, F. and al. (2021). A reality check on long-term thermochemical heat storage for household applications. *Renewable and Sustainable Energy Reviews*, doi.org/10.1016/j.rser.2020.110683
- Shuli, L. and al. (2022). Thermal performance study of thermochemical reactor using net-packed method. *Renewable Energy*, doi.org/10.1016/j.renene.2021.09.115
- Sungkook, H. and al. (2022). Investigation of open-type 1kW-scale thermochemical heat storage system with zeolite 13X for power-to-heat applications. *Journal of Mechanical Science and Technology (KSME)*, DOI 10.1007/s12206-022-0842-y



Experimental Study on Thermal Storage System with Sand and Al-Si Alloy for Coal-fired Plant Retrofit Carnot Battery

Cho Junhyun^{1,*}, Choi Bongsu¹, Oh Bong Seong¹, Ra Ho-Sang¹, Na Sun Ik¹, Shin Hyungki¹, Baik Young-Jin¹ and Lee Gilbong¹

¹ Korea Institute of Energy Research (KIER), 152 Gajeong-ro, Yuseong-gu, Daejeon, South Korea

*Corresponding author e-mail: jhcho@kier.re.kr

Abstract

In the retrofitting of coal-fired power plants into Carnot batteries, materials and unit modules for high-temperature thermal storage systems were studied. The standard inlet condition of steam turbines in South Korean coal-fired power plants, which is 538°C, led to the selection of sand as a material that is cost-effective and capable of withstanding high temperatures. Sensible heat storage systems, such as those made from sand or concrete, are economically feasible but suffer from the disadvantage of a decrease in temperature during continuous heat discharge. To compensate for this and to maintain the inlet temperature of steam turbines in coal-fired plants, an Al-Si Alloy, which can utilize the latent heat phase in this temperature range, was incorporated, resulting in the formation of a composite thermal storage module. Through accelerated preliminary tests, it was confirmed that the temperature is maintained around 577°C by utilizing the latent heat phase, and it was observed that performance remained above 90% even after 10 cycles.

Keywords: Carnot Battery, Coal-fired Power Plant Retrofit, ESS, Sand Thermal Storage, Al-Si Alloy

Introduction

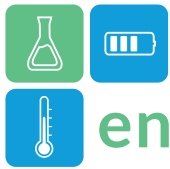
According to the 10th Electric Power Supply Plan announced by the Ministry of Trade, Industry and Energy in South Korea, all coal-fired power plants are scheduled to be decommissioned by 2050. Furthermore, there is a requirement for 20.85GW of long-duration power storage systems, excluding pumped-storage generation, to be developed by 2036. Retrofitting these coal-fired plants into Carnot Batteries, which involves converting excess renewable energy into heat, storing it, and then utilizing the existing steam power generation systems of the plants to regenerate electricity, offers a feasible solution. This innovative approach could create large-scale, cost-effective, long-duration Energy Storage Systems (ESS) by leveraging the substantial stranded assets of the decommissioned plants. This study presents preliminary experimental research on thermal storage material modules necessary for the implementation of this system.

Coal-fired Power Plant Retrofit Carnot Battery

For large-scale, long-duration Energy Storage Systems (ESS), the Levelized Cost of Storage (LCOS) is a key performance indicator. The U.S. Department of Energy (DOE) has set a technology development goal to reduce LCOS below the cost of commercial pumped-storage

hydroelectricity (0.1\$/kWh), aiming for a target of 0.05\$/kWh. LCOS consists of capital expenditures (CAPEX), operational expenditures (OPEX), and the costs associated with total roundtrip efficiency (RTE) losses. Among these, the most significant is CAPEX. Therefore, it is essential to design a system that minimizes CAPEX. Retrofitting coal-fired power plants into Carnot Batteries, which utilize existing infrastructure such as steam power generation systems, cooling systems, water treatment facilities, transmission and distribution equipment, and sites, is being considered as a strategy that can significantly reduce CAPEX. In this context, choosing a thermal storage system with lower CAPEX is crucial, and materials like concrete and sand are being evaluated for high-temperature thermal storage due to their cost-effectiveness

The main steam of South Korea's standard coal-fired power plant must be supplied at a level of 538±16°C and 246 bar. However, low-cost sensible heat storage media such as concrete or sand in a single thermal storage system have the characteristic of decreasing temperature as heat is discharged. To address this, a thermal storage module design was developed that mixes particulate sand with an Al-Si alloy containing 12.6% silicon, which has a eutectic point at 577°C. This design aims to utilize latent heat at steam production



temperatures, improve thermal conductivity, and enhance energy density.

Experimental Setup of Thermal Energy System with Sand and Al-Si Alloy

The melting characteristics of Al-Si alloy vary with the silicon content, and a composition of Al 87.4wt% and Si 12.6wt% exhibits a eutectic point at 577°C, where the latent heat is 483 kJ/kg.[1] This value is higher than the melting heat of ice, which is 335 kJ/kg. Previous research has primarily focused on Al-Si alloys as a standalone material [1,2], with limited studies on their combination with sand in a composite thermal storage system. To design a composite thermal storage system that combines the sensible heat storage of sand with the latent heat storage of the Al-Si alloy, preliminary tests were conducted on accelerated charging-discharging heat cycles by mixing sand with the Al-Si alloy to examine the thermal storage characteristics and degradation. The density of sand is 1445 kg/m³, and that of Al-Si ranges from 2500 to 2700 kg/m³. Due to the density difference and repeated phase changes, there is a possibility of aluminium flowing downwards through the pores of the sand under gravity. In our module design, the grain size of sand was selected carefully to ensure that the structure and thermal properties are maintained even after cyclic tests.

For this purpose, a heating device capable of heating the material with an electric heater was constructed as shown in Figure 1. A chamber to contain the material inside the heater was fabricated from SUS310s material 100A pipe, 200mm in height. K-type thermocouples (A-class) were installed at various locations inside the chamber, both centrally and on the inner surface, to measure the temperature of the sample. A data logging system (Yokogawa GP10) and LabVIEW were used for heater control and real-time monitoring.

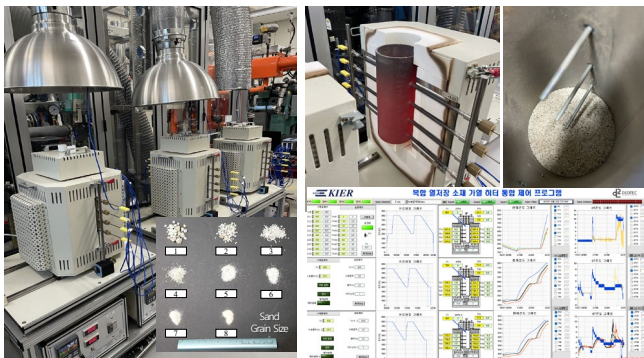


Figure 1: Experimental setup of a charging-discharging heater

For the accelerated tests, cyclic heat charging and discharging were conducted between 400 and 800°C, around the target thermal storage temperature of 577°C. The heating was controlled by an electric heater at a rate of 10°C/min, and after maintaining at 800°C for 3 hours, cooling occurred naturally at approximately -1°C/min. Various sample combinations were subjected to 10 cycles of accelerated cyclic testing, and the heat storage performance was compared between the 1st and 10th cycles. After mixing the samples, the first cycle of melting was defined as cycle 0. For performance comparison, heating of 1 and 10 cycle were carried out at approximately 2.5°C/min under the same heat input conditions (same electric heater output).

Results and Discussion

Experiments were conducted with 1x1x1 cm cubic samples of Al-Si 12.6% alloy, combined with various sand samples. Ultimately, a unit module was designed and fabricated as shown in Fig. 2. The sand sample of size 3 (1-2 mm) was mixed with the Al-Si alloy samples, and to prevent the alloy from flowing downwards, the finest size sand, number 8 (<0.1 mm), was layered between each layer. This can be easily understood as analogous to spreading cream between layers of a Christmas cake. In fact, this idea was inspired by the use of very dense particles of sand as molds in commercial Al-Si casting processes, where sand is used as the mold.

Temperature data for the 1st and 10th cycles measured at the central point of the thermal storage module sample are displayed in Fig. 3. Position 1 is at the top, and position 7 is at the bottom. As can be seen in Fig. 3, a latent heat phase maintaining temperature near 577°C was confirmed at all locations. This suggests the potential for stable production of the 538°C steam supplied to the steam turbine.

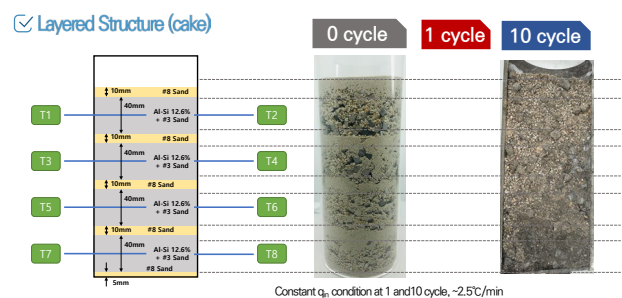


Figure 2: Layered structure of sand and Al-Si alloy module

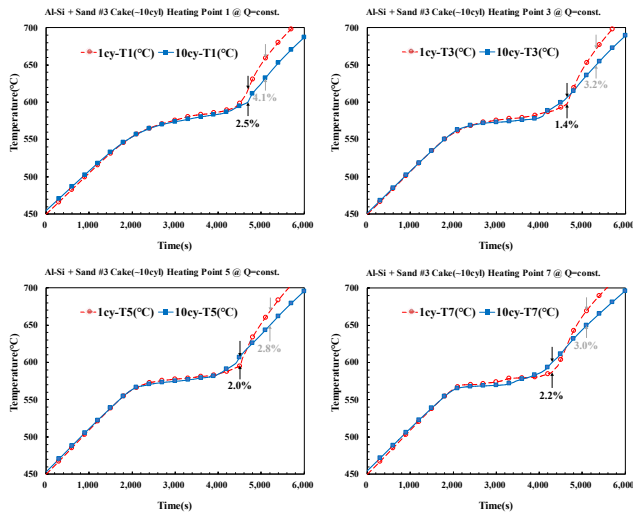


Figure 3: Temperature data for the 1st and 10th cycles

Furthermore, after 10 accelerated cycles, the latent heat formation phase was maintained at all positions, with the difference confirmed to be within a maximum of 4.1% across all sections. Based on this, it can be confirmed that the internal structure of the sample is also maintained, and the combination of sand and Al-Si alloy is still intact as seen in the cross-sectional picture of the sample in Fig. 2

Conclusions

For the application of a Carnot battery retrofit for coal-fired power plants, we designed a composite thermal storage module using sand, a low-cost thermal storage material, and an Al-Si 12.6% alloy with a eutectic point of 577°C. The feasibility was confirmed through preliminary testing

Acknowledgment

This work was supported by the Development Program of the Korea Institute of Energy Research (KIER C4-2429) and by the Korea Institute of Energy Technology Evaluation and Planning (KETEP) and the Ministry of Trade, Industry & Energy (MOTIE) of the Republic of Korea (No. 20202020800200).

References

- Gokon, N. and al. (2015). Cyclic properties of thermal storage/discharge for Al-Si alloy in vacuum for solar thermochemical fuel production. *Energy Procedia*. Elsevier, doi: 10.1016/j.egypro.2015.03.145
- Wang, Z. and al. (2017). Thermal reliability of Al-Si eutectic alloy for thermal energy storage. *Materials Research Bulletin*. Elsevier, doi/10.1016/j.materresbull.2017.07.040

Experimental investigation of a façade-integrated adsorption system for solar cooling

O. Boeckmann^{1,*}, S. Weber², A. Schedler³, M. Schaefer¹

¹ University of Stuttgart, IGTE, Pfaffenwaldring 31, 70569 Stuttgart, Germany

² University of Stuttgart, IABP, Pfaffenwaldring 7, 70569 Stuttgart, Germany

³ University of Stuttgart, IBK2, Keplerstraße 11, 70174 Stuttgart, Germany

*Corresponding author e-mail: boeckmann@igte.uni-stuttgart.de

Abstract

Due to its high demand for resources and energy, the building sector accounts for almost 40% of the global carbon dioxide emissions. Therefore, in order to achieve the ambitious climate protection goals, it is essential to reduce the required amount of building material in the construction of future buildings as well as to operate these lightweight buildings more energy efficiently or, if possible, energy self-sufficiently. Against this background, a novel, façade-integrated adsorption system for solar cooling of lightweight buildings is being developed and experimentally investigated within the Collaborative Research Centre 1244 "Adaptive skins and structures for the built environment of tomorrow" at the University of Stuttgart. The proposed adsorption system combines the functionality of energy storage and cold production, with minimum occupation of inner building space.

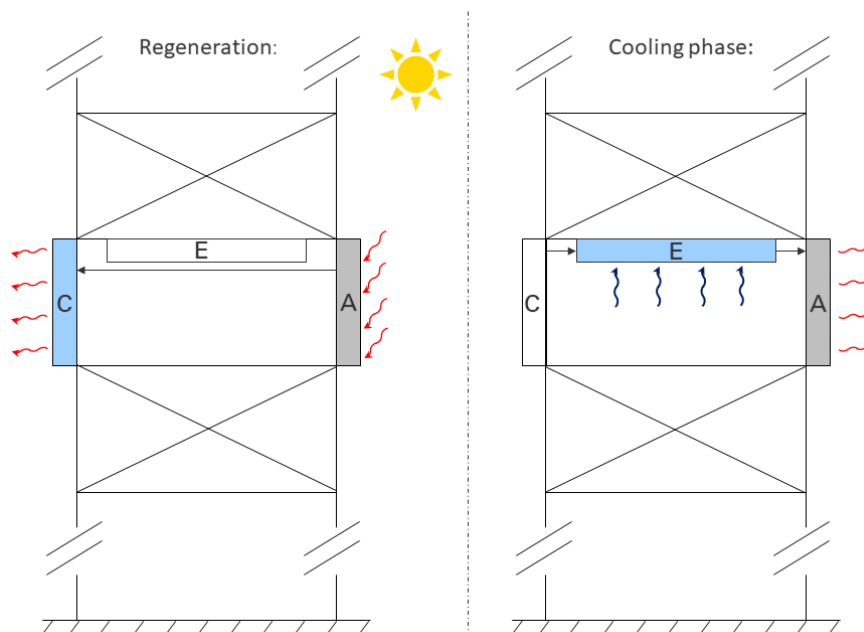
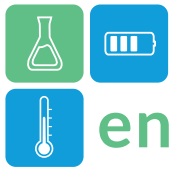


Figure 1: Design scheme and operating principle of the façade-integrated adsorption chiller

The adsorption system consists of the three components adsorber, condenser and evaporator, refer to Figure 1. The adsorber and the condenser are integrated as panel-shaped elements into the building façade. The particular challenge lies in the efficient absorption of solar irradiation by the adsorber during the regeneration phase and the sufficiently high heat release to the ambient during cooling operation. The evaporator is installed as a cooling ceiling in the building. For cooling, the evaporator is connected to the adsorber, whereby the cooling power can be controlled by throttling the vapor mass flow.

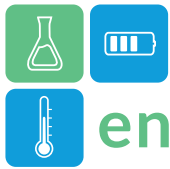
After the detailed simulation of a reference case confirmed the general functionality of the proposed cooling system, a first prototype is built in a tempered laboratory environment. The facade area of this prototype is one m² for each component. In order to precisely measure the cooling power of the system, the evaporator



is installed at the ceiling of a test chamber with a floor area of 6m^2 and a height of 2.8m, which is highly insulated with both, mineral wool and vacuum insulation panels. Further, it is equipped with several thermocouples to measure the temperature distribution and can be heated in a controlled manner. The adsorber is placed at the outside of the test chamber and is regenerated using a 1m^2 field of heating wires, which allows to set the regeneration power between 0 and 2000W. The condenser is also placed outside of the test chamber and is cooled by free convection inside the laboratory.

The experimental studies are carried out under realistic boundary condition. The regeneration phase takes place for 6 hours as it would be the case for an adsorber installed at a façade with a direction of South-East. In the subsequent cooling phase, a cooling power of around 50W per square meter can be kept constant for 14 hours. This power level is limited by the heat transfer between the evaporator and the room to be cooled as well as by the lower set point limit for the water temperature inside the evaporator of 15°C . If this limit is set to lower values, a cooling power of above 100W per square meter is found.

This work introduces the working principle as well as the prototype set-up and presents measurement results, which provide the practical proof of concept of the proposed cooling system.



Experimental study of heat transfer enhancement in a latent heat thermal energy storage using metal wool

Alessandro Ribezzo¹, Matteo Morciano¹, Gabriel Zsembinszki², Sara Risco Amigó², Saranprabhu Mani Kala², Emiliano Borri², Luca Bergamasco¹, Matteo Fasano¹, Eliodoro Chiavazzo¹, Cristina Prieto³, Luisa F. Cabeza^{2,*}

¹ Department of Energy, Politecnico di Torino, Corso Duca degli Abruzzi 24, 10129 Torino, Italy

² GREiA Research Group, University of Lleida, Pere de Cabrera s/n, 25001-Lleida, Spain

³ University of Seville, Department of Energy Engineering, Camino de los Descubrimientos s/n, 41092, Seville, Spain

*Corresponding author e-mail: luisaf.cabeza@udl.cat

Abstract

Effective utilization of renewable energy sources demands a thermal energy storage system with improved thermal performance and efficiency. Low charging and discharging rates are major challenges involved with the heat exchanger. Modifying the heat exchanger design by including fillers, metal foams, and heat pipes was found to impact the thermal performance favourably. This experimental study employs copper metal wool as fillers for the heat exchanger to enhance thermal performance. Three different configurations of a heat exchanger unit have been developed with n-octadecane as the phase change material. The performance of the heat exchanger unit was assessed with a lab-scale experimental setup. Significant reduction in charging and discharging time was observed with the incorporation of copper metal wool. Overall, the implementation of the heat exchanger comprising metal wool improved the performance of the thermal energy storage system.

Keywords: Metal wool, Heat exchanger, Thermal energy storage system, Phase change material

Introduction

Thermal energy storage (TES) technologies classify heat storage into sensible, latent, or thermochemical categories according to process leveraged (Amir et al., 2023). In detail, latent heat thermal energy storage utilizes phase change materials (PCMs) to efficiently stockpile waste heat and/or renewable energy sources. The heat exchanger design, energy storage medium, and heat transfer fluid are the three crucial components of the TES system (Kuravi et al., 2013). However, selecting heat transfer fluid and energy storage material relies on the desired application's working temperature range (H. Zhang et al., 2016).

Low charging and discharging rates are the primary problems strongly associated with the TES system, regardless of the category (Yang et al., 2023). Improving the thermal transport properties of the TES system is a continuous research interest for many researchers since its end-use applications are not limited to a particular segment. However, researchers have proposed several methods to increase the heat transfer properties of the TES system, but the thirst to improve the system's efficiency has not decreased. A

versatile technique consists in using fins to increase the thermal transfer. However, the incorporation of fins, metal foams, nanoparticles, heat pipes, metal wool etc., into the heat exchanger is still under research (Gasia et al., 2019; Khedher et al., 2022; Saini et al., 2023; J. Zhang et al., 2023). Mahdi et al. numerically investigated the performance of the PCM upon integration with fin-assisted foam strips. The author developed four different cases of heat exchanger units obtained with combinations of foams and fins and observed a 9% to 58% reduction in melting time (Mahdi et al., 2022). Belazreg et al. observed a maximum 48% reduction in melting time upon the inclusion of Y-shaped fins to the heat exchanger unit (Belazreg et al., 2022).

This work focuses on using metal wool as fillers for the heat exchanger of a latent heat TES unit. Three different heat exchanger configurations have been developed with n-octadecane as the PCM. Charging and discharging characteristics of the heat exchanger unit have been acquired using a lab-scale experimental setup.

Materials and method

Materials

N-octadecane ($\text{CH}_3(\text{CH}_2)_{16}\text{CH}_3$), purchased from Alfa Aesar, Germany, was loaded in the heat exchanger setup as the PCM. It has a melting point of $27.7\text{ }^\circ\text{C}$ with a latent heat capacity of 243.5 J/g (Adine & El Qarnia, 2009).

Copper metal wool purchased from STAX, Germany, was used as fillers. The metal wool consists of aligned fibres, each of them having a thickness of $60\text{ }\mu\text{m}$, a thermal conductivity of $383\text{ W/(m}\cdot\text{K)}$, and a density of 8.9 g/cm^3 .

Experimental setup

The research facilities available at the GREiA research group of the University of Lleida, Spain, have been used to acquire data related to the performance of the heat exchanger. The setup comprised a condenser unit (Zanotti model GCU2030ED01B), a buffer tank built with two 3-kW electric heaters, circulating water pumps, a flow meter, thermocouples (PT100) within the heat exchanger and in the inlet and outlet section of the heat transfer fluid and the heat exchanger. The selection of the heat transfer fluid is typically based on the working temperature window of the application. This study chose n-octadecane with a melting point of $27.7\text{ }^\circ\text{C}$ as PCM. Its operating temperature window typically ranges between 15 to $45\text{ }^\circ\text{C}$. Accordingly, water was chosen as the heat transfer fluid.

The water target temperatures were obtained by means of the built-in heaters and the condenser unit. Hence, this allows the preparation of the heat transfer fluid for the heat exchanger unit during the charging and discharging cycles. The heat transfer fluid flow rate was maintained constant ($\sim 3\text{ L/min}$) for both the charging and discharging cycles. The inlet and outlet temperature of the heat transfer fluid associated with the heat exchanger and the temperature of the PCM were measured with thermocouples. The data acquisition system connected to the computer integrates all the thermocouples and stores the experimental measurements with time step of 10 seconds.

Heat exchanger design

A shell-and-tube heat exchanger was used in the experimentation. The shell consisted of 1050 aluminium alloy and had dimensions of $250\times 85\times 210\text{ mm}$ (length \times depth \times width), whereas 10 parallel 16 mm diameter copper tubes were housed inside the shell. More details regarding the heat exchanger can be found in (Gasia et al., 2019). The charging and discharging characteristics have been acquired for three different

heat exchanger configurations. The first configuration is a simple shell-and-tube heat exchanger loaded with n-octadecane as the PCM. The other two configurations include the use of copper metal wool as filler to increase heat transfer. One configuration distinguishes from the other in the way how the metal wool convolutes around the heat exchanger tubes. However, the orientation of metal wool was laid perpendicular to the heat exchanger tubes to increase the heat transfer in the radial direction. Figure 1 shows the three different configurations of the heat exchanger. The mass of PCM loaded in the heat exchanger ($\sim 2.1\text{ kg}$) was maintained the same for all configurations. Configuration 3 has a high packing factor as compared to configuration 2 since the mass of metal wool integrated in configuration 3 (0.43 kg) is higher than that of configuration 2 (0.24 kg).

During the charging cycle, the tank was heated to $46\text{ }^\circ\text{C}$ with the built-in electrical heaters and once the tank reached the target temperature, the hot water was pumped at 3 L/min through the tube side of the heat exchanger. The PCM temperature at the beginning of each charging cycle was around $15\text{ }^\circ\text{C}$.

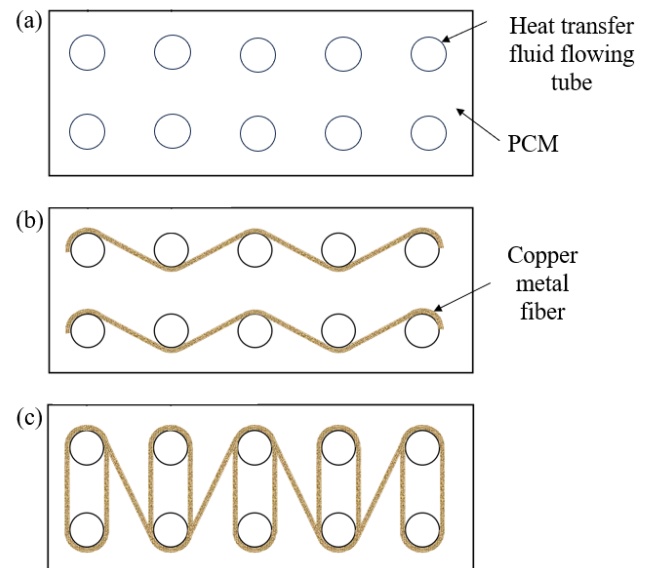


Figure 1. Schematic representation of the heat exchanger unit: (a) Configuration 1 - heat exchanger with only PCM, (b) Configuration 2 - heat exchanger with metal wool and PCM in design 1, (c) Configuration 3 - heat exchanger with metal wool and PCM in design 2.

During the discharge cycle, the buffer tank was brought below $15\text{ }^\circ\text{C}$ with the condenser unit to facilitate discharging. Once the tank reached the target temperature, the cold water was pumped at 3 L/min through the tube side of the heat exchanger. The PCM temperature at the beginning of each discharging cycle was around $45\text{ }^\circ\text{C}$.



Measurements exploring the temperature window of 15 to 45 °C and 45 °C to 15 °C were considered for the analysis of the heat exchanger performance during the charging and discharging cycles. The charging and discharging cycles were repeated three times storing the temperature measurements for every process.

Results and discussion

Figure 2 and Figure 3 show the temperature measured within the heat exchanger vs time for all three heat exchanger configurations during the charging and discharging cycles. The thermocouple was placed at a central part of the heat exchanger with a view to measure the average temperature of the PCM. The selected temperature range (15 °C to 45 °C) covers the typical phase change process (solid to liquid during charging and liquid to solid during discharging) of n-octadecane.

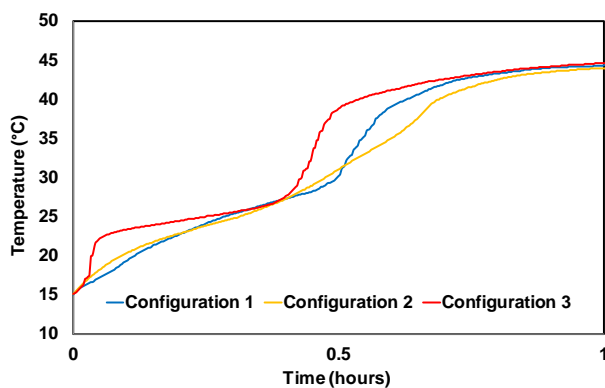


Figure 2. Temperature vs time during the charging cycle.

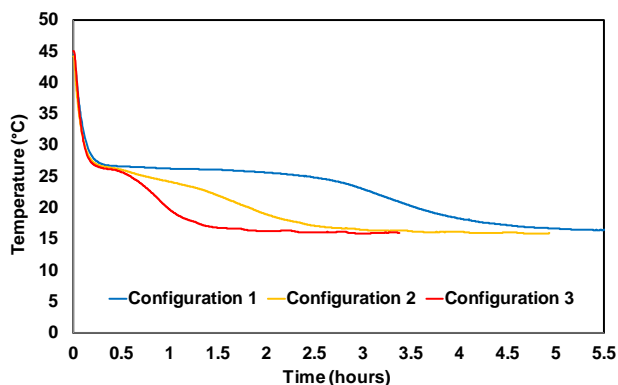


Figure 3. Temperature vs time during the discharging cycle.

During the charging cycle, the heat exchanger that contained only n-octadecane (configuration 1) showed a lower charging rate during the initial and final phase of melting. Amid configurations 2 and 3, the heat exchanger with the design of configuration 3 showed a higher charging rate and required a lower time for

phase transition. Furthermore, the latent and sensible heat components are distinct from the configuration 3 charging curve.

During the discharging cycle, the heat exchanger that contained only n-octadecane (configuration 1) required longer discharge time than the other configurations. The temperature variation with time was similar for all heat exchanger configurations during the initial phase of the discharging cycle. However, after the onset of the solidification process, the temperature change with time was much faster for the heat exchanger with configuration 3.

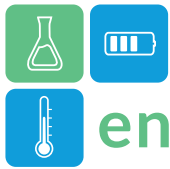
The inclusion of high thermally conductive metal wool in the heat exchanger unit reduced the charging and discharging time. The heat exchanger with configuration 3 significantly reduced charging time (16%) and discharging time (397%) with respect to configuration 1 (only PCM). The reduction could stem from the metal wool in configuration 3 covering the outer wall of the heat exchanger the most compared to another configuration.

Conclusions

Three different configurations of heat exchanger units have been developed and tested using copper metal wool as a filler. The heat exchanger was loaded with n-octadecane as the phase change material for all three configurations. The charging and discharging characteristics of the heat exchanger unit have been acquired using a lab-scale experimental setup. The performance of the heat exchanger was analysed within the temperature window of 15 °C to 45 °C. The heat exchanger with the highest amount of metal wool (configuration 3) showed reduced charging and discharging time compared to other configurations. The increase in heat transfer surface area with the addition of copper metal wool was one of the key factors in reducing charging and discharging time. The other prominent factors are the strength and thermal conductivity of the metal wool.

Acknowledgments

This project was funded by the European Union's Horizon Europe Research and Innovation Programme under grant agreement 101084182 (HYBRIDplus). Views and opinions expressed are however those of the author(s) only and do not necessarily reflect those of the European Union or CINEA. Neither the European Union nor the granting authority can be held responsible for them.

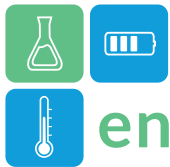


This work is partially supported by ICREA under the ICREA Academia programme. The authors would like to thank the Departament de Recerca i Universitats of the Catalan Government for the quality accreditation given to their research group (2021 SGR 01615).

GREiA is certified agent TECNIO in the category of technology developers from the Government of Catalonia.

References

- Adine, H. A., & El Qarnia, H. (2009). Numerical analysis of the thermal behaviour of a shell-and-tube heat storage unit using phase change materials. *Applied Mathematical Modelling*, 33(4), 2132–2144. <https://doi.org/10.1016/j.apm.2008.05.016>
- Amir, M., Deshmukh, R. G., Khalid, H. M., Said, Z., Raza, A., Muyeen, S. M., Nizami, A.-S., Elavarasan, R. M., Saidur, R., & Sopian, K. (2023). Energy storage technologies: An integrated survey of developments, global economical/environmental effects, optimal scheduling model, and sustainable adaption policies. *Journal of Energy Storage*, 72, 108694. <https://doi.org/10.1016/j.est.2023.108694>
- Belazreg, A., Abderrahmane, A., Qasem, N. A. A., Sene, N., Mohammed, S., Younis, O., Guedri, K., Nasajpour-Esfahani, N., & Toghraie, D. (2022). Effect of Y-shaped fins on the performance of shell-and-tube thermal energy storage unit. *Case Studies in Thermal Engineering*, 40, 102485. <https://doi.org/10.1016/j.csite.2022.102485>
- Gasia, J., Maldonado, J. M., Galati, F., De Simone, M., & Cabeza, L. F. (2019). Experimental evaluation of the use of fins and metal wool as heat transfer enhancement techniques in a latent heat thermal energy storage system. *Energy Conversion and Management*, 184(February), 530–538. <https://doi.org/10.1016/j.enconman.2019.01.085>
- Khedher, N. Ben, Mahdi, J. M., Majdi, H. S., Al-Azzawi, W. K., Dhahbi, S., & Talebizadehsardari, P. (2022). A hybrid solidification enhancement in a latent-heat storage system with nanoparticles, porous foam, and fin-aided foam strips. *Journal of Energy Storage*, 56, 106070. <https://doi.org/10.1016/j.est.2022.106070>
- Kuravi, S., Trahan, J., Goswami, D. Y., Rahman, M. M., & Stefanakos, E. K. (2013). Thermal energy storage technologies and systems for concentrating solar power plants. *Progress in Energy and Combustion Science*, 39(4), 285–319. <https://doi.org/10.1016/j.pecs.2013.02.001>
- Mahdi, J. M., Najim, F. T., Aljubury, I. M. A., Mohammed, H. I., Khedher, N. Ben, Alshammari, N. K., Cairns, A., & Talebizadehsardari, P. (2022). Intensifying the thermal response of PCM via fin-assisted foam strips in the shell-and-tube heat storage system. *Journal of Energy Storage*, 45, 103733. <https://doi.org/10.1016/j.est.2021.103733>
- Saini, P., Dhar, A., Powar, S., & Doddamani, M. (2023). Cesaro fins parametric optimization for enhancement in the solidification performance of a latent heat storage system with combined fins, foam, and nanoparticle. *Energy Reports*, 9, 5670–5687. <https://doi.org/10.1016/j.egy.2023.04.375>
- Yang, M., Moghimi, M. A., Loillier, R., Markides, C. N., & Kadivar, M. (2023). Design of a latent heat thermal energy storage system under simultaneous charging and discharging for solar domestic hot water applications. *Applied Energy*, 336, 120848. <https://doi.org/10.1016/j.apenergy.2023.120848>
- Zhang, H., Baeyens, J., Cáceres, G., Degrève, J., & Lv, Y. (2016). Thermal energy storage: Recent developments and practical aspects. *Progress in Energy and Combustion Science*, 53, 1–40. <https://doi.org/10.1016/j.pecs.2015.10.003>
- Zhang, J., Cao, Z., Huang, S., Huang, X., Han, Y., Wen, C., Honoré Walther, J., & Yang, Y. (2023). Solidification performance improvement of phase change materials for latent heat thermal energy storage using novel branch-structured fins and nanoparticles. *Applied Energy*, 342, 121158. <https://doi.org/10.1016/j.apenergy.2023.121158>



From Heat Storage to Heat Sink: The Role of Phase Change Materials in Battery Thermal Management

Apoorva Balwani^{1, *}, Tridib Ambardar¹

1Centre for Research in Energy Science & Technology (CREST), Pluss Advanced Technologies, IMT Bawal, India

*Corresponding author e-mail: apoorva.balwani@pluss.co.in

With the widespread adoption of EVs, focus has shifted towards improving thermal management in lithium ion (LiB) battery packs. Phase change material (PCM) assisted passive cooling of LiBs offers promise in developing volumetrically and economically lean battery packs for light EVs such as 2-wheeler and 3-wheeler e-bikes. However, integrating PCMs in high-rate cooling applications may require a lateral shift from their traditional role of energy reservoirs. In this report, we investigate the interconnected role of energy density and thermal conductivity of phase change materials in mitigating thermal runaway propagation in commercial battery packs comprising of cylindrical LiBs (form factor: 18650 & 21700) through hybrid (machine learning + physics) simulations. Our results show the lack of a linear dependence on either property in preventing thermal runaway, while benchmarking them against conventional pack filler materials, viz. thermally conducting potting materials and insulating materials. Although a facile interpretation of these results would be to assume superiority of simpler filler materials, we argue that when thermal runaway propagation and regular thermal management are considered in tandem, PCMs arise as superior passive cooling solutions. In this manner, our study provides a framework to execute future investigations in correlating the thermal diffusivity of the PCMs with the high-speed cooling demands in electronics and laser applications.

Keywords: Electric vehicles, Phase change materials, Heat sink, Simulations, Thermal energy storage

Introduction

The need for careful thermal management of lithium-ion batteries, especially for battery chemistries with nickel-magnesium-cobalt (NMC) cathode is one of great concern and particularly well-understood. These battery chemistries are quite prone to degradation in performance, life, and safety with increasing temperatures, where thermal excesses over critical temperatures can often result in vigorous and potentially harmful thermal runaway reactions. Packed in close density, such as in an electric vehicle application, thermal runaway events in ‘rogue’ cells run the risk of driving enough heat into neighbouring cells to cause thermal runaway to occur in those cells, causing an explosive, cascading event that puts the passengers’ lives in jeopardy. As such, an immediate challenge for battery engineers is designing battery packs which maximize energy density while ensuring robust thermal management across all cells, as well as risk mitigation in the event of explosion/damage in one or several members of the battery pack resulting in propagation of thermal runaway reactions.

While conventional methods of temperature control, viz. liquid cooling and air cooling are relevant here, these active cooling measures apply a cost penalty on

the volumetric, economic and performance efficiency of the vehicle. As such, their utility is limited to larger commercial vehicles such as cars and trucks. When it comes to two-wheelers, three-wheelers, and other smaller transport applications (such as drones), passive cooling of battery packs is the viable approach. Generally, this method utilizes either ‘filler’ materials that occupy the negative space between cells in the battery pack or naturally driven air convection through this space. A large body of literature elucidates the specific impact of each of these different types of passive coolants. While air cooling is found to be economical, the lack of thermal homogeneity across the cells during operation is a disadvantage of this approach. On the other hand, fillers that have been investigated have ranged from insulating materials to thermally conductive materials to phase change materials. Notably, Li et. al (2019) used aluminium plates in battery modules as heat sinks and found thermal mass and contact resistance to be crucial design parameters. Separately, Pegel and coworkers (2023) incorporated potting material with low thermal conductivity between large format, tables cylindrical cells and found that they mitigated thermal runaway to neighbouring cells by preventing convective heat



transfer from vented gases. In use of PCMs, use of paraffin PCMs is most extensively covered (Mei et al, 2023), where paraffin is found to delay the onset of thermal runaway and the delay scales with the amount of PCM loading.

Thus, while interstitial filler materials have been holistically investigated, the strategy underlying their usage has been either in terms of a) preventing heat from rogue cell from spreading to neighbouring cells, or b) quickly drawing excess heat from rogue cells and homogenizing temperatures across the battery pack. PCMs have mostly belonged to the latter group of materials in these reports, however, rather than concentrating heat near the damaging cells, these materials absorb the heat, largely normalizing the local temperatures. With some intuition and insight, it is clear that while insulating and localizing the heat generation is the more effective strategy in preventing cascaded thermal runaway reactions, these materials can impose similar effects on the battery pack during regular operation and raise local temperatures in the vicinity of cells, in effect worsening the performance and accelerating their deterioration. On the other hand, highly conductive fillers, and high thermal conductivity heat exchangers may have an upper limit to how much heat can be thrown out during a thermal runaway event.

High thermal conductivity PCM composites, such as those presented by Hallaj and other members of the AllCell research team propose an alternative approach to incorporating PCMs in battery packs and marry the heat resisting and the heat conducting approach in a singular material. Building on their reports, the authors of this work attempt to fill knowledge gaps regarding the precise nature of these thermal composites by elucidating the role of thermal buffering versus thermal exchange in the context of mitigation of thermal runaway propagation. A series of battery packs are simulated in a hybrid physics thermal simulation model, where pack size, thermal conductivity, thermal capacity and intercell distance are varied while a preselected cell in the pack is forced to go into thermal runaway via heating method. By quantifying the impact of the thermal runaway event on the overall pack temperatures, number of neighbouring cells that went into thermal runaway, and venting profiles, we investigate how the PCM thermal properties are required to scale with pack design variables for efficacious performance. Specifically, we attempt to address the following questions;

1. What is the minimum pack specific thermal energy density that prevents thermal runaway propagation?

2. What is the minimum thermal conductivity of filler material to prevent thermal runaway propagation?
3. Is the minimum thermal conductivity requirement from above independent of pack size and cell to cell distance?
4. Which is better for preventing thermal runaway propagation: PCM with high heat capacity and low thermal conductivity or PCM with high thermal conductivity and low heat capacity?

Methodology

Oorja, a hybrid thermal simulation software for modelling thermal physics in battery packs was employed for the purpose of this study. Three cylindrical NMC cells, viz. Samsung 50E 21700 (5 Ah capacity), Samsung 40T 21700 (4 Ah capacity), and LG 18650 (2.2 Ah capacity) were chosen and their drive cycles as well as thermal runaway data as obtained from accelerated rate calorimetry (HWS protocol: heat 2.5 m, wait 30 m, seek 10 m, temperature step 5 K) were fed into the software for model training. Oorja employs simplified lumped model of heat generation, wherein the model parameters are trained using the fed data to replicate thermal runaway events during simulation phase with minimal computation load. After the training completed, battery packs of various sizes, cell types, filler types and cell to cell distances were designed. Pack sizes were varied from 9 cells to 121 cells, cell to cell distance was varied from 0.05 mm to 2.8 mm, and filler types were varied from air to insulating PUF to thermally conductive potting material ($k = 3 \text{ W/m.K}$) to various grades of a PCM savE OM50 from Pluss Advanced Technologies Ltd., where the thermal conductivity of the PCM varied between 0.14 W/m.K to 20 W/m.K , while the latent heat capacity varied between 10 kJ/kg to 195 kJ/kg . Finally, thermal runaway tests were simulated in all battery packs by heating the central cell with a constant heating power of 50 W until runaway event, and the simulations were studied for a period of 20,000 seconds ($\sim 5.5 \text{ h}$).

Results

Figure 1 shows the temperature evolution of all the cells in a 36 cell pack in presence of no filler material or external cooling mechanism. Figure 2 shows temperature evolution in cells for the same design, except in presence of savE OM50, with an average latent enthalpy of 195 kJ/kg and thermal conductivity of 0.21 W/m.K . The onset of thermal runaway in the selected cell is delayed by three times in presence of the PCM, while the impact of thermal incursion of the vented heat on neighbouring cells is also significantly minimized. Similarly, other results enlisted in this



study will effectively show that the same PCM, when reduced in thermal capacity by half and with approximately forty-fold higher thermal conductivity does not allow any cell, including target cell to go into thermal runaway over a span of 10,000 seconds of non-stop heating. A corollary to this result the one where no PCM was utilized but a potting material of equivalent thermal conductivity was incorporated. Herein, while the cells do not undergo thermal runaway, the overall temperature increment is much higher than that for the high thermal conductivity PCM composite, suggesting that a filler with a given thermal conductivity acts essentially like a large heat exchanger, where PCM incorporation improves the effective heat removal rate of the heat exchanger.

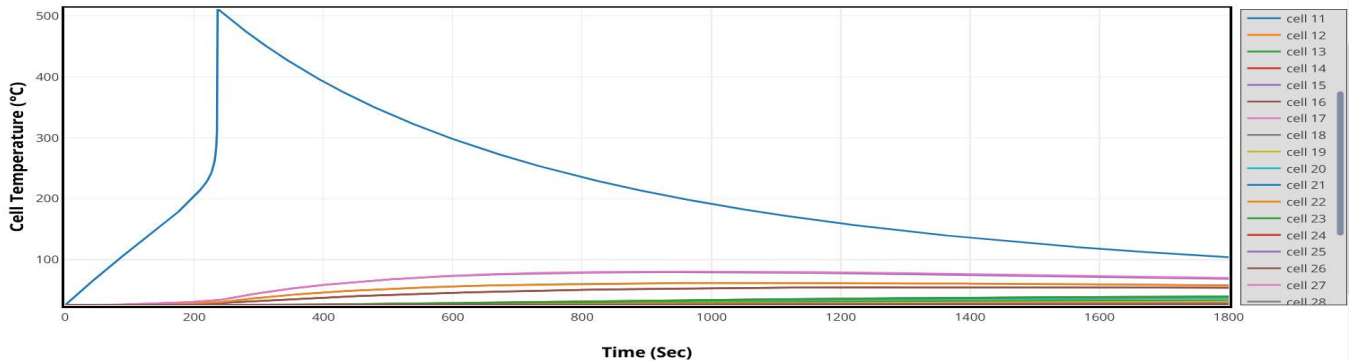
Conclusions

This paper presents evidence to suggest that the proper approach to designing passively cooled battery packs requires a rigorous effort towards maximizing its thermal conductivity. However, the laws of nature put restrictions on the upper limit of thermal conductivity for any given material. In this light, incorporation of PCM offers a bypass to the material design constraint,

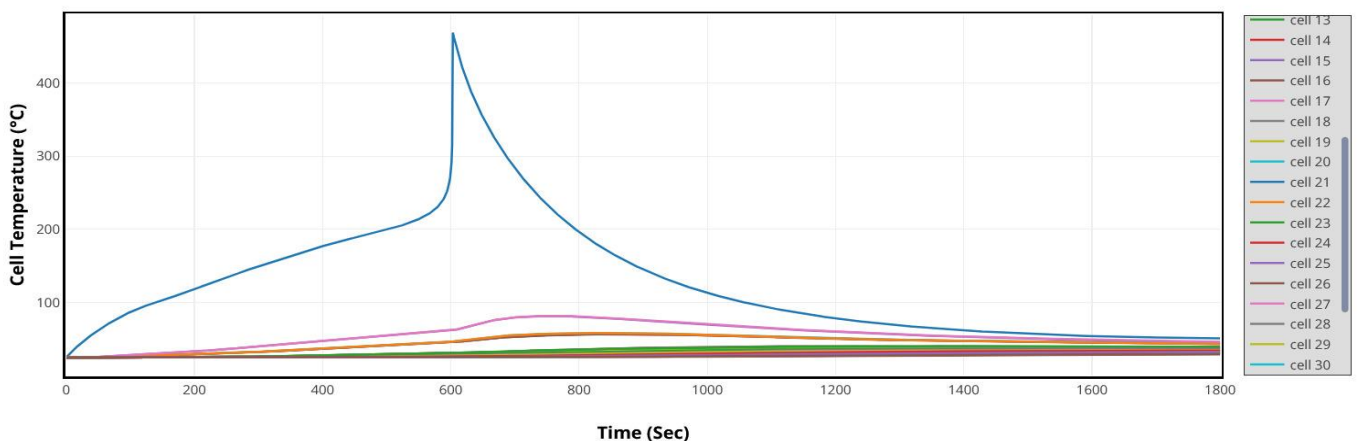
effectively allowing the filler-heat exchanger to behave, albeit transiently, like it is oversized, allowing the filler material to arrest all thermal runaway energy and minimize thermal incursions throughout the battery pack.

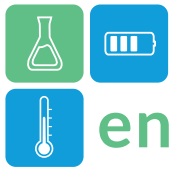
References

- Kim, J. and al. (2022) A comprehensive numerical and experimental study for the passive thermal management in battery modules and packs, Journal of the electrochemical society, doi.org/10.1149/1945-7111/ac9ee4.
- Mei, J. and al. (2023) Experimental study on the effect of passive retardation method for thermal runaway mitigation of lithium ion battery, Applied thermal engineering, doi.org/10.1016/j.applthermaleng.2023.120861.
- Pegel, H. and al. (2023). Extensive experimental thermal runaway and thermal propagation characterization of large formate tables cylindrical lithium ion cells with aluminum housing and laser welded endcaps, Journal of the electrochemical society, doi.org/10.1149/1945-7111/ad0cd3.



(Top) Figure 1 Thermal evolution of different cells during runaway event in battery pack with air, (Bottom) Thermal evolution of different cells during runaway event in a PCM battery pack; selected data shown for clarity.





Genetic Algorithm Based Optimization of a Closed Sorption Heat Storage System Using COMSOL Multiphysics® and MATLAB

Elham Abohamzeh¹, Georg Frey¹

¹ Chair of Automation and Energy Systems, Saarland University, Saarbrücken, Germany

Abstract

Sorption storage systems have gained significant attention for heat storage of solar energy in recent years. The benefit of this technology is long-term energy storage with negligible heat loss and high energy density compared to other thermal energy storage techniques. This study discusses how a CFD solver, COMSOL Multiphysics, and a Genetic Algorithm (GA) optimization tool written in MATLAB are combined to optimize the design of a sorption heat storage system. GA aids a design that maximizes the efficiency, useful energy, and outlet temperature, while the volume of the used sorption materials remains as low as possible. The model developed in the CFD solver simulates the adsorption reaction between zeolite and water and the heat and mass transfer phenomena in the designed prototype. GA with MATLAB iterates over different values of the variables and checks the optimality of the design. If a global optimal is not reached, MATLAB changes the design based on GA rules. Then, the new set is fed back to COMSOL to evaluate the performance of the reactor through updated geometry, boundary conditions, mesh generation and numerical simulations. GA uses the results to find the best combination of variables that minimizes the objective function value, which means it is looking for the design that gives the best performance according to the defined metrics. This analysis helped us achieve 21% higher energy output, 15% higher efficiency and 2 K higher average temperature for the heat transfer fluid outlet while maintaining a constant system volume.

Keywords: Genetic algorithm optimization, Sorption Heat Storage, Computational Fluid Dynamics, Zeolite.

Introduction

One of the critical challenges humanity faces involves addressing the growing need for energy while ensuring that future generations have access to adequate sustainable energy resources. This objective can be realized by relying more on renewable energy sources and optimizing their use. A substantial portion of energy usage is categorized as low-temperature thermal energy. Therefore, improved management of this energy through thermal energy storage systems could play a significant role in enhancing the overall efficiency of industrial economies and energy usage in buildings. Between thermal energy storage technologies, sorption heat storage has been found to have great potential for short-term (daily) and long-term (seasonal) storage applications and has been proposed as a promising approach to minimize the temporal mismatch between solar energy supply and space heating demand. However, it is still at an early stage of research and development compared to other heat storage technologies. Optimizing these systems with the aim of maximizing efficiency and energy output within the smallest feasible volume is beneficial. This is particularly crucial for integration in buildings where installation space is limited, and the system's volume presents a significant challenge. The goal of this work is to explore the possibility of combining genetic algorithm-based optimization with

computational fluid dynamics (CFD) to optimize the geometry of a designed sorption heat storage system.

Mathematical Procedures

In the present study, MATLAB is selected as a connection tool between performance prediction and GA. COMSOL is chosen as calculation software for heat storage performance since it can be easily interfaced with MATLAB language. The developed automated program aims to find the optimum design of the system.

Model development in COMSOL

A three dimensional CFD model has been developed to simulate the adsorption process of zeolite/water pair and heat and mass transfer in the reactor during the process. In a sorption heat storage, the process of adsorption begins with the evaporation of water vapor in the evaporator, placed at the bottom of the reactor. The water vapor flows into the reactor and is adsorbed in the pores of the dry zeolite. The released energy from this reaction is extracted by the heat transfer fluid (HTF) flowing in the heat exchanger. The geometry of the prototype, the computational meshes used for simulations and the computational domain including the bed filled with zeolite 13X, and the heat exchanger containing HTF are presented in **Error! Reference source not found.** The system consists of a reactor with 540 mm length and 400 mm diameter, a heat

exchanger, and a fixed bed with zeolite particles, where the reaction between the zeolite and water takes place. The heat exchanger has a 14-layer two-row helical-shaped tube. The inner and outer coil diameters are 220 and 320 mm, respectively. The tube itself has a diameter of 16 mm and a thickness of 1 mm. An opening with an 84,3 mm diameter is considered from the evaporator to the reactor. This design would be considered as a reference case for the optimization problem, discussed in the next sections.

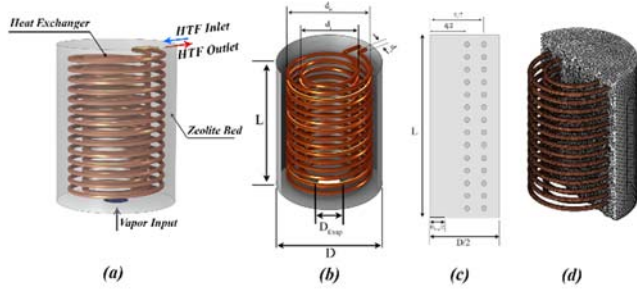


Figure 1: (a) Computational domain (b) 3D Geometry (c) 2D axisymmetric Geometry (d) Computational grid

Governing Equations

The Linear Driving Force (LDF) model is used for calculating the adsorbed amount X (Glueckauf, 1955):

$$\frac{\partial X}{\partial t} = k_{LDF} [X^* - X] \quad (1)$$

where X^* is the equilibrium adsorption capacity and X is the amount of adsorbed water. K_{LDF} is defined as:

$$K_{LDF} = \frac{15}{r_p^2} D_{ref} \exp\left(-\frac{E_a}{RT}\right) \quad (2)$$

where r_p is the radius of the zeolite particles, D_{ref} is the reference diffusivity, and E_a is the characteristic energy. Dubinin's theory is used for calculating the equilibrium water uptake (Do, 1998) :

$$X^* = X_0 \exp\left(-B \left(\frac{T}{T_{sat}} - 1\right)^n\right) \quad (3)$$

Where X_0 is the maximum adsorption capacity and B and n are fit coefficients for the zeolite/water pair.

The mass balance equation for the transport of the adsorbed gas can be formulated as (Çağlar, Yamalı, & Baker, 2013):

$$\begin{aligned} \varepsilon_{eff} \frac{\partial T_s}{\partial t} - D_{eff} \nabla^2 c + \nabla(c \cdot u) \\ = - \frac{(1 - \varepsilon_{eff}) \rho_s}{M_w} \frac{\partial X}{\partial t} \end{aligned} \quad (4)$$

where c is the water vapor concentration, D_{eff} is the effective diffusion coefficient, ρ_s is the density of the adsorbent, M_w is the molar mass of water vapor.

Three different regions are considered: the adsorbent bed, the HTF, and the HTF tube. The energy equations for the adsorbent bed can be written as [4]:

$$\begin{aligned} (\varepsilon_{eff} \rho_f C_f + (1 - \varepsilon_{eff}) \rho_s C_s \\ + (1 - \varepsilon_{eff}) \rho_s C_l X) \frac{\partial T_s}{\partial t} \\ + \rho_f C_{p,f} u \cdot \nabla T_s - k_{eff} \nabla^2 + \frac{h_i A_i}{V_s} (T_s - T_t) \quad (5) \\ + Q_{ambient} \\ = (1 - \varepsilon_{eff}) \rho_s \frac{\partial X}{\partial t} |\Delta H| \end{aligned}$$

where ΔH is the reaction enthalpy. Further details about the governing equations, the 3D simulation and validation of the developed model have been presented in (E. Abohamzeh, 2023).

2D axisymmetric model

A simplified 2D axisymmetric model is further proposed based on three-dimensional simulations with much lower computational time and cost. The 2D axisymmetric geometry is presented in Figure 1. (c). The results from 3D and 2D axisymmetric simulations in terms of loading and adsorption bed temperature are presented in Figure 2.

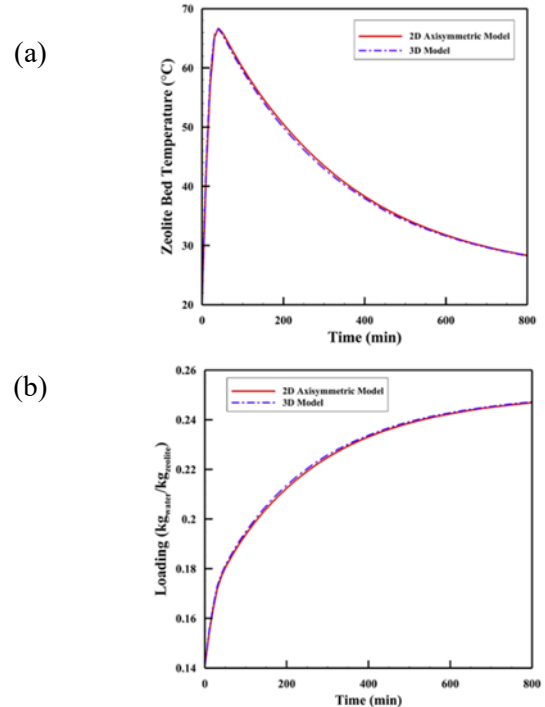


Figure 2: Comparison of the results from 3D model and 2D axisymmetric model in terms of (a) bed temperature and (b) loading

The results presented in Figure 3 show the very high accuracy of the simplified 2D model. This model is used for conducting the GA optimization, enabling the simulations with minimal computational resources.

Optimization Scheme

In this work, GA, which uses a mathematical model of a biological evolution theory to obtain an optimal solution, is selected for the optimization process. To get an optimized result for the system performance, GA and CFD solver were linked with a MATLAB code.

Design variables

The deciding factors for the performance of the system are released energy, efficiency, and outlet reachable temperature. For this purpose, parameters that need to be optimized are identified and parameterized within the COMSOL environment. The design variables for this study are for the reactor: length (L), diameter (D), and opening from the evaporator into the reactor (D_{Evap}); for the heat exchanger: tube diameter (d_t), inner coil diameter (d_i) outer coil diameter (d_o), and the number of tubes (NT) in each row. Table. 1 presented the detailed information of these variables.

Table 1: Design variables and their optimization bounds.

Variables	d	D	L	D_{Evap}	D_i	D_o	NT
	(mm)	(mm)	(mm)	(mm)	(mm)	(mm)	
Lower Bound	8	400	220	20	16	72	10
Upper Bound	32	600	1320	300	300	504	18

Objective function

The goal is to increase the useful released energy and efficiency during the adsorption process while keeping the volume to a minimum. Based on the optimization goal, the fitness function is defined as:

$$100 * \left(\left(\frac{E_c}{E_{ci}} \right) \left(\frac{\eta}{\eta_i} \right)^{n_\eta} \left(\frac{VR}{VR_i} \right)^{n_{VR}} \right)^{\frac{1}{n_\eta + n_{VR} + 1}} \quad (6)$$

Where E_c is the useful energy transferred to the HTF during adsorption and E_{ci} is the useful released energy in the initial (reference case) which is presented in CFD section, η is the efficiency of adsorption process and η_i is the efficiency of reference case. VR is the volume of the bed containing zeolite particles based on the selected design variables and VR_i is the volume of the reference case. A schematic of the optimization

process is presented in Figure 3. The process is started by defining the CFD model within COMSOL, where the physical parameters, boundary conditions, and governing equations are established to simulate the fluid dynamics scenarios. Concurrently, GA has been set up in MATLAB, designed to optimize these parameters. During the optimization process, MATLAB interacts with COMSOL via the LiveLink interface, where MATLAB serves as the master controller guiding the search for the optimal solution. Each potential solution generated by the GA in MATLAB is sent to COMSOL, which then runs the CFD simulation with the given set of parameters. The results of each simulation, such as efficiency and flow characteristics, are evaluated in MATLAB, which uses this performance data to evolve the population towards better solutions over successive generations. This iterative loop continues, with the GA in MATLAB refining the parameter set and COMSOL evaluating the performance of these parameters, until the optimization criteria are reached.

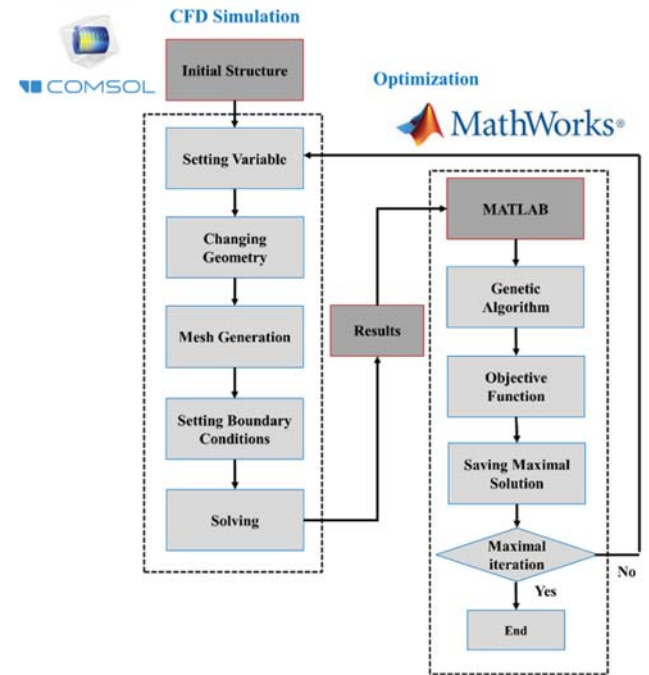


Figure 3: The flowchart of the optimization process.

Results and Discussion

The results of GA optimization are presented in this section. The optimization was conducted considering 7 design variables and carried out 2000 evaluations with a population size of 100 for each generation. According to the first results, the maximum number of HEX loops selected by GA is 18 which is upper bound defined for this variable, and the diameter of the reactor equal to

400 mm which is the defined lower bound. Therefore, these variables have been excluded and the optimization process is executed again. The optimal value resulting from GA is reported in Table 2.

Table 2: Optimal values for the variables

Variables	d	D	L	D _{Evap}	Di	Do	NT
	(mm)	(mm)	(mm)	(mm)	(mm)	(mm)	
Ranges	8-32	400	220-1320	16-300	40-280	72-504	18
Optimal values	20	400	605	274	200	340	18

The results show that in a constant volume, E_c increases by 21% and η increases by 15%, and the average temperature of the HTF outlet shows an increase of 2 K. The temperature contours for the initial design and the optimal cases are shown in Figure 4.

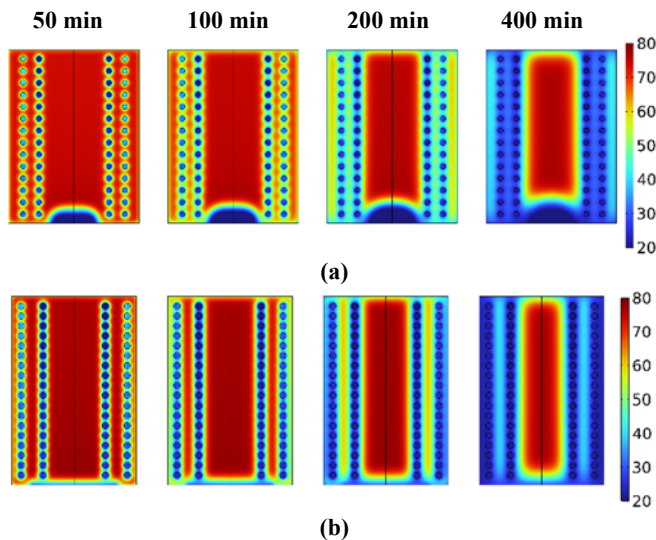


Figure 4: Temperature contours for average bed temperature in (a) design before optimization and (b) optimized case

As can be seen, the optimum opening from the evaporator into the reactor enables a uniform distribution of water vapor in the reactor, and also a uniform temperature distribution, and due to the more effective reaction between water and zeolite, a higher temperature can be achieved during the adsorption process. Also, due to the more optimal design of the heat exchanger, more effective cooling is possible by HTF, as a result, more energy is transferred to HTF and E_c increases, leading to decreasing the bed temperature and based on Dubinin-Astakhov equation, by decreasing the temperature of adsorbent, the adsorption

capacity augments. Therefore, more water can be adsorbed, and more adsorption energy can be released.

Conclusions

This study discusses the development of an automated method for obtaining maximum energy and efficiency in a sorption storage system by combining COMSOL and GA optimization tool written in MATLAB. Both 3D and 2D axisymmetric models are developed in CFD solver, and upon verifying the high accuracy of 2D model, it was employed for simulations, resulting in a substantial reduction in computational time. The automated method builds the geometry automatically, generates computational meshes, updates the boundary conditions, and provides the objective function values by solving partial differential equations with processes that are all linked to a GA program in the MATLAB environment. In the optimal design of the system, a 21% increase in useful energy and a 15% improvement in efficiency is achieved due to more uniform water vapor and heat distribution within the reactor, and better heat transport between the adsorption bed and HTF.

References

- Çağlar, A., Yamalı, C., & Baker, D. K. (2013). Two dimensional transient coupled analysis of a finned tube adsorbent bed for a thermal wave cycle, *International journal of thermal sciences*, 73, 58-68.
- Do, D. D. (1998). Adsorption analysis: Equilibria and kinetics (with cd containing computer MATLAB programs). *World Scientific*, 2.
- E. Abohamzeh, S. E. Hosseinzadeh, G. Frey (2023). 3-Dimensional Analysis of Coupled Heat and Mass Transfer in a Thermochemical Heat Storage System. Munich: *COMSOL Conference*.
- Glueckauf, E. (1955). Theory of chromatography. Part 10.—Formulæ for diffusion into spheres and their application to chromatography51. *Transactions of the Faraday Society*, 51, 1540-1551.
- Kant, A., Shukla, A., Rindt, C. C., & Smeulders, D. M. (2020). Analysis and optimization of the closed-adsorption heat storage bed performance. *Journal of Energy Storage*, 32, 101896.



GeoBOOST: Pioneering Efficient Geothermal Solutions through Barrier Mitigation in Europe

Henk Witte^{1,*}, Riccardo Pasquali², Borja Badenes³ (on behalf of the GEOBOOST Consortium Members)

¹Groenholland Geo-energysystems Ltd, Valscherkade 26B, 1059VD Amsterdam, the Netherlands

²GeoServ, Unit 26 The Village Mill Enterprise Park, Rathnew, Ireland

³ ICT vs Climate Change research group - Instituto de Aplicaciones de las Comunicaciones Avanzadas (ITACA), Universitat Politècnica de València, Camino de Vera S/N, 46022 Valencia, Spain

*Corresponding author e-mail: henk.witte@groenholland.nl

Keywords: Geothermal energy, Renewable heating and cooling, technical catalogue, SWOT analysis, policy framework.

1. Introduction

The EU LIFE21 project GEOBOOST: Boosting geothermal heat pumps to mainstream cost-effective and efficient renewable heating and cooling in buildings, comprises a consortium of research institutes, companies and organisations from Belgium, Spain, Germany, Ireland, Sweden, Austria, the Netherlands, and Poland. The main objective of the project is to unlock barriers to geothermal heat pumps that are often neglected by policy makers, despite being the most energy efficient and cost-effective RES Heating and Cooling solution available

The Fit for 55 package calls for a greater than 40% target for renewable energy sources by 2030, it also calls for increased primary (39%) and final (36%) energy savings to be achieved defined in the Energy Efficiency Directive (EED). Accelerating proven and cost-effective, energy efficient renewable heating and cooling technologies will be key to the successful achievement of these targets.

Having been pioneered in Europe in Sweden in the 1980's, shallow (or low-enthalpy) geothermal systems (SGE's) have, during the past 50 years, proven to be very energy efficient and cost effective solutions for heating and cooling of buildings.

Usually the shallow geothermal system is made up of a closed-loop (borehole heat exchanger or shallow horizontal ground heat exchanger) or open-loop (aquifer systems) coupled to a heat pump that uses the low-temperature shallow geothermal source to provide the temperatures required for heating, domestic hot water production or cooling (although cooling can often be provided directly) to end users.

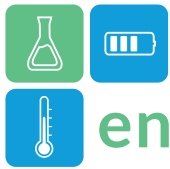
The uptake of SGE systems in countries such as the Netherlands, Germany, Switzerland, Poland and Austria has accelerated in the past decades, with a

similar development in many other countries. Despite the success of shallow geothermal systems, there are still many barriers to the wider uptake of heating and cooling by renewable energies (RES HC). These include: ineffective policy measures, institutional barriers, lack of financial support and incumbent power having designed markets around fossil fuel utilisation rather than capital-intensive RES HC.

The GEOBOOST project does not develop new technologies but will develop analysis and guidelines to identify market topologies, regulatory and policy frameworks, financial frameworks, training courses and technology and business solutions based on the current state-of-art of SGE systems (Open loop and closed loop systems) in Europe. Building on these key-stones policy makers, utilities and market developers will be able to assess the potential of and select the most appropriate SGE-HC solution.

Whilst GEOBOOST does not develop new technologies, it undertakes a detailed analysis supported by guidelines to identify market topologies, regulatory and policy frameworks, financial frameworks, training courses as well as technology and business solutions based on the current state-of-art of SGE systems in Europe. Building on these key-stones policy makers, utilities and market developers will be able to assess the potential of and select the most appropriate SGE-HC solution.

One of the first results of GEOBOOST is a Technical Catalogue. This highlights the diverse methods and technologies used to activate the ground source energy system that are dependent on building type and usage (energy requirements), local conditions and heat pump systems, and the difficulties associated with selecting an optimal solution or comparing and evaluating project proposals. A detailed technical



catalogue of technologies, including different types of storage technologies (ATES/BTES), drilling methods and other enabling components of the system is required. In addition, boundary conditions for application of different technologies should be available and a Strength and Weaknesses (SWOT) analysis provided.

The main results of the Technical Catalogue developed will be presented including an overview of the different technologies considered and their key performance indicators, factors for success and limitations. The SWOT analysis identifies the risk zone, match field and competitive advantage zones for different shallow geothermal technologies, showing that shallow geothermal energy systems have a clear competitive advantage for many of the key and supporting technologies whilst clearly indicating to the industry which of these can be improved to achieve competitive advantage.

The results of this GeoBOOST task will be combined with data from a recent study performed in the Netherlands where a quantitative environmental and economic comparison between different heating and cooling technologies has been made.

2. Methodology

This section will detail the systematic approach taken by the GEOBOOST project to analyse the current landscape of geothermal energy technologies. It will describe the development process of the Technical Catalogue, including the criteria for technology selection and the framework for evaluating different geothermal systems in varied European contexts.

The main methodology to create the Technical Catalogue (TC) has been through collaboration between an international team of experts, based on the experience in different countries. A TC has been developed covering virtually all aspects of SGE systems: heat pump technology, control systems, SGE systems including open loop (Aquifer Thermal Energy Storage) and closed loop (Borehole Heat Exchangers, Borehole Thermal Energy Storage, Horizontal Ground Heat Exchangers, circulation media and drilling technologies. For different usage types and climate zones a qualitative assessment of the potential of the different SGE systems has been developed.

A SWOT analysis has been performed to provide a detailed evaluation of where the different SGE systems have a competitive advantage or where they can be brought into the competitive advantage zone with limited effort.

3. Results

As a starting point different SGE systems were classified (table 1) according to most promising locality type where locality is loosely equivalent to building density and available land space for SGE installation.

	Urban	Village	Rural
Open Loop	++	+	+/-
Closed loop, BTES	+	+	+
Closed loop, BHE	+	++	++
Closed loop, HORIZONTAL	-	+/-	+
Closed loop, RING	-	+/-	+
Closed loop, SPIRAL	-	+/-	++

Table 1. Indication of types of geothermal systems per locality type. Dark green (++): very suitable, light green (+): suitable; yellow (+/-): may be suitable; red (-): not or limited suitability.

Open Loop : aquifer systems. Closed loop: BTES (Borehole Thermal Energy Store) systems, BHE (Borehole Heat Exchanger systems), Shallow horizontal heat exchanger systems, Ring: Shallow Ring collector heat exchanger systems (Slinky), Spiral: Spiral (including Earth-Basket) type heat exchangers.

A second classification considered the application type and associated thermal capacity (Table 2).

In practice SGE is routinely applied in a wide range of different applications and capacities. Even for small (single family houses) systems are often realized in large numbers (typical size of a development in the Netherlands can range from 30 to 300 houses, larger developments of up to 2500 houses are not rare).

	SFH	MFH	T1	T2	I&A	HCN
Capacity (kW)	3 - 15	15 - 350	50 - 800	800 - 2500	> 2500	> 2500
Open Loop	+	+	+	++	++	++
Closed loop, BTES	-	++	++	+/-	+/-	+/-
Closed loop, BHE	++	++	++	-	-	-
Closed loop, HORIZONTAL	+	+/-	-	-	-	-
Closed loop, RING	+	+/-	-	-	-	-
Closed loop, SPIRAL	+	+/-	-	-	-	-

Table 2. Indication of type of application suitable for different geothermal technologies. SFH: Single Family House; MFH: Multi Family House; T1: Small and medium scale Tertiary; T2: Large scale Tertiary; I&A: Industrial and Agricultural, HCN: Heating / Cooling Networks. (Tertiary buildings: larger buildings such as offices, hospitals etc).

In addition to providing an overview of typically applied technologies, the Technical Catalogue also lists a number of new developments that will increase



efficiency and widen implementation. These are amongst others:

- Development of dual-source heat pumps (ground or ground water and air) such as pioneered in the H2020 project Geotēch (Corberán et al, 2018; Alonso et al 2022)
- Other hybridizations with e.g. Solar-assisted heat pumps (Besagni, 2019).
- Development of an acoustic heat pump (Blue Heart Heatpump) and high-temperature heat pumps suitable for retrofit applications.
- Advanced control systems based on Machine Learning or Model Predictive Control.
- New ground heat exchanger technologies, including developments for deeper systems (higher strength materials, composites), new coaxial piled GHX (GEO4CIVIC project¹), and higher conductivity pipe materials (Badenes et al 2020).
- New or improved drilling methods such as the “Easy Drill” method (Pockele et al. 2021, Galgaro et al. 2022) and radial drilling methods that require less surface area for the installation (Sokolnicka and Derwich 2010).

3.1 SWOT Analysis

A Strengths, Weaknesses, Opportunities and Threats (SWOT) analysis is used as an assessment tool of ground source heat pump (GSHP) technologies reviewed as part of the GeoBOOST project that include: borehole heat exchangers, ground water heat pumps, aquifer & borehole thermal energy storage, horizontal collectors, heat pumps, drilling technologies and hybridisation. The qualitative SWOT methodology highlights the viability of increased deployment of shallow geothermal solutions focussing on barriers to implementation (threats and weaknesses) as well as the technology advantages (strengths and opportunities) over other renewables. Aspects related to the delivery, completion and operation of GSHP systems are assessed against a set of pre-defined categories. These are weighted out of 100 and the applicability of each technology scored based on the available information with respect to the deployment of GSHPs in the European market. The delivery aspects of the technologies are broadly considered in the SWOT as follows:

- Use of different geothermal collector technologies
- Heat pumps & hybrid technology implementations
- Drilling Technologies
- Availability resource against energy requirements;
- Construction phase and supply chain;

- Replication of solutions and integration with other technologies;
- Environmental Impacts;
- Financial Aspects – CAPEX & OPEX
- Operational Life;
- Technology Awareness;
- Regulatory and Permitting requirements

The SWOT analysis provides a means of assessing the suitability of the GSHP technologies by identifying potential matches with respect to non-technical aspects and aligning these with the needs of the market. The outcome demonstrates the competitive advantages the technologies considered and their future role in the deployment across Europe.

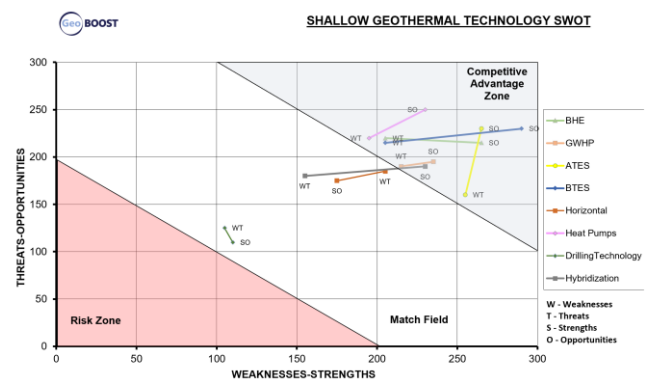


Figure 1: Geothermal Technology SWOT Analysis results

4. Conclusions

The technical catalogue developed in the GeoBOOST project provides policy makers, architects and project developers as well as engineers working on shallow geothermal energy systems a complete overview of possible application types and available technologies. It provides a first stepping-stone for enhancing both general and qualitative as well as detailed quantitative background to SGE technologies.

SWOT analysis reveals (Figure 1) vertical BHEs and BTES as competitive despite higher CAPEX, due to their adaptability to various ground conditions. The GWHPs and ATEs systems have overall increased potential for meeting the decarbonisation of the heating and cooling sector, however increased permitting and the resource availability to match user demand are threats to future deployment. Horizontal collectors requiring a larger surface area restrict the potential for deployment.

Heat pumps, noted for their efficiency, already have a competitive market advantage compared to other heating and cooling technologies, offering lower

¹ <https://geo4civhic.eu/>



operating costs, environmental impact and improved air quality due to their high efficiencies. The opportunities for the heat pump technologies are strengthened by the existing awareness and deployment of the technology in the built environment and the ability to integrate GSHPs with other renewables and district heating networks. The specific lack of awareness from key market actors of ground source heat pump technology represents a clear common threat to further uptake from competing air source heat pumps. Similarly, the higher CAPEX of GSHPs is a key threat compared to lower cost solutions like ASHPs, despite the latter generally having higher operational costs than GSHP solutions.

Hybrid solutions of air source and ground source show promise in urban areas, optimizing efficiency in challenging geothermal conditions where geothermal deployment is challenging. Hybridisation also offers improved optimisation of heating and cooling systems, maximising operational efficiencies.

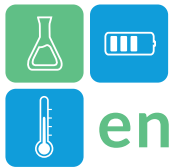
The review of drilling technologies indicates potential market growth and increased deployment. However, the completion time for the construction works and some of the environmental impacts related to noise, vibration and emissions from mostly diesel fired engines represent a threat. Opportunities for improvement in drilling are focussed on emerging market solutions based on the electrification of drilling equipment as well as innovative drilling solutions focussed on reducing drilling and completion timelines for geothermal systems.

Acknowledgement

The GeoBOOST project is financially supported by the European Commission (LIFE21-CET, Grant no. 101077613). The authors would like to acknowledge the valued input of all GeoBOOST project members and especially the GeoBOOST project reviewers of the deliverable H. Javadi (Universitat Politècnica de València) and C. Steiner (Geosphere Austria).

References

- Besagni, G., Croci, L., Nesa, R., Molinaroli, L. (2019). Field study of a novel solar-assisted dual-source multifunctional heat pump. *Renewable Energy* 132: 1185 – 1215.
- Corberán, J. M., Cazorla-Marín, A., Marchante-Avellaneda, J., & Montagud, C. (2018). Dual source heat pump, a high efficiency and cost-effective alternative for heating, cooling and DHW production. *International Journal of Low-Carbon Technologies*, 13(2), 161-176. <https://doi.org/10.1093/ijlct/cty008>
- Alonso, L., Peña, X., Trebilcock, F., Hernandez, J., & Agirre, A. (2022). Performance evaluation of a R-290 dual-source heat pump for heating and cooling. *CLIMA 2022 Conference*. <https://doi.org/10.34641/clima.2022.381>
- Borja Badenes, Burkhard Sanner, Miguel Ángel Mateo Pla, José Manuel Cuevas, Flavia Bartoli, Francesco Ciardelli, Rosa M. González, Ali Nejad Ghafar, Patrick Fontana, Lenin Lemus Zuñiga, Javier F. Urchuegúa (2020). Development of advanced materials guided by numerical simulations to improve performance and cost-efficiency of borehole heat exchangers (BHEs), *Energy*, Volume 201, 2020, 117628, ISSN 0360-5442, <https://doi.org/10.1016/j.energy.2020.117628>.
- Pockele, G. Mezzasalma, D. Righini, J. Verduyck, F. Cicolin, G. Cadelano, A. Galgaro, G. Dalla Santa, M. De Carli, G. Emmi, A. Bernardi, (2020). Innovative coaxial heat exchangers for shallow geothermal, in: *Proceedings of World Geothermal Congress 2020*.
- Galgaro A., Di Sipio E., Carrera A., Dalla Santa G., Ramos Escudero A., Cuevas J.M., Pasquali R., Sanner B., Bernardi A., European and municipal scale drillability maps: A tool to identify the most suitable techniques to install borehole heat exchangers (BHE) probes, *Renewable Energy* 192, pp. 188-199
- Sokolnicka B., Derwich P., (2010) Ekologiczne ciepło, System GRD Traco-Technik, *Inżynieria Bezwykopowa* 4, 66-68.



GIS-Based GSHP Sizing and Estimation Tool: Facilitating Non-Expert User Engagement and Technology Dissemination

Borja Badenes^{1*}, Teresa Magraner¹, Adela Ramos^{1,2}, Cristina de Santiago³, Helena Van Den Berg¹

¹ ICT vs Climate Change research group - Instituto de Aplicaciones de las Comunicaciones Avanzadas (ITACA), Universitat Politècnica de València, Camino de Vera S/N, 46022 Valencia, Spain

² Departamento de Física aplicada y tecnología naval. Grupo de materiales avanzados para la producción y almacenamiento de energía. Universidad Politécnica de Cartagena. *Pza. del Cronista Isidoro Valverde. Edif. La Milagrosa C.P. 30202 Cartagena*

³ Instituto Geológico y Minero de España, C/ Ríos Rosas 23, 28003, Madrid, España

*Corresponding author e-mail: borbaba@upv.es

Abstract

Currently, there are several tools for the simulation of ground source heat pump (GSHP) installations, such as software programs or analytical methods. However, this software requires a high/expert user level and a prior collection of data on the characteristics of the installation. Through the application of Geographic Information Systems (GIS), the introduction, administration, analysis, and cartographic representation of the data necessary for GSHP simulation can be achieved in an automatic and personalised way without the user's expert inputs. This work presents the development of an energy simulation tool for estimating the GSHP potential in the region of Valencia (Spain), based on the IGSHPA analytical methodology and oriented towards a non-technical profile. The tool is designed modular using GIS that allows its easy use and subsequent integration with other modules such as photovoltaic energy. The general objective of this development is to fight against one of the main non-technological barriers to geothermal energy, namely the lack of dissemination, awareness and proximity to the non-expert public.

Keywords: SGE (shallow geothermal energy), GSHP (ground source heat pumps), Geographic Information Systems (GIS), Sizing and Estimation Tool

1 Introduction

Shallow geothermal energy is a competitive, clean, local, and long-term stable source of renewable thermal energy. It is increasingly recognised for its pivotal role in decarbonising the heating and cooling sector. Owing to its high efficiency, the ability to synergize with other renewable energy sources, and its potential for high renewable cooling production, shallow geothermal energy is a key component in Europe's strategy for renewable heating and cooling, as outlined in the Strategic Research and Innovation Agenda (SRIA) published by RHC – ETIP in 2020. Moreover, the European Union, in its REPowerEU plan, has recently prioritized integrating geothermal energy in buildings to lessen Europe's reliance on Russian fossil fuels. However, the market share growth of shallow geothermal energy is hindered by several barriers, including the lack of legislative framework, high installation costs, shortage of skilled personnel (specific training), limited awareness and visibility of the technology, and the absence of effective market monitoring tools.

Several tools currently exist for simulating geothermal heat pumps installations, such as software programs [1] and analytical methods [2]. However, this software requires a high/expert user level and prior data collection regarding the installation's characteristics. The application of Geographic Information Systems (GIS) can automate the introduction, management, analysis, and cartographic representation of the data necessary for geothermal installation simulation (in this case, geological, hydrogeological, climatic data, etc., all requiring a spatial positioning system), in a customized manner, without the need for expert user knowledge. The research group has collaborated on the creation of geothermal potential maps within the framework of the H2020 European projects it has participated in: "Cheap-GSHPs" [3], "GEOCOND" [4], and "GEO4CIVHIC" [5]. In Spain, there have been several proposals for the application of GIS systems in the field of geothermal energy, both at the national and regional levels. However, in these cases, their application to geothermal heat pump systems (shallow geothermal energy) is limited and excludes any estimation/simulation of installation performance.

This simulation tool estimates the geothermal potential of heating and cooling installations using ground source heat pumps (GSHPs). This tool will provide valuable insights into the geothermal potential of the site, investment costs, energy, and economic savings (return on investment), renewable energy production, and avoided CO₂ emissions (see Figure 1). Should the installation proceed, these preliminary findings will require validation and further refinement.

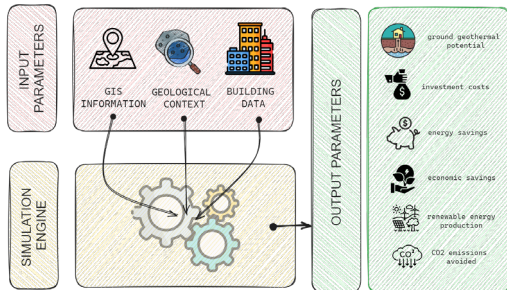


Figure 1: Diagram of the tool

The proposed tool will be based on a set of customised data specific to the building's location: (i) spatial data (either directly read or pre-processed), including geological and hydrogeological context, soil conductivity, and ground temperature. (ii) climatic data. (iii) building data, such as the type of building and its surface area.

2 Methodology

2.1 Preliminary maps: Lithology, groundwater depth and average thermal conductivity

Lithologies are traditionally converted to thermal conductivities for subsequent geothermal studies, considering a standard density and dry state (total absence of water in the pores) to simplify the process. However, the presence, amount, and condition of water in the ground (soils or rocks) play a crucial role in their thermal behaviour [6].

To consider both lithostratigraphic and hydrogeological aspects, the continuous lithostratigraphic map of Spain (scale 1:200.000) was used as the base map (InfoIGME - Servicios de mapas).

Then, a piezometric map was created by collecting and analysing historical data from 275 georeferenced piezometers in the Spanish piezometric monitoring network, hosted by the Ministry of the Environment. This allowed the differentiation of the thermal conductivities of saturated and unsaturated materials.

Once the groundwater table depth is known, all the ground over it is dry while the ground below it is saturated. Dry and saturated thermal conductivity values were assigned to each lithology of the map. To do this, the geological material-dependent thermal

conductivities ranges recommended for Ground Source Heat Exchangers (GSHE) by the Swiss Standard (SIA, 2010), the German Standard (VDI 4640-1, 2010), and the Spanish standard (UNE 100715, 2014) were consulted. The 25% lowest value of the recommended ranges was assigned to the dry state, whereas 75% of the range was assigned to the saturated state of every lithology (Figure 2).

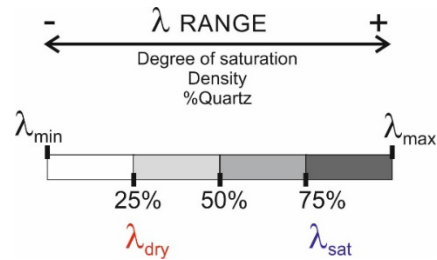


Figure 2: Degree of water saturation

Assuming that the total borehole length is surrounded by outcropping lithology, the average ground thermal conductivity λ_{ave} can be calculated by the weighted mean of the thermal conductivity of the upper dry part and the lower saturated part crossed along the GHE:

$$\lambda_{ave} = \frac{(\lambda_{dry} \cdot h_{dry}) + (\lambda_{sat} \cdot h_{sat})}{h_{total}}$$

Where λ and h are the thermal conductivity and the thickness of the stratigraphic unit in dry state (over the groundwater level) and below the groundwater level, respectively (Figure 3).

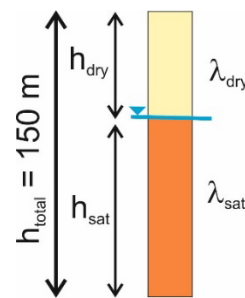


Figure 3: Average ground thermal conductivity

2.2 GIS Techniques in Data Acquisition

Geographic Information Systems (GIS) are computer-based tools used to store, visualise, analyse, and interpret geographic data [7]. In the context of estimating the geothermal potential of heating and cooling installations, GIS provides a comprehensive framework for integrating geological, hydrological, climatic, and building data. Through the following techniques the data can be collected, and modified as necessary, for the estimation tool:



Attribute management: Attribute management in GIS involves the organisation and manipulation of databases linked to spatial features. In the estimation of geothermal potential, this includes handling key data from different cartographic data sources. As mentioned above, lithology, and water level are essential for the estimation of geothermal conductivity. Lithology, which describes the geological composition of an area, is crucial for understanding subsurface conditions affecting thermal conductivity. Water level information, obtained from the Spanish piezometric network, is a vectorial layer of points requiring careful management. The management and/or integration of the necessary attributes of lithology and water level provides a foundation for subsequent analyses.

Spatial interpolation: Spatial interpolation is a GIS technique used to estimate values for locations where data points are not available. In the context of geothermal potential estimation, water level data from the piezometric network is sparse and requires interpolation for a continuous representation. Spline with tension interpolation, a type of radial basis function, is applied to generate a continuous water level layer for the entire study area.

Map algebra and overlay analysis: Map algebra involves manipulating and analysing data through mathematical operations [8]. In the context of geothermal potential estimation, map algebra is essential for combining and analysing various datasets, such as lithology, water level, ground temperature, etc. This allows for the creation of composite layers that provide a more comprehensive understanding of geothermal characteristics of the site. By applying map algebra, researchers can derive new layers that highlight areas with high geothermal potential based on the interaction of different factors. Nevertheless, map algebra is primarily associated with raster data, where spatial information is represented as a grid of cells, each with a specific value.

Web mapping: To ensure accessibility for the public, the integration of GeoServer [9], an open-source GIS server, with the Leaflet JavaScript library facilitates the creation of an online interactive web mapping application. This application offers an intuitive and user-friendly platform for visualising geothermal potential and other relevant information. GeoServer plays a crucial role by serving geospatial data, including layers derived from uploaded raster or vectorial data. These layers are configured and stylised to meet specific cartographic requirements, providing a comprehensive and visually appealing representation of the data. In the web application, Leaflet enhances the

user experience with an intuitive and responsive mapping interface. Leveraging Leaflet's capabilities, users can easily interact with GeoServer-served layers, performing actions such as zooming, panning, toggling, and clicking to explore different layers within the estimation tool.

2.3 Building data

The developed tool focuses on the analysis of residential buildings. Based on the cadastral information available in GIS databases (building typology, built surface area, number of floors and year of construction) and on the climatic zone where the GSHP installation is located, the demand for heating and cooling is evaluated. To this end, eleven different climatic zones in Comunitat Valenciana have been identified, in accordance with the Spanish Technical Building Code, and eight construction periods depending on the applicable regulations (before 1900, between 1900-1940, 1940-1960, 1960-1979, 1979-2006, 2006-2019 and after 2019), which determine different thermal transmittances of the building envelope (enclosures and glazing). For each combination of climatic zone and year of construction, two building typologies were simulated using HULC software [10], which is the most complete official tool in Spain for energy performance analysis, since it is used for the issuance of energy performance certificates in both new and existing buildings. The building typologies analysed are the most common in the region: two-store single-family home between party walls and apartment building between party walls with interior patios (Figure 4).

In summary, to determine the thermal needs, 176 simulations were carried out, obtaining the monthly and hourly energy demand for heating and cooling per square metre. These results have been implemented in a GIS database to, when the user select any location, the heating and cooling needs can be assessed based on the cadastral data and the climatic zone.



Figure 4: Two store single-family home between party walls and apartment building between party walls with interior patios, building typology modelled in HULC

3 Results and Discussion

3.1 Data Output and Tool Functionality

This tool is designed to estimate key aspects of geothermal heat pump installations, providing valuable data on the geothermal potential of the site, necessary drilling depth, and associated costs. It also projects



potential energy savings, economic benefits, and reductions in CO₂ emissions.

Additionally, the tool calculates the possible renewable energy generation and outlines available subsidies and their amounts. This comprehensive approach allows users, particularly those without technical expertise, to make informed decisions about geothermal installations, understanding both the financial and environmental implications. The estimation tool simplifies the complexity surrounding geothermal energy projects, facilitating easier access to and comprehension of this sustainable energy source.

4 Conclusions

The GIS-based GSHP sizing and estimation tool represents as a significant innovation, particularly in simplifying the process of geothermal heat pump installation for non-expert users. Integrating Geographic Information Systems (GIS) for accurate, location-specific data, this tool makes the complex task of sizing and estimating GSHP installations more accessible and less daunting. The user-friendly nature of the tool addresses a critical barrier in the commitment geothermal technology: the lack of technical knowledge among potential users. By demystifying the complexities and offering reliable estimates, it empowers users to confidently consider and adopt geothermal solutions.

The modular design of this tool not only caters to current needs but also allows for future integration with other renewable energy technologies. This adaptability ensures its long-term utility and relevance in the rapidly evolving landscape of renewable energy solutions. It is more than just a utility for sizing and estimation; it is a step towards making renewable energy technologies such as GSHPs more mainstream and user-friendly.

In conclusion, the development of this tool marks a pivotal moment in the promotion of sustainable energy solutions. The success of this tool underscores the potential and importance of user-friendly technological innovations in achieving broader environmental and sustainability goals.

Acknowledgment

We acknowledge the funding received from the Universitat Politècnica de València (UPV), through VICERRECTORADO DE INVESTIGACION, for the project "GEOSIMVAL - SIMULADOR DEL POTENCIAL GEOTÉRMICO DE UNA

INSTALACIÓN DE CLIMATIZACIÓN EN LA COMUNITAT VALENCIANA."

References

- [1] Earth Energy Design, EED.
<https://buildingphysics.com/eed-2/>
- [2] IGSHPA (International Ground Source Heat Pump Association) (2009): "Ground source heat pump residential and light commercial: design and installation guide". <https://igshpa.org/>
- [3] Sipio, Eloisa & Galgaro, Antonio & Teza, Giordano & Destro, Elisa & De Carli, Michele & Chiesa, Sergio & Zarrella, Angelo & Emmi, Giuseppe & Manzella, Adele. (2015). Empirical modeling of maps of geo-exchange potential for shallow geothermal energy at regional scale. *Geothermics*. <https://doi.org/10.1016/j.geothermics.2015.06.017>
- [4] Ramos-Escudero, A., García-Cascales, M.S, Cuevas, J. M., Urchueguía, J.F. y Sanner, B. GIS-Supported evaluation and mapping of the physical parameters affecting shallow geothermal systems efficiency at a continental scale. *Proceedings European Geothermal Congress 2019*. <https://europeangeothermalcongress.eu/wp-content/uploads/2019/07/287.pdf>
- [5] A. Galgaro, E. Di Sipio, A. Carrera, G. Dalla Santa, A. Ramos Escudero, J.M. Cuevas, R. Pasquali, B. Sanner, A. Bernardi. European and municipal scale drillability maps: A tool to identify the most suitable techniques to install borehole heat exchangers (BHE) probes, *Renewable Energy*. <https://doi.org/10.1016/j.renene.2022.04.120>
- [6] Farouki, O.T. (1986). *Thermal properties of soils*. Trans Tech Publications. D-3392 Clausthal-Zellerfeld, Germany. 136 pp. ISBN 0-87849-055-8
- [7] What is GIS? [<https://cdc.gov/gis/what-is-gis.htm>] (accessed 01/11/2024)
- [8] Mennis, J. (2022). *Grid Operations and Map Algebra*. The Geographic Information Science & Technology Body of Knowledge (3rd Quarter 2022 Edition). John P. Wilson (Ed.). DOI: <https://doi.org/10.22224/gistbok/2022.3.1>
- [9] Geoserver, 2024. *Geoserver user manual*. [<https://docs.geoserver.org/latest/en/user/>] (accessed 01/11/2024)
- [10] Herramienta unificada LIDER-CALENER (HULC), (n.d.). <https://www.codigotecnico.org/Programas/HerramientaUnificadaLIDERCALENER.html> (accessed January 10, 2024).



Graphite Based Encapsulation Concept for a High Temperature Metallic Latent Thermal Energy Storage System

Veronika Stahl^{1,*}, Werner Kraft¹, Frank Nees¹, Julius Feine¹, Anastasios Katourtzidis¹,
Nuria Navarrete², Carolina Villada²

1 German Aerospace Center (DLR), Institute of Vehicle Concepts, Pfaffenwaldring 38-40, 70569
Stuttgart, Germany

2 German Aerospace Center (DLR), Institute of Material Physics in Space, Linder Höhe, 51170 Cologne,
Germany

*Corresponding author e-mail: veronika.stahl@dlr.de

Abstract

Developing metallic latent thermal energy storage for replacement of battery capacity might enhance battery electric buses or trains by reduction of storage investment costs, mass and volume. However, they are based on metallic Phase Change Materials which are highly corrosive to structural materials such as conventional steel-based alloys. Building a long-term stable encapsulation growing out of lab-scale is one of the critical steps to enhance this promising storage technology. In this work, efforts were made to design and manufacture a storage prototype with storage material encapsulation based on different graphite grades. The stability and functionality of the prototype was proven over 26 phase change cycles under conditions similar to the application.

Keywords: Thermal energy storage, Metallic phase change material, Compatibility, Electric Vehicles

Introduction

Current battery-powered electric buses and trains have drawbacks compared to conventional diesel buses and trains due to their high investment costs and limited range, which are dependent on the ambient temperature, especially when heating is required. (Kraft et al. 2020b; Yang et al. 2022)

By replacing the battery capacity dedicated to heating with a Metallic Latent Thermal Energy Storage based on metallic Phase Change Materials (mPCM), the investment costs for electric buses and trains and the battery mass and volume can be reduced. (Kraft et al. 2020a)

Rawson et al. (2020b) found that the eutectic Al - 12.5 wt.% Si (AlSi₁₂) with a melting point of 577 °C is the optimal eutectic mPCM for an operating temperature range up to 660 °C regarding latent heat of fusion, energy density and cost. However, liquid Al-Si alloy is highly corrosive to metals such as steel base-materials. (Fukahori et al. 2016; Dindi et al. 2020; Tiwari und Periaswaym 2023)

This is an essential challenge as material compatibility and encapsulation is crucial for good performance, long lifetime and low cost (Perraudin et al. 2015).

One approach to address corrosivity of mPCM is to apply protective ceramic coatings on the structural encapsulation. Tiwari und Periaswaym (2023) report

failure of Al₂O₃ ceramic coating and dissolution of steel substrate in AlSi₁₂ and Rea et al. (2018) suggest that ceramic coatings could fracture due to thermal gradients or volume change and react which makes extended life cycle tests necessary.

Building a long-term stable mPCM encapsulation growing out of the lab-scale is still lacking in literature.

In this study we tackled an alternative approach and investigate a mPCM encapsulation concept using a graphite liner. Graphite is very common in industry and an attractive encapsulation material due to its low cost. Rawson et al. (2020a) found in static reaction experiments that there was no reaction between graphite and AlSi₁₂ after 336 hours at 650 °C under argon atmosphere.

The mPCM encapsulation ideally should be cheap, easily producible, resistant to corrosion and thermal gradients, ensure high performance and safe to handle.

Materials and Methods

Prototype setup and materials

Figure 1 illustrates the investigated prototype setup which is an intermediate scale between very small lab samples and application scale. 2.45 kg of AlSi₁₂ (Supplier: Oetinger Aluminium) are placed in a box shaped encapsulation out of Alloy A-286 stainless

steel with graphite liner. The graphite liner shall protect the steel cover from degradation by liquid metal corrosion and the stainless steel cover shall maintain an inert atmosphere in order to prevent the graphite liner from oxidation by ambient air. The hooded-shaped upper part of the graphite liner is made from Sigrafine R7660 and the bottom plate at the interface to the heat exchanging structures is made from Sigrafine R7510 graphite grade both supplied by SGL Carbon. Between these two graphite parts a gasket made from Sigraflex TH (Supplier: SGL Carbon) was placed in order to prevent liquid metal leakage.

The steel cover is closed on the bottom side with a steel plate. In one configuration the steel plate had integrated electrical heaters (4 x 600 W) for charging heat only, in another configuration the steel plate was featured with additional air-fluid channels for discharging heat. The heat extraction characteristics of this prototype were investigated by Nees et al. (2023).

The steel hood and plate were joint with screws and a gasket made from Sigraflex APX (Supplier: SGL Carbon) was used in order to prevent impermeability to gas as the prototype is operated under argon atmosphere. All steel parts are surrounded by a microporous insulation made from TH1000+ (Supplier: Thermoline Manufaktur).

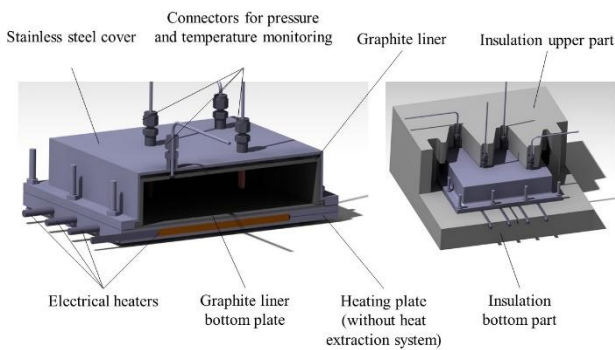


Figure 1: 3D CAD model of the storage prototype without heat extraction system in sectional view (left) and with part of the insulation (right).

Table 1 lists the properties of the storage design both with and without heat extraction system for a temperature range of 20–650 °C. The values refer to the outside of the insulation as the system boundary. The insulation was neglected when determining the storage capacity.

Table 1: Properties of storage prototype with/without heat extraction system (WAS)

Property	Without WAS	With WAS
Storage capacity	1.57 kWh	1.82 kWh

Mass	14.4 kg	17 kg
Volume	16.6 l	18.2 l
Grav. energy density	109.6 Wh/kg	107 Wh/kg
Vol. energy density	94.8 Wh/l	100 Wh/l
Dimensions	329 mm x 329 mm x 153.7 mm	329 mm x 329 mm x 167.7 mm

Methods

A thermal analysis of both graphite grades was performed. The heat capacity was measured using a differential scanning calorimeter (DSC) NETZSCH DSC 404C under argon atmosphere (50 ml/min) with graphite crucibles and perforated lids. The samples were about 20–25 mg and a 20 K/min heating rate was applied. The heat capacity was determined by the ratio method comparing the samples to a sapphire calibration standard. The thermal diffusivity was determined using a light flash apparatus Netzsch LFA 467 HT Hyperflash under argon atmosphere.

The experimental investigation of the prototype was performed in a custom-built test stand.

Results and Discussion

Thermal Properties of Graphite

The temperature dependent heat capacity of the two used graphite grades in the temperature range of 50–690 °C is shown in Figure 2. The heat capacity curves were fit into a cubic model. The standard error of the curve fit model is 0.019 kJ/kg·K for R7510 and 0.013 kJ/kg·K for R7660 respectively.

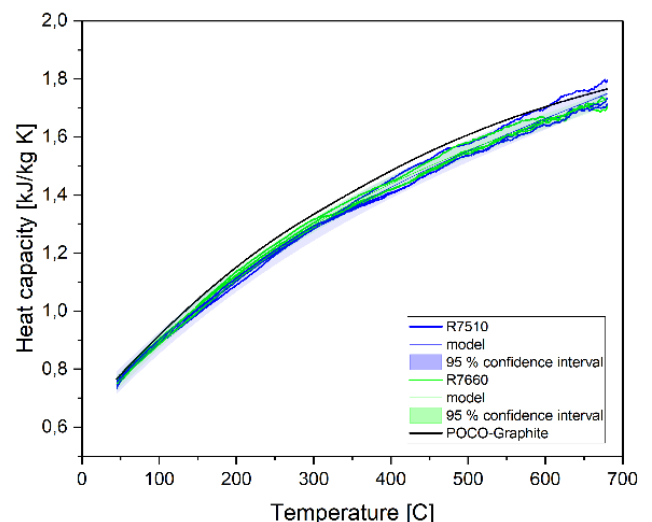


Figure 2: Heat capacity for the graphite grades R7510 and R7660. The lines represent the models with the 95 % confidence interval for each grade.

The temperature dependent thermal diffusivity of the two used graphite grades in the temperature range of 20–698 °C is shown in Figure 3. The thermal diffusivity curves were fit into a cubic model. The

standard error of the curve fit model is 0.888 mm²/s for R7510 and 0.439 mm²/s for R7660 respectively.

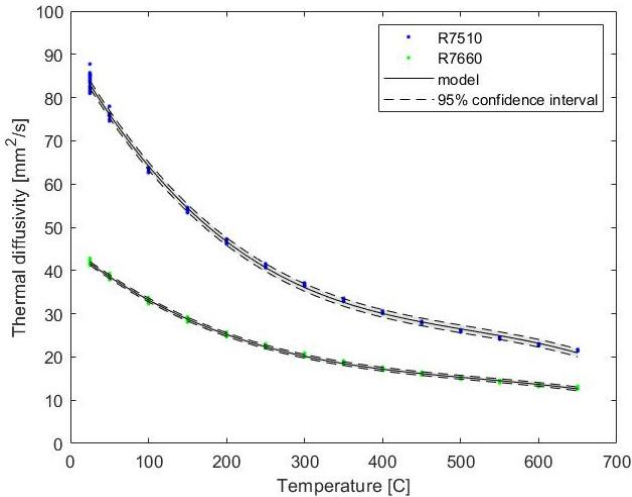


Figure 3: LFA results for the graphite grades R7510 and R7660. The lines represent the model for each grade and the upper and lower dotted lines are the 95 % confidence interval.

Prototype performance

The individual manufactured parts of the prototype are displayed in Figure 4 and the prototype integrated in the test stand is shown in Figure 5. Filling of the mPCM was done by positioning solid mPCM-blocks in the graphite housing (see Figure 7 left).

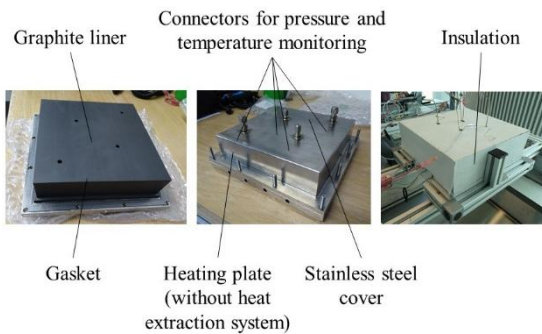


Figure 4: Individual parts of the storage prototype without heat extraction system before testing.

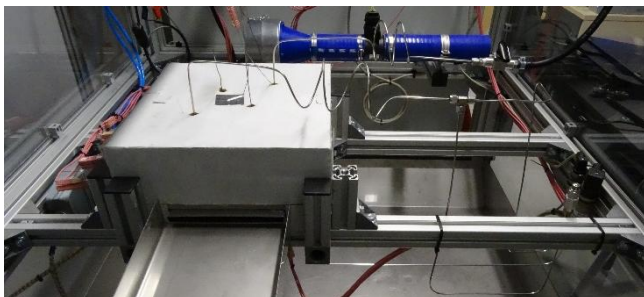


Figure 5: Prototype with heat extraction system and insulation integrated in the test stand

Several experiments were performed. The accumulation of the temperature load higher than 100 °C over all experiments is shown in Figure 6. The prototype has completed 26 phase change cycles in total and time in molten state was about 50 hours. No mass change of the graphite components was observed over the experimental procedure. No leakage occurred and no damage at any part of the prototype could be observed which is shown exemplarily for the graphite liner in Figure 7 and the graphite plate in Figure 8.

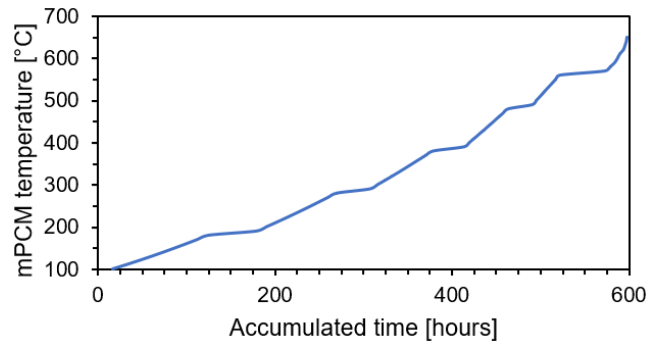


Figure 6: Accumulated temperature load higher than 100 °C the prototype has experienced in total.

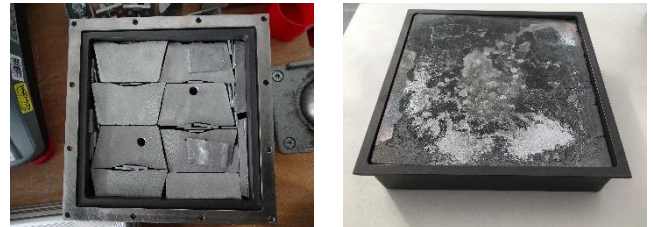


Figure 7: mPCM blocks placed in graphite liner in steel hood before (left) and after (right) test program.

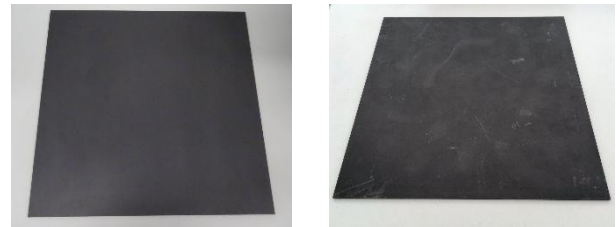


Figure 8: Graphite plate before (left) and after (right) test program.

Conclusions

An encapsulation concept for AlSi₁₂-based latent thermal energy storage based on a graphite liner was successfully built in a mid-scale size. For interfaces with or without heat exchanging function graphite grades with different thermal diffusivity values were



measured, while the temperature dependent heat capacity values were similar for both grades. After about 600 h of experiments, 26 cycles and around 50 h in liquid state no mass change of the prototype encapsulation was observed.

Further research for transfer to application scale is necessary.

Acknowledgment

This research was funded by the EFRE (Europäischer Fonds für regionale Entwicklung) Leitmarkt Wettbewerb Nordrhein-Westfalen Mobilität.Logistik within the project „LatHe.GO“ and by Baden-Württemberg’s Department of Trade and Industry within the project “THS-Bus”.

References

Dindi, Abdallah; Lopez Ferber, Nicolas; Gloss, Daniel; Rilby, Erik; Calvet, Nicolas (2020): Compatibility of an Aluminium-Silicon metal alloy-based phase change material with coated stainless-steel containers. In: *Journal of Energy Storage* 32, S. 1–18. DOI: 10.1016/j.est.2020.101961.

Fukahori, Ryo; Nomura, Takahiro; Zhu, Chunyu; Sheng, Nan; Okinaka, Noriyuki; Akiyama, Tomohiro (2016): Thermal analysis of Al–Si alloys as high-temperature phase-change material and their corrosion properties with ceramic materials. In: *Applied Energy* 163, S. 1–8. DOI: 10.1016/j.apenergy.2015.10.164.

Kraft, Werner; Rawson, Anthony; Stahl, Veronika; Vetter, Peter; Kargl, Florian; Sonnekalb, Michael; Best, Pascal (2020a): Thermal high-performance storages as heating systems for electric buses. In: *Proceedings of 8th Transport Research Arena TRA 2020*.

Kraft, Werner; Stahl, Veronika; Vetter, Peter (2020b): Thermal Storage Using Metallic Phase Change Materials for Bus Heating—State of the Art of Electric Buses and Requirements for the Storage System. In: *Energies* 13 (11), S. 3023. DOI: 10.3390/en13113023.

Nees, Frank; Feine, Julius; Katourtzidis, Anastasios; Stahl, Veronika; Kraft, Werner (2023): Heat Extraction Characteristics Of A Small Scale Metallic

Latent Heat Thermal Energy Storage System. In: *Proceedings of the 17th International Heat Transfer Conference 2023*. DOI: 10.1615/IHTC17.430-40.

Perraudin, David Y. S.; Binder, Selmar R.; Rezaei, Ehsan; Ortonaa, Alberto; Haussener, Sophia (2015): Phase Change Material Systems for High Temperature Heat Storage. In: *Chimia* 69 (12), S. 780–783. DOI: 10.2533/chimia.2015.780.

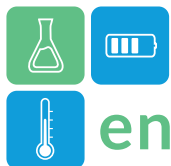
Rawson, Anthony Joseph; Gläsel, Tina; Nowak, Benedikt; Boon, David; Stahl, Veronika; Kargl, Florian (2020a): The Compatibility of Metallic Thermal Storage Materials and Housing Materials: A Computational Survey and Accelerated Reaction Experiments. In: Xiaobo Chen, Yulin Zhong, Lei Zhang, John A. Howarter, Alafara Abdullahi Baba, Cong Wang et al. (Hg.): *Energy Technology 2020: Recycling, Carbon Dioxide Management, and Other Technologies*. Cham: Springer International Publishing (The Minerals, Metals & Materials Series), S. 15–29.

Rawson, Anthony Joseph; Kraft, Werner; Gläsel, Tina; Kargl, Florian (2020b): Selection of compatible metallic phase change materials and containers for thermal storage applications. In: *Journal of Energy Storage* 32, S. 101927. DOI: 10.1016/j.est.2020.101927.

Rea, Jonathan E.; Oshman, Christopher J.; Olsen, Michele L.; Hardin, Corey L.; Glatzmaier, Greg C.; Siegel, Nathan P. et al. (2018): Performance modeling and techno-economic analysis of a modular concentrated solar power tower with latent heat storage. In: *Applied Energy* 217, S. 143–152. DOI: 10.1016/j.apenergy.2018.02.067.

Tiwari, Vivek; Periaswaym, Srinivasan (2023): Compatibility of structural materials with AlSi12 alloys-based phase change material and increasing the corrosion resistance by ceramic coatings. In: *Journal of Energy Storage* 2023 (72), Artikel 108526, S. 1–8. DOI: 10.1016/j.est.2023.108526.

yang, shan; Mach, Stefan von; Buschbeck, Jan; Donner, Sylvio; Kraft, Werner (2022): Thermische Hochleistungsspeicher für batterieelektrische Schienenfahrzeuge. In: *ZEVrail* 2022 (146), S. 43–49.



High Temperature PCMs for industrial steam systems

- Extended abstract -

Herbert Zondag^{1,2,*}, Michel van der Pal¹, Gertjan Herder¹, Robert de Boer¹

¹TNO, Westerduinweg 3, 1755 LE Petten, The Netherlands

²TU Eindhoven, Den Dolech 2, 5612 AZ Eindhoven, The Netherlands

*Corresponding author e-mail: herbert.zondag@tno.nl

Abstract

Several materials were selected and tested for application as high temperature PCM in the temperature range 150-300°C. Promising results in terms of stability of melting temperature and solidification heat were found for hydroquinone, pentaerythritol and tin. For the hydroxide mixture NaOH/KOH, degradation was found, but this may be related to the mixing ratio, further investigation is needed. For phthalic acid, fast degradation was found.

Keywords: PCM, process steam, industry

Introduction

In industry, large amounts of process steam are used for process heating and mechanical drive, particularly in the temperature range of 140-300°C. This steam demand can be strongly fluctuating, particularly when applied in combination with batch processing or periodic steam cleaning. To limit the required steam boiler capacity and enhance process efficiency, it can be beneficial to add heat storage in the process, that is charged when steam demand is low, and discharged when steam demand is high, allowing the steam boiler to run in a more continuous mode.

Traditionally, steam accumulators are used as buffer in a steam driven process. However, steam boilers are very bulky and have the disadvantage that the steam produced declines in temperature and pressure during the discharge. These disadvantages can be solved by applying high temperature PCM storage, using a PCM that solidifies slightly above the required steam temperature, causing the storage to be more compact while the storage temperature and pressure are more constant.

Since industrial process steam is used at different temperature levels, it is convenient to have a range of PCM materials meeting these temperature levels, while at the same time being stable and low-cost, while thermal conductivity should be sufficient to meet the required thermal power. This triggered the present investigation into high temperature phase change materials.

Methodology

The methodology consisted of three steps:

1. First, a literature search was carried out, indicating potentially interesting materials.
2. Next, the indicated materials were classified according to their chemical structure, and literature data for other materials with similar structures was found. Also, for all materials, an indicative assessment was made of the material costs per kJ of melting enthalpy, allowing us to focus on more low-cost materials. Often, such low-cost materials are materials that are produced in bulk as feedstock for the chemical industry.
3. Finally, selected materials were tested in DSC over multiple cycles, to establish characteristics such as melting point, supercooling, cyclic stability and material degradation.

Results & discussion

Literature study

For the temperature range 150-300°C, different classes of materials can be applied as PCM. Typical classes are:

1. Organic materials. In order to have sufficiently high melting points, the connection between the molecules in the organic material should be relatively strong, typically by O-H bonding. As a general rule, the larger the number of OH groups, the higher the melting temperature. Typical materials are sugar alcohols and dicarboxylic acids (having a much higher melting point than monocarboxylic acids). But also aromatic (poly)acids (e.g. phthalic acid) and their corresponding anhydrides, (poly)hydroxybenzenes (phenols) and aromatic hydroxy acids (e.g. salicylic acid) have high melting points.

- Inorganic salts, such as nitrate mixtures or hydroxide mixtures. Pure nitrate salts and pure hydroxide salts have a too high melting point, but eutectic mixtures of these materials melt at a lower temperature. However, applying a chemical mixture also tends to reduce the melting enthalpy, so testing is needed.
- Metals, such as tin and bismuth, as well as alloys of e.g. tin and lead can also be used. A point of attention is the relatively low melting heat of metals per kg, although this is partially compensated by their high density, resulting in acceptable melting heat per volume. Metals as PCM can be characterised as rather heavy and relatively costly, but with a good thermal conductivity.

Based on temperature range, costs and the scanty information available from literature on stability, a first selection was made for further testing, as shown in the table below.

Table 1: PCM materials selected for testing

PCM Material	T _{melt} (°C) (Literature)	DH _{melt} (kJ/kg) (Literature)	ref
Adipic acid	152	233	Waschull, 2009, 2010
NaOH/KOH	170	213	Kenisarin, 2010
Hydroquinone	172	225	Gil, 2014
Pentaerythritol	188	244	Ventikaraj, 2017
Phthalic acid	208	315	-
Tin (Sn)	232	59	Shamberger, 2020

Of these materials, adipic acid was already successfully tested in a previous publication (Zondag, 2022) and turned out to show promising characteristics and stable performance; these test results will not be repeated here. The other materials will be reported below.

DSC experiments

For a NaOH/KOH mixture of 50%/50%, a series of 10 DSC cycles was carried out with a gold cup with pierced lid (preliminary cycles in aluminium cup showed corrosion of the cup); the results are shown in Figure 1 and Figure 2. The melting temperature shows a slight decline of 170°C to 165°C. However, more problematic is the observation that the measured values for the melting and solidification enthalpies are much lower than the literature values and show a further decline of 12% over cycle 2 to 10. It is presently not clear what causes this difference. However, it is likely

that the determination of the mixing ratio was affected by the hygroscopic nature of the hydroxides (water take-up from the air during handling of the samples affected the measurement of the component mass), resulting in a non-eutectic composition. Due to project constraints this material was not examined further.

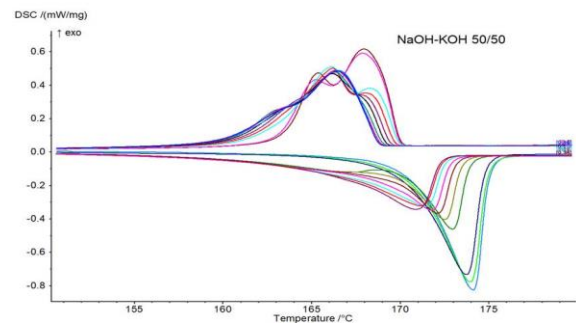


Figure 1: Cycling of NaOH/KOH mixture, pierced gold cup.

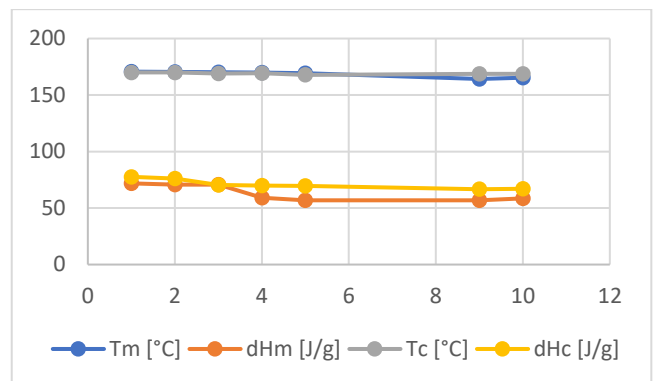


Figure 2: Cycling of NaOH/KOH mixture, pierced gold cup.

Hydroquinone was tested in DSC over 10 cycles, as shown in Figure 3 and 4. The material showed a relatively stable onset of the melting at about 167°C, as well as a very stable enthalpy on solidification of 197 kJ/kg. However, significant hysteresis was found between melt and solidification, that may require the addition of a nucleating agent.

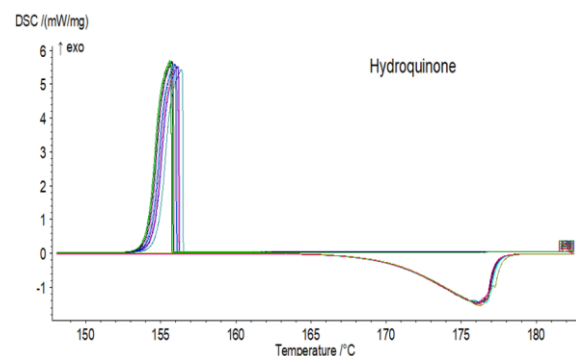


Figure 3: Cycling of hydroquinone, aluminium cup.

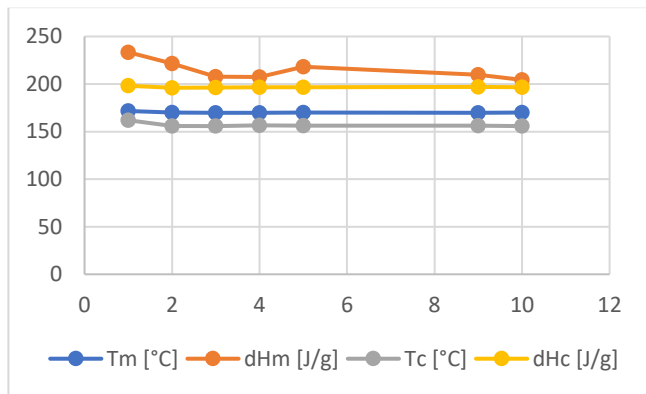


Figure 4: Cycling of hydroquinone, aluminium cup.

Pentaerythritol was tested in DSC over 10 cycles, as shown in Figure 5 and 6. The melting and solidification peaks have an unusual shape, which is probably related to the fact that this is a solid-solid transition (the only one in the present overview), affecting the recrystallization rate. Also, hysteresis was present in the phase transition. The results for the solid-solid transition show a stable melting temperature of 173°C but a slight decline in solidification enthalpy of 7.5% (from 230 kJ/kg to 212 kJ/kg) over cycle 2 to 10.

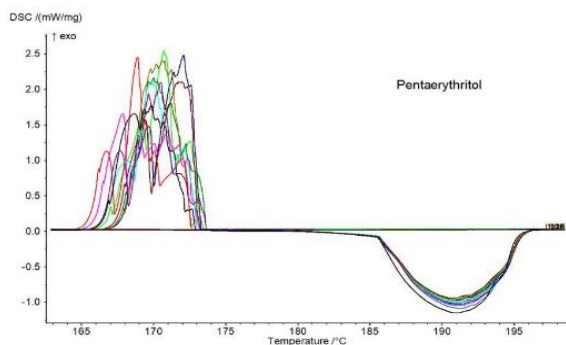


Figure 5: Cycling of pentaerythritol, aluminium cup.

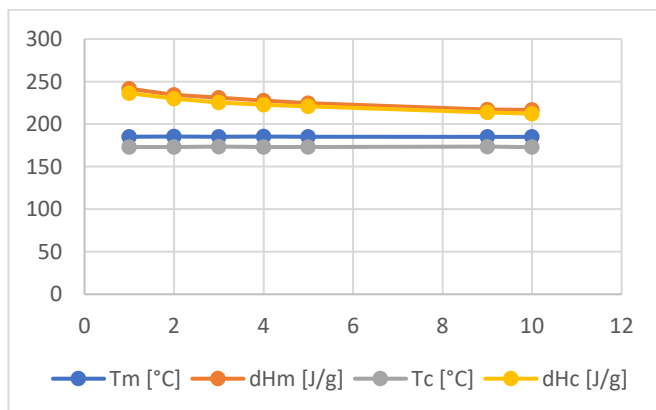


Figure 6: Cycling of pentaerythritol, aluminium cup.

In addition to the solid-solid transition of pentaerythritol, also the solid-liquid transition at 260°C was tested for use as PCM, but this showed a significant mass loss due to almost complete evaporation of the sample.

Phthalic acid was also tested in DSC, as shown in Figure 7. Unfortunately, the material very quickly degraded; after the first cycle no more melting was observed. This may be due to phthalic acid converting to phthalic anhydride at high temperature, releasing water vapor. It was hoped that the water vapor pressure built up in the cup would stop this conversion, but it turned out after the measurements that the built up pressure had caused a leak in the cup, whereby the water vapor could escape. It is hypothesised that with a better closed cup, this might be avoided, but due to project constraints, no further tests on the material were carried out.

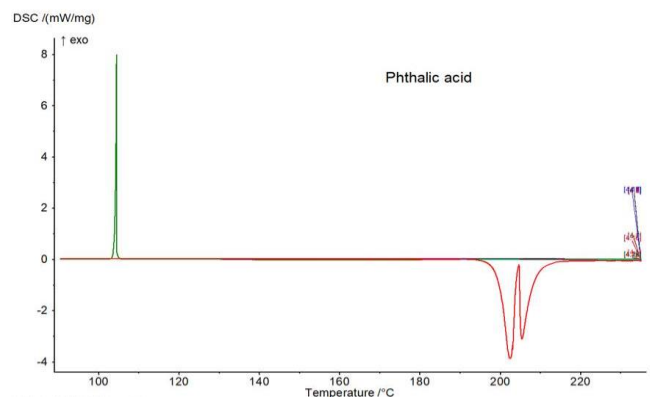


Figure 7: Cycling of phthalic acid, aluminium cup

For tin, a high purity sample was tested in DSC over 10 cycles, as shown in Figure 8 and 9. The performance of the material in terms of melting temperature and enthalpy is very stable, at respectively 232°C and 56 kJ/kg. However, a very significant supercooling was found. Possibly, this may be suppressed by nucleating additives.

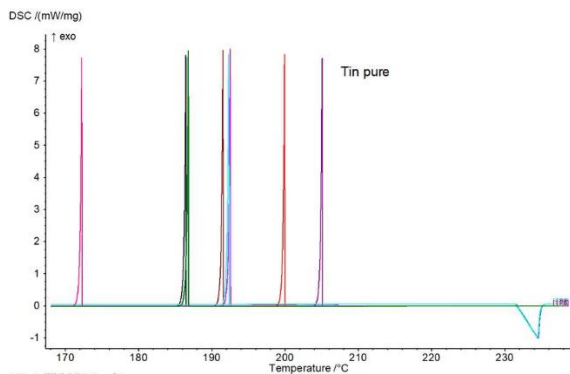


Figure 8: Cycling of tin (Sn), aluminium cup.

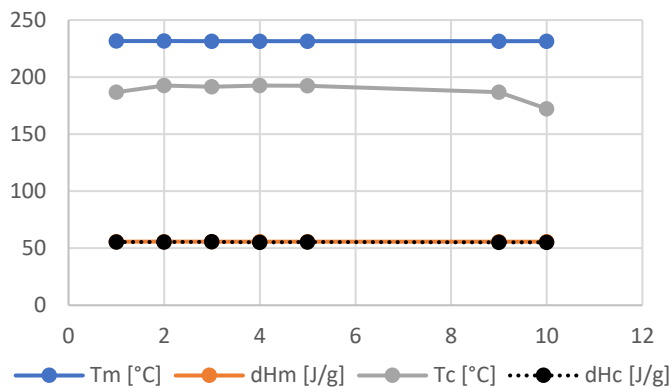


Figure 9: Cycling of tin (Sn), aluminium cup.

Conclusions

On the 5 tested PCM materials, the following conclusions are drawn:

1. NaOH/KOH: the material is rather corrosive and hygroscopic and showed a change in DSC curves, as well as a decline in melting temperature and solidification enthalpy. Also, the measured crystallization enthalpy was unexpectedly low (about 70 kJ/kg). It seems that the material is less suitable as PCM. However, the lacking stability may be related to the used ratio of NaOH/KOH; if the material is not in the eutectic composition, degradation is to be expected.
2. Hydroquinone: the material has a stable onset of the melting at about 167°C, as well as a very stable enthalpy on solidification of 197 kJ/kg. The material seems suitable as PCM.
3. Pentaerythritol: the solid-solid transition at 185°C is potentially suitable as PCM, although it shows hysteresis and some decline in enthalpy was visible over cycles. The solid-liquid transition at 260°C showed strong degradation and seems unsuitable.
4. Phthalic acid: the material showed strong degradation over repeated melting/solidification,

caused by side reactions. It is hypothesised that these might be suppressed by using a pressure tight cup, but this still needs to be confirmed.

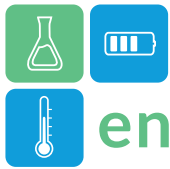
5. Tin: the melting temperature is very stable, as is the melting enthalpy. However, the very pure sample showed considerable supercooling.

Acknowledgements

This research was partially financed from the energy transition budget of the municipality of Rotterdam, subsidy Nr.: SUB.20.10.00037.SBSA. The remainder was financed with TNO SMO-funding.

References

- Gil, A., et al. (2014). Experimental analysis of hydroquinone used as phase change material (PCM) to be applied in solar cooling refrigeration, international journal of refrigeration <http://dx.doi.org/10.1016/j.ijrefrig.2013.05.013>
- Kenisarin, M.M. (2010). High-temperature phase change materials for thermal energy storage, Renewable and Sustainable Energy Reviews <https://doi.org/10.1016/j.rser.2009.11.011>
- Shamberger, P.J. and Bruno, N.M. (2020). Review of metallic phase change materials for high heat flux transient thermal management applications, Applied Energy <https://doi.org/10.1016/j.apenergy.2019.113955>
- Venkataraj, K.P. and Suresh, S. (2017). Experimental study on thermal and chemical stability of pentaerythritol blended with low melting alloy as possible PCM for latent heat storage, Experimental Thermal and Fluid Science <https://doi.org/10.1016/j.expthermflusci.2017.05.018>
- Waschull, J. et al. (2009). Investigation of Phase Change Materials for Elevated Temperatures. Proceedings from Effstock 2009, Stockholm.
- Waschull, J. et al. (2010). Development of a Heat Storage Material for Elevated Temperatures. Proceedings from Eurosun 2010, Graz.
- Zondag, H.A., et al. (2022). Testing of an industrial PCM heat storage prototype using adipic acid-graphite. Proceedings from IRES 2022, Dusseldorf.



High Temperature Thermal Energy Storage with Phase Change Materials in Concentrated Solar Power System: A Case Study

Lianying Shan^{1,*}, Tomokazu Nakamura², Takahiro Nomura², Justin Ningwei Chiu¹

¹ Department of Energy Technology, KTH Royal Institute of Technology, Brinellvägen 68, SE-10044 Stockholm, Sweden

² Faculty of Engineering, Hokkaido University, Kita 13 Nishi 8, Kita-ku, Sapporo 060-8628, Japan

*Corresponding author e-mail: lianying@kth.se

Abstract

Thermal energy Storage has received widespread attention for its role in integrating variable solar energy. Latent heat thermal energy storage with phase change materials (PCMs) is regarded as a promising technology. In this study, two novel metal-based microencapsulated PCMs with melting temperatures of 577 °C and 520 °C are analysed for their application in the 650 °C next-generation solar power plant. Five storage units with different Al-Si to Al-Cu-Si volume ratios (1:0, 0:1, 1:1, 2:1) and height/diameter ratios (3:2, 2:3) are designed and benchmarked under the actual operating conditions, with the charge and discharge cut-off temperatures set for the return loop at 376 °C and 456 °C. The results show that the case with single Al-Si PCM leads to higher average outlet temperature, which is good for steam generation, while the case with single Al-Cu-Si PCM shows higher storage capacity. The thermal performance of the cascaded models with two PCMs exhibit a compromise between high outlet temperature and high storage capacity. The height/diameter ratio of 3:2 shows the best performance considering outlet temperature and stored heat capacity.

Keywords: Thermal Energy Storage, Phase Change Material, High Temperature Application, Thermal Performance

1. Introduction

With the expanding integration of solar energy in the electricity grid, it is necessary to alleviate the disadvantage of solar intermittency for a reliable power system (Achhari and El Fadar 2020; Bashiri Mousavi et al. 2021). Thermal energy storage (TES) is considered as a promising technology that can be implemented in Concentrated Solar Power (CSP) plants to improve dispatchability and cycle efficiency (Mostafavi Tehrani et al. 2019; Shen, Mazhar, and Liu 2022).

In order to increase the efficiency and to have a better performance, Kolb (2011) proposed a 650 °C next-generation solar power tower with ultra-supercritical Rankine cycle. Latent heat thermal energy storage (LHTES) has attracted much attention due to the high energy density of phase change material (PCM) and single-tank configuration. Nomura et al. (2017, 2019) developed a metal-based micro-encapsulated phase change material (MEPCM) with Al-25wt%Si as core and Al₂O₃ as the shell. The MEPCM with a melting point of 577 °C can be a potential storage material for the next-generation high temperature TES with lower corrosion characteristics as compared to salt-based PCMs. Tiwari et al. (2021) designed a shell-and-tube

LHTES with Al-12wt%Si as PCM and SaltStream-700 as heat transfer fluid (HTF) for the next-generation 650 °C solar power tower plants. They investigated the performance of the system under actual operating conditions with cut-off temperatures and different geometric parameters and HTF flow rates.

There are limited references to commercially available PCMs. In this study, two novel metal-based MEPCMs developed by Hokkaido University are evaluated as potential candidates. They are placed in cylindrical tank as high temperature thermal energy storage materials for the next-generation 650 °C CSP.

2. Methodology

The thermal performance of the MEPCMs in a packed bed is analysed with COMSOL 6.0 in this work.

2.1 Thermophysical Properties

In this study, two aluminium-based metal alloys with spherical microencapsulation and Al₂O₃ shell are chosen as the PCMs. A closed void inside the PCM core allows volume expansion during phase change processes, accounting for 0.5% of the volume of the spherical encapsulation (Nomura et al. 2017). One of the PCMs (Al-Si) is composed of 75 wt% Al and 25 wt% Si with melting temperature of 577 °C. The other PCM (Al-Cu-Si) is a ternary alloy with melting

temperature of 520 °C consisting of 68.1 wt% Al, 26.5 wt% Cu and 5.4 wt% Si. An improved sodium hydroxide (NaOH) (Hyme Energy ApS n.d.) is chosen as the HTF in this study. The melting point of NaOH is 318 °C with the maximum operating temperature up to 700 °C. The thermophysical properties of these two PCMs and HTF are summarized in Table 1.

Table 1: Thermophysical properties of PCMs and HTF

Properties	Al-Si	Al-Cu-Si	NaOH
Diameter [mm]	10	10	
Density [kg/m ³]	1850	3640	2100
Melting temperature [°C]	577	520	318
Melting temperature interval [°C]	10	18	
Solidification temperature [°C]	542	513	
Solidification temperature interval [°C]	16	32	
Latent heat [J/g]	253.9	177.5	
Thermal conductivity in solid phase [W/(m·K)]	1.60	2.35	1.10
Thermal conductivity in liquid phase [W/(m·K)]	2.36	2.35	
Heat capacity in solid phase [J/(kg·K)]	1177	1050	
Heat capacity in liquid phase [J/(kg·K)]	2265	1450	2100

2.2 Thermal Storage Unit

Two-dimensional axisymmetric model with PCM packed in a cylindrical tank is performed in this study. The layouts of a single model and a cascaded model are exhibited in Figure 1. The packed bed porosity is set as 0.4.

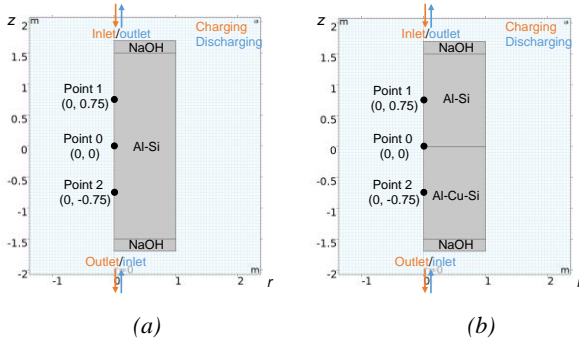


Figure 1: Layouts of LHTES tanks: (a) single-PCM model, Case 1; (b) cascaded model, Case 3

In this study, five cases with different volume ratios of Al-Si to Al-Cu-Si and height/diameter (H/D) ratios are considered:

1. Case 1: single Al-Si (volume ratio 1:0) with H/D of 3:2;
2. Case 2: single Al-Cu-Si (volume ratio 0:1) with H/D of 3:2;
3. Case 3: volume ratio of 1:1 with H/D of 3:2;
4. Case 4: volume ratio of 2:1 with H/D of 3:2;
5. Case 5: volume ratio of 1:1 with H/D of 2:3.

The thermal power of the PCM storage is calculated with the temperature variations of HTF at the inlet and outlet as shown in Eq. (1). By time integrating Eq. (1), the stored and released heat can be calculated.

$$\dot{q} = \dot{m}c_{pf}(T_{in} - T_{out}) \quad (1)$$

where \dot{q} is the heat storage or release rate, [W]; \dot{m} is the mass flow rate of HTF, [kg/s]; T_{in} and T_{out} are the inlet and outlet temperature of HTF, respectively, [K].

Dimensionless thermocline thickness (ξ) in Eq. (2) is used to evaluate the designed storage tank. The thermocline thickness (z_{tt}) are the height with dimensionless temperature difference (δ) in the range of $0.15 < \delta < 0.85$ (Musser and Bahnfleth 2001), as shown in Eq. (3).

$$\xi = z_{tt}/H \quad (2)$$

$$\delta = [T(z) - T_{dis,in}]/(T_{ch,in} - T_{dis,in}) \quad (3)$$

where H is the height of the PCM domain, [m]; $T(z)$ is the temperature at height of z , [K]; $T_{ch,in}$ is the inlet temperature during charge, [K]; $T_{dis,in}$ is the inlet temperature during discharge, [K].

2.3 Governing Equations

The packed bed materials can be seen as porous media, composed of PCM (solid) and HTF (fluid). The flow of HTF is governed by non-Darcian Ergun equation. The model is based on local non-equilibrium heat transfer mechanism. The governing equations for energy conservation are shown in Eq. (4)-Eq. (7).

$$\theta_s \rho_s c_{ps} (\partial T_s / \partial t) + \nabla \cdot \mathbf{q}_s = q_{sf} (T_f - T_s) + \theta_s Q_s \quad (4)$$

$$\mathbf{q}_s = -\theta_s k_s \nabla T_s \quad (5)$$

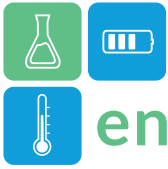
$$\varepsilon_p \rho_f c_{pf} (\partial T_f / \partial t) + \rho_f c_{pf} \mathbf{u} \cdot \nabla T_f + \nabla \cdot \mathbf{q}_f = q_{sf} (T_s - T_f) + \varepsilon_p Q_f \quad (6)$$

$$\mathbf{q}_f = -\varepsilon_p k_f \nabla T_f \quad (7)$$

where θ_s is the PCM volume fraction; ε_p is the porosity; ρ_s and ρ_f are the densities of PCM and HTF, [kg/m³]; c_{ps} and c_{pf} are the specific heat capacities of PCM and HTF at constant pressure, [J/(kgK)]; T_s and T_f are the temperatures of PCM and HTF, [K]; \mathbf{q}_s and \mathbf{q}_f are the conductive heat fluxes of PCM and HTF, [W/m²]; k_s and k_f are the thermal conductivities of PCM and HTF, [W/(mK)]; q_{sf} is the interstitial convective heat transfer coefficient, [W/(m³K)]; Q_s and Q_f are the heat sources of PCM and HTF, [W/m³].

2.4 Boundary Conditions

In this work, the cut-off temperatures of the HTF at the outlets, which are 376 °C for charging process and 456 °C for discharging process, are applied to simulate the actual operation, as proposed in (Tiwari et al. 2021).



The ambient temperature is set as 25 °C and the maximum charging time is set to 14 h. The remaining 10 h in a day are used for discharge.

The initial temperature of the storage unit is set to 325 °C at the first charge cycle to ensure liquid state of the HTF. The inlet temperature of the HTF is 650 °C with mass flow rate of 1 kg/s (flow through time of 10556 s). The charging process stops when the outlet temperature of the HTF reaches 376 °C. After reaching the cut-off temperature, the inlet and the outlet become adiabatic, and no HTF flows in or out. During discharge, the initial conditions are taken from the end of previous charge at 14 h. The HTF flows from the bottom with the same mass flow rate and is set at 336 °C. The discharging process stops when the outlet temperature drops to 456 °C. Same as in the first charge cycle, there is no inflow or outflow of the HTF after cut-off. This completes the first 24-hour cycle. The initial condition of the second charge is the end of the first discharge at 24 h.

The numerical model is run with the following assumptions:

1. The PCMs are homogenous and isotropic;
2. NaOH as the HTF is considered as incompressible;
3. There is no heat loss through the shell;
4. For spherical pellet packed bed, the interstitial heat transfer coefficient (h_{sf}) between PCM and HTF is estimated with the correlation in Eq. (8).

$$h_{sf} = [d_p/(k_f Nu) + d_p/(\beta k_s)]^{-1} \quad (8)$$

where d_p is the diameter of pellet, [m]; Nu is the Nusselt number; β is a constant with $\beta = 10$ for spherical particles.

3. Results and Discussion

The sensitivity of mesh and time step are performed. Considering the calculation precision and calculation time, the mesh elements of 21600 (mesh quality of 1 due to conformity of mesh to model geometry) and the maximum time step of 6 s are chosen. In this section, the thermal performance of three charge/discharge cycles for the five cases are simulated and compared. The negative value of heat means heat release during discharge.

3.1 Single-PCM to Cascaded-PCM Performance

The simulation results of the three cycles in single-PCM model Case 1 are shown in Figure 2 and Figure 3. Focusing on the third cycle, the third charging process stops at 52.3 h with heat storage of 10.1 GJ. The PCM at point 1 (T_{s1}) is completely melted and the latent heat fully utilized. While point 0 and point 2 are still in mushy state or solid phase. The overall liquid fraction at cut-off is 0.39, increasing to 0.42 at the end

of the charge cycle at 62 h due to heat transfer in idling between 52.3h and 62 h. During the third discharge, the heat release stops at 68.04 h with all the PCM entirely solidified. The volume average temperature is 336.4 °C with heat release of 12.0 GJ.

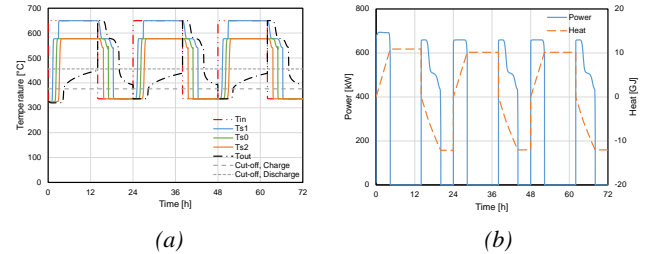


Figure 2: Three cycles of Case 1: (a) temperature; (b) power and heat

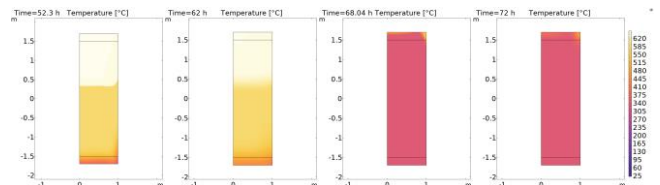


Figure 3: Temperature distribution of Case 1

Figure 4 and Figure 5 display the simulation results of cascaded model Case 3. The third cycle stops at 52.88 h for charge with heat storage of 11.5 GJ. The liquid fraction of Al-Si is 0.89 and most of the Al-Si has melted, while the liquid fraction of Al-Cu-Si is only 0.33. The discharge process stops at 68.72 h with heat release of 12.9 GJ. Same as in Case 1, all the PCM has solidified.

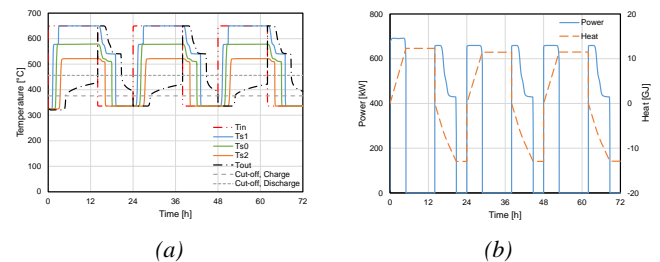


Figure 4: Three cycles of Case 3: (a) temperature; (b) power and heat

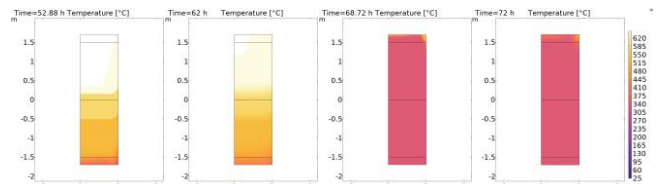


Figure 5: Temperature distribution of Case 3

3.2 Sensitivity Analysis

The temperature difference with different PCM volume ratios and H/D ratios are shown in Figure 6. Ignoring the idling after cut-off, the outlet temperature variation of charge process has no significant difference among the five cases except for the cut-off time.



During the discharge process, at beginning, case 2 maintains a higher temperature (>640 °C) for the longest time of 2.9 h (max 53% longer), but it is also the one with the fastest temperature drop after that. These is due to the higher heat storage capacity and lower freezing temperature. Case 1, Case 3~Case 5 have almost the same temperature trend during the first half of the discharge period. While Case 1 has the highest outlet temperature from 60% to 98% discharge period due to only Al-Si, followed by Case 4.

During the full discharge cycle, Figure 6 shows that Case 1 has the highest average outlet temperature of 599.2 °C, followed by Case 4 of 593.1 °C, while Case 2 has the lowest of 574.3 °C. The average outlet temperatures between five cases are Case1>Case4>Case3>Case5>Case2.

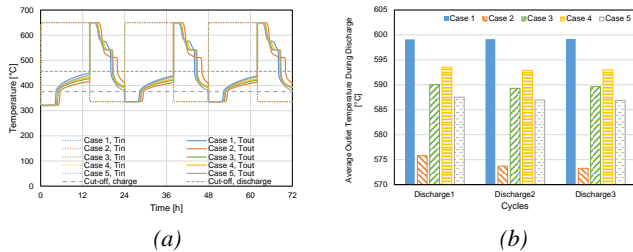


Figure 6: Temperature: (a) inlet and outlet temperature variation; (b) Average outlet temperature during discharge

Considering the heat storage or heat release capacity, Figure 7 (a) displays the capacity of five cases. It can be seen that Case 2 has the highest heat capacity, 24% higher than the lowest Case 1. Although Al-Si has larger latent heat, its density is smaller. With the same volume, Al-Cu-Si has higher theoretical heat capacity than Al-Si. Due to this, the heat capacity of Case 3 is 3% higher than Case 4.

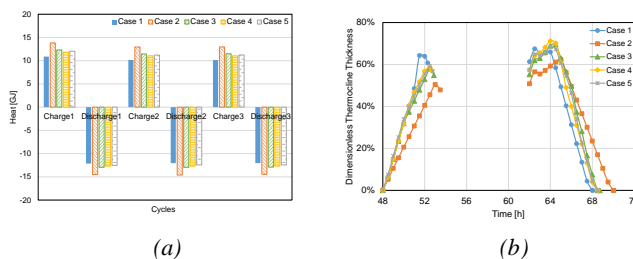


Figure 7: Heat and thermocline: (a) heat capacity; (b) dimensionless thermocline thickness

The dimensionless thermocline thickness variation of the third cycle is shown in Figure 7 (b). During charging process, Case 2 has the smallest dimensionless thermocline thickness, which is 0~50% of the PCM domain height, while the other cases have similar variation till 51 h. After that, the thermocline of Case 2 is the largest. During discharging process, Case 2 has the smallest dimensionless thermocline thickness

of 51%~59% of the PCM domain height during the first quarter of discharge period, while it becomes the largest in the second half of the discharge. Case 1 performs better in the second half with the smallest thermocline thickness. Case 3~Case 5 show similar trends.

4. Conclusions

In this study, the thermal performance of five storage unit designs with different Al-Si to Al-Cu-Si ratios and H/D ratios have been analysed. The results show that single Al-Si PCM (Case 1) has the highest average outlet temperature, 24.9 °C higher than single Al-Cu-Si (Case 2). Case 2 shows higher Al-Cu-Si mass, leading to higher storage heat capacity. The cascaded design shows thermal performance in between Case 1 and Case 2. Considering the effect of H/D ratio, the average outlet temperature of higher H/D ratio (Case 3) is 2.5 °C higher than lower H/D ratio (Case 5), and Case 3 shows a slightly larger heat capacity as compared to Case 5.

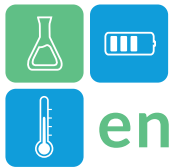
For further work, the impact of hysteresis on the thermal performance should be considered. An optimal design of storage unit can then be implemented.

Acknowledgment

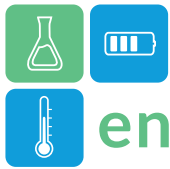
Lianying Shan would like to express her gratitude to the China Scholarship Council (CSC) and the Karl Engvers Foundation for the doctoral funding. This paper is based on results obtained from a project, JPNP20005, subsidized by the New Energy and Industrial Technology Development Organization (NEDO).

References

- Achkari, O., and A. El Fadar. 2020. "Latest Developments on TES and CSP Technologies – Energy and Environmental Issues, Applications and Research Trends." *Applied Thermal Engineering* 167(October 2018):114806. doi: 10.1016/j.applthermaleng.2019.114806.
- Bashiri Mousavi, Shadi, Mahdiah Adib, M. Soltani, Amir Reza Razmi, and Jatin Nathwani. 2021. "Transient Thermodynamic Modeling and Economic Analysis of an Adiabatic Compressed Air Energy Storage (A-CAES) Based on Cascade Packed Bed Thermal Energy Storage with Encapsulated Phase Change Materials." *Energy Conversion and Management* 243(January):114379. doi: 10.1016/j.enconman.2021.114379.
- Hyme Energy ApS. n.d. "New Molten Salt Storage for the Energy Transition." Retrieved



- (<https://www.hyme.energy/technology>).
- Kolb, Gregory. 2011. *An Evaluation of Possible Next-Generation High Temperature Molten-Salt Power Towers*. Albuquerque, NM, and Livermore, CA (United States): Sandia National Laboratories. doi: 10.2172/1035342.
- Mostafavi Tehrani, S. Saeed, Yashar Shoraka, Karthik Nithyanandam, and Robert A. Taylor. 2019. “Shell-and-Tube or Packed Bed Thermal Energy Storage Systems Integrated with a Concentrated Solar Power: A Techno-Economic Comparison of Sensible and Latent Heat Systems.” *Applied Energy* 238(January):887–910. doi: 10.1016/j.apenergy.2019.01.119.
- Musser, A., and W. P. Bahnfleth. 2001. “Parametric Study of Charging Inlet Diffuser Performance in Stratified Chilled Water Storage Tanks with Radial Diffusers: Part 1—Model Development and Validation.” *HVAC and R Research* 7(1):31–49. doi: 10.1080/10789669.2001.10391428.
- Nomura, Takahiro, Nan Sheng, Chunyu Zhu, Genki Saito, Daiki Hanzaki, Takehito Hiraki, and Tomohiro Akiyama. 2017. “Microencapsulated Phase Change Materials with High Heat Capacity and High Cyclic Durability for High-Temperature Thermal Energy Storage and Transportation.” *Applied Energy* 188:9–18. doi: 10.1016/j.apenergy.2016.11.025.
- Nomura, Takahiro, Julalak Yoolerd, Nan Sheng, Hiroki Sakai, Yuta Hasegawa, Miki Haga, and Tomohiro Akiyama. 2019. “Al/Al₂O₃ Core/Shell Microencapsulated Phase Change Material for High-Temperature Applications.” *Solar Energy Materials and Solar Cells* 193(November 2018):281–86. doi: 10.1016/j.solmat.2018.12.023.
- Shen, Yongliang, Abdur Rehman Mazhar, and Shuli Liu. 2022. “Comprehensive Review on Cascaded Latent Heat Storage Technology: Recent Advances and Challenges.” *Journal of Energy Storage* 55(PD):105713. doi: 10.1016/j.est.2022.105713.
- Tiwari, Vivek, Aakash C. Rai, and P. Srinivasan. 2021. “Parametric Analysis and Optimization of a Latent Heat Thermal Energy Storage System for Concentrated Solar Power Plants under Realistic Operating Conditions.” *Renewable Energy* 174:305–19. doi: 10.1016/j.renene.2021.04.073.



Highly Accurate Simulation of the Flow Effects during Loading with Swirl

Felix Oestreich¹, Thorsten Urbaneck^{1,*}

¹ University of Technology Chemnitz, Department of Mechanical Engineering, Professorship of Applied Thermodynamics, Reichenhainer Straße 70, Chemnitz, Germany

*Corresponding author e-mail: thorsten.urbaneck@mb.tu-chemnitz.de

Abstract

The use of thermal energy storage in the district heating supply increases system efficiency. In the district heating supply, so-called slim hot water storage tanks can achieve this goal. This requires efficient storage tanks with low internal and external losses. Due to the special storage tank geometry, disadvantageous flow effects (e.g. wall flow) occur during loading (high internal losses). To overcome these fluid mechanical challenges, Platzer and al. (2023) propose swirl loading. This causes the loading fluid to enter the storage tank in a rotating manner. The flow changes fundamentally. This is where this article comes in. A storage tank is modeled and simulated by numerical flow simulation CFD with Ansys CFX. As a result, the vortex flows in the diffuser (e.g. longitudinal, transverse and Görtler vortices) become visible for the first time. The storage simulation shows the transient development of thermal stratification with vortex effects (e.g. Kelvin-Helmholtz vortices, head-nose structure, free shear layers).

Keywords: Thermal energy storage, loading, radial diffuser with guiding elements, swirl, CFD, LES

Introduction

A massive expansion of the district heating supply is necessary to achieve the European climate targets. This often involves the use of generators that supply electricity and heat, e.g. motorized combined heat and power plants. Waste heat is generated here during electricity-led operation. This can be stored using thermal energy storage systems and later made available to the district heating network (increased efficiency, decoupling of generation and demand). This function is realized in the district heating supply by so-called slim hot water storage tanks (dished bottom according to DIN (2012), slim design, pressure vessel up to 20 bar, operating temperature up to 200 °C, production in the factory (storage tank type b1, Urbaneck 2020)). The advantages mentioned above require efficient storage tank operation (low internal and external storage losses). This article deals with the minimization of internal losses by improving the thermal stratification behaviour. Thermal stratification with the narrowest possible transition area between the hot and cold zones is an indicator of low mixing processes during loading. Minimizing these mixing processes during loading plays a key role in minimizing internal storage losses. Lohse (2012) and Brähmer (2012) investigated loading with conventional radial diffusers in slender hot water storage tanks using numerical flow simulation. The

work identifies disadvantageous flow effects due to the slim storage tank shape, such as a pronounced wall jet. This wall jet stimulates mixing processes and thus increases the internal storage losses. To overcome this flow problem, Platzer and al. (2023) suggest loading with swirl. The investigations by Oestreich and al. (2022) showed the flow behavior in the diffuser and in the storage tank, the effects on thermal stratification and the advantages. This article is intended to provide a more detailed description of the flow processes. This knowledge is essential in order to better understand the causes and effects of swirl loading and the build-up of thermal stratification.

Methodology

The modeling and simulation of the flow and heat transfer of a 360° diffuser model, a single guiding channel and a storage segment is carried out with Ansys CFX (Ansys, 2019). The turbulence is modeled using the coarse structure simulation approach (Nicoud, 1999). This calculates large vortices and models small vortices. The computational domain and important boundary conditions are shown in Figure 1.

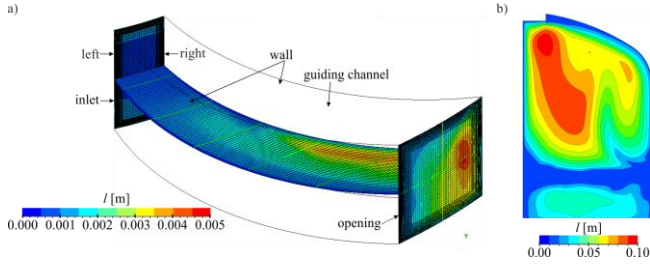


Figure 1: Turbulent integral length scale for a) single guiding channel with boundary conditions, b) storage (centred on the X-axis)

The integral turbulent length scale Eq. (1) provides information on the size of the vortices and computational cells. The Courant number Eq. (2) and Peclet number Eq. (3) are used to assess the grid quality and convergence behavior of the solution (Ferziger, 2019, Ansys, 2011).

$$l = C_{\mu}^{3/4} \frac{k^{3/2}}{\epsilon} \quad (1)$$

$$Cr = \frac{U \cdot \Delta t}{X} \quad (2)$$

$$Pe = \frac{U \cdot X}{\alpha_w} \quad (3)$$

The Q -criterion Eq. (4) is used to represent the turbulent structures (Ansys, 2011).

$$Q = C_Q \cdot (\Omega^2 - S^2) \quad (4)$$

Results and Discussion

The flow effects in the diffuser are shown in Figure 2. Due to the reflection of the inlet flow on the upper diffuser plate, the behavior changes from laminar to turbulent. The impact creates a dust area on the upper diffuser plate (Figure 1 top right, blue). Screw structures are visible in the guiding channels (Figure 1 bottom right)

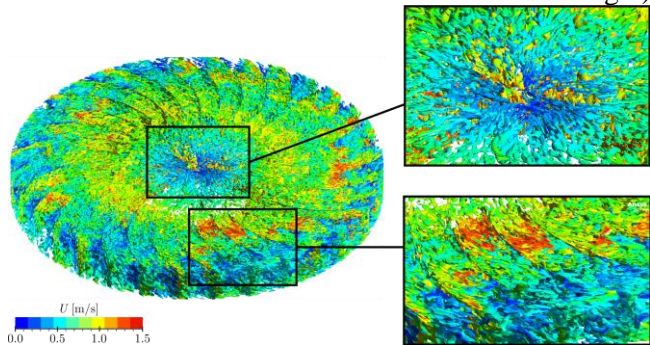


Figure 2: Flow effects in the radial diffuser with internal elements visualised with the Q -criterion (400 s^{-2}) and coloured according

to the magnitude of the velocity (isometric view), detailed view top right: flow at the upper diffuser plate, bottom right: guiding channel with outflow

The flow effects in the guiding channel are shown in Figure 2. The friction between the fluid and the concave curved wall causes Görtler vortices (G) (Saric 1994). The effect of a centrifugal force excites so-called transverse vortices (Q) in the center of the guiding channel. These are more energetic than the Görtler vortex. The main flow pushes the cross vortex out of the guiding channel. A pressure gradient is created away from the concave curved wall. Longitudinal vortices (L) are formed there, which flow back into the guiding channel. The vortex effects mentioned occur simultaneously and influence each other. As a result, the vortices form so-called helical structures (HP).

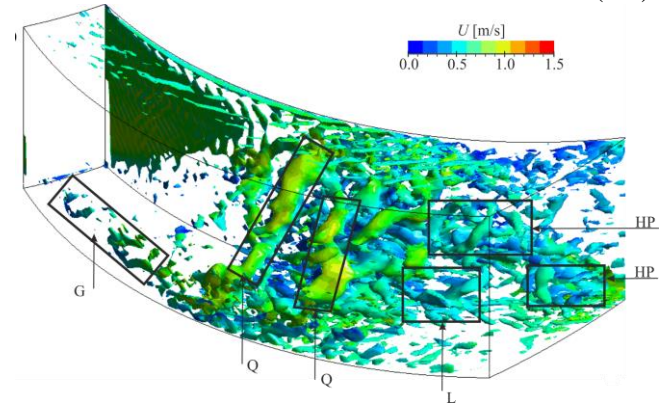


Figure 3: Flow effects in a representative guiding channel visualised with the Q -criterion ($Q = 1400 \text{ s}^{-2}$) and coloured according to the magnitude of the velocity, significant flow effects

are marked with *G...* Görtler vortex, *Q...* cross vortex, *L...* longitudinal vortex, *HP...* Helical Pairing

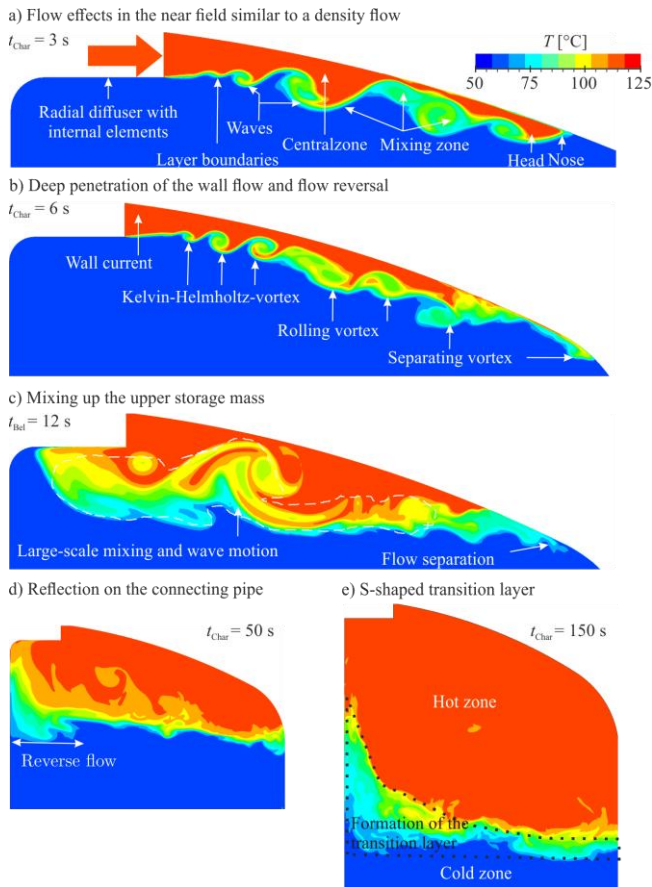


Figure 4: Flow effects during swirl loading in the slim hot water tank with dished bottom at different times with significant flow effects

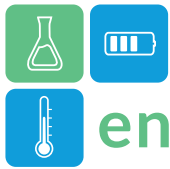
The flow in the storage is shown in Figure 4. The charging fluid is fed into the storage. The buoyancy forces act due to the density differences. As a result, the flow is directed towards the top of the storage tank. Due to the swirl flow, a red area forms over the diffuser height near the diffuser outlet (Figure 4 a)). This is not the case with conventional radial diffusers. Vortices roll up at the layer boundary as a result of shear forces. The radial velocity component causes the flow to advance at the top of the storage. A higher head is formed there compared to the leading nose. This behavior is known from density flows in cold water storage tanks (Urbanek 2009). Here, the head-nose formation occurs in reverse (horizontally mirrored) to the density flow in flat-bottom tanks. The occurrence of the so-called Lap-Gap-Structure cannot be clearly demonstrated. This is probably due to the high velocity of the wall jet, which closes the gap quickly. Shorter evaluation intervals in the simulation are necessary for the detection to be successful. After 6 s, Kelvin-Helmholtz vortices are formed in the free shear layers (Figure 4 b)). The resolution of these

instabilities confirms the high quality of the computational grid. In the wake of the flow, further vortices detach. The radial velocity component ensures that the flow penetrates deep into the storage chamber. In Figure 4 c), the flow along the tank wall comes to a standstill due to the buoyancy force. Vertical penetration is then not possible. The charging fluid is deflected horizontally. Due to the temperature difference, it undergoes vertical acceleration. The flow then penetrates into the center of the tank. This process is associated with strong mixing effects. The intensity is shown in Figure 4 c), as heavier or colder areas lie above lighter, warmer areas. Wave movements are the result. The mixing effects and undulations increase with increasing operating variables (volume flow, temperature). At the end of this phase, the mixing area extends to the connecting pipe (Figure 4 d)). There, reflection occurs again in conjunction with mixing effects. After 150 s, an S-shaped transition layer forms (Figure 4 e)). This is typical for loading with swirl. When the rotation of the storage mass no longer has any influence, the transition layer flattens out into a straight line. Further vortices form at the lower end of the boundary layer.

Conclusions

Slim hot water storage tanks with dished ends play a key role in increasing the efficiency of district heating networks, among other things. This requires high storage efficiency. This demands a narrow transition layer with low internal losses during loading. Oestreich and al. (2022) showed that swirl loading can make a significant contribution. The detailed description of the flow effects of swirl loading in the radial diffuser with guiding elements and in the storage tank has not yet been clarified. This article closes this gap.

The investigations are carried out using numerical flow simulation with Ansys CFX. LES is used to model the turbulence. Due to the demanding flow in the storage tank (temperature, volume flow), increased discretization effort is required. The Peclet and Courant numbers as well as the integral turbulent length scale were to be taken into account when creating the model. As a result, longitudinal, transverse and Görtler vortices in the guiding channel could be identified for the first time. The storage simulation shows a similar behavior of a density flow with a pronounced head-nose structure, Kelvin-Helmholtz vortices and free shear layers. The results confirm the previous work and extend it significantly. Future work should clarify the characteristics of the flow effects shown with variable operating variables.



Acknowledgment

The underlying collaborative project is funded by the Federal Ministry of Education and Research (BMBF) under the number 03SF0623A/B/C on the basis of a resolution of the German Bundestag. Project management is carried out by the Project Management Organisation Jülich (PtJ). The responsibility for the content of this publication lies with the authors.

The authors gratefully acknowledge the GWK support for funding this project by providing computing time through the Center for Information Services and HPC (ZIH) at TU Dresden.

Nomenclature

Constant	C_Q	-
Constant	C_μ	-
Coordinate	X, Y, Z	m
Courant number	Cr	-
Height	h	m
Peclet number	Pe	-
Pressure	p	Pa
Q-criterion	Q	1 s^{-2}
Shear rate	S	1 s^{-1}
Temperature	T	$^\circ\text{C}$
Thermal conductivity	α	$\text{m}^2 \text{ s}^{-1}$
Time	t	s
Turbulent dissipation rate	ε	$\text{m}^2 \text{ s}^{-2}$
Turbulent kinetic energy	k	$\text{m}^2 \text{ s}^{-2}$
Turbulent length scale	l	m
Velocity	U	m s^{-1}
Vorticity	Ω	1 s^{-2}

References

ANSYS, Inc.: ANSYS CFX-Solver Theory Guide. Release 14.0. 2011.

ANSYS, Inc.: ANSYS CFX 2019 R2. Canonsburg (USA), 2019.

Brähler, C., Urbaneck, T., Lohse, R.: Influence of Geometry and Operation Parameters on Thermal Stratification. *Euro Heat and Power* 4 (2012), pp. 30–36. ISSN: 1630-

0200.

DIN 28011:2012-06: Gewölbte Böden - Klöpperform. Berlin. Beuth Verlag, 2012.

Ferziger, J., Peric, M.: *Computational Methods for Fluid Dynamics*. 4th Edit. Springer, Cham, 2019. ISBN: 978-3-319-99693-6. DOI: <https://doi.org/10.1007/978-3-319-99693-6>.

Lohse, R., Urbaneck, T., Brämer, C., Platzer, B. Effects during loading of hot water storages with a high aspect ratio *EuroHeat&Power*, English Edition VWEW Energieverlag Vol. 9, Issue 3 (2012). pp. 42–47. ISSN 1613-0200.

Nicoud, F., Ducros, F.: Subgrid-Scale Stress Modelling Based on the Square of the Velocity Gradient Tensor. *Flow Turbulence and Combustion* 62 (Sep.1999), pp. 183–200. DOI: 10.1023/A:1009995426001.

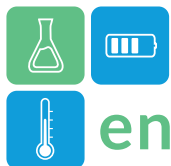
Oestreich, F., Urbaneck, T.: Loading Slim Hot Water Tanks With and Without Swirl Generation – First Results. In: *Proceedings of EuroSun 2022 – ISES and IEA SHC 14th International Conference on Solar Energy for Buildings and Industry*. International Solar Energy Society (Hrsg.). Kassel, 2022, Tagungsband, S. 1384–1395, 2023, review. – ISBN 978-3-982 0408-8-2. doi: 10.18086/eurosun.2022.08.08. url: <http://proceedings.ises.org>.

Platzer, B.; Findeisen, F.; Urbaneck, T.; Winkler, T.: Verfahren und Vorrichtung zum Be- und/oder Entladen eines thermische Energiespeichers. Europäisches Patent, EP37044, erteilt am 07.06.2023.

Saric, W. S.: Görtler Vortices. *Annual Review of Fluid Mechanics* 26:1, pp. 379–409 (1994).

Urbaneck, T., Möller, H.; Kressner, T.; Platzer, B.: Kaltwasserspeicher mit radialen Diffusoren. Teil 2a: Schichtungsaufbau im Nahfeld - Grundlagen, Physik, Simulation. *HLH* Vol. 60, Issue 6 (2009), pp. 32–36.

Urbaneck, T.: Water Tank Stores for Medium/Large Application. In: *Reference Collection in Earth Systems and Environmental Sciences*, Elsevier (2020). ISBN: 9780124095489.



IMPROVED THERMOPHYSICAL AND MECHANICAL PROPERTIES IN LiNaSO_4 COMPOSITES FOR THERMAL ENERGY STORAGE

Maria Taeño^{1*}, Ariba Adnan¹, Cristina Luengo¹, Ángel Serrano¹, Jean-Luc Dauvergne¹, Paola Crocomo¹, Ali Huertas¹, Stefania Doppiu¹ and Elena Palomo del Barrio^{1,2}

¹ Center for Cooperative Research on Alternative Energies (CIC energiGUNE), Basque Research and Technology Alliance (BRTA), Alava Technology Park, Albert Einstein 48, 01510 Vitoria-Gasteiz, Spain

² Ikerbasque, Basque Foundation for Science, 48013 Bilbao, Spain

*Corresponding author e-mail: mtaeno@cicenergigune.com

Abstract

In order to enhance the mechanical properties of the LiNaSO_4 compound, composites comprising MgO and expanded graphite (EG) as dispersed phases and LiNaSO_4 as matrix, have been prepared through a simple ball milling process. The characteristic microstructure of MgO and the high degree of crystallization of EG, confers to the composites a mechanical stability which lead to an increase in the Young's modulus (almost three times higher) compared to the pure LiNaSO_4 . These materials are proposed as suitable candidates for thermal energy storage applications at high temperatures (400-550 °C). The addition of 5 wt.% of MgO or 5% of EG had a small influence on the solid-solid phase change temperature and enthalpy, however other thermal properties such as the specific heat capacity was increased, opening the field of application of these materials.

Keywords: solid-solid PCMs, mechanical properties, thermal energy storage, MgO, EG600

Introduction

The exploration of phase-change materials (PCMs) for thermal energy storage has been a subject of extensive research in recent decades (1-3). Compared to sensible heat storage, PCMs offer advantages such as higher energy density at nearly constant temperature, with cost-effective solutions compared to thermochemical storage (6-8). Solid-liquid PCMs, undergoing melting/solidification, have been widely used due to their high phase change enthalpy, although they face challenges such as leakage and low thermal conductivity that leads to expensive heat exchanger or macro-encapsulation solutions. In contrast, solid-solid PCMs present an opportunity of reducing the cost of the storage system by eliminating the need for macro-encapsulation or heat exchangers. Comprehensive reviews of solid-solid PCMs can be found in recent works by Fallahi and al. (9) and Usman and al. (10.) An ideal solid-solid PCM must exhibit not only high phase transition enthalpy and thermal conductivity but also stability during heating/cooling cycles, compatibility with heat transfer fluid, and mechanical stability. In this regard, LiNaSO_4 -based solid-solid transitions have shown great potential for thermal energy storage applications at high-temperature (10-12). However, despite reported thermal properties

such as transition enthalpy, specific heat capacity, thermal conductivity, and thermal expansion, the mechanical behavior, and the efforts to improve the thermophysical properties have not been thoroughly explored. The addition of conductive nanostructures, such as magnesium oxide (MgO), aluminum oxide (Al_2O_3), copper (Cu), copper oxide (CuO), gold (Au), silver (Ag), titanium oxide (TiO_2), zinc oxide (ZnO), or expanded graphite (EG), has been widely investigated in the past to improve thermal conductivity in inorganic PCMs (13-17). It has also been shown that porous ceramics like MgO or Al_2O_3 , in addition to increasing thermal conductivity, enhance the mechanical strength of pure PCMs. This study explores the influence of binders, both carbon-based (EG) and ceramic-based (MgO), on the thermophysical and mechanical properties of LiNaSO_4 .

Methodology

The enthalpy values of different composites, containing pure LiNaSO_4 and different additives, were evaluated to select the most promising binders. EG600 and MgO were chosen for further investigation based on the enthalpy values of the corresponding composites. The samples were prepared following a mechanical process (ball milling for 15 minutes) by

adding a 5 wt.% of the corresponding binder to the stoichiometric compound LiNaSO_4 (previously synthesized) followed by uniaxial compression of the powder's mixture.

Results and Discussion

As already mentioned in the introduction, the mechanical properties of LiNaSO_4 stoichiometric compound (referred as to LNS_50:50 thereafter) have not been previously reported. Therefore, one of the aims of this work is to study the behaviour of this material under compression tests. Figure 1 shows the compressive deformation vs. compressive stress curves for five samples of the pure LNS_50:50 stoichiometric compound.

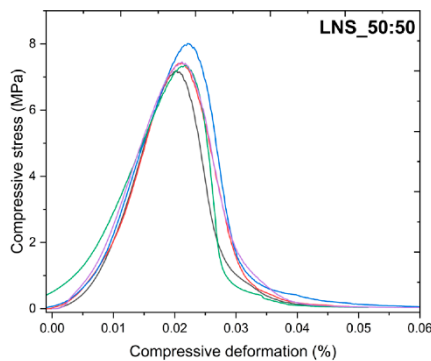
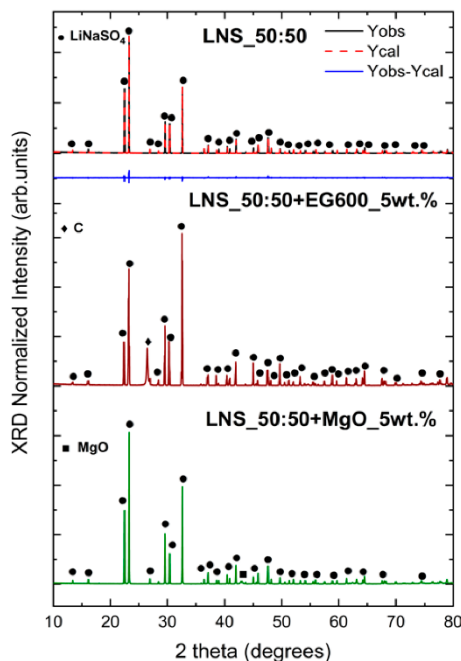


Figure 1: Compressive deformation vs. compressive stress curves for the LNS_50:50 stoichiometric compound.

The deformation-stress curves of the five samples exhibit notable similarity and a good reproducibility. Analyzing the slope of each curve facilitates the straightforward calculation of Young's modulus. The average Young's modulus and yield point values are determined as 494 MPa and 7.5 MPa, respectively.



d, no comparative analysis with existing literature data is feasible. To ensure that the addition of EG600 and MgO does not alter the structural properties of the pure LNS_50:50 stoichiometric compound, X-ray diffraction (XRD) analysis was conducted post-synthesis of the composites. Figure 2 presents the XRD results for both the pure LNS_50:50 and the corresponding Rietveld refinement, allowing for a comprehensive comparison.

Figure 2: XRD patterns for LNS_50:50 pure sample, LNS_50:50+EG600_5wt.% and LNS_50:50+MgO_5wt.%.

The X-ray diffraction analysis confirms the presence of the LiNaSO_4 stoichiometric compound (ICSD 14364) in all three samples. Additionally, in the XRD pattern of the LNS_50:50+EG600_5wt.% sample, the graphite phase (ICSD 76767) exhibits the most prominent peak at 26.4° , while the XRD pattern of the LNS_50:50+MgO_5wt.% sample reveals the most intense peak of MgO (ICSD 9863) at approximately 43° . As anticipated, the relative intensity of these peaks is significantly lower than that of the LiNaSO_4 peaks, owing to the limited amount of added binder. These findings strongly suggest that the incorporation of both binders does not result in the formation of undesired secondary phases, highlighting the chemical compatibility of the materials. This conclusion is further supported by the Differential Scanning Calorimetry (DSC) results depicted in Figure 3. The samples containing the binders were subjected to a

Since this is the first time that the mechanical properties of this material have been reported

pre-treatment at 550 °C for 30 minutes before the DSC measurements, reinforcing the chemical stability and compatibility of the materials.

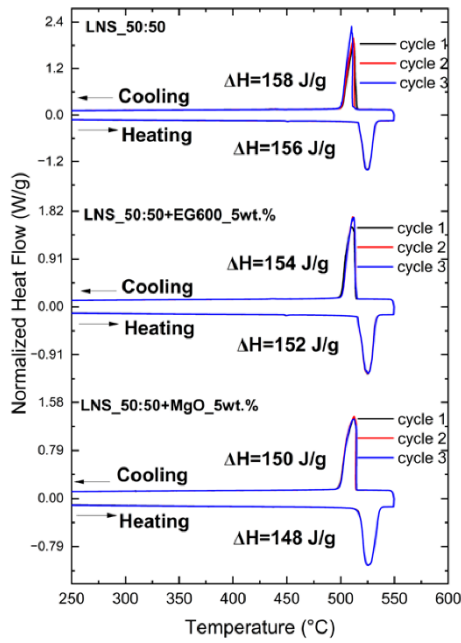


Figure 3: DSC curves for LNS_50:50, LNS_50:50+EG600_5wt.%, and LNS_50:50+MgO_5wt.%, including the enthalpy values.

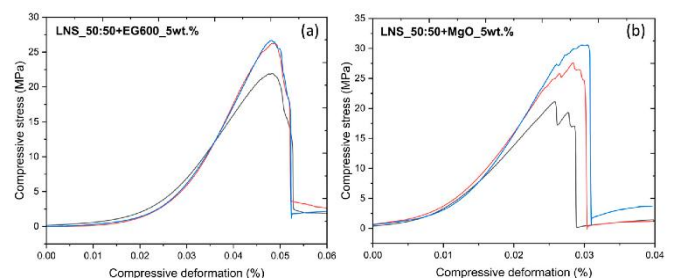
The results indicate that the introduction of the binders has no impact on the stoichiometry of pure LNS_50:50. Additionally, the thermal stability of all the samples remains consistent across three cycles, with no noteworthy variations. The energy associated with the solid-solid transition in pure LNS_50:50 agrees with previously reported experimental values. As anticipated, the enthalpy values for binder-containing samples (152 J/g for LNS_50:50+EG600 and 148 J/g for LNS_50:50+MgO) are slightly lower than those for pure LNS_50:50 due to the presence of inert additives (5 wt.%). Moreover, there are no significant differences in the transition temperature (approximately 518 °C for all samples), and no apparent subcooling was observed. Table 1 presents the average enthalpy values (across three cycles) with a standard deviation below 2% for all measurements and the specific heat capacities.

Table 1: Enthalpy values from DSC heating and cooling cycles and specific heat capacities.

Sample	$\Delta H_{\text{heating}}$ (J/g)	$\Delta H_{\text{cooling}}$ (J/g)	C_p (J/g·K)
LNS_50:50	156	158	1.60
LNS_50:50+EG600_5wt.%	152	154	1.62
LNS_50:50+MgO_5wt.%	148	150	1.67

Sample	$\Delta H_{\text{heating}}$ (J/g)	$\Delta H_{\text{cooling}}$ (J/g)	C_p (J/g·K)
LNS_50:50	156	158	1.60
LNS_50:50+EG600_5wt.%	152	154	1.62
LNS_50:50+MgO_5wt.%	148	150	1.67

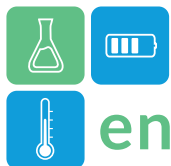
In the case of specific heat capacities measurements, each sample underwent three repetitions, and the results generally exhibited a margin of error within $\pm 5\%$, falling within the measurement accuracy of the DSC. Table 1 presents the specific heat capacity for the three samples at 540 °C, where the α -LiNaSO₄ cubic phase forms. The theoretical value for the pure LiNaSO₄ cubic phase is 1.50 J/g·K, according to data from FactSage 8.2, and consistent with both the experimental value obtained in this study and the value reported (18). However, the addition of binders results in an increase of specific heat capacities, as shown in Table 1. This increase is likely attributed to the substantial specific heat capacities of EG600 and MgO powders. Prior studies have indicated that the increase of specific heat capacity in modified salt is not solely tied to the properties of nano-MgO but also involves the adsorption of nanoparticles on the salt, leading to the formation of a solid layer. As previously stated, one of the primary goals of this study is to improve the mechanical characteristics of pure LNS_50:50. To achieve this objective, similar compression tests, as previously outlined, were conducted on samples containing EG600 and MgO. Figure 4a displays the compressive deformation versus compressive stress curves for LNS_50:50+EG600_5wt.%, while Figure 4b illustrates the corresponding curves for LNS_50:50+MgO_5wt.%. Measurements with an



error exceeding 10% were excluded, resulting in Figures 4a and 4b showcasing only the curves from experiments with minimal error.

Figure 4: Compressive deformation vs. compressive stress curves for (a) LNS_50:50+EG600_5wt.% and (b) LNS_50:50+MgO_5wt.%.

Table 2 shows the average values for Young's modulus and the yield point, with values for



LNS_50:50 included as references. It is noteworthy that the average Young's modulus values in Table 2 confirm the reproducibility of the measurements across different samples. However, there is a noticeable dispersion in the values of the yield point, leading to consideration of average values primarily for comparison with the pure PCM. The results indicate a significant increase in both Young's modulus and yield points for the two composites. A higher Young's modulus signifies greater stiffness, resulting in smaller deformations. The enhancement of mechanical properties in inorganic PCMs with the addition of EG or MgO has been previously documented by various researchers.

Table 2: Average values of Young's modulus and yield point for pure LNS_50:50, LNS+EG600_5wt.%, and LNS+MgO_5wt.%.

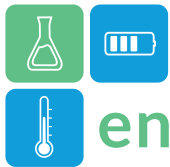
Sample	Young's modulus (MPa)	Yield Point (MPa)
LNS_50:50	494	7.5
LNS_50:50+EG600_5wt.%	1177	24.9
LNS_50:50+MgO_5wt.%	1508	24.7

Conclusions

This study investigated the potential of LiNaSO₄-based composites with MgO and EG600 as binders for high-temperature thermal energy storage applications. The results demonstrated that the addition of MgO or EG600 had a minimal impact on the phase transitions of LiNaSO₄ but significantly enhanced mechanical properties. The composites exhibited nearly threefold higher Young's modulus compared to pure LiNaSO₄, making them promising candidates for compact and cost-effective thermal storage systems. Further research should focus on optimizing the binder content and exploring the long-term stability and cycling performance of these composites in practical applications.

References

- Pielichowska, K.; Pielichowski, K. (2014) Phase Change Materials for Thermal Energy Storage. *Prog. Mater.* 65, 67–123
- Faraj, K.; Khaled, M.; Faraj, J.; Hachem, F.; Castelain, C. (2021) A Review on Phase Change Materials for Thermal Energy Storage in Buildings: Heating and Hybrid Applications. *J. Energy Storage*, 33, 101913.
- Wu, S.; Yan, T.; Kuai, Z.; Pan, W. (2020) Thermal Conductivity Enhancement on Phase Change Materials for Thermal Energy Storage: A Review. *Energy Storage Mater.* 25, 251–295.
- Umair, M.M.; Zhang, Y.; Iqbal, K.; Zhang, S.; Tang, B. (2019) Novel Strategies and Supporting Materials Applied to Shape-Stabilize Organic Phase Change Materials for Thermal Energy Storage—A Review. *Appl. Energy*, 235, 846–873.
- Magendran, S.S.; Khan, F.S.A.; Mubarak, N.M.; Vaka, M.; Walvekar, R.; Khalid, M.; Abdullah, E.C.; Nizamuddin, S.; Karri, R.R. (2019) Synthesis of Organic Phase Change Materials (PCM) for Energy Storage Applications: A Review. *Nano-Struct. Nano-Objects*, 20, 100399.
- Eslami, M.; Khosravi, F.; Fallah Kohan, H.R. (2019) Effects of Fin Parameters on Performance of Latent Heat Thermal Energy Storage Systems: A Comprehensive Review. *Sustain. Energy Technol. Assess.* 47, 101449.
- Koçak, B.; Fernandez, A.I.; Paksoy, H. (2020) Review on Sensible Thermal Energy Storage for Industrial Solar Applications and Sustainability Aspects. *Sol. Energy*, 209, 135–169.
- Desai, F.; Sunku Prasad, J.; Muthukumar, P.; Rahman, M.M. (2021) Thermochemical Energy Storage System for Cooling and Process Heating Applications: A Review. *Energy Convers. Manag.* 229, 113617.
- Fallahi, A.; Guldentops, G.; Tao, M.; Granados-Focil, S.; Van Dessel, S. (2017) Review on Solid-Solid Phase Change Materials for Thermal Energy Storage: Molecular Structure and Thermal Properties. *Appl. Therm. Eng.* 127, 1427–1441.
- Usman, A.; Xiong, F.; Aftab, W.; Qin, M.; Zou, R. (2022) Emerging Solid-to-Solid Phase-Change Materials for Thermal-Energy Harvesting, Storage, and Utilization. *Adv. Mater.* 34, 2202457.
- Doppiu, S.; Dauvergne, J.-L.; Serrano, A.; del Barrio, E. (2019) The Li₂SO₄-Na₂SO₄ System for Thermal Energy Storage. *Materials*, 12, 3658.
- Sadeghi, G. (2022) Energy Storage on Demand: Thermal Energy Storage Development, Materials, Design, and Integration Challenges. *Energy Storage Mater.* 46, 192–222.
- Cheng, P.; Chen, X.; Gao, H.; Zhang, X.; Tang, Z.; Li, A.; Wang, G. (2021) Different Dimensional Nanoadditives for Thermal Conductivity Enhancement of Phase Change Materials:



enerstock

ENERSTOCK 2024

The 16th IEA ES TCP International Conference on Energy Storage

June 5–7, 2024

Lyon, France

- Fundamentals and Applications. *Nano Energy*, 85, 105948.
14. Nazir, H.; Batool, M.; Bolivar Osorio, F.J.; Isaza-Ruiz, M.; Xu, X.; Vignarooban, K.; Phelan, P.; Inamuddin; Kannan, A.M. (2019) Recent Developments in Phase Change Materials for Energy Storage Applications: A Review. *Int. J. Heat. Mass. Transf.* 129, 491–523.
 15. Trisaksri, V.; Wongwises, S. (2007) Critical Review of Heat Transfer Characteristics of Nanofluids. *Renew. Sustain. Energy Rev.* 11, 512–523.
 16. Boualou, R.; Agalit, H.; Samaouali, A.; El Youssfi, A.; El Alami, K. (2019) Doping Effect of Magnesium Oxide (MgO) on the Enhancement of the Thermal Storage Properties of Sodium Nitrate (NaNO₃). *AIP Conf. Proc.* 2190, 020069.
 17. Hu, Z.; Zou, Y.; Xiang, C.; Sun, L.; Xu, F.; Jiang, M.; Yu, S. (2022) Stabilized Multifunctional Phase Change Materials Based on Carbonized Cu-Coated Melamine Foam/Reduced Graphene Oxide Framework for Multiple Energy Conversion and Storage. *Carbon Energy*, 4, 1214–1227.
 18. Bayón, A.; Liu, M.; Sergeev, D.; Grigore, M.; Bruno, F.; Muller, M. (2019) Novel Solid–Solid Phase-Change Cascade Systems for High-Temperature Thermal Energy Storage. *Sol. Energy*, 177, 274–283.



Jawad Rabbi^{1,*}, Gholamhossein Kahid Baseri¹, José Luiz Lara Cruz¹, Magnus Rotan², Ragnhild Sæterli², Jorge Salgado-Beceiro², Frida Vullum-Bruer², Alexis Sevault², Jean-Pierre Bédécarrats¹

¹ Université de Pau et des Pays de l'Adour, E2S UPPA, LaTEP, Laboratoire de Thermique, Énergétique et Procédés, 64000 Pau, France

² SINTEF Energy Research, Postboks 4761 Torgarden, 7465 Trondheim, Norway.

*Corresponding author e-mail: jawad.rabbi@univ-pau.fr

Abstract

Phase change materials used in thermal energy storages may undergo supercooling. This phenomenon arises when a liquid does not crystallize at the solid-liquid equilibrium temperature (melting point) but at a lower temperature. The degree of supercooling is defined as the difference between the crystallization temperature and solid-liquid equilibrium temperature. It can be quantified by measuring the temperature of crystallisation of the material with thermocouples placed inside or outside of the sample. Mostly, in thermal systems, whether industrial or at laboratory scale, the thermocouples are installed inside the sample and may impact the supercooling. In this research, the influence of the position of the thermocouple probes on the supercooling of distilled water is studied. A volume of 3 ml contained in tubes with an internal diameter of 10 mm is considered. The effect of the thermocouple is investigated using the distilled water samples immersed in a bath containing a fluid at a controlled temperature. It was found that the average degree of supercooling of distilled water with thermocouples placed inside was less than the degree of supercooling of samples with thermocouples attached on the outside. The second objective is to study the effect of the cooling rate of the sample. The first results showed that varying the cooling rate from 1°C/min to 0.166°C/min had no significant effect on the degree of supercooling.

Keywords: Thermal Energy Storage, Phase Change Materials, Supercooling, Thermocouples

Introduction

The importance of renewable energy is evident by the climate change. Thermal energy storage (TES) plays the vital role in the renewable energy systems to reduce the intermittency and increase the efficiency of the system (Cabeza, 2021). Latent heat thermal energy storage (LHTES) is an alternative to sensible heat storage because of its high energy storage capacity and its ability to store large amounts of energy within a small temperature range in the storage medium. The materials used in LHTES are called phase change materials (PCMs) (Mehling & Cabeza, 2008). PCMs face several problems, of which supercooling is one of the major challenges. When PCMs undergo a phase change process from liquid to solid, they are expected to solidify at the solid-liquid equilibrium temperature. But, in some situations the temperature of PCM decreases below this point without crystallization occurring. The temperature difference between solid-liquid equilibrium temperature and the crystallization temperature is called the degree of supercooling (Sandnes & Rekstad, 2006). This phenomenon of supercooling is illustrated in Figure. 1. The crystallization in the PCM will happen once the nucleation of a solid nuclei occurs. There are two

types of nucleation process, homogeneous and heterogeneous nucleation (Safari et al., 2017). A homogeneous nucleation happens when a liquid is uniformly cooled below its freezing point without the presence of any nucleation sites that may otherwise lead to solidification. Unlike a heterogeneous nucleation, the solid nuclei form independently of an existing solid object. On the other hand, a heterogeneous nucleation is the term used to describe the nucleation when cooling liquid comes in contact with foreign substances such as the surface of fins, heat exchangers and other structures (Shamseddine et al., 2022).

Disadvantages of Supercooling

Supercooling can be both advantageous and disadvantageous depending upon the application. Following are two major disadvantages associated to this phenomenon (Zahir et al., 2019).

1. Freezing temperature out of the system's operating range.
2. Extra energy consumption

The most inconvenient drawback is the fact that the temperature range at which a system operates, may not include the freezing point of the supercooled PCM. The second problem introduced into energy

consumption as the liquid PCM requires an extra energy input to lower the temperature below its freezing point, which can be a significant energy expenditure in some cases (Zahir et al., 2019).

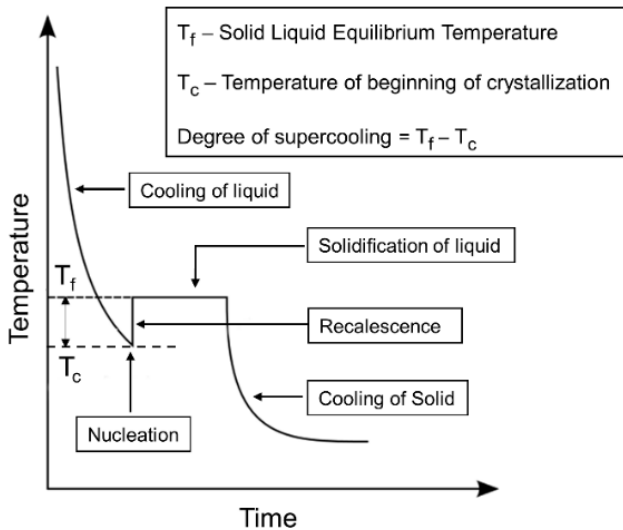


Figure 1. Evolution of the temperature inside a PCM for a cooling process.

Factors Affecting Supercooling

Nucleation can be triggered in PCMs by various mechanisms. It is important to mitigate supercooling for the applications when it is not desired. Factors affecting the supercooling have to be studied. The following factors have most significant role on supercooling.

1. Volume
2. Surface roughness of the container
3. Thermal history
4. Purity of PCM
5. Cooling Rate

Research Objectives

Due to volume dependence of supercooling, the laboratory scale results are not directly applicable for larger volumes and configurations in real systems. To predict supercooling of real systems, the dependence of supercooling on various factors will be analysed at laboratory scale and will be extrapolated to a larger scale using statistical modelling. This research corresponds with one of the objectives of the PCM STORE project to have more knowledge about PCMs used in real systems and to develop thermal energy storage systems. This article presents the results from the first part of this project, which is to analyse laboratory scale dependence of supercooling on various factors. Thermocouples are used to record temperature of PCMs in research facilities and in real applications. It is well established that foreign surfaces may impact the supercooling of PCMs.

actual degree of supercooling. Therefore, the objective of this study is to find the impact of the location of the thermocouple in the PCM samples. This is done by measuring the degree of supercooling with and without thermocouples placed in the PCM samples. In addition to the impact of the thermocouple probe, the effect of cooling rate on supercooling is also investigated.

Materials and Methodology

Experimental Setup

Distilled water is used as PCM inside test tubes made of polypropylene. The inner diameter and thickness of the tubes are respectively 10 mm and 1mm. Each tube is filled with a volume of water of 3 ml. Two different configurations are made (Figure 2). The first configuration has one thermocouple outside the sample at location of 1.5 ml. The second configuration has two thermocouples, one inside, in the water and one outside on the external wall, both at the location of 1.5 ml. T type thermocouples are used. Classical wire probe thermocouples are installed outside, held close to the wall of the tube with a zip-tie. Rigid probe thermocouples are used inside to ensure that the probes are in exactly the right position.

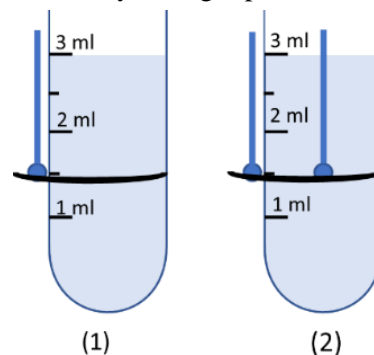


Figure 2: Different configuration of samples (1) One thermocouple probe outside (2) Two probes, one inside and one outside

Configuration 1 is used to measure the actual degree of supercooling, since there is no foreign object present inside the sample, but this measurement includes the thermal gradient across the tube wall. Configuration 2 measures the temperature difference between the external wall of the tube and the centre of the PCM. Data of configuration 2 can be used to estimate the degree of supercooling inside the samples when there is no probes inside. This configuration also gives the degree of supercooling influenced by the thermocouple probe. This is summarized in Table 1. In our work, the heat transfer fluid (HTF) used is an aqueous solution (50% water) of monoethylene glycol (Neutragel®).

Configuration	Location of Thermocouple	Purpose
1	Outside	To find actual supercooling
2	Inside and outside	To determine thermal gradient, and assess the impact of the probe on the supercooling

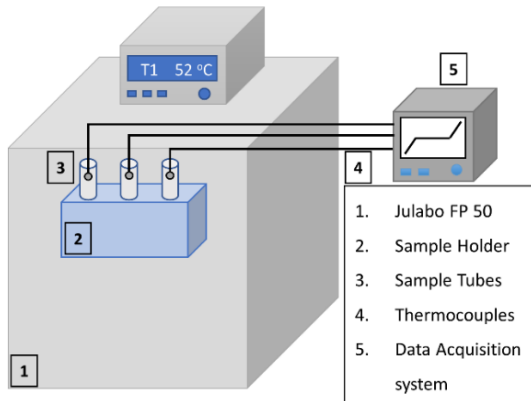


Figure 3: Experimental setup

Figure 3 shows the experimental setup. A refrigerated heating circulator (Julabo FP 50) including a bath is used to control the temperature of the HTF inside it. A sample test tube holder was immersed directly in the bath, the water sample tubes are placed in the tube holder. These tubes have thermocouples at different locations depending upon the different configurations as given in Table 1. Total 16 tubes are placed in the tube holder for distilled water. Data acquisition system KEYSIGHT DAQ970A is used to record the temperature of the samples versus time. Accuracy of thermocouples is found to be $\pm 0.1^\circ\text{C}$.

Methodology

A temperature cycle was applied on the cooling bath containing the HTF. As already mentioned, a rack with the distilled water samples was placed in the cooling bath. The temperature of the sample was recorded, and the degree of supercooling was measured by the difference between the temperature of crystallization and the melting point (as explained in Figure. 1). The experiment was repeated 19 times to have a statistical average value of the degree of supercooling for each configuration. The details of the experiments are summarized in Table 2. The schematic of applied cycle is shown in Figure 4. Different cooling rates were applied. The cooling rate is defined in Eq. 1 and is also illustrated in Figure 4.

$$\text{Cooling Rate} = \frac{\Delta T}{\Delta t} \quad \#(1)$$

ΔT is the difference in the highest temperature and lowest temperature of the bath. Δt is the time in which

temperature.

Table 2: Total Number of Results

	Cooling Rate ($^\circ\text{C}/\text{min}$)		
	1	0.5	0.166
No. of Samples	16	16	16
No. of Cycles	19	19	19

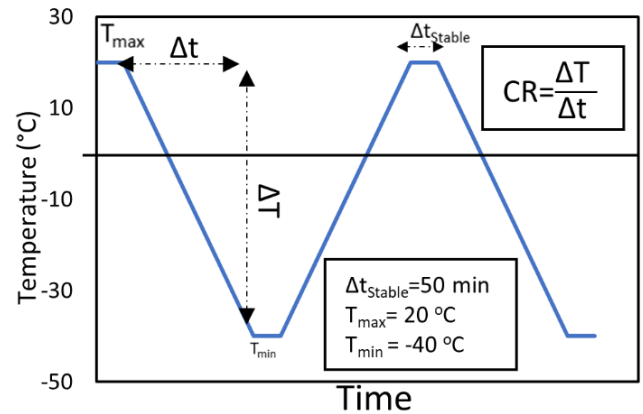


Figure 4: Temperature cycle applied on the bath and explanation of the cooling rate.

The error bounds for the results are calculated by combining the error of the thermocouple and the standard error of statistical data.

Results and Discussion

Effect of Thermocouple Probe

The effect of the thermocouple probe on the degree of supercooling is studied using different configurations. If the degree of supercooling of the sample with only outside probe (configuration 1) is higher than the degree of supercooling of the sample having one probe inside and one outside (configuration 2), this indicates that the probe located in the sample decreases the degree of supercooling. Figure 5 and Table 3 show that for all the cooling rates, the samples with the probes located only outside (configuration 1) have higher degree of supercooling than the samples having the double probes (configuration 2). This means that the probes located inside the sample tube are affecting or decreasing the degree of supercooling of distilled water samples with volume of 3 ml. The temperature difference between the inside and the outside of the tube increases when the cooling rate increases. This means that the measurement of the temperature of the outer wall of the tube does not necessarily correspond to the crystallisation temperature of the PCM at high cooling rates. The temperature gradients across the tube wall must therefore be considered to determine the true PCM supercooling.

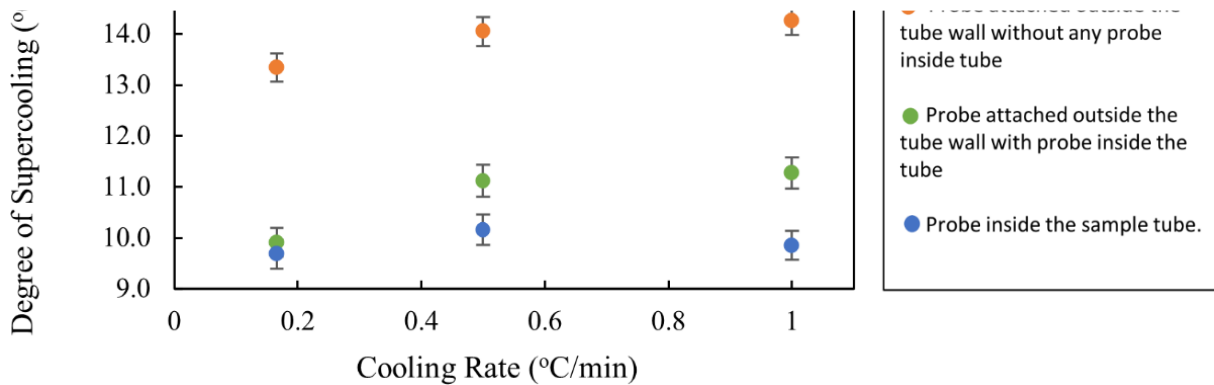
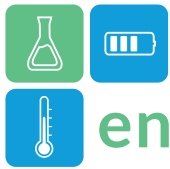


Figure 5: Degree of supercooling of the distilled water samples with and without a thermocouple probe inside the sample

Table 3. Experimental results.

Cooling Rate (°C/min)	Temperature difference between the probe inside and outside. (°C)	Difference in supercooling recorded outside for the two configurations. (°C)
0.166	0.2	3.5
0.5	1.0	3.0
1	1.4	3.0

Figure 5 clearly shows that the degree of supercooling does not change significantly by varying the cooling rate over the range of cooling rates studied.

Conclusions

PCM Store is a project seeking to enable widespread implementation of TES into energy systems aiding the green transition. For PCM based TES, it is necessary to know the dependence of different parameters on supercooling of the PCM and the impact in different sized systems. Extrapolating laboratory data using statistic modelling will help predict supercooling of real systems. In this study, the influence of a thermocouple probe on the degree of supercooling in tubes with 3 mL of distilled water samples have been experimentally evaluated. It was observed that a thermocouple probe located inside the sample tube decreases the degree of supercooling of distilled water. It was also observed that the studied cooling rates had no significant impact on the degree of supercooling. To determine the true supercooling of a material, no intrusive measurement should be made, and the external wall temperature measurement should be re-evaluated, taking into account the thermal gradient across this wall, particularly for high cooling rates.

Acknowledgment

This project has received funding from the European Union's Horizon 2020 research and innovation

programme under the Marie Skłodowska-Curie Actions, Grant agreement No 945416 and was carried out through the research project KSP PCM-STORE (308847) supported by the Research Council of Norway and industry partners. PCM-STORE aims at building knowledge on novel PCM technologies for thermal energy storage systems.

References

- Cabeza, L. F. (2021). Advances in thermal energy storage systems: Methods and applications (Second edition). Woodhead Publishing. doi.org/10.1016/B978-0-12-819885-8.00002-4
- Mehling, H., & Cabeza, L. F. (2008). Heat and cold storage with PCM: An up to date introduction into basics and applications. Springer. doi.org/10.1007/978-3-540-68557-9
- Safari, A., Saidur, R., Sulaiman, F. A., Xu, Y., & Dong, J. (2017). A review on supercooling of Phase Change Materials in thermal energy storage systems. Renewable and Sustainable Energy Reviews, 70, 905–919. doi.org/10.1016/j.rser.2016.11.272
- Sandnes, B., & Rekestad, J. (2006). Supercooling salt hydrates: Stored enthalpy as a function of temperature. Solar Energy, 80(5), 616–625. doi.org/10.1016/j.solener.2004.11.014
- Shamseddine, I., Pennec, F., Biwole, P., & Fardoun, F. (2022). Supercooling of phase change materials: A review. Renewable and Sustainable Energy Reviews, 158, 112172. doi.org/10.1016/j.rser.2022.112172
- Zahir, Md. H., Mohamed, S. A., Saidur, R., & Al-Sulaiman, F. A. (2019). Supercooling of phase-change materials and the techniques used to mitigate the phenomenon. Applied Energy, 240, 793–817. doi.org/10.1016/j.apenergy.2019.02.045



Impact of Using Different Phase Change Materials on a PCM-HX's Performance

Ryan L. Callaghan, Maxim Belinson, Dominic Groulx*

Dalhousie University, Mechanical Engineering Department, Halifax, Canada

*Corresponding author e-mail: dominic.groulx@dal.ca

Abstract

One of the foci of research in the latent heat thermal energy storage (LHTES) community is the search for comparative metrics and design rules for those systems. On the experimental side, LHTES systems have been characterized using different geometries, different operating conditions (temperatures, mass flow rate) and typically using one phase change material (PCM). The work presented in this extended abstract adds one additional layer of data by characterizing a LHTES system using two different PCMs: dodecanoic acid ($T_m = 43^\circ\text{C}$) and 1-octadecanol ($T_m = 57^\circ\text{C}$). For the characterization work, the initial and charging/discharging temperatures were selected to be similar for both PCMs in relation to their respective melting temperature. Results shows interesting differences between the power curves obtained in relation to the phase transition of both PCMs, the thermal conductivity and latent heat of both PCMs, and the possible impact and onset of natural convection during charging for both PCMs.

Keywords: Latent Heat Thermal Energy Storage, Phase Change Materials, Targeted Experimental Characterization.

Introduction

The use of thermal energy storage (TES) systems is attractive when heat is the required output. Some applications for these types of systems include optimization of building heating, (Morovat *et al.*, 2019) solar thermal energy (Joseph *et al.*, 2016) and waste heat recovery (Yan *et al.*, 2020). The use of phase change materials (PCMs) as the heat storage medium is a promising approach, leading to latent heat thermal energy storage (LHTES).

The central problem in the development of PCM heat exchangers today is due to the difficulties in modelling the complex nature of the heat transfer in these systems leading to the development of LHTES systems achieving the required heat transfer rates for their given application, *i.e.*, the *rate problem* (Groulx, 2018). Researchers have attempted to characterize LHTES using both experimental and numerical methodologies: looking at different heat exchanger geometries (Patil, 2020; Wołoszyn *et al.*, 2021) as well as variation of operating parameters (Al-Abidi *et al.*, 2014; Herbinger & Groulx, 2022).

One aspect that has not been thoroughly addressed is the impact of the PCM used in the LHTES, and its properties, on the characterization of the system and on the development of comparative metrics/design rules. Aside from a few studies (Gürel, 2020; Raud *et al.*, 2017), to the author's knowledge, very little research has been done exploring the effect of PCM properties on the performance LHTES system and none have attempted to reduce the data using performance indicators.

This paper will explore the use of two different types of PCM in the same LHTES system under the same representative operating conditions. The observed effects will be used to attempt to explore relationships between heat transfer rates, stored energy and PCM properties.

Methodology

Phase change materials

The first PCM selected to be used in this research was dodecanoic acid. Many previous research projects done at the Lab of Applied Multiphase Thermal Engineering (LAMTE) have used this PCM (Herbinger & Groulx, 2022; Patil, 2020; Skaalum & Groulx, 2020). A review of various PCMs used in literature was performed to select a second PCM. The most important factors considered when choosing the second PCM were the difference of thermophysical properties from dodecanoic acid, the cost and whether supercooling was a possibility. Ultimately, 1-octadecanol was chosen as the second PCM. The properties of both 1-octadecanol and dodecanoic acid can be seen in Table 1.

Experimental setup and procedure

A diagram of the experimental setup is presented in Fig. 1. This figure shows a water bath which is both the heater and chiller for the heat transfer fluid (HTF). The bath also contains a pump which responsible for circulating the HTF into the heat exchanger through *Hot Side* tubing (in red on the figure). Temperature measurements of the HTF are made at the inlet and outlet of the PCM-TES system using RTD probes.

Table 1: Properties of dodecanoic acid (Desgrosseilliers et al., 2013) and 1-octadecanol (Kahwaji et al., 2017)

Thermophysical Properties	Dodecanoic acid	1-octadecanol
Density (solid)	930 ± 20 kg/m ³	862 ± 86 kg/m ³
Density (liquid)	885 ± 20 kg/m ³	805 ± 81 kg/m ³
Heat capacity (solid)	1.95 ± 0.2 kJ/kg·K	1.75 ± 0.175 kJ/kg·K
Heat capacity (liquid)	2.4 ± 0.03 kJ/kg·K	2.49 ± 0.249 kJ/kg·K
Thermal conductivity (solid)	0.160 ± 0.004 W/m·K	0.29 ± 0.029 W/m·K
Thermal conductivity (liquid)	0.150 ± 0.004 W/m·K	0.21 ± 0.021 W/m·K
Heat of fusion	184 ± 9 kJ/kg	218 ± 21.8 kJ/kg
Melting temperature	43.0 ± 1.5 °C	57 ± 1.5 °C

The water then exits the heat exchanger containing the PCM via the *Cold Side* tubing (in blue) returning to the bath for heating/cooling. A bypass loop (in green) is used to initialize the HTF temperature at the start of each experiment.

Data gathered based on the experimental results are used to calculate the power exchanged $Q(t)$ from the HTF to and from the system:

$$Q(t) = \dot{m}c_p\Delta T \quad (1)$$

with \dot{m} being the HTF mass flow rate, c_p being the HTF heat capacity and ΔT the difference between the inlet and outlet HTF temperatures. The total energy stored or recovered by the system is calculated using a simple integration of power over time.

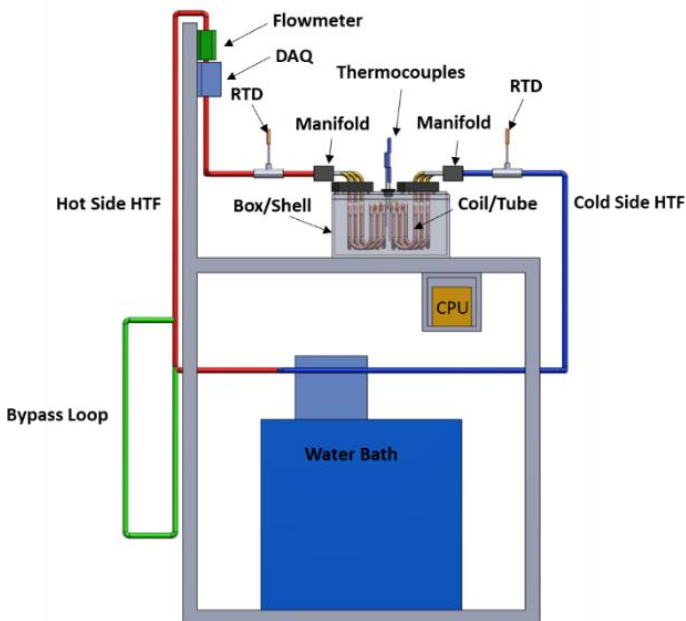


Figure 1: Schematic representation of the experimental setup

$$E = \int_{t_{initial}}^{t_{final}} Q(t)dt \quad (2)$$

In order to focus the study on the effects of PCM properties on the system's performance and characterization, all other variables which affect the system's performance, such as geometry, flow rate (L/min), insulation, and heat loss, were kept constant or accounted for using common assumptions.

Figure 2 shows all the combination of initial and charging/discharging temperatures used for the characterization of the system, all expressed in relation to the PCM's melting temperature.

The experimental procedure for each individual trial is to first initialize the PCM temperature by turning on the water bath to the correct initial temperature and pumping HTF through the heat exchanger until it is reached. Once the PCM is at the initial temperature (verified using the thermocouples embedded in the PCM) the water bath is changed over from the main loop to the bypass loop using valves. The water bath is then set to the final temperature, allowing the HTF to reach the final temperature within the bypass loop. Once the HTF has reached the final temperature, the valves are changed back to the main loop and simultaneously the LabVIEW program is started, recording the data as characterization of the LHTES starts.

Finally, once the system has reached steady-state (fully charged or discharged - PCM has reached the final temperature and constant power exchange over time), the trial is complete and the system is prepared for the next experimental run, essentially starting back at the top of this list.

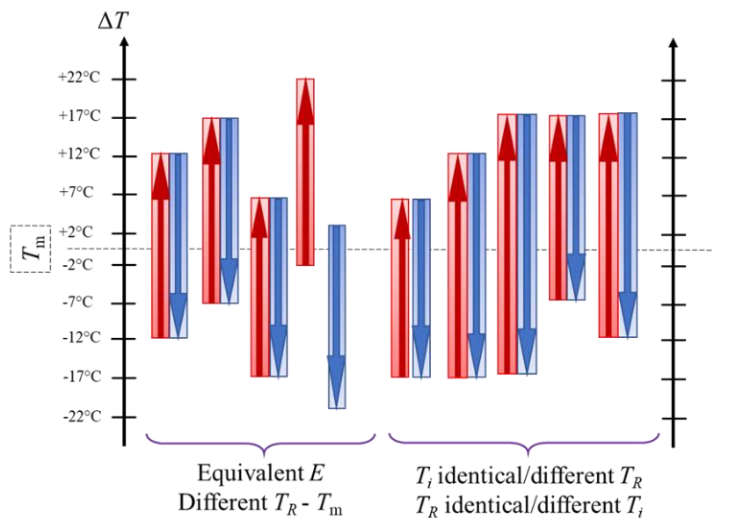


Figure 2: Temperature used for charging and discharging experiments based on PCM's melting temperature

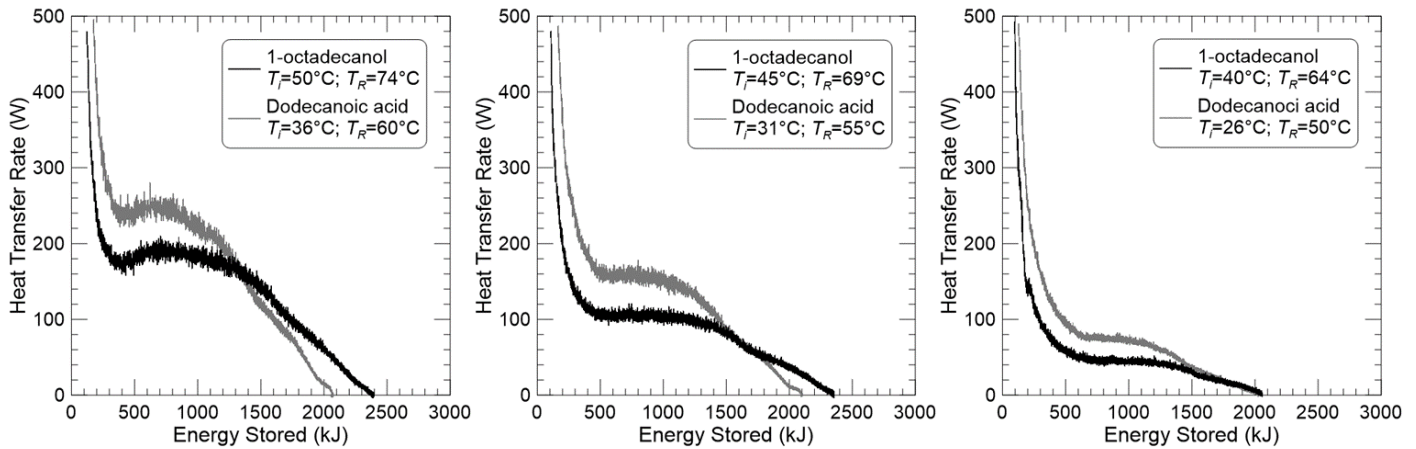
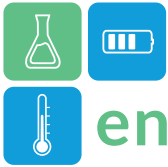


Figure 3: Power curve vs stored energy in charging experiments for dodecanoic acid and 1-octadecanol

Results

The results of the experiments using dodecanoic acid and 1-octadecanol are presented in the form of instantaneous power against the energy stored (or discharged) by the system. Results from similar characterization experiments for both PCMs (similar temperature differential in relation to the melting temperature) are presented on the same figures.

Charging

Figure 3 displays heat transfer results as a function of the stored energy for charging experiments with three combinations of initial (T_i) and HTF (T_R) temperatures. The shape of the power curve is typical of charging experiments: instantaneous peak in power initially due to the large difference between the cold outlet temperature exiting and the warm inlet temperature entering the system, followed by a rapid decrease in power as the PCM temperature begins to increase until it reaches the PCM melting temperature, an inflection point followed by a plateau when the PCM starts to melt and natural convection starts dominating heat transfer, and a final steady decrease in power and the system reaches its full charge.

The heat transfer of dodecanoic acid is initially greater than that of 1-octadecanol. However, as the trial continues, 1-octadecanol shows greater heat transfer rates closer to the end of the experiment. 1-octadecanol shows larger energy storage values for the duration of the experiments in all but one of the experiments presented. The larger energy storage observed in the 1-octadecanol points to the larger latent heat value for this PCM compared to dodecanoic acid. The larger thermal conductivity of 1-octadecanol compared to dodecanoic acid would suggest that this PCM would lead to higher heat transfer rates, especially in the solid

phase. However, this is not the case. This points to two related explanations. One, the viscosity of 1-octadecanol (0.01 Pa·s) is greater than dodecanoic acid (0.008 Pa·s), diminishing the impact of natural convection during melting (Yaws, 2003). Second, 1-octadecanol sees two transition temperature during melting, a first one at 55°C (solid-solid) and a second at 58°C (solid-liquid) (Kahwaji *et al.*, 2017), so more energy is needed to reach a liquid phase in the melt, again delaying the onset of natural convection.

Discharging

Much like the charging experiments, the heat transfer rates of the discharging trials follow a typical trend. Figure 4 displays results for discharging experiments of various initial (T_i) and HTF (T_R) temperatures.

The heat transfer is dominated by conduction, and continuously decreases in magnitude as the trial progresses. No plateau is observed in these experiments due to the minimal effect of natural convection. Similar to the results of the charging trials, the discharging results show dodecanoic acid offering a higher heat transfer rate at the start of the experiment, with 1-octadecanol's heat transfer rate surpassing it near the end of the experiment. Again, and for the same reason, more energy is discharged from the 1-octadecanol experiments.

The observed reduction in heat transfer rate for 1-octadecanol is a result of the two phase transition temperatures, the second one occurring after solidification, a solid-solid transformation at 50°C (Kahwaji *et al.*, 2017). Therefore, during solidification, less energy is needed for 1-octadecanol to become solid and the temperature differential between the HTF and the solid-liquid PCM happens for a shorter period of time, leading to an overall smaller heat transfer rate.

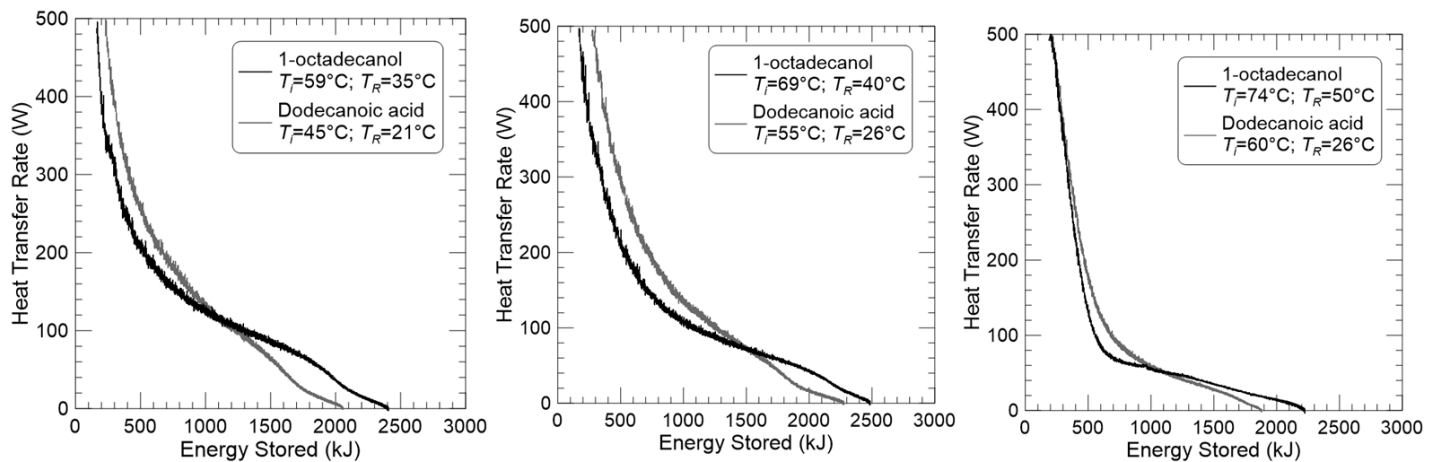
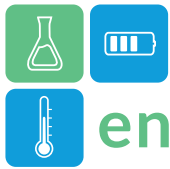


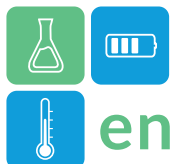
Figure 4: Power vs discharged energy in discharging experiments for dodecanoic acid and 1-octadecanol

Conclusion

This study evaluated the effect of PCM properties on an LHTES system with all other variables kept constant. The results determined that for both charging and discharging experiments, 1-octadecanol showed larger energy storage while exhibiting a smaller heat transfer rate. The effects of PCM viscosity in charging, and multiple phase changes in discharging, account for this smaller heat transfer rate. From these results, future work will look at comparative metrics and performance indicators from a PCM properties point of view.

References

- Al-Abidi, A. A., *et al.* (2014). Experimental study of melting and solidification of PCM in a triplex tube heat exchanger with fins. *Energy and Buildings*, 68, 33-41.
- Desgrosseilliers, L., *et al.* (2013). Dodecanoic acid as a promising phase-change material for thermal energy storage. *Applied Thermal Engineering*, 53(1), 37-41.
- Groulx, D. (2018). The rate problem in solid-liquid phase change heat transfer: Efforts and questions toward heat exchanger design rules. Proceedings of the 16th International Heat Transfer Conference (IHTC-16), Beijing, China, 16.
- Gürel, B. (2020). A numerical investigation of the melting heat transfer characteristics of phase change materials in different plate heat exchanger (latent heat thermal energy storage) systems. *International Journal of Heat and Mass Transfer*, 148, 119117.
- Herbinger, F., & Groulx, D. (2022). Experimental comparative analysis of finned-tube PCM-heat exchangers' performance. *Applied Thermal Engineering*, 211, 118532.
- Joseph, A., *et al.* (2016). Characterization and real-time testing of phase-change materials for solar thermal energy storage. *International Journal of Energy Research*, 40(1), 61-70.
- Kahwaji, S., *et al.* (2017). *Thermophysical Properties, Chemical Compatibility and Thermal Stability of Phase Change Materials Selected for Fanless Cooling of Portable Electronics*
- Morovat, N., *et al.* (2019). Simulation and performance analysis of an active PCM-heat exchanger intended for building operation optimization. *Energy and Buildings*, 199, 47-61.
- Patil, A. (2020). *Experimental study of coil and shell phase change material heat exchanger* Dalhousie University. Halifax, 131.
- Raud, R., *et al.* (2017). Design optimization method for tube and fin latent heat thermal energy storage systems. *Energy*, 134, 585-594.
- Skaalum, J., & Groulx, D. (2020). Heat transfer comparison between branching and non-branching fins in a latent heat energy storage system. *International Journal of Thermal Sciences*, 152, 106331.
- Wołoszyn, J., *et al.* (2021). Enhanced heat transfer in a PCM shell-and-tube thermal energy storage system. *Applied Thermal Engineering*, 196, 117332.
- Yan, S.-R., *et al.* (2020). Energy efficiency optimization of the waste heat recovery system with embedded phase change materials in greenhouses: a thermo-economic-environmental study. *Journal of Energy Storage*, 30, 101445.
- Yaws, C. L. (2003). Yaws' Handbook of Thermodynamic and Physical Properties of Chemical Compounds. In: Knovel.



Influence of host matrices on the thermochemical energy storage capacity of novel organic salt hydrate

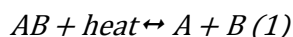
Emanuele Previti^{1,*}, Juan M. Coronado², Emanuela Mastronardo¹, Candida Milone¹, Luigi Calabrese¹
1 Department of Engineering, University of Messina, Contrada di Dio 98166, Messina, Italy
2 Instituto de Catálisis y Petroleoquímica (ICP-CSIC), Calle de Marie Curie 28049, Madrid, Spain
*Corresponding author e-mail: emanuele.previti@studenti.unime.it

The interest of scientific community towards materials for thermochemical heat storage has grown significantly in recent years. For low-temperature applications hydrated inorganic salts are commonly used. However, the large-scale employment of this kind of materials is limited by some operational challenges. Hydrated organic salts with a low solubility in water constitute a valid alternative for overcoming deliquescence problems. In this perspective, Calcium Lactate Pentahydrate constitutes a promising candidate considering its high energy density. For surpassing the slow salt hydration kinetics, five Calcium Lactate based hybrid materials were proposed. The performances of the synthesized materials were evaluated under both static and dynamic vapour conditions. In Calcium Lactate composite materials, a positive effect was encountered in terms of the amount of water uptaken with benefits also on the hydration kinetics.

Keywords: Calcium Lactate Pentahydrate, Silica Gel, Sepiolite, Graphite, Carbon Nanotubes

Introduction

Rising energy costs and concerns about pollution from energy production have prompted the international community to take steps to reduce energy consumption. From this perspective, the problem of energy waste is a central issue in the global process of improving energy efficiency. Thermal energy storage (TES) systems are particularly adequate for applications in buildings and industrial processes to store thermal energy for later use. Thermochemical energy storage represents an appealing alternative to sensible and latent heat storage systems. The technology is based on a reversible chemical reaction as shown in Eq.1.

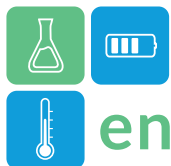


During the direct process the species AB undergoes an endothermic reaction, that represent the “charge step”, in which the waste heat is stored; on the contrary, the reverse (exothermic) reaction represents the “discharge stage”, in which the previously stored energy is released (Milone and al., 2018). For low temperatures applications hydrated inorganic salts are commonly employed. Despite the high energy released and the low-price availability of these materials they present some operational challenges related to their deliquescence, which causes, among the other issues, agglomeration and corrosion. For

these reasons, Mastronardo and al. (2022) proposed the employment of hydrated organic salts with a low solubility in water as a solution for overcoming deliquescence issues.

In view of this new strategy, we are studying the properties of Calcium Lactate Pentahydrate (CL) as novel promising material for thermochemical energy storage applications (Patent pending P02276IT-01-ds). This hydrated organic salt is an abundant, inexpensive and environmentally safe material. CL presents a high energy density (1.5 GJ m^{-3}) and no problems related to deliquescence or corrosion. The employment of CL as excipient in drugs and Calcium source was extensively studied in literature. In addition, its slow hydration kinetics was investigated by Sakata and al. (2005) concluding that the rate limiting step during the process is likely to be the diffusion of water in the solid phase. In the present work different hybrid Calcium Lactate based materials with five different matrices were prepared. The hosts effects on the thermochemical energy storage capacity of CL and their influence on hydration kinetics of the salt were evaluated. In particular the auxiliary materials are used for separating Calcium Lactate particles and triggering hydration process, avoiding, possibly, agglomeration issues.

Methodology



For preparing the hybrid materials with Calcium Lactate two different classes of host have been used: mineral and carbonaceous matrices. Among materials of mineral origin, Silica Gel (SG) and Sepiolite (SEP) were chosen for their high hydrophilicity and capacity of sorbing water even at low relative humidities (Zhang, 2023; Fujiwara and Sato, 1992). On the other hand, as carbonaceous matrices Exfoliated Graphite (EG), Graphite Oxide (GO) and functionalized Carbon Nanotubes (CNT) were employed. The capability of aforementioned matrices on enhancing thermochemical energy storage capacity was investigated by our group in MgO/H₂O/Mg(OH)₂ chemical heat pumps systems (Mastronardo and al., 2016; Mastronardo and al., 2016).

CL has been supplied by Sigma Aldrich. SG and SEP have been furnished by Siogel and Tolsa SA (Spain), respectively. EG has been supplied by TIMREX C-THERM 002 TIMCAL Ltd. Carbon Nanotubes were prepared by Catalytic Chemical Vapor Deposition using isobutane (i-C₄H₁₀) as carbon source, in the presence of Fe dispersed on the Al₂O₃ catalyst, and then washed to remove catalyst residues (Messina and al., 2008). The functionalization of carbonaceous matrix was carried out through oxidation of CNT in nitric acid vapor (HNO₃) at T=135 °C for 120 min according to procedures described in literature (Milone and al., 2015). Similarly, EG surface was treated through Hummers' method (Hummers and Offeman, 1958) for introducing oxygenated groups on it, thus obtaining GO.

The hybrid materials have been prepared by two different procedures accordingly to the group of matrices. For all the prepared samples, a load of 90% wt. of CL was added to 10% wt. of host. The so obtained materials are listed in Table 1 with the respective codes and contents (% wt.).

Table 1: Codes and contents (% wt.) of prepared hybrid materials.

Codes	%wt. of CL	Matrix	%wt. of Matrix
CL90SG10	90	Silica Gel	10
CL90SEP10	90	Sepiolite	10
CL90EG10	90	Exfoliated Graphite	10
CL90GO10	90	Graphite Oxide	10
CL90CNT10	90	Carbon Nanotubes	10

The mineral precursors were added through an impregnation procedure, drop casting a water solution (100 g dm⁻³) of CL onto the matrix surface. On the other hand, Carbon type materials were mixed with the salt in ethanol for 1 h and the obtained solution

was slowly evaporated by rotavapor. As a final step in both procedures, hybrid materials were grinded to obtain fine powders.

The performances of the synthesized materials were evaluated by both static and dynamic conditions of vapour. For analysis in static conditions a closed system has been employed. It includes a thermogravimetric analyser (Setaram Themys One) customized with a pump for the evacuation and an evaporator. The analysis consists of a ramp 10 K min⁻¹ to 353 K followed by an isotherm of 4h at this temperature. During these steps, the sample, previously dehydrated, is kept under vacuum (~1.6 Pa) for removing any moisture or gases adsorbed. At the end of isotherm, the evacuation is stopped and the evaporator (P_{evaporator} = 2300 Pa) is opened. A subsequent cooling to 298 K (by 5 K min⁻¹) occurs followed by a final 3h isotherm at 298 K. The increment of mass and heat recorded during the cooling phase are related to hydration process of sample.

The dynamic conditions were investigated by a Dynamic Vapour Sorption (DVS Vacuum) analyser. The instrumental setup consists of a micro-balance (precision 0.1 mg) and a water vapor pressure flow control system within the sample holder chamber. The whole system is placed in a temperature-controlled box and maintained at 303 K. The sample, before water adsorption, was activated (degassed) at 353 K in vacuum (~ 0.1 Pa) for 3h to determine its dry weight. Subsequently, a valve connecting the evaporator, containing liquid water, and the sample chamber was opened. Isothermal tests were performed at increasing partial pressures (p/p₀ from 0.002 to 0.9). The pressure is kept constant during each step until the sample weight reaches equilibrium (Calabrese and al., 2022).

Results and Discussion

The hydration behaviour of CL and its composites, obtained in static conditions of vapour (P_{evaporator} = 2300 Pa), was recorded during the final cooling and isothermal steps and it is showed in Figure 1.

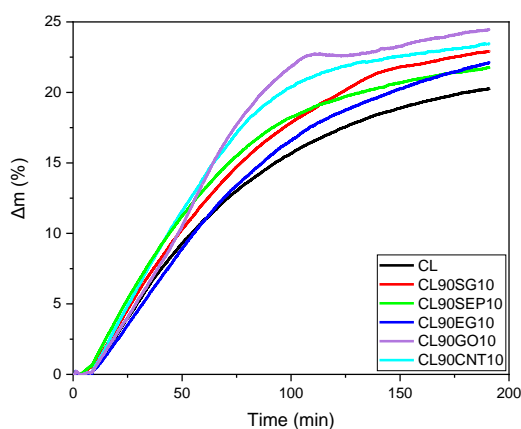


Figure 1: Influence of matrices on Calcium Lactate hydration process measured in static conditions of vapour.

The Δm (%) reported in Figure 1 was normalized considering the content of CL in each composite material. Greater mass increases of composites compared to CL (black line) is observed which reflect also on the composites' kinetics. A positive effect of both mineral and carbonaceous matrices in terms of water absorption was found, but it is more evident on the carbonaceous-based materials. We cannot exclude that the matrices themselves are partly contributing to certain water uptake. For a quantitative determination of their contribution, further analyses are ongoing.

The heat of hydration (exothermic process) recorded during the final cooling and isothermal steps in static conditions of vapour is listed in Table 2. The enthalpy of hydration was calculated as the integral over time of the measured heat flow and normalized respect the dry content of CL in each composite material.

Table 2: Enthalpy of hydration measured for hybrid materials in static conditions of vapour.

Material	Enthalpy of hydration (J g^{-1})
CL	538
CL90SG10	474
CL90SEP10	616
CL90EG10	568
CL90GO10	583
CL90CNT10	514

In Figure 2 are reported the hydration curves measured in dynamic conditions of vapour for Calcium Lactate and its composites.

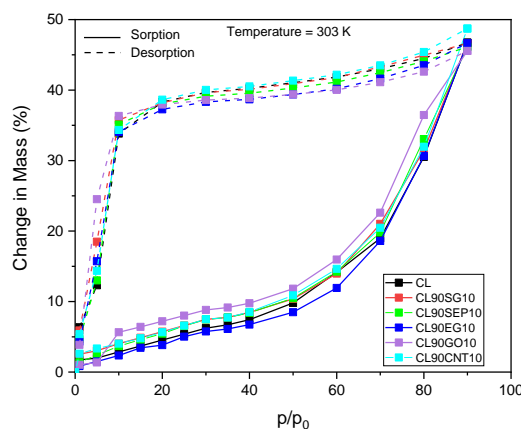


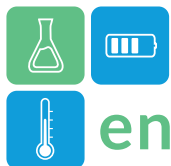
Figure 2: Influence of matrices on Calcium Lactate hydration process measured in dynamic conditions of vapour.

The curves were obtained in the increasing range of partial pressures from 0.002 to 0.9 at the temperature of 303 K and they were normalized considering the content of CL in each composite material. The ascending solid lines, shown in Figure 2, refer to the vapor absorption process; on the contrary, the descending dashed curves refer to the subsequent desorption process. A large hysteresis was observed for both CL and all composites, most likely attributed to a kinetic barrier. In Figure 2, no changes in the trend of the curves were observed, resulting in an almost zero effect of matrices on the hydration kinetics of the salt in dynamic vapour conditions. Further studies will be conducted to determine the degree of hydration of the materials under different vapor partial pressure and temperature conditions.

Ongoing activities are focused on structural and morphological characterization of composite materials. Powder X-Ray Diffraction (PXRD) and Scanning Electron Microscopy (SEM) analysis with Energy Dispersive X-ray spectroscopy (EDX) will be used for understanding the distribution of CL onto matrices surfaces. Infrared spectroscopy will be used for the chemical characterization of composite materials.

Conclusion

The synthesis of five different hybrid materials for thermochemical energy storage applications was presented. Each composite is made up by 90 %wt. of Calcium Lactate Pentahydrate (CL) and 10 %wt. of auxiliary material. Two different classes of host have been used as additive materials. Among mineral materials, Silica Gel (SG) and Sepiolite (SEP) were chosen. As carbonaceous matrices Exfoliated Graphite (EG), Graphite Oxide (GO) and functionalized Carbon Nanotubes (CNT) were employed. The



performances of the synthesized materials were evaluated by both static and dynamic conditions of vapour. A positive effect of matrices in terms of water absorption of composites was found, in static vapour conditions, as also witnessed by enthalpy values measured. Further investigations will be focused on quantifying the contribution of each host material on hydration process.

Nomenclature

Abbreviations	Definitions
TES	Thermal Energy Storage
CL	Calcium Lactate Pentahydrate
SG	Silica Gel
SEP	Sepiolite
EG	Exfoliated Graphite
GO	Graphite Oxide
CNT	Carbon Nanotubes
PXRD	Powder X-Ray Diffraction
SEM	Scanning Electron Microscopy
EDX	Energy Dispersive X-ray spectroscopy

References

- Calabrese, L. and al. (2022). Deviceful LiCl salt hydrate confinement into a macroporous silicone foam for low-temperature heat storage application. *Journal of Science: Advanced Materials and Devices*. <https://doi.org/10.1016/j.jsamd.2022.100463>
- Fujiwara, I. and Sato, M. (1992). Adsorption of Water Vapor on Sepiolite for Chemical Heat Pumps. *Journal of Chemical Engineering of Japan*. <https://doi.org/10.1252/jcej.25.609>
- Hummers, W. and Offeman, R. (1958). Preparation of graphitic oxide. *Journal of the American Chemical Society*. <https://doi.org/10.1021/ja01539a017>
- Mastronardo, E. and al. (2022). Organic Salt Hydrate as a Novel Paradigm for Thermal Energy Storage. *Energies*. <https://doi.org/10.3390/en15124339>
- Mastronardo, E. and al. (2016). Thermochemical Performance of Carbon Nanotubes Based Hybrid Materials for MgO/H₂O/Mg(OH)₂ Chemical Heat Pumps. *Applied Energy*. <https://doi.org/10.1016/j.apenergy.2016.08.041>
- Mastronardo, E. and al. (2016). Efficiency Improvement of heat storage materials for MgO/H₂O/Mg(OH)₂ Chemical Heat Pump. *Applied Energy*. <https://doi.org/10.1016/j.apenergy.2015.10.066>
- Messina, G. and al. (2008). Large-scale production of high-quality multi-walled carbon nanotubes: role of precursor gas and of Fe-catalyst support.

- Diamond and Related Materials. <https://doi.org/10.1016/j.diamond.2008.01.060>
- Milone, C. and al. (2018). Chapter - Recent Advancements in Materials and Systems for Thermal Energy Storage, Springer, https://doi.org/10.1007/978-3-319-96640-3_3
- Milone, C. and al. (2015). Highly Versatile and Efficient Process for CNT Oxidation in Vapor Phase by Means of Mg(NO₃)₂ - HNO₃ - H₂O Ternary Mixture. *Fullerenes, Nanotubes and Carbon Nanostructures*. <https://doi.org/10.1080/1536383X.2013.858132>
- Sakata, Y. and al. (2005). Characterization of dehydration and hydration behavior of calcium lactate pentahydrate and its anhydrate. *Colloids and Surfaces B: Biointerfaces*. <https://doi.org/10.1016/j.colsurfb.2005.10.004>
- Zhang, Y. and al. (2023). Performance analysis of a lab-scale adsorption desalination system using silica gel/LiCl composite. *Desalination*. <https://doi.org/10.1016/j.desal.2022.116278>



Influence of operating conditions on the melting front movement in tube-in-tube latent thermal energy storage heat exchangers

Julie Van Zele^{1,2,*}, Maité Goderis^{1,2}, Kenny Couvreur^{1,2}, Wim Beyne^{1,2}, Michel De Paepe^{1,2}
1 Department of Electromechanical, Systems and Metal Engineering – UGent, Ghent, Belgium
2 FlandersMake@UGent – Core lab EEDT-MP, Leuven, Belgium
*Corresponding author e-mail: julie.vanzele@ugent.be

Analytical models describing the phase change front movement during melting or solidification can potentially provide a framework for sizing latent thermal energy storage (LTES) heat exchangers. However, limited data are available in literature on the phase change front movement. Therefore, a tube-in-tube LTES heat exchanger is experimentally tested. In the setup, water flows through the inner tube as heat transfer fluid and the shell contains a paraffin RT35HC as phase change material. During an experiment, the movement of the phase change front is tracked over time using a camera. It is seen that each front-curve shows an S-shape with a linear part which represents a quasi-steady state regime of the moving speed. To gain a better understanding of the phase change front dynamics, the influences of the varying operating conditions on this front speed were analysed. Only for the HTF inlet temperature, a clear linear trend was found: higher HTF inlet temperature results in higher front speed. As the HTF Reynolds number increases, the front speed first decreases at Reynolds numbers between 2500 - 5000 and at Reynolds numbers higher than 5000, the front speed increases again. However, there are many fluctuations present in the results. Lastly, a higher initial PCM temperature increases the front speed.

Keywords: Latent thermal energy storage, phase change material, tube-in-tube heat exchanger, phase change front movement, characterisation

Introduction

Thermal energy storage systems play a crucial role in realizing a sustainable and carbon-neutral future by bridging the gap between heat supply and demand. There are three main types of thermal energy storage: sensible, latent and thermochemical storage (Karami, 2020). Latent thermal energy storage (LTES) uses a phase change to store thermal energy. As the temperature rise in operation is quite small, they can store 4 to 10 times more energy per unit mass than STES at the same temperature difference (Regin, 2008).

Despite the potential of LTES systems, their successful integration into the market has been mainly hampered due to sizing difficulties. Classical heat exchanger theory cannot be employed due to the non-linear and transient behaviour of LTES systems (A. Castell and C. Solé, 2015). Hence, extensive experimental and numerical testing is primarily performed nowadays. However, in recent years, attempts have been made to develop predictive methods for sizing LTES heat exchanger systems. These methods focus for example on predicting an average effectiveness (Tay, 2012) or the total phase change time (Raud, 2017), but they are

unable to fully predict the performance indicators of the system as a function of time.

A recent analytical method, developed by Beyne et al. (Beyne, 2023), offers a promising approach for sizing LTES systems by linking the location of the phase change front as a function of time to the local phase change fraction over time. The latter is integrated to obtain the overall phase change fraction of the entire LTES system. As a result, the method relates the evolution of the phase change front to the (instantaneous) internal energy change of the phase change material (PCM) volume and thus to the heat transfer rate between the heat transfer fluid (HTF) and PCM. This provides a complete characterisation of the LTES system based on a thorough understanding of the phase change process. On the other hand, limited data are available in literature on the phase change front movement. Hence, this study aims to enhance our understanding of phase change front dynamics, particularly by analysing the influences of the operating conditions on its movement.

Set-up description

The set-up consists of a 1 m long tube-and-tube heat-exchanger where water flows as HTF through an inner

tube and PCM is located in the outer tube. The copper inner tube has an outer diameter of 15 mm and a wall thickness of 2 mm and is concentrically placed in a transparent polycarbonate tube, which has an outer diameter of 60 mm and a wall thickness of 3 mm. As PCM, the paraffin RT35HC supplied by Rubitherm is used (Rubitherm GmbH, 2023). The PCM has a phase change range of 34 to 36 °C. The tube-in-tube heat exchanger contains 1.497 kg of PCM with a total latent heat capacity of 360 kJ.

A camera is placed in front of the heat exchanger on a linear slider to monitor the position of the melting front along the entire tube length. The assembly is arranged in a large box filled with insulation granules to reduce the thermal losses (Vermiculite, 2023). Figure 1 gives a schematic representation.

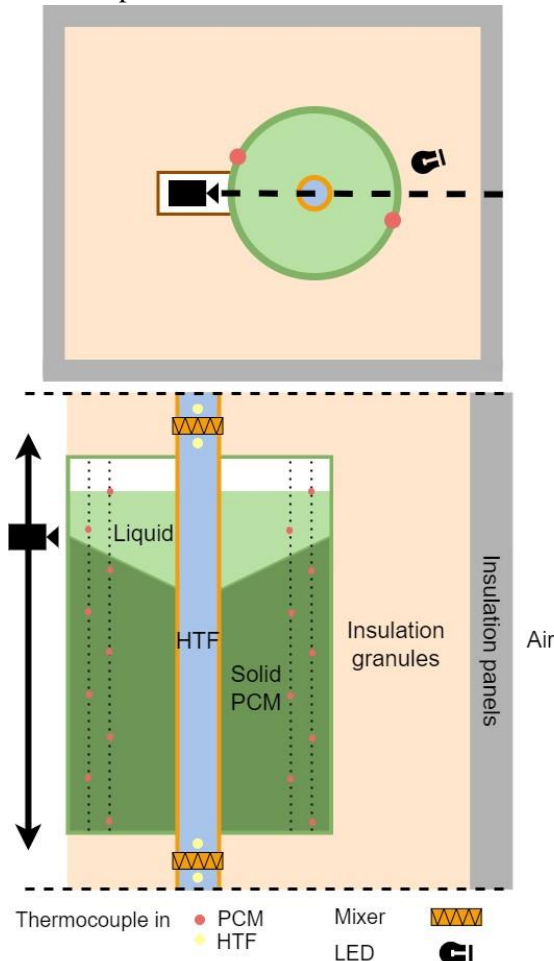


Figure 1: Schematic representation of PCM heat exchanger unit.

The HTF bulk temperature at the inlet and outlet of the heat exchanger is measured using two mixers and four normal and two differential 1.5-mm K-type thermocouples. The HTF mass flow rate is measured using a coriolis flowmeter of the type Proline Promass F 300. The temperature distribution within the PCM is

tracked using 18 K-type thermocouples placed at nine different heights and two depths. All thermocouples are calibrated to 0.15 °C.

Due to practical challenges in visually observing the phase change front during solidification tests, this study only focuses on melting experiments. Similar problems have been noted in literature (Longeon, 2013).

Experimental methodology

A series of melting experiments have been performed in which the HTF mass flow rate (\dot{m}_{HTF}), HTF inlet temperature ($T_{inlet,HTF}$) and initial PCM temperature ($T_{PCM,initial}$) were varied.

Table 1 depicts the different values of HTF mass flow rate HTF and inlet temperature HTF to investigate the influence of these parameters of the heat transfer. In total 16 different experiments were conducted therefore.

Table 1: The values of $T_{inlet,HTF}$ and \dot{m}_{HTF} to investigate their influences.

$T_{inlet,HTF}$ [°C]	50	55	60	65
\dot{m}_{HTF} [kg/h]	20	30	55	80

To examine the influence of turbulent conditions as well, three additional experiments are performed as shown in Table 2. The three HTF mass flow rates correspond to a Reynolds number of 10000, 15000, 20000, respectively.

Table 2: The different \dot{m}_{HTF} to investigate the influence of turbulent conditions in the HTF tube at $T_{inlet,HTF} = 55$ °C and $T_{PCM,initial} = 26$ °C.

\dot{m}_{HTF} [kg/h]	159	235	313
------------------------	-----	-----	-----

Finally, three extra experiments were conducted sharing the same mass flow rate and inlet temperature of the HTF to analyse the initial temperature of PCM.

Table 3: The experimental matrix to investigate the influence of the initial PCM temperature at $T_{inlet,HTF} = 65$ °C and $\dot{m}_{HTF} = 30$ kg/h.

$T_{PCM,initial}$ [°C]	32	25	18
------------------------	----	----	----

During each experiment, the vertical position of the phase change front at the outer diameter of the PCM tube is tracked over time by the camera. The front position is defined as the vertical distance covered by the phase change front, beginning at the inlet of the HTF tube.

Figure 2 shows the observed phase change front movement during a complete melting experiment with operating conditions: $T_{inlet,HTF} = 50$ °C, $\dot{m}_{HTF} = 30$ kg/h and of $T_{PCM,initial} = 26$ °C.

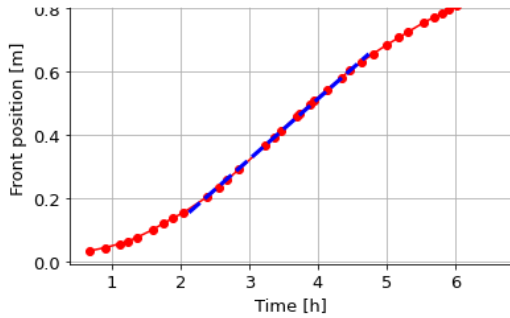


Figure 2: Movement of the phase change front and linear approximation (blue dotted line) for a charging experiment

Three different melting phases can be distinguished. During the start of the experiment the moving speed of the phase change front increases until a quasi-steady state regime is obtained where the moving speed is constant. Near the end of the experiment the moving speed decreases again. These three observed phases make the typically obtained S-shaped curve. In the remainder of this paper, the focus is on this quasi-steady state regime and a linear fit is proposed. The linear approximation for one of the experiments is shown as the blue line in Figure 2. This regime can be characterized by its slope, which represents the front movement speed. This front speed is an important parameter because it is related to the change in internal energy of the PCM volume.

The visual observation of the front position has an error of 1 mm, which is only a small percentage of the total height of the heat exchanger (1%). Therefore, the error on the front position and moving speed are considered to be negligible and not mentioned further.

Data reduction and analysis

The influence of HTF inlet temperature, HTF mass flow rate, and initial PCM temperature on the front movement speed are shown in Figures 4, 5 and 6.

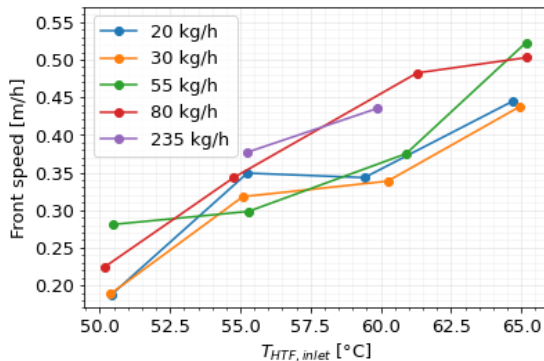


Figure 3: Influence of $T_{inlet,HTF}$ on the front speed during melting experiments for different \dot{m}_{HTF} .

A pronounced tendency can be identified between the HTF inlet temperature and phase change front movement. A higher $T_{HTF, inlet}$ results in a higher front speed as the overall heat transfer during the complete

experiment is enhanced by the larger temperature difference between HTF and PCM. Figure 3 even suggests a linear relationship between the speed and $T_{HTF, inlet}$.

A high HTF mass flow rate (Reynolds number) enhances forced convection in the HTF tube, and thus overall heat transfer, meaning the front speed movement should be higher. However, as the mass flow rate increases, the temperature difference across the HTF tube will decrease, reducing the buoyancy force in the liquid PCM. At the same time, the smaller temperature difference between HTF inlet and outlet increases the temperature difference between the HTF and PCM along the entire length of the tube, and thereby possibly increasing the overall heat transfer. All these effects contribute to the complexity of predicting a simple relationship between the HTF mass flow rate and phase change front.

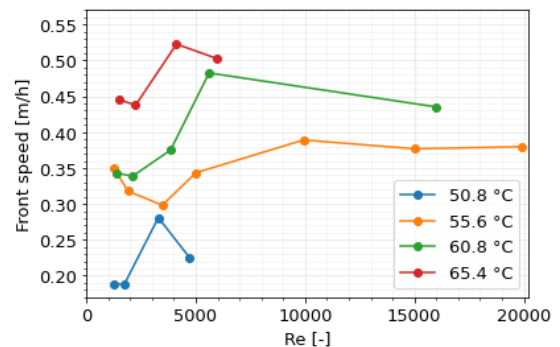


Figure 4: Influence of Reynolds number (\dot{m}_{HTF}) on the front speed during melting experiments for different $T_{inlet,HTF}$.

It can be inferred from Figure 4 that a higher Reynolds number results in a higher front speed. Between the laminar and turbulent conditions, the distinction can be seen. However, (big) fluctuations are present between the Reynolds numbers 2500 and 5000, meaning no clear trend can be established. In addition, it can be seen that the moving speed, and consequently the rate of change in internal energy of the PCM volume, is more sensitive to a change in the HTF inlet temperature than to a change in mass flow rate, which is consistent with literature (Kalapala, 2018). However, further research is required to obtain a better comprehension.

Figure 5 shows that a higher $T_{PCM, initial}$ corresponds to a higher front speed. This is the opposite of what one would expect, as a higher $T_{PCM, initial}$ causes the temperature difference between the PCM and HTF to be smaller and thus a smaller overall heat transfer. On the other hand, it should be noted that $T_{PCM, initial} = 32$ °C is very close to the phase change range. Again, further research is needed to investigate the combination of all the influences.

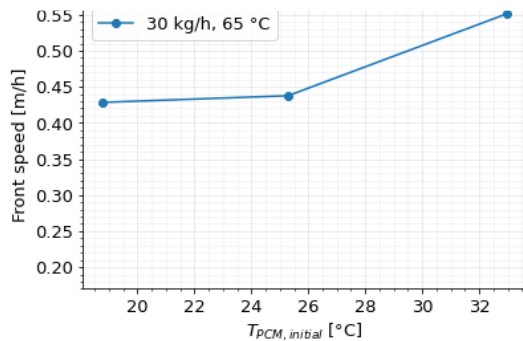
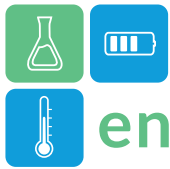


Figure 5: Influence of $T_{PCM,initial}$ on the front speed during melting experiments for the same $T_{inlet,HTF}$ and \dot{m}_{HTF} .

Conclusions

A series of melting experiments have been performed in which the HTF mass flow rate, HTF inlet temperature and initial PCM temperature were varied. During each experiment, the movement of the phase change front was tracked over time using a camera. It was seen that each front-curve shows an S-shape with a linear part which represents the quasi steady state regime of the moving speed. To gain a better understanding of the phase change front dynamics, the influences of the varying operating conditions on this front speed were analysed. Only for the HTF inlet temperature, a clear linear trend was found: higher HTF inlet temperature results in higher front speed. As the HTF mass flow increases and consequently the Reynolds number, the front speed first decreases at Reynolds numbers between 2500 - 5000 and at Reynolds numbers higher than 5000, the front velocity increases again. However, there are many fluctuations present in the results. Lastly, a higher initial PCM temperature increases the front movement speed. Further research is required to gain a deeper understanding of the combination of all the influences.

Acknowledgments

This research was partially funded by a FWO grant (1SHBC24N) for strategic basic research and a FWO grant (1246924N) for junior postdoctoral research of the Research Foundation – Flanders, Belgium. The financial support is gratefully acknowledged. This work has been partially funded by the grant agreement No. 101103921 (HEATERNAL project) of the European Union's Horizon 2020 research and innovation programme.

Furthermore, the authors would like to express their gratitude and appreciation to the technical staff of Ghent University, especially Frederik Martens, Bart Van Daele, and Thomas Blancke for building and maintaining the setup used to obtain the discussed experimental data.

References

- A. Castell and C. Solé. (2015). 11 - design of latent heat storage systems using phase change materials (PCMs). In e. L. F. Cabeza, *Advances in Thermal Energy Storage Systems* (pp. 285–305). Woodhead Publishing.
- Beyne, W. (2023). An approximate analytical solution for the movement of the phase change front in latent thermal energy storage heat exchangers. *Energy Storage*, 106132.
- Kalapala, L. (2018). Influence of operational and design parameters on the performance of a PCM based heat exchanger for thermal energy storage – A review. *Energy Storage*, 497–519.
- Karami, R. (2020). Experimental investigation of the effect of perforated fins on thermal performance enhancement of vertical shell and tube latent heat energy storage systems. *Energy Conversion and Management*, 112679.
- Longeon, M. (2013). Experimental and numerical study of annular pcm storage in the presence of natural convection. *Applied Energy*, 175-184.
- M. Heyhat, F. Kowsary, A. Rashidi, S. A. V. Esfehiani, and A. Amrollahi. (2012). Experimental investigation of turbulent flow and convective heat transfer characteristics of alumina water nanofluids in fully developed flow regime. *International Communications in Heat and Mass Transfer*, 1272–1278.
- Raud, R. (2017). Design optimization method for tube and fin latent heat thermal energy storage systems. *Energy*, 585-594.
- Regin, A. F. (2008). Heat transfer characteristics of thermal energy storage system using pcm capsules: A review. *Renewable and Sustainable Energy Reviews*, 2438–2458.
- Rubitherm GmbH. (2023, December 19). Retrieved from <https://www.rubitherm.eu/en/productcategory/organische-pcm-rt>
- Tarragona, J. (2021). Experimental analysis of a latent thermal energy storage system enhanced with metal foam. *Energy Storage*.
- Tay, N. H. (2012). An effectiveness-NTU technique for characterising tube-in-tank phase change thermal energy storage systems. *Applied Energy*, 309-319.
- Vermiculite. (2023, December 16). Retrieved from <https://shop.deschacht.eu/nl-be/7921/vermiculite-g3-medium-9kg-100l>



Innovative transient modelling of concrete-based solid medium for thermal energy storage systems

Pablo D. Tagle-Salazar^{1,2}, Cristina Prieto^{2*}, Luisa F. Cabeza¹

¹ GREiA Research Group, Universitat de Lleida, Pere de Cabrera s/n, 25001, Lleida, Spain

² University of Seville, Department of Energy Engineering, Camino de los Descubrimientos s/n, 41092, Seville, Spain

*Corresponding author e-mail: cprieto@us.es

Abstract

Global warming poses a critical challenge, demanding sustainable solutions to reduce greenhouse gas emissions. Concentrated Solar Power (CSP), a zero-emission technology, integrates seamlessly with Thermal Energy Storage (TES) systems, ensuring plant reliability for industrial heat processes and electricity generation, despite solar intermittence. In contemporary discourse, several authors have posited that TES employing concrete as the storage medium has emerged as a promising alternative to conventional two-tank systems utilizing molten salts. This paper introduces an inventive transient model designed to simulate a concrete TES block, utilizing a configuration previously outlined in the literature, which addresses both constructive and operational challenges inherent in concrete TES systems, thereby contributing to the advancement of this technology. The model identifies optimal heat transfer conditions near the transitional-to-turbulent flow regime. Additionally, the temperature distribution within the solid medium consistently exhibits a diagonal pattern, with the hottest point at the HTF inlet.

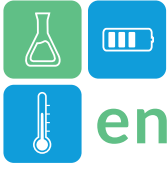
Keywords: Sensible heat thermal energy storage, solid medium, transient modelling.

Introduction

Global warming, often considered one of the greatest challenges facing humanity today, has spurred an urgent need for sustainable solutions to mitigate its adverse effects. As countries strive to meet climate change targets and reduce greenhouse gas emissions, the increased utilization of renewable energy sources has emerged as a paramount strategy. Among the array of renewable energy technologies, Concentrated Solar Power (CSP) stands out as a potential contributor in this context (IEA, 2010; Mehos et al., 2017). What sets CSP apart from other solar energy technologies is its unique capability to generate zero-emission high-temperature heat for industrial processes and electricity. A distinguishing feature that positions CSP as a key player in the renewable energy landscape is its seamless integration with Thermal Energy Storage (TES) systems. However, CSP is not without its challenges, primarily stemming from the intermittence of solar radiation, especially during nighttime or cloudy periods. It is in this critical juncture that TES systems emerge as a solution, as they ensure the continuity and reliability of CSP plants by meeting energy demand even when solar input is insufficient. These factors collectively underscore the essential role of CSP and TES systems in addressing the multifaceted challenges of global warming and transitioning toward a more sustainable energy future.

The field of thermal energy storage incorporates a diverse array of technologies, with three primary categories at its core: sensible heat, latent heat, and thermochemical heat storage. Among these, sensible heat storage stands as the most widely deployed system, often employing a two-tank configuration with molten salt as the storage medium. An alternative approach within sensible heat storage involves the use of solid media materials, where conventional concrete emerges as an economically attractive choice due to its widespread availability, significant thermal mass per unit volume, and cost-effectiveness. Moreover, concrete materials exhibit robust thermal stability during high temperature cycling and display commendable durability (Wang et al., 2023).

(Cabeza et al., 2022) identified various challenges associated with concrete TES technology, including on-site construction, thermal expansion of pipe materials in direct contact with concrete, operational constraints of the Heat Transfer Fluid (HTF), and HTF migration into solid medium in tubeless modules. In response to these issues, the authors proposed a modular block featuring a square-prism configuration with a circular aperture and advocated for the use of air as the HTF. This modular block design streamlines fabrication, construction, and assembly processes, addressing the aforementioned operational concerns. The current study introduces a novel transient model,



incorporated into a software tool, and calibrated utilizing the findings presented by (Cabeza et al., 2022) within the context of the proposed modular configuration.

Methodology

In modelling concrete TES, two essential components demand consideration: the HTF and the solid media. The subsequent mathematical models, accompanied by their relevant constraints and assumptions, are detailed here. These models have been incorporated into OpenModelica to enable efficient simulations of the storage system.

Heat transfer model in solid media

Within the context of solid media, the thermal model is underpinned by a bi-dimensional thermal resistance-capacitance network, as shown in Figure 1a. This approach postulates the concrete as an isotropic medium characterized by temperature-dependent thermo-physical properties, except for density, which is held as constant. The concrete block is geometrically conceptualized as a right prism with regular polygons serving as the base. Notably, this simplified model omits several complex phenomena, including but not limited to the effects of cracking, fluid migration, mass loss of aggregates, thermal stresses, and other pertinent factors.

The concrete medium is discretized into small elements (i.e. nodes), where r_{nodes} and z_{nodes} are the number of elements in radial and axial directions, respectively. The energy balance within an individual node is mathematically expressed as indicated in Equation (1). While the concrete is assumed to be well-insulated at its extremities (i.e., at $z = 0$ and $z = L$), it is permitted to absorb or transmit heat through its inner and outer surfaces. In the axial direction, the governing equation aligns with Fourier's law of conduction heat transfer, and in the radial direction, heat conduction is influenced by the shape factor S , as denoted in Equation (2). The boundary condition is defined as surfaces with uniform heat flow in the radial boundaries (Equation (4)). Equation (5) delineates the capacity factor, a metric expressing the proportion of energy retained within the solid media relative to the maximum storage capacity of the module, quantified as a percentage.

$$-\dot{q}_{i+1} + \dot{q}_{i-1} - \dot{q}_{j+1} + \dot{q}_{j-1} = \dot{q}_{sto,i} \quad (1)$$

$$\dot{q}_i = kA_i (T_{i-1,j} - T_{i,j})/\Delta z ; \dot{q}_j = kS_j \Delta z \quad (2)$$

$$\dot{q}_{sto,i} = \rho C_p (A_i \Delta z) \partial T_{i,j} / \partial t \quad (3)$$

$$\begin{cases} \dot{q}_{i,0} = \dot{q}_{i,in} \\ \dot{q}_{i,r_{nodes}+1} = \dot{q}_{i,out} \end{cases} ; \forall i = [1, z_{nodes}] \quad (4)$$

$$C_f = \frac{\int (\sum \dot{q}_{sto,i}) dt}{m \int_{T_{cold}}^{T_{hot}} C_p dT} \times 100\% \quad (5)$$

The computation of the shape factor leverages the algorithm expounded by (Hirbodi & Jafarpur, 2020). This algorithm facilitates the determination of the shape factor for a prismatic-hollow cylinder featuring inner and outer cross-sections comprising n-sided regular polygons or circular geometries. Consequently, the concrete block is subject to discretization in the radial direction, as visualized in Figure 1b. In scenarios involving a circle-polygon configuration (as used for this study), the number of sides of the polygon exhibits a doubling pattern as the radial progression approaches the circular side. This deliberate augmentation in the number of sides is implemented with the aim of refining the fidelity of simulation outcomes to the authentic temperature distribution characteristic of configurations of this nature.

Heat transfer model in HTF

The heat transfer model for the HTF considers a fluid flowing in the inner part of the solid media. It delineates a discretization of the fluid into small volumes referred to as “nodes,” as illustrated in Figure 1c. The model assumes constant properties of the fluid along each node, emphasizing incompressibility and adherence to Newtonian fluid dynamics. Equation (6) expresses the energy balance for each node. Uniformity in heat flow through the lateral surface is posited, and subsequently, the total convection heat flow is apportioned by dividing it among the number of sides constituting the external surface of the solid media. Importantly, the model makes the specific assumption of a horizontally oriented pipe, thereby neglecting the influence of height variations.

$$\begin{aligned} m_i \frac{\partial h_i}{\partial t} + \dot{m} [h_i - h_{i-1} + (v_i^2 - v_{i-1}^2)/2] \\ = -\bar{h}_{conv} A_l (T_{f,i} - T_{s,i}) \end{aligned} \quad (6)$$

The thermophysical properties of the fluid exhibit dependency on both temperature and pressure for gaseous substances, while for liquids, such properties are exclusively functions of temperature. The nodal convection heat transfer coefficient, denoted as \bar{h}_{conv} , considers all flow regimes: laminar, transitional, and turbulent. To ensure continuity across these distinct regimes, correlations governing this coefficient were meticulously chosen, thus maintaining consistency throughout the entirety of the three flow regimes.

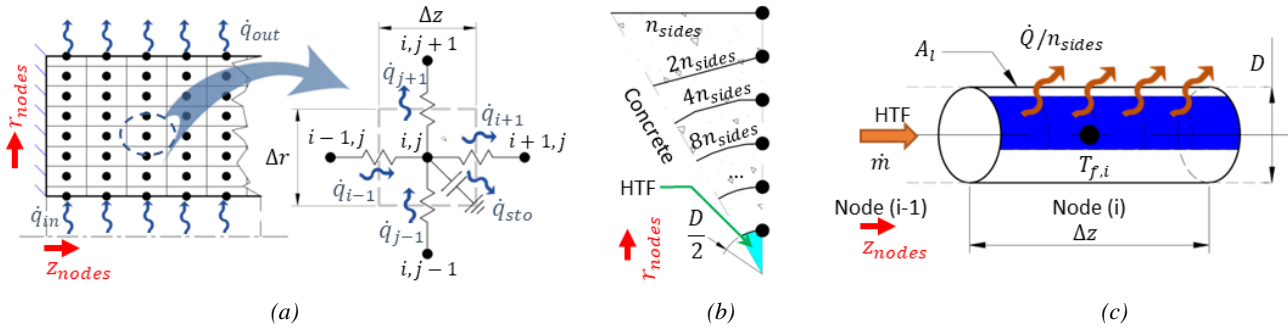


Figure 1. Concrete TES. (a) Thermal resistance-capacitance network in solid media, (b) Discretization in radial direction in solid media, (c) Discretization of the HTF

Concrete TES block

The conceptualization of the concrete TES block involves a modular design featuring direct-fit connections (male/female), as depicted in Figure 2 (dimensions in mm). This particular configuration enables straightforward assembly through block stacking. The tubeless nature of the block is implemented to mitigate mechanical stresses arising from the thermal expansion of pipes, while the integration of air as the HTF serves to pre-emptively address issues related to fluid migration. The properties of the concrete used in simulations are 1.01 W/m·K for thermal conductivity, 2306 kg/m³ for density, and 0.837 kJ/kg·K for specific heat capacity. In the interest of computational simplification, this study omits the consideration of direct-fit connections. Consequently, the analysed configuration of the block under examination assumes a right square-prism shape with a central circular aperture.

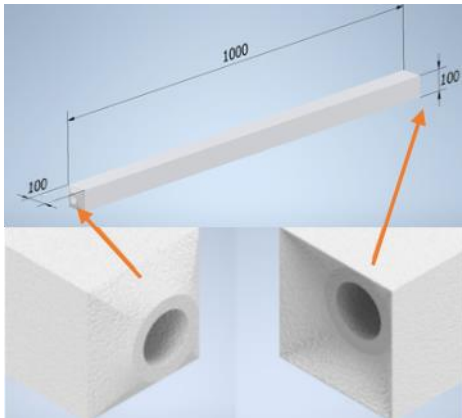


Figure 2. Conceptual concrete block (Cabeza et al., 2022)

Results

Optimization of the concrete block

To mitigate the impact of a coarse mesh and enhance computational efficiency, a sensitivity analysis is conducted. The simulation conditions involve a step increment in the inlet temperature from 265 °C to 450 °C at $t = 0$. The initial condition in the HTF entails

a uniform temperature distribution along its length at 265 °C. To ascertain the optimal conditions for heat transfer, a simulation is conducted to examine the relationship between the capacity factor and fluid velocity. Subsequently, with the optimized velocity, a sensitivity analysis is executed to assess the impact of varying the number of nodes in both axial and radial directions on the capacity factor. Following the determination of an appropriate node configuration, a further simulation is carried out to identify the optimum fluid velocity. This iterative algorithm is repeated until the fluid velocity converges to a state of negligible change. Particularly in this aspect, the designation of the concrete block as "charged" is contingent upon the outlet temperature reaching 80 % of the initial temperature difference.

Figure 3 illustrates the outcomes of the analysis. Initially, the optimal heat transfer is observed at a velocity of 6 m/s (Figure 3a), yielding a capacity factor of approximately 42.7 % and a corresponding time of 1.89 hours to achieve the specified conditions. Velocities below 2.4 m/s result in higher capacity factors, but the charging time for these conditions becomes impractically long for solar applications (higher than 5 hours). In Figure 3b, the capacity factor is noted to increase asymptotically with the number of axial nodes and decrease with radial nodes, nearing the asymptote around 200 nodes in axial direction. Conversely, in the radial direction, the change is negligible with number of nodes higher than 20. Then 200 and 20 are selected as the number of nodes in axial and radial directions, respectively, for further analysis.

Simulation of the modular concrete TES block

In the simulation of the concrete block, all conditions remain consistent in previous section, with the only modification being that the concrete block is designated as "fully charged" upon reaching a capacity factor of 99 %. Subsequently, temperature distribution in the concrete is derived. Fluid velocity is 6 m/s for optimum heat transfer conditions.

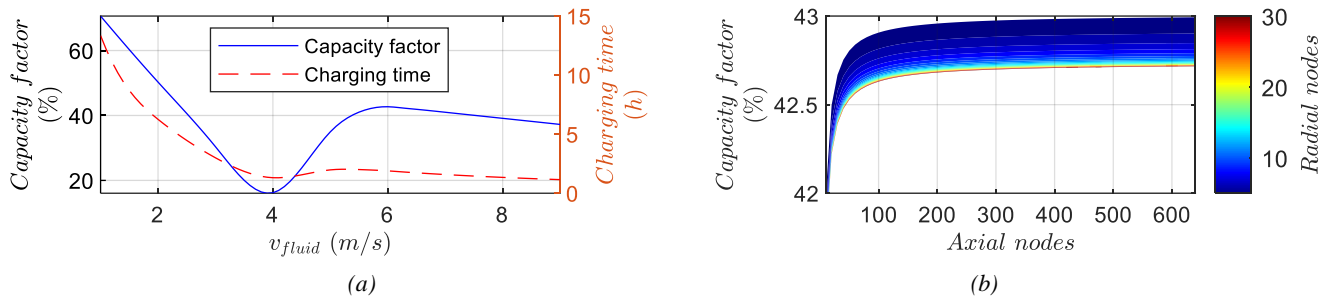
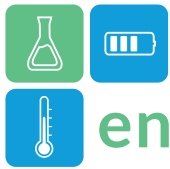


Figure 3. Optimization analysis. (a) Fluid velocity and charge time, (b) Sensitivity analysis of number of nodes in axial and radial directions

Figure 4 shows the temperature distribution in a section of the concrete module corresponding to a "half-charged" state ($C_f = 50\%$), achieved after 2.36 hours of charging. As anticipated, the region in direct contact with the fluid at the inlet exhibits the highest temperature, while the outer surface near the fluid outlet remains cooler throughout the simulation. The temperature difference between these points is approximately $37.6\text{ }^\circ\text{C}$ at the displayed status, closely aligning with the predicted value of $50\text{ }^\circ\text{C}$, visually estimated by (Cabeza et al., 2022). Notably, the maximum temperature difference occurs at 1.48 hours, reaching a value of $39.1\text{ }^\circ\text{C}$. After this time, the temperature difference decreases up to $2.1\text{ }^\circ\text{C}$ when the module is at "fully-charged" state.

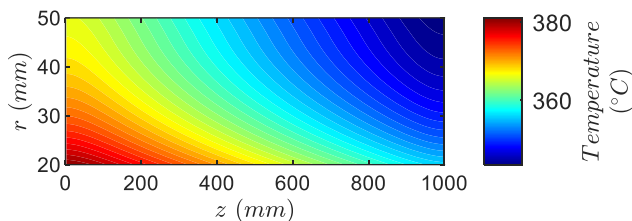


Figure 4. Temperature distribution in solid medium

Conclusions

A bidimensional transient heat transfer model for a concrete module utilizing air as the HTF is presented, encompassing its limitations, assumptions, and mathematical formulations. In comparison to a previous analysis of prismatic geometry, the current study reveals that the model identifies optimal heat transfer conditions in the vicinity of the transitional-to-turbulent flow regime ($Re \approx 3355$). Moreover, the model demonstrates greater sensitivity to the number of nodes in the axial direction than in the radial direction. The temperature distribution within the solid medium consistently exhibits a pattern where the hottest and coolest points are diagonally opposite, with the hottest point in contact with the HTF at the inlet.

Acknowledgments

This work is part of PCI2020-120695-2 project funded by Ministerio de Ciencia e Innovación—Agencia

Estat de Investigación (MCIN/AEI/10.13039/501100011033) and by the European Union "NextGenerationEU/PRTR". This work was partially funded by the Ministerio de Ciencia e Innovación - Agencia Estatal de Investigación (AEI) (PID2021 123511OB C31 - MCIN/AEI/10.13039/501100011033/FEDER, UE and RED2022-134219-T). This work is partially supported by ICREA under the ICREA Academia programme. The authors from University of Lleida would like to thank the Catalan Government for the quality accreditation given to their research group GREiA (2021 SGR 01615). GREiA is a certified agent TECNIO in the category of technology developers from the Government of Catalonia.

References

- Cabeza, L. F., Várez, D., Zsembinszki, G., Borri, E., & Prieto, C. (2022). Key Challenges for High Temperature Thermal Energy Storage in Concrete—First Steps towards a Novel Storage Design. *Energies*, *15*(13), 4544.
- Hirbodi, K., & Jafarpur, K. (2020). A simple and accurate model for conduction shape factor of hollow cylinders. *International Journal of Thermal Sciences*, *153*, 106362. <https://doi.org/https://doi.org/10.1016/j.ijthermalsci.2020.106362>
- IEA. (2010). *Technology Roadmap: Concentrating Solar Power*. OECD Publishing. <https://doi.org/10.1787/9789264088139-en>
- Mehos, M., Turchi, C., Vidal, J., Wagner, M., Ma, Z., Ho, C., Kolb, W., Andraka, C., & Kruiuzenga, A. (2017). *Concentrating Solar Power Gen3 Demonstration Roadmap*.
- Wang, S., Abdulridha, A., Naito, C., Quiel, S., Suleiman, M., Romero, C., & Neti, S. (2023). Enhancement of conventional concrete mix designs for sensible thermal energy storage applications. *Journal of Energy Storage*, *61*, 106735. <https://doi.org/10.1016/J.EST.2023.106735>



Engineering Considerations and Preliminary Design

Mateo Sanclemente¹, Silvia Trevisan¹ and Rafael Guedez¹

¹ KTH Royal Institute of Technology, Department of Energy Technology, 100 44 Stockholm, Sweden.

E-Mail: mateosl@kth.se

Abstract

The present work introduces the preliminary laboratory design of a heat upgrade process using a Stirling Cycle heat pump and three thermal energy storage units. Heat is upgraded to 250°C by recovering heat from a medium-temperature water vector. Then, this heat is used for charging a thermal energy storage unit which can be utilized for various industrial heat applications, such as steam production or hot air drying.

Keywords: Heat upgrade, thermal energy storage, heat pump.

Introduction

Heat upgrade technologies are becoming increasingly relevant as one of the ways to meet the high energy demand required by industry. The development and installation of these technologies represent a double benefit. First, by using renewable energy sources, it contributes to reducing fossil fuel consumption. Second, heat for industrial processes is a market where other renewable-based technologies, such as solar, are encountering limitations [1].

Commercial heat pumps can effectively upgrade heat up to 120°C [2]. Nowadays, a wide part of the industrial sector requires higher temperatures, 150-250°C [3]. In this work, heat is upgraded up to 150-250°C using a high-temperature Stirling heat pump (HTHP) that uses helium, which drastically enlarges the industrial exploitability of waste heat upgrade systems. The integration of innovative thermal energy storage (TES) solutions will ensure a reliable, flexible, and customizable heat delivery with full decoupling from any waste heat recovery and renewables availability, which is an usual challenge in various industrial sectors. The authors introduce the concept by describing the preliminary design and engineering steps for the installation and commissioning of such a novel laboratory-scale facility. This work is a stepping-stone towards a comprehensive experimental investigation.

Methodology

Figure 1 shows the proposed the system. The central units of the system are the HTHP, one low-temperature thermal energy storage (LT-TES) at 70°C, one medium-temperature thermal energy storage at 155°C (MT-TES), and one high-temperature thermal energy storage (HT-TES) at 245°C. The LT-TES is located on the cold side (left) of the HTHP while the MT-TES and HT-TES units are on the hot side (right) of the HTHP.

The laboratory rig is designed to deliver about 200kW of heat to produce steam or hot drying air. For practical reasons, the rig will use a heat exchanger as a heat sink instead of a steam generator to avoid handling steam in the laboratory. In the same perspective, an electric tracing is used to simulate the heat coming from a waste heat stream. The system is designed to use pressurized water as heat transfer fluid (HTF) in both circuits.

Figure 1 shows four modes of operation: (1) charging of the TES units and producing steam in black lines, (2) discharging in red lines, (3) only charging without delivering heat to the heat sink in yellow lines, and (4) heat is delivered only to the heat sink while all TES units are fully charged in blue lines. It is important to highlight that the system is designed to be flexible and to operate in different conditions.

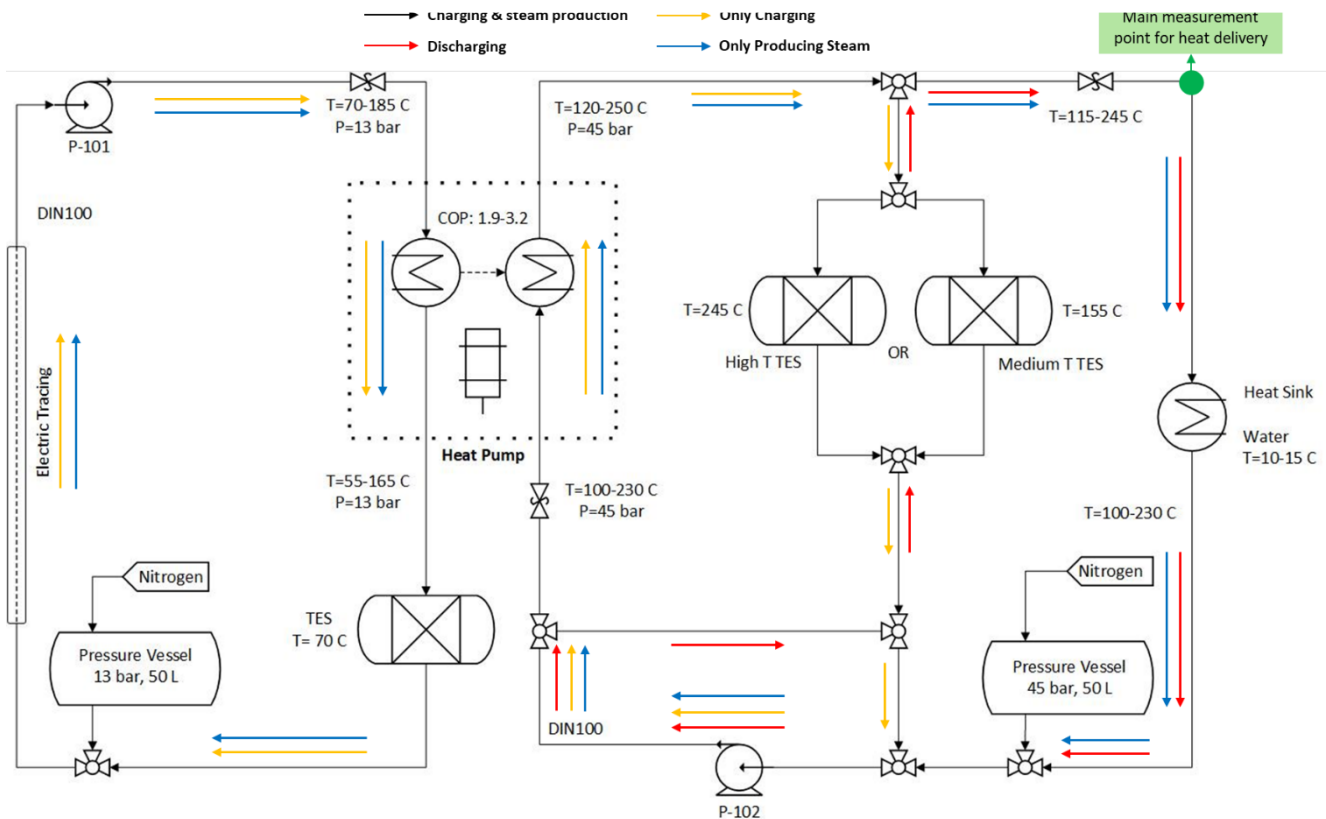


Figure 1. Proposed laboratory rig layout with different operation modes indicated in colours.

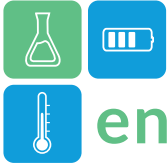
The system has three TES units with different melting temperatures: one with a phase change material (PCM) at 245°C, a second with a PCM at 155°C, and a third with a PCM at 70°C, giving the system more flexibility to store heat in a wider range of temperatures. For a given running cycle only one TES on the hot side (i.e. medium-temperature and high-temperature TES) can be used depending on the temperature of the system, meaning that only one can be charged or discharged while running the system. The LT-TES can be used at any time. This research also investigates the performance of the system when upgrading heat to 250°C while achieving a coefficient of performance (COP) of 2.8; for this, a maximum source temperature of 185°C must be used for the temperature lift.

When starting the system, the electric tracing on the cold side will heat the HTF to the required inlet temperature of the cold side of the HTHP ($T_{C,in}=70-160^{\circ}\text{C}$ as seen in Figure 1). Pump-101 will start running the circuit through the cold heat exchanger of the HTHP and, parallelly, pump-102 will also start running the hot circuit while a steady state of the cold side is reached. Then, the HTHP will start, heat is transferred to the pressurized water reaching temperatures of 120-250°C, and finally, delivering it to the heat sink. Also,

when the circuit reaches temperatures of 160-250°C it can be used for charging the respective MT-TES and HT-TES units.

For each source temperature, several sink temperatures are reached using four different average COPs: 1.95, 2.25, 2.55, and 3.0. It is known that for all heat pumps lower temperature lifts ($T_{H,out}-T_{C,in}$), and larger ratios ($T_{C,in}/T_{H,out}$) lead to higher coefficients of performance [4]. For example, a $T_{H,out}$ of 303°C is achieved with a COP of 2.0 and a source temperature of 120°C while a $T_{H,out}$ of 178°C is achieved with COP of 3.0 with the same source temperature.

When T_C and T_H have been defined for the boundary cases, it is possible to calculate the different parameters of the system by performing energy balances on the different components.



The design starts with the heat sink heat exchanger which has been designed to deliver 200kW. The maximum inlet temperature is 250°C, and the maximum outlet temperature is 230°C. Thus, it is possible to calculate the mass flow of water inside the liquid and the heat losses by

$$Q = \dot{m}_H c_{pl} (T_{H,out} - T_{H,in}) \quad (1)$$

Where $T_{H,out}=250^\circ\text{C}$, $T_{H,in}=230^\circ\text{C}$ and $Q=200\text{kW}$.

By equalizing equation (1) to zero and solving for \dot{m} , the mass flow of the circuit can be obtained.

Then, for the Heat Pump

ΔT between the inlet and outlet temperature of the HTF on both heat exchangers of the HTHP is considered equal to 20°C, which maintains the COP. The design must consider the minimum and maximum conditions of temperature and COPs (1.9-3.2) for calculating the mass and outlet temperature of water on the cold side of the heat pump. The equations involved in the heat pump are

$$Q_H = \dot{m}_H c_{pH,in} (T_{H,out} - T_{H,in}) \quad (2)$$

Then using COP = 1.9 and 3.2 it is possible to calculate Q_C using equation (2) and to determine $T_{C,out}$ by

$$Q_C = \dot{m}_C c_{pC,in} (T_{C,in} - T_{C,out}) \quad (3)$$

Considering that \dot{m}_C can be equal to \dot{m}_H , $T_{C,out}$ is obtained. The mass flow can be set to keep a reasonable velocity of the fluid inside the circuit (0,25-1 m/s) and the $T_{L,out}$ is calculated from the respective energy balance.

One important consideration for the laboratory rig design is the selection of the HTF and, in this case, water is selected as it is non-flammable and does not have toxic risk. To work with water, the circuits must be pressurized above the saturation pressure ($P_{saturation}$) at the given temperatures, otherwise, vapour will be produced. Therefore, two scenarios for the pressure are foreseen: the first one for building the desired pressure before the start-up; and the second, to compensate for the pressure losses within the circuit. For the latter, the segment thermal losses and the friction losses can be calculated for a given length, pipe diameter and flow regime.

Water pumps

For each pump, the corresponding segment loss is determined by

$$\Delta P = \frac{f L \rho V^2}{2 D_i} \quad (4)$$

Where D_i is the internal pipe diameter, L is the pipe length, V is the velocity of the fluid, ρ is the density of the fluid, and f is the friction factor for internal flow.

calculated by

$$V = \frac{\dot{v}}{\pi \left(\frac{D_i}{2}\right)^2} \quad (5)$$

Where \dot{v} is the flow rate in m^3/s , and the power of the pump is calculated as

$$\dot{W}_p = \Delta P \cdot \dot{v} \quad (6)$$

Pressure Water Vessels

For the pressure vessel, the volume is calculated using the following heuristic.

$$V_{pv} = 6 \dot{m} \quad (7)$$

Then for a 20% filled capacity, a vessel of 50 L is enough.

As main components of the system, two centrifugal pumps are used for controlling water flow and overcome pressure losses within the circuit. This involves one pump on each side. As mentioned before, the water circuits must be pressurized above $P_{saturation}$ at the highest temperature, in the case of the cold side a pressure vessel at 13 bars will be used, and on the hot side, a pressure vessel at 45 bars will be used. Minor components such as valves and sensors are considered for control purposes. The system foresees N1. T-port valve and N.1 Pressure relief valve (PRV) on the cold side, and the hot side: N.7 T-port valves for connecting the circuit with both TES. N.2 PRV for pressure control, one before the HTHP and one before the heat sink heat exchanger. Key measurement points ought to be before and after the HTHP on both sides. The main temperature measurement point is indicated in Figure 1 as a green dot. Several manometers for pressure measurements are included in the design. Additionally, one flowmeter for flow control is considered after each pump on both sides of the system.

Boundary Conditions

The HTHP enables a COP between 1.9 and 3.2 for temperature ratios of 1.1-1.5 ($T/T \text{ }^\circ\text{K}$) providing sufficient heat to produce high-quality steam for heating, drying or distillation processes. From the previous methodology, a total of thirteen (N.13) operational scenarios have been identified as boundary conditions. Each respective COP characterizes a T_C , T_H and temperature ratio as shown in Figure 2.

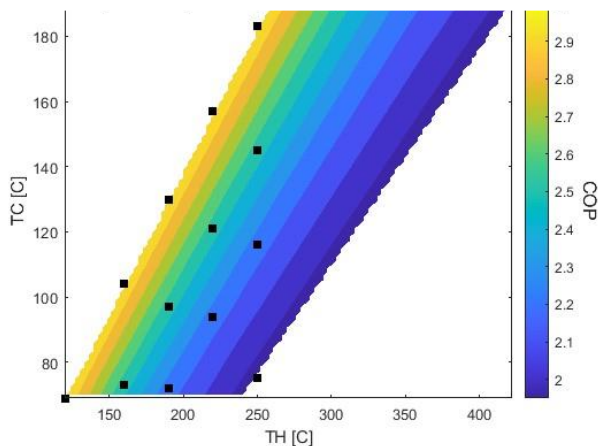
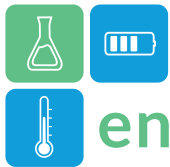


Figure 2. Operational scenarios for the HTHP

The thirteen cases have been chosen according to the industrial cases that this work is investigating. The first one is a dairy factory located in Greece, where the waste stream has a temperature of 70°C, and the heat is to be delivered at 200°C for steam production. The second is a fish-related product factory in Norway, where the waste stream has a temperature of 90°C, and heat is to be delivered at 250°C to produce hot drying air. Within these cases, two are limit cases that express the minimum and maximum flow rate of water needed in the system, Case 9 and Case 13 as shown in Table 1.

Table 1. Boundary cases.

Case	Case 9	Case 13	Units
COP	3.0	3.0	
$T_{c,in}$	70	183	°C
$T_{H,out}$	120	250	°C
H ₂ O mass flow	8211	5145	kg/h
H ₂ O volumetric flow	2,42	1,79	L/s

Conclusions

The present work introduces the preliminary laboratory design of a heat upgrade process using a Stirling Cycle heat pump and two thermal energy storage units. The boundary conditions have been identified from the basic engineering. Future work will be focused on designing the control strategy and consolidating the P&ID of the system including valves, sensors, and operational manual of the system.

This project has received funding from the European Union’s Horizon Europe research and innovation programme under grant agreement NO 101103552.

References

- [1] M. Martín, “Challenges and opportunities of Solar thermal energy towards a sustainable chemical industry,” *Comput. Chem. Eng.*, vol. 165, p. 107926, Sep. 2022, doi: 10.1016/J.COMPCHEMENG.2022.107926.
- [2] C. Arpagaus, F. Bless, M. Uhlmann, J. Schiffmann, and S. S. Bertsch, “High temperature heat pumps: Market overview, state of the art, research status, refrigerants, and application potentials,” *Energy*, vol. 152, pp. 985–1010, Jun. 2018, doi: 10.1016/J.ENERGY.2018.03.166.
- [3] G. Kosmadakis, “Estimating the potential of industrial (high-temperature) heat pumps for exploiting waste heat in EU industries,” *Appl. Therm. Eng.*, vol. 156, pp. 287–298, Jun. 2019, doi:10.1016/J.APPLTHERMALENG.2019.04.082.
- [4] M. Nilsson, “Simplified pumped thermal energy storage using a two-way Stirling cycle,” *J. Energy Storage*, vol. 73, p. 108994, Dec. 2023, doi: 10.1016/J.EST.2023.108994.



Interpretable Reinforcement Learning Control for Battery Storage in Grid-Interactive Communities

Ken Takahashi^{1,*}, Hiroyuki Ichikawa¹, Shintaro Ikeda², Ryoza Ooka³

1 The University of Tokyo, Graduate School of Engineering, Department of Architecture, 4-6-1 Komaba, Meguro-ku, Tokyo 153-8505, Japan

2 Mikoto Strategy Corporation, 1-5-6 5F KS Floor, Kudan Minami, Chiyoda-ku, Tokyo, 102-0074, Japan

3 The University of Tokyo, Institute of Industrial Science, 4-6-1 Komaba, Meguro-ku, Tokyo 153-8505, Japan

*Corresponding author e-mail: kentak@iis.u-tokyo.ac.jp

Abstract

Grid-interactive communities (GIC) are increasingly adopting battery storage systems to enhance the resilience and efficiency of their energy networks. Leveraging the CityLearn framework for grid-interactive efficient buildings, recent advances in reinforcement learning (RL) research have demonstrated promising results in optimizing energy consumption and reducing carbon emissions. However, the lack of transparency in Artificial Intelligence (AI) algorithms has hindered trust and adoption in real-world applications. This paper introduces an innovative interpretable RL technique, utilizing SHAP (SHapley Additive exPlanations), to enhance trust and acceptance of AI-driven solutions in optimizing battery storage for GIC by providing insights into the decision-making process. Through understanding model results, our approach empowers stakeholders to efficiently contribute to ongoing optimization and enhancement of energy storage control, addressing transparency concerns associated with AI.

Keywords: Explainable Artificial Intelligence, Reinforcement Learning, Battery Storage Controls, Grid-Interactive Communities

Introduction

Grid-interactive communities (GIC) are increasingly adopting battery storage systems to enhance the resilience and efficiency of their energy networks. However, optimizing the operation of these systems remains a complex challenge, demanding advanced control strategies integrating Artificial Intelligence (AI). Advancements in reinforcement learning (RL) research in control systems for GIC have demonstrated promising results in optimizing energy consumption and reducing carbon emissions (Wu et al. 2023). However, the opacity of AI models makes it challenging to understand why specific control values were chosen at a given moment, even for experts, leading to reluctance and hindering widespread adoption, particularly in critical systems like energy management (Chen et al. 2023).

The emergence of highly advanced AI models, such as ChatGPT, has heightened societal concerns about transparency and understanding AI-driven actions. Especially in critical systems like energy management, increased reliance on AI is anticipated to prompt regulatory measures. The EU AI Act,

passed in June 2023, underscores the necessity for accountability, safety, and transparency in AI applications as it becomes increasingly integrated into daily life (Heymann et al 2023).

In light of these considerations, this study aims to enhance the reliability of AI for the proliferation of RL systems, ensuring user confidence. To address the opacity in AI decision-making, Explainable AI (XAI) is employed. The application of XAI allows understanding why specific control values were chosen, potentially identifying areas where the model failed to optimize. Focusing on these decision processes enables users to comprehend and trust AI control mechanisms, striving for more effective and reliable operation.

Methodology

This study introduces the interpretable RL (IRL) control framework for AI-based energy storage controls as presented in Figure 1. The Soft-Actor Critic (SAC) algorithm was employed for the reinforcement learning control that combines entropy regularization and off-policy learning, providing a stable and sample-efficient approach for continuous

action spaces, making it well-suited for tasks like battery control in dynamic environments (Haarnoja. T et al. 2018). Then for each control action, the SHapley Additive exPlanations (SHAP), introduced by Lundberg and Lee 2017, was utilized to explain the SAC model’s decision. SHAP is a widely used interpretability tool in machine learning, rooted in the concept of Shapley values. By leveraging SHAP, one can discern the influence of each observation or state variable on the agent’s decision-making process. This approach provides a valuable understanding of the relative importance of different observations in shaping the agent’s actions, enhancing transparency and interpretability in reinforcement learning models.

Using the explanations provided by the SHAP, the study will answer the following questions one may have about why the model made specific control decisions.

1. Which observations has the highest impacted on deciding the control value?
 - Which observation specifically contributed to decide when to charge the battery?
 - Which observation specifically contributed to decide when to discharge the battery?
2. Which observations had a low impact on the control decision where a higher impact is expected?
3. What are possible solutions to improve the control of the battery storage based on the above findings?

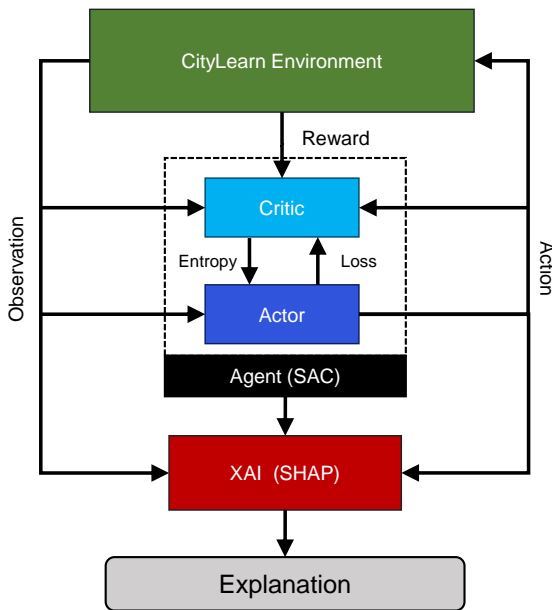


Figure 1: Diagram of the workflow for IRL control

Case Study

This study utilizes the dataset from the NeurIPS 2022 CityLearn Challenge to optimize the battery charge state for residences in a grid-interactive community

located in California (Nweye and al., 2023). The study takes the lighting and appliance load or the non-shiftable electrical load and the solar photovoltaic (PV) generation data from five residences equipped with 6.4 kWh battery and 5 kW PV generation each. The goal of the study is to control the State of Charge (SoC) of the batteries in each residence to minimize the overall electricity cost and CO₂ emissions for the entire district.

The SAC model was trained on one month of data from 5/1 -5/31 and evaluated on one week of data from 6/5-6/11. The observations from the CityLearn environment used to determine the battery state action is listed in Table 1. The reward function for the SAC presented in Eq. (1) penalized the total electricity cost P and carbon emission G for each household i of N buildings. α, β are the weight factors for each objective and was given equal weight for this study.

$$Reward = - \sum_{i=1}^N \alpha P + \beta G : \alpha = \beta = 1 \# (1)$$

For comparison, a baseline case without battery storage and a simple rule based control (RBC) was used. The RBC charges during the daylit hours from 6AM to 2PM at the rate of 11% of the max battery capacity per hour, and discharges at all other hours at the rate of 6.7%.

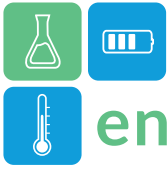
Table 1: Observations from CityLearn Environment

Observation	Observation point
Month, weekday, hour	Current
Diffuse/direct solar [W/m ²]	Current, 6h, 12h forecast
Carbon intensity [kgCO ₂ /kWh]	Current
Non-shiftable load per house [kWh]	Current
Solar generation per house [kWh]	Current
Battery SoC per house [-]	Current
Electricity pricing [\$/kWh]	Current, 6h, 12h forecast

Results

Reinforcement learning control results

In comparison to a baseline without battery storage, the SAC model demonstrated 30% reductions in energy consumption, 33% reduction in CO₂ emissions, and a 38% reduction in power costs. Even when compared to the RBC model, significant reductions were observed in each category. Examining the control patterns in Figure 3, the RBC model exhibited a gradual charge-discharge pattern, while the SAC model demonstrated relatively rapid control. In most cases, these controls fell within the expected pattern of charging during the day and discharging at night. However, for Home 7, the control pattern exhibited



slightly unexpected behavior; discharging in the middle of the day on weekdays and not charging the battery at all on the weekends, which deviates from a human operator may control the battery.

Therefore, the study shifts focus on Home 7, where SHAP was used to provide insights into the contribution of each observation to the model's decision-making, identifying potential issues with the current control and suggesting improvements to the model based on the unexpected control pattern.

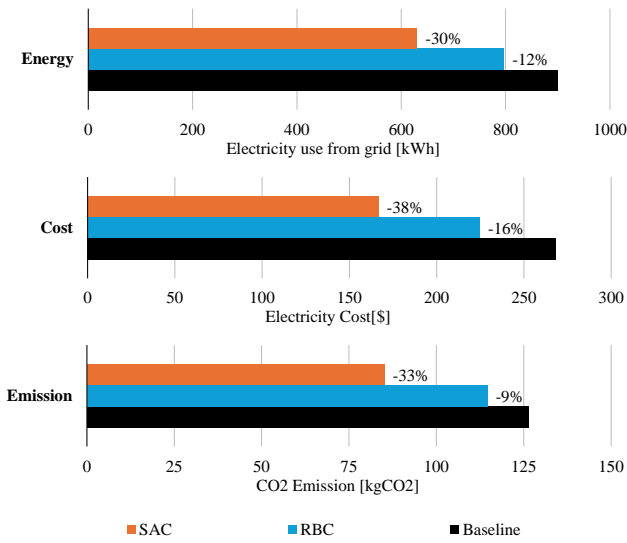


Figure 2: Energy, Cost, and Emission results of the RBC and RLC

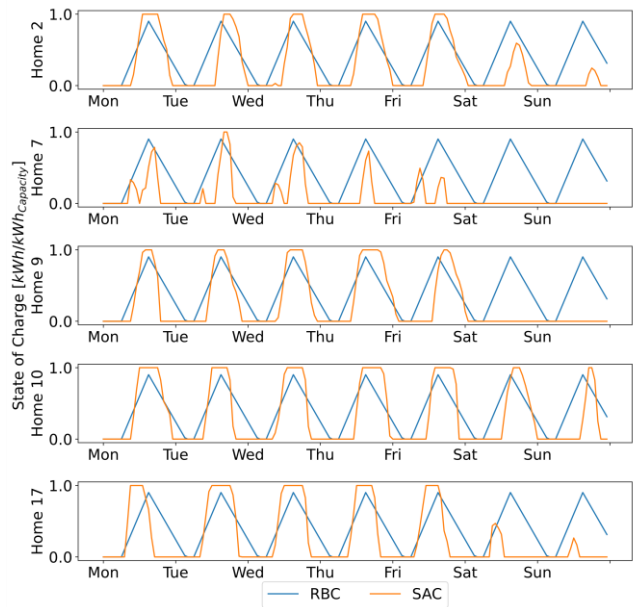


Figure 3: Battery State of Charge for each household

Interpreting the results with SHAP

Figure 4 illustrates the variations in the contribution of features that were significant in controlling Home 7 during the test period. The colored scatter plots after

the top two plots show the SHAP values from each hour of each observation. SHAP values are additive, thus can be directly interpreted at the amount added to the control action. Positive values in red represent additional charging due to the observation value and negative values in blue represent discharging.

It is evident from the figure that the home tends to charge during periods of high diffuse solar radiation and when electricity prices are expected to increase 12 hours later. Conversely, discharging is observed when the current electricity prices and the home's load is high. From this figure, it can be observed that the discharging in the middle of the day occurred due to the high electrical load in the middle of the day, and no charging occurred on the weekends because the electricity pricing forecast was lower.

On the other hand, Figure 5 illustrate the features with low contributions for Home 7. From the figure, it is observed that the contributions of the residence's own battery state and carbon intensity were low, and solar generation had no contribution to the control decision.

Based on the results of the SHAP analysis, the following issues were observed, and suggestions were made to improve the model and bring the control strategy closer to what a human will expect:

- SAC attempts to discharge when the battery is empty.
 - Apply a penalty to the reward function when the battery is empty for prolonged periods.
- The solar power generation is not contributing at all. Instead, the diffuse solar radiation, which is in correlation, plays a significant role.
 - Adjustment of the features used in observations.
- The contribution of carbon intensity is low.
 - Adjustment of the weights in the reward function.

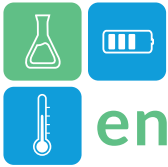
Conclusions

The application of XAI methods, such as SHAP values, has enabled us to objectively identify improvements that were previously based on speculation alone. The use of IRL has the potential to clarify the influence of features on control values, contributing to a better understanding of the internal structure of AI models.

References

Chen, Z et al. (2023) Interpretable machine learning for building energy management: A state-of-the-art review. *Advances in Applied Energy*. doi.org/10.1016/j.adapen.2023.100123.

Haarnoja, T. et al. (2018) Soft Actor-Critic: Off-Policy Maximum Entropy Deep Reinforcement Learning with a Stochastic Actor. *Computing*



ENERSTOCK 2024
The 16th IEA ES TCP International Conference on Energy Storage
June 5–7, 2024
Lyon, France

- Research Repository. Information Processing Systems.
doi.org/10.48550/arXiv.1801.01290. doi.org/10.48550/arXiv.1705.07874
- Heymann, F. et al. (2023) Operating AI systems in the electricity sector under European's AI Act – Insights on compliance costs, profitability frontiers and extraterritorial effects. Energy Reports. doi.org/10.1016/j.egy.2023.11.020
- Lundberg, S. and Lee, S. (2017) A unified approach to interpreting model predictions. Advances in Neural Information Processing Systems. doi.org/10.18738/T8/0YLJ6Q.
- Wu, A. et al. (2023) Heterogeneous Multi-Agent Reinforcement Learning for Grid-Interactive Communities. Association for Computing Machinery. doi.org/10.1145/3600100.3626276.

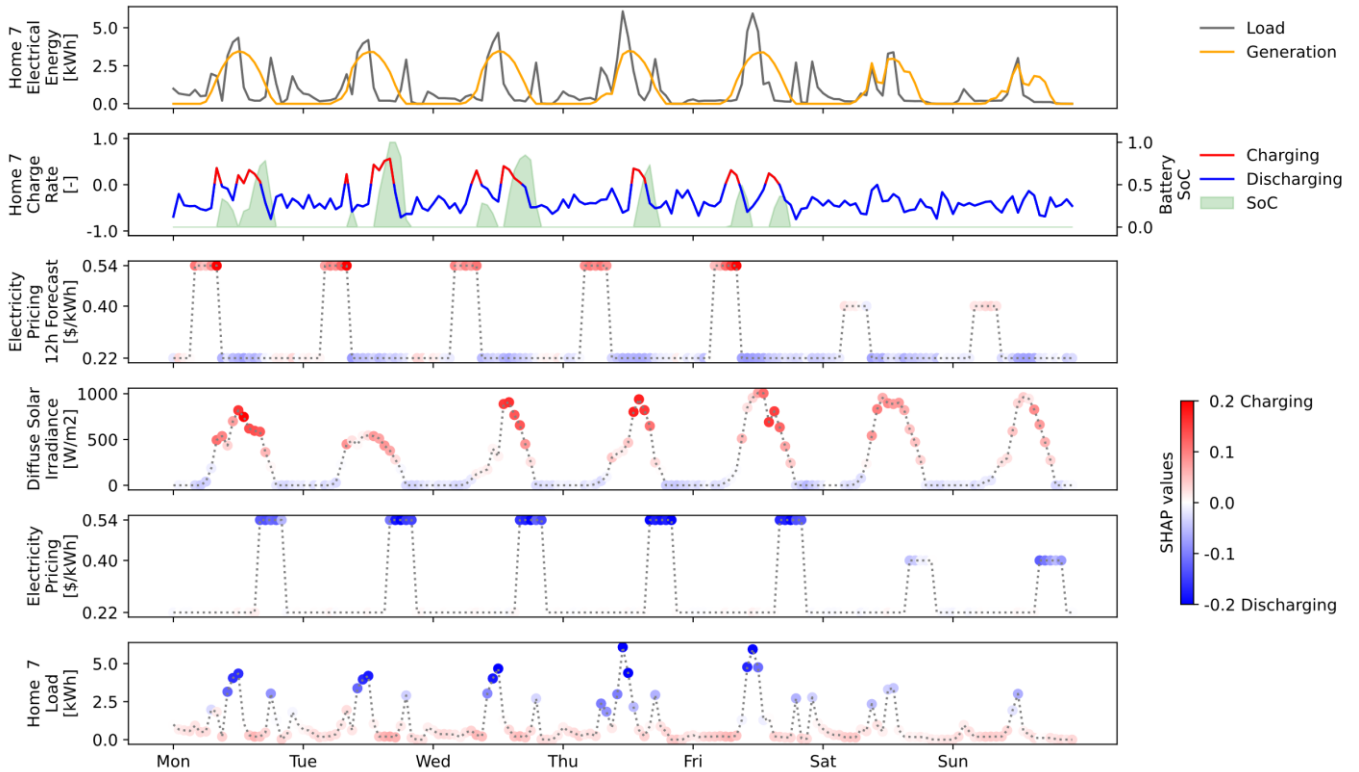
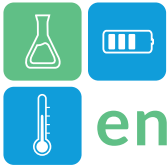


Figure 4: Observations from the test period that showed high contributions to the control decision for Home 7. The darker shade represents a higher contribution to the control decision of the model.

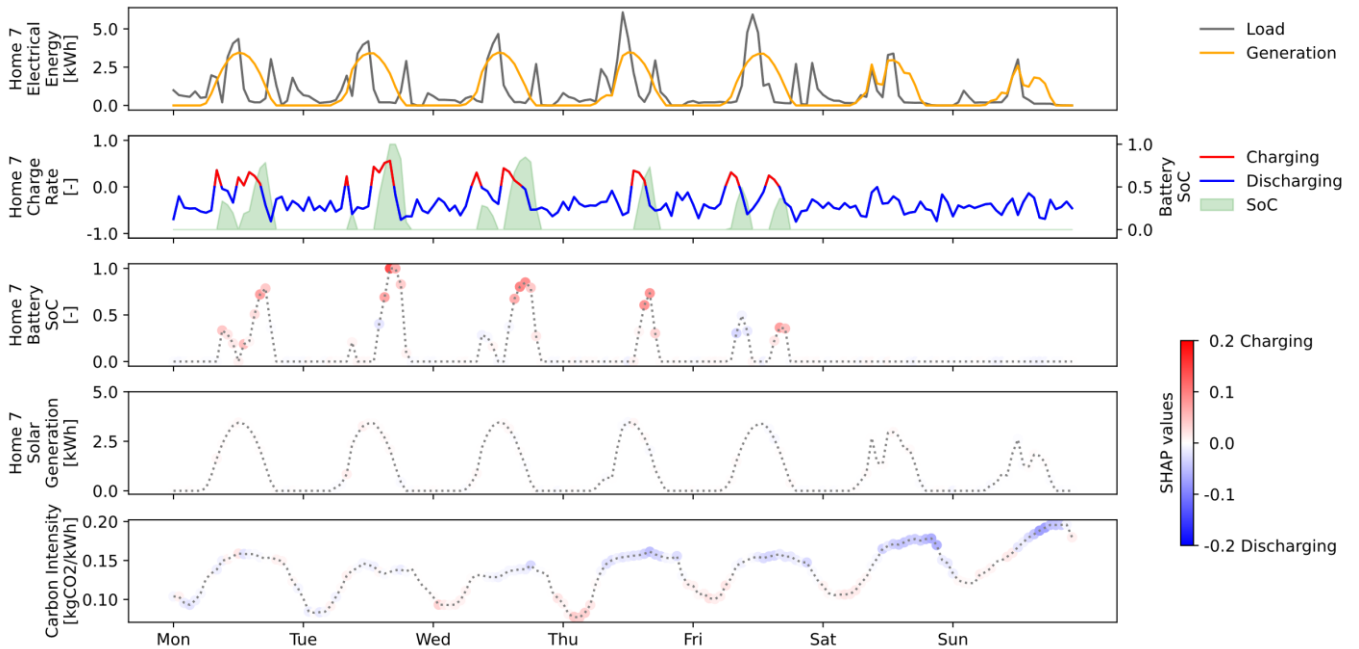


Figure 5: Observations from the test period that showed low contributions to the control decision for Home 7 where a higher contribution would have been expected.



Inventory data generation for prospective lifecycle design thorough full-year simulation of Carnot Battery with Al-Si based PCM

Shoma Fujii^{1,2}, Yuichiro Kanematsu³, Yasunori Kikuchi^{1,2,3*}, Justin NingWei Chiu⁴,
Tomokazu Nakamura⁵, Takahiro Nomura⁵

1 Institute for Future Initiatives, The University of Tokyo, 7-3-1 Hongo, Bunkyo-ku Tokyo, 113-8654, Japan

2 Department of Chemical System Engineering, The University of Tokyo, 7-3-1 Hongo, Bunkyo-ku Tokyo, 113-8656, Japan

3 Presidential Endowed Chair for “Platinum Society”, The University of Tokyo, 7-3-1 Hongo, Bunkyo-ku Tokyo, 113-8656, Japan

4 Department of Energy Technology, KTH Royal Institute of Technology, Brinellvägen 68, SE-10044 Stockholm, Sweden

5 Faculty of Engineering, Hokkaido University, Kita 13 Nishi 8, Kita-ku, Sapporo 060-8628, Japan

*Corresponding author e-mail: ykikuchi @ifi.u-tokyo.ac.jp

Abstract

As one of the emerging technologies, the Carnot battery is subjected to prospective life cycle assessment and design for further technology development in conjunction with other mature and competitive technologies. The objective of this study is to generate inventory data through annual simulations using a case study of a Carnot battery with Al-Si based phase change material with high temperature and high heat storage density. A price following model was developed to simulate Carnot batteries with use of solar and wind energy as heat charging sources, and inventory data is collected for system evaluation, such as average spot electricity price. When solar power is used as the heat charging source, an average economic benefit of 160% between spot price differences can be obtained due to time shift in storage and energy utilization.

Keywords: Thermal energy storage, Price following model, High temperature heat storage

Introduction

Early implement of various emerging technologies is required to achieve a sustainable society. Emerging technologies need to be evaluated prospectively and then compared with other technologies from the viewpoint of their lifecycle environmental impacts (Kikuchi and al., 2020) and fed back into technology development, and it is important to generate inventory data that reflects technology information with appropriate granularity and accuracy. Carnot battery, as one of the emerging technologies, is considered one of the essential storage technologies in increasing the penetration of large scale intermittent renewable energy plants such as solar and wind power (Novotny and al., 2022). The Carnot battery is a technology that stores renewable energy-derived power as heat and then recovers it as electricity. Recently, Al-Si alloy based microencapsulated phase change material (MEPCM) with melting temperature 577 °C and high heat storage density has been developed (Nomura and al., 2015) and are being experimentally investigated.

The objective of this study is to generate inventory data for a prospective life cycle assessment and design of a Carnot battery using Al-Si based PCM, and for this purpose, a full year simulation of a system that uses renewable energy as heat source to the storage and electricity as output has been constructed.

Material and methodology

Figure 1 depicts the “Power to Heat to Power” concept envisioned in this study. A fixed bed packed with MEPCM is set as a heat charging and discharging device. When charging heat, the air is heated with electricity derived from renewable energy sources and vented into the MEPCM packed bed. The properties of MEPCM and steam conditions are shown in Table 1. During heat discharging, high-temperature air as the heat transfer medium of about 650 °C is produced, and steam is generated utilizing a heat exchanger, which is then introduced into a steam turbine for electricity generation. For the annual simulation, a price following model has been constructed. A fixed period of time is

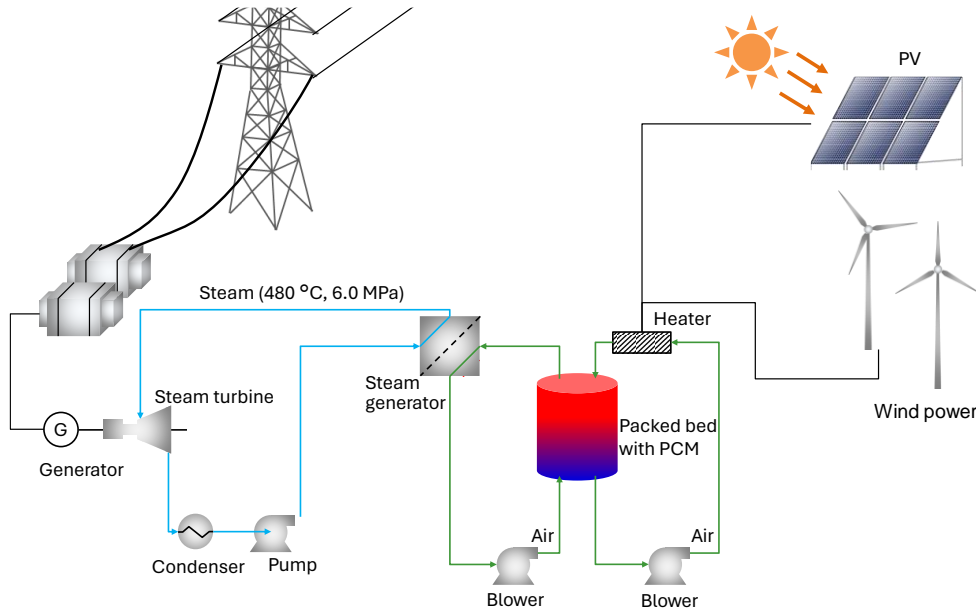


Figure 1: Schematic of Carnot Battery using packed bed with Al-Si based PCM.

set during which the storage level is balanced (168 hours in this case study) and the expected heat storage amount within that period is controlled according to the spot electricity price. The maximum and minimum load (set at 20% of the maximum load) of the steam turbine, and the maximum and minimum limits of the heat charging capacity were set, and the charged heat was allocated for heat discharging within a week to satisfy these conditions. For example, if the flow rate of steam exceeding the maximum load of the turbine is allocated at a certain time, it is reallocated first to other times of the day with higher spot electricity prices, then for surpluses that could not be fully satisfied, heat input cuts and additional power purchase from the grid were considered. As a case study, a system that takes in 500 GWh per year from two renewable energy sources, solar and wind power, has been considered with data from Hokkaido Electric Power Company (Renewable Energy Institute, 2024) in Japan.

Table 1: Properties of MEPCM and condition of steam.

Properties	Unit	Value
Specific heat for solid/liquid phase	J g ⁻¹ K ⁻¹	1.15/2.36
Latent heat of solidification	J g ⁻¹	254
Melting point	°C	577
Maximum/Minimum temperature	°C	650/300
Pressure of generated steam	MPa	6.0
Temperature of generated steam	°C	480

Result and discussion

Figure 2 show an example of the calculation results for a four-day period extracted from the annual simulation. It can be seen that when solar power generation is used as the heat charging source, Figure 2(a), heat input occurs during the daytime, while the heat is discharged according to the spot price satisfying the maximum and minimum load constraints on the turbine. Since the current spot electricity price in Japan is strongly influenced by the situation of solar power generation, it can be seen that the model is based on charging heat at low electricity prices and heat discharging at night when prices are high. On the other hand, in the case where wind power is used as the energy charging source, although the stored energy is discharged according to the spot electricity price, it is not always possible to charge the heat when prices are low, as shown in Figure 2(b).

Table 2 shows the average spot electricity prices for storage charging and discharging in two cases. When solar power is used as the heat charging source, it is strongly affected by the price-following model, in which heat is charged when the spot electricity prices are low and heat is discharged when the spot electricity prices are high, indicating that the average spot electricity price at discharging is more than 1.6 times higher than at charging. On the other hand, when wind power is used as the heat charging source, the average spot electricity prices of heat charging and discharging are almost the same. Since the round-trip efficiency of the Carnot battery is about 30-40% (taken as about 35% in this study), it is difficult to introduce the system

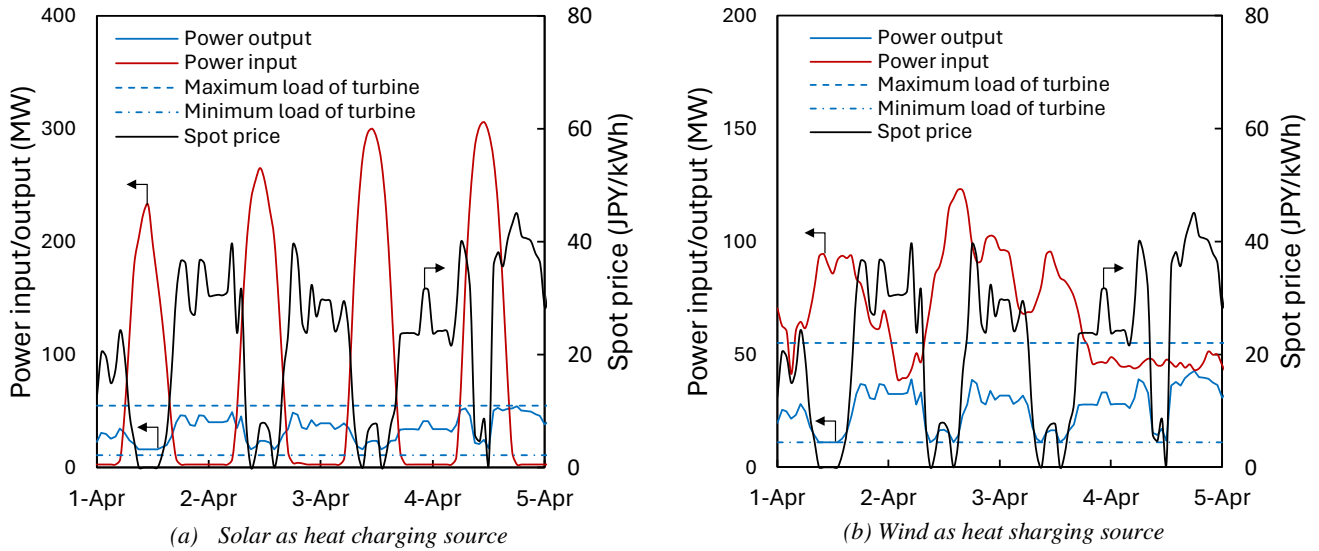
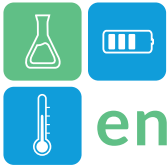


Figure 2: Result of 4 days simulation extracted from annual Carnot battery simulation.

under the current spot electricity price scheme, but many regions in Japan have already started to implement variable renewable energy output control, and this price difference is expected to widen in the future making the introduction of Carnot batteries more significant.

Table 2: Result of average spot electricity prices in charging and discharging periods.

Heat source	Average spot electricity price in charging period [JPY/kWh]	Average spot electricity price in discharging period [JPY/kWh]
Solar	14.4	23.4
Wind	20.6	22.9

Conclusions

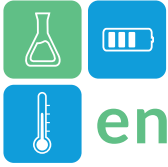
In this study, the annual simulation model for the Carnot battery using PCM was developed and a calculation model of heat charging and discharging control strategy based on a price-following model has been successfully constructed. The results can be used as inventory data for the prospective life cycle design of Carnot battery as one of the prominent emerging technologies. By reflecting on more detailed technical information in the model and by visualizing life cycle greenhouse gas, resource consumption impacts and other midpoint impact categories, it will be possible to further strive for technology development and allow inputs for future policy making.

Acknowledgment

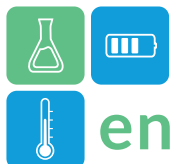
This work was supported by the New Energy and Industrial Technology Development Organization (NEDO, Grant number JPNP20005), the Environment Research and Technology Development Fund (Grant Number JPMEERF20213R01) of the Environmental Restoration and Conservation Agency of Japan, JST PRESTO (Grant Number JPMJPR2278), JSPS KAKENHI Grant-in-Aid for Early-Career Scientists (Grant Number JP22K18061) and JST COI-NEXT (Grant Number JPMJPF2003). The activities of the Presidential Endowed Chair for “Platinum Society” at the University of Tokyo are supported by Mitsui Fudosan Corporation, Sekisui House, Ltd., East Japan Railway Company, and Toyota Tsusho Corporation.

References

- Kikuchi, Y. and et al., (2020), Application of technology assessments to co-learning for regional transformation: a case study of biomass energy systems in Tanegashima, Sustain. Sci., <https://doi.org/10.1007/s11625-020-00801-1>
- Nomura, T. and et al., (2015), Microencapsulation of Metal-based Phase Change Material for High-temperature Thermal Energy Storage Scientific Reports, <https://doi.org/10.1038/srep09117>
- Novotny, V. and et al., (2022) Review of Carnot Battery Technology Commercial Development, Energies, <https://doi.org/10.3390/en15020647>
- Renewable Energy Institute, (2024), Power Supply & Demand Chart, <https://www.renewable-ei.org/en/statistics/electricity/#demand> (Accessed on Jan. 2024)



ENERSTOCK 2024
The 16th IEA ES TCP International Conference on Energy Storage
June 5–7, 2024
Lyon, France



Investigating the relation between the crystallisation velocity and the hysteresis of phase change materials with two polyethylene glycols

Stefan Hiebler¹, Henri Schmit^{1,*}, Stefanie Tafelmeier¹, Peter Hoock¹
1 ZAE Bayern, Walther-Meissner-Str.6, 85748, Garching, Germany
*Corresponding author e-mail: henri.schmit@zae-bayern.de

Abstract

In this work, the relation between the hysteresis of PCM and their crystallisation velocity is investigated with two types of polyethylene glycol: PEG 2000 and PEG 10 000. Calorimetric measurements via differential scanning calorimetry (DSC) show that a notable temperature difference between the enthalpy curves during crystallisation and melting, i.e. the hysteresis, persists even for unusually low heating/cooling rates. The temperature-dependent crystallisation velocities measured for different supercooling temperatures show that the crystallisation velocities for PEG 2000 are generally higher than those for PEG 10 000. A simple explicit finite differences model incorporating the crystallisation velocity was programmed. This simulation tool can be used to simulate DSC enthalpy curves that show good agreement with the measured curves. From the obtained results, it can be concluded, that the crystallisation velocities of the two PEGs, which are too low at supercooling below about 10 K, are the cause of the apparent hysteresis.

Keywords: Thermal Energy Storage, Phase change material, Crystallisation velocity, Hysteresis, Supercooling

Introduction

Phase change materials (PCM) allow storing and releasing large amounts of heat in a narrow temperature range and are therefore attractive for thermal energy storage (TES). For a successful and widespread implementation of latent heat TES, some properties of PCM have to be better understood. In enthalpy measurements, a more or less pronounced temperature difference between the enthalpy curves during crystallisation and melting, the so-called hysteresis, can be observed for PCM. In the design and simulation of latent heat TES, the hysteresis can lead to some issues, especially if the PCM is not completely melted or crystallised, as it is the case with partial cycles that can occur in applications.

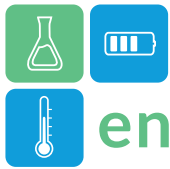
In a recent review article (Klimes and al., 2020) it is mentioned that hysteresis is not considered in most of the reported simulations with PCM. In the same article, it is stated that if hysteresis is considered in the models, it is mostly done via a temperature-dependent enthalpy or effective heat capacity function for both heating and cooling. In the case of incomplete phase change, the model then toggles between the curves for heating and cooling. Additionally, the authors mention that only few models consider both hysteresis and supercooling. However, the authors do not mention the incorporation of the crystallisation velocity in any of the models. This shows that there is a need for a different modelling approach regarding hysteresis of PCM.

Here, it is proposed to incorporate a temperature-dependent crystallisation velocity into a model. One of the challenges thus consists in experimentally obtaining the temperature-dependent crystallisation velocities of PCM as a function of the degree of supercooling. The goal of this work is to develop a model that can simulate hysteresis and thus be able to model partial cycles of PCM.

Materials and methods

In the introduction, it was mentioned, that one of the goals of this work was to experimentally determine the temperature-dependent crystallisation velocity of PCM. Therefore, several requirements have to be met by the investigated PCM. First, it should show a considerable degree of supercooling. Additionally, PCM with a spatially homogeneous crystal growth are required since a homogeneously propagating phase front can be more easily measured and simulated with a one-dimensional model. Therefore, two polyethylene glycols with spherulitic crystal growth (Pielichowski and al., 2002) with known supercooling and hysteresis (Hennemann and al., 2012) were chosen: PEG 2000 and PEG 10 000. The number behind PEG thereby indicates the average molecular weight.

Polyethylene glycol 2000 for synthesis (8.21037.1000), batch number S6394537 147, from Merck was used as PEG 2000. Poly(ethylene glycol) (P6667-500G), batch number BCBC5864, from Sigma-Aldrich was used as PEG 10 000.



Calorimetric data for both PEGs is needed to assess e.g. the amount of the hysteresis. The calorimetric measurements were carried out via differential scanning calorimetry (DSC) with a DSC Q2000 from TA Instruments. According to the manufacturer's recommendation, the enthalpy and temperature calibration was performed with indium. Further information on the measurement uncertainty of the DSC Q2000 at ZAE Bayern is e.g. provided by Rathgeber and al. (2014). A constant stream of nitrogen (50 ml min^{-1}) was applied as flushing gas.

Both PEGs were introduced as solids into DSC crucibles. Around 3.5 g and 3.9 g were used for PEG 2000 and PEG 10 000, respectively. Since the origin of the hysteresis between melting and crystallisation of PCM is not fully understood, several heating/cooling rates were chosen to verify if the hysteresis persisted even for comparatively small heating/cooling rates. Thus, it can be shown, that the hysteresis is also an inherent material property and not only due to the dynamic nature of DSC measurements. The following heating/cooling rates were chosen: 8, 4, 2, 1, 0.5, 0.25, 0.1, and 0.05 K min^{-1} . It has to be noted that heating/cooling rates below 0.5 K min^{-1} are unusual due to a growing signal to noise ratio. Indeed, 2 K min^{-1} is the standard heating/cooling rate at ZAE Bayern with the DSC Q2000 (e.g. Schmit and al., 2018), and no calibration is usually performed for heating/cooling rates below 0.5 K min^{-1} . Therefore, in the following, it was chosen not to include heating/cooling curves measured with heating/cooling rates below 0.5 K min^{-1} . However, some relevant numerical values relying on DSC measurements with lower heating/cooling rates are listed in the following.

The temperature-dependent crystallisation velocity was determined with an optical stereo microscope SteREO Discovery.V12 from Zeiss equipped with a heating stage. The challenge consists in determining the crystallisation velocity for different degrees of supercooling. Therefore, the sample has to reliably crystallise at a given supercooling. To this end, a hot-wire method was developed. An electrically heatable wire was placed on top of the coverslip of the microscope sample. After fully crystallising the sample at a sufficiently low temperature, the temperature of the heating stage is then set to a specific temperature below the melting temperature. Subsequently, a power supply is used to heat the wire. As a consequence, a part of the sample is melted whereas the remaining crystalline parts leave an interface between the two phases. After the power supply has been turned off and the wire cools down, the sample crystallises starting from those

interfaces. The crystallisation velocity for a specific temperature is then determined optically using the AxiosVision Software (Release 4.8.2).

A simple explicit finite differences model using the enthalpy method was programmed which incorporates the crystallisation velocity during the crystallisation process.

An enthalpy-temperature curve for a heating rate of 0.5 K min^{-1} was used for each of the PEGs for the simulation. During crystallisation the amount of crystallised PCM was calculated with the help of the temperature-dependent crystallisation velocity. With the knowledge of the ratio between liquid and solid PCM a new enthalpy curve depending on the specific heat capacities of the liquid and solid PCM was calculated. With this new enthalpy curve the temperature change was calculated.

With this algorithm a simple simulation of the DSC Q2000 was programmed and heating and cooling measurements were simulated according to the real measurements.

Results and discussion

PEG 2000 and PEG 10 000 were both measured with different heating/cooling rates via DSC. Figure 2 shows a selection of the resulting enthalpy curves for PEG 2000. For clarity reasons, only the three heating/cooling rates of 4, 2 and 0.5 K min^{-1} are shown.

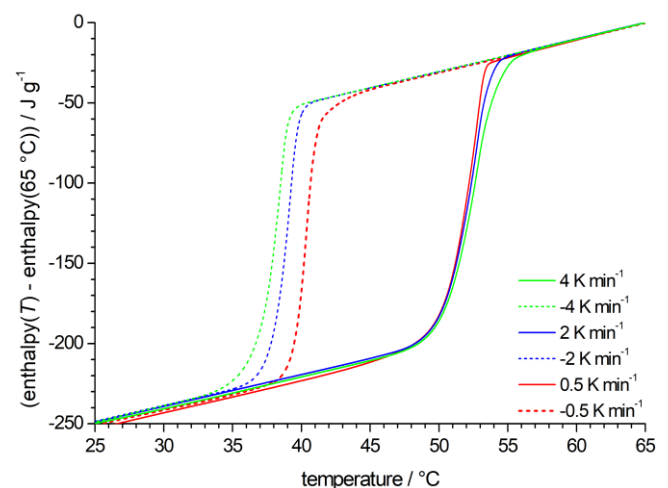


Figure 1: Enthalpy curves during heating (straight lines) and cooling (dashed lines) for different heating/cooling rates obtained via DSC for PEG 2000

From the enthalpy curves in Figure 1 it can be seen that the temperature difference between melting and crystallisation decreases as expected with decreasing heating/cooling rate. The difference is reduced from around 15 K at 8 K min^{-1} to less than 3 K at 0.05 K min^{-1} . Thus, even at this unusually small heating/cooling rate a considerable hysteresis persists.

This leads to the conclusion that a part of the observed hysteresis is an inherent material property in the case of PEG 2000.

Figure 2 shows a selection of the resulting enthalpy curves for PEG 10 000. For clarity reasons, only the four heating/cooling rates of 4, 2 and 0.5 K min⁻¹ are shown.

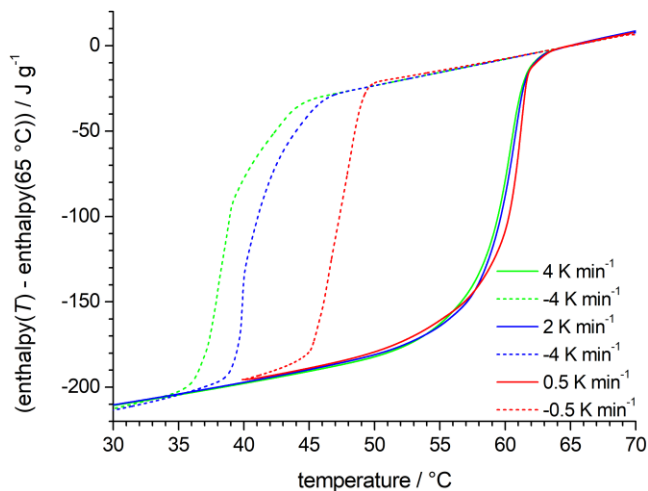


Figure 2: Enthalpy curves during heating (straight lines) and cooling (dashed lines) for different heating/cooling rates obtained via DSC for PEG 10 000

Again, the temperature difference between melting and crystallisation decreases with decreasing heating/cooling rate (Figure 2). The difference is reduced from over 20 K at 8 K min⁻¹ to around 10 K at 0.05 K min⁻¹. These values show that PEG 10 000 has a higher hysteresis compared to PEG 2000, especially at the lowest heating/cooling rate. Again, it can be stated that part of the observed hysteresis is an inherent material property.

The crystallisation velocities of PEG 2000 and PEG 10 000 were measured with the hot-wire method and the optical stereo microscope as described above. The crystallisation velocity in function of the supercooling for both PEGs is shown in Figure 3. For PEG 2000 and PEG 10 000 a substantial supercooling of around 8 K is needed to obtain a crystallisation velocity of around 1 mm min⁻¹. With further supercooling, the crystallisation velocity increases further for both PEGs. However, the crystallisation velocity of PEG 2000 is considerably higher than that of PEG 10 000 for the same supercooling. For e.g. 14 K supercooling, the crystallisation velocity of PEG 2000 is more than two times higher than that of PEG 10 000. The difference in crystallisation velocity with increasing molecular weight of the PEG was expected. Indeed, it is known from literature (Hiebler and al., 2014) that the single to multiple folding of

macromolecules in the solid-state body as it is the case for PEGs with a molecular weight of 2000 g mol⁻¹ and higher hampers the crystallisation. Furthermore, it is interesting to point out that PEG 10 000, with a higher hysteresis than PEG 2000, also shows generally lower crystallisation velocities for the same supercooling.

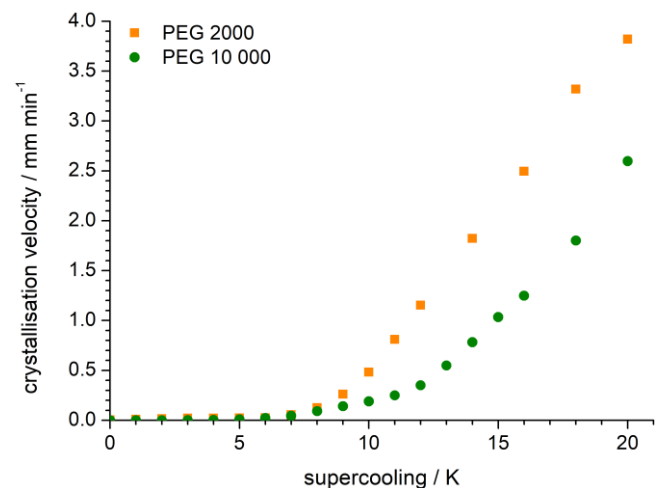


Figure 3: Comparison of the crystallisation velocities of PEG 2000 (orange squares) and PEG 10 000 (green circles) in function of the supercooling

The simple model shows a good agreement between the heating and cooling curves for both PEGs (Figure 4 and Figure 5).

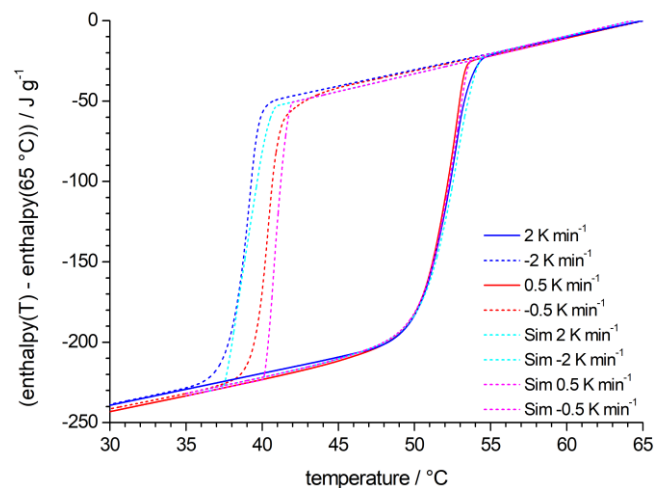


Figure 4: Comparison between measurement and simulation for PEG 2000

Above all, the very good agreement in the heating measurements shows that the heat transport in the samples is sufficient to obtain only a slight deviation between the different heating rates used. During crystallisation it can be clearly seen that the crystallisation rate is not sufficient to crystallise the sample even at the lower heating rates used here, as long as the crystallisation velocity is below about 0.2 mm min⁻¹. Since the crystallisation velocity for



both PEGs increases only above this value at supercooling of more than 10 K, this leads to an apparent hysteresis between the heating and cooling curves, which does not disappear even for comparatively low heating rates in heat flow DSC.

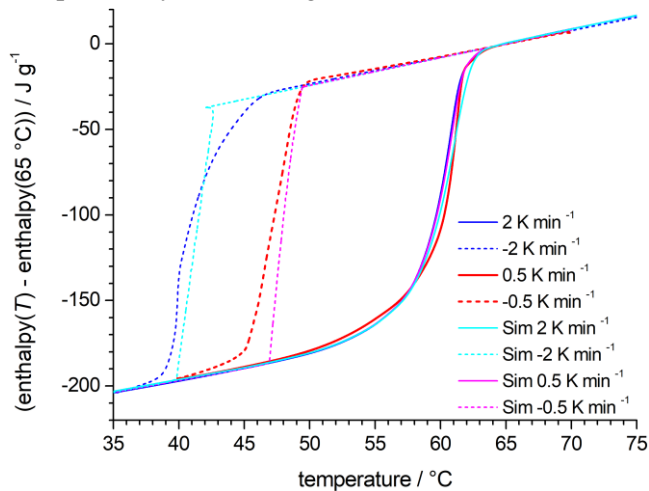


Figure 5: Comparison between measurement and simulation with PEG 10 000

Conclusions

In this work, the relation between hysteresis of PCM and their crystallisation velocity was investigated with two types of polyethylene glycol PEG 2000 and PEG 10 000. The enthalpy curves of both PEGs were obtained with different heating/cooling rates via DSC. The enthalpy curves show a rate dependent hysteresis, which is still present down to a heating/cooling rate as low as 0.05 K min^{-1} . This shows, that the hysteresis is a material inherent property for both PEGs.

The temperature-dependent crystallisation velocities of PEG 2000 and PEG 10 000 for different degrees of supercooling were measured with a self-developed hot-wire method with an optical stereo microscope. The measurements show that both PEGs require a substantial supercooling of around 8 K to attain crystallisation velocities around 1 mm min^{-1} . Thereby, PEG 2000 shows generally higher crystallisation velocities than PEG 10 000.

A simple explicit finite differences model using the enthalpy method was programmed which incorporates

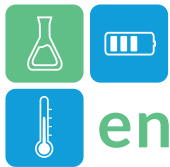
the crystallisation velocity during the crystallisation process. This simulation tool can be used to simulate DSC curves that show good agreement with the measured curves. From the obtained results, it can be concluded, that the crystallisation velocities of the two PEGs, which are too low at supercooling below about 10 K, are the cause of the apparent hysteresis.

Acknowledgment

This work is part of the project PCM-Metro-2 and was supported by the Federal Ministry for Economic Affairs and Climate Action under the project code 03ET1584A. The responsibility for the content of this publication is with the authors.

References

- Hennemann, P. and al. (2012). Experimental study on poly-ethylene glycols to investigate their potential as phase change materials. Proceedings from Innostock 2012. Lleida (ES), 16-18 May 2012.
- Hiebler, S. and al. (2014). Schlussbericht: Entwicklung neuartiger PCM, formstabiler PCM und PCM Verbundmaterialien mit verbesserter Wärmeleitfähigkeit (EnFoVerM), FKZ 0327851 D.
- Klimes, L. and al. (2020). Computer modelling and experimental investigation of phase change hysteresis of PCMs: The state-of-the-art review. Applied Energy. doi.org/10.1016/j.apenergy.2020.114572
- Pielichowski, K. and al. (2002). Differential scanning calorimetry studies on poly(ethylene glycol) with different molecular weights for thermal energy storage materials. Polymers for Advanced Technologies. doi.org/10.1002/pat.276
- Rathgeber, C. and al. (2014). Measurement of enthalpy curves of phase change materials via DSC and T-History: When are both methods needed to estimate the behaviour of the bulk material in applications? Thermochimica Acta. doi.org/10.1016/j.tca.2014.09.02
- Schmit, H. and al. (2018). Influence of different basic raw materials from technical to laboratory grade on the maximum storage capacity of $\text{CaBr} \cdot 6\text{H}_2\text{O}$. Thermochimica Acta. doi.org/10.1016/j.tca.2018.10.026



Investigation of a thermochemical storage system for the use of solar energy in domestic applications

Philip Andreas Patschg¹, Tobias Niederkofler^{1,2,*}, Aldo Giovannini¹, Roman Lackner²

1 Department of Environmental, Process, and Energy Engineering, Management Center Innsbruck,
Maximilianstrasse 2, Innsbruck, 6020, Austria

2 Material Technology Innsbruck, University of Innsbruck, Technikerstrasse 13, Innsbruck, 6020, Austria

*Corresponding author e-mail: tobias.niederkofler@mci.edu

Abstract

Space heating and domestic hot water constitute the primary thermal energy demands in residential buildings. Traditionally met by fuel-based technologies, a paradigm shift toward renewable heating systems is crucial in the face of global warming and the finite nature of fossil fuels. This study explores the potential of thermochemical storage systems integrated with solar energy to address these demands. Assessing the feasibility of such a system involves a comprehensive analysis of relevant parameters. The investigation encompasses three main categories: firstly, elucidating the demand and requirements of a detached house in Austria based on building standards; secondly, evaluating the solar potential at an Austrian site through the consideration of photovoltaic and solar thermal systems at various operating conditions; and thirdly, estimating key characteristics of a potential thermochemical storage system. Magnesium sulfate is examined as thermochemical storage material in the storage system, reflecting common representations in various studies. The synthesis of this information underscores the viability of thermochemical storage solutions for long-term solar energy storage in domestic applications.

Keywords: Solar Energy Integration, Renewable Heating Systems, Thermochemical Storage Systems

Introduction

The rising global energy demand and the heavy dependency on fossil fuels are contributing to drastic climate changes worldwide. Globally, the residential sector is responsible for approximately 40 % of the primary energy consumption, which corresponds to 24 % of the world's total CO₂ emissions (Saheb, 2011). Thereby, energy consumption is primarily driven by the demand for space heating and domestic hot water. To meet this demand, several renewable energy systems are available nowadays. However, with the integration of renewable energy sources, new challenges arise due to the intermittent nature of their supply. While solar energy can meet thermal energy needs throughout the year, seasonal fluctuations hinder the exploitation of its full potential. Therefore, the development of new energy storage solutions plays a crucial role in the expansion of solar energy systems. Addressing this challenge, thermochemical energy storage emerges as a promising solution, offering high energy density and long-term storage with minimal losses (Böhm & Lindorfer, 2019). N'Tsoukpoe et al. (2014) and Visscher & Veldhuis (2005) identified magnesium sulfate as one of the most promising materials for long-term energy storage in domestic applications. Hence, magnesium sulfate is considered

as thermochemical storage material (TCM).

This work aims to provide a holistic view of a monovalent heating system for a detached house located in Innsbruck, Austria. The consideration is based on a system level, not specifically on individual components. Additionally, operating parameters and building service requirements for a thermochemical energy storage system are determined. Therefore, the thermal requirements of a reference detached house are elaborated in terms of the energy demand for space heating and domestic hot water. Based on the annual thermal energy demand the potential solar energy yield is estimated for different system requirements. Further, the energy flow of the system is elaborated, including the demand, the supply from solar collectors, and the auxiliary energy for the sorption storage. Based on the determined informations, the feasibility of the system is examined.

Methodology

Basic values for the evaluation of the system parameters are elaborated based on data from the literature. For the reference detached house shown in Figure 1, specific sources relating to the European and Austrian situation and regulations are selected (European Parliament, 2010; Schöber et al., 2022). In

addition, literature on heating and air conditioning technology applied in practice is used to enable a practical approach in further consideration (Ihle et al., 1996; Schlagnitweit & Wagner, 2015).

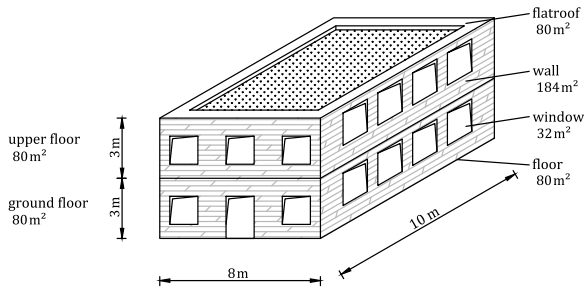


Figure 1: Reference detached house located in Innsbruck (Austria), with a living area of 140 m² and a target useful heating energy demand of 30 kWh m⁻² a⁻¹.

Based on this information, the transmission heat loss and the ventilation heat loss of the defined reference building are calculated. Besides the heat losses, heat gains from radiation through windows and internal gains from equipment are determined for structural components and internal equipment through the GEQ software (Zehentmayer Software GmbH, 2023). Thermal gains of the building are calculated based on the geometry, location, and orientation of the defined reference building. Further, the thermal energy yield is calculated for this reference house using the software T*SOL (Valentin Software, 2021). The collector orientation is considered in southern direction with an inclination of 30°. Thereby, solar potential is compared for a solar thermal collector system (evacuated tube collector, type MP-tec VRK12,) and a photovoltaic system (silicon polycrystalline collector, type example collector 260 W_p). Whereas the transformation from electric into thermal energy for the photovoltaic system is considered using resistance heaters with an efficiency of 100 % (Dinçer, 2018). Thereby, the magnesium sulfate dehydration temperature of 150 °C is considered.

To address the building's energy gap, an open-loop thermochemical storage system is employed. The applied storage system is shown in Figure 2, comprising a reactor, heat exchangers (HEX), a humidifier, and a fan. The reactor, central to the process, facilitates sorption and desorption reactions. In desorption mode, solar-heated air is blown through the reactor, releasing humid air into the environment. In sorption mode, conditioned air is used for an ideal reaction environment. Internal heat exchangers maintain constant conditions, and a second heat exchanger draws energy from the reactor outlet air.

After this, the process air still retains sufficient energy for an adiabatic humidifier to restore initial air conditions, completing the cycle. For the reactor, a thermal power output of 2 kW is assumed. However, only about 70 % of the energy initially supplied during the desorption process can be recovered during the adsorption (Gaeini et al., 2017). Referring to Ihle et al. (1996), a pressure drop of 1100 Pa is estimated for the system components. Further, a fan efficiency of 0.7 is assumed.

Operating conditions are selected to avoid salt deliquescence during the reaction. Magnesium sulfate is considered one promising thermochemical energy storage material due to its suitable material properties. However, to achieve good reaction kinetics a high relative humidity is necessary. Research indicates that levels above 85 % are needed to achieve complete hydration to magnesium sulfate heptahydrate (Linnow et al., 2014). Therefore, an inlet air condition of 25 °C and 90 % relative humidity is assumed for the process.

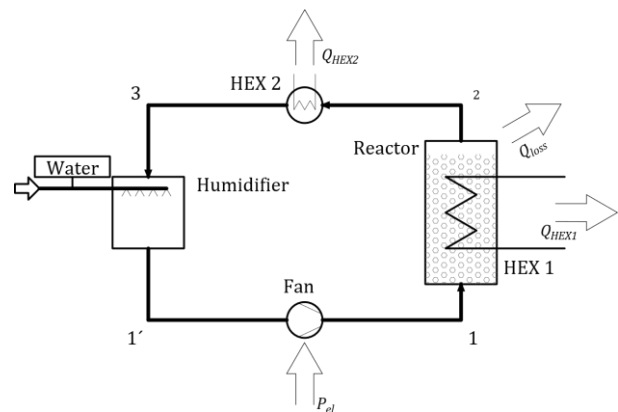


Figure 2: Schematic of the thermochemical storage system.

Results and Discussion

For the reference detached house, we determined a total thermal energy demand of 10153 kWh a⁻¹, of which space heating accounts for 5072 kWh a⁻¹ at a temperature of 30 to 40 °C and domestic hot water accounts for 5081 kWh a⁻¹ at a temperature of 60 °C. By taking solar and internal gains into account, a space heating energy demand of 5134 kWh a⁻¹ results. The total space heating demand equivalent to 5072 kWh a⁻¹ corresponds to a value of 32 kWh m⁻² a⁻¹. Hence, despite the rough estimation and numerous assumptions made throughout the calculation, this appears to be a good representation of the monthly energy demand for a “nearly zero energy building”, where a target value of 30 kWh m⁻² a⁻¹ is defined (European Parliament, 2010). As visible, from the total

solar yield of 11443 kWh a^{-1} , about 7143 kWh a^{-1} are consumed immediately, and 4300 kWh a^{-1} are stored with the applied system. Thereby, 30 % of the stored energy is lost during the sorption reaction (Q_{loss}). Moreover, auxiliary energy describes the energy demand of the fan throughout the year. To meet this energy needs, a comparison of the determined thermal and electrical solar yield per collector is conducted. The thermal yield for solar thermal collectors for the target temperatures $80 \text{ }^\circ\text{C}$, $110 \text{ }^\circ\text{C}$, and $140 \text{ }^\circ\text{C}$ is displayed in Figure 4. Thereby, a decrease in efficiency with increasing target temperature is observed. As shown in Figure 4, the photovoltaic system shows a better performance than the solar thermal system for the required dehydration temperature of $150 \text{ }^\circ\text{C}$. Additionally, the flat photovoltaic curve offers advantages by producing more energy during the heating season, reducing the reliance on extensive storage solutions for space heating. In this scenario, the photovoltaic system requires 34 collectors to achieve an energy yield of 11443 kWh a^{-1} , to cover the thermal energy demand and compensate the losses. In the last step, the performance of the designated salt hydrate is evaluated for the configuration depicted in Figure 2. In examining the performance of magnesium sulfate within the specified system, Table 1 provides a comprehensive overview of key performance indicators for seasonal energy storage. The storage volume (V_{TCM}) is particularly crucial in system design, especially for seasonal heat storage considerations.

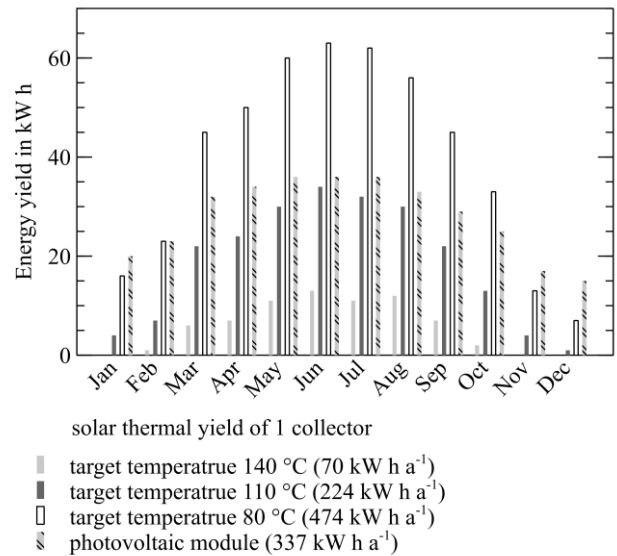


Figure 4: Comparison of the potential energy yield of different system requirements throughout the year (energy yield per collector).

Notably, MgSO_4 exhibits a very high energy density of 2.3 GJ m^{-3} for the reaction from heptahydrate to monohydrate (van Essen et al., 2009). This results in a storage volume of 6.7 m^3 . In a similar study conducted by Ferchaud et al. (2012), the authors investigated the utilization of magnesium chloride as TCM for seasonal heat storage. Thereby, the thermal energy demand of 1368 kWh a^{-1} for a passive house standard ($\sim 15 \text{ kWh m}^{-2} \text{ a}^{-1}$) was considered. Results showed that a packed-bed reactor with a volume of 8.5 m^3 enables

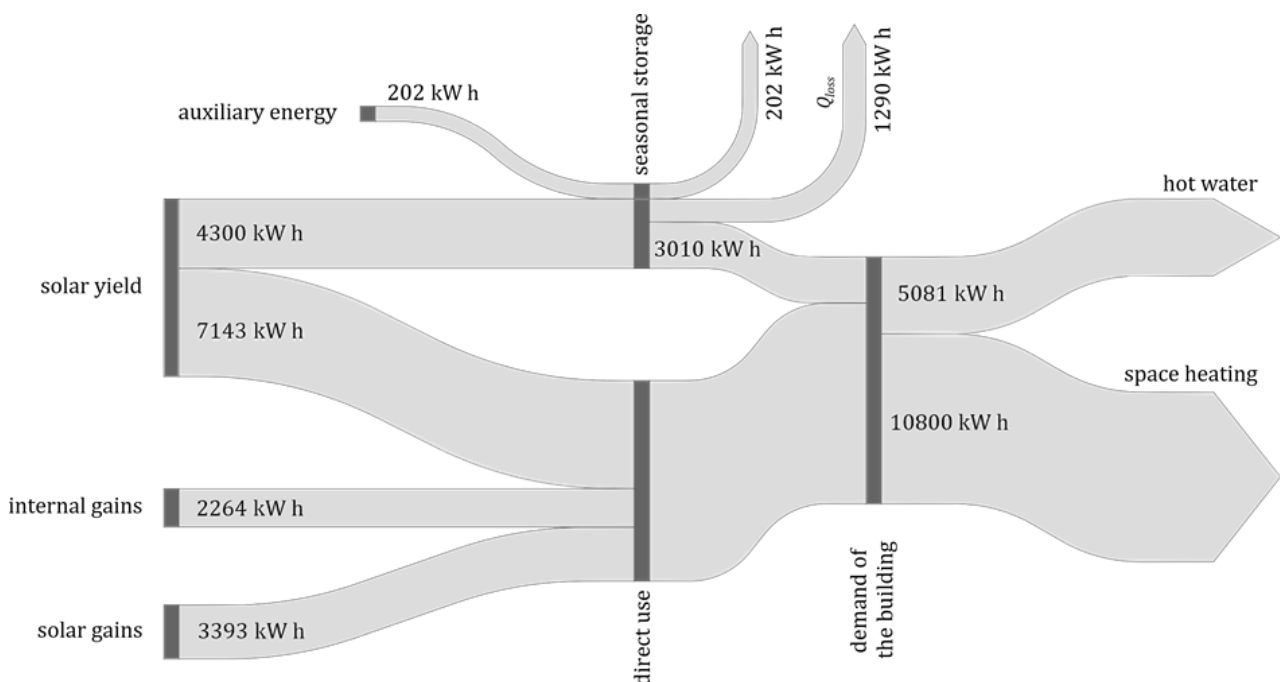


Figure 3: Energy flow chart based on the data of the reference house, with values for the seasonal heat storage exemplary displayed for the thermochemical storage material (TCM) magnesium sulfate.



the storage of the required energy. However, in their calculation the authors assumed a bed porosity of 50 %. Besides the required storage volume, Table 1 enumerates values for water and air demand for the storage system throughout the year.

Table 1: Data on the performance of magnesium sulfate heptahydrate as storage material, at a dehydration temperature of 150 °C.

Material	MgSO ₄	Unit
Energy stored	Q_{storage} 4300	kWh
Reactor power	P_{reactor} 2	kW
Operating hours	t 2150	h
Storage volume	V_{TCM} 6.7	m ³
Molar water demand	\dot{n}_{TCM} 24.54	mol h ⁻¹
Water mass flow	$\dot{m}_{\text{H}_2\text{O}}$ 2326	g h ⁻¹
Air mass flow	\dot{m}_{air} 258.4	kg h ⁻¹
Sorption energy	Q_{HEX} 3010	kWh a ⁻¹
Energy losses	Q_{loss} 1290	kWh a ⁻¹
Fan energy demand	E_{fan} 202	kWh a ⁻¹

Conclusions

In conclusion, this thesis delves into the potential of a thermochemical energy storage system, specifically tailored for domestic applications. The examination adopts a holistic approach, focusing on three key segments. Firstly, the energy demand of a reference detached building in Austria is scrutinized monthly, considering the desired temperature levels for space heating and domestic hot water. Subsequently, a thorough investigation into a photovoltaic and solar thermal system is conducted under varying operating conditions to align with the building's energy demand. The analysis reveals that under higher operating conditions for thermochemical energy storage, the overall efficiency of the solar thermal system diminishes, potentially making a photovoltaic system with an electric heater more feasible. Comparing energy yield and demand, approximately one-third of the system's energy output needs to be stored seasonally, prompting consideration for a thermochemical storage system. A comprehensive assessment of magnesium sulfate within the storage system highlights promising performance indicators. While installation costs may pose a consideration, the lack of concrete information on actual system installation costs prevents further exploration. Despite the substantial storage volume proposed, the feasibility of implementing such storage in a domestic building appears realistic.

References

- Böhm, H., & Lindorfer, J. (2019). Techno-economic assessment of seasonal heat storage in district heating with thermochemical materials. *Energy*, 179, 1246–1264. <https://doi.org/10.1016/j.energy.2019.04.177>
- Dinçer, İ. (Ed.). (2018). *Comprehensive energy systems*. Elsevier. <https://www.sciencedirect.com/science/referenceworks/9780128149256>
- European Parliament (2010). Directive 2010/31/EU of the European Parliament and of the Council of 19 May 2010 on the energy performance of buildings (recast) (Richtlinie L 153). Official Journal of the European Union.
- Ferchaud, C. J., Zondag, H. A., Veldhuis, J., & Boer, R. de (2012). Study of the reversible water vapour sorption process of MgSO₄·7H₂O and MgCl₂·6H₂O under the conditions of seasonal solar heat storage. *Journal of Physics: Conference Series*, 395, 12069. <https://doi.org/10.1088/1742-6596/395/1/012069>
- Gaeini, M., Javed, M. R., Ouwerkerk, H., Zondag, H. A., & Rindt, C. (2017). Realization of a 4kW thermochemical segmented reactor in household scale for seasonal heat storage. *Energy Procedia*, 135, 105–114. <https://doi.org/10.1016/j.egypro.2017.09.491>
- Ihle, Bader, & Golla. (1996). *Tabellenbuch Sanitär, Heizung, Lüftung*. Gehlen.
- Linnow, K., Niermann, M., Bonatz, D., Posern, K., & Steiger, M. (2014). Experimental Studies of the Mechanism and Kinetics of Hydration Reactions. *Energy Procedia*, 48, 394–404. <https://doi.org/10.1016/j.egypro.2014.02.046>
- N'Tsoukpoe, K. E., Schmidt, T., Rammelberg, H. U., Watts, B. A., & Ruck, W. K. (2014). A systematic multi-step screening of numerous salt hydrates for low temperature thermochemical energy storage. *Applied Energy*, 124, 1–16. <https://doi.org/10.1016/j.apenergy.2014.02.053>
- Saheb, Y. (2011). *Modernising building energy codes to secure our global energy future: The IEA Policy Pathway Series* (2011).
- Schlagnitweit, & Wagner. (2015). *Heizungs- und Lüftungstechnik: Installations- und Gebäudetechnik. Jugend & Volk*. <https://permalink.obvsg.at/AC12637018>
- Schöber, Braun, Glaser, Hama, Heuberger, Hofbauer, Kronsteiner-Mann, & Vollmann. (2022). *Wohnen: Zahlen, Daten und Indikatoren der Wohnstatistik*. https://www.statistik.at/fileadmin/user_upload/Wohnen-2021.pdf



ENERSTOCK 2024
The 16th IEA ES TCP International Conference on Energy Storage
June 5–7, 2024
Lyon, France

Valentin Software. (2021). T*SOL (Version R4) [Computer software]. <https://valentin-software.com/produkte/tsol/>

van Essen, V. M., Zondag, H. A., Gores, J. C., Bleijendaal, L. P. J., Bakker, M., Schuitema, R., van Helden, W. G. J., He, Z., & Rindt, C. C. M. (2009). Characterization of MgSO₄ Hydrate for Thermochemical Seasonal Heat Storage. *Journal of Solar Energy Engineering*, 131(4), Article 041014. <https://doi.org/10.1115/1.4000275>

Visscher, K., & Veldhuis, J. (Eds.) (2005). Comparison of candidate materials for seasonal storage of solar heat through dynamic simulation of building and renewable energy system.

Zehentmayer Software GmbH. (2023). GEQ (Version 2023.23) [Computer software]. <https://www.geq.at/>



Large Scale Testing of Refractory Bricks for Molten Salt Thermal Energy Storage

Christian Odenthal¹, Freerk Klasing¹, Alexander Bonk², and Thomas Bauer¹

¹German Aerospace Center (DLR), Linder Höhe, 51147 Köln

²German Aerospace Center (DLR), Pfaffenwaldring 38, 70569 Stuttgart

*Corresponding author e-mail: christian.odenthal@dlr.de

Abstract

In this work the large-scale testing of refractory bricks in a molten salt-based thermocline thermal energy storage system is presented. Refractory brick could overcome issues associated with packed-bed type thermal energy storage systems such as thermal ratcheting or higher void fractions. Thermal cycling and stand-by behavior of 17 tons of refractory bricks is investigated with the test facility for thermal energy storage in molten salts (TESIS) at DLR in Cologne. A stable thermocline was established which showed a good agreement to a 1D-model previously implemented in MATLAB. The thermocline is stratified evenly over the cross-sectional area. It is shown that also over longer stand-by periods of several days the stratification of the thermocline remains stable.

Keywords: Thermal Energy Storage, Thermocline, Refractory Bricks

Introduction

Presently, molten salt thermal energy storage is extending its reach into innovative application areas. In addition to its initial utilization in concentrating solar power (CSP), it is also finding application in transforming traditional power plants into Power-to-Heat-to-Power storage facilities. This versatile technology is being employed for decoupling industrial processes from supply and demand and enhancing the flexibility of chemical plants (Bauer et al., 2021).

One important key aspect is the reduction of storage costs. Since the overall costs are mainly driven by the molten salt inventory, the highest cost reduction potential lies in substituting a large fraction of the molten salt by a cost-effective filler material. A common approach is the utilization of a packed bed as storage material. Since such packed bed has the ability to move, the adverse effect of thermal ratcheting may arise. That is when the tank walls expand due to thermal expansion, followed by thermal contraction due to cyclic temperature variations. A packed bed may expand alongside with the tank walls but can prevent their contraction, leading to stains inside the tank walls and eventually to plastic deformation. Some other limitations of a packed bed are the limited void fraction and the difficulty to partly remove the packed bed for tank inspections.

One simple solution is the utilization of regularly shaped refractory bricks. With such bricks no

ratcheting occurs, the bricks could be partly removed and very low void fractions can be realized.

Within the project “Newline” cost effective refractory bricks have been identified and two of the most promising candidate materials were inserted into the TESIS (test facility for thermal energy storage in molten salts) plant at DLR in Cologne.

Methodology

The aim of the present experiments was to investigate the performance of refractory bricks with molten salts at elevated temperatures of up to 560°C. Solar salt as storage medium has been used with a temperature range between 290°C and 560°C.

The geometry of the refractory bricks was designed previously during the first project phase. The target design has a low void fraction of 10 % and small flow channels with 10 mm hydraulic diameter. Two layers of prototype bricks with the target design made of a novel storage material developed by the project partner Kraftblock were produced. Below that layer mainly clinker bricks as shown in Figure 1 have been used.

These clinker bricks are readily available but do not have the ideal geometry as the final void fraction (including gaps between the bricks) is around 40% and the hydraulic channel diameter is about 14 mm. The material was placed inside three baskets with a perforated floor to allow molten salt to pass through.

The baskets were then stacked into the TESIS facility. An overview of the setup is shown in Figure 2.

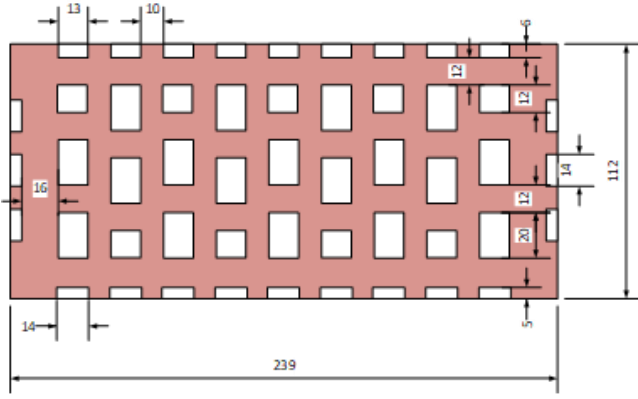


Figure 1: Dimensions of the investigated clinker bricks

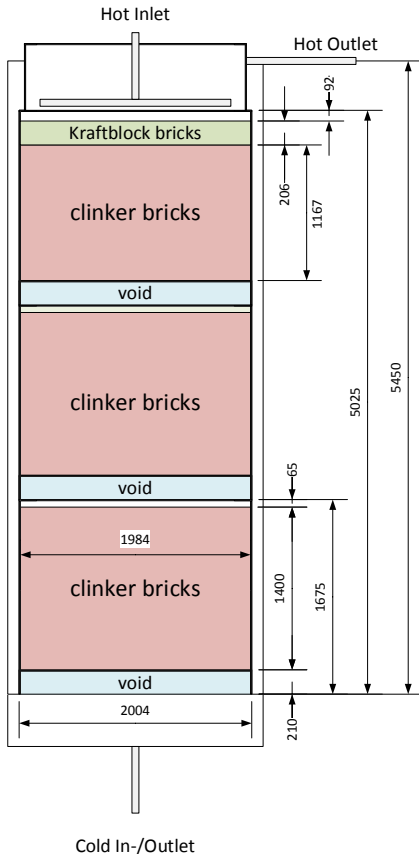


Figure 2: Sketch of the TESIS refractory bricks inventory inside the TESIS test tank

Besides the experiments, a 1D Matlab code has been developed (Odenthal et al., 2023) and the experiments were used for its validation. The model consists of the partial differential equations for the fluid (f) as given by equation (1)

$$\varepsilon \rho_f c_f \frac{\partial T_f}{\partial t} = -\rho_f c_f v_{0,x,f} \frac{\partial T_f}{\partial x} + \lambda_{\text{eff},x} \left(\frac{\partial^2 T_f}{\partial x^2} \right) + \dot{Q}'_{f-s} \quad (1)$$

and the solid (s), see equation (2):

$$(1 - \varepsilon) \rho_s c_s \frac{\partial T_s}{\partial t} = -\dot{Q}'_{s-f} \quad (2)$$

Herby \dot{Q}'_{s-f} is the heat flow between the fluid and the solid, $\rho_f c_f$ and $\rho_s c_s$ are the volumetric heat capacities for the fluid and solid, $v_{0,x,f}$ is the free flow velocity of the fluid, $\lambda_{\text{eff},x}$ the effective conductivity and ε the void fraction. The equations are transformed into a system of ordinary differential equations by spatial discretization and solved with Matlab.

Results and Discussion

In a first experiment the thermal energy storage has been discharged with molten salt at a temperature of 290°C starting with a uniform temperature of 560°C, as depicted in Figure 3. As can be seen, the thermocline remains very steep at the top of the packing area, which is likely due to the thermodynamically optimal geometry of the Kraftblock packing material. Within the clinker brick layer, the stratification diminishes slightly as the heat transfer into the clinker bricks is lower. The agreement with the model is good within the upper part of the storage volume but shows some deviations towards the end of the storage volume leaving some room for further refinement of the model. The cause is likely due to lacking data of physical properties of the clinker bricks.

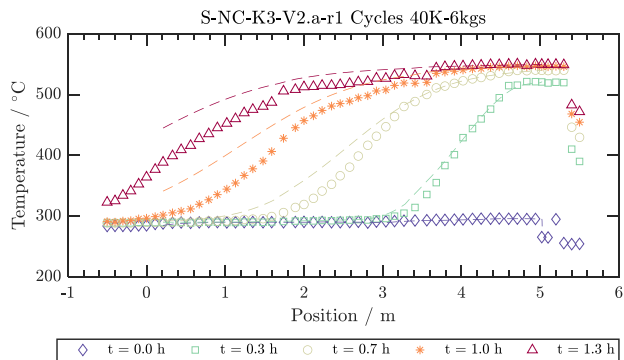


Figure 3: Temperature curves during the discharge cycle with 6kg/s mass flow and 40K cut-off temperature. Simulation (lines) and measured values (markers)

In the next experiment the stand-by behavior is investigated.

Figure 4 shows the temperature distribution inside the storage tank after 4 hours of stand-by time with a freshly created thermocline. The stratification of the thermocline is evenly distributed in radial direction.

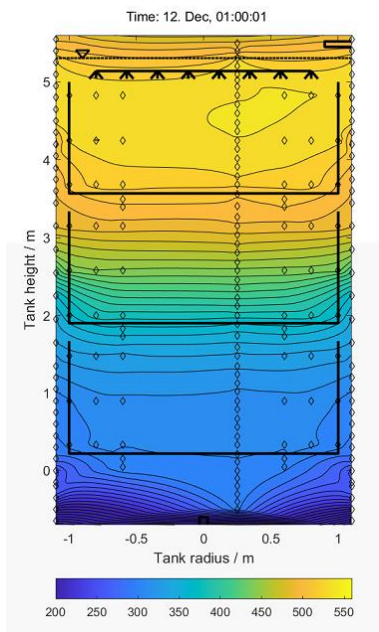


Figure 4: Interpolated temperature field after 4 hours of stand-by

This stratification also remains after 1 day of additional stand-by time, only the overall temperature level is reduced due to heat losses to the environment (see Figure 5).

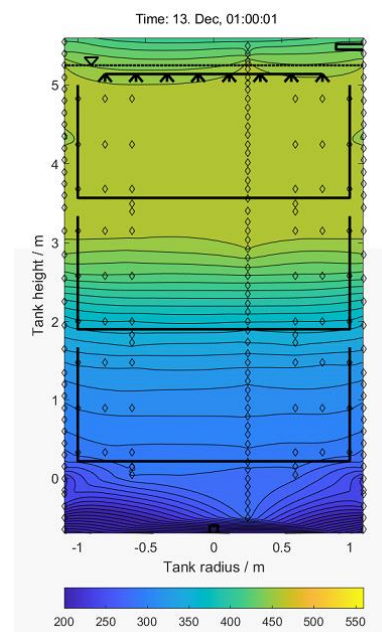


Figure 5: Interpolated temperature field after 28 hours of stand-by

Conclusions

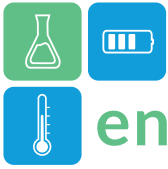
The experiments have shown that a good stratification can be achieved with refractory bricks as storage material and molten salt as heat transfer medium. In comparison to the 1D-model a good agreement can be found with the Kraftblock material section but further research in the physical properties of the clinker material is necessary. During stand-by periods the thermocline remains stable and does not show signs for the onset of stronger free convection.

Acknowledgment

The authors thank the German Federal Ministry for Economic Affairs and Energy for the financial support given to this work in the project Newline (03EE5057A)

References

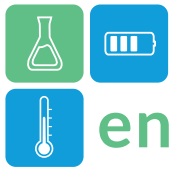
- Bauer, T., Odenthal, C., Bonk, A., 2021. Molten Salt Storage for Power Generation. *Chemie Ingenieur Technik* 93, 534–546. <https://doi.org/10.1002/cite.202000137>
- Odenthal, C., Tombrink, J., Klasing, F., Bauer, T., 2023. Comparative study of models for packed bed molten salt storage systems. *Applied Thermal Engineering* 226, 120245.



ENERSTOCK 2024
The 16th IEA ES TCP International Conference on Energy Storage
June 5–7, 2024
Lyon, France

<https://doi.org/10.1016/j.applthermaleng.2023>

.120245



LargeTESmtk: A comprehensive modeling toolkit for large-scale thermal energy storage systems

Michael Reisenbichler-S.^{1,2,*}, Franz Wotawa², Keith O'Donovan^{1,3}, Carles Ribas Tugores¹, Franz Hengel¹

¹ AEE - Institute for Sustainable Technologies, Feldgasse 19, 8200 Gleisdorf, Austria

² Institute of Software Technology, Graz Univ. of Technology, Inffeldgasse 16b/II, 8010 Graz, Austria

³ Modelon Deutschland GmbH, Agnes-Pockels-Bogen 1, 80992 München, Germany

*Corresponding author e-mail: m.reisenbichler@ae.at

Abstract

Large-scale underground thermal energy storage systems offer the flexibility to store large amounts of renewable energy to bridge the natural gap between supply and demand. However, to exploit the full potential of this technology, numerical simulations are required along the whole design process.

Hence, we have developed the LargeTESModelingToolkit (LargeTESmtk), a novel Modelica-based toolkit for modeling and simulating large-scale pit and tank thermal energy storage. This first comprehensive Modelica library in the field provides the flexibility and tools needed to develop new storage models tailored to the desired application. It also offers researchers and industrial users pre-built storage models for simulation studies to answer the relevant questions for optimized storage and system-level design.

This paper presents the toolkit's key features, structure, and underlying modeling approaches. Moreover, we discuss the models' validation and show the toolkit's application with an exemplary simulation case study.

Keywords: Modelica library, Modeling toolkit, Large-scale thermal energy storage, Pit TES, Tank TES

Introduction

The integration of large-scale underground thermal energy storage (TES) systems offers a high potential to massively increase the share of renewable energy in our future energy systems. They can provide the flexibility needed to store volatile renewable energy sources for a few days as well as on a seasonal basis, bridging the natural gap between supply and demand (Schmidt et al., 2018). At the same time, they also offer a high economic attractiveness for storing large amounts of heat due to economies of scale and a certain flexibility in site selection due to attractive underground integration without free-standing tall structures. In contrast, the large volumes involved lead to high investment costs, which require fundamental planning from the component to the system level. Experimental investigations in the design phase are limited due to the size of these storage technologies and the long time periods in question. Therefore, numerical simulations are used throughout the whole design process (Dahash et al., 2019).

Modelica¹ is an equation-based, object-oriented, and multi-domain modeling language that inherently facilitates high reusability, expandability, and adaptability of the produced models. Therefore, with Modelica's

features and capabilities, large-scale TES modeling on the storage and system level can be taken to the next level.

However, currently, available models are still scattered, limited in functionality and flexibility (e.g., in the choice of geometries), focused on specific applications, or have not yet undergone a comprehensive validation process. Hence, we have developed the LargeTES-ModelingToolkit (LargeTESmtk), a comprehensive Modelica-based toolkit for the modeling and simulating large-scale pit and tank TES (Reisenbichler-S. et al., 2023). In addition to an easy-to-use Modelica library with scientifically proven, pre-built storage models for researchers and industrial users, the toolkit is also intended to provide the foundation and tools for developing new storage models customized to the wanted application.

The LargeTESmtk modeling toolkit

Figure 1 provides an overview of the LargeTESmtk. Displayed in the centre is the basic structure of each storage model, consisting of the two main models for the fluid and ground domain, surrounded by an extract

¹ <https://modelica.org/> (accessed: January 10, 2024)

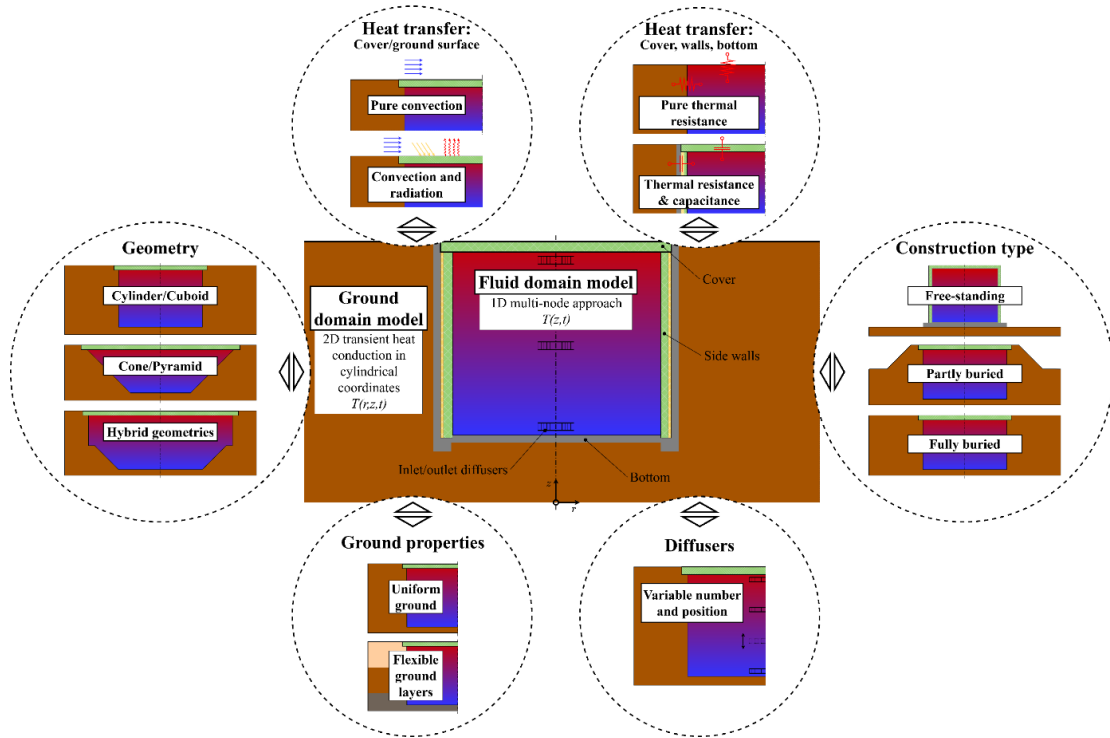


Figure 1: Overview and features of the LargeTESmtk (Reisenbichler-S. et al., 2023)

of available model configuration options. Along with other features, the library should provide a wide range of configuration options in terms of geometry (e.g., cylindrical, conical, or hybrid geometries), heat transfer mechanisms (e.g., pure convection or combined convection and radiation) or ground properties (e.g., uniform ground or specific ground layers) that can be tailored specifically to the wanted application and level of detail. Figure 2 shows the top-level structure and selected sub-packages of the corresponding Modelica library of the toolkit.

The developed models with the LargeTESmtk are to be applied in parameter studies, sensitivity and techno-economic analyses for optimized design on storage and system level. This may include addressing important storage design questions regarding the volume, geometry, insulation quality of the cover, side walls, and bottom, or the number and position of inlets and outlets (i.e., diffusers). In addition, for instance, the investigation of long-term effects (e.g., the development of storage performance in the first years of operation during the heat-up of the surrounding ground) of different system integration concepts (e.g., post-heating concepts via large heat pumps) or storage operation strategies is possible.

Methodology

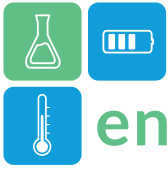
In the following, we discuss the modeling approaches, the validation of the models, and the simulation case study.



Figure 2: Modelica library structure (Reisenbichler-S. et al., 2023)

Main modeling approaches

For both main models (i.e., the fluid and ground domain model) the finite difference method (FDM) is used to solve the governing basic partial differential equations (PDE). The so-called 1D multi-node approach, which is widely used in dynamic system simulation, is applied to model the fluid domain. For the ground domain, the basic mathematical description and the governing equations follow the partial differential equations of two-dimensional transient heat conduction



in cylindrical coordinates with constant thermophysical properties. For further details and explanations regarding the applied modeling approaches, please refer to the publication by Reisenbichler-S. et al. (2023).

Validation of the models

To validate and assess the accuracy of the developed tank TES (TTES) model, a validation case study was conducted comparing the simulation results with real measurement data of the Danish pit TES (PTES) in Dronninglund (Reisenbichler et al., 2021). Furthermore, the TTES model of the LargeTESmtk was part of a cross-comparison study of various large-scale TES models from different simulation tools (e.g., COMSOL Multiphysics, TRNSYS) in a scenario with generic boundary conditions (Ochs et al., 2022). Recently, as part of IEA ES TCP Task 39 "Large Thermal Energy Storages for District Heating", a comprehensive cross-comparison study with models from various simulation tools, including the TTES and PTES models of the LargeTESmtk under standardized test procedures was conducted by (Schmidt et al., 2024).

Overall, a good agreement between the LargeTESmtk models, the measurement data, and the other models could be demonstrated. Further validation studies (including further comparisons with measurement data from real TES systems) are in progress.

Simulation case study

One main application area of the storage models is the integration into system simulations. Thereby, the interaction of the storage together with other system components (e.g., large heat pumps, district heating systems) is evaluated on the system level. However, in this paper, we demonstrate the application of the library models through an exemplary simulation case study on the storage level. The study compares the performance of TTES and PTES with cylindrical and conical fluid

geometry under different operation modes ranging from short-term to seasonal storage operation.

As the focus is on the storage level, other system components, such as heat supply units and heat consumers (e.g., the district heating system), are neglected. Instead, simplified generic charging and discharging profiles based on real storage application scenarios are applied for the different operation modes. For further details on the investigated operation modes, applied model parameters, and boundary conditions, please refer to the publication by Reisenbichler-S. et al. (2023).

Results and Discussion

Figure 3 shows the used models and the resulting annual storage efficiencies of the simulation case study depending on the operation mode (i.e., number of nominal storage cycles) ranging from short-term to seasonal storage operation. The annual storage efficiency η is defined as the annual discharged energy Q_{dis} divided by the annual charged energy Q_{ch} :

$$\eta = \frac{Q_{dis}}{Q_{ch}} \quad (1)$$

The expected trend that a higher number of storage cycles leads to higher storage efficiency can be seen for both storage types. The short-term operation with 120 nominal storage cycles shows the highest efficiencies with values above 99%. With fewer storage cycles, the storage utilization decreases, and the actual storage phases become longer, resulting in the lowest storage efficiency for the seasonal operation, whereby the storage efficiency only falls below 90% starting from a number of four storage cycles. The lowest efficiency is about 58% for the PTES case. In general, as expected, the TTES performs better than the PTES. One main reason for that is the lower surface-to-volume ratio of the cylindrical geometry compared to the conical geometry. At high storage cycle numbers, there is only a

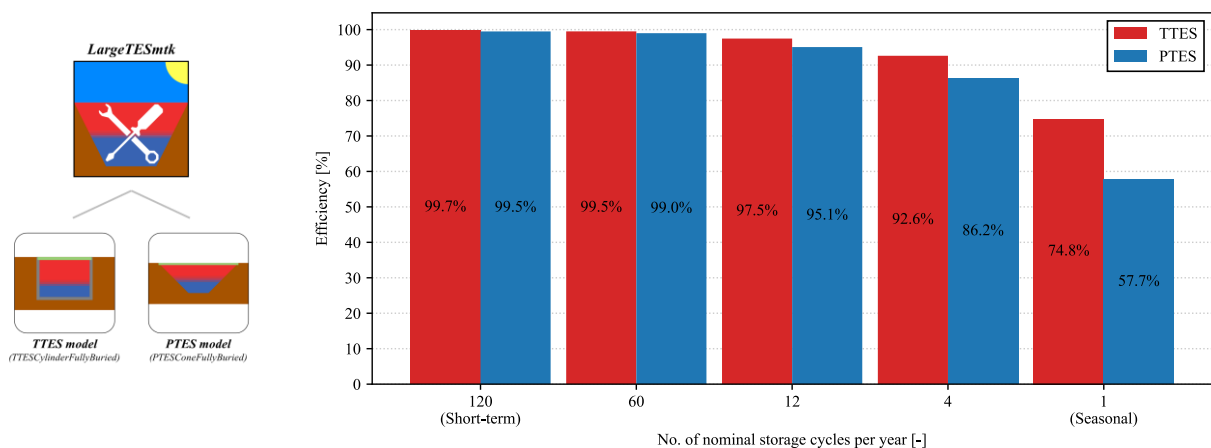


Figure 3: Used models and annual storage efficiencies ranging from short-term to seasonal storage operation of the simulation case study (Reisenbichler-S. et al., 2023).



slight difference between the storage types, but for the seasonal storage operation, the difference between TTES and PTES is considerable at about 17%.

The purpose of this rather small simulation case study was mainly to show the application of the storage models of the library. Storage parameters such as volume, height-to-diameter ratio, ground properties or insulation level, which can have a high impact on the storage efficiency, were not evaluated. However, this simulation case study can serve as a basis for these broader parameter studies and with the provided models and flexibility of the LargeTESmtk, the study may also be extended to other storage geometries or combined with additional system components for evaluations on system level.

Conclusions

This study introduced the LargeTESmtk, a comprehensive Modelica-based toolkit for the modeling and simulation of large-scale PTES and TTES at storage and system level for researchers and industrial users. Besides the pre-built storage models, the provided sub-models and the wide range of model configuration options allow high flexibility in the modeling process and facilitate the development of new models specifically tailored to the desired application. The library models are to be applied in simulation studies to address relevant storage design questions (e.g., regarding the proper storage geometry or insulation quality) or to investigate different system concepts to achieve an optimized design at storage and system level.

The accuracy of selected library models has been shown with excerpts from completed and ongoing validation case studies, including measurement data of real TES, and cross-comparison studies with other storage models. Further studies in this regard are underway. To demonstrate the application of the LargeTESmtk, an exemplary simulation case study was conducted comparing the performance of PTES and TTES under different operation modes ranging from short-term to seasonal storage operation. As expected, the simulation case study showed that the storage efficiency drops with seasonal operation compared to short-term operation and that the TTES generally performs better than the PTES.

The toolkit is currently still undergoing a continuous development process. As shown in this paper, many features and models are already available, but some of the presented models and features (e.g., hybrid geometries) still need to be added and subjected to validation studies. Furthermore, it is intended to make the library available to everyone soon.

Acknowledgment

This work was mainly funded by the Austrian Research Promotion Agency (FFG) in the framework of the program “Forschungspartnerschaften Industriennahe Dissertationen 2020 - 6. AS Forschungspartnerschaften“ as part of the project “DevMoTES” (Project No. 878848).

References

- Dahash, A., Ochs, F., Janetti, M. B., & Streicher, W. (2019). Advances in seasonal thermal energy storage for solar district heating applications: A critical review on large-scale hot-water tank and pit thermal energy storage systems. *Applied Energy*, 239, 296–315. <https://doi.org/10.1016/j.apenergy.2019.01.189>
- Ochs, F., Dahash, A., Tosatto, A., Reisenbichler, M., O'Donovan, K., Gauthier, G., Skov, C. K., & Schmidt, T. (2022). Comprehensive Comparison of Different Models for Large-Scale Thermal Energy Storage. *Proceedings of the International Renewable Energy Storage Conference 2021 (IRES 2021)*, 36–51. <https://doi.org/10.2991/ahe.k.220301.005>
- Reisenbichler, M., O'Donovan, K., Ribas Tugores, C., van Helden, W., & Wotawa, F. (2021). Towards more efficient modeling and simulation of Large-scale Thermal Energy Storages in future Local and District Energy Systems. *Proceedings of the 17th IBPSA Conference*, 2155–2162. <https://doi.org/10.26868/25222708.2021.30911>
- Reisenbichler-S., M., Wotawa, F., O'Donovan, K., Tugores, C. R., & Hengel, F. (2023). LargeTES-ModelingToolkit: A Modelica Library for Large-scale Thermal Energy Storage Modeling and Simulation. *Proceedings of the 15th International Modelica Conference*. The 15th International Modelica Conference, Aachen (DE). <https://tinyurl.com/LargeTESmtkModelicaCon23>
- Schmidt, T., Dahash, A., Tosatto, A., Ochs, F., Gauthier, G., Sifnaios, I., Thornton, J., Reisenbichler-S., M., Van der Wilk, S., & Klöck, M. (2024). *Results of test case simulations (in press)* (Deliverable C3a; Task 39 - Large Thermal Energy Storages for District Heating: Subtask C - Round Robin Simulation). IEA ES TCP. <https://iea-es.org/task-39/deliverables/>
- Schmidt, T., Pauschinger, T., Sørensen, P. A., Snijders, A., Djebbar, R., Boulter, R., & Thornton, J. (2018). Design Aspects for Large-scale Pit and Aquifer Thermal Energy Storage for District Heating and Cooling. *Energy Procedia*, 149, 585–594. <https://doi.org/10.1016/j.egypro.2018.08.223>

Layered manganese dioxide as a versatile heat-storage material utilizing environmental water vapor

Norihiko L. Okamoto^{1,*}, Hiroki Yoshisako², Kazuya Tanaka³, Tetsu Ichitsubo^{1,3}

¹Tohoku University, Institute for Materials Research, Katahira, Aoba-ku, Sendai, Japan

²Tohoku University, Graduate School of Engineering, Aramaki, Aoba-ku, Sendai, Japan

³Japan Atomic Energy Agency, Advanced Science Research Center, Tokai, Japan

*Corresponding author e-mail: nlokamoto@tohoku.ac.jp

Abstract

We have discovered that layered manganese dioxide (birnessite, $\delta\text{-K}_{0.33}\text{MnO}_2 \cdot n\text{H}_2\text{O}$) can store/release heat through an intercalation mechanism, in which water molecules in a moist atmosphere are inserted into and removed from the interlayers. The material has an excellent balance of various properties required for heat-storage materials, such as low heat-storage temperature, high thermal energy density, good charge/discharge rate, and good cyclic properties. The material initially contains 0.83 mol of interlayer water molecules per $\text{K}_{0.33}\text{MnO}_2$ and releases them by absorbing heat at around 120°C. After the first heating/cooling cycle, the material can reversibly release and absorb 0.50 mol of water molecules per $\text{K}_{0.33}\text{MnO}_2$, resulting in a volumetric energy density exceeding 1,000 MJ/m³. We also analysed crystal structures of $\text{K}_{0.33}\text{MnO}_2$ before and after heat treatment by atomic-resolution scanning transmission electron microscopy. We have elucidated that the interlayer K cations, which are initially disordered due to a site competition with water molecules in the as-synthesized state, exclusively occupy the most stable sites in a tripled periodicity in the absence of water molecules during heat treatment, hindering the excess water to re-intercalate in the subsequent thermal cycle process.

Keywords: Heat-storage material, Birnessite, Water intercalation, Scanning transmission electron microscopy

Introduction

Thermal storage materials, which can store waste heat energy and release it as needed, can be classified to several different types, including sensible heat, phase-change, chemical reaction, and chemisorption (Sadeghi, 2022). Although chemical-reaction and chemisorption types have a high heat storage energy density, their heat-storing (i.e., charging) temperature is too high and, furthermore, they lack cyclability and reversibility due to deliquescence and large volume distortion by including a large amount of water molecules (Steiger et al., 2008). Phase-change materials using sensible heat or latent heat usually show excellent reversibility of heat absorption/release but have low heat storage energy density and difficulty in maintaining the heat-stored state (Paris et al., 1993, Tokoro et al., 2015). Therefore, a new material with a new heat storage mechanism that has all the properties required for heat storage materials (low charging temperature, high heat-storage energy density, good rate property, good cyclability, environmental compatibility, etc.) is desired for recovery and reuse of low-temperature waste heat.

Based on our previous study on the phase stabilities of various polymorphs of manganese dioxide (MnO_2) with different crystal structures (Hatakeyama et al., 2022), we have demonstrated that K-containing layered manganese dioxide (birnessite, $\delta\text{-K}_x\text{MnO}_2$) shown in Figure 1(a) can be used as a high-performance thermal storage material possessing the above properties (Hatakeyama et al., 2022). In addition, it has also been found that the heat release and absorption reactions of layered manganese dioxide are caused by an intercalation mechanism in

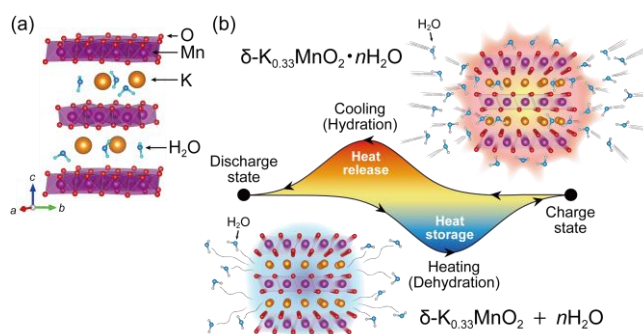
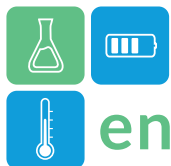


Figure 1: (a) Crystal structure of layered manganese dioxide $\delta\text{-K}_{0.33}\text{MnO}_2 \cdot n\text{H}_2\text{O}$. (b) Schematic illustration of the heat storage and release reactions by the water-molecule deintercalation-intercalation mechanism.



which water molecules in the moist atmosphere are inserted into and removed from the interlayer of MnO_2 slabs (Figure 1(b)).

Here, we present our recent study on how the K-containing layered manganese dioxide was identified to be an excellent heat-storage material utilizing the water intercalation mechanism (Hatakeyama et al., 2022). We also show the crystal structure analysis of the K-containing layered manganese dioxide before and after heat-treatment by atomic-resolution scanning transmission electron microscopy (STEM) to elucidate the origin of an irreversible capacity of water intercalation observed after the initial thermal cycle (Okamoto et al., 2023).

Methodology

Materials preparation

$\delta\text{-MnO}_2$ was prepared according to the literature by Gaillot *et al.* (Gaillot et al., 2004). KMnO_4 (Wako Chemical) crystalline powder was thermally decomposed at 700 °C in air. The as-decomposed powder sample and the powder sample heat-treated in air at 250°C to release all the water molecules will be called a “pristine” and “heat-treated” samples, respectively, throughout the paper.

Materials characterization

X-ray powder diffraction (XRD) analysis was performed using a SmartLab diffractometer (Rigaku) with $\text{Mo-K}\alpha$ radiation. In-situ XRD analysis at controlled temperatures was carried out at a heating rate of 5 K/min. The samples were placed in ambient air atmosphere (60%RH@24°C) or dry N_2 atmosphere during measurement. Atomic-resolution STEM imaging was made with a spherical-aberration-corrected JEM-ARM200F microscope (JEOL).

Thermal analyses under dry or moisture condition

Thermogravimetric analysis under controlled humidified N_2 atmosphere (70%RH@25°C) was performed using Thermo plus EVO2 TG-DTA8122/HUM-1 (Rigaku). The rate capability was measured for the first six cycles at a heating rate of 10–100 K/min whereas cooling rate was fixed at 5 K/min. Cyclability was subsequently assessed up to 16th cycles at a heating rate of 20 K/min and cooling rate of 5 K/min.

Results and Discussion

TG-DTA in a humidity-controlled atmosphere

Deintercalation and intercalation behaviour of water molecules in K-containing layered manganese dioxide was analysed by thermogravimetric analysis in a

humidity-controlled N_2 atmosphere (Hatakeyama et al., 2022). The endothermic reaction during heating was accompanied by a decrease in weight and the exothermic reaction during cooling was accompanied by an increase in weight, which indicates that the endothermic reaction observed in Figure 2(a) at around 160°C was associated with the deintercalation of water molecules. The weight of the sample decreased by about 13% during the first cycle, but the weight did not completely recover even after lowering the temperature. The weight loss during the second and subsequent cycles was about 8%. Assuming that all the water of crystallization is released at 260°C to form $\text{K}_{0.33}\text{MnO}_2$, the molecular weight of water in the as-synthesized sample is 0.83 mol per $\text{K}_{0.33}\text{MnO}_2$ composition ($\text{K}_{0.33}\text{MnO}_2 \cdot 0.83\text{H}_2\text{O}$). It was estimated to be 0.5 mol ($\text{K}_{0.33}\text{MnO}_2 \cdot 0.50\text{H}_2\text{O}$) in the hydrated state after the second cycle. Thus, there exists an irreversible capacity of 0.33 mol of water in the 1st cycle. The reason for the irreversible capacity will be discussed at the end of the Results and Discussion section. The fact that the dehydration is completed within 2 minutes at the highest heating rate (100 K/min) indicates that the diffusion of water molecules within the material is extremely rapid. As shown in

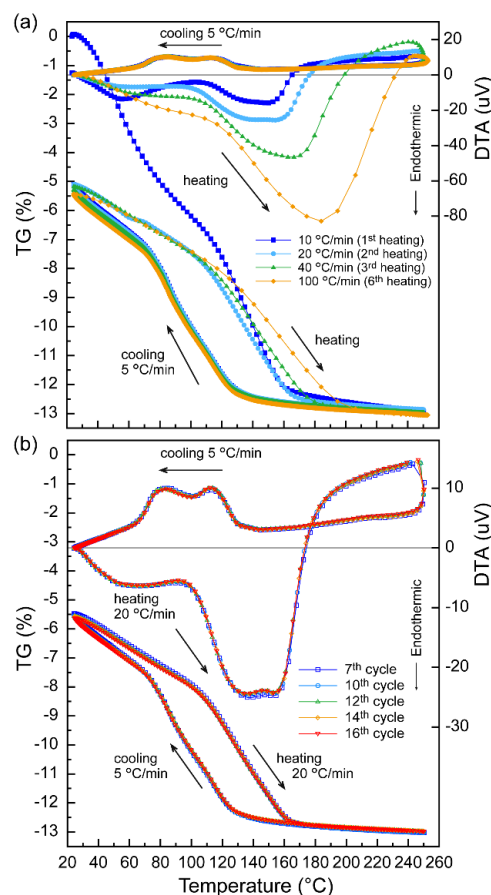


Figure 2(b), the changes in the TG-DTA values followed almost the same trajectory from the 7th to the 16th cycle, indicating that the cycle characteristics were also excellent.

In-situ XRD in humid and dry atmospheres

In order to investigate the structural changes during thermal cycle, in-situ high-temperature X-ray diffraction measurements were performed in humid and dry atmospheres (Hatakeyama et al., 2022). First, the X-ray diffraction measurements with heating-cooling cycles were performed in air at a relative humidity of 60% @24°C. Figure 3(a) shows the colour map of the diffraction intensity. The diffraction angles of 002 and 004 reflections of the layered $K_{0.33}MnO_2$ discontinuously increase at $\sim 140^\circ\text{C}$ during heating and discontinuously decrease at $\sim 160^\circ\text{C}$ during cooling. On the other hand, the diffraction angle of 100 reflection around 16.5° is invariant regardless of temperature. These indicate that the interlayer distance decreases/increases with keeping the in-plane (a -axis) lattice constant during the water deintercalation and intercalation during heating/cooling. Under a dry nitrogen atmosphere, as shown in Figure 3(b), after the c -axis lattice constant is decreased due to the dehydration reaction during the first-cycle heating, the a - and c -axis lattice constants remained unchanged even after repeating heating and cooling processes. However, when the sample was exposed to a humid atmosphere after two thermal cycles, the interlayer distance returned to its original value within a few minutes. This also indicates that the change in interlayer distance during heating and cooling is due to the deintercalation/intercalation of water molecules.

Interlayer K cation ordering induced by heat-treatment

Figures 4(a) and (b) show the atomic-resolution HAADF-STEM images of the pristine and heat-treated samples, respectively, taken along the $[1\bar{1}00]$ direction (Okamoto et al., 2023). The atomic columns with the brightest contrast in the images correspond to

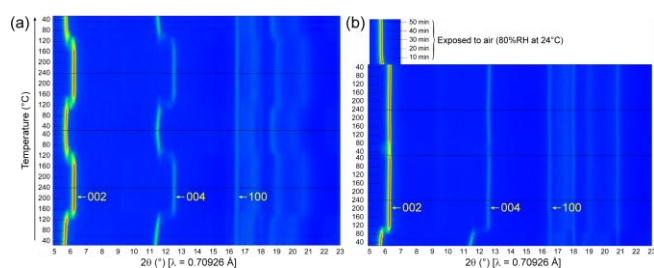


Figure 3: In-situ high-temperature X-ray diffraction measurements (a) in humid air (60%RH@25°C) and (b) in dry nitrogen.

Mn atoms in the MnO_2 layer while those with a relatively bright contrast between the MnO_2 layers correspond to the interlayer K cations. The contrast of interlayer K cations for the heat-treated sample (Figure 4(b)) is discrete as indicated by solid yellow arrows. The interlayer K cations are arranged in an ordered manner with a tripled periodicity along the a -axis, which can be confirmed by the intensity profiles along the lines connecting positions Y–Z as shown in Figure 4(d). On the other hand, some interlayer positions for the pristine sample show ambiguous contrast as indicated by open yellow arrows (Figure 4(a)). For comparison, the intensity profiles along the lines connecting positions W–X are shown in Figure 4(c). This ambiguous contrast does not mean a deficiency of the interlayer K cations but the disordered arrangement of the K cations since the heat treatment should not increase the K content. The

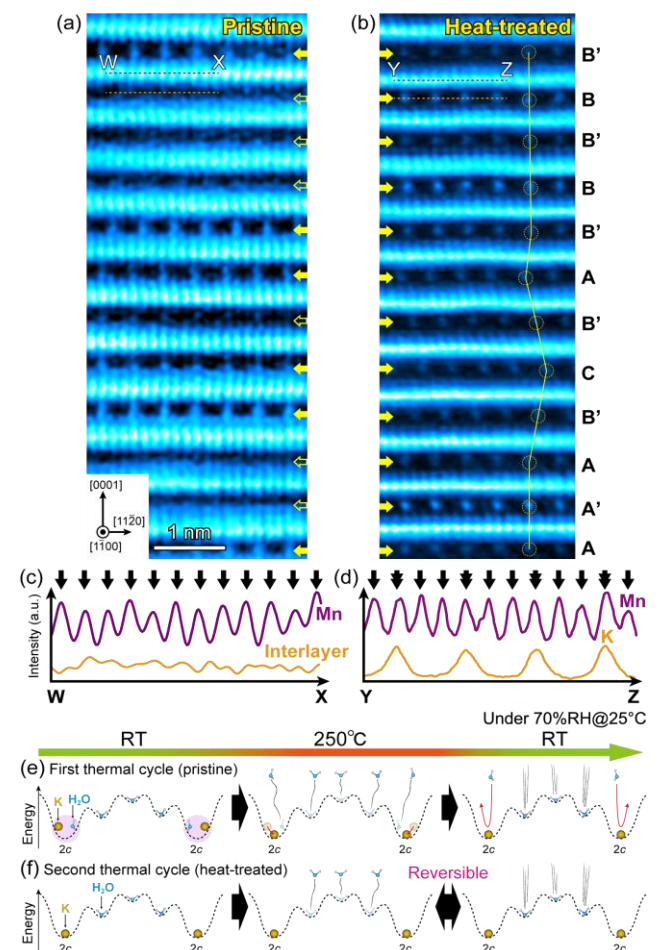
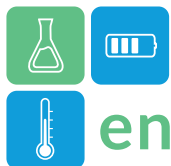


Figure 4: Atomic-resolution HAADF-STEM images of (a) pristine and (b) heat-treated samples taken along the $[1\bar{1}00]$ direction. (c,d) Intensity profiles along the lines connecting positions W–X in (a) and Y–Z in (b), respectively. Schematic illustrations showing the release/absorption of water molecules from/to $K_{0.33}MnO_2$ during heating/cooling TG-DTA measurements for the pristine sample (e) in the 1st cycle and (f) in the subsequent cycles. In the initial state, the interlayer K cation and excess water molecule are competing for the 2c site (left-hand side).



interlayer K cations with positional disorder became regularly arranged at one-third of the preferential sites (Wyckoff $2c$ in the space group $P6_3/mmc$) after the heat treatment. This infers that the heat treatment allows the K cation to move from its metastable position to the most stable position ($2c$ site) in the absence of water molecules. In the pristine state, conversely, the interlayer K cations and excess water molecules are considered to compete for the $2c$ site, resulting in the disordered arrangement of K cations as schematically shown on the left-hand of Figure 4(e) (Okamoto et al., 2023).

The irreversible capacity of water molecules (0.33 mol) described above can be considered due to the structural relaxation involving the interlayer K cations (Okamoto et al., 2023). In the as-synthesized state, the excess water molecules (0.83 mol per $K_{0.33}MnO_2$) prevent the interlayer K cations from occupying the most stable $2c$ sites, as indicated by pink circles in Figure 4(e). The K cations are randomly arranged between the MnO_2 layers. Some of the intercalated water molecules are at a relatively shallow potential energy surface and the other water molecules competing with the interlayer K cations for the $2c$ sites are at a relatively deep potential energy surface. When the sample is exposed to elevated temperatures, the intercalated water molecules are completely released, and the K cations readily move to the most stable $2c$ sites, introducing the ordered arrangement with the tripled periodicity within the interlayer space as evidenced by the STEM observation (Figure 3(b)). After such structure relaxation, some of the released water molecules cannot return to their original positions as shown on the right-hand of Figure 4(e). Thus, heat treatment at high temperatures causes the structure relaxation and the irreversible capacity of water molecules. After the heat treatment at $250^\circ C$, the same amount of water molecules is reversibly released and absorbed in the subsequent heating/cooling cycles (Figure 4(f)). To minimize the irreversible capacity of water intercalation, and hence, to increase the thermal energy density, replacing interlayer K cations with other species and/or optimizing the interlayer cation content that change the interaction between interlayer cations and water molecules will be effective.

Conclusions

We have demonstrated that the mechanism of “water intercalation” in heat storage materials is very advantageous in terms of their reversibility and reaction rate. Although not shown in this proceeding

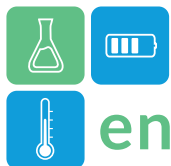
due to space limitation, the reversible heat-storage capacity is at least $1,000 \text{ MJ/m}^3$ (Hatakeyama et al., 2022), which is the best among phase-change type heat-storage materials. Furthermore, $\delta\text{-}K_{0.33}MnO_2$ of the layered structure is superior as a heat-storage material in terms of environmental resistance (oxide cannot be degraded in by environmental oxygen and water). Thus, the excellently balanced $\delta\text{-}K_{0.33}MnO_2$ utilizing moisture/water in an open system will pave the way for the application of heat storage technology exploiting low-grade waste heat.

Acknowledgments

N.L.O. and K.T. acknowledge that this work was supported by the Japan Science and Technology Agency (JST) ALCA-Next Program (grant number: JPMJAN23A3).

References

- Gaillot, A. C., Drits, V. A., Plançon, A. and Lanson, B. (2004). Structure of synthetic K-rich birnessites obtained by high-temperature decomposition of $KMnO_4$. 2. Phase and structural heterogeneities. *Chem. Mater.* 10.1021/cm035236r.
- Hatakeyama, T., Okamoto, N. L. and Ichitsubo, T. (2022). Thermal stability of MnO_2 polymorphs. *J. Solid State Chem.* 10.1016/j.jssc.2021.122683.
- Hatakeyama, T., Okamoto, N. L., Otake, S., Sato, H., Li, H. Y. and Ichitsubo, T. (2022). Excellently balanced water-intercalation-type heat-storage oxide. *Nat. Commun.* 10.1038/s41467-022-28988-0.
- Okamoto, N. L., Yoshisako, H. and Ichitsubo, T. (2023). Effect of interlayer K ordering on water intercalation behavior in δ -type layered manganese dioxide. *Energy Storage Mater.* 10.1016/j.ensm.2023.102912.
- Paris, J., Falardeau, M. and Villeneuve, C. (1993). Thermal Storage by Latent-Heat - a Viable Option for Energy-Conservation in Buildings. *Energy Sources.* 10.1080/00908319308909014.
- Sadeghi, G. (2022). Energy storage on demand: Thermal energy storage development, materials, design, and integration challenges. *Energy Storage Mater.* 10.1016/j.ensm.2022.01.017.
- Steiger, M., et al. (2008). Hydration of $MgSO_4$ center dot H_2O and generation of stress in porous materials. *Cryst. Growth Des.* 10.1021/cg060688c.
- Tokoro, H., et al. (2015). External stimulation-controllable heat-storage ceramics. *Nat. Commun.* 10.1038/ncomms8037.



Lignin modified ecological coating as thermal barrier in container materials for sorption heat pumps.

Sara Amini^{1,*}, Xabier Erdocia², Fabio Hernández¹, Jalel Labidi¹, Ángel G. Fernández¹.

1 Biorefinery Processes Research Group, Chemical and Environmental Engineering Department, Faculty of Engineering Gipuzkoa, University of the Basque Country UPV/EHU, Plaza Europa 1, 20018 Donostia, Spain

2 Biorefinery Processes Research Group, Department of Applied Mathematics, Faculty of Engineering Bilbao, University of the Basque Country UPV/EHU. Rafael Moreno “Pichichi”, 3, 48013 Bilbao, Spain

*Corresponding author e-mail: sara.amini@ehu.eus

Abstract

Corrosion issues have significant economic and environmental impacts. Therefore, proposals for reducing corrosion rates are becoming increasingly important. Additionally, there is a growing emphasis on developing coatings of renewable origin (green coatings) for use on metal surfaces to slow down corrosion. This work proposes the use of coatings based on modified (silanized) lignin to reduce the corrosion rate of metal surfaces in sorption heat pumps that use sorption salt ($\text{MgSO}_4 \cdot 7\text{H}_2\text{O}$). Tests were carried out in a highly corrosive environment, where the salt is completely dehydrated, to verify the effectiveness of the coatings. The study results demonstrate the silanization of lignin and the effectiveness of the coating in reducing the corrosion rate of metals in the proposed sorption heat pump.

Keywords: Green coatings, Lignin coating, Corrosion mitigation, Sorption heat pumps.

Introduction

The corrosion of metals affects the economic growth of a country. The global corrosion cost in 2016 was estimated at \$2.5 trillion (USD), according to a study from NACE (Koch et al., 2016). However, nowadays this cost has increased reaching up to \$3 trillion (USD), which is around 3.5% of the 2020 world Gross Domestic Product (GDP). In addition to the economic costs, corrosion has a negative impact on the environment and increases the human footprint, as well as the emission of greenhouse gases (GHG). Due to the corrosion of metal parts, replacement must occur, increasing the production of GHG during the recycling, smelting, manufacturing and transportation of the new materials to be used in the affected zone. Therefore, it is very important to increase the durability of materials under industrial environments to reduce both economic costs and environmental impact (Solvay, 2023).

One of the most commonly employed methods is the use of protective coatings that are placed on the metal surface based on organic (plastics) and inorganic molecules (Ndukwe, 2022). These coatings have the ability to modify the corrosion potential and the electric resistance (Carlos De Haro et al., 2019).

Inorganic coatings predominantly contain chromium, aluminium, nickel or other metal ions. However, these coatings are in decline (especially those based on chromium VI or hexavalent chromium), due to their high toxicity, price, negative environmental impact or limited lifetime (Carlos De Haro et al., 2019)

On the other hand, organic coatings can be classified into the following categories: polymeric, hybrid sol-gel, nano and green coatings (Olajire, 2018). Due to the toxicity of some inorganic and organic coatings, green inhibitors or green coatings, such as natural products obtained from plant extracts or the use of renewable products are being targeted by researchers.

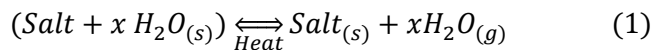
Green corrosion inhibitors are biodegradable coatings used on top of metallic surfaces to prevent corrosion. They do not contain heavy metals nor other toxic compounds. In this direction, the use of lignin has been highlighted due to their interesting properties. Lignin is an abundant natural polymer, mainly used in surfactants, adhesives and dispersants although there are some green applications as plastic replacement and packaging systems that are under study.

An innovative application of lignin has been focused on corrosion protective coatings. This protection can be applied under metal surfaces since lignin presents some

interesting properties as water impermeability, hydrophobicity and film forming ability. Some recent research work has discussed the feasibility of incorporating lignin as anticorrosive substance, in the formulation of coatings placed on top of metallic surfaces (Dastpak et al., 2018). The quantities of added lignin varies from case to case.

One way to improve the adhesion properties of the lignin coating to the metal surface and to improve its anticorrosive properties is by silanization of the lignin. Thermal energy storage (TES) based on chemical energy is an alternative to sensible or latent heat TES. These systems have higher density and longer storage times, as well as lower thermal dissipation. Thermochemical TES involves a reversible reaction. When the reaction proceeds in one direction, the system becomes endothermic (charging state). Conversely, when the reaction proceeds in the opposite direction, the system releases energy and becomes exothermic (discharge state).

Dehydration of hydrated salts enables the storage and release of heat at low temperatures. The process is described by the following reaction.



Sorption heat pump systems are a type of thermal energy storage (TES) system that utilise a physicochemical reaction to generate and store energy. The system consists of a sorbent reactor, which is heated to evaporate the sorbate (water) and transfer the resulting vapour to the condenser during the charging phase. The condensed water is then evaporated in the condenser, causing the sorbate to flow back into the sorbent reactor in a gaseous state, thus generating heat (Figure 1).

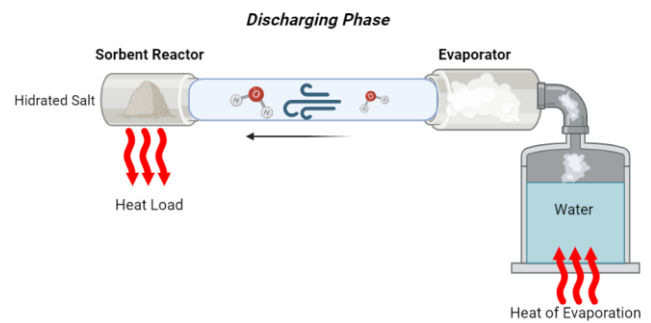
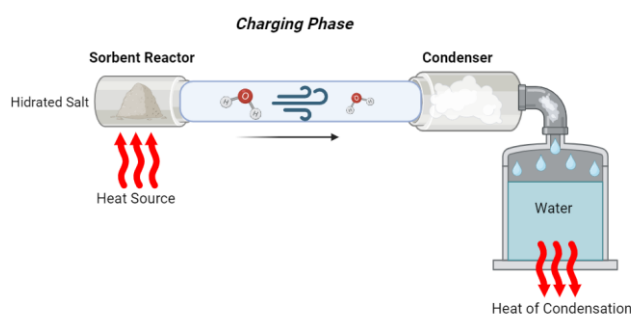


Figure 1: Sorption TES cycle (Charging and Discharging phase)

Modified lignin-based coatings have been proposed as a mechanism to reduce the corrosion rate of metal surfaces in sorption pumps. Relevant characterisations and tests have been carried out to verify the improvement.

Methodology

The lignin was extracted from Eucalyptus wood chips using the organosolv method (Figure 2). In the reactor a mixture of 100 g of raw material, with a particle size greater than or equal to 4 mm, and 600 g of a solvent mixture of EtOH/H₂O (50%w) was prepared. The reaction was carried out at 200°C for 75 minutes. Then, the mixture was cooled at room temperature up to 30°C and 530 mL of black liquor was recovered.

Organosolv lignin was extracted from the black liquor using acidified water (pH=2). The acidified water was prepared by mixing 1060 mL of distilled water with approximately 30 mL of glacial acetic acid. The organosolv black liquor was then added to the acidified water, which enabled the precipitation of lignin and its subsequent extraction. The resulting mixture was vacuum filtrated and the lignin was left in the oven (50°C) for 3 days.

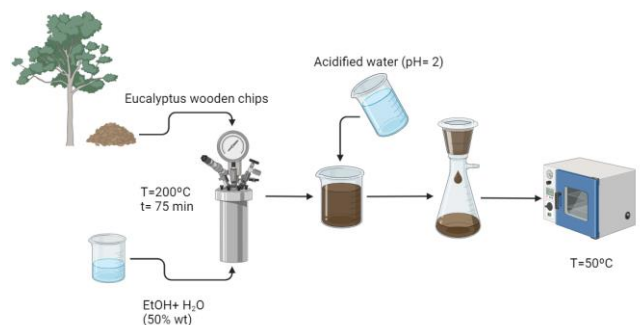


Figure 2: Diagram of organosolv lignin extraction from eucalyptus.



After extracting the lignin from the black liquor, it was modified through silanization. Lignin was silanized in a single step using ATS (3-Aminopropyl triethoxysilane). The reaction was carried out in a round bottom flask equipped with a thermometer and a magnetic stirrer. In this case, 1 g of lignin was dispersed in 100mL of an ethanol solution (10% v) with 10 μ L of sulphuric acid. The amount of ATS needed was calculated with the following equations, taking into account the molecular weight (MW) of the compounds (Eq. (2) and Eq. (4)) and the optimum molar relation between them (Eq. (3)).

$$\text{Lignin (mol)} = \text{Lignin (g)} / \text{Lignin MW} \quad (2)$$

$$\text{ATS (moles)} = \text{Lignin (mol)} * 5 \quad (3)$$

$$\text{ATS (g)} = \text{ATS (moles)} * \text{ATS MW} \quad (4)$$

After mixing the different compounds, the resulting solution was placed under continuous stirring at 70°C (with reflux) for 24 hours. Finally, the already silanized lignin could be recovered through acid precipitation, adding twice as much acidified water (pH=2), and its subsequent filtration and neutralization.

Several 250-hour tests were conducted to compare the corrosion rate of the selected sorption pump materials, carbon steel and brass. Electrochemical tests were performed, including electrochemical impedance spectroscopy (EIS) and linear polarization resistance (LPR), on the metal surfaces of the sorption systems with and without the silanized lignin coating. The tests were conducted under highly corrosive conditions, after almost complete dehydration of the salt, where the corrosive power is at its highest. The operating conditions of the selected salt, magnesium sulfate heptahydrate ($\text{MgSO}_4 \cdot 7\text{H}_2\text{O}$), were 130°C and 20 mbar.

The lignin samples were analysed by FTIR spectroscopy in order to characterise the different chemical bonding in within the lignin structure, demonstrating the success of the modifications. FTIR was used in transmittance mode and was performed

using a Spectrum Two spectrometer (Perkin Elmer). Spectra were recorded from 4000 cm^{-1} to 600 cm^{-1} at a spectral resolution of 8 scans.

Additionally, it has been used an energy-dispersive X-ray spectroscopy (EDS) in order to obtain MAPS of composition, connected to SEM (Model SmartEDX from ZEISS). In order to identify the different oxides and spinels in cross-sectional coating samples after corrosion tests, X-ray diffraction (XRD) technique has been also used (PANalytical Xpert PRO equipment).

Results and Discussion

After characterising the samples using FTIR, we obtained the following graphs (Figure 3 and Figure 4). To verify the silanisation of the lignin, we analysed an unmodified organosolv lignin sample (EOL) and a silanised organosolv lignin sample (EOLS).

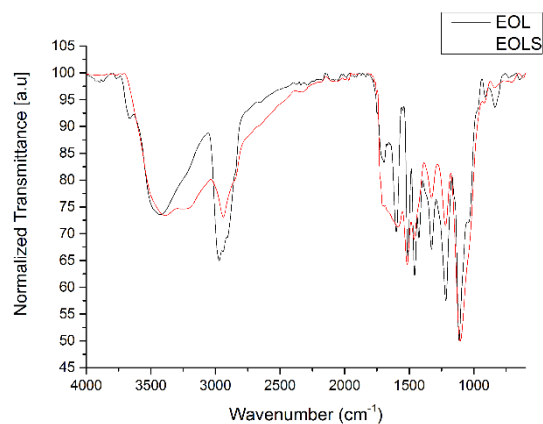


Figure 3: FTIR graph comparing modified and unmodified organosolv lignin.

Figure 3 shows differences between the two samples, indicating the modification of the organosolv lignin. However, the most significant peaks are found in the fingerprint area of the graph (Figure 4). The lignin that has been treated with silane exhibits a more prominent peak at a wavenumber of 1100 cm^{-1} , which is attributed to the Si-O-C bonds (Cichosz & Masek, 2020). Additionally, there is a peak at 696 cm^{-1} indicating the vibration of the C-Si-C bonds (Issa & Luyt, 2019).

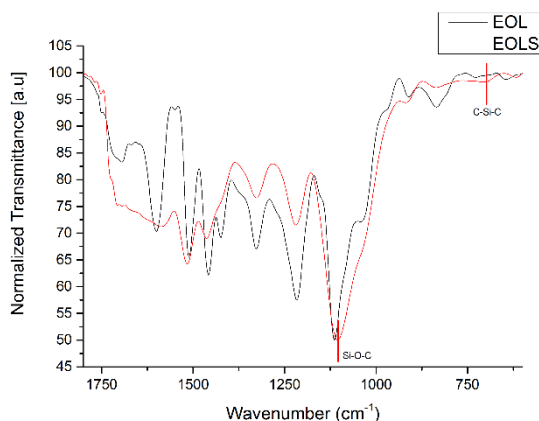
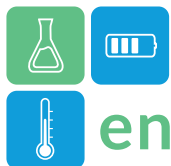


Figure 4: Amplified fingerprint region of the FTIR graphs.

EIS and LPR were successfully applied in the material tested in order to understand the corrosion mechanism in the sorption materials as well as to obtain the corrosion rate in the alloys with and without lignin modified coatings.

Conclusions

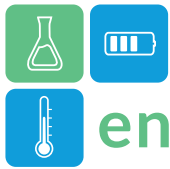
The modification of lignin was successful in reducing the corrosion rate of the alloys in contact with the sorption salt proposed.

Acknowledgment

Dr. Angel G. Fernández wants to acknowledge the financial support from RyC 2020-28787-I funded by MCIN/AEI /10.13039/501100011033 and ESF “Investing in your future”.

References

- Carlos De Haro, J., Magagnin, L., Turri, S., & Griffini, G. (2019). Lignin-Based Anticorrosion Coatings for the Protection of Aluminum Surfaces. *ACS Sustainable Chemistry and Engineering*, 7(6), 6213–6222. <https://doi.org/10.1021/acssuschemeng.8b06568>
- Cichosz, S., & Masek, A. (2020). Superiority of cellulose non-solvent chemical modification over solvent-involving treatment: Application in polymer composite (part II). *Materials*, 13(13), 1–19. <https://doi.org/10.3390/ma13132901>
- Dastpak, A., Yliniemi, K., Monteiro, M. C. de O., Höhn, S., Virtanen, S., Lundström, M., & Wilson, B. P. (2018). From waste to valuable resource: Lignin as a sustainable anti-corrosion coating. *Coatings*, 8(12). <https://doi.org/10.3390/COATINGS8120454>
- Issa, A. A., & Luyt, A. S. (2019). Kinetics of alkoxy silanes and organoalkoxy silanes polymerization: A review. *Polymers*, 11(3). <https://doi.org/10.3390/polym11030537>
- Koch, G., Varney, J., Thompson, N., Moghissi, O., Gould, M., & Payer, J. (2016). International measures of prevention, application, and economics of corrosion technologies study. *NACE International Impact, February*, 1–216.
- Ndukwe, A. I. (2022). Green Inhibitors for Corrosion of Metals in Acidic Media: a Review. *Academic Journal of Manufacturing Engineering*, 20(2), 36–50.
- Olajire, A. A. (2018). Recent advances on organic coating system technologies for corrosion protection of offshore metallic structures. *Journal of Molecular Liquids*, 269, 572–606. <https://doi.org/10.1016/j.molliq.2018.08.053>
- Solvay. (2023, June 28). *Corrosion Awareness Day 2022 - The Cost of Corrosion and How Chemistry Can Help*. <https://www.solvay.com/en/solutions-market/industrial/surface-treatment/metal-treatment/corrosion-awareness-day-2022>



Liquid metals – efficient heat transfer fluids for high-temperature heat storage

Klarissa Niedermeier^{1,*}, Margaux Zehnder¹, Franziska Müller-Trefzer¹, Frank Fellmoser¹, Martin Lux¹,
 Markus Daubner¹, Thomas Wetzel^{1,2}

1 Institute for Thermal Energy Technology and Safety (ITES), Karlsruhe Institute of Technology (KIT),
 Hermann-von-Helmholtz-Platz 1, 76344 Eggenstein-Leopoldshafen

2 Institute of Thermal Process Engineering (TVT), KIT, Kaiserstraße 12, 76131 Karlsruhe, Germany

*klarissa.niedermeier@kit.edu

Abstract

As the share of fluctuating renewable energy in the energy system grows, the significance of energy storage systems in bridging the gap between energy supply and demand rises. Among proposed energy storage systems, thermal energy storage offers a relatively simple, cost-effective, and efficient method for storing energy in the form of heat. The storage systems can help stabilizing heat distribution networks, facilitate sector integration, and can be utilized in heat-to-power-to-heat systems. However, especially for high temperatures above 500 °C research is still ongoing and is focussing on storage concepts, configurations, and materials for those elevated temperatures. The contribution will present an overview of the ongoing research at the Karlsruhe Liquid Metal Laboratory that develops high-temperature heat storage concepts using liquid metals as heat transfer fluids.

Keywords: Heat storage, Packed bed, Liquid metal, Heat transfer

Introduction

The Karlsruhe Liquid Metal Laboratory (KALLA) at the Karlsruhe Institute of Technology (KIT) specializes in studying heat storage systems that utilize liquid metals as heat transfer fluids. That includes the development and demonstration of storage concepts, testing of materials and components that are in contact with liquid metals and fundamental heat transfer investigations.

Due to their extensive liquid state temperature range and exceptional heat conductivity, liquid metals can efficiently serve as heat transfer fluids in packed bed thermal energy storage systems (Bozorg, Coventry, and Torres, 2023).

Materials and Methods

Among the liquid metals, lead (Pb), lead-bismuth eutectic (Pb_{44.5}Bi_{55.5}), sodium (Na) and tin (Sn) are most promising for the use in thermal energy storage systems based in their liquid state temperature range, their material costs, thermophysical data and operational experience (Niedermeier, 2023). Therefore, they are focused on in this contribution.

Table 1 gives examples of liquid metals with melting temperatures of ca. 100–330°C and evaporation temperatures of ca. 880–2700°C. This shows the broad

possible temperature range, in which liquid metal could generally be used.

Table 1: Temperature regions of selected liquid metals (Pacio and Wetzel, 2013).

	Melting temperature	Evaporation temperature
Pb	327 °C	1743 °C
Pb _{44.5} Bi _{55.5}	125 °C	1533 °C
Na	98 °C	883 °C
Sn	232 °C	2687 °C

In addition to that, the thermal conductivity of liquid metals is excellent, which makes them superior heat transfer fluids. Table 2 shows that the thermal conductivity λ of selected liquid metals is in the range of ca. 13–46 W/mK.

Table 2: Thermophysical properties of selected liquid metals (at 600°C) (Pacio and Wetzel, 2013).

	c_p , kJ/(kgK)	λ , W/(mK)	ρ , kg/m ³	μ , 10 ⁻³ Pas
Pb	0.15	18.8	10 324	1.55
Pb _{44.5} Bi _{55.5}	0.15	12.8	9660	1.08
Na	1.25	46.0	808	0.21
Sn	0.24	33.8	6330	1.01

In order to demonstrate the applicability of liquid metals in packed bed thermal energy storage systems at high temperatures (above 500°C), several steps are undertaken:

First, a proof-of-concept of the thermal energy storage is performed on a lab-scale (thermal capacity 1 kWh) including a filler material screening to identify compatible material (Müller-Trefzer et al., 2022). A photo of the experimental test rig at KALLA is shown in Figure 1.

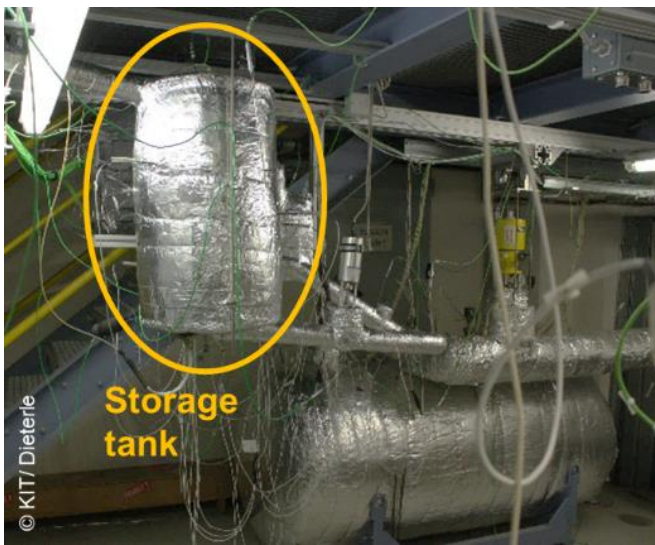


Figure 1: Test rig with integrated storage system, adapted from Müller-Trefzer et al., 2022; photo: Dieterle/KIT.

Based on the findings of the lab-scale experimental results, the storage concept will be demonstrated on a larger scale with 100 kWh thermal capacity.

In parallel, materials and components are to be tested in a 700°C liquid Pb loop, which is currently being set up at KALLA in order to extend the temperature limits for corrosion resistant material (Niedermeier et al., 2023). A simplified 3D drawing of the test loop is shown in Figure 2.

Furthermore, in-depth heat transfer investigations are undertaken to improve the state-of-the-art on heat transfer correlations in a packed bed that is flown through by liquid metal.

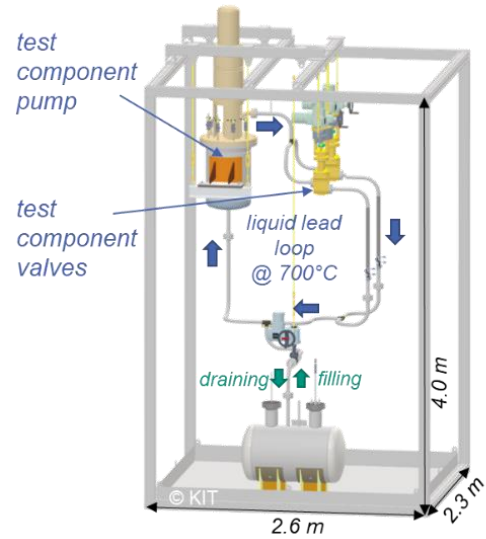


Figure 2: 3D design of the liquid-lead-containing parts of the high-temperature (700 °C) test rig LIMELIGHT, adapted from Niedermeier et al., 2023.

Results and Discussion

The contribution will provide an overview of the current activities of the Karlsruhe Liquid Metal Laboratory (KALLA) regarding high temperature heat storage and will highlight the following aspects:

- The discussion will cover the outcomes from testing a laboratory-scale prototype utilizing ceramic filler material with liquid lead-bismuth as the heat transfer medium.
- The presentation will also feature the design and the set-up of a pilot-scale demonstrator with a thermal capacity of 100 kWh.
- Furthermore, the construction progress of a high-temperature material and component test loop, operating at 700°C with liquid lead, will be presented.
- Finally, the design and set up of a test rig for heat transfer investigations in the packed bed will be shown.

Conclusions

The use of liquid metals for heat transfer offers notable benefits such as superior heat transfer rates and the ability to operate at high temperatures. However, challenges arise concerning material compatibility, particularly at temperatures above 600°C. Hence, our focus lies in showcasing heat storage systems across various scales, from laboratory to pilot, while thoroughly testing materials and components like pumps and valves that interact with liquid metals under these conditions.

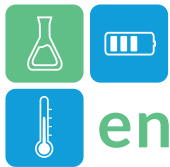


Acknowledgment

The authors would like to acknowledge the funding for the research on high-temperature material and component testing within the project LIMELISA (grant number 03EE5050C), which is granted by the German Federal Ministry for Economic Affairs and Climate Actions (BMWK).

References

- Bozorg, Mehdi V., Joe Coventry, and Juan F. Torres. 2023. "Thermal Energy Storage in a Tightly Packed Bed with Sodium as the Heat Transfer Fluid: A Numerical Study." *Applied Energy* 352:121879. doi: 10.1016/j.apenergy.2023.121879.
- Müller-Trefzer, Franziska, Klarissa Niedermeier, Markus Daubner, and Thomas Wetzel. 2022. "Experimental Investigations on the Design of a Dual-Media Thermal Energy Storage with Liquid Metal." *Applied Thermal Engineering* 213:118619. doi: 10.1016/j.applthermaleng.2022.118619.
- Niedermeier, Klarissa. 2023. "A Perspective on High-Temperature Heat Storage Using Liquid Metal as Heat Transfer Fluid." *Energy Storage* e530. doi: 10.1002/est2.530.
- Niedermeier, Klarissa, Martin Lux, Anisa Purwitasari, Alfons Weisenburger, Markus Daubner, Franziska Müller-Trefzer, and Thomas Wetzel. 2023. "Design of the LIMELIGHT Test Rig for Component Testing for High-Temperature Thermal Energy Storage with Liquid Metals." *Processes* 11(10):2975. doi: 10.3390/pr11102975.
- Pacio, J., and Th. Wetzel. 2013. "Assessment of Liquid Metal Technology Status and Research Paths for Their Use as Efficient Heat Transfer Fluids in Solar Central Receiver Systems." *Solar Energy* 93:11–22. doi: 10.1016/j.solener.2013.03.025.



Long-term stability investigation of capric acid as potential phase change material

Hamza Ayaz^{a*}, José Lara Cruz^a, Jorge Salgado-Beceiro^b, Magnus Rotan^b, Ragnhild Sæterli^b, Fride Vullum-Bruer^b, Alexis Sevault^b and Jean-Pierre Bedecarrats^a

^a Université de Pau et des Pays de l'Adour, E2S UPPA, LaTEP, Laboratoire de Thermique, Énergétique et Procédés, 64000 Pau, France

^b SINTEF Energy Research, Postboks 4761 Torgarden, 7465 Trondheim, Norway.

*Corresponding author e-mail: hamza.ayaz@univ-pau.fr

Abstract

Thermal battery that utilizes solid-liquid phase change material (PCM) is getting more attention by storing a large amount of thermal energy during the solid-liquid phase change. Among other parameters, the stability of the PCM is an important factor that has a direct influence on the overall performance of the thermal battery. Therefore, the stability of PCM is investigated by different research groups, but scattered data can be found regarding the protocol utilized. The objective of this study is to investigate the stability of a PCM by performing various tests and conclude a standard stability procedure for organic PCMs. The stability protocol in this work includes accelerated thermal cycling (impact of the phase transition on the thermal properties in successive cycles), and thermal stress test (influence of the higher temperature). The PCM under investigation is an organic PCM (capric acid) which is commercially available and widely utilized in thermal energy storage applications. The factors (different cooling rates, different volumes of the sample) involved in the accelerated thermal cycling were investigated and the results show that these factors do not influence the thermal properties of the organic PCM. Capric acid shows good thermal stability during the thermal stress but a decrease in the thermal properties was observed after 1000 thermal cycles. The result can be helpful for the research community engaged with the stability investigation of organic PCM.

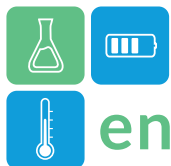
Keywords: Thermal energy storage, Phase change material, Capric acid, Accelerated thermal cycling, Thermal stress test

Introduction

Thermal energy storage based on phase change materials (solid-liquid phase change) has great potential in many applications. The different groups of solid-liquid phase change materials (PCMs) include organic and inorganic PCMs [1]. The prerequisites for selecting a reliable PCM for any thermal energy storage application include its phase change equilibrium temperature, amount of energy stored during phase transition, and stability of the PCM. Moreover, certain materials with relevant thermal properties have poor long-term stability. These PCMs, when exposed for a long duration to environmental conditions or repeated solidification/melting thermal cycles, have a negative impact on their storage capacity [2]. It is therefore essential to test the cyclic stability of these PCMs before incorporating them into a real-time application. The successful use of the storage system depends greatly on the reliability and thermal stability of the PCMs used. It is a real challenge to evaluate the stability of PCMs [3]. The stability investigation of the PCM can be performed in conditions that are close to the real application conditions to better investigate its performance. The

different test conditions include the temperature interval, contact with the environment, temperature ramp, and compatibility of the PCM with the storage container [4,5]. Different protocols are utilized to investigate the stability of PCM. A technical review summarized a total of 18 different experimental devices and conditions for the investigation of the stability of PCM. The different factors considered were the amount of PCM utilized (0.5 ml to 154 L), the temperature ramp (0.05 to 50 °C/min), thermal cycles each day (1 to 140), and various storage container materials [6]. After utilizing the PCM sample in the experimental devices for testing, the thermal properties were investigated with differential scanning calorimetry (DSC) [7]. However, another protocol is to directly perform cyclic stability in the DSC without utilizing additional experimental devices.

To present, no standard guidelines are presented in the open literature on how to perform stability tests for the PCM (amount of sample used, temperature ramp). In this work, the accelerated thermal cycling protocol was optimized, and the stability of an organic PCM (capric acid) was investigated. The accelerated



cooling/heating rates and different amounts of sample. The thermal stress (to put a PCM in liquid phase at a temperature higher than the phase change equilibrium temperature) experiment was performed to observe the temperature influence on the thermal properties. This work aims to perform a stability investigation for organic PCMs and conclude a general protocol to analyse the stability of organic PCM for thermal energy storage applications.

Methodology (Materials and method)

Capric acid ($C_{10}H_{20}O_2$) is a medium-chain fatty acid also known as decanoic acid with a phase change equilibrium temperature near 30°C . The studied capric acid (98% purity) procured from Sigma Aldrich [8] was utilized without any further purification.

Accelerated thermal cycling and thermal stress test

A refrigerated heating circulator (Julabo FP 50) was used to perform accelerated thermal cycling. The minimum and maximum temperatures were 0°C and 50°C . Initially the cooling machine was kept at 0°C for 20 mins to have thermal equilibrium which was followed by linear temperature ramp and after achieving 50°C the temperature was kept uniform for 20 mins and vice versa for the reverse cycle. The plastic test tubes were considered as the PCM sample container. The accelerated thermal cycling experiment is performed in two parts. First, different linear temperature ramps (0.5 , 1 and $2^\circ\text{C}/\text{min}$) and sample weights (5g and 50g) were considered to investigate its influence on the thermal cycling process. The results will be used to define the best parameters (temperature ramp and PCM quantity) for the complete study of the PCM stability with a thermal cycling experiment of 1000 cycles.

The thermal stress test was performed at a controlled temperature environment in an oven (DHG-9032) with an uncertainty of $\pm 0.5^\circ\text{C}$. The sample size of 35g is filled in glass bottles and exposed to a temperature above its phase change equilibrium temperature to observe the temperature influence on the PCM stability. A temperature of 50°C was set in the oven which is 20°C above the phase change equilibrium temperature and three samples were investigated. The experiment lasted ninety days, and one different sample had to be taken out after each thirty days. To find out if the PCM was stable, additional characterization was performed on the removed sample.

Characterization of the PCM

A standard procedure was followed to obtain the thermal properties of PCM with a Differential

SCALPHEX (SETARAM). The thermograph acquired with the DSC gives detailed information about the thermal properties of the PCM. The temperature program consists of a temperature range (0 – 60°C) with a linear ramp of $0.5^\circ\text{C}/\text{min}$. The samples of PCM from the accelerated thermal cycling and thermal stress experiment were subjected to DSC to investigate the thermal properties. For each test, a total of 5 thermal cycles were performed in the DSC. The average thermal properties of the 5 thermal cycles are presented with an absolute uncertainty of $\pm 0.2^\circ\text{C}$ for the phase change temperature and a relative uncertainty of 1.3% for the phase change enthalpy. The uncertainty was calculated by performing a DSC analysis of distilled water and comparing the standard data available for the sample.

Results and Discussion

DSC characterization of the PCM

The phase change process for solidification and melting of capric acid before the accelerated thermal cycling and thermal stress experiments is shown in Figure 1. The onset phase change equilibrium temperature (solid to liquid) $T_{\text{onset,m}}$ was $31.8 \pm 0.2^\circ\text{C}$ whereas the phase change equilibrium enthalpy $\Delta_{\text{fus}}H$ was $156 \pm 2\text{ J/g}$. The onset crystallisation temperature (liquid to solid) $T_{\text{onset,s}}$ was $25.7 \pm 0.2^\circ\text{C}$, and its phase change enthalpy $\Delta_{\text{sol}}H = 163 \pm 2\text{ J/g}$. The difference in the phase change values is due to the degree of supercooling. Due to the erratic behavior of the degree of supercooling, it is not considered in this work and the results presented were deduced by analyzing the phase change process during melting. The thermal properties reported in this work have the same tendency as reported by other research groups [9-10]. 5 cycles were performed in the DSC for this analysis and the average values are presented.

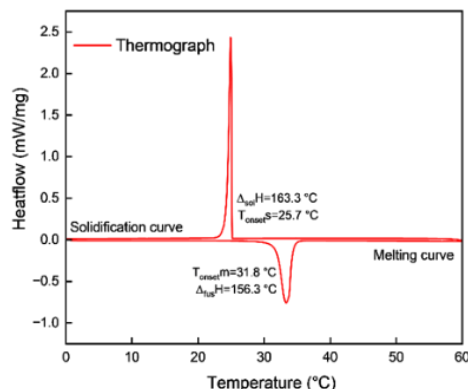


Figure 1 Thermograph of the capric acid before thermal cycling

Thermal cycling of the Capric acid

The thermal cycling process consists of several parameters that can directly influence the accelerated

thermal cycling performed [5]. The results for the two selected parameters (different heating/cooling rates and volume) are presented. Initially, different masses of the PCM sample which were 5 g and 50 g of capric acid went through the thermal cycling process and the results are presented in Figure. 2. The heating/cooling rate was fixed at 2 °C/min for 40 thermal cycles. The results indicate that the different mass of the PCM has no impact on the thermal cycling process. In the following experiment, the amount of PCM was fixed at 5 g whereas the different cooling/heating rates (0.5, 1, and 2 °C/min) were employed in the system. The results are presented in Figure 3 with the values of $T_{onset,m}$ and $\Delta_{fus}H$. The peaks in the graph show that there is no significant difference in the thermal properties of capric acid determined after cycles at different heating/cooling rates. So low volume and high cooling/heating rates can be selected to accelerate the whole process.

Based on these results, the optimized accelerated thermal cycling uses 5 g volume and 2 °C/min heating/cooling rate. A long-term accelerated thermal cycling was performed for capric acid which consists of 1000 cycles. The results of 1000 thermal cycles for capric acid are presented in Figure 4 and Figure 5. The results indicate that degradation takes place with successive thermal cycles which is mainly observed through the decrease in the phase change enthalpy. The maximum variation in the $T_{onset,m}$ is 2.83% whereas for $\Delta_{fus}H$ it was 11.13%. This result will help in designing a latent heat thermal energy storage system for the long term.

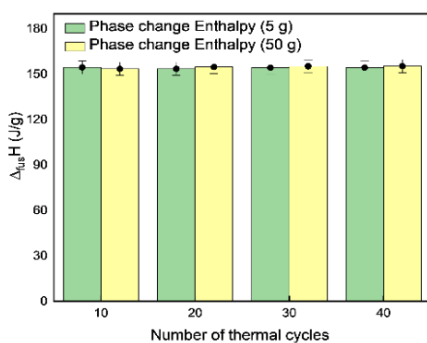


Figure. 2 Thermal cycling performed for different volumes of capric acid

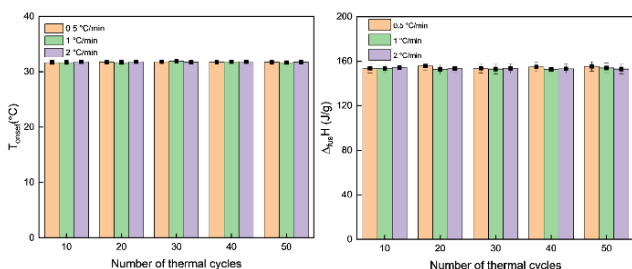


Figure. 3 Thermal cycling performed for heating/cooling rates of capric acid

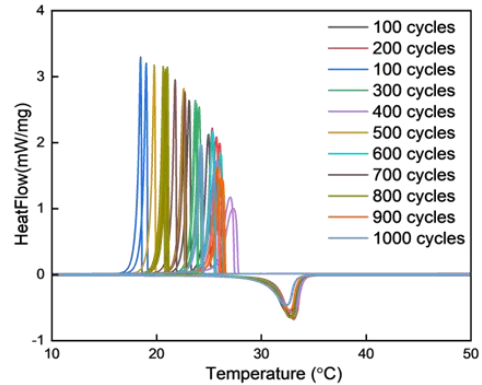


Figure. 4. Thermal cycling performed for 1000 thermal cycles of capric acid

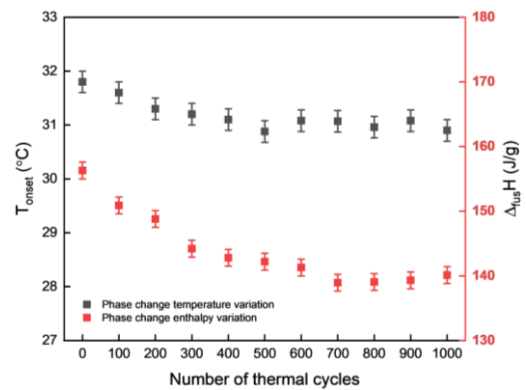


Figure. 5 Thermal properties variation for 1000 thermal cycles

Thermal stress analysis of Capric acid

6

The thermal stress test results are shown in Figure and Figure 7. The DSC thermograph for the three samples that were analyzed after 30, 60, and 90 days did not show much variation in the thermal properties of the sample. The result indicates that capric acid is thermally stable and will not degrade if the temperature of the latent heat thermal energy storage system increases to 50 °C due to thermal fluctuation.

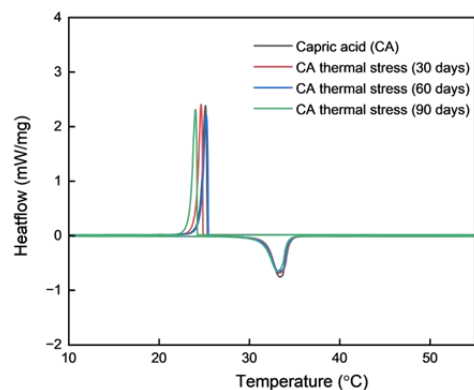


Figure. 6 Thermal stress of the capric acid

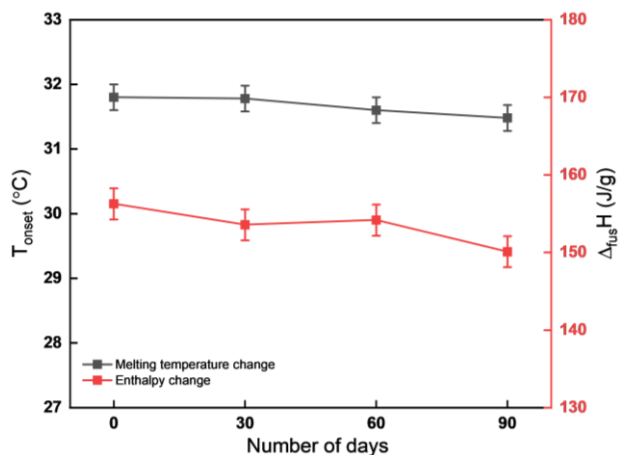
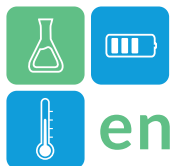


Figure. 7 Thermal properties variation of the capric acid during thermal stress

Conclusions

The goal of this work was to perform the stability investigation of an organic PCM and deduce a general protocol. The stability of capric acid was investigated by performing accelerated thermal cycling and thermal stress tests. The accelerated thermal cycling protocol was optimized by investigating different parameters whereas the result shows similar thermal properties. Based on the results, the 2 °C/min cooling/heating rates and 5 g volume was selected which reduced the duration of the accelerated thermal cycling. The results of 1000 thermal cycles show a maximum variation of 2.83% for phase change equilibrium temperature and an 11.13% reduction in the phase change equilibrium enthalpy. The thermal stress test performed indicates that capric acid is stable and did not show any significant change in the thermal properties. In future work, the extensions include performing different characterizations (FT-IR, NMR) to investigate the chemical profile of the PCM and compare the results whether the change in thermal properties is due to chemical degradation. The results will be helpful for the research community working on the stability investigation of organic PCM for latent heat thermal energy storage applications.

Acknowledgment

This project has received funding from the European Union's Horizon 2020 research and innovation program under the Marie Skłodowska Curie Actions, Grant Agreement No. 945416 and was carried out through the research project KSP PCM-STORE (308847) supported by the Research Council of Norway and industry partners. PCM-STORE aims at building knowledge of novel PCM technologies for thermal energy storage systems.

References

1. H. Ayaz, V. Chinnasamy, Y. Jeon, H. Cho, Thermo-physical studies and corrosion analysis of caprylic acid–cetyl alcohol binary mixture as novel phase change material for refrigeration systems, *Energy Reports* 8 (2022). doi.org/10.1016/j.egy.2022.05.239.
2. L. Miró, C. Barreneche, G. Ferrer, A. Solé, I., Martorell, L.F. Cabeza, Health hazard, cycling and thermal stability as key parameters when selecting a suitable phase change material (PCM), *Thermochim Acta* (2016). doi.org/10.1016/j.tca.2016.01.014.
3. L. Quant, G. Diarce, L. Bouzas, J.-P. Bédécarrats, A. García-Romero, Long-term assessment of the thermal stability of sodium nitrate-urea eutectic phase change material, *Solar Energy Materials and Solar Cells* 230 (2021). doi.org/10.1016/j.solmat.2021.111261.
4. R. Bayón, E. Rojas, Development of a new methodology for validating thermal storage media: Application to phase change materials, *Int J Energy Res* 43 (2019). doi.org/10.1002/er.4589.
5. C. Rathgeber, A. Grisval, H. Schmit, P. Hoock, S. Hiebler, Concentration dependent melting enthalpy, crystallization velocity, and thermal cycling stability of pinacone hexahydrate, *Thermochim Acta* 670 (2018). doi.org/10.1016/j.tca.2018.10.025.
6. C. Rathgeber, S. Hiebler, R. Bayón, L.F. Cabeza, G. Zsembinszki, G. Englmaier, M. Dannemand, G. Diarce, O. Fellmann, R. Ravotti, D. Groulx, A.C. Kheirabadi, S. Gschwander, S. Höhle, A. König-Haagen, N. Beaupere, L. Zalewski, Experimental devices to investigate the long-term stability of phase change materials under application conditions, *Applied Sciences (Switzerland)* 10 (2020). doi.org/10.3390/app10227968.
7. M. Majó, R. Sánchez, P. Barcelona, J. García, A.I. Fernández, C. Barreneche, Degradation of fatty acid phase-change materials (PCM): New approach for its characterization, *Molecules* 26 (2021). doi.org/10.3390/molecules26040982.
8. Sigma aldrich, Capric acid (Sigma aldrich), <https://www.sigmaaldrich.com/FR/fr/product/sigma/c1875> (accessed January 17, 2024).
9. C. Cárdenas-Ramírez, M.A. Gómez, F. Jaramillo, Comprehensive analysis of the thermal properties of capric-myristic, lauric-myristic and palmitic-stearic acids and their shape-stabilization in an inorganic support, *J Energy Storage* 34 (2021). doi.org/10.1016/j.est.2020.102015.
10. P. Sarafoji, V. Mariappan, R. Anish, K. Karthikeyan, P. Kalidoss, Characterization and thermal properties of Lauryl alcohol – Capric acid with CuO and TiO₂ nanoparticles as phase change material for cold storage system, *Mater Lett* 316 (2022). doi.org/10.1016/j.matlet.2022.132052.

Long term performance of the HT BTES plant at Xylem in Emmaboda, Sweden

Olof Andersson^{1,*}, Niklas Håkansson², Leif Rydell³

1 Geostrata HB, Kärrsångarvägen 14 SE 247 35 S Sandby, Sweden

2 Xylem Inc, Stålvägen SE 361 41 Lindås, Sweden

3 Reikab AB, Skruvbyvägen 5 SE 365 94 Skruv, Sweden

*Corresponding author e-mail: olle.geothermal@hotmail.com

Abstract

The Emmaboda High Temperature, Borehole Thermal Energy Storage (HT-BTES), was taken into operation in 2010. Up till 2017 it was primarily used for chilling the industrial process and only a small fraction of the waste heat was recovered for space heating of the industrial buildings. By installing extraction heat pumps in 2018 the recovery factor has been increased to approx. 75 % up till 2023

Keywords: HT-BTES, waste heat storage, industrial process cooling, storage efficiency

Introduction

The Emmaboda High Temperature Borehole Thermal Energy Storage (HT-BTES) is owned and operated by Xylem Water Solutions Inc. It was designed and constructed 2008-2010. The goal was at that time to store waste heat from the industrial processes in the summer season to be used for space heating replacing bought district heating. It was taken into operation in the autumn 2010.

The planning, design, construction, and operational experiences of the plant have been presented at five former Stock Conferences (Andersson et al., 2009; Andersson et al., 2012, Nordell et al., 2015 and Andersson et al 2018). In these papers the basis for design, the expected and the actual outcome of the system can be found, as well as operational technical problems and solutions.

In 2013-2015 the technical and thermal function of the storage was analyzed in a special research program funded by The Swedish Energy Agency (Nordell et al., 2016). In this study it was strongly recommended to install a heat pump system in order to have an improved storage efficiency as well as to minimize the technical risks.

In 2018 the heat pump system for extraction of stored heat was installed. The system performance after this installation was monitored for three years as a part of an international research program (IEA HPT Annex 52). The results from this study, covering three full heating seasons, indicated a considerable improvement of using the storage for heat extraction

from the BTES, but also an increased capacity for BTES used for cooling of the industrial processes (Andersson et al 2021). In the current paper the results from this study are summarized with some up-dated data of the storage efficiency added.

The concept using BTES

The original goal was to use the BTES system for seasonal storage of waste heat in order to decrease the dependence of external district heat. A second goal was to minimize the usage of cooling towers that are used for disposal of heat from the cooling system in the factories. The concept is illustrated in Figure 1.

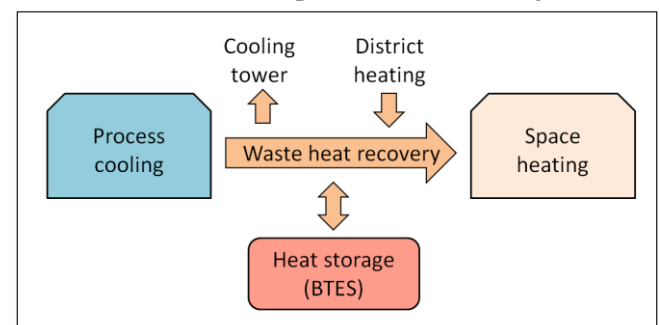


Figure 1: The concept of using BTES for seasonal storage of waste heat and less use of the cooling tower (Andersson et al 2021).

The BTES system description

The BTES consists of 140 boreholes to a depth of 150 m and with a borehole space of 4 m. The boreholes are divided into seven sections (A-G) with 20 holes in each (Figure 2). The three inner sections was planned

to have the highest temperature with the four outer ones to act as a buffer zone with slightly lower temperatures. The idea behind this lay-out is to adjust the extraction temperature to fit the demand. To achieve this function control valves are placed on the larger manifold pipes in the storage central, as shown in the Figure 2.

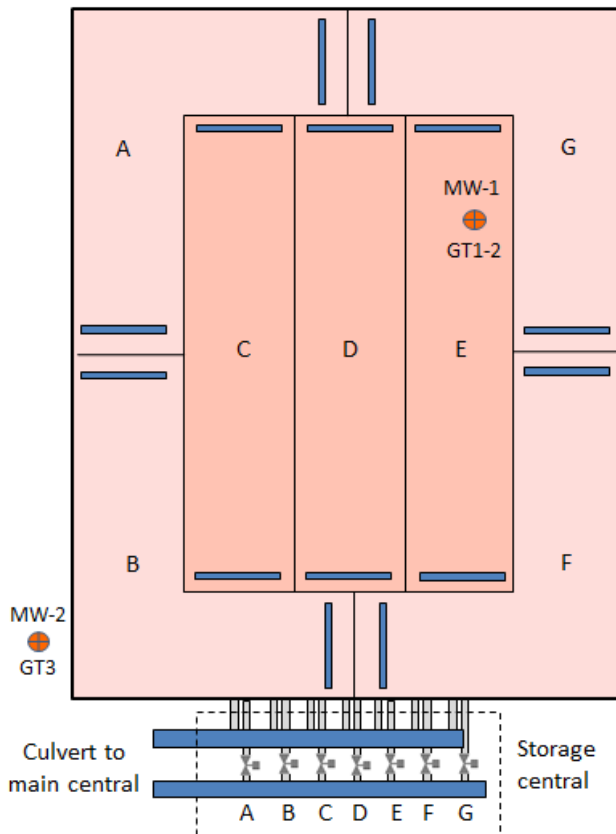


Figure 2: Design of the borehole storage with seven sections (A-F). Each section has 20 boreholes of which two are in series. The boreholes are connected with OD 40 pipes and ends up to OD 90 field manifolds at both section ends (blue). MW: Monitoring well. GT: Temperature sensor (Andersson et al 2021)

The borehole heat exchangers are of coaxial type and consist of double pipes with an intermediate insulation of non-convective water, kept in place by swelling rubber rings.

An advantage using this type of BHE is that it allows for reversed flow direction. Thus, the highest storage temperature can always be found at the bottom of the storage (Figure 3).

Another advantage is that the thermal resistance is less compared to conventional U-pipes. The resistance of the coaxial heat exchanger was measured by thermal response tests to be 0.02 K(W/m), while U-pipes commonly have values around 0,08.

The storage has a top cover of sand on which an insulation layer of foam glass is placed. It ends up with organic soil. The foam glass, 0,4 m thick, is covered by a plastic sheet to keep the surface of the storage dry.

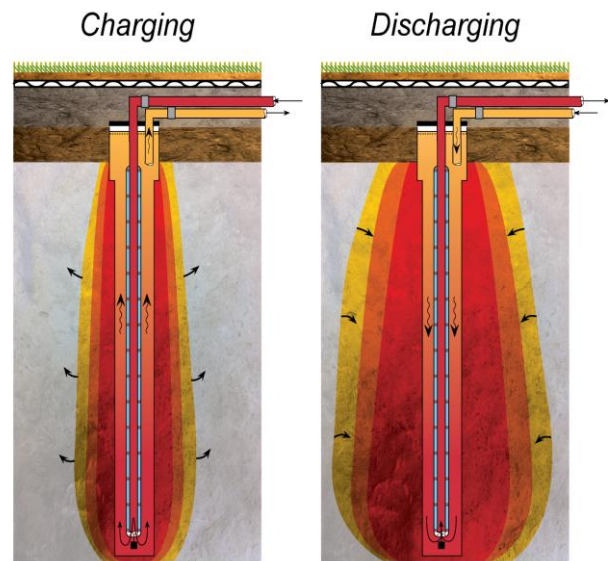


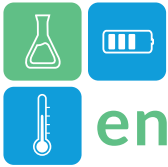
Figure 3: The flow is reversed when discharging compared to charging. That makes the temperature being the warmest at the bottom that reduces heat losses and provides the highest possible temperature at extraction of heat (Andersson et al 2012)

Monitoring system

For measuring the storage temperature there are two monitoring wells (MW), one inside and one a few meters outside the storage. In these wells temperature sensors are installed (GT1-3 in Figure 2). Furthermore, supply and return temperatures to and from each of the sections are measured, as well as the pressure in the two assembly pipes in the storage central.

From the main technical central, about 200 m from the storage, the heat carrier is circulated through an insulated steel culvert using a frequency-controlled circulation pump. Heat is supplied to and extracted from the storage through a heat exchanger (HEX). On the secondary side of the HEX the internal heating grid is connected, with the enforced extraction heat pumps included as part of the BTES system. There are eight heat pumps in parallel, all together representing a maximum capacity of approximately 800 kW.

In the system there are sensors for measurements of temperatures, flow rates and pressures for all fluid circuits. In addition, electricity consumption for the heat pumps and circulation pumps on each side of the



HEX is measured, making it possible to evaluate the performance factor (SPF) for each separate function of the system.

Results and discussion

BTES storage efficiency and thermal behaviour

The annual heating and cooling provided by the BTES the last seven storage cycles (Sept 01-Oct 31), is shown in Figure 4.

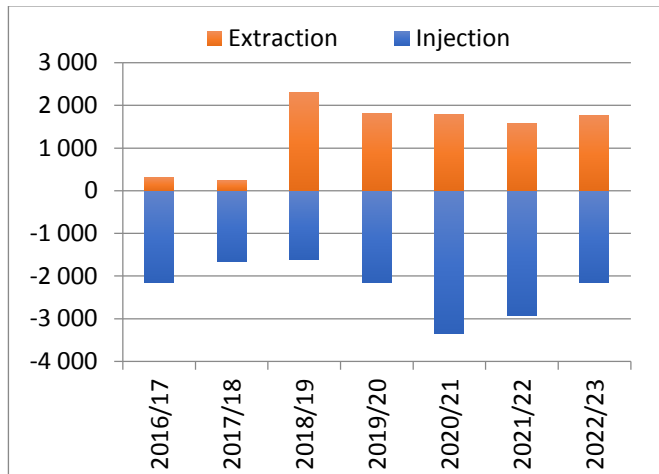


Figure 4: Annual injected and extracted heat (MWh) the last seven years (Sept 01-Aug 31)

Prior to the heat pump installation, the cycles 2016/17 and 2017/18 3 820 MWh was stored while only 549 MWh was recovered. These figures give a storage performance factor of 0,14 while the following five years using the heat pumps for extraction with 12 200 MWh stored and 9 200 MWh recovered ends up with a mean performance factor of 0,75.

The poor recovery several years prior to the heat pump installation was caused by a too low supply temperature to be used for space heating. The less extraction these years resulted in an expansion of stored heat indicated by the monitoring well MW2. This well is located 10 m away from the storage and the temperature is shown as a red line in Figure 5. By more extraction in 2018 the temperature drops from a value of 32 down to 25 °C.

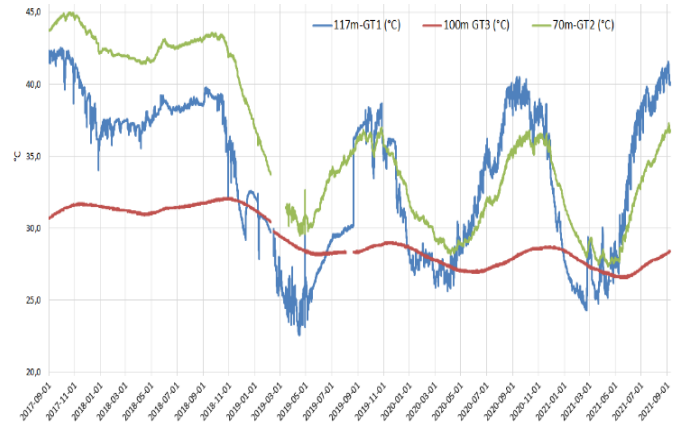


Figure 5: The development of storage temperature from the cycle 2017-18 up to 2020/21 (Andersson et al 2021)

The blue and green lines represent temperatures at different levels inside storage, see former Fig. 2. These measurements indicate in general that the working temperature of the BTES has been decreased to be in the order of 40-20°C since the heat pump system was installed.

The thermal profile during extraction mode was studied in February- April 2019 using fibre-optics in the same monitoring wells (Ramstad et al 2023). The result at the beginning of these measurement is shown in Figure 6

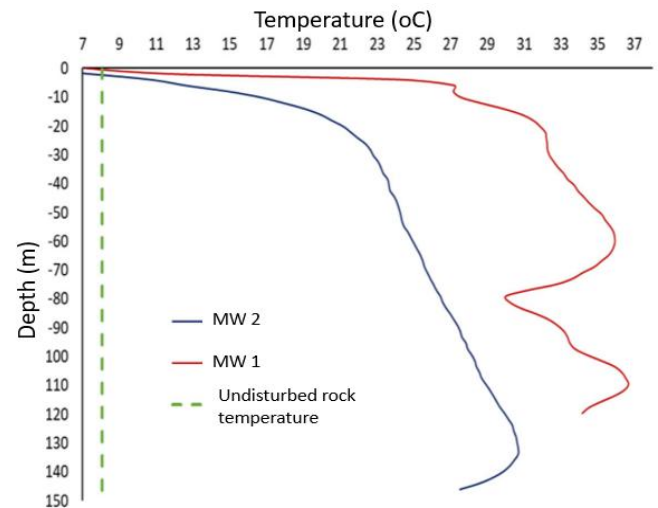


Figure 6: Temperature profiles in the monitoring wells MW1 and 2 from February 9, 2019 (Ramstad et al 2023)

The temperature profile from MW2 outside the storage indicate an even increase of temperature to the storage bottom. Also, in MW1 inside the storage, a similar increase was measured. However, in this case there are several depths with lowered temperatures, especially around 75 m and at the end of the borehole. These are evaluated to be caused by a close distance to a couple of the active BTES boreholes (Ramstad



2023). The explanation is that MW1 at construction was drilled into another borehole at a depth of 117 m and for that reason was abandoned as a production borehole and used as a monitoring well instead.

Performance of the heat pump system

The system consists of 8 units in parallel and uses the BTES as a source of heat. On the evaporator side the incoming temperature is designed for 28/20°C, while the condenser side is designed for 45/55°C. However, the actual temperature demand for heating fluctuates as a function of the out-door temperature. The heat pumps are specially designed regarding the unusual high evaporator temperature. The nominal capacity of the heat pump system is 480 kW. However, with respect to the high evaporator temperature the measured capacity is about 800 kW all units included.

The mean seasonal COP of the heat pump system was evaluated to be around 5,0 the first three years of operation (Figure 7). Up till now (2023) the system has continued with practically the same COP.

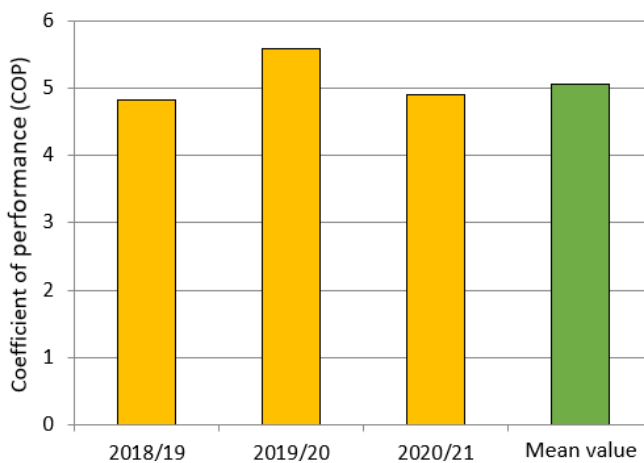


Figure 7: COP of the heat pump system the first three years of operation (Andersson et al 2021)

Conclusions

The extraction heat pump system increased the heat extraction from 400 up to 1 800 MWh annually.

By lowering the BTES working temperature, the usage for cooling has been improved significantly.

The increased extraction of heat and lowering of BTES working temperature by means of using extraction heat pumps have improved the BTES

thermal efficiency from a performance factor of 0,14 up to 0,75.

Acknowledgment

This paper is mainly a result from the project IEA HPT Annex 52 - *Long-term performance monitoring of GSHP systems for commercial, institutional, and multi-family buildings*. The authors gratefully acknowledge the financial support from the Swedish Energy Agency.

References

- Andersson, O. Rydell, L. Algotsson, T. (2009). *Efficient usage of waste heat by applying seasonal energy storage (BTES) at ITT W & WW AB, Emmaboda, Sweden*. Proceedings of the 11th Int. Conf. on Energy Storage, Stockholm, June 14-17, 2009.
- Andersson, O. Rydell, L. (2012). *The HT-BTES plant at Xylem in Emmaboda, Sweden. Experiences from design, construction, and initial operation*. Proceedings of the 12th Int. Conf. on Energy Storage, Lleida, Spain, May 14-15, 2012.
- Nordell, B. Andersson, O. Rydell, L. Liuzzo Scorp, A. (2015). *Long-term Performance of the HT-BTES in Emmaboda, Sweden*. Proceedings of the 13th Int. Conf. on Energy Storage, Beijing, China, May 19-22, 2015.
- Nordell, B. Liuzzo Scorp, A. Andersson, O. Rydell, L. Carlsson, B. (2016). *The HT BTES plant in Emmaboda. Operation and Experiences 2010-2015*. Water Resources Engineering. Luleå University of Technology, Research Report.
- Andersson, O. Rydell, L. Håkansson, N (2021). *Case study report for the Xylem HT-BTES plant in Emmaboda, Sweden*. [Microsoft Word - Andersson et al 2021 Case Study Report Annex 52 HT BTES Xylem Sweden Final.docx \(heatpumpingtechnologies.org\)](#)
- Ramstad, R.K. Justo-Alonso, M. Andersson, O. Acuña, J. Sokuca, M. Håkansson, N. Midttømme, K. Rydell, L (2023). *The borehole thermal energy storage at Emmaboda, Sweden : First distributed temperature measurements*. Science and Technology for the Built Environment, (2023) 29, 146–162



Replacing Fossil-Fueled Combined Heat and Power Plants with Malta's Pumped Heat Energy Storage Technology to Provide Clean Power and District Heat

Janina Hippler-Nettlau^{1,*}, Finn Runkel¹

¹ Malta Hochtemperatur Wärmepumpen Stromspeicher GmbH, Am Brainergy Park 1, 52428 Jülich, Germany

*Corresponding author e-mail: janina.hippler-nettlau@maltainc.com

Abstract

This paper analyses the potential integration of a 100 MW_{el} 36-hour Malta Pumped Heat Energy Storage (PHES) system into the district heating network of the city of Hamburg, Germany, using energy from an offshore windfarm located nearby that would otherwise be curtailed for charging. Publicly available data showing the times when curtailment instructions were given by the transmission grid operator are used to determine the hours during which the storage system shall be charged. Malta's proprietary hourly performance model was used to simulate the behaviour and performance of different plant configurations. It is shown that this configuration could avoid the curtailment of 227 GWh_{el} of wind energy per year. The system could provide 117 GWh_{el} of electricity to the grid in times when less renewables are available, as well as 72 GWh_{th} of thermal energy for Hamburg's district heating network. Compared to the coal-fired combined heat and power (CHP) plant that shall be replaced, this system could reduce the annual CO₂ emissions by 101,400 tonnes.

Keywords: Energy Storage, Curtailment, Green Heat, District Heating, Decarbonization

Introduction

In addition to the EU climate and energy targets for 2030 and the objective of climate-neutrality by 2050, as set in the European Climate Law (EU, 2021), some member states such as Germany have set even more ambitious targets to be climate neutral by 2045 (BMUV, 2021). To reach these objectives, further targets on the build-out of renewables together with a phase-out of coal have been established. The transition from fossil-fuelled to renewable electricity generation impacts not only the power sector, but also the decarbonization of the heat sector. The retirement of coal power plants, among them many that are operated in a CHP mode to supply heat for district heating, and the electrification and increased build-out of district heating systems using renewable heat will require the implementation of new, innovative technologies. One of the technical solutions that provides flexible power and heat is Malta's Pumped Heat Energy Storage (PHES).

There are many locations in Germany with high installed onshore and offshore wind capacity, e.g. in the states of Schleswig-Holstein and Lower Saxony, where not all the available renewable electricity can be transmitted to consumers on windy days due to the lack of grid capacity. In these cases, wind turbines have to be curtailed. In 2020, 5,820 TWh of

renewable energy were already curtailed across Germany (Bundesnetzagentur, 2023). This figure will continue to rise in the future with the increasing expansion of renewables. In the medium- and long-term, long duration energy storage (LDES) systems will be needed to provide green power and heat in times of low solar radiation and low wind. Detailed meteorological studies of the site analysed in this paper were carried out, showing that such periods frequently occur for up to five days or more. The curtailed energy could be used to charge a Malta M100 PHES system in the city of Hamburg, which comprises a large district heating network. For the example studied in this paper, a large CHP plant near Hamburg is considered, which is still using hard coal for the time being, but shall phase-out coal by 2025 and switch to sustainable energy sources. This paper studies the integration of a 36-hour 100 MW_{el} Malta PHES system ("M100"), storing only otherwise curtailed wind energy, into Hamburg's district heating system, providing 24/7 green heat as well as green power in times of low wind energy availability to the city of Hamburg.

Technical Concept for the M100 to Provide Electricity and Green Heat

Malta's PHES technology, also called M100, is a long duration energy storage system of 100 MW_{el} net AC

synchronous discharge power designed to meet grid-scale energy storage needs for various market applications. This technology brings stability and resiliency to the grid by alleviating load mismatch between demand and generation and providing grid services, such as frequency and voltage control, rotating inertia (in German: “Momentanreserve”) and short circuit current. It uses molten salt and a coolant to store variable renewable energy that has been converted to thermal energy (heat and cold) through the Charge Heat Pump and reconverts it into dispatchable synchronous power and process heat through the Discharge Heat Engine, as illustrated in Figure 1. The M100 can operate at any power between minimum rated power (25% of nominal charge power and 35% of nominal discharge power) and full rated power for both charge and discharge as application demands.

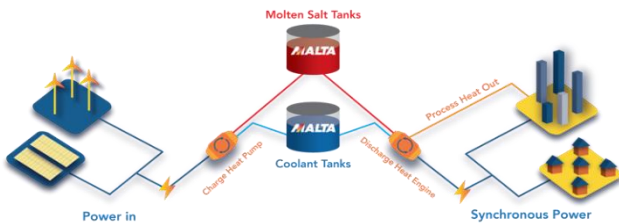


Figure 1: Conceptual diagram of the Malta charge and discharge sequence

The added value of Pumped Heat Electricity Storage over battery storage systems is that its charge and discharge turbomachinery trains offer all the flexible power generation abilities of gas turbine cycles. Malta PHES can provide the following storage services:

- Electricity storage (energy shifting, arbitrage, reserve power, ramping),
- Auxiliary services (synchronous inertia, frequency control, short circuit current),
- Additional supply of process heat for the decarbonization of industrial processes.

Malta PHES fully replaces conventional gas-fired power plants and CHP plants by providing dispatchable power and heat. A 3D view of the M100 plant is shown in Figure 2. The storage duration is easily scalable and customizable to specific applications by just increasing the size and number of the salt and coolant tanks.



Figure 2: 3D view of Malta M100 plant with 12-hour storage duration

While in discharge mode, discharge heat at 121°C is extracted from the system to be used as industrial process heat or for district heating systems. As indicated in the red oval in Figure 3, the discharge heat is extracted from the main system in the Heat Rejection Heat Exchanger downstream of the recuperator. A Discharge Heat Heat Exchanger (DHHX) is used to extract heat from the hydronic fluid (Paratherm- MR) from the discharge heating subsystem when the Malta system is in discharge mode. The secondary side of this DHHX is expected to be water so the DHHX is a liquid-to-liquid type. The heat can be distributed directly to the end-use facilities and/or stored in a hot water storage tank.

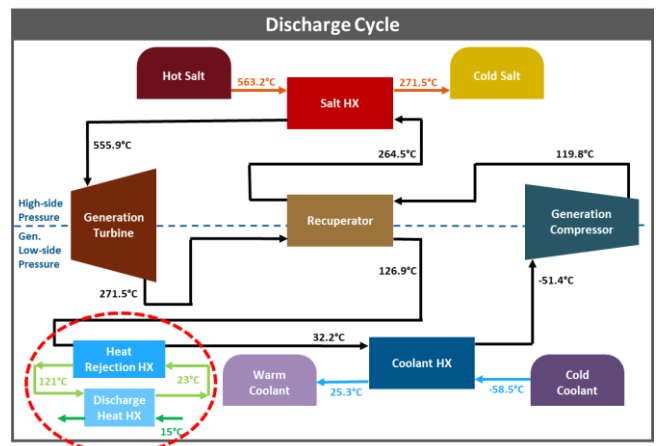
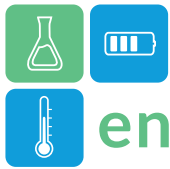


Figure 3: Extraction of discharge heat from the discharge cycle

If the whole temperature range is used, up to 81 MW_{th} of heat can be extracted at full rated condition. Additional storage and backup heating are options to ensure covering a 24/7 heat delivery. To optimize the use of the Malta discharge heat, a combination of a high and a low temperature heating network would ensure that the heat is used in its full temperature range.



Modelling Methodology

For this study, the curtailment instructions (German: Einspeisemanagement, “EinsMan”) for the offshore wind farm “Borkum West 2” of the year 2020 were considered as a typical year for reference. The data is made available publicly in a minutely resolution by the Transmission System Operator (TSO) TenneT who operates this part of the German transmission grid (TenneT). It was assumed that the storage system shall be charged at full rated power whenever EinsMan occurs and discharged at full rated power when no EinsMan takes place.

The system was simulated in Malta’s proprietary detailed thermodynamical performance model on an hourly basis. The model calculates the charge and discharge cycle efficiencies and the working fluids’ mass flows and temperatures based on the ambient conditions and the conditions of the storage media, e.g. hot salt temperature, cold coolant temperature etc, in every hour individually. It also considers startup times and ramp rates. The thermodynamics of the charge and discharge cycles are simulated in Epsilon, considering actual performance parameters, such as heat transfer coefficients and isentropic efficiencies provided by Original Equipment Manufacturers (OEMs).

In order to optimize the system configuration from a techno-economic perspective, the storage duration was varied in two-hour steps between 10 and 72 hours. The Levelized Cost Of Electricity (LCOE) was calculated for each configuration. Sensitivity analyses were carried out, varying the total installed cost of the system and the cost of charge energy. Apart from the LCOE, attention was given to the annual operation hours of the storage system and the total amount of electrical and thermal energy that can be made available by the system.

Results and Discussion

The wind farm was curtailed for 1440 hours in the year 2020. The variation of the storage duration shows that the LCOE reaches its minimum with a storage duration of 26 hours, as shown in Figure 4.

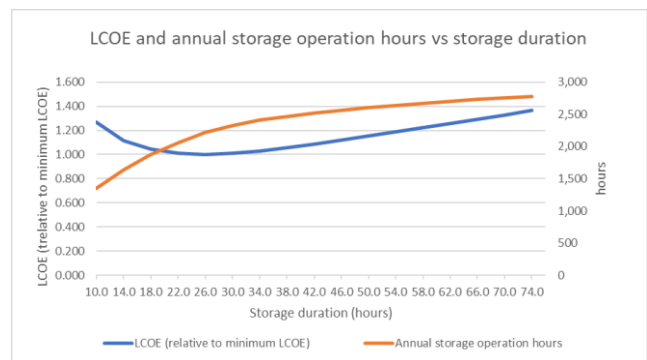


Figure 4: LCOE (relative) & annual operation hours of Malta M100 vs. storage duration

From this point on, with increasing storage duration, there are less and less annual operation hours during which this additional storage capacity can be used. The LCOE is not shown in absolute numbers (EUR/MWh), but relatively to the lowest LCOE. This is because the values strongly depend on the assumptions for the installation and operation cost of the storage system. A cost estimate for this specific site and configuration was not carried out at this stage and will be done in a second step after a detailed techno-economic pre-feasibility study. The LCOE also depends on the price of the energy used for charging. With the current German regulations, wind farm operators get paid for the curtailed energy, and it may not be used to charge storage systems. It can be expected, though, that this regulation will change in the near future and that otherwise curtailed energy will be made available to storage systems at a very low price. There are no reliable predictions for these prices available. Nevertheless, as mentioned above, the LCOE is not the only parameter to be taken into consideration. The number of operation hours and thereby the amount of electrical and thermal energy delivered by the storage shall be as high as reasonably possible. The operation hours increase with increasing storage duration, but the curve flattens out notably beyond 36 hours. Therefore, a 36-hour storage system has been chosen as recommended for this study.

With this configuration, out of the 1440 hours of EinsMan, 1195 hours could be used to charge the storage system, corresponding to 83.0% of the available hours. A total of 227 GWh_{el} of otherwise curtailed wind energy could be stored. 117 GWh_{el} would be returned to the electricity grid, while 72 GWh_{th} of thermal energy could be used in the district heating network, see Figure 5. The overall energy losses result in 39 GWh. This corresponds to a roundtrip efficiency (power-to-heat-to-power-and-heat) of 83.3%. As this energy storage plant would



replace a hard coal-fired power plant, assuming an average specific CO₂ emission of hard coal of 867 g/kWh_{el}, the CO₂ reduction results in 101,400 t per year.

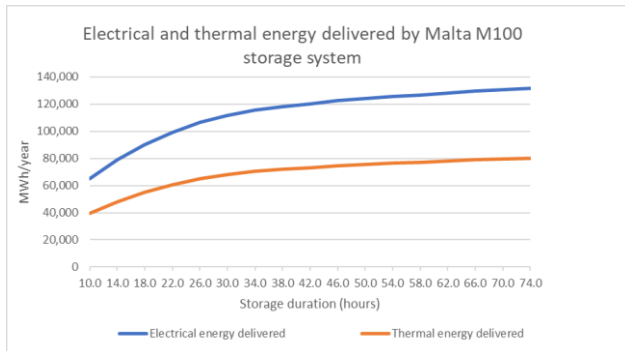


Figure 5: Electrical and thermal energy provided by Malta M100 vs storage duration

As can be seen in Figure 6, most curtailment occurs in winter between November and March, matching very well the Hamburg district heating heat demand curve.

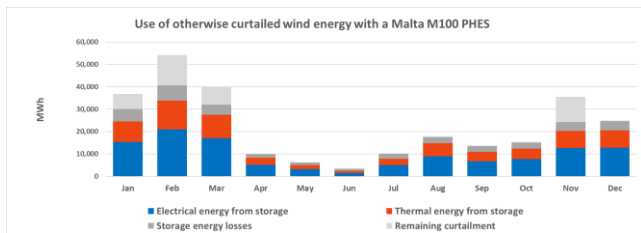


Figure 6: Monthly distribution of otherwise curtailed wind energy stored in the Malta M100 PHEs system

It shall be noted that in addition of only using otherwise curtailed energy, the storage system discussed here could be used in further situations, e.g., it could be charged when electricity market prices are low and discharged when prices are high, independently of the occurrence of curtailment. This will increase the annual operation hours and hence decrease the LCOE. Further analyses with future market prices, taking into account the increasing penetration of renewable generators and the decommissioning of existing fossil-fuelled power plants, will be conducted in a next step.

Conclusions

The study that was carried out shows that a large part of wind energy from an offshore wind farm in Northern Germany that would otherwise be curtailed can be stored in a long duration energy storage system and be made available in the forms of electricity and heat at a later stage, when renewable resources are

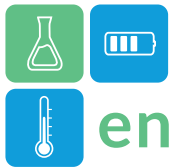
low and energy demand is high. It is shown that the occurrence of excess wind energy is much higher in winter, thereby matching very well the heat demand in a district heating network.

As more and more renewable power plants are installed, energy storage systems are necessary to avoid further curtailment. As shown in this example, there are energy storage technologies that can balance electricity supply and demand while also providing grid services and heat, thus being able to fully replace fossil-fuelled CHP plants.

A precise cost estimate for this specific site and configuration was not carried out at this stage and will be done in a second step after a detailed techno-economic pre-feasibility study. The business case depends on the development of future market prices and on potential additional revenue streams, such as arbitrage, frequency services, and payments for capacity or rotating inertia (“Momentanreserve”). In most scenarios analysed, a green premium in the form of a feed-in tariff or a Contract for Difference (CfD) is necessary to make a project like the one described in this paper economically feasible under the current market conditions. Nevertheless, LDES systems are absolutely essential to reach the EU climate and energy targets and to make the transition to climate neutrality possible.

References

- EU (2021). Regulation (EU) 2021/1119 of the European Parliament and of the Council of 30 June 2021 establishing the framework for achieving climate neutrality and amending Regulations (EC) No 401/2009 and (EU) 2018/1999 (‘European Climate Law’)
- Bundesministerium für Umwelt, Naturschutz, nukleare Sicherheit und Verbraucherschutz (2021). [bmu.de/gesetz/bundes-klimaschutzgesetz](https://www.bmu.de/gesetz/bundes-klimaschutzgesetz)
- Bundesnetzagentur: Quartalsbericht (2023). Netzentpassmanagement, Viertes Quartal 2022
- TenneT – Eisman-Einsatzberichte. netztransparenz.tennet.eu/de/strommarkt/transparenz/transparenz-deutschland/berichte-marktrelevante-informationen/einspeisemanagement-einsaetze-nach-14-eeg/eisman-einsatzberichte



Manufacturing Composites for High-Temperature Thermal Energy Storage applications From lab to pilot scale

M. E Navarro Rivero^{1,*}, Argyrios Anagnostopoulos¹, Abdalqader Ahmad¹, Yelaman Maksum¹, Shivangi Sharma¹, and Yulong Ding¹

¹ Birmingham Centre for Energy Storage & School of Chemical Engineering, University of Birmingham, Birmingham B15 2TT, United Kingdom

*Corresponding author e-mail: h.navarro@bham.ac.uk

Abstract

Industrial thermal processes constitute 18.9% of the EU's total energy demand. Recovering waste heat from these processes could allow the reuse of 400 TWh annually. Thermal Energy Storage (TES) can address energy-intensive industries, like foundries, by storing their waste heat in a cost-effective thermal form, balancing generation and demand in industrial processes. Among TES technologies, Composite Phase Change Materials (CPCMs), which involve encapsulating PCMs in a porous matrix, are a promising solution to achieve high thermal energy storage density systems. However, there is a lack of available information regarding the relationship between manufacturing process parameters and TES materials performance. This study evaluates the scaling-up process of CPCMs formulated with two different PCMs, NaNO₃ and Solar Salt, and a matrix, a mixture of MgO and waste foundry sand. The scaled-up process reveals the effect of particle size on the microstructure and the mechanical properties of the CPCMs over the working temperature range (T_{amb} to 400 °C). The higher the particle size, the higher the tensile strength below the melting point. However, above the melting point, the CPCM with smaller particle sizes presents higher tensile strength.

Keywords: Composite phase change materials, waste heat recovery, large-scale manufacturing

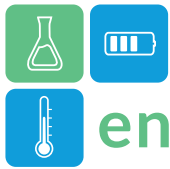
Introduction

According to the European Union (EU), the industrial sector contributes to 27% of the total energy consumption and is responsible for 30% of CO₂ emissions related to heat (International Energy Agency (IEA), 2022). Within this sector, industrial thermal processes represent 70% of the overall energy demand, equivalent to 18.9% of the total energy demand in the EU (Malinauskaite et al., 2019). Recovering the waste heat from these thermal processes will allow 400 TWh per year to be reused.

Energy-intensive industries, such as foundry industries pose significant challenges towards Net Zero targets. Thermal energy storage (TES) is able to address such a challenge by storing waste heat in a cost-effective thermal form, thus facilitating the balance of mismatching generation and demand in industrial processes (Renewable and Agency, n.d.). Among TES technologies, latent heat TES (LHTES) uses the phase change of a material (PCM), to absorb/release heat isothermally during its transition, most commonly between solid and liquid. However, PCMs suffer from poor thermal conductivity, volume expansion,

corrosion, and subcooling in some cases. These challenges can be partially overcome by encapsulating the PCMs in a porous matrix, typically ceramic, carbon or metallic materials (Jacob and Bruno, 2015); or more recently using materials coming from waste or by-products such as red mud (Anagnostopoulos et al., 2021), phosphogypsum (Anagnostopoulos et al., 2022) or fly ash (Gutierrez et al., 2016). The resulting materials are called composite phase change materials (CPCMs). Waste foundry sand is another waste that has been proposed as part of CPCMs. It is a by-product/waste from the casting of ferrous and non-ferrous components. The sand used in casting moulds can be recycled reaching an average internal recycling rate of up to 80-98 %. However, after cycles, it is disposed of in landfills (Siddique and Noumowe, 2008).

Despite the efforts from both academic and industrial sectors to deploy Composite Phase Change Materials (CPCM) into the market, the available options remain limited, and their cost remains high (Jiang et al., 2021). Moreover, there is a lack of available information regarding the relationship between manufacturing



process parameters and TES materials performance. This emphasizes the importance of comprehending the impact of manufacturing process parameters on the performance of CPCMs at a commercial scale, particularly for the implementation of TES in waste heat recovery applications.

This study evaluates the scaling-up process of CPCMs formulated with two different PCMs, NaNO_3 and Solar Salt, and a matrix, a mixture of MgO and waste foundry sand. The aim is to assess how manufacturing process parameters, during the transition from laboratory to commercial scale, influence the performance of CPCMs.

Methodology

Materials

The CPCMs are formulated using two PCMs, NaNO_3 with a melting point of 308°C and Solar Salt (a mixture of NaNO_3 and KNO_3 60/40 mass ratio). NaNO_3 and KNO_3 were purchased from Sigma-Aldrich at a chemical grade purity ($>99.9\%$). The matrix was formulated using MgO and sand. MgO was purchased from VWR International Limited and the sand was obtained from “Boro Foundry”, a 60-year West Midlands (UK) specialist that manufactures ferrous and non-ferrous castings and machined parts.

Methods

The CPCMs, a mixture of sand, MgO and PCM grains were mixed in different proportions following two different procedures: At lab scale, they were milled in an Agatha mortar, compressed at 28 MPa for 1 min, in a 50x10 mm diameter pellet and heated at 80°C for 2 hours to remove moisture followed by a heating up to 400°C for 1 hour. When scaling up, it was used a large ball mill with alumina balls to mix and a semi-automatic hydraulic die press to shape 60x45 mm pellets. The same heating profile was followed. The lab scale samples can be seen in Figure 1 and the scaled-up manufactured pellets composition can be seen in Table 1.

Table 1: CMCP formulated composition

Sample	PCM (%)	MgO (%)	Sand (%)
CPCM1	(NaNO_3 - KNO_3)-40	40	20
CPCM2	NaNO_3 -40	40	20

Characterization

The CPCM bulk density is calculated by obtaining the respective pellet's mass and dimensions (volume). The

porosity of the CPCM is then calculated using the density ratio.

The specific heat capacity, melting point and latent heat were measured using a Differential Scanning Calorimetry (DSC) in a DSC3 Mettler Toledo from 20 to 400°C , a heating rate of 10°C min in aluminium crucibles under nitrogen atmosphere.

Compressive strength was measured using LS100 Lloyd Instruments Co., Ltd. testing machine. Tests are performed until breakage (rupture) by applying constant load.

The IR thermal images were taken with a FLIR TG297 and the microstructure was analysed using a secondary electron microscopy (SEM) TM3030 Hitachi and an optical microscope (OM) Zeiss AXIO A1 microscope.

Results and Discussion

Morphology and microstructure



Figure 1. Pictures of lab-scale manufactured 50 mm pellets

A study at lab scale was done to assess the mechanical stability of the different formulations after the heat treatment. An example of the produced pellets can be seen in Figure 1. The amount of PCM ranged from 40 to 55 wt. % and the amount of sand from 15 to 25 wt. %. The formulated pellets showed that a high amount of PCM and sand led to cracks and leakage of the PCM, resulting in poor shape stability.



Figure 2. Pictures of 50 mm pellets scaling up manufacturing process; right CPCM1 and left CPCM2.

Figure 2 shows an example of the scaled-up manufactured pellets, CPCM1 on the right and CPCM2 on the left. After further analysis with optical and SEM microscopes, see Figure 3, it can be

seen that the two CPCMs have a different microstructure and pore sizes. This is due to a different grain size during the milling and mixing process. The silica particles size, identified by EDX, differ in one order of magnitude; CPCM1 has silica particles ranging around 50 μm , whereas CPCM2 ranges around 300 μm . We can deduce that during manufacturing, the raw materials have been processed differently, and ground up to a different particle size before being pressed into 60 mm pellets.

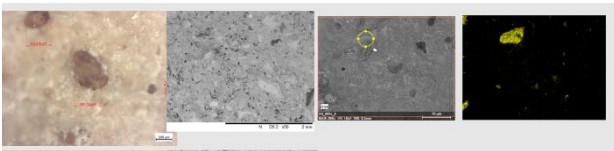
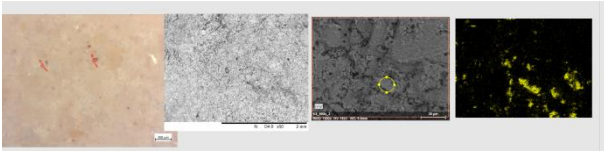


Figure 3. OM (first left), SEM pictures (middle) and EDX (right) of CPCM1 (up) and CPCM2 (bottom) of scaled-up manufactured 50 mm pellets.

Thermal Properties

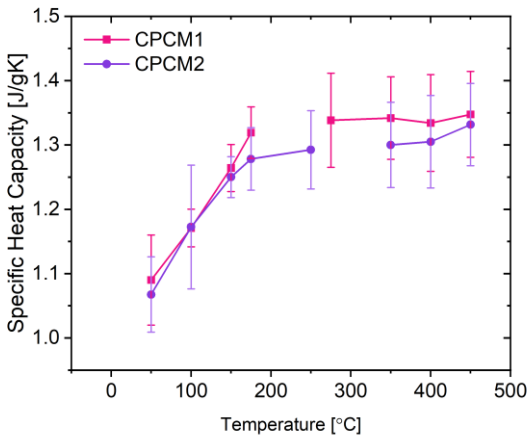


Figure 4. Specific heat capacity of CPCM1 and CPCM2 before and after the PCM melting point.

The specific heat capacity (C_p) is a key parameter influencing CPCM performance in TES systems. The C_p was measured over a temperature range of 50–400 $^{\circ}\text{C}$, see Figure 4. The CPCM1, with solar salt, exhibited a C_p , from an initial 1.06 J/gK to 1.29 J/gK, after the phase transition, the C_p remained quasi-constant at 1.29 J/gK. CPCM2, with NaNO_3 , showed a C_p of 1.09 J/gK at 25 $^{\circ}\text{C}$, up to 1.37 J/gK till the phase transition reached 1.34 J/gK. CPCM1 has a lower C_p than

CPCM2 (1.09 versus 1.22, and 1.3 versus 1.35 J/gK). Regarding the latent heat, CPCM1 composites, had a lower latent heat than CPCM2, as expected, with values of 39 ± 1.1 and 59 ± 2.6 J/g respectively.

Mechanical properties

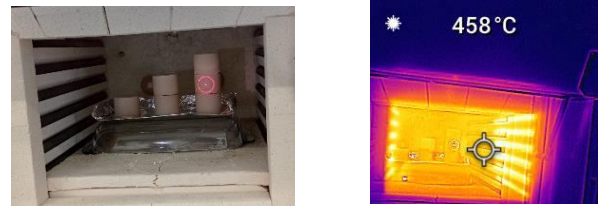


Figure 5. CPCM scale-up manufactured at high temperatures.

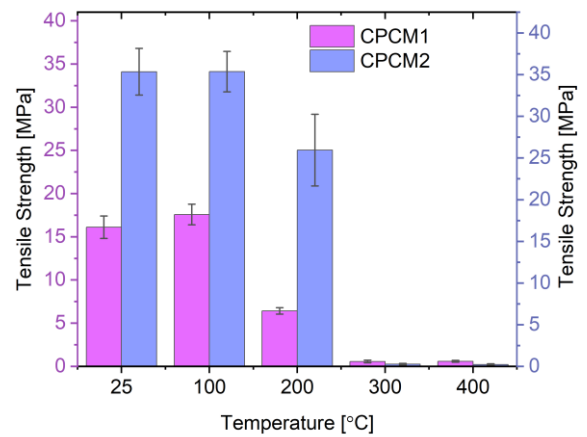


Figure 6. CPCMs tensile strength with temperature.

The mechanical properties of the composites will define the final TES system configuration and how the samples are shaped and placed inside the TES tank. To study the CPCM shape stability, it is necessary to explore their properties within the working temperature range. To do so, the samples were mechanically tested at different working temperatures, as can be seen in Figure 6. For the CPCM1, the tensile strength at ambient temperature was 16.10 MPa and decreased slightly when temperature increased up to 6.42 MPa at 200 $^{\circ}\text{C}$. After the melting point (220 $^{\circ}\text{C}$), the values reached 0.56 MPa (300 $^{\circ}\text{C}$). CPCM2, with a bigger particle size, have a tensile strength of 35.37 MPa at ambient temperature and 25.95 at 200 $^{\circ}\text{C}$. Above the melting point (308 $^{\circ}\text{C}$), the tensile strength is reduced drastically below 0.30 MPa (400 $^{\circ}\text{C}$). CPCM2 has half of the tensile strength of CPCM1 at high temperatures.



Conclusions

This research assesses the viability of incorporating waste foundry sand into thermal energy storage waste heat recovery systems and studies the effect of process parameters on the performance of the TES material. The valorisation of the sand not only presents a cost-effective and sustainable substitute for natural sand but also presents the usage of waste materials as an alternative for high-temperature thermal energy storage materials. The scaling-up process shows that:

- The particle size of the materials greatly affects the microstructure of the CPCMs after sintering and consequently the mechanical properties. Although the tensile strength of the CPCMs decreases significantly at temperatures above the melting point, due to the phase change of the molten salt, the pellets can keep the shape up to a certain maximum packing number. Thus reducing the number of mechanical support needed, such as trays, in high-temperature applications.
- The energy storage density of the CPCMs from Tamb up to 400 °C for CPCMs1 reaches 516 ± 4.5 kJ/kg and CPCMs2 samples reach 542 ± 8.3 kJ/kg, with melting points around 308 and 220 °C respectively.

This study shows the effect of the scaling-up process on the thermal and mechanical performance of the CPCMs, where the mechanical properties are greatly affected by the grain size and the large equipment specifications.

Acknowledgement

The authors would like to acknowledge Transforming Foundation Industries Network+ in the context of THERMCAST and SANDTHERM projects (EPSRC grant EP/V026402/1). Additionally, the authors would like to acknowledge Borofoundry Ltd. for their support during the projects.

References

Anagnostopoulos, A., Navarro, M., Ahmad, A., Ding, Y., Gaidajis, G., 2022. Valorization of phosphogypsum as a thermal energy storage

material for low-temperature applications. *J. Clean. Prod.* 342, 130839.

Anagnostopoulos, A., Navarro, M.E., Stefanidou, M., Ding, Y., Gaidajis, G., 2021. Red mud-molten salt composites for medium-high temperature thermal energy storage and waste heat recovery applications. *J. Hazard. Mater.* 413, 125407.

Gutierrez, A., Miró, L., Gil, A., Rodríguez-Aseguinolaza, J., Barreneche, C., Calvet, N., Py, X., Fernández, A.I., Grágeda, M., Ushak, S., Cabeza, L.F., 2016. Industrial waste materials and by-products as thermal energy storage (TES) materials: A review. In: *AIP Conference Proceedings*. AIP Publishing LLC, p. 050019.

International Energy Agency (IEA), 2022. Global CO₂ emissions rebounded to their highest level in history in 2021. *Glob. Energy Rev. CO₂ Emiss.* 2021 1–3.

Jacob, R., Bruno, F., 2015. Review on shell materials used in the encapsulation of phase change materials for high-temperature thermal energy storage. *Renew. Sustain. Energy Rev.* 48, 79–87.

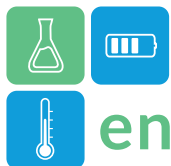
Jiang, Z., Navarro Rivero, M.E., Anagnostopoulos, A., She, X., Liu, X., Xuan, Y., Ding, Y., 2021. Fabrication of form-stable composite phase change materials for thermal energy storage by direct powder incorporation with a preheating process. *Powder Technol.* 391, 544–556.

Malinauskaite, J., Jouhara, H., Ahmad, L., Milani, M., Montorsi, L., Venturelli, M., 2019. Energy efficiency in industry: EU and national policies in Italy and the UK. *Energy* 172, 255–269.

Renewable, I., Agency, E., n.d. *INNOVATION OUTLOOK THERMAL ENERGY*.

Sabour, M.R., Derhamjani, G., Akbari, M., Hatami, A.M., 2021. Global trends and status in waste foundry sand management research during the years 1971-2020: a systematic analysis. *Environ. Sci. Pollut. Res.* 28, 37312–37321.

Siddique, R., Noumowe, A., 2008. Utilization of spent foundry sand in controlled low-strength materials and concrete. *Resour. Conserv. Recycl.*



Mechanochemical synthesis of layered hybrid organic-inorganic perovskites for thermal energy storage materials

R. Salgado-Pizarro, J. Manosa, C. Barreneche, A.I. Fernández*, C. Barreneche

1 Departament de Ciència de Materials i Química Física, Secció de Ciència de Materials, Facultat de Química, Universitat de Barcelona, C/ Martí i Franquès 1-11, 08028, Barcelona, Spain

*Corresponding author e-mail: ana_inesfernandez@ub.edu

Abstract

This study evaluates the mechanochemical synthesis method to produce layered hybrid organic-inorganic perovskites (LHOIPs) that work as solid-solid phase change materials. These materials can store energy due to polymorphism transitions and are suitable for cooling electronics. Three synthesis routes, two solvent-based and mechanochemical, are evaluated, comparing the crystal structure and the thermal properties. The mechanochemical sample presents some impurities and lower specific heat capacity. However, we can significantly reduce energy consumption through this route compared to the two other solvent-based methods. These results show the potential of mechanochemical synthesis to produce this material, highlighting its energy-efficient synthesis process.

Keywords: Layered Hybrid Organic-Inorganic Perovskites (LHOIP), Mechanochemistry, Thermal Energy Storage (TES), Solid-Solid Phase Change Materials (ss-PCM).

Introduction

Solid-solid phase change materials (ss-PCM) are great candidates as thermoregulators since they do not require encapsulation or shape stabilisation. Also, the corrosion issues may be reduced, and the absence of a second material to shape stabilisation or encapsulation allows faster charging and discharging (Mastani Joybari et al., 2015; Putra et al., 2019; Sciacovelli et al., 2018). Organometallics ss-PCMs, especially layered hybrid organic-inorganic perovskites (LHOIPs), present unique structural characteristics and tailored properties (Huan et al., 2016; Mao et al., 2019; Pedesseau et al., 2016).

In this study, we evaluate an alternative synthesis route through mechanochemical synthesis to obtain the LHOIPs to work as solid-solid PCMs, $(C_{12}H_{28}N)_2CuCl_4$. Here, we compare three synthesis routes to obtain this product and analyse the crystal structure and thermal properties.

Materials and methods

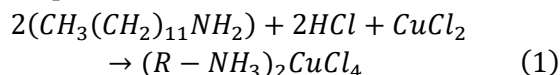
Materials

N-dodecylamine 98% (N° CAS 124-22-1) from Acros Organics. Copper (II) chloride dehydrated (N° CAS 10125-13-0) was purchased from VWR international, hydrochloric acid 37 % (N° CAS 7647-01-0) from Labbox and anhydrous methanol (max. 0.003 % H₂O) (N° CAS 67-56-1) from Merck Group.

Solvent-based synthesis

Two different solvent-base syntheses were performed in this study. The conventional synthesis (Conv.)

comprises refluxing the reagent products' stoichiometry amount 337 K for 4 hours, followed by successive recrystallisation steps in anhydrous methanol (He et al., 2010). The optimised synthesis (Optm.) is described in the study (Salgado-Pizarro et al., 2023). Both synthesis follows the stoichiometry reaction, Eq.1.



Mechanochemical synthesis

The mechanochemical synthesis (MC) was performed in a RETSCH PM100 planetary ball mill with a 250 mL alumina grinding jar with 27 alumina balls of 10 mm diameter. The stoichiometric amount of the reagents was added into the grinding jar, along with 70 mL of anhydrous methanol. The synthesis was performed at 300 rpm during 12 min. Then the product was poured into a petri dish and dried for seven days and subsequently 30 minutes at 60 °C in an oven. The final dried product was ground with an agate mortar.

Characterisation

The crystalline structure was determined from 298 K to 378 K, with a ΔT of 20 K by X-ray powder diffraction (XRD) conducted in a PANalytical X'Pert PRO MPD θ/θ powder diffractometer of 240 mm of radius. The thermal characterisation was done with a differential scanning calorimeter (DSC) from Mettler Toledo. A 300 K to 380 K heating ramp at 1 K·min⁻¹ was set to determine the polymorphic transitions. The specific heat was determined from 310 to 350 K, each 10 K,

using the approach established by Ferrer et al. (Ferrer et al., 2017).

Results and discussion

Crystal structure

Figure 1 displays the XRD spectra of the samples of the three synthesis methods. It can be observed that the main peak of the component is present in all the samples. However, some impurities of unreacted CuCl_2 can be detected in the MC sample, peak around 16° (Engberg & Staffansson, 1970).

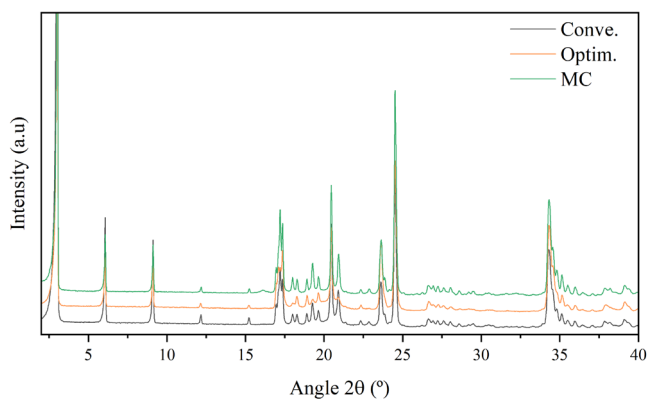


Figure 1: XRD spectra of the samples by three synthesis methods.

Thermal characterisation

The enthalpy and the peak temperature of the three samples are presented in Figure 2. The first transition presents an enthalpy around 60 Jg^{-1} at 329.8 K ; the second transition, 11 Jg^{-1} at 337.2 K , is present in all the samples. No significant changes can be observed in the enthalpy or peak temperature values. However, higher values of enthalpy can be detected in the Optim. sample, this could be due to slight differences in the crystallisation step.

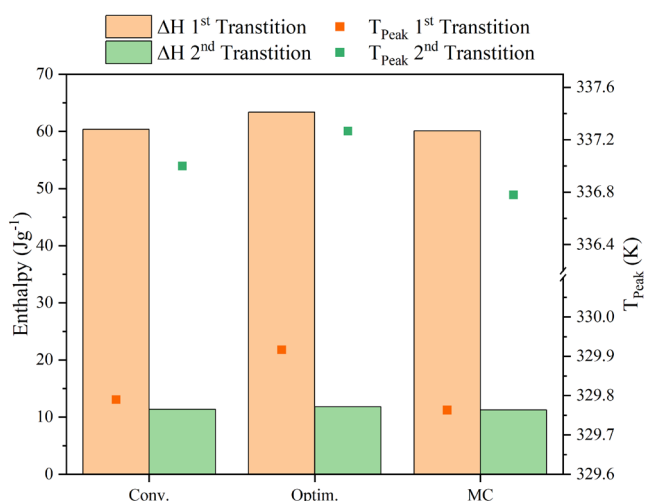


Figure 2: Enthalpy and peak temperature of the three synthesis methods.

The specific heat values and the heat flow curves of the three samples are presented in Figure 3. Regarding the specific heat, similar values are presented in all the samples. Where an increase of the specific heat is detected at temperatures close to the polymorphic transitions, and after the values are stabilised, however, lower values are detected in the MC sample, this may be attributed to a reduced crystal size compared to the other two samples. Since the crystallisation and crystal growth in this sample are produced during grinding, the grinding process can limit these phenomena.

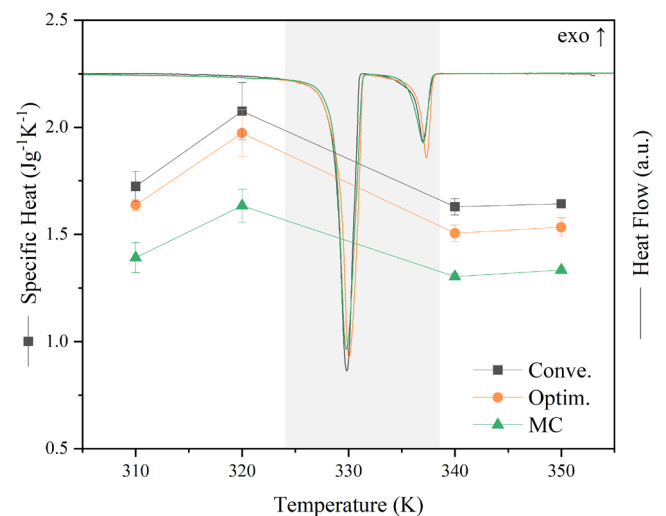


Figure 3: Specific heat values and heat flow curves of the three synthesis methods.

Conclusions

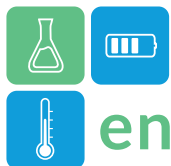
This work tries to analyse the viability of producing LHOIPs as solid-solid PCMs by mechanochemical synthesis.

The XRD and DSC results show that the product can be obtained by mechanochemistry. However, some impurities and lower specific heat values are obtained in the MC sample.

However, by the MC method, we are able to decrease the energy consumption per kg of sample radically. The energy required for Conv., Optim. and MC are 7870.63 , 1725.67 and $106.64 \text{ MJ}\cdot\text{Kg}^{-1}$, respectively. Further investigations should be performed to determine the optimal parameter for the MC and assess scalability through this method. The finding demonstrates the viability of producing LHOIPs as solid-solid PCMs via mechanochemical synthesis, emphasising the energy-efficiency of the process.

Acknowledgments

The authors thank the Catalan Government for the quality accreditation given to their research group DIOPMA (2021 SGR 00708). DIOPMA is a certified



agent of TECNIO in the category of technology developers from the Government of Catalonia. The authors are grateful to the CCiTUB for the equipment or measurements of XRD.

This work is partially supported by the grant PID2021-123511OB-C32 funded by MCIN/AEI/10.13039/501100011033 and, as appropriate, by "ERDF A way of making Europe" and the PhD grant PRE2019-087336 funded by MCIN/AEI/10.13039/501100011033 and, as appropriate, by "ESF Investing in your future" of R. Salgado-Pizarro.

References

- Engberg, Å., & Staffansson, L.-I. (1970). An X-Ray Refinement of the Crystal Structure of Copper(II) Chloride Dihydrate. *Acta Chemica Scandinavica*, *24*, 3510–3526. <https://doi.org/10.3891/acta.chem.scand.24-3510>
- Ferrer, G., Barreneche, C., Solé, A., Martorell, I., & Cabeza, L. F. (2017). New proposed methodology for specific heat capacity determination of materials for thermal energy storage (TES) by DSC. *Journal of Energy Storage*, *11*, 1–6. <https://doi.org/10.1016/j.est.2017.02.002>
- He, D., Di, Y., Yao, Y., Liu, Y., & Dan, W. (2010). Crystal Structure, Low-Temperature Heat Capacities, and Thermodynamic Properties of Bis(dodecylammonium) Tetrachlorocuprate ($C_{12}H_{28}N$)₂CuCl₄ (s). *Journal of Chemical & Engineering Data*, *55*(12), 5739–5744. <https://doi.org/10.1021/jc100699g>
- Huan, T. D., Tuoc, V. N., & Minh, N. V. (2016). Layered structures of organic/inorganic hybrid halide perovskites. *Physical Review B*, *93*(9), 094105. <https://doi.org/10.1103/PhysRevB.93.094105>
- Mao, L., Stoumpos, C. C., & Kanatzidis, M. G. (2019). Two-Dimensional Hybrid Halide Perovskites: Principles and Promises. *Journal of the American Chemical Society*, *141*(3), 1171–1190. <https://doi.org/10.1021/jacs.8b10851>
- Mastani Joybari, M., Haghghat, F., Moffat, J., & Sra, P. (2015). Heat and cold storage using phase change materials in domestic refrigeration systems: The state-of-the-art review. *Energy and Buildings*, *106*, 111–124. <https://doi.org/10.1016/j.enbuild.2015.06.016>
- Pedesseau, L., Saponi, D., Traore, B., Robles, R., Fang, H.-H., Loi, M. A., Tsai, H., Nie, W., Blancon, J.-C., Neukirch, A., Tretiak, S., Mohite, A. D., Katan, C., Even, J., & Kepenekian, M. (2016). Advances and Promises of Layered Halide Hybrid Perovskite Semiconductors. *ACS Nano*, *10*(11), 9776–9786. <https://doi.org/10.1021/acsnano.6b05944>
- Putra, N., Rawi, S., Amin, M., Kusriani, E., Kosasih, E. A., & Indra Mahlia, T. M. (2019). Preparation of beeswax/multi-walled carbon nanotubes as novel shape-stable nanocomposite phase-change material for thermal energy storage. *Journal of Energy Storage*, *21*, 32–39. <https://doi.org/10.1016/j.est.2018.11.007>
- Salgado-Pizarro, R., Barreneche, C., & Fernández, A. I. (2023). Synthesis optimisation of copper-based layered perovskites as thermal energy storage materials. *Materials Today Chemistry*, *30*, 101491. <https://doi.org/10.1016/j.mtchem.2023.101491>
- Sciacovelli, A., Navarro, M. E., Jin, Y., Qiao, G., Zheng, L., Leng, G., Wang, L., & Ding, Y. (2018). High density polyethylene (HDPE) — Graphite composite manufactured by extrusion: A novel way to fabricate phase change materials for thermal energy storage. *Particuology*, *40*, 131–140. <https://doi.org/10.1016/j.partic.2017.11.011>



Membrane-Encapsulated Salt Hydrate: An Anti-agglomeration Approach to Enhance Cyclability

Behrooz Elahi^{1,*}, Mohammad Mehrali¹

¹ (University of Twente, Department of Thermal and Fluid Engineering), Drienerlolaan 5, 7522 NB, Enschede, The Netherlands

*Corresponding author e-mail: b.elahi@utwente.nl

Abstract

Heat has a crucial effect on the general energy consumption in the world. Hence, the need for an environmentally friendly and energy-efficient substitute is on the rise as far as reducing carbon footprints is concerned, where thermochemical materials (TCM) can be a viable option. Potassium carbonate (K_2CO_3) has shown the most promising characteristics for seasonal heat storage due to its high energy density, cost-effectiveness, and reaction safety. However, due to the accruing of salt crystal clumping after a few hydration/dehydration cycles, the operational life cycle of K_2CO_3 is challenged with diminished energy density and kinetics of hydration. In the present study, to mitigate this challenge, a new encapsulation strategy based on membrane science is used to address both agglomeration mitigation and preservation of crystal integrity without limiting the water vapour diffusion inside the crystal by employing a separative polymeric layer. This research introduced the encapsulation process along with suitable crystal morphology with a focus on optimal pore structure and hydration kinetics as a mechanism for optimizing the efficiency of transport of water vapour. The key results of this research provide a cheap and easy-to-implement method to prevent agglomeration while preserving the cyclic performance characteristics of salt hydrates for heat battery application.

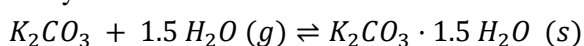
Keywords: Thermochemical materials, Salt hydrate, Heat battery, Cyclic performance

Introduction

Heat accounts for the largest portion of the world's final energy consumption, contributing nearly 50% to the total global energy consumption. Domestic heating is directly responsible for 80% of CO_2 emissions in buildings (Eurostat 2021, IEA 2022). To comply with international climate agreements, the enhancement of renewable heat consumption sources must occur at a rate 2.5 times faster than currently planned (Eurostat 2021).

Thermochemical energy storage (TCES), which utilizes reversible chemical reactions, is a viable option among different sustainable heat storage techniques. This method employs solid substances called thermochemical materials (TCMs) that retain heat as chemical potential energy. It offers a significant advantage in terms of heat storage density and minimal losses over long durations, particularly when compared to sensible and latent heat storage systems. (Frazzica and Cabeza 2018)

The salt hydrate identified as the most promising option for seasonal heat storage is potassium carbonate (K_2CO_3) by considering energy density, power output, price and material safety (Donkers, Sögütöglu et al. 2017). The reversible thermochemical reaction can be given by:



In this study, the main focus is on the development of cyclable Thermochemical Materials (TCM), as they offer a sustainable and long-term heat storage solution for household applications (Scapino, Zondag et al. 2017).

During repeated cycles of operation, the clumping of salt crystals can lead to a decrease in energy density and alter the hydration kinetics. To address this, a novel approach inspired by membrane science has been adopted. This method involves creating a porous, separative layer between the salt particles, which still permits the passage of water vapour into the core structure. The impact of water addition to the coating solution and the choice of solvent in this process was examined through a study focusing on the resulting morphological and hydration kinetic changes. The focused criteria are pore structure and kinetic as well as hydration completion to ensure that the transport of the water vapour to and from the salt is as efficient as possible while at the same time ensuring the coating structure helps in preventing agglomeration of the salt crystals. This study is dedicated to understanding how these properties significantly affect the performance and efficiency of potassium carbonate. This understanding is vital for enhancing and refining the application of these materials in advanced heat storage solutions.

Materials and Methods

Materials

High-purity Potassium carbonate sesquihydrate (ACS reagent, 99%) was purchased from Sigma-Aldrich, USA. Dimethyl sulfoxide (DMSO, ACS (99.9 % min)), N, N-Dimethylacetamide, (DMAC, (99.5%, extra pure)) was obtained from Thermo Scientific. Polyethersulfone (PES) ($m_w = 90$ kDa, $T_g = 225$ °C, E7020, Ultrason) was purchased from BASF SE, Germany.

Preparation

The saturated solutions of potassium carbonate were prepared using MiliQ water in which the salt was dissolved and heated to 80°C. By maintaining a temperature of 80°C, this method minimizes evaporation while leveraging the benefits of enhanced

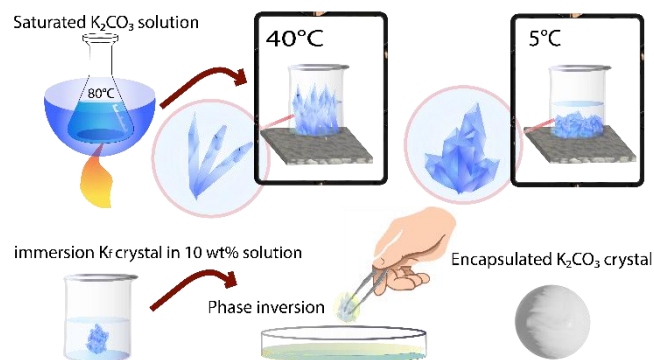


Figure 1: K_2CO_3 crystallization and encapsulation process schematic

solubility. The crystals were formed by using two different methods. The first method involved rapidly cooling the saturated solution in a refrigerator set to 5°C. This approach was designed to encourage quick crystal growth, potentially leading to unique crystal forms due to the rapid changes in solubility. The second approach, called K_f , was gradually cooled down in a climate chamber at 0.5K/min until it reached a temperature of 40°C. This slower cooling rate was chosen to explore how gradual changes in solubility might influence the crystals' shape. However, it's important to note that the climate chamber's relative humidity was not regulated, introducing an additional variable that could impact crystal growth.

The central objective of using these two different cooling modes was to see how cooling rate and environmental conditions influence the hydration behaviour of the potassium carbonate crystals as well as their kinetics. Detailed conditions for these experiments are outlined in Table 1 and displayed in Figure 1.

Table 1: Potassium carbonate crystal formation parameters.

Sample Name	Cooling Method	Final Temperature	Environment
K_S	Rapidly placed at 5°C	5°C	Fridge environment
K_F	0.5K/min to 40°C	40°C	Climate chamber

K_S crystals were chosen as the primary material for encapsulation. The crystals were placed in a petri dish and dried in a convection oven at 160°C to dehydrate and convert residual $KHCO_3$ to K_2CO_3 . The encapsulation process entailed creating a polymeric solution by dissolving 10% Polyethersulfone (PES) in DMSO and DMAC. Following this, MiliQ water was incrementally added into the solution in 1% steps from 0 wt% to 2 wt%. To achieve a uniform solution, a 16-hour resting period in an Erlenmeyer flask was employed to allow for the release of any trapped air bubbles. The immersion time was maintained constant in the coagulation bath, thereby ensuring that no salt dissolution occurred. In total, six samples were prepared using the parameters mentioned in Table 2, each with distinct cooling methods and environmental conditions to investigate their effects on crystal morphology and hydration kinetics.

Table 2: Membrane solution parameters.

Sample	Solvent	Water in solution (wt %)
C_0	DMSO	0
C_1	DMAC	0
C_2	DMSO	1
C_3	DMAC	1
C_4	DMSO	2
C_5	DMAC	2

Characterization

The pore morphology was analyzed on both the PES coating structure and salt crystals. Imaging was conducted using JEOL JSM-6010LA scanning electron microscope (SEM), located in Tokyo, Japan, with an operating voltage of 10 kV. The PES membrane film underwent cryogenic treatment with liquid nitrogen to decrease molecular mobility and increase brittleness. This procedure was designed to prevent distortion of the pore microstructure, ensuring a clear cross-sectional view. Moreover, the membrane was coated with a 5nm layer of Pt/Pd to enhance its electrical conductivity and minimize charge build-up.

The hydration kinetics and cyclic performance of the samples were evaluated using Differential Scanning Calorimetry (DSC) and Thermogravimetric Analysis (TGA). The DSC assessed the hydration enthalpy at

30°C and relative humidity of 31%, which is the average water vapor pressure in boreholes during winter. The dehydration was performed at 100°C to ensure the samples were completely dehydrated. Simultaneous measurements were made using the STA Netzsch 449, F3, Jupiter instrument. During these tests, air flowed at a rate of 300 ml per minute through the samples, both in the hydration and dehydration phases in the STA furnace.

Results and Discussion

Morphology

The SEM images (Figures 3a-d) present morphological characteristics of potassium carbonate crystals grown through two distinct cooling regimes. Figures 3a and 3b depict crystals resulting from a slow cooling process (K_s), where the solute was cooled at a rate of 0.5K/min to an isotherm temperature of 40°C. The obtained crystal structures are notably larger with smoother surfaces compared with K_f crystals which indicates a slower cooling rate promotes orderly crystal growth (Barakan, Ayaluey et al. 2021). Moreover, the uniform shape and structure indicate that the growth of each crystal is a process controlled by kinetics, where every facet of the crystal develops in equilibrium with its environment (Beving, Romme et al. 2022).

Figures 3c and 3d represent a distinctly different crystalline structure formed in a 5°C environment. The observed K_f microstructure forms of needle-like shapes. This points towards a growth process that is limited by diffusion, where a swift increase in supersaturation overtakes the systematic incorporation of solute ions into the crystal lattice. These needle-like structures hint at crystal shapes that are kinetically trapped, typically emerging under conditions of rapid changes in the environment. The red circles in Figure 3d indicate the presence of many defects forming in a non-equilibrium cooling stage with a brighter colour around the crack edges due to dehydration and water presence under high vacuum conditions in the SEM chamber. Blue circles point out an uncontrolled nucleation and growth in this cooling regime.

To gain deeper insights into the porous layer coating encapsulated salt crystals, the coating layer structure was investigated.

Figure 4b observed the formation of a dense layer instead of a porous one, unlike with DMSO. This difference in behaviour can be attributed to a higher affinity of DMAC with PES, leading to a denser and more cohesive polymer solution.

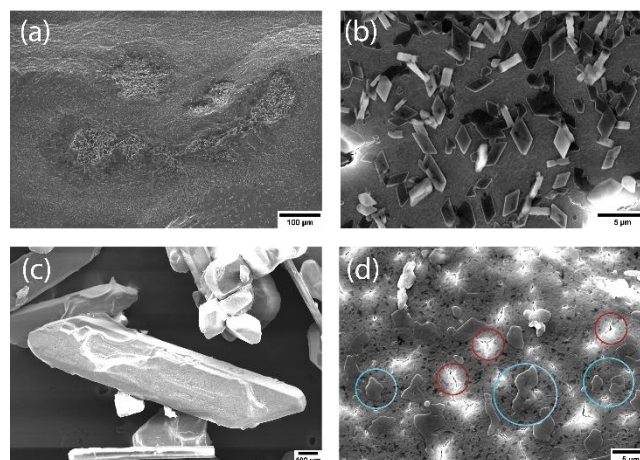


Figure 3: K_2CO_3 crystals SEM morphology. (a-b) K_s , (c-d) K_f

Introducing water to a PES/DMSO solution is key for porous membrane layer formation through phase inversion, as it helps to tune microstructure. Optimal PES at 10wt% polymer concentration to avoid thick, slow-forming layers, water enhances surface phase inversion kinetics for finer pores. Inner shell kinetics protect K_2CO_3 granules' structure.

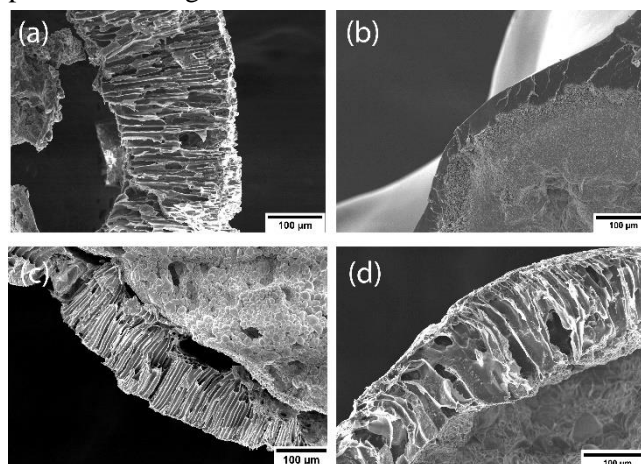


Figure 4: PES encapsulated layer morphology change. a) C_0 b) C_1 c) C_2 d) C_3

The best results were observed for C_2 at 1 wt% water concentration (Figure 4c), balancing phase inversion kinetics and polymer interaction, ensuring a uniform pore structure. Higher concentrations lead to rapid, irregular phase separation, while lower concentrations yield less structured porous layers, as seen in Figure 3d.

Hydration kinetics

The water uptake of K_s and K_f measurements was performed under cyclic hydration and dehydration. The cyclic performance of larger K_s is conducted over longer time intervals due to diffusion-limited kinetics (Gaeini, Zondag et al. 2016, Gaeini, Shaik et al. 2019). A notable distinction was observed in the TGA results outlined in Figure 5. Hydration and dehydration

behaviours between large crystals (Figure 5a) and needle-like structures (Figure 5b) through multiple cycling. The large crystals initially show a lower water uptake, which could be indicative of less active surface sites or a denser packing that impedes water penetration. With successive cycles, the mass change increases, suggesting the formation of microcracks, as evidenced by the gradual increase in surface area exposed to hydration. This phenomenon is likely due to thermal stresses leading to structural fracture, which facilitates faster water uptake and surface reactions. In contrast, the needle-like structures present a high surface-to-volume ratio that diminishes over time, as the needles agglomerate, confirming a decrease in hydration reaction rate over time due to the reduced exposure of active sites (Schuttlefield, Cox et al. 2007).

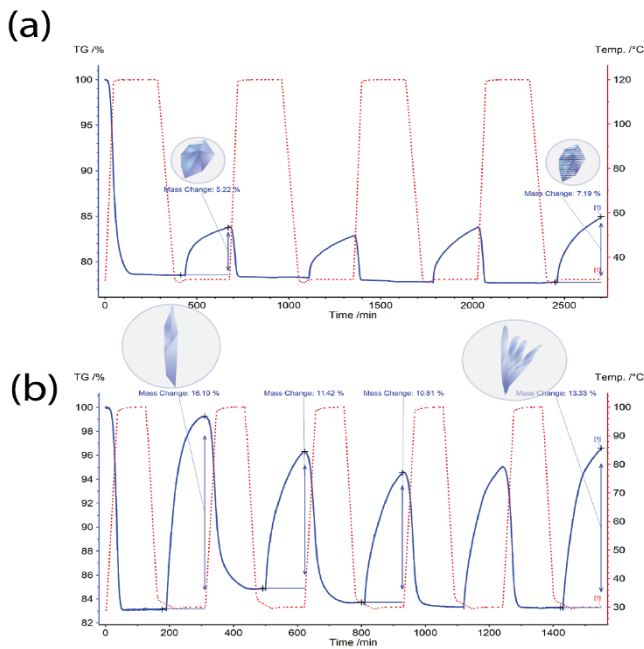


Figure 5: The Mass change % vs time. (a) K_s crystals (b) K_f crystals

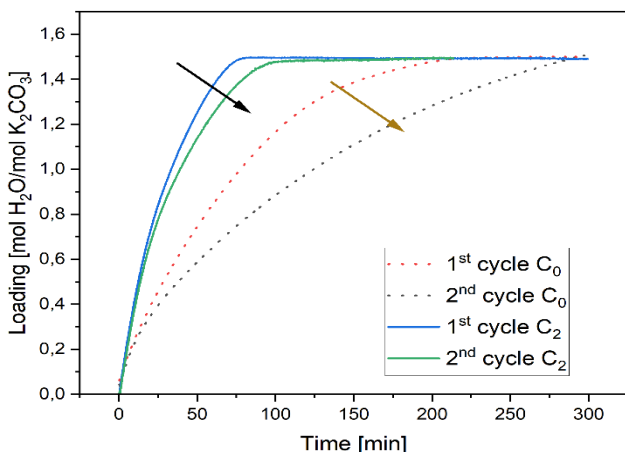


Figure 6: Two-cycle hydration behaviour of encapsulated K_f crystals

The Figure 6. graph presents water sorption kinetics for potassium carbonate K_f coated with a porous membrane, comparing two sample types across consecutive cycles. For sample C_0 , there is a visible decrease in water uptake from the first to the second cycle, indicated by the lower peak in the second cycle (black arrow). This trend could be either indicative of pore blockage or K_2CO_3 crystal agglomeration over time.

In contrast, sample C_2 maintains almost consistent water sorption capacity between cycles (green line), suggesting the presence of a more robust and stable membrane structure at 1 wt% water concentration. Overall, both coating compositions can be used for thermochemical materials, especially, K_2CO_3 particles for heat storage cyclic applications. The porous water permeable layer successfully allowed water vapor to enter and permeate inside the salt crystals and made fully hydration possible.

Conclusions

In this study, several techniques were employed to select the most effective crystal and agglomeration inhibitor morphology to improve the performance of cyclic hydration. Two distinct potassium carbonate crystal morphologies were grown to deeply analyse the microstructural behaviour for further encapsulation step. The rapid cooling and growth limited scheme shows a higher surface-to-volume ratio resulting in a higher active surface for hydration bond formation with water molecules.

An innovative membrane science-inspired encapsulation method was developed in this study to form a separative porous layer on the salt particle surface. This layer prevents direct contact among ionic salt atoms by a porous and water-permeable layer. The PES polymer was used to promote the porous layer formation via phase inversion with various water content in the coating solution. The hydration completion by this method demonstrated that porous salt crystal encapsulation can be a cost-effective and easy-to-implement technique for increasing the life cycle of K_2CO_3 particles.

Future studies can investigate the porous encapsulation performance under rigorous conditions and closer to the real heat battery condition on a larger scale.



enerstock

ENERSTOCK 2024

The 16th IEA ES TCP International Conference on Energy Storage

June 5–7, 2024

Lyon, France

References

Barakan, S., M. N. Ayaluey, S. Shayanfar and V. Aghazadeh (2021). "Production and characterisation of sodium and potassium carbonate salts from carbonation alkaline aluminate liquor." Mineral Processing and Extractive Metallurgy **131**(3): 211-219.

Beving, M., J. Romme, P. Donkers, A. Frijns, C. Rindt and D. Smeulders (2022). "Experimental and Numerical Validation of the One-Process Modeling Approach for the Hydration of K₂CO₃ Particles." Processes **10**(3).

Donkers, P. A. J., L. C. Sögütöglü, H. P. Huinink, H. R. Fischer and O. C. G. Adan (2017). "A review of salt hydrates for seasonal heat storage in domestic applications." Applied Energy **199**: 45-68.

Eurostat. (2021). "Energy consumption in households." from <https://ec.europa.eu/>.

Frazzica, A. and L. F. Cabeza (2018). Recent advancements in materials and systems for thermal energy storage: an introduction to experimental characterization methods, Springer.

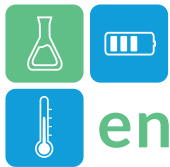
Gaeini, M., S. A. Shaik and C. C. M. Rindt (2019). "Characterization of potassium carbonate salt hydrate for thermochemical energy storage in buildings." Energy and Buildings **196**: 178-193.

Gaeini, M., H. A. Zondag and C. C. M. Rindt (2016). "Effect of kinetics on the thermal performance of a sorption heat storage reactor." Applied Thermal Engineering **102**: 520-531 % @ 1359-4311.

IEA. (2022). "The Netherlands-Countries & Regions - IEA n.d." from <https://www.iea.org/countries/the-netherlands>

Scapino, L., H. A. Zondag, J. Van Bael, J. Diriken and C. C. M. Rindt (2017). "Sorption heat storage for long-term low-temperature applications: A review on the advancements at material and prototype scale." Applied Energy **190**: 920-948.

Schuttlefield, J. D., D. Cox and V. H. Grassian (2007). "An investigation of water uptake on clays minerals using ATR-FTIR spectroscopy coupled with quartz crystal microbalance measurements." Journal of Geophysical Research: Atmospheres **112**(D21).



Metallic phase change material (PCM) for high temperature applications, selection, synthesis and characterisation.

Kyran Williamson^{1,*}, Angel Serrano Casero¹, Paola Zimmermann Crocomo¹, Artem Nikulin¹, Francesco Torre¹, Laura Teodorescu², Grégory Largiller², Elena Palomo Del Barrio¹

¹Centre for Cooperative Research on Alternative Energies (CIC energiGUNE), Basque Research and Technology Alliance (BRTA), Alava Technology Park, Albert Einstein 48, 01510 Vitoria-Gasteiz, Araba,

²Univ. Grenoble Alpes, CEA, LITEN, DTCH, LCST, 38000, Grenoble, France

*Corresponding author e-mail: kwilliamson@cicenergigune.com

High heat of fusion metal alloy phase-change materials (PCMs) within the 700-800°C temperature range are chosen for integration with ceramic refractories, forming the core component of a thermal energy storage (TES) unit. Applications targeted by this EU-HEATERNAL project are the steel, aluminium and ceramics industries. The selected PCMs, are a key component of a novel TES prototype consisting of a composite including metal alloy PCMs contained within ceramic refractory bricks. This innovation aims to enhance energy density by 350%, surpassing traditional ceramic bricks, and aims for rapid implementation by 2030. The project targets a 50kWh prototype (TRL5) and up-scaled storage system models connected to factories. This presentation delves into the phase change material selection process and criteria specific to the 700-800°C temperature range, highlighting the impact of synthesis and dendrite growth on latent heat measurements of Cu.Si based PCMs.

Keywords: Metallic alloys, Characterization, TES, PCM

Introduction

The selection of PCMs for thermal energy storage is made after revising the materials characteristics and their storage capacity -i.e. melting temperature, heat transfer and so on [1]. Latent heat storage (LHS) is an efficient method of storing thermal energy in which a phase-change material (PCM) stores or releases heat during an isothermal solid-to-liquid or liquid-to-solid phase transition [2]; compared to sensible storage, it enables higher volumetric energy densities.

Based on previous research [3], it was observed that alloys have higher latent heat of fusion than pure metals thanks to their higher entropy of mixing.

The combination of refractory materials and Phase Change Materials (PCMs) in the HEATERNAL thermal energy storage system (TESS) achieves a synergistic blend of sensible and latent heat storage. In the pursuit of optimizing efficiency and stability through repeated cycles, compatible combinations are explored by examining existing ceramic formulations designed for use with metal alloys.

A preliminary selection of PCM composite metal alloys for an operating temperature range of 700°C - 800°C is reported in this context. The selection

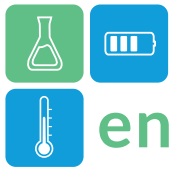
process is guided by key performance indicators (KPIs) such as cost, heat storage capacity (> 400 kWh/m³), proven lifetime (> 1000 hours), low energy & CO₂ footprint, non-toxicity, safety, and ease of recyclability.

Based on the above factors, the chosen metals for evaluation include Al, Cu, Fe, Si, Mn, and Ti, along with their respective alloys. This study centres on the selection, synthesis, and optimization of characterization techniques aimed at maximizing the latent heat of these materials, especially in the temperature range of 700-800 °C.

Methodology

Initial CALPHAD Screening

A preliminary assessment using the CALPHAD approach, utilizing FactSage Thermochemical Software allowed us to determine theoretical liquidus projection phase diagrams. This analysis enabled the prediction of the expected enthalpy of fusion within the temperature range of 700-800°C (see Figure 5). However, it should be considered that even if FactSage can offer a theoretical database regarding



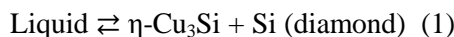
the thermophysical characteristics, depending on the selected databases, some discrepancies between the results and literature have been noted.

Metal alloy synthesis

The Cu-Si system has been the subject of previous research because of its important applications in technology [4–7]. The binary alloy provides great thermophysical characteristics, due to the strong heat storage capacity of silicon and the superior thermal conductivity of copper. As a result, Cu-Si alloys that melt at temperatures higher than 650°C are excellent TES materials [8]. The metals used in synthesis were ordered from HMW Hauner GmbH & Co. KG Gewerbering 36 as granules with a purity of 99.999% and diameter of 1-5 mm.

In the context of this limited abstract, the binary eutectic composition of $\text{Cu}_{83}\text{Si}_{17}$ with a theoretical melting point of 809.1 °C and enthalpy of fusion of 232.6 J/g has been selected.

The expected reaction is as follows[7],



The eutectic alloys $\text{Cu}_{83}\text{Si}_{17}$ (%wt) were prepared by three synthesis methods: solid-state, blowtorch and rapid inductive synthesis.

Solid-State Synthesis Method:

Pure Cu (granules 99,99%, HMW Hauner) and pure Si (granules 99,99%, HMW Hauner) were **weighed to a total of three grams** and placed in graphite crucibles within a tube furnace (carbolite). The samples were heated at 10 K/min from room temperature to $T=1200$ °C, under a nitrogen flow (80mL/min) and held isothermally for 3 hours.

Blowtorch Synthesis:

Approximately two grams of metals were placed in an alumina crucible. After, the samples were heated using a blowtorch, until reaching a molten state. Borax powder flux was added to ensure the homogeneity and to prevent oxidation. The molten alloy was carefully transferred to a graphite crucible for rapid cooling and recovery.

Rapid Inductive Synthesis:

Metals in the appropriate ratio were heated in a 30 μL alumina crucible coated with graphite. The crucible was placed within a quartz tube connected to primary

vacuum (10^{-3} mbar), an induction heater was used to heat the alloys to an estimated temperature of ($\geq 1600^\circ\text{C}$) in ~ 10 s.

Simultaneous thermal analysis(STA):

The thermal analysis was performed using a STA 449 F3 JUPITER (Netzsch), where each sample was placed in alumina crucible (30 μL), heated at $10^\circ\text{K}/\text{min}$ and thermally cycled three times between 900°C and 700°C . The samples were under a nitrogen flow (80mL/min) to prevent oxidation. The sample mass ranged from 42-240 mg.

Scanning Electron Microscopy (SEM):

Scanning electron microscopy (SEM) was performed using an FEI QUANTA 250, working between 5 and 30 kV, and operated in high vacuum mode. The SEM is equipped with Schottky field emission gun and Everhart-Thornley detector for (secondary electrons).

Results

DSC results for the 83% Cu copper-silicon binary (Figure 1) revealed notable differences among synthesis methods. The DSC analysis showed two separate peaks, suggesting a slightly off-eutectic composition, maybe due to partial oxidation under air so weighing errors or partial completion of the targeted alloy. Larger total masses used in the blowtorch and furnace synthesis reduce the proportional uncertainty, however these DSC results don't demonstrate any heterogeneity.

The induction sample presented the highest latent heat at approximately 178.9-210.6 J/g, suggesting it is closer to the eutectic point.

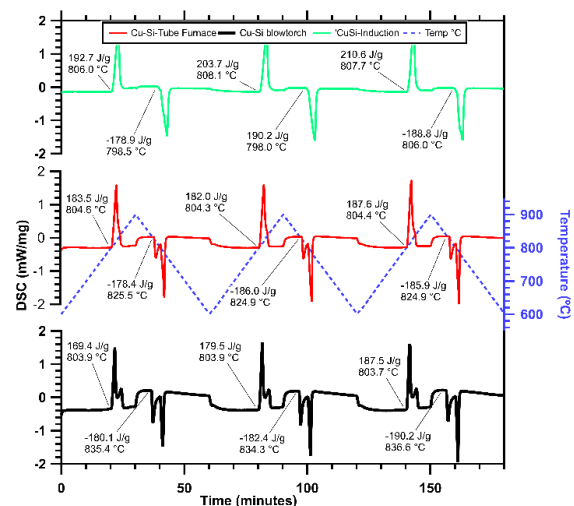


Figure 1: DSC thermograph results of Cu-Si binary alloy synthesised via (top):induction:(middle)tube furnace:(bottom) Blowtorch.

The SEM observations of the samples revealed various microstructures, as it can be seen in Figure 2, Figure 3, and Figure 4. Notably present in each composition are characteristic dark dendrites, featuring an atomic composition of 1.46% Cu and 98.54% Si, existing within a $\text{Cu}_3\text{Si}-\eta''$ matrix. This matrix, comprising 78.67% Cu and 21.33% Si, signifies a eutectic reaction. Figure 2 displays a composition with larger dendrites dispersed sparingly throughout the sample as observed in other works [4]. In Figure 3, larger dendrites are observable, while Figure 4 show a significant proportion of smaller dendrites and a porous structure. These dendrites are indicative of samples exposed to rapid cooling, a result of the small sample size in the DSC crucible and immediate removal of the heat source as the induction heater is switched off.

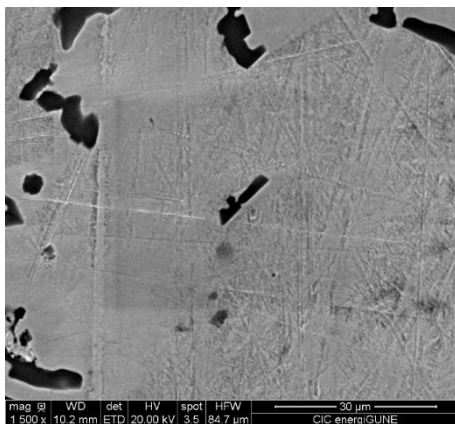


Figure 2: SEM image of $\text{Cu}_{83}\text{Si}_{17}$ eutectic composition synthesised by blowtorch method

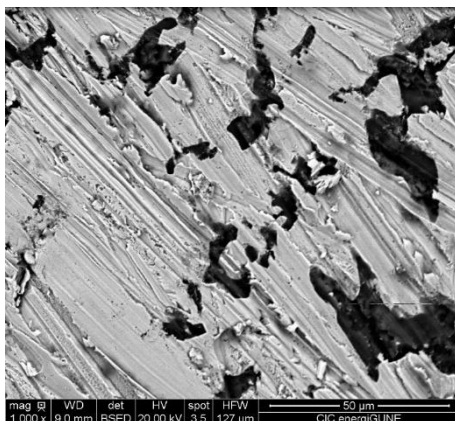


Figure 3: SEM image of $\text{Cu}_{83}\text{Si}_{17}$ eutectic composition synthesised by furnace method

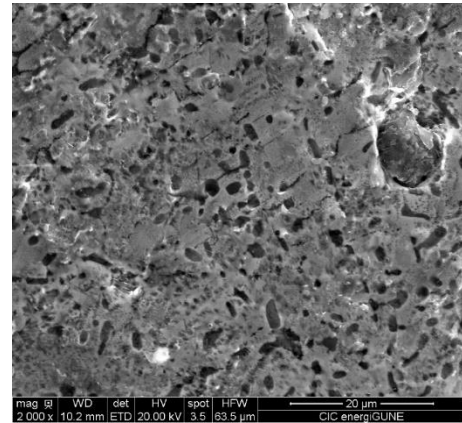


Figure 4: SEM image of $\text{Cu}_{83}\text{Si}_{17}$ eutectic composition synthesised by induction method.

The finer dendritic structures, evident in SEM images, contribute to an increased solid-liquid interface per unit volume. This heightened interface, where latent heat is absorbed or released during solidification, can result in a potentially higher latent heat in alloys with smaller dendrites. Additionally, the refined microstructure associated with smaller dendrites impacts the distribution of phases and atom arrangement, further influencing variations in latent heat compared to alloys with coarser dendritic structures [9].

Conclusions

The binary eutectic $\text{Cu}_{83}\text{Si}_{17}$ emerges as a promising high enthalpy phase change material suitable for incorporation into HEATERNAL PCM ceramic composite bricks.

During the preliminary stages of latent heat analysis in PCM selection, it is crucial to exercise caution in the choice of synthesis methods. Variations in latent heat recordings may be attributed to incomplete eutectic formation or the influence of dendritic growth. As a key component of the HEATERNAL TES system it is important to consider the effects on the measurement of latent heat when up-scaling to a larger system.

Acknowledgment

This document has been prepared within the framework of IEA ES TCP. This project has received funding from the European Union's Horizon Europe

research and innovation programme under grant agreement No 101103921, HEATERNAL.

References

- [1] S. Khare, M. Dell'Amico, C. Knight, S. McGarry, Selection of materials for high temperature latent heat energy storage, *Solar Energy Materials and Solar Cells* 107 (2012) 20–27. <https://doi.org/10.1016/j.solmat.2012.07.020>.
- [2] R. Fukahori, T. Nomura, C. Zhu, N. Sheng, N. Okinaka, T. Akiyama, Thermal analysis of Al–Si alloys as high-temperature phase-change material and their corrosion properties with ceramic materials, *Applied Energy* 163 (2016) 1–8. <https://doi.org/10.1016/j.apenergy.2015.10.164>.
- [3] X. Li, H. Wang, H. Wang, S. Kim, K. Esfarjani, Z. Ren, G. Chen, Metallic Composites Phase-Change Materials for High-Temperature Thermal Energy Storage, in: American Society of Mechanical Engineers Digital Collection, 2013. <https://doi.org/10.1115/ES2013-18395>.
- [4] L. Soldi, A. Laplace, M. Roskosz, S. Gossé, Phase diagram and thermodynamic model for the Cu–Si and the Cu–Fe–Si systems, *Journal of Alloys and Compounds* 803 (2019) 61–70. <https://doi.org/10.1016/j.jallcom.2019.06.236>.
- [5] X. Yan, Y.A. Chang, A thermodynamic analysis of the Cu–Si system, *Journal of Alloys and Compounds* 308 (2000) 221–229. [https://doi.org/10.1016/S0925-8388\(00\)00983-X](https://doi.org/10.1016/S0925-8388(00)00983-X).
- [6] K. Sufryd, N. Ponweiser, P. Riani, K.W. Richter, G. Cacciamani, Experimental investigation of the Cu–Si phase diagram at $x(\text{Cu}) > 0.72$, *Intermetallics* 19 (2011) 1479–1488. <https://doi.org/10.1016/j.intermet.2011.05.017>.
- [7] B. Hallstedt, J. Gröbner, M. Hampl, R. Schmid-Fetzer, Calorimetric measurements and assessment of the binary Cu–Si and ternary Al–Cu–Si phase diagrams, *Calphad* 53 (2016) 25–38. <https://doi.org/10.1016/j.calphad.2016.03.002>.
- [8] Y. Ge, N. Sheng, C. Zhu, Macroencapsulated Cu Si phase change material by in situ alloying formation for high temperature thermal energy storage over 800 °C, *Journal of Energy Storage* 72 (2023) 108258. <https://doi.org/10.1016/j.est.2023.108258>.
- [9] R. Trivedi, W. Kurz, Dendritic growth, *International Materials Reviews* (1994). <https://doi.org/10.1179/imr.1994.39.2.49>.

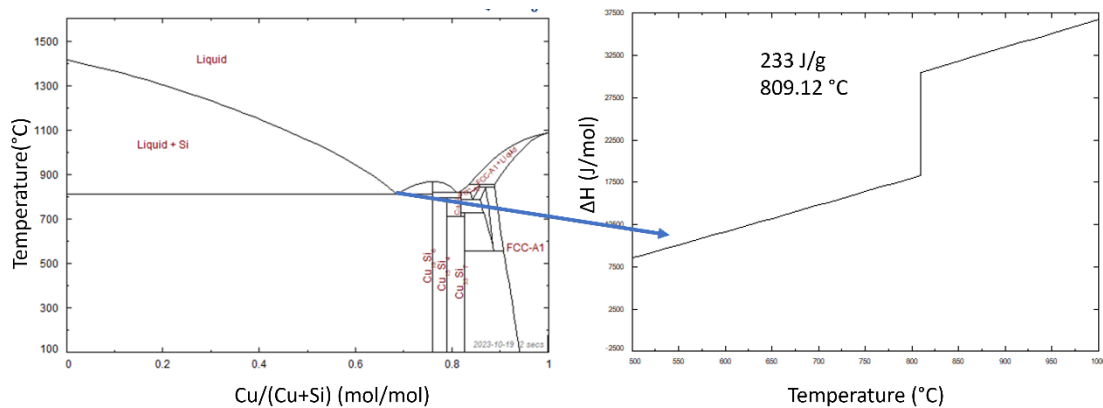


Figure 5: CALPHAD calculations of the copper – silicon binary system generated using FACTSage databases FTlite and ELEM the calculated enthalpy of the eutectic $\text{Cu}_{83}\text{Si}_{17}$ (wt%) is highlighted



Methodology for integrating renewable energy and thermal storage systems in the electricity market

M. Carmen Pavón-Moreno^{1,*}, Antón Lopez-Roman¹, Cristina Prieto^{1,*}

¹ Department of Energy Engineering, University of Seville, 41092 Sevilla, Spain

*Corresponding author e-mail: mpavonm@us.es; cprieto@us.es

Abstract

The integration of hybrid renewable energy sources with energy storage devices in the electricity market has become an important topic nowadays. The intermittent nature of renewable energy makes the need for storage and a methodology that allows optimized operation of each of the energy sources and storage become especially important. To address these challenges, a plant configuration is proposed that combines wind, photovoltaic and solar thermal technology, complemented by electric heaters and storage systems. This article proposes a methodology that optimises the approaches for each of the operating situations of the analysed plant model, maximizing the integration of renewable energy in the current electricity market and defining a series of strategies to achieve the proposed the objective of reducing the use of conventional energy sources.

Keywords: Hybridization, Grid dispatchability, Decarbonization, Thermal Energy Storage

Introduction

Nowadays, the energy transition path is being followed worldwide with short-term goals of decarbonization and integration of renewable energy (Mufutau Opeyemi, 2021). Therefore, it is worth exploring whether renewable energy is ready to support the power demand and satisfy the requirements of the electricity market (Maisanam et al., 2021).

The changes in which the world energy sector is immersed mean that the different renewable technologies that exist to face this challenge cannot be considered competition among themselves (Xu et al., 2022). Said technologies must be considered as complementary, with hybridization being the strategic key to the development of renewable electricity generation plants with high dispatchability and competitive costs compared to conventional plants based on fossil fuels (Ju et al., 2017).

Industrial processes, unlike the tertiary and residential sectors, demand a higher proportion of heat than electricity. This is why the integration of renewable energy into these processes must consider thermal components that replace fossil generation systems.

In this matter, the integration between renewable energy sources and thermal storage systems is one of the solutions being evaluated (Zurita et al., 2020). The combination of technologies such as wind, photovoltaic and solar thermal will provide a high degree of flexibility to the final solution (Liu et al., 2023). In addition, the proposed hybridization will

achieve a drastic reduction in final costs while maintaining a high level of dispatchability due to the presence of large capacity storage systems (Valenzuela et al., 2017).

However, the excessive increase of renewable energy in power grids will produce curtailment, or situations of oversupply, which could even cause negative electricity market prices (Prokhorov & Dreisbach, 2022), long-term thermal storage takes on double relevance. This is presented as a key solution to address the challenges associated with the intermittency of renewable sources, making it essential to ensure the robustness of the electricity supply and stable capacity of the energy mix (Zhai et al., 2017). To further improve the dispatchability of a hybrid system and reduce wasted renewable energy during times of lower electricity prices, electric heaters are being incorporated into the system with the aim of transforming excess electrical energy into thermal energy that can be stored (Liu et al., 2019; Pardillos-Pobo et al., 2023).

To challenge these objectives, this study proposes a plant configuration that combines wind, photovoltaic, and solar thermal technology, complemented by electric heaters and storage systems. Managed by an optimization model of renewable hybrid plant operation strategies that can guarantee the correct balance of the grid by using energy storage systems.

Plant Description

The plant model analysed is made up of wind farm, photovoltaic and solar thermal technology, complemented by electric heaters and storage systems, as shown in Figure 1. All technologies used have a certain maturity, except the operation of the electric salt heater, which in the scope of this study will be analysed in detail. Finding a degree of synergy between all of them, together with the needs of the current electricity market, is essential to achieve the objective proposed.

Electrical energy production is carried out through the wind farm, the photovoltaic plant, and the power block of the solar concentration plant. Priority is given to non-manageable renewable generation, such as photovoltaic and wind. These technologies will be connected to the grid and at the same time to the electric storage and heater. Electric storage in electric batteries, which provide a quick response to cover the transitions of electricity generation with different renewable technologies, providing grid stability.

Regarding concentrated solar power technologies, parabolic trough collectors are used because they are more commercially proven and less risky. However, it can reach lower temperature, the series connected electric heater is used to provide the same temperature range as in the solar tower configuration.

The thermal energy storage system comprises two molten salts tanks. One of them contains the salt at a higher temperature (hot tank) and the other one accumulates the salt at a lower temperature (cold tank). Large capacity thermal storage in molten salts through an innovative configuration that includes the fast reactive electric heater for heating solar salts. This module will allow to charge the thermal storage by means of wind, photovoltaic energy to or the grid itself, according to the operation strategies that will be analysed in the following section.

Electrification plus thermal storage allows the direct generation of electricity and heat simultaneously and the release of heat on a delayed basis. This makes it possible to significantly increase renewable penetration in processes.

The proposed solution achieves the integration of renewable energy in the current electricity market, with the fundamental role of thermal storage.

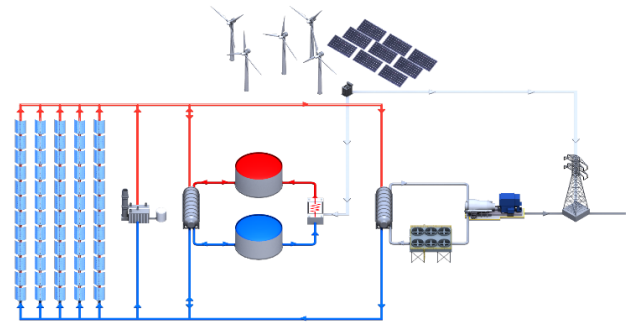


Figure 1. Scheme of the analysed plant

Methodology

This article provides a methodology to design the optimal operation of the plant presented above, integrated into the characteristics of the current electricity market, Figure 2. Short-term management optimization models of renewable hybrid configurations will be developed that can guarantee the correct balance of the grid using electric battery systems, with fast and short operation, as well as thermal storage of molten salts, which guarantee a longer storage time and more stability.

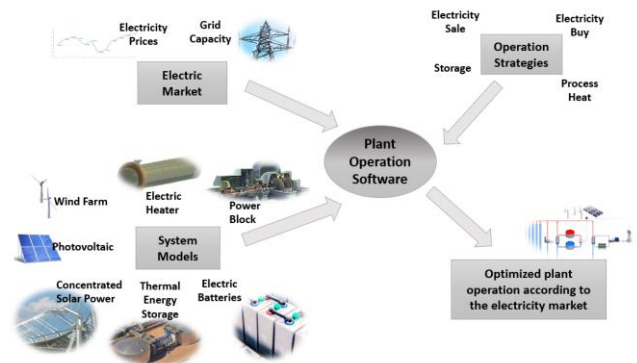
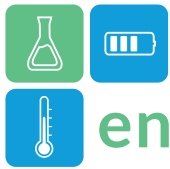


Figure 2. Proposed methodology

Firstly, the behaviour of each of the systems has been analysed: renewable energy production, power block, solar thermal, storage, both thermal and electrical, as well as the electric heater. This last equipment requires a complementary study, since it is not yet commercialized, it is necessary to know its real behaviour, such as knowing possible dead zones, freezing of salts, corrosion, degradation. A model has been obtained for each of the systems which, based on certain input variables evaluates the behaviour of each of them and, therefore, of the plant.

Subsequently, the characteristics of the current electricity market have been studied, to define



operating strategies. The phenomenon defined above as curtailment, for grid power generators, is the reduction of production below what could have been produced, because the transmission grid is not capable of supporting the full production of renewable generation. Therefore, the methodology will always analyse the grid capacity and the prices of the electricity market.

The evaluation of the electricity market and the plant's energy generation, mainly depending on meteorological conditions, are incorporated into the plant's operation optimization software, determining at each moment which strategy is the most convenient to carry out. Therefore, it is necessary to develop operation strategies that allow maximum use of renewable production, minimizing possible curtailment situations, adding value to long-term thermal storage.

The main operating strategies are presented in Figure 3 (orange rectangles), as well as the systems that are involved in them.

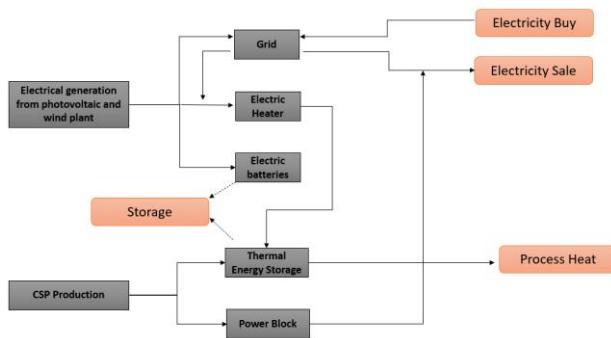


Figure 3. Definition of operation strategies

The input variables for decision making are renewable generation and the state of the electricity market, in terms of price curve and available grid capacity.

The main operating strategies are based on the storage charging cycle mode, since as we said previously, thermal storage is the key to decarbonization. The discharge cycle mode will be determined by the process, the storage gives up its energy (*Process Heat*).

During the period of maximum production, if the price of electricity is low, the thermal storage is charged first (*Storage*). For this purpose, both the concentrating solar effect and other renewable energy sources are used, passing it through the electric heater in the latter case. The temperature of the salts stored in the hot tank can also be increased with this equipment. Electricity can be purchased from the grid to charge storage if required (*Electricity Buy*). The objective is to obtain enough stored energy for subsequent consumption during peak periods of electricity prices.

If the price of electricity is high and there is energy production, both from photovoltaics and wind, as well as CSP, it can be poured into the grid (*Electricity Sale*). Previously, it is necessary to also leave the TES charged.

Heat storage allows electricity from low demand or very low prices to be transferred to times of high demand and more competitive prices. Therefore, it is possible to increase the use of renewable energy, minimize the cost of operating the processes, or even obtain a certain benefit from the sale of energy. The surplus electrical energy generated represents an opportunity that can be exploited through storage systems and increases the value of the electrical surplus.

The objective of optimization is to minimize energy costs, aligned with the current energy transition objectives and the electric market requirements.

Conclusions

This study proposes a plant configuration that combines wind, photovoltaic, and solar thermal technology, complemented by electric heaters and storage systems. Managed by an optimization model of renewable hybrid plant operation strategies that can guarantee the correct balance of the grid by using energy storage systems.

A methodology has been presented that allows the integration of renewable energies in the current electricity market. The surplus of electrical energy generated represents an opportunity that can be exploited using storage systems, in which the conversion of potential discharges of electrical energy of renewable origin into thermal energy or other types of energy represents an opportunity. The objective of optimization is to minimize energy costs, aligned with the current energy transition objectives and the electric market requirements.

This proposal can be implemented in a multitude of CSP plants that currently exist, the changes would involve only the generation of renewable energy and incorporate some elements, such as the electric heater. In this way, the decarbonization objectives currently proposed and the integration of renewable energies in the electricity market would be achieved, without wasting them their generation potential at curtailment moments.



Acknowledgment

This work was partially funded by the Ministerio de Ciencia e Innovación de España (TED2021-132216A-I00).

References

- Ju, X., Xu, C., Hu, Y., Han, X., Wei, G., & Du, X. (2017). A review on the development of photovoltaic/concentrated solar power (PV-CSP) hybrid systems. *Solar Energy Materials and Solar Cells*, *161*, 305–327. <https://doi.org/10.1016/j.solmat.2016.12.004>
- Liu, H., Zhai, R., Fu, J., Wang, Y., & Yang, Y. (2019). Optimization study of thermal-storage PV-CSP integrated system based on GA-PSO algorithm. *Solar Energy*, *184*, 391–409. <https://doi.org/10.1016/j.solener.2019.04.017>
- Liu, H., Zhai, R., Patchigolla, K., Turner, P., Yu, X., & Wang, P. (2023). Multi-objective optimisation of a thermal-storage PV-CSP-wind hybrid power system in three operation modes. *Energy*, *284*. <https://doi.org/10.1016/j.energy.2023.129255>
- Maisanam, A. K. S., Biswas, A., & Sharma, K. K. (2021). Integrated socio-environmental and techno-economic factors for designing and sizing of a sustainable hybrid renewable energy system. *Energy Conversion and Management*, *247*. <https://doi.org/10.1016/j.enconman.2021.114709>
- Mufutau Opeyemi, B. (2021). Path to sustainable energy consumption: The possibility of substituting renewable energy for non-renewable energy. *Energy*, *228*. <https://doi.org/10.1016/j.energy.2021.120519>
- Pardillos-Pobo, D., González-Gómez, P. A., Laporte-Azcué, M., & Santana, D. (2023). Thermo-economic design of an electric heater to store renewable curtailment in solar power tower plants. *Energy Conversion and Management*, *297*. <https://doi.org/10.1016/j.enconman.2023.117710>
- Prokhorov, O., & Dreisbach, D. (2022). The impact of renewables on the incidents of negative prices in the energy spot markets. *Energy Policy*, *167*. <https://doi.org/10.1016/j.enpol.2022.113073>
- Valenzuela, C., Mata-Torres, C., Cardemil, J. M., & Escobar, R. A. (2017). CSP + PV hybrid solar plants for power and water cogeneration in northern Chile. *Solar Energy*, *157*, 713–726. <https://doi.org/10.1016/j.solener.2017.08.081>
- Xu, T., Gao, W., Qian, F., & Li, Y. (2022). The implementation limitation of variable renewable energies and its impacts on the public power grid. *Energy*, *239*. <https://doi.org/10.1016/j.energy.2021.121992>
- Zhai, R., Liu, H., Chen, Y., Wu, H., & Yang, Y. (2017). The daily and annual technical-economic analysis of the thermal storage PV-CSP system in two dispatch strategies. *Energy Conversion and Management*, *154*, 56–67. <https://doi.org/10.1016/j.enconman.2017.10.040>
- Zurita, A., Mata-Torres, C., Cardemil, J. M., & Escobar, R. A. (2020). Assessment of time resolution impact on the modeling of a hybrid CSP-PV plant: A case of study in Chile. *Solar Energy*, *202*, 553–570. <https://doi.org/10.1016/j.solener.2020.03.100>



Modeling multi-basin water-gravel thermal energy storages with STORE

Christoph Bott^{1,*}, Peter Bayer¹

1 Martin Luther University Halle-Wittenberg, Applied Geology, Von-Seckendorff-Platz 3, 06120 Halle, Germany

*Corresponding author e-mail: Christoph.Bott@geo.uni-halle.de

Abstract

Seasonal thermal energy storage is crucial for the global energy transition, addressing the intermittent nature of renewable sources like solar thermal and wind power. As communities embrace sustainable yet variable sources, efficient energy storage becomes essential for grid stability, reducing reliance on fossil fuels, and optimizing energy utilization. Meeting high requirements for modern district heating systems is vital, but the substantial costs of new systems hinder global market availability. Here, the innovative concept of reusing existing basin structures in transforming areas represents an opportunity that has been overlooked so far. For multiple, subdivided infrastructure compounds, challenges for design, construction, and operation are apparent. We introduce the component-based STORE model for simulating various water-gravel thermal energy storage combinations. This facilitates a realistic computer-based implementation to scrutinize crucial technical issues like optimal interconnection and insulation designs. Effects of multi-storage systems and their thermal interference are analyzed, revealing ideal combinations and optimal modes of operation. Accordingly, the study deduces favorable application windows for combined basin structures and strategies to enhance overall efficiency.

Keywords: Seasonal thermal energy storage; Water gravel storage; Energy transformation; Site development

Introduction

Seasonal thermal energy storage

Thermal energy storage (TES) serves daily to seasonal demands, with short-term storage prevalent especially in residential and industrial buildings. Large-scale seasonal thermal energy storage (sTES) involves one or two cycles per year. It optimizes locally generated thermal energy for decentralized district heating and cooling (DHC) networks and can integrate sources like industrial waste heat, data centers, solar thermal, or geothermal. Economically viable sTES require low installation costs, high capacity levels, efficient heat transfers, sustainable materials, and high efficiency (Bott and al., 2019).

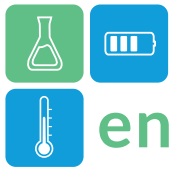
Geothermal sTES utilize the natural subsurface through aquifer or borehole heat exchangers (ATES, BTES) or water-filled caverns (CTES). They depend strongly on suitable site conditions, e.g., for BTES, the absence of groundwater (Fleuchaus and al., 2018). As site-independent solutions, three artificial, ground-based, large-scale concepts are: (i) pit TES involve sloped pits sealed with plastic foils, filled with water, and insulated at the top, (ii) tank TES are highly insulated facilities with various geometries based on static structures, and (iii) water-gravel thermal energy storages (WGTES) feature a two-component filling and, indirect charging/discharging systems (Bott and al., 2019).

Reno-sTES and multi-sTES

In past sTES projects, large expenses were incurred through excavation, static components, and sealing layers, reducing economic viability (Schmidt, 2012). To overcome this issue, a novel approach involves reusing idle structures: Reusing existing infrastructure as renovated “Reno-sTES” could eliminate cost-intensive steps associated with new constructions. Further, multiple basins may exist in locations with existing infrastructures, posing new research questions for combined “multi-sTES”. One case for this is the IN-Campus (Faigl and al., 2019) in Ingolstadt, Germany. There, compound concrete basins, formerly used for wastewater treatment, are available (Figure 1), and currently investigated for reuse as “Reno-WGTES”.



Figure 1: Multi-basin of infrastructures at the IN-Campus (Germany), pictured from different angles (Stettner and al. 2016).



When multiple separate basin setups are available, various sTES combinations with different configurations, designs, and operation strategies (i.e., hydraulic connections) can be explored. Thus, the system allows subdividing one basin into multiple sub-sTES, enabling different designs and optimized layouts for specific applications. Modelling tools for assessing different layouts, however, are rare or computationally intense.

STORE-Model

Concept and features

Accurate simulation is vital for reliable sTES planning. In this respect, existing models are often limited concerning the complexity systems, especially those with varied geometries. To address these issues, the currently developed model “STORE” (Bott and al., 2022) takes a new 2.5-D approach, combining the benefits of a building component-based resolution with extensive parameterization and versatile evaluation capabilities. In contrast to complex, computationally intensive 3-D numerical models, STORE simulates sTES building components, linked by process-based transfer functions, governing thermal energy exchange, and determining the thermal regime (Figure 2).

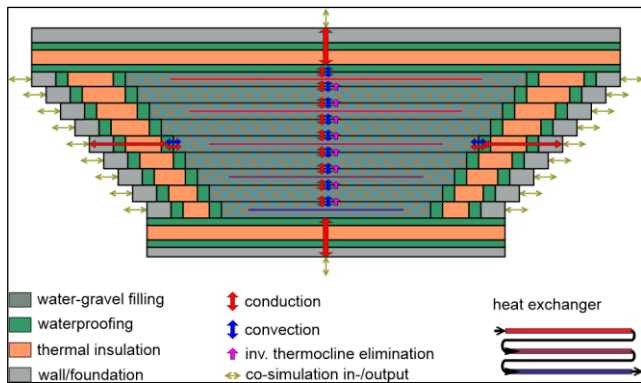


Figure 2: STORE-Model with modified boundary conditions for co-simulation (after Bott and al., 2022; 2023).

Accordingly, STORE is structured as a vertically layered representation for the filling, and it is further organized – on each layer – in four pre-defined spatial directions (i.e., north/east/south/west for a cuboidal structure). Each of these directions contains the building components of the sTES shell as thermal masses. Between these, the heat transfer processes (i.e., convection, and conduction) are simulated. Analytical models and standard correlations for heat exchangers implement the operation strategy of the storage (i.e., charging/discharging). Further details of the model design as well as its representation in implemented in Simscape can be found in Bott and al. (2022).

A novel development (Bott and al., 2023) adopts a co-simulation approach, combining STORE with a 3-D numerical multi-physics model, implemented in COMSOL. The latter simulates thermal processes and subsurface water flow in the ambient sTES environment, whereby co-simulation is facilitated by a functional mock-up unit. Thereby, the co-simulation benefits from minimum computational demands due to different optimal time steps in the model components.

Enhancement: The multi-STORE model

Multi-sTES may represent subdivided infrastructure compounds. Optimization of their design, construction, and operation represents a challenge. Different temperature levels and thermal losses of the individual structures have to be considered and monitored. To simulate multi-sTES with STORE, restructuring and adjustments to the existing version are necessary.

As an example, we assume a network of three adjacent basins. Thus, in the Simscape implementation, the filling is separated into three sub-systems and internal walls are added, including sealing and insulation components. This allows the basins to be segregated, enabling different temperature levels with reduced interaction. Furthermore, each filling is considered to have individual heat exchangers. Here the flexible parameterization of STORE proves to be advantageous, as each sub-basin may be designed differently (e.g., materials used, insulation thicknesses, heat exchanger levels, etc.).

Thermal energy transfer to the environment within the COMSOL model is also adjusted for each basin (Figure 3). To this end, the specific partial interface areas to the ground are assigned to the individual sub-basins on each layer in the relevant directions. All other processes are consistent with the description presented by Bott and al. (2023).

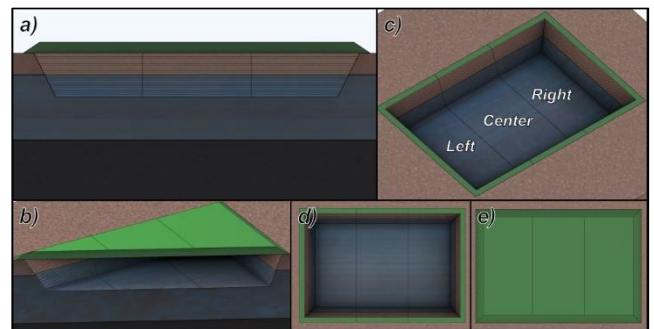
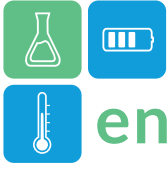


Figure 3: Different illustrations (a–b: side views, c–e: top views with and without top cover) of the (COMSOL-) multi-sTES model.

Using the enhanced STORE model, it is now possible to study temperature adjustments for each sub-basin, and this way to optimize the overall efficiency of the compound sTES. Therefore, the data considered for



evaluating the multi-sTES model includes individual filling temperatures, the individual heat losses of the single basins, as well as the recovered energy quantities.

Parameter study

Reference case design

The composite system consisting of three sub-basins considered in this study is a steeply sloped pit (slope angle 1:0.5) with a depth of 4 m (Figure 3). The combined length is 20 m, and each basin has the same width of 10 m. The total volume is around 1,542 m³.

As typical for WGTES, all sub-basins are filled with a water-gravel mixture (effective thermal conductivity $\lambda_{\text{eff}} = 2.4 \text{ W m}^{-1} \text{ K}^{-1}$, heat transfer coefficient for convection $\alpha = 20 \text{ W m}^{-2} \text{ K}^{-1}$, specific heat capacity $c_p = 1,545 \text{ J kg}^{-1} \text{ K}^{-1}$, density $\rho = 1,928 \text{ kg m}^3$). For insulation, foam glass gravel ($\lambda_{\text{eff}} = 0.05 \text{ W m}^{-1} \text{ K}^{-1}$, $\rho = 160 \text{ kg m}^3$, $c_p = 900 \text{ J kg}^{-1} \text{ K}^{-1}$) is used, enclosed by a 0.0015 m thick PVC foil. The insulation has a thickness of 0.5 m at the top and 0.3 m at the bottom in all scenarios. The external walls of the overall composite system are also equipped with insulation measuring 0.3 m. The supporting structure of the reused pit is made of concrete ($\lambda_{\text{eff}} = 1.0 \text{ W m}^{-1} \text{ K}^{-1}$, $c_p = 1,000 \text{ J kg}^{-1} \text{ K}^{-1}$, $\rho = 2,600 \text{ kg m}^3$), whereby the self-supporting roof and external walls are 0.2 m thick, the internal walls measure 0.1 m, and the foundation has a thickness of 0.3 m. The multi-sTES is covered with a 1.5 m thick layer of dry soil ($\lambda_{\text{eff}} = 1.4$, $c_p = 2,000 \text{ J kg}^{-1} \text{ K}^{-1}$, $\rho = 2,100 \text{ kg m}^3$).

Around the storage facility, the subsurface is modeled as consisting of three layers with standard values for soil types (Figure 3). The bottom layer consists of 8 m of impermeable clay ($\lambda_{\text{eff}} = 2.2$, $c_p = 2,250 \text{ J kg}^{-1} \text{ K}^{-1}$, $\rho = 2,500 \text{ kg m}^3$, hydraulic conductivity $K = 1 \cdot 10^{-10} \text{ m s}^{-1}$, porosity $n = 0.05$). The fully saturated gravel layer above (thickness of 6.75 m, $\lambda_{\text{eff}} = 1.8 \text{ W m}^{-1} \text{ K}^{-1}$, $c_p = 2,400 \text{ J kg}^{-1} \text{ K}^{-1}$, $\rho = 2,200 \text{ kg m}^3$, hydraulic conductivity of $K = 1 \cdot 10^{-3} \text{ m s}^{-1}$, $n = 0.28$), represents a stagnant aquifer without groundwater flow. The vadose zone consists of sand and is 2.25 m thick ($\lambda_{\text{eff}} = 1.4 \text{ W m}^{-1} \text{ K}^{-1}$, $c_p = 2,000 \text{ J kg}^{-1} \text{ K}^{-1}$, $\rho = 2,100 \text{ kg m}^3$, $K = 5 \cdot 10^{-5} \text{ m s}^{-1}$, porosity of $n = 0.45$). The lateral size of the COMSOL model is set to two times the multi-sTES length and width.

Environmental and operational boundary conditions

The multi-storage facility is operated with vertically evenly distributed, indirect heat exchanger coils on five levels and with a diameter of 0.05 m. In total, the surface area of the heat exchangers for all sub-sTES amounts to around 2,000 m². Synthetic load profiles are

used for the simulation (Figure 4), whereby the supply temperature of the charging flow (from around the beginning of March to around mid-September) equals 90 °C while the discharge flow temperature reaches 45 °C during the rest of the year.

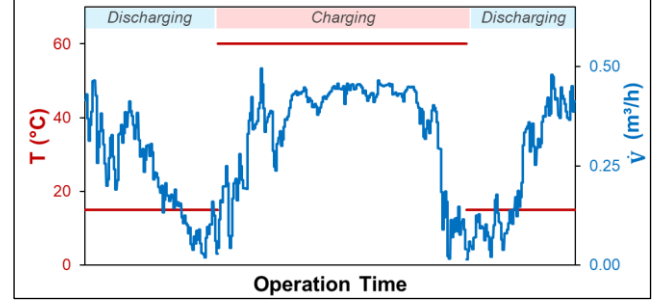


Figure 4: sTES operation datasets used in the parameter study.

Similarly, synthetic input data is applied to model the environmental boundary conditions of the storage facility. To this end, the annual air temperature profile is calculated by Eq. 1:

$$T = 10 - 10 \cos\left(\frac{2\pi t}{8760}\right) \quad (1)$$

Similarly, to represent seasonally and daily varying solar irradiation, the following Eq. 2 is used:

$$\ddot{q} = 0.8 - 0.8 \cos\left(\frac{2\pi t}{24}\right) + 0.8 - 0.8 \cos\left(\frac{2\pi t}{8760}\right) \quad (2)$$

Scenarios for hydraulic connection and insulation

An overview of the scenarios considered in this study is presented in Table 1. They consist of a variable arrangement of the hydraulic combination of the sub-WGTES (either in series from left to right (Figure 3c), or in parallel). Furthermore, the scenarios include cases where the central basin is isolated from the others by employing internal thermal insulation. In this cascaded multi-storage setup, the central basin is intended to be partly insulated by surrounding sub-sTES.

Table 1: Scenarios of the parameter study presented in this paper.

Scenario ID	Insulation	Hydraulic connection
P-I	Internal walls: high	Left Center Right
S-I	Internal walls: high	Center → Left → Right
P-0	Internal walls: low	Left Center Right
S-0	Internal walls: low	Center → Left → Right

Five years of operation of the multi-sTES are simulated for all scenarios. In this process, the Simscape model is run with hourly time steps, while a communication step size of 14 days is utilized for the co-simulation.

Results

Hydraulic interconnection

Results of the STORE simulations show that operation with serial charging and discharging yields an 8.8% increase in efficiency for the uninsulated compound system (S-0: 50.2% vs. P-0: 46.2%, Figure 5a). In this

S-0 scenario, the amount of energy recovered is 280 MWh, which is 13.5% more than in scenario P-0 with a parallel hydraulic connection (247 MWh).

The temperatures of the sub-TES are most different in the serial scenarios: In scenario S-I, the maximum range of the mean temperatures of 8.3 K between the sub-basins is reached (left: 36.2 °C, center: 45.7 °C, right: 27.9 °C). In contrast, the mean temperatures are distributed more uniformly in the scenarios with parallel operation, where the highest compound sTES maximum temperature is obtained (P-0: 52.5 °C).

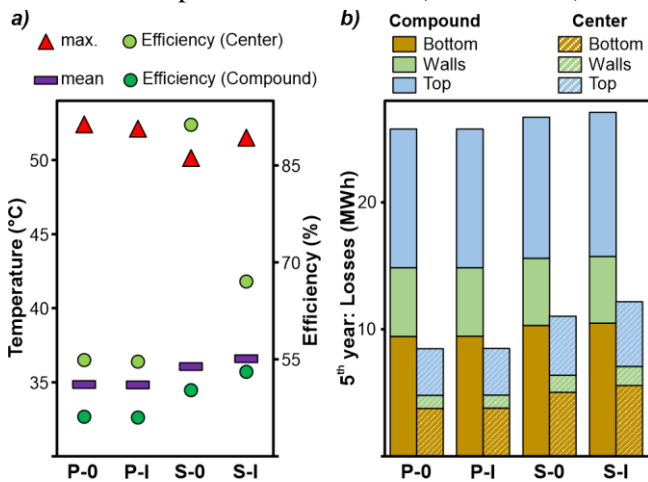


Figure 5: Key results overview: Temperatures and efficiency over the total operation period (a); losses in the last simulated year (b).

Benefits of central basin insulation

Further, results show that insulation of the central basin can be beneficial: the efficiency in scenario S-I increases to the maximum value of 91.3% for the central basin (Figure 5a). In this case, the basin is efficiently insulated by its surrounding sub-sTES. Conversely, despite the increased temperatures, the scenarios with central basin insulation show no increase in thermal losses of the multi-sTES in the last simulated year (Figure 5b), amounting to 25.8 MWh for scenarios P-I / PI, and 26.7 MWh or 27.1 MWh for scenarios S-0 and S-I, respectively.

Insulating the central basin finally increases the mean filling temperatures in the central basin in the last simulated year. They reach 47.7 °C and 36.9 °C in scenarios S-I and P-I, respectively, compared to 44.2 °C and 36.8 °C in the uninsulated S-0 and P-0 scenarios, respectively, thus raising the capacity of the sub-sTES.

Conclusions

Reusing existing infrastructures for seasonal thermal energy storage (sTES) can reduce costs, but it limits design flexibility. Therefore, innovative approaches are required. One example of this is multi-sTES, which

consists of combined reused basin structures. In this case, research challenges involve designing, planning, and operating of this sTES solution.

Here, we present an enhanced version of the STORE model, to study the coupling of multiple sub-sTES units. Results of an exemplary case study reveal insights into the benefits of different hydraulic interconnections (parallel, serial) for charging and discharging and internal insulation variations of a multi-sTES consisting of three sub-WGTES facilities. While efficiencies can be increased by about 7.0%, and 5th-year losses reduced by 1.3 MWh (5.1%), it can be concluded for the example case that a design of the multi-sTES with serial hydraulic interconnection and internal insulation of the central sub-basin is most technically efficient.

For implementing multi-sTES, future research has to focus on technical issues (e.g., detailed hydraulics, optimal control implementation), and further work needs to analyze the potential benefits of multi-sTES with flexible operation and design compared to static integration of single units.

Acknowledgments

The authors thank Ryan Pearson for language edits. This study is financially supported by the EU Horizon Europe project INTERSTORES (no. 101136100).

References

- Bott, C. and al. (2019). State-of-technology review of water-based closed seasonal thermal energy storage systems. *Sust. Energ. Rev.*, 113, 109241.
- Bott, C. and al. (2022). Component-based modeling of ground-coupled seasonal thermal energy storages. *Appl. Therm. Eng.*, 118810.
- Bott, C. and al. (2023). Influence of thermal energy storage basins on the subsurface and shallow groundwater. *J Energy Storage*, under review.
- Faigl, M. and al. (2019). IN-Campus - Innovative Technologien, Smarte Energie: Stand: April 2019. AUDI Werksplanung / Planung Energie und Gebäudetechnik, Ingolstadt.
- Fleuchaus, P. and al (2017). Worldwide application of aquifer thermal energy storage – A review. *Sust. Energ. Rev.*, 94, 861-876.
- Schmidt, T. (2012). Große saisonale Wärmespeicher. In: 11. Tagung Wärme- & Kälteversorgung in der Energiestrategie Schweiz, 26.1.2012, Biel-Bienne.
- Stettner, C. and al. (2016). Untersuchungsbericht zur Zustandsbewertung der Behälter auf dem ehemaligen Bayernölgelände in Ingolstadt: Projektnummer 154094CS. Zilch + Müller Ingenieure GmbH, München.



Modelling of heat and moisture transfer through the lid of Pit Thermal Energy Storages

Tom Brand, Magdalena Berberich, Dirk Mangold
Solites, Stuttgart, Germany

Corresponding author e-mail: brand@solites.de

Abstract

In the past, in some Pit Thermal Energy Storages (PTES) a failed lid construction had to be replaced. In most cases, the reason for the failure of the lid is the accumulation of moisture in the thermal insulation with a resulting increase in heat loss. The presence of moisture inside of the lid has various causes, such as leaks in the synthetic liner, installation of an already moist insulating material and water vapour diffusion through the synthetic liner. Past studies according to Ochs et al. and Bauer et al. have shown that water vapour diffusion increases significantly, especially at high temperatures above 60 °C. At the same time, at high temperatures, the heat loss increases significantly due to the mechanism of the heatpipe effect. In order to avoid possible moisture accumulation and the associated damages, a simulation model for heat-coupled mass transfer is in development as part of the Efficient Pit research project (FKZ 03EN6007B – BMWK), which can appropriately represent the heat and mass transfer in PTES covers at high temperatures. In the course of Efficient Pit, data is to be collected from two laboratory PTES for comprehensive validation. The general aim is to develop an open-source tool as a planning support tool to support planners and investors for PTES.

Keywords: Pit Thermal Energy Storage, heat and moisture transfer, simulation, solar district heating, seasonal heat storage

Introduction

The concept of sensible heat storage for district heating networks has been investigated in Europe since the 1970s. (IEA DHC Annex XII, 2018) Pit Thermal Energy Storages (PTES) are considered to have the greatest potential due to their high flexibility of location and comparatively low construction costs but have still not achieved market-ready status.

Most of the cost are related to the construction of the lid. The lid has the task of reducing the heat losses of the PTES. Thus the materials are exposed to temperatures up to 95 °C and high concentrations of moisture due to diffusion through the floating liner.

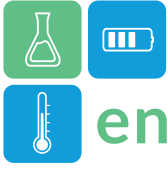
In the past, some lids had to be replaced after only a few years of operation because of moisture accumulation inside of the lid (Sifnaios, 2022). In few cases the storage has been taken out of service completely.

The presence of moisture inside of the lid had various causes, such as leaks in the floating- or topliner, installation of an already moist insulating material and water vapour diffusion through the synthetic liner at high temperatures, example see figure 1 (Sørensen, 2015, Sifnaios, 2022).



Figure 1: Shrinkage of an insulation material in Marstal - Solites

Unlike the other causes, the latter cannot be avoided by proper execution during the construction process. When using synthetic liners, there is currently no material that can withstand the high temperatures and moisture loads and at the same time guarantee a complete water vapour diffusion tightness. Past studies have shown that water vapour diffusion through the synthetic liner increases significantly with rising temperatures, especially above 60 °C (Ochs, 2009).



At the same time, at such high temperatures the heat transport inside of the insulation materials increases significantly due to the mechanism of the heatpipe effect which describes the interaction of spatially separated vaporisation and condensation of water in the insulation material as a porous medium. (Bauer et al. 2012)

Methodology

The target is to provide the general public with a validated calculation tool that describes the heat-coupled mass transfer in porous media, i.e. the insulation layers with appropriate accuracy.

This target is to be achieved in four steps:

1. Elaboration of the theoretical fundamentals of heat and mass transfer at elevated temperatures
2. Development of the model environment
3. Verification and validation with real data
4. Development of a user-friendly tool and publication

Theoretical Fundamentals

The numerical approach of heat-coupled mass transfer has been used in building physics since 1978 in (Krischer, 1994). Based on the model according to Krischer, the models according to Künzel and Grünewald were further developed (Künzel, 1994, Grünewald, 1997).

The scope of this study differs from the classic building physics approach, as temperatures above 60 °C are rarely relevant in building physics. In addition, moisture contents in the range of capillary water to supersaturation frequently occur in PTES lid constructions.

Ochs was the first to investigate heat and mass transfer with regard to the covering of PTES, taking into account material-specific, non-linear temperature dependencies above 60 °C (Ochs et al., 2009). The findings and results of Ochs are used as a reference in the development of the simulation model.

In the building sector, hygroscopic materials with small pore radii are often used (concrete, EPS, etc.) and therefore the advective component can be neglected. This approach without the consideration of convection is used in many established calculation tools.

However, the use of macroporous or bulk insulation materials is still state of the art, see PTES in Gram, Vojens, etc.. The high permeability of bulk materials like foam glass gravel (FGG) or expanded clay is associated with a higher convective fraction in the

mass- and energy-balance. This effect increases significantly, especially at elevated temperatures. For this reason, convective heat and mass transfer is also taken into account in this work in comparison to existing calculation tools.

Development of the model

The heat-coupled mass transfer in this work is described with a two-phase and two-component model (2p2c) based on the open-source calculation framework DuMu^x (dumux.org, 2023). The phases regard the aggregate states liquid and gaseous of the two components air and water. For both phases the heat-coupled mass transfer is described by the implicit solution of partial differential equations of the energy and mass balance. Both transport equations are strongly dependent on each other and cannot be solved separately.

Mass-balance:

$$\begin{aligned} & \phi \cdot \frac{\partial(\sum_{\alpha} \rho_{\alpha} \cdot X_{\alpha}^{\kappa} \cdot S_{\alpha})}{\partial t} \\ & - \sum_{\alpha} \nabla \cdot \left\{ \rho_{\alpha} \cdot X_{\alpha}^{\kappa} \cdot \frac{k_{r\alpha}}{\mu_{\alpha}} \cdot K(\nabla p_{\alpha} - \rho_{\alpha} \cdot g) \right\} \\ & - \sum_{\alpha} \nabla \cdot \left\{ \rho_{\alpha} \cdot D_{\alpha,pm}^{\kappa} \cdot \nabla X_{\alpha}^{\kappa} \right\} = 0 \end{aligned} \quad (1)$$

Energy-balance:

$$\begin{aligned} & \phi \cdot \frac{\partial(\sum_{\alpha} \rho_{\alpha} \cdot u_{\alpha} \cdot S_{\alpha})}{\partial t} + (1 - \phi) \cdot \frac{\partial \rho_s \cdot c_s \cdot T}{\partial t} \\ & - \sum_{\alpha} \nabla \cdot \left\{ \rho_{\alpha} \cdot h_{\alpha} \cdot \frac{k_{r\alpha}}{\mu_{\alpha}} \cdot K(\nabla p_{\alpha} - \rho_{\alpha} \cdot g) \right\} \\ & - \sum_K \nabla \cdot \left\{ D_{pm}^K \cdot \rho_g \cdot h_g^K \cdot \nabla X_g^K \right\} \\ & - \nabla \cdot (\lambda_{pm} \cdot \nabla T) = 0 \end{aligned} \quad (2)$$

Verification and Validation

Two different scenarios in 1D and 2D were considered for an initial verification of the model. For the 1D approach, reference was made to a simulation example according to (Ochs et al., 2009). In this approach, the transient moisture distribution in the thermal insulation of a heat storage is investigated under the influence of varying storage temperatures. Different simulation models (WUFI, DELPHIN, Ochs et al., DuMu^x) are compared with each other.

For the 2D analysis, a qualitative simulation of thermal conductivity tests in FGG at the IGTE of the University of Stuttgart was carried out. (Bauer et al., 2012) The aim was to verify whether inhomogeneities in the void distribution and the resulting flow paths of the water vapour can be accurately reproduced.

Figure 2 shows a thermal image recording of a 32/64 mm FGG bulk insulation in side profile. The storage side is imitated using a heating plate with a constant temperature at the bottom. The temperature distribution is measured and additionally visualized over the height of the FGG bulk insulation at different water contents by infrared thermography. (Bauer et al., 2012)

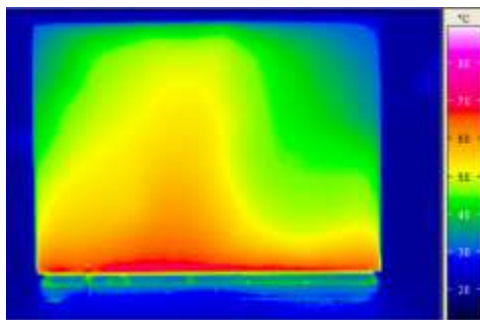


Figure 2: Thermal imaging of the heat conduction tests in FGG bulk insulation at the ITW University of Stuttgart (Bauer et al., 2012)

Humidity and temperature data in lids of PTES are currently very limited. Consequently, as part of the Efficient Pit research project, extensive measurements of temperature and humidity distributions are to be carried out in the lids of two large laboratory PTES. Under real conditions, the PTES are charched with hot water at up to 95 °C. Different heat insulating materials such as bulk insulations or sheet insulating materials are to be investigated.

Results and Discussion

Figure 3 shows the results of a qualitative, simulative reproduction of the thermal conductivity tests at the ITW. According to the tests, the formation of flow paths could be simulated due to inhomogeneities in the void distribution in coarse FGG fills. It could also be shown with a high conformity of the investigations that heat conduction in coarse FGG fills is no longer the dominant heat transfer mechanism, but that a strongly inhomogeneous temperature distribution occurs due to convection. Both the experiments and the simulations verified the heatpipe effect due to gravity.

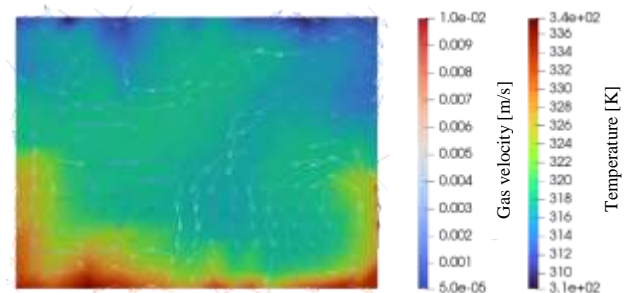


Figure 3: Own results of the simulative reproduction using DuMu^x of an FGG fill according to investigations at the ITW (Bauer et al., 2012)

In general, good agreement could be achieved with the temperature measurement results and the here shown comparison of the simulations and the thermal imaging of (Bauer et al. 2012). The verification was based on a qualitative approach due to high uncertainties in the material specifications.

An important prerequisite for modelling is an accurate characterization of the insulating material. Important variables for porous materials are the moisture storage function to describe the material moisture, the proportion of cavity accessible for mass transfer and information on the permeability of the porous medium. It has been shown that the determination of such parameters is currently associated with increased effort and is often only carried out under standard conditions. Consequently, methods must be developed in the future to characterize insulating materials at elevated temperatures.



Conclusions

- A model that represents reasonable heat and mass transfer processes in insulation layers at temperatures up to 95 °C could be created in DuMu^x
- The model provides an accurate representation of important heat transfer processes such as the heatpipe effect at high temperatures
- First verification were done by comparing DuMu^x in a 1D case with other established models and a qualitative comparison to thermal conductivity test at the ITW Stuttgart in a 2D view.
- Further validation will be carried out via the laboratory PTES of the Efficient Pit research project
- Material characteristics are often only determined for standard conditions; there is a need to develop new methods at elevated temperatures

Acknowledgment

This project has received funding from the German Ministry for Economic Affairs and Climate Action on the basis of a decision by the German Bundestag.

The sole responsibility for the content of this publication lies with the authors. It does not necessarily reflect the opinion of the funding organizations. Neither the funding organizations nor the authors are responsible for any use that may be made of the information contained therein.

References

Efficient Pit FuE, Forschungsvorhaben FKZ 03EN6007B des BMWK, Laufzeit 1.9.2021 bis 31.8.2025, Solites, Stuttgart

IEA DHC Annex XII, (2018) – Design Aspects for Large-Scale Aquifer and Pit Thermal Energy Storage for District Heating and Cooling. - <https://doi.org/10.1016/j.egypro.2018.08.223>

Ioannis Sifnaios (2022) – Dronninglund water pit thermal energy storage dataset - <https://doi.org/10.1016/j.solener.2022.12.046>

Per Alex Sorensen et al. (2015) - New cover solution for the pit heat storage in Marstal - EUDP File no. 63011-0089 | PlanEnergi 9520 Skørping

Fabian Ochs ITW (2009) - Modelling Large-Scale Thermal Energy Stores – Dissertation Universität Stuttgart - ISBN: 978-3-8322-8834-1

Bauer et al. (2012) – Solarthermie2000Plus: Wissenschaftlich-technische Begleitung des Förderprogramms Solarthermie2000Plus zu solar unterstützter Nahwärme und Langzeit-Wärmespeicherung – FKZ 0329607P

Krischer, O. et al. (1978) – Die wissenschaftlichen Grundlagen der Trocknungstechnik. Dritte Auflage, Springer-Verlag Berlin 1978.

Künzel (1994) – Verfahren zur ein- und zweidimensionalen Berechnung des gekoppelten Wärme- und Feuchtetransports in Bauteilen mit einfachen Kennwerten – Dissertation Universität Stuttgart | Wufi.de

John Grunewald (1997) – Diffusiver und konvektiver Stoff- und Energietransport in kapillarporösen Baustoffen – Dissertation TU Dresden 1997 – ISBN 3860051911, 9783860051917

DuMu^x - <https://dumux.org/>



Modelling of thermal storage systems using artificial intelligence

Edgar Felipe Rojas Cala, Ramón Bejar, Emiliano Borri, Carles Mateu, Luisa F. Cabeza*

GREiA Research Group, Universitat de Lleida, Pere de Cabrera s/n, 25001 Lleida, Spain

*Corresponding author e-mail: luisaf.cabeza@udl.cat

Abstract

In the search for new alternatives to optimize the TES tank design process, a study was carried out implementing the use of neural networks to reduce the resources and costs of modelling using CFD programs. For this purpose, an initial design of a basic TES tank was selected and a neural network based on the U-net model was trained to model the state of the design three seconds after the initial state provided by the user. The neural network model trained in this study has been shown to be capable of modelling TES tanks, but more robust models need to be generated in order for this technology to be easily integrated into any TES tank design process.

Keywords: TES tanks, Thermal energy storage (TES), artificial intelligence, neuronal networks

Introduction

Regardless of the energy source, structure or composition of a thermal energy storage (TES) system, they all have a storage tank (Cabeza et al., 2015), this component is crucial in the TES system, as the efficiency and ability to optimally using this type of energy depends on the tank capabilities and characteristics. Given the above, it is understandable that the design process of these tanks is time consuming and requires skilled personnel with knowledge of the different areas, and it is also understandable that this process requires computational modelling tools to understand the behaviour of the tank without wasting resources on prototypes with a high probability of failure.

However, even with all this technology and manpower, the design and modelling process for TES tanks is still long, tedious and costly (Pompei et al., 2023). If the process needs to be scaled up or simply made more competitive, current design and modelling methods are inadequate. There may be many solutions, but there is one that may stand out due to its low cost in resources (human or computational), time and novelty. This solution is the use of artificial intelligence for modelling in the TES tank design process.

To understand why the use of artificial intelligence, and more specifically neural networks, is an optimal solution for achieving scalability and reducing the resource consumption of the TES tank modelling process, it is necessary to understand how TES tanks are currently modelled using computational tools. Presently, computational modelling is based on the analytical representation of the behaviour of the TES tank; that is, it makes use of a number of mathematical

equations that model the behaviour over time of the different materials to be modelled; finally, it solves several higher order equations for multiple points located in a space that represents the TES tank. The computer solves finite equations in finite time spaces for finite elements within what it understands to be a deposit (Mostafazadeh et al., 2018; Salvadore et al., 2013).

On the other side, neural networks use a single matrix equation which, thanks to its characteristics, can model an infinite number of behaviours, because it does not care about the number of variables it handles, but about the "weight" that the variable has within the matrix equation (Usman et al., 2021; Wessels et al., 2020a, 2020b). Once trained, the neural network is capable of modelling the behaviour of the reservoir regardless of the scenario (even if it was not included in the training of the neural network). This modelling solution not only allows different scenarios to be tested without the need to develop new behavioural equations, but also significantly reduces the time, manpower and computing infrastructure required, as the network, once trained, does not require any further adjustment or intervention by third parties, nor does it require large processors or memory to run (Oktay et al., 2018; Romano & Baysal, 2022a, 2022b).

This paper presents the implementation of neural networks in the TES tank modelling process for a specific case study, where we want to model the behaviour of a TES tank in two dimensions, with two materials, a simple geometry and over a period of 3 seconds; in order to compare the results, a comparison is made with a modelling carried out using computational fluid dynamics (CFD) tools, specifically

the COMSOL program. The paper also mentions the future work of this implementation and the benefits it can bring to the field of thermal energy storage.

Materials and methods

With the aim of developing a new alternative for modelling TES tanks, a first attempt to model a basic design was carried out (Figure 1), the tank had a rectangular shape with a length (L) of 0.14mm by a width (H) of 0.24 through which water enters and exits, the inlet dimensions (b) were 0.02 mm, in the centre of the tank there was a concrete circle with a diameter (D) of 0.10 mm which acts as thermal energy storage material. The tank releases the thermal energy stored in the concrete through the water circulating at a given speed.

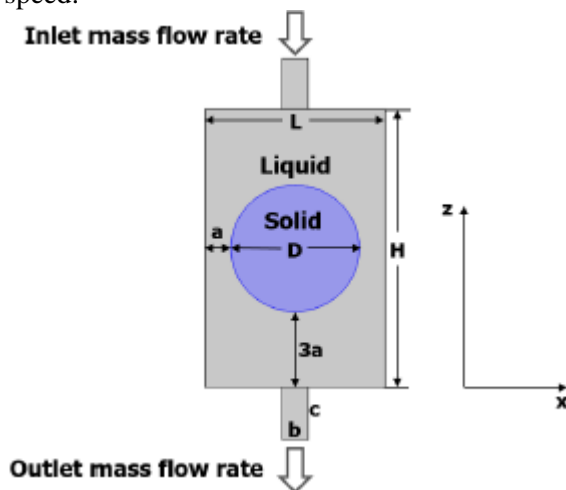


Figure 1: Design proposal for a two-dimensional, single-use TES tank, with Cartesian guidelines

Once the prototype to be modelled was obtained, it was necessary to have a large amount of data on the behaviour of the tank; this is due to the fact that the development of neural networks requires a training process that is usually accompanied by an enormous amount of "data", which are basically the properties that the artificial intelligence (AI) needs to be able to learn and interpret. In this case, it was determined that the neural network should be able to interpret properties such as the initial temperature of the water and the concrete, the input speed and the initial state of the concrete, in order to interpret the behaviour of the tank after a period of time. For this purpose, the COMSOL software was used, a CFD solution tool capable of solving high-level equations for the behaviour of the materials inside a given TES tank. This programme has the functionality of displaying the resolution of these equations in the TES tank in the form of images. Thanks to this tool it was possible to

obtain the behaviour of the tank for different values of liquid temperature (variations of 10 degrees Kelvin between 283 K and 323 K), concrete temperature (variations of 10 degrees Kelvin between 333 K and 373 K) and different values of water velocity (measured in Reynolds number with variations of 200, 350, 700, and 900).

The last parameter required by the neural network is to know how much time to model, since not only the network should be able to model the tank, but also to be able to interpret the behaviour of the tank over time; for this case study it was decided to use a modelling interval of 3 seconds. Eventually, the neural network should be able to model and simulate in the same way as a CFD program such as COMSOL; this idea can be explained as shown in Figure 2.

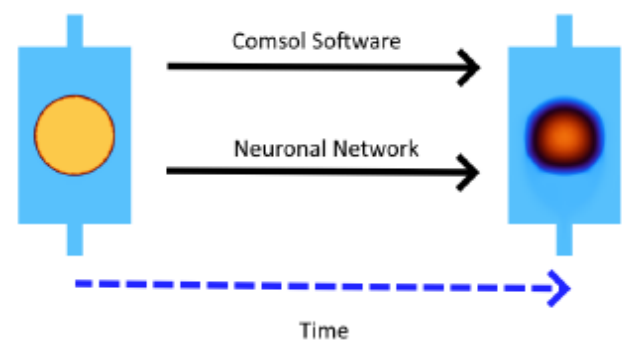


Figure 2: Graphical conceptualisation of the objective of the work, where the aim is to realise the function of a CFD simulator by means of an implementation with artificial intelligence.

Once a data set was obtained thanks to the CFD COMSOL program, it was organised according to the characteristics that the neural network had to learn, such as the initial state of the tank, represented by an image, and the initial values of the initial temperature of the water, the concrete and finally the fluid velocity (represented by the Reynolds number). For the neural network, these properties were the input values of the network and the output of the network was a picture of the behaviour of the tank three seconds in the future.

Once the inputs and outputs of the neural network were understood, the architecture of the network model to be used must be structured; this will determine the ability of the network to learn and understand the behaviour to be modelled. This architecture allows the network to compute each pixel of the image and reconstruct it in such a way that the neural network learns to interpret the image as a set of interconnected elements; in this

case, since the colours of the image represent the temperature values, the process carried out by the U-net is essential for the network to understand the image as a deposit with temperature changes as a whole and not to learn behaviours separately. This model architecture was modified to allow the neural network to learn the behaviour based on the initial values of the initial water temperature, the concrete and the fluid velocity. A schematic of the model architecture used to build the neural network is shown in Figure 3.

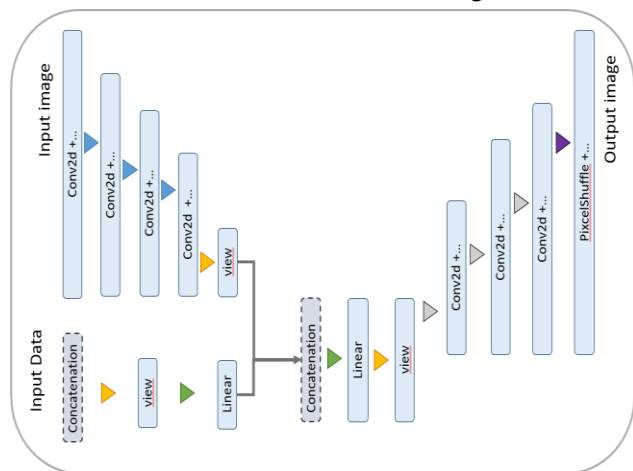


Figure 3: Proposed model architecture for development of neural network modelling the behaviour of the TES-tank used

The next step was to train the neural network; this process involves running the database through the neural network a large number of times, with the network adjusting the weighting parameters of each feature to be learned at each attempt until the output is as expected. At the end of the process, the neural network is said to be trained and ready to make inferences on new data.

Results and Discussion

After the training, the weights and other parameters can be exported for use anywhere, the storage space required does not exceed 1 Gb, and the computational resources required do not exceed those of a conventional office computer; this shows that the neural network application, once trained, is able to reduce the computational requirements for tank modelling using CFD programs.

Data inference for the new neural network requires data to be organised: an image of the initial state, the initial temperature values of the materials involved and the fluid velocity. This makes the use of a neural network, which requires no prior knowledge, preferable to a CFD simulation, which requires knowledge of both the programme and the material properties.

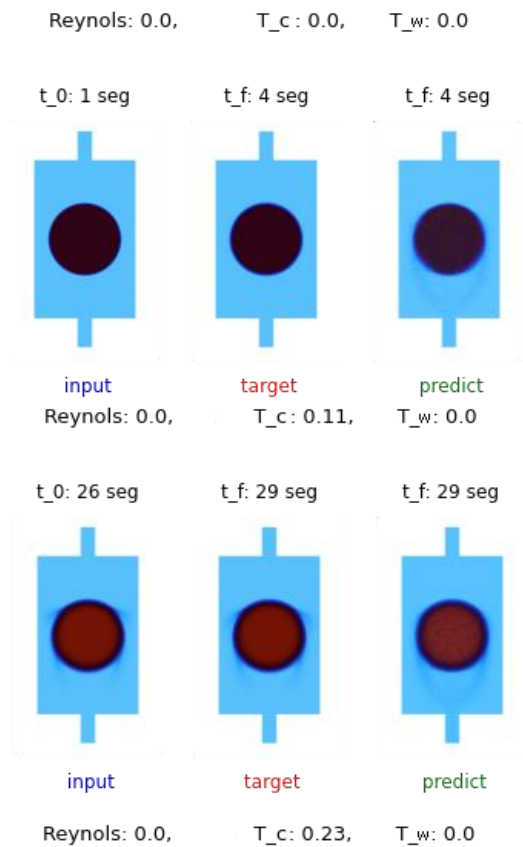


Figure 4: Proposed model architecture for development of neural network modelling the behaviour of the TES-tank used

To observe the effectiveness of the neural network, the inference process was performed on a dataset of images with different water and concrete temperature values and different Reynolds velocity values. The results represent the modelling of the tank 3 seconds after the initial time. Figure 4 shows three results obtained where the initial value of the concrete temperature and the initial time have been changed, organised in the different rows of the image; each column of the image refers (from left to right) to the initial state of the tank, the final state modelled by CFD and the final state modelled by AI. Although the neural network shows regions where the pixels have certain colour variations, in general it can be said that it has learned the behaviour of the reservoir optimally.

Finally, with all the general data set, a comparison was made between the images generated with CFD and those obtained by neural network inference; the similarity of each pixel was analysed in order to see how similar the images obtained by inference were to a CFD simulation. As can be seen in Figure 5, over the simulated time the images generated by inference tend to be more similar to those generated by CFD, a behaviour that may be due to the fact that the bulk of the data represents steady-state behaviour of the



reservoir, making it a pattern that may overstrains the model in some way.

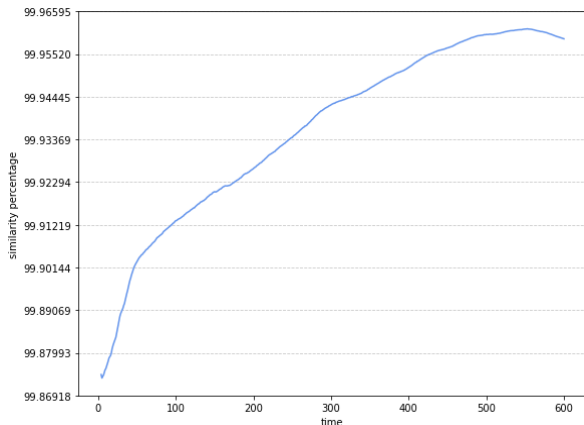


Figure 5: Percentage similarity between images generated by CFD and the proposed neural network over simulation time

Conclusions

Although the results are not entirely as expected at present, it was demonstrated that artificial intelligence is capable of reproducing such complex behaviours as the modelling of TES tanks. Currently, the neural network used to model these tanks requires modifications and more hours of work to perfect the final result, in addition to rethinking the database to reduce the impact of steady state in the training of the network.

Currently, there is an opportunity to improve design processes in technologies such as TES tanks through the use of these new tools, although they are still at an early stage, in the future this neural network can be used to model more complex behaviours, with multiple variables and without the need for more resources, reducing the time required and allowing scalability of processes never before seen in this area.

Acknowledgment

This study received funding from European Union's Horizon Europe research and innovation program within project SUSHeat (101103552).

The authors would also like to thank the Generalitat de Catalunya for the quality accreditation granted to their research group (2021 SGR 01615). GREiA is certified agent TECNIO in the category of technology developers of the Government of Catalonia. This work is partially supported by ICREA under the ICREA Academia programme.

References

- Cabeza, L. F., Martorell, I., Miró, L., Fernández, A. I., & Barreneche, C. (2015). Introduction to thermal energy storage (TES) systems. In *Advances in Thermal Energy Storage Systems* (pp. 1–28). Elsevier.
<https://doi.org/10.1533/9781782420965.1>
- Mostafazadeh, B., Marti, F., Liu, F., & Chandramowliswaran, A. (2018). Roofline Guided Design and Analysis of a Multi-stencil CFD Solver for Multicore Performance. *2018 IEEE International Parallel and Distributed Processing Symposium (IPDPS)*, 753–762.
<https://doi.org/10.1109/IPDPS.2018.00085>
- Oktaý, O., Schlemper, J., Folgoc, L. Le, Lee, M., Heinrich, M., Misawa, K., Mori, K., McDonagh, S., Hammerla, N. Y., Kainz, B., Glocker, B., & Rueckert, D. (2018). *Attention U-Net: Learning Where to Look for the Pancreas*. *Midl*.
<http://arxiv.org/abs/1804.03999>
- Pompei, L., Nardecchia, F., & Miliozzi, A. (2023). Current, Projected Performance and Costs of Thermal Energy Storage. *Processes*, 11(3).
<https://doi.org/10.3390/pr11030729>
- Romano, J. P., & Baysal, O. (2022a). Convolutional-neural-network-based Auto-encoder for Synthetic Upscaling of Computational Fluid Dynamics Simulations. *AIAA Science and Technology Forum and Exposition, AIAA SciTech Forum 2022*.
<https://doi.org/10.2514/6.2022-0186>
- Salvadore, F., Bernardini, M., & Botti, M. (2013). GPU accelerated flow solver for direct numerical simulation of turbulent flows. *Journal of Computational Physics*, 235, 129–142.
<https://doi.org/https://doi.org/10.1016/j.jcp.2012.10.012>
- Usman, A., Rafiq, M., Saeed, M., Nauman, A., Almqvist, A., & Liwicki, M. (2021). Machine Learning Computational Fluid Dynamics. *33rd Workshop of the Swedish Artificial Intelligence Society, SAIS 2021*.
<https://doi.org/10.1109/SAIS53221.2021.9483997>
- Wessels, H., Weißenfels, C., & Wriggers, P. (2020a). The neural particle method – An updated Lagrangian physics informed neural network for computational fluid dynamics. *Computer Methods in Applied Mechanics and Engineering*, 368, 113127.
<https://doi.org/10.1016/j.cma.2020.113127>

Molecular Dynamics Simulation of the Polyvinyl Alcohol Template Effect in n-Octadecane Phase Change Slurry Crystallization

Moritz Kick^{1,*}, Stefan Gschwander¹

¹ Fraunhofer ISE, Heidenhofstraße 2, Freiburg, Germany

*Corresponding author e-mail: moritz.kick@ise.fraunhofer.de

Abstract

Supercooling in small droplets limits the advantage of Phase Change Slurries (PCS) over sensible storage. The surfactant Polyvinyl alcohol (PVA) shows effective supercooling reduction in contrast to other surfactants that usually require a nucleation additive to yield similar results. Recent studies propose a structural template effect that is investigated with Molecular Dynamics (MD) Simulation on the atomic scale. Through MD, insights to structural assembly and crystallization within PCS droplets allow for mechanism exploration. N-Octadecane is simulated in the OPLS-AA/L force field alongside PVA and the results indicate a strong bonding of the PVA backbone to PCM droplets. The PCM nucleation is triggered earlier close to the contact zone and provides the seed for succeeding crystallization. This enables the search for nucleation-supporting surfactants with strong supercooling reduction.

Keywords: Molecular Dynamics Simulation, Phase Change Slurry, Dispersion, Nucleation, Template Effect

Introduction

Supercooling is observed frequently in Phase Change Slurries (PCS) with small particles.[1–4] PCS with Polyvinyl alcohol (PVA) have shown little supercooling compared to PCS with similar particle sizes below 3 μm and different surfactants.[5] Supercooling reduction is an ongoing research field that usually leads to the incorporation of seed materials into the droplets.[6, 7] Therefore, a surfactant that effectively stabilizes the slurry and eliminates the need for seeds is very desirable. A template effect of the PVA carbon backbone was proposed to offer a heterogeneous crystallization surface for the PCM molecules to form nucleation sites easily.[8] To understand the mechanism in n-Octadecane/PVA slurries, Molecular Dynamics (MD) Simulations were used to observe the crystallization process.

Methodology

The software GROMACS (version 2021 [9–11], OPLS-AA/L force field [12], with CUDA 10.4 support) was used to run MD Simulations on a Workstation with AMD EPCY 7702P (64 core) and dual NVIDIA RTX Titan graphics accelerators. Visual representations were made with VMD 1.9.3.[13]

The single components were modelled in a chemical structure editor and converted to the GROMACS input format with a custom python script. Each component was pre-optimized with the steepest descent algorithm and in an NVT ensemble (constant number of particles

N, volume V and temperature T). The systems of interest were then assembled from the single components, e.g. a PCM surface with PVA in proximity (Figure 1, water in “empty” space hidden) with periodic boundary conditions (PBC).[9]

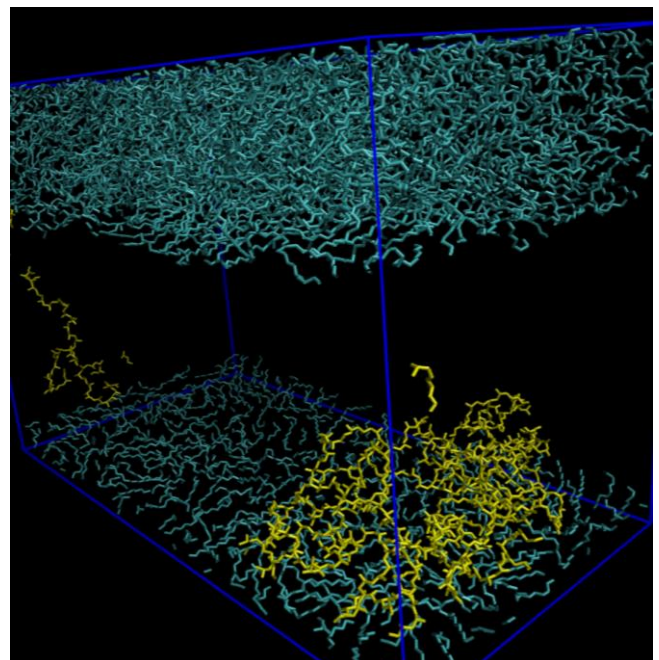


Figure 1: N-Octadecane (cyan) surface of 900 molecules with a single PVA molecule (yellow) attached. PBC apply and water is hidden. © 2023 FHG ISE, M. Kick

The final configuration was equilibrated in an NPT ensemble (constant pressure P instead of volume) above melting temperature to get an unbiased system. The temperature was then lowered in steps of 10 K

until crystallization occurred, indicated by highly ordered PCM molecules. The trajectory of the system was evaluated visually near the phase change to follow the PCM-PVA interaction. To simulate a PCS droplet in water, PCM and PVA were placed in a larger simulation box and the remaining space was filled with H₂O molecules. For water, the TIP3P model [15] was considered. A comparison with alcohol ethoxylate surfactants was done in the same way to see why they do not exhibit the template effect.

Results and Discussion

The reference simulations of pure n-Octadecane (C₁₈) take more than 100 ns in some instances to crystallize and must be cooled approx. 20 K below the literature melting point of 302 K. This can happen due to nucleation being a rare stochastic event especially in small volumes. Additionally, finite size effects can lead to temperature deviance when a molecule interacts with itself in a small simulation box.[14]

The simulation of a single PVA molecule on a n-Octadecane surface confirms the backbone making good contact with the PCM. The PCM crystallization starts in proximity of the PVA backbone and still requires 20 K lower temperatures. There is a thin PCM layer between the forming seed and the PVA, so a single PVA molecule does not influence the PCM crystallization, apparently.

Therefore, a starting configuration of PVA with a cluster of 4 molecules is investigated. We observe the formation of a partially ordered structure during cooling (Figure 3). This crystal-like PVA cluster can then initiate faster PCM crystallization, even at a simulation temperature of 300 K (Figure 2). This leads to the conclusion that the PVA backbone provides a suitable template.

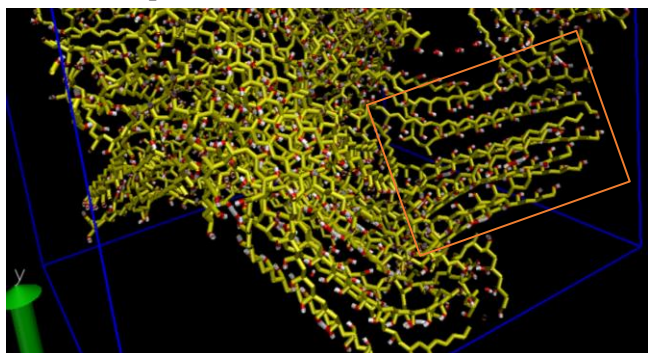


Figure 3: Partially crystalline PVA (orange box).
 © 2023 FHG ISE, M. Kick

Comparing it against the polymer surfactant Poloxamer 407 with a block copolymer structure shows a better nucleation support of the PVA. The difference in the

polymers is the position of their oxygen atoms. In the Poloxamer they are contained in the backbone, so there is no homogeneous part long enough to match the PCM. The oxygen atoms instead introduce a slightly different atom spacing which does not exactly match with the PCM and its crystal structure.

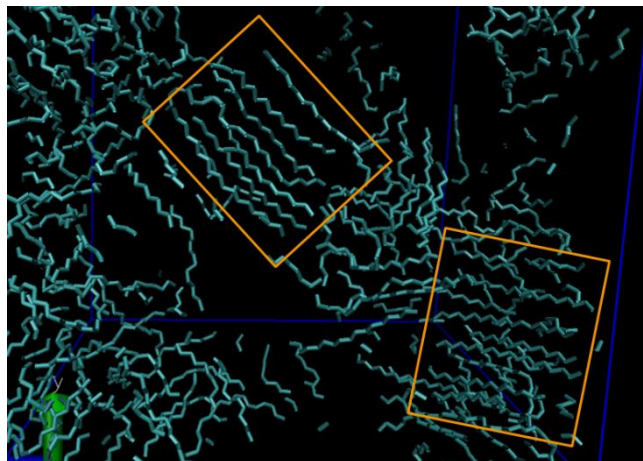


Figure 4: N-Octadecane crystallites (orange boxes) formed in contact with the PVA carbon backbone (hidden).
 © 2023 FHG ISE, M. Kick

However, other surfactants do have long carbon chains as well, for example, ethoxylated alcohols are frequently used in emulsion stabilization. To see why they do not exhibit nucleation support at all, 1-Dodecanol (C₁₂OH) with 3 ethoxy units (Laureth-3) was simulated on a PCM droplet in water (Figure 5).

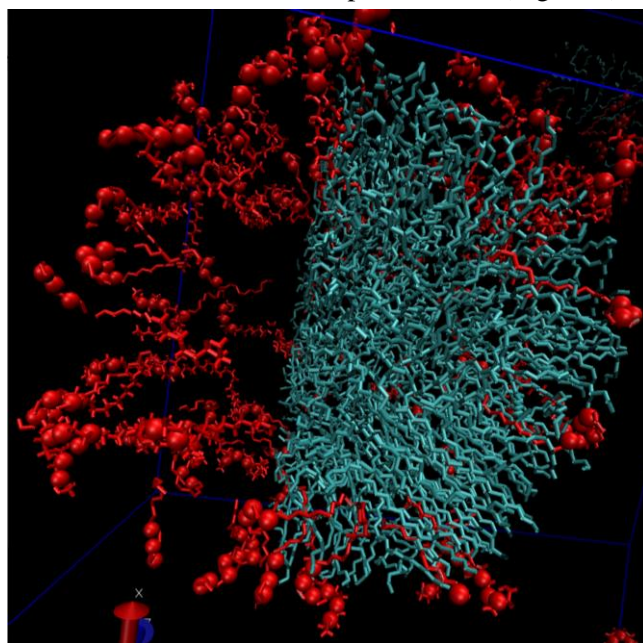


Figure 5: PCM droplet (cyan) cut in half with Laureth-3 (red) on its surface. The Laureth-3 oxygen atoms (large beads) of the hydrophilic part reach into the water (hidden) and the lipophilic part reaches into the droplet. © 2023 FHG ISE, M. Kick.

This PCS droplet reveals that the surfactant (and the whole class of ethoxylated alcohols) does not align parallel to the surface but instead reaches into the droplet orthogonally and sometimes bend/fold inside. In small droplets the curvature is high, so that the space for PCM crystallization between surfactant molecules is vanishing. Therefore, the PCM cannot benefit from any structural similarities to the surfactant (Figure 6). Furthermore, the droplet surface is expected to be covered by surfactant completely, which means any potential nucleation at the oil-water interface is usually blocked as well.

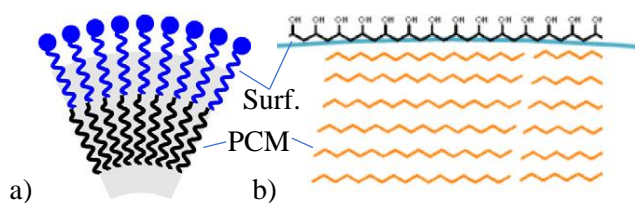


Figure 6: a) Small particles do not allow for parallel crystal patterns due to the curvature angle. Thus, the formation of highly ordered molecule clusters which lead to nucleation is prevented. Reproduced from © 2011 ZAE Bavaria, Günther et al.[16] b) This is not happening with PVA aligned parallel to the surface. Reproduced from © 2018 FHG ISE, G. Hagelstein.[8]

Conclusions

The nucleation supporting “template effect” is strong in PVA, especially. This is found to originate in parts of the carbon backbone providing a crystal-like structure longer than the PCM chains that are aligned parallel to the oil-water surface. Oxygen atoms (and potentially other hetero atoms) in the template structure lead to structural mismatch and decreased efficiency. Surfactants that reach into the droplets do not support or even inhibit crystallization. Further investigation into the exact structure matching and the effect of hetero atoms can be done.

Acknowledgment

We are grateful for the funding of this work by the German Federal Ministry for Economic Affairs and Climate Action and administrative support given by the Projektträger Jülich (FKZ 03ET1596).

Nomenclature

PCM: Phase Change Material

PCS: Phase Change Slurry

PVA: Polyvinyl alcohol

GROMACS: Groningen Machine for Chemical Simulations

OPLS-AA/L: Optimized Potentials for Liquid Simulations, all atom, optimized for long hydrocarbons
CUDA: Compute Unified Device Architecture (Nvidia GPU API)

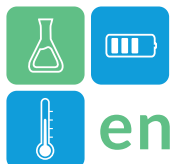
TIP3P: Transferable Intermolecular Potential with 3 Points

PBC: Periodic Boundary Conditions

AMD: Advanced Micro Devices

References

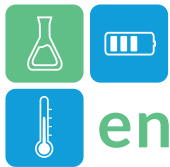
- Gschwander S, Niedermaier S, Gamisch S et al. (2021) Storage Capacity in Dependency of Supercooling and Cycle Stability of Different PCM Emulsions. *Applied Sciences* 11:3612. <https://doi.org/10.3390/app11083612>
- Günther E, Schmid T, Mehling H et al. (2010) Subcooling in hexadecane emulsions. *International Journal of Refrigeration* 33:1605–1611. <https://doi.org/10.1016/j.ijrefrig.2010.07.022>
- Dash L, Anna Mahanwar P (2021) A REVIEW ON ORGANIC PHASE CHANGE MATERIALS AND THEIR APPLICATIONS. *IJEAST* 5. <https://doi.org/10.33564/IJEAST.2021.v05i09.045>
- Berdja M, Hu J, Hamid A et al. (2021) Investigation on the anti-supercooling effect of sodium polyacrylate as an additive in phase change materials for the applications of latent heat thermal energy storage. *Journal of Energy Storage* 36:102397. <https://doi.org/10.1016/j.est.2021.102397>
- Wang F, Lin W, Ling Z et al. (2019) A comprehensive review on phase change material emulsions: Fabrication, characteristics, and heat transfer performance. *Solar Energy Materials and Solar Cells* 191:218–234. <https://doi.org/10.1016/j.solmat.2018.11.016>
- Huang L, Petermann M, Doetsch C (2009) Evaluation of paraffin/water emulsion as a phase change slurry for cooling applications. *Energy* 34:1145–1155. <https://doi.org/10.1016/j.energy.2009.03.016>
- Delgado M, Lázaro A, Mazo J et al. (2012) Review on phase change material emulsions and microencapsulated phase change material slurries: Materials, heat transfer studies and applications. *Renewable and Sustainable Energy*



Reviews 16:253–273.

<https://doi.org/10.1016/j.rser.2011.07.152>

8. Hagelstein G (2018) Untersuchung zum Kristallisationsverhalten in n-Octadecan-Wasser-Dispersionen: INAUGURALDISSERTATION
9. Abraham MJ, Murtola T, Schulz R et al. (2015) GROMACS: High performance molecular simulations through multi-level parallelism from laptops to supercomputers. *SoftwareX* 1-2:19–25. <https://doi.org/10.1016/j.softx.2015.06.001>
10. Berendsen H, van der Spoel D, van Drunen R (1995) GROMACS: A message-passing parallel molecular dynamics implementation. *Computer Physics Communications* 91:43–56. [https://doi.org/10.1016/0010-4655\(95\)00042-e](https://doi.org/10.1016/0010-4655(95)00042-e)
11. GROMACS development team GROMACS Documentation: Release 2019.6
12. Siu SWI, Pluhackova K, Böckmann RA (2012) Optimization of the OPLS-AA Force Field for Long Hydrocarbons. *J Chem Theory Comput* 8:1459–1470. <https://doi.org/10.1021/ct200908r>
13. William Humphrey, Andrew Dalke, Klaus Schulten (1996) VMD - Visual Molecular Dynamics. *Journal of Molecular Graphics* 14:33–38
14. Crystallization Behaviors of n-Octadecane in Confined Space_Crossover of Rotator Phase from Transient to Metastable Induced by Surface Freezing_Xie_2008
15. Jorgensen WL, Chandrasekhar J, Madura JD et al. (1983) Comparison of simple potential functions for simulating liquid water. *The Journal of Chemical Physics* 79:926–935. <https://doi.org/10.1063/1.445869>
16. Günther E, Huang L, Mehling H et al. (2011) Subcooling in PCM emulsions-Part 2: Interpretation in terms of nucleation theory. *Thermochimica Acta* 522:199–204. <https://doi.org/10.1016/j.tca.2011.04.027>



Monitoring results of energy-efficient demonstration buildings with thermal activated building mass as energy storage

C. Rohringer^{1,*}, W. Becke¹, P. Gruber¹, P. Lampersberger², M. Mayr², D. Wolfesberger²

1 AEE – Institute for Sustainable Technologies (AEE INTEC)

Feldgasse 19, 8200 Gleisdorf, Austria

Tel.: +43 (0) 3112 - 5886 - 662

*e-Mail: c.rohringer@aee.at

2 e7 energy innovation & engineering

Walcherstraße 11/43, 1020 Vienna, Austria

e-Mail: paul.lampersberger@e-sieben.at

Abstract

Thermal activated building mass (TAB) as a technology is predominantly used for heating and cooling, despite its capabilities to function as an efficient thermal energy storage. The Austrian project BTTAB, as well as the Austrian led IEA ES Task 43, deal with analysing and further developing the capabilities of TAB as energy storage and its integration into thermal and electrical networks. Both activities aim at learning from existing implementations and generalizing the results to provide scientifically based planning, construction and control methods for refurbishment and new construction. TAB can offer its storage capacity as much needed flexibility to thermal grids, and via heat pumps as sector coupling technology, also to electrical grids. This paper highlights the methodology and first results of the monitoring of 18 energy-efficient demonstration buildings with thermally activated building mass as energy storage in Austria.

Keywords: Thermal Energy storage, Thermal activated building mass, TABs, Flexibility, Sector coupling

Introduction

The expansion of renewable energy generation and extensive energy storage options are central cornerstones of the energy transition. Thermal component activation can be a key aspect of this, as it can be used multifunctionally as a heating and cooling supply system and as a storage system for fluctuating renewable energies. These applications not only offer enormous potential for the integration of renewable energies and waste heat, but also promise a high level of economic attractiveness and are convincing due to their simplicity in implementation, operation and utilisation.

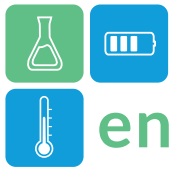
In order to investigate these properties of TAB in real buildings, 18 demonstration buildings distributed across Austria were selected for monitoring and surveys in the BTTAB study (Becke et al. 2023). On the one hand, it is intended to provide information on the performance of the storage and energy flexibility potential and, on the other hand, to generate important findings with regard to user comfort, user satisfaction, economic aspects in construction and operation as well as functionality.

Methodology

To begin with, information was obtained about the technical building systems and any existing measurement and metering equipment in the 18 demonstration buildings and the modalities for providing measurement data were clarified.

In the next step, based on the experience of the project partners AEE INTEC and e7, a detailed monitoring concept was drawn up to answer the relevant aspects relating to energy generation, heat and cold output and storage via TAB and comfort in reference rooms. In addition, a simplified measurement method for the quick and cost-effective determination of the operating temperature in reference rooms (key comfort criterion) was developed, tested and subsequently applied in all demonstration buildings.

In addition to energy and comfort monitoring, a user questionnaire was developed to survey and analyse the subjective satisfaction of building users, which is used in the 18 demonstration buildings. Targeted surveys of stakeholders (investors, planners, contractors) complete the creation of a comprehensive and well-founded knowledge base.



Results and discussion

The demonstration buildings differ not only in their type of use, but also in the application of TAB in combination with the energy supply concept. In the ongoing work of the BTTAB study, the differences are being worked out and compared with the monitoring results. The TAB technologies used are categorised according to the following distinguishing features:

- Activated components and type of installation of the TAB
- utilisation for heating and/or cooling
- type of control strategy of the TAB.

Findings already obtained from energy and operational monitoring as well as statements on the use of storage potential are analysed and contextualised with the building structure, use and energy generation system and combined with the results from the comfort monitoring of reference areas within the buildings. The results from the simplified measurement method for determining the operative temperature of reference rooms are analysed and compared with the results of the comfort measurement in accordance with ISO 7730. Although the monitoring of some demonstration buildings is still ongoing and the surveys have not yet been completed, many results can already be provided that are of great importance for the planning, design and operation of future buildings with TAB.

Based on the available results, the following statements can be made:

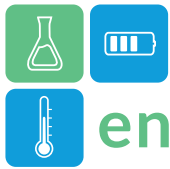
- The TABS analysed are well-functioning systems
- The users feel very comfortable in these buildings
- TABS offer optimal conditions for the utilisation of renewable energies, such as optimal temperature levels for heating and cooling, reduced peak loads compared to other available supply systems in combination with a high storage capacity.
- In order to maximise the storage potential of TAB, more sophisticated control strategies need to be introduced.

Conclusions

The BTTAB project shows that monitoring is highly relevant for innovative buildings with new technologies such as TAB. The monitoring of energy and comfort parameters proves to be an ideal instrument for monitoring the control operation of buildings, the individual technologies used and the interaction of complex system structures. Monitoring makes it possible to assign energy consumption to specific control settings of individual components or to specific user behaviour, to quickly localise faults and, if necessary, to take countermeasures in system operation or user behaviour. The effectiveness of implemented measures can also be quickly checked with the monitoring system at system level. The aim of energy and comfort monitoring is to continuously improve technical building operation and comfort conditions, to become more resource-efficient and to pass on the knowledge gained for future building projects.



Figure 1: Overview of the 18 Austrian Demonstration buildings of BTTAB and their use category. Copyright © AEE INTEC



ENERSTOCK 2024
The 16th IEA ES TCP International Conference on Energy Storage
June 5–7, 2024
Lyon, France

Acknowledgment

The work published in this paper is financially supported by the Österreichischen Forschungsförderungsgesellschaft (FFG) as part of the "Stadt der Zukunft" programme through the study "BTTAB - Broad-based testing of energy-efficient demonstration buildings with thermally activated building components".

The Task Manager, Subtask B Lead and task participation for IEA ES Task 43, carried out by Austria, are financed by the Austrian Federal Ministry for Climate Action, Environment, Energy, Mobility, Innovation and Technology under grant agreement FO999898192 "IEA ES Task XX: Standardisierte Nutzung von Gebäudemasse als Speicher für erneuerbare Energien und Netzflexibilität".

References

Becke, W. et al. (2023), BTTAB - Breit angelegte Erprobung von energieeffizienten Demonstrationsgebäuden mit thermisch aktivierten Bauteilen. Verfügbar in: <https://nachhaltigwirtschaften.at/en/sdz/projects/bttab.php> (accessed 24.11.2023)



Multi-scale experimental characterization and management of the supercooling of Isosorbide as Phase Change Material for thermal energy storage

Arnaud Bruch^{1,*}, Fabrice Bentivoglio¹, Baptiste Boit², Awa Sy¹

¹ Univ Grenoble Alpes, CEA, LITEN, DTCH, LCST, F-38000 Grenoble, France

*Corresponding author e-mail: arnaud.bruch@cea.fr

Abstract

This study experimentally investigates the thermal behaviour of Isosorbide as potential storage material for PCM (Phase Change Material) Thermal Energy Storage (TES). The characterization has been made at 3 different scales, i.e. material (10.3 mg), lab-scale (400 g) and TES prototype (37 kg) scales. At all scales, significant supercooling is observed. N₂ bubbling during discharge is then proved to be an effective way of managing the supercooling by triggering the crystallization. However, this also leads to a temperature homogenization in the PCM volume. Experimental tests at prototype scale show that this homogenization is not an issue for TES performances as it allows to recover energy at higher temperatures during discharge.

Keywords: Phase Change material, supercooling, isosorbide, bubbling, crystallisation triggering

Introduction

The transformation of the global energy system in line with the Paris Agreement implies rapid and significant changes in the energy use. In particular, the need of reducing the carbon emissions into the atmosphere is now consensual and widely accepted, which involves higher share of renewable energy sources and the promotion of high energy-efficient systems (IPCC 2023). In this context, Thermal Energy Storage (TES) gains more and more attention with an exponential number of publications (Calderon et al. 2019).

TES solutions are typically categorized by the physical phenomenon used to store energy, i.e. sensible, latent or thermochemical heat. Sensible and thermochemical heat TES are highest and lowest maturity level TES technologies, respectively. Due to its high storage density combined with a high maturity level (close to the industrial application), latent heat TES is gaining interest for residential and urban heating network applications where space is a high constraint.

PCM storages for residential application requires low temperature PCM, with melting temperature typically in the range 40 – 70°C. Isosorbide could be considered as a good candidate. It is a bio-based material obtained from starch that is non-toxic, non corrosive, environmentally friendly with an adequate melting temperature (63°C) and a high enthalpy of fusion (>110 J/g). Its liquid density is high

(1.33kg/m³) leads to a high volume storage density (>40kW.h/m³).

Nevertheless, Isosorbide exhibits supercooling. Supercooling is the characteristic of a material to remain liquid below its freezing temperature. This characteristic is problematic for thermal storage applications even if it can be, in specific cases, used on purpose (Safari et al. 2017). The supercooling rate is defined as the difference between the theoretical solidification temperature and the lowest temperature reached during liquid phase. Numerous parameters impact this characteristics, such as the sample size (Adachi et al. 2014), the cooling rate (Tayler et al. 2016, Guzman and Braga 2005) or the material history through thermal cycling (Wada et al. 1983, Wada et al. 1984).

Authors have developed some strategies to reduce supercooling such as the addition of specific additives (Fashandi and Leung 2018), the bubbling (Duquesne et al. 2019), the mechanical agitation or bubbling combined with seeding (Piquard et al. 2023). The efficiency of these technics depends on the PCM, in particular on the capacity of the PCM to do primary nucleation or not.

This study focuses on the experimental characterization of the supercooling behaviour of Isosorbide. Multi-scales experiments have been conducted, from material characterization device to PCM TES prototype. .

Experimental characterization of Isosorbide

The experimental characterization of the Isosorbide is made from small scale to prototype scale.

The first analysis performed on Isosorbide is a DSC analysis. A sample of 425 mg of Isosorbide has been submitted to heating/cooling/heating cycles on a DSC module at thermal rate of 0.1°C/min.

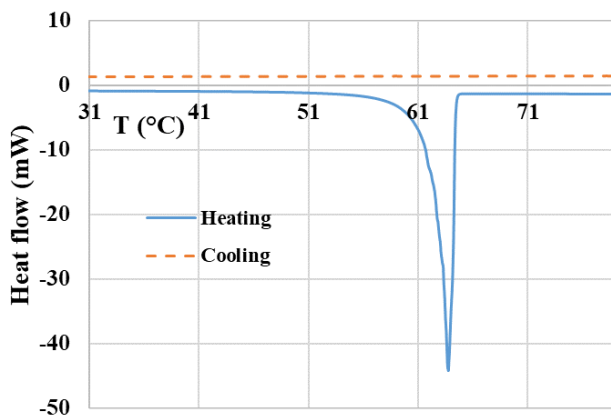


Figure 1: DSC analysis of Isosorbide.

Starting from 30°C, the Isosorbide sample is heated up to 78°C, highlighting a phase change in the temperature range of 60-65°C, with a corresponding enthalpy change of 110 J/g, which is very close to the theoretical enthalpy of fusion. Upon cooling at 0.1°C/min, no crystallization is observed when the sample reaches 30°C. Unfortunately, it was possible to cool the sample at lower temperatures and, thus, it was not possible to quantify precisely the supercooling rate of Isosorbide. In any case, a high level of supercooling (> 30°C) that is clearly not acceptable for most of thermal applications has been observed.

However, supercooling is known to be enhanced in small volumes (Adachi et al. 2014). Thus, experiments have been performed at intermediate scale (400 mL of Isosorbide) on a dedicated test bench (see Figure 2). The facility is composed of a double-walled metallic cylindrical crystallizer connected to a thermal bath using silicone oil (SilOil M40) as heat transfer fluid. Two thermocouples measure the inlet and outlet temperatures of the thermal oil and nine thermocouples (T-type 1 mm) are immersed in the PCM sample at different positions to follow the thermal behavior (see (Piquard et al. 2022) for a complete description). Supercooling and triggering of crystallization are managed through bubbling, i.e. injection of N₂ at the bottom of the vessel with a needle.

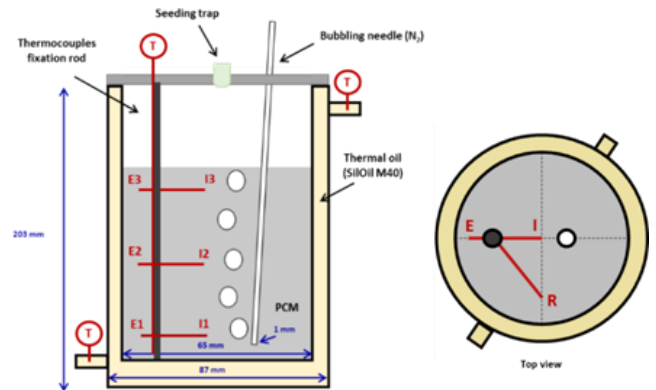


Figure 2: Intermediate scale device used to study overcooling management

The experimental results first bring to light that without triggering system the supercooling of isosorbide is broken anyway (Figure 3, top), meaning that Isosorbide does homogeneous primary nucleation. However, crystallization happens after a long time of latency (> 1000s) and more than 30°C of supercooling rate. In addition, the latency time and supercooling rates are not repeatable: tests with identical conditions (see Table 1) lead to different values, highlighting the stochastic specificity of supercooling rupture by homogeneous primary nucleation.

Table 1: Characteristics of crystallization triggering and reproducibility, with and without bubbling.

	Latency time (s)	Triggering T (°C)
Without bubbling Test 1	477	38.8
Without bubbling Test 2	1014	32.6
With bubbling Test1	133	56.5
With bubbling Test2	139	56

With the addition of N₂ bubbling during the cooling phase (Figure 3, bottom), the temperature supercooling and the time latency are strongly reduced (from 30°C and 1000s without bubbling to 5°C and less than 150s with bubbling) and the results are more repeatable (see Table 1). Bubbling also homogenises the temperature field inside the experimental container during the first 1700s as illustrated in Figure 3.

These results at intermediate scale open the opportunity to a supercooling rate management at the scale of a TES. Then it has been tested as PCM in a prototype of PCM TES based on tube and shell technology, presented in Figure 4. It consists on a 2.15 m high heat exchanger placed inside a 0.22 m

diameter cylindrical shell. The heat transfer fluid (water) circulates inside the tubes and exchanges heat with the PCM contained in the shell. The heat exchanger is made of a bundle of 7 finned tubes (20 mm of internal diameter tube, 0.4 mm thick aluminium fins, 10 fins par inch, external fin diameter of fin of 57.4 mm) as illustrated in Figure 4.

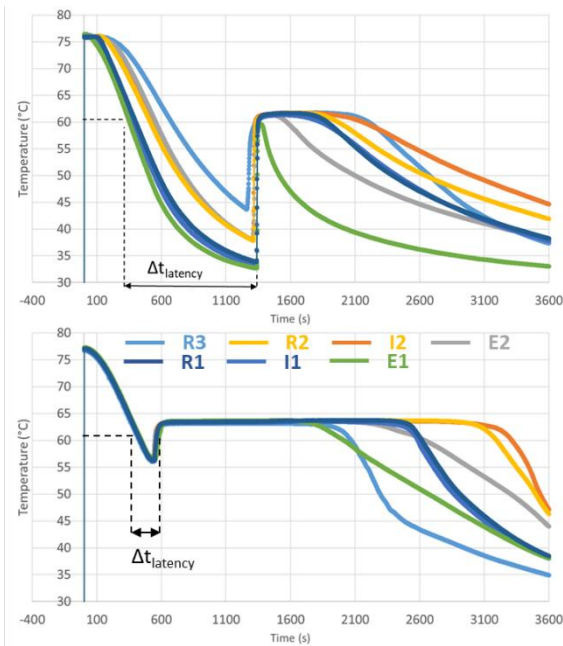


Figure 3: Typical results obtained in cooling, with (bottom) and without (top) use of N₂ bubbling (1 NL/min) to trigger the Isosorbide crystallization.

The TES prototype is equipped with thermocouples on water and PCM sides (see Figure 4 for the positions of the TC inside the PCM). The bubbling is made by using a N₂ injection device at the bottom of the prototype, below the PCM.

Typical results obtained with and without bubbling are presented in Figure 5 (water temperatures) and (PCM temperatures). Initially heated at 82°C, the TES is cooled with a 100 kg/h flow of water varying between 22°C and 30°C. The tests with bubbling are performed with 5 NL/min of N₂ flow rate.

Without bubbling, the results exhibit a solidification front moving from the bottom (inlet in discharge) to the top (outlet in discharge) of the storage tank. There is no temperature plateau as expected with the solidification of a PCM, but a temperature drop followed by a temperature peak, corresponding to the supercooling and its rupture. This behaviour is observed on both PCM and water sides.

On the PCM side, the rupture of supercooling leads to temperature increases until values close to the melting temperature (55-60°C), with or without bubbling.

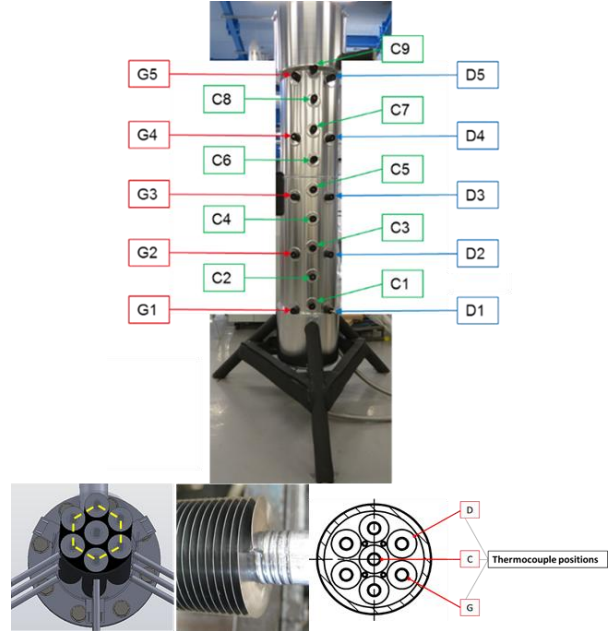


Figure 4: Prototype of PCM TES, with focus on the tubes bundle, the tubes fins and the TC instrumentation.

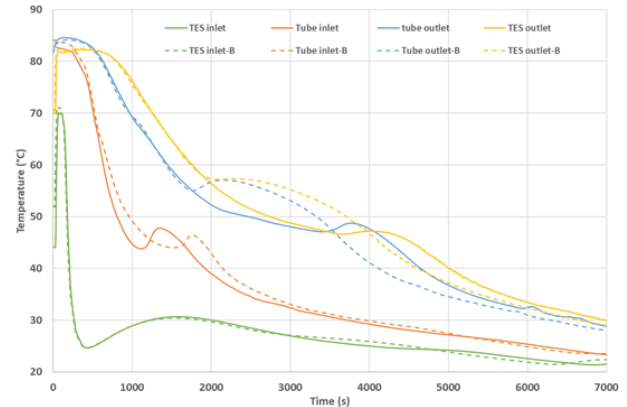
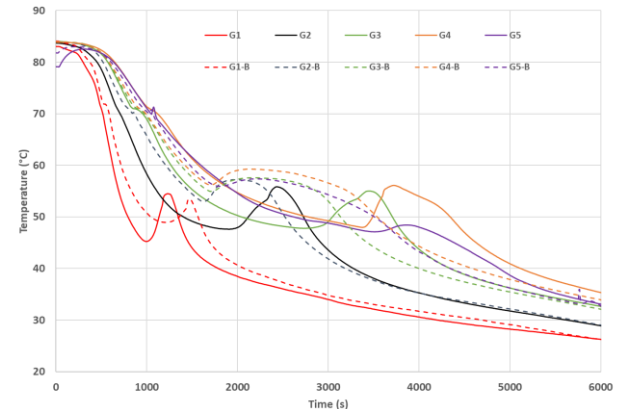


Figure 5: Temporal evolution of the water temperature, with and without bubbling. "B" refers to tests with bubbling.



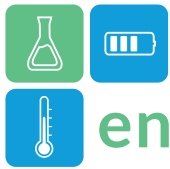


Figure 6: Temporal evolution of the PCM temperature, with and without bubbling.

Adding bubbling leads to a completely different behaviour: there is no more propagation of a solidification front and, except on the bottom of the TES (“Tube inlet” in Figure 5 and “G1” in

), a single temporal evolution of temperature is observed on the whole TES height. Crystallization is triggered at the same time in all the PCM (about 1750 s on

). At the beginning of the test, the outlet temperature of the storage is the same, but it becomes higher after the crystallisation triggering thanks to an earlier triggering.

Adding bubbling increases the water outlet temperature during the second part of a discharge of the storage, such parameter being of prime importance for certain application such as domestic hot water for example.

Conclusion

Due to its thermal, safety and environmentally friendly properties, Isosorbide is considered as a potential good candidate as a storage material for residential application. However, Isosorbide exhibits supercooling, which may limit its use.

This paper presents the experimental results of the thermal behaviour of Isosorbide at 3 different scales, from material characterization to thermal storage characterization. Important supercooling has been reported at all scales. N₂ bubbling allows efficient triggering of crystallization, increases reproducibility, but leads to a global thermal homogenization of the TES.

Next steps will include more experimental tests and the evaluation of the global benefits of triggering the crystallization, depending on the process constraints and limits.

Acknowledgment

This work is supported by the EU Horizon 2020 project “Compact bio-based thermal energy storage for buildings” (ComBioTES) (No. 864496).

References

Adachi T., Daudah D., and Tanaka G., Effects of Supercooling Degree and Specimen Size on Supercooling Duration of Erythritol, *ISIJ Int.*, vol. 54, n° 12, p. 2790- 2795, 2014.

Taylor R.A., Tsafnat N., and Washer A., Experimental characterisation of sub-cooling in hydrated salt

phase change materials, *Appl. Therm. Eng.*, vol. 93, p. 935- 938, janv. 2016.

Guzman J.J.M and Braga S.L., Supercooling Water in Cylindrical Capsules, *Int. J. Thermophys.*, vol. 26, n° 6, p. 1781- 1802, nov. 2005.

Wada T., Kimura F. and Matsuo Y., Studies on Salt Hydrates for Latent Heat Storage. IV. Crystallization in the Binary System CH₃CO₂Na–H₂O, *Chem. Soc. Jpn.*, p. 3827- 3829, déc. 1983.

Wada T., Matsunaga, and Matsuo Y., Studies on Salt Hydrates for Latent Heat Storage. V. Preheating Effect on Crystallization of Sodium Acetate Trihydrate from Aqueous Solution with a Small Amount of Sodium Pyrophosphate Decahydrate, *Chem. Soc. Jpn.*, p. 557- 560, 1984.

IPCC, 2023: Summary for Policymakers. In: Climate Change 2023: Synthesis Report. Contribution of Working Groups I, II and III to the Sixth Assessment Report of the Intergovernmental Panel on Climate Change [Core Writing Team, H. Lee and J. Romero (eds.)]. IPCC, Geneva, Switzerland, pp. 1-34.

Calderón A. , Barreneche A. ,Hernández-Valle K., Galindo E., Segarra M. and Fernández A.I., Where is Thermal Energy Storage (TES) research going? – a bibliometric analysis, *Sol Energy* (2019).

Safari A., Saidur R., Sulaiman F.A., Yan Xu and Joe Dong, A review on supercooling of Phase Change Materials in thermal energy storage systems, *Renewable and Sustainable Energy Reviews*, Volume 70, 2017, Pages 905-919.

Fashandi M. and Leung S.N., Sodium acetate trihydrate-chitin nanowhisker nanocomposites with enhanced phase change performance for thermal energy storage, *Sol. Energy Mater. Sol. Cells*, vol. 178, p. 259- 265, mai 2018.

Piquard L., Gagnière E., Largiller G., Mangin D. and Bentivoglio F., Triggering Xylitol crystallization in a 42 kWh shell and tubes latent heat thermal energy storage system, *Appl. Therm. Eng.*, vol. 221, p. 119802, févr. 2023.

Piquard L., Gagnière E., Largiller G., Mangin D. and Bentivoglio F., Xylitol used as phase change material: Nucleation mechanisms of the supercooling rupture by stirring, *Journal of Energy Storage*, vol. 48, art. 1039022, 2022.

Duquesne M., Palomo Del Barrio E., Godin A., Nucleation triggering of highly undercooled xylitol using an air lift reactor for seasonal thermal energy storage. *Appl. Sci.* 2019, 9, 267.

Nanofabrication of Multi-Shells Hollow CuO Microspheres for an Enhanced Cyclic Redox Reaction in High-Temperature Thermochemical Heat Storage Applications

Hassan Agalit^{1,*}, Samuel D Widijatmoko², Gary A. Leeke², Yongliang Li^{1,*}

¹ Birmingham Centre for Energy Storage (BCES) & School of Chemical Engineering, University of Birmingham, Birmingham B15 2TT, UK

² School of Chemical Engineering, University of Birmingham, Birmingham B15 2TT, UK

*Corresponding authors e-mail: h.agalit@bham.ac.uk, and y.li.1@bham.ac.uk

Abstract

Thermochemical energy storage systems relying on the CuO/Cu₂O redox reaction offer a promising solution for decarbonizing high-temperature applications (around 1000 °C). However, the predominant challenge with this material is the occurrence of sintering, impeding cyclic operation and significantly reducing storage efficiency after multiple cycles, as documented in the literature. This study presents a straightforward one-pot synthesis process for hollow CuO microspheres to improve the cyclic performance of thermochemical heat storage systems based on the CuO/Cu₂O redox. A distinctive aspect of this work, compared to previous investigations, is the absence of any doping material in the final product, resulting in a remarkably high energy density of approximately 747 kJ/kg. The formation of multi-shelled hollow CuO microspheres was confirmed through Scanning Electron Microscopy (SEM) techniques. Furthermore, the synthesized material exhibited stable cyclic performance after 10 cycles, as demonstrated using the Simultaneous Thermal Analysis (STA) apparatus.

Keywords: Hollow CuO microspheres; Hydrothermal synthesis; Thermochemical seasonal storage; Nanofabrication;

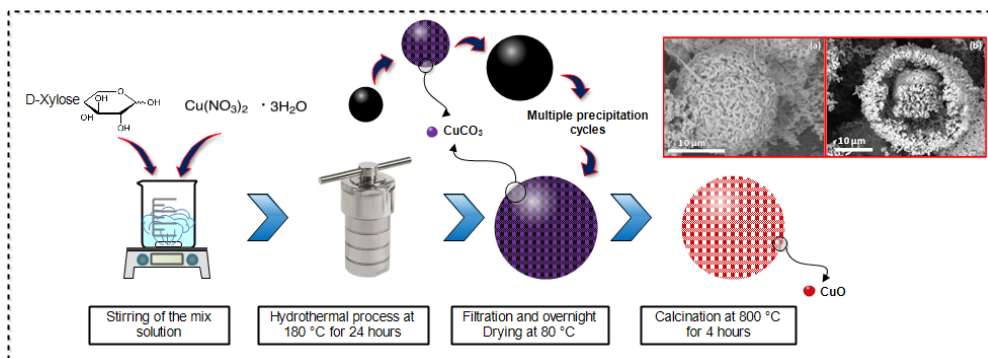


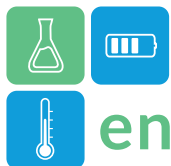
Figure 1: Synthesis process of the Multi-Shells Hollow CuO Microspheres.

Introduction

Decarbonizing high-temperature heat sectors poses a significant challenge, currently heavily dependent on fossil fuels such as natural gas (Gigantino et al., 2020). However, there is a positive outlook with the declining costs of renewables, like wind turbines, and a substantial anticipated increase in installed capacities. Consequently, a substantial surplus of curtailed renewable electricity output is expected during periods of low demand. To solve the previous decarbonisation equation, a reliable storage technology is needed at high operating temperature (~ 1000 °C) (Forsberg et

al., 2017). In this context, energy storage systems based on the reversible thermochemical redox reaction CuO/Cu₂O is a promising solution thanks to its very high reported energy density (810.2 kJ/kg) and its incorporation of ambient air as the oxidation reagent (Carrillo et al., 2019; Wu et al., 2018). In addition, copper is abundant, non-toxic and have relatively low prices.

A primary obstacle for this material involves the sintering issue arising from the elevated reduction temperatures of CuO (~1000 °C), nearing its melting point (~1232 °C). This leads to diminished gas-solid



reaction surface area and, consequently, a significant decline in reaction efficiency after multiple cycles (Agrafiotis et al., 2016). The state-of-the-art solution to address the sintering problem involves physically or chemically doping CuO with metal oxides possessing notably high Tamman temperatures, such as MgO, Al₂O₃, and YSZ (Gigantino et al., 2020; High et al., 2022). However, both doping approaches result in materials with reduced energy density due to the relatively high content of the doping materials.

In this study, we present a straightforward one-pot chemical route to synthesize a multi-shelled hollow microsphere structure of CuO without the use of any dopant. The synthesis process is initially outlined, followed by a discussion of essential material characterizations. Additionally, the cyclic performance of the developed materials is demonstrated within the temperature range of 900–950 °C after 10 redox cycles. Finally, an assessment of the microstructure of the cycled materials is provided.

Experimental

Materials and synthesis process

In a typical synthesis process of the Multi-Shells Hollow CuO Microspheres (Figure 1), D-xylose, 99+% C₅H₁₀O₅ (40 mmol; Sigma Aldrich) were dissolved in 15 ml of deionized (DI) water under vigorous stirring for 20 min. Then, Copper (II) Nitrate Tetrahydrate Cu(NO₃)₂ · 3H₂O, (17 mmol; Sigma Aldrich) was added to the previous mixture and stirred for another 20 minutes. The obtained solution was transferred to a 50 ml PTFE (Poly Tetra Fluoroethylene) lined stainless-steel autoclave from CES (Cambridge Energy Solutions), which was placed in an oven at 180 °C for 24–36 hours. After cooling down to room temperature, the content of the reactor (black carbonaceous powder) is washed multi-times with Deionized (DI) water, then once with Ethanol. The obtained black powder was dried overnight at 80 °C and subsequently calcined at 800 °C for 4 hours with a slow heating rate of (i.e. 2 °C/min from room temperature up to the isothermal temperature) to remove the carbonaceous template and obtain the Multi-Shells Hollow CuO Microspheres.

Materials Characterisation techniques

The morphologies and elemental mapping of the investigated materials were analysed by Scanning Electron Microscopy (SEM) using a Hitachi TM3030 microscope, which is coupled to an Energy Dispersive X-ray Spectrometer (EDX), QUANTAX 70 Xflash@ 430-H from Bruker. The different analysis were operated at high vacuum mode, with a magnifications

up to 15.0kx and an accelerating voltage of 15 kV. Prior to the analysis the samples were coated with a 5–10 nm layer of Au coating using Q150R ES Plus – Rotary Pumped Coater from Quorum.

The phase composition of the materials was determined by X-ray powder diffraction (XRD) technique by means of the Bruker D8 Advance Diffractometer in Bragg-Brentano geometry (θ - 2θ), using Cu K α 1 radiation. The data were collected between 10° and 90° in 2θ with a step size of 0.02° and counting time of 8 s per step.

The thermochemical properties of the materials (e.g. Redox enthalpies) were measured using a the Simultaneous Thermal Analyzer NETZSCH STA 449 F3 Jupiter. In a typical test run, 10–20 mg of sample is loaded in a 85 μ l platinum crucible and heated from room temperature to 950 °C at a rate of 10 °C/min, followed by a 30 min isothermal under 50 ml/min flow of N₂ gas to ensure the full reduction of CaO materials. Then, the furnace temperature is cooled down to 900 °C at a rate of 10 °C/min, followed by a 5 min isothermal, without changing the previous gas flow and temperature conditions, to allow for the stabilization of the furnace temperature. Afterwards, an isothermal of 20 min is followed, where the flow is switched to Air and introduced into the furnace environment at the same previous temperature to perform the oxidation cycle. Another 5 min isothermal is followed where we go back to the initial gas flow condition to stabilize the environment get it ready for the following reduction cycle. In order to perform Redox cycles, the previous steps are repeated accordingly.

Results and Discussion

Nanofabrication of CuO hollow microspheres

As depicted in Figure 2, the successful synthesis of multi-shelled hollow CuO microspheres was achieved with two hydrothermal durations: (a) 24 hours and (b) 36 hours. An extended synthesis period led to an increased diameter of the microspheres, featuring distinct outer surface characteristics. In the upcoming sections, the two microspheres are denoted as hCuO/a and hCuO/b, respectively.

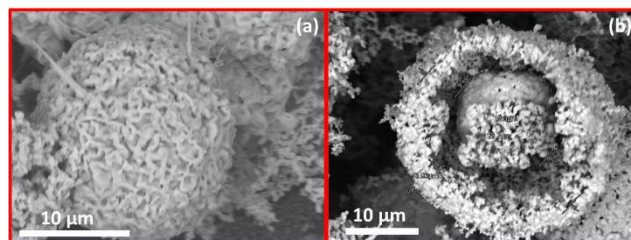


Figure 2: SEM analysis of one Multi-Shells Hollow CuO Microsphere for two hydrothermal synthesis time (a) 24 hours (hCuO/a) and (b) 36 hours (hCuO/b).

Characterisation of CuO hollow microspheres

Figure 3, displaying XRD analysis, demonstrates the attainment of a singular crystallographic phase of CuO (Tenorite). Additionally, the EDS elemental analysis clearly illustrates the chemical map of the multi-shelled hollow CuO microspheres (hCuO/b), comprising Cu and O atoms. Similar XRD and EDS results were obtained for hCuO/a.

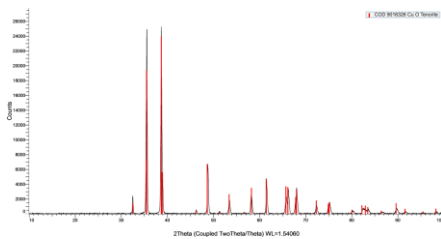


Figure 3: XRD analysis of the multi-Shells Hollow CuO Microspheres.

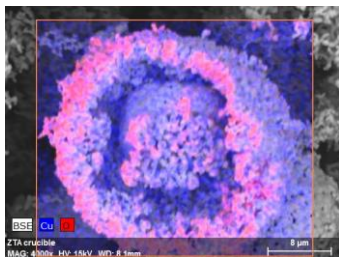


Figure 4: EDS elemental analysis of the multi-Shells Hollow CuO Microspheres.

Assessment of the cyclic redox performances

As outlined in the experimental section, hCuO/a underwent 10 cycles within the temperature range of 900-950 °C to evaluate its cyclic redox performance. As depicted in Figure 5, the multi-shelled hollow CuO microstructure demonstrates superior cyclability behaviours in comparison to the reference CuO material (Agrafiotis et al., 2016). Notably, the reoxidation capacity is maintained after 10 cycles without a reduction in energy storage density, distinguishing it from chemically doped CuO materials (High et al., 2022). As described in the experimental section, hCuO/a was cycled 10 times between in the temperature range of 900-950 °C to assess its cyclic redox performances. Similar results were obtained for the material hCuO/b.

Based on these results, the initial conclusion can be drawn that the sintering effect has been significantly

mitigated solely due to the hollow microsphere structure of CuO.

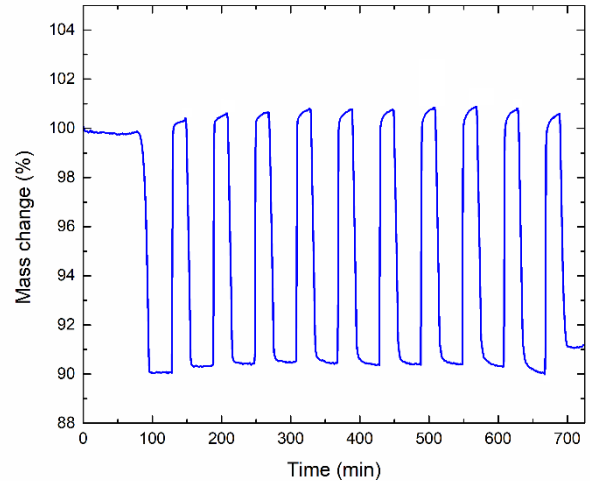


Figure 5: performances of the Multi-Shells Hollow CuO Microspheres under 10 cycles of Redox operation in the temperature range of 900-950 °C.

Microstructure cyclic performances

At the end of the cycling test in STA apparatus, which is described in the previous sub-section, hCuO/a sample was collected and subjected to an SEM analysis to investigate and understand any eventual change occurring to its microstructure. From Figure 6, after 10 cycles of Redox reactions, the hollow microspheres are dismantled into an association of shoulder blade like microstructures which highly porous and presenting a high surface area. No sign of sintering is shown in the obtained cycled microstructure which reinforce the conclusion from the previous subsection. In fact, the multi-shells hollow CuO microstructure is less prone to sintering phenomenon at high reduction temperatures. This might be due to the micrometric distancing between the CuO grains in the hollow CuO microstructure.

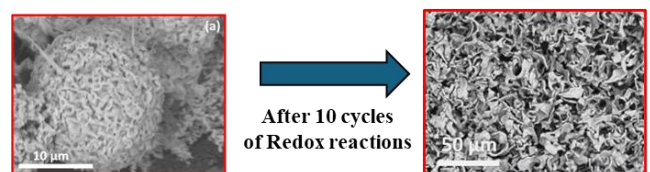
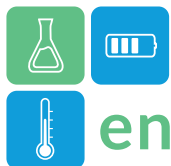


Figure 6: SEM analysis of the multi-Shells Hollow CuO Microspheres after 10 Redox cycles in the temperature range 900-950 °C. (a) before cycling, and (b) after cycling.



Conclusions

In conclusion, in this study multi-shelled hollow CuO microspheres were successfully synthesized through a straightforward one-pot process, without the need for any dopant. The newly developed microstructure demonstrated superior cyclic redox performance over 10 cycles when compared to the reference CuO material for potential applications in high-temperature thermochemical storage (Agrafiotis et al., 2016). Additionally, the synthesized materials exhibited a higher energy density (approximately 747 kJ/kg), closely approaching the reported literature value for the CuO/Cu₂O pair (~816 kJ/kg) (Gigantino et al., 2020). This experimentally obtained energy density is 59% higher than that of physically doped material (~470 kJ/kg) (Gigantino et al., 2020), and 87% higher than that of chemically doped material (~400 kJ/kg) (High et al., 2022).

SEM analysis of the hCuO/a material after 10 cycles revealed the transformation of its initial hollow microspheres into a highly porous microstructure resembling shoulder blades. Notably, there was no evidence of sintering, explaining the sustained redox efficiency over 10 cycles in the STA apparatus. These promising outcomes suggest that the sintering effect has been significantly alleviated solely due to the hollow microsphere structure of CuO, without the need for any doping agent. Further analyses are required to confirm the continued excellent cyclic performance over an extended number of cycles.

Acknowledgment

The research leading to these results has received funding from the Engineering and Physical Sciences Research Council (EPSRC), United Kingdom through the Plasma Assisted Thermo-CHEmical energy storage for Carnot batteries (PATCH) Project: (EP/W027887/1).

References

- Agrafiotis, C., Roeb, M., Sattler, C., 2016. Exploitation of thermochemical cycles based on solid oxide redox systems for thermochemical storage of solar heat. Part 4: Screening of oxides for use in cascaded thermochemical storage concepts. *Solar Energy* 139, 695–710.
- Carrillo, A.J., González-Aguilar, J., Romero, M., Coronado, J.M., 2019. Solar energy on demand: a review on high temperature thermochemical heat storage systems and materials. *Chemical reviews* 119, 4777–4816.
- Forsberg, C.W., Stack, D.C., Curtis, D., Haratyk, G., Sepulveda, N.A., 2017. Converting excess low-price electricity into high-temperature stored heat for industry and high-value electricity production. *The Electricity Journal* 30, 42–52.
- Gigantino, M., Sas Brunser, S., Steinfeld, A., 2020. High-temperature thermochemical heat storage via the CuO/Cu₂O redox cycle: From material synthesis to packed-bed reactor engineering and cyclic operation. *Energy & Fuels* 34, 16772–16782.
- High, M., Patzschke, C.F., Zheng, L., Zeng, D., Gavalda-Diaz, O., Ding, N., Chien, K.H.H., Zhang, Z., Wilson, G.E., Berenov, A.V., 2022. Precursor engineering of hydrotalcite-derived redox sorbents for reversible and stable thermochemical oxygen storage. *Nature Communications* 13, 5109.
- Wu, S., Zhou, C., Doroodchi, E., Nellore, R., Moghtaderi, B., 2018. A review on high-temperature thermochemical energy storage based on metal oxides redox cycle. *Energy conversion and management* 168, 421–453.



Numerical analysis of an off-grid positive temperature cold room coupled with latent thermal energy storage for food preservation

Gianluca Slaviero^{1,2,*}, Dario Traverso², Franco Traverso², Marco Noro¹, Claudio Zilio¹, Simone Mancin¹
¹ Department of Management and Engineering, University of Padova, Str.lla S.Nicola 3, Vicenza, 36100, Italy

² Genius Cold Srl, Via Postumia 9/B, Carmignano di Brenta (PD), 35010, Italy

*Corresponding author e-mail: gianluca.slaviero@phd.unipd.it

Abstract

The interest in Phase Change Materials (PCMs) is constantly growing in recent years thanks to their capacity of store large quantities of thermal energy per volume unit. PCMs are also promising candidates for developing a new concept of off-grid cold room only powered by solar power. This type of cold storage could be a game changer in remote area of developing countries, where almost one third of the food produced annually is wasted due to various inefficiencies of the cold chain or instabilities of the power grid. This study aims to develop a TRNsys-based numerical analysis of a positive temperature cold room for food preservation, coupled with a Latent Thermal Energy Storage (LTES), with different control strategies of the PV-powered system in various location of Africa and Italy. Coupling of the cold room with the PCM storage enabled the temperature control of the ambient during the nights and in low irradiation days.

Keywords: PCM, Thermal energy storage, off-grid cold room, food preservation

Introduction

Several areas of Africa suffer from poor agricultural development, mainly due to the difficulty of keeping the harvested products at a controlled temperature. As reported by Calati et al. (2023), Food and Agricultural Organization of United Nations (FAO) estimates that 1/3 of the food produced annually, about 1.3 billion tons, is wasted and that more than 800 million people suffer from malnutrition. Moreover, resulting Food Waste and Loss (FWL) play an important role in the climate change problem, accounting for the 8-10% of the total greenhouse gas (GHG) emission, about 4.4 Gt CO₂-eq, annually. In developing countries, waste of perishable food, is mainly associated by various inefficiencies of the cold chain that is usually powered by diesel generators or by unstable grid. This research is focused on study different control strategies to couple a positive temperature cold room with an ice storage, served by a chiller powered only by photovoltaic (PV) panels in TRNsys. The simulation demonstrated that is possible to maintain a 50 m³ cold room at a constant temperature of 5 °C overnight, without the aid of grid power.

Methodology

In Figure 1, a simplified schematic representation of the numerical model developed in TRNsys is presented. Within the software, the modeling of the component involves the use of predefined types that are characterized by parameters, inputs, and outputs. Type 56 in this model represents a single zone building that simulates 50 m³ food preservation room with a height and width of 2.6 m, and a length of 7.5 m. The walls are modelled as commercially available insulation panels manufactured by Cosma Impianti (Italy). These panels are considered to be massive, with a thermal conductivity of 0.034 W m⁻¹ K⁻¹, a density of 40 kg m⁻³, and a thickness of 0.2 m.

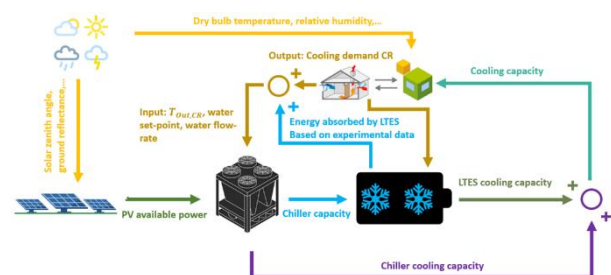
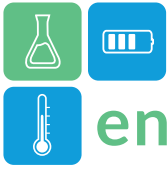


Figure 1: Schematic representation of the TRNsys model.



In TRNbuild, a Cooling Type with a constant setpoint of 5 °C is added, with a cooling power limited to the input provided by the chiller and the latent storage capacity. Type 15-6 is included to provide weather data from Meteororm for the selected location (Mogadishu, Somalia). Initially, Type 605-v2a was chosen for the air-cooled chiller characterization, but it was later modified into a user-defined type (Type 203) to accommodate variations in PV generation. The rated cooling capacity of the refrigeration unit is set at 2 kW for all simulations. The added functionality to this type includes the calculation of an internal parameter called the PV Signal. This function is designed to limit the electrical power input to the chiller only when PV power is available. A new type for the latent storage was developed within TypeStudio. Type 205 is based on experimental analysis conducted by Righetti et al. (2023) who run several charging and discharging tests of a 18 kWh roll bond based LTES filled with bio-based PCM. The storage in TRNsys takes as parameters the maximum storage capacity and the initial state of charge and has an embedded control structure. Eq. 1 and Eq. 2 describes the amount of power that the LTES can absorb or release as function of the solid fraction, defined as “s”, for a 18 kWh LTES.

$$P_{out,LTES} = 12.285s^3 - 9.045s^2 + 4.68s \quad (1)$$

$$P_{in,LTES} = -10.69s^3 + 25.917s^2 - 23.31s + 8.25 \quad (2)$$

This particular type of roll bond based LTES allows to scale the power input and output based on the size of the storage itself. For a 36 kWh storage for example, all the coefficient in Eq. 2 and 3 would be doubled. The considered PV array is composed by multiple modules connected in parallel configurations. A short technical description of the PV modules is reported in Table 1.

Table 1: PV modules datasheet

Supplier and Model	Silfab SLA230
Max Power Output [W]	230
Max op. voltage [V]	29.50
Max op. current [A]	7.80
Open circuit voltage [V]	37.40
Short circuit current [A]	8.30
V _{oc} [%/K]	-0.35
I _{sc} [%/K]	0.03
NOCT [°C]	45

Results

The photovoltaic signal that drives the compressor, as well as the PV and chiller power profiles, are depicted in Figure 2, portraying a weekly simulation. This function showcases the electrical power generated by the PV system that can be utilized to operate the chiller based on the compressor unit size. In the case presented, a refrigeration unit with a rated capacity of 2 kW is examined, paired with 10 PV modules connected in parallel.

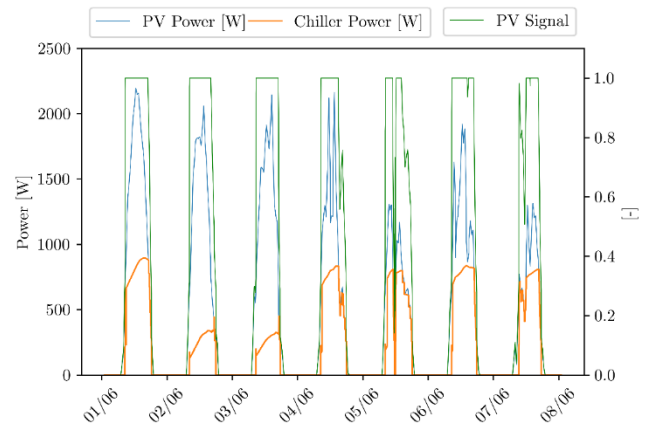


Figure 2: PV power output and Refrigeration Unit absorbed power during the first week of June with ten PV modules in parallel.

It is noteworthy to mention that on the 5th of June, for instance, the PV electrical power output is lower compared to other days, resulting in the PV function dropping below the lower threshold for set partial loading of 20% for the chiller, causing it to shut off. This scenario prompts the activation, during daylight hours, of the discharging mechanism of the LTES, as demonstrated in Figure 3.

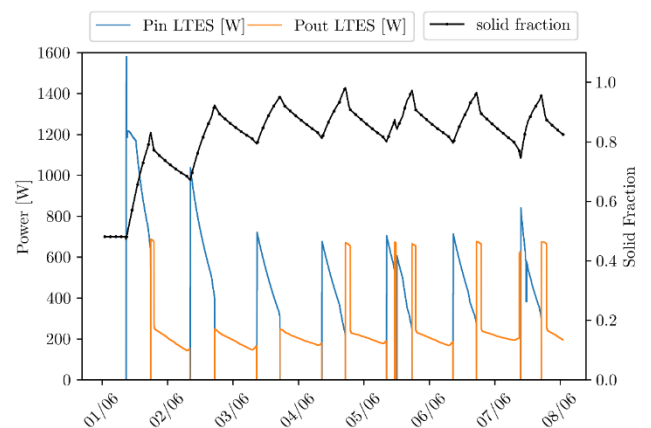
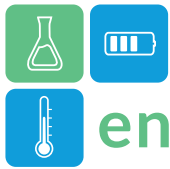


Figure 3: Charging and discharging cycles of the LTES in a weekly simulation.

In the diagram of Figure 3, P_{in} denotes the thermal power absorbed by the LTES from the chilled fluid, while P_{out} quantifies the thermal power output supplied



by the storage to the cold room. Both parameters are determined based on the solid fraction, which is the ratio between the ice mass to the total mass of water and ice within the storage. Throughout the week-long simulation, the ice storage's initial solid fraction is established at 0.5 to emphasize the charging and discharging cycles. Figure 4 illustrates the initial setup of the photovoltaic (PV) array, featuring 6 modules connected in parallel and a LTES capacity of 27 kWh. In this setup, the power generated by the solar array is insufficient to meet both the cooling needs of the refrigerator unit and the required charging ratio for the storage. As a result, the temperature of the cold storage exceeded the 5°C set point, particularly occurring in July for a total of 851 hours. The average solid ice fraction throughout the year is 0.574.

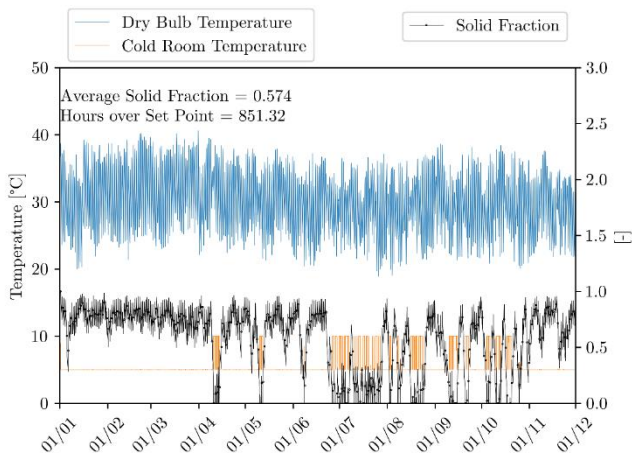


Figure 4: Year long simulation with 6 modules of PV panels.

A solution with 12 PV panels (Figure 5) can achieve complete grid independence throughout the year. The instances of internal temperature exceeding the set point can be primarily attributed to initial numerical errors, which will be corrected in the next release of the model. The duration of temperatures above 5 °C is slightly over 30 minutes and never surpasses 10 °C. Through the parametric study, it was determined that a high average solid fraction is essential for ensuring a consistent energy supply to the room in this particular roll-bond design. As demonstrated in equations 2 and 3, the solid fraction of ice directly impacts the thermal power output delivered to the cold room. For instance, when the solid fraction is 1, the LTES can provide approximately 7.9 kW of power, whereas at a solid fraction of 0.5, the power output drops to just 1.6 kW, nearly five times less.

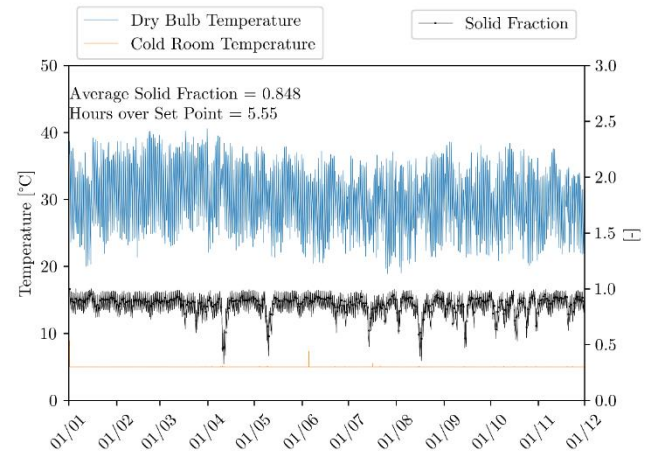


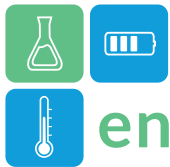
Figure 5: Year-long simulation with 12 modules of PV panels.

Conclusions

This study introduces a new numerical model for an off-grid positive-temperature cold room designed for food preservation. The model is integrated with an air-cooled chiller and a 300 kg ice thermal energy storage system. The primary focus of this study was to develop a tool that can simulate the potential use of off-grid food preservation technologies in rural areas of Africa, where the local power supply is unreliable or dependent on diesel generators, which are costly and have high greenhouse gas emissions. The use of ice-based cold storage systems offers a promising solution for off-grid food preservation and distribution. As part of this study, a 50 m³ positive temperature cold room was simulated using TRNsys software, coupled with a commercially available LTES system filled with water, having a total energy capacity of 27 kWh. The LTES system was incorporated into the simulation as a new type in TRNsys using TypeStudio. Different simulations were conducted, with different configurations of the PV arrays. The results indicate that the use of 6 PV modules connected in parallel does not allow to reach the off-grid target. This resulted in 35 days where the temperature exceeded the set point of 5 °C. The most effective solution was found to be the use of 12 modules PV array, which enabled complete power independence from the grid with only 5.5 hours of temperature exceeding the setpoint. These instances were primarily at the start of the simulation and were attributed to control issues that will be addressed in the upcoming model release.

Acknowledgment

Authors acknowledge financial support from Smart PhD 2023, co-funded by Fondazione Cassa di Risparmio di Padova e Rovigo, Intesa San Paolo S.p.A.



ENERSTOCK 2024
The 16th IEA ES TCP International Conference on Energy Storage
June 5–7, 2024
Lyon, France

References

Righetti, G., Zilio, C., Guarda, D., Feo, D., Auerbach, M., Butters, M., & Mancin, S. (2023). Experimental analysis of a commercial size bio-based latent thermal energy storage for air conditioning. *Journal of Energy Storage*, 72, 108477.

<https://doi.org/10.1016/j.est.2023.108477>

Michele Calati, Development and optimization of porous structures for efficient thermal energy storage using phase change materials (PCMs) for refrigerated transport applications, PhD Thesis, University of Padua, 2023.

Numerical and dynamic energy modeling for performance analysis of an integrated photovoltaic/thermal-heat pump system

Soowon Chae¹, Yujin Nam^{1,*}

¹Department of Architectural Engineering, Pusan National University, Busan 46241, Republic of Korea

*Corresponding author e-mail: namyujin@pusan.ac.kr

Abstract

In this study, we address the challenge of thermal management in photovoltaic-thermal (PVT) systems, particularly focusing on the impact of thermal energy storage (TES) on system efficiency. Traditional TES designs often employ a simplified single or limited-node approach, which can lead to inaccuracies in performance prediction. To overcome this, we developed a detailed numerical model that simulates TES behavior in PVT systems more accurately. Our model utilizes a convection heat diffusion approach tailored for PVT systems, where energy balance is calculated based on net heat transfer influenced by mass flow in a Cartesian coordinate framework. We considered both forced and natural convection scenarios, analyzing the effects of different node configurations on heat transfer. We validated our model by assessing PVT system performance under various typical conditions. The findings reveal that our model reliably predicts PVT efficiency with minimal variation due to changes in flow rate, marking a substantial advancement in PVT system design and analysis.

Keywords: Photovoltaic-thermal system, Thermal energy storage, Numerical modelling, Convection heat transfer

Introduction

Global challenges have heightened the focus on renewable energy, particularly photovoltaic (PV) systems, which efficiently convert solar energy to electricity but suffer efficiency losses at higher temperatures. Traditional cooling solutions like heat dissipation fans are both inefficient and consume significant energy (Tripanagnostopoulos and al., 2002).

To address these limitations, researchers have developed the photovoltaic/thermal (PVT) system. This innovative approach not only manages PV cell heat but also repurposes the waste heat for practical applications like heating and domestic hot water. Especially when combined with a heat pump (HP) in a hybrid system, PVT can significantly improve energy efficiency in these applications. However, the performance of these hybrid systems is closely tied to the temperature and flow rate of the fluid from the thermal energy storage (TES) (Chae and al., 2023).

Previous studies have highlighted the economic benefits of integrating PVT with HP, including shorter payback periods. Yet, a gap remains in accurately modeling TES, often simplified to one-dimensional due to computational constraints. This simplification can misrepresent fluid flow characteristics and lead to inaccuracies in system performance predictions.

Our research develops an advanced TES model, optimized for both computational efficiency and

accuracy in building energy simulations. By integrating this TES model with key components of the PVT-HP system, we evaluated its performance in real-time scenarios. This approach enhanced the accuracy of temperature dynamics, leading to more precise PVT efficiency predictions and supporting stakeholders in optimizing energy production and financial outcomes.

Methodology

Figure 1 illustrates the system's configuration and interconnections of its components, providing a visual representation of how they are integrated and operate together.

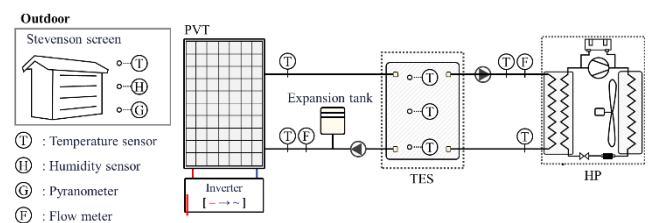


Figure 1: Schematic of an integrated PVT-HP system

In the PVT system, PV cells generate electricity via the photoelectric effect, and thermal energy is collected by a fluid circulating through a tube attached to an absorber plate beneath the PV cells. The TES system consists of a vertical cylindrical tank filled with water, designed to interact with up to two fluid streams

without an immersed heat exchanger. The HP operates by transferring heat from the storage tank to meet the heating load, employing a shell-and-coil mechanism coupled with compression work. The detailed specifications and design features of the PVT-HP integrated system are based on an actual building located in Busan, South Korea, and are presented in Table 1.

Table 1: Design Specifications and Component Details of the Integrated PVT-HP System.

Components	Parameters	Value
PVT	Number of modules	10
	Number of fluid tubes	14
	Length of the collector	2 m
	Width of the collector	1 m
	Module angle	45 °
	Module azimuth	130 °
TES	Height	1 m
	Volume	0.3 m ³
Pump	Head	11 m
	Power rating	180 W
HP	Compressor type	Scroll
	Compressor power	3 kW
	Refrigerant	R-410a

PVT simultaneously generates electricity and collects thermal energy by integrating PV cells with tubes and absorbers for fluid flow. Figure 2 illustrates this dual-function architecture, highlighting both the electricity and heat collection processes.

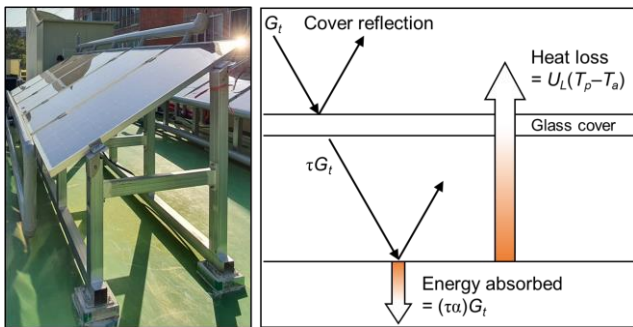


Figure 2: Schematic of the P/T model

The heat collection (q_{PVT}) amount and power generation (P_{PV}) amount are calculated as follows based on the calculated module solar radiation, observed outdoor temperature, and physical property information of the materials that make up the PVT.

$$q_u = \dot{m}_{PVT} C_p (T_{PVT,out} - T_{PVT,in}) \quad (1)$$

$$P_{PV} = (\tau\alpha)_n \eta_{PV} A_{PVT} I_{PVT} \quad (2)$$

We employed polynomial regression and a Multilayer Perceptron (MLP) to predict the outlet refrigerant conditions in a heat pump system. Polynomial regression focused on linear relationships, while the MLP, designed with z-score normalization, a single-neuron output layer, and Leaky ReLU activation with L2 regularization, tackled complex nonlinear patterns, using mean square error for loss assessment. Training of the MLP ceased after 500 epochs when no further decrease in validation error was noted.

Our study also described a shell-and-coil heat exchanger design for effective thermal energy transfer in a heat pump system, utilizing a TES. Water circulates through the shell, and refrigerant through the coil, with refrigerant flow and compressor efficiency influenced by initial conditions determined from shell temperature and compressor data. Despite potential inaccuracies in short-term operational predictions, these were considered minor in terms of overall system performance. The shell-and-coil model, using the finite volume method for detailed temperature and pressure calculations, optimized computation through improved spacing. Figure 3 depicts this counterflow shell-and-coil configuration.

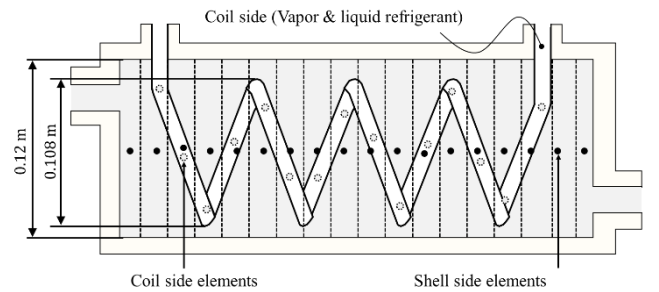


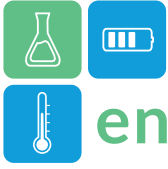
Figure 3: Schematic of the shell and coil model

When the heat pump's circulator pump is active, the refrigerant's heat absorption in the coil (q_{coil}) from the shell side is calculated using the total thermal resistance ($R_{S\&C}$) and the temperature difference between the shell and coil fluids. The equation is:

$$q_{coil} = \frac{1}{R_{S\&C}} (T_{shell} - T_{coil}) \quad (3)$$

In this equation, T_{shell} is the shell side water temperature, and T_{coil} is the coil side refrigerant temperature.

This version succinctly explains the process of calculating heat transfer and thermal resistance in the heat pump system, maintaining the technical details while reducing the overall length.



HP coefficient of performance (COP) and refrigerant flow rate are calculated as follows:

$$COP = \frac{q_{coil} + W_{comp}}{W_{comp}} \quad (4)$$

Here, W_{comp} is power rating of compressor.

Accurate heat transfer analysis in our TES model requires precisely defined control parameters for each node. We calculated centroid locations and heat transfer for each control volume using differential methods in the Cartesian coordinate system. The dimensions of finite elements on the x- and y-axes dynamically adjust to the number of central angles set by the user. Our finite element model accounts for heat transfer through conduction and convection, as well as node mixing, ensuring adherence to momentum and energy balance principles. Figure 4 illustrates the heat transfer flow between nodes.

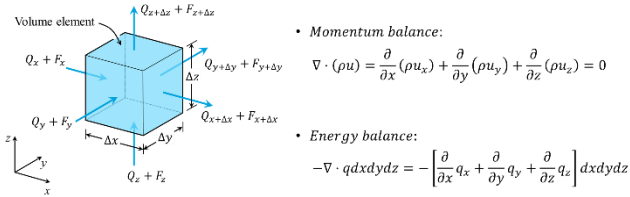


Figure 4: Schematic diagram of heat flow in TES elements

We optimized the finite elements in the TES numerical model using Particle Swarm Optimization (PSO). PSO constraints were set based on achieving momentum and energy balance, and aligning with experimental results. The PSO process includes initialization, evaluation, and updating phases. It begins with generating a swarm of 'particles', each representing a specific central angle size in the TES model. In the evaluation phase, the performance of each particle is assessed. The update phase recalculates the velocity and position of each particle, considering both the particle's own best position and those of its neighbors, and iterates this process until reaching the maximum number of predetermined iterations.

Results and Discussion

The accuracy of the numerical model for the HP, which plays a significant role in the performance of the integrated PVT-HP system, was examined. The method of accuracy assessment adopted was the Coefficient of Variation of the Root Mean Square Error (CV(RMSE)) as recommended by ASHRAE Standard 14. The accuracy verification results for heating and cooling were 11.95% and 3.59%, respectively. These results significantly satisfy the accuracy criterion, exceeding

the maximum allowable value of 30% suggested by ASHRAE Standard 14 (Chae and al., 2023). Figure 6 shows the accuracy verification results of the heat pump numerical model performed based on actual measurement data.

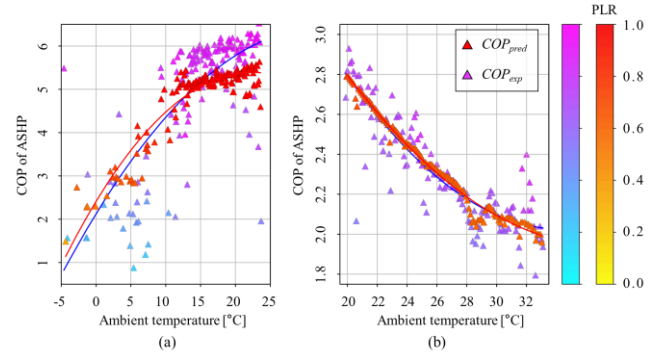


Figure 5: Heat pump heating and cooling performance analysis: (a) heating season (b) cooling season.

The performance and temperature gradient analysis of the integrated PVT-HP system was thoroughly conducted, focusing on the dynamics of the heat storage operations of the PVT and the heating functionalities of the HP. This analysis was performed on a representative day in December to evaluate the system's effectiveness in winter conditions. The protocol requires that heating begins when the TES temperature exceeds a set shell temperature of 30°C, with a 5°C deadband to ensure stability and efficiency. The initiation of heat storage occurs when the PVT temperature surpasses the TES temperature by the deadband, and continues only if the captured heat exceeds ten times the power consumption of the PVT circulator pump.

To evaluate the impact of different flow rates on system performance, flow rates of 20, 30, 40, and 50 liters per minute (LPM) were analyzed. Figure 6 shows the temperature fluctuations within the TES, the operational dynamics of the circulator pump, and detailed phases of heat storage and supply. The figure labels sections (a) through (d), each depicting the performance for flow rates of 20 to 50 LPM, respectively. This detailed analysis helps in optimizing the system for enhanced performance and sustainability by illustrating how various flow rates affect the thermal dynamics and efficiency of the integrated PVT-HP system.

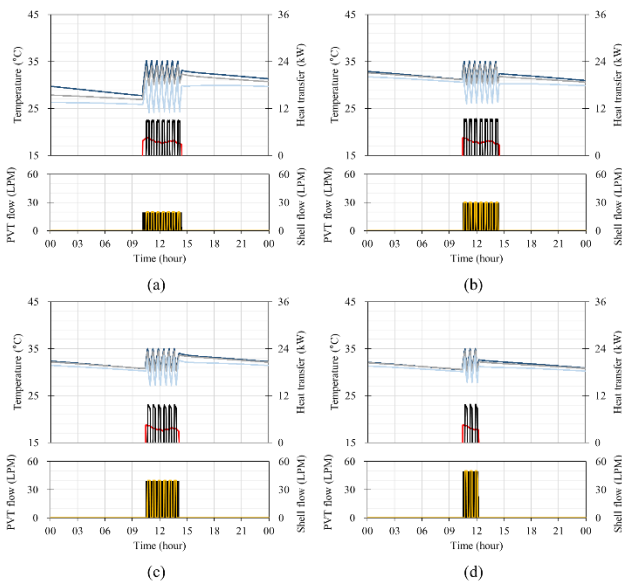


Figure 6: Representative days' flow-based performance analysis

Higher flow rates in the PVT system typically decrease vertical temperature gradients in the TES, analyzed using a three-dimensional TES model to account for horizontal flow effects. Our study, which analyzed temperature differences between the TES's upper and lower nodes under various conditions, found that increased flow rates enhance the vertical momentum of the fluid from the PVT, quickly elevating TES temperatures. This not only narrows the temperature difference between the TES and PVT, reducing heat storage frequency and volume, but also potentially raises the PVT inlet temperature, affecting operational efficiency. Additionally, higher TES temperatures may hinder achieving necessary temperatures at the shell inlet, limiting heating operations and reducing q_{coil} . Strategic adjustment of the circulator pump's flow rate based on environmental conditions can significantly improve system performance.

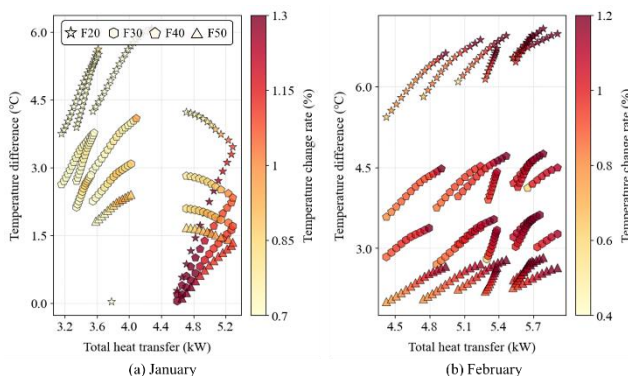


Figure 7: Schematic diagram of heat flow in TES elements

Conclusions

In conclusion, our study's three-dimensional TES model significantly enhances the accuracy of fluid dynamics predictions within TES systems. This model's ability to capture fluid temperature changes in all directions improves the precision of fluid state predictions for systems like heat pumps and PVT, even over brief time sequences.

The findings address a crucial gap in energy simulation, particularly in achieving high-interpretation accuracy for second-level time sequences. By more accurately reflecting real-world conditions, our TES model facilitates the practical implementation of digital twin technology and high-performance control technologies, like those using Multilayer Perceptron (MLP), in actual energy systems.

However, challenges remain. While effective on high-performance computers, implementing 3D TES models in standard micro control units (MCUs) used in heating and air conditioning systems is currently impractical due to computational and thermal limitations. Real-world application may thus require either remote control of MCUs through protocols like Modbus or further simplification of the TES model. These adaptations are essential for applying our research in practical settings and advancing energy-efficient technology.

Acknowledgment

This work was supported by the National Research Foundation of Korea(NRF) grant funded by the Korea government(MSIT). (No.2021R1A2C2014259)

References

- Tripanagnostopoulos, Y. and al. (2002) Hybrid photovoltaic/thermal solar systems. *Solar energy* 72.: 217-234, [https://doi.org/10.1016/S0038-092X\(01\)00096-2](https://doi.org/10.1016/S0038-092X(01)00096-2).
- Chae, S. and al. (2023). Economic and environmental analysis of the optimum design for the integrated system with air source heat pump and PVT. *Case Studies in Thermal Engineering*, 103142, <https://doi.org/10.1016/j.csite.2023.103142>.



Numerical investigation about the electrical heating of a molten salt mixture for thermal energy storage applications

Mattia Cagnoli^{1,*}, Roberto Grena¹, Michela Lanchi¹, Giuseppe Vecchi², Roberto Zanino³
1 ENEA, via Anguillarese 301, Roma, Italia

2 Politecnico di Torino, Dipartimento Energia, corso Duca degli Abruzzi 24, Torino, Italia

3 Politecnico di Torino, Dipartimento di Elettronica e Telecomunicazioni, corso Duca degli Abruzzi 24, Torino, Italia

*Corresponding author e-mail: mattia.cagnoli@enea.it

Abstract

Thermal energy storage (TES) is an effective technology to decouple the energy produced by intermittent renewable sources and the users' demand. TES systems are easily coupled with the concentrated solar power technology, which produces thermal energy. In hybrid renewable-based plants, CSP mainly charges the TES, while photovoltaic panels and/or wind power generates electricity to the grid. The electricity overproduction can be profitably exploited to further charge the TES. This work investigates the electrical heating of a molten salt mixture (solar salt), which is a common storage medium in TES systems. Advantages and disadvantages of the electrical heating technologies (Joule effect, microwaves, induction) have been identified by means of a theoretical analysis discussed in this manuscript. Microwaves heating seems the best compromise between technological feasibility and potential performance. An experimental device has been commissioned to study the salt thermal behaviour under microwave heating. The design of such an experimental device has been assisted with a dedicated numerical multi-physics model that solve both the electromagnetic and the thermal-fluid-dynamic problem; the computed results are presented here.

Keywords: Thermal Energy Storage, Molten salt, Electrical heating, Microwave

Introduction

Global warming imposes shifting from fossil fuels to renewable sources. A major drawback in using renewables is the intermittence in the energy source that makes difficult matching the energy production and the users' demand. Thermal energy storage (TES) is an effective technology to make the renewable energy dispatchable since it allows storing the surplus of energy produced, which is released on demand.

Among the renewables technologies, concentrated solar power (CSP) can be easily and profitably coupled with a TES system. This is because CSP directly produces thermal energy at medium-high temperature. The CSP plus TES technology is commercially available, as proven by the large number of plants built and operated worldwide (Alami et al., 2023). The storage medium is typically a mixture of molten salt, whose melting point is about 120-240 °C, depending on the salt mixture, and the maximum operating temperature is below 600 °C (Giaconia et al., 2021).

Recently, the hybridization of CSP plants with other renewable technologies that generate electricity, like photovoltaic (PV) and wind power, is gaining interest. In such hybrid systems, the CSP is focused on charging

the TES, while the other renewables systems mostly provide low-cost electricity to the grid. The electricity overproduction can be potentially stored in the TES increasing the profitability of the plant (Riffelmann et al., 2022). This implies converting the electrical energy into heat. For this purpose, different electrical heating techniques can be applied, namely:

- Joule effect
- Induction heating
- Microwave heating

Heat pumps are not very suitable in this case because of the large temperature difference between the available heat recovery temperature (ambient air) and the required salt temperature, which is typically up to about 550 °C (Giaconia et al., 2021; Hamid et al., 2023).

In this work, the electrical heating of a molten salt mixture, namely the solar salt (60%w NaNO₃, 40%w KNO₃), has been numerically investigated. This work aims at identifying the advantages and disadvantages of the electrical heating technologies applied to molten salt, with the purpose of determining the most promising option in terms of technology maturity and potential performance. Once identified the most

promising method for the electrical heating of molten salt, a numerical study is conducted to assist in the design of an experimental device able to prove the feasibility of the proposed technology.

The experimental device has been commissioned; it is going to be installed and operated at the ENEA Research center “Casaccia” in 2024.

Methodology

The three possibilities for electric salt heating were investigated with a preliminary scrutiny.

A model of Joule heating was built, computing the maximum power transferable to salt at a given bulk temperature, with the constraint that the film temperature of the salt cannot exceed the maximum allowed temperature (565 °C), above which salt decomposition becomes significant. Natural convection from horizontal heating elements was assumed. The heat transfer is very poor when the salt bulk temperature approaches its maximum working temperature, showing that the method can be applied only for a preliminary heating of the salt, but cannot satisfyingly heat the storage up to 550 °C;

Preliminary computations on induction heating show that direct induction could be an interesting path for future research, but requires some additional investigations and presents difficulties due to the poor electrical conductivity of the salt and to the interaction of the heating element with the salt. Indirect induction presents the same problem with film temperature as Joule heating;

Microwave heating seems to be feasible, given the preliminary work of Rodríguez-García et al. (2021); it guarantees a volumetric heating without problems of film temperature, and it is suitable to be tested on a lab-scale. So, microwave heating was selected.

A lab-scale device has been commissioned to experimentally study the thermal behavior of molten salt exposed to microwaves. The experimental device consists of a cylindrical tank partially filled with molten salt. A 3 kW magnetron generates microwaves with a 2.45 Hz frequency, which are directed to the top of the cylindrical tank by means of a rectangular WR340-type waveguide. The waveguide is provided with a ceramic window to prevent salt vapours from rising along the waveguide. Figure 1 shows a scheme of the experimental device.

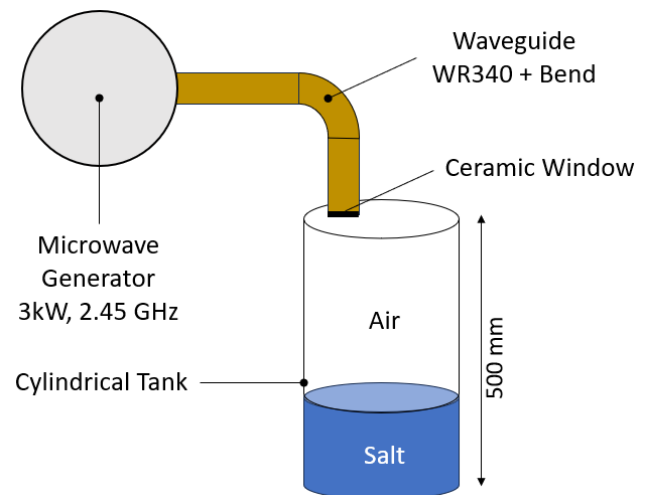


Figure 1: Scheme of the experimental device

A numerical 3D multi-physics model has been developed with COMSOL to assist in the design of the device. The numerical analysis aims at (i) evaluating how the design parameters affect the electromagnetic performance of the device and (ii) estimating the temperature distribution in the salt mixture under microwave heating. The model solves the Maxwell’s equations to determine the electric field in the device (salt and air regions) and, consequently, the power dissipated in the molten salt. The latter becomes the thermal driver of the thermal-fluid-dynamic study, which solves the dynamic mass, momentum and energy balance equations in the molten salt domain. The computational domain consists of half of the cylindrical tank because of the symmetry. A representative portion of the waveguide has been also considered. For the thermal-fluid-dynamic study, the computational domain is reduced only to the salt region. Suitable boundary conditions have been applied and the mesh independence of the results has been checked. The salt dielectric properties have been taken from (Rodríguez-García et al., 2021). Figure 2 and Figure 3 show the computational domain and the boundary conditions applied in the electromagnetic and thermal-fluid-dynamic model, respectively.

In the electromagnetic study, the coefficient of reflection, also known as scattering parameter (S11), has been considered as the performance indicator. This term provides a measure of the electromagnetic waves that are reflected back through the waveguide. The higher the absolute value of S11 the higher the power dissipated in the salt mixture.

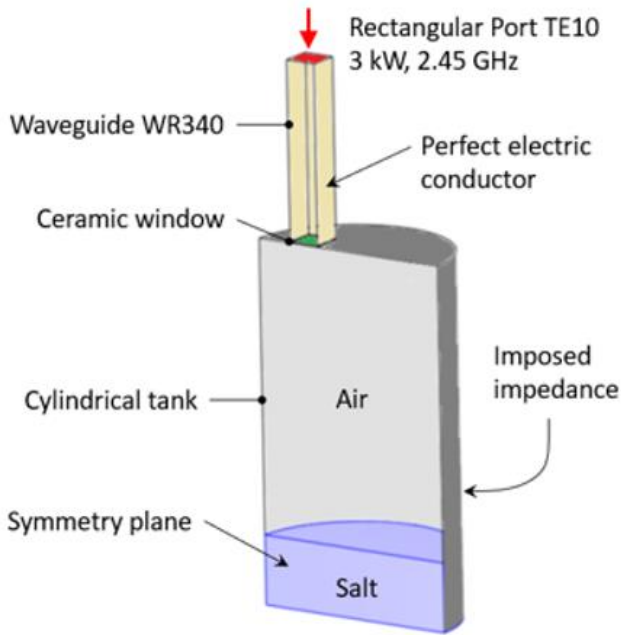


Figure 2: Computational domain and boundary conditions applied to the electromagnetic model

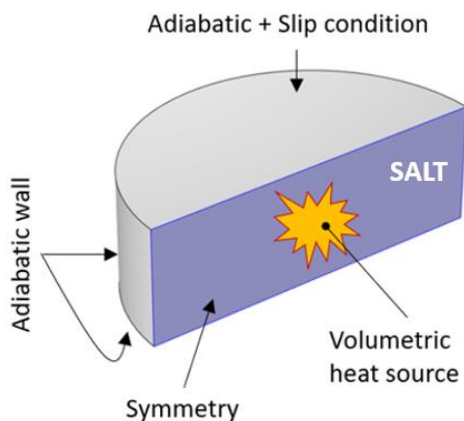


Figure 3: Computational domain and boundary conditions applied to the thermal-fluid-dynamic model

First, the model has been exploited to maximize the absolute value of S_{11} by means of an extensive parametric study. The parametric space examined includes:

- Tank diameter: 200 – 283 mm
- Salt volume at 280 °C: 6 – 12 liters
- Waveguide position along the vertical direction: immersed – salt free surface – over the salt
- Waveguide position along the radial direction: tank axis – half radius

In addition, the presence (or absence) of a metallic grid to confine the heated salt has been considered. The tank height has been fixed at 500 mm.

The best performing configuration has been considered in the thermal-fluid-dynamic study, which provides an estimation of the velocity field and of the temperature distribution in the salt volume during a test transient of 7 minutes.

Results and Discussion

An example of the results of the parametric study is provided in Figure 4. The greatest benefit is obtained moving the waveguide over the salt because of the air volume between the end of the waveguide and the salt. This volume of air helps the spread of the microwaves before reaching the salt volume resulting in a lower fraction of electromagnetic waves reflected back in the waveguide. The metal grid cannot be applied if the waveguide ends over the salt level. Finally, the best performing configuration corresponds to the configuration with the maximum diameter (283 mm), 6 liters of salt and the waveguide located over the salt level at a distance from the tank axis equal to half a radius. In addition, it was observed that moving the ceramic window upward from the end of the waveguide of about a wavelength (~ 12 cm) leads to a reduction of the reflected waves ($S_{11} = -26.5$ dB). In the optimized configuration, about 99 % of the electrical power is dissipated in the salt.

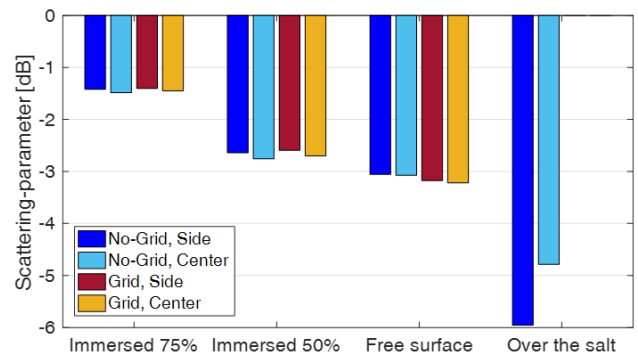


Figure 4: Computed scattering parameter varying the waveguide vertical and radial position, considering the presence or the absence of a metallic grid to confine the heated salt

The volumetric heat source obtained from the electromagnetic simulation is then exploited in the thermal-fluid-dynamic model as thermal driver. At the end of the test transient (7 minutes), the computed salt temperature distribution is shown in Figure 5. It can be observed that the salt temperature increases with the height, due to the distribution of the volumetric heat source. This mostly inhibits the natural convection in the salt region. For this reason, an impeller is planned to be installed in the experimental device, to promote the mixing making the salt temperature more uniform.

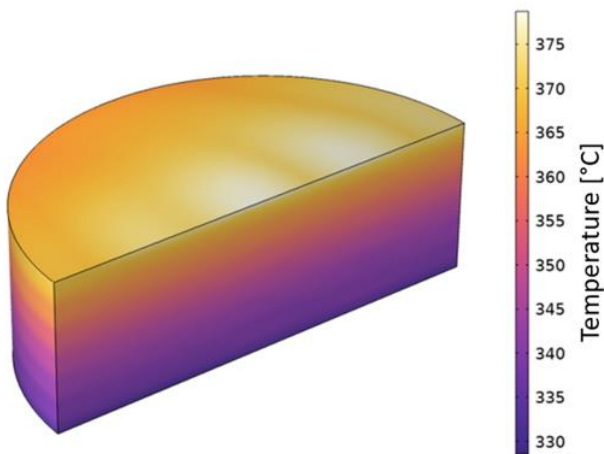
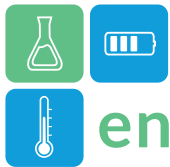


Figure 5: Temperature distribution in the salt at the end of a 7 minutes transient

Conclusions

This work deals with the issue of the electrical heating of a molten salt mixture (solar salt) for thermal energy storage applications, in the context of a hybrid (CSP + PV/wind) renewable energy plant.

Microwave heating was selected since it allows a volumetric heating of the salt, eliminating the power limitations due to the film temperature of heating elements when conduction/convection is exploited (e.g., Joule effect or indirect induction). In addition, it is more easily realisable on lab-scale in comparison to direct induction, whose feasibility needs to be investigated further.

To prove the feasibility of the microwave heating of the molten salt mixture, a lab-scale experimental device has been commissioned. The design of such a device has been assisted by a dedicated 3D numerical multi-physics model, which has been developed using COMSOL. The model solves the electromagnetic problem, determining the power dissipated in the salt, which is then exploited as thermal driver in the thermal-fluid-dynamic study, which provides the velocity field and the temperature distribution in the salt. The model allowed identifying the configuration of the experimental device that maximizes the power dissipated in the salt. The estimated salt temperature distribution does not promote the natural convection;

for this reason, an impeller is being installed in the experimental device.

Acknowledgements

This work was funded by the Italian Ministry of Environment and Energy Security through the «National Electric System Research» Programme, Project 1.9 “Solar thermodynamics” 2022-2024 implementation plan

References

- Alami, A.H., Olabi, A.G., Mdallal, A., Rezk, A., Radwan, A., Rahman, S.M.A., Shah, S.K., Abdelkareem, M.A., 2023. Concentrating solar power (CSP) technologies: Status and analysis. *Int. J. Thermofluids* 18, 100340. doi:10.1016/j.ijft.2023.100340
- Giaconia, A., Tizzoni, A.C., Sau, S., Corsaro, N., Mansi, E., Spadoni, A., Delise, T., 2021. Assessment and Perspectives of Heat Transfer Fluids for CSP Applications. *Energies* 14, 7486. doi:10.3390/en14227486
- Hamid, K., Sajjad, U., Ulrich Ahrens, M., Ren, S., Ganesan, P., Tolstorebrov, I., Arshad, A., Said, Z., Hafner, A., Wang, C.C., Wang, R., Eikevik, T.M., 2023. Potential evaluation of integrated high temperature heat pumps: A review of recent advances. *Appl. Therm. Eng.* 230, 120720. doi:10.1016/j.applthermaleng.2023.120720
- Riffelmann, K.J., Weinrebe, G., Balz, M., 2022. Hybrid CSP-PV plants with integrated thermal storage. *AIP Conf. Proc.* 2445, 030020-1–9. doi:10.1063/5.0086610
- Rodríguez-García, M.M., Bayón, R., Alonso, E., Rojas, E., 2021. Experimental and Theoretical Investigation on Using Microwaves for Storing Electricity in a Thermal Energy Storage Medium, in: *SolarPACES 2021 Proceedings*.

Numerical investigation of porous media layers for improved stratification within cold storage

Sebastian Gamisch^{1,*}, Parshva Atulbhai Parekh¹, Stefan Gschwander¹

¹Fraunhofer Institute for Solar Energy Systems ISE, Heidenhofstr. 2, 79110 Freiburg, Germany

*Corresponding author e-mail: sebastian.gamisch@ise.fraunhofer.de

Abstract

In fluid based sensible thermal energy storages a pronounced thermal stratification is crucial for the utilization of the energy content of the storage. This work investigates a porous sheet to improve the initialization of the thermal stratification in a cuboid shaped storage tank with a slotted pipe diffuser. Water is used as storage medium. Numerical simulations are performed with a two-dimensional model of the tank, to observe the influence of different placements and configurations of the porous sheet. The thickness of the transition zone between the warm upper and cold lower part, named thermocline thickness, is used to quantify the thermal stratification. The thermocline thickness can be reduced by limiting the mixing volume at the inlet. For the inclined placement of the sheet, the thermocline thickness can be reduced by 42 % from 0.12 m to 0.07 m compared to the storage without sheet.

Keywords: computational fluid dynamics, sensible thermal energy storage, thermocline, porous sheet

Introduction

In a single-tank thermal energy storage (TES) with liquid storage medium the fluid is separated due to buoyancy forces in a warmer upper region and colder lower region. The transition zone between the two temperature zones is known as thermocline (Pacheco et al. 2002) (see Figure 1). Higher exergy content and utilization of the energy content of the TES are associated with smaller thermocline thickness (Haller et al. 2009).

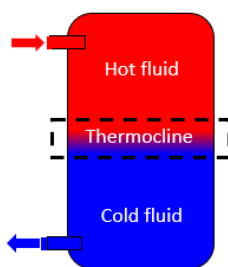


Figure 1: Schematic representation of different zones in TES tank

During the charging and discharging process, the initialization of thermocline region is significantly impacted by inlet jet mixing and plume entrainment due to high inlet velocities (Hollands and Lightstone 1989). In order to mitigate these adverse effects, suitable technological remedies are required. Therefore, several authors studied the impact of diffusers, baffles, stratifiers and porous sheet structures in the vicinity of the inlet.

Implementation of porous sheet structures can enhance the thermal stratification by restricting the inlet jet mixing zone and homogenizing the fluid flow. Using two-dimensional (2D) computational fluid dynamics (CFD) simulations, Lou et al. (2020) analysed the effect of perforated structures mounted in a single tank TES system. It was observed that with optimization of the perforated plate by having smaller holes in the middle domain of the tank and larger holes near the wall of the tank can significantly reduce the thermocline zone. Pathade et al. (2020) investigated the influence of two different perforated dampers on thermal stratification, which are mounted along with a radial diffuser in a cylindrical storage tank. It is concluded that horizontal dampers are not as impactful as vertical dampers to break the inlet jet momentum and improve the stratification.

In this paper, the thermal stratification of warm (35 °C) and cold (20 °C) water in a cuboid shaped storage tank during charging is studied using 2D CFD simulations. The tank is equipped with a slotted pipe diffuser. A porous sheet is utilized to restrict the inlet jet mixing zone and homogenize the incoming fluid flow.

Model description

A two-dimensional axisymmetric cuboid shaped tank with a height of 1 m, a width of 1 m and a depth of 2 m is investigated (see Figure 2) using the commercial software package COMSOL Multiphysics (Version 6.1). The slotted pipe diffuser is a semi-circular design with a slit as inlet to the storage. The slit has a width of

5 mm, and the center of the diffuser h_{tube} is at a height of 0.98 m. The axisymmetric model of the tank without any porous sheet arrangement is termed as the base case model.

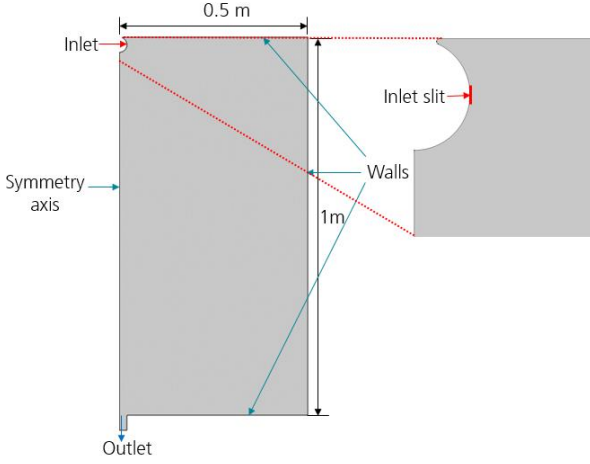


Figure 2: TES Model (left) and detail of the inlet slit (right).

A horizontal and an inclined placement of the porous sheet are examined. Both placements are shown in Figure 3.

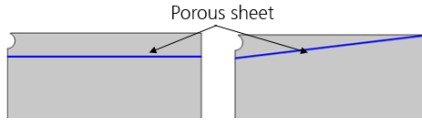


Figure 3: TES with porous sheet: horizontal placement (left) and inclined placement (right)

Governing equations

Transient simulations are executed by employing coupled laminar fluid flow and heat transport. Here, as the working fluid is water, incompressible fluid flow with a constant density is assumed. The mass, momentum and energy conservation equations solved for the base model in this investigation are, respectively

$$\rho \nabla \mathbf{u} = 0, \quad (1)$$

$$\rho \frac{\partial \mathbf{u}}{\partial t} + \rho (\mathbf{u} \nabla) \mathbf{u} = \nabla [-p \mathbf{I} + \mu (\nabla \mathbf{u} + (\nabla \mathbf{u})^T)] + \rho \cdot \mathbf{g}, \quad (2)$$

$$\rho c_p \frac{\partial T}{\partial t} + \rho c_p \mathbf{u} \nabla T + \nabla (-k \nabla T) = 0, \quad (3)$$

where $\mathbf{u} = u(u_x, u_y)$ is the velocity vector, ρ is the density of the fluid, t stands for time, p denotes the pressure, μ is the dynamic viscosity, T is the temperature, \mathbf{g} is the gravitational acceleration, c_p is the specific heat of the fluid at constant pressure, and k is the thermal conductivity of the fluid.

When a porous sheet is introduced, the mass conservation equation remains unchanged as shown in eq. (1). The fluid flow through the porous material is treated using Darcy-Forchheimer's equation which

extends Darcy's law to consider an additional pressure drop resulting from inertial losses, based on the acceleration and deceleration of the fluid as it flows through the tortuous path of a porous medium (Huang et al. 2020)

$$-\nabla p = \frac{\mu}{\kappa} \mathbf{u} + \rho \left(\frac{C_F}{\sqrt{\kappa}} \right) \mathbf{u}^2, \quad (4)$$

where C_F is the Forchheimer parameter and κ is the permeability of the porous sheet. The momentum conservation equation, solved for fluid flow through porous media, is

$$\frac{1}{\varepsilon_p} \rho \frac{\partial \mathbf{u}}{\partial t} + \frac{1}{\varepsilon_p} \rho (\mathbf{u} \nabla) \mathbf{u} \frac{1}{\varepsilon_p} = \nabla \left[-p \mathbf{I} + \mu \frac{1}{\varepsilon_p} (\nabla \mathbf{u} + (\nabla \mathbf{u})^T) - \frac{2}{3} \mu \frac{1}{\varepsilon_p} (\nabla \mathbf{u}) \mathbf{I} \right] - \left(\frac{\mu}{\kappa} + \rho \left(\frac{C_F}{\sqrt{\kappa}} \right) |\mathbf{u}| \right) \mathbf{u} + \rho \mathbf{g}, \quad (5)$$

where ε_p is the porosity of the porous material. The equation for the Forchheimer parameter is

$$C_F = \frac{1}{2} a b^{-1/2} \varepsilon_p^{-3/2}, \quad (6)$$

with the constants $a = 1.75$ and $b = 150$.

Boundary conditions

The initial temperature of the cold water T_{tank} is set at 20 °C. A uniform inlet flow rate \dot{V}_{in} of 5.333 m³/h and a constant inlet temperature T_{in} of 35 °C are assumed. At the outlet, an atmospheric pressure condition is applied whereas at the walls, no-slip boundary conditions and adiabatic thermal conditions are applied. Heat losses to the ambient are neglected. A symmetry boundary condition is applied on the left side.

A mesh independence study is performed in the CFD simulation for the base case TES at the given flow rate. Four different mesh types are generated. The deviation in terms of thermocline thickness after 50 % of charging is shown in Figure 4. For the finest mesh a thermocline thickness d_{tc} of 12 cm is achieved. The maximum deviation is around 178.22 % between coarsest and finest mesh whereas lowest deviation is around 13.48 %. Hence, the finest mesh is used for further analysis, assuming that the results are not significantly dependent on the mesh size for this choice.

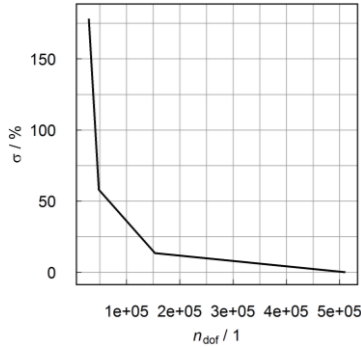


Figure 4: Deviation of thermocline thickness σ (from the result with the finest mesh) vs. number of degrees of freedom n_{dof}

Results and Discussion

Different case for the porous medium were investigated. The variations of porosity, permeability and Forchheimer parameter are listed in Table 1. The values are based on geometric variations of the porous layer. κ and C_F are dependent on ε_p .

Table 1: Investigated porous layer properties

Case	ε_p	κ (m ²)	C_F
1	0.2022	3.2088×10^{-11}	0.7854
2	0.3180	3.4458×10^{-10}	0.3983
3	0.3735	4.5114×10^{-10}	0.3129
4	0.4933	1.0588×10^{-9}	0.2062
5	0.6122	6.2083×10^{-9}	0.1492

First the TES without porous medium shown in Figure 2 and TES with horizontal placement of porous medium shown in Figure 3 (left) are analysed. For the porous sheet Case 3 with $\varepsilon_p = 0.3735$, the development of the thermocline thickness d_{tc} with respect to time for up to 30% charging of the TES is shown in Figure 5.

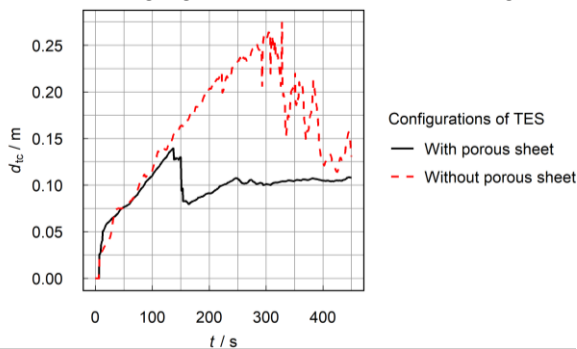


Figure 5: Thermocline thickness d_{tc} against time t for different configurations of TES (horizontal placement and case 3).

According to the graph, d_{tc} is nearly the same until 150 s. Afterwards the fluid impacts the opposite wall of the storage. With the porous sheet the thermocline thickness is reduced compared to the system without sheet, as the mixing zone is limited and the vertical downward flow is homogenized. Further the hot fluid mixes with cold fluid below the porous sheet, increasing thermocline thickness slightly until 250 s.

After that, the basically stable thermocline zone moves downward in the storage. For the system without sheet, the thermocline thickness increases as the fluid mixes within a larger volume in the storage. After 450 s, d_{tc} with the porous sheet is around 3 cm less as compared to base case model.

Further, three different vertical positions h_{porous} between 0.85 and 0.959 m of the horizontally placed porous sheet within the TES were investigated. Figure 6 shows a significant variation of d_{tc} for the different variations of h_{porous} . Here, Case 3 is applied. For $h_{porous} = 0.85$ m d_{tc} rises steadily until 300 s. Because of the larger mixing zone above the sheet, the mixing time of the hot and cold fluid is increased, resulting also in a larger d_{tc} of up to 17 cm at 400 s. When the porous sheet is placed more closer to diffuser ($h_{porous} = 0.959$ m), mixing area above porous medium is reduced leading to an earlier homogenized downward flow and smaller d_{tc} of 8 cm after 450 s.

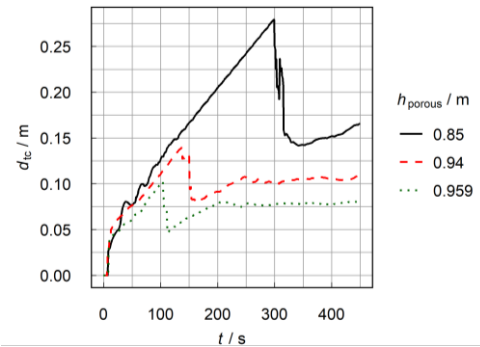


Figure 6: Thermocline thickness d_{tc} against time t for different vertical positions h_{porous} of the sheet

Figure 7 shows d_{tc} against time for different porosities ε_p (Cases 1 to 5) of the horizontal sheet. It can be observed that cases with $\varepsilon_p < 0.4933$ perform similarly. At 450 s comparatively higher thermocline thickness are observed as compared to cases with $\varepsilon_p \geq 0.4933$. After already around 120 s d_{tc} is lower for cases with $\varepsilon_p \geq 0.4933$ than other cases, owing to improved mixing of fluid above the porous sheet. The flow pattern above the porous layer changes with the porosity. With smaller porosities, the layer acts more like a rigid wall that exerts higher shear forces on the inlet flow. As a result, the liquid comes into contact with the porous layer earlier and therefore flows through it sooner leading to larger d_{tc} . With larger porosities, the highly permeable layer has less influence on the horizontal inlet flow. The fluid remains longer above the sheet for mixing. This results in a better stratification. However, the variation in

porosity doesn't have significant impact on the thermal stratification.

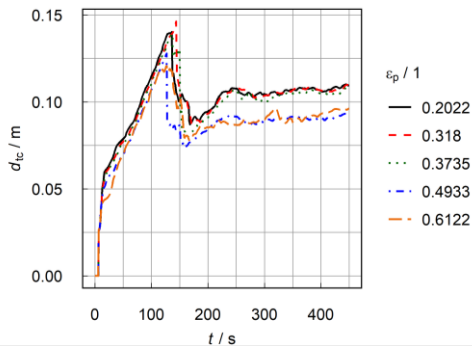


Figure 7: Thermocline thickness d_{tc} against time t for porosity variation of the sheet

To further reduce the mixing area above the porous sheet, an inclined placement (Figure 3 (right)) of the porous sheet is studied. Figure 8 shows the evolution of d_{tc} over time for the horizontal and inclined configurations for ϵ_p of 0.3735 (Case 3) and h_{porous} of 0.94 m, where the vertical position of the inclined placement is defined by the edge at the symmetry boundary condition, (see Figure 3).

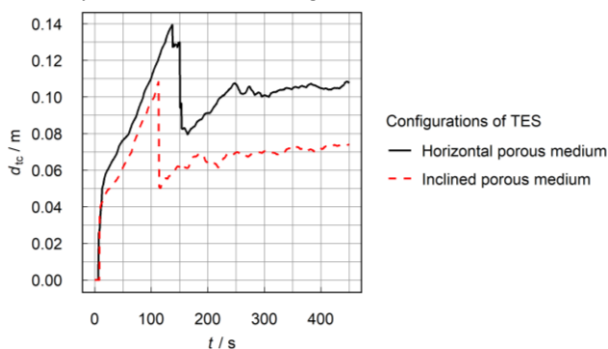


Figure 8: Thermocline thickness d_{tc} against time t for horizontal and inclined placement of the porous sheet

For the inclined placement, d_{tc} is significantly lower compared to horizontal sheet. The fluid comes earlier into contact with the inclined sheet which homogenizes the flow earlier. The inclined placement achieves a 3 cm smaller d_{tc} compared to horizontal placement after 450 s.

Conclusion

The thermal stratification in a cuboid storage tank with slotted pipe diffuser and porous sheet beneath is investigated numerically. Horizontal placement as well as inclined were examined. The following conclusions are obtained:

- Insertion of a horizontal porous sheet accelerates the formation of the stratification and results in a more stable and 3 cm lower thermocline thickness after 30 % of charging.

- For a lower thermocline thickness, a reduced mixing region is needed. Thus, the porous sheet should be placed as close as possible to diffuser.
- Variation in porosity does not have a vital impact on thermal stratification, with slightly better stratification for higher porosity/permeability.
- An inclined placement of the sheet can further reduce the mixing region resulting in a thermocline thickness of around 7 cm after 30 % of charging, again ca. 3 cm lower than in the horizontal configuration.

Acknowledgment

The authors are grateful for the funding of the project Optimus by the German Federal Ministry for Economic Affairs and Climate Protection. Many thanks also to the project management organization Jülich (PtJ) for their administrative support.

References

- Haller, Michel Y.; Cruickshank, Cynthia A.; Streicher, Wolfgang; Harrison, Stephen J.; Andersen, Elsa; Furbo, Simon (2009). Methods to determine stratification efficiency of thermal energy storage processes – Review and theoretical comparison. *Solar Energy*. DOI: 10.1016/j.solener.2009.06.019.
- Hollands, K. G. T.; Lightstone, M. F. (1989). A review of low-flow, stratified-tank solar water heating systems. *Solar Energy*. DOI: 10.1016/0038-092X(89)90151-5.
- Huang, Ting; Du, Pengbin; Peng, Xinkai; Wang, Peng; Zou, Gaofeng (2020). Pressure drop and fractal non-Darcy coefficient model for fluid flow through porous media. *Journal of Petroleum Science and Engineering*. DOI: 10.1016/j.petrol.2019.106579.
- Lou, Wanruo; Fan, Yilin; Luo, Lingai (2020). Single-tank thermal energy storage systems for concentrated solar power: Flow distribution optimization for thermocline evolution management. *Journal of Energy Storage*. DOI: 10.1016/j.est.2020.101749.
- Pacheco, James E.; Showalter, Steven K.; Kolb, William J. (2002). Development of a Molten-Salt Thermocline Thermal Storage System for Parabolic Trough Plants. *Journal of Solar Energy Engineering*. DOI: 10.1115/1.1464123.
- Pathade; Swati, Maurya; R.S. (2020). Improving Thermal Performance of Chilled Water Storage Tank-A Numerical Study. *International Journal of Mechanical and Production Engineering Research and Development (IJMPERD)*.



Numerical modelling of a Pit Thermal Energy Storage used for performance guarantee.

Nathan Fournier^{1,*}, Pierre Garcia¹, Alexis Gonnelle¹, Jianhua Fan², Simon Furbo²

1. Newheat, 10 allées de Tourny, 33300 Bordeaux, France

2. DTU Construct, Technical University of Denmark, Brovej, Building 118, 2800 Kgs. Lyngby, Denmark

*Corresponding author e-mail: nathan.fournier@newheat.fr

Abstract

Water pit thermal energy storage (PTES) is a long-term heat storage technology that synergises with fluctuating renewable energy sources. PTES numerical models are crucial at every stage of project development but can be challenging due to long computational time. By balancing numerical efficiency and prediction accuracy, this work aims to develop a PTES model suitable for system-based analysis. The model was developed based on open-source Modelica libraries in the Dymola environment and validated against data from Dronninglund PTES. The model predicts accurately the key performance indicators of the PTES: the charged and discharged energies and the water region temperatures, with absolute deviations of less than 3% for the energies. The computational time is of 75s for a yearly simulation. The model has been used for a performance guarantee in an opportunity study for PTES integration into district heating network (DH-N), showing the relevance of considering the performance sensibility to design parameters such as lid conductivity and soil characteristics.

Keywords: Water pit thermal energy storage, Numerical model, Modelica, Measurement validation, Performance guarantee.

Introduction

Large Thermal Energy Storages (LTES) constitute a strong enhancer for renewable energy development for heating applications, by reducing seasonal mismatch (Dahash, A. et al. 2023), offering flexibility to the DH-N and enabling power-to-heat potential. PTES is one type of LTES consisting of a large water volume (typically from 10 000 to 500 000 m³) dug into the ground and covered by an insulation lid. The excavated soil is reused to build up banks and increase the storage volume. The advantages of PTES are the possibility to be installed almost everywhere, its affordability due to partial burying, and the possibility to achieve high efficiencies after a steady state is reached.

An appropriate modelling tool is crucial for preliminary studies and techno-economical evaluation of energy systems. PTES models can be divided in two categories: detailed computational fluid dynamics models and simplified multi-node models. Computational fluid dynamics (CFD) modelling tools, such as ANSYS Fluent and COMSOL, provide a detailed overview of the PTES behaviour over time as these models are typically 3D but they lead to high numerical complexity and computational time, thus are too costly to be used for system-level analysis. "Coarse models" which simplified assumptions are introduced to obtain a balance between prediction accuracy and

turnover time. The frequently used system simulation tools are Transient System Simulation (TRNSYS), MATLAB/Simulink and Dymola (based on Modelica language).

Modelica is an object-oriented language used especially for complex multi-domain systems modelling. It is an equation-based, acausal and object-oriented modelling language, which facilitates reuse of pre-existing knowledge. Only a few models have been developed for PTES in Modelica, none being validated and available open-source or commercially. Dahash et al. validated a model before studying some key parameters on LCOS (Dahash et al. 2022). Reisenbichler et al. (2021) also created a model following a similar approach. It was compared to existing TRNSYS models for validation purpose. Finally, Formhals et al. (2020) developed an open-source library in for modelling underground thermal energy storage systems (MoSDH). This open-source library served as inspiration for the PTES model introduced in this paper.

The literature highlights the lack of a publicly available and robust PTES model with a quick computational time in Modelica language. Therefore, a PTES model would facilitate pre-feasibility investigations, design, and optimization of energy systems with PTES.

The aim of the model is to achieve a good balance between prediction accuracy and numerical efficiency. This paper will present the steps of model development, spanning between modelling, validation, sensitivity analysis and present its use for an opportunity study.

Model description

The water region is represented by a thermally stratified tank component. The PTES, which usually has a reverse truncated-pyramid shape, is simplified to a cylindrical shape to reduce the computational time. The IBPSA library provides a tank storage which is discretized in layers along the depth of the storage, following Equation 1, where $T(z, t)$ is the temperature of the layer at depth z and time t , v the velocity of the flow, λ the thermal conductivity of the medium, c_p its thermal capacity, ρ its density and \dot{q}_{los} the volumetric heat flow rate to the ambient.

$$\frac{\partial T(z, t)}{\partial t} + v \frac{\partial T(z, t)}{\partial z} = \frac{\lambda}{\rho c_p} \frac{\partial^2 T(z, t)}{\partial z^2} + \frac{\dot{q}_{los}}{\rho c_p} \quad (1)$$

To account for the actual geometry of a PTES, the heat loss term through a face of the storage has been adapted by considering the area of this face as if it was a corresponding truncated pyramid, instead of the cylinder modelled. The equation is presented hereafter with Q_{loss} the heat losses through a face of the storage, A_{pyr} the area of this face for a truncated pyramid with the same volume and height, λ_{ins} the insulation thermal conductivity, d_{ins} its thickness and ΔT the temperature difference between the two sides of the face

$$Q_{loss} = \frac{A_{pyr} * \lambda_{ins}}{d_{ins}} \Delta T \quad (2)$$

The soil region is developed based on the global model technique from MoSDH library. It meshes the soil in two dimensions (radial and axial), following the axial symmetry simplification used in the model.

The meshing is defined in each direction by the number of nodes, the size of the first one, and the increase factor from one another. Each node follows the heat equation, with V , $T_{cell}(t)$, ρ , and c_p , its respective volume, temperature, density, and specific heat capacity. R_k and T_k are the resistance to an adjacent node and its temperature.

The meshing is defined in each direction by the number of nodes, the size of the first one, and the increase factor from one another. Each node follows the heat equation, with V , $T_{cell}(t)$, ρ , and c_p , its respective volume, temperature, density, and specific heat capacity. R_k and

T_k are the resistance to an adjacent node and its temperature.

$$V \rho c_p \frac{\partial T_{cell}(t)}{\partial t} = \sum_k \frac{T_k(t) - T_{cell}(t)}{R_k} \quad (3)$$

Finally, the boundary conditions have been defined as follows:

- Inner boundary: adiabatic, due to the symmetry considered.
- Top boundary: consideration of a convective heat flux at the surface of the PTES, with a prescribed ambient temperature at the boundary.
- Outer and bottom boundaries: Undisturbed Soil Temperature Model from the Buildings library.

The resulting model meshing is introduced in Figure 1. The default values used for the meshing have been calculated following a sensitivity analysis to reach an asymptotic finite element method response, to avoid unwanted effects from boundary conditions for example.

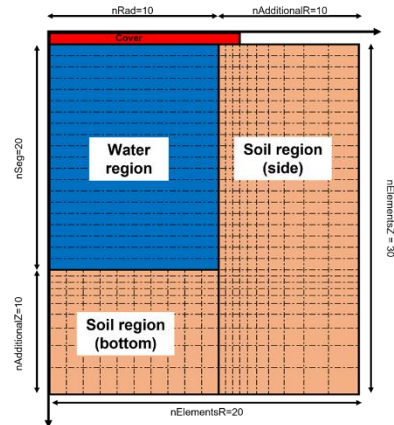


Figure 1: Meshing of the PTES model.

Robust key performance indicators (KPIs) are necessary to understand the performance of a storage, which can be complex to represent. Task 39 from the IEA Energy Storage collaboration programme, untitled “Large Thermal Energy Storages for District Heating”, is producing an exhaustive list of KPIs for thermal storages and guidelines for their use. One of those is the energy efficiency (η_E), an indicator used for measuring the performance of a storage, knowing its charged (E_{cha}) and discharged (E_{dis}) energies and its internal energy variation (ΔE_{st}).

$$\eta_E = \frac{E_{dis}}{E_{cha} - \Delta E_{st}} \quad (4)$$

Results and Discussion

Validation

The developed PTES model is validated against data from a PTES in Dronninglund (Denmark) which is part of a solar heating plant. The measured data has been post-processed by Sifnaios, I. et al. (2023) to reach a consistent dataset. The plant was built by Dronninglund Fjernvarme, a consumer-owned company responsible for the DH network for 1,350 consumers (Tschopp, D. et al. 2020). The plant has been operating since May 2014 and aims to reach a 50% solar fraction. It was created to demonstrate that combining large-scale solar plants and PTES could ensure stable heat supply for DH networks. Its plant system design is introduced in Figure 2. The PTES is approximately 60,000 m³; its depth is 16 m, and it is shaped as a reversed truncated pyramid with a squared base. The length of the top and bottom surfaces are respectively 90 m and 26 m, leading to a side slope of 26.6°.

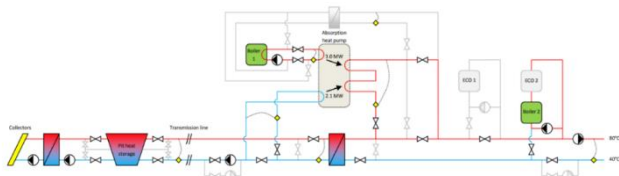


Figure 2: Dronninglund thermal plant system design.

The validation of the model is conducted after one year of pre-heating using the data from 2015. The pre-heating will establish a reasonable temperature profile in the PTES and in the soil region. Then, the simulation is conducted for the years 2015 and 2016.

Table 1 presents the results of the validation; the model underestimates the charged and discharged energies by less than 3%. The relative differences of charged and discharged energies varied between -3.1% to -4.1% for 2015 and -1.3% to -1.7% for 2016. This result confirms the importance of validating the model over several years to highlight the differences from one year to the other and the likely diminishing influence of the initialization method.

Table 1: 2015 & 2016 measured and simulated energy balances.

Energy [GWh]	Meas.	Sim.	Difference [%]
Charged	23.54	23.02	-2.2
Discharged	21.70	21.05	-3.0
Internal change	-0.54	-0.43	+19.5
Thermal losses	2.38	2.40	+0.7
Top losses	1.62	1.56	-3.7
Efficiency [%]	89.9	89.6	-0.3

Figure 3 presents the comparison between the measured and simulated temperatures within the PTES closest to each diffuser. The model precisely represents the temperature close to the diffusers, which explains

the accuracy observed in the energy analysis. The main differences between the measured and simulated profiles occur when the PTES has large temperature fluctuations, that the model tends to underestimate due to numerical diffusion induced by the limited number of layers. The same exercise was conducted for each sensor within the storage and all the coefficient of determination calculated have a value higher than 0,95.

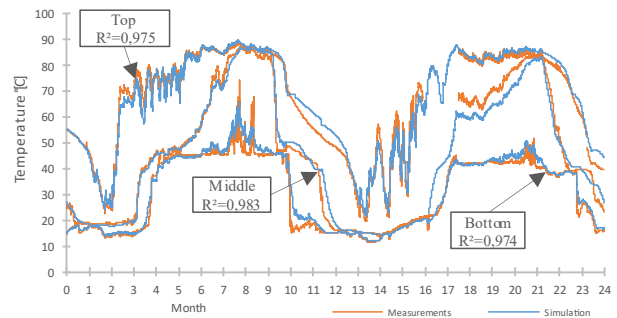


Figure 3: Temperature profile within the PTES at the sensor closer to each diffuser.

As discussed in the introduction, the computational time is of a major importance for system simulation. After optimizing the settings of the Dymola compiler, a one-year simulation on a computer equipped with a 4-core 11th Gen Intel® Core™ i7 processor, lasts approximately 75 s.

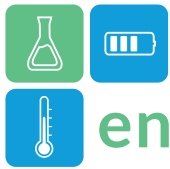
To confirm its relevance for providing such a guarantee, a second round of model evaluation against operation data from Marstal PTES in 2019 was conducted. The lid has been changed the following year due to significant damage in the original one. By fitting the lid thermal conductivity to a value which is consistent with its observed condition, the model turned out to provide results as accurate as those observed for Dronninglund validation.

Opportunity study

The model was used by Newheat to provide a performance guarantee in an opportunity study for a (DH-N) in France. In this project, the implementation of a PTES is considered for increasing the use of excess energy from various sources instead of gas. Thus, the storage is a mean to increase the renewable share in the energy balance of the network.

The PTES considered has a volume of 430,000 m³, which would make it the biggest in the world as of today; a depth of 25 m, a slope of 1:2, and includes two diffusers at the storage's top and bottom.

To provide a performance guarantee to the DH-N operator, a sensitivity analysis was conducted on two categories of parameters:



- Those which can vary over time (random or degradable): ambient temperature and lid conductivity.
- Those which were uncertain at this stage of the project: soil characteristics (thermal conductivity and capacity).

For each of those parameters, a range was estimated from a reference to a worse case, based on literature and information from suppliers, creating several scenarios. Five-years simulations were conducting for each. Table 2 shows the energy balance and efficiency of the storage for the second year (after one year of preheating), for three scenarios with worsening parameters (light grey) regarding PTES performance. It shows that the KPIs (light green) can vary significantly due to uncertainty or potential degradation of several parameters.

Table 2: Energy balances for several sets of parameters.

Scenario	1	2	3
Lid U-value [W/(m ² .K)]	0.17	0.17	0.20
Soil conductivity [W/(m.K)]	2.5	5.1	5.1
Soil capacity [kJ/(kg.K)]	1.0	1.4	1.4
Charged energy [GWh]	28.7	29.3	29.3
Discharged energy [GWh]	23.2	22.2	21.8
Losses [GWh]	4.8	6.1	6.6
Efficiency	83.0%	78.4%	76.9%

This study enabled the definition of a performance guarantee based on the model simulation results. It varies depending on the years and operating conditions due to the sensibility of the storage performance to those.

Conclusions

The main goal of this work was to develop a PTES model adapted for preliminary studies at system level in Modelica language. It has been validated against operating data from Dronninglund storage, showing a deviation lower than 3% regarding yearly energy balances and an acceptable fit for temperature levels within the PTES. Moreover, its computational time within an energy system model has an order of magnitude of one minute per year, which is acceptable. Thus, this model can be used for system simulations including PTES. Finally, the work introduces a performance guarantee conducted with this model for a DH-N project in France. It displayed the importance of considering the performance sensibility to several key parameters, thus, confirming the need for a system integrated PTES model available for early project stages to reach a performance guarantee which avoids

to many risks for the developer and is interesting for the customer.

Acknowledgment

This study was partly funded by the Danish Energy Agency through EUDP grants ‘IEA ECES Annex 39 LTES’ (no. 64018-0134), ‘Participation in the IEA SHC Task 68 on efficient solar district heating systems’ (no. 134-21027) and ‘Participation in the IEA ES TCP Task 41 on Economics of Energy Storage’ (no. 134223-495989). The authors want to express their deepest gratitude to Dronninglund Fjernvarme for providing the data used for validation. The authors also want to acknowledge Alessandro Maccarini, Ioannis Sifnaios, Michael Reisenbichler, Abdulrahman Dahash and Julian Formhals who took time at different stages of the project to provide insights and advice based on their research.

References

- Dahash, A. et al. “Advances in seasonal thermal energy storage for solar district heating applications: A critical review on large-scale hot-water tank and pit thermal energy storage systems”. In: Applied Energy 239 (Apr. 2019), pp. 296–315. issn: 0306-2619. doi: 10.1016/J.APENERGY.2019.01.189.
- Dahash, A. et al. “Simulation-based design optimization of large-scale seasonal thermal energy storage in renewables-based district heating systems.” Unit of Energy Efficient Buildings, Department of Structural Engineering and Material Sciences, University of Innsbruck, 2020.
- Formhals, J. et al. “A modelica toolbox for the simulation of borehole thermal energy storage systems”. In: Energies 13 (9 May 2020). issn: 19961073. doi: 10.3390/en13092327.
- Guo, H. and al. (2023) Chapter One - Effect of thermal storage and heat exchanger on compressed air energy storage systems in Advances in Heat Transfer, Elsevier, doi: 10.1016/bs.aiht.2023.02.003.
- Sifnaios, I. et al. (2023) ‘The Impact of Large-Scale Thermal Energy Storage in the Energy System’. Applied Energy 349 (November 2023): 121663. doi: 10.1016/j.apenergy.2023.121663.
- Reisenbichler, M. et al. “Towards More Efficient Modeling and Simulation of Largescale Thermal Energy Storages in Future Local and District Energy Systems.” 2021.
- Tschopp, D. et al. “Large-scale solar thermal systems in leading countries: A review and comparative study of Denmark, China, Germany and Austria”. In: Applied Energy 270 (2020). issn: 03062619. doi: 10.1016/j.apenergy.2020.114997.



Numerical simulations for improvements of the experimental system for testing adsorption heat storage materials

Urška Mlakar^{1,*}, Alenka Ristic², Uroš Stritih¹

1 University of Ljubljana, Faculty of Mechanical Engineering, Laboratory for heating, sanitary and solar technology and air conditioning, Aškerčeva cesta 6, 1000 Ljubljana, Slovenia

2 National Institute of Chemistry, Laboratory for adsorbents, Hajdrihova ulica 19, 1000 Ljubljana, Slovenia

*Corresponding author e-mail: urska.mlakar@fs.uni-lj.si

Abstract

In order to reduce the share of fossil resources consumed, countries strive to increase the share of renewable energy sources used. Energy storage is inevitable to bridge the problem of availability of energy sources and energy demand, which can be achieved with the help of renewable energy sources. In this paper, open adsorption storage is discussed. Using the results of the experiments, the numerical model of the open adsorption system is validated for the multiple tests of using adsorbents. The numerical model will enable improvements to be made to the experimental system. The numerical model is created in the Ansys software environment.

Keywords: Numerical simulations, experimental system, adsorption, adsorbents, heat storage

Introduction

Half of the world's final energy demand is used for heating and cooling purposes. In March 2023, an agreement was reached between the European Parliament and the Council to strengthen the EU Renewable Energy Directive. The agreement raises the EU renewable energy target for 2030 to at least 42.5%, which is equivalent to doubling the current share of renewable energy in the EU (European Commission, 2023). Due to the fluctuating availability of renewable energy sources, a solution must be found to include them in the supply chain for the provision of final energy for heating and cooling buildings. Thermal energy storage technologies can play a key role in this. There are three technologies of thermal energy storage (TES), which are sensible, latent and thermochemical storage. In this contribution focus will be on thermochemical storage. In thermochemical storage, energy is stored through reversible sorption processes or chemical reactions. Therefore, high reaction/adsorption enthalpies can be utilised to achieve higher energy storage density, making it suitable for large-scale applications. In this method, the heat loss during the energy storage process is almost zero (Crespo et al., 2023). The selection of a suitable adsorbent and adsorbate is very important. The most important properties of the adsorbent are high energy density for high thermal storage, low charging temperature for low energy consumption, high uptake

of sorbate and that it is environmentally friendly if we have open systems and easy to handle as well as non-toxic (Stritih & Mlakar, 2018). Another key advantage of thermochemical storage is its compactness. For the same amount of storage energy, thermochemical storage requires a volume ten times smaller than sensible storage and at least twice as much as latent storage.

One of the main challenges in the field of thermochemical energy storage is to improve synergies by optimising TCM materials within the systems. Different TCM classes (Gunasekara et al., 2021) have been investigated; some of them need to be further explored to understand cycling stability, cost reduction opportunities and improved performance by combining materials.

In this contribution, we would like to present our ongoing work on a numerical model to improve the experimental system, which we will use to test different materials for thermochemical energy storage.

Some of the other numerical models developed so far have been moving bed adsorption reactors (Reichl et al., 2016) for an open system using Ansys, sorption dynamics in adsorption chillers (Freni et al., 2012) and another open packed bed reactor (Gaeini et al., 2016) using COMSOL.

Methodology

Experimental system

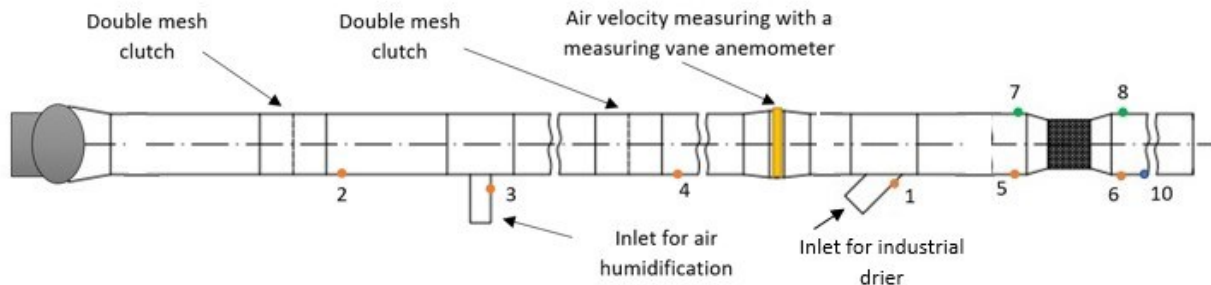


Figure 1: Scheme of the experimental system for open adsorption heating storage

Figure 1 shows the scheme of the experimental system for testing adsorbents. At the entrance of the pipe, we have a fan that ensures the desired air flow through the measuring system. This is followed by a double mesh coupling to ensure a steady flow of air. Next comes the supply pipe for supplying moist air during the discharge phase. The air humidifier, manufactured by Gorenje, is connected with the experimental line via an inlet pipe, which is currently not fixed to the main structure of the track due to the search for the most suitable inlet solution, as it must be appropriately adjusted according to the different phases (Moist air inlet – the pipe is in use; We do not supply moist air – the humidifier is removed and the inlet is sealed). This is followed by a second coupler with a double mesh, to ensure a steady flow of air behind the humid air supply.

The next elements of the experimental system are two diameter adjustment channels for the flow meter. The channel in front of the meter increases the diameter from 100 to 110 mm, while the channel behind the meter reduces the diameter back to 100 mm. This is followed by the supply of hot air with an industrial dryer, which allows the air to be heated during the charging or drying phase of the material being tested. The used industrial dryer is manufactured by Black&Decker and fits nicely on the hot air supply due to the groove that the mouth of the industrial dryer has. At the end of the experimental line, there is a key part where we can insert the tested material.

The material testing section consists of a channel to reduce the diameter from 100 mm to 80 mm and a channel to increase the diameter again to 100 mm. Behind the part of the experimental system where we test the material is a 700 mm long outlet channel. The numbers in the scheme indicate the individual measuring points, where they are: (1) Inlet temperature of the industrial hair dryer (charging phase); (2)

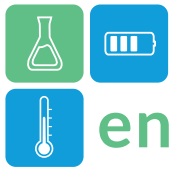
Temperature before air humidification; (3) Humid air inlet temperature (discharge phase); (4) Temperature in front of the measuring vane; (5) Temperature before entering the bulk material; (6) Temperature at the exit from the material dump; (7) Pressure before entering the bulk material; (8) Pressure at the exit from the material dump; (9) Relative humidity at the entrance to the bulk material and (10) Relative humidity at the exit from the bulk material. Figure 2 shows the prepared experimental system in the laboratory that was described throughout the current chapter.



Figure 2: Experimental system in the laboratory

Numerical simulations

After the experimental part, we are currently planning to create a numerical model to perform numerical simulations that would contribute to a better



understanding of the processes during the experiment. This would provide important information on how the experimental system could be improved to obtain more effective and efficient conditions for testing and later use of the materials' in a practical real application system as well.

We will take two different approaches to research and perform numerical simulations. On the one hand, we want to simulate what happens to the individual granules in the area of the experimental system, where the material test part is located. For this example, simulations are performed at the granule level, which normally use stochastic approaches (Rindt & Gaastra-Nedeia, 2015). The higher the level of the simulations, the more approximation models we need.

In the second step, we want to simulate the entire bulk of the porous material. For this part, simulations are performed at the reactor level. The relevant equations consist of energy balances for the vapour and the grains as well as a mass balance for the grains. Figure 3 shows three examples of the adsorption of the bulk of zeolites that are to be tested and simulated with the numerical model.

In the first part of the research, the experiments and simulations will focus on zeolites, as they are the most commonly available porous TCMs that can be found in the literature for correlations if needed. Later, other TCMs will be tested and simulated. For our simulations we will use the Ansys software environment.



Figure 3: Bulks with different amounts of tested material

Expected results

When the work is completed, we would like the model to allow simulations of the adsorption dynamics in the adsorbent's bulk. Through simulations we would like to gain insight into the results of the pressure drop in the material's bulk, temperatures and the water loading lift achieved by the adsorption/desorption process.

Conclusions

A suitable numerical model is being developed for the current experimental system, which will provide the research group with advantages in future work. These would be:

- To have an experimental system and a numerical model for testing new materials for open adsorption heat storage.
- Understanding the importance of the single grain in the experimental system.
- To have a model for simulations in bulk of porous material.
- Understand the limitations and possible improvements of the experimental system or numerical model.

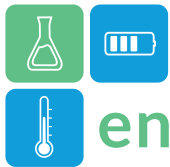
The experiments and simulations will initially be carried out on zeolites and later on other sorption materials.

Acknowledgments

This study was financially supported by Slovenian Research Innovation Agency - SRIA - through project number L1-7665 and research program Nanoporous materials P1-0021.

References

- Crespo, A., Fernández, C., Vérez, D., Tarragona, J., Borri, E., Frazzica, A., Cabeza, L. F., & Gracia, A. De. (2023). Thermal performance assessment and control optimization of a solar-driven seasonal sorption storage system for residential application. *Energy*, 263. <https://doi.org/https://doi.org/10.1016/j.energy.2022.125382>
- European commission. (2023). *European Green Deal: EU agrees stronger legislation to accelerate the rollout of renewable energy*. Official Website of the European Union. https://ec.europa.eu/commission/presscorner/detail/en/IP_23_2061
- Freni, A., Maggio, G., Cipiti, F., & Aristov, Y. I. (2012). Simulation of water sorption dynamics in adsorption chillers : One , two and four layers of loose silica grains. *Applied Thermal Engineering*, 44, 69–77. <https://doi.org/10.1016/j.applthermaleng.2012.03.038>
- Gaeini, M., Zondag, H. A., & Rindt, C. C. M. (2016). Effect of kinetics on the thermal performance of a sorption heat storage reactor. *Applied Thermal*



enerstock

ENERSTOCK 2024

The 16th IEA ES TCP International Conference on Energy Storage

June 5–7, 2024

Lyon, France

- Engineering*, 102, 520–531.
<https://doi.org/10.1016/j.applthermaleng.2016.03.055>
- Gunasekara, S. N., Barreneche, C., Fernández, A. I., Calderón, A., Ravotti, R., Risti, A., Weinberger, P., Paksoy, H. Ö., Koçak, B., Rathgeber, C., Chiu, J. N., & Stamatou, A. (2021). Thermal Energy Storage Materials (TESMs)— What Does It Take to Make Them Fly? *Crystals*, 1–34.
<https://doi.org/https://doi.org/10.3390/cryst11111276>
- Reichl, C., Lager, D., Englmaier, G., Zettl, B., & Popovac, M. (2016). Fluid dynamics simulations for an open-sorption heat storage drum reactor based on thermophysical kinetics and experimental observations. *Applied Thermal Engineering*, 107, 994–1007.
<https://doi.org/10.1016/j.applthermaleng.2016.06.119>
- Rindt, C. C. M., & Gaastra-Nedea, S. V. (2015). Modeling thermochemical reactions in thermal energy storage systems. In *Advances in Thermal Energy Storage Systems: Methods and Applications*. Woodhead Publishing Limited.
<https://doi.org/10.1533/9781782420965.3.375>
- Stritih, U., & Mlakar, U. (2018). Technologies for Seasonal Solar Energy Storage in Buildings. In *Advancements in Energy Storage Technologies* (pp. 51–75). InTech.
<https://doi.org/10.5772/intechopen.74404>



Optimizing the size of a heat storage tank for a district heating system

Anastasija Jocić², Luka Bregar¹, Eneja Osterman¹, Uroš Stritih^{2,*}

1 Interenergo d.o.o., Tivolska cesta 48, 1000 Ljubljana, Slovenia

2 Faculty of Mechanical Engineering, University of Ljubljana, Aškrčeva Cesta 6, 1000 Ljubljana, Slovenia

*Corresponding author e-mail: uros.stritih@fs.uni-lj.si

Abstract

The operation of systems using wood biomass often requires the installation of larger heat storage systems. This article addresses the optimization of the size of a sensible heat storage tank for district heating (DH) systems. Using a validated simulation model with TRNSYS, we conducted multiple simulations of the thermal response and efficiency of heat storage tanks of different sizes in the DH system in the town of Lenart, Slovenia. The simulation results for different sizes of heat storage tanks were evaluated and compared using various indicators. The DH network of the system is currently around 5,000 m long. The system itself incorporates a heat storage tank with a volume of 50 m³. According to the simulation results for this size of heat storage tank, the discharge effectiveness is 55%, and additional heat from the oil boiler is 19.6 MWh and the return on investment (ROI) is 5.7 years.

Keywords: heat storage, district heating (DH), TRNSYS simulation, model validation

Introduction

Sensible heat storage involves increasing the temperature of a medium without a phase change. Choosing the right storage medium is vital, with water being a favourable option for residential and multi-unit heating systems due to its high specific heat capacity, low cost, and temporal stability.

Studies on sensible heat storage in District Heating (DH) systems have explored optimization solutions and their impact on energy efficiency. One study by

M. Leško et al. [1] focused on managing a sensible heat storage tank to optimize DH system operation, demonstrating cost savings and increased electricity production. Another case study by K. Sartor et al. [2] addressed the co-production of electricity and heat from biomass in a DH network, estimating potential energy savings and associated costs. Despite a 13-year payback time, this approach did not meet the research criteria.

In the DH system of the town of Lenart, Slovenia, the main heating source is an Urbas biomass boiler with a nominal capacity of 3.5 MW. In addition to the biomass boiler, there is also an extra light fuel oil boiler with a nominal capacity of 3.5 MW. The oil boiler serves as a backup for peak coverage, operates during transitional periods, and functions in the event of a biomass boiler failure. The heating plant is responsible for heating a DH network approximately 5,000 meters long.

Annually, the system supplies around 7,400 MWh of thermal energy to 500 consumers. In 2020, the DH system in Lenart upgraded its capacity with two sequentially connected tanks, each with a volume of 25 m³. The primary objective of installing the heat storage tank was to reduce the use of electricity from the oil boiler and consequently improve the economic efficiency of the system.

The main advantages of these tanks are that they can cover peak demand loads in the system with their heat reserves, therefore assisting the primary biomass boilers in their operation.

This study aims to numerically evaluate whether such kind of storage tank is feasible to install in the DH system or not and if the chosen size of it was optimal.



Figure 1: DH boiler room in the town of Lenart, Slovenia
Copyright © 2022 Ekoenergo d.o.o.[3]

Research methods

Numerical simulations

To conduct simulations, we utilized the simulation tool TRNSYS. Using predefined models known as Types, we assembled a simulation model in which we simulated the thermal response and operational efficiency of heat storage tanks of various sizes in the mentioned DH system.

We designed the simulation to allow the import of real operational data from the DH system for any chosen period. The imported data should describe the system's operation at a 15-minute interval. Using the imported data in the simulation, we depict the operation of the heat source (boiler), DH system, and the operation of valves RV1 and MV1. By importing accurate data, the user can simulate the response and efficiency of heat storage tanks of various sizes for the DH system.

Operation of the heat source

The data was exported from the heat meter, indicated as Q1 in the lower diagram of Figure 2.

Operation of the simulation

The simulation operates by defining certain input parameters with data. These parameters include the inlet temperature and fluid flow from the heat source, as well as the inlet temperature and fluid flow from the heat consumer. Two additional input parameters are the control signals for valves MV1 and RV1. The remaining values are the result of the simulation performed by the TRNSYS program using the established modules.

Validation of the model

Since we developed the entire simulation model from scratch and it hasn't been validated by the creators of the TRNSYS program or other experts, we conducted self-validation before running various simulations. Validation was performed using a previously established simulation model and experimental data obtained from the existing heating system through the SCADA.

We compared experimental data obtained from the lower temperature sensor in the heat storage tank with simulation data for the temperature in the lower segment of the tank (segment N=10). The validation was performed for 96 hours in December 2021. During this period, in the early morning hours, there was a peak load on the system, resulting in the emptying of the heat storage tank, which helped supply heat to the network

alongside the wood biomass boiler. After the completion of the tank emptying, the tank was refilled during the day and night.

We have decided to validate the model using two indicators: the percentage of the mean absolute error (MAPE) and the coefficient of determination or R-squared (R^2). The obtained value of MAPE is 3.0%. Our prediction is very accurate, as the value of 3.0% falls below 10%, classifying our result into the category of very accurate predictions.

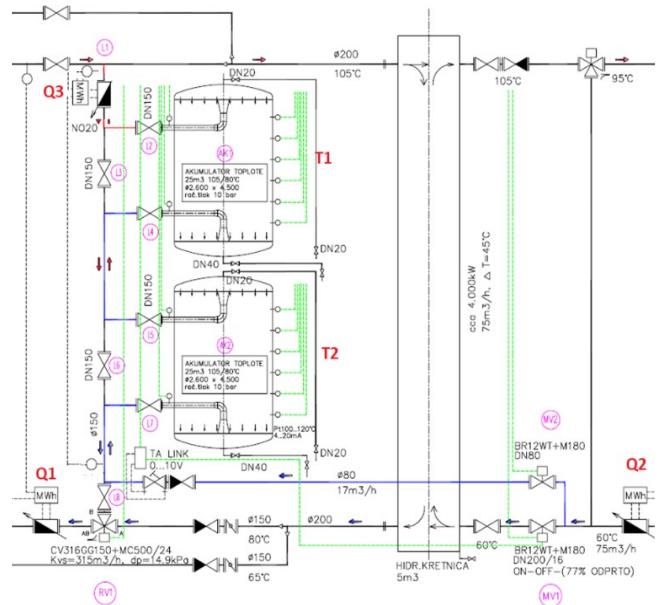


Figure 2: Connection scheme of the storage tank and valves

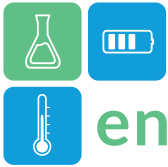
The second indicator we calculated as part of the model validation is the R^2 or coefficient of determination. In the calculation of the determination coefficient R^2 we obtained a value of 0.86. The obtained R^2 coefficient value is greater than 0.7, classifying our simulation model among models with very good prediction accuracy [4].

Results and discussion

We simulated the response and efficiency of heat storage tanks of various sizes based on the operation of the selected DH system and evaluated them using the three described indicators.

Coverage of the deficit of the heat storage tank

This indicator was used to describe the response of heat storage tanks of various sizes to the operation of the DH



system for the specified 14-day operating period in terms of water reserves in each tank.

From the results in Figure 3, it can be observed that the efficiency of the emptying process of the heat storage tank initially increases with the expansion of the tank volume. The volume of the tank in the range between 0 m³ and 50 m³ is small enough for the tank to be filled. However, for tank volumes greater than 75 m³, the efficiency curve starts to rise less steeply.

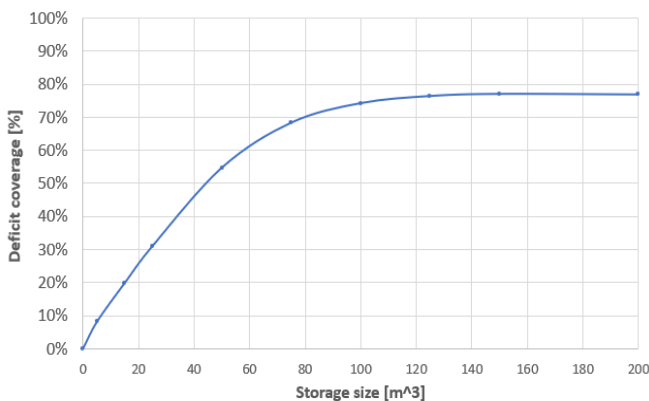


Figure 3: Graph of tank emptying efficiency depending on tank size

From the results in Figure 3, it can be observed that the efficiency of the emptying process of the heat storage tank initially increases with the expansion of the tank volume. The efficiency, or the amount of heat from the heat storage tank relative to the heat deficit in the network, increases with the increase in tank volume. In the first phase, the curve rises steeply. This is expected because as the volume of the heat storage tank increases, the stock of stored sensible heat also increases, which is released and supplied directly to the network during the emptying process. The volume of the tank in the range between 0 m³ and 50 m³ is small enough for the tank to be filled at a sufficiently high temperature throughout the entire volume during the filling regime, ensuring that it can assist the operation of the wood biomass boiler during emptying. For a heat storage tank volume of 50 m³, the emptying efficiency is approximately 55%. However, for tank volumes greater than 75 m³, the efficiency curve starts to rise less steeply. For a tank size of 100 m³, the curve becomes almost horizontal and does not rise further up to a tank size of 200 m³. The efficiency of emptying the tank concerning the system's needs does not increase further and even remains constant at around 75%, despite the increase in the volume of the heat storage tank. The decline in the slope of the curve and the consequent cessation of the increase in emptying

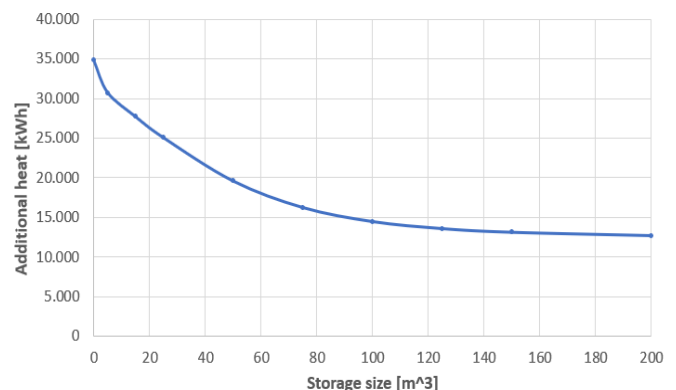
efficiency for larger tank volumes occur because the tank, due to its size, does not reach a sufficiently high temperature throughout the volume during the filling process.

As a consequence, we have a partially heated heat storage tank that then releases as much heat during emptying as it has stored within. Although the heat storage tank could potentially store much more heat due to its size, it remains only partially heated. This indicates that the heat storage tank is likely too large and oversized for the given heating system. Because there is too much water in the tank and it cannot be fully heated by the given biomass boiler, the efficiency does not increase further. With further increases in the volume of the storage tank, the trend even reverses. Efficiency begins to decline as the excessively large volume of water leads to a lower temperature of stored water in the tank. However, with an increased volume, heat losses from the tank further contribute to a deterioration in performance.

Based on the results and interpretation from the previous paragraph, we can see that increasing the heat storage tank for the Lenart system is cost-effective up to a maximum tank size of 100 m³. At this volume, the curve significantly flattens and begins to grow slowly. This indicates that we have achieved maximum efficiency in relation to the size of the heat storage tank. At a volume of 100 m³, we achieve an efficiency of 74%. In conclusion, based on the results from the first indicator, the optimal heat storage tank for our system is between 50 m³ and 100 m³.

Required additional heat from the auxiliary heating source

Through simulation and the Type 6 module, we calculated data on the required additional thermal energy from the auxiliary heat source for each size of the heat storage tank.



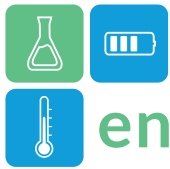


Figure 4: Graph of the required additional heat from the reserve heat source compared to the volume of the heat storage tank.

Based on the obtained results, we can see that with the increase in the volume of the heat storage tank, there is a decrease in the need for additional heat from the auxiliary heating source or the oil-fired boiler. As seen in Figure 4, the trend of the curve on the graph is inversely proportional to the curve from the first indicator.

Economic Indicator (ROI)

The third indicator in determining the optimal size of the heat storage tank is the economic indicator. Within this indicator, we calculated the financial savings in the case of installing a heat storage tank of various sizes and compared it with the investment. With this comparison, we calculated the simple payback period of the investment in such a heat storage tank. The results from the second indicator, representing the additional energy needed from the oil boiler in a 14-day interval, were recalculated and converted into annual costs for oil (heating season) according to Eq. 1.

The annual cost for oil for each size of the heat storage tank is determined by the equation:

$$C_{oil,i,year} = V_{oil,i,year} \cdot P_{oil} \quad (1)$$

The reference value for calculating savings was the cost of oil when the heat storage tank was not present in the system. This cost amounts to 43,449 EUR per year.

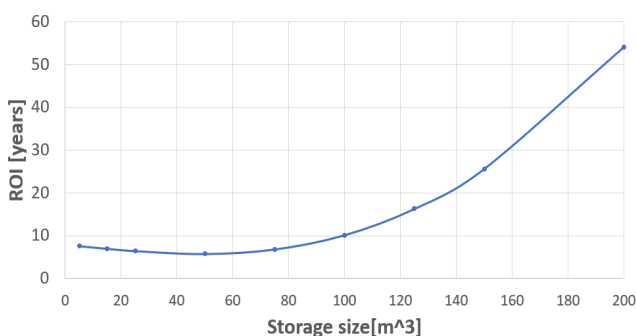


Figure 5: Graph of ROI payback period depending on the size of the storage tank

Based on the simulation results, it can be seen that, from an economic perspective, the optimal size for the

thermal storage tank in the Lenart DH system is 50 m³, resulting in a payback period of 5.7 years.

Conclusions

In this study, we explored the storage of sensible heat based on a practical case - the DH system in Lenart, Slovenia. The said system allowed us to prepare simulations using TRNSYS based on experimental data.

Based on the simulations we can conclude that a thermal storage tank with 75 m³ is optimal, with a discharge effectiveness of 68%. However, beyond 75 m³, the discharge effectiveness is around 75% indicating that larger tanks are oversized for the said heating system. Further analysis considered the amount of additional heat required from an auxiliary heating source to achieve the desired temperature. Results showed that larger thermal storage tanks supply more heat to the network, reducing the need for additional heat from the auxiliary heater.

The study also delved into the economic analysis of installing the DH system boiler room, calculating annual financial savings brought by the thermal storage tank. The largest tank, with a size of 200 m³, yielded the maximum savings of 27,565 EUR/year. Past investment data determined construction values for all simulated tank sizes. The simple payback period of investments (ROI) was calculated, revealing that the 50 m³ tank has the shortest payback period at 5.7 years.

References

- [1] Leško, M., Bujalski, W., & Futyma, K. (2018). Operational optimization in district heating systems with the use of thermal energy storage. *Energy*, 165, 902–915.
- [2] Sartor, K., & Dewallef, P. (2018). Integration of heat storage system into district heating networks fed by a biomass CHP plant. *Journal of Energy Storage*, 15, 350–358.
- [3] Web page Ekoenergo d.o.o., accessible at: <https://ekoenergo.si/nasi-sistemi/lenart/>, [viewed 01.06.2022].
- [4] D. S. Moore, W. I. Notz, M. A. Flinger, *The basic practice of statistics*, Third edition, W. H. Freeman and Company, New York.



Performance enhancement of a Latent Heat Thermal Energy Storage for Domestic Hot Water production

Bénédicte Champel*, Arnaud Bruch, Fabrice Bentivoglio
Univ. Grenoble Alpes, CEA, LITEN, DTCH, LCST, 38000 Grenoble

*Corresponding author e-mail: benedicte.champel@cea.fr

Abstract

This study numerically investigates different ways to enhance the discharge performance of a Latent Heat Thermal Energy Storage for Domestic Hot Water production, from a design point of view. A dynamic model of the storage, built on Dymola platform, is used to assess the impacts of the Phase Change Material and the hydraulic path on the useful capacity of the storage and its discharge efficiency. We show that using RT 70 HC (melting temperature 70°C) instead of octadecanol (melting temperature 58°C) permits to increase storage useful capacity by 38%. We also show that useful capacity is further increased by 14% if Heat Transfer Fluid flow is arranged in 3 passes instead of 1. The study concludes that, by integrating all these features into an optimal design, it is possible to boost storage performance for Domestic Hot Water production.

Keywords: Phase change material, Octadecanol, RT 70 HC, Dymola, multi-pass

Introduction

In the context of climate change, the substitution of carbon technologies by low-carbon alternatives for energy production becomes critical. In Europe, thermal end uses represent a major part of households total energy consumption, of which more than 50% comes from fossil fuels (Eurostat, 2021). In this context, thermal energy storage (TES) at residential scale is a way to reduce fossil fuels consumption, either by facilitating the integration of solar thermal (storing the produced excess renewable energy until times of high heat demand), or by adding flexibility to heat pumps (so that electricity consumption can be decoupled in time from heat consumption).

Most of today's thermal storage facilities are sensible storages using water as storage media as it is the cheapest and most mature technology. Latent heat TES (LHTES) however is gaining interest for households for which its high storage density is a strong advantage.

The main research areas to improve the performance of LHTES systems concern phase change materials (PCMs) characterization and heat transfer enhancement techniques to overcome PCM low thermal conductivity (Khademi et al, 2022, Xu et al, 2022). Our study focuses on the optimisation of the storage component itself, a research field that has so far been less studied.

The application targeted for this study is domestic hot water (DHW) production. The discharge process of

LHTES targeting DHW production has already been studied both experimentally and numerically (Almagour et al, 2018 and 2021, Dogkas et al, 2020, Fadl et al, 2019 and 2021, Passaro et al, 2022). The impacts of heat transfer fluid (HTF) inlet temperature and flow rate on storage performance have been assessed. However, previous studies considered fixed HTF flow rates, while DHW production is rather characterized by a fixed discharge power. In addition, HTF inlet temperature and flow rate are fixed by the application, and therefore an improvement of TES performance by optimizing their values is not achievable in real life.

The objective of the present study is to investigate numerically different ways of enhancing discharge performance of a LHTES for DHW production, from a design point of view, focusing on the impacts of PCM melting temperature and of the tube network arrangement. An optimal design is proposed and its performance compared to that of the Reference.

Presentation of Use Case, design and model

Use Case and sizing requirements

Our study focuses on the use of LHTES to provide DHW for a single-family house. The storage is assumed to be initially charged at a temperature of 75°C using internal electrical heater. It is discharged in order to provide hot water to the users, with an objective of fixed flow rate (12L/mn) and water temperature at the tap (40°C). Cold water temperature

is assumed to be 12°C (discharged power is thus approx. 23kW). The storage capacity requirement is fixed at 9kWh that corresponds to the daily DHW need for a 5-persons household (ADEME, 2022).

One peculiarity of LHTES is that temperature of the water flowing out of the TES in discharge decreases with time. In order to supply water at a constant temperature at the tap, cold water flow is divided into two streams (as shown in Figure 1): the first stream flows through the TES while the second one bypasses it. The share of input flow rate bypassing the storage is controlled so that the mixing temperature corresponds to the application temperature. It is maximum when the storage is fully charged. It then decreases with time, following the reduction in temperature of water at storage outlet. When TES outlet temperature decreases below target temperature, it is not possible any more to achieve the target temperature by mixing.

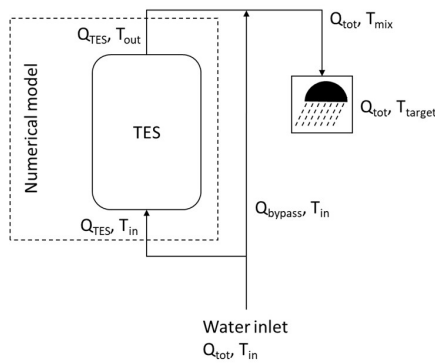


Figure 1: General concept of DHW Use Case in discharge (dashed line indicates the scope of the numerical model)

Reference Storage Design

The storage global design is based on the tube-and-shell single pass heat exchanger concept, because of its technological maturity and compacity (Bentivoglio et al, 2021). In this concept, the TES consists of a tube bundle in which the HTF is flowing, surrounded by the PCM embedded in the shell. Finned tubes are used in order to improve the thermal conductivity of the medium out of the tubes (NematpourKeshteli et al, 2022). In addition, internal hydraulic inserts are placed inside the tubes to reduce the fluid flow section and increase HTF velocity and then the convective heat transfer coefficient. The geometry of the tubes and hydraulic inserts used are the following: hydraulic insert diameter of 13.5mm, tube inner and outer diameters of 20.6mm and 25.4mm, helical aluminium fins (10 fins per inch, fins height of 15.9mm, fins mean thickness of 0.4mm).

Octadecanol is selected as reference PCM (properties are presented in Table 1).

Table 1 : PCM thermophysical properties

	Octadecanol	RT-70 HC	Stearic Acid
Melting temperature [°C]	58	70	70
Storage heat capacity [kJ/kg] (latent + specific heat)	In the range [12 – 75]°C		
	372	392	200
Density [kg/m3]	789	825	892

Table 2 and Table 3 present the main characteristics, and general indicators regarding mass and energy, of the Reference Case design.

Table 2 : Reference Case Design parameters

Number of tubes	37	Tube network	67.2mm
PCM	Octadecanol	Shell diameter	0.47m
Tubes' height	1.37m	Average PCM height	1.27m

Table 3 : Stored Energy – Reference Case

	Volume [L]	Mass [kg]	Energy between 40°C and 75°C[kWh]	Energy between 12°C and 75°C[kWh]
PCM	184	146	13.0	15.1
Steel	21	166	0.9	1.6
Aluminum	12	33	0.3	0.5
Water	49	48	2.0	3.5
TOTAL	266	393	16.2	20.7

Numerical modelling

A dynamic model, that allows to account for the dynamic heat transfer between PCM and HTF, has been developed in Dymola simulation platform. The model has been fully described and validated in Da Col et al, 2023.

The Dymola model is used to simulate the discharge process of the PCM storage. Two indicators are defined in order to compare the different designs:

- The useful capacity, defined as the cumulative energy discharged until the moment when water outlet temperature falls below the target temperature of 40°C.
- The discharge efficiency, defined as the ratio between the useful capacity and the total energy stored between 40°C and 75°C (i.e. 16.2 kWh, see Table 3).

Results and Discussion

Reference Case

In the reference case (Figure 2), the outlet temperature remains at 75°C during the first 7 minutes of the

discharge. Then it decreases sharply and reaches 45°C after 17mn. From that time, the evolution of water outlet temperature with time is gentler, and reaches 40°C after 23mn. At that time, 8.9kWh have been discharged from the storage. After that, even if some energy continues to be discharged, the temperature provided is lower than 40°C, despite the fact that part of the PCM is still at a temperature higher than 40°C (given the low heat exchange coefficient between HTF and PCM). The TES can then be considered as empty for DHW use.

The Useful capacity of this storage is 8.9kWh. This represents only 55% of the energy stored between 40°C and 75°C.

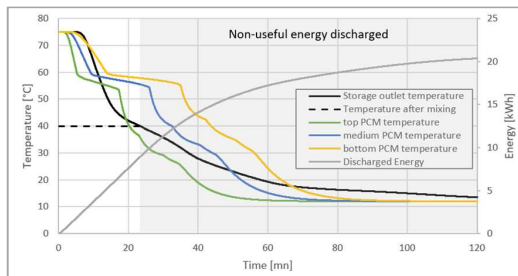


Figure 2 : Discharge performance of Reference Case

Impact of the PCM

The use of RT 70 HC or Stearic Acid instead of Octadecanol has been tested. The thermophysical properties of these PCMs are presented in Table 1.

As can be seen in Table 4, the PCM mass in the LHTES is slightly higher for RT 70 HC and Stearic Acid than for Octadecanol, due to their higher density. The energy stored is 7% higher for RT 70 HC and 5% lower for Stearic Acid than it was for Octadecanol. However, the increase in Useful Capacity is much higher: +38% for RT 70 HC, and +24% for Stearic Acid. This is confirmed by the increase in Discharged Efficiency: 55% for Octadecanol and 71% for RT 70 HC and Stearic Acid. This feature can be explained by the improved heat exchange between PCM and HTF (due to their higher temperature difference), and the fact that energy is retrieved at a higher temperature because of the higher melting temperature of these PCMs compared to that of Octadecanol.

Impact of tube network arrangement

Multi-pass hydraulic paths are then tested instead of the single-pass in Reference Design. A 3-pass and a 37-pass options are tested, as presented in Figure 3.

It is clear from Table 4 that Discharge Efficiency is higher for multi-pass circuits. Indeed, it reaches 77% for the 3-pass circuit. For the case where all the tubes are hydraulically in series, it could even reach 102%

(thanks to the recovery of PCM heat below 40°C at the inlet of the storage, then heated-up above 40°C through the storage). This improvement is due to the increased HTF velocity that boosts heat exchange between HTF and PCM.

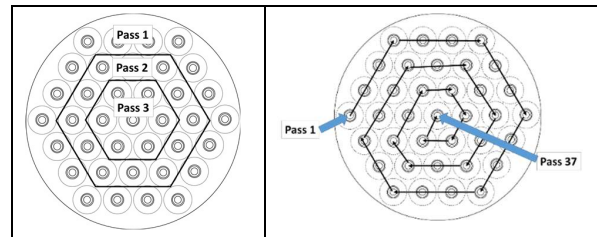


Figure 3 : Simulated tube network arrangements: Three passes - left and 37 passes (all tubes in series) - right

Table 4: Impact of PCM and tube network arrangement on LHTES performance

PCM	Octadecanol			RT 70 HC	Stearic Acid
	Single pass	3-pass	37 pass	Single pass	
PCM Mass [kg]		146		152	165
Energy stored between 40°C and 75°C [kWh]		16.2		17.4	15.4
Useful capacity [kWh]	8.9	12.4	16.5	12.3	11.0
Discharge efficiency	55%	77%	102%	71%	71%

Optimal Case

An improved arrangement is proposed, based on the features that have been shown to improve the recovery of energy at a higher temperature: use of a higher melting temperature PCM (RT 70 HC is chosen rather than Stearic Acid because of its higher storage density), and 3-pass hydraulic pattern.

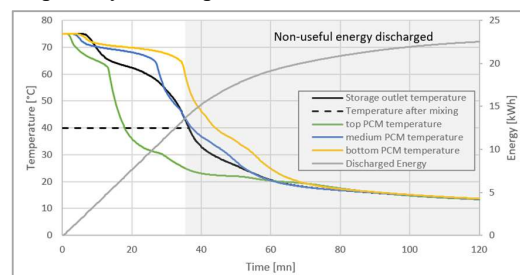
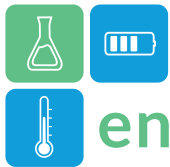


Figure 4 : Discharge performance of Optimal Case

As can be seen in Figure 4, the modifications made in the TES greatly improve energy recovery compared to the Reference Case. This leads to a huge improvement in storage Useful Capacity (+57% compared to



reference), and Discharge Efficiency, as can be seen in Table 5.

Table 5 : Stored energy and useful energy for the Reference Case and the Optimal Case

	Reference Case	Optimal Case
Hydraulic pattern	Single pass	Three pass
PCM	Octadecanol	RT 70 HC
Energy stored between 40°C and 75°C [kWh]	16.2	17.4
Useful capacity [kWh]	8.9	14.0
Discharge efficiency	55%	80%

Conclusions

In DHW applications, the temperature at which energy is retrieved from TES is of major importance. Indeed, only the energy retrieved above a given temperature (depending on the user) is useful. In such applications, two approaches can be chosen to increase the useful storage capacity: increase the energy stored in the TES (by increasing PCM quantity or thermophysical properties), or increase the share of stored energy that can be retrieved above a given temperature level.

This study has shown that, for a given design, the use of a PCM with a higher melting temperature on the one hand, and multi-pass flow path on the other hand, drastically increase the useful energy in discharge and the discharge efficiency.

Acknowledgment

This work is supported by the EU Horizon 2020 project “Compact bio-based thermal energy storage for buildings” (ComBioTES) (No. 864496).

References

Eurostat (2021), Energy consumption in households, https://ec.europa.eu/eurostat/statistics-explained/index.php?title=Energy_consumption_in_households#Use_of_energy_products_in_households_by_purpose

Khademi, A. et al. (2022), A brief review on different hybrid methods of enhancement within latent heat storage systems, *Journal of Energy Storage*, doi: 10.1016/j.est.2022.105362.

Xu, C. et al (2022), Review on thermal conductivity improvement of phase change materials with enhanced additives for thermal energy storage, *Journal of Energy Storage*, doi: 10.1016/j.est.2022.104568.

Amagour, M. E. H. et al (2021), Numerical investigation and experimental validation of the

thermal performance enhancement of a compact finned-tube heat exchanger for efficient latent heat thermal energy storage, *Journal of Cleaner Production*, doi: 10.1016/j.jclepro.2020.124238.

Amagour, M. E. H. et al (2018), Experimental investigation and comparative performance analysis of a compact finned-tube heat exchanger uniformly filled with a phase change material for thermal energy storage, *Energy Conversion and Management*, doi: 10.1016/j.enconman.2018.03.041.

Dogkas G. et al. (2020), Development and experimental testing of a compact thermal energy storage tank using paraffin targeting domestic hot water production needs, *Thermal Science and Engineering Progress*, doi: 10.1016/j.tsep.2020.100573.

Fadl M. and Eames P. C. (2019), An experimental investigation of the heat transfer and energy storage characteristics of a compact latent heat thermal energy storage system for domestic hot water applications, *Energy*, doi: 10.1016/j.energy.2019.116083.

Fadl, M. et al (2021), Thermal performance analysis of compact thermal energy storage unit-An experimental study, *International Journal of Heat and Mass Transfer*, doi: 10.1016/j.ijheatmasstransfer.2021.121262.

Pássaro, J. et al. (2022), Effect of fins and nanoparticles in the discharge performance of PCM thermal storage system with a multi pass finned tube heat exchange, *Applied Thermal Engineering*, doi: 10.1016/j.applthermaleng.2022.118569.

ADEME (2022), Guide technique Les besoins d'eau chaude sanitaire en habitat individuel et collectif

Bentivoglio, F. et al (2021), Design and operation of a 180 kWh PCM heat storage at the Flaubert substation of the Grenoble urban heating network, *Applied Thermal Engineering*, doi: 10.1016/j.applthermaleng.2020.116402.

NematpourKeshтели, A. et al (2022), Enhancing PCMs thermal conductivity: A comparison among porous metal foams, nanoparticles and finned surfaces in triplex tube heat exchangers, *Applied Thermal Engineering*, doi: 10.1016/j.applthermaleng.2022.118623.

Da Col, A. et al (2023), Modelling a latent heat thermal storage demonstrator and identification of the model key-parameters, *Journal of Energy Storage*, doi.org/10.1016/j.est.2023.109239



Performance of high-temperature thermochemical systems based on carbonates and mixed oxides in fluidized bed reactors.

R. Liberatore^{1,*}, M. Lanchi¹, S. Sau¹, N. Corsaro¹, A. Spadoni¹, A.C. Tizzoni¹

¹ENEA – Italian National Agency for New Technologies, Energy and Sustainable Economic Development, Lungotevere Thaon di Revel, 76, 00196 Rome, Italy

Abstract

The main objective is to develop a high-temperature storage system (600-900°C) by conducting thermochemical reactions in a fluidized bed reactor operating in a bubbling bed regime. Actually, the fluidized bed reactor configuration is technologically more complex than a fixed bed one. Still, it allows us to overcome the main critical issues encountered, effectively guaranteeing a greater exchange surface and heat transfer between HTF and TCM.

Two TCM (Thermo-Chemical Material) systems have been here proposed, to highlight the different operating conditions in terms of temperature, pressure, and heat transfer fluid (HTF), in such a way as to explore a wide range of potential applications.

The first reactive chosen system is the calcium oxide/calcium carbonate (CaO/CaCO₃) system dispersed in an inert matrix of Mayenite (a calcium aluminate with the formula Ca₁₂Al₁₄O₃₃), called TCM1, the second TCM is made up of an oxide-based on manganese and aluminium according to the formula MnAl₂O₄/MnAl₂O_{4-δ} (TCM2). For this purpose, the optimal grain size of the powders of the CaO-Mayenite/CaCO₃ (TCM1) system was identified, to guarantee effective fluidization inside the reactor. The effect of particle size was also investigated on key process parameters, such as carbonation reaction conversion, cycling resistance, and reaction enthalpy. A preliminary estimate of the energy storage densities of the two TCMs has been proposed, to evaluate and compare their potential and fields of application. Finally, the sizing of the prototype reactor was carried out.

Keywords: TES; Thermochemical Storage; Fluidized Bed Reactor; carbonates; metal oxides.

Introduction

High-temperature thermochemical energy storage (HT-TCES) technology is based on reversible gas-solid chemical reactions which, in the present activity, operate between about 600 to 900°C. They allow thermal energy to be stored in the form of chemical energy through discharge and charge cycles:

- for the charging phase (endothermic decomposition reaction) the necessary heat can be provided by renewable sources (e.g.: CSP concentrating solar power systems) or by thermal waste from high-temperature industrial processes;
- for the discharge (exothermic reaction) the heat released can be exploited directly by heat exchange with the heat transfer fluid or integrated with direct (Brayton) or indirect (Rankine) power cycles (power block) to produce electricity.

In this topic, two TCM (Thermo Chemical Material) systems have been proposed, to highlight their action in different operating conditions in terms of temperature, pressure and HTF, to explore a wide range of potential applications.

The first reactive chosen system is the calcium oxide/calcium carbonate (CaO/CaCO₃) application dispersed in an inert matrix of Mayenite (a calcium aluminate with the formula: Ca₁₂Al₁₄O₃₃), called TCM1, the second TCM is made up of an oxide based on manganese and aluminium with the formula MnAl₂O₄/MnAl₂O_{4-δ} (TCM2) as described by Morabito and al. (2020), whose particular stoichiometry AB₂O₄ (A=Mg₂₊, Mn₂₊; Fe₂₊, Zn₂₊; B=Al₃₊ cation) is generally indicated with the name of "spinel". The reactions involved and the applicable temperature range are detailed in Table 1. The values refer to the latest calculations carried out for a proper test campaign.



Table 1: Proposed thermochemical storage materials and operating parameters.

TCM	Discharge	Discharge T (°C)	Charge	Charge T (°C)	HTF
1	CaO+CO ₂ →CaCO ₃ +Heat	600-830 (P=1 atm)	CaCO ₃ +Heat →CaO +CO ₂	740-900 (P=1 atm)	CO ₂ /Air
2	MnAl ₂ O _{4-δ} + (δ/2) O ₂ →MnAl ₂ O ₄ +Heat	650-700°C* (P=1 atm)	MnAl ₂ O ₄ +Heat → MnAl ₂ O _{4-δ} + (δ/2) O ₂	760-780°C* (P=1 atm)	Air

Materials and method

TCM1 based on CaO-Mayenite/CaCO₃ was prepared according to the wet synthesis method (sol-gel) described by Spadoni and al. (2023) using a simplified and potentially scalable method.

Three sets of powder samples with a distribution within a range of: 100-250, 180-250 and 250-500 μm were synthesised. On these samples, preliminary fluidization tests were carried out at room temperature in a cylindrical transparent borosilicate reactor in which a significant amount of material was included (10 g). Based on the outcome of the tests, the most appropriate average diameter was selected.

On the other hand, TCM2 was obtained with Aluminium nitrate and Manganese Acetate, after calcination. These powders were studied in terms of morphological and thermophysical properties, from a pre- and post- thermal cycle by chemical-physical tests on the redox systems, including:

- X-ray diffraction analysis, before and after the thermal cycles of charge and discharge. This analysis, after cycling, highlighted the stability of the material which remained as it was, even after thermogravimetric tests (TGA) with prolonged charge/discharge cycles;
- SEM microscopy + EDS microanalysis to define its morphology, structure and stability or degradation after the above-mentioned cycles;
- thermogravimetric analysis (TGA) to study the energy density, reaction yield and stability.

20g of MnAl₂O₄ were then prepared with the right morphological characteristics and dimensions to be subsequently pelletized.

The determination of the heat involved in the reaction was carried out through thermal analysis in TGA/DSC, simulating the carbonation reaction on the real sample which will be inserted inside the fluidized bed reactor at 700°C, as the diameter of the particles. Similarly, for TCM2 considering granules with an average diameter between 100-250 μm, simulating the charging reaction between 650 and 780°C (Delise and al., 2021). The heat involved during the reaction was determined experimentally in the TGA/DSC in which the heat flux was recorded as time varied during the reaction examined. For TCM1, the reaction is carried out at a fixed temperature T, equal to 700°C. Concerning TCM2, the reaction takes place between 650°C and 780°C. The process heat obtained corresponds to the value of the integral of the area under the recorded heat flow curve.

$$Q_r = \int_{t_0}^{t_f} HF(t) dt$$

The density of the powders, necessary to design the fluidized bed reactors was determined by Martinez and al. (2019) for a system very similar to TCM1 also including the intra-particle porosity (67.1%): 890 kg/m³, while the research of Liberatore and al. (2024) reports the density of the TCM2: 29.497 mol/m³ corresponding to 5073 kg/m³ considering a molecular weight of 172 g/mol.

The energy storage density (Sd), understood as "effective" energy released per unit volume of the material, was determined experimentally by measuring the amount of heat involved during the reaction.

The energy storage density can therefore be calculated through the following relationship:

$$Sd = \rho \cdot Q_r$$

where:

Q_r , is the process heat involved (kJ/g)

ρ , is the density of the material (g/cm³)

For fluidized bed reactors (Perry and al., 2008; Levenspiel and al., 1999), there are various kinds of possible configurations: boiling bed (bubbling bed), circulating bed and entrained bed. The first kind, the "bubbling fluidized bed" configuration, was chosen because it has the following advantages: high exchange coefficients, high control over reaction times and temperatures, and above all easier and more economical management of the solids since the escape of the solids from the reactor is not

foreseen and consequently the installation of expensive auxiliary treatment equipment for the entrained solids is not necessary. A lab-scale prototype reactor was designed in terms of diameter, bed height, particle transport height, positioning of thermocouples, and quantity of fluidization fluid to perform the necessary experiments. The sizing was evaluated based on desired power, pressure, quantity of reagent mass, particle size, degree of vacuum, kind of desired fluidization and therefore minimum and maximum fluidization speed.

Results and Discussion

Preliminary fluidization tests were carried out at room temperature in a transparent cylindrical reactor (Figure 1).

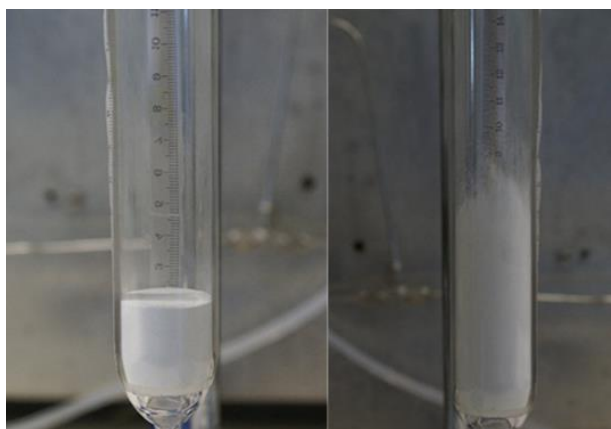


Figure 1. Preliminary fluidization tests with an average diameter of 180-250 μm

The 100-250 μm sample gave rise to a leakage of the dust out of the reactor (elutriation phenomenon), with a mass loss of approximately 20%.

For powders with a diameter between 250-500 μm , no phenomena of dust leakage from the reactor are observed.

The fragmentation resistance property was also investigated by estimating the average size of the granules before and after the fluidization test.

In addition, the value of the sample size, expressed as the average obtained on 20 replicates (1 measurement for each granule) and standard deviation showed that there are no significant differences between the two means (Table 2). It has been concluded that the room-temperature granules had good fragmentation resistance during room-temperature fluidization tests.

Table 2. particles sizes before and after fluidization

TC [μm]	Before [μm]	After [μm]
180-250	234 \pm 28.2	213 \pm 28.7
250-500	469 \pm 49.5	497 \pm 16.6

The storage energy density of TCM1 and TCM2 are shown in Table 3.

The final value of the volumetric storage density, expressed in kWh/m^3 , is given by the contribution of the reaction heat, the sensible heat, the density of the material and the void fraction into the reaction bed (0.4 for the TCM1 and 0.46 for TCM2).

The temperature range considered for sensible heat includes the input of the HTF temperature (air or CO_2/air) and the temperature corresponding to the start (on-set) of the reaction turning point.

It is possible to note that the chosen materials show good properties for energy storage, particularly the TCM1 with particles of 180-250 μm diameter.

It is worth noticing that the final value of the volumetric energy density, is given by the contribution of the process heat and the density. For TCM1, a high contribution of process heat is found, while for TCM2 the largest contribution is given by the density.

The reaction conditions will be further optimized in the experimentation which will concern the fluidized bed reactor, planned in the next activities.

Table 4 shows the sizing of the Inconel prototype reactor at the lab scale.

Table 3. Comparison of storage energy densities for TCM1 and TCM2

TC [μm]	TCM1 180-250	TCM1 250-500	TCM2 100-250
Heat of reaction [MJ/kg]	1.817	1.292	0.109
Temperature of reaction [$^{\circ}\text{C}$]	700	700	650-780
Density [kg/m^3]	890	890	5073
Conversion	0.53	0.53	1
Energy density by DHr [kWh/m^3]	272	194	48
Temperature range for usable sensible heat [$^{\circ}\text{C}$]	600-780	600-780	600-800
Sensible heat [kWh/m^3]	21.4	21.4	122
Total energy density [kWh/m^3]	290.4	212.4	170

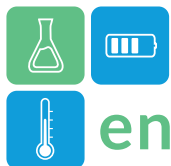


Table 4. Results obtained for the sizing of the prototype reactor.

Parameter	value	Measure unit
Inlet gas (in mass)	0.85	g/s
Inlet gas (in mol)	0.030	mol/s
Inlet gas (in volume)	0.0006	m ³ /s
Inlet gas (in volume)	40.191	NL/min
Section	0.0012	m ²
Minimum fluidization velocity	0.0486	m/s
Terminal velocity	0.629	m/s
Velocity for bubbling bed	0.486	m/s
Reactor diameter	4.0	cm
Material (mass)	10	g
Fluidized bed volume	25	cm ³
Fluidized bed height	2.04	cm
Transport disengaging height	0.5	m
Total height	0.52	m

Conclusions

The research activities here described led to the development and characterization of two kinds of promising materials in terms of environmental impact, as well as chemical and physical stability. The first reactive system, the carbonate/calcium oxide system supported on an inert matrix (CaO/CaCO₃-Mayenite), is usable in the thermal range of 700-900 °C, including the calcination step, while the mixed oxide of manganese and aluminium (MnAl₂O₄/MnAl₂O_{4-δ}, spinel structure) allows heat to be stored and released at lower temperature [650-780 °C] and [600-800 °C] including also the exploitable sensible heat. A theoretical analysis was carried out for both proposed reactive systems, to evaluate their performance in fluidized bubbling beds using pelletized powders of optimal average diameter. The latter was estimated based on an analysis aimed at evaluating the effect of particle size on the main process parameters, such as the minimum fluidization speed and the dimensions of the reactor. For this purpose, for carbonates, the reaction yield, in the charging and discharging phases, of a batch of selected powders was obtained in a thermobalance in the optimal dimension, while, for the mixed oxide system, the experimental data was taken into consideration.

The energy density evaluation showed similar performance for the two systems. Even though

TCM1 has more heat of reaction per mass unit, the not total conversion, the high porosity and so the low density, impact negatively on its heat of reaction per volume unit and affects also the supplementary heat provided by the sensible heat at equal reactor volume.

In parallel, in this line of activity, the specifications of the experimental device, at a lab scale, were presented. They are representative of the operation of a fluidized bed reactor, intended for verifying the performance of the two reactive systems under examination in the next future.

Acknowledgement

This work was funded by the Italian Ministry of Environment and Energy Security through the «National Electric System Research» Programme (RdS) – Integrated Project 1.2 “Electrochemical and thermal storage technologies”, 2022-2024 implementation plan.

References

- Delise, T. and al. (2021). Performance of an Indirect Packed Bed Reactor for Chemical Energy Storage. *Materials*, 14, 5149.
- Levenspiel, O. (1999). *Chemical Reaction Engineering*, John Wiley & Sons.
- Liberatore, R. and al. (2024). Fluidized bed reactor sizing using manganese aluminium spinel for thermochemical storage. *Journal of Energy Storage* 78 110039
- Martinez and al. (2019). Performance and operating limits of a sorbent-catalyst system for sorption-enhanced reforming (SER) in a fluidized bed reactor. *Chemical Engineering Science* 205 94–105.
- Morabito, T., and al. (2020). Chemical CSP storage system based on a manganese aluminium spinel. *Solar Energy* 197 462–471.
- Perry R.H., Green D.W. (2008). *Perry’s Chemical Engineers’ Handbook*, McGraw-Hill.
- Spadoni A. and al. (2023). Thermochemical heat storage through CaO-Mayenite/CaCO₃ system: Thermal performances comparison for two synthesis methods; *Journal of Energy Storage*, 72, 108386.



Phase change material integrated underground thermal energy storage in heating and cooling applications: A review

Haoyang Dong*, Saman Nimali Gunasekara, Justin NingWei Chiu

KTH Royal Institute of Technology, School of Industrial Engineering and Management, Department of Energy Technology, Brinellvägen 68, Stockholm, Sweden

*Corresponding author e-mail: haoyangd@kth.se

Abstract

This study reviews advancements in the use of phase change materials (PCMs) in underground thermal energy storage (UTES) systems. The primary application forms include vertical and horizontal ground heat exchangers (GHEs) and PCM underground storage units. The paper emphasises the diverse potential of PCMs in UTES by selecting representative research that investigates various types of PCMs and their integration concepts. It highlights the role of PCMs in enhancing storage density and improving system efficiency.

Keywords: Phase change materials, Underground thermal energy storage, Ground heat exchangers

Introduction

The ongoing transition toward carbon-neutral heating and cooling represents a significant step in sustainable energy practices (IRENA, IEA and REN21, 2020). As a crucial part of the energy chain, thermal energy storage (TES) plays a role in mitigating mismatches between thermal energy production and consumption in time and space (Guelpa and Verda, 2019). This becomes increasingly relevant as renewable energy sources, known for their intermittent nature, occupy a larger fraction of the energy supply. PCMs are noted for their high storage density, attributed to their latent heat properties and the ability to maintain a small temperature swing during the phase change process. Phase change material (PCM) implementation in buildings is observed in various applications, including building envelopes, solar thermal collectors, storage tanks, and heat exchangers (Gu *et al.*, 2023). Another widely implemented TES approach is Underground TES (UTES), recognized for its extensive storage capacity. UTES is typically employed to store surplus heat from renewable sources or industrial waste heat, often serving as a seasonal storage solution (Mahon *et al.*, 2022).

Merging PCM with UTES technology has been an expanding field of research in the last decades, aiming to harness the benefits of both technologies. Despite great progress, there is a scarcity of comprehensive literature reviews on this subject. This study seeks to fill this gap by compiling and analysing research on PCM-integrated UTES. In this extended abstract, research in the past two decades, mostly in the past three years, is selected. It categorizes the application of

PCM into two distinct areas: PCM-enhanced ground heat exchangers (GHEs) and standalone PCM storage units. The study further explores various methods of leveraging latent heat in UTES, highlighting their principal characteristics. This comprehensive review aims to provide a clearer understanding of PCM's role in UTES, contributing to the broader objectives of realising sustainable energy storage solutions.

PCM-enhanced GHEs

GHEs are designed to transfer heat to or from the ground, either vertically or horizontally. Horizontal GHEs are typically installed in shallow ground layers, whereas vertical ones can extend hundreds of meters underground. Their installation involves drilling or digging to position circulation pipes. (Sarbu and Sebarchievici, 2016)

The space around these pipes, often filled with sand, soil, or water, presents an opportunity to implement PCM for modifying and controlling the thermal properties of a GHE system.

PCM-enhanced borehole heat exchangers

A borehole is a man-made structure that supports borehole heat exchangers (BHEs), extending deep into the ground. The substance typically used to fill the void between BHE and the ground is grout, often comprising sand, soil, or groundwater. Research shows using suitable PCMs as grout can enhance storage density and reduce the number of required boreholes. For example, Qi *et al.* (2016) simulated the thermal performance of three PCM types (commercial paraffin RT27, a mixture of capric and lauric acids, and a mixture of n-decanoic acid and lauric acid). Simulation



shows the PCMs have a stable temperature due to their small thermal effect radius, showing advantages over ordinary soil in certain applications. Deng et al. (2023) measured the performance of three shape-stabilized PCMs (hexadecane, heptadecane and octadecane) as grouts, noting an increase in the coefficient of performance (COP) of ground source heat pumps (GSHPs) due to reduced temperature fluctuations. Their research also highlighted how the initial ground temperature influences the thermal performance of PCM. It suggests that the PCM selection and its operational temperature range should depend on the ground's initial temperature, which correlates with latitude. Žirgulis et al. (2023) compared the thermal activities of four PCM-grout types, varying in PCM ingredients (microencapsulated PCM and shape-stabilised PCM) and proportions. They noted a balance between increased storage capacity and reduced conductivity, indicating an optimal PCM ratio for a specific annual heat injection and extraction balance.

In contrast to using PCMs as grout, Daneshazarian and Berardi (2023) used a numerical model to place 12 nanoparticle-enhanced PCM pipes around U-pipe loop heat exchangers. Their simulation suggested that the storage capacity of a borehole thermal energy storage (BTES) field with 296 BHEs (243 meters) could be matched by 197 nanoparticle-enhanced PCM BHEs (163 meters). The shorter drilling length and less open space needed imply lower installation costs and requirements.

Typically, BHEs operate above the water freezing point to prevent damage from volume changes in frozen groundwater. However, Fong et al. (2019) explored the feasibility of storing cold by actively freezing groundwater. Their experimental model used a bayonet tube heat exchanger in a vertical GHE, similar to a borehole. Their study observed fluctuating heat transfer across different seasons, particularly when external temperatures exceed ground temperatures, which emphasises the importance of an integrated control system to manage such fluctuations.

PCM-enhanced energy pile

In recent decades, there has been growing interest in energy piles (EPs), which integrate shallow BHEs into a building's structural foundation. These are also known in some literature as geothermal EPs (Saaly and Maghoul, 2019; Al Hajaj and Ziad Saghir, 2023), thermal caissons (Alavy *et al.*, 2021), or pile-foundation heat exchangers (Shukla *et al.*, 2021). EPs offer a cost-effective alternative to traditional borehole fields, primarily by cutting the expenses of drilling. Their primary function is to store heat in the building's

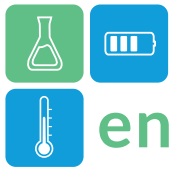
shallow ground area for various durations – from hours to months. This stored heat can then be utilized as a heat source during winter and as a cooling source in summer.

In the early applications, energy was stored as sensible heat in mediums like concrete and mortar. Gao et al. (2008) studied the thermal characteristics of four types of pipe configurations in concrete piles in experiments and simulations. Therein, the W-shaped type was adopted and used in a group of 5500 EPs. Hamada et al. (2007) studied three types of heat exchangers in mortar-filled piles, and U-tubes were adopted in real installations. In Germany, a large installation of around 950 EPs was monitored (Duus and Schmitz, 2021). With free cooling through the ground, the COPs of the two heat pump systems have increased continuously from 3.3 and 3.3 to 3.7 and 3.9 from 2014 to 2017.

Extensive research has been conducted to enhance the storage density and capacity of EPs through the integration of PCMs within their structure. Alavy et al. (2021) validated a numerical model against the world's first EP installation using PCM. This system utilized paraffin (with a melting temperature of 5 to 7 °C) in closed pipes. The design features the PCM within four steel pipes symmetrically arranged in a concrete-filled EP, with U-pipe heat exchangers immersed in the PCM (Shukla *et al.*, 2021). A follow-up study by Alavy, Shirazi and Rosen (2023) conducted a 10-year simulation of this structure, showing notable differences in fluid temperatures entering the heat pump in winter: -0.9 °C for EPs with PCM, compared to -12.7 °C for those without PCM.

In a different design, the PCM is contained within four symmetric tube containers, with U-pipe heat exchangers positioned externally and integrated into cement paste (Mousa, Bayomy and Saghir, 2022). A one-year numerical simulation was conducted to evaluate this structure's performance. The addition of PCM (RT5HC) increased heat pump COP by 5.3%. Ongoing research continues to explore this design. In 2023, Al Hajaj and Ziad Saghir (2023) developed and simulated models in experimental size and found a 42.2 to 46.2% increase (under different heat transfer fluid flow rates) in the energy store by using this design.

Bandeira Neto, Fei and Narsilio (2024) explored another configuration of EPs through numerical analysis. This configuration included a combination of traditional EPs (without PCM) and piles embedded with PCM (used solely for heat/cold storage). This layout minimizes interference between EPs by spacing them farther apart (1.05-meter spacing) while the inclusion of PCM piles enhances the overall storage



capacity. The proposed system has improved heat pump performance by placing the PCM piles that are only used for storing energy between traditional EPs. However, the performance increase was not obvious, likely due to the limited size of the EPs, which constrained the quantity of PCM used.

Han et al. (2022) developed a composite of C50 concrete mixed with MicroPCM, analysing its thermal and mechanical properties. They found that adding 1% by weight of MicroPCM was optimal, maintaining high mechanical strength in the EPs while enhancing geothermal energy collection by 5% in cooling mode. Chang et al. (2024) examined the bearing performance of EPs made with Gum Arabic and polyethylene glycol 600 compared to traditional EPs. The former demonstrated a smaller decrease in load capacity after 343 thermal-cold cycles.

PCM-enhanced horizontal ground heat exchangers

Bottarelli et al. (2022) conducted experiments comparing paraffin and hydrated salts with sand as backfill materials for flat-panel GHEs. Their results indicated that PCMs can effectively compensate for solar energy shortfalls in challenging weather conditions. Cao et al. (2023) numerically investigated various pipe configurations in phase change plates and the evolution of the solid-liquid interface, designed for storing cold to cool the upper part of tunnel lining GHEs.

Underground PCM storage units

In most applications of PCMs in UTES, PCM acts as a supplementary technology to enhance thermal properties. However, some studies have also focused on using PCM (especially ice) as the primary storage medium in underground units. Gu et al. (2022) designed and conducted experiments and simulations on an ice storage tank buried in shallow ground, intended for storing cold for use in a solar greenhouse during summer. Griesbach, König-Haagen and Brüggemann (2022) introduced a novel numerical analysis of a system combining a heat pump with underground ice energy storage (500 m³). This study is notable for its exploration of the system's operation independently of solar energy and its evaluation of the potential to use waste heat from non-residential buildings.

Conclusion and future research direction

This paper has provided a comprehensive overview of the current state of PCM-enhanced GHEs and underground PCM storage units. Innovative concepts of PCM integration are emerging in the recent two decades ranging from material using, configurations

and arrangements in space, applications in different GHEs. Research has covered mostly numerical investigation and lab-scale experiments of the new concepts. The integration of PCMs in various UTES systems represents a great advancement in enhancing the efficiency and sustainability of the overall systems.

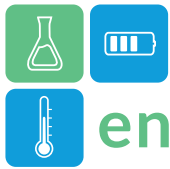
Further research can be done in 1. Techno-economic and life cycle analysis: The most critical research gap lies in conducting thorough techno-economic and life cycle analyses of PCM-enhanced geothermal systems. These analyses would provide valuable insights into the cost-effectiveness, environmental impact, and long-term sustainability of these systems, guiding future development and implementation. 2. Long-term performance monitoring and numerical modelling: continuous monitoring and advanced modelling of both short-term and long-term thermal performance of PCM-enhanced systems are essential. This will help in understanding their behaviour over extended periods and under different environmental conditions, leading to optimized designs and operational strategies. 3. Identification of optimal PCMs: Research should focus on identifying PCMs that operate efficiently within desired temperature ranges and can withstand numerous thermal cycles. Emphasis should be on low-cost, environmentally friendly materials that can be easily integrated into existing geothermal systems.

Acknowledgment

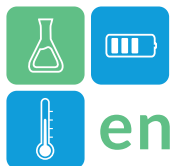
The work is funded by the Swedish Energy Agency. Geothermica EraNET Project: HECTAPUS- Heating Cooling Transition and Acceleration with Phase Change Energy Utilization Storage (Project number P2022-01044)

References

- Alavy, M. et al. (2021) 'Assessment of a novel phase change material-based thermal caisson for geothermal heating and cooling', *Energy Conversion and Management*, 234, p. 113928. Available at: <https://doi.org/10.1016/j.enconman.2021.113928>.
- Alavy, M., Shirazi, P. and Rosen, M.A. (2023) 'Long-term energy performance of thermal caisson geothermal systems', *Energy and Buildings*, 292, p. 113152. Available at: <https://doi.org/10.1016/J.ENBUILD.2023.113152>.
- Bandeira Neto, L.A., Fei, W. and Narsilio, G.A. (2024) 'Improving thermal performance of groups of energy screw piles with phase change materials', *Applied Thermal Engineering*, 236, p. 121874. Available at: <https://doi.org/10.1016/J.APPLTHERMALENG.2023.121874>.
- Bottarelli, M. et al. (2022) 'Role of phase change materials in backfilling of flat-panels ground heat exchanger', *Renewable Energy*, 189, pp. 1324–1336. Available at: <https://doi.org/10.1016/J.RENENE.2022.03.061>.



- Cao, Z. *et al.* (2023) ‘Thermal behavior of phase change plates using tunnel lining GHEs for cool storage: Effect of pipe design parameters and PCM latent heat’, *Energy and Buildings*, 301, p. 113737. Available at: <https://doi.org/10.1016/J.ENBUILD.2023.113737>.
- Chang, H. *et al.* (2024) ‘Analysis of the effect of multiple thermal-cold cycles on the bearing performance of phase change energy piles’, *Geothermics*, 116, p. 102858. Available at: <https://doi.org/10.1016/J.GEOTHERMICS.2023.102858>.
- Daneshazarian, R. and Berardi, U. (2023) ‘Nano-enhanced thermal energy storage coupled to a hybrid renewable system for a high-rise zero emission building’, *Energy Conversion and Management*, 291, p. 117301. Available at: <https://doi.org/10.1016/J.ENCONMAN.2023.117301>.
- Deng, Z. *et al.* (2023) ‘Numerical analysis of borehole heat exchanger using a single shape-stabilized phase change material in heating and cooling seasons’, *Journal of Energy Storage*, 70, p. 107897. Available at: <https://doi.org/10.1016/J.EST.2023.107897>.
- Duus, K. and Schmitz, G. (2021) ‘Experimental investigation of sustainable and energy efficient management of a geothermal field as a heat source and heat sink for a large office building’, *Energy and Buildings*, 235, p. 110726. Available at: <https://doi.org/10.1016/J.ENBUILD.2021.110726>.
- Fong, M. *et al.* (2019) ‘On the performance of ground coupled seasonal thermal energy storage for heating and cooling: A Canadian context’, *Applied Energy*, 250, pp. 593–604. Available at: <https://doi.org/10.1016/J.APENERGY.2019.05.002>.
- Gao, J. *et al.* (2008) ‘Thermal performance and ground temperature of vertical pile-foundation heat exchangers: A case study’, *Applied Thermal Engineering*, 28(17–18), pp. 2295–2304. Available at: <https://doi.org/10.1016/J.APPLTHERMALENG.2008.01.013>.
- Griesbach, M., König-Haagen, A. and Brüggemann, D. (2022) ‘Numerical analysis of a combined heat pump ice energy storage system without solar benefit – Analytical validation and comparison with long term experimental data over one year’, *Applied Thermal Engineering*, 213, p. 118696. Available at: <https://doi.org/10.1016/J.APPLTHERMALENG.2022.118696>.
- Gu, H. *et al.* (2023) ‘Review on heat pump (HP) coupled with phase change material (PCM) for thermal energy storage’, *Chemical Engineering Journal*, 455, p. 140701. Available at: <https://doi.org/10.1016/j.cej.2022.140701>.
- Gu, X. *et al.* (2022) ‘Design and Performance Analysis of a Seasonal Ice Storage System for Cooling Chinese Solar Greenhouses’, *JARQ*, 56(2), pp. 147–161. Available at: <https://www.jircas.go.jp> (Accessed: 21 November 2023).
- Guelpa, E. and Verda, V. (2019) ‘Thermal energy storage in district heating and cooling systems: A review’, *Applied Energy*, 252, p. 113474. Available at: <https://doi.org/10.1016/j.apenergy.2019.113474>.
- Al Hajaj, Z. and Ziad Saghir, M. (2023) ‘Numerical study on the influence of embedded PCM tubes on the energy storage properties of the geothermal energy pile’, *International Journal of Thermofluids*, 20, p. 100416. Available at: <https://doi.org/10.1016/J.IJFT.2023.100416>.
- Hamada, Y. *et al.* (2007) ‘Field performance of an energy pile system for space heating’, *Energy and Buildings*, 39(5), pp. 517–524. Available at: <https://doi.org/10.1016/J.ENBUILD.2006.09.006>.
- Han, C. *et al.* (2022) ‘Characteristics and energy performance of novel MicroPCM C50 energy pile in cooling mode’, *Energy and Buildings*, 274, p. 112442. Available at: <https://doi.org/10.1016/J.ENBUILD.2022.112442>.
- IRENA, IEA and REN21 (2020) *Renewable Energy Policies in a Time of Transition: Heating and Cooling*. Available at: www.irena.org (Accessed: 19 December 2023).
- Mahon, H. *et al.* (2022) ‘A review of thermal energy storage technologies for seasonal loops’, *Energy*, 239, p. 122207. Available at: <https://doi.org/10.1016/j.energy.2021.122207>.
- Mousa, M.M., Bayomy, A.M. and Saghir, M.Z. (2022) ‘Long-term performance investigation of a GSHP with actual size energy pile with PCM’, *Applied Thermal Engineering*, 210, p. 118381. Available at: <https://doi.org/10.1016/J.APPLTHERMALENG.2022.118381>.
- Qi, D. *et al.* (2016) ‘Numerical investigation on thermal performance of ground heat exchangers using phase change materials as grout for ground source heat pump system’, *Applied Thermal Engineering*, 106, pp. 1023–1032. Available at: <https://doi.org/10.1016/J.APPLTHERMALENG.2016.06.048>.
- Saaly, M. and Maghoul, P. (2019) ‘Thermal imbalance due to application of geothermal energy piles and mitigation strategies for sustainable development in cold regions: a review’, *Innovative Infrastructure Solutions*, 4(1), pp. 1–18. Available at: <https://doi.org/10.1007/S41062-019-0224-1/FIGURES/8>.
- Sarbu, I. and Sebarchievici, C. (2016) ‘Ground-Source Heat Pump Systems’, *Ground-Source Heat Pumps*, pp. 71–128. Available at: <https://doi.org/10.1016/B978-0-12-804220-5.00005-9>.
- Shukla, S. *et al.* (2021) ‘Performance characterization of novel caisson-based thermal storage for ground source heat pumps’, *Renewable Energy*, 174, pp. 43–54. Available at: <https://doi.org/10.1016/J.RENENE.2021.04.075>.
- Žirgulis, G. *et al.* (2023) ‘Temperature evolution around four laboratory-scale borehole heat exchangers grouted with phase change materials subjected to heating–cooling cycles: An experimental study’, *Journal of Energy Storage*, 74, p. 109302. Available at: <https://doi.org/10.1016/J.EST.2023.109302>.



Prediction and experimental characterization of a peritectic mixture of sodium acetate trihydrate and sodium nitrate to be used as phase change material

Christoph Rathgeber^{1,*}, Henri Schmit¹, Stefan Hiebler¹, Medine Ilbas², Anabel Palacios², Poppy O'Neill³
¹ Bavarian Center for Applied Energy Research (ZAE Bayern), Walther-Meissner-Str. 6, 85748 Garching, Germany

² Lucerne School of Engineering and Architecture, Technikumstrasse 21, 6048 Horw, Switzerland

³ Cowa Thermal Solutions AG, Platz 4, Technopark Luzern, Root CH-6048, Luzern, Switzerland

*Corresponding author e-mail: christoph.rathgeber@zae-bayern.de

Abstract

In the research project *EuteQ*, the modified BET model was applied to calculate solid-liquid phase diagrams of mixtures of salt hydrates and salts. Particular interest was given to a peritectic composition in the system sodium acetate + sodium nitrate + water. Sodium acetate trihydrate alone offers a high enthalpy of fusion of around $260 \text{ J} \cdot \text{g}^{-1}$ at a melting temperature of $58 \text{ }^\circ\text{C}$. The predicted peritectic mixture was tested and validated with differential scanning calorimetry measurements. In addition, density measurements were performed, and a preliminary nucleating agent screening test revealed that disodium hydrogen phosphate reduces the supercooling of the peritectic to 6 K. With a melting temperature of $49 \text{ }^\circ\text{C}$, the peritectic is suitable for domestic hot water storage systems. It is to be noted that the thermal cycling stability of peritectics should be investigated under application-oriented conditions before they are used as PCM.

Keywords: Thermal Energy Storage, Phase Change Materials, Salt Hydrates, Modified BET Model, Nucleating Agent

Introduction

Latent heat storage using phase change materials (PCM) provides thermal energy storage systems with high storage capacities in small temperature ranges. Most of the PCM used in applications undergo a phase change from solid to liquid and vice versa storing heat in repeated melting and crystallization processes. To select a suitable PCM, both melting and crystallization have to match the temperature range of the intended application.

In the temperature range from 0 to $100 \text{ }^\circ\text{C}$, salt hydrates are generally cheaper and offer higher volumetric melting enthalpies than organic PCM. Mixtures of salt hydrates and salts are being investigated to adapt the melting temperature of known salt hydrates for a specific application. To identify interesting mixture compositions and to reduce the experimental effort, prediction models are applied to calculate solid-liquid phase diagrams.

In the research project *EuteQ*, the modified BET model was applied to calculate the solid-liquid phase diagrams of mixtures of salt hydrates and salts. The modified BET model has proven to be able to predict phase diagrams of salt hydrate mixtures over a wide

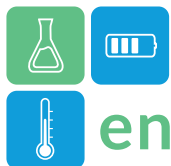
composition and temperature range (Rathgeber (2022)).

Sodium acetate trihydrate ($\text{NaCH}_3\text{COO} \cdot 3\text{H}_2\text{O}$) offers a high melting enthalpy of around $260 \text{ J} \cdot \text{g}^{-1}$ at a melting temperature of $58 \text{ }^\circ\text{C}$ (Schmit et al. (2020)). Particular interest was given to a peritectic composition in the system sodium acetate + sodium nitrate + water ($\text{NaCH}_3\text{COO} + \text{NaNO}_3 + \text{H}_2\text{O}$). With a melting temperature of about $49 \text{ }^\circ\text{C}$, the peritectic composition is suitable for domestic hot water storage systems.

To validate the melting temperature of the calculated peritectic composition and measure its enthalpy change upon melting, measurements via differential scanning calorimetry (DSC) were carried out.

Measurements of the liquid density were performed to determine the volumetric enthalpy change of the peritectic.

Supercooling is a phenomenon by which the crystallization temperature of the PCM is below the melting temperature (Rathgeber et al. (2015)). In the *EuteQ* project, a nucleating agent screening was performed on the sodium acetate trihydrate and sodium nitrate peritectic to observe the influence of common nucleating agents on the crystallization behaviour.



Methodology

Calculation of solid-liquid phase diagram of the system sodium acetate + sodium nitrate + water

To calculate solid-liquid phase diagrams of salt hydrate mixtures, a thermodynamic model needs to predict both the water and salt activities over the concentration and temperature range of interest. In this work, calculation of liquidus temperatures is based on the law of mass action with activities derived from the modified BET model as done by Rathgeber (2022). As a prerequisite, the solid phases (salt hydrates, anhydrous salts, double salts) that occur in the investigated temperature and concentration range have to be known.

In a binary system salt + H₂O, a peritectic is found at the intersection of the liquidus curves of two solids that do not correspond to a local temperature minimum. Accordingly, in a ternary system salt A + salt B + H₂O, a peritectic is found at the intersection of the liquidus surfaces of three solid phases that do not correspond to a local temperature minimum.

The solid-liquid phase diagram of the system NaCH₃COO + NaNO₃ + H₂O was calculated using the BET parameters and solubility constants listed in Table 1 and Table 2, respectively.

Table 1: BET parameters r and ε of sodium acetate (NaCH₃COO) and sodium nitrate (NaNO₃).

Salt	r / -	ε / kJ·mol ⁻¹	Ref.
NaCH ₃ COO	3.66	-1.296	this work
NaNO ₃	1.55	-2.018	Rathgeber (2022)

Table 2: Solubility constants of the solid phases within the system NaCH₃COO+NaNO₃+H₂O.

Solid phase	$\ln K_s$ / -	Ref.
NaCH ₃ COO	$-6.4458+0.0111 \cdot (T/K)$	this work
NaCH ₃ COO·3H ₂ O	$-17.8159+0.0372 \cdot (T/K)$	this work
NaNO ₃	$-9.2948+0.0258 \cdot (T/K)$ $-1.6795 \cdot 10^{-5} \cdot (T/K)^2$	Rathgeber (2022)

DSC measurements

Three repetitions of the five different compositions of NaCH₃COO (>98% Merck), NaNO₃ (>98% Merck) and deionized water, as found in Table 3 were prepared in 10 mL falcon tubes. Each sample was subjected to DSC measurements at 2 K·min⁻¹ for melting temperature measurements and 10 K·min⁻¹ for enthalpy measurements.

Table 3: Compositions of samples within the system NaCH₃COO+NaNO₃+H₂O measured via DSC.

Sample #	wt.% NaCH ₃ COO	wt.% NaNO ₃	wt.% H ₂ O
1	56.25	3.25	40.50
2	53.50	7.50	39.00
3	50.75	11.75	37.50
4	47.50	16.50	36.00
5	45.00	20.00	35.00

The compositions of samples 1 to 5 lie roughly on the connection line from NaCH₃COO·3H₂O to NaNO₃. Samples 1 to 3 correspond to compositions along the boundary between the liquidus surfaces of NaCH₃COO and NaCH₃COO·3H₂O, with sample 1 close to NaCH₃COO·3H₂O and samples 2 and 3 in the direction of the peritectic composition. Sample 4 has a composition corresponding to the peritectic, taking into account the accuracy of sample preparation. The composition of sample 5 lies in the region of the liquidus surface of NaNO₃.

Density measurements

Samples were prepared by mixing the required amounts of salts and deionized water. NaCH₃COO and NaNO₃ (Merck, “for analysis”) were used together with deionized water to prepare a sample with a composition corresponding to the peritectic of the ternary system NaCH₃COO + NaNO₃ + H₂O.

Liquid densities were measured with a DMA 4500 M from Anton Paar calibrated with deionized water. Thereby, densities are measured with an estimated accuracy of $d\rho=0.0002 \text{ g}\cdot\text{cm}^{-3}$ in terms of density and $dT=0.05 \text{ K}$ in terms of temperature. Measurements were carried out above 60 °C to prevent crystallization of the sample inside the density meter.

Tests of Nucleating Agents

To find an appropriate nucleating agent for the peritectic system, two common nucleating agents (Guarda et al. (2023), Hua et al. (2018)) for the bulk salt hydrate in the system, NaCH₃COO·3H₂O, were tested to see their influence on the crystallization temperature of the peritectic. Four 50 mL samples were prepared by mixing the appropriate peritectic composition of NaCH₃COO (>98% Merck), NaNO₃ (>98% Merck) and deionized water into falcon tubes. To the first sample, no nucleating agent was added. To the second sample, 3 wt.% of Na₃PO₄ (96% Merck) was added as a nucleating agent, and to the third sample 3 wt.% of Na₂HPO₄ (≥99% Merck). To the fourth sample, 1.5 wt.% of Na₃PO₄ and 1.5 wt.% of Na₂HPO₄ were added. The samples were placed in a thermal cycling unit (details to be found in O’Neill et al. (2021)) and cycled between 25 and 65 °C at a heating and cooling rate of 0.5 K·min⁻¹.

Results

Predicted phase diagram and peritectic composition

The calculated phase diagram of the system NaCH₃COO + NaNO₃ + H₂O is shown in Figure 1. Such three-dimensional drawings with the ordinate as temperature axis and the base as the composition triangle facilitate the interpretation of solid-liquid

phase diagrams. Although coordinates cannot be read off directly, the temperature profile of the phase boundary lines is illustrated. The liquidus surfaces of the occurring solid phases are plotted with contour lines at intervals of 10 K. The liquidus surfaces were calculated down to a minimum temperature of 270 K.

In the system $\text{NaCH}_3\text{COO} + \text{NaNO}_3 + \text{H}_2\text{O}$, one peritectic was identified. The ternary peritectic corresponds to the composition where the solid phases of NaCH_3COO (liquidus surface in orange, marked with “1”), $\text{NaCH}_3\text{COO}\cdot 3\text{H}_2\text{O}$ (blue, “2”), and NaNO_3 (red, “3”) are in equilibrium with aqueous salt solution of the same composition. Its calculated composition is 46.75 wt% $\text{NaCH}_3\text{COO} + 16.75$ wt% $\text{NaNO}_3 + 36.5$ wt% H_2O . The calculated peritectic temperature is 52.55 °C. In Figure 1, the peritectic is marked with a yellow sphere.

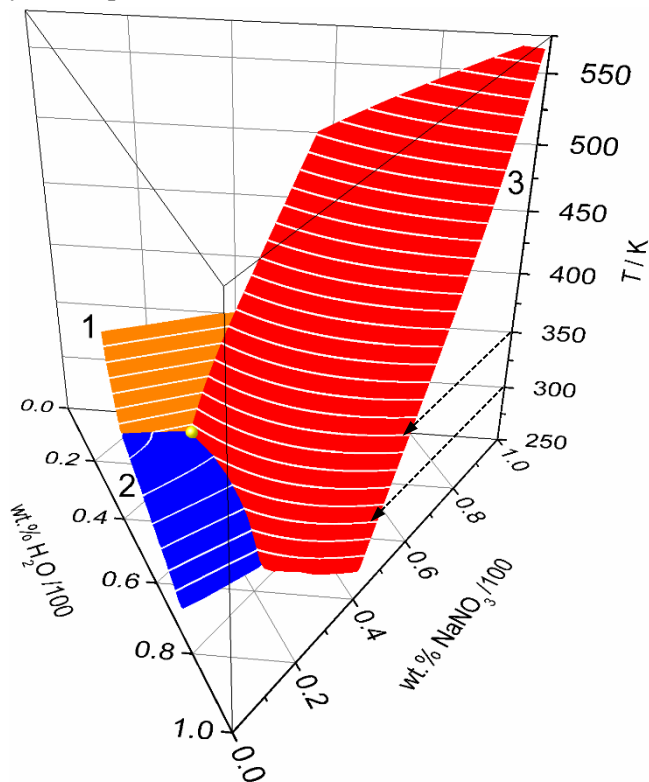


Figure 1: Calculated solid-liquid phase diagram of the system $\text{NaCH}_3\text{COO} + \text{NaNO}_3 + \text{H}_2\text{O}$ with peritectic composition (yellow sphere); liquidus surfaces of NaCH_3COO (1, orange), $\text{NaCH}_3\text{COO}\cdot 3\text{H}_2\text{O}$ (2, blue), and NaNO_3 (3, red). Dashed arrows indicate the contour lines at 300 and 350 K.

DSC measurements

Figure 2 shows the melting temperatures and enthalpies measured via DSC compared with the predicted, calculated temperatures. Uncertainty bars indicated for melting temperatures and enthalpies correspond to the standard deviations of the three measurements carried out for each composition.

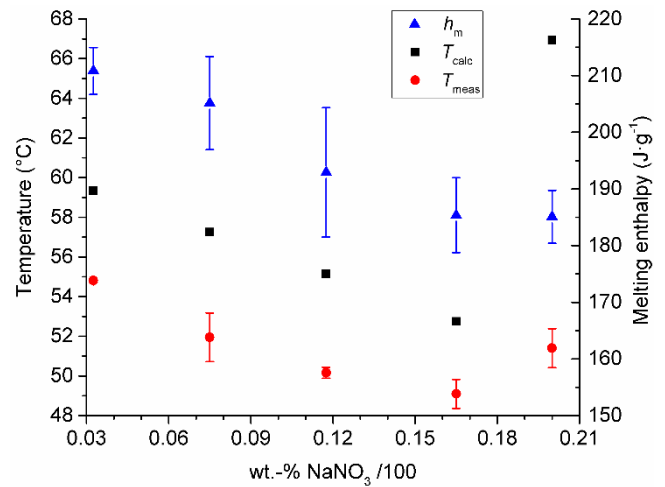


Figure 2: Measured (red circles) and calculated (black squares) melting temperatures and measured melting enthalpies (blue triangles) of samples listed in Table 3.

Of the samples measured, the one with 16.5 wt.% NaNO_3 has a composition closest to the calculated peritectic composition (referred to as “peritectic sample”). The measured onset temperature of the melting peak is 49 °C, and the melting enthalpy is $(185 \pm 7) \text{ J}\cdot\text{g}^{-1}$.

Overall, the measurement results support the calculated phase diagram: Of the samples measured, the peritectic sample has the lowest calculated and the lowest measured melting temperature. The deviations between calculated and measured temperatures are mainly a consequence of comparing onset temperatures of melting peaks obtained from dynamic measurements with calculated solubility limits at equilibrium state.

Measured melting enthalpies decrease with increasing NaNO_3 content due to the melting enthalpy of NaNO_3 ($178 \text{ J}\cdot\text{g}^{-1}$ according to ICTAC Working Group (1999)) being lower than the melting enthalpy of $\text{NaCH}_3\text{COO}\cdot 3\text{H}_2\text{O}$.

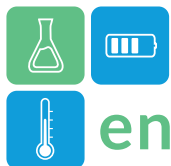
Density measurements

The measured liquid density of the peritectic composition in the system $\text{NaCH}_3\text{COO} + \text{NaNO}_3 + \text{H}_2\text{O}$ are given in Table 4.

Table 4: Measured liquid density ρ of the peritectic in the system $\text{NaCH}_3\text{COO} + \text{NaNO}_3 + \text{H}_2\text{O}$.

$T / ^\circ\text{C}$	$\rho / \text{g}\cdot\text{cm}^{-3}$
60	1.3628
65	1.3587
70	1.3546
75	1.3505
80	1.3464
85	1.3422

Depending on the upper application temperature of a storage tank based on this peritectic, the volumetric



melting enthalpy is calculated as the product of the mass-related melting enthalpy and the liquid density. For example, with $\rho = 1.35 \text{ g}\cdot\text{cm}^{-3}$ at $75 \text{ }^\circ\text{C}$, the volumetric melting enthalpy is $h_m = (250 \pm 9) \text{ J}\cdot\text{cm}^{-3}$.

Tests of Nucleating Agents

The results from the nucleating agent test can be observed in Figure 3. The figure includes two representative cooling curves for the analyzed samples with and without nucleating agents.

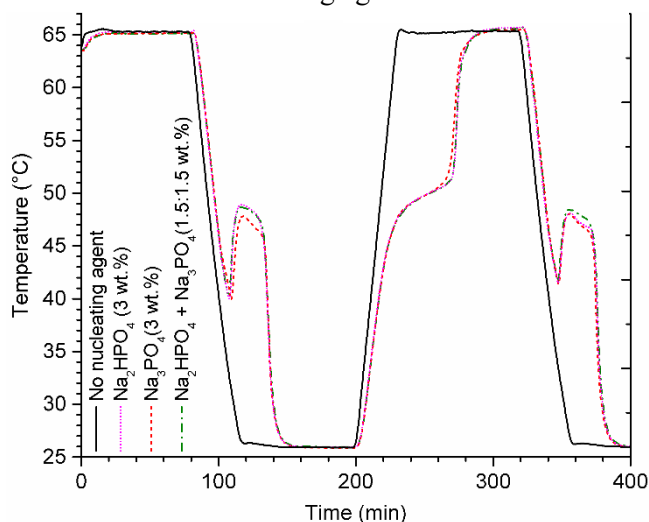


Figure 3: Nucleating agent cycling testing with Na_3PO_4 , Na_2HPO_4 at 3 wt.% and a combination of 1.5 wt.% of Na_3PO_4 and 1.5 wt.% Na_2HPO_4 against a reference sample without nucleating agent.

Without nucleating agents (solid black line), the peritectic mixture does not crystallize between 65 and 25 $^\circ\text{C}$. The addition of Na_3PO_4 or Na_2HPO_4 reduces the degree of supercooling, with Na_3PO_4 inducing an average supercooling degree of 8 K (dashed red line), and Na_2HPO_4 of 6 K (dotted blue line). The combination of Na_3PO_4 and Na_2HPO_4 (dotted-dashed olive line) does not show any added benefit.

Conclusions

In this work, the modified BET model was applied to calculate the solid-liquid phase diagram of the system $\text{NaCH}_3\text{COO} + \text{NaNO}_3 + \text{H}_2\text{O}$. In this system, a peritectic composition of 46.75 wt% $\text{NaCH}_3\text{COO} + 16.75 \text{ wt}\% \text{ NaNO}_3 + 36.5 \text{ wt}\% \text{ H}_2\text{O}$ with a melting temperature at around 52 $^\circ\text{C}$ was predicted.

In DSC measurements, an onset melting temperature of 49 $^\circ\text{C}$ and a melting enthalpy of $(185 \pm 7) \text{ J}\cdot\text{g}^{-1}$ were obtained. The addition of 3 wt.-% Na_3PO_4 , Na_2HPO_4 , or a mixture of both salts as nucleating agent reduced the supercooling of the peritectic significantly.

This peritectic should be subjected to thermal cycling stability tests under application-oriented experimental conditions. Thermal cycling stability is an essential

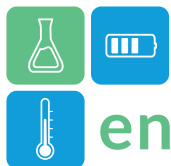
requirement for a PCM. In the case of peritectics, a separation of different solid phases could occur during repeated melting and crystallization cycles.

Acknowledgments

The work of ZAE Bayern was supported by the German Federal Ministry of Education and Research under the project code 01QE2252C. The work of Cowa Thermal Solutions AG and HSLU was made possible through the project *EuteQ* project ID 1853 from *Eurostars 3 Call 2*. The responsibility for the content of this publication is with the authors.

References

- Guarda, D., Righetti, G., Mancin, S., Fenk, B., O'Neill, P., Worlitschek, J., ... & Schuetz, P. (2023). Systematic analysis of the stability of Sodium Acetate Trihydrate as Phase Change Material during thermal cycling. In Proceedings of the 26th International Congress of Refrigeration.
- Hua, W., Zhang, X., Muthoka, M. J., & Han, X. (2018). Preparation and performance analysis of modified sodium acetate trihydrate. *Materials*, 11(6), 1016. doi/10.3390/ma11061016.
- ICTAC Working Group (1999). Reference materials for calorimetry and differential thermal analysis. *Thermochimica Acta*, 331(2), 93-204. doi/10.1016/S0040-6031(99)00009-X.
- O'Neill, P., Stamatou, A., Bonjour, J., Fischer, L., & Revellin, R. (2021). The effect of surfactant selection in phase change dispersions. In 13th IIR PCM Conference.
- Rathgeber, C., Schmit, H., Miró, L., Cabeza, L. F., Gutierrez, A., Ushak, S. N., ... & Hauer, A. (2015). Analysis of supercooling of phase change materials with increased sample size—Comparison of measurements via DSC, T-History and at pilot plant scale. In Proceedings of the 13th International Conference on Energy Storage Greenstock, Beijing, China (pp. 19-21).
- Rathgeber, C. (2022). Mischungen aus Salzhydraten und Salzen als Phasenwechselmaterialien: Thermodynamische Modellierung und experimentelle Untersuchung von fest-flüssig Phasendiagrammen. (Doctoral dissertation, Technical University Berlin). doi/10.14279/depositonce-16629.
- Schmit, H., Rathgeber, C., Hock, P., & Hiebler, S. (2020). Critical review on measured phase transition enthalpies of salt hydrates in the context of solid-liquid phase change materials. *Thermochimica Acta*, 683, 178477. doi/10.1016/j.tca.2019.178477



Proposal of advanced electrochemical techniques for improved monitoring control in sorption materials for TES systems

Angel G. Fernández^{1,*}, Sara Amini¹, Mikel Alberro²

1 University of the Basque Country UPV/EHU, Gipuzkoa Engineering Faculty, Department of Chemical and Environmental Engineering, Plaza Europa 1, 20018, Donostia-San Sebastián, Spain

2 University of the Basque Country UPV/EHU, Gipuzkoa Engineering Faculty, Department of Electronic Technology, Plaza Europa 1, 20018, Donostia-San Sebastián, Spain

*Corresponding author e-mail: angelgabriel.fernandez@ehu.eus

Abstract

The optimization of control and monitoring performance of industrial thermal energy storage (TES) systems is one of the main challenges in the energy industrial technology. In this work, we have applied different electrochemical techniques for a better understanding of the hydrated/dehydrated processes in sorption materials (highlighting cyclic voltammetry and chronoamperometry). Additionally, the corrosion behaviour of different sorption salts, was monitored using electrochemical impedance spectroscopy due to the aggressive impurities usually formed in chloride and bromide containing salts. Electrochemical techniques were successfully applied to understand both, hydration/dehydration process and corrosion mechanism in contact with commercial alloys.

Keywords: Sorption materials, Molten salts, Electrochemical monitoring techniques

Introduction

Thermal energy storage (TES) has become as one of the main important development for the energy industry, since it has the potential to overcome the existing mismatch between energy production and demand for discontinuous energy sources, solar thermal, at high temperature, and/or variable loads, for medium thermal energy demand in buildings. It is therefore evident that this component is gaining a crucial role in the development of highly efficient thermal energy systems (Ibrahim et al, 2008). The optimal performance and control of this parameter in industrial environments has been a hot topic in the last decades and the proposal of electrochemical monitoring techniques has been studied in different storage environments. In this direction, this work is focused on the use of electrochemical techniques to control sorption materials (50-180°C) and molten salts (390-700°C). Sorption materials have gained popularity since energy density potential, price and workability, identifying MgCl₂, SrBr₂ and MgSO₄ as some of the most promising candidates for thermochemical TES, applied to heat pumps to reduce the energy consumption in smart buildings (N'Tsoukpoe et al, 2014). For salt hydrate-based sorption heat storage, salt hydrates form new crystal structures by dissociating or absorbing water molecules, and this process realizes the storage or

release of thermal energy. The operating principle can be classified into charging (desorption or dehydration) and discharging (sorption or hydration) processes. Additionally to the formation of corrosive specimens in the proposed sorption salts, there is a lack of knowledge in the hydrate/dehydrate control processes for a better optimization during the charge/discharge cycles in the corresponding application. In this sense, the combination of different electrochemical techniques were used to evaluate the hydration/dehydration reactions in an accurate way and the corrosion mechanism in different commercial alloys, due to the halide content in the sorption salt proposed.

Methodology

A combination of the following electrochemical measurements will be performed for a better understanding of the sorption and corrosion process:

- **Chronoamperometry (CA):** CA is used to study the kinetics of chemical reactions, diffusion processes, and adsorption. CA is a controlled current technique where the potential is the variable determined as a function of time. The constant current will be applied between the specially designed electrochemical electrodes used during the project, obtaining curves ($E_{we} = f(t)$), that correspond to the redox potential of the electroactive species (Tian et al, 2020).

- **Electrochemical impedance spectroscopy (EIS):** The greatest advantage of this technique is the low intensity of excitation signal used which causes minimal disruption in the electrochemical system state, constituting a non-destructive technique and reducing the error associated with the measurement process. Impedance spectra obtained by this method is adjusted to an electrical circuit of a combination of resistors and capacitors (equivalent circuits), in order to interpret the corrosion processes (Andrade et al, 2010; Orazem et al, 2018) and the behaviour of the coating formed.

- **Linear polarization resistance (LPR):** A small voltage (or polarization potential) is applied to an electrode in solution. The current needed to maintain a specific voltage shift (typically 10 mV) is directly related to the corrosion on the surface of the electrode in the solution, and the corrosion rate can also be calculated instantaneously, according the Butler-Volmer equation (Zeng et al, 2001; Anderko et al, 2004).

These innovative techniques have been applied in situ in the sorption conditions, defined for each salt and integrated in a specially designed sorption reactor. The experimental set-up is shown in Figure1.

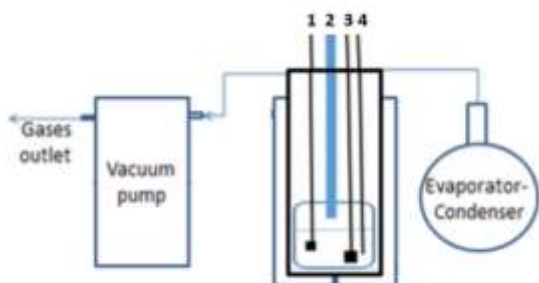


Figure 1: Sorption set-up including 1 (working electrode), 2 (thermopar), 3 (counter electrode) and 4 (reference electrode)

The sorption reactor can be modified to the specific hydration/dehydration conditions under temperature and pressure. Table 1 shows the sorption salts selected for this work as well as their storage properties and testing conditions.

Table 1: Sorption salts selected

Sorption Material	m.p. (°C)	λ (W/(m·K))	ΔH (kJ/kg)	C_p (kJ/kg K)	Corrosion Test (°C/mbar)
SrBr ₂ *6H ₂ O	88.6	0.71	347	0.98	78/129
MgCl ₂ *6H ₂ O	115	0.57	255	2.61	167

The container materials tested in this sorption proposed salts were carbon steel (A1) stainless steel (AISI 304) and brass with the following chemical composition.

Table 2: Chemical composition of the alloy tested

Material	Fe	Cr	Ni	Cu	Zn
A1	Bal.	0.05	0.05	-	-
AISI 304	Bal.	18.1	8.07	-	-
Brass	0.02	-	0.03	Bal.	36.43

The corrosion tests were carried out during 500h to obtain the corrosion rate through linear polarization resistance technique. CA and CV were applied at different thermal and pressure cycles from room temperature to 200°C in order to monitorize the hydration/dehydration processes.

Scanning electron microscopy (SEM) and X-ray diffraction (XRD) were used to analyse the corrosion products formed in the alloy surface.

Results and discussion

Corrosion tests are under operation and the electrochemical techniques were successfully applied. The preliminary results show a higher corrosion rate in MgCl₂*6H₂O due to the formation of MgOHCl, an aggressive impurity that was detected by XRD. Cronoamperimetry and cyclic voltammetry results were used for a better understanding of the sorption process, confirming the water molecules release and the formation of MgOHCl through the following reaction at 167°C:



Conclusions

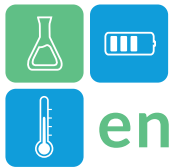
The use of advanced electrochemical techniques could be an interesting option to control the hydrate/dehydration processes in sorption salt for innovative heat pumps and evaluate the life cycle of the components materials due to the halide content of some of the most promising sorption candidates.

Acknowledgment

Dr. Angel G. Fernández wants to acknowledgement the financial support from RyC 2020-28787-I funded by MCIN/AEI/10.13039/501100011033 and ESF "Investing in your future".

References

Anderko, A and al., A general model for the repassivation potential as a function of multiple



enerstock

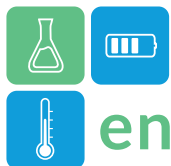
ENERSTOCK 2024

The 16th IEA ES TCP International Conference on Energy Storage

June 5–7, 2024

Lyon, France

- aqueous solution species. *Corrosion Science* 46, 2004, 1583-1612.
- Andrade, C and Martínez, I. Techniques for measuring the corrosion rate (polarization resistance) and the corrosion potential of reinforced concrete structures. *Non-Destructive Evaluation of Reinforced Concrete Structures: Non-Destructive Testing Methods*, 2010.
- Ibrahim, H and al., Energy storage systems—Characteristics and comparisons, *Renewable and Sustainable Energy Reviews*, 2008, 12, pp: 1221–1250.
- N'Tsoukpoe, K.E. and al., A systematic multi-step screening of numerous salt hydrates for low temperature thermochemical energy storage. *Applied Energy*, 2014, 124, pp: 1–16.
- Orazem, M., An integrated approach to electrochemical impedance spectroscopy. *Electrochimica Acta*, 2008. 53: p. 7360–7366.
- Tian, R., Using chronoamperometry to rapidly measure and quantitatively analyse rate-performance in battery electrodes. *Journal of power sources*, 2020, 468, pp: 228220
- Zeng, C.L., Electrochemical impedance models for molten salt corrosion. *Corrosion Science*, 2001, 43: p. 787-801.



Protic dialkylammonium-based ionic liquids as promising solid-solid phase change materials for thermal energy storage: synthesis and thermo-physical characterization.

Jorge L. Lopez-Morales¹, Jonatan Perez-Arce¹, Angel Serrano¹, Jean-Luc Dauvergne¹, Nerea Casado^{2,3}, Aginmariya Kottarathil¹, Elena Palomo Del Barrio^{1,3}, Eduardo J. Garcia-Suarez^{1,3}

¹Center for Cooperative Research on Alternative Energies (CIC energiGUNE), Basque Research and Technology Alliance (BRTA), Alava Technology Park, Albert Einstein 48, 01510 Vitoria-Gasteiz, Spain.

²POLYMAT, University of the Basque Country UPV/EHU, Avenida Tolosa 72, 20018 Donostia-San Sebastián, Spain

³IKERBASQUE, Basque Foundation for Science, Plaza Euskadi 5, 48009 Bilbao, Spain.

Abstract

The surge in renewable energy usage, notably solar and wind, needs effective energy storage systems to address their discontinuous nature. Thermal energy storage, particularly using phase change materials (PCMs), is a focal area of research. While most PCMs undergo solid-liquid transitions, leading to leakage concerns and increased costs for containment, a novel class of PCMs, organic ionic plastic crystals (OIPCs), with solid-solid transitions has emerged to mitigate these challenges. Despite limited literature and availability of OIPCs for Thermal Energy Storage (TES), we present the synthesis and thorough characterization of nine OIPCs based on dioctylammonium cation paired with various organic and inorganic acids as anions. In this work, we studied key thermal properties of PCMs, including latent heat, transition temperature, subcooling, thermal conductivity, and energy storage density. The evaluation covers also thermal stability and reliability through thermal cycling. Among the OIPCs, [DOA][NO₃], [DOA][Cl], and [DOA][FOR] stand out with energetic solid-solid transition enthalpies, demonstrating their potential as PCMs for TES systems below 45 °C.

Keywords: Phase Change Materials; dialkylammonium salts; Thermal Energy Storage; ionic liquids; organic ionic plastic crystals.

Introduction

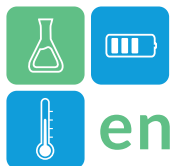
The anticipated global increase in population until 2100, coupled with a rising demand for energy, translates the use of fossil fuels as an energy source unsustainable. Apart from the finite nature of fossil fuels, the inevitable release of substantial CO₂ amounts intensifies the greenhouse effect¹. Abuse of fossil fuels not only leads to global warming but also needs mitigation to prevent adverse effects on living organisms². Consequently, the scientific community seeks innovative, disruptive, and efficient energy solutions to mitigate the impacts on both the planet and living beings.

In this context, the focus has been on alternative sustainable energy sources such as solar, wind, sea, or biomass, and significant progress has been made in recent decades. However, most renewable energy sources are inherently intermittent or seasonal due to reliance on daily weather and climatic conditions. This intermittency increases the critical need for efficient energy storage to use generated energy on

demand. Currently, two main methods for storing energy exist: electrical (EES) and thermal (TES) energy storage³.

While most attention has been directed toward EES, the potential of TES has been underestimated until now. Thermal energy storage can manifest as sensible (SHS), latent (LHS), or thermochemical (THS) heat. LHS stands out for its high energy density storage at a constant temperature, minimal energy loss, and compact storage systems. Phase change materials (PCMs), play a crucial role in this context, covering applications across temperatures from 0 °C to above 1000 °C^{4,5}.

However, most employed PCMs involving solid-liquid transitions (SL-PCMs) exhibit significant limitations related to containment and volume increase during the phase transition. A new class of PCMs undergoing solid-solid transitions (SS-PCMs), known as organic ionic plastic crystals (OIPCs), has emerged to address these issues⁶. Unlike SL-PCMs, SS-PCMs, particularly OIPCs, offer more compact



TES systems and potentially avoid the costs associated with SL-PCM containmentment.

The organic ionic plastic crystals (OIPCs), offer advantages such as negligible or low vapor pressure and easy functionalization, making them adaptable to specific temperature ranges and compatible with various heat transfer fluids⁷

This study focuses on synthesizing and characterizing a series of OIPCs formed by combining dioctylammonium ([DOA]) cation with both organic and inorganic anions. Unlike previous studies limited to inorganic anions combined with alkylammonium salts, this work explores the use of organic anions. The primary objective is to assess key thermal and physical properties of the prepared OIPCs for their potential use as PCMs in TES systems for thermochemical heat storage at temperatures below 55 °C.

Experimental section

Synthesis of dialkylammonium salts

The organic ionic compounds were synthesized following a slightly modified procedure reported by Steinert et al⁸. In a typical experiment, the desired amount of the dioctylamine was placed in a round bottom flask with a magnetic stirrer placed in an ice bath. After, 1.03 equivalents of the corresponding acid were added dropwise. Then the ice bath was removed, and the mixture was allowed to stir at room temperature overnight. Finally, the product was filtered off and washed several times with distilled water until neutral pH to remove the excess of unreacted acid. The obtained product was dried in an oven at 60 °C until constant weight and kept under dried atmosphere until further use.

Nuclear Magnetic Resonance analyses

¹H and ¹³C{¹H} NMR spectra were recorded on a BRUKER Avance II 300 MHz (¹H at 300 MHz and ¹³C{¹H} at 75 MHz). The chemical shifts were reported in ppm (δ).

Density measurements

The true density of the prepared dialkylammonium salts was determined by using an AccuPyc-Micrometrics AccuPyc gas displacement pycnometer. For the density measurement, 310 mg to 750 mg of the sample was placed in a 1 ml chamber as He was employed as probe gas.

Melting point measurements

The melting point of all the compounds was measured in an SRS Optimelt instrument. The measurement was

carried out in two steps. In a first step, a temperature scan from room temperature to 200 °C at a heating rate of 5 °C/min. Then the melting point was determined in a second step by heating the sample in the established temperature range set in the first step at 1 °C/min.

Thermalgravimetric analysis (TGA)

The thermal stability of the compounds was determined by TGA in a Netzsch ASCII instrument. The sample (10 to 20 mg) was placed in an open alumina crucible and heated from room temperature to 110 °C at a heating rate of 10 °C/min under N₂ atmosphere (60 ml/min). Afterward, the sample was heated from 110 °C to 600 °C with a heating rate of 5 °C/min. Decomposition temperature was determined by the onset temperature defined according to ISO 11358-1.

Differential scan calorimetry (DSC) analysis

DSC was used to determine the transition/melting temperatures, latent heat, and specific heat capacities of the obtained OIPC. A power-compensation DSC Q2500 from TA Instruments was employed with sealed Al crucibles. The mass of the samples was ca. 9 mg. Argon (50 ml/min) was employed as the purge gas. Each sample was submitted to three heating and cooling cycles, from -40 °C to 70 °C or 110 °C depending on the previously registered melting point, with a heating/cooling rate of 5 °C/min. The transition temperatures are determined by the onset temperature of corresponding endothermic peaks in the DSC-thermograms, whereas the latent heat is calculated by integrating the latter assuming a linear baseline. The specific heat capacity was registered 5 °C before the first phase transition, both in heating and cooling.

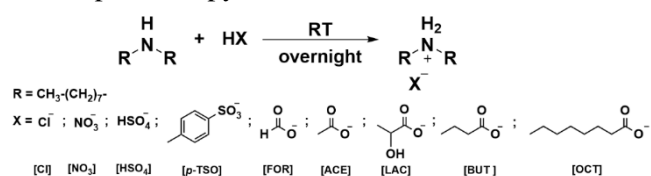
Thermal conductivity

The thermal conductivities of the organic ionic compounds were determined by Transient Plane Source (also known as Hot Disk). The size of the sensor and samples, the heating power, and the measurement time were chosen according to the norm ISO 22007-2:2015⁹. Measurements were carried out with a Hot Disk TPS 2500S instrument equipped with a Kapton 7577 F1 sensor (radius 2.001 mm) subjected to a heating power of 15 mW for 20 s. This sensor was sandwiched between two pelletized compound samples. At least 3 measurements for each compound were performed at room temperature by moving the samples between each test. The recorded data were processed using the Hot Disk Software (version 7.4.0.10).

Results and discussion

Synthesis of Dialkylammonium Salts and Structural Characterization

The cation source chosen for the synthesis of OIPCs was dioctylamine (DOA, C8), selected for its size, symmetry, and aliphatic chain length. As for the anion source, nine different acids were employed, including three inorganic acids, one organic sulfonic acid, and five organic carboxylic acids. The synthesis followed a modified procedure (**Scheme 1**) reported by Steinert and co-workers in 2005⁸, involving acid-base neutralization to obtain the desired protic ionic compounds. The resulting compounds were isolated with high yields, and their structural characterization and purity were confirmed using ¹H and ¹³C{¹H} NMR spectroscopy.



Scheme 1.

The investigation focuses on the impact of different anions on the thermo-physical properties of the prepared OIPCs, with potential applications discussed in the field of thermal energy storage as solid-solid phase change materials (SS-PCMs).

Thermal Stability

The thermal stability of OIPCs is a crucial consideration for their application in thermal energy storage. The decomposition temperatures at 0.1 wt.%, 1.0 wt.%, and 5.0 wt.% mass loss for the prepared OIPCs were determined and are presented in **Table 1**. The thermal stability was found to be influenced by the specific anion present. The order of decomposition temperatures (onset) was observed as [p-TSO] > [HSO₄] > [Cl] > [NO₃] > [LAC] > [OCT] > [ACE] > [BUT] > [FOR]. Interestingly, the thermal stability of OIPCs with inorganic acid anions ([HSO₄], [p-TSO]) was higher compared to carboxylate anions.

Anion	[Cl]	[NO ₃]	[HSO ₄]	[p-TSO]	[FOR]	[ACE]	[LAC]	[BUT]
T _{0.1} (°C)	116.3	114.9	137.8	136.4	114.0	110.6	121.0	111.1
T _{1.0} (°C)	139.4	134.1	209.1	254.7	124.4	117.9	149.3	123.1
T _{5.0} (°C)	214.2	166.3	251.1	312.4	143.9	138.9	175.9	141.1
dT _{dec.} (onset) (°C)	229.5	201.9	268.7	338.9	139.4	155.7	195.3	151.3

Table 1.

Melting Point

The difference between solid-solid transition and melting temperatures of OIPCs provides insights into their operating temperature range. OIPCs exhibited melting temperatures ranging from below room temperature to approximately 235 °C. Carboxylate anions resulted in lower melting points, while inorganic anions yielded the highest melting points, particularly [DOA][Cl] (234.1 °C). [DOA][BUT] was found to be liquid at room temperature.

Thermal Conductivity

Thermal conductivity, a critical parameter influencing heat transfer rates in thermal energy storage systems, was determined at 25 °C for the prepared OIPCs. The thermal conductivities ranged from 0.180 W/mK to 0.373 W/mK (**Figure 1**).

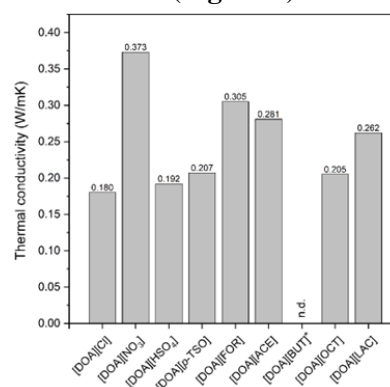
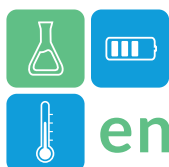


Figure 1.

Differential Scanning Calorimetry and Storage Density

Differential Scanning Calorimetry (DSC) was employed to evaluate the main thermal properties of the OIPCs. **Table 2** presents onset temperatures, enthalpies, and specific heat values for solid-solid transitions, as well as melting temperatures. The prepared OIPCs exhibited low-temperature transitions, with [DOA][NO₃] having the highest at 41.4 °C and [DOA][Cl] the lowest at 20.0 °C. Limited subcooling (1.8 °C to 6.3 °C) was observed for most OIPCs.

	[DOA][Cl]		[DOA][NO ₃]		[DOA][FOR]	
T _{onset} ^{heating} (°C)	1.8	20.0	9.7	41.4	10.6	29.7
T _{onset} ^{cooling} (°C)	4.1	18.3	19.1		23.5	
Subcooling (°C)	1.8		22.4		6.3	
ΔH _{heating} (J/g)	3.5	97.7	22.3	134.3	5.5	52.9
ΔH _{cooling} (J/g)	35.2	59.8	152.3		49.8	



$C_{p,TP}$ (J/g°C)	1.5	1.5	1.7
$C_{p,HTP}$ (J/g°C)	1.9	2.1	2.1
$T_{melting}$ (°C)	234.1	167.0	58.6

Table 2

The thermal energy storage density, representing the amount of energy stored per unit volume, was calculated for each OIPC. [DOA][Cl], [DOA][NO₃], and [DOA][FOR] demonstrated high storage densities of 91.9 J/cm³, 162.5 J/cm³, and 58.4 J/cm³, respectively.

Reliability

To assess the reliability of the OIPCs, [DOA][Cl], [DOA][NO₃], and [DOA][FOR] underwent 50 heating/cooling cycles. DSC thermograms for the 1st and 50th cycles showed consistent onset temperatures for the main solid-solid transitions. While [DOA][FOR] exhibited a slight decrease in latent heat (6.2%), [DOA][NO₃] and [DOA][Cl] experienced less than 4% loss (Figure 4). Based on these results, the OIPCs were deemed reliable for at least the first 50 cycles, meeting the cycling category F of the RAL-GZ 896 (Quality Association PCM)¹⁰.

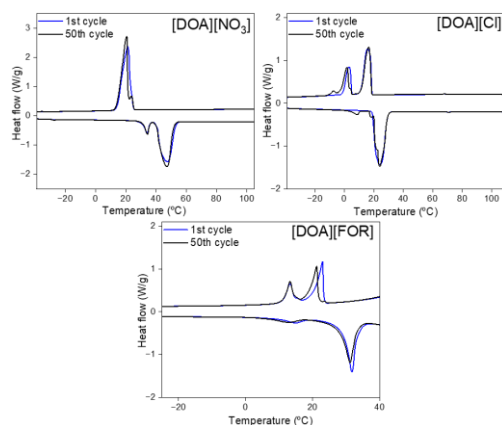


Figure 4

Compatibility with Water

The compatibility of OIPCs with water is crucial for their applicability in thermal energy storage systems. Eight of the prepared OIPCs showed no solubility in water, and [DOA][BUT], liquid at room temperature, was also not miscible in water. This enhances the overall performance of these OIPCs in TES systems by avoiding costly encapsulation methods and maintaining efficient heat transfer rates with water.

Conclusions

Based on the obtained results, [DOA][NO₃],

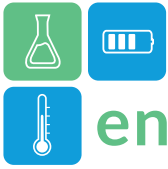
[DOA][Cl], and [DOA][FOR] OIPCs exhibit favorable properties, positioning them as potential candidates for integration into low-temperature Thermal Energy Storage (TES) systems. These materials not only showcase high energy storage densities but also demonstrate a considerable operating range, characterized by substantial differences between their solid-solid transition and melting points. Moreover, they prove to be reliable through a minimum of 50 thermal cycles. Additionally, the successful utilization of organic-based anions with [DOA] counterions in crafting OIPCs with solid-solid transitions has been validated. This opens up the prospect of exploring other organic compounds, serving as both cations or anions, enabling the precise adjustment of Solid-Solid Phase Change Materials (SS-PCMs) on demand. This adjustment can be achieved by fine-tuning transition temperatures and incorporating specific functionalities through the modification of organic moieties, given their facile functionalization.

Acknowledgments

Financial support from the Basque Government (KK-2021/00064 & KK-2022/00089) is gratefully acknowledged for funding this research.

References

- (1) T.R. Anderson, E. Hawkins, P.D. Jones, *Endeavour*, 2016, 40(3), 178-187.
- (2) L. Al-Ghussain, *Environmental Progress & Sustainable Energy*, 2019, 38(1), 13-21.
- (3) H.A. Behabtu, M. Messagie, T. Coosemans, M. Bercibar, K.A. Fante, A.A. Kebede, J. Van Mierlo, *Sustainability*, 2020, 12, 10511-10531.
- (4) H. Jouhara, A. Żabnieńska-Góra, N. Khordehgah, D. Ahmad, T. Lipinski, *International Journal of Thermofluids*, 2020, 5-6, 100039-100065.
- (5) K. Matuszek, M. Kar, J.M. Pringle, D.R. MacFarlane, *Chem. Rev.*, 2023, 123(1), 491-514.
- (6) J.M. Pringle, P.C. Howlett, D.R. MacFarlane, M. Forsyth, *J. Mater. Chem.*, 2010, 20, 2056-2062.
- (7) S.K. Singh, A.W. Savoy, *Journal of Molecular Liquids*, 2020, 297, 112038-112051.
- (8) S. Steinert, W. Voigt, R. Glausch, M. Neuschütz, *Thermochimica Acta*, 2005, 435, 28-33.
- (9) ISO 22007-2:2015, *Plastics-Determination of Thermal Conductivity and Thermal Diffusivity-Part 2: Transient Plane Heat Source (HotDisc) Method* (International Organization for Standardization, Geneva, 2015)



ENERSTOCK 2024
The 16th IEA ES TCP International Conference on Energy Storage
June 5–7, 2024
Lyon, France

(10) R.A.L. Gütesicherung, 2018, Phase Change
Materials RAL-GZ 896. RAL German Institute for

Quality Assurance and Certification: Sankt Augustin,
Germany.



enerstock

ENERSTOCK 2024

The 16th IEA ES TCP International Conference on Energy Storage

June 5–7, 2024

Lyon, France

Recent advance on metal/alloy based micro-encapsulated phase change materials for middle-high temperature applications

Takahiro Nomura*

Faculty of Engineering, Hokkaido University, Kita 13 Nishi 8, Kita-ku, Sapporo 060-8628, Japan

*Corresponding author e-mail: nms-tropy@eng.hokudai.ac.jp

Abstract

Middle-high temperature latent heat storage technology is one of the key technologies for thermal management technologies in a broad sense. Our research group have been developing middle-high temperature latent heat storage technology using metals/alloys as Phase Change Materials (PCMs) which operating temperature are about 200-800°C. Especially, we are developing microencapsulated PCMs (MEPCMs); the core is metals/alloys with about 10-60 μm diameter and the shell is various ceramics with complete chemical and mechanical stability. Moreover, pellet, grains, and honeycombs type PCM composites with matrix of the MEPCM are developed. This article mainly introduces the recent advance of the MEPCM based middle-high temperature latent heat storage technology.

Keywords: Thermal energy storage; Latent heat storage; High temperature heat storage; Microcapsule; Composite

Introduction

Considerable installations of various renewable energies in the power network and establishment of advanced energy saving technologies in industrial processes are strongly needed to achieve carbon neutrality. Middle–high temperature thermal energy storage technology is one of the key thermal management technologies for achieving these future energy systems. Latent heat storage, based on the latent heat of the solid–liquid phase transition of a phase change material (PCM) is a promising thermal energy storage technology based on the high heat storage density and function of converting intermittent energy sources like renewable energy and industrial waste heat to a constant temperature heat source at the phase changing temperature of a PCM.

As middle-high temperature PCMs, metals/alloys are promising candidates from their large latent heat, high thermal conductivity, and relatively small volume expansion/shrinking during solid-liquid phase changing. However, the high corrosivity of liquid metals/alloys is serious technical barrier to utilize them as PCMs and design the heat storage unit.

From the other viewpoints, advanced thermal energy storage materials, such as PCMs and chemical heat storage materials, have different temperature ranges

suitable (or usable) for use depending on their respective materials, due to their principles. On the other hand, there is an urgent need to develop universal technologies with a large ripples effect towards carbon neutrality by 2050. In addition, following the example of heat storage systems installing solid sensible heat storage materials such as hot air furnaces and regenerative burners implemented in industry, the perspective of designing systems that are as simple as possible and to extent flexible for deployment in large or wide-ranging applications is also considered an important factor. Another important factor to be considered in the field of industrial waste heat utilization is how to efficiently recover heat from "dirty high-temperature heat sources", including dust and other substances that are highly exergy but have to be cooled using conventional technology. Here, too, robust properties that can be handled 'roughly' to some extent, such as solid sensible heat storage materials, will be needed.

From these viewpoints our research group is developing core-shell type microencapsulated PCMs (MEPCMs), in which core is composed of metal/alloy microparticles and shell is composed of ceramics with excellent corrosion resistance against the liquid cores. This manuscript mainly introduces the recent advance of the MEPCM based middle-high temperature latent

heat storage technology from viewpoints of both material development and its applications.

Lineup of MEPCMs

Figure 1 shows preparation procedures of MEPCMs. Combinations of a hydrothermal process (Nomura et al., 2017) or a dry process (Jeem et al., 2024) to fabricate precursors and a heat-oxidation process to metals or alloys microparticles as the raw materials are proposed for preparing MEPCMs. Figure. 2 shows the lineup of MEPCM reported in our previous studies. MEPCMs with different operating temperature ranges can be fabricated simply by changing the composition of the core PCMs. So far, MEPCMs have been successfully produced using Ga (T_m , melting point: 29.5°C) (Dong et al., 2022), Sn (T_m : 232°C) (Jeem et al., 2024), Zn-Al (T_m : 420-500°C) (Kawaguchi et al., 2020), Al-Cu-Si (521°C) (Shimizu et al., 2024), Al-Si (T_m : 577°C) (Nomura et al., 2015), Al-Ni (T_m : 640°C) (Shimizu et al., 2022), Al (T_m : 660°C) (Nomura et al., 2019), and Cu-Si (T_m : 780°C) (Aoki et al., 2024) as

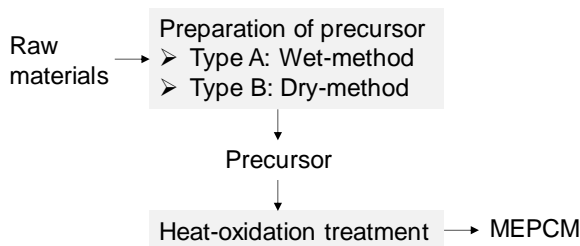


Figure1: Preparation procedures of MEPCMs.

raw materials.

MEPCM composites

A MEPCM has a core-shell structure with a ceramic (mainly metal oxide such as Al_2O_3) shell filled with an alloy PCM core. The diameter of a MEPCM is several tens of micrometres. Therefore, MEPCMs can be handled as ceramic micro-particles and can be applied

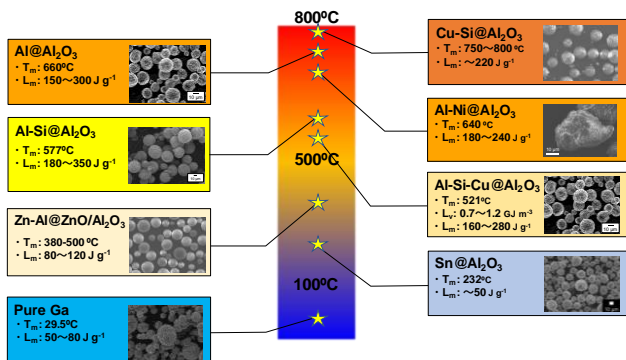


Figure2: Recent advances of MEPCMs with various operating temperatures.

to existing ceramic moulding processes. Using the MEPCM as a raw material, various types of PCM composites have been developed, including pellets, grains, and honeycombs shown in Figure 3. These PCM composites have a heat storage density approximately 2 - 5 times higher than that of conventional solid heat storage materials, such as rock, concrete, and Almina bricks.

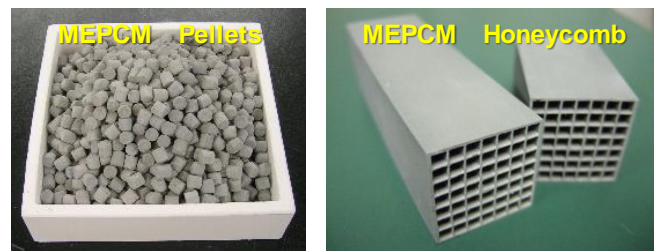


Figure3: MEPCMs composites (Private communication: NIPPON SHOKUBAI CO., LTD.)

Cyclic performance

Cyclic durability of MEPCMs and MEPCM composites is the most important performance to use them in practical applications. We designed an automatic cyclic heating and cooling machine to investigate the durability of MEPCM composites. Figure 4 shows an overview of the apparatus (Kawaguchi et al. 2024) The apparatus comprised six rotatable heater sections and a stage section that could be raised or lowered after the MEPCM composites were set in place. Six heaters were set to alternately blow air above or below melting temperature of the MEPCM composites for a predetermined time. Using this machine, one cycle of melting and solidification can be completed in about 2 minutes. For an Al-Si based MEPCM composite, 10000 cycles cyclic durability was confirmed.

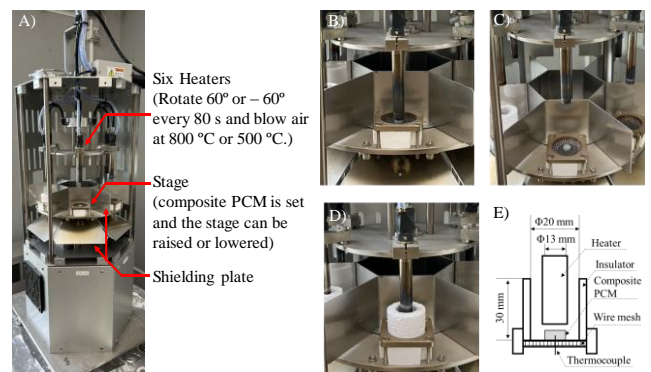
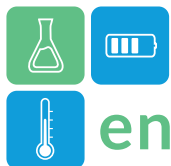


Figure4: Overview of an automatic cyclic heating and cooling machine for MEPCM composites (Kawaguchi et al. 2024).



Summary

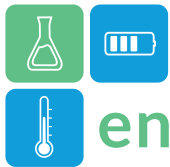
There are great expectations for innovations in heat utilization technology towards the realization of carbon neutrality, with thermal energy storage, heat transport and thermal management as keywords in a wide range of application areas. This paper outlined the recent development of metal/alloy-based MEPCM, which not only has high performance as a thermal energy storage material, but also has the potential to be used as a retrofit material in existing heat utilization systems. MEPCMs are "thermal engineering material" that has the potential to pioneer a new technical basis for heat utilization that crosses various technological domains.

Acknowledgment

This work was supported by the New Energy and Industrial Technology Development Organization (NEDO, Grant number JPNP20005, Grant number JPNP20003), JSPS KAKENHI (Grant Number 22H00306 and 22K18993).

References

- Aoki, M. et al. (2024). High-temperature ternary Cu–Si–Al alloy as a core–shell microencapsulated phase change material: fabrication via dry synthesis method and its thermal stability mechanism. *Material Advances*. DOI: 10.1039/D3MA00788J
- Dong, X. et al. (2022). Optimized Preparation of a Low-Working-Temperature Gallium Metal-Based Microencapsulated Phase Change Material. *ACS Omega*.
<https://doi.org/10.1021/acsomega.2c02801>.
- Jeem, M. et al. (2024). Shell-Driven Localized Oxide Nanoparticles Determine the Thermal Stability of Microencapsulated Phase Change Material. *ACS Applied Material Interfaces*.
<https://doi.org/10.1021/acsaami.3c17129>
- Kawaguchi T. et al. (2020). Microencapsulation of Zn-Al alloy as a new phase change material for middle-high-temperature thermal energy storage applications. *Applied Energy*.
<https://doi.org/10.1016/j.apenergy.2020.115487>
- Kawaguchi T. et al. (2024). Composite phase change material based on Al alloy with durability of over 10,000 cycles for high-temperature heat utilization. *Journal of Energy Storage*.
<https://doi.org/10.1016/j.est.2023.109635>.
- Nomura T. et al. (2015). Al/Al₂O₃ core/shell microencapsulated phase change material for high-temperature applications. *Solar Energy Materials and Solar Cells*.
<https://doi.org/10.1016/j.solmat.2018.12.023>.
- Nomura, T. et al. (2017). Microencapsulated phase change materials with high heat capacity and high cyclic durability for high-temperature thermal energy storage and transportation. *Applied Energy*.
<https://doi.org/10.1016/j.apenergy.2016.11.025>.
- Nomura T. et al. (2019). Microencapsulation of Metal-based Phase Change Material for High-temperature Thermal Energy Storages. *Scientific Reports*. DOI: 10.1038/srep09117.
- Shimizu Y. et al. (2022). Al–Ni alloy-based core-shell type microencapsulated phase change material for high temperature thermal energy utilization. *Solar Energy Materials and Solar Cells*.
<https://doi.org/10.1016/j.solmat.2022.111874>
- Shimizu Y. et al. (2024). Novel microencapsulated ternary eutectic alloy-based phase change material. *Journal of Energy Storage*.
<https://doi.org/10.1016/j.est.2023.109535>



Reduction of the Winter Gap Problem - Energy Efficiency vs. Energy Flexibility

Fabian Ochs^{1,*}, Alice Tosatto², Mara Magni³

1 University of Innsbruck, Technical Engineering, Energy Efficient Building, Technikerstr. 13, 6020 Innsbruck, Austria

*Corresponding author e-mail: fabian.ochs@uibk.ac.at

Abstract

The decarbonization of the building sector is linked to the electrification of buildings, thus increasing the stress on the electric grid. The increasing share of PV and wind utilization for electricity generation introduces a supply-demand mismatch, resulting in the so-called winter gap. Mitigating grid stress involves implementing energy efficiency measures such as deep thermal renovation and efficient heat pump systems. Energy storage on building level, either activating the thermal mass or utilizing space heating buffers or domestic hot water stores, or batteries, allows peak shifting. While shifting loads to periods with low energy price and/or with high share of renewables can have a beneficial micro-economic effect, on the macro-economic scale and from the grid perspective such a positive effect cannot be demonstrated. The simulation-based analyses based on building and building stock models indicate that building-wise energy storage and load shifting do not relevantly reduce the grid peak load (PL) but rather increase the total electricity demand. Hence, grid flexibility does not reduce the required grid and electricity generation capacity. Contrariwise, efficiency measures, significantly reduce the energy demand, the PL and thus the winter gap. These findings highlight the importance of implementing ambitious policies to foster energy efficiency measures in the building sector and understanding the building sector as the important column of the energy policy.

Keywords: Building Stock, Energy Efficiency, Heat Pump, Energy Storage, Load Shifting, Flexibility, Winter Gap

Introduction

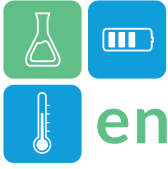
The decarbonization of the building stock is one of the major future challenges (Abbasi et al. 2021). The decarbonization of the district heating and electricity system is challenging and requires the integration of renewables and also the integration of electrical and thermal energy storage, both on energy system and on building level (Kurnitski et al. 2011, Ochs et al. 2022). If connection to district heating is not possible, deep thermal renovation and the replacement of fossil-based heating systems by heat pump (HP) systems for space heating (SH) and or domestic hot water (DHW) preparation are the most promising options for the decarbonization of the building stock (Wemhöner et al. 2019, Ochs et al. 2023b).

With the electrification of buildings (and mobility) and the integration of PV, buildings will represent an important part of the electricity system, representing both a load and a source and the impact on the electric system becomes increasingly relevant. Energy flexibility (of buildings) has been intensively studied within the last decades. The main objective is improving the grid stability, which faces challenges with increasing share of renewables on the one hand and electrification of buildings and mobility on the

other hand. Li et al. (2021) presented a comprehensive review of energy flexibility options in residential buildings.

Through energy storage, energy flexibility in buildings has the potential to provide additional capacity for energy grids, and integrate RE sources in energy systems. The main challenge is providing thermal comfort, reducing thermal losses while ensuring an economic benefit for the building owner/operator and the utility, see (IEA EBC, Annex 67). In times of availability of abundant and cheap renewable electricity buildings can be (slightly) overheated (thermal mass activation) or thermal/electric storage capacities can be charged such that in peak power times or when renewable energies are scarce, the load can be reduced. Several energy storage options are available in buildings. A small DHW store can cover the daily DHW demand and serve as a night/day storage. The set point temperature of the DHW store and of an optional SH buffer can be increased to increase the storage capacity. In addition, the thermal mass of the building can be activated by increasing the set point from e.g. 20 °C or 22.5 °C to maximum 25 °C or 26 °C. Furthermore, batteries can be used to store surplus electricity on a day/night basis (Ochs et al. 2023a).

This contribution compares the effect of efficiency measures



and energy flexibility options in terms of the reduction of the PL of the building stock and the so-called winter gap (see Feist, 2013).

Method

Overview

The methodology of this study is summarized in Fig. 1.

Building Categories	Building Characteristics	Building Model	Building Stock Model	KPIs
<ul style="list-style-type: none"> SFH sMFH IMFH Office Hotel 	<ul style="list-style-type: none"> SH, DHW Appliances thermal mass heat emission HVAC System Cooling PV Storage <ul style="list-style-type: none"> Thermal Electric 	<ul style="list-style-type: none"> average/specific building lumped mass R 2* RC single/multi-zone Floor heating Thermal activation Control (on-off, PI) MPC, external signal 	<ul style="list-style-type: none"> Superposition of Building Load Curves Baseline Efficiency Path Flexibility options 	<ul style="list-style-type: none"> Load Curve Analysis Peak Load Storage Efficiency LCF/SCF SRI

Figure 1: Structure and method

Energy flexibility – external signal-based control

Energy flexibility options are distinguished in “shift” and “shed” (IEA HPT Annex 67). In this context “shift” means that energy consumption is increased before a PL occurs such that during usual PL times the building load can be decreased (i.e. overheating, followed by a period of reduced consumption). “Shed” instead would just cut the peak, which would lead to a reduced indoor temperature during the usual peak period. In buildings “shed” is not an option as violation of the thermal comfort (TC) is assumed to be no acceptable.

Weather (ambient temperature, solar radiation, wind speed) and thus the load and the RE availability can be predicted few days ahead with sufficiently good accuracy. Prior to expected PLs (i.e. low ambient temperature) and/or high energy prices (i.e. low RE availability) an external signal could be used to overheat the buildings. The set point temperature of the indoor temperature and or the buffer storage and the DHW store can be increased: e.g. by $\Delta T_{SP} = 3.5$ K to max. 6 K for the indoor temperature and/or by $\Delta T_{SP} = 10$ K for the buffer and the DHW storage temperature.

$$T_{SP} = T_{SP} + \Delta T_{SP} \cdot (\text{signal} == 1) \quad (1)$$

This will increase the average building and or storage temperature and as a consequence, also the thermal losses and the total energy demand (E_{flex}).

$$E_{flex} = E_{ref} + E_{loss} \quad (2)$$

The thermal losses depend on the type of storage and the storage duration. In case of activation of the thermal mass of the building the thermal losses depend on the time constant τ i.e. the envelope quality (EQ) and the thermal mass (TM).

$$\tau = \frac{(m \cdot c)_{eff}}{\sum UA + \rho \cdot c \cdot V \cdot n_{eff}} \quad (3)$$

Thus, flexibility options will increase the energy demand, but the additional energy demand and some of the reference energy demand ($E_{ref} \cdot a$) might be provided at lower cost or with higher share of RE and thus with lower CO₂ emissions.

$$\Delta_{C/CO_2} = f_{C/CO_2} \cdot E_{ref} - (1 - a) \cdot f_{C/CO_2} \cdot E_{ref} - a \cdot f_{C/CO_2}^* \cdot E_{ref} - f_{C/CO_2}^* \cdot E_{loss} \quad (4)$$

The energy cost or CO₂ savings Δ_{C/CO_2} depend on the difference of the cost or CO₂ factor at PL f and non-peak times f^* on the losses and on the share of energy shift a which is a function of the storage duration, which is the time between the point of time when the heating is switched on again after the external signal driven heating and the point of time when the external signal is set back ($\text{signal} == 0$).

$$\Delta \tau = t(\text{heat on}) - t(\text{signal} == 0) \quad (5)$$

The resulting storage capacity is the difference in energy

$$Q_{out} = Q_{ref}(t(\text{heat on})) - Q_{ref}(t(\text{signal} == 0)) \quad (6)$$

The thermal storage efficiency is the ratio of heat output and input and the electric storage efficiency the ratio of electric output and input. The electric efficiency depends on the thermal efficiency and on the HP performance (COP).

$$\eta_{th} = Q_{out}/Q_{in} \quad (7)$$

$$\eta_{el} = W_{out}/W_{in} \quad (8)$$

The load cover factor (LCF) and supply cover factor (SCF) indicate the grid load reduction (with the remaining load mainly occurring in winter time) and the PV self-consumption (with the remaining excess power mainly occurring in summer time):

$$LCF = W_{PV,own}/W_{load,tot} \quad (9)$$

$$SCF = W_{PV,own}/W_{PV,tot} \quad (10)$$

Building Categories and Building Characteristics

Table 1 summarizes the building categories and the building characteristics are listed in Table 2.

Table 1: Building categories with No. of storeys, treated area (A_T) and available area for onsite PV (A_{PV})

SFH	sMFH	IMFH	office	Hotel
2	3	10	8	3
144	543	1659	1100	672
54	109	166	103	168

Table 2: building characteristics

Age	Renovation level	HVAC System	RE and Storage
Pre 1919	Existing	Heat Pump (HP)	PV
1920-1944	Partly renovated	Direct Electric (DE)	Thermal storage
1945-1960	Fully renovated	Deep renovated	Battery
1061-1980	Deep renovated	Biomass	
1981-1990	New	(Bio)	
1991-2000		District Heating (DH)	
2001-2010			
Post 2011			

Building and Building Stock Model

The dynamic building model is implemented in Matlab and the resulting system of differential equations is solved using Matlab ODE solvers on sub-hourly time step. The heat load is interpolated to hourly values. Two types of models are implemented (Magni et al. 2022, Ochs et al. 2023a): a simplified 1 zone lumped capacity models (R) and a 1 zone 2* models (R-C). The building model parameters are read from PHPP, which has been developed for each building category, each building age and for each energy standard. DHW demand is based on EN 16147 tapping profiles (profile M) and the profile for appliances is based on APCS.

The building stock model is derived by superposition of load curves of individual buildings with different shares of building categories, characteristics (thermal envelope, heating system, PV, storage) as well as with and without external control signal. Table 3 summarizes the share of buildings for the building stock model for scenario BAU and BEST (Tosatto et al. 2023).

Table 3: Share of building categories and heating system in % (m²/m²) - Scenario BAU

SFH	sMFH	IMFH	office	Hotel
HP + DE				
25.9	7.8	8.3	9.9	2.1
Bio + DH				
18.3	5.8	9.8	10.1	2.1

- Scenario BEST

SFH	sMFH	IMFH	office	Hotel
HP + DE				
27.2	8.3	8.8	10.0	2.2
Bio + DH				
17.0	5.3	9.2	9.9	2.1

Results

The resulting load curves of the average building - (a) time series and (b) sorted total electricity demand - are shown in Fig.2 for the scenario BAU and BEST. A significant peak power reduction, 2643 W instead of 4441 W (i.e. ca. 40 %) is achieved from BAU to BEST.

Integration of PV (and batteries) leads to a further reduction of the grid load; however, a relevant reduction can be seen only in terms of energy (52 % in case of BAU and 65 % in case of BEST), but not in terms of peak load (3% in case of BAU and 9 % in case of BEST). Figure 3 shows exemplarily an energy flux diagram (Sankey) for a sMFH with PV, BIPV and battery. In spite of a relevant reduction of the electric energy required from the grid, the integration of PV and battery has only a minor effect on the PL and no relevant effect on the grid demand in winter (i.e. the winter gap).

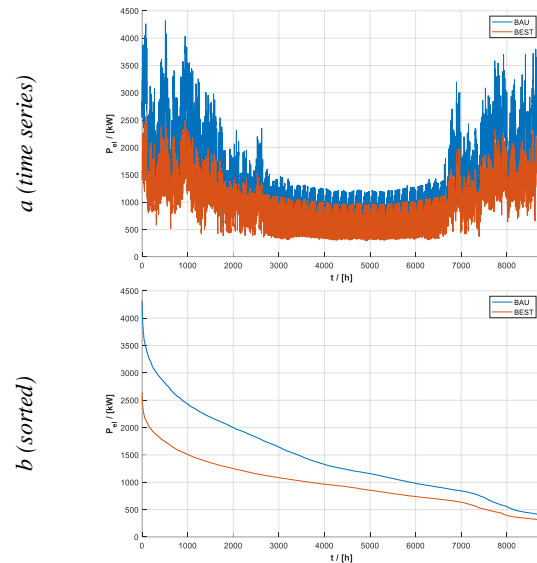


Figure 2: Load Curves (total electricity demand) for the average building for the scenarios BAU and BEST, a: time series, b: sorted

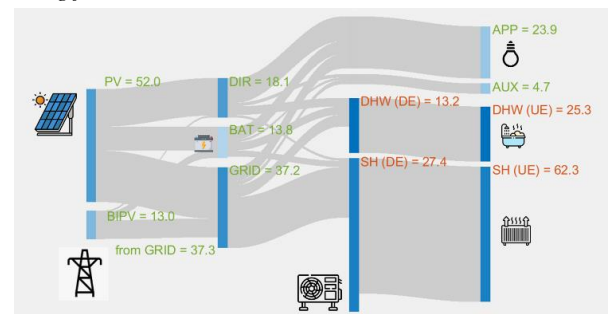


Figure 3: Sankey diagram (based on Ranran 2022) of the BAU sMFH (62 kWh/(m² a)), with A/W-HP; PV (22 kW_p), BIPV (8 kW_p) and Battery (26.7 kWh)

Figure 3 compares the electric load curve with different efficiency and RE measures: envelope/MVHR (PH w/ and PH w/o MVHR, BAU, BEST), heat generation (DE, A-HP, GW-HP) and PV, BIPV, battery using the IMFH as example. Table 4 compares accordingly, the achieved load reduction of a selection of different efficiency and RE measures. Additionally, the corresponding theoretical load reduction through flexibility (i.e. load shifting) is shown.

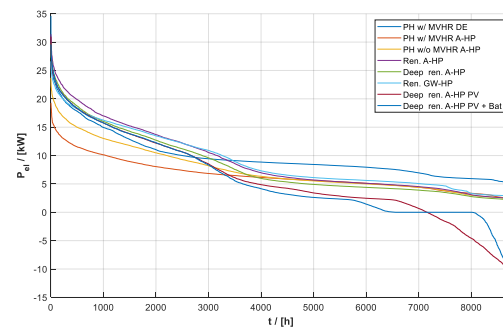


Figure 3: Electric load curves for the case IMFH New (i.e. PH w/ and w/o MVHR), as well as renovated (BAU) and deep renovated (BEST) with different efficiency and RE measures

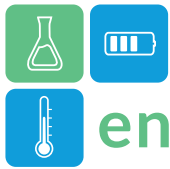


Table 4 summarizes the grid load reduction depending on the building envelope quality, the type of heating system using the SFH as an example.

Table 4: Relative grid peak load reduction with respect to the reference (renovated BAU, DE) in % using the SFH as an example with different efficiency and RE measures

	DE	A-HP+DE	A-HP	GW-HP
Efficiency				
PH	43	63	66	71
PH w/o MVHR	35	58	61	66
Deep ren. BEST	8	46	49	57
Renovated BAU	0	41	44	51
PV				
PH	54	65	66	71
PH w/o MVHR	35	58	59	65
Deep ren. BEST	12	46	48	56
Renovated BAU	-1	40	45	49
PV + Battery				
PH	53	65	66	69
PH w/o MVHR	39	57	61	65
Deep ren. BEST	9	45	49	58
Renovated BAU	-1	40	43	52

Conclusions

The decarbonization of the building sector is strongly connected to the electrification of buildings and district heating. Thus, the stress on the electric grid will increase. The effect of energy efficiency and energy flexibility on the electric grid is analyzed and compared using building and building stock models. From the micro-economic perspective load shifting can have some positive impact (i.e. a reduction of the purchased electricity), however, from the grid point of view (i.e. macro-economic perspective) building-wise energy storage (both external signal-based overheating of thermal building mass or other thermal storage capacities and batteries) is less relevant. The peak of the electric load curve cannot be significantly reduced compared to the influence of efficiency measures. A load shift from night to day is possible and allows better integration of volatile renewables, but the need to provide the peak grid capacity and the provision of peak power plants and/or central storage is hardly reduced. Instead, efficiency measures such as deep thermal renovation, MVHR or heat pumps do relevantly reduce the PL and also the winter gap and thus have also relevant influence on the grid peak capacity. Efficiency measures lead to a significant reduction of the load thus also to energy cost reduction and reduction of CO₂ emissions. In buildings with high energy demand the winter gap is significantly longer and higher than in very efficient buildings with efficient and well-dimensioned equipment.

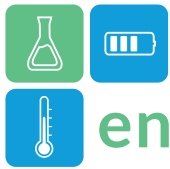
Acknowledgment

This research was possible through funding of the Austrian FFG project PhaseOut and ACRP INTEGRATE as well as

IEA HPT Annex 61 and IEA EBC Annex 83.

References

- M.H. Abbasi, Abdullah B., M.W. Ahmad, A. Rostami, J. Cullen (2021). Heat transition in the European building sector: Overview of the heat decarbonisation practices through heat pump technology. Sustainable Energy Technologies and Assessments.
- W. Feist, Energy concepts – Passive House in comparison, 2013 Conference Proceedings 17
- J. Kurnitski, A. Saari, T. Kalamees, M. Vuolle, J. Niemelä, T. Tark, T. (2011). Cost optimal and nearly zero (nZEB) energy performance calculations for residential buildings with REHVA definition for nZEB national implementation. Energy and Buildings, 43(11).
- H. Li, Z. Zhe, T. Hong, M. A. Piette, Energy flexibility of residential buildings: A systematic review of characterization and quantification methods and applications, Advances in Applied Energy, 2021.
- M. Magni, F. Ochs, W. Streicher, Comprehensive analysis of the influence of different building modelling approaches on the results and computational time using a cross-compared model as a reference, Energy and Buildings, Volume 259, 15 March 2022, 111859.
- F. Ochs, M. Magni, G. Dermentzis (2022) Integration of heat pumps in buildings and district heating systems - Evaluation on a building and energy system level, Energies 15 (11), 3889
- F. Ochs, A. Tosatto, M. Magni, E. Venturi, G. Dermentzis, (2023) Heat Pumps, Photovoltaics and Energy Storage in Buildings - Load Characteristics and Flexibility Options on District Level; EuroSun 2022, Kassel
- F. Ochs, N. Franzoi, G. Dermentzis, W. Monteleone, M. Magni, (2023), Monitoring and simulation-based optimization of two multi-apartment NZEBs with heat pump, solar thermal and PV, Journal of Building Performance Simulation, 1-26
- A. Tosatto, F. Ochs, W. Streicher, M. Magni, E. Venturi, Methodology for the calculation of energy scenarios to achieve carbon neutrality in the building stock, IBPSA 2023, Shanghai
- APCS <https://www.apcs.at/de/clearing/technisches-clearing/lastprofile> (visited 2023)
- EN 16147 Heat pumps with electrically driven compressors - Testing, performance rating and requirements for marking of domestic hot water units
- EU-SRI: https://energy.ec.europa.eu/topics/energy-efficiency/energy-efficient-buildings/smart-readiness-indicator_en (visited 2023)
- IEA EBC Annex 67, Energy Flexible Buildings; <http://www.annex66.org/> (visited 2023).
- Ranran Wang (2022). Sankey Diagram (<https://www.mathworks.com/matlabcentral/fileexchange/75813-sankey-diagram>), MATLAB Central File Exchange. Retrieved October, 2022.



Renewal planning method of air-conditioning heat source system with diurnal water thermal storage for demand response in an existing building

Mio Imaida^{1,*}, Hideharu Komoda², Hideki Tanaka¹
 1 Nagoya University, Furo-cho, Chikusa-ku, Nagoya City, Japan
 2 Kajima Corporation, 6-5-30 Akasaka, Minato-ku, Tokyo, Japan
 *Corresponding author e-mail: yz.54j.4835@s.thers.ac.jp

Abstract

This paper examines a planning method for the renewal of air conditioning heat source systems that takes demand response into account, based on the use of building operation data, and calculates the provided electric power based on the simulation results of DR operation using diurnal water thermal energy storage. Furthermore, with the aim of increasing the provided electric power and the success rate of DR, the introduction of storage batteries was examined, and findings leading to a proposal for a capacity selection method are reported.

Keywords: Demand Response, Water Thermal Storage, Capacity planning

1. Introduction

In order to cope with the construction of a decarbonized society, there is an increasing reliance on natural variable power sources such as solar power generation. Therefore, building facilities are also expected to play a role in adjusting electricity supply and demand. In addition, buildings must be able to significantly reduce their energy consumption when the vast stock of building stock is upgraded.

In this study, a case study was conducted on a renewal plan for air-conditioning heat source system with diurnal water thermal energy storage (TES) that takes demand response (DR) into consideration, assuming a response to the future demands of the electricity supply and demand adjustment market.

2. Planning flow for the renewal project

Fig.1 shows the planning procedure for the renewal of the air conditioning heat source system in an existing building, taking DR into consideration. Since the subject is an existing building, data confirmation and analysis are conducted based on the actual building operation data. The maximum design load is calculated from the past record data, and the capacity of heat source equipment is determined. A diurnal water TES is assumed as a DR-capable system configuration.

3. Target building and heat source load

An actual office building that owns a water thermal heat storage tank was used as the target building. An outline of the building is shown in Table 1. The actual cooling and heating load of the subject building was

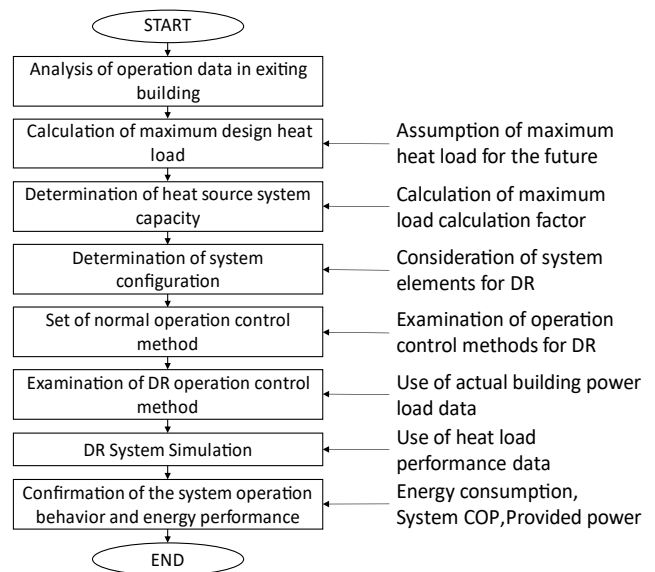


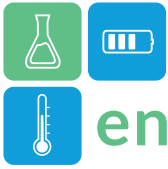
Fig.1 System planning procedure

Table 1 Outline of subject building

Location	Minato-ku, Tokyo (Completed in 2012)
Building scale	30 floors above ground, 3 floors below ground
Total floor area	53,337 m ² (Office : 47,982 m ² , Residence: 5,794 m ²)
Main uses	Offices, apartments, and retail stores

Table 2 Target Systems

Equipment name	Capacity
Centrifugal chillers with INV control	809 kW×3
Air-cooled heat pump	750 kW×3
Water storage tanks	726 kW (231 m ³ ×3)
Chilled water system Heat exchanger for heat storage and radiation	726 kW×2
Heating water system Heat exchanger for heat storage and dissipation	360 kW×2



confirmed based on the actual operation data for the last 7 years (2015-2021). Heat source equipment capacity was calculated based on actual operation data for 2020. The capacity of the heat source equipment per unit gross building floor area was assumed to be 60.3 W/m² for the chilled water system and 60.1 W/m² for the hot water system.

4. System configuration and operation method

The assumed diurnal water TES is shown in Table 2 and the system diagram in Fig.2. The water storage tank is operated for 10 hours from 22:00 to 8:00 for heat storage and for 8 hours from 9:00 to 17:00 for heat release. The system has three water storage tanks. In summer, the three tanks are used for cooling; in winter, two water storage tanks are used for heating and one tank is used for cooling.

During the daytime in summer, the cooling load is met by the heat release from the heat storage tank and the turbo chiller, and the nighttime chilled water load and summer hot water load are met by the air-cooled heat pump. During the daytime in winter, the heating load is met by the heat release from the heat storage tanks and air-cooled heat pumps, and the air-cooled heat pumps are operated during the nighttime.

The chilled water load in winter will be met in the same way as in summer daytime. When multiple heat source units are operated in both summer and winter, parallel pert road operation is used.

5. DR operation analysis overview

In the assumed DR operation menu, the amount of power reduction due to DR operation is predicted on the previous day, and the electric power value that can be provided during the DR operation time (provided power) on the following day is declared to the aggregator. On the day of the DR operation, the aggregator gives 45 minutes' notice before the DR operation starts, and then the DR operation continues for 3 hours. During the DR operation period, the results are evaluated every 30 minutes (every hour in this study), and the DR success is determined if the power received is within ±10% of the target power.

The power provided by DR operation is calculated as the reduction in power consumption during DR hours relative to the normal operation of the heat source system. The amount of heat that can be released from the water TES during the DR operation period is assumed to be twice that of normal operation. DR time periods are assumed to be 1) Peak power hours and 2) Evening hours, when electricity demand increases sharply and solar power generation decreases.

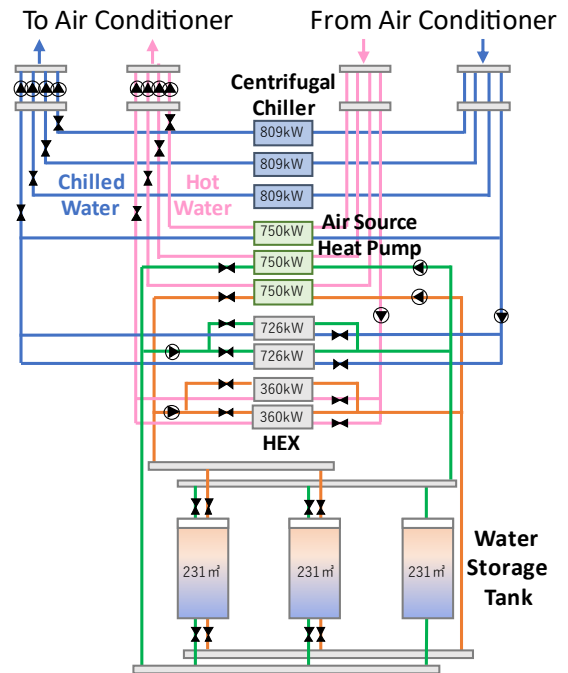


Fig.2 System Diagram

Table 3 DR operation heat release schedule

	Summer Period	Winter Period
Peak hours	9:00-13:00(heat release) 13:00-16:00 (DR heat release) 16:00-17:00(heat release)	9:00-12:00 (DR heat release) 12:00-17:00(heat release)
Evening pattern 1	12:00-17:00(heat release) 17:00-20:00 (DR heat release)	11:00-16:00(heat release) 16:00-19:00 (DR heat release)
Evening pattern 2	9:00-14:00(heat release) 14:00-17:00(stoppage) 17:00-20:00 (DR heat release)	9:00-14:00(heat release) 14:00-16:00(stoppage) 16:00-19:00 (DR heat release)

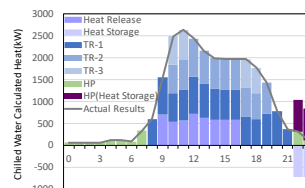


Fig.3 Normal operation
Summer peak day Chilled water
production heat output

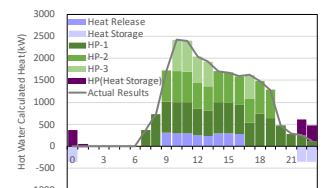
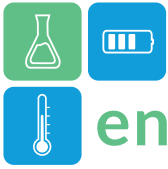


Fig.4 Normal operation
Winter peak day Hot water
production heat output

Peak hours are assumed to be 13:00-16:00 in summer and 9:00-12:00 in winter. Evening hours are assumed to be 17:00-21:00 in summer and 16:00-20:00 in winter. Since the capacity of the water TES is provided based on the assumption of 8-hour heat radiation, if DR operation is conducted during the Evening hours, the remaining amount of thermal heat in the tank will run out before the DR hours due to normal heat radiation during the daytime. Therefore, in order to obtain the



storage heat amount during the DR time period, the heat release time period is adjusted in the following two ways.

Pattern 1: Delay the entire heat release time

Pattern 2: Stop heat release before the DR time period

The heat release schedule for each operation pattern is shown in Table 3. DR operation was considered only on representative days for summer and winter peak days, mid-summer and severe winter periods, and low heat load days. Based on actual operating data, the summer peak day was selected as 8/17, the winter peak day as 1/6, the mid-summer day as 8/28, the severe winter day as 1/22, the summer low load day as 10/1, and the winter low load day as 3/18.

6. Evaluation of DR performance

6.1. Calculation method of provided power

A simulation model for the target system was constructed using the LCEM tool, a simulation program for air-conditioning systems developed by MILT (2014). Measured outdoor air conditions, actual heat source load, and secondary water consumption were used as boundary conditions.

In order to obtain the provided power, the power consumption other than air-conditioning was separated from the actual power consumption data of the building at each time of the day. To this data, the power consumption of the new air conditioning heat source system obtained from the simulation results is added, and this is the new power consumption of the building for ordinary daily use (normal operation) after the facility is upgraded. This building power consumption is compared with the power consumption during DR operation, and the power provided is calculated as the amount of power reduction during the DR time period.

6.2. System operating behaviour

The heat value of chilled water production on summer peak days during normal operation is shown in Fig.3, and the heat value of hot water production on winter peak days is shown in Fig.4. Fig.5(a) through 10(a) show the heat produced on summer and winter peak days when DR operation is performed for each operation pattern, with the amount of heat released doubling during the DR time period. The building power consumption on summer and winter peak days during DR operation is shown in Fig.5(b) to 10(b). By increasing the heat release during DR hours, the number of electric heat sources in operation can be reduced or the power output can be curtailed to generate the power provided. Evening pattern 1 stops

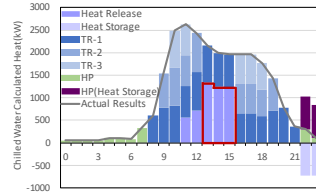


Fig.5(a) Peak hours
 Summer peak day Chilled water production heat output

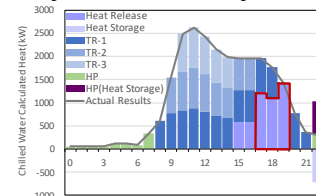


Fig.6(a) Evening pattern 1
 Summer peak day Chilled water production heat output

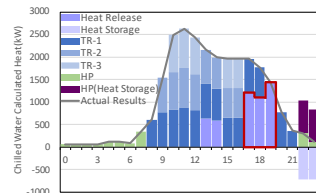


Fig.7(a) Evening pattern 2
 Summer peak day Chilled water production heat output

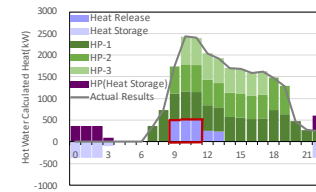


Fig.8(a) Peak hours
 Winter peak day Hot water production heat output

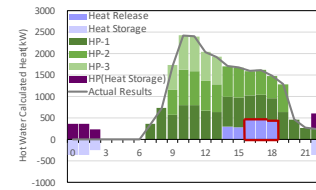


Fig.9(a) Evening pattern 1
 Winter peak day Hot water production heat output

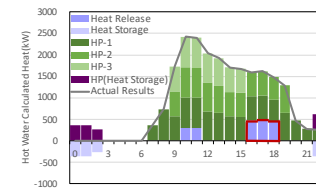


Fig.10(a) Evening pattern 2
 Winter peak day Hot water production heat output

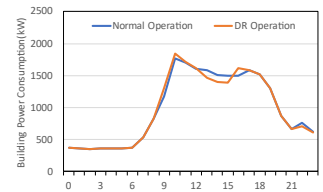


Fig.65b) Peak hours
 Summer peak day Building power consumption

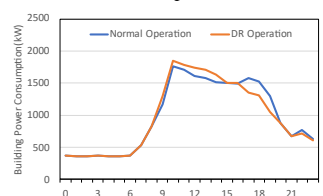


Fig.6(b) Evening pattern 1
 Summer peak day Building power consumption

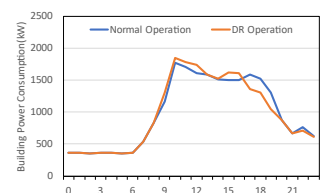


Fig.7(b) Evening pattern 2
 Summer peak day Building power consumption

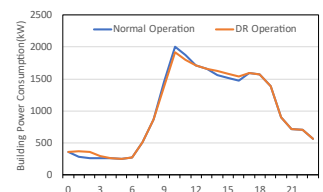


Fig.8(b) Peak hours
 Winter peak day Building power consumption

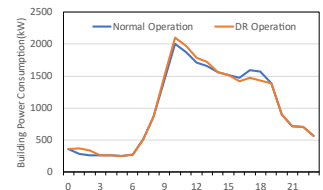


Fig.9(b) Evening pattern 1
 Winter peak day Building power consumption

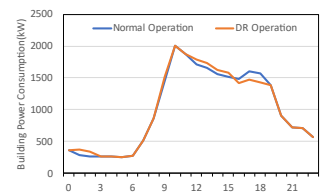
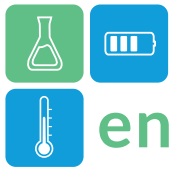


Fig.10(b) Evening pattern 2
 Winter peak day Building power consumption



heat release in the morning, and Evening pattern 2 stops heat release just before DR operation, so power consumption during that time period is higher than in normal operation.

6.3. Provided power

The daily (in 3 hours) provided power during DR operation delivered was evaluated according to its quantities and low variability. Variation was defined as the difference between the maximum and minimum hourly provided power (hourly average power) for three hours on a representative day. Fig.11(a) shows the provided power for a representative day during peak hours, evening pattern 1, and evening pattern 2. Fig.11(b) shows the provided power and the frequency of occurrence of the variation when DR operation was conducted every day for the entire year. Note that days with no provided power throughout the day are excluded from the annual provided power and the frequency distribution of variations in the figure.

Fig.11(a) shows that there was no significant difference in the provided power on representative days for Evening pattern 1 and pattern 2. The provided power ranged from 40kW to 110kW during the peak hours in winter and from 30 kW to 160 kW in the evening.

In summer, the peak hours ranged from 0kW to 130kW, and in the Evening from 40kW to 260kW. Fig.11(b) shows that the annual provided power was in the 90kW range for both Peak hours and Evenings. However, Peak hours are below 150kW, and evenings appear in the 260kW range. The annual variation was in the 10kW range during Peak hours and in the 70kW range in the Evening. It was confirmed that both provided power and variability were large in the Evening.

6.4. Storage battery utilization and capacity

The provided power offerings to be declared to the aggregator on the previous day would be the minimum of the three-hour power offerings predicted on the previous day, given that the power available for supply specified by the aggregator in the next day's DR operation (DR success) would be met.

In order to absorb such minor fluctuations in the provided power and increase the success rate of DR, the introduction of storage batteries should be considered. From Fig.11(b), for example, if 90% of the variation occurring on each day of the year were to be met, a storage battery which has a capacity of 90 kW output would need to be installed during Peak hours, 80 kW during Evening pattern1 and pattern 2 as an assist of in DR operation.

7. Conclusion

A DR operation with diurnal water TES simulation was conducted using actual heat load and weather condition data as boundary condition, and a renewal planning method for the air conditioning heat source system that takes DR into consideration was examined. The simulation results showed that the provided power during DR hours varied. Therefore, the introduction of storage batteries was considered in order to stabilize the provided power and increase the success rate of DR. Furthermore, we presented findings that lead to the proposal of a method for selecting the capacity of storage batteries.

Control methods of real-time DR operation for heat source systems with TES including battery and optimization of system design methods are future study.

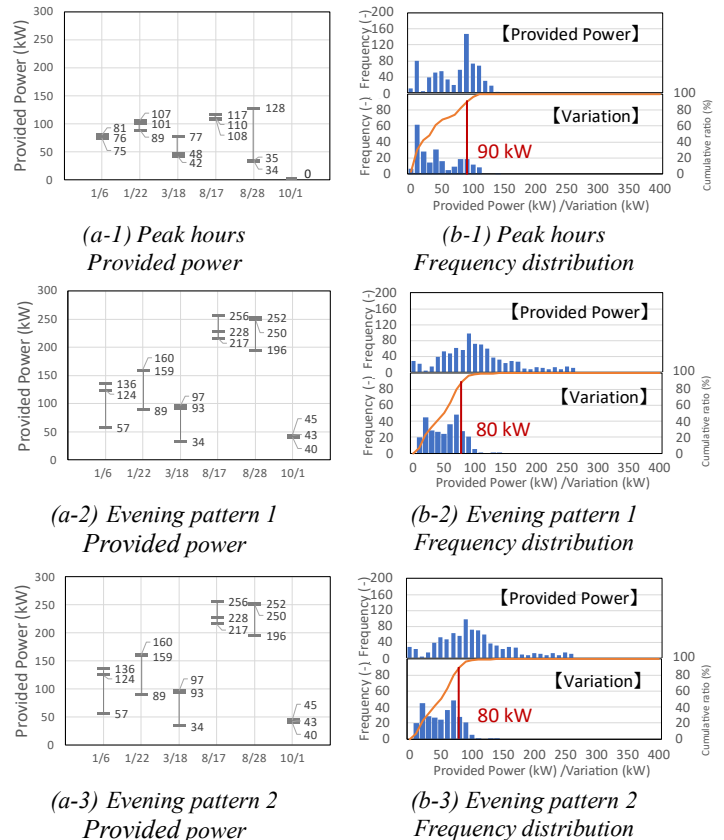
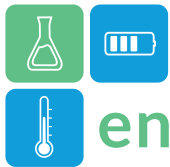


Fig.11 Provided power for a representative day
 Frequency distribution of provided power and variation

References

MILT: Ministry of Land, Infrastructure, Transport and Tourism, Japan (2014), LCEM Tool; Energy simulation tool of Air-conditioning system for Life Cycle Energy Management
https://www.mlit.go.jp/gobuild/sesaku_lcem_lcemtool_index.htm



Rheological study on xylitol crystallization by seeding and shearing for its use as PCM: Influence of shear rate, temperature and seed size

Miguel Navarro^{1,*}, Marta Martí¹, Mónica Delgado^{1,2}, Ana Lázaro¹,

¹Aragón Institute for Engineering Research (I3A), Thermal Engineering and Energy Systems Group, University of Zaragoza, Agustín de Betancourt Building, C/María de Luna 3, 50018, Zaragoza, Spain

²Centro Universitario de La Defensa, Academia General Militar, Ctra Huesca S/N, 50090, Zaragoza, Spain

*Corresponding author e-mail: miguel.navarro@unizar.es

Abstract

Energy storage is a key component of the energy systems that includes renewable sources as their energy source. Xylitol is a sugar alcohol with very high potential to work as energy storage material by storing energy as latent heat; as xylitol has high phase change enthalpy and density. However, xylitol suffers from undercooling and low crystallization rate, which hinder its capabilities. Studies on triggering xylitol crystallization have been conducted, and the seeding and shearing technique is an appropriate technique to promote and accelerate crystallization. This work will study crystallization in a stress-controlled rheometer and will analyse the influence of shear, temperature, and gap on nucleation rate, and will show how lower gaps and temperatures lead to higher nucleation rates, while the dependence of shear on nucleation rate is not clear.

Keywords: Xylitol, Crystallization, Rheometer, Phase Change Material, Thermal Energy Storage

1. Introduction

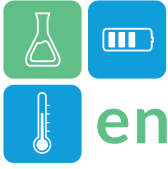
In the search for the decarbonization of society, energy storage plays a key role, as renewable energy sources are intermittent in nature, which produces a de-synchronization between the generation of energy and demand. Energy storage can help solve this problem, as it can be used as load shifting by storing excess energy. There are several ways to store energy, but this work focuses on latent heat thermal energy storage, by using xylitol, a sugar alcohol (SA), as a phase change material, using the solid-to-liquid phase change.

Xylitol, as well as other SA, are promising materials for energy storage in several applications, like solar or waste heat applications; as xylitol has a high energy density (100kWh/m³) and a melting temperature of 92°C [2]. However, xylitol has two main drawbacks, which are common among many SAs, which are undercooling and low crystallization rates. Xylitol has a stable undercooling, which means that crystallization does not start unless some external action triggers it; and the low crystallization rate of xylitol makes the thermal power very low. To overcome these drawbacks, some techniques have

been researched, like bubbling, stirring or adding additives [3], [4], [5]. In this work, the combined technique of seeding and shearing is used for crystallization triggering and acceleration [1].

Crystallization is a process made of two different sub-processes: nucleation and crystal growth. Nucleation, which refers to the formation of crystals in the liquid, is divided too in two different nucleation processes, primary nucleation (spontaneous formation) and secondary nucleation (formation from pre-existing crystals). Also, crystallization is a stochastic process, which means that the same initial conditions of the system can result in two different crystallization times. However, as a first approach, this work aims to study nucleation by classical nucleation theory, as it can give insights into how each initial condition (temperature, shear rate...) can affect crystallization.

For the analysis of the influence of different conditions on the induction time of the crystallization, a stress-controlled rheometer is used in combination with the shearing and seeding technique. Although crystallization is a system-specific process, meaning that the quantitative results would be different, this analysis could give insights into the critical variables



influencing xylitol crystallization, and highlight which variable should be taken into account when scaling the system.

2. Materials and Methods

2.1 Xylitol

Xylitol is a 5-carbon sugar alcohol, with a chemical formula of $C_5H_{12}O_5$ and a CAS Number of 87-99-0. Xylitol is used currently as the food additive E967, but is a very promising PCM. Xylitol used in this study was purchased from Alpha Aesar with a purity of 99%. The seeds used were obtained by using a mortar and pestle to break xylitol crystals from the bulk and sieve them.

2.2 Stress-controlled rheometer and testing conditions.

The tests are conducted in a stress-controlled rheometer (AR-G2 model from TA Instruments), coupled with a Peltier plate for the temperature control of the sample, and a parallel plate of 40mm as the geometry. This geometry allows for a simple loading of the sample and it allows the use of the seeding and shearing technique.

The sample is loaded in the rheometer in different steps. First, half of the xylitol sample is molten with the Peltier plate, and the geometry is lowered until it touches the xylitol. By doing this, the geometry is heated and the probability of crystallization by contact with a cold surface is reduced. After the temperature of molten xylitol has reached the test temperature, the geometry is raised, and the seed and the other half of the sample, pre-melted in an oven, are added. The geometry is lowered again and the experiment starts.

The shear rates selected in this work are 1, 10 and 100 s^{-1} , the gap (which is the distance between the geometry and the Peltier plate) is 1000 and 600 μm , and the temperatures selected are 70, 75, 80, 85 and 90°C. Seed size is 300 μm , and the seeds are obtained as described in section 2.1.

2.3 Induction time definition

Crystallization is not an instantaneous process, and there is a delay between the start of the activation system and the changes in the properties of the sample due to crystallization. As such, induction time is the variable that characterizes this delay between the start of the activation system, and the start of crystallization.

The identification of the starting of crystallization by observing a change in one measured magnitude can be affected by the procedure itself among the properties

of the sample. This means that different measurement procedures and different sensors can lead to different induction times measurements, even if the same system is analysed. In this work, as the system used for the nucleation study is a rheometer, the induction time is calculated from the viscosity curve. As crystallization is a process where the sample turns solid from the liquid state, viscosity is related to crystallization as higher solid fractions mean higher viscosity.

In this work, induction time is calculated as the intersection between the baseline and the tangent at the inflexion point of the viscosity-time curve.

2.4 Nucleation Rate Modelling

The experimental nucleation rate calculated in this work ($J[1/s \cdot m^3]$) uses the Kashchiev formula [6], which uses induction time of crystallization (t_{ind} [s]), crystal growth (G [m/s]) and the minimum solid fraction detected α_{crit} , as depicted in Eq. 1.

$$J = \frac{\alpha_{crit}}{\frac{\pi}{3} \cdot G^3 \cdot t_{ind}^4} \#(1)$$

For the calculation of the solid fraction, as the system measures viscosity, the Krieger-Dougherty [7] formula can be used, as the solid fraction is thought to be small at the induction time. The Krieger-Dougherty formula is:

$$\mu_{susp} = \mu_m \cdot \left(1 - \frac{\varphi}{\varphi_{max}}\right)^{-[\mu] \cdot \varphi_{max}} \#(2)$$

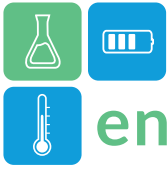
Where μ_{susp} is the viscosity of the suspension, μ_m is the viscosity of the liquid, φ is the solid volume fraction, φ_{max} is the maximum packing fraction and $[\mu]$ is the intrinsic viscosity. φ corresponds with α_{crit} in Eq. 1.

For the nucleation modelling of xylitol crystallization, the model proposed by Piquard[4], derived from the equation Mullin[8] and Mersmann[9] developed for undercooled and supersaturated solutions. This crystallization model is shown in Eq. 2.

$$J = \frac{A}{\eta(T)} \cdot e^{\left[\frac{-B}{T \cdot (T_m - T)^2}\right]} \#(3)$$

Where J is the nucleation rate, η is the viscosity, which is a function of temperature, T_m is the phase change temperature and T is the temperature of the sample. A and B are experimental constants, which are calculated from the experimental test.

The calculation of A and B parameters results from a linear fitting of Eq. 3. Creating a new variable X (equation 4), and taking natural logarithms, the rearranged equation is:



$$X = T_m \cdot (T_m - T_{sub})^2 \quad (4)$$

$$X \cdot \ln(J \cdot \eta(T_{sub})) = X \cdot \ln(A) - B \quad (5)$$

Eq. 5 has the form of a linear function, where the independent variable is X, and dependent variable is $X \cdot \ln(J \cdot \eta)$, the slope is $\ln(A)$ and the intercept is B. Parameters A and B can be calculated from the fitting of the equation to a straight line.

3. Results

3.1 Induction times

Induction times are represented in Figure 1. The results are divided by shear rate (1, 10 and 100s⁻¹) and gap (Gap 1=600 μm or Gap 2=1000 μm).

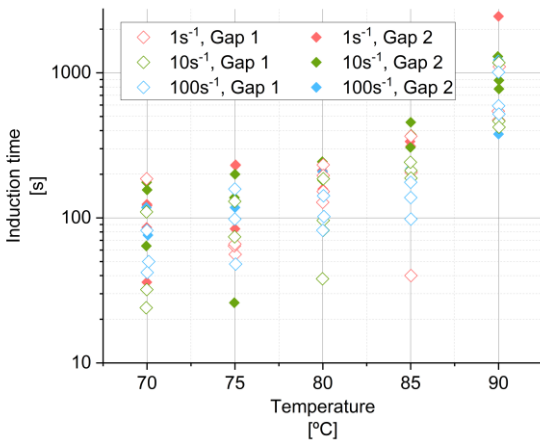


Figure 1. Induction time vs temperature of all the tests conducted

Figure 1 shows the test conducted at 90°C has the highest induction times, and the trend of the data is that lowering the sample temperatures leads to a decrease in induction time. It is also seen that the relationship between temperature and crystallization is not linear. The data points show a big variance at each temperature which can mean that the influence of shear rate is not clear.

3.2 Nucleation modelling

The nucleation model used to obtain the results was discussed in subsection 2.4. Figures 2 and 3 show the effect of the gap and the effect of shear on the experimental and modelled nucleation. The combination of both effects can be shown in Figure 4.

In all three figures, the nucleation model shows that crystallization is slower near the phase change temperature of xylitol (92°C), and a maximum crystallization time between 70 and 75°C. Figure 2 shows that shorter gaps lead to an increase in the

crystallization rate, and Figure 3 shows that higher shear rates lead to faster induction of crystallization at low undercoolings. Even though an ANOVA test has not been conducted yet, the influence of shear rate on crystallization does not seem significant.

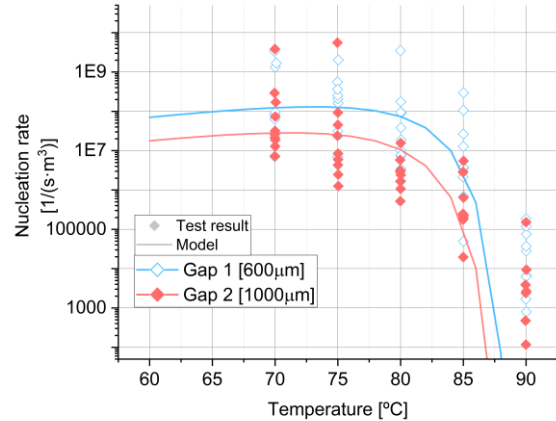


Figure 2. Nucleation rate for two different gaps

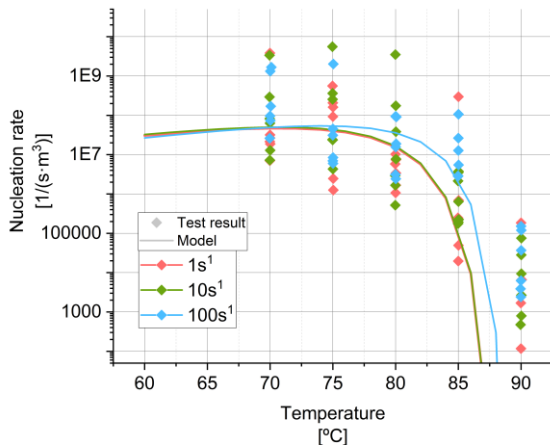


Figure 3. Nucleation rate for three different shear rates.

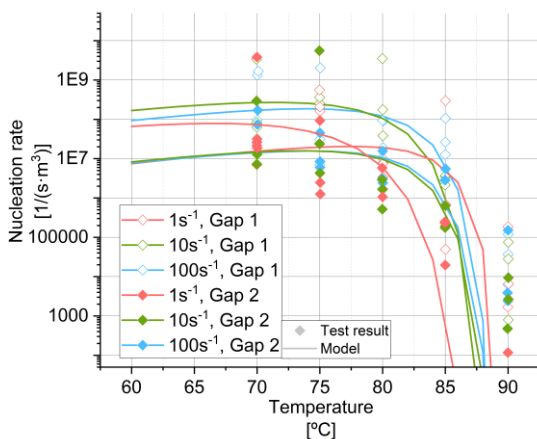


Figure 4. Nucleation rates for the different experimental parameters

4. Conclusion

As shown in both induction time and nucleation modelling, temperature is an important factor in crystallization. Crystallization at small supercooling is very low, as can be seen in Figure 1, with a minimum induction time of 377 seconds and a maximum of 2500 seconds. There is a trend shown in all the figures, in which lower temperatures than 90°C lead to lower induction rates. However, while the nucleation model shows a maximum in nucleation rate at approximately 70°C, that trend is not as visible in Fig.1, as there is no data at 60°C or lower. More tests at lower temperatures are recommended, to confirm if there is a maximum of 70°C, or if the crystallization at 70°C has reached its maximum and stays constant from then on.

Figure 2 shows that the lower gap leads to higher nucleation rates. Lower gaps mean that there is not much space for the seed to move in the liquid sample, which results in more collisions between the seed and the steel geometry. The nucleation rate is related to the number of collisions between solid and geometry, which could explain why higher gaps lead to lower nucleation rates.

In Figure 3 it is observed that the influence of the shear rate in crystallization is not very clear at low temperatures. However, the model shows there is a dependence on the shear rate of nucleation rate, but only at temperatures near the melting point of xylitol.

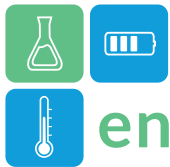
The variability of results is also very high for each temperature. Although some trends can be implied from the nucleation modelling, the variation between tests with the same operating conditions is very high, which can influence the nucleation model. A probabilistic approach for determining the nucleation rate should help understanding better the influence of each parameter on crystallization.

5. Acknowledgements

This work has been partially financed by the State Research Agency (SRA) and the European Regional Development Fund (ERDF). Research Projects: PID 2020-15500RB-I00, TED2021-131061B-C31, and TED2021-131061B-C32. Miguel Navarro acknowledges the funding from the Ministry of Science, Innovation and Universities of Spain through the grants for pre-doctoral contracts for the training of doctors contemplated in the State Training Subprogramme of the State Programme to Develop, Attract and Retain Talent, within the framework of the State Plan for Scientific, Technical and Innovation Research 2021–2023, reference PRE2021-097131. The authors would like to acknowledge the use of the Servicio General de Apoyo a la Investigación-SAI, Universidad de Zaragoza.

6. References

- [1] Delgado, M. et al. (2021) «Triggering and acceleration of xylitol crystallization by seeding and shearing: Rheo-optical and rheological investigation», *Solar Energy Materials and Solar Cells*, vol. 220, p. 110840, 2021, doi: 10.1016/j.solmat.2020.110840.
- [2] Zhang, H. H. et al. (2017) «Experimental and in silico characterization of xylitol as seasonal heat storage material», *Fluid Phase Equilibria*, vol. 436, pp. 55-68 doi: 10.1016/j.fluid.2016.12.020.



enerstock

ENERSTOCK 2024

The 16th IEA ES TCP International Conference on Energy Storage

June 5–7, 2024

Lyon, France

- [3] Navarro, M. (2023) et al. «Comparative study on bubbling and shearing techniques for the crystallization of xylitol in TES systems», Results in Engineering, vol. 17, p. 100909, doi: 10.1016/j.rineng.2023.100909.
- [4] Piquard, L. et al. «Xylitol used as phase change material: Nucleation mechanisms of the supercooling rupture by stirring», Journal of energy storage, vol. 48, pp. 103922-103922 doi: 10.1016/j.est.2021.103922.
- [5] Seppälä A. et al. (2010) «The effect of additives on the speed of the crystallization front of xylitol with various degrees of supercooling», Experimental Thermal and Fluid Science, vol. 34, n.o 5, pp. 523-527, doi: 10.1016/j.expthermflusci.2009.11.005.
- [6] Kashchiev, D. (2000) Nucleation: basic theory with applications. Oxford: Butterworth Heinemann.
- [7] Krieger, I. M. and Dougherty, T. J., «A Mechanism for Non-Newtonian Flow in Suspensions of Rigid Spheres», Transactions of the Society of Rheology, vol. 3, n.o 1, pp. 137-152, mar. 1959, doi: 10.1122/1.548848.
- [8] Mullin, J. W. (2002) «Crystallisation, 4th Edition Butterworth Heinemann: Oxford, UK. 600 pp. ISBN 075-064-833-3.», Org. Process Res. Dev., vol. 6, n.o 2, pp. 201-202, mar. 2002, doi: 10.1021/op0101005.
- [9] Mersmann, A. (1996), «Supersaturation and Nucleation», Chemical Engineering Research & Design, vol. 74, pp. 812-820



Selection of suitable inorganic materials to be applied as PCMs in high temperatures thermal energy storage system

Franklin R. Martinez Alcocer^{1,2}, Emiliano Borri¹, Svetlana Ushak^{2,3}, Cristina Prieto⁴, Luisa F. Cabeza^{1*}

¹ GREiA Research Group, University of Lleida, Pere de Cabrera s/n, 25001-Lleida, Spain

² Centre for Advanced Research in Lithium and Industrial Minerals, University of Antofagasta, Avenue Universidad de Antofagasta 02800, Antofagasta, Chile

³ Departamento de Ingeniería Química y Procesos de Minerales University of Antofagasta, Avenue Universidad de Antofagasta 02800, Antofagasta, Chile.

⁴ University of Seville, Department of Energy Engineering, Camino de los Descubrimientos s/n, 41092, Seville, Spain

*Corresponding author e-mail: luisaf.cabeza@udl.cat

Abstract

Current CSP plants can improve their production process by incorporating two molten salt tanks. However, using phase change materials (PCM) is more efficient since latent heat has a higher energy density than sensible heat. To implement this technology, it is necessary to use PCMs in the range of 300 °C to 600 °C. Inorganic salts are optimal for this aim due to their high energy storage density. From the scientific literature, data sheets of commercial PCMs, and others developed using FactSage, seventy-seven potential materials were collected. In the EU-funded project HYBRIDplus a latent heat thermal energy storage (LHTES) cascade system was proposed with the implementation of five PCMs with different melting temperatures. This study presents the PCM selection methodology developed based on the evaluation of the primary system requirements, thermal properties of the PCMs, compatibility of the PCMs with other materials, safety, and environmental considerations, as well as costs.

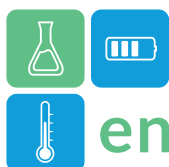
Keywords: Thermal energy storage, Inorganic PCM, Latent Heat TES cascade system, CSP plants

Introduction

In recent decades, concentrated solar power (CSP) plants have advanced their technologies by incorporating two molten salt tanks into their production processes for storing thermal energy in a purely sensible way (Prieto and Cabeza 2019). The implementation of molten salt tanks represents 12% of the total installation costs (IRENA (2021), 2021). However, replacing these molten salt tanks with a single tank composed of phase change materials (PCM) with different melting temperatures (in a cascade configuration) represents a more efficient alternative. This is attributed to the higher energy density of latent heat compared to sensible heat, which means that a greater amount of thermal energy can be stored with a smaller amount of material (Prieto and Cabeza 2019). To implement this technology, it is necessary to find PCMs with melting temperatures in the range of 300 °C to 600 °C (traditional operating temperature range of CSP plants) (Banerjee et al. 2022). Literature shows that there are many materials that can be used as phase change materials PCMs, but researchers still struggle to choose the adequate materials. The PCM selection

methodologies usually considers a limited number of factors as relevant, which are melting enthalpy, melting temperature, and the amount of energy that can be stored and released. However, from an application and material handling point of view, other factors are also crucial in the PCM selection methodology, such as hygroscopicity, metal compatibility (corrosion), level hazard, cost, and thermal and atmospheric stability. Moreover, during the initial process of identifying potential PCMs, it is common to obtain many potential materials. However, carrying out the full characterization for all these potential candidates involves significant economic investment, time, effort, and dedication. In this context, the need for a selection methodology which allows to identify/disregard those materials which do not worth a full characterisation and exhaustive analysis for the final selection arises.

In the EU-funded project HYBRIDplus (GA 101084182) a latent heat thermal energy storage (LHTES) cascade system was proposed with the implementation of five PCMs with different melting temperatures to store heat for CSP plants.



In contrast to traditional PCM selection methodologies, this study presents a new methodology which considers a more comprehensive point of view and allows to identify in the first stages candidates which are not worthy to fully characterize was developed for the selection of suitable PCMs to be implemented in a latent heat thermal energy storage (LHTES) cascade system.

Materials

Inorganic PCM

In this research study, a total of sixty-seven potential inorganic compounds, such as: nitrates, carbonates, chlorides, hydroxides, sulphates, nitrates, fluorides, and their eutectic mixtures, were evaluated as candidates for use as PCM in the LHTES cascade system. These materials were sourced from scientific literature, and commercial PCM datasheets, and some were developed using the FactSage software.

Methodology

The methodology developed to carry out the PCM selection has the steps shown in Figure 1.

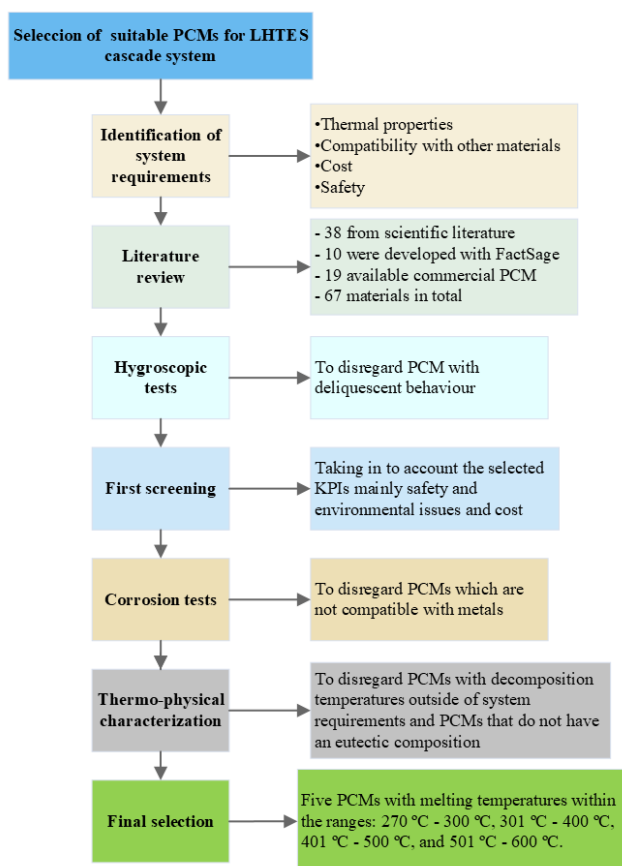


Figure 1. Methodology for selection of suitable PCM

Identification of LHTES cascade system

In the cascade concept, the phase change temperatures are divided into four distinct temperature ranges: 270 °C to 300 °C, 301 °C to 400 °C, 401 °C to 500 °C, and 501 °C to 600 °C. To ensure an optimal TES system design based on working conditions, other essential parameters have to be considered:

1. High latent heat storage capacity (i.e., phase change enthalpy)
2. Easiness in handling and not imposing health hazard
3. Thermal cycling stability: thermal properties need to remain almost constant during a certain number of thermal cycles
4. Thermal stability: maximum working temperature of at least 50 °C below the range of operation
5. Compatibility with the metal selected for the metal wool and the storage container that will contain the PCM
6. Suitable price
7. Atmospheric stability: PCM should be stable in the atmospheric conditions of the storage container

Literature review

To identify potential materials for application as PCMs within the temperature range of 270 °C to 600 °C for the LHTES cascade system, an exhaustive search was conducted. This search encompassed a comprehensive review of scientific literature, an examination of commercial PCM datasheets, and the creation of eutectic mixtures using FactSage software.

Hygroscopic test

Hygroscopic tests consist of weighing approximately five grams of each chemical and leaving them exposed to atmospheric conditions (19 °C, 70 % RH) for eight hours. Every hour a record of the mass of each chemical was taken. After eight hours of exposure to the environment, chemicals were placed in the oven at 200 °C for twelve hours in order to dry the samples. Finally, after twelve hours, the chemicals were weighed again.

First property assessment

To carry out the characterization and experimental tests for all materials identified, a very large number of experiments needs to be developed. Therefore, it was necessary to carry out a deep screening in order to select the most promising materials to carry out the experimental tests. The selection was done considering the most relevant variables: hazard level, properties drawbacks, price (€/kJ), and melting enthalpy.

Corrosion test

Static corrosion was evaluated by the immersion method. A sample (approximately 0.3 g) of metal wool was placed in crucibles, which were filled with 15 g of solid PCM. All crucibles were then placed in the oven

at 50 °C above their melting temperature to ensure that the PCM was in a liquid state. The samples were immersed in the liquid PCM for one week, one month, and three months. The evaluation of results in this study is only qualitative (visual inspection) because the fibres used are very thin, and it was not possible to clean the passivated oxide layer as indicated in the standard ASTM G1-03.

Initially, a first screening of a one-week test with stainless steel fibres was carried out. With those samples that pass the test, the test is repeated for one week, one month and three months. With the samples that did not pass the three-month test, the first one-week screening is repeated but with alloy 20. With those samples that pass the test, the test is repeated for one week, one month and three months again. With the samples that did not pass the three-month test, the first screening of one week is repeated with stainless steel but in an inert atmosphere. With those samples that pass the test, the test is repeated for one week, one month and three months again. With the samples that did not pass the three-month test, the first screening is repeated for one week in an inert atmosphere but with alloy 20. With those samples that pass the test, the test is repeated for one week, one month and three months again.

Thermophysical characterization of PCM

Thermophysical characterisation tests were carried out by thermogravimetric analysis (TGA) on the TGA-DSC 3+ (Mettler Toledo). About 10 mg of sample were deposited in 70 µl sapphire crucibles and the experiments were carried out in an inert N₂ atmosphere. This equipment allows the decomposition temperature of the sample to be determined and has a balance with an accuracy of ±0.00001 g which allows the mass loss associated with the decomposition process to be quantified. In addition, this equipment simultaneously performs DSC measurements. The accuracy of the equipment is ±0.1 °C for temperature results and ±3 J/g for enthalpy results. The measurement parameters collected from these measurements were: decomposition temperature, melting enthalpy and melting temperature. The thermal behaviour of the samples could also be analysed.

Final selection criteria

The LHTES cascade system developed in the project HYBRIDplus will involve the implementation of five PCMs. For this final selection of PCMs, the results obtained in the thermophysical characterisation tests, compatibility with other materials and the KPIs defined based on the system requirements were evaluated. The

KPIs defined for this system are: thermal properties, compatibility with other materials, safety and environmental issues, and costs.

Results

Literature review

67 potential materials were obtained, 38 from scientific literature, 10 were developed with FactSage Educational version 8.3, and 19 available commercial PCM.

Hygroscopic test

Figure 2 shows an example of a PCM with deliquescent behaviour, LiBr in this case, during the hygroscopic test. At the beginning LiBr has a dry appearance. However, after one hour of being exposed to the environment, the appearance of humidity can be noticed, the first liquid drops appear. After four hours, the appearance of humidity in LiBr is more evident. Furthermore, after eight hours, it can observe clearly that LiBr looks completely wet, forming a puddle of water around the salt. Finally, after the drying process, LiBr increased its volume, and its appearance is different to the initial one. Results were translated to mass change. Materials behave differently with prior drying than without prior drying, absorbing a higher percentage of water after 8 hours of exposure to the environment. LiBr absorbed 19.64 % of humidity (with prior drying) in 8 hours (0.98 g H₂O), and 14.94 % of humidity (without prior drying) in 8 hours (0.77 g H₂O).

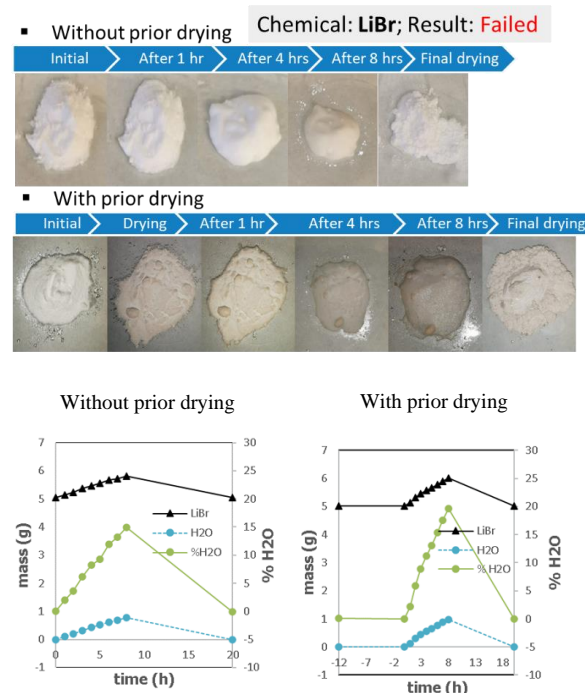


Figure 2. LiBr Hygroscopic test

First property assessment

From the 67 potential materials initially identified, 29 materials were disregarded (8 PCMs identified as deliquescent and 21 with hazard level 3) reducing the number of potential candidates to 38 real candidates for which full characterisation and compatibility tests with potential metals with which they will be in contact (corrosion test) were performed.

Corrosion test

Figure 3 shows an example of the results of the 1-week corrosion test of one of the PCMs, in the case of a eutectic mixture of $\text{KNO}_3\text{-KCl}$ (94-6wt.%). The stainless-steel fibers after one week of being immersed in this PCM were disintegrated, while the Alloy 20 fibers retained their integrity. Therefore, the 3-month test will be carried out with Alloy 20 metal fiber.

Conclusions

This study presents a novel PCM selection methodology that considers crucial factors related to the application and handling of materials, including hygroscopicity, hazard level, and corrosion resistance. The application of this new methodology to the presented case study has allowed the identification of 38 real potential PCM candidates for which it is worthy to carry out a full thermophysical characterisation and exhaustive analysis, out of an initial group of 67 potential PCMs.

Acknowledgments

This project was funded by the European Union’s Horizon Europe Research and Innovation Programme

under grant agreement 101084182 (HYBRIDplus). Views and opinions expressed are however those of the author(s) only and do not necessarily reflect those of the European Union or CINEA. Neither the European Union nor the granting authority can be held responsible for them. Franklin R. Martinez Alcocer thanks the National Doctorate Scholarship for foreign students ANID 2021 Folio 21211932 for the financial support in the research. This work is partially supported by ICREA under the ICREA Academia programme. The authors would like to thank the Catalan Government for the quality accreditation given to their research group (2017 SGR 1537). GREiA is certified agent TECNIO in the category of technology developers from the Government of Catalonia.

References

Banerjee, Bikash, Sushovan Chatterjee, Jinia Datta, and Sabarni Dutta Saha. 2022. “Application of Phase Changing Materials in a CSP Plant for Thermal Energy Storage: A Review on Recent Developments.” *Materials Today: Proceedings* 62: 3502–7. <https://doi.org/10.1016/j.matpr.2022.04.306>.

IRENA (2021). 2021. “Renewable Capacity Statistics 2021.” Abu Dhabi.

Prieto, Cristina, and Luisa F. Cabeza. 2019. “Thermal Energy Storage (TES) with Phase Change Materials (PCM) in Solar Power Plants (CSP). Concept and Plant Performance.” *Applied Energy* 254: 113646. <https://doi.org/10.1016/j.apenergy.2019.113646>.









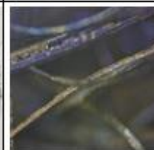

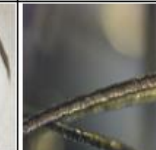
PCM	Stainless steel 314		Stainless steel 434		Alloy 20	
Before tests						
$\text{KNO}_3\text{-KCl}$ (94-6wt. %)						
Comments (Test temperature)	Failed (T= 340 °C)		Failed (T= 340 °C)		Passed (T= 340 °C)	

Figure 3. Results of corrosion test

Selection of the storage system for industrial steam supply with heat pumps

Dimitri Nefodov¹, Haochen Wang¹, Markus Richter¹, Robin Berlin¹, Thorsten Urbaneck¹

¹ Professorship Applied Thermodynamics, Department of Mechanical Engineering, Chemnitz University of Technology, 09107 Chemnitz, Germany

*Corresponding author e-mail: thorsten.urbaneck@mb.tu-chemnitz.de

Abstract

This paper deals with a typical heating process in industry. For this purpose, various heat pump storage systems are presented and investigated. In addition to the classic Ruths storage system, hybrid storage systems with phase change materials are also used. By decoupling the supply of heat from production over time, the authors aim to achieve low-emission and energy-efficient heat supply in industry. The simulation of the system is performed with the software EBSILON®Professional.

Keywords: Heat pump, Ruths Steam Storage, PCM, Simulation, EBSILON®Professional

Introduction

In industrial process heat supply, steam is often used as the heat transfer medium. However, their production requires a relatively large amount of energy (Bazzanella, 2017). For example, in 2019, process heat accounted for approximately 66.7% of the energy consumption of German industry (BMWK, 2021). With the European Union aiming to reduce annual greenhouse gas emissions by 55% by 2030 and Europe aiming to be carbon neutral by 2050, the supply of process heat to industry must be given greater attention. Within the framework of the KETEC project (Research Platform for Refrigeration and Energy Technology) (Urbaneck et al., 2023), concepts for the realisation of the highly available, low-emission and energy-efficient provision of steam for industrial processes based on heat pump-storage systems, among other things, are being fundamentally investigated.

The solution approach provides for the use of a heat pump storage system. Steam generation is provided by a high-temperature heat pump. The produced steam is buffered in a storage system to increase flexibility in steam generation and supply, with a minimum steam temperature of 140 °C. The heat pumps can currently only achieve good performance coefficients with low steam temperatures and high heat source temperatures. This limits the usable temperature difference, which has a negative effect on the Ruths steam storage. To increase the storage capacity in the small temperature range, steam storage can be combined with phase change materials (PCM). Such approaches are known as hybrid storage in the literature. A promising configuration of the Ruths storage with external PCM storage is shown in Figure 1.

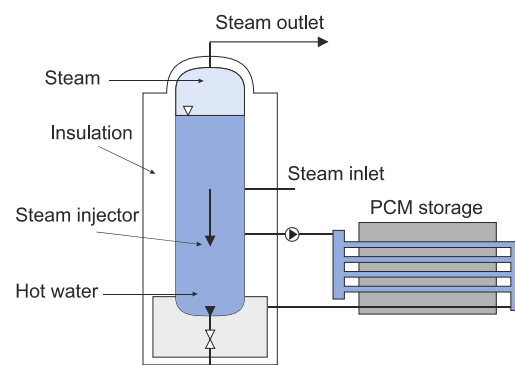


Figure 1: Combination of the Ruths storage with external PCM storage (hybrid storage) (modified according to Buschle et al. (2006a,b))

Modelling and Boundary Conditions

The Ruths storage unit with the externally arranged PCM storage unit (material data derived from the PCM RT80HC (Iqony, 2023) and adjusted for the melting point of 130 °C) supplies a sterilization process from the food industry as an example. In the process should be handled cans of tomato soup. According to assumptions, 4000 doses fit into the autoclave with a chamber volume of 2.2 m³. The autoclave with a starting temperature of 20 °C is supplied with steam for approx. 160 minutes (theoretical assumption) until the target temperature (mean temperature) of around 121 °C is reached. The temperature must be maintained for a period of 10 to 20 minutes to kill all microorganisms (Figure 2) (Bender et al., 2020).

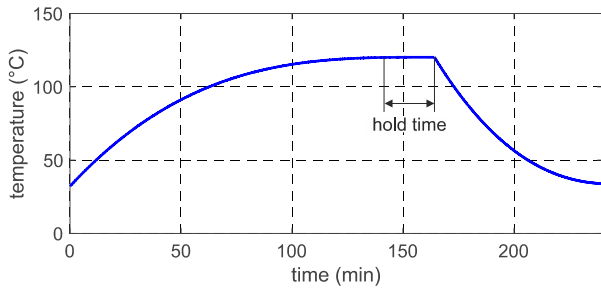


Figure 2: Exemplary temperature curve of a batch sterilization process (modified according to Bender et al. (2020))

A high-temperature heat pump with a relatively low supply temperature of 140 °C serves as the steam generator. A system without a storage tank (designation: R-WP) and a system with a Ruths storage tank (designation: R-RS, 25 m³) are defined as references. The model with the hybrid storage is shown in Figure 3. A parameter study (Figure 4) was carried out for dimensioning the system R-PCM with the software EBSILON®Professional. Possible combinations of PCM storage mass and Ruths storage volume, which fulfil the above mentioned target criteria, are marked in blue. For further examinations, interpretation according to Figure 4 (Point L) applies. By using the PCM storage with a PCM mass of around 3500 kg, the volume of the Ruths storage can be reduced from 25 m³ to approx. 16 m³.

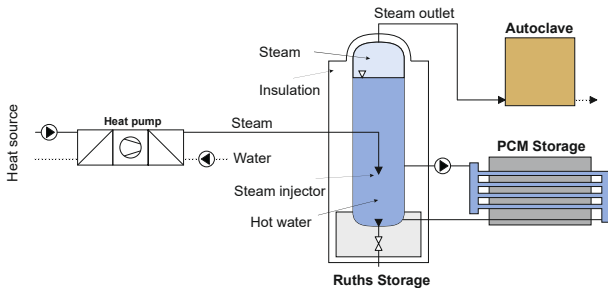


Figure 3: Hybrid storage system R-PCM

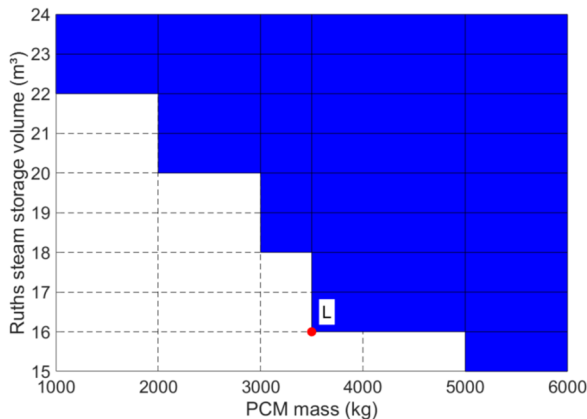


Figure 4: Results of the parameter study for the dimensioning of the hybrid storage (EBSILON simulation)

Results and Discussion

In order to better illustrate a difference to steam production with a storage tank, the initial state (variant R-WP) is to be simulated. The investigation provides a variation of the steam mass flow from 0.010 to 1.000 kg/s. The course of the average autoclave temperature over time for different loading mass flows is shown in Figure 5. At a steam mass flow of 0.075 kg/s, the target temperature is reached in 148 minutes. Thus, this mass flow is initially considered as the reference value.

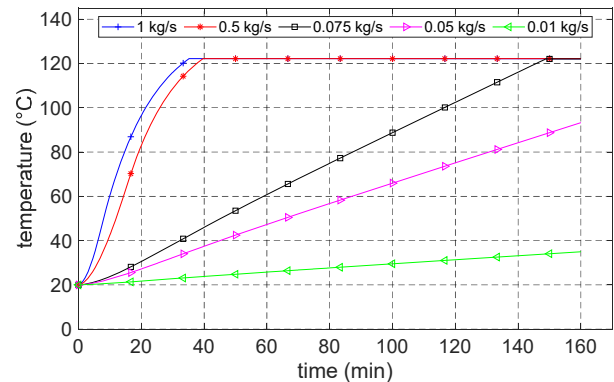


Figure 5: Curves of the average autoclave temperature for different steam mass flows during the sterilization process (variant R-WP)

The simulation results for the hybrid storage system are shown in Figure 6. The autoclave reaches the target temperature of 121 °C in 159 minutes. The liquid level in the Ruths storage tank drops by 5.87%. It is noticeable that the average temperature in the Ruths storage tank remains relatively high at the end of the charging process at approx. 127 °C. Lower temperatures can probably be achieved through further optimization of the operation.

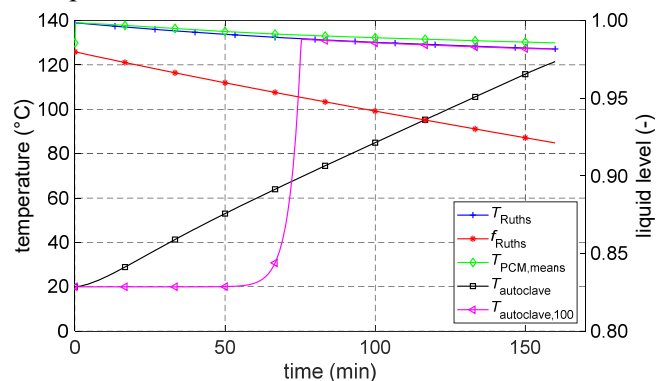
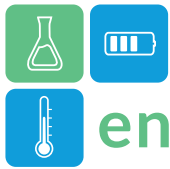


Figure 6: Temperature and level curve during discharging of the hybrid storage system and sterilisation process (variant R-PCM)

Figure 7 shows the loading time for the Ruths storage system R-RS and the hybrid storage system R-PCM. The assumption is that the heat pump can only deliver a limited mass flow of steam of 0.070 kg/s. With the



system according to variant R-RS the Ruths storage tank is heated from 121 °C to 139 °C in around 185 minutes. The liquid level increases by 4.85% (variant R-RS) or 26.58% (variant R-PCM). As expected, a decisive disadvantage occurs when loading the hybrid storage system. The loading time here is around 572 minutes. In order to increase the rate of storage loading, further operational optimization or modifications to the storage design are required.

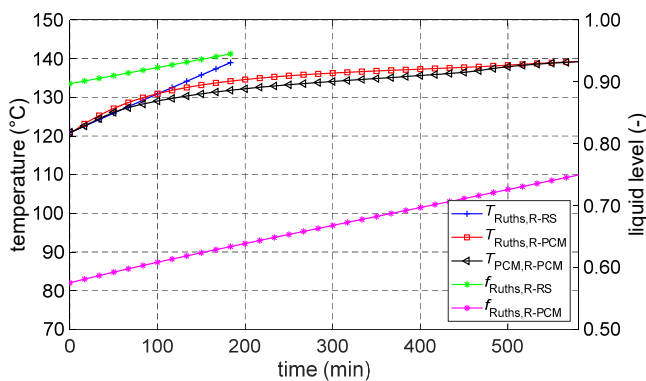


Figure 7: Curve of temperatures and liquid level during storage loading for variant R-RS and variant R-PCM

Conclusions

It is possible to produce the steam by using a high-temperature heat pump and store it for further purposes. Hybrid storage systems are suitable for steam storage. Such heat pump-storage systems can be used in various industries, such as the food industry.

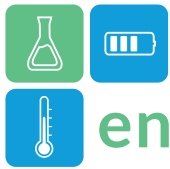
Due to the fact that the heat pumps can currently supply only relatively low steam temperatures, the usable temperature difference on the side of the Ruths storage tank and thus its storage capacity is limited. An additional PCM storage expands the storage capacity in this small temperature range and allows to take a larger amount of steam out of the Ruths storage. One disadvantage of the Ruths storage is that as discharge progresses, the storage tank temperature sinks. Further optimizations of the steam supply are planned.

Acknowledgment

The research work is funded by the Federal Ministry of Education and Research (BMBF) under the reference 03SF0623A/B/C on the basis of a resolution of the German Bundestag. Project management is provided by Projektträger Jülich (PtJ). The authors would like to express their gratitude for the funding, support and cooperation.

References

- Bazzanella, M. and Ausfelder, F. (2017). Low carbon energy and feedstock for the European chemical industry. Technologische Studie, DECHEMA Gesellschaft für Chemische Technik und Biotechnologie e.V., Frankfurt am Main.
- Bender, B. and Göhlich, D. (Ed.) (2020). *Dubbel Taschenbuch für den Maschinenbau 3: Maschinen und Systeme*. Berlin, Heidelberg: Springer Berlin Heidelberg. - ISBN 978-3-662-59714-9.
- Buschle, J., Steinmann, W. D. and Tamme, R. (2006). Latent heat storage for process heat applications. 10th International Conference on Thermal Energy Storage ECOSTOCK 2006. New Jersey, USA.
- Buschle, J., Steinmann, W. D. and Tamme, R. (2006). Latent Heat Storage for Process Heat Applications. DLR – German Aerospace Center. The Tenth International Conference on Thermal Energy Storage, Atlantic City.
- Federal Ministry for Economic Affairs and Climate Action (BMWK, 2021). *Energieeffizienz in Zahlen. Entwicklungen und Trends in Deutschland 2021*. https://www.bmwk.de/Redaktion/DE/Publikationen/Energie/energieeffizienz-in-zahlen-entwicklungen-und-trends-in-deutschland-2021.pdf?__blob=publicationFile&v=6 [accessed: 22.02.2023].
- Hofmann, R., Dusek, S., Gruber, S. and Drexler-Schmid, G. (2019). Design Optimization of a Hybrid Steam-PCM Thermal Energy Storage for Industrial Applications. *Energies*, 12 (5), p. 898. - ISSN 1996-1073.
- Iqony Solutions GmbH (2023). *EBSILON®Professional 16 P1*.
- Niknam, P. H. and Sciacovelli, A. (2023). Hybrid PCM-steam thermal energy storage for industrial processes – Link between thermal phenomena and techno-economic performance through dynamic modelling. *Applied Energy*, 331, p. 120358. - ISSN 03062619.
- Urbaneck, T., Matthes, M., Richter, M., Hempel, O., Safarik, M., Franzke, U., Noack, R., Honke, M., Müller, M., Henninger, S., Schossig, P., Henning, H.-M., de Oliveira, H. T., Morgenstern, A., Nienborg, B., Gschwander, S., Engelmann, P. and Benndorf, G. (2023). *www.ketec.online*. Website of the joint project [accessed: 03.06.2023].



Sensible/latent hybrid heat storage using molten nitrate and Al alloy-based phase-change material

Yuto Shimizu^{1,*}, Melbert Jeem², Takahiro Nomura²

1 Graduate School of Engineering, Hokkaido University, Kita 13 Nishi 8, Kita-ku, Sapporo, 060-8628, Japan

2 Faculty of Engineering, Hokkaido University, Kita 13 Nishi 8, Kita-ku, Sapporo, 060-8628, Japan

*Corresponding author e-mail: y.shimizu2241@eng.hokudai.ac.jp

Abstract

Thermal energy storage (TES) has attracted attention as a renewable energy storage technology. Although sensible heat storage (SHS) is the most developed TES, alloy-based latent heat storage (LHS), which combines higher heat storage density and thermal conductivity, has attracted attention. Particularly, microencapsulated phase-change materials (MEPCMs) have the advantage of being treated as ceramic powders even when the alloys melt. Therefore, we conceived the possibility of developing a liquid sensible/alloy-based latent hybrid heat storage with improved thermal properties by mixing MEPCM with a molten nitrate. In this study, NaNO₃–40% KNO₃ (solar salt) and Al–Cu–Si-based MEPCM were mixed, and their thermal properties were evaluated. Consequently, in the molten solar salt, MEPCM functioned as a LHS material. The mixed sample (solar salt–28vol.% MEPCM) was estimated to have a heat storage density of 1.04 GJ m⁻³ at $\Delta T = 250$ °C, which is approximately 1.5 times higher than that of the solar salt alone.

Keywords: Latent heat storage, Sensible heat storage, Phase-change material, Microcapsule, Molten nitrate

Introduction

Advancements in thermal storage technology are essential for effective storage and utilization of unused heat and renewable energy related to carbon neutrality. Sensible heat storage (SHS) is a primary technology used for high-temperature thermal energy storage (TES). In concentrating solar power plants with a class of 1000 MWh, molten nitrate SHS is implemented (Guillot and al., 2012). NaNO₃–40mass%KNO₃ (solar salt), with a melting point (T_m) of 220 °C, is mainly used for molten nitrate SHS. Solar salt is used at temperatures below 565 °C, the typical thermal decomposition temperature.

Although SHS is the mainstream in TES, latent heat storage (LHS) using alloy-based phase-change materials (PCMs), which have a higher heat storage density and higher thermal conductivity, have attracted attention. However, alloy-based PCMs are difficult to handle because of their solid–liquid phase transition and high corrosivity. The microscale to macroscale encapsulation of alloy-based PCMs has been investigated to solve these issues (Nomura and al., 2015; Zhang and al., 2014; Zhou and al., 2022).

Among alloy-based encapsulated PCMs, microencapsulated PCMs (MEPCMs), in which the alloy core is covered by a ceramic shell, are promising

TES materials with excellent handling, chemical stability, and formability. In particular, Al alloy-based MEPCMs (Al–Si [Nomura and al., 2015], Al–Zn [Kawaguchi and al., 2020], and Al–Cu–Si [Shimizu and al., 2024]), which have been developed previously, are attractive because they can be fabricated in two simple steps: 1) chemical conversion treatment and 2) heat oxidation treatment. In addition, Al alloy-based MEPCMs with mainly α -Al₂O₃ shells exhibit excellent thermal and chemical stability and can be used as ceramic powders even when the core Al alloy melts. Because it can be handled as a ceramic powder, bottom-up formation is also possible using MEPCM (Sakai and al., 2020).

Based on the above, we considered the possibility of molten nitrate sensible–alloy-based latent hybrid heat storage, in which both the heat storage density and thermal conductivity were improved by mixing MEPCMs with molten nitrate. This hybrid heat storage material has the potential of being used in the same facilities as conventional molten nitrate SHS systems. In this study, an Al–Cu–Si alloy-based MEPCM was mixed with a solar salt, and its structure and thermal storage properties were investigated. The Al–Cu–Si MEPCM was selected because it has a melting point of 517 °C (Shimizu and al., 2024), which ranges between

220 and 565 °C, the typically operating temperature range of solar salts.

Methodology

Al–29.5%Cu–6.0%Si (mass%) alloy powder (particle size of <math><45 \mu\text{m}</math>) was used as a raw material for MEPCM. The MEPCM precursor was obtained by stirring 50 g of raw alloy powder in boiling distilled water (pH: 8.0) for 3 h as a chemical conversion treatment. An NH_3 solution with a concentration of 1 M was used to adjust the pH of the distilled water. The MEPCM precursor sample was heated to 1000 °C at $10 \text{ }^\circ\text{C min}^{-1}$ in an O_2 atmosphere and maintained for 3 h to obtain the MEPCM sample. Three grams of the MEPCM sample was placed in an Al_2O_3 crucible, along with 1.8 g of NaNO_3 and 1.2 g of KNO_3 raw powder. The mixed powder sample was maintained at 250 °C for 1 h and at 350 °C for 5 h to dehydrate and melt the mixed NaNO_3 (T_m : 308 °C) and KNO_3 (T_m : 334 °C). The samples were then heat-treated at 560 °C for 1 h above the melting point of the Al–Cu–Si alloy-based MEPCM (517 °C). All heat treatments, including dehydration, were performed in an Ar atmosphere. The obtained samples were analyzed using X-ray diffraction (XRD), scanning electron microscopy (SEM), energy-dispersive X-ray spectroscopy (EDS), and differential scanning calorimetry (DSC). For simplicity, the final mixed sample of the solar salt and MEPCM is denoted SS-ME MIX.

Results and Discussion

The XRD measurements showed that only the MEPCM components of Al, Si, Al_2Cu , $\alpha\text{-Al}_2\text{O}_3$, and CuAl_2O_4 and the solar salt components of NaNO_3 and KNO_3 were detected in the SS-ME MIX. Quantitative analysis via XRD revealed that the amount of CuAl_2O_4 formed was lower than one-tenth that of $\alpha\text{-Al}_2\text{O}_3$.

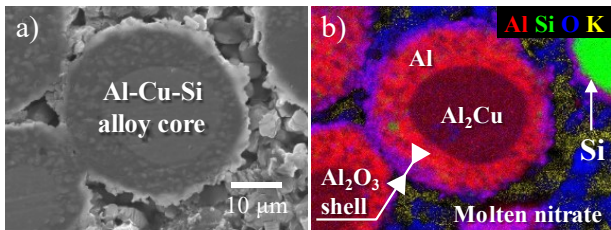


Figure 1: a) SEM image and b) EDS elemental mapping of SS-ME MIX cross-section.

Figure 1 shows the a) SEM image and b) EDS elemental mapping of the SS-ME MIX cross-section. Figure 1 a) SEM image and b) EDS mapping show that the Al alloy particles dispersed in the nitrate were Al–Cu–Si alloys, and the particles were covered with an Al oxide layer. Therefore, even after heat treatment at 560 °C, which exceeds the melting point of the core

alloy, the MEPCM in SS-ME MIX maintained its microcapsule structure in molten nitrate. The above XRD and SEM-EDS observations indicate that the SS-ME MIX contains nitrate and Al–Cu–Si alloy core/Al-oxide shell-type MEPCM dispersed in the nitrate.

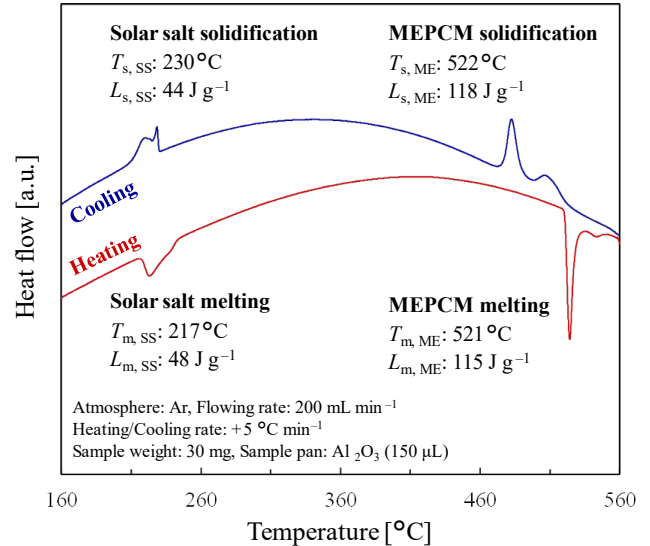
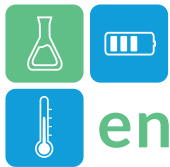


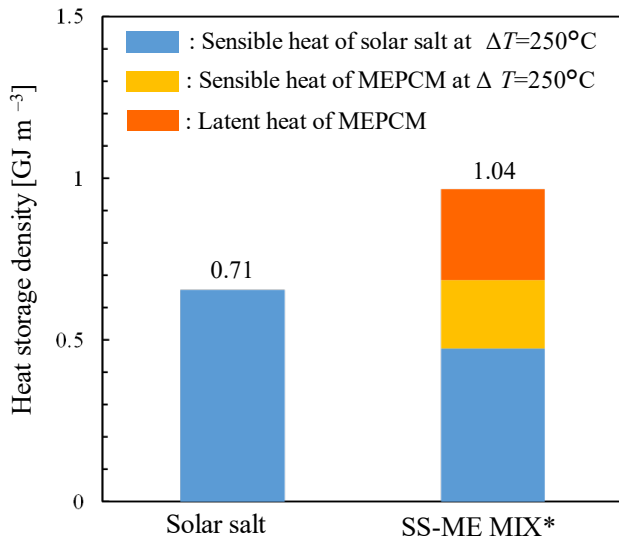
Figure 2: Heating and cooling DSC curves of SS-ME MIX (The melting and solidification temperatures (T_m and T_s) were evaluated at onset temperature, respectively).

Figure 2 shows the DSC curves for heating and cooling of the SS-ME MIX. During the heating and cooling stages, melting and solidification peaks corresponding to the solar salt and Al–Cu–Si alloy MEPCM were observed in the DSC curves of the SS-ME MIX. Solar salt and MEPCM have melting points of 217 °C ($T_{m,SS}$) and 521 °C ($T_{m,ME}$), respectively, and corresponding melting latent heat capacities of 48 J g^{-1} ($L_{m,SS}$) and 115 J g^{-1} ($L_{m,ME}$). Moreover, during the cooling process, the solar salt and MEPCM have solidification points of 230 °C ($T_{s,SS}$) and 522 °C ($T_{s,ME}$), with solidification latent heat capacities of 44 J g^{-1} ($L_{s,SS}$) and 118 J g^{-1} ($L_{s,ME}$), respectively. The melting and solidification points were evaluated at the onset temperature. These DSC measurements confirmed that the MEPCM operated as an LHS material in the solar salt liquid. Therefore, SS-ME MIX can be used as a liquid-sensible/alloy-based latent hybrid heat-storage material with solar salt and Al–Cu–Si alloys.

Figure 3 shows the estimated volume-based heat-storage density at $\Delta T = 250 \text{ }^\circ\text{C}$ for the solar salt alone and SS-ME MIX. In this study, the volume ratio of solar salt to MEPCM in the SS-ME MIX was 28 vol.% MEPCM based on the XRD quantitative analysis. As shown in Figure 3, SS-ME MIX has a heat storage density of 1.04 GJ m^{-3} , which is higher than that of solar salt alone (0.71 GJ m^{-3}). Thus, the heat storage



density can be increased by approximately 1.5 times by mixing approximately 30% of the Al–Cu–Si MEPCM with solar salt. This result also suggests that the heat storage density increases with the addition of the MEPCM to solar salt.



*Solar salt–28 vol.% MEPCM (XRD quantitative analysis value)

Figure 3: Estimated volume-based heat storage density at $\Delta T = 250^{\circ}\text{C}$ for solar salt alone and SS-ME MIX.

Conclusions

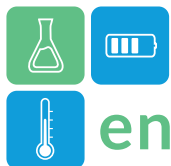
An Al–Cu–Si MEPCM with a melting point of approximately 520°C was mixed with solar salt, a high-temperature liquid SHS material, and the structural and thermal storage properties of the mixture were investigated. The Al–Cu–Si alloy core/Al oxide shell-type MEPCM maintained its capsule structure in the solar salt melt and functioned as an LHS material. SS-ME MIX (solar salt–28 vol.% MEPCM) has an estimated heat storage density of 1.04 GJ m^{-3} at $\Delta T = 250^{\circ}\text{C}$, which is approximately 1.5 times higher than that of solar salt alone.

Acknowledgments

This study was partially supported by a JPNP20003 project subsidized by the New Energy and Industrial Technology Development Organization (NEDO), JSPS KAKENHI (Grant Number: JP23KJ0050) and the Light Metal Educational Foundation, Japan.

References

- Guillot, S. and al. (2012) Corrosion effects between molten salts and thermal storage material for concentrated solar power plants, *Applied Energy*, doi.org/10.1016/j.apenergy.2011.12.057.
- Kawaguchi, T. and al. (2020) Microencapsulation of Zn–Al alloy as a new phase change material for middle-high-temperature thermal energy storage applications, *Applied Energy*, doi.org/10.1016/j.apenergy.2020.115487.
- Nomura, T. and al. (2015) Microencapsulation of metal-based phase change material for high-temperature thermal energy storage, *Scientific Reports*, doi.org/10.1038/srep09117.
- Sakai, H. and al. (2020) Fabrication of heat storage pellets composed of microencapsulated phase change material for high-temperature applications, *Applied Energy*, doi.org/10.1016/j.apenergy.2020.114673.
- Shimizu, Y. and al. (2024) Novel microencapsulated ternary eutectic alloy-based phase change material, *Journal of Energy Storage*, doi.org/10.1016/j.est.2023.109535.
- Zhou, X. and al. (2022) Encapsulated copper-based phase-change materials for high-temperature heat storage, *ACS Omega*, doi.org/10.1021/acsomega.1c06751.
- Zhang, G. and al. (2014) Encapsulation of copper-based phase change materials for high temperature thermal energy storage, *Solar Energy Materials and Solar Cells*, doi.org/10.1016/j.solmat.2014.05.012.



Small-scale field demonstration of zeolite based mobile thermochemical energy storage

Shoma Fujii^{1,2*}, Sogo Saito³, Kazuki Matsui³, Takao Nakagaki³, Yasunori Kikuchi^{1,2,4}

1 Institute for Future Initiatives, The University of Tokyo, 7-3-1 Hongo, Bunkyo-ku Tokyo, 113-8654, Japan

2 Department of Chemical System Engineering, The University of Tokyo, 7-3-1 Hongo, Bunkyo-ku Tokyo, 113-8656, Japan

3 Department of Modern Mechanical Engineering, Waseda University, 3-4-1 Okubo, Shinjuku-ku, Tokyo, 169-8555, Japan

4 Presidential Endowed Chair for “Platinum Society”, The University of Tokyo, 7-3-1 Hongo, Bunkyo-ku Tokyo, 113-8656, Japan

*Corresponding author e-mail: shoma.fujii@ifi.u-tokyo.ac.jp

Abstract

In order to make effective use of unused heat below 200 °C, a mobile thermochemical energy storage system that regenerates unused heat into industrial process steam using a zeolite water vapor adsorption/desorption cycle is being considered. A small-scale demonstration test of a zeolite flow rate of 15 kg/h class for a zeolite boiler, a heat discharging device employing a moving bed and indirect heat exchange system, was conducted. As a result of the steam generation test, continuous generation of pressurized steam at 0.2 MPa was achieved, and heat gain of more than 15% was confirmed relative to the enthalpy of steam introduced for adsorption heat generation.

Keywords: Zeolite, Heat exchanger, Adsorption

Introduction

Cascading use of unused heat from industry, biomass plants, and waste incineration plants in the region will play an important role in decarbonization by using local resources. While most industrial waste heat in Japan is below 200 °C (Thermat, 2019), there is also significant demand for heat at lower temperatures, including hot water and low-temperature steam. Hot water can be replaced by industrial waste heat or heat pumps, but steam, which is particularly in demand in industry, is a highly effective substitute, and it is important to regenerate waste heat as steam. One thermal energy storage material that can recover waste heat below 200 °C is an adsorbent. However, although many thermal energy storage systems using adsorbents have been studied (Kuznik and al., 2018), most of them have been heat discharging systems designed to replace low-temperature heat demand such as space heating, hot water heating, and hot dry air, etc. A fixed-bed system that use adsorbents to regenerate low-temperature waste heat below 200 °C as steam has been developed (Nakaso and al., 2015), however, there are few examples of continuous steam generation that can be used as an alternative to existing boilers.

In order to realize continuous generation of pressurized steam, a zeolite boiler, a heat discharging device

employing a moving bed and indirect heat exchange system, has been considered (Fujii and al., 2019) that can regenerate unused heat below 200 °C as pressurized steam below 150 °C.

In this study, a small-scale field demonstration of a zeolite-based mobile thermochemical energy storage system (About 1/100 of commercial scale on a zeolite flow basis) that regenerates unused energy derived from sugarcane residue (sugarcane bagasse) as steam, one of the examples of a local resource, was conducted.

Material and methodology

Figure 1 shows an overview of a small-scale field demonstration of a mobile thermochemical energy storage system between a sugar mill and a cleaning plant using LPG boilers in one of Japan's southwestern islands, Tanegashima. A preliminary test of a zeolite boiler with a zeolite flow rate of 15 kg/h installed in the cleaning plant on the island was conducted, and the adsorbed zeolite, after heat discharging was transported to the sugar mill. During the sugar milling period, unused energy derived from sugarcane bagasse at the sugar mill was used to charge heat. To simplify the test, a hot-air generator driven by surplus electricity derived from sugarcane bagasse was used to generate hot air. The stored zeolite was transported by a small car to the

cleaning plant about 8.5 km away during the maintenance period of the sugar mill, when there was no traffic of sugar cane trucks. The cleaning plant operates an LPG boiler and consumes about 0.2 MPa of steam. A zeolite boiler was operated at a zeolite flow rate of 15 kg/h to continuously produce pressurized steam using zeolite charged during the operating hours of the sugar mill to demonstrate a small-scale mobile thermochemical energy storage system. Type 4A zeolite with a diameter of around 2 mm was used in these tests.

First, on the heat charging side, the unused energy from the sugar mill was charged using a heat charging device named heat charger, employing a moving bed counter-current contact system as shown in Figure 1. Since the mass balance and numerical analysis of the heat charger demonstration test have already been reported (Fujii and al., 2021), experiments to verify the heat charger system with constant water uptake of input zeolite, were not conducted in this case, and the heat charger was simply used to charge heat in the zeolite. Zeolite was fed from the top of the heat charger after preliminary tests of the zeolite boiler, where the feed water uptake of input zeolite was not constant. The heat storage temperature was set to 180 °C.

Next, heat-charged zeolite were transported to the cleaning plant for a steam generation test. Figure 2 shows a schematic diagram of the zeolite boiler. The zeolite boiler uses a moving bed indirect heat exchange system. The heat-charged zeolite is continuously fed from the top. Steam from the existing boiler is depressurized to atmospheric pressure and injected into the zeolite bed from the top. The zeolite absorbs the

injected steam and generates adsorption heat. A heat exchanger is installed in the zeolite bed, and room temperature water is fed into the heat exchanger from the bottom. The adsorption heat generated by the zeolite is transferred to the internal water supply through the heat exchanger, the water in the heat exchanger evaporates, and pressurized steam is delivered from the top. As described above, pressurized steam can be continuously generated using zeolite while using an inexpensive atmospheric pressure tank, and fuel can be reduced by generating steam with a higher enthalpy than that of the injected steam. It is also possible to use humidified air instead of the steam generated by existing boilers.

A zeolite boiler with a scale of 15 kg/h zeolite flow rate (hereafter referred to as a small-scale zeolite boiler) was designed. A rectangular stainless-steel chamber with a cross section of 290 mm x 290 mm and a height of 750 mm was manufactured for the small-scale zeolite boiler. A 490 mm height plate-finned tubular heat exchanger was installed in the chamber as shown in Figure 2. The steam injection port was mounted at $x=0$ mm (i.e., above the heat exchanger), and superheated steam generated by the existing boiler was injected through the injection port. The chamber was surrounded by glass wool insulation. The demineralized water was pressurized by a pump and supplied to the heat exchanger in the zeolite boiler and the injection steam generator. Six K-type thermocouples were set to measure the axial temperature distribution in the zeolite bed. The temperature at the top of the heat exchanger was inserted from the top of the chamber and the center

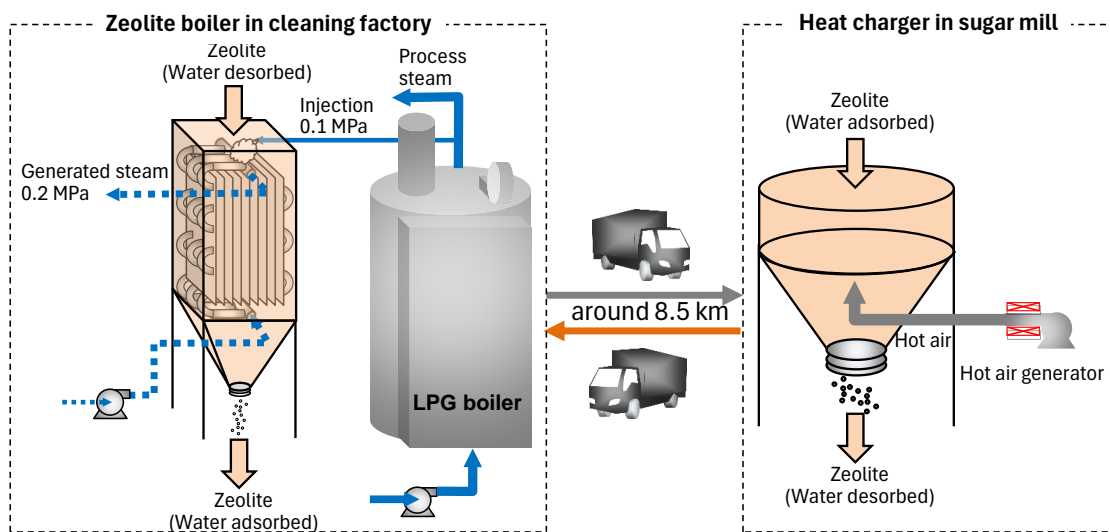


Figure 1: Schematic of zeolite boiler and picture of plate-finned heat exchanger

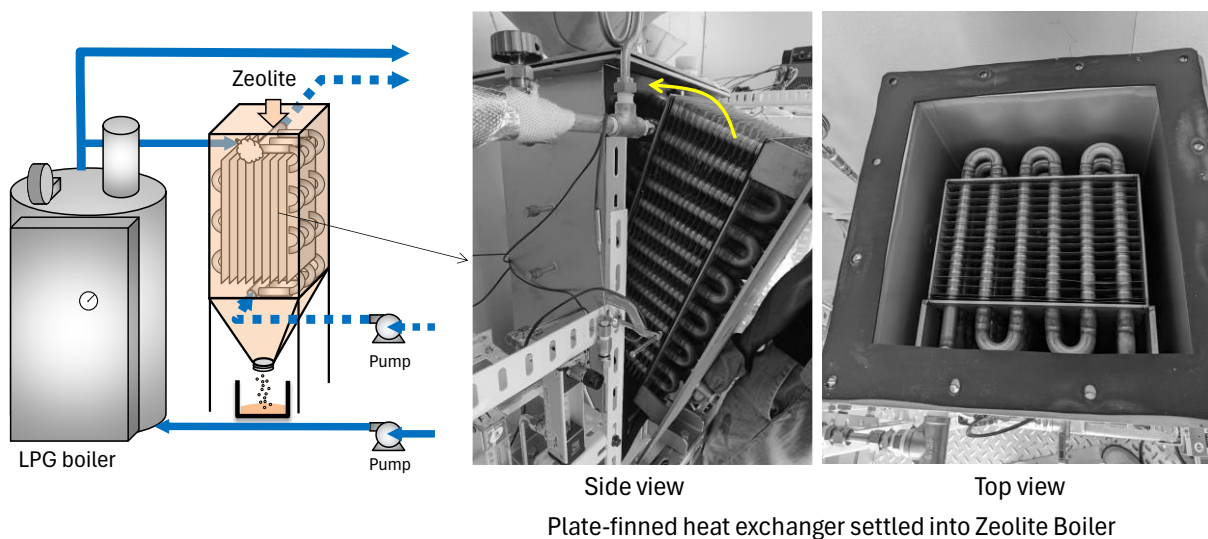


Figure 2: Schematic of zeolite boiler and picture of plate-finned heat exchanger

temperature of the chamber was measured. The other five thermocouples were placed in the center of the fins at positions $x = 30, 146, 260, 374,$ and 490 mm from the top. The temperatures of the feed water, generated steam, and injected steam were measured by K-type thermocouples, and a logger recorded these temperatures every 10 seconds. Water uptake into the zeolite at inlet and outlet and mass flow rate of the zeolite were measured every 30 minutes.

The injected steam was maintained at superheated steam in the bypass line and then introduced into the zeolite boiler with a quick switch of the valve. Simultaneously, a particle discharger was started to exhaust the zeolite and the experiment was initiated. When the outlet steam from the heat exchanger reached superheat under ambient pressure, the back pressure valve was controlled to begin pressurizing the generated steam to 0.2 MPa. Once the generation of pressurized superheated steam was confirmed and the temperature inside the zeolite boiler was stabilized, steady-state operation was conducted for 1 hour.

Result and discussion

As a result of heat charging test with hot air generated by electricity derived from sugarcane bagasse, the amount of adsorption amount at exhaust point of heat charger was confirmed to be constant at about 0.035 kg/kg and about 200 kg of zeolite could be regenerated. Regenerated zeolite was transported to the cleaning factory from the sugar mill for the zeolite boiler test.

The zeolite boiler test was conducted under the following conditions: 15 kg/h of dried zeolite flow rate, 1.9 kg/h of injection steam flow rate, 2.3 kg/h of

supplied water flow rate. Figure 3 shows the results of the mass balance of dry zeolite and adsorbed water during the test. Zeolite was discharged stably during the test. Adsorbed water gradually increased and reached a steady state in 4.0 hours after the start of the test. Data from 5 hours after the start of the experiment showed that the amount of water adsorbed on the zeolite was 0.161 kg/kg, and since 0.163 kg/kg was expected from the experimental conditions, it was confirmed that almost the injected steam was adsorbed. Figure 4 shows the axial temperature distribution after reaching steady state 4-5 hours after the start. It can be seen that the zeolite exceeds $200\text{ }^{\circ}\text{C}$ at the top, then the temperature gradually decreases due to heat transfer and is discharged at about $110\text{ }^{\circ}\text{C}$ at the bottom. During steady-state operation, pressurized steam under 0.2 MPa could be continuously generated. The enthalpy of the generated steam was increased by more than 15% relative to the enthalpy of the injected steam.

In the region of $x = 0.260\text{--}0.374$ m, the temperature of the zeolite hardly changes. This is considered to be because the feedwater in the heat exchanger reached the saturation temperature of $120\text{ }^{\circ}\text{C}$ at a feedwater pressure of 0.2 MPa, is in the phase change region where the water temperature is constant, and the adsorption is almost complete. There was little heat exchange between the zeolite and the feedwater in this region, suggesting that the heat transfer area of the heat exchanger was excessive under the experimental conditions. There is a lateral temperature distribution of the zeolite bed between the fins, but the measurement point is at the center between the fins, and the zeolite temperature is expected to be measured at $5\text{--}6\text{ }^{\circ}\text{C}$ higher than the saturation temperature of $120\text{ }^{\circ}\text{C}$.

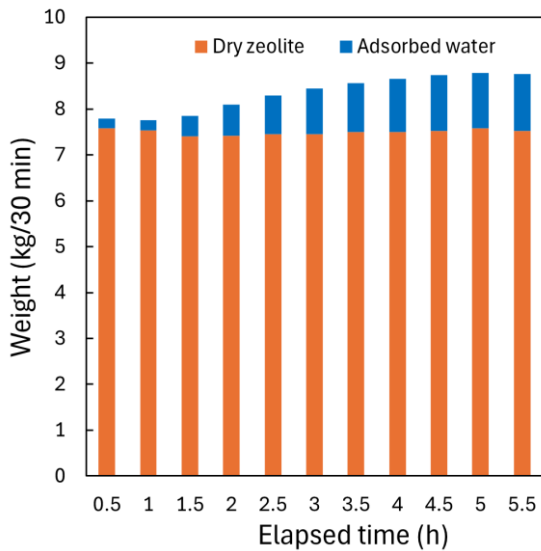


Figure 3: Mass balance result of zeolite boiler test

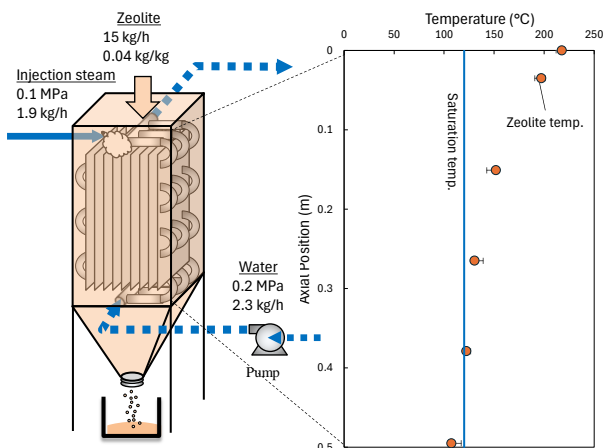


Figure 4: Axial temperature distribution inside zeolite boiler

Conclusions

The small-scale field demonstration of a mobile thermochemical energy storage system using zeolite to regenerate unused heat as industrial process steam was conducted. Continuous generation of pressurized steam at 0.2 MPa was achieved at a zeolite flow rate of 15 kg/h at the cleaning plant using zeolite stored with unused energy derived from sugar cane at a sugar mill, demonstrating the potential of using local low-temperature unused energy to regenerate it as industrial steam.

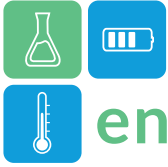
Acknowledgment

The field tests were supported by Shinko sugar mill Co. Ltd. and Kyouseikoubou-Sarukango (the cleaning

plant). This work was supported by the Environment Research and Technology Development Fund (Grant Number JPMEERF20213R01) of the Environmental Restoration and Conservation Agency of Japan, JST PRESTO (Grant Number JPMJPR2278), JSPS KAKENHI Grant-in-Aid for Early-Career Scientists (Grant Number JP22K18061) and JST COI-NEXT (Grant Number JPMJPF2003). The activities of the Presidential Endowed Chair for “Platinum Society” at the University of Tokyo are supported by Mitsui Fudosan Corporation, Sekisui House, Ltd., East Japan Railway Company, and Toyota Tsusho Corporation.

References

- Fujii, S., and al. (2019), Design of zeolite boiler in the thermochemical energy storage and transport system utilizing unused heat from sugar mill, *Applied Energy*, <https://doi.org/10.1016/j.apenergy.2019.01.104>
- Fujii, S., and al. (2021), Bench-scale demonstration test and design of a moving bed counter-flow heat exchanger for unused energy from a sugar mill (in Japanese), *Kagaku Kogaku Ronbunshu*, <https://doi.org/10.1252/kakoronbunshu.47.191>
- Kuzunik, F., and al. (2018), A review on recent developments in physisorption thermal energy storage for building applications, *Renewable Sustainable Energy Reviews*, <https://doi.org/10.1016/j.rser.2018.06.038>
- Nakaso K. and al. (2015), Performance of a novel steam generation system using a water- zeolite pair for effective use of waste heat from the iron and steel making process. *ISIJ Int.* <https://doi.org/10.2355/isiinternational.55.448>.
- Thermat, (2019), Survey of Exhaust Heat in the Industrial Sector (in Japanese)



Solar heating and cooling with latent heat storage for temporary shelters

Halime Paksoy^{1,*}, Khamid Mahkamov², Gülfeza Kardaş¹, İbrahim Südaş³, Sedat Emir¹, Gizem Biçer Göktepe¹, Özge Güngör¹, Fatma Alma¹, Filiz Hoplamaz¹, Shine Win Naung², Irina Makhkamova²

¹Çukurova University, Faculty of Art and Sciences, Chemistry Department, Adana, Türkiye

²University of Northumbria at Newcastle, United Kingdom

³Barış Enerji Sistemleri A.Ş., Adana Türkiye

*Corresponding author e-mail: hopaksoy@cu.edu.tr

Abstract

Temporary shelters with comfort conditions are needed for millions of people around the world who are forced to continue their lives away from their homes affected by natural disasters or other geopolitical problems. Such dwellings can be off-grid without any proper infrastructure. Solar energy with thermal energy storage (TES) can be used as a source to provide heating and cooling in such places. In this paper, the concept development for solar heating cooling systems for temporary shelters is presented. The system being developed uses solar thermal collectors for both heating and cooling. Solar thermal collectors are used in horizontal orientation to benefit from night-time radiation for cooling. Two latent heat storage tanks are used for hot and cold storage. Phase Change materials (PCMs) with different melting points suitable for heating and cooling are used in TES units. In on-going studies, modelling, optimization of components and long-term tests are carried out.

Keywords: Temporary shelter, solar energy, thermal energy storage, heating, radiative cooling, night-time radiation, phase change material

Introduction

In the past year, millions of people around the world are affected by sudden onset of natural disasters such as earthquakes, hurricanes, floods, forest fires. The climate crisis is accelerating some of these disasters in number and strength. These people have to migrate into new areas and find shelter. Geopolitical changes happening around the world also increase the number of refugees who need temporary shelters. According to United Nations High Commissioner for Refugees (<https://www.unhcr.org/refugee-statistics/>) forcibly displaced people worldwide reached to 110 million in mid 2023.

Solar energy has been used in heating and cooling of buildings in many previous studies. For more efficient and uninterrupted supply of solar energy thermal energy storage (TES) has to be included in the system. (Mehling and Cabeza, 2005). These systems can be active and passive. In active systems HTF circulates between solar collectors and TES during sunny hours to store heat. Heat is released to the ambient through distribution system in the building with another network when sun is not available. Backup heaters or heat pumps can be used in some of these systems (Osterman et al., 2015). In passive systems, building materials or elements act as TES units and operate based on the day and night time temperature differences (Stritih et al., 2018).

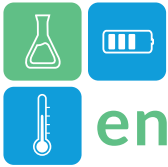
Among the TES methods, latent heat storage providing high storage capacity and isothermal behaviour is preferred in compact building application (Tyagi et al., 2007).

Temporary buildings for disaster relief have minimal living space with limited space for TES units. In this paper, we present solar heating and cooling concept we have developed for shelters in refugee camps in Adana, Türkiye. System description, components and operation modes are described.

Methodology

Solar heating and cooling concept for temporary shelter in Adana, Türkiye includes the following components:

- Cabin: Similar living area that is used in temporary shelters of refugee camps in Türkiye was considered. Prefabricated cabin with dimensions of 3x7x2.8 m insulated with glass wool was chosen for this purpose.
- Harnessing solar energy: 8 flat plate solar collectors with dimensions of 1940x940x100 mm, painted absorber surface with 4 mm tempered glass cover
- Distribution system in cabin: 4 fan coils in serial connection
- Latent heat storage: Two tanks – one for hot and one for cold - with heat exchanger coils and about 1 ton of PCM are used. PCMs with different melting points suitable for heating and cooling are selected.



- Pumps: Two pumps – one for circulating HTF from/to solar collectors to TES tanks and the other for circulating HTF from/to TES tanks to fan coils.
- 2-way valves: Control flow of heat transfer fluid based on the operation modes.
- Monitoring system: Temperatures at 12 points in each TES tank, inlet, outlet, indoor, outdoor and fan coils are measured with PT100 thermocouples. Flow rates in solar and fan-coil networks are also measured. Energy consumption of pumps and fans are also monitored.

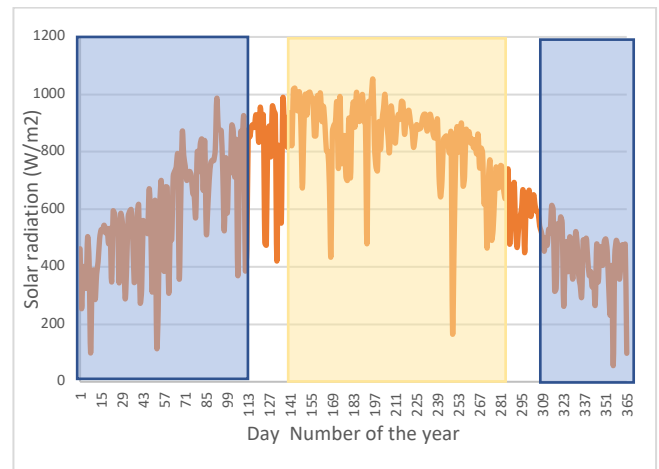
Results and Discussion

Concept developed here is based on thermal energy storage of solar energy for heating and cooling by making use of temperature difference between day and night. Weather conditions – mainly solar radiation and air temperature – of the region defining the operation are shown in Figure 1 (produced with Meteornorm 7.1) is shown. In Adana, solar radiation (Figure 1 a) can go up to 1048 W/m² with an annual average value of 678 W/m². There are 192 days with solar radiation above this average. In air temperature distribution given in Figure 1(b), maximum and minimum curves correspond to day-time and night-time, respectively.

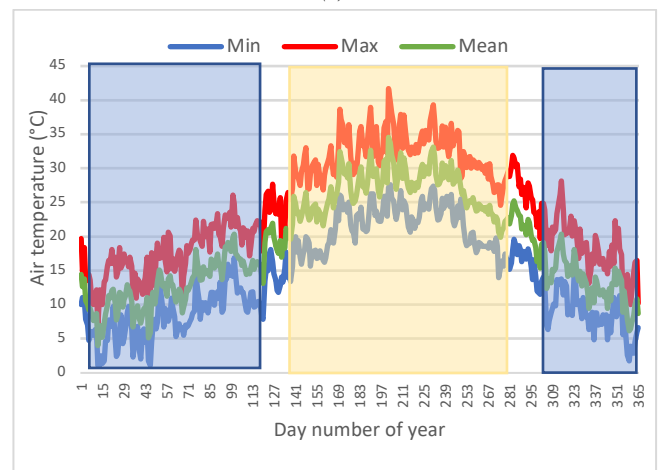
Figure 1 is roughly divided into heating season (blue) and cooling season (yellow). For transition season with no heating or cooling no colour is used.

Our concept is developed to provide heating and cooling according to the seasons illustrated in Figure 1. In heating season, during the day solar heat is stored to be used for heating shelter during night-time. Adana being in solar-belt region has abundant solar radiation for this purpose (Figure 1(b)). In the cooling season, during the night cooled water by night-time radiation is used for cooling the shelter during the day. Solar thermal collectors are used for harvesting both solar heat and cold. Infrared radiation released from solar collectors during night cools down the heat transfer fluid below the ambient temperature. This is known as radiative cooling, which can lead to decrease of temperature of heat transfer fluid in the solar collector by 5°C below ambient and can be achieved even at ambient night-time conditions of 29°C with 100% relative humidity. (Dong et al., 2019). Figure 1(b) shows that night-time temperature during cooling season is around 25°C in Adana, which shows a significant potential for radiative cooling.

For an effective night-time radiation, solar collectors have to be in horizontal position. Flexible pipe shown in Figure 2 is used together with solar collector assembly to adjust the slope to desired value.



(a)



(b)

Figure 1: Weather parameters in Adana, Türkiye produced with Meteornorm 7.1 a) Daily mean solar radiation distribution b) Daily mean air temperature distribution



Figure 2: Flexible pipe to adjust slope of the solar collectors

Figure 3 shows the following components brought together in a cabin similar to temporary shelters used in refugee camps: 1) Solar collectors, 2) Hot TES tank, 3) Cold TES tank, 4) Fan coils. The system aims to provide 24 kWh cooling or heating when requested, which makes it possible to provide thermal comfort during 10-hour period.



Figure 3: System concept 1) Solar collector, 2) Hot TES tank, 3) Cold TES tank, 4) Fan coils

The operation modes of the system are illustrated in Figure 4. There are two heat transfer fluid circulation networks: 1) Network 1: Solar collector to/from TES tanks 2) Network 2: TES tanks to/from fan coils. In heating mode (Figure 4 a), during the day solar energy is stored in hot TES. Network 1 transfers heat from solar collectors to hot TES. At night time stored heat is recovered. Network 2 transfers heat from hot TES to fan coils to be delivered to the shelter. In cooling mode (Figure 4 b), during the night cold is stored in cold TES. Network 1 transfers cold produced by night-time radiation of horizontal solar collectors to cold TES. At day time stored cold is recovered. Network 2 transfers cold from cold TES to fan coils to be delivered to the shelter.

Control of the system is done based on temperature measurements. Heat storage is continued while temperature at the inlet to hot TES (coming from solar collector) is above the melting temperature of the PCM in hot TES. For cold storage, inlet temperature should be below freezing point of the PCM in cold TES.

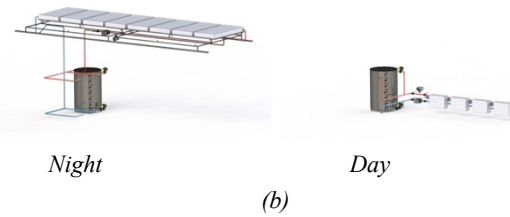
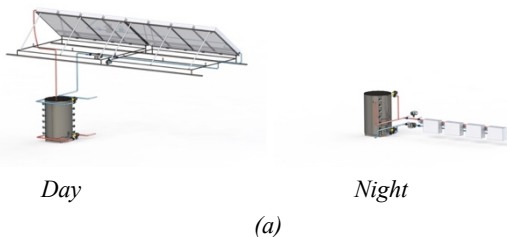


Figure 4: Operation modes a) Heating mode; b) Cooling mode

Conclusions

The concept developed for heating and cooling of a temporary shelter using solar energy is presented here. The system relies on ambient weather conditions that have high solar energy abundance and suitable day and night temperature differences. Using compact TES with latent heat storage is important for such applications with limited space availability.

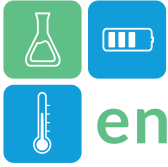
Further studies on optimization of system parameters and evaluating monitoring is on-going. Considering growing demand for such temporary dwellings for natural disasters, results can give some sustainable solutions to decrease dependence on fossil fuels and any other central grids.

Acknowledgment

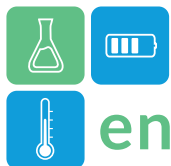
The authors would like to acknowledge funding provided by TÜBİTAK (Project No: 218M182), British Council (Project ID: 414707599), HECTAPUS project funded by TÜBİTAK (Project No:122N750/222N357) under the umbrella of GEOTHERMICA Joint Call Smart Energy Systems ERA-Net and Çukurova University Research Fund (Project No: FBA-2024-16523).

References

- Dong,M., Chen,N., Zhao,A., Fen,S., Chen,Z. (2019). Nighttime radiative cooling in hot and humid climates. *Optics Express*, 27(22), 31587.
- Mehling, H., Cabeza, L. F. (2008). Heat and cold storage with PCM. *Heat and mass transfer*, 11-55.
- Osterman,E., Butala,V., Stritih,U. (2015). PCM thermal storage system for ‘free’ heating and cooling of buildings. *Energy and Buildings*, 106, 125–133.
- Stritih,U., Tyagi,V, Stropnik,R., Paksoy,H.Ö., Haghghat,F., Mastani,J. (2018). Integration Of Passive Pcm Technologies For Net-Zero Energy Buildings. *Sustainable Cities and Society*, 41, 286–295.
- Tyagi, V. V., Buddhi, D. (2007). PCM thermal storage in buildings: A state of art. *Renewable and Sustainable Energy Reviews*, 11(6), 1146–116.



ENERSTOCK 2024
The 16th IEA ES TCP International Conference on Energy Storage
June 5–7, 2024
Lyon, France



Solid-Solid Phase Change Materials for the Thermal Management of Li-Ion Batteries

Ali Saad¹, Clément Weick¹, Thomas Pietri¹, Grégory Largiller^{1,*}

¹Univ. Grenoble Alpes, CEA, Liten, 38000, Grenoble, France

*Corresponding author e-mail: Gregory.LARGILLER@cea.fr

Abstract

With the escalating demand for high-performance lithium-ion (Li-ion) batteries across diverse applications, ensuring effective thermal management is imperative for safety, longevity, and optimal functionality. Current literature limitations underscore the crucial necessity for innovative solutions, leading to the exploration of solid-solid phase change materials (SS-PCMs). This study focuses on the potential of hybrid organic-inorganic layered perovskites, a unique class of SS-PCMs, for thermal management in Li-ion batteries. These materials boast higher thermal stability, minimizing the risk of leakage and enhancing overall safety. Moreover, they offer improved energy density, extended cycle life, and efficient heat absorption/release. This research delves into the synthesis, characterization, and future perspectives of integrating these materials into various battery components for optimized thermal control and enhanced overall performance.

Keywords: Li-ion batteries, thermal management, SS-PCMs, hybrid layered perovskites.

Introduction

Thermal energy storage is a critical concern, especially given the prevalence of heat-intensive processes in final energy applications. Latent heat storage, characterized by a high enthalpy of phase change, presents distinct advantages over sensitive storage methods, offering energy densities three to five times higher. The isothermal nature of latent heat storage, coupled with the ability to adjust temperatures through material design, renders it suitable for applications like thermal management in Li-ion batteries. The demand for high-performance Li-ion batteries has seen a significant rise across diverse applications, underscoring the critical need for efficient thermal management. This is essential not only for ensuring safety but also for enhancing the longevity and optimal functionality of these batteries. In this context, phase change materials (PCMs), particularly hybrid solid-solid PCMs (SS-PCMs) like 2D perovskites, have emerged as promising candidates for thermal energy storage (Wankhede et al., 2022). These materials exhibit reversible transitions between crystalline and semi-crystalline or amorphous states, displaying minimal volume variation and the absence of a liquid phase related leakages. Notably, they offer enhanced energy density, extended cycle life, and efficient heat absorption and release, making them valuable for advanced thermal energy storage applications (Fallahi et al., 2017).

Despite being identified as promising materials for thermal management in the 1980s (Busico et al., 1980),

employing 2D perovskites as hybrid SS-PCMs have received little attention until now (Seo et al., 2022). In fact, hybrid SS-PCMs with a generic chemical formula $(C_nH_{2n+1}NH_3)_2M^II X_4$ (M = divalent metal; X = halogen) have demonstrated potential for heat transfer with controllable phase change temperatures (Landi and Vacatello, 1975). This paper discusses the synthesis, characterization, and potential of copper and zinc-based solid-solid phase change materials for thermal management in today's applications.

Methodology

Hybrid SS-PCMs $(C_nH_{2n+1}NH_3)_2M^II X_4$, where M =Cu, Zn; X =Cl; n =12, 16 were synthesized via solution chemistry. The synthesis involved the mixing of inorganic salts (zinc chloride, copper chloride - SigmaAldrich) and alkyl amines (dodecylamine, hexadecylamine - SigmaAldrich) in ethanol under reflux conditions at elevated temperatures (70-82°C), with the addition of slight quantities of HCl (37%). Notably, the synthesis protocol was implemented at different scales, ranging from 50 mL to 600 mL, ensuring scalability and reproducibility. Four hybrid SS-PCMs were synthesized:

- Bis(n-dodecylammonium)Tetrachlorocuprate $(C_{12}H_{28}N)_2CuCl_4$ (denoted as CuC12)
- Bis(n-dodecylammonium)Tetrachlorozincate $(C_{12}H_{28}N)_2ZnCl_4$ (denoted as ZnC12)
- Bis(n-hexadecylammonium)Tetrachlorocuprate $(C_{16}H_{34}N)_2CuCl_4$ (denoted as CuC16)
- Bis(n-hexadecylammonium)Tetrachlorozincate $(C_{16}H_{34}N)_2ZnCl_4$ (denoted as ZnC16)

The obtained SS-PCMs underwent a comprehensive characterization using a multi-technique approach. Thermal performance was assessed using micro-differential scanning calorimetry (DSC, Setaram, Calvet 3D) and simultaneous thermal analysis (STA coupling TGA and DSC, Jupiter F3-Netzsch). The structural features were investigated using X-ray diffraction (XRD, Bruker D8 Advance), attenuated total reflection (ATR, Bruker Invenio), small-angle X-ray scattering (SAXS, Xenocs), and synchrotron techniques. Scanning electron microscopy (SEM, Zeiss LEO 1530) was used for microscopic analyses.

Results and Discussion

Batches of CuC12, CuC16, ZnC12, and ZnC16 synthesized at different scales between 50 and 600 mL were characterized by ATR and XRD. The obtained XRD patterns exhibited characteristic peaks corresponding to the parent materials despite the increase in synthesis scale (Figure 1), signifying the reproducibility and scalability of the followed synthesis protocol for each of the four-studied SS-PCMs. Similarly, no changes in the recorded ATR profiles were observed, indicating the preserved structure and coordination after the scale up.

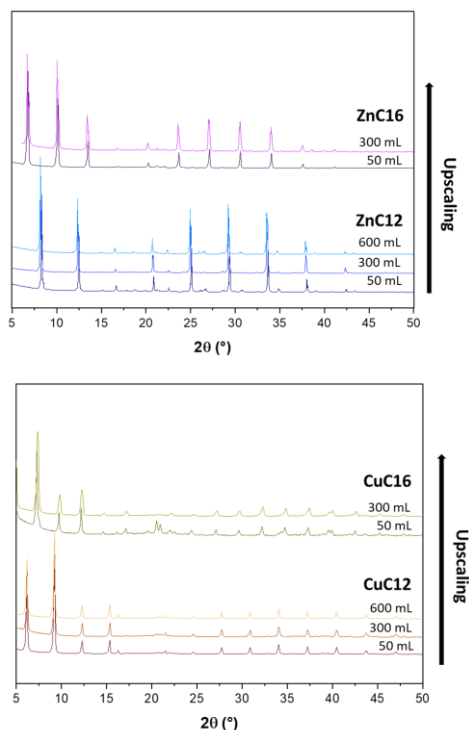


Figure 1: PXRD results showing the reproducibility of synthesis protocol at different synthesis scales.

Moreover, the thermal performance of the different materials was studied by STA and DSC. The obtained results revealed an increase in the transition temperature with the increase in the alkyl chain length

for both Cu and Zn based materials. The effect of the cation on the configuration was also observed. Copper-based samples presented transition temperatures lower than those of zinc based ones (Figure 2).

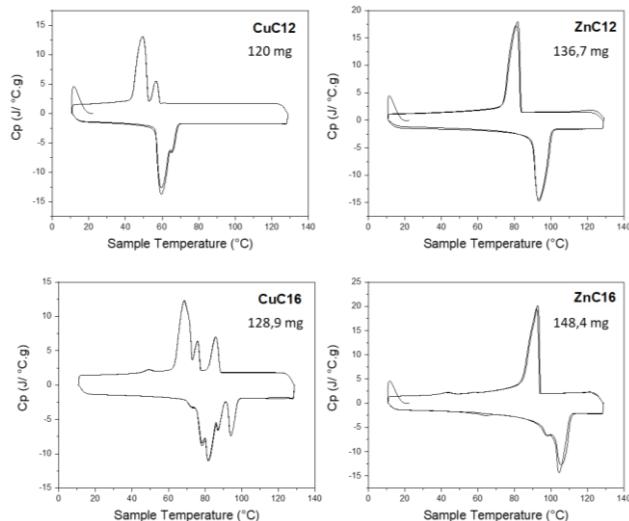


Figure 2: DSC profiles recorded after two consecutive cycles between 10-130°C at a rate of 1 Kmin⁻¹. Measurements were performed under air in closed crucibles.

Correspondingly, STA measurements have shown that the synthesized samples presented a high thermal stability up to 3 times the transition temperature in case of copper, and 2 in case of zinc (Figure 3).

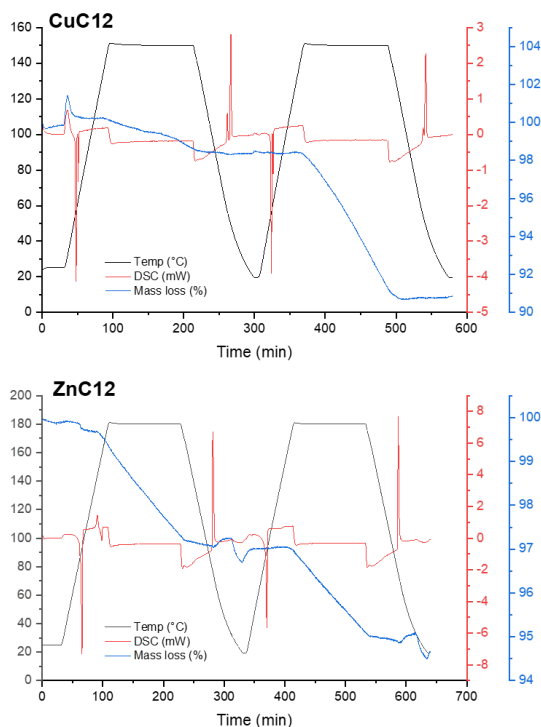


Figure 3: STA measurements recorded on CuC12 (26.3 mg) and ZnC12 (27.5 mg) after 2 cycles under air between 25-130°C at a rate of 2 Kmin⁻¹.

Table 1: Summary of results obtained by DSC and STA.

	CuC12	CuC16	ZnC12	ZnC16
ΔH (J/g)	72	72/103	85	80/100
T_{melting} ($^{\circ}\text{C}$)	54-56	69-71	80-83	92-95
Thermal Stability	150 $^{\circ}\text{C}$	150 $^{\circ}\text{C}$	180 $^{\circ}\text{C}$	180 $^{\circ}\text{C}$

Based on the obtained results, CuC12 can be nominated as an ideal material for thermal management of Li-ion batteries. CuC12 presents a phase transition temperature around 55 $^{\circ}\text{C}$ and a thermal stability at a temperature up to three times higher than its transition temperature with no degradation or liquidification. Further efforts are being put on the mechanical characterization of these materials, and a preliminary prototype is being under studies (Figure 4).

Conclusions

This study presents hybrid materials with high latent heat storage efficiency and thermal stability, even at temperatures double their transition temperature. Their unique thermal properties allow versatile shaping for optimized thermal exchanges, especially in Li-ion batteries. The employed advanced characterization techniques provided detailed insights into the materials' structure and behavior; the energy and transition temperature depend on both the length of the aliphatic chain and the nature of the cation. The possible successful design of the first thermally stable Li-ion battery employing SS-PCMs accentuates the innovative potential of these materials. Our work sets the stage for further exploration and optimization, emphasizing their transformative impact on energy storage technologies in terms of efficiency and

scalability. Future research may focus on refining synthesis methods, exploring additional applications, and advancing integration into diverse energy storage systems. Finally, it is worth mentioning that a pioneering commercial-scale synthesis protocol using 20L reactors is under investigation.

Acknowledgment

This document has been prepared within the context of Institut Carnot, Energies de Futur, projects.

References

- Busico, V., Carfagna, C., Salerno, V., Vacatello, M., Fittipaldi, F., 1980. The layer perovskites as thermal energy storage systems. *Solar Energy* 24, 575–579.
- Fallahi, A., Guldentops, G., Tao, M., Granados-Focil, S., Van Dessel, S., 2017. Review on solid-solid phase change materials for thermal energy storage: Molecular structure and thermal properties. *Applied Thermal Engineering* 127, 1427–1441.
- Landi, E., Vacatello, M., 1975. Metal-dependent thermal behaviour $\text{Ln}(\text{n-CnH}_{2\text{n}+1}\text{NH}_3)_2\text{MCl}_4$. *Thermochimica Acta* 13, 441–447.
- Seo, J., McGillicuddy, R.D., Slavney, A.H., Zhang, S., Ukani, R., Yakovenko, A.A., Zheng, S.-L., Mason, J.A., 2022. Colossal barocaloric effects with ultralow hysteresis in two-dimensional metal-halide perovskites. *Nature Communications* 13, 2536.
- Wankhede, S., Thorat, P., Shisode, S., Sonawane, S., Wankhede, R., 2022. A study of different battery thermal management systems for battery pack cooling in electric vehicles. *Heat Transfer* 51, 7487–7539.

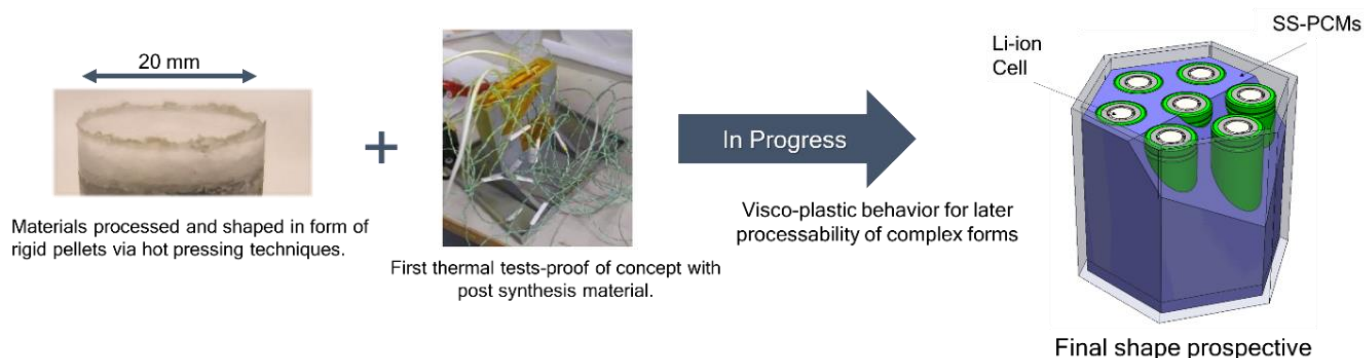


Figure 4: Work in progress covering the testing and shaping of materials for applying in a Li-ion battery system.



Solidification enhancement by changing fin structures using Straight and Y-shaped fins for M-TES applications

İsmail Demirkiran^{1,*}, Erdal Çetkin¹

¹ İzmir Institute of Technology, Department of Mechanical Engineering, Urla, İzmir 35430, Türkiye

*Corresponding author e-mail: ismaildemirkiran@iyte.edu.tr

Abstract

This study explores heat transfer enhancement by incorporating fins into the design. Two types of fin configurations (one with four straight fins ($N_{fin}=4$) and another with a single Y-shaped fin ($N_{fin}=1$)) and two different sizes of these configurations are evaluated based on their performance in the solidification process. Key findings indicate that the Y-shaped fin configuration outperforms the 4-fin design regarding the solidification process, even though it uses fewer daughter fins. Interestingly, the current study also revealed that lowering the temperature of the cold surface is more influential on the solidification process than changing the fin structure. These results offer new insights into cost-effective design and packing strategies for M-TES tanks.

Keywords: Melting/Solidification, Phase Change Material, Latent Heat Storage, Y-shaped fins, CFD

Introduction

In recent years, almost all people from different parts of the world have begun to experience the extreme weather events caused by global warming more perceptibly. This tendency has led decision-makers to develop subsidies and investments in renewable energy technologies. However, recent military conflicts in Eastern Europe and the Middle East threaten the energy supply line, leading to coal-based energy investments again due to energy security. Conversely, clean energy investments and electric vehicle sales have increased by 40% and 500%, respectively, compared to 2020. Even so, the attempts are not enough to reach the aim of restricting global warming to 1.5°C (Wright 1986).

While industry releases waste heat to the environment, the building sector continues to meet heating/cooling needs from fossil fuels. M-TES systems are heat carriers that load waste heat from industrial facilities and transport it to buildings. The primary limitation of M-TES tanks is their weight. According to the transportation regulations set in China, temperatures beyond 100°C are considered dangerous, and the maximum value, including truck weight, is 49 tons (Guo et al. 2022). Therefore, the storage density of the thermal battery should be as high as possible. Hence, Phase Change Materials (PCMs) are promising as a storage medium due to their high storage capability in small volumes, abundance, non-toxicity, and non-flammability. Erythritol is found as the most appropriate candidate for M-TES applications. On the other hand, almost all PCMs (excluding metallics) suffer from low thermal conductivity. Although there

are various heat transfer enhancement methods, the chosen one should provide low manufacturing and material cost, low weight, and durability to make M-TES tanks economically feasible and competitive. Therefore, many researchers are going towards inserting metal fins in PCM units. One of the first studies that employs Erythritol compares uncovers the superiority of longitudinal fins in comparison to annular fin during melting process for horizontally arranged shell-and-tube storage tank (Agyenim, Eames, and Smyth 2010). The study of (Demirkiran and Cetkin 2021) shows that tube allocation and alteration in shell shape cause a reduction in melting time due to appropriate spacing for natural convection. Still, the geometrical changes negatively influence the solidification process of Erythritol, whose thermal conductivity is significantly lower in the liquid phase. (Nie, Deng, and Liu 2020) investigated the effect of fin location using the same number of fins in a circular shell-and-tube heat exchanger during melting and solidification processes. The results show that top-located fins perform better than other fin arrangements in both melting and solidification processes. On the contrary, our previous research (Demirkiran, Rocha, and Cetkin 2022) stated that the PCM domain is created sufficiently large not to prevent melting growth with partial melting, and charging time is limited to 30 min to mimic M-TES operations. The results show that top-located fins accelerate the melting process more than bottom-located fins, and its melting front shape leads to packing tubes eccentrically and in rectangular compartments. (Zheng et al. 2023) conducted a

comprehensive numerical and experimental study including various fin parameters for a medium-temperature application in a rectangular shell-and-tube heat exchanger. The authors imply that the fin structure should be determined considering the PCM amount at the corners since it remains unmelted/unsolidified during the charging/discharging process and takes almost 50% of the process times.

Many studies in the literature endeavour melting and solidification processes by developing designs by fin and cavity shapes such as Arc-shaped, Fibonacci, and Sinusoidal. However, most researchers do consider manufacturing complexity and material costs enough. The present work aims to seek and find an appropriate fin structure for not only melting but also solidification processes using the same amount of high-conductive material, maybe even less. Two different straight fin structures ($N_{fin}=4$) and two different Y-shaped fin structures ($N_{fin}=1$) are numerically compared in 2D space by carrying out a 30min-charging process and subsequent solidification process in a horizontally oriented rectangular shell-and-tube TES tank. Then, the performance of proposed fin structures at different solidification boundary conditions is examined. The results give insight into how to pack finned tubes in an M-TES tank and seek a common appropriate fin structure for melting and solidification.

Numerical Model

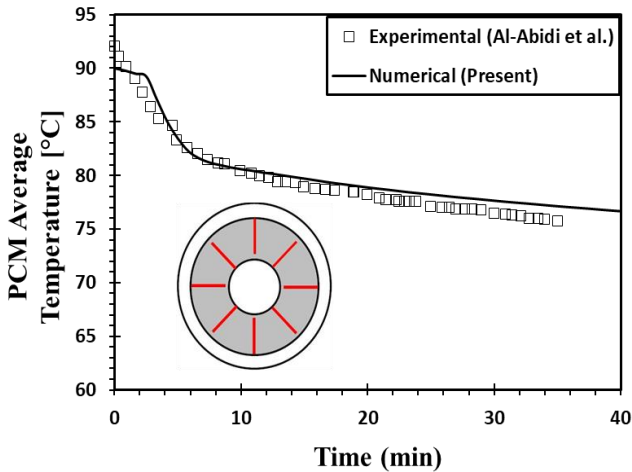


Figure 1. Numerical validation of Al-Abidi et al. (Al-Abidi et al. 2014) comparing PCM average temperatures during solidification.

Figure 2 shows the proposed fin structures, and L_T represents the total fin length. The tube is centered at the 120x120mm rectangular cavity, and its inner and outer diameters are 20mm and 22mm, respectively. In (4-fin) cases, long fins have 21mm, and short fins have

11mm lengths. In both (Y)-shaped designs, the mother-fin length is 22mm, but mother-fin lengths are 15mm and 21mm for the 3rd and 4th cases, respectively. The annular region is filled with Erythritol as PCM, and the tube and fins are made of copper. Transient solidification simulations are analyzed in 2D space using ANSYS Fluent 19.2, which employs the enthalpy-porosity technique to solve melting/solidification problems. The geometry is modeled vertically symmetric to avoid high computational costs. The numerical model is simplified by assuming the setup below:

- Liquid PCM behaves as an incompressible and Newtonian fluid, and flow is in a laminar regime.
- Boussinesq approximation is activated to account for density-driven buoyancy forces and natural convection.
- The isothermal phase change process uses an average melting temperature of 117.7°C.
- Supercooling is neglected in solidification process.

$$\frac{\partial \rho}{\partial t} + \nabla \cdot (\rho u) = 0 \quad (1)$$

$$\rho \frac{\partial u}{\partial t} + \rho(u \cdot \nabla)u = -\nabla P + \mu(\nabla^2 u) - \rho_{ref} \beta g(T - T_{ref}) - C_{mushy} \frac{(1-f)^2}{f^3 + b} u \quad (2)$$

$$\rho \frac{\partial h}{\partial t} + \nabla \cdot (\rho u h) = \nabla \cdot (k \nabla T) + \frac{\partial(\rho H)}{\partial t} + \nabla \cdot (\rho u H) \quad (3)$$

The equations (1), (2), and (3) are mass, momentum, and energy equations. Mesh and time independency tests are satisfied for three different mesh densities (69027, 89124, 107930 nodes) and three different time step sizes (tss) (0.05, 0.1, 0.15s), respectively, for solidification of bare tube cases. Max. error between the different nodes is 1.5%, while each tss perfectly matches. Hence, simulations are done by using tss=0.1s. Further information and detailed explanation about governing equations, geometry sizes, thermophysical properties of Erythritol and copper, and employed numerical algorithms can be found in our previous study (Demirkiran, Rocha, and Cetkin 2022) in much more detail.

The present numerical model for the solidification process is validated against to the data obtained from experiment of (Al-Abidi et al. 2014) starting subsequent discharging process with setting inner and outer tube temperatures as 61.8°C just after melting simulation is ended. The error is 2.8% at the beginning

of the process and max. error is 3.3%, so there is a good match between numerical model and experiment.

Results and Discussion

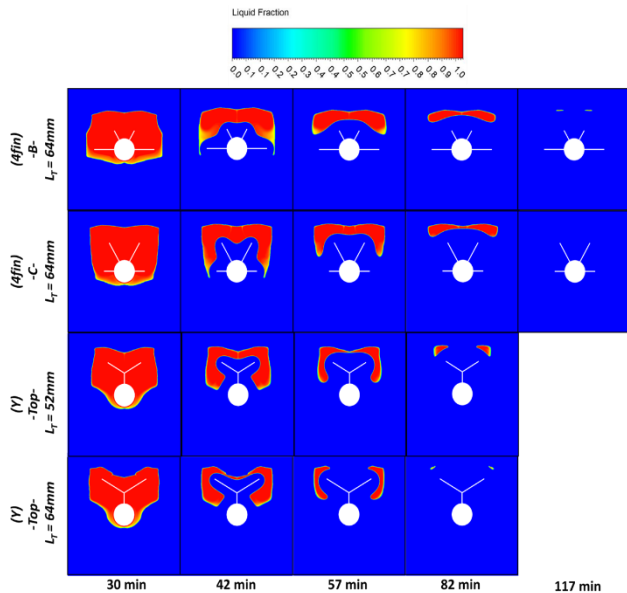


Figure 2. Liquid fraction contours of proposed fin structures during the solidification process. Red and blue represent PCM's liquid and solid phases, respectively.

All cases in Figure 2 firstly are charged by setting the inner tube at 136.7°C (20°C higher than the initial temperature) for 30 minutes of melting time. As demonstrated in contour graphs, the PCM in the cavity is not fully melted, but the liquid fraction values are same even if each has distinct melting front shapes. In addition, average PCM temperature for all cases are around 119°C for all cases. Hence, solidification process starts with same initial conditions. Figure 3a show the liquid fraction evolution in time when the inner tube surface is exposed to 30°C. At the beginning of the process, solidification starts at the tube and fin surface and there is no observable difference between the cases as expected. As time goes on, the solidified regions take shape with respect to fin structures. The melting front are wider along x-direction and upper y-direction in (4-fin)-B and (4-fin)-C configurations, respectively. Therefore, solidified regions similarly grow faster in those directions. The solidification rate is higher than Y-shape fin configurations due to the existence of side fins in (4-fin) configurations. However, solidification becomes more difficult after the solid-liquid interface gets far away from fin and tube surfaces. That is because as the distance increases between the interface and fins, the solid PCM starts to behave as insulation even if thermal conductivity of solid Erythritol is almost 2 times greater than of liquid

form. It can be inferred that although high-conductive fins are employed and the temperature gradient is set quite high (30°C to 119°C), nonuniform settlement of fin structure does not show a good performance as expected. As stated in the study of Zheng et al. (Zheng et al. 2023), influence of parameters such as fin material, fin number, or fin thickness decreases if there is a gap between unsolidified PCM and cold surfaces. On the other side, relatively uniform-distributed Y-shaped fins surpass this handicap. Since natural convection only acts at the beginning of the solidification and is effective rather at lower parts of the cold surfaces (Yazici et al. 2014), it is more critical for fins to reach far points away during the discharging process. As seen in Figure 3a, Y-shaped fins shows significantly better performance, the solidification times are 39% and 24% less than (4-fin) configurations with 64mm and 52mm total fin length cases. Melting fronts grow in upward direction due to existence of natural convection circulations. However, in (4-fin) configurations, only fin tips can reach this far region. As for Y-shaped fins, the daughter fins can occupy PCM more and solidification can be carried out effectively. Even daughter fin lengths lessen, solidification rate is still higher than (4-fin) cases. Therefore, preference of Y-shaped fins instead of (4-fin) configuration with straight fins causes cost reduction and more space for PCM inside the tank.

In order to assess the influence of cold temperature exposed to the inner tube, another strategy is tried starting solidification processes with 97.7°C (20°C less than Erythritol melting temperature). The purpose is to understand which factor has the greater impact on solidification: fin structure or inner tube temperature. Figure 3b shows that if the exposed temperature is elevated from 30°C to 97.7°C, net solidification times increase to its 4.2-4.5 times higher values for each fin cases. Only (4-fin)-B configuration shows slightly worse performance than the others. Almost the same change in solidification times revealed that the proposed different fin structures did not create a significant difference compared to the boundary temperature.

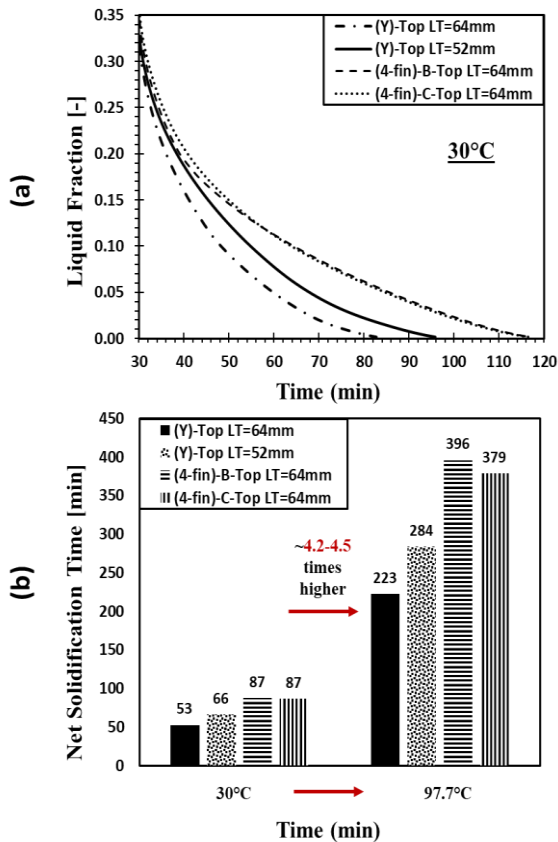


Figure 3. (a) Evolution of PCM liquid fraction values during solidification process, (b) net solidification times of proposed fin structures at the boundary temperatures of 30°C and 97.7°C.

Conclusion

The main outcomes are as follows:

- Y-shaped fins show up to 39% higher performance than (4-fin) configurations during solidification even if daughter fin lengths are shortened. It is desirable due to reduced investment cost and more space appearance for PCM.
- On the contrary to the common thought in literature, Y-shaped fins can be preferred instead of increasing the number of fins for enhancement in melting/solidification processes.
- The effect of boundary temperature has more influence than the change in fin structure during the solidification process.

References

Agyenim, Francis, Philip Eames, and Mervyn Smyth. 2010. "Heat Transfer Enhancement in Medium Temperature Thermal Energy Storage System Using a Multitube Heat Transfer Array."

Renewable Energy 35 (1): 198–207. <https://doi.org/10.1016/j.renene.2009.03.010>.

Al-Abidi, Abduljalil A., Sohif Mat, K. Sopian, M. Y. Sulaiman, and Abdulrahman Th Mohammad. 2014. "Experimental Study of Melting and Solidification of PCM in a Triplex Tube Heat Exchanger with Fins." *Energy and Buildings* 68 (PARTA): 33–41. <https://doi.org/10.1016/j.enbuild.2013.09.007>.

Demirkıran, İsmail Gürkan, and Erdal Cetkin. 2021. "Emergence of Rectangular Shell Shape in Thermal Energy Storage Applications: Fitting Melted Phase Changing Material in a Fixed Space." *Journal of Energy Storage* 37 (May): 102455. <https://doi.org/10.1016/j.est.2021.102455>.

Demirkıran, İsmail Gürkan, Luiz Alberto Oliveira Rocha, and Erdal Cetkin. 2022. "Emergence of Asymmetric Straight and Branched Fins in Horizontally Oriented Latent Heat Thermal Energy Storage Units." *International Journal of Heat and Mass Transfer* 189. <https://doi.org/10.1016/j.ijheatmasstransfer.2022.122726>.

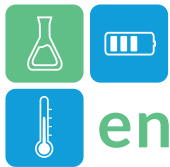
Guo, Shaopeng, Jun Zhao, Alexandre Bertrand, and Jinyue Yan. 2022. "Mobilized Thermal Energy Storage for Clean Heating in Carbon Neutrality Era: A Perspective on Policies in China." *Energy and Buildings* 277: 112537. <https://doi.org/10.1016/j.enbuild.2022.112537>.

Nie, Changda, Shengxiang Deng, and Jiangwei Liu. 2020. "Effects of Fins Arrangement and Parameters on the Consecutive Melting and Solidification of PCM in a Latent Heat Storage Unit." *Journal of Energy Storage* 29 (June): 101319. <https://doi.org/10.1016/J.EST.2020.101319>.

Wright, Vincent P. 1986. "World Energy Outlook.," 23–28.

Yazici, Mustafa Yusuf, Mete Avci, Orhan Aydin, and Mithat Akgun. 2014. "On the Effect of Eccentricity of a Horizontal Tube-in-Shell Storage Unit on Solidification of a PCM." *Applied Thermal Engineering* 64 (1–2): 1–9. <https://doi.org/10.1016/J.APPLTHERMALENG.2013.12.005>.

Zheng, Siyu, Songrui Li, Meng Li, Rui Dai, Mingshan Wei, and Ran Tian. 2023. "Experimental and Numerical Investigation of a Rectangular Finned-Tube Latent Heat Storage Unit for Carnot Battery." *Journal of Energy Storage* 71 (December 2022): 108092. <https://doi.org/10.1016/j.est.2023.108092>.



Specific heat capacity variability analysis of Chilean copper slag for packed-bed thermal energy storage applications

Valentina Segovia^{1,*}, José Miguel Cardemil¹, Ana Inés Fernández²

1 Departamento de Ingeniería Mecánica y Metalúrgica, Pontificia Universidad Católica de Chile, Av. Vicuña Mackenna 4860, Macul, 7810000, Santiago, Chile

2 Departament de Ciència de Materials i Química Física, Secció de Ciència de Materials, Facultat de Química, Universitat de Barcelona, C/ Martí i Franquès 1-11, 08028, Barcelona, Spain

*Corresponding author e-mail: vosegovia@uc.cl

Abstract

This study presents an analysis of the specific heat capacity of copper slag samples sourced from a Chilean foundry, intended as a filler material for packed-bed thermal energy storage. Copper slag, known for its heterogeneity, exhibits considerable variability in its thermophysical properties. In this investigation, various statistical descriptive indicators are employed to examine how the specific heat capacity varies with temperature within the range of 100°C to 450°C. Furthermore, the elemental composition of a copper slag sample is analysed using SEM mapping and EDS analysis. The findings reveal a significant concentration of iron in the sample. Moreover, the specific heat capacity exhibits an upward trend with increasing temperature, albeit accompanied by a growing variability across the temperature range.

Keywords: Packed-Bed Thermal Energy Storage (PBTES), Sensible Heat Storage Materials (SHSM), Heterogeneous material characterization

Introduction

In the search for new materials for Sensible Heat Thermal Energy Storage (SHTES), several authors have explored the utilization of slags from metallurgical industries, including steel slag, carbide slag, and copper slag (Yaxuan et al., 2022; Alkan et al., 2022; Lopez Ferber et al., 2022; Ortega-Fernández et al., 2019), highlighting the techno-economic benefits of their implementations. These benefits include wider temperature ranges of operation and significant cost reductions compared to the use of nitrite salts, as these residue materials have low to negligible costs (Ortega-Fernández et al., 2015). Among these alternatives, copper slag, derived from the pyrometallurgical process of copper extraction, has exhibited promising properties for applications in Packed-Bed Thermal Energy Storage (PBTES) (Calderón-Vásquez et al., 2021).

In Chile, where the copper industry is the main export of the country, the production of copper slag reaches significant volumes annually. Approximately, 5.6 million metric tons (MT) of copper are produced annually, of which 1.2 million MT correspond to copper from pyrometallurgy (COCHILCO, 2023). Roughly 2.2 tons of copper slag are generated per ton of copper extracted (Gorai et al., 2003), estimating an annual production of 2.64 million MT of copper slag in

Chile. Despite its abundance, this material has no further use after its production, posing a challenge for the mining industries.

The use of this industrial residue as filler material for PBTES has been shown to be an alternative with a high apparent specific heat capacity ranging from 0.9 to 1.45 [J/gK] in the study presented by Calderón-Vásquez et al. (2021). Additionally, this article assessed a 1-D model of a copper slag packed-bed, reporting high exergy efficiency results during long-term operation cycles. However, copper slag presents limited information regarding its performance at high temperatures for SHTES applications. Moreover, the application of the material "as received" presents challenges stemming from its heterogeneous characteristics, resulting in variability in its thermophysical properties.

In the following work, a statistical analysis of the variability of the specific heat capacity of copper slag is conducted, along with image analysis and chemical characterization of its main elements.

Material and methods

Material sampling

To analyse the specific heat capacity, copper slag rocks in their original state ("as-received") were ground to a suitable size for Differential Scanning Calorimetry

(DSC) analysis. After milling, the material was mixed and separated to obtain 12 random samples of copper slag. Additionally, a randomly selected sample of copper slag rock was polished for SEM/EDS analysis.

Characterization methods and data fitting

The specific heat capacity was determined using the dynamic method with a DSC PerkinElmer 600. The analysis spanned temperatures from 100°C to 450°C, with a heating rate of 20°C/min. Measurements were conducted under a nitrogen atmosphere with a flux of 50 ml/min, following the guidelines outlined in ASTM E-1269 and employing sapphire as a reference material. Thermal stabilization was achieved by subjecting each sample to three heating cycles, as described in Calderón-Vásquez et al. (2021), with data from the third cycle used for specific heat capacity analysis. Heat flux curves (baseline, reference, and sample) were processed using Python software and fitted to Equation 1 as specified in the ASTM standard for specific heat capacity estimation (c_p).

$$c_p = c_{p(st)} \frac{m_{st}(Q_b - Q_s)}{m_s(Q_b - Q_{st})} \quad (1)$$

In the equation, $c_{p(st)}$ represents the specific heat capacity of the standard reference material (sapphire), m_{st} denotes the mass of the standard reference material, m_s stands for the mass of the sample, and Q corresponds to the measured heat flux by the DSC in [mW]. Subscripts "b," "st," and "s" indicate the baseline, reference material, and sample, respectively.

For elemental composition, mapping, and Energy-Dispersive Spectroscopy (EDS) analysis, results were obtained using an Oxford Maxin Ultra 40 sensor coupled with Field Emission Scanning Electron Microscopy (FE-SEM; GeminiSEM 360).

Results and Discussion

Elemental composition, mapping and quantification

Figure 1 displays the SEM image captured for a sample of copper slag. The material exhibits a regular and compacted topography, with the presence of small grains in the upper half of the image. Furthermore, the elemental composition mapping depicted in Figure 2 indicates a relatively homogeneous distribution of identified elements, with few concentrated grains. Table 1 presents the EDS results corresponding to the spectra shown in Figure 1. Grains such as Spectre 1, Spectre 2, and Spectre 3 exhibit varying Fe compositions, which are inversely proportional to the Si percentage. Therefore, Spectre 1, identified and semi-quantified, is likely a silicate grain, whereas Spectre 3, with a significantly higher Fe percentage,

corresponds to an iron oxide grain. Regarding Spectre 6, which represents the mean value of the elements identified, a substantial percentage of Fe is evident. Overall, based on the image mapping and semi-quantification, it can be inferred that copper slag is predominantly composed of iron oxides and silicates, consistent with compositions reported in the literature (Gorai et al., 2003). However, for a more detailed composition analysis, additional chemical analysis methods should be employed, such as X-Ray Fluorescence (XRF).

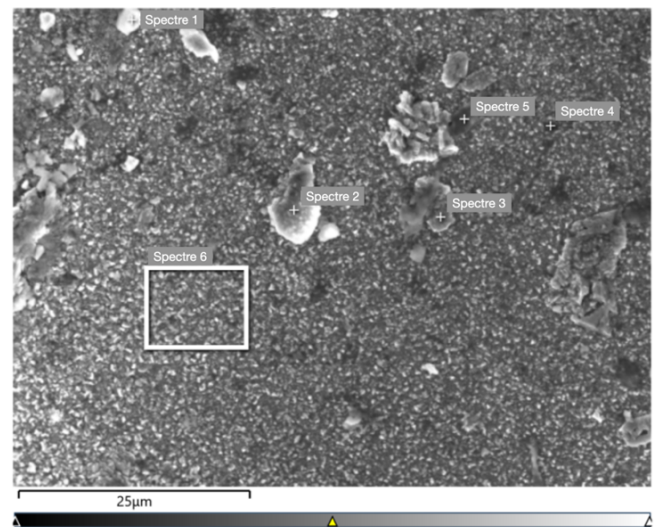


Figure 1: SEM image of copper slag sample.

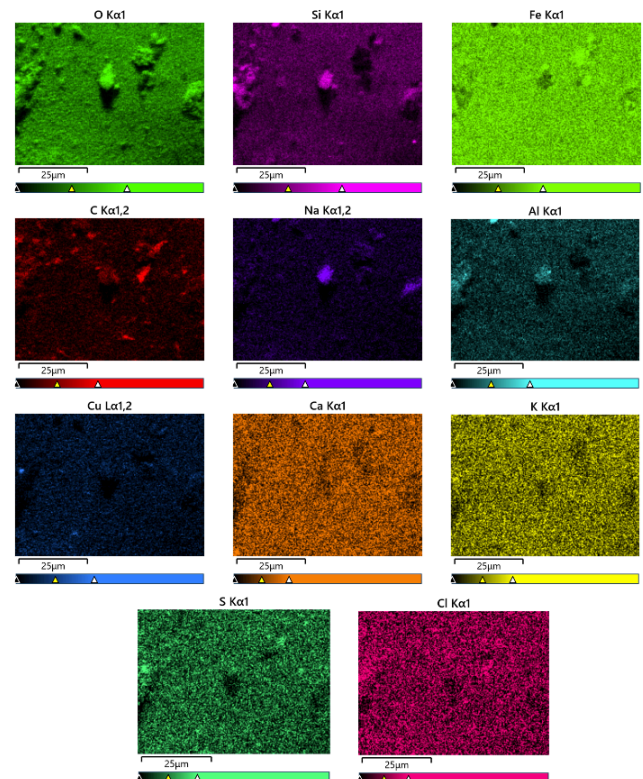


Figure 2: FE-SEM mapping of a copper slag sample.

Table 1: EDS semi-quantitative chemical analysis results of the different spectres points and area selected in Figure 1. Results marked in red are values with low reliability, as determined by the EDS software.

Element	Sp.1	Sp.2	Sp.3	Sp.4	Sp.5	Sp.6
O	45.7	38.7	21.2	28.4	19.9	25.3
Fe	4.0	26.0	72.3	44.0	38.7	53.8
Si	25.2	9.6	0.7	5.3	4.4	5.1
C	9.4	12.5	4.9	13.3	28.8	5.8
Al	8.5	1.4	0.3	1.0	0.7	0.9
Na	6.3	6.4	-	1.4	1.6	1.1
Ca	0.4	1.0	0.3	1.7	1.5	1.9
K	0.4	0.7	0.2	1.0	1.0	1.0
Cl	0.2	0.1	-	0.2	0.6	-
Cu	-	2.5	0.2	2.7	1.7	4.5
Pb	-	1.1	-	-	-	-
Mg	-	-	-	0.6	-	-
S	-	-	-	0.2	1.1	0.3
Ti	-	-	-	0.2	-	0.2

Specific heat capacity results and analysis

The results from DSC analysis are presented in Figure 3, illustrating the mean and standard deviation of specific heat capacity (c_p) curves across the temperature range from 100°C to 450°C. In the graph, the interquartile range of c_p results are highlighted in the yellow area, representing the range between the 25th and 75th percentiles. Notably, the interquartile range tends to increase with temperature, except for the data point at 450°C, where a slight decrease is observed. Examining the mean c_p curve, we observe a gradual increase from 0.67 [J/gK] at 100°C to 0.86 [J/gK] at 450°C. This increasing trend aligns with the expected behaviour for a thermally stable solid, indicating a greater capacity to store heat as temperature rises. The values obtained are consistent with those reported by Navarro et al. (2012). It's noteworthy that the standard deviation for each data point also rises with temperature, indicating a greater dispersion of data at higher temperatures. The standard deviation ranges from 0.13 [J/gK] at 100°C to 0.27 [J/gK] at 450°C, underscoring the increasing variability as temperature increases. Furthermore, the median curve is depicted alongside the mean curve. Interestingly, the median curve surpasses the mean curve from 100°C to 300°C, after which it declines and becomes lower than the mean curve. This asymmetrical distribution suggests a skewness in the data distribution, with a tendency towards higher values at lower temperatures and lower values at higher temperatures. Around 300°C, the distribution appears to be relatively symmetrical, indicating a more balanced and likely normally distributed dataset.

In general, the c_p behaviour of the copper slag samples exhibits a consistent increase with temperature, and the data can be accurately represented by a third-degree polynomial function. However, an interesting observation arises beyond 300°C, where the slope of the mean curve appears to decrease, suggesting a possible trend towards decreasing c_p values at 450°C.

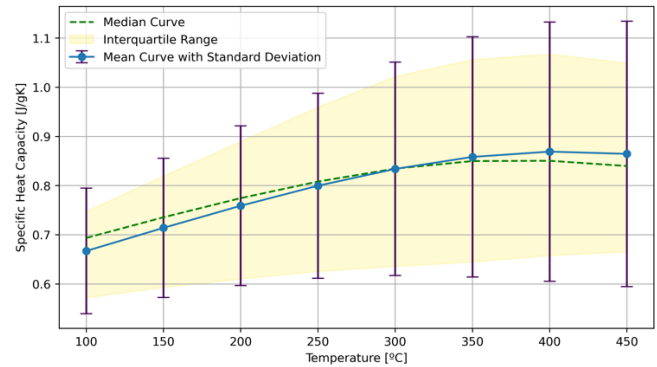


Figure 3: Specific Heat Capacity results for copper slag samples.

Conclusions

It is concluded that the copper slag samples analysed show an elemental composition in agreement with what is expected from the literature with a relatively large iron weight percentage. In terms of elemental composition, is relatively homogeneous. However, additional chemical analyses are required to gain deeper insights into its composition.

Regarding the results of specific heat capacity, although the values align with those documented for other copper slag and slag types in existing literature, it's important to highlight a significant variability, particularly evident with rising temperatures. This variability is likely attributed to the inherent heterogeneity of copper slag.

However, despite the dispersion of the data, the behaviour of the curves remains stable and can be effectively modelled using a third-degree polynomial function. Nonetheless, conducting an analysis at higher temperatures could provide further insights into the specific heat capacity behaviour of copper slag, potentially enhancing our understanding of its thermal properties across a wider temperature range.

Acknowledgment

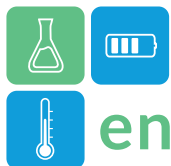
The authors thank the financial support from project ANID/FONDEF/ ID22110200 "RadTES-CS/Radial Packed-Bed Thermal Storage System Using Copper Slag as Storage Medium". A.I. Fernández also thanks the project PID2021-123511OB-C32 funded by



MCIN/AEI/10.13039/501100011033 and, as appropriate, by "ERDF A way of making Europe". The authors are also grateful to UTEM (Universidad Tecnológica Metropolitana) for FE-SEM and EDS measurements. In addition, V. Segovia would like to acknowledge the Doctoral Scholarship ANID-BECAS/Doctorado Nacional/21232013.

References

- Alkan, G., Mechnich, P., Lucas, H., Knoblauch, N., Sommerfeld, M., Flucht, F., Pernpeintner, J., Sergeev, D., Müller, M., & Friedrich, B. (2022). Assessment of Metallurgical Slags as Solar Heat Absorber Particles. *Minerals*, 12(2), 121. <https://doi.org/10.3390/min12020121>
- ASTM International. (s. f.). *ASTM E1269-11, Standard Test Method for Determining Specific Heat Capacity by Differential Scanning Calorimetry*. <https://doi.org/10.1520/E1269-11R18>
- Calderón-Vásquez, I., Segovia, V., Cardemil, J. M., & Barraza, R. (2021). Assessing the use of copper slags as thermal energy storage material for packed-bed systems. *Energy*, 227, 120370. <https://doi.org/10.1016/j.energy.2021.120370>
- COCHILCO. (s. f.). *Producción cobre de fundición mundial y Chile* [Microsoft Excel spreadsheet]. Recuperado 9 de noviembre de 2023, de <https://www.cochilco.cl/Paginas/Estadisticas/Bases%20de%20Datos/Producción-Minera.aspx>
- COCHILCO. (s. f.). *Producción cobre de mina mundial y Chile* [Microsoft Excel spreadsheet]. Recuperado 9 de noviembre de 2023, de <https://www.cochilco.cl/Paginas/Estadisticas/Bases%20de%20Datos/Producción-Minera.aspx>
- Gorai, B., Jana, R. K., & Premchand. (2003). Characteristics and utilisation of copper slag—A review. *Resources, Conservation and Recycling*, 39(4), 299-313. [https://doi.org/10.1016/S0921-3449\(02\)00171-4](https://doi.org/10.1016/S0921-3449(02)00171-4)
- Lopez Ferber, N., Al Naimi, K. M., Hoffmann, J.-F., Al-Ali, K., & Calvet, N. (2022). Development of an electric arc furnace steel slag-based ceramic material for high temperature thermal energy storage applications. *Journal of Energy Storage*, 51, 104408. <https://doi.org/10.1016/j.est.2022.104408>
- Navarro, M. E., Martínez, M., Gil, A., Fernández, A. I., Cabeza, L. F., Olives, R., & Py, X. (2012). Selection and characterization of recycled materials for sensible thermal energy storage. *Solar Energy Materials and Solar Cells*, 107, 131-135. <https://doi.org/10.1016/j.solmat.2012.07.032>
- Ortega-Fernández, I., Wang, Y., Durán, M., Garitaonandia, E., Unamunzaga, L., Bielsa, D., & Palomo, E. (2019). Experimental validation of steel slag as thermal energy storage material in a 400 kWh prototype. 200026. <https://doi.org/10.1063/1.5117741>
- Ortega-Fernández, I., Calvet, N., Gil, A., Rodríguez-Aseguinolaza, J., Faik, A., & D'Aguanno, B. (2015). Thermophysical characterization of a by-product from the steel industry to be used as a sustainable and low-cost thermal energy storage material. *Energy*, 89, 601-609. <https://doi.org/10.1016/j.energy.2015.05.153>
- Yaxuan, X., Huixiang, W., Yuting, W., Jinhua, Z., Haimeng, L., Qian, X., Xingxing, Z., Chuan, L., & Yulong, D. (2022). Carbide slag based shape-stable phase change materials for waste recycling and thermal energy storage. *Journal of Energy Storage*, 50, 104256. <https://doi.org/10.1016/j.est.2022.104256>



Stability Evaluation of Cation-exchanged Zeolites through Repeated Experiment of Heat Charging and Discharging

Seong-Eun Kim^{1,*}, Sung-Kook Hong¹, Kang-Hee Cho², Dae-Hun Chung¹, Si-Won Yoon¹, Duck-jae Wei¹
1 Korea Institute of Energy Research, Gajeong-ro, Yuseong-gu, Daejeon, 34129, Korea
2 In-ha University, Inha-ro 100, Michuhol-gu, Incheon, 22212, Korea
*se.kim@kier.re.kr

Abstract

In the application of thermal energy storage technology, the primary constraint is the energy density and stability of the thermal storage medium. It is very important to develop high-density materials with stable performance. Therefore, in the present study, Cation-exchanged zeolites containing lithium or magnesium have been developed. The Cation-exchanged zeolite with magnesium shows higher water adsorption and heat storage capacity. To test the material stability of the Cation-exchanged zeolite, a cycle test apparatus was set up and a total of 100 cycle tests were carried out. It was confirmed that the performance of the cation-exchanged zeolite was stable under this operating condition.

Keywords: Thermo Chemical Material, Thermal Energy Storage, Cation-exchange

Introduction

The key to achieving global carbon neutrality is the active utilisation of waste heat generated in the industrial sector. The total waste heat potential in the European Union is about 300 TWh/year, with about 60 % in the range of 100°C to 500°C. Effective reuse of this waste heat can save significant energy consumption. (Papapetrou, M and al., 2018) In order to effectively utilise waste heat, it is important to solve the inconsistency between time and space, and heat storage technology is required to solve this problem. What needs to be solved in thermal energy storage technology is to develop a heat storage material that is stable and has a high storage density. Therefore, research was conducted to confirm the stability of heat dissipation while improving the performance of zeolite-based heat storage materials. (S.Z, Xu and al., 2018; Huizhong, Z and al., 2020; Dongshuai, H and al., 2021) A zeolite material was developed to improve the heat storage density by cation exchange of lithium and magnesium, and its stability was evaluated by performing 100 cycles thermal charging and discharging tests.

Material and Test Equipment

The material used in the study was zeolite 13X, a bead with a diameter of 3 to 5 mm, purchased from Jisim Tech. (South Korea). Based on the base zeolite 13X, Cation-exchanged zeolite was prepared using magnesium nitrate and lithium nitrate from Sigma Aldrich (Germany). Thermal Gravimetric Analysis (TGA) and Differential Scanning Calorimetry (DSC) analyses were carried out to measure the basic desorption properties of the prepared zeolite.

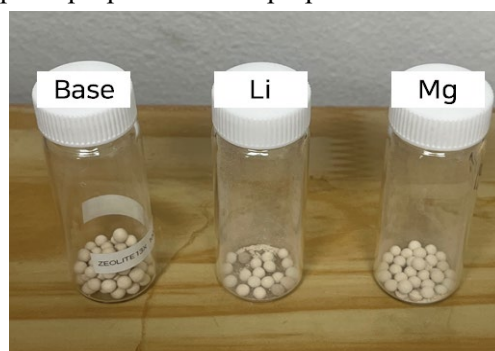


Figure 1, Base material and Cation-exchanged material

The equipment for testing the stability of the zeolite was constructed as shown in Figure 2. The repeatability test rig consists of a reactor, a buffer tank, a vacuum pump and a steam generator. A heat storage material was filled inside the reactor and the temperature and

pressure changes of the working fluid during the heat charging and discharging process inside the reactor were confirmed by a sensor. At that time, the experiment was carried out using a heater for heat discharging and a steam generator for heat charging. During the discharging (adsorption) process, steam of 120°C is supplied and adsorption occurs. During the charging (desorption) process, the temperature of 250°C and a vacuum atmosphere of 0.1 bar (abs) is maintained by means of a heater and a vacuum pump. The samples that had undergone 100 cycles of charging and discharging were analysed again by DSC and compared with the samples that had undergone 1 cycle.

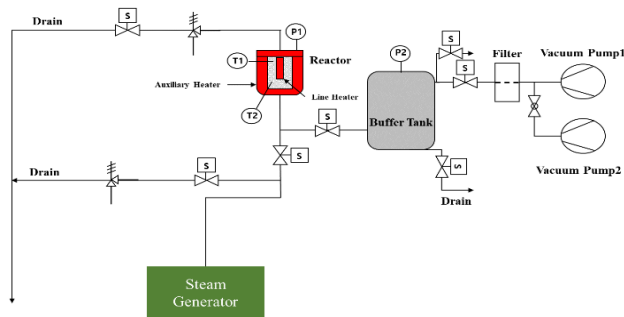


Figure 2, Equipment schematic diagram

Results and Discussion

Figure 3(A) shows the TGA profiles of zeolite 13X in different cation forms. These profiles indicate that most water molecules are desorbed below 573 K, with two step decreases observed at 353 K and 433 K. However, the extent of water desorption below 573 K varies depending on the cation type in zeolite 13X. For base zeolite 13X with Na^+ , the weight loss (corresponding to the percentage of water adsorbed) is about 21.0 wt%. Upon ion exchange with Li^+ , Mg^{2+} the weight loss is about 26.5% and 27.1%, respectively. This means two Cation-exchanged materials have absorbed more water. Figure 3(B) is the DSC results graph of zeolite materials after cation exchange with lithium and magnesium. The base zeolite 13X exhibits a distinct bimodal shape, indicative of uniform micropore sizes within the zeolite 13X. Zeolite materials exchanged with cations also displayed DSC curves similar to the base zeolite 13X, showing a bimodal shape. Meanwhile, it was observed that the heat storage capacity of the zeolite material Cation-exchanged with magnesium was improved compared to base zeolite 13X by 18%. (Youn. Y and al., under revision)

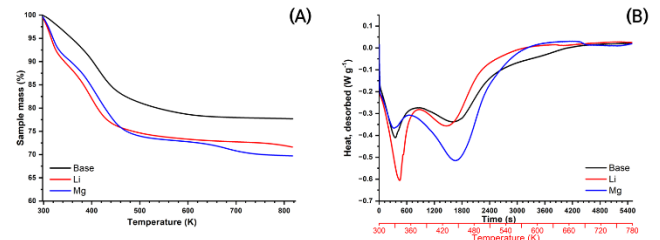


Figure 3, Isotherm graph and DSC result of the Cation-exchanged material (Youn. Y, under revision)

Figure 4 is a graph of the enthalpy ratio for base zeolite and cation-exchange zeolite with lithium, and magnesium, respectively. The enthalpy ratio is the ratio between the desorption calorific value after the 1 cycle and the desorption calorific value after the 100 cycles. The enthalpy change of the base zeolite 13X was measured to be within 99%, and it was confirmed that even in the case of the newly prepared ionized zeolite, it was slightly reduced to within 3 and 5% in the case of lithium and magnesium, respectively, showing stable performance.

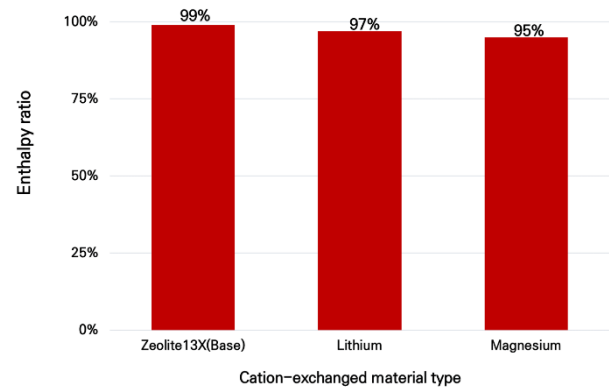
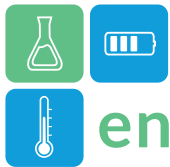


Figure 4, Graph of Enthalpy ratio for Cation-exchanged materials

Conclusions

To address better performance in heat storage system, high-density thermal storage materials were developed by using ionization. The lithium Cation-exchanged zeolite demonstrated advantages in low-temperature heat storage, while the magnesium Cation-exchanged zeolite proved to be suitable for high-temperature storage.

Cycling test rig was set up to evaluate the stability of the developed materials. DSC analyzed samples that had undergone 100 charging and discharging processes. In terms of enthalpy ratio, there is a slight difference of less than 5%, but it shows stable performance. In the near future, we plan to check the performance of



cation-exchanged zeolites in many more cycling tests under different operating conditions.

Acknowledgment

This material is based upon work supported by the research funding from Korea Institute of Energy Research (KIER) (project number GP2021-0020).

References

- Papapetrou, M. and al. (2018). Industrial waste heat: Estimation of the technically available in the EU preindustrial sector, temperature level and country, Applied Thermal Engineering, doi.org/10.1016/j.applthermaleng.2018.04.043
- S.Z, Xu. and al. (2018). A zeolite 13X/magnesium sulfate-water sorption thermal energy storage device for domestic heating, Energy Conversion and Management, doi.org/10.1016/j.enconman.2018.05.077
- Huizhong, Z. and al. (2020). Water sorption on composite material “zeolite 13X modified by LiCl and CaCl₂”, Microporous and Mesoporous Materials, doi.org/10.1016/j.micromeso.2020.110109
- Dongshuai, H. and al. (2021). Molecular dynamics study on water and ions transport mechanism in nanometer channel of 13X zeolite, Chemical Engineering, doi.org/10.1016/j.cej.2021.129975
- Youn, Y. and al. Significant Improvement of Adsorption Thermal Energy Storage of Zeolite by Simple Cation Exchange, Inducing Strong Polarization of Water, Journal of Energy Storage. (under revision)



Stability test of three different phase change material emulsions

Stefan Gschwander*

Fraunhofer ISE, Heidenhofstr. 2, Freiburg, Germany

*Corresponding author e-mail: stefan.gschwander@ise.fraunhofer.de

Abstract

Phase Change Material Slurries (PCMS) are mixtures of a carrier fluid and a dispersed PCM. This contribution reports on the development of three different PCM emulsions slurries (PCME) for the operation temperature ranges of 10 to 18 °C, 20 to 28 °C and 45 to 50 °C with the focus on the PCME stability tested under conditions close to those appearing in applications. Therefore, a hydraulic test system containing a centrifugal pump, plate type heat exchangers, membrane expansion vessel and several valves is used to circulate the PCME in a loop while it is heated above the melting and cooled down below the crystallization temperature range. To determine the stability frequently taken samples are analysed via laser diffraction on their particle size distribution and differential scanning calorimetry (DSC) is used to determine the effect of the cycling on the dispersed PCM's melting and crystallization behaviour. All tested PCME show within the 10000 tested cycles a high stability in particle sizes as well as in the phase transition behaviour.

Keywords: Thermal Storage, Phase Change Material Slurry, Emulsions, Stability

Introduction

PCMS and PCME in general are widely discussed to be used as heat carrier and storage fluid. Compared to other PCM solutions, PCMS offer the potential to be used in hydraulic grids like water but with higher heat storage and transport capacities within a defined temperature range. There is a lot of information on stability against separation of PCME but less for the stability under phase transition and shear stress which applies in a real hydraulic piping networks. (Zhang et al. 2021) for example described the development of PCM emulsions with particle sizes in the nanometre scale using hexadecane as the PCM. The stability was tested by cooling it down in an ice bath and then it was heated up again. The emulsion showed a high stability against separation applying this test. (Delgado et al. 2013) applied tests to a microencapsulated PCM slurry (mPCMS) using a rotational rheometer with a plate-plate geometry in oscillatory mode. She found an exponential relationship between creaming percentage and the elastic module. (Gschwander et al. 2021) applied also a rotational rheometer test to PCME where a cup-cylinder geometry was used to apply a defined shear rate to the emulsion while it was frequently heated and cooled above and below the melting and crystallisation temperature range. Particle size measurements with samples before and after the test revealed the stability of the emulsion. (Kong et al. 2017) made a field test using mPCMS with 6 to 11 % of microcapsules in water for a ground source heat

pump system. An improvement of coefficient of performance of up to 4.9 % and no significant degradation of the slurry during operation with more than 127,000 cycles was observed.

In this work a hydraulic test facility is used to study the degradation under phase transition and shear stress applied to the PCME.

Methodology

The test facility's hydraulic system, shown in Figure 1, has a fill volume of four litres for PCME. The PCME is cycled between two heat exchangers with the help of a centrifugal pump. So, in every circulation the PCE is once heated up above the melting and cooled down below the crystallization temperature range. In the experiments the volume flow is controlled to 150 l/h, so every hour 37.5 cycles are completed summarizing to 900 in a day. Temperatures are measured directly inside each in- and outlet of both heat exchangers by using Pt100 sensors, which are calibrated to an uncertainty of +/- 0.05 K, the volume flows are measured by using a magnetic inductive volume flow meter (Krone Optiflux 5000) with an accuracy of 0.15% for the measured value. Pressure drop is measured on the PCME side (secondary side) of the heat exchanger which is cooling the PCME to monitor blocking of the heat exchanger due to PCME degradation. The temperatures of the primary warm sides are controlled by a heater (Weinreich WTD) and

the cold side is controlled by using a thermostat (Huber Unistat 510). All data is acquired with a Keysight 34970A data acquisition system equipped with two 20 channel multiplexer modules 34901A for temperature, volume flow and pressure measurement and a multifunction module 34907A for controlling the pump, the heater and the thermostat.

The analyses of sample which are taken during the cycling test is done by enthalpy determination using a DSC Q2500 from TA-Instruments and the particle size distribution is measured by using the light scattering system LS13320 from Beckman Coulter.

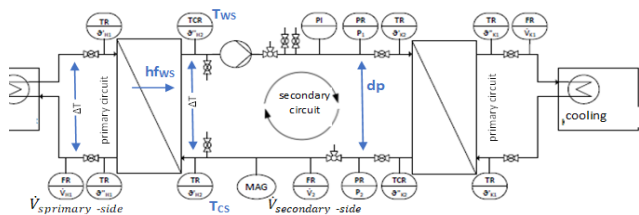


Figure 1: Schematic drawing of the hydraulic test facility to cycle the PCME.

The heat flow into the slurry is determined by the volume flow and temperature difference measured in the heating circuit since this circuit is operated by pure water which properties are well known. Earlier investigation using water also in the secondary loop showed no significant heat loss to the ambient due to the high efficiency of the heat exchangers and its insulation with 20 mm of Armaflex ($\lambda = 0.035$) in addition with a 20 mm polystyrol insulation ($\lambda = 0.032$) on top of the Armaflex.

Table 1 gives an overview over the investigated PCMEs. The labels indicate the temperature range of phase transition. As PCM 1-Octadecene from H&R, Parafol 18-97 from Sasol Wax and RT50 from Rubitherm was dispersed in a quantity of 35 wt.% each.

Table 1: The investigated emulsions. All Emulsions contain a fraction of 35 wt.% PCM. Phase transition includes both the temperature range of melting and the solidification.

Label	PCM	Phase transition range	Enthalpy not cycled / after cycling
Emu10-16	Octadecene	10 – 16 °C	47 kJ/kg / 42 kJ/kg
Emu20-28	Parafol 18-97	20 – 28 °C	76 kJ/kg / 74 kJ/kg
Emu45-50	RT50	45 – 50 °C	50 kJ/kg / 46 kJ/kg

Results and Discussion

Figure 2 to Figure 10 showing the results for all three tested emulsions with three figures for each emulsion:

The first shows the measurement data from the test facility, the second the particle size distribution determined for the samples taken from the test facility and the third figure shows the DSC results for the samples.

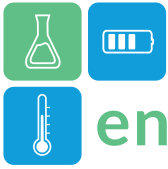
In the standard test procedure, the lower and upper temperature is controlled to be close to the temperature range of the dispersed PCM's phase transition. All tests were done with the target to reach 10,000 cycles, so each test was in operation over 11 to 12 days. The emulsions are rated as stable when the pressure drop measured over the heat exchanger which cools down the PCME is not changing during the test, when the particle sizes stay below $1 \mu\text{m}$ and when there is no continuous change of phase transition behaviour visible for the samples taken from the test facility.

In general, all experiments show no change in pressure drop which cannot be attributed to changes in the flow rate or to temperature variation caused by the control of the heat and cooling devices. Emu10-16 and Emu20-28 showing neglectable changes in particle size distribution for the samples taken (Figure 3, Figure 6). The phase transition behaviour shows minor changes between the untreated emulsion and the first sample taking from the test facility for all three PCME. During the test the phase transitions stay stable for all samples taken. The visible changes are due to variations in the water content, which can arise while applying the sample to the DSC crucible.

A closer look on the enthalpy results of Emu10-16 reveal that the supercooling is increased after it was applied to the test facility (Figure 10). This is indicated by a small shift of the crystallization curve to lower temperatures. But for the later samples it stays stable again.

Compared to Emu10-16 Emu20-28 shows two steps in the phase transition: The main between 20 and 23 °C and the second between 7 and 8 °C. This second phase transition is not visible in the bulk (not shown here) and becomes visible when the PCM is emulsified, due to the confined volume of PCM in the particles (Hagelstein and Gschwander 2017). As this second phase transition is at low temperature, it might not be accessible in many applications and the enthalpy in it is lost for the application.

Figure 8 to Figure 10 showing the results for the Emu45-50. The particle size is varying much more than for the other two emulsions, which indicates a less stable emulsion but since the particle size distribution stays below $1 \mu\text{m}$ and because it keeps constant after 2700 cycles it is also rated as stable. The enthalpy



curves show a bit more supercooling for the cycled samples than the non-cycled samples. Already the first sample taken from the test facility shows a bit more supercooling but compared to this, negligible changes are visible for the further samples taken. The enthalpy curve for the sample taken at 6300 cycles shows much bigger differences in comparison to the other samples and because samples taken later showing the same behaviour than the ones taken before it is rated as an

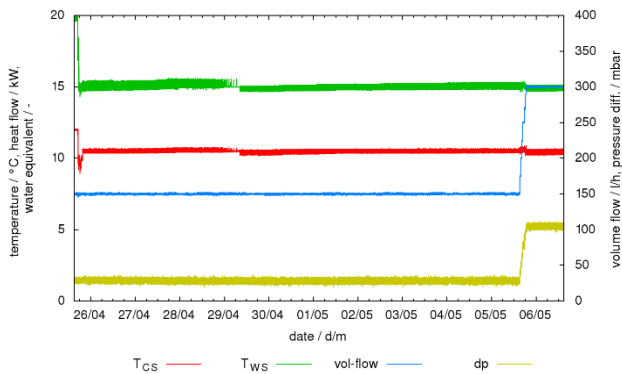


Figure 2: Temperatures, volume flow pressure drop measured during the experiment with a PCME containing 35 wt.% of Octadecene (Emu10-16).

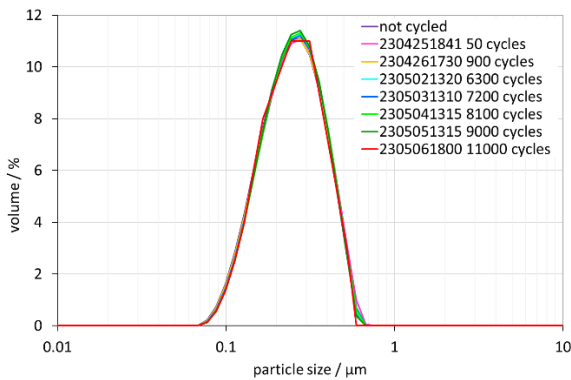


Figure 3: Development of the particle size distribution for the Octadecene emulsion (Emu10-16).

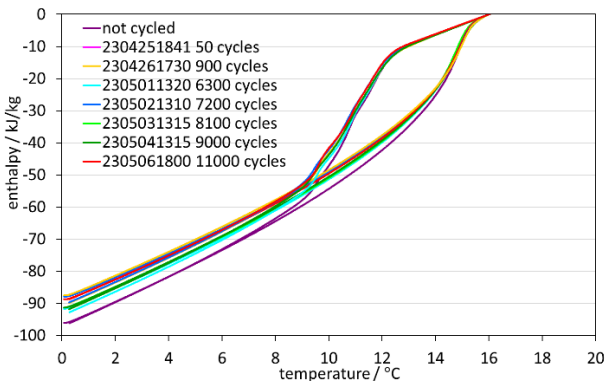


Figure 4: Enthalpy curves determined for the Octadecene emulsion samples taken during the test (Emu10-16).

outlier attributed to a nonstable DSC baseline. So, compared to the other two emulsions Emu45-50 shows a bit more variations in particle sizes and in supercooling. But together with the result of the particle size measurement the emulsion can be stated also as stable.

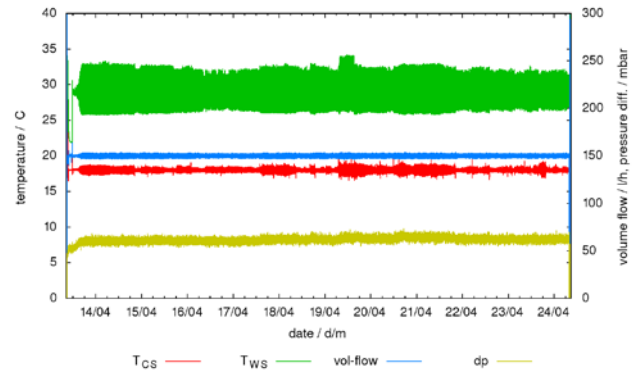


Figure 5: Temperatures, volume flow pressure drop measured during the experiment with a PCME containing 35 wt.% of Parafol 18-97 (Emu20-28).

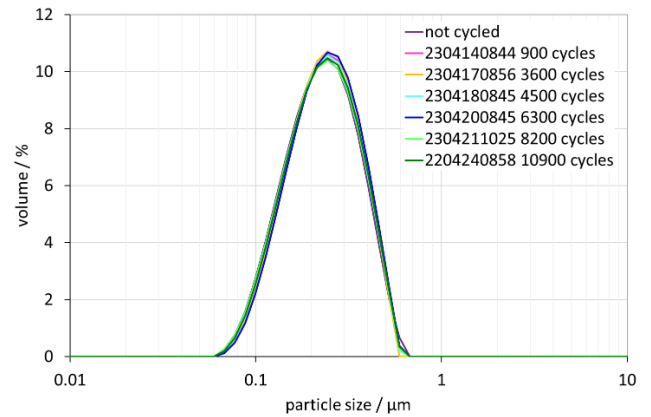


Figure 6: Development of the particle size distribution for the Parafol 18 emulsion (Emu20-28).

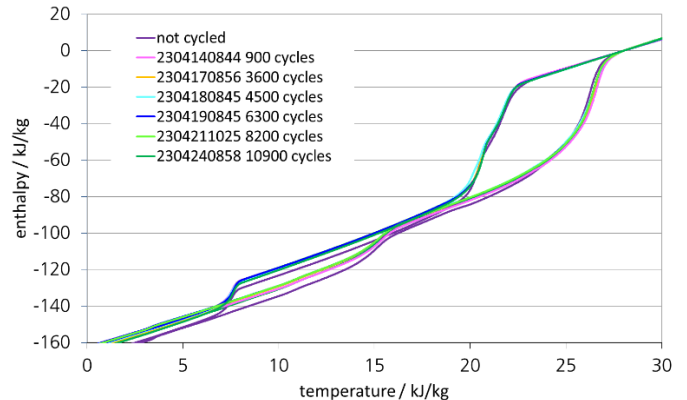


Figure 7: Enthalpy curves determined for the Parafol 18 emulsion samples taken during the test (Emu20-28).

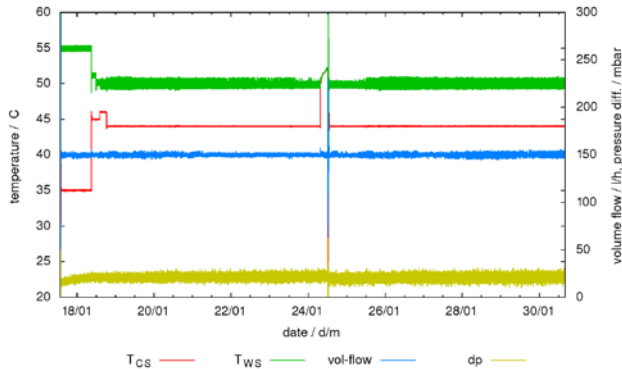
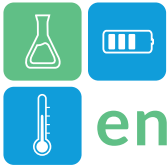


Figure 8: Temperatures, volume flow pressure drop measured during the experiment with a PCME containing 35 wt.% of RT50 (Emu45-50).

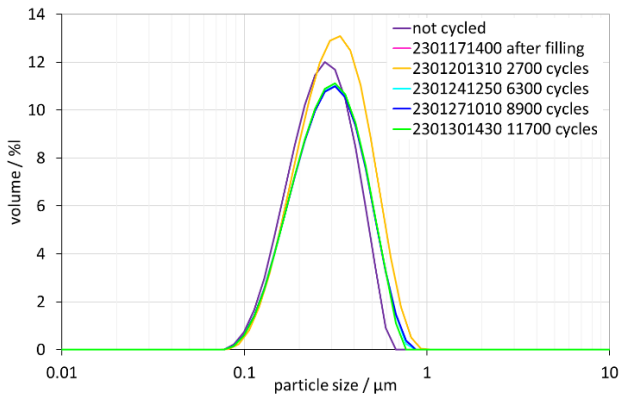


Figure 9: Development of the particle size distribution for the RT50 emulsion (Emu45-50).

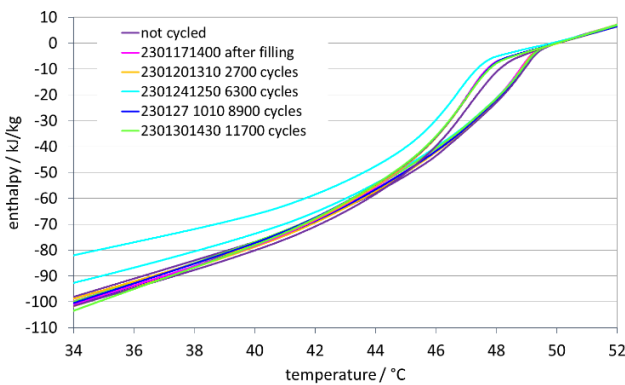


Figure 10: Enthalpy curves determined for the RT50 emulsion samples taken during the test (Emu45-50).

Conclusions

Three different PCME have been tested in a hydraulic test facility under conditions close to those arising in

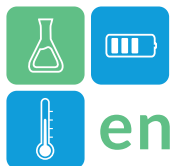
applications. The PCME are containing different PCMs with different melting temperatures. All three PCME are designed to be used withing small temperature ranges and therefore they are tested in temperature ranges which are close to the phase transition ranges of the emulsified PCMs. All three PCME were tested on their stability by applying at least 10,000 cycles which contain the phase transition but also high shear rates due to the circulation in the hydraulic loop. Even though all three emulsions can be considered as stable, Emu10-16 and Emu20-28 show hardly any changes in particle size and enthalpy curves, while Emu45-50 shows somewhat greater variations in particle size.

Acknowledgment

The Author is grateful for the funding of the project Optimus by the German Federal Ministry for Economic Affairs and Climate Protection. Many thanks also to the project management organization Jülich (PtJ) for their administrative support.

References

- Delgado M, Lázaro A, Peñalosa C, Mazo J, Zalba B, 2013. Analysis of the physical stability of PCM slurries. *International Journal of Refrigeration*, 36 (6), 1648–1656.
- Gschwander S, Niedermaier S, Gamisch S, Kick M, Klünder F, Haussmann T, 2021. Storage Capacity in Dependency of Supercooling and Cycle Stability of Different PCM Emulsions. *Applied Sciences*, 11 (8), 3612.
- Hagelstein G, Gschwander S, 2017. Reduction of supercooling in paraffin phase change slurry by polyvinyl alcohol. *International Journal of Refrigeration*, 84, 67–75.
- Kong M, Alvarado JL, Thies C, Morefield S, Marsh CP, 2017. Field evaluation of microencapsulated phase change material slurry in ground source heat pump systems. *Energy*, 122, 691–700.
- Zhang X, Niu J, Wu J, 2021. Evaluation and manipulation of the key emulsification factors toward highly stable PCM-water nano-emulsions for thermal energy storage. *Solar Energy Materials and Solar Cells*, 219, 110820.



Study of solid-state transition kinetics of supercooled neopentyl glycol by infrared thermography

Jean-Luc Dauvergne^{1,*}, Sergio Santos-Moreno^{1,2}, Elena Palomo del Barrio^{1,3}

1 Centre for Cooperative Research on Alternative Energies (CIC energiGUNE), Basque Research and Technology Alliance (BRTA), Alava Technology Park, Albert Einstein 48, 01510 Vitoria-Gasteiz, Spain

2 TECNALIA, Basque Research and Technology Alliance (BRTA), Parque Tecnológico de San Sebastián, 20009 Donostia-San Sebastián, Spain

3 Ikerbasque, Basque Foundation for Science, 48013 Bilbao, Spain

*Corresponding author e-mail: jldauvergne@cicenergigune.com

Abstract

Compact and cost-effective thermal energy storage (TES) systems can leverage the characteristics of plastic crystals, including their solid-solid transitions, high latent heat, and tuneable transition temperatures. For this reason, plastic crystals have been widely investigated in the past. However, their kinetics of phase transition and the influence of the processing on this key parameter for assessing the discharging rate of these systems remains underexplored. This study presents an infrared thermography-based approach to quantify this parameter but also to better understand the phenomena driving the solid-solid transitions.

Keywords: Solid-solid phase change material, Neopentyl glycol, Kinetics of transition, Supercooling, Infrared thermography

Introduction

Latent heat thermal energy storage (LHTES) offers a suitable compromise between energy storage density, maturity of the technology, and cost compared to sensible and thermochemical storage. LHTES uses storage materials absorbing or releasing heat by a phase change process, often from solid to liquid but also from a solid phase to another solid phase. The main advantage of solid-solid PCMs over liquid-solid PCMs is that they do not leak, allowing the design of much cheaper storage systems as there is no need for heat exchangers or macro-encapsulation solutions.

Among the phase change materials (PCMs) with solid-solid transitions, plastic crystals (Timmermans, 1961) show a great potential due to their high latent heat and adjustable temperatures of transition. In this category, neopentyl glycol, pentaglycerine, and pentaerythritol have been widely studied due to their high potential for LHTES (Chandra, 2002; Benson, 1986). However, neither the kinetics of the phase transitions of these materials, nor the impact of the processing method on these kinetics have been previously studied.

In this study, the effects on the phase transition kinetics of pressing and casting, two common processing methods, are evaluated for the neopentyl glycol (NPG) by using an infrared thermography-

based approach. Two solid phases are reported for this plastic crystal, also known as 2,2-Dimethyl-1,3-propanediol, the low temperature ordered crystalline phase (monoclinic) and the high temperature disordered plastic phase (face-centered cubic). As this plastic crystal can present on the order of 10 °C of subcooling, i.e., its phase transition during cooling is lower than the theoretical phase transition temperature, the kinetics of transitions were studied and quantified at different degrees of subcooling.

Material and methods

Materials

Neopentyl Glycol (99% of purity) was supplied by Merck (St. Louis, Missouri, USA) and used as received. The main properties of this plastic crystal are shown in Table 1.

Table 1: Main properties of Neopentyl Glycol (Serrano, 2019).

Formula	Phase transition temperature (onset, °C)	Mass-specific enthalpy (kJ/kg)	Degree of supercooling (°C)
C ₅ H ₁₂ O ₂	41	126	ca. 7 (measured for the samples used of this study)

Pellet-shaped samples of NPG were produced following two different protocols, by pressing (denoted “Pressed” in the following) and by casting

(denoted “Casted” in the following), to evaluate a possible impact of the preparation method on the results:

- Pressing: the raw PCM was hand ground using a mortar and a pestle. The obtained powder was then pressed using a manual uniaxial press (5 tons for 30 seconds) and a pellet die (\varnothing 2 cm). The mass and thickness of the samples were ca. 0.4 g and ca. 1.4 mm, respectively (Figure 1, left).
- Casting: NPG samples were prepared by melting / solidification of the PCM. A high temperature gasket of the desired thickness (ca. 1.4 mm) was notched, placed on a hot plate maintained at a temperature above the melting temperature of the NPG (>130 °C) and covered with a glass slide. The powdered Neopentyl Glycol was then deposited in contact with the joint notch and the capillary forces induced by the presence of the glass slide allowed the progressive filling of the joint by the molten NPG. When the seal was totally filled, the hot plate was switch off, and the sample cooled freely. After crystallization of the NPG, the set sample/joint was detached from the plate and the pellet was separated from the joint (Figure 1, right).



Figure 1: Samples obtained by pressing (left) and casting (right).

Methods

An experiment for studying the kinetics of phase transition (see Figure 2) consists in placing the pellet-shaped NPG samples in subcooled state underneath an infrared camera (cooled InSb FLIR A6752sc configured for data acquisition in the calibrated temperature range -20 °C to 55 °C, spatial resolution of 48 μm by pixel), activating the phase transition with an external solicitation (e.g., cold finger) and observing their thermal behaviours in the infrared spectrum. Accurate thermal regulation of the samples was insured using a heat exchanger (aluminium, 4 cm x 4 cm) connected to a refrigerated / heating circulator (Julabo 601F, temperature stability of ± 0.03 °C). To mitigate background effects and parasitic environmental infrared reflections, the heat exchanger was black painted with a high emissivity graphite coating (Kontakt Chemie Graphit 33, CRC Industries Deutschland GmbH).

To activate the plastic to crystal transition, a “L-shaped” arm (stainless steel), thermally regulated at a lower temperature than the subcooled NPG, was used. The arm was fixed to a stepper motor (400 steps per revolution without delay to minimize the impact duration). The end of this arm was welded to obtain a spherical shape and thus reduce the impact area on the sample. To regulate the temperature of the arm, the latter was partly immersed (i.e., excluding its tip to prevent droplets from being projected on impact) in a bath of water. The temperature of the water, and therefore of the arm, was regulated to reach 10 °C at the arm’s tip (temperature monitored thanks to a type K thermocouple inserted in the welding) using a heat exchanger immersed in the bath. This heat exchanger was connected to a second refrigerated / heating circulator (Julabo 1000F, temperature stability: ± 0.03 °C).

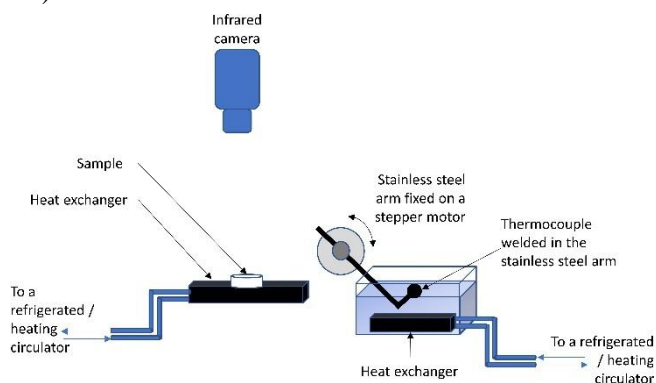


Figure 2: Sketch of the experimental setup.

During the first step of the experimental protocol the sample was heated up above its crystal to plastic transition temperature (55 °C in this work for a crystal to plastic transition temperature of ca. 40 °C), and then cooled down ($2\text{K}/\text{min}$) and stabilized (10 minutes) at a chosen temperature below the same transition temperature (sample in subcooled state, from 34 to 38 °C in 1 °C steps in this work). In the second step, after sample temperature stabilization, the transition from plastic to crystal phase was initiated by locally cool down the sample thanks to the cold “L-shaped” arm. It should be noted that during some randomly chosen experiments, samples were preliminary impacted, 2 to 3 times, by the end of the arm maintained at a higher temperature than the sample. During this verification step, it was never possible to activate the phase transition, which shows that the mechanical impact alone does not play a role in this activation but that it is induced by the local

cooling. An experiment ended when the complete transition of the sample has been observed.

Finally, postprocessing of the obtained infrared data was carried out using an ad-hoc algorithm to automatically identify the plastic to crystal transitions areas and/or interfaces. This sequential algorithm, developed with GNU Octave 6.3.0 (Eaton, 2020) and its image processing toolkit (“image package” 2.12.0), can be summarized as follow:

1. For each image of the infrared movie, a disc-shaped mask was applied to separate the cylindrical sample from its background: all values outside the mask are then removed from the processing.
2. By applying a threshold, the image was binarized and the isolated pixels were removed.
3. Using the remaining pixels as a mask (label), corresponding raw values recorded by the infrared camera can be extracted and post-processed. The GNU Octave function “regionprops” allows to retrieve useful properties from this label as its surface (in pixels), its boundaries or its centre of mass to convert it in equivalent disk as used in the following.
4. Knowing the acquisition frequency of the infrared camera and the radii of the equivalent circles (converted from pixels to mm) at two distinct times, corresponding transition kinetic can be calculated.

The different steps of the algorithm are illustrated in Figure 3.

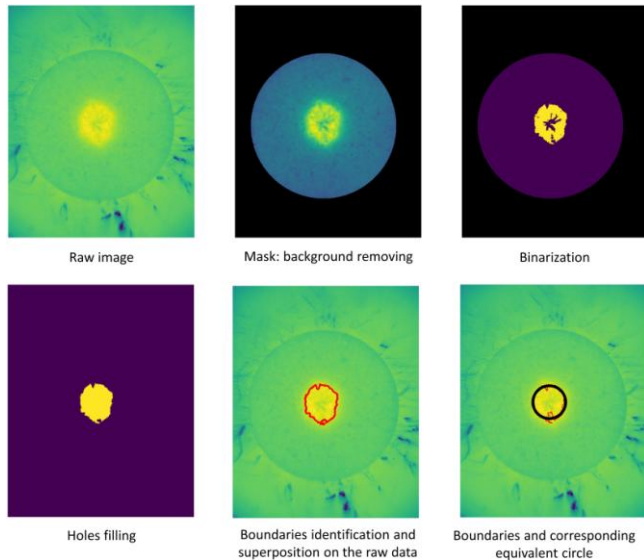


Figure 3: Illustration of the main steps of the algorithm developed to retrieve the transition kinetics.

The accuracy of the automatic detection of areas / interfaces have been checked by superposition of the raw data and the results from the algorithm with the naked eye.

Results and discussion

Following the experimental protocol detailed in the previous section, phase transitions of the casted and pressed samples were recorded at different subcooling temperatures. Figure 4 shows an example of the obtained infrared data.

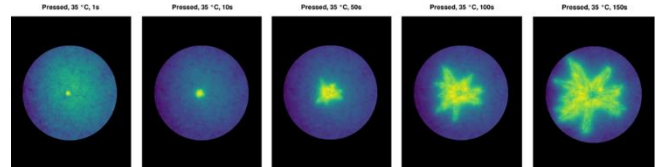


Figure 4: Transition evolution for a pressed sample stabilized at 35 °C. Recorded images, with background subtraction, at 1, 10, 50, 100 and 150s after arm impact.

Figure 5 presents the time evolutions of the plastic-crystal interface (equivalent circle radius) while corresponding velocities are summarized in Table 2.

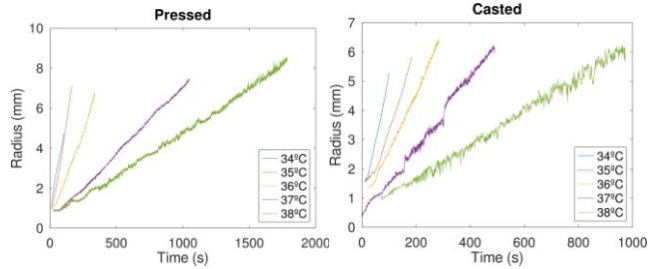


Figure 5: Temporal evolution of the plastic-crystal interface (equivalent circle radius) for samples maintained at different temperatures: Pressed samples (left); Casted samples (right).

These results show the clear impact of the degree of subcooling on the velocity of transition: the latter increases drastically with the degree of subcooling. It should be noted that at the lowest temperatures (highest degrees of subcooling), quantifications are less accurate as the time to perform the tracking is greatly reduced. The second important concerns the process used to produce the samples. Thus, the measured velocities of the casted samples are generally slightly higher than those of the pressed ones, but with differences of the order of uncertainties.

Table 2: Kinetics of plastic to crystal transitions for both pressed and casted samples at different temperature of the sample.

Sample	Temperature of the sample (°C)	Kinetics of plastic to crystal transition (mm/s)
Pressed	34	0.037
Pressed	35	0.042
Pressed	36	0.018
Pressed	37	0.007
Pressed	38	0.004
Casted	34	0.043
Casted	35	0.026
Casted	36	0.020

Casted	37	0.012
Casted	38	0.006

If the results obtained show that infrared thermography is a powerful tool for quantifying the kinetics of transitions of solid-solid phase change materials such as plastic crystals, more information can be retrieved. Thus, complementary information among which the evolution of a temperature profile on the radius of a sample over time can be obtained. To do so, a rigorous prior calibration must be carried out to accurately convert the raw radiometric data from the infrared camera into sample surface temperatures. Figure 6 illustrates two experiments, with both pressed and casted samples impacted at a stabilized temperature of 36 °C.

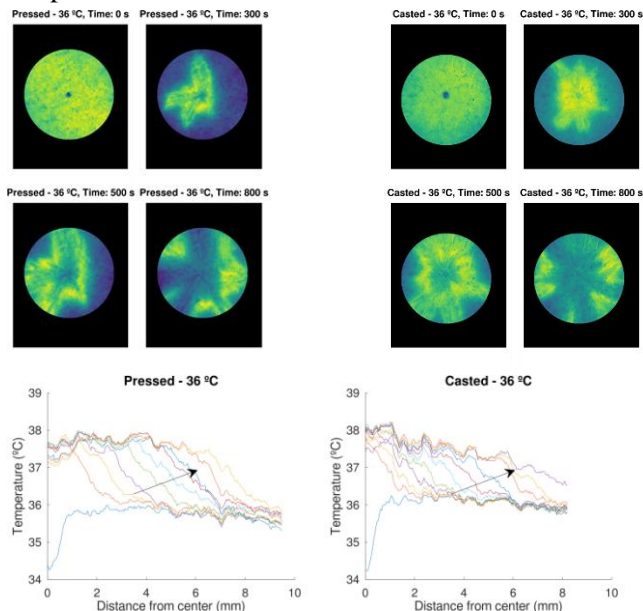


Figure 6: Top: Infrared raw data recorded a time 1, 300, 500 and 800 s after the arm impact. Bottom: Profiles of temperatures along a radius of the samples (36 °C) during the first 300 s of the experiment. Plots are equally spaced in time (32 s). Black arrows indicate the time evolution: Left) Pressed samples; Right) Casted samples.

The first profile (1s after the arm impact, blue curve in Figure 6) shows the local cooling of the sample due to the cold impact. It can be noted that the measured temperature is already higher than the arm due to the immediate start of the transition after impact (at $t=0$ s). Afterwards, the temperature at the impact point increases to reach a temperature (ca. 38 °C) close to the crystal-plastic transition temperature (ca. 40 °C), but slightly lower due to a competition with both heat losses with the environment and the heat exchanger always maintained at a lower temperature than this transition temperature. Over time, the temperature along the radius increases up to the transition

temperature from near to near until it reaches the border of the sample. Naturally, when the transition is completed locally (first at the point of impact and then from near to near), the local temperature decreases to reach the temperature of the heat exchanger.

Conclusions

This study shows the suitability of using infrared thermography to quantify the phase transition kinetics of solid-solid PCMs-based LHTES.

For NPG, we show that the kinetics of phase transition from the disorder phase to the crystalline phase are strongly dependent on the degree of subcooling, increasing from 0.006 mm/s approx. at low subcooling (38 °C), to 0.04 mm/s approx. at 34 °C. In addition, the performed study indicates that the preparation method (casting vs. pressing) has no significant effect on the kinetics of phase transition.

This study paves the way for a generalization of the proposed approach to other solid-solid PCMs, their mixtures, the raw material used (e.g., grain size) or to quantify the effects of additives.

Acknowledgment

The research was funded by the Department of Economic Development, Sustainability and Environment of the Basque Government (Programa Elkartek 2023, KK-2023/00063).

This research was funded by: FEDER/Ministerio de Ciencia e Innovación – Agencia Estatal de Investigación, SWEET-TES project (RTI2018-099557-B-C21).

References

- Timmermans, J. (1961). Plastic crystals: a historical review. *Journal of Physics and Chemistry of Solids*, 18(1), 1-8. doi.org/10.1016/0022-3697(61)90076-2
- Chandra, D., and al. (2002). Heat capacities of “plastic crystal” solid state thermal energy storage materials. doi.org/10.1524/zpch.2002.216.12.1433
- Benson, D. K., and al. (1986). Solid state phase transitions in pentaerythritol and related polyhydric alcohols. *Solar Energy Materials*, 13(2), 133-152.
- Serrano, A., and al. (2019). Neopentyl glycol as active supporting media in shape-stabilized PCMs. *Materials*, 12(19), 3169.
- Eaton, J. W., and al. (2020). GNU Octave version 6.1. 0 manual: a high-level interactive language for numerical computations. URL <https://www.gnu.org/software/octave/doc/v6.1>.



Study on Estimation of Time-Specific CO₂ Emission Factors and New Operation of Thermal Energy Storage System.

Haruki YAMANASHI¹, Masaya NISHIKAWA, PhD²

¹ Graduate Student, Department of Architecture, Tokyo Denki University

² Associate Professors, Department of Architecture, Tokyo Denki University

*Corresponding author e-mail: yamanashi.env@gmail.com

Abstract

This study reports on the estimation of time-specific CO₂ emission factors and the new operation of a TES system. The purpose of this study was to calculate more accurate CO₂ emissions and to examine the effective use of excess power generated by VER. First, we identified the amount of electricity generated by each power generation method in Japan to determine the prevalence of VRE. Next, to analyse the trend in each region, we defined the time-specific CO₂ emission factors based on the amount of electricity generated and the amount of fuel consumed and clarified the trend of TSCE factors. In addition, a comparison of energy consumption trends of building uses was made to examine the effect of the TSCE factors on the CO₂ emissions of building uses. Then, estimates were made regarding the operation of buildings with TES systems. As a result, it was found that direct feed operation during the daytime has the potential to reduce CO₂ emissions.

Keywords: CO₂ emission factor, Thermal storage tank, Renewable energy, Excess power

1. Introduction

1.1. Introduction

Renewable energies become increasingly widespread to realize a decarbonized society, and the expansion of solar power generation is particularly remarkable in Japan. The reduction effect of fossil fuel consumption by solar power generation facilities is reflected in the CO₂ emission factors calculated by each electric utility company in accordance with the law [1], but this value is based on an annual average. On the other hand, solar power generation is a variable renewable energy (VRE) which generation volume changes depending on weather conditions. In other words, the ratio of VRE to total electricity generation is fluctuating from time to time, and CO₂ emission per unit of electricity are also changing. Therefore, the amount of CO₂ emitted by a building during operation can be more accurately estimated, by determining CO₂ emission factors that accounts for the variability.

In this study, we attempted to calculate time-specific CO₂ emission factors (hereinafter denoted as TSCE factors) that take variability into account, for estimating more accurate CO₂ emissions from buildings. Specifically, the TSCE factors were calculated by examining the amount of electricity generated by each power source at each time of day. Then, for the purpose of determining the actual CO₂ emission trends of buildings, we estimated the hourly CO₂ emissions for

several building uses by applying TSCE factors. In addition, with a view to utilizing the data for building facility operation, a model building with thermal energy storage (TES) was set up to investigate the impact of heat source operational differences on CO₂ emissions from the building.

1.2. Survey of Power Generation Status

Figure 1 shows the annual trends in power source composition in Japan, and CO₂ emissions from power generation. Since FY 2016, total electricity generation and CO₂ emissions have been on a decreasing trend. CO₂ emissions have decreased by 29%.

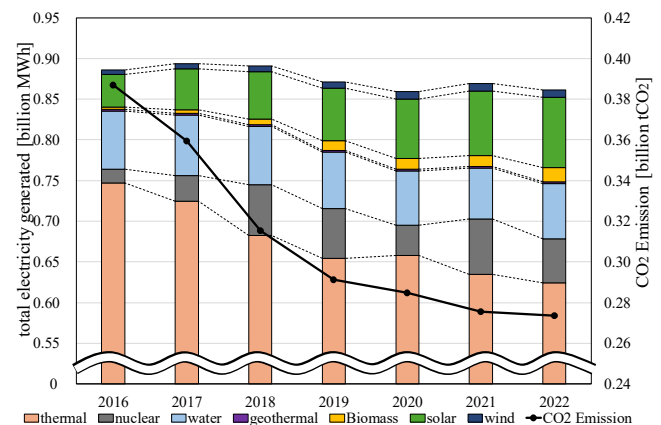
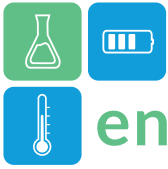


Figure 1 the annual trends in power source composition including the source of thermal power, and CO₂ emissions in Japan.



It's because the ratio of renewable energy has increased. For example, solar power generation increased by 56% and has been on an increasing trend throughout the period.

2. Methodology

2.1. CO₂ Emission Factor of Thermal Power Generation

The top 11 electric power companies account for about 80% of thermal power generation in Japan, and they publish annual totalized values of fuel consumption and power generation related to thermal power generation. Therefore, in this study, we calculated the annual average CO₂ emission factors for thermal power generation based on the data from these companies. The calculation formula is shown in Equation (1).

$$\alpha_{CO_2} = \frac{\sum(F_n \cdot E_n)}{T_n} \quad (1)$$

Where α_{CO_2} is CO₂ emission factor of thermal power (kgCO₂/kWh); F_n is annual totalized fuel consumption (kg,L,m³/year); E_n is emission factors by fuel (kgCO₂/kg,L,m³); T_n is annual total generation from thermal power (kWh/year).

2.2. Calculation of TSCE Factors

TSCE factors were calculated based on actual supply and demand data [2] published by electric utility companies in each region. The data consisted of area demand by time of day and power generation by source (nuclear, thermal, Water, geothermal, biomass, solar, wind, pumped storage, and connection lines). Connection lines that interconnect different region are excluded from the total power generation of the receiver. We calculated the factors using the sender's data with reference to the law[1]. In addition, only thermal power generation was assumed to emit CO₂, and the calculation was performed using Equation (2).

$$\beta_{TCO_2} = \frac{(T_m \cdot \alpha_{CO_2})}{G_m} \quad (2)$$

Where β_{TCO_2} is TSCE factors (kgCO₂/kWh); T_m is thermal power generation at time-m (kWh/h); G_m is total amount of electricity generated at time-m (kWh/h).

2.3. Analysis Method and Conditions

2.3.1. Analysis conditions of TSCE factors

Japan is an East Asia country comprising archipelago over 3,000 km along the Pacific coast. which makes it possible to observe a wide range of meteorological. Environmental standards in Japan are divided into eight categories [3]. This study calculated annual average CO₂ emission factors for each region and compared trends. Next, we analysed monthly CO₂ emission factor trends and TSCE factor trends focuses on the area including Tokyo.

2.3.2. Trend Analysis by Building Use

In calculating the CO₂ emissions by building use when considering the TSCE factors, Tokyo was selected as representative region based on the power source composition and climate characteristics. Data for energy use of buildings was referenced from DECC [4]. The building use categories were set as offices, commercial buildings, and hospitals. The area classification was 10,000m² or more. CO₂ emissions were calculated by multiplying the hourly power consumption by the TSCE factors. The highest and lowest factor's days were selected in the month as the conditions for comparison. The highest is the day with the largest ratio of thermal power generation in a day, and the lowest is the day with the lowest TSCE factor recorded in each month. In addition, we compare these days to annual average factors [5].

2.3.3. Comparison of TES Operations

One university in Tokyo was used as the model building. Table 1 shows an overview of the system. The main hours of use are from 8am to 10pm. Refer to the FY2022 operational results, a comparison was made between 2 cases. One case is that the heat load is treated with the heat stored in the nighttime TES operation (10pm-8am), and another case is that all the heat is treated in the daytime by direct feed operation (8am-10pm). In making comparison, the remaining heat in TES was excluded from the calculation, and the heat source system COP was simply assumed from outdoor air condition and heat source load rate. The evaluation was set on a sunny day in May, as it has the lowest TSCE factors.

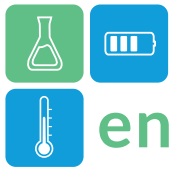
Table 1 Building and TES system Outline

TES	Capacity [m ³]	Thermal capacity [MJ]	Total floor area[m ²]
chilled water	1,559.0	72,140	101,100
hot water	919.1	13,500	

3. Results

3.1. TSCE Factors

Figure 2 shows Comparison of the annual average of TSCE factors and published factors in FY2022. When compared to the published factors, we can confirm that the difference is less than 10% except Kansai and Shikoku. The Tokyo region generated the largest amount of electricity, with average annual TSCE factor of 0.454. The Kansai region has the lowest TSCE factor at 0.299 because it uses nuclear power generation in addition to renewable energy. The Kyushu region has the highest ratio of non-thermal power generation to total power generation. The monthly power source composition ratio and monthly average TSCE factors are shown in Figure 3.



The month with the largest share of solar power generation is May, and the monthly average TSCE factor in May is the lowest. The power source composition ratio and TSCE factor are shown in Figure 4. The time with the highest ratio of non-thermal power generation was 11am on May 4, recording 63.1%. The time with the lowest TSCE factor was also the same time, recording 0.173. TSCE factors were classified by 0.01 unit, and the frequency of occurrence of the factors and the percentage of each month are shown in Figure 5. 0.30 and lower values accounted for about 11.8% of the total, of which about 47.4% were spring values. The highest frequency was 0.44. The trend of the power source composition, solar radiation, and TSCE factors on a representative day is shown in Figure 6. In the case of rainy weather, the TSCE factors exceeds the annual average factor for 21 hours, while it is 12 hours in the case of sunny weather. In addition, the TSCE factors decreases during the daytime as the amount of solar power generation changes, with a larger decrease in the factors when solar radiation is higher.

3.2. Trend of CO₂ Emissions by Building Use

The trend of average power consumption per unit area and CO₂ emissions are shown in Figure 7. When calculating using published values, the trend is the same as for electricity consumption because the values do not change during the day and night. In the case of the high-trend TSCE factors, CO₂ emissions do not decrease during the daytime, so the trend is similar to the published value. The TSCE factors is higher than the published value for most of the time, so the daily CO₂ emissions are higher than the published value. At the low-trend TSCE factors, the factors drop significantly at noon, and CO₂ emissions are lower than published values. In addition, offices show little difference in electricity consumption throughout the year, but CO₂ emissions decrease in March, April, and May, which is related to the TSCE factor. In winter, offices' emissions tend to increase in the morning and evening, and the same is true for hospitals. On the other hands, department stores and supermarkets' emissions are highest in the evening throughout the year.

3.3. The Comparison of TES Operations

The results for a representative day are shown in Figure 8. The cumulative CO₂ emissions for nighttime TES operation was 7.37[kg CO₂/day], while the cumulative CO₂ emissions for direct feed operation was 6.94 [kg CO₂/day], a decrease of about 6%. In direct feed operation, daytime CO₂ emissions increase more slowly than in the nighttime TES operation. This is because the TSCE factors is lower during the daytime.

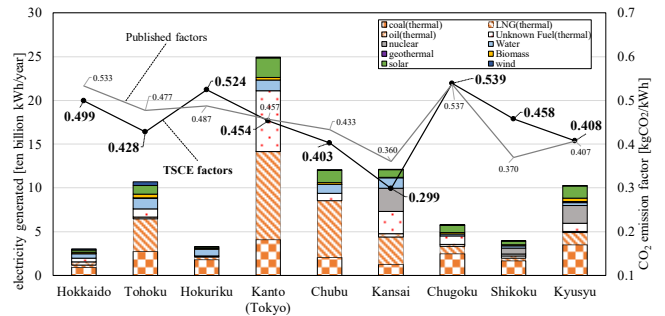


Figure 2 Comparison of CO₂ emission factors and annual power generation by source for each region

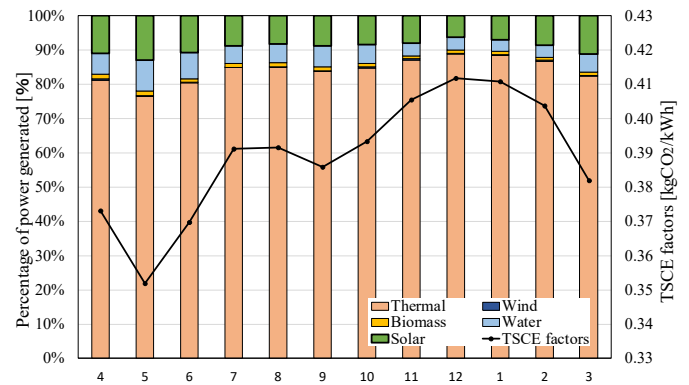


Figure 3 The monthly power source composition ratio and monthly average TSCE factors in Tokyo

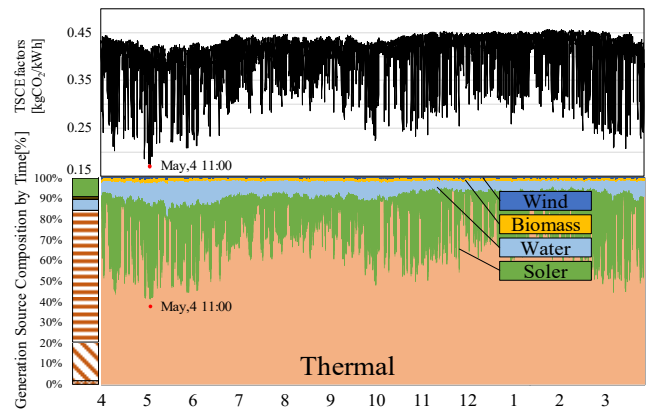


Figure 4 Power source composition and TSCE factors in Tokyo.

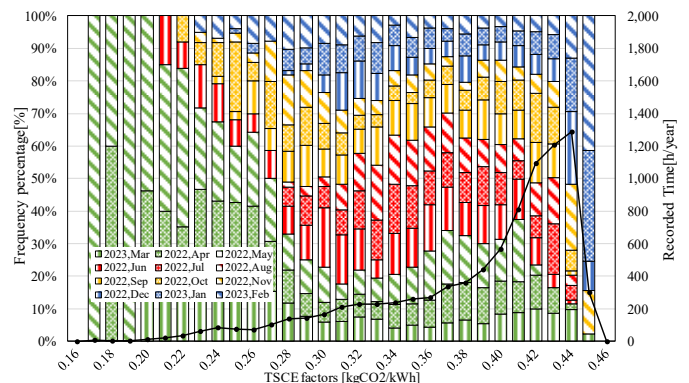
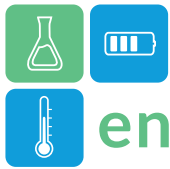


Figure 5 the frequency of occurrence of the factors and the percentage of each month in Tokyo



The result shows that the hourly CO₂ emissions during the daytime decrease more in direct feed operation than in the case of nighttime TES operation. However, the direct feed operation on a cloudy day during the same period resulted in a 1.3% increase. Therefore, it is considered that the direct feed operation may reduce CO₂ emissions when sufficient solar radiation can be secured and TSCE factor is low enough.

4. Conclusions

TSCE factors were estimated based on annual power generation and fuel consumption, and the TSCE factors tends to decrease at the spring season in Japan. The TSCE factors in each region were different because each region has a different power source composition. Also, we found that there are different characteristics on CO₂ emissions trend in several building uses. Furthermore, CO₂ emissions were roughly estimated based on different TES operations. It was found that when surplus electricity from solar power generation is created on sunny days, direct feed operation has the potential to reduce CO₂ emissions. In addition, there is room to consider various patterns, such as setting the ratio of nighttime TES operation and direct feed operation according to the future VRE penetration rate and analysing seasonal trends.

References

- [1]. Ministry of the Environment - (2022), Law Concerning the Promotion of Measures to Cope with Global Warming
- [2]. Hokkaido Electric Power, Inc. Homepage, Tohoku Electric Power Co, Inc. Homepage, Hokuriku Electric Power Co, Inc. Homepage, TEPCO Power Grid, Inc. Homepage, Chugoku Electric Power Co, Inc. Homepage, Chubu Electric Power Miraiz Co, Inc. Homepage, KEPCO, Inc. Homepage, Shikoku Electric Power Co, Inc. Homepage, Kyushu Electric Power Co, Inc. Homepage – (2022) Area Supply and Demand Results,
- [3]. Ministry of Land, Infrastructure, Transport and Tourism – (2019) Law Concerning the Improvement of Energy Consumption Performance of Buildings, <https://www.mlit.go.jp/jutakukentiku/house/shoenehou.html>
- [4]. Japan Sustainable Building Consortium – (2007-2018), Database for Energy Consumption of Commercial buildings, <https://www.jsbc.or.jp/decc/decc.html>
- [5]. Ministry of the Environment - (2022), List of calculation methods and emission factors, <https://ghg-santeikohyo.env.go.jp/calc>

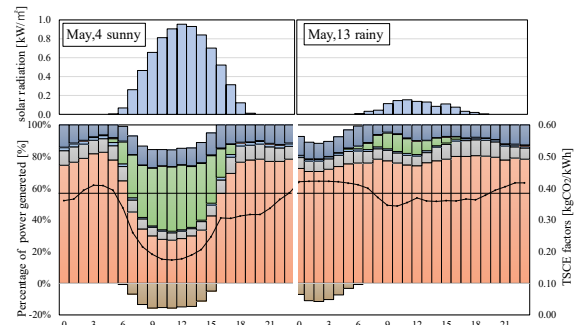


Figure 6 The trend of the power source composition, solar radiation, and TSCE factors in Tokyo

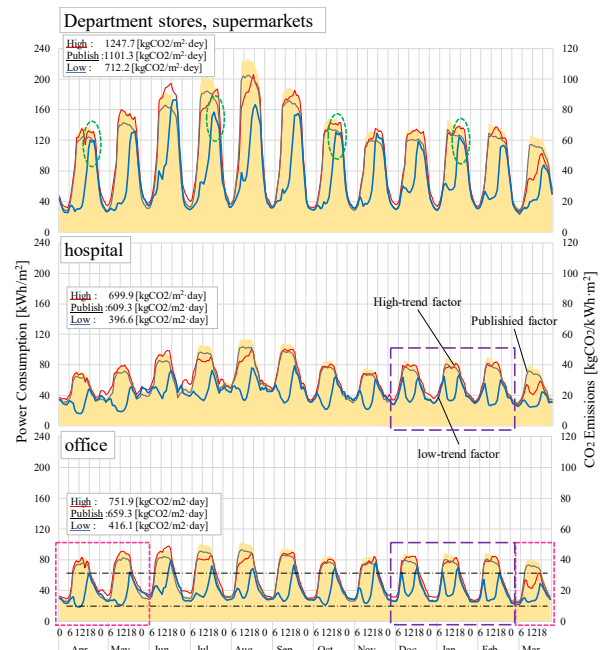


Figure 7 The trend of average power consumption per unit area and CO₂ emissions

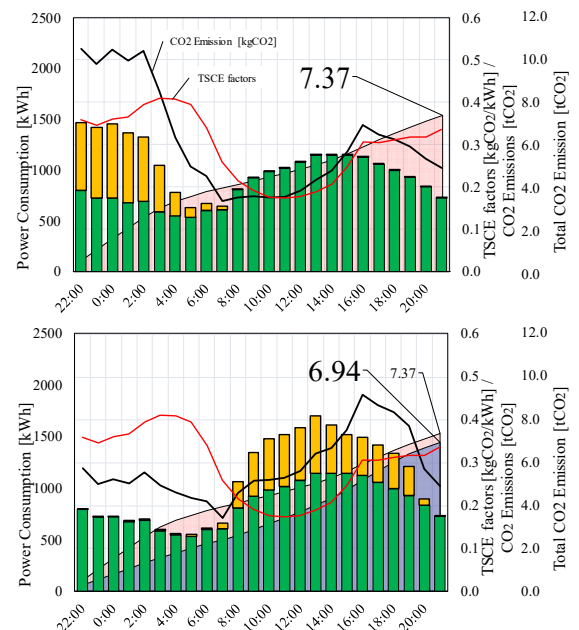
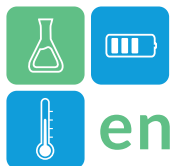


Figure 8 The results for a representative day in May



Supercooling suppression of Al-Si phase change material for efficient thermal energy storage and practical applications

Joshua Chidiebere Mba^{1*}, Kaixin Dong¹, Yuto Shimizu², Minako Kondo¹, Tomokazu Nakamura¹,
Melbert Jeem¹, Takahiro Nomura¹

1 Faculty of Engineering, Hokkaido University, Kita 13 Nishi 8, Kita-Ku, Sapporo, 060-8628, Japan.
2 Graduate School of Engineering, Hokkaido University, Kita 13 Nishi 8, Kita-Ku, Sapporo, 060-8628,
Japan.

*Corresponding author e-mail: mbajoshuac@eng.hokudai.ac.jp

Abstract

Rapid socioeconomic development and the incessant global energy crisis demand renewable energy alternatives to harvest, store, and save energy to meet the world's energy demand and supply. Latent heat thermal energy storage (LHTES) is an efficient means to store and utilize renewable energy for later use. Metals and alloy-based phase change materials (PCMs) such as thermo-responsive Al-Si PCMs show great potential for LHTES and utilization. However, practical uses are militated against by supercooling. To date, supercooling suppression of metal-alloy based PCMs is rarely reported despite the large heat storage density per unit volume, high thermal conductivity, and exceptional thermal stability. Herein, we present a method to introduce TiO₂ additives to Al-Si PCMs via high-speed impact blending. Following heat oxidation treatment, the addition of 3wt.% TiO₂ showed the best supercooling suppression effect. The results demonstrate the development of Ti-doped Al-Si MEPCMs with high latent heat capacity and an excellent suppression of supercooling, paving way for efficient practical uses.

Keywords: Thermal energy storage, supercooling, phase change materials, latent heat storage, renewable energy

Introduction

The incessant high energy demand across the globe, the environmental impacts of fossil fuels and the need to explore renewable energy sources to ensure sustainable energy access and security are trending topics around the world. Though the most utilized source of energy, fossil fuels are unsustainable, non-renewable and pose lots of challenges to the environment including environmental pollution, carbon emission and the associated climate change among others (Kerr, R. A., 2007). Moreover, the recent global energy crisis calls for advanced broad range of renewable energy. Consequently, the resort to renewable, and sustainable sources of energy such as solar, wind, geothermal bioenergy, tidal, thermal energy etc to mitigate these challenges (Owusu et al., 2016).

Thermal energy storage (TES) using phase change materials (PCMs) is one of the key energy storages approaches capable of constant utilization of renewable energy for diverse applications including waste heat recovery, centralized solar power generation, heavy electronics equipment cooling, as well as use in

buildings, medical and agricultural applications etc (Chavan et al., 2022; Sun et. al., 2023). Metal and alloy-based PCMs such as thermo-responsive Al-Si PCMs show great promise for latent heat thermal energy storage and utilization for diverse applications. Nevertheless, supercooling phenomenon limits efficient use of Al-Si PCMs for thermal energy storage systems. It reduces crystallization temperature, preventing efficient release of stored energy. Previously, Nomura et al. (2017) reported the synthesis of Al-25mass%Si MEPCM via two steps of boehmite treatment and heat-oxidation treatment in an O₂ atmosphere. The melting point and the latent heat of the MEPCMs were 573 °C and 247 J·g⁻¹, respectively, however, the MEPCMs displayed a supercooling degree of approximately 49 °C, a bottleneck for practical uses. Supercooling mitigation is therefore critical for practical applications.

Currently, organic PCMs can be doped with nanoparticles in the shell and core materials to reduce the effect of supercooling, however, most metals and alloy based PCMs have inorganic wall materials, particularly those synthesized by self-oxidation

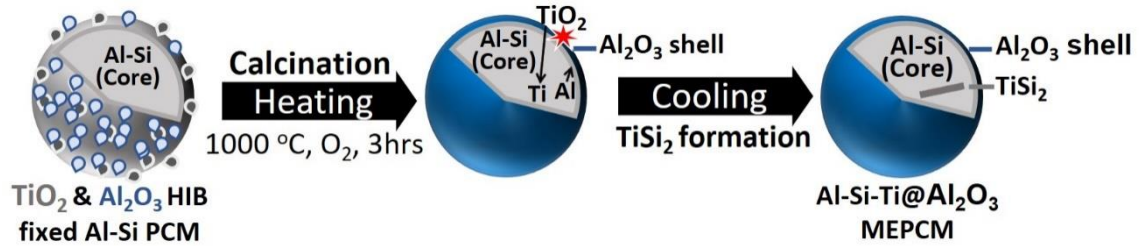


Figure 1: Illustration of synthesis of Ti-doped Al-Si-Ti@Al₂O₃ MEPCM via novel high-speed impact blending and heat oxidation treatment.

method, preventing the introduction of nucleating agents via doping to forestall supercooling. In alloy casting field, it was reported that Al intermetallic compounds such as TiAl₃, ZrAl₃, VAl₁₀, NiAl₃, CrAl₇, and B₂Al are possible nucleating agents for Al (Marcantoni et al., 1970). Such intermetallic compounds can alter the nucleation kinetics during the Al-25mass%Si phase transition. Hence, this study to mitigate the supercooling of Al-25mass%Si PCMs for efficient thermal energy storage and utilization via Ti-doping, demonstrating successful supercooling suppression of Al-25mass%Si MEPCMs.

Materials and method

Ti-Doped Al-25mass%Si microencapsulated PCMs (MEPCMs) were fabricated via high-speed impact blending (HIB) and heat oxidation treatment (Figure 1). First, a hybridizer was used to adhere 3wt.% TiO₂ additive and Al₂O₃ (shell material) on the microparticles utilizing high-velocity mechanical forces to promote adhesion among particles. Next, 100 mg of the hybridized samples were heated in an Al₂O₃ crucible from room temperature to 1000 °C at a rate of 10 °C min⁻¹ for 3 hrs and subsequently cooled using thermo-balance apparatus (TGA/DSC 1, Mettler Toledo, USA). The phase composition of the prepared Al-Si-Ti@Al₂O₃ MEPCMs were characterized by Powder X-ray diffraction. Following, the morphology and surface structure were assessed by field-emission scanning electron microscopy. The latent heat capacities were determined using thermogravimetric analysis and differential scanning calorimetry.

Results and Discussion

Figure 2a represents the SEM image and EDS elemental mapping of 3wt.% Ti-doped Al-25mass%Si MEPCMs, depicted as Al-Si-3Ti@Al₂O₃. The MEPCMs show good morphology and evenly covered surfaces with α-Al₂O₃ shell. Further, the EDS elemental mapping of the MEPCMs depicts Al, Si, O, and Ti as major constituents of the MEPCMs, indicating successful synthesis of Ti-doped MEPCMs. The XRD patterns of the MEPCMs showed Al, Si, α-

Al₂O₃ and TiSi₂ as the components of the material. Figure 2b shows the SEM image and EDS elemental mapping of cross-section of the MEPCM after heat oxidation treatment, revealing the presence of Ti inside the MEPCM's core. During calcination, the adhered Ti oxides on the surfaces of the microcapsules were reduced to the metallic phase Ti by Al (i.e., Al is oxidized by the adhered TiO₂), resulting in the precipitation of Ti into the core of the MEPCMs. The observed Ti was colocalized with Si inside the cores. This colocalization led to the formation of TiSi₂ phase during the cooling process, not only observed in the cores but also detected by the XRD. The formed TiSi₂, an intermetallic compound is solid at high temperatures above the eutectic temperature of Al-25mass%Si in the Ti-doped MEPCMs and is implicated as the heterogenous nucleating agent responsible for the

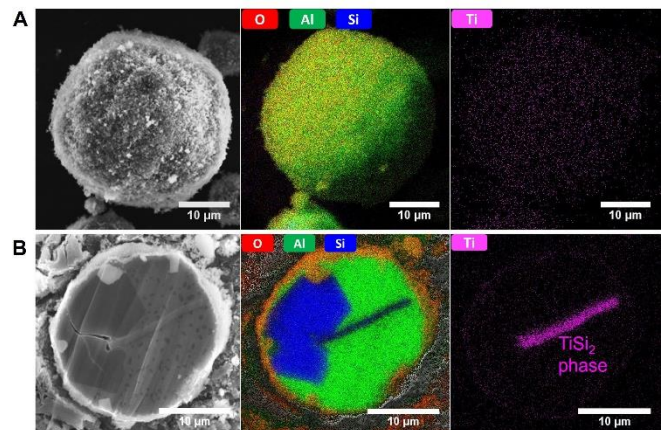


Figure 2: (a) SEM and EDS elemental mapping of Al-Si-3Ti@Al₂O₃ MEPCM. (b) SEM and EDS elemental mapping of cross-sectioned Al-Si-3Ti@Al₂O₃ MEPCM. Al, Si, Ti, and O represent aluminium, silicon, titanium, and oxygen, respectively.

suppression of the established supercooling of Al-25mass%Si MEPCMs. Further, the heat storage capacity of the Ti-doped MEPCMs and the control sample (Al-Si@Al₂O₃) were investigated. Compared to MEPCMs with Ti doping, the DSC curves show 3 main exothermic peaks with the first exothermic peaks of the Ti-doped MEPCMs being broader and starting at

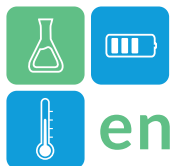


Table 1: Summary of melting and solidification starting temperatures, supercooling degree and latent heat of fusion of Al-Si@Al₂O₃ and Al-Si-3Ti@Al₂O₃ MEPCMs evaluated from DSC curves.

Sample	Melting temp. (°C)	Solidification temp. (°C)	Latent heat (Jg ⁻¹)	Supercooling degree (°C)
Al-Si@Al ₂ O ₃	578.44	553.20	274.23	25.24
Al-Si-3Ti@Al ₂ O ₃	578.46	578.10	267.19	0.36

higher temperatures. The peak broadening is attributed to the distribution of freezing temperatures in each MEPCM. The shift of the solidification temperatures to higher temperatures indicate suppression of supercooling. Summary of the melting/solidification starting temperatures, the latent heat of fusion (ΔH) and the supercooling degree of the MEPCMs determined from the DSC curves are shown in Table 1, depicting successful fabrication of MEPCMs with high latent heat capacity and excellent suppression of supercooling. The addition of 3wt.% TiO₂ resulted in over 98% reduction of supercooling of Al-25mass%Si MEPCMs prepared via hybridization and heat oxidation treatment method.

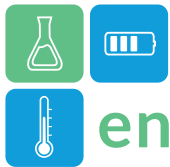
Conclusion

We successfully synthesized a Ti-doped Al-25mass%Si MEPCMs via high-speed impact blending and heat oxidation treatment. The TiO₂ additive fixed on the surfaces of Al-Si microparticles were reduced by Al during heat oxidation treatment, resulting in the colocalization of the metallic Ti with Si and the consequent nucleation of the doped MEPCMs by the resultant TiSi₂ inside the core. The introduction of Ti into the MEPCMs led to broadening of the exothermic peaks and shift to a higher solidification temperature. Consequently, the supercooling of Al-25mass%Si microencapsulated PCMs was successfully reduced from 25.24 °C to 0.36 °C, following 3wt.% TiO₂ addition. The results show that the introduction of TiO₂ to Al-25mass%Si MEPCMs suppressed the existential supercooling, a major drawback in practical applications of metals and alloys PCMs in latent heat thermal energy storage systems.

In conclusion, this study demonstrates a facile approach to introduce impurities into metals and alloy based MEPCMs using hybridization and heat oxidation treatments, with a great promise to forestall the supercooling of other metals and metal alloy based MEPCMs for efficient latent heat thermal energy storage and practical utilization.

References

- Chavan, S. et al. (2022). A comprehensive review on current advances of thermal energy storage and applications. *Alexandria Engineering Journal*. <https://doi.org/10.1016/j.aej.2021.11.003>.
- Kerr R. A. (2007). Climate change. Global warming is changing the world. *Science*. <https://doi.org/10.1126/science.316.5822.188>.
- Marcantoni, J. A. et al. (1970). Nucleation of aluminium by several intermetallic compounds. *Journal of Institute of metals*.
- Nomura, T. et al. (2017). Microencapsulated phase change materials with high heat capacity and high cyclic durability for high-temperature thermal energy storage and transportation. *Applied Energy*. <https://doi.org/10.1016/j.apenergy.2016.11.025>.
- Owusu, P. A. et al. (2016). Cogent Engineering. A review of Renewable energy sources, sustainability issues and climate change mitigation. <https://doi.org/10.1080/23311916.2016.1167990>.
- Sun, M. et. al. (2023). A review on thermal energy storage with eutectic phase change materials: fundamentals and applications. *Journal of Energy Storage*. <https://doi.org/10.1016/j.est.2023.107713>.



Surface engineering for TES application enhancement.

Lorena Betancor, Sergi Dosta*, Camila Barreneche

University of Barcelona, Faculty of Chemistry, Department of Materials Science and Physical Chemistry,
Martí i Franqués, 1, floor 7, Barcelona, Spain.

*Corresponding author e-mail: sdosta@ub.edu

Abstract

The increasing global awareness of the environmental and social impact of fossil fuels has intensified the demand for clean and sustainable energy sources. In this context, Concentrating Solar Power (CSP) plants with thermal storage systems (TES) systems have emerged as a cost-effective and promising technology. This review explores the pivotal role of coatings in these types of plants, covering various coating techniques and evaluating their applications, advantages, limitations and Technology Readiness Level (TRL).

Keywords: Coatings, Thermal Energy Storage, Concentrated Solar Power, Thermal Spray

Introduction

Nowadays, the population is increasingly aware of the environmental and social impacts of fossil energy sources (International Energy Agency (IEA), 2022). In this context, concentrating solar power (CSP) plants have emerged as a promising and efficient technology. However, in order to maximize its effectiveness, continuous advances have been required. An example of this was the emergence of thermal energy storage (TES) systems to harness the energy even in times when there is no sun (H. L. Zhang et al., 2013). In addition, specialized coatings have been applied to improve the efficiency and durability of the plants.

Coatings can be used in CSP technology to reduce corrosion in all system components and enhance plant performance by improving effectiveness properties (Atkinson et al., 2015; Walczak et al., 2018). Similarly, surface engineering can help to increase the economic viability of CSP systems.

The main objective of the review is to present an overview on the state of the art of surface engineering studies and developments applied to CSP plants and outstand some of the main potential added value that this discipline can contribute to CSP improvement.

SCOPE and Structure of the review

The scope of this review is to summarize the different applications of coatings in CSP plants. For a better classification, they are organized according to the application techniques. In addition, the advantages and limitations of each deposition technique will be

detailed in order to create a perspective of the level of maturity for each specific application.

There are several techniques available to create a proper coating for such a function but are those ones listed below which are relevant to be implemented in CSP plants components: vapor deposition techniques, laser deposition techniques, sol-gel, thermal spray and other deposition techniques (spray, paint or slurry).

These coatings can be used in the following applications:

- Corrosion resistance. High-temperature molten salts are generally used to store heat and generate electricity (Ding et al., 2018). These cause corrosion problems in different elements of the plant (heat exchangers, piping and thermal storage systems). The use of coatings significantly reduces this problem.
- Selective coatings for solar receivers. Dark and/or high absorbance coatings increase the amount of heat captured in CSP plants (Galindo et al., 2021), improving efficiency and reducing LCOE (Boubault et al., 2017).
- Improve effective properties. Coatings can be applied to modify the properties (conductivity and emissivity) of TES systems (Trevisan et al., 2021).

Implementation in CSP plants

Corrosion resistance

One of the main problems of CSP plants is caused by corrosion by molten salts at high temperatures. Molten salts corrosion is complex and depends on the salt composition, thermodynamic and substrate materials



(Ding et al., 2018, 2019; Liu et al., 2016). Coatings are crucial in protecting CSP components, improving performance and reducing costs.

Slurry

Slurries for corrosion resistance application in CSP plants are recommended as a proper solution. However, these types of coating are still an option with a lot of potential to be explored since it is not cost-efficient yet.

Thermal spray

Thermal spraying is a technique that has been widely developed for a long time and with excellent results against corrosion in general and against corrosion in the solar field in particular. It is also economical and effective on a large scale, thanks to its versatility in terms of materials.

Sol-gel

The usage of sol-gel for corrosion resistance application in CSP plants are recommended due to its flexibility in terms of substrates and environments. However, the requirement to apply several layers may limit its application on certain materials.

Vapor Deposition Techniques (CVD and PVD)

Vapor deposition techniques have proven to be suitable due to their ability to generate different coating thicknesses as a measure to reduce corrosion. Nevertheless, their use in this type of plant is more developed in the selective solar absorber area.

Selective coatings for solar receivers

The amount of sunlight captured by materials and converted into heat is crucial to the efficiency of CSP plants. Coatings can be applied to improve thermal properties and increase the amount of heat captured. Optimizing absorbers can achieve up to 65% efficiency in this type of plants (Burlafinger et al., 2015). These coatings must exhibit a number of characteristics: stability, longevity, comply with regulations and cost-effective (Atkinson et al., 2015). The most prominent materials use as selective absorbers are nanocomposites (Oelhafen & Schüler, 2005), transition oxides, nitrides and nitride oxides (H. L. Zhang et al., 2013; K. Zhang et al., 2017).

Sol-gel

The use of sol-gel coatings as selective solar absorbers is a versatile and effective option. In addition to improving the optical properties of the absorbers, it also provides protection against corrosion. However, it is an energy-intensive and less environmentally friendly technique.

Vapor Deposition Techniques (CVD and PVD)

Vapor deposition techniques are recommended for this type of application due to their technological maturity and good optical properties. However, the requirement for heat treatment may limit their application in certain materials.

Dip-coating

The use of solar absorbing coatings applied by dip coating is an economical and simple solution. Although it is not as developed as other techniques, it has huge potential.

Spraying methods

The use of spray coatings for solar receivers is effective, provided that the materials allow it. That is why it is not a widely used technique in this area.

Laser deposition

Laser deposited coatings are recommended for this application due to their robustness and optical properties. This is a more novel and expensive set of techniques due to its requirement for specific equipment.

Improve effective properties

The application of coatings in TES systems is not widespread in the research world. However, the work of Trevisan et al. on the use of coatings in packed beds is noteworthy, establishing a link between coating emissivity, conductivity, and particle size (Trevisan et al., 2021). Some of the coating materials studied such as Nitinol, SS 304, HIE-Coat 840MX and Pyro-Paint 634-ZO resisted elevated temperatures and thermal cycles (Trevisan, Wang, & Laumert, 2022; Trevisan, Wang, Zhao, et al., 2022).

Discussion

In general, coatings are an economical and effective solution for improving the efficiency of CSP plants. In addition to a wide variety of coating materials, they offer excellent properties.

- Thermal spray is a technique that allows a wide variety of substrates (stainless steels, alloy steels, composites, biological and ceramic materials) and coatings, especially alloys and superalloys (Inconel 625). Its application as an anticorrosive barrier in TES units stands out, since it performs well in different salts ($\text{Na}_2\text{SO}_4\text{-V}_2\text{O}_5$, $\text{NaCl-KCl-Na}_2\text{SO}_4$, $\text{NaNO}_3\text{-KNO}_3$) and in a temperature range of 300-850 °C.

- Sol-gel is a technology that, due to the fact that it can be used as a barrier against corrosion and as a selective solar absorber, allows the use of different materials. The most prominent are substrates of stainless steels,



alloys and non-ferrous metals and ceramic coatings, multilayers and metal oxides. Although their use is limited to solar salt up to 500 °C, these materials have excellent optical properties (absorptivity, 0.85-0.95 and emissivity, 0.12-0.15).

- PVD and CVD coatings cover a wide range of ceramic materials, alloys and multilayers. They act as a measure to prevent corrosion in solar salt up to 500-600 °C. In addition, they are also used as solar absorbers due to their high absorptivity (0.85-0.96) and low emissivity (0.02-0.18).

- Slurry technique has been studied to reduce corrosion in thermal storage tanks with molten salts (KNO_3 - NaNO_3 , NaCl - KCl) at 600°C. The aluminides deposited on stainless steels, alloys and superalloys (Inconel 600) stand out.

- Dip-coating is a technology with good results used as solar absorbers at temperatures of 250-500 °C, due to its absorptivity close to 0.95. Mostly ceramic coatings, oxides and non-ferrous metals are used. Substrates are usually non-ferrous metals or stainless steels, although glass can also be used.

- Laser techniques are novel in the field of selective solar absorbers. They allow a wide temperature range of 350-650 °C with absorptivities of 0.80-0.90 and emissivities of 0.03-0.12. The most commonly used materials are ceramic multilayers on stainless steel and non-ferrous metal substrates.

- Spray coatings can resist high temperatures of 650-750°C. That is the reason for their usefulness as solar absorbers. The main materials used are oxides, polymers and multilayers on stainless steel and Inconel 625.

However, there is no optimal deposition technique; it depends on the particular requirements of the plant, the materials used and the operating parameters. The constant progress in this field is remarkable thanks to the various advances in new techniques and combination of materials, thus allowing to adapt the coatings to the requirements of each plant. However, further research is still needed in order to optimize the techniques and improve their performance under real conditions (thermal cycling, wider range of salts and corrosive environments). Similarly, future research can be focused on the development of more sustainable and environmentally friendly materials, as well as directed towards new fields and new combinations of materials.

Conclusions

Overall, coatings demonstrate multifaceted potential within CSP plants, serving as a protective layer against

corrosion and improving thermal storage properties, enhancing plant performance and durability.

Regarding its anticorrosive function, thermal spray technique stands out as the most prominent due to its cost-effectiveness and large-scale use. Sol-gel also shows satisfactory results; however, adhesion is limited by the number of layers. Vapor-phase deposition techniques offer a variety of layer thickness coatings but may require high-temperature heat treatments. Slurry deposition, while environmentally friendly, can present durability and efficiency problems.

As selective solar absorbers, sol-gel shows remarkable versatility and good optical properties. CVD and PVD offer mature technology with optimal optical properties and high-temperatures robustness. Dip coating and spray deposition show potential and offers cost-effective selective properties. Finally, laser deposition allows the creation of robust coatings with suitable optical properties but may require specialized equipment and professionals.

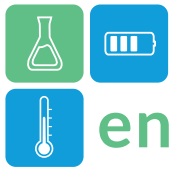
Lastly, the use of coatings to improve the properties of TES systems is a novel and underexplored option. This application has been shown to be essential in this type of system.

Acknowledgments

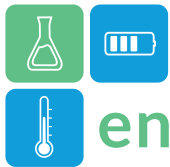
The authors would like to thank the Catalan Government for the quality accreditation given to their research group DIOPMA (2017 SGR 0118, 2021 SGR 00708). DIOPMA is a certified agent TECNIO in the category of technology developers from the Government of Catalonia. This work has been partially funded by the Spanish government PID2021-123511OB-C32 (MINECO/FEDER, UE) and CHINA.

References

- Atkinson, C., Sansom, C. L., Almond, H. J., & Shaw, C. P. (2015). Coatings for concentrating solar systems - A review. In *Renewable and Sustainable Energy Reviews* (Vol. 45, pp. 113–122). Elsevier Ltd. <https://doi.org/10.1016/j.rser.2015.01.015>
- Boubault, A., Ho, C. K., Hall, A., Lambert, T. N., & Ambrosini, A. (2017). Durability of solar absorber coatings and their cost-effectiveness. *Solar Energy Materials and Solar Cells*, 166, 176–184. <https://doi.org/10.1016/j.solmat.2017.03.010>
- Burlafinger, K., Vetter, A., & Brabec, C. J. (2015). Maximizing concentrated solar power (CSP) plant overall efficiencies by using spectral selective absorbers at optimal operation



- temperatures. *Solar Energy*, 120, 428–438. <https://doi.org/10.1016/j.solener.2015.07.023>
- Ding, W., Bonk, A., & Bauer, T. (2019). Molten chloride salts for next generation CSP plants: Selection of promising chloride salts & study on corrosion of alloys in molten chloride salts. *AIP Conference Proceedings*, 2126. <https://doi.org/10.1063/1.5117729>
- Ding, W., Bonk, A., Gussone, J., & Bauer, T. (2018). Electrochemical measurement of corrosive impurities in molten chlorides for thermal energy storage. *Journal of Energy Storage*, 15, 408–414. <https://doi.org/10.1016/j.est.2017.12.007>
- Galindo, R. E., Krause, M., Niranjan, K., & Barshilia, H. (2021). Solar selective coatings and materials for high-temperature solar thermal applications. *Sustainable Material Solutions for Solar Energy Technologies: Processing Techniques and Applications*, 383–427. <https://doi.org/10.1016/B978-0-12-821592-0.00011-X>
- Liu, M., Steven Tay, N. H., Bell, S., Belusko, M., Jacob, R., Will, G., Saman, W., & Bruno, F. (2016). Review on concentrating solar power plants and new developments in high temperature thermal energy storage technologies. In *Renewable and Sustainable Energy Reviews* (Vol. 53, pp. 1411–1432). Elsevier Ltd. <https://doi.org/10.1016/j.rser.2015.09.026>
- Oelhafen, P., & Schüler, A. (2005). Nanostructured materials for solar energy conversion. *Solar Energy*, 79(2), 110–121. <https://doi.org/10.1016/j.solener.2004.11.004>
- Trevisan, S., Wang, W., & Laumert, B. (2021). Coatings utilization to modify the effective properties of high temperature packed bed thermal energy storage. *Applied Thermal Engineering*, 185. <https://doi.org/10.1016/j.applthermaleng.2020.116414>
- Trevisan, S., Wang, W., & Laumert, B. (2022). A high-temperature thermal stability and optical property study of inorganic coatings on ceramic particles for potential thermal energy storage applications. *Solar Energy Materials and Solar Cells*, 239. <https://doi.org/10.1016/j.solmat.2022.111679>
- Trevisan, S., Wang, W., Zhao, X., & Laumert, B. (2022). A study of metallic coatings on ceramic particles for thermal emissivity control and effective thermal conductivity enhancement in packed bed thermal energy storage. *Solar Energy Materials and Solar Cells*, 234. <https://doi.org/10.1016/j.solmat.2021.111458>
- Walczak, M., Pineda, F., Fernández, Á. G., Mata-Torres, C., & Escobar, R. A. (2018). Materials corrosion for thermal energy storage systems in concentrated solar power plants. In *Renewable and Sustainable Energy Reviews* (Vol. 86, pp. 22–44). Elsevier Ltd. <https://doi.org/10.1016/j.rser.2018.01.010>
- International Energy Agency (IEA). (2022, October). *World Energy Outlook 2022*. <https://www.iea.org/reports/world-energy-outlook-2022>
- Zhang, H. L., Baeyens, J., Degève, J., & Cacères, G. (2013). Concentrated solar power plants: Review and design methodology. In *Renewable and Sustainable Energy Reviews* (Vol. 22, pp. 466–481). Elsevier Ltd. <https://doi.org/10.1016/j.rser.2013.01.032>
- Zhang, K., Hao, L., Du, M., Mi, J., Wang, J. N., & Meng, J. ping. (2017). A review on thermal stability and high temperature induced ageing mechanisms of solar absorber coatings. In *Renewable and Sustainable Energy Reviews* (Vol. 67, pp. 1282–1299). Elsevier Ltd. <https://doi.org/10.1016/j.rser.2016.09.083>



Swedish State-of-the-Art on Ground-source De-Icing and Snow Melting Systems

Signhild Gehlin^{1,*}, Olof Andersson², Bijan Adl-Zarrabi³

1 The Swedish Geoenery Center, Hedvig Möllers gata 12, 22355 Lund, Sweden

2 Geostrata HB, Kärrsångarvägen 14 SE 247 35 S Sandby, Sweden

3 Chalmers university of technology, 41296 Gothenburg, Sweden

*Corresponding author e-mail: signhild.gehlin@geoenergicentrum.se

Abstract

Sweden is part of the on-going International Energy Agency (IEA) Energy Storage (ES) collaboration project Task 38 – Ground Source De-Icing and Snow Melting Systems for Infrastructure, running 2021-2024. A recent outcome of the project is a State-of-the-Art report on snow melting and de-icing using the ground as a heat source in Sweden. This paper summarizes the main content of the Swedish State-of-the-art report.

Keywords: Sweden, ground-source, de-icing, IEA ES Task 38

Introduction

Sweden, together with Türkiye, Germany, Italy and Belgium, is taking part in the on-going International Energy Agency (IEA) Energy Storage (ES) collaboration project Task 38 – Ground Source De-Icing and Snow Melting Systems for Infrastructure (Adl-Zarrabi et al. 2022). Task 38 is running 2021-2024. A recent outcome of the project is a Swedish State-of-the-Art report on snow melting and de-icing using the ground as energy source (Andersson et al. 2024).

Snow and ice melting with heated surfaces is a well-used method to prevent slip accidents with pedestrians as well as vehicles. There are two basic commercial types of surface heating systems: electric heated pavement (EHP), and hydronic heated pavement (HHP). Electric systems use resistance wires or mats to generate heat, while hydronic systems use a fluid circulated through pipes.

Carlsson et al. (2016) report that the number of fall accidents on heated pedestrian streets were 67-100% lower compared to unheated pedestrian streets in four Swedish cities in different climate zones. Such surface heating can be provided with hydronic systems as well as with electric cables. Task 38 has the focus on hydronic systems, heated with the ground as a source for heating, e.g. from boreholes or groundwater. Sweden is one of the world leading countries in geothermal energy use from shallow ground sources and has a long tradition of designing shallow geothermal energy systems and underground thermal energy storage systems for space heating (Gehlin et al 2022). As part of Task 38 an overview of the practice

and potential for using the underground as an energy source for de-icing and snow-melting in Sweden has been made. The aim is to increase the use of ground source de-icing, and to replace electric de-icing and snow-melting systems.

The use of electricity for snow and ice melting was introduced in the time when the electricity price in Sweden was much lower than today. Large EHP systems are now rarely used and existing systems are shut down or replaced by hydronic systems. Applications for smaller electric systems, such as for icicle prevention on roofs, ice-melting in gutters and for de-icing of railway switches, are still used.

HHP systems in Sweden are mostly using heat from the return pipe of district heating (DH) as the heat source and are so far mainly used for pedestrian streets. Andersson et al. (2023) list 22 HHP systems in Swedish city centers installed between the 1960's and 2020, and with heated areas of 3000-184 000 m². The total heated area of these 22 systems is approximately 600 000 m². The required heating capacity for these applications is in the range 200-400 W/m², depending on the local winter climate conditions, system design, operation and control.

The earliest and also largest of the 22 listed HHP systems is in the city center of Västerås in the middle parts of Sweden. Installations began in 1964 and the heated surface was expanded over the years to reach 320 000 m² in 1985, when it was as largest. After energy prices increased in the late 1980s and 1990s, large parts of the system that were not co-financed by property owners were shut down. In recent years the system has expanded anew. As of today, the Västerås HHP system covers 184 000 m² divided in 11



substations and operates from October 15th to April 15th (Andersson et al., 2023).

Another application of hydronic systems for de-icing and snow-melting is for keeping sports field (e.g. for soccer) free from snow and ice to prolong the season for games and practice. A survey made by the Swedish Football Association (Svenska Fotbollsförbundet 2018) counts at least 1 000 fields with artificial turf in Sweden, of which at least 83 are winter heated (approximately 8%).

Ground source HHP Systems

There are only a handful Swedish examples in which heat from the ground is used in HHP systems for de-icing and snow-melting, and a few experimental studies that have been performed on both existing and planned applications. These studies apply either boreholes in rock (closed loops) or groundwater (open loops) as heat source and thermal energy storage medium and provide important knowledge for further market development.

A HHP served by a ground source heat pump (GSHP) system is estimated to use 70-80% renewable heat from the ground source. The remaining energy is electric energy for running the compressors. Underground thermal energy storage (UTES) systems such as borehole thermal energy storage (BTES) and aquifer thermal energy storage (ATES) may, depending in their design, use an even higher fraction of renewable energy than a GSHP system.

Arlanda Airport (ATES)

In an experimental study at Stockholm Arlanda Airport (Persson 2007) the influence of multiple variables at a HHP system for airplane gates was investigated, and to what extent heat from an ATES system could be used to keep the gates free from ice and snow. Whether the HHP could also be used as solar collectors for charging the warm side of the ATES system with solar heat was also investigated. The aquifer temperature at +20°C could efficiently be utilized to keep the ground at +3°C by increasing the system flow rate. The total extracted solar heat would be approximately 50% of the heat used to keep the gates heated and free from snow and ice in the winter season. In 2009 a HHP system for de-icing of gates at Arlanda Airport was also installed as part of the larg ATES system for heating and cooling of the airport building that was installed that year (Andersson, 2009). The HHP system, in which heat from the ATES system is used, covers an area of 100 000 m² of which some 75 000 m² are gates at Terminal 2 and 5 and the rest is used for entrances, etc. Previously, the heat was supplied by a local district

heating system (Swedavia 2016). The HHP system in this design is not used as a solar collector at the gates.

Tranarpsbron

In 2014 the Swedish Transport Administration initiated research and development of ground heating systems for particularly vulnerable road sections and bridges (Trafikverket 2014a) after a severe car accident occurred on the bridge Tranarpsbron in southern Sweden that year. The simulation tool CoupModel was used in a case study to investigate the cost for heating a bridge deck in Gothenburg (Halvors länk). In this case three options for keeping the bridge heated, combined with traditional snow clearance, were simulated, analyzed, and cost calculated (Trafikverket 2014b). The Tranarp bridge accident also led to a feasibility study for heating of the bridge with geothermal energy (Togård 2014). The simulation study used CoupModel to calculate the heat and mass transfer for the bridge deck, combined with a large borehole thermal energy system (BTES) as heat source. It was concluded that such a solution was not economically feasible at the time of the study.

The Östersund HERO test site

In 2017 an experimental test site for road heating with solar heat stored in boreholes in the ground was constructed in Östersund in the middle parts of Sweden (Johnsson 2019). The test site, called HERO (Heating Road with Stored Solar Energy) consists of a 20 m long and 3.5 m wide section of a minor road. The paved surface is used to collect solar heat in the summer and the heat is stored in four boreholes of 210 m depth in crystalline rock on the side of the road part. The objective of the test plant was to collect data for verification of a simulation model that was developed prior to the tests. The test results indicated that it is possible to harvest more solar energy in the summer than needed during the winter if the system is controlled in an efficient way. The measured energy demand in the winter was consistent with the simulated energy demand, but only half of the energy supplied to the system originated from the BTES because the supply temperature from the boreholes was lower than required.

Entrances and ramps

Some commercial and institutional buildings that use GSHP, BTES or ATES systems for space heating and cooling, also serve smaller HHP systems for de-icing and snow-melting at entrances and ramps, etc. One example of such a system is the administrative building Kristallen in Lund, constructed in 2013 (Sweco, 2012). It has a steep pedestrian and bicycle ramp leading from



the railway station to the building. When the weather cause slippery road conditions the ramp is kept heated using heat from the BTES system that serves the building. Another example is the prison in Helsingborg, constructed 2012. A 60 m² recreation area on the roof deck and a 40 m² ramp to the garage are heated by the building's ATES system (Norrporten, 2009). Several IKEA warehouses use HHPs supplied by the building BTES systems to keep entrances free from snow and ice (IKEA, 2010).

Sports fields

Examples of sports fields, especially fields with artificial turf, using the ground as an energy source for ice and snow melting are still rare in Sweden, but there is a growing interest for such applications. One example is Backavallen sports facility in Katrineholm in middle Sweden. A BTES system with 91 boreholes of 180 m depth, and a storage capacity of about 1 700 MWh was installed in 2009. Some 400 MWh of heat is collected from subsurface pipping in the soccer field in summertime. The remaining heat is waste heat from making indoor ice for the ice hockey, curling field, and outdoor ice bandy facilities (SENS, undated).

A similar system is used at Kungsängen sports center, where 40 boreholes of 180 m depth are used with waste heat from an ice machine. Other examples are Täby football arena (90 boreholes to 300 m depth) and Torvalla arena (91 boreholes to 230 m depth), (Svensk Geoenergi 2018). In Hallsberg in middle Sweden a football field is heated by groundwater from wells draining the sport facility area (Carlsson, 2010). Groundwater is pumped from three wells and disposed in a small river after heat extraction. The maximum flow rate is 35 l/s and the temperature is constant at about +8°C throughout the year. The groundwater picks up condenser heat from the ice hockey rink chiller, increasing the temperature to +14°C. The maximum supply temperature to the football field is +14°C and the lowest return temperature is +3,5°C. Hence the system provides a maximum heating capacity around 1 500 kW, and keeps the turf unfrozen at an outdoor temperature of -12°C.

Conclusions

HHP systems are widely used for snow and ice prevention in various applications in Sweden. Although HHP systems using the ground as a heat source are still rare, the potential for such systems is promising. The additional investment cost for the drilling may be compensated for by the low operating cost of the ground source heated systems, and the heat from the ground is a local and renewable resource.

Ground source snow melting and de-icing systems have a promising market potential for transport infrastructure, such as walking paths, sensitive road parts, bridge decks, parking areas, ramps and entrances. In addition, there is a significant market potential for ground source HHP applications for sports fields (e.g. soccer) with artificial turf.

Acknowledgment

This work is part of the international collaboration project IEA ES Task38 - Ground Source De-Icing and Snow Melting Systems for Infrastructure. The authors gratefully acknowledge the financial support for their work from the Swedish Energy Agency, Grant 51491-1, and from their employers.

References

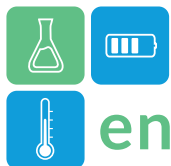
- Adl-Zarrabi, B., Gehlin, S., Van den Bergh, W., Cetin, A., Staudacher, L. (2022). Ground Source De-Icing and Snow Melting Systems for Infrastructure. *Transport Research Procedia* 2022.
- Andersson, O. (2009.) *The ATES Project at Stockholm Arlanda Airport - Technical Design and Environmental Assessment*. Proceedings of ECES conference Effstock, June 6-9, Stockholm.
- Andersson, O., Gehlin, S., Hellström, G., Adl-Zarrabi, B., Carlsson, A., Kalantar, A. (2023). State-of-the-Art: Sweden: Ground-Source De-Icing and Snow Melting Systems for Infrastructure. Final report. December 2023. IEA ES Task38 Report. http://media.geoenergicentrum.se/2024/01/Annex-38_SOTA-Sweden_Final-report-Dec-2023-Publ.pdf?_ga=2.254797134.718641499.1705419278-1472001483.1591185555
- Carlsson, A., Sawaya, B., Koveca, J., Andersson, M. (2016). *Skadereducerande Effekt av Uppvärmda Trottoarer, Gång- och Cykelstråk*. Slutrapport projekt TRV 19843, Chalmers 2016.
- Carlsson, B. (2010). *Föredrag Hallsbergs kommun avseende grundvattenuppvärmd fotbollsplan*. [Microsoft Word - Föredrag-svff-markvärme \(svenskfotboll.se\)](https://www.svenskfotboll.se/medlemsomradet/nyheter/2010/09/2010-09-20-foredrag-svff-markvarme)
- Gehlin, S., Andersson, O., Rosberg, J-E. (2022). *Geothermal Energy Use- Country Update for Sweden*. European Geothermal Congress in Berlin Oct. 17-20, 2022.
- IKEA. (2010). *Standard design room book*. Internal document (not published)
- Johnsson, J. (2019). *Low temperature deicing of road infrastructure using renewable energy*. Doctoral Thesis at Chalmers University of Technology. ISBN 978-91-7905-168-6



enerstock

ENERSTOCK 2024
The 16th IEA ES TCP International Conference on Energy Storage
June 5–7, 2024
Lyon, France

- Norrporten. (2009). *Bygghandling, Ritning V-53-1-002* dated 2009-12-07 (not published).
- Persson, F. 2007. *Analys av Markvärmesystem på Arlanda Flygplats*. Examensarbete vid Lunds Tekniska Högskola, Juni 2007.
- SENS (Undated). *Energy Storage In-A-Box*. Downloaded 2023-10-19. Backavallen energilager_iab_backavallen.pdf (sens.se)
- Svensk Geoenergi (2018). *Tema: Geoenergi och idrott*. Nr.1 2018. http://media.geoenergicentrum.se/2018/05/SvGeo_1_2018-web.pdf?_gl=1*ey12js*_ga*MTQ3MjAwMTQ4MjY4xNTkxMTg1NTU1*_ga_PG87BHCGEN*MTcwNTQ5NTY1OS41ODcuMS4xNzA1NDk1NjY4LjAuMC4w&_ga=2.123961866.1065470018.1705483216-1472001483.1591185555
- Svenska Fotbollsförbundet (2018). *Inventering av konstgräsplaner och fotbollshallar konstgräs i Sverige*. Rev. 2018-06-27.
- Sweco. (2012). *Underlag för dimensionering av värme till ramp och gång och cykelväg*. PM 2012.09-13 (not published)
- Swedavia, (2016). Verbal information from Kent Arvidsson, November 2016.
- Togård, C. (2014). *Geoenergisystem för uppvärmning av broar - En fallstudie över Tranarpsbron*. Examensarbete vid KTH, Stockholm.
- Trafikverket (2014a). *Halkfria vägar Förstudie. Solvärme och värmelagring för miljöanpassad halkbekämpning*. ISBN 978-91-7467-646-4
- Trafikverket (2014b). *Halkfria vägar Etapp 2. Energi och systemanalys med kostnader. Solvärme och värmelagring för miljöanpassad halkbekämpning*. ISBN 978-91-7467-647-1



Synergistic Approaches to Modulate Transition Temperatures in Enhanced Organic Plastic Crystals

Angel Serrano^{1,*}, Eduardo J. Garcia-Suarez^{1,2}, Ander Centeno-Pedraza¹, Jonatan Perez-Arce¹, Elena Palomo del Barrio^{1,2}

1 Centre for Cooperative Research on Alternative Energies (CIC energiGUNE), Basque Research and Technology Alliance (BRTA), Alava Technology Park, Albert Einstein

48, 01510, Vitoria-Gasteiz, Spain

2 Ikerbasque, Basque Foundation for Science, 48013, Bilbao, Spain

*Corresponding author e-mail: aserrano@cicenergigune.com

Abstract

Organic plastic crystals (OPCs) exhibit significant potential for latent heat thermal energy storage (TES). These molecules undergo reversible solid-phase transitions characterized by unusually large enthalpies (110 J/g - 300 J/g) within the temperature range of 44 °C to 185 °C. These unique characteristics position them as ideal candidates to drive future solid-state thermal batteries. This study explores diverse strategies to tailor the transition temperature of these materials. The ability to fine-tune these temperatures not only facilitates the design of versatile solutions but also extends the use of OPCs to applications requiring temperatures beyond the typical operational range of solid-solid phase change materials (PCMs). Among the strategies investigated are the blending of OPCs in binary mixtures, the utilization of fatty acids, and the doping with functionalized solid microparticles. These approaches unlock synergistic benefits, including enhanced energy storage capacity and improvement in thermal conductivity.

Keywords: Solid-solid PCM, Latent heat, Thermal Energy Storage

Introduction

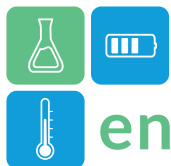
Increasing the compactness of TES systems and the development of versatile solutions have the potential to revolutionize the energy market by enabling modular plug-and-play TES systems. Enhanced compactness reduces the spatial footprint and simplifies the transportation of TES systems. Meanwhile, achieving versatility would eliminate the need for costly and complex individualized studies for different applications and target temperatures, as an optimal material or compound for thermal storage had to be determined for each temperature. Both compactness and versatility can be addressed through material development. In the case of TES systems and considering the aforementioned goals, PCMs are the key materials to be modified.

Currently, the most commercially viable TES technologies are based on solid materials, particularly those utilizing the sensible heat of substances such as rocks, sand, bricks, or concrete. These materials are cost-effective, and their solid-state simplifies the TES system, potentially eliminating the need for a heat exchanger. In a more ambitious approach, solid-solid

PCMs combine the compactness of PCMs with the simplicity and low cost of solid materials.

One promising category of solid-solid PCMs is organic plastic crystals (OPCs). These molecules undergo reversible solid-phase transitions from a low-temperature ordered structure to a high-temperature orientationally disordered phase called plastic phase. The solid phase transition in these plastic crystals takes place at temperatures between 44 °C to 185 °C, and it is characterized by an unusually large enthalpy of transition, ranging from 110 J/g to 300 J/g. OPCs have attracted significant attention for material improvement strategies in terms of energy storage capacity and versatility (Serrano et al. 2019, 2021, 2022, and 2024).

In terms of versatility, these materials are combined in binary and ternary systems to modify their transition temperature within an established range (44-185 °C) defined by the base materials. In addition to the mentioned strategy, this study explores novel approaches to temperature adjustment, aiming to expand the utilization of these materials to temperature ranges beyond the initially set limits of the base materials. These approaches include the



utilization of fatty acids and doping through functionalized microparticles. Beyond adjusting their transition temperature, these strategies enable us to achieve synergistic advantages, such as increased energy storage capacity and a significant enhancement in thermal conductivity.

Materials and methods

Materials and composite preparation

NPG (2,2-Dimethyl-1,3-propanediol), PG (1,1,1-tris(hydroxymethyl)ethane) and PE (2,2-bis(hydroxymethyl)-1,3-propanediol) are supplied by Sigma-Aldrich and used as solid-solid PCM. These materials are also known as neopentylglycol, pentaglycerine, and pentaerythritol, respectively.

Lauric acid provided by Sigma-Aldrich was used as fatty acid, and different functionalized microparticles (graphene oxide, reduce graphene oxide...), were used for the doping of the OPCs.

Characterization

The thermal properties of the obtained composites, including latent heat and transition temperatures, were assessed using Differential Scanning Calorimetry (DSC). The samples underwent heating/cooling cycles at a rate of 5°C/min in a power-compensation DSC Q2500 from TA Instruments, utilizing sealed aluminum crucibles. The sample mass was approximately 9 mg, and Argon (50 ml/min) served as the purge gas.

To determine the thermal conductivity of the samples at room temperature, the transient hot disk method was employed. Measurements were conducted on cylindrical-shaped samples with a diameter of 22 mm and a thickness of 5 mm, using a TPS 2500 S instrument equipped with a Kapton sensor (diameter: 2.001 mm, sensor type 7577). A power of 20 mW was applied to the rear face of the sample for 20 s.

For microstructure analysis, samples were imaged using a scanning electron microscope Quanta 200 FEG operating in low vacuum mode at 10 kV, featuring a backscattered electron detector (BSED) and large field low vacuum detector (LFD). Operational conditions were carefully selected to prevent paraffin melting during the study.

Fourier Transform Infrared Spectroscopy (FTIR) analysis and variable temperature solid-state nuclear magnetic resonance (ssNMR) experiments were conducted to gain insights into the behavior of the composites and the interaction between the compounds comprising them.

Results and discussion

The adjustment of transition temperature through the combination of different OPCs has been extensively documented. An example is the PE:PG system, which enables coverage of discharge temperatures ranging from 78 °C to 180 °C (Figure 1). However, the processing required to obtain these binary systems, as well as their stability under thermal cycling, has been overlooked to date. The results indicate that combinations of OPCs still present unresolved aspects, such as variation in subcooling or instability during cycling depending on the cooling rate. These phenomena are assessed through DSC and NMR techniques to delve deeper into their understanding.

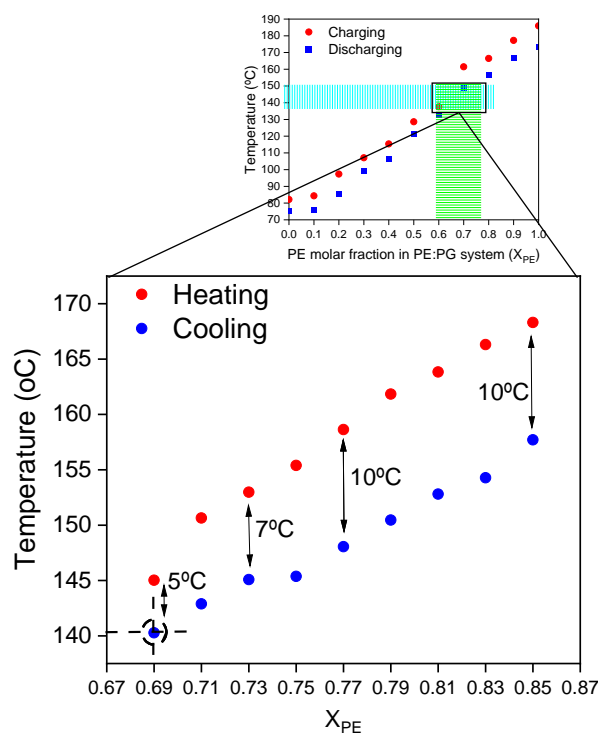


Figure 1. Example of tailoring the discharging transition temperature of the PE:PG binary system, $X_{PE0.67-0.87}$.

Another strategy for formulating OPCs involves the use of fatty acids. In this case, the effect of employing lauric acid to adjust the transition temperature of NPG is demonstrated (Figure 2). The use of this fatty acid not only reduces the transition temperature of NPG from 42°C to 34°C but also increases the phase change enthalpy of the compound by 37%. The interaction between both compounds is evaluated through FTIR, NMR, and DSC. The incorporation of the fatty acid gives rise to a eutectic, which, despite exhibiting the desired thermal properties, loses its solid-solid phase transition property.

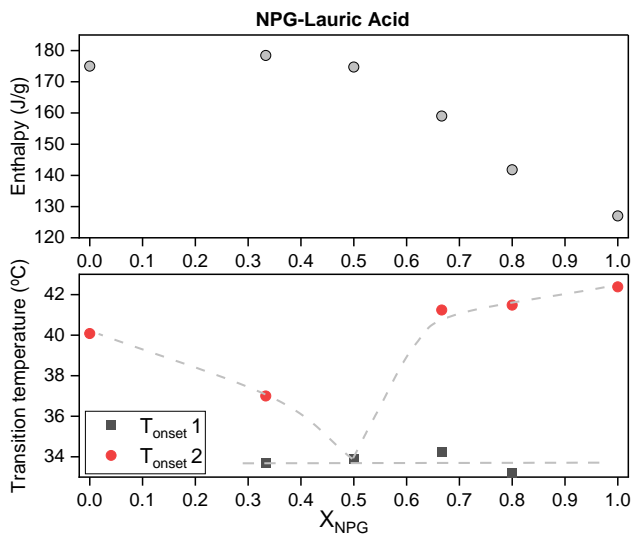


Figure 2. Enthalpy (top) and transition temperatures (bottom) of NPG-Lauric ac. system.

Finally, based on observations made while working with fatty acids, the use of microparticles functionalized with acid groups is proposed to decrease the transition temperature of both NPG and PG (Figure 3). Preliminary results demonstrate the potential of these particles to adjust the transition temperature while maintaining the solid state and increasing the thermal conductivity of the final composite.

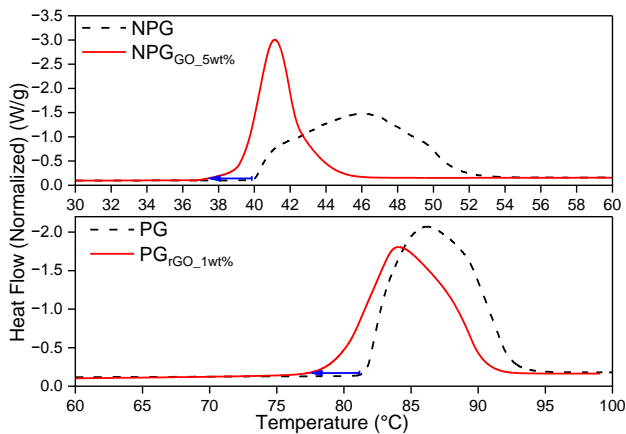


Figure 3. DSC thermograms of NPG and NPG+GO (5wt%) (top), and PG and PG+rGO (1wt%) (bottom).

Conclusions

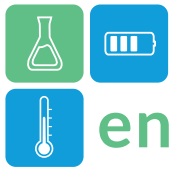
The findings presented herein contribute to the broader understanding of OPCs and facilitate their extended utilization across a variety of TES applications.

Acknowledgment

The research is funded by the Department of Economic Development, Sustainability and Environment of the Basque Government (Programa Elkartek 2023, KK-2023/00063).

References

- A. Serrano, M. Duran, J.L. Dauvergne, S. Doppiu, E.P. Del Barrio, Tailored transition temperature plastic crystals with enhanced thermal energy storage capacity, *Sol. Energy Mater. Sol. Cells.* 220 (2021) 110848. <https://doi.org/10.1016/j.solmat.2020.110848>.
- A. Serrano, I. Garrido, S. Santos, M. Duran, J.-L. Dauvergne, M. Carmona, E. Palomo Del Barrio, Effect of processing on microstructure and mechanical properties of pentaglycerine based solid-solid phase change materials, *J. Energy Storage.* 55 (2022) 105677. <https://doi.org/10.1016/J.EST.2022.105677>.
- Á. Serrano, S. Santos, J.L. Dauvergne, J.M. López del Amo, M. Durán, M. Taño, S. Doppiu, E. Palomo Del Barrio, Effect of processing on thermal properties of pentaglycerine-based solid-solid phase change materials, *Mater. Today Energy.* 39 (2024) 101472. <https://doi.org/10.1016/J.MTENER.2023.101472>
- A. Serrano, J.-L. Dauvergne, S. Doppiu, E. Palomo Del Barrio, Neopentyl Glycol as Active Supporting Media in Shape-Stabilized PCMs, 2019. <https://doi.org/10.3390/ma12193169>.



Synergistic effect of textile-reinforced mortar and phase change materials in buildings

Rabeb Ayed¹, Emiliano Borri², Salwa Bouadila¹, Luisa F. Cabeza^{2,*}, and Mariem Lazaar¹

¹ Centre de Recherches et des Technologies de l'Energie, Technopole de Borj-Cédria, BP : 95, Hamam Lif, Ben Arous, Tunisia

² GREiA Research Group, Universitat de Lleida, Pere de Cabrera s/n, 25001 Lleida, Spain

*Corresponding author: luisaf.cabeza@udl.cat

Abstract

The use of phase change materials (PCMs) and thermal insulation represents a critical way to improve thermal inertia, promoting near-zero energy efficient buildings. This study investigated the effectiveness of PCMs panels and textile-reinforced mortar in improving the thermal behaviour of buildings under harsh summer conditions. Various configurations were studied, from the use of PCMs panels or textile-reinforced mortar in the construction of building roofs to a hybrid approach incorporating both. The results indicate that the integration of textile-reinforced mortar into the roof structure brings a comparable improvement to the installation of a 4-cm thick PCMs board, resulting in a temperature reduction of 3% compared to the reference scenario. In particular, the synergistic combination of PCMs installation and thermally enhanced mortar results in an even more significant temperature drop of around 5%, highlighting the potential of this dual strategy for improved thermal management in building design under harsh climatic conditions.

Keywords: Phase change materials; Thermal insulation; Building applications; Textile fibers; Cement mortar.

1. Introduction

In the realm of enhancing thermal dynamics for energy-efficient and nearly-zero energy buildings, the strategic integration of phase change materials (PCMs) and thermal insulation emerges as a pivotal practical opportunity. In fact, numerous studies underline the potential of PCMs to improve the energy efficiency and thermal behaviour of buildings (Stropnik et al., 2019). However, despite these advantages, phase change materials face significant limitations, including stability (Devanuri et al., 2020) and integration issues. From an alternate perspective, it is acknowledged that attaining near zero energy buildings requires thermal insulation (Amani and Kiaee, 2020). Therefore, several studies investigate the combination of thermal insulation and PCMs in construction. Jia et al. (Jia et al., 2021), for instance, numerically studied the effect of incorporating different thermal insulation materials and PCMs in brick walls. The results showed that the incorporation of the insulation materials increased the thermal resistance while PCMs increased the thermal inertia, resulting in significant improvements in the thermal behaviour of the bricks. Similarly, Kalbasi and Afrand (Kalbasi and Afrand, 2022) studied the efficiency of walls with integrated insulation, PCMs or a combination of both and found that PCMs perform better in summer and insulation is more effective in

winter. Meshgin et al. (Meshgin et al., 2012) investigated the addition of PCMs and rubber particles to cement mortar. The results of thermal conductivity analysis show a decreasing trend of thermal conductivity of rubberized mortar with decreasing size of rubber particles. The introduction of phase change material results in a clear peak in the thermal conductivity curve exactly at the melting point of the PCM. When examining the thermal properties, it is clear that the rubber particles play an essential role in reducing the thermal conductivity of the mortar. Conversely, the PCMs contribute to increasing its thermal capacity.

To improve thermal efficiency, this study investigates the potential of PCMs panels and textile-reinforced mortar in building roof. Textile-reinforced mortar consists of a composite material made from textile fibre waste and a cementitious matrix (Ayed, Borri, et al., 2023). This combination has proven effective in improving the thermal properties of building elements (Ayed, Bouadila, et al., 2023). Four different scenarios were studied. The first one represents a reference room test with a 10-cm thick concrete roof. The second scenario represents a room whose roof is built with a layer of textile-reinforced mortar on a layer of concrete. The third scenario represents a room in which a PCM board was integrated into the concrete roof. The last

scenario investigates a room where a PCM panel has been integrated in the roof between a layer of concrete and a layer of textile-reinforced mortar. The comparison was done based on the improvement in indoor air temperature of a test room. Overall, this research aims to enhance understanding regarding the potential benefits of integrating phase change materials and textile fibres in buildings.

2. Methodology

This study aims to employ numerical modelling, using COMSOL Multiphysics software, to examine the influence of cement mortar reinforced with textile fibres and PCMs on the thermal behaviour of a test room in summer. This numerical analysis is based on a previous experimental study carried out on a self-contained cabin room with a volume of 1 m³ on northern Tunisia at the Energy Research and Technology Center in Borj Cedria. The experimental test room, shown in Figure 1(a), consists of brick walls coated with a 2 cm thick layer of cement mortar on both sides and a roof made of a 10 cm thick layer of concrete.

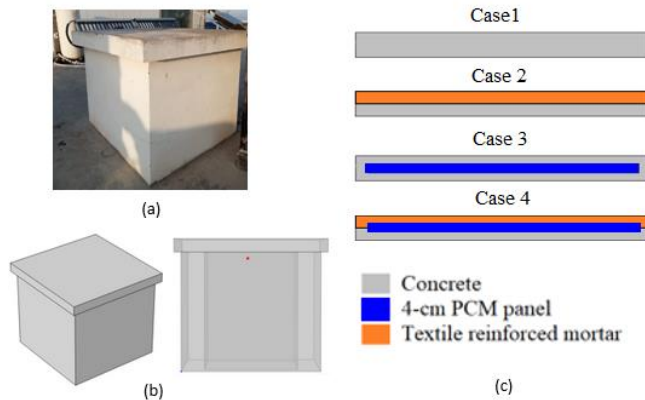


Figure 1: (a) Experimental room, (b) 3D geometry designed with COMSOL and (c) studied roof configurations.

The approach taken in this study is to change the roof configuration each time through one of the configurations listed below:

- **Scenario 1:** A reference test room that is an exact copy of the experimental space utilized to validate the numerical model.
- **Scenario 2:** A room whose roof is built with a 5-cm thick layer of cement mortar, reinforced with 40% textile fibres by volume, on a 5-cm thick layer of concrete.
- **Scenario 3:** A room in which a 4-cm thick PCM board was integrated into the 10-cm thick concrete roof.
- **Scenario 4:** A room where a 4-cm thick PCM panel has been integrated in the roof between a 5-cm thick layer of

concrete and a 5-cm thick layer of textile-reinforced mortar.

A three-dimensional (3D) geometry was developed (Figure 1(b)) and a time-dependent study was selected for this numerical study. This analysis included conjugate heat transfer component, phase change material feature, the laminar flow module, and the surface-to-surface radiation function. Investigating how changes in room configuration (Figure 1(c)) affect the thermal environment focused on assessing air temperature changes. Table 1 represents the thermal properties of the used materials.

Table 1: Thermal properties of the used materials.

Material	PCM DS5001X	Textile reinforced mortar	Concrete
Solid thermal conductivity [W/m·K]	0.2	0.91	1.8
Liquid thermal conductivity [W/m·K]	0.13	-	-
Solid heat capacity [J/kg·K]	1700	1815	880
Liquid heat capacity [J/kg·K]	2153	-	-
Latent heat [kJ/kg]	130	-	-
Density [kg/m ³]	995	1690	2300

3. Results and Discussion

3.1. Climatic conditions and model validation

The meteorological conditions considered in the numerical simulation are those recorded at the test site on the day of the experiment. Figure 2 shows the climatic conditions at the experimental site. This experimental measurement took place on a typical summer day with outdoor temperatures fluctuating between 33 °C and 22 °C, accompanied by a maximum solar radiation of about 960 W/m².

Figure 3 portrays a comparison between the predicted mid-cabin air temperature variation in Scenario 1 and the temperature observed through experimental measurements. This graph shows a consistent pattern between the numerical and experimental with a root mean square error of 0.48. This consistency of results supports the reliability of the model in anticipating heat transfer within the intended space.

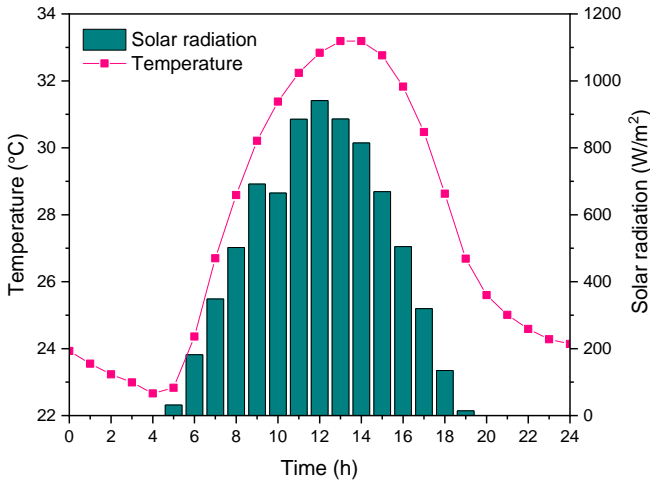
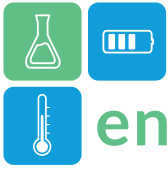


Figure 2: Variations of the external air temperature and the solar radiation at the experimental site.

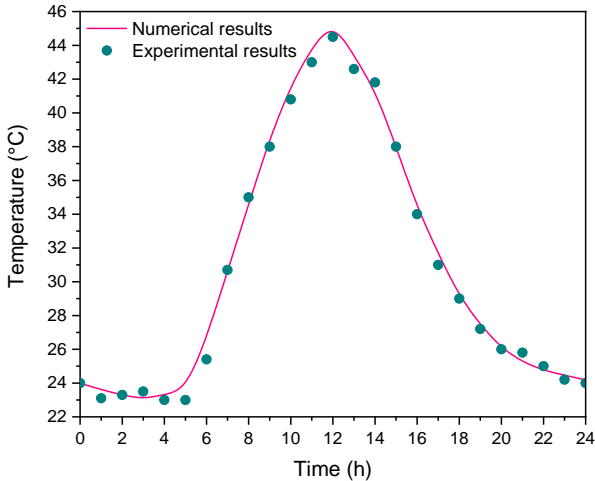


Figure 3: Experimental and numerical results comparison.

3.2. Evaluation of the effect of adding textile-reinforced mortar in a building roof

Figure 4 shows a comparison of air temperature fluctuations across the four scenarios. Since the changes occur in the architectural composition of the roof, the temperature change was evaluated at a location close to the roof (Figure 1(b)). Figure 5 represents an enlargement of Figure 4 from 10 a.m. to 2 p.m. As shown in the graphic, replacing a 5 cm thick concrete layer with thermally reinforced mortar resulted in a similar temperature drop as installing a 4 cm thick PCM board on the concrete roof. In fact, both scenarios 2 and 3 show a 3% decrease in maximum temperature compared to scenario 1. However, these two cases show different time periods, which is related to the thermal properties of phase change materials. It is noteworthy that a room in which a 4 cm thick PCM panel has been integrated into the roof between a 5 cm thick layer of concrete and a 5 cm thick layer of textile-reinforced mortar has the lowest air temperature

fluctuations, resulting in a maximum temperature reduction of 5% compared to scenario 1.

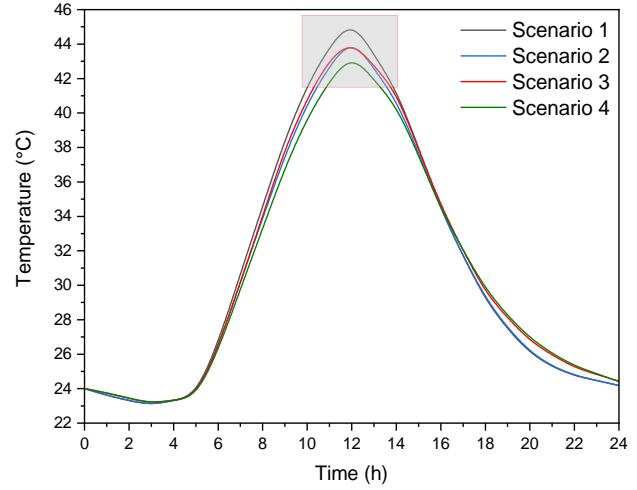


Figure 4: Comparison of air temperature variations in the four scenarios.

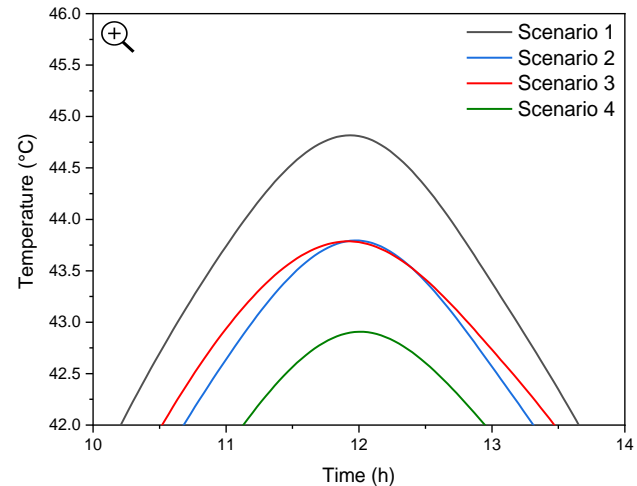


Figure 5: Air temperature variations in the four scenarios from 10 a.m. to 2 p.m.

4. Conclusion

This research examines the incorporation of phase change material (PCM) and thermal insulation to improve thermal dynamics in energy efficient buildings. Numerical simulations were conducted to evaluate different configurations, including standalone PCM panels or textile-reinforced mortar and their combined use for building roofs. The results show that by adding textile-reinforced mortar into the roof structure, a temperature reduction of 3% is achieved, similar to a 4 cm thick PCM board. A more significant temperature drop of 5% occurs when both PCM and thermal insulation are integrated, demonstrating potential synergies in reducing heat influx for



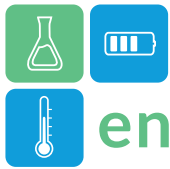
improved energy efficiency in building design under adverse climatic conditions.

Acknowledgement

This study was supported by the Thermal Processes Laboratory of the Research and Technology Center of Energy (CRTE) in Tunisia. Funded by the European Union's Horizon Europe Research and Innovation Programme under grant agreement No. 101086302 (CSTO2NE). Views and opinions expressed are however those of the author(s) only and do not necessarily reflect those of the European Union or REA. Neither the European Union nor the granting authority can be held responsible for them. The authors from University of Lleida would like to thank the Catalan Government for the quality accreditation given to their research group (2021 SGR 01615). GREiA is certified agent TECNIO in the category of technology developers from the Government of Catalonia. This work is partially supported by ICREA under the ICREA Academia programme.

References

- Amani N and Kiaee E (2020) Developing a two-criteria framework to rank thermal insulation materials in nearly zero energy buildings using multi-objective optimization approach. *Journal of Cleaner Production* 276. Elsevier: 122592. DOI: 10.1016/J.JCLEPRO.2020.122592.
- Ayed R, Borri E, Gasa G, et al. (2023) An Experimental Study on the Thermo-mechanical Properties of Cement Mortar with Textile Fibers for Building Applications. *RILEM Bookseries* 43: 1153–1162. DOI: 10.1007/978-3-031-33211-1_103.
- Ayed R, Bouadila S, Skouri S, et al. (2023) Recycling Textile Waste to Enhance Building Thermal Insulation and Reduce Carbon Emissions : Experimentation and Model-Based Dynamic Assessment. DOI: 10.3390/buildings13020535.
- Devanuri JK, Gaddala UM and Kumar V (2020) Investigation on compatibility and thermal reliability of phase change materials for low-temperature thermal energy storage. *Materials for Renewable and Sustainable Energy* 9(4). Springer International Publishing: 1–16. DOI: 10.1007/s40243-020-00184-4.
- Jia C, Geng X, Liu F, et al. (2021) Thermal behavior improvement of hollow sintered bricks integrated with both thermal insulation material (TIM) and Phase-Change Material (PCM). *Case Studies in Thermal Engineering* 25(January). Elsevier Ltd: 100938. DOI: 10.1016/j.csite.2021.100938.
- Kalbasi R and Afrand M (2022) Which one is more effective to add to building envelope: Phase change material, thermal insulation, or their combination to meet zero-carbon-ready buildings? *Journal of Cleaner Production* 367. Elsevier: 133032. DOI: 10.1016/J.JCLEPRO.2022.133032.
- Meshgin P, Xi Y and Li Y (2012) Utilization of phase change materials and rubber particles to improve thermal and mechanical properties of mortar. *Construction and Building Materials* 28(1). Elsevier: 713–721. DOI: 10.1016/J.CONBUILDMAT.2011.10.039.
- Stropnik R, Koželj R, Zavrl E, et al. (2019) Improved thermal energy storage for nearly zero energy buildings with PCM integration. *Solar Energy* 190. Pergamon: 420–426. DOI: 10.1016/J.SOLENER.2019.08.041.



System and Component Model Development of a Secondary Loop System with Buried Thermal Energy Storage Tank

Pouria Moghimi¹, Jeffrey D. Spitler^{2,*}, Christian K. Bach³

¹ Oklahoma State University, PhD Student, Mechanical and Aerospace Engineering School, USA

^{2,3} Oklahoma State University, Faculty, Mechanical and Aerospace Engineering School, USA

*Corresponding author e-mail: Spitler@okstate.edu

Abstract

Heating Ventilation and Air Conditioning (HVAC) represents the largest share of residential buildings' final energy consumption. Storage of thermal energy can facilitate renewable electricity generation by providing a way to mitigate renewable's intermittent nature. In this research, we are researching integration of a buried and stratified thermal energy storage tank with a residential-scale water-based secondary loop system providing cooling. Simulations are conducted to compare the performance of an Above-Ground (AG) thermal energy storage (TES) tank vs a buried-in-the-ground TES tank. The in-tank model is validated with our experimental data for charging, storage, discharging and adverse feed temperature scenarios. Case studies are presented for Stillwater, Oklahoma and Chicago. Results show that a buried tank of volume 2 m³ with insulation thickness of 13mm can provide a round-trip efficiency of 93 and 101% for single-family houses in Stillwater and Chicago respectively. This is 14 and 22% higher than an AG tank with the same insulation.

Keywords: Thermal Energy Storage (TES), buried-in-the-ground TES, Above-ground TES, Secondary loop

Introduction

The intermittent and non-dispatchable nature of renewable electrical energy generation is a key challenge to maintaining electrical grid stability. Grid-scale electrical storage is not currently feasible, but a potential solution is the use of load-side TES. Given the increasing interest in TES solutions, efficient numerical models are needed for accurately modelling TES systems as a new component of buildings' HVAC system.

While residential heating and cooling distribution systems are commonly air-based in the USA, water-based secondary loop systems integrated with TES offer many benefits - low-cost, no intermediate heat exchanger between the TES and distribution system; easy zoning of the house. Outdoor air-to-water heat pumps can use flammable refrigerants, and allow plug-and-play installation, so that the unit can be swapped out and serviced in shop. Review of the literature shows that integration of the TES with an HVAC system can help reduce peak energy consumption and cycling of the system, yet there is the risk that total energy consumption can be increased due to TES losses. If this increased energy consumption occurs while renewable electricity is available, the TES may still lower carbon footprints. Also, taking the advantage of low-cost time-of-use utility pricing during off-peak hours can

compensate for higher initial cost of the system (Alghamdi and al., 2022). However, extra space needed for an AG storage tank may be undesirable.

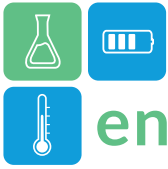
In this research, we are studying the feasibility of an alternative solution: a buried-in-the-ground and fully stratified tank made from HDPE (similar technology to ground heat exchangers). Design guidance will then be needed for this novel approach in selection of the optimum tank design (shape and aspect ratio), burial depth, insulation thickness, etc.

In this presentation, we model a buried TES integrated with other components of a secondary loop system serving a residential building. Model validation is discussed. Storage efficiency of the tank will be compared for buried vs AG tanks with different insulation levels during the cooling season.

Methodology

Overview

Firstly, we developed a 1-Dimensional (1D) model for in-tank simulations. Our goal was to develop a comprehensive, yet simple model capable of modeling the TES in all operation scenarios: charging, discharging, and storage during the time between charging and discharging. Our experimental facility is used to examine the model's predictive capabilities for these scenarios. This model is also used as the AG TES model. To model a buried tank, this model is coupled



to a 2D cylindrical model of the surrounding ground. The two models are coupled by assuming that the soil temperature remains constant for a given time step (dt_{soil}), calculating heat losses from the tank to soil for a given number of tank time steps ($N = dt_{soil} / dt_{tank}$) and updating soil boundary conditions for the next soil time step calculations. Typical time steps are 60 s and 600 s for the tank and soil, respectively. Additionally, a system model is developed for integrating the TES tank with other components of a secondary loop system for charging and discharging the tank. Here, we will examine the system performance for the cooling mode during summer. Comparisons will be made for AG vs buried TES tanks that are fully charged and discharged daily during this period.

In-tank Model

Accurately modeling a stratified tank is the first step in our simulations. We assumed that for a well-designed inlet and outlet diffuser design, the temperature profile in the radial direction of the tank will be uniform (this assumption is examined later in results). Hence, the temperature changes along the tank's height in the z -direction (Figure 1, left). The finite volume method (FVM) is used for numerical modeling of the problem.

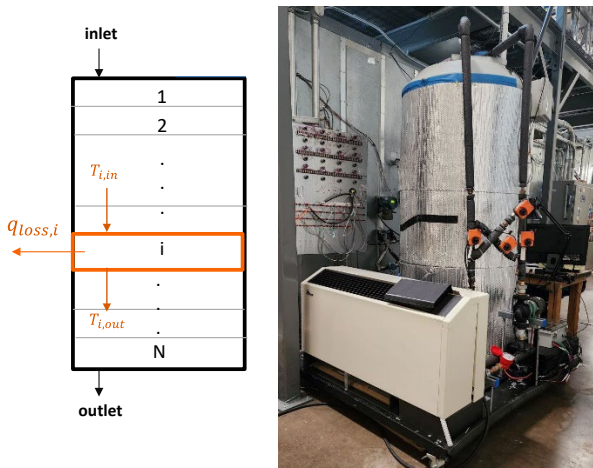


Figure 1: TES tank, left: Segmented numerical model and right: Above ground TES experimentation apparatus

We employed a hybrid scheme for numerical discretization of the governing equations (Versteeg et al., 2007). The hybrid scheme automatically selects between an upwind scheme (accurate in advection dominant flows: charging and discharging modes in our problem) or a central scheme (accurate in diffusion dominant flows: storage mode). Also, a simplified approach (Newton 1995) is used to account for buoyancy when thermal inversion occurs. The simplified approach checks for thermal inversion, and, when it occurs, mixes every two cells with a thermal inversion, and sets the temperature of these two

segments equal to their average temperature. This procedure is repeated till no thermal inversion exists in that tank time step.

TES Tank Experimental Test Bed

A test bed capable of automatically replicating charging, storage and discharging modes is developed for validating the 1D tank model (Figure 1, right). A 5.3 kW (1.5-tons) heat pump is used for cooling/heating of the water in the tank. Four two-way valves allow the mode selection between charging and discharging based on the operation mode, e.g., in charging during cooling mode, cold water enters the tank from bottom diffuser and warm water is discharged from the top diffuser. Forty calibrated digital ds18b20 temperature sensors measure temperatures inside the tank with accuracy of $\pm 0.5^\circ\text{C}$ from -10°C to $+85^\circ\text{C}$.

Twenty are located on a temperature tree close to the wall and the other half are located on a temperature tree in the middle of the tank at the same vertical locations. Additionally, temperatures at the inlet and outlet of the tank and heat pump are measured.

Ground Model

Heat transfer in the ground is modeled in 2D cylindrical coordinates. A grid with finer mesh in regions closer to the tank and coarser mesh in the far field is generated to save computational resources in the far field where temperature gradients are small (Figure 2). A modeled undisturbed ground temperature (UGT) is used to determine the initial and boundary conditions of the ground as a function of depth, location and day of the year. (Xing and Spitler, 2015)

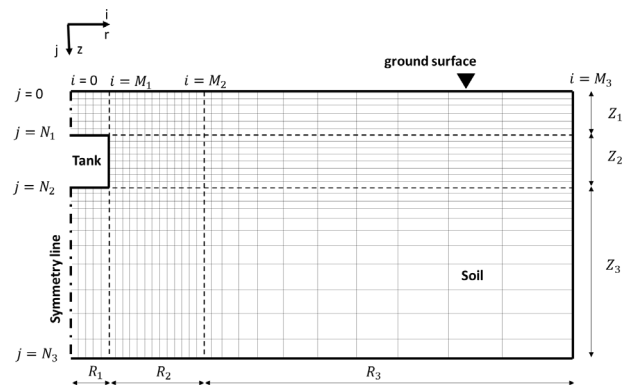


Figure 2: Problem domain-grid generation

Secondary Loop System Model and Control Strategy

The system model (Figure 3) incorporates the other components with separately calculated cooling loads. The system model consists of an Air to Water Heat Pump (AWHP), TES tank (buried or AG) and indoor hydronic coil. For the AWHP, we are using

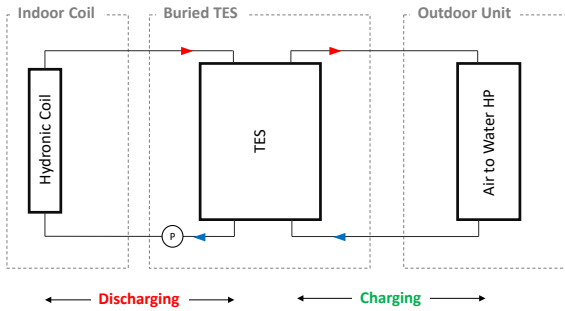
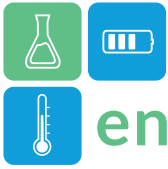


Figure 3: Secondary loop system with TES

performance data of a commercially available heat pump, with nominal 12.3 kW (3.5 tons) of refrigeration capacity.

The indoor coil is a hydronic heat exchanger component adapted from ACHP (ACHP’s documentation, 2011). For purposes of demonstrating the results, the AWP starts to run at 2 a.m to charge the tank until the average temperature inside the tank reaches a target setpoint temperature. Discharging mode starts at 2 p.m to maintain indoor temperatures using the secondary loop until the tank reaches to a discharge setpoint temperature. Energy extracted from the tank divided by energy needed for charging the tank is used to calculate the round-trip efficiency (RTE) of the tank as a key performance indicator.

Results and Discussion

The 1D in-tank model has been validated with experimental measurements made in the test apparatus shown in Figure 1. Sample validation results for charging and storage modes are presented in Figure 4.

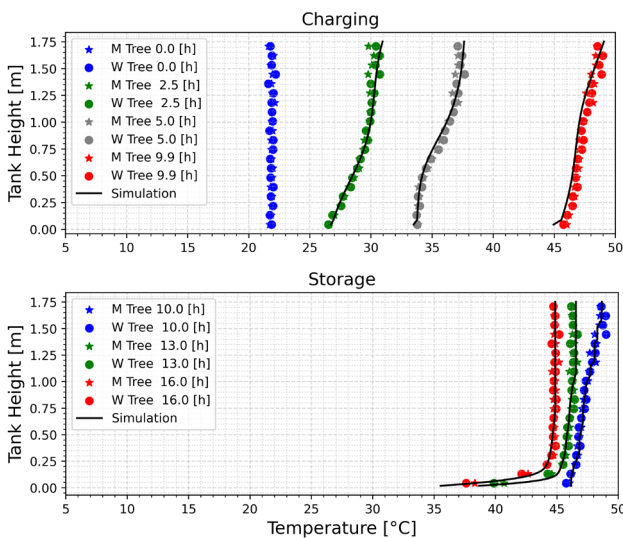


Figure 4: In-tank model validation-time in hours [h]

Temperature profile inside the tank as a function of time is shown where M Tree and W Tree represent the

middle and wall temperature trees, respectively. The legend shows elapsed times since the start of charging. Maximum RMSE for the results is 0.46 °C for the data shown in Figure 4.

As can be seen, temperature in W and M trees are almost the same, indicating the validity of the 1D assumption. To examine the accuracy of Newton’s (1995) simplified approach, tests with adverse feed temperatures were also conducted (e.g. feeding hot water from bottom). Model accuracy similar to that shown in Figure 4 is obtained, indicating the high performance of the simplified approach.

Sample results for the coupled ground-tank model are shown in Figure 5. Temperature contours show both in-tank and ground temperatures in °C.

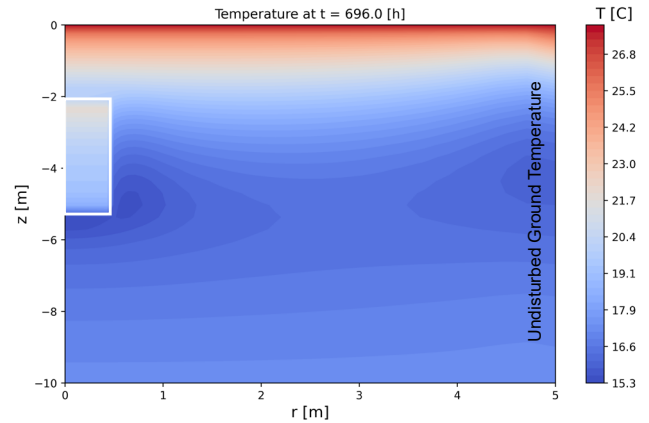


Figure 5: Temperature contour in the problem domain

System simulations are conducted for two locations in the USA: Stillwater, OK, and Chicago, IL. A buried tank with 13 mm insulation is compared with an AG tank with different insulation thicknesses. This is to see how much extra insulation is needed if the tank is installed above ground. Simulation assumptions are presented in Table 1.

Table 1: Simulation setup and assumptions.

Variable	Value	Explanations
Tank Volume	2 m ³	Cylindrical tank with 0.5 m radius and 3.37 m height
Tank burial depth [m]	2 m	Z ₁ in Figure 2
Operation Period	Summer	June 1 to Sept. 1
Charging Setpoint Temp.	7 °C	Average temperature inside the tank
Discharging Setpoint Temp.	20 °C	Average temperature inside the tank
Insulation	$k = 0.04 \frac{W}{m.K}$	Polyurethane foam

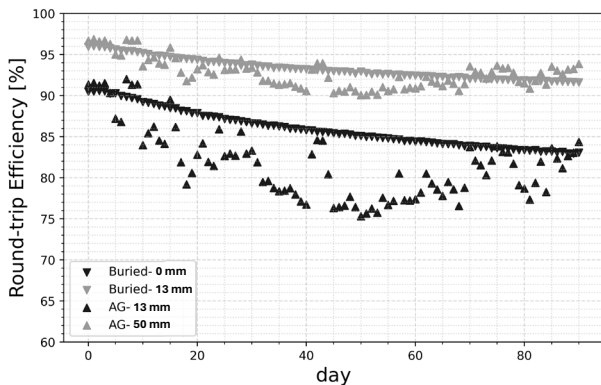
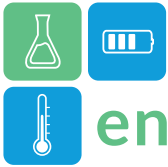


Figure 6: Daily RTE during cooling season, Stillwater, OK.

The daily variations of RTE during the cooling season are shown in Figure 6 for Stillwater for several cases. Both the buried tank and AG tank are subject to ambient temperature variations. The AG tank is exposed to outdoor air without solar radiation (e.g. located in a carport).

The buried tank, however, shows less fluctuation – the RTE drops as the cooling season progresses, due to an increase in UGT over the summer. Although we cool down the ground surrounding the tank during charging period, the far-field UGT increases its temperature leading to higher heat gains to the tank in summer. Table 2 summarizes the results for the entire cooling season for Stillwater and Chicago.

Table2: Summary table, RTE [%] for the entire cooling season.

Insulation [mm]	Buried TES		Above-Ground TES		
	0	13	13	25	50
Stillwater, OK	86%	93%	82%	88%	93%
Chicago, IL	102%	101%	88%	92%	95%

As can be seen in Table 2, the TES tank has higher overall RTE in Chicago in comparison with Stillwater, which is due to lower ambient and ground temperatures in Chicago. The Chicago system with buried TES has RTE exceeding 100% due to low ground temperatures in Chicago. This is for an idealized case where the tank is fully charged and discharged each day. This condition is nearly met for Stillwater with the 2m³ tank, but not for Chicago. Therefore, the high seasonal RTEs may be considered an upper limit for the building loads and tank size. For Stillwater, burying the tank with 13mm insulation can provide the same RTE as an AG tank with 50mm insulation.

Conclusions

A system model capable of simulating the integration of buried or AG TES tanks with other components of a

secondary loop is developed. With the validated in-tank model, a daily charging/discharging scenario is simulated throughout the cooling season. Results for Stillwater and Chicago show that:

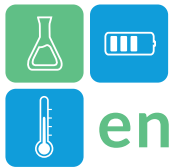
- Burying the tank can save aboveground space and lower ground temperatures, compared to the ambient air, can result in lower heat gains to the tank in the cooling season.
- As a result, the buried tank has a higher RTE than an AG tank for the same insulation thickness. The trend of change in RTE is also more stable and predictable for the buried tank and this can be an advantage for predictability of the system and its charging/discharging controls.
- RTE for the AG tank fluctuates with ambient temperature. However, RTE drops for the buried tank as we go through the cooling season indicating that the increase in UGT is the dominant phenomena around the tank.
- Low ground temperatures in Chicago are favorable for the cooling performance of the tank, but these values depend on a daily cycle that fully charges and discharges the tank. Further investigation is planned to optimize the tank size, design, controls, and economics for a range of locations.

Acknowledgment

Support of the Center for Integrated Building Systems (CIBS) at OSU and its industry members is gratefully acknowledged. An undergraduate capstone design team developed the preliminary version of the experimental test bed.

References

- Alghamdi, K. I. and al., (2022), "Water-Based Thermal Energy Storage for Heating and Air-Conditioning Applications in Residential Buildings: Review and Preliminary Study". International Refrigeration and Air Conditioning Conference. Paper 2345.
- Bell, I., (2011), ACHP Documentation, <https://achp.readthedocs.io/en/latest/ACHPComponents/CoolingCoil.html>, accessed 11/20/2023.
- Newton, B. J., (1995), Modelling of Solar Storage Tanks, U. Wisc.-Madison, MS Thesis.
- Versteeg, H. K. and al., (2007) An Introduction to Computational Fluid Dynamics, The Finite Volume Method, 2nd Edition, Pearson Education Limited.
- Xing, L. and Spitler, J. D., (2017), Prediction of undisturbed ground temperature using analytical and numerical modelling. Part I: Model development and experimental validation, Science and Technology for the Built Env., 23:5, 787-808.



Test rig for investigating the optimisation of operating strategies for steam supply with passive Latent Heat – Thermal Energy Storages

Larissa Dietz*, Michael Fiss, Fatima Mata-Marquez, Inga Bürger, Andrea Gutierrez
German Aerospace Center (DLR), Pfaffenwaldring 38-40, 70569 Stuttgart, Germany,
corresponding author e-mail: larissa.dietz@dlr.de

Abstract

The shell and tube heat exchanger design is one of the most popular designs for passive latent heat thermal energy storage systems [1]. Nevertheless, the simultaneous transient phenomena in the heat transfer fluid (HTF) and phase change material (PCM) during the operation of these systems are not yet fully understood. Therefore, a finned single-tube LH-TES test section was designed and built. The test rig has a charging and discharging infrastructure for the operation with water and steam as HTF and PLUSICE A133 as PCM. Also, several thermocouples were strategically installed to record the temperature of both, the PCM and the HTF. The temperature measurement network inside the LH-TES for detecting the phase change front in the PCM was determined based on Fluent® simulations of the cross-section and measurement results generated with a small test container. Additional thermocouples in the HTF-flow are used to monitor the coupled behaviour of PCM and HTF. Using this test rig optimised operating strategies are studied, based on an indirect operating parameter, namely the dominant heat transfer surface, and validation data for numerical design models is generated.

Keywords: PCM, steam supply, operation strategies, passive LH-TES

Introduction

The shell and tube heat exchanger is one of the most popular designs used for thermal energy storage units in industrial applications [1]. It can be used for Latent Heat – Thermal Energy Storage (LH-TES) systems where the storage medium is a phase change material (PCM), which is provided in the shell of the device. The optimal design of such passive TES and a controlled dynamic operation is only possible if the transient phenomena occurring in the PCM and in the heat transfer fluid (HTF) during the charging and discharging process of the storage unit are known in detail, as they determine the thermal power profile of the system. A test rig was designed and built to investigate the influence of an indirect transient operation parameter in LH-TES systems with a two-phase HTF on the thermal charging and discharging power: The so-called *dominant heat transfer surface*. It can be adjusted by the HTF mass flow rate as well as by the temperature difference between the HTF inlet temperature and the PCM phase change temperature. This work presents the results of the test section design based on numerical simulations and experiments with a small test container.

Materials and Methods

PCM and HTF

The storage material in the test section is PLUSICE A133, a polyethylene glycol, supplied by Phase Change Material Products Ltd, with a melting temperature of 133 °C and a phase change enthalpy of 200 kJ/kg (Figure 1). The HTF is demineralised water.



Figure 1: PLUSICE A133, an organic pure and single chain length compound.

Infrastructure

In Figure 2, the infrastructure for operating the test section is shown. To charge the storage element, the pump transports the water to the evaporator where saturated steam is generated. The steam is superheated

using an electrical heating wire to avoid condensation before reaching the tube inlet and then flows into the top of the test tube. It condensates and the released energy is transferred to the solid PCM in the storage part of the test rig which then melts. Depending on the state of charge of the PCM, the water leaves the bottom of the tube gaseous, liquid or as a two-phase fluid. In the subsequent tube-in-shell condenser, the fluid is condensed and/or cooled down to 60 °C and fed back into the cycle. During discharging, the HTF inlet temperature is established in the electrical preheater and the saturated liquid water flows through the tube in the opposite direction, entering at the bottom of the tube.

The special feature of the steam cycle is the possibility to control the mass flow rate of the HTF and pressure in the system simultaneously with the help of a back-pressure regulator (a) and mass flow rate control valves during charging (b)/during discharging (c). HTF mass flow rate, inlet and outlet pressures and temperatures as well as the mass flow rate and inlet and outlet temperatures of the cooling water flowing through the condenser are recorded with the Siemens PLC system SIMATIC S7-1500.

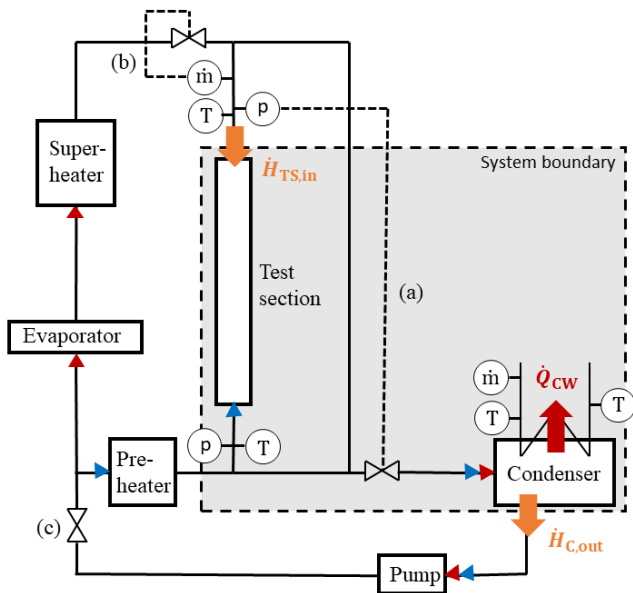


Figure 2: Steam/water infrastructure for the charging and the discharging of the test section with system boundaries for the calculation of the storage power.

Test section

The storage element to be investigated consists of a pressure steel tube with clamped-on aluminium fins embedded in a steel container filled with the storage material. As seen in Figure 3, the container is 2 m long and a set of temperatures is measured on each of

the five levels, L1 to L5, distanced by 30 cm from each other in axial direction. To measure the temperature representatively at all relevant positions, a self-tailored container design was developed, as can be seen in Figure 4. It contains mounting possibilities for thermocouples in the pressure tube, at the tube wall and in the PCM on each level.

Based on the results of numerical simulations in Fluent® and temperature measurements in the test container, the relevant thermocouple positions were chosen for the test rig shown in Figure 3. This is explained in the section Results and Discussion.

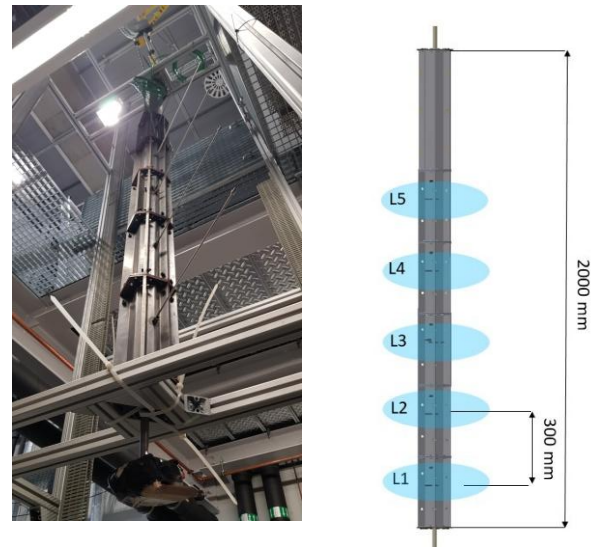


Figure 3: Schematic and photograph of the test section.



Figure 4: Schematic and photograph of the test container.

Determination of the thermal storage power

The thermal power of the test section during charging and discharging is calculated using an energy balance for system boundaries that include the storage element itself and the condenser as shown in Figure 2. Due to the difficulty of determining the steam fraction in two-phase flows, enthalpy flow rates in the two-phase HTF are avoided this way. Furthermore, the cooling cycle of the condenser is designed to determine precisely the dissipated heat. Thus, the thermal power

of the storage element can be calculated precisely based on Equation 1.

$$\dot{Q}_{HTF \rightarrow PCM} = \dot{H}_{TS, \epsilon} - \dot{H}_{C, out} - \dot{Q}_{CW} \quad (1)$$

Results and Discussion

The goal of the temperature measurements in the PCM is to generate representative data for the determination of the phase change front with a limited number of thermocouples in the cross-section. In Figure 5 (left) the initially planned positions for temperature measurements are marked. The necessity of placing thermocouples in all the intended positions was checked using further Fluent® simulations of the cross-section. The results shown that there are two bundles of similar temperature curves, which can be represented by one measurement only. Thus, the number of thermocouples per cross-section was reduced significantly as can be seen in Figure 5 (right), from 95 to 59 thermocouples. The purposes for all measurement positions are listed in

Table 1.

Table 1: Thermocouple positions and corresponding functions.

Position	Function
3.1, 3.2	Checking uniform heating of fins
1.1	Differentiating 1p/2p flow in tube
1.2	Estimating of aggregate state of HTF
1.3, 2.3, 2.1, 2.3R, 2.4R, 2.7R, 2.2	Determining of phase change front position/State of Charge
1.3', 2.1', 2.4R', 2.7R', 2.2'	Checking Symmetry of phase change front

References

- Li, Q., et al., *A review of performance investigation and enhancement of shell and tube thermal energy storage device containing molten salt based phase change materials for medium and high temperature applications*. Applied Energy, 2019. **255**.

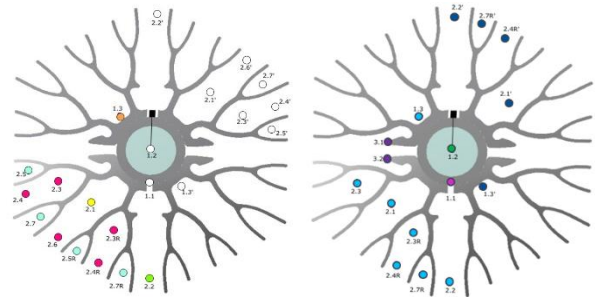


Figure 5: Original measurement cross-section (left side) and cross-section with a reduced number of thermocouples (right side).

Conclusions

A single-tube test section and the corresponding charging and discharging infrastructure were designed and built. The test rig consists of a finned pressure tube that uses water and/or steam as HTF and the storage container is filled with the PCM PLUSICE A133. The evaluation method to determine the (charging/discharging) thermal power of the storage was developed in this study. The temperature measurement network in the LH-TES to measure the phase change front in the PCM was strategically installed. Using the new test rig, experiments to test optimized operation strategies based on the so-called *dominant heat transfer surface* and to generate experimental validation data for numerical models will be performed and presented in 2024.

TESTING AND ANALYSIS OF A DUAL-TUBE LATENT HEAT STORAGE SYSTEM

Maike Johnson, Konstantinos Theologou, Jonas Tombrink, Larissa Dietz*, Andrea Gutierrez
 German Aerospace Center (DLR), Pfaffenwaldring 38-40, 70569 Stuttgart, Germany,
 *Corresponding author e-mail: larissa.dietz@dlr.de

Abstract

In order to effectively charge and discharge a latent heat thermal energy storage, there must be a driving temperature difference between charging and discharging, resulting in a higher charging than discharging temperature. For a system using differing charging and discharging media, this was made possible through the development of a dual-tube concept. A storage unit was designed, tested and built integrating two tube registers with connecting fins, showing the feasibility of such a system. An axially finned tube was created for this, allowing for heat conduction via highly conductive aluminium directly between the circuits, as well as heat transfer between the heat transfer fluid and the phase change storage material (eutectic mixture of lithium and potassium nitrate). Data from the experimental analysis is shown and discussed.

Keywords: PCM storage; latent heat; dual-tube; axial aluminium fins; heat transfer fluid

Introduction

The shell-in-tube design is widely used for the implementation of passive latent heat thermal energy storage (LH-TES) systems [1]. In a review by Li et al. [1] on the performance of LH-TES with salt-based phase change materials (PCM) for medium and high temperatures in this arrangement, most of the heat exchangers – although they differ in detail – have flow in one direction during charging and in the other during discharging as displayed in Figure 1.

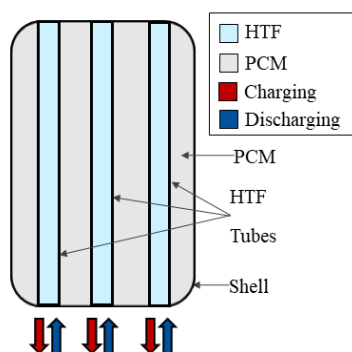


Figure 1 Schematic of charging and discharging flow directions in a single-tube LH-TES unit.

This results in a number of challenges when integrating such storages into a system. Firstly, there are difficulties when switching from charging to discharging mode or vice versa. The HTF tubes – and connecting welds – may be exposed to large and rapid changes in pressure and temperature during the changeover. This leads to significant stress on the tubes and can cause damage.

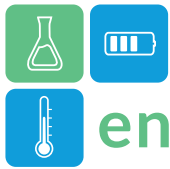
Differing heat transfer fluids (HTF) may be in use in the system integration – for example feedwater and condensate, possibly contaminated with lubricants.

These challenges can be alleviated through the integration of a separate closed loop for the storage system, necessitating additional valves, heat exchangers and control systems, and inducing an additional temperature gradient between charging and discharging, which may not be feasible from a system point of view.

In this paper, a dual-tube LH-TES concept [2] is proposed as a solution. As it can be charged and discharged via separate tubes using different refrigerants, extra valves, heat exchangers and system control components are not needed, temperature differences between charging and discharging are minimized and material stresses are reduced. Garcia et al [2] also recognize the advantages of a double-tube heat exchanger for the integration of solar heat into steam processes.

Methodology

This LH-TES was designed for the coupling of a high-temperature heat pump and an organic Rankine cycle, in order to create a flexible energy management system, as discussed by Weller et al. in [3]. The heat pump upgrades heat, theoretically electrically powered by renewable energies, thereby evaporating the refrigerant. This condenses in the LH-TES, thereby charging the storage. When energy is dispatched again, the other refrigerant is pumped



through the LH-TES, evaporating it and discharging the storage. This is then condensed in the organic Rankine cycle while converting a portion of the thermal energy to electricity. Excess heat can be further transferred to a system such as a district heating network. The coupling of these systems required not only the driving temperature difference between the charging and discharging cycles in the LH-TES, but also differing refrigerants as well as lubricants for the heat pump and organic Rankine cycle machines. To this end, the system was developed, built and tested.

The LH-TES unit is designed as a dual vertical shell-and-tube heat exchanger embedded in the PCM. Here, this was a eutectic mixture of potassium and lithium nitrate salt. This system allows for condensation and evaporation of the two working fluids in the storage tubes at small temperature differences with respect to the melting temperature of the PCM on the shell side, in order to minimize entropy generation in the system. Hence, the heat transfer efficiency between the PCM and working fluid is maximized.

Axial aluminum fins connect the two tube systems and are immersed in the PCM storage media. These improve the heat transfer between the PCM and the working fluid in the heat exchanger tubes, since nitrate salts generally have a low thermal conductivity in the range of 0.5 W/m/K [4]. In the desired temperature range, aluminum is a suitable fin material, due to its high thermal conductivity (~210 W/m/K) and formability. Figure 2 shows a dual tube assembly consisting of two fin segments and two steel tubes attached by spring steel clips [5]; Figure 3 **Erreur ! Source du renvoi introuvable.** the storage integrated into the lab. The design parameters of the unit are summarized in Table 1.



Figure 2 Dual-tube assembly consisting of steel tubes and aluminum fins.



Figure 3 Latent heat storage integrated into the lab.

Table 1: As-built design parameters of the dual-tube latent heat storage.

Property	Quantity
Storage capacity	approx. 160 kWh
Heat exchanger type	Tube bundle with separate circuits for charging and discharging
Heat exchanger configuration	Vertical tube pairs integrated in PCM volume and connected to headers
Effective tube length	3 m
Storage material (PCM)	Eutectic of KNO_3 - LiNO_3 (67 wt% - 33 wt%), melting temperature 133 °C
PCM mass	approx. 4400 kg

Results and Discussion

Figure 4 shows the discharging and charging of the unit using the thermocouple measurements D4C, D4NE, D4S and D4SW around a central tube over the height of the storage.

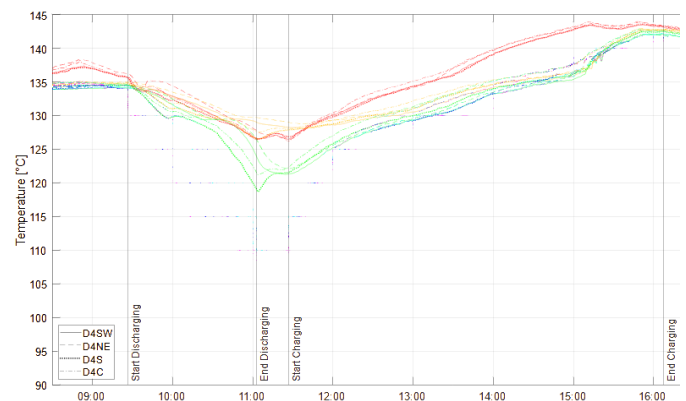


Figure 4 Temperature distribution of the thermocouple measurements at different positions around a central tube-pair at the measurement levels 1/top to 6/bottom in red, orange, green, turquoise, blue and purple during a discharging and charging cycle (right).

The corresponding thermocouple positions can be seen in Figure 5. Melting and solidification fronts through the cycle phases and the differences in the solidification and melting plateau during phase change become apparent.

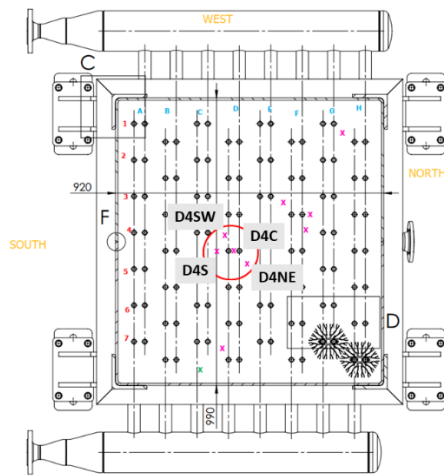


Figure 5 Cross-section of the storage showing the positions of the thermocouples, the temperature measures of which are shown in Figure 4.

Conclusions

This set of results as well as further experiments show the feasibility of the dual-tube concept, allowing for coupling of systems with a minimization of necessary driving temperature difference and increased system simplicity. The dual-tube design can be developed further for the flexible energy management system developed here, as well as for coupling separate processes in industrial processes.

Acknowledgment

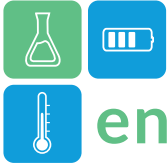
The work presented in this paper is a result of research activities of the CHESTER Project (www.chester-project.eu) which received funding from the European Union's Horizon 2020 research and innovation programme under grant agreement No 764042.

References

Uncategorized References

1. Li, Q., et al., A review of performance investigation and enhancement of shell and tube thermal energy storage device containing molten salt based phase change materials for medium and high temperature applications. *Applied Energy*, 2019. **255**.
2. Fiß, M. and M. Johnson, *Wärmespeichervorrichtung und Verfahren zum Speichern oder Bereitstellen von Wärme mittels einer Wärmespeichervorrichtung*, in <https://depatisnet.dpma.de/DepatisNet/depatisnet?action=pdf&docid=DE102017213718B4>

3. Weller, T., et al. *Design, build and initial testing of a novel energy management system*. in *Heat Powered Cycles Conference*. 2021. Bilbao, Spain.
4. Mehling, H. and L.F. Cabeza, *Heat and cold storage with PCM - An up to date introduction into basics and applications*. Heat and Mass Transfer. 2008, Berlin Heidelberg: Springer.
5. Bauer, T. and B. Hachmann, *Heat Transfer Tube*, in <https://data.epo.org/publication-server/document?iDocId=4682841&iFormat=0>, E.P. Office. 2014. EP 2 510 302 B1.°



ENERSTOCK 2024
The 16th IEA ES TCP International Conference on Energy Storage
June 5–7, 2024
Lyon, France



The IN-Campus: A lighthouse site for re-used infrastructures as seasonal thermal energy storage

Christoph Bott^{1,*}, David Hoffmann¹, Christoph Trinkl², Tobias Schrag², Simon Müller²,
Markus Faigl³, Rainer Strobel⁴, Peter Bayer¹

1 Martin Luther University Halle-Wittenberg, Applied Geology, Von-Seckendorff-Platz 3, 06120 Halle, Germany

2 Ingolstadt University of Applied Sciences, Institute of new Energy Systems, Esplanade 10, 85049 Ingolstadt, Germany

3 AUDI AG, Factory planning, Auto-Union-Str. 1, 85045 Ingolstadt, Germany

4 Planungsgruppe M+M AG, Technical consulting, Hanns-Klemm-Str. 1, 71034 Böblingen, Germany

*Corresponding author e-mail: Christoph.Bott@geo.uni-halle.de

Abstract

Densely populated and industrialized areas face high energy requirements and often land use conflicts. At the same time, as part of the energy transition and the transformation of industries, disused infrastructure systems, and industrial facilities can be integrated into new energy supply systems that serve multiple users. Many brownfield sites are regarded as attractive for transformation into modern, innovative urban districts or industrial campuses with district heating and cooling. For these, seasonal thermal energy storage represents an important component, ideally with a high share of renewable energy and a high degree of autarky. As an example, we introduce the IN-Campus site, located in Ingolstadt, Germany, and present the Reno-sTES concept, which is to be implemented at the site. The strategy of re-using idle infrastructures as seasonal storage systems will be applied to reduce construction, renovation, and demolition costs while implementing a modern low-temperature district heating network. We present the characteristics of the site, describe its key features and history, and provide an overview of the planned tasks for site development and implementation of the proposed seasonal energy storage concept.

Keywords: Seasonal thermal energy storage; Water gravel storage; Energy transformation; Site development

Introduction

Transformation of districts and energy systems

The transformation of the energy market is interconnected with the transformation of building stock and industry (e.g., car industry towards e-mobility, phasing out of subsurface storage of fossil fuels). Consequently, energy supply solutions strive for mutual benefits during the evolution of commercial or industrial districts and redeveloped brownfields. In this respect, an innovative approach involves continuous utilization of idle or disused structures for the development and optimization of new or retrofitted energy systems.

Large-scale, closed-loop, seasonal thermal energy storage in artificial basin structures

Storing thermal energy offers great potential for enhancing efficiency and increasing the use of renewable energies for various applications. Recently, increasing attention has been focused on sensible seasonal thermal energy storage (sTES), as this solution is particularly attractive for energy systems with significant excess thermal energy in summer (e.g.,

due to a high share of solar thermal energy) (Bott et al., 2019).

Besides geological storage options (borehole thermal energy storage, aquifer thermal energy storage), the following technical variants represent sTES in artificial basin structures: pit thermal energy storages (PTES), tank thermal energy storages (TTES) and water-gravel thermal energy storages (WGTES), each of which offers individual (geo-)thermal properties and advantages (Dahash et al., 2019). The evolution and further development of these ground-based, closed-loop, large-scale sTES is fundamental for reliable low-carbon heat supply and may be supported via the new Reno-sTES concept.

The Reno-sTES concept

Energy systems under transformation represent a dynamic field with varying demands. There, storage and energy systems evolve over several years, and both may be expanded and/or changed in functionality (concerning, e.g., scales, timespans, temperatures, flow rates, heat vs. cold demand). This sets high requirements on the flexibility of sTES, or, on the other

hand, offers particular opportunities for sTES that are not perfectly tailored for a given operational mode.

Transformation processes are related to enormous demolition and renovation costs, while re-use strategies have a high potential for cost reduction. This strategy has already been realized in principle for former gravel pits that after gravel mining serve as PTES (Ulbjerg, 2017). An alternative approach is to utilize idle structures for the further development and optimization of energy systems by converting them to sTES facilities. In particular, existing basin facilities with piping systems are highly attractive. Sites with tanks, pools, or basins can be converted as part of a technical upcycling (“Reno”) process (Dressel et al., 2018).

However, re-using existing structures restrains the flexibility of the sTES design (e.g., optimization of surface/volume ratio). In this case, efficiency predictions are complex and need to be tailored to the given site conditions. Innovative approaches to increase the efficiency of individual components, and new strategies, are required since conventional planning practices are often not suitable. Challenges relate to the degree of freedom in sTES type selection, planning, installation, and operation strategy, altogether with the necessary integration into a highly optimized local district energy system.

The IN-Campus

The location presented in this study is located in Bavaria (Germany). A former refinery site in a commercial district of the city of Ingolstadt is being transformed into a research and development (R&D) campus of around 75 ha (Figure 1), which hosts up to 70 non-residential, large buildings (offices, workshops, industrial labs, test benches, computer center, etc.).



Figure 1: Construction phases at the IN-Campus (a; available basins highlighted in red), and pictures of the available basin structures (b: basin A, c: basin D). Aerial image: LDBV (2023).

The IN-Campus is a prime example of land transformation processes: brownfields and existing structures are being redeveloped, and land reclamation is managed by both public and industrial partners.

Development and expansion of the IN-Campus (Figure 1) are divided into four construction phases. Up to 70 buildings will be constructed and used for innovative R&D applications, many of these as prominent showcases of the modernizing car industry. During the currently ongoing first construction phase, the first buildings are being completed, offering space for 1,400 workers (Faigl et al., 2019). As a result, the energy requirements of the various buildings will evolve dynamically, which poses challenges for the planning and implementation of the energy system, and an adaptive planning strategy for optimal energy supply is needed.

Energy system

The energy supply at the site is planned to be highly autarkic, low-carbon, and efficient. The aim is to supply at least 85% of thermal energy via renewable sources and to employ peak shaving and load-shifting mechanisms actively (PGMM, 2018). Thus, the conventional approach to energy supply is being replaced by a smart system to connect various energy sources and sinks (Figure 2). Thereby, the supply of electricity, cooling, and heating is not implemented via conventional direct connections, but via combinations of energy forms, and different storage solutions.

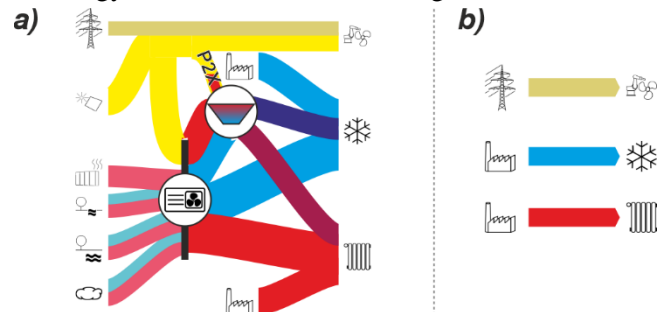


Figure 2: The smart energy system of the IN-Campus (a), compared to a conventional, direct energy system (b).

For controlled thermal energy distribution of decentralized sources and sinks (e.g., heat pumps, waste heat from a data center, solar thermal) an uninsulated low-exergy grid (5–30 °C) is being constructed. During the planning phase, thermal energy demands were estimated at 26 MW for cooling and 20 MW for heating at the end of the last construction phase. Given the climatic conditions and high construction standards, the demand for cooling will exceed the heating demand by up to 30% (PGMM, 2018).

The benefits of sTES are apparent: Unlike costly cooling of excess energy, sTES facilities offer a key element in the energy system to acknowledge peak shaving and load shifting. Thereby, sTES promotes

sector coupling and enhances the efficiency of the overall system.

Available basin infrastructures

At the site, basins formerly used for storing water for firefighting, and for wastewater treatment (activation, clarification, post-aeration; Figures 1 and 4) are available. These structures may be utilized as sTES with a total volume of almost 32,300 m³ (excl. internal components, Table 1) (Stettner et al., 2016).

Table 1: Dimensions of the basin (compounds) at the IN-Campus.

Basin	Length (m)	Width (m)	Height (m)	Volume (m ³)
A-B-C	59.6	102.6	3.2	17,176
D-E-F	59.6	38.3	3.2	5,839
G	52.0	26.4	2.0	2,299
H	75.0	16.0	5.5	6,960

Reno-sTES at the IN-Campus

Conceptual approach

Reno-sTES is introduced as a storage category that is based on recycling, reusing, and/or renovating existing infrastructure to serve as thermal energy storage in a modern district heating or cooling network. The development of conceptual Reno-sTES scenarios is subject to site-specific boundary conditions, where volume, geometry, and ambient conditions are predefined in the case of re-used infrastructures. Further boundary conditions are given by the energy system and constraints for storage operation (e.g., number of storage cycles, supply/return temperatures, volumetric flow rates).

For the IN-Campus project and due to its complex energy system structure, a multifunctional solution for heat and cold storage, operating both seasonally and as a short-term buffer, is required. In contrast to conventional strategies, this Reno-sTES system will not only store heat generated by solar energy but also excess thermal energy at different temperatures from a variety of sources.

As part of the first construction phase, the heat storage focuses on the A-B-C basin compound (Figure 1). Given the public accessibility of the area, it is essential to design a concept for securing and integrating the basins into the surrounding landscape. At the same time, preliminary structural investigations prove that the basins are in a suitable condition to be transformed into a Reno-sTES (Stettner et al., 2016).

Besides these multiple constraints, many dependent and independent parameters remain for the optimum design of Reno-sTES facilities. These concern the selection of materials and methods that affect the design of each component of the system.

Storage integration and potential

Investigations of the first construction phase yield positive results and a recommendation to implement storage solutions at the location. The Reno-sTES can be integrated directly into the LowEx grid. This enables, for example, cooling in early summer to optimize the efficiency of decentralized heat pumps. Furthermore, waste heat from central refrigerating units to operate the local cooling network can be extracted via a separate local heating network. Also, a direct supply of waste heat from the Ingolstadt waste incineration plant is available. This renewable source can provide high temperature levels for rapid heating of the Reno-sTES facility in summer.

Planned site development

In the first step, starting in 2024, the existing basin compound “A-B-C” will be transformed into a system with detailed monitoring, and it will be connected to the energy system (Figure 3). Aiming to implement a differentiated sTES compound, sub-basins A+B will be upgraded to a fully buried, indirectly charged/discharged WGTES basin (filling: re-used, on-site gravel) that is sealed with re-used plastic foils from site remediation activities on all sides with re-used plastic membranes. By implementation as WGTES, the basin surfaces can be used as green spaces or for parking. Basin C will be transformed and integrated as a study case to optimize technical elements and to test different, innovative insulation materials.

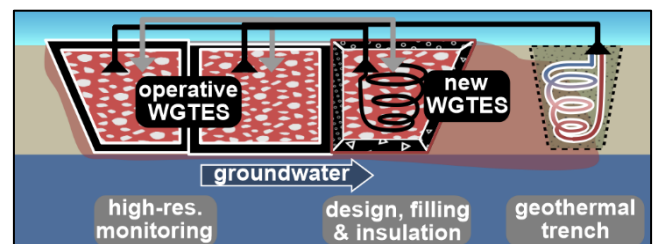


Figure 3: Planned realization of the A-B-C basin compound as Reno-sTES system with complementary research activities.

Monitoring and complementary R&D activities

In general, innovative efforts at the IN-Campus can focus on an optimized, flexible transformation of basin structures and optimum sTES integration, while potentials for re-use as sTES facilities can be explored for further on-site structures.

Basin C will be equipped with a high-resolution thermal and moisture monitoring appliance, which will reveal hydraulic and thermal conditions in the Reno-sTES and, particularly, at the walls to track lateral thermal losses and insulation performance to all sides.

The monitoring will be complemented by groundwater monitoring wells to measure the temperature evolution



into the surrounding underground due to potential thermal loss since the basin's foundations are located beneath the groundwater level. In the groundwater downstream (5–10 m), a geothermal trench will be installed down to the depth of the sTES and connected via a monitored geothermal heat pump with the energy system (Figure 3). The focus of the innovation at IN-Campus is on optimized basin transformation, and flexible combined Reno-sTES integration, ground waste heat recycling, preparation of further storage (basins D–H), integration in the expanding energy system. Here, it is advantageous that the entire IN-Campus is a dynamic project that will successively be expanded in further construction phases. This allows demonstration options for optimized, combined use of multi-sTES in a modern, evolutionary environment.

Conclusions

During the energy transition and industrial transformation processes, areas with a need for novel solutions for seasonal thermal energy storage are emerging. The IN-Campus, one example of a such location, represents a unique opportunity for the further development of the sTES technology. There it is possible to test the novel Reno-sTES, which involves strategic conversions of idle basin structures into seasonal thermal storage. Altogether, the IN-Campus represents a unique field laboratory/demonstration for storage design, monitoring, and further developments. The required adaptive planning of energy supply will be ideally realized by the support of applied research activities that validate and demonstrate innovative concepts. For this purpose, the IN-Campus offers a valuable demonstration target and may become the benchmark of an upcoming sustainability strategy for site development with Reno-sTES.

Acknowledgments

The authors acknowledge Ryan Pearson for language edits. The present study is financially supported by the EU Horizon Europe project INTERSTORES (project no. 101136100).

References

- Bott, C. and al. (2019). State-of-technology review of water-based closed seasonal thermal energy storage systems. *Renewable and Sustainable Energy Reviews*;113:109241.
- Dahash, A. and al (2019). Advances in seasonal thermal energy storage for solar district heating applications: A critical review on large-scale hot-water tank and pit thermal energy storage systems. *Applied Energy*;239:296–315.
- Dressel, I. and al. (2018). Dressel I, Bott C, Bayer P. Converting idle infrastructure to large scale seasonal heat storage systems. In: 45th IAH Congress; 2018.
- Faigl, M. and al. (2019). IN-Campus - Innovative Technologien, *Smarte Energie*: Stand: April 2019. AUDI Werksplanung/Planung Energie und Gebäudetechnik, Ingolstadt.
- LDBV (2023). Digitales Orthophoto DOP40 (WMS). Landesamt für Digitalisierung, Breitband und Vermessung, München.
- PGMM (2018). IN-Campus - Fortschreibung innovatives Energiekonzept: Ergebnisse Stand Entwurf. Planungsgruppe M+M AG, Böblingen.
- Stettner, C. and al. (2016). Untersuchungsbericht zur Zustandsbewertung der Behälter auf dem ehemaligen Bayernoilgelände in Ingolstadt: Projektnummer 154094CS. Zilch + Müller Ingenieure GmbH, München.
- Ulbjerg, F. (2017). Heat storage pits: Cheap and efficient energy with heat storage pits. Ramboll Group, Copenhagen.



Figure 4: Aerial view of the available basin structures at the IN-Campus. Aerial image: LDBV (2023).

Thermal discharge performance of a composite foam in an indirect fixed-bed reactor for thermochemical energy storage

Shigehiko Funayama^{1,*}, Tsukasa Sugiyama², Tsuyoshi Izaki², Hana Saeki², Kenta Tomita², Kazuya Fujii², Soichiro Tamano², Takashi Kato¹, Hiroki Takasu¹, Yukitaka Kato¹

1 Laboratory for Zero-Carbon Energy, Institute of Innovative Research, Tokyo Institute of Technology, 2-12-1-N1-22, O-okayama, Meguro-ku, Tokyo, 152-8550, Japan

2 Graduate Major in Nuclear Engineering, Tokyo Institute of Technology, 2-12-1-N1-22, O-okayama, Meguro-ku, Tokyo, 152-8550, Japan

*Corresponding author e-mail: funayama.s.aa@m.titech.ac.jp

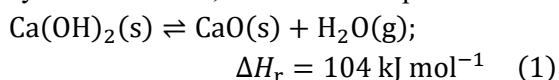
Abstract

This experimental study explores the thermal discharge power density of an indirect fixed-bed reactor employed for thermochemical energy storage. Composite foam blocks were prepared by utilizing calcium hydroxide and silicon-impregnated silicon carbide foams. The reactor demonstrated a thermal discharge power density of $0.25 \text{ kW L}_{\text{material}}^{-1}$ during the hydration of calcium oxide.

Keywords: Thermochemical energy storage, Calcium hydroxide, Composite foam, Molten salt

Introduction

Thermochemical energy storage involving calcium oxide/calcium hydroxide ($\text{CaO}/\text{Ca}(\text{OH})_2$) enables the storage of thermal energy through the dehydration of $\text{Ca}(\text{OH})_2$ and subsequent discharge of energy via the reverse hydration of CaO , described in Eq. 1.



To enhance heat transfer and stabilize the bulk properties of storage materials, the authors had previously synthesized composites using $\text{Ca}(\text{OH})_2$ and silicon-impregnated silicon carbide (Si-SiC) foams (Funayama, S. et al., 2023). In this study, we prepared a composite foam with an energy capacity 21 times higher than that of the previously reported composite foam. Furthermore, we successfully discharged thermal energy using the developed composite foam in an indirect fixed-bed reactor. Our objective was to investigate the discharge power density of the reactor during the hydration of CaO .

Materials and methods

Materials

In this study, a calcium hydroxide slurry with a solid content of 60 wt% was employed. The Si-SiC foam featured a foam porosity of 92% and mean pore diameter of $400 \mu\text{m}$. Cylindrical foam blocks measuring 55 mm in diameter and 50 mm in height were prepared, incorporating a 7 mm diameter hollow channel at the center of each block to serve as the

water-vapor channel (see Figure 1). The foam samples were immersed in a $\text{Ca}(\text{OH})_2$ slurry under vacuum and subsequently dried to eliminate water from the slurry. Ten composite blocks were prepared to form a rod with a length of 500 mm. The heat transfer fluid (HTF) utilized was a molten salt known as HITEC.

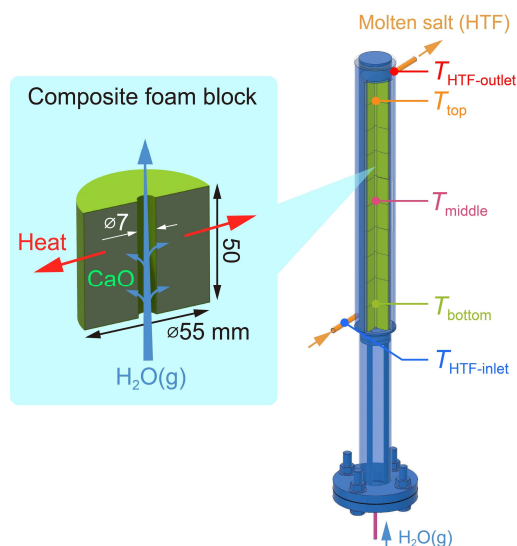


Figure 1: Composite foam blocks (denoted in green) in the indirect fixed-bed reactor.

Experimental setup and procedure

In this study, an indirect fixed-bed reactor equipped with a double-tube heat exchanger was utilized. The 10 composite blocks were positioned within the inner tube, and the HTF flowed upward between the inner and outer tubes at a rate of 0.10 L min^{-1} . The locations of

the primary thermocouples are illustrated in Figure 1. Water vapor, at approximately 200 kPa, was introduced from the bottom of the reactor to initiate CaO hydration. The quantity of water consumed during hydration, essential for calculating the conversion, was determined by measuring the water level of the evaporator. For a more detailed description of the setup, readers are referred to our previous publication (Funayama, S. et al., 2024).

Results and discussion

The primary temperatures, pressure, and conversion are depicted in Figure 2. The initial temperature was set at 350 °C. Subsequent to the introduction of water vapor to the reactor for 0 min, the material temperatures (T_{top} , T_{middle} , and T_{bottom}) experienced a rapid increase. Middle temperature T_{middle} reached 541 °C when the pressure reached 179 kPa, indicating a close agreement between the achieved temperature and the equilibrium temperature corresponding to the water vapor pressure.

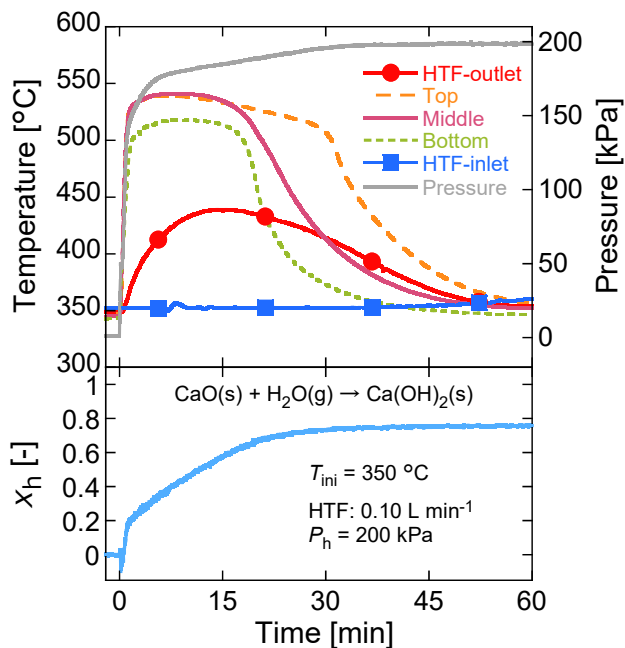


Figure 2: Temperature, pressure, and conversion during hydration at 200 kPa pressure.

The temperature at the bottom was lower than that in the other layers, which can be attributed to the cooling effect of the entering water vapor. The temperature plateau observed at the top of the bed endured for the longest duration, indicating the completion of hydration from the bottom to top of the bed. The HTF collected the heat generated during hydration, and its outlet temperature reached 439 °C after approximately 15 min, resulting in an 87 °C temperature difference between the inlet and outlet. Hydration seemed to be complete around 40 min, with an achieved conversion

of 76%. The thermal discharge power density of the reactor during CaO hydration is illustrated in Figure 3. The power density exhibited an increase corresponding to the difference between the inlet and outlet HTF temperatures, reaching 0.25 kW $L_{material}^{-1}$ at 15 min.

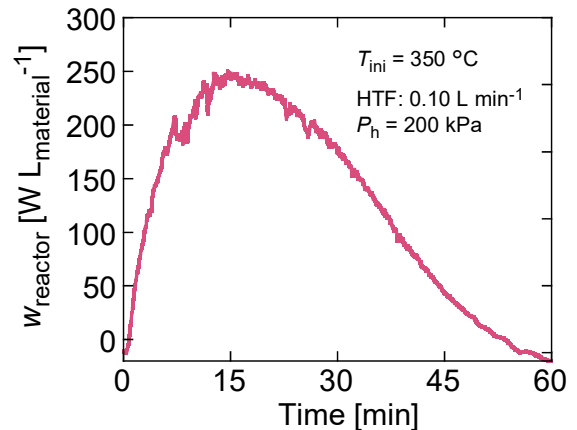


Figure 3: Thermal discharge power density of the reactor.

The results of this study can serve as a benchmark for enhancing power density. Furthermore, these results will be instrumental in constructing a numerical model of the reactor, a crucial step for advancing the scale-up of the reactor and multiplying the reaction tubes in future studies.

Conclusions

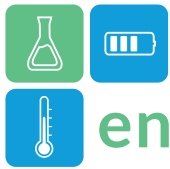
We examined the performance of an indirect fixed-bed reactor for thermochemical energy storage. We synthesized composite blocks using $Ca(OH)_2$ and Si-SiC foam, possessing an energy capacity 21 times higher than that of a previously reported composite. Molten salt served as the HTF. The reactor demonstrated a discharge power density of 0.25 kW $L_{material}^{-1}$ during the hydration of CaO, resulting in a maximum temperature difference of 87 °C between the HTF inlet and outlet.

Acknowledgment

This study was supported by the JST-Mirai Program, Grant Number JPMJMI21E4, Japan.

References

- Funayama, S. et al. (2023) Calcium hydroxide and porous silicon-impregnated silicon carbide-based composites for thermochemical energy storage, Applied Thermal Engineering, 220, 119675, doi.org/10.1016/j.applthermaleng.2022.119675.
- Funayama, S. et al. (2024) Thermal energy storage with flexible discharge performance based on molten-salt thermochemical energy storage, Applied Thermal Engineering, 238, 121947, doi.org/10.1016/j.applthermaleng.2023.121947.



enerstock

ENERSTOCK 2024
The 16th IEA ES TCP International Conference on Energy Storage
June 5–7, 2024
Lyon, France

Thermal Energy Storage as a Service Business Model for Food Supply Chain Decarbonisation

Xinfang Wang^{1,*}

1 Birmingham Energy Institute, School of Chemical Engineering, University of Birmingham, Edgbaston, Birmingham, UK. B15 2TT.

*Corresponding author e-mail:
x.wang.10@bham.ac.uk

Abstract

Cooling and the cold chain are essential for majority of food across the supply chain, from the producer to the consumer, to ensure food safety and nutrition, and to reduce food loss and waste through storing food at the low temperature required and extend its shelf life. It is estimated that around 30% of food is lost due to limitations in the cold chain globally (FAO, 2015). The global cold chain is expanding rapid to meet the demand for cooling. Energy is required to produce the cooling to meet the demand, including for the food production, refrigerated transport, cold stores, retail sites, homes, and workplaces and so on. It is estimated that energy used for refrigerating food accounts for around 8% of power usage globally and is responsible for 2.5% of direct and indirect GHG emissions worldwide (IRENA, 2020).

The cost of energy to deliver the cooling required is significant. For example, energy cost accounts for around 11% of the production value of dairy products (Dallemand et al., 2015). Thermal energy storage (TES) could play a significant role in reducing GHG emissions of the food cold chain, with applications in short, medium, and long terms. TES enables integrating renewable energy across all stages of the cold chain and increasing the flexibility of refrigeration loads to meet

the demand at peak times. Examples of applications include thermal storage for freight containers (Huang and Piontek, 2017; University of Birmingham, 2018), and demand side management at commercial retail sites (Axiom Cloud, n.d.). Due to the high cost of technological innovation and application of TES in the cold chain, innovative new business models are needed to help address the financial challenge. The research here develops service-oriented business model - TES as a service business model - to overcome the high investment cost of applying TES technologies to reduce energy and GHG emissions across the food supply chain. The service-oriented business model clearly identifies the ownership, responsibilities of operation and maintenance, as well as skills and training required by various stakeholders across the cold chain.

Compared with traditional sale-purchase or lease-rental business models, the service-oriented business model allows the opportunity for small businesses and individuals to adopt TES technology and cooling equipment without the burden of high up-front cost. This improves the inclusivity, equality, and diversity of stakeholders of multiple sizes to be engaged in the innovative TES technology and application. It would also improve the performance and reliability of the cooling system with improved maintenance from the providers, who could maintain ownership of the equipment and be responsible for second life use and end of life disposal. The service-oriented business model can be flexible to be replicated and scaled up to wider regions globally, playing an essential role for reducing energy use and GHG emissions of the food supply chain whilst reducing food loss and waste worldwide.

Keywords: Thermal storage, Business model, Emission reduction



enerstock

ENERSTOCK 2024
The 16th IEA ES TCP International Conference on Energy Storage
June 5–7, 2024
Lyon, France

References

Axiom Cloud (n.d.). *Axiom Cloud: Apps for Commercial Refrigeration*. Virtual Battery Case Study – Multi-site Grid Services Event. <https://docsend.com/view/dw695qyn8atvt6wn>. (accessed 31st January 2024).

Dallemand, J. et al. (2015). *Energy Use in the EU Food Sector: State of Play and Opportunities for Improvement*. JRC Science and Policy Report. DOI: 10.2790/158316.

FAO (2015). *Global Initiative on Food Loss and Waste Reduction*. Food and Agriculture Organization of the United Nations (FAO), <https://www.fao.org/3/i4068e/i4068e.pdf>. (accessed 31st January 2024).

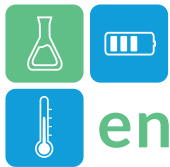
Huang, L. and Piontek, U. (2017). Improving Performance of Cold-chain Insulated Container with Phase Change Material: An Experimental Investigation. *Applied Sciences*, Vol. 7, Issue 12, p. 1288, DOI: 10.3390/app7121288.

IRENA (2020). *Innovation Outlook: Thermal Energy Storage*. International Renewable Energy Agency, Abu Dhabi.

University of Birmingham (2018). *UK and China Scientists Develop World-first Cold Storage Road/Rail Container*. www.birmingham.ac.uk/news/latest/2018/12/scientist-s-develop-world-first-cold-storage-roadrail-container.aspx. (accessed 31st January 2024).

Endnotes

The research work is being carried out between January and May 2024, with results and analysis being ready for presenting in June 2024 at the ENERGYSTOCK conference. An extended abstract and full report will also be ready before the ENERGYSTOCK conference in June 2024.



Thermal energy storage in energy communities: a perspective overview through a bibliometric analysis

Luca Brunelli¹, Emiliano Borri², Anna Laura Pisello³, Andrea Nicolini⁴, Carles Mateu², Gabriel Zsembinski², Luisa F. Cabeza^{2,*}

¹CIRIAF-Interuniversity Research Centre, University of Perugia, Via G. Duranti 63, 06125 Perugia, Italy

²GREiA Research Group, Universitat de Lleida, Pere de Cabrera s/n, Lleida, Spain

³EAPLAB at CIRIAF-Interuniversity Research Centre, University of Perugia, Via G. Duranti 63, 06125 Perugia, Italy

⁴Department of Engineering, UNIPG—University of Perugia, Via Goffredo Duranti 93, 06125 Perugia, Italy

*Corresponding author e-mail: luisaf.cabeza@udl.cat

Abstract

The escalating climate crisis demands immediate countermeasures. Renewable energy communities (RECs), introduced by the European Renewable Energy Directive (RED II), emerge as a democratic innovation to enhance energy control and sharing. This study focuses on defining the perspective of thermal energy storage in RECs, emphasizing economic viability over electric batteries. This study aims to define the role of thermal energy storage in renewable energy communities. Existing literature on thermal storage lacks terms specific to these communities. While studies on renewable energy communities haven't fully explored thermal energy storage potential, the general expression of the keyword "energy storage" indicates an unexplored avenue. This research delves into thermal energy storage technologies, crucial in the current energy transition, to optimize renewable energy utilization.

Keywords: Thermal energy storage; energy communities; renewable energy

Introduction

Year after year, the climate crisis represents an increasingly concrete threat for which it is now urgent to take countermeasures. In the context of climate change mitigation, energy is one of the sectors where emission reductions can have the greatest short-term effects.

This is why there is an increasing need for a transition to renewable energy sources and a consequent shift away from fossil fuels.

The European Union manifested this objective in recent years through the "Clean Energy Package" and the "Fit for 55", measures promoted by the European Commission that set a perspective of climate neutrality from fossil fuels from 2050 onwards.

In this context, renewable energy communities (RECs) represent a social innovation capable of advancing more equitable models for managing, consuming, and producing energy, enhancing democratic decision-making and control over renewable energy, and placing it in the hands of communities and individuals.

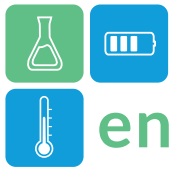
Introduced by the European Renewable Energy Directive (RED II), RECs are legal entities that are based on open and voluntary participation.

The main objective of a REC is to maximise the sharing of energy produced through renewable energy sources

(RES) in a collective self-consumption scheme. However, the use of RES entails the usual problem of solving the time mismatch between production and user demand for energy.

To overcome this problem, it is possible to use energy storage systems, whereby the energy produced by renewable plants is stored and then used when required.

Thermal energy storage (TES) systems are also relevant in this context. With the use of a heat pump, it is possible to convert electrical energy into a heat carrier, storing it to meet the heat demand of a utility. This solution proves to be more sustainable than the installation of an electric storage battery. This is evidenced by Fambri et. al (Fambri et al., 2023), who in their work compare the use of an electric battery and a heat pump thermal energy storage system in a REC. The results showed that the profits from the increase in self-consumption of the energy community were not sufficient to compensate for the high investment cost of the electric battery. On the contrary, the TES solution, although less performing from an energy point of view, was found to be economically convenient. Therefore, the main objective of this study is to define the perspective of thermal energy storage in renewable energy communities to maximize the share of renewable sources.



Materials and methods

In this study, the database Scopus was used as a reference with the last access on 12 January 2024. In order to identify research trends and gaps in the application of TES in energy communities, two queries were formulated and reported in Table 1. A first query was used to collect bibliometric data related to the studies on TES in buildings including districts (Borri et al., 2021). A second, more specific query, was then formulated to draw the state of the art of TES specifically in energy communities. In this study, bibliometric data were used to identify the main trends in the number of publications. In order to identify the research gaps, keywords were visually mapped and analysed through the open-source software VOSviewer (Van Eck & Waltman, 2022).

Table 1: Query used in the Scopus database

Topic	Query
TES in buildings and districts	TITLE-ABS-KEY (“thermal energy storage*” AND (“building*” OR “built environment” OR “district*” OR “municipal*” OR “neighbourhood”) AND NOT (“aircraft” OR “transport* application” OR “transport sector”))
Renewable energy communities	"energy communit*" AND "renewable*"

Results

This section reports the results of the bibliometric analysis done with the methodology described above. Figure 1 shows the number of documents published in the field of thermal energy storage applied to buildings and districts.

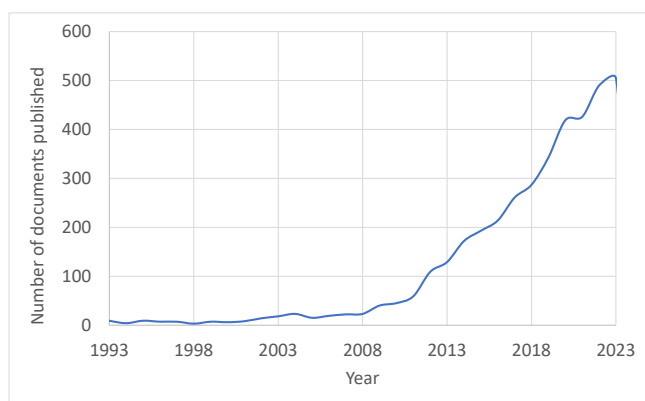


Figure 1. Number of documents published in thermal energy storage

The number of publications started to rise after 2008 reaching more than 500 documents published only in the year 2023. This demonstrates that TES is gaining momentum in the built environment application being a pivotal component of the energy transition. The number of documents published related renewable energy communities (RECs) is shown in Figure 2.

Results show that this topic only gained interest recently after 2018. This can be related to the release of the European Renewable Energy Directive (RED II) which introduced the concept of renewable energy communities.

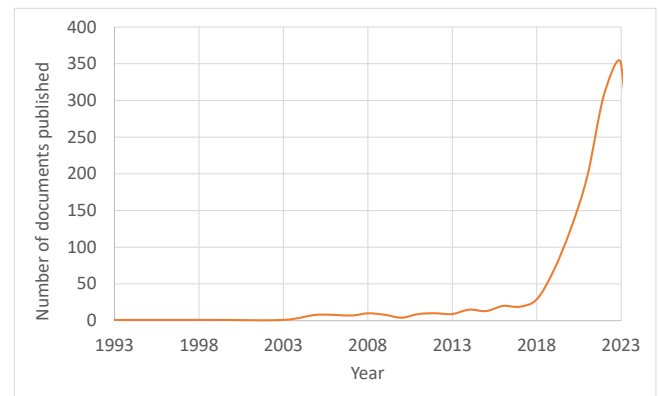


Figure 2. Number of documents published in renewable energy communities

Figure 3 shows the co-occurrence of keywords obtained through the software VOSviewer for the first query related to TES in buildings and districts. In the right part of the figure (green cluster) is possible to notice that a lot of studies are related to the development and the improvement of storage materials, in particular phase change materials (PCMs). On the right side of the figure, is possible to notice the TES applications which include district heating, (red cluster) demand side management, cogeneration and heating and cooling in buildings (blue cluster). From the figure, there are no terms appearing in terms of renewable energy communities although there are keywords such as smart grids, microgrid and sector coupling that can be related to the integration of TES in a wider context than a single building.

The co-occurrence of keywords related to renewable energy communities is shown in Figure 4. In this case, the keyword related to energy storage is only generic without any specific term related to thermal energy storage. This gives room for more investigation highlighting a substantial gap. Keywords shown in the figure studies are mostly related investigate to the role of prosumers in the energy market. However, it is interesting the link between energy communities and micro-grid and smart grids which could link renewable energy communities with the implementation of thermal energy storage in the built environment.

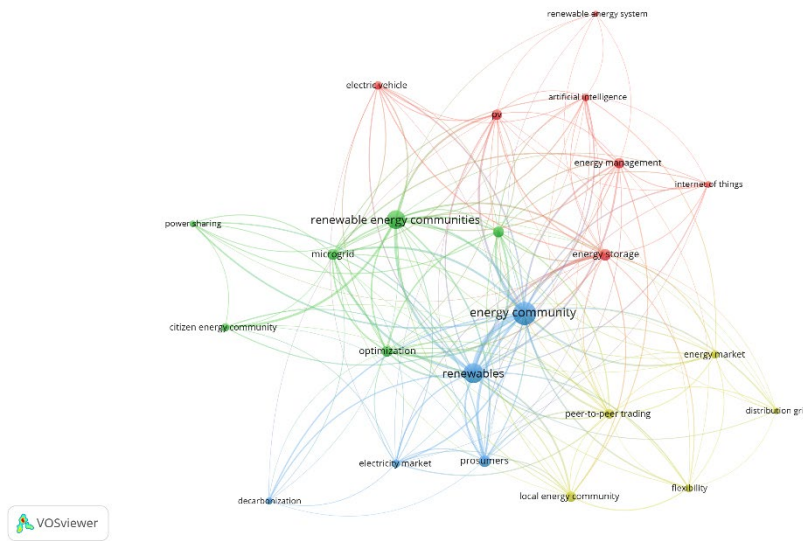


Figure 3. Co-occurrence of keywords related to renewable energy communities

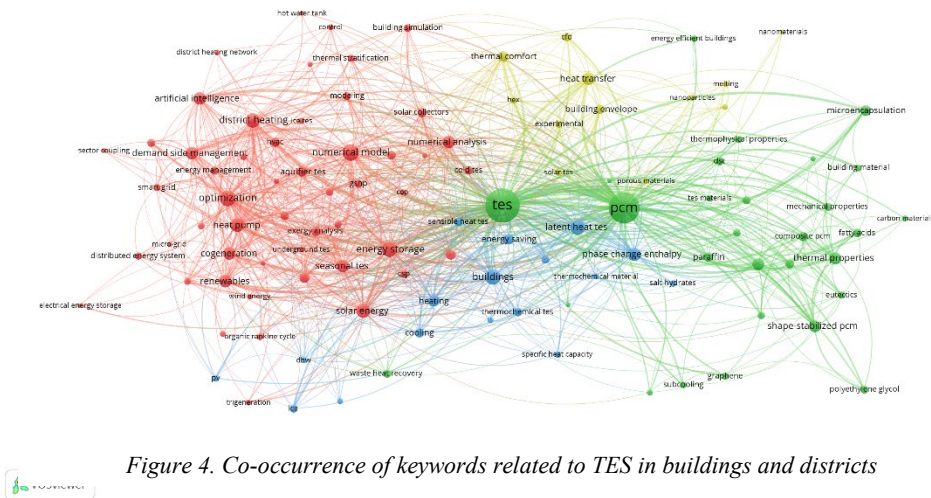


Figure 4. Co-occurrence of keywords related to TES in buildings and districts

Currently, the figure shows that the implementation of energy storage in energy communities is linked with solar technologies (photovoltaic) which implementation can be optimized with the use of artificial intelligence.

Conclusions

This study aims to define the perspective of thermal energy storage in renewable energy communities. This topic has seen a significant increase in publications since 2018 after the introduction of specific European directives. Observing the literature on thermal energy storage in buildings and districts, there are no terms directly related to renewable energy communities which identify a research gap. However, from the analysis of keywords, some terms emerge that refer to a broader concept beyond individual buildings and can be addressed in the context of renewable energy sharing. This highlights a possible compatibility between TES and renewable energy communities in



terms of future research. On the other hand, studies on renewable energy communities still did not fully explore the potential of thermal energy storage. They include the concept of "energy storage," but through a general approach, considering different types of storage, without focusing specifically on TES. . This gives room for potential investigation of thermal energy storage technologies which constitute a concrete tool for improving the performance of a renewable energy community, increasing the sharing of renewables among community members.

Acknowledgment

This work was partially funded by the Ministerio de Ciencia e Innovación - Agencia Estatal de Investigación (AEI) (PID2021-123511OB-C31 - MCIN/AEI/10.13039/501100011033/FEDER, UE). The authors at the University of Lleida thank the Generalitat de Catalunya for the quality accreditation granted to the GREiA research group (2021 SGR 01615). GREiA is a TECNIO-certified agent in the category of technological development of the Gobierno de Cataluña. This work is partially supported by ICREA inside the program ICREA Academia.

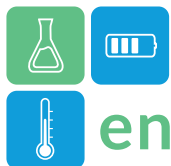
References

Borri, E., Zsembinszki, G., & Cabeza, L. F. (2021). Recent developments of thermal energy storage

applications in the built environment: a bibliometric analysis and systematic review. *Applied Thermal Engineering*, 189(116666).

Fambri, G., Marocco, P., Badami, M., & Tsagkrasoulis, D. (2023). The flexibility of virtual energy storage based on the thermal inertia of buildings in renewable energy communities: A techno-economic analysis and comparison with the electric battery solution. *Journal of Energy Storage*, 73, 109083.

Van Eck, N., & Waltman, L. (2022). *VOSviewer: Manual for VOSviewer Version 1.6.18*. Leiden University Press: EZ Leiden, Netherlands. <https://www.vosviewer.com/>



Thermal Energy Storage with Molten Salts: Predictive Models for thermo-physical properties

R. Liberatore^{1,*}, S. Sau¹, A.C. Tizzoni¹, A. Spadoni¹, E. Veca¹, E. Mansi¹, T. Delise¹, M. Battaglia², N. Corsaro¹, C. D'Ottavi², S. Licocchia²

¹ENEA – Italian National Agency for New Technologies, Energy and Sustainable Economic Development, CR Casaccia, Lungotevere Thaon di Revel, 76, 00196 Rome, Italy

² University of Rome Tor Vergata - Department of Chemical Science and Technologies, Via della Ricerca Scientifica 1, Roma, Italy

Abstract

The aim of this work was the development and validation of predictive models for the description of the chemical-physical properties of molten salt mixtures suitable as thermal heat storage means, starting from the behaviour of the individual components.

Mixtures of binary, ternary and quaternary molten salts were selected, characterized, and studied as an alternative to the currently most used binary formulation ("Solar salt": $\text{NaNO}_3\text{-KNO}_3$).

Given the numerousness of the possible multicomponent mixtures produced, it was necessary to prepare and validate tools that allow the prediction of important thermo-physical parameters of these thermal fluids such as density, viscosity, conductivity, and thermal capacity, leading to the reduction of costs and times of experimental campaigns.

Keywords: Molten salt; TES; Thermo-Physical Properties; Modelling; Sensible Heat.

Introduction

Molten nitrate salts, or more typically their mixtures, have melting points and thermophysical properties that make them suitable to be used as heat exchange and storage fluids in thermodynamic solar systems operating at medium-high temperatures, i.e. below 600°C (Delise and al., 2019). In the last years, various mixtures composed of nitrates/nitrites have been studied and developed to lower of their freezing point compared to the most used material called "Solar Salt" which has sodium and potassium nitrate as components.

The key features of these materials are their good thermal characteristics, chemical stability, low toxicity, and low cost, but they have a relatively high freezing point, i.e. start of solidification, being around 240°C .

This last aspect represents an issue both regarding the cost of night-time thermal backup, given that the melt must not solidify, and for the start-up and maintenance operations of the plant (for example, emptying lines and tanks). For these reasons and considering the possible usefulness of low-melting fluids for applications at lower temperatures,

mixtures with lower freezing points, usually lower than 150°C , have been proposed in recent years.

Given the variety of possible feasible mixtures, a practical selection method is needed. The content of this work concerns the development and the experimental validation of predictive models which, starting from the properties of the individual components, allow the thermophysical characteristics of mixtures of nitrates and nitrites to be established as a function of their composition.

In fact, since the ternaries and quaternaries of possible practical interest are particularly numerous, it is practically impossible to determine the chemical-physical parameters for each of them. It is, therefore, necessary to validate simulation tools that allow obtaining the required properties, given the mole fractions of the selected mixture.

This work describes the models developed for the calculation of specific heat, density, viscosity, and thermal conductivity. Regarding the first three points, an experimental campaign was preliminarily carried out aimed at filling the gaps present in the scientific literature regarding these data, and, more generally, at obtaining a minimum number of values, which would allow an appropriate validation of the proposed predictive systems.

On the other hand, the experimental measurement of the thermal conductivity of molten salts represents, in general, a significant problem, and it was not possible to carry it out with the instrumentation currently available, so, in this case, only the few data were used of available literature; the result obtained is however valid and certainly useful for the intended purpose.

Materials and method

Binary and ternary mixtures reported in Table 1 were characterized against their thermophysical features, experimentally measuring heat capacity, viscosity, and density, in the temperature range from the solidification temperatures up to the maximum thermal stability values (Delise and al., 2020 – Tizzoni and al., 2020).

Sodium nitrate NaNO_3 and calcium nitrate tetrahydrate $\text{Ca}(\text{NO}_3)_2$ were supplied by Sigma Aldrich (99% purity), while potassium nitrate KNO_3 and sodium nitrite NaNO_2 by Fluka (99% purity).

The mixtures were prepared by mixing the individual components previously dried in a ventilated oven in appropriate proportions. Approximately 10 grams of salts were placed in a Pyrex glass flask, the system was heated, and the salts mixed until the mixture was completely melted (350-380 °C), and quickly cooled to room temperature.

Table 1: Molten salts selected and studied in this work (Delise and al., 2020 – Tizzoni and al, 2020).

	KNO_3	NaNO_3	NaNO_2	$\text{Ca}(\text{NO}_3)_2$
	Molar fraction			
KNO_3	1			
NaNO_3		1		
NaNO_2			1	
Solar Salt - NaNO_3 - KNO_3	0.36	0.64		
NaNO_3 - NaNO_2		0.40	0.60	
KNO_3 - NaNO_2	0.40		0.60	
NaNO_3 - $\text{Ca}(\text{NO}_3)_2$		0.70		0.30
KNO_3 - $\text{Ca}(\text{NO}_3)_2$	0.70			0.30
Hitec® NaNO_3 - KNO_3 - NaNO_2	0.44	0.07	0.49	
Hitec XL® NaNO_3 - KNO_3 - $\text{Ca}(\text{NO}_3)_2$	0.50	0.21		0.30

To determine the specific heat of the salt mixtures, a DSC differential calorimeter (Differential Scanning Calorimetry, DSC1, Mettler Toledo) was used. The experimental density measurements were performed based on Archimedes' principle, using an indirect method (Figure 1).

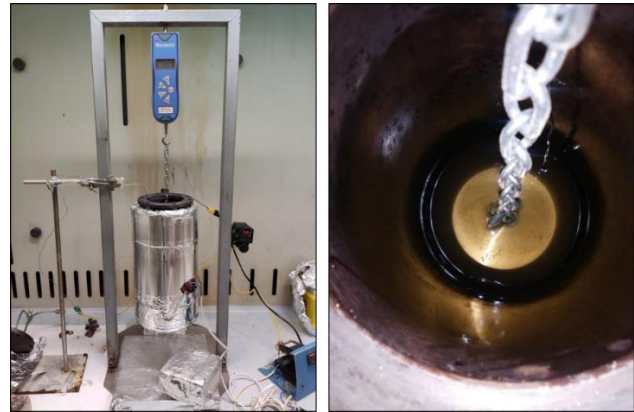


Figure 1: Experimental setup for measuring density: in particular, the dynamometer, the container and the submerged weight are shown.

Viscosity was determined experimentally, using an AR 2000ex rheometer.

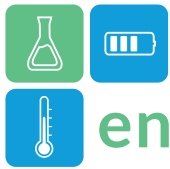
Thermal conductivity has not been evaluated experimentally, but methods to estimate it have been studied and validated, starting from the density measurements, the calculation of the molar volume described for binary mixtures (Zhao and al., 2016), and the sum on the mole fractions of the conductivities of the individual components for ternary and quaternary mixtures (Di Giulio and al., 1992). The modelling results were compared with experimental values present in the scientific literature.

Results and Discussion

The equations used for modelling the thermochemical properties studied, are summarized in Table 2.

Table 2: Equations used for modelling the thermochemical properties studied.

Properties	Models *
Cp	$cp_x = \sum X_j * cp_j$
Density	$V_{m,x} = \sum X_j * V_{m,j}$
Viscosity	$\mu/\mu_0 = (1 + a\sqrt{c} + bc)e^{\frac{f_{EX}}{RT}}$



Heat conductivity

$$\lambda_{mix} = \sum_{i=0}^m \chi_i \lambda_i$$

* for all j components in the mixture

To illustrate the experimental validations of the models developed, some significant results relating to the ternary Hitec® and Hitec XL® mixtures are reported in the following figures.

The simulation of the specific heat, exploiting the rule of additivity of the values of the pure components that constitute it, has proven to be a valid predictive tool, capable of modelling the behaviour of binary, ternary and quaternary mixtures in a range of error within 5%.

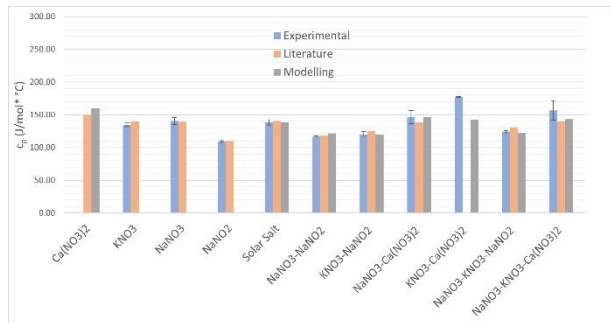


Figure 2. Heat capacity: comparison between experimental data, literature and modelling results for the binary and ternary mixtures considered in this work.

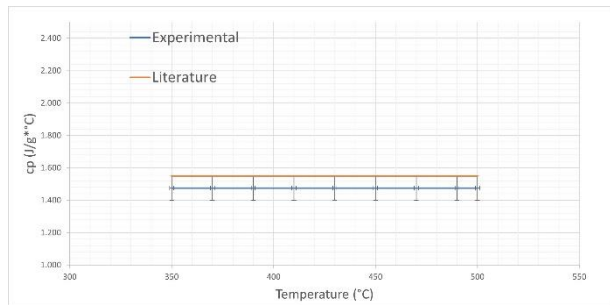


Figure 3. Heat capacity: comparison between experimental data and modelling results for Hitec® mixture.

Modelling the density of mixtures involves the determination of the molar volume of the individual pure components, obtained experimentally, and then their subsequent use in the development of the calculation of the molar volume of the mixtures and their density. This predictive tool also proved to be very accurate and capable of simulating the behaviour of many mixtures of practical interest for the field of application of this work.

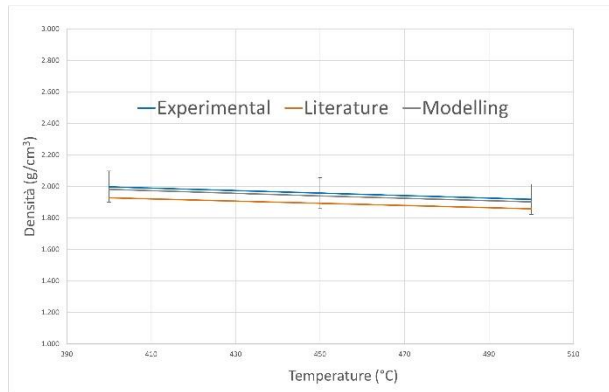


Figure 4. Density: comparison between experimental data and modelling results for Hitec XL® mixture.

The modelling of viscosity, starting from the density and viscosity properties of the pure components, gave good results for the salts studied that do not contain calcium nitrate. In fact, for the latter, this approach diverges at low temperatures, making its use inappropriate. A second model was therefore taken into account, considering the interaction between solute and solvent for mixtures containing Ca(NO₃)₂, based on the liquid state theory. The results of this second modelling were satisfactory only for calcium nitrate mole fractions higher than 0.3, while for lower values the model still needs to be studied and requires further experimental data to make it a tool for general use.

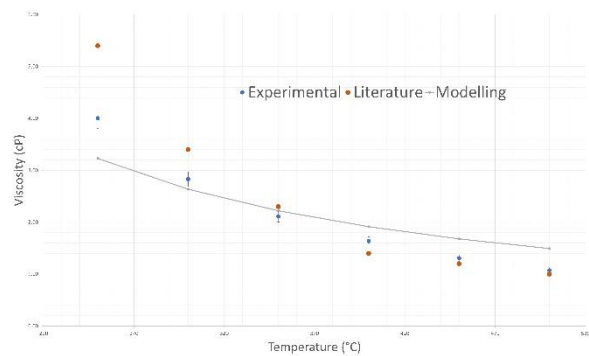


Figure 5. Viscosity: comparison between experimental, literature data and modelling results for Hitec® mixture.

Concerning the thermal conductivity, it was not possible to measure the values experimentally, but the predictive model was developed starting from the experimental density data for the binary mixtures and applying the molar volumetric additivity rule for the other multicomponent mixtures considered, obtaining good results from comparison with the values reported in the scientific literature.

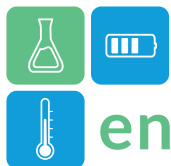


Table 3. Heat conductivity: comparison between literature data and modelling results for Hitec ® mixture.

			Conductivity (W/m*°C)	Conductivity (W/m*°C)
KNO ₃	NaNO ₃	NaNO ₂	Literature	Modelling
0.44	0.07	0.49	0.510 *	0.479

* Wang and al. (2012)

Conclusions

The aim of this work was the development and validation of predictive models for the description of the chemical-physical properties of molten salt mixtures suitable as thermal energy storage mean starting from the behaviour of the individual components.

Mixtures of binary, ternary and quaternary molten salts were selected, characterized, and studied. Given the large number of possible multicomponent mixtures produced, it was necessary to prepare and validate tools that allow the prediction of important thermo-physical parameters of these thermal fluids such as density, viscosity, conductivity, and thermal capacity, allowing the reduction of costs and times of experimental campaigns.

In this work, the values of specific heat, density and viscosity were experimentally measured, and data from scientific literature were used for the study of thermal conductivity.

The experimental values obtained allowed the development and therefore the subsequent validation of the predictive models for the mixtures considered; these were then further verified also as predictive tools for further multi-component molten nitrate mixtures, whose values are reported in the scientific literature.

It is therefore possible to conclude that the development of predictive models for specific heat, density, viscosity, and thermal conductivity of molten salt mixtures starting from the properties of the individual components has proven to be an important tool, useful both for completing missing data in the scientific literature and for the identification of innovative formulations to be used not only as thermal energy storage at medium temperature but also for heat transfer fluid for CSP applications.

Acknowledgment

This work was funded by the Italian Ministry of Environment and Energy Security through the «National Electric System Research» Programme (RdS) – Project 1.9 and the Integrated Project 1.2 “Electrochemical and thermal storage technologies”, 2022-2024 implementation plan.

References

- Delise, T. and al. (2019). Thermophysical, environmental, and compatibility properties of nitrate and nitrite containing molten salts for medium temperature CSP applications: A critical review. *J. Eur. Ceram. Soc.*, vol. 39, no. 1, pp. 92–99, doi: 10.1016/j.jeurceramsoc.2018.07.057.
- Delise, T. and al. (2020). Modeling the Total Ternary Phase Diagram of NaNO₃–KNO₃–NaNO₂ Using the Binary Subsystems Data,” *Int. J. Thermophys.*, vol. 41, no. 1, pp. 1–20, Jan. 2020, doi: 10.1007/s10765-019-2577-2.
- Tizzoni, A.C. (2020). Report RdS/PTR(2020)/255. Sviluppo di fluidi termici avanzati per CSP: modelli predittivi per il calcolo del calore specifico, densità e viscosità di miscele di sali fusi partendo dai componenti singoli.
- Zhao, Q. G. and al. (2016). A theoretical model for predicting the thermal conductivity of binary molten salts. *Int. J. Heat Mass Transf.* 92 639–642
- Di Giulio, R.M. and al. (1992). A rough hard-sphere model for the thermal conductivity of molten salts. *Int. J. Thermophys.* 13, 855
- Wang, T. and al. (2012), Thermal conductivity of the ternary eutectic LiNO₃–NaNO₃–KNO₃ salt mixture in the solid state using a simple inverse method, *Solar Energy Materials and Solar Cells*, Volume 102, Pages 201-207, ISSN 0927-0248.



Thermal modelling of the discharge of a 180kWh latent thermal energy storage demonstrator

Amandine Da Col^{1,2}, Fabrice Bentivoglio^{2,*}, Benoît Stutz²

¹ Univ. Grenoble Alpes, CEA, LITEN, DTCH, 38000 Grenoble, France

² Université Savoie Mont-Blanc, LOCIE Laboratory, UMR 5271, CNRS, 73370 Le Bourget-du-Lac, France

*Corresponding author e-mail: fabrice.bentivoglio@cea.fr

Abstract

This paper presents a comparison between numerical and experimental results for the discharge of a 180 kWh latent thermal energy storage. The numerical model has been presented and validated for different charging cases in a previous paper. It is a 1.5D model with a 1D homogeneous approach for the heat transfer fluid combined with a 1.5D approach for the phase change material. The heat transfer fluid used is water and the phase change material is RT70HC. The paper focus on the modelling of the phase-change during discharges, as the RT70HC has two solidification peaks. The model reproduces the total energy unloaded during a discharge with an accuracy of 95% and a root-mean-square error of 3 kW on outlet power.

Keywords: Numerical modelling, Thermal energy storage, Phase-change material, System-scale

Introduction

District heating networks (DHN) are an interesting solution to reduce CO₂ emissions of buildings in dense areas by providing them a way to better integrate decarbonized heat (Schmidiger and al., 2020). The main challenges resides in the shift between production and demand, and in the management of the consumption peaks in the morning and evening due to domestic hot water and heating (Martinez, 2022). Currently, they are mainly managed using fossil fuel boilers.

Thermal Energy Storage (TES) are a key component to better manage these peaks. It could smooth the urban heating network load by charging when the demand is low and supplying during peak demand. Thus, renewable energy systems like biomass, heat pumps or geothermal energy could more often operate in conditions closer to nominal conditions, gaining life-expectancy and efficiency (Guelpa and Verda, 2019). In addition, renewable and intermittent sources like wasted heat or waste incineration could be better exploited by storing their production during periods of low demand instead of sometimes being lost.

Among the different technologies developed for DHN, latent heat TES allows to store energy with a high density. It is particularly adapted in urban areas where space is generally limited.

This paper presents the validation of a numerical model of a Latent Heat TES (LHTES) against experimental data coming from a large scale demonstrator. The numerical model has been previously presented and

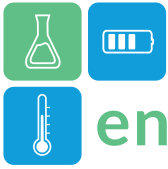
validated for different charging cases (Da Col and al, 2023). The present paper focuses on the discharging mode. This model aims to be a fast and precise tool for future design of latent heat thermal energy storages, reducing the need for computer-demanding CFD studies.

Methodology

A numerical 1.5D model has been developed on the DYMOLA software. It simulates a 180 kWh LHTES demonstrator based on shell-and-tubes technology with monophasic water as heat transfer fluid (HTF), RT70HC as the phase-change material (PCM) and aluminium fins to enhance the conductive heat transfer in the PCM. The flow inside the tubes is annular to enhance the convective heat transfer and ensure being in a forced convection laminar flow regime. A more detailed description of the demonstrator (geometry, thermocouples positions...) can be found in Bentivoglio and al (2021).

31 charge and discharge tests have been carried out on the demonstrator during the experimental campaign. In discharging mode, the cold water enters the bottom of the system by a collector. A shattering plate ensures that the flow is sufficiently distributed inside the collector to reduce the disparity of the mass flowrate between the 367 tubes.

The DYMOLA model is based on a 1D model to simulate the HTF and a conductive 1.5D model to represent the steel tube, the radial aluminium fins and the free PCM. CFD simulations are used to feed the



DYMOLA model with reduced data for the equivalent material composed by the PCM and the radial fins.

The heat exchange between the HTF and the tube is determined by the correlation from Muzychka and Yovanovich (2004). It takes into account the entrance region with an asymptotic model and is adapted to an annular fluid section.

The numerical results are compared to experimental data at macroscopic (power and energy) and local (outlet temperature and PCM temperatures) scales.

Da Col and al. (2023) concluded that the key parameters of the model are the discretization of the collectors, the convection heat transfer coefficient between the HTF and the tube, and the PCM thermal capacity model. Thus, one of the main challenges of the discharge case is to investigate the solidification behaviour of the RT70HC. Several tests had showed that this PCM has two distinct solidification plateaus. Jadal (2020) demonstrated that it is because two different species composed the material. Then, DSC tests were run in order to construct a numerical model of the material in solidification for the DYMOLA model, with the same method previously used in Da Col and al. (2023).

Results and Discussion

Thermal capacity model

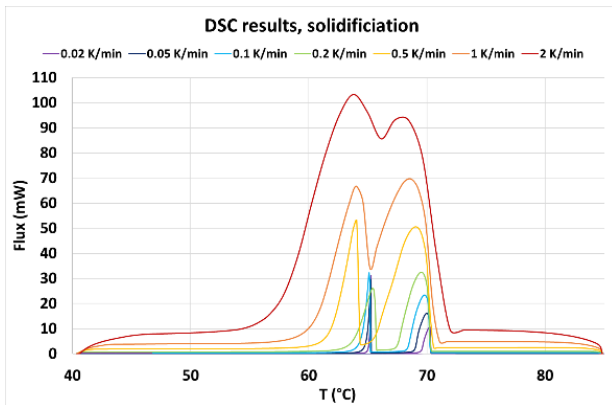


Figure 1: Differential Scanning Calorimetry results in solidification, for different temperature slopes

The DSC tests were run with temperature slopes from -0.02 K/min to 2 K/min on a same sample of 111 mg. The two phase-changes plateaus appear clearer when the solidification rate is slower. The aim was to develop a thermal capacity model that includes the two phase-changes. Integrating these results following Hu and Argyropoulos (1996) and Kahwaji and al (2021) recommendations lead to the numerical model presented in the Figure 2. It is written in the software as a table associating 8 temperatures from 50 to 80 °C

to a value of thermal capacity. Between two temperature points, the software does a linear interpolation to determine the thermal capacity.

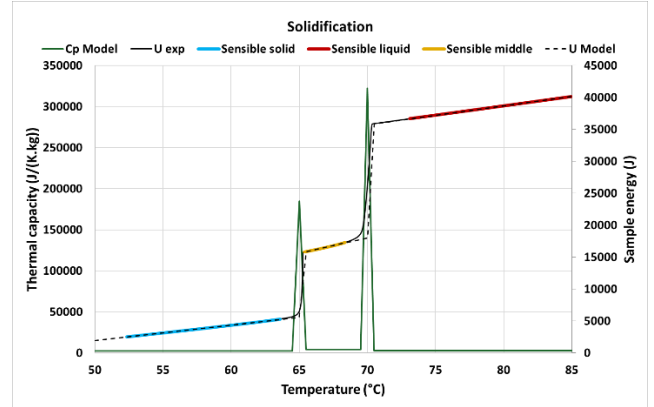


Figure 2: Numerical model for thermal capacity with integrated latent heat, based on experimental result

Constant power discharge

The first experimental case is a discharge where the mass flowrate at the bottom of the system is regulated in order to extract 25 kW from the system. Figure 3 shows the power and energy extracted from the thermal storage, calculated according to equations (1) and (2).

$$\dot{q}_{htf} = \dot{m} \times C_{p\text{average}}(T_{in} - T_{out}) \quad (1)$$

$$q = \int_0^t \dot{q}_{htf} dt \quad (2)$$

At first, the power is superior to this value because of the minimum mass flowrate of the pump. After 2 hours of operation, the flow control adjusts the extracted power to the set point. After 5h30 of operation, the maximum flowrate is reached and it is no longer possible to adjust the extracted power to the setpoint.

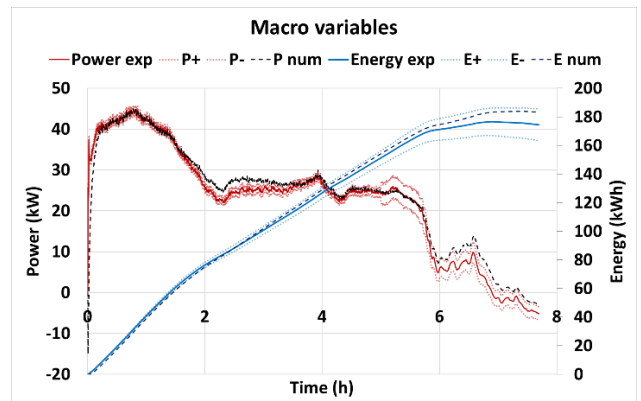


Figure 3: Power and energy extracted, with uncertainties range, with constant power discharge

The results of the comparison between the model and the experimental points are presented in the Figure 3, the Figure 4 and the Figure 6. Globally the results are in very good agreement. The root-mean-square (RMS)

error between experimental and numerical results is 2.96 kW for thermal power, and the difference in total energy extracted is 8.17 kWh, i.e. 4.68 % of the total energy. The RMS error on outlet temperature, shown on Figure 4, is 1.1°C.

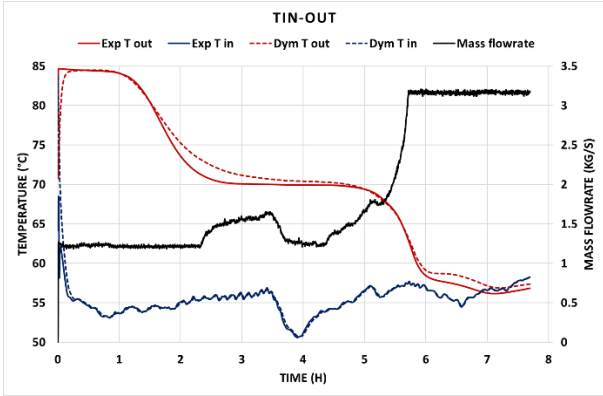


Figure 4: Inlet and outlet temperatures of the system

Locally, there is a good agreement between local and experimental results, as shown in Figure 6. The major error is situated on “PCM2” thermocouples, the one located at the longest distance from the tube: it is probably because the model considers the edge of a cylinder with a radius of 32.2 mm whereas the real distance between the thermocouple “PCM2” and the centre of the tube is 35.45 mm, as illustrated in Figure 5. The linear thermal resistance between the edge of the fins (28.75 mm radius) and the end of the free PCM (35.45mm) is then 0.65 K/W numerically and 1.2 K/W experimentally, i.e. a difference of 54.2%.

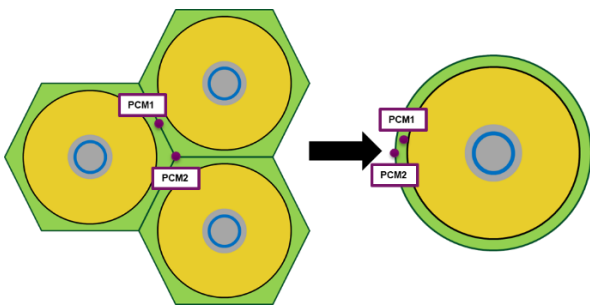


Figure 5: Positions of the thermocouples PCM1 and PCM2 in the system (left) and in the model (right)

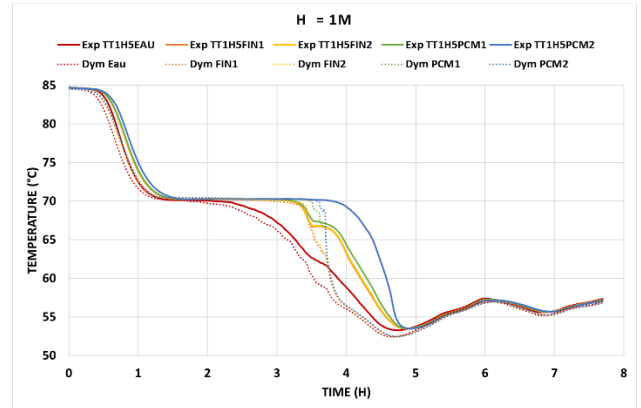


Figure 6: Local temperature of water, tube, fins and free PCM at 1 meter height

This difference does not affect much the macroscopic results nor the water temperature in the tubes, as shown in Figure 7 and Figure 7. There is a good agreement between experimental and numerical results at all levels.

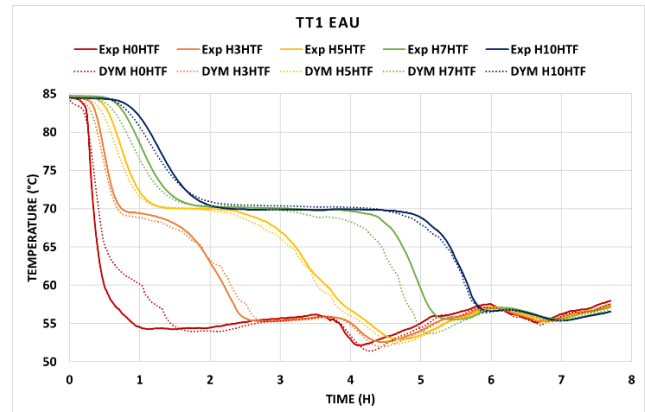


Figure 7: Water temperature inside the tube for different heights, each section being 0.5m higher than the previous, with $H_0 = 0m$.

Constant flowrate discharge

The second experimental case is a discharge where the mass flowrate at the bottom of the system is set to 0.6 kg/s. Results are presented in Figure 8 and Figure 9.

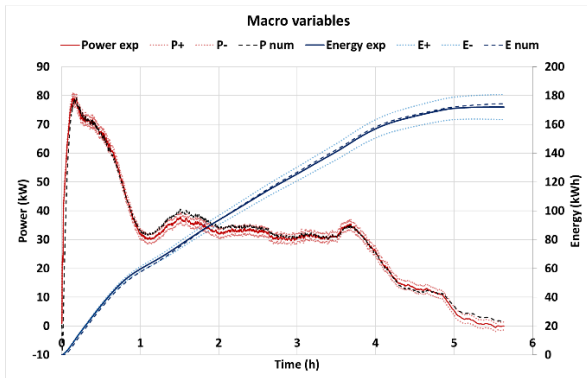
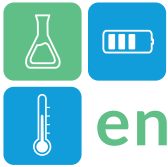


Figure 8: Macroscopic variables of the system, power and energy extracted, with uncertainties range, compared with numerical results.

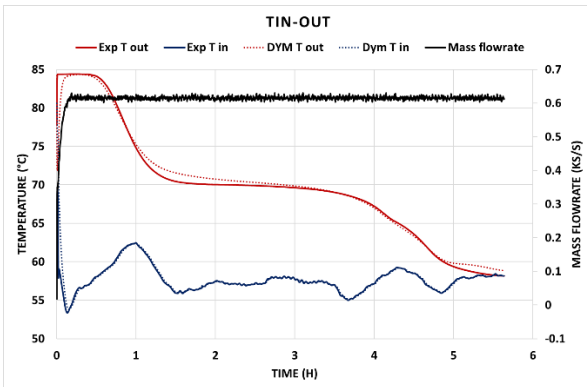


Figure 9: Inlet mass flowrate and temperature, and outlet temperature of the system

For this case, the RMS error on the power is 3.01 kW, the difference between numerical and experimental energy extracted is 2.98 kWh, i.e. 1.73 % of the total energy. The RMS error on outlet temperature is 1.62 °C.

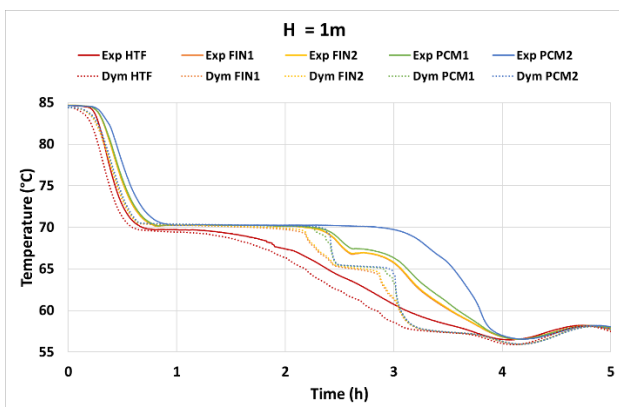


Figure 10: Local temperature in the HTF, fins zone and free PCM, at 1m height

Locally, the model reproduces the two solidifications plateaus of Figure 10 with a good agreement in terms of relative plateaus' length. This confirms that we can not neglect these two solidifications. Figure 11 illustrates the macroscopic results difference between the model that considers one solidification (1 peak) and

our current model (2 peaks). Table 1 compiles the major criteria used to compare experimental and numerical data. It shows that the 1 peak model is still acceptable, but the 2 peaks model is slightly better.

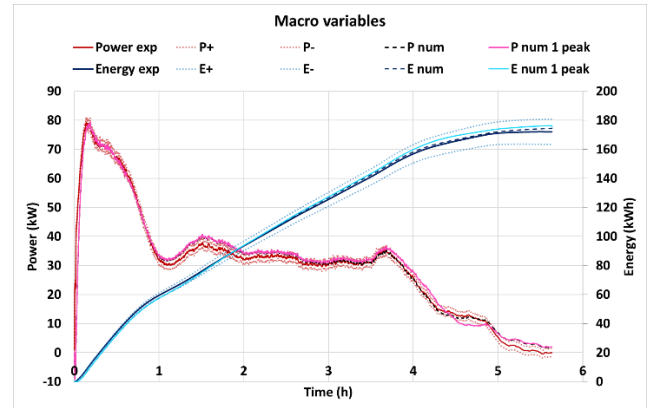


Figure 11: Macro variables, comparison between the two thermal capacity models

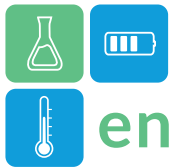
Table 1: Comparison between errors of the two thermal capacity models

Model	RMS on T (°C)	RMS on P (kW)	dE (kWh - %)
1 peak	1.67	3.22	3.59 – 2.08%
2 peaks	1.62	3.01	2.98 – 1.73%

Conclusions

This 1D fluid – 1.5D PCM numerical model is able to reproduce with a good agreement the experimental results for two kind of discharges, at constant flow rate and constant power. The relative error for the energy extracted is <5 %, the RMS errors on power and temperature are <3 kW and <2°C. The PCM thermal capacity model with two peaks reproduces well the thermal behaviour of the system and is an improvement compared to a model with only one peak.

This 1D fluid – 1.5D PCM model and the methodology used to determine its parameters are then validated for the charges and discharges of a latent thermal energy storage based on tube and shell technology. Thus, this method is relevant to design these systems with a reduced computer time: it requires only about 10 minutes to simulate 6 hours of operation of the whole system.



enerstock

ENERSTOCK 2024

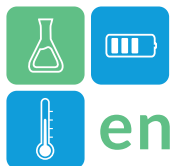
The 16th IEA ES TCP International Conference on Energy Storage

June 5–7, 2024

Lyon, France

References

- Bentivoglio, F. and al. (2021). Design and operation of a 180 kWh PCM heat storage at the Flaubert substation of the Grenoble urban heating network. *Applied Thermal Engineering*. doi.org/10.1016/j.applthermaleng.2020.116402
- Da Col, A, and al. (2023). Modelling a latent heat thermal storage demonstrator and identification of the model key-parameters. *Journal of Energy Storage*. doi.org/10.1016/j.est.2023.109239
- Guelpa, E. and Verda V. (2019). Thermal energy storage in district heating and cooling systems: A review. *Applied Energy*. doi.org/10.1016/j.apenergy.2019.113474
- Hu, H., and Argyropoulos S.A. (1996). Mathematical modelling of solidification and melting: a review. *Modelling and Simulation in Material Science and Engineering*. doi.org/10.1088/0965-0393/4/4/004
- Jadal, M. (2020). Caractérisation thermique d'un échangeur-stockeur constitué d'un matériau à changement de phase dans une structure conductrice.
- Kahwaji, S., and al. (2021). Thermal property determination for phase change materials. *The Journal of Chemical Thermodynamics* 160, 106439. doi.org/10.1016/j.jct.2021.106439
- Martinez, S., and al. (2022). Demand-side flexibility in a residential district: What are the main sources of uncertainty? *Energy and Buildings*. doi.org/10.1016/j.enbuild.2021.111595
- Muzychka, Y.S., and Yovanovich, M.M. (2004). Laminar Forced Convection Heat Transfer in the Combined Entry Region of Non-Circular Ducts. *Journal of Heat Transfer*. doi.org/10.1115/1.1643752
- Schmidiger, P., and al. (Press release, 2020). L'extension du réseau de chauffage de Saint-Louis intégrera l'EuroAirport. <http://www.r-cu.fr/wp-content/uploads/2021/04/CP-Extension-reseau-chaaleur-St-Louis.pdf>



Thermal response of layered hybrid organic-inorganic perovskites as solid-solid phase change materials

R. Salgado-Pizarro¹, H. Navarro², C. Barreneche^{1*}, A.I. Fernández¹

¹ Departament de Ciència de Materials i Química Física, Secció de Ciència de Materials, Facultat de Química, Universitat de Barcelona, C/ Martí i Franquès 1-11, 08028, Barcelona, Spain

² Birmingham Center of Energy Storage, School of Chemical Engineering, University of Birmingham, Birmingham, UK

*Corresponding author e-mail: c.barreneche@ub.edu

Abstract

This work investigates layered hybrid organic-inorganic perovskites (LHOIPs) as solid-solid phase change materials, which can store energy due to polymorphism transitions and are suitable candidates for cooling electronics. Here, we evaluate the polymorphic transition of these materials, mainly focusing on the reorganisation that takes place during the transition and its implications on the thermal properties. Three different compounds will be evaluated $(C_{12}H_{28}N)_2CuCl_4$, $(C_{14}H_{32}N)_2CuCl_4$ and $(C_{16}H_{36}N)_2CuCl_4$, where XRD and Raman were used to understand the reorganisation of the alkylammonium chain and the laser flash and differential scanning calorimetry to analyse the thermal response. An increase in cell volume during the polymorphic transition is detected, leading to a decrease in the thermal diffusivity and an increase in the specific heat capacity.

Keywords: Layered Hybrid Organic-Inorganic Perovskites (LHOIP), Organometallic materials, Thermal Energy Storage (TES), Solid-Solid Phase Change Materials (ss-PCM).

Introduction

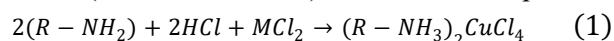
Solid-solid phase change materials (ss-PCM) are great candidates as thermoregulators since they do not require encapsulation or shape stabilisation. Also, the corrosion issues may be reduced, and the absence of a second material to shape stabilisation or encapsulation allows faster charging and discharging (Mastani Joybari et al., 2015; Putra et al., 2019; Sciacovelli et al., 2018). Organometallics ss-PCMs, especially layered hybrid organic-inorganic perovskites (LHOIPs), present unique structural characteristics and tailored properties (Huan et al., 2016; Mao et al., 2019; Pedesseau et al., 2016).

Understanding phase transitions of the LHOIPs at the molecular level remains an area that requires further investigation, given the limited existing literature on the subject. This study addresses these knowledge gaps by presenting a perspective on the polymorphic transitions in LHOIPs. To achieve our research objectives, we conducted a comprehensive analysis of phase transitions, including crystal transformation and the study of alkylammonium movement using X-ray diffraction and Raman spectroscopy during phase transformation. Additionally, we measure the thermal conductivity in the proximity of phase transitions and the specific heat capacity.

Materials and methods

Synthesis and sample preparation

The synthesis of the LHOIP, ss-PCM, following the procedure described in the study (Salgado-Pizarro, Barreneche, et al., 2023), following the stoichiometry reaction, Eq.1. The reactants n-dodecylammonium 98%, n-tetradecylammonium 98% and n-hexadecylammonium 90% were acquired from Acros Organics, copper (II) chloride dehydrated from VWR international, hydrochloric acid 37% from Labbox and anhydrous methanol (max 0.003% H₂O) from Merk Group.



The nomenclature used to identify each component was CuC_X, where X represents the length of the alkylamine used.

Characterisation

The crystalline structure was determined from 298 K to 378 K, with a ΔT of 20 K by X-ray powder diffraction (XRD) conducted in a Anton Paar XRDynamic 500 equipped with an Anton Paar CHC plus+ Cryo 2 θ/θ powder diffractometer. The molecular structure was studied by a Raman spectroscopy coupled with a hot stage, which was used and measured from 298 to 378 K and measured every 20 K. The thermal

characterisation was done with a differential scanning calorimeter (DSC) from Mettler Toledo. A 300 K to 380 K heating ramp at 1 K·min⁻¹ was set to determine the polymorphic transitions. Moreover, the thermal diffusivity was measured by laser flash, LFA 427 from Netzsch, from 300 to 380 K. The laser voltage was set at 650 V and a pulse of 0.8 ms.

Results and discussion

Crystal and molecular structure

Figure 1 displays the XRD and Raman spectra and the samples' heat flow curves, highlighting the temperatures where the XRD and Raman spectra were taken.

Figure 1 (a) presents the crystal structure's evolution over the polymorphic transition. The samples present a movement of the (0 0 1) plane to lower values, meaning that the interlayer distance between the perovskites layer is increased, which can be related to a conformational change of the alkylamine chain (Bochalya et al., 2019). Three main hypotheses can be used to explain these changes: (I) an increase of the initial tilting of 40° of the alkylamine chain between the perovskite layer and the ammonium group (Ciajolo et al., 1976); (II) trans conformation to a conformation with gauche conformation, which results on an increasing of the length of the interlayer distance (Li et al., 2021); (III) full/partial disorganisation of the alky chain with a combination of the two phenomena (I) and (II), recalling a polymer melting (Needham et al., 1984).

Moreover, an amorphous halo around the 16-18° diffraction peaks can be detected, mainly in the CuC₁₆ sample. The halo is detected after the polymorphic transition, which can be related to the full/partial disorganisation of the alky chain, which resembles the amorphous halo present in the amorphous linear polymers.

Figure 1 (b) presents the Raman spectra of the samples over the temperature. The range from 700 to 1700 cm⁻¹ is selected because it is the range where the main alkylamine bands can be detected. From 298 K to 318 K, no significant changes are detected. However, close to the polymorphic transition temperatures, the signal decreases. The 1062 cm⁻¹ band, related to the C-C vibration on a trans planar chain, is mainly lost by increasing the temperature, meaning that this organisation changes and may acquire a gauche conformation. Other evidence of this behaviour is the decreased intensity at 1465 cm⁻¹ related to the CH₂ bending to the molecular coupling of trans conformation (Li et al., 2021).

Thermal characterisation

Figure 2 presents the thermal diffusivity (α) results, including a tendency curve discarding the result close to the polymorphic transition. A drop in the values from room to transition temperature is detected. Above the polymorphic transition, the thermal diffusivity values stabilise around 0.1 mm²·s⁻¹ over the temperature. The minimum values are detected close to the phase transition. No clear tendencies can be extracted regarding the length of the alkylamine.

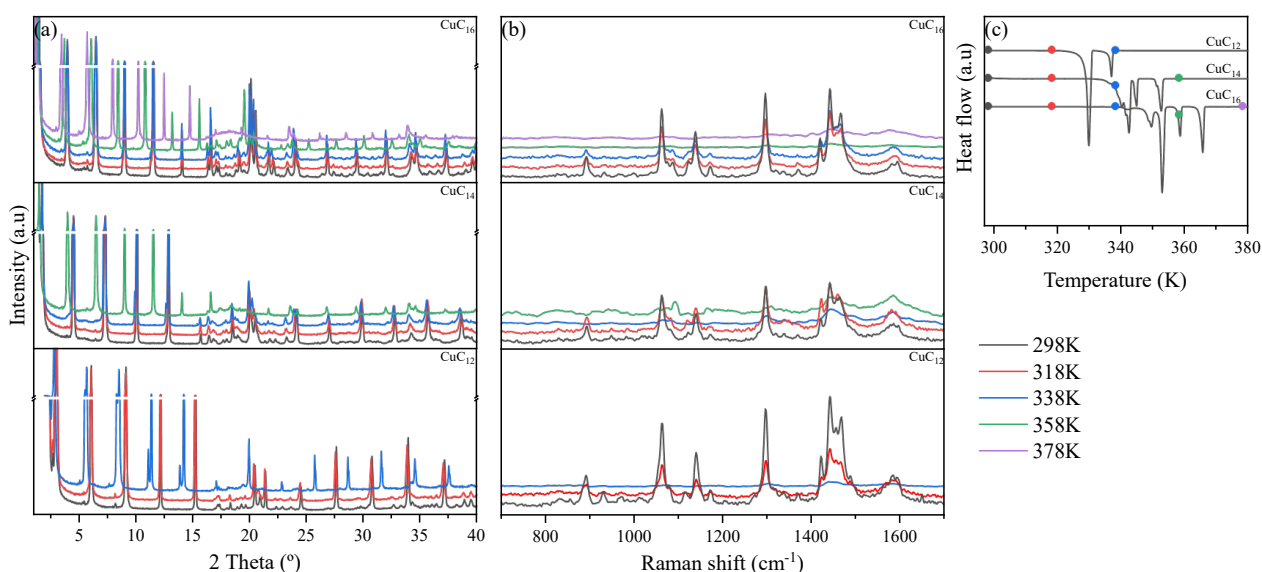


Figure 1: (a) XRD spectra over temperature; (b) Raman

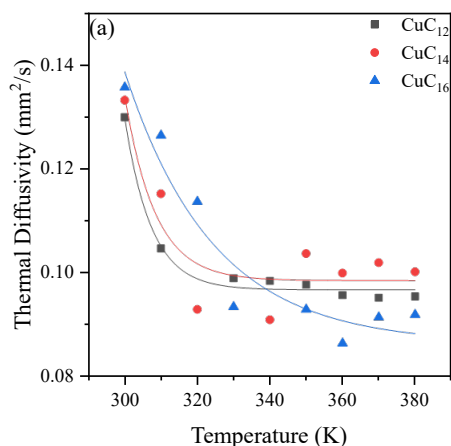
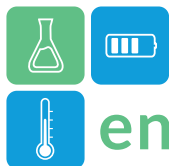


Figure 2: (a) Thermal diffusivity values over temperature.

Table 1 presents the specific heat capacity (C_p) and the calculated density (ρ), thermal diffusivity (α) and thermal conductivity (λ).

The specific heat presents an inverse relation between the length of the alkylamine, as reported in previous studies (Salgado-Pizarro et al., 2023). Concerning the density of the samples, a decrease is observed by increasing the temperature, which is directly related to the reorganisation of the alkylamine chain to a less dense structure. The thermal conductivity presents values around $0.2 \text{ W}\cdot\text{m}^{-1}\cdot\text{K}^{-1}$ that mostly remain constant over the temperature.

Table 1: Summary of the density, specific heat capacity and thermal conductivity results.

Sample	ρ (g/m^3)	Temp. (K)	α (mm^2/s)	C_p (J/gK)	λ (W/mK)
CuC ₁₂	1.23	300	0.130	1.71	0.27
	1.23	320	0.071	2.41	0.21
	1.22	340	0.099	1.94	0.23
	1.22	360	0.096	1.88	0.22
CuC ₁₄	1.19	300	0.133	1.47	0.23
	1.19	320	0.093	2.04	0.23
	1.17	360	0.100	1.97	0.23
CuC ₁₆	1.17	380	0.100	2.06	0.24
	1.19	300	0.136	1.37	0.22
	1.19	320	0.114	1.64	0.22
CuC ₁₆	1.17	360	0.086	2.17	0.22
	1.17	380	0.092	1.81	0.20

Conclusions

This work tries to understand the polymorphic transition on the selected LHIOP in order to work as solid-solid PCMs.

Throughout the XRD analysis, we detected an increase in the c-axis of the crystal structure during the polymorphic. As a result of the XRD and the Raman results, it is concluded that the transition mainly occurs

due to the chain's reorganisation. The reorganisation may be attributed to different factors such as the tilting angle of the chain, its conformation or full/partial disorder. In the thermal diffusivity results, a decrease is detected due to the alkylamine chain's reorganisation, which produces a decrease in the thermal conductivity and an increase in the specific heat.

Furthermore, supplementary studies should be performed to completely comprehend the molecular motion of the alkylamine chain and its implications in the thermal characteristics to be used as thermal energy storage materials.

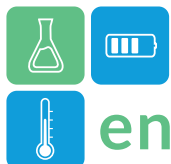
Acknowledgements

The authors thank the Catalan Government for the quality accreditation given to their research group DIOPMA (2021 SGR 00708). DIOPMA is a certified agent of TECNIO in the category of technology developers from the Government of Catalonia. The authors are grateful to the CCiTUB for the equipment or measurements of XRD.

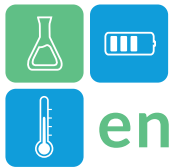
This work is partially supported by the grant RTI2018-093849-B-C32 and PID2021-123511OB-C32 funded by MCIN/AEI/10.13039/501100011033 and, as appropriate, by "ERDF A way of making Europe" and the PhD grant PRE2019-087336 funded by MCIN/AEI/ 10.13039/501100011033 and, as appropriate, by "ESF Investing in your future" of R. Salgado-Pizarro.

References

- Bochalya, M., Kanaujia, P. K., Vijaya Prakash, G., & Kumar, S. (2019). Structural and optical diversity in copper halide-based ferromagnetic inorganic-organic layered hybrids. *Journal of Solid State Chemistry*, 273(March), 219–225. <https://doi.org/10.1016/j.jssc.2019.03.012>
- Ciajolo, M. R., Corradini, P., & Pavone, V. (1976). Comparative studies of layer structures: the crystal structure of bis(monodecylammonium) tetrachloromanganate (II). *Gazzetta Chimica Italiana*, 106(9–10), 807–816.
- Huan, T. D., Tuoc, V. N., & Minh, N. V. (2016). Layered structures of organic/inorganic hybrid halide perovskites. *Physical Review B*, 93(9), 094105. <https://doi.org/10.1103/PhysRevB.93.094105>
- Li, J., Barrio, M., Dunstan, D. J., Dixey, R., Lou, X., Tamarit, J.-L., Phillips, A. E., Lloveras, P., Li, J.,



- Dunstan, D. J., Dixey, R., Phillips, A. E., Lou, X., Barrio, M., Tamarit, J.-L., & Lloveras, P. (2021). Colossal Reversible Barocaloric Effects in Layered Hybrid Perovskite $(\text{C}_{10}\text{H}_{21}\text{NH}_3)_2\text{MnCl}_4$ under Low Pressure Near Room Temperature. *Advanced Functional Materials*, *31*(46), 2105154. <https://doi.org/10.1002/ADFM.202105154>
- Mao, L., Stoumpos, C. C., & Kanatzidis, M. G. (2019). Two-Dimensional Hybrid Halide Perovskites: Principles and Promises. *Journal of the American Chemical Society*, *141*(3), 1171–1190. <https://doi.org/10.1021/jacs.8b10851>
- Mastani Joybari, M., Haghighat, F., Moffat, J., & Sra, P. (2015). Heat and cold storage using phase change materials in domestic refrigeration systems: The state-of-the-art review. *Energy and Buildings*, *106*, 111–124. <https://doi.org/10.1016/j.enbuild.2015.06.016>
- Needham, G. F., Willett, R. D., & Franzen, H. F. (1984). Phase transitions in crystalline models of bilayers. 1. Differential scanning calorimetric and x-ray studies of $(\text{C}_{12}\text{H}_{25}\text{NH}_3)_2\text{MCl}_4$ and $(\text{C}_{14}\text{H}_{29}\text{NH}_3)_2\text{MCl}_4$ salts ($\text{M} = \text{Mn}^{2+}, \text{Cd}^{2+}, \text{Cu}^{2+}$). *The Journal of Physical Chemistry*, *88*(4), 674–680. <https://doi.org/10.1021/j150648a012>
- Pedesseau, L., Saponi, D., Traore, B., Robles, R., Fang, H.-H., Loi, M. A., Tsai, H., Nie, W., Blancon, J.-C., Neukirch, A., Tretiak, S., Mohite, A. D., Katan, C., Even, J., & Kepenekian, M. (2016). Advances and Promises of Layered Halide Hybrid Perovskite Semiconductors. *ACS Nano*, *10*(11), 9776–9786. <https://doi.org/10.1021/acsnano.6b05944>
- Putra, N., Rawi, S., Amin, M., Kusri, E., Kosasih, E. A., & Indra Mahlia, T. M. (2019). Preparation of beeswax/multi-walled carbon nanotubes as novel shape-stable nanocomposite phase-change material for thermal energy storage. *Journal of Energy Storage*, *21*, 32–39. <https://doi.org/10.1016/j.est.2018.11.007>
- Salgado-Pizarro, R., Barreneche, C., & Fernández, A. I. (2023). Synthesis optimisation of copper-based layered perovskites as thermal energy storage materials. *Materials Today Chemistry*, *30*, 101491. <https://doi.org/10.1016/j.mtchem.2023.101491>
- Salgado-Pizarro, R., Svobodova-Sedlackova, A., Fernández, A. I., & Barreneche, C. (2023). Designing thermal regulation materials: Investigating alkylamine length in polymorphic layered hybrid organic-inorganic perovskites. *Journal of Energy Storage*, *73*, 109156. <https://doi.org/10.1016/j.est.2023.109156>
- Sciacovelli, A., Navarro, M. E., Jin, Y., Qiao, G., Zheng, L., Leng, G., Wang, L., & Ding, Y. (2018). High density polyethylene (HDPE) — Graphite composite manufactured by extrusion: A novel way to fabricate phase change materials for thermal energy storage. *Particuology*, *40*, 131–140. <https://doi.org/10.1016/j.partic.2017.11.011>



Thermo-mechanical assessment of steels under service conditions in hot tanks used in CPS.

Sergio Andrés Ardila-Parra^{1,*}, Cristina Prieto², Ana Inés Fernández¹

¹Universitat de Barcelona, Faculty of Chemistry, Department of Materials Science and Physical Chemistry, Martí i Franqués, 1, floor 7, Barcelona, Spain.

²Universidad de Sevilla. Department of Energy Engineering, Camino de los Descubrimiento s.n., 41092 Sevilla, Spain

*Corresponding author e-mail: sergioardila@ub.edu

Abstract

The design of a methodology and development of the necessary test setup to replicate the service conditions of the steels employed in solar salt storage tanks is presented. In Concentrated Solar Power (CSP) systems, hot tanks contain molten salt at a high temperature of about 560°C. The structural steel used to fabricate these tanks confronts the challenges of a harsh environment: high temperature and corrosive conditions of the molten salt environments. Due to the lack of explicit standards for selecting the right material and dimensions of the tanks, simulations combined with experimental approaches play a pivotal role in the process of selecting optimal material. The core of this research lies in the emulation of the conditions of a furnace that allows external loads to be applied to the sample, while salt is heated. The low thermal conductivity of the molten salt limits heat transfer, the main aim of the research is to design a furnace capable of ensuring maximum temperature over the steel sample allowing mechanical loading.

Keywords: TES, CSP, Molten Salt, Heat Transfer.

Introduction

Thermal Energy Storage (TES) systems are focused on addressing the availability of renewable energies, solving the intermittent nature of it. Concentrated Solar Power (CSP) incorporates two tanks with cold and hot molten salt, the temperature in the hot tank is the more critical aspect by reaching a temperature up to 560°C (Cabeza et al., 2015).

The design of this specific type of tank is not regulated by any standard, API 650 allows a maximum temperature of 260°C (*Welded Steel Tanks for Oil Storage*, 2003) but is usually implemented with some adjustments. Several tanks have failed in recent years involving leakage of molten salts and other accidents, resulting in economic losses and affecting the right operation of the plants (Wan et al., 2020).

Evaluating failure modes of AISI 347H, one of the austenitic steels used in the fabrication of hot tanks for CSP, could be challenging because of the complex and extreme conditions presented in the service. This research presents an approach to assess the durability of the steel by the implementation of a device capable

of heating the steel in contact with molten salt at high temperatures while tensile stress is applied.

The design and development of this kind of device brings some problems related mainly to the behavior of the molten salt. The device must keep the molten salt inside, avoiding leakages and the salt in contact with the steel should be at a temperature close to the service temperature of 560°C without exceeding it to prevent salt degradation. A previous experience was conducted previously with a plain steel and a lower temperature that gave us some insights for a new design (Prieto et al., 2018).

Methodology

The solar salt thermal conductivity is:

$$k = 0.39 + 1.9 \cdot 10^{-4}T \#(1)$$

Where k is the conductivity in $W/m \cdot K$ (Wan et al., 2020). For a temperature of 560°C, the conductivity of the salt is $0.4964 W/m \cdot k$. Austenitic Steel AISI 347H has a thermal conductivity of $16.3 W/m \cdot k$ which is a considerable difference and can affect heat transfer, according to material software *ANSYS SELECTOR*.

Heat transfer for the device developed is based on the heat conduction from a hot source to the molten salt that finally heats the 347H sample. Cylindrical conduction is defined by the equation:

$$Q = \frac{2\pi KL(T_i - T_o)}{\ln\left(\frac{r_o}{r_i}\right)} \quad \#(2)$$

Where q is the flux of heat [W], K is the conductivity of the material, L is the length of the cylinder, T_1 is the internal temperature, T_2 is the external temperature, and r_1 and r_2 are the radial distance where these temperatures are located. Figure 1. Shows these variables and dimensions (Yunus A. Çengel, 2011.).

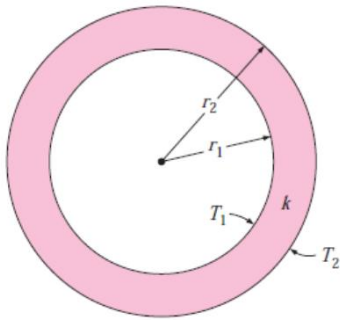


Figure 1: Conduction in cylinders
 Copyright © Çengel Yunus - Heat and mass transfer.

Due to the necessity of maintaining a temperature in the salt in contact with the sample close enough to 560°C, the difference between the temperature outside the cylinder and inside must be minimal. This constraint is due to the degradation of molten salt, as mentioned before. Corrosion over the sample will increase considerably when molten salt degradation occurs, (Bonk et al., 2018)

Results and Discussion

Different geometry configurations were simulated using FEM commercial software to minimize the temperature difference and to achieve a maximum temperature on the surface of the stainless-steel sample.

The temperature field of each design was analysed to determine the critical aspects of the geometry. According to Equation 2, increasing the length of the cylinder minimizes the temperature difference, this measure is limited by the dimensions of the sample. The dimensions of the sample were taken from standards ASTM E8 (Designation: E8/E8M – 13a

Standard Test Methods for Tension Testing of Metallic Materials 1, n.d.) making the sample as long as possible, the following figure shows the final dimensions implemented.

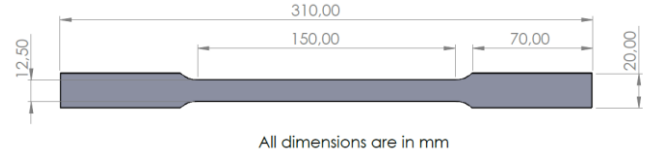


Figure 2: Sample dimensions.

In general, increasing the dimensions of the cylinder will increase the heat transfer area, and will minimize the temperature difference. However, increasing the diameter of the cylinder is not viable because the distance between the molten salt at maximum temperature will be larger and the low conductivity of the molten salt will decrease the temperature on the surface of the sample. The following figure shows the temperature distribution of the molten salt inside a furnace design and around the sample.

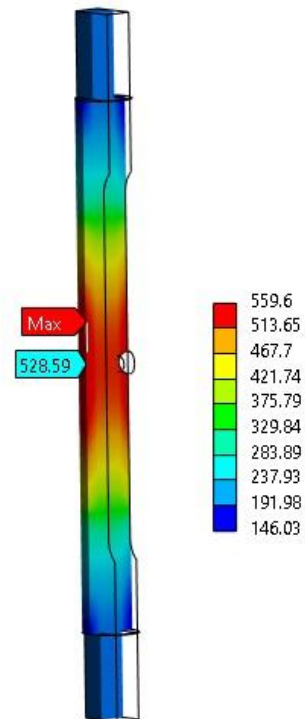


Figure 3: Temperature distribution over the salt.

Figure 3 shows a temperature drop at the upper and the lower extremities. These low temperatures are needed to maintain in the solid state the salt, avoiding in this way the leakage to meet both operational and



safety requirements. A refrigeration circuit using water as a refrigerant was implemented to remove heat employing convection, two furnace inner chambers allow cooling walls in contact with the salt without mixing it with water. The distance between these two zones was maximized to avoid affecting the heat transfer in the middle of the sample as shown also in Figure 2.

Several designs were evaluated to maximize the temperature of the salt in contact with the sample. Figure 4 shows the final design, the diameter of the internal cylinder, and the distance and areas of the convection zones were optimized to reduce the drop in temperature and to keep solidified salt at the extremities.

The material's selection for the furnace wall is an ongoing task. Previous work (Prieto et al., 2018) used quartz as a transparent wall was aimed. Some issues with its durability at higher temperatures need to be analysed.

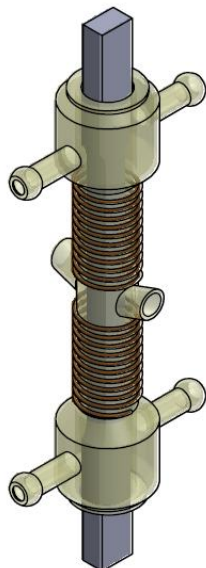


Figure 4: Final design.

Conclusions

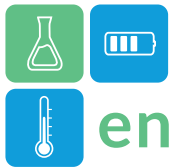
Design of components in Thermal Energy Storage (TES) systems within concentrated solar plants required an integration of heat transfer dynamics, material selection, and structural design. The culmination of this research effort is presented by a

design, engineered to withstand combined thermal and mechanical loads.

The final design maintains a temperature close to 530°C on the sample surface without exceeding the degradation temperature of 560°C on the molten salt.

References

- Bonk, A., Braun, M., Hanke, A., Forstner, J., Rückle, D., Kaesche, S., Sötz, V. A., & Bauer, T. (2018). Influence of different atmospheres on molten salt chemistry and its effect on steel corrosion. *AIP Conference Proceedings*, 2033. <https://doi.org/10.1063/1.5067097>
- Cabeza, L. F., Martorell, I., Miró, L., Fernández, A. I., & Barreneche, C. (2015). Introduction to thermal energy storage (TES) systems. In *Advances in Thermal Energy Storage Systems: Methods and Applications* (pp. 1–28). Elsevier Inc. <https://doi.org/10.1533/9781782420965.1>
- Designation: E8/E8M – 13a. (2011.). *Standard Test Methods for Tension Testing of Metallic Materials* 1. https://doi.org/10.1520/E0008_E0008M-13A
- Prieto, C., Barreneche, C., Martínez, M., Cabeza, L. F., & Fernández, A. I. (2018). Thermomechanical testing under operating conditions of A516Gr70 used for CSP storage tanks. *Solar Energy Materials and Solar Cells*, 174, 509–514. <https://doi.org/10.1016/j.solmat.2017.09.029>.
- Standard, A. P. I. (2013). *Welded tanks for oil storage.* American Petroleum Institute 1220.
- Wan, Z., Wei, J., Qaisrani, M. A., Fang, J., & Tu, N. (2020). Evaluation on thermal and mechanical performance of the hot tank in the two-tank molten salt heat storage system. *Applied Thermal Engineering*, 167. <https://doi.org/10.1016/j.applthermaleng.2019.114775>
- Yunus A. Çengel_ Afshin J. Ghajar. (2011). *Heat and mass transfer.* Mc Graw Hill.



Thermochemical energy storage in a CSA-based cementitious material

Noé Beaupere^{1,*}, Alexandre Malley-Ernewein¹, Tamar Nahhas¹, Stéphane Ginestet¹, Gabriel Samson¹,
Martin Cyr¹

¹Université de Toulouse, UPS, INSA, LMDC (Laboratoire Matériaux et Durabilité des Constructions de Toulouse), 135, Avenue de Rangueil, 31 077 Toulouse cedex 4, France

*Corresponding author e-mail: beaupere@insa-toulouse.fr

Abstract

Thermochemical energy storage materials are found promising due to their high capacity of storage. Ettringite ($3\text{CaO} \cdot \text{Al}_2\text{O}_3 \cdot 3\text{CaSO}_4 \cdot 32\text{H}_2\text{O}$) presents additional benefits of a moderate temperature of storage (60°C) and an affordable price that may fit the prerequisites to store renewable energies for space heating or domestic hot water production. CSA (Calcium Sulfo-Aluminate) cement was used as a thermochemical energy storage media. A prototype was built to evaluate the storage properties of a monolith made of CSA cement paste. A hot dinitrogen flow would be produced, to dehydrate CSA cement and store energy. By adding water vapor to the nitrogen, the energy could then be released on demand. To facilitate the diffusion of the gas flow, the cement monolith was foamed, increasing its permeability. It was shown that about 43 MJ/m^3 (12 kWh/m^3) could be released within two days when the material was hydrated.

Keywords: Thermochemical energy storage; ettringite cementitious material; hydration-dehydration;

Introduction

The possibility of energy release by ettringite was demonstrated by Struble and Brown [1], who found a heat of hydration close to $1,4 \text{ MJ/kg}$. The process involved is the dehydration of ettringite ($3\text{CaO} \cdot \text{Al}_2\text{O}_3 \cdot 3\text{CaSO}_4 \cdot 32\text{H}_2\text{O}$) into meta-ettringite ($3\text{CaO} \cdot \text{Al}_2\text{O}_3 \cdot 3\text{CaSO}_4 \cdot 12\text{H}_2\text{O}$), resulting in the physical and chemical desorption of water. Dehydration of the material goes by step, as demonstrated by Zhou and Glasser [2]. It was found that dehydration was complete (20 molecules evaporated) as a temperature of 57°C was experienced by the material in a dry atmosphere (partial pressure of vapor of 800 Pa).

The high heat of reaction and adequate temperature for energy storage resulted in the development of several prototypes. These prototypes involve either closed (Figure 1 (a)) or open-systems (Figure 1 (b)). At EMPA was developed a closed-system prototype involving a 6 m^3 cement block, releasing 216 MJ/m^3 on discharge [3]. Two other prototypes of 0.005 m^3 were developed at LMDC. The first was a closed-system, showing 220 MJ/m^3 on discharge, while the

second was an open-system prototype for better efficiency on release (421 MJ/m^3), that was foamed material (76% porosity) [4]. No aging was found for these samples after 10 cycles. To allow the gas to go through the material, the material was foamed, resulting in a porosity of 53%, and a density of 600 kg/m^3 instead of 1800 kg/m^3 for the bulk material.

This paper presents the study of a new prototype, developed to characterize open-system at a larger scale.

Materials and method

Production of the cementitious monolith

The material considered is ettringite, based on CSA cement (Vicat, Alpenat R²). The material was mixed with water, and a foaming agent (hydrogen peroxide, J.T. Baker®). A monolith of 0.047 m^3 was obtained, which was assumed to contain about 68% of ettringite [5]. A resin was applied on the edges for sealing and forcing the heat transport fluid to cross the material. Due to scale-up from 0.005 m^3 samples, the porosity was decreased to 53%, for a density of 0.869 and a compressive strength of about 3.5 MPa .

Development of a prototype

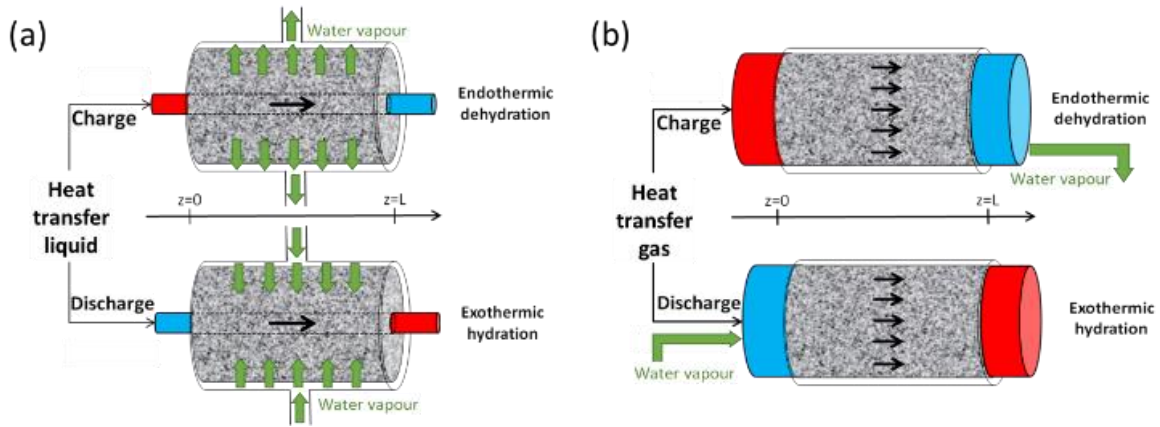


Figure 2. (a) closed configuration and (b) open configuration.

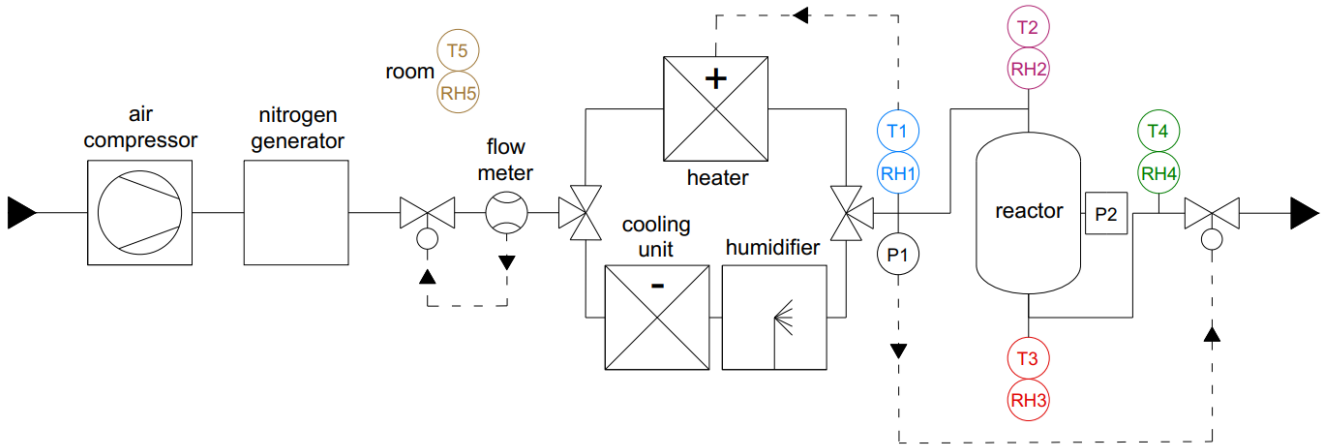


Figure 1. Schematic description of the different components of the prototype. The dashed path with arrows corresponds to the retroaction of the measurement on flow, pressure, or heating, of nitrogen. The colors of the sensors correspond to their curves in the following figures.

A fully new prototype was used for this characterization, presented in Figure 2. The cementitious monolith was placed in the reactor, and different elements were placed before for heat transfer gas conditioning. A dinitrogen flow was considered instead of air to avoid carbonation of ettringite which would lead to a decrease of the storage capacity of the material. Once produced, a 3-way valve was used to conduct the gas either throughout “heater” or “cooler+humidifier” unit. On one side, the heater was used to increase the temperature of the gas, which would dehydrate the reactive material. On the other side, the humidifier allows for water vapor mixing with the heat transport fluid. Along the path, several sensors were positioned for measuring and controlling by PID the parameter of the heat transport fluid. A flowmeter (Azbil, MCF0150) and a manometer, named P1 on Figure 2 (S+S Regeltechnik, SHD-SD I-10), each connected to a hydraulic valve to control flow and pressure. To evaluate the quantity of energy stored, five temperature/relative humidity (RH)

sensors (Galltec Mela, SZKA.0H model) were positioned before and after the reactor, as seen in Figure 3.

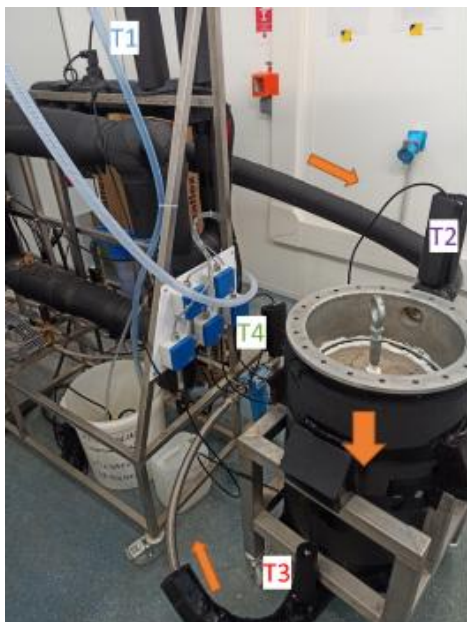


Figure 3. Photo with the distribution of the Pt100/humidity sensors (T1, T2, T3, and T4). The arrows represent the direction of the gas flow. The font colors correspond to the color of the curves in the following figures

Results and Discussions

Temperature and relative humidity calibration

Before the experiments, the calibration of the temperature and humidity sensors was performed. For the calibration in temperature, the probes were immersed in a thermostatic bath filled with water. A nitrile glove was used to avoid penetration of liquid water in the probe, as shown in Figure 4 (a). The probes were tested with 4 temperatures of 30; 45; 60 and 75 °C and left immersed for ten minutes for each temperature. In parallel, the calibration in relative humidity was carried out by immersing the probes in an insulated volume containing air saturated by solutions of salts (Figure 4 (b)). The 3 solutions of salt considered were NaOH, MgCl₂ and NaCl, producing a relative humidity of 9; 33 and 75%.

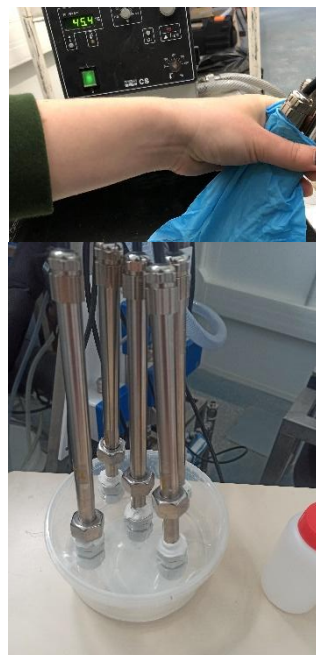


Figure 4. Calibration in (a) temperature and (b) humidity of the sensors

For temperatures, a standard deviation of ± 0.15 K from the set point was found, and for humidity, the deviation was about 0.5%RH, these data were consistent with the datasheet.

Charge curve

The experiment of thermochemical charge and discharge was then carried out by respectively heating and hydrating a cementitious monolith. This experiment was performed by fixing a nitrogen flow of 0.5 bars and 12 Nm³/h (flow rate given for standard conditions). The evolution of the temperatures for the heating curve is presented in Figure 5. A temperature of 60 °C is immediately reached before the material, while a temperature of 50 °C was found after the material, due to the thermal inertia of cement. After stabilization, the remained temperature gap between inlet (T2 = 63 °C) and outlet (T3 = 52 °C) may be explained by heat loss.

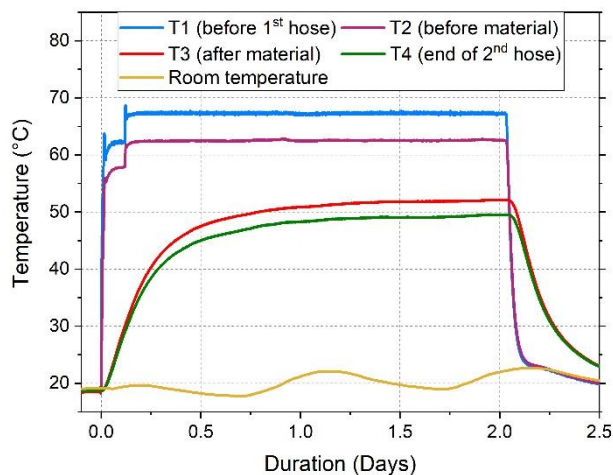


Figure 5. The temperature evolution during heating (storage) of the cementitious material. The position of the probe can be seen in Figure 3 and Figure 4

Cooling to ambient temperature

After two days at a setpoint of 70 °C, the sensible heat stored is released by stopping the heater. In order to determine the quantity of heat released, heat capacity measurements were performed using DSC (Netzsch, STA 449 F3 Jupiter). It was found a heat capacity of about 850 J/kg/K. With a weight of 36 kg, the cooling of the monolith to ambient temperature released about 2.2 MJ/m³ (0.61 kWh/m³) considering a decrease in temperature from 55 to 20 °C.

Discharge curve

The release of heat is initiated by adding water vapour to the heat transport fluid. In Figure 6 is presented the evolution of the temperature difference between the inlet and the outlet of the reactor, during the heat release step. A difference of +7 °C is found a few hours after the release of energy. The heat extraction is facilitated by forced convection using a heat transport gas passing through the material. After one day, a stabilization of this difference is found around 1 °C.

By integrating the energy released from the monolith (36 kg; 0.047 m³) over time, about 1.83 MJ (0.51 kWh) can be released by physical and chemical sorption from the material. This corresponds to 43 MJ/m³ (12 kWh/m³), a thermochemical energy storage of about 20 times more than the sensible energy storage capacity.

To reach the theoretical value of energy release, several technological improvements of the prototype and the material are expected. This could involve an increase in the permeability of the material, relative

humidity in the heat transport gas during discharge, or thermal insulation.

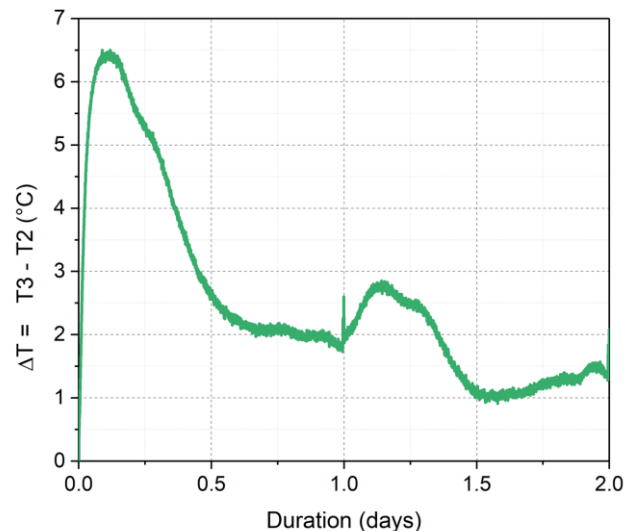
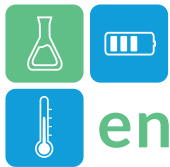


Figure 6. Evolution of the temperature difference $\Delta T = T3$ (reactor outlet) - $T2$ (reactor inlet)

Conclusions

This repeatable reaction of hydration from meta ettringite to ettringite shows promising results for thermochemical energy storage at large scale, at a temperature adapted to residential and industrial applications. The capability of energy release from a large-scale material has been demonstrated for an innovative prototype. This prototype involves the use of heat transport fluid for the mass transfer of water vapor, also called an open-system, resulting in a release of 43 MJ/m³.

The cementitious material is also cheap, easy to produce, and presents a mechanical resistance of 3.5 MPa. In addition to a self-supporting material, its applications scope is larger as the material can be used as large-scale storage tank. Able to store energy without heat loss when it is insulated from water vapor, this material can be easily used for thermal energy transport to another location.

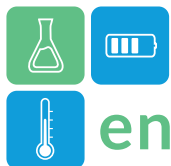


Acknowledgment

This work is financially supported by the Occitanie Region (France) in the framework of the PROTEuS (PROTOTYPE Energy Storage) project, Programme opérationnel FEDER-FSE Midi-Pyrénées et Garonne 2014-2020. The authors also thank Toulouse Tech Transfer for their financial support.

References

- [1] L. J. Struble and P. W. Brown, ‘Heats of dehydration and specific heats of compounds found in concrete and their potential for thermal energy storage’, *Solar Energy Materials*, vol. 14, no. 1, pp. 1–12, Aug. 1986, doi: 10.1016/0165-1633(86)90008-0.
- [2] Q. Zhou and F. P. Glasser, ‘Thermal Stability and Decomposition Mechanisms of Ettringite at’, *Cement Concrete Res.*, vol. 31, pp. 1333–1339, 2001, doi: 10.1016/S0008-8846(01)00558-0.
- [3] J. Kaufmann and F. Winnefeld, ‘Seasonal heat storage in calcium sulfoaluminate based hardened cement pastes – experiences with different prototypes’, *Journal of Energy Storage*, vol. 25, p. 100850, Oct. 2019, doi: 10.1016/j.est.2019.100850.
- [4] K. Ndiaye, S. Ginestet, and M. Cyr, ‘Experimental evaluation of two low temperature energy storage prototypes based on innovative cementitious material’, *Applied Energy*, vol. 217, pp. 47–55, May 2018, doi: 10.1016/j.apenergy.2018.02.136.
- [5] K. Ndiaye, M. Cyr, and S. Ginestet, ‘Development of a cementitious material for thermal energy storage at low temperature’, *Construction and Building Materials*, vol. 242, p. 118130, May 2020, doi: 10.1016/j.conbuildmat.2020.118130.



Thermochemical energy storage properties of $\text{Ca}_2\text{AlMnO}_{5+\delta}$

Keita Tanahashi^{1,2*}, Yu Matsuba¹, Melbert Jeem², and Takahiro Nomura²

1 Graduate School of Engineering, Hokkaido University, Kita 13 Nishi 8, Kita-ku, Sapporo, 060-8628, Japan

2 Faculty of Engineering, Hokkaido University, Kita 13 Nishi 8, Kita-ku, Sapporo, 060-8628, Japan

*Corresponding author e-mail: k.tanahashi@eng.hokudai.ac.jp

Abstract

Thermochemical energy storage, employing redox reactions, has garnered attention as a heat storage technology for application in concentrating solar power plants. Perovskite oxides, identified as among the most promising candidate materials, exhibit advantages in terms of cost and the reversibility of the reaction. However, achieving a low oxygen partial pressure is essential to enhance the reaction yield, consequently leading to an increase in the overall system cost. In this study, we synthesized $\text{Ca}_2\text{AlMnO}_{5+\delta}$ and its Fe-doped or Y-doped compounds, investigating their redox reactions. All compounds demonstrated significant redox reactivity in response to temperature variations alone. In addition, elemental doping allowed the reaction temperature to be tuned, increasing the choice of optimal materials for each storage system.

Keywords: Thermochemical energy storage, Redox, Oxygen storage materials, Brownmillerite

Introduction

Concentrating solar power (CSP) plants, which combine thermal energy storage to utilize intermittent and non-dispatchable sunlight, are expected to be widely used from the perspective of energy supply continuity. Thermal energy storage (TES) can be divided into sensible heat storage (SHS), latent heat storage (LHS), and thermochemical energy storage (TCES). TCES technology, which can store and release thermal energy by reversible chemical reactions, has prominent advantages such as high thermal energy storage capacity, large working temperature range, long-term storage period, and long transport possibilities (Carrillo and *al.*, 2019). To date, various TCES systems have been studied, including hydration/dehydration systems (e.g., $\text{CaO}/\text{Ca}(\text{OH})_2$ and $\text{MgO}/\text{Mg}(\text{OH})_2$), carbonation/decarboxylation systems (e.g. CaO/CaCO_3 , SrO/SrCO_3), and redox systems (e.g., $\text{Co}_3\text{O}_4/\text{CoO}$ and $\text{Mn}_2\text{O}_3/\text{Mn}_3\text{O}_4$) (Wu and *al.*, 2023). From a cost perspective, redox systems that utilize air as a reactant are attracting increasing attention because they do not require a gas storage management system (Imponenti and *al.*, 2017).

Early material research on redox systems was conducted on simple transition metal oxides, such as $\text{Co}_3\text{O}_4/\text{CoO}$ and $\text{Mn}_2\text{O}_3/\text{Mn}_3\text{O}_4$, and their mixtures. However, their use is limited by their high cost and low cycling stability (Carrillo and *al.*, 2014). In recent years,

perovskite oxides represented by the chemical formula $\text{ABO}_{3-\delta}$, whose δ value changes depending on temperature and oxygen partial pressure, have been widely studied (Imponenti and *al.*, 2017; Mastronardo and *al.*, 2020; Chen and *al.*, 2021). These compounds have the potential to undergo reversible redox reactions with elemental compositions abundant on Earth. Unlike simple transition metal oxides, perovskites have the characteristic that δ changes gradually over a wide temperature range. Although this characteristic allows the effect of chemical heat storage to be obtained over a wide temperature range, if the temperature range used is limited to a narrow range, the change in δ may be small and the amount of chemical heat storage may not be able to be used sufficiently. Additionally, many studies of $\text{ABO}_{3-\delta}$ perovskite oxides utilize low oxygen partial pressure gases to obtain larger δ changes. This requires a closed environment, such as a TCES system that uses hydrates or carbonates, which leads to higher costs.

We propose to use $\text{Ca}_2\text{AlMnO}_{5+\delta}$ (CAMO) as a heat storage material for TCES systems. Among perovskites, this compound has a brownmillerite structure, in which some of the BO_6 octahedra are orderly replaced with layers composed of BO_4 tetrahedral chains (Saito and *al.*, 2017). In the CAMO, the B site is occupied by Mn and Al atoms that are alternately stacked in layers. The oxygen release phase ($\delta = 0$) consists of MnO_6

octahedral layer and AlO_4 tetrahedral layer. In the oxygen storage phase ($\delta = 0.5$), every other AlO_4 tetrahedral layer in the oxygen release phase takes in oxygen and changes to an AlO_6 octahedral layer. CAMO has attracted attention as a material for oxygen production because it has an inexpensive elemental composition and can store or release up to 3.3wt% oxygen (Motohashi and *al.*, 2013). However, no studies have been conducted on its use as a heat storage material.

In this study, we investigated the redox reactions of CAMO and CAMO doped with Fe or Y. Additionally, the advantages and disadvantages compared with those of other metal oxides are discussed.

Methodology

We synthesized $\text{Ca}_2\text{AlMnO}_{5+\delta}$ (CAMO), $\text{Ca}_2\text{AlMn}_{0.9}\text{Fe}_{0.1}\text{O}_{5+\delta}$ (CAMFO-Fe0.1), and $\text{Ca}_{1.9}\text{Y}_{0.1}\text{AlMnO}_{5+\delta}$ (CYAMO-Y0.1) using solution combustion synthesis (SCS) and heat treatment (Tanahashi and *al.*, 2021). Using $\text{Ca}(\text{NO}_3)_2 \cdot 4\text{H}_2\text{O}$ (99.9%), $\text{Al}(\text{NO}_3)_3 \cdot 9\text{H}_2\text{O}$ (98.0%), 50wt% aqueous $\text{Mn}(\text{NO}_3)_2$, $\text{Fe}(\text{NO}_3)_3 \cdot 9\text{H}_2\text{O}$ (99.9%), $\text{Y}(\text{NO}_3)_3 \cdot 6\text{H}_2\text{O}$ (99.9%), and glycine ($\text{C}_2\text{H}_5\text{O}_2\text{N}$) (99.0%) as starting materials, they were mixed with distilled water at the stoichiometric ratio of each compound. The samples were then heated to 400 °C to obtain a precursor powder. The precursor powder was heated in air for 12 h at 1250 °C followed by 12 h at 1250 °C in Ar (the samples as prepared). Furthermore, oxidized samples were obtained by heating a part of the samples as prepared at 450 °C for 3 h in O_2 .

Powder X-ray diffraction (XRD, Rigaku MiniFlex, Cu $\text{K}\alpha$) measurements were used for crystal phase identification and structural analysis. Thermogravimetry curves were measured in air or oxygen at heating and cooling rates of ± 2 °C/min using a thermogravimetric (TG) analyzer (Mettler Toledo TG-DSC3). Pressure-composition temperature (PCT) characteristics were obtained using Sieberts' method (Tanahashi and *al.*, 2021). The enthalpy changes ΔH for each reaction were calculated from the van't Hoff plot based on the PCT curves.

Results and Discussion

Figure 1 shows the XRD patterns of CAMO, CAMFO-Fe0.1, and CYAMO-Y0.1 (a) as-prepared and (b) oxidized. The insets in Figures (a) and (b) show schematic diagrams of the crystal structures of the CAMO oxygen release and storage phases, respectively. In Figure 1(a), all the as-prepared samples show almost the same diffraction pattern with no impurity peaks, which corresponds to the reference

peaks of the oxygen release phase of CAMO. The same was true for the oxidized samples in Figure 1(b), which matched the reference peak of the CAMO oxygen storage phase. Therefore, we successfully doped the CAMO with the target elements. In Figure 1(b), a (020) peak, indicated by an arrow, appears in all the oxidized samples. This peak indicates that oxygen was stored in the AlO_4 tetrahedral layers, and ordered AlO_6 octahedral layers were formed, as shown in the inset of Figure 1(b). The intensity of the (020) peak of the sample CAMFO-Fe0.1 oxidized was weaker than that of the other samples. Carvalho and *al.* reported that by doping CAMO with Fe, the Mn and Al layers are partially disturbed, and these atoms are mixed in each layer (M. D. Carvalho and *al.*, 2008). Therefore, it is believed that the orderliness of the AlO_6 octahedral layer in the oxygen storage phase of CAMFO-Fe0.1, decreased.

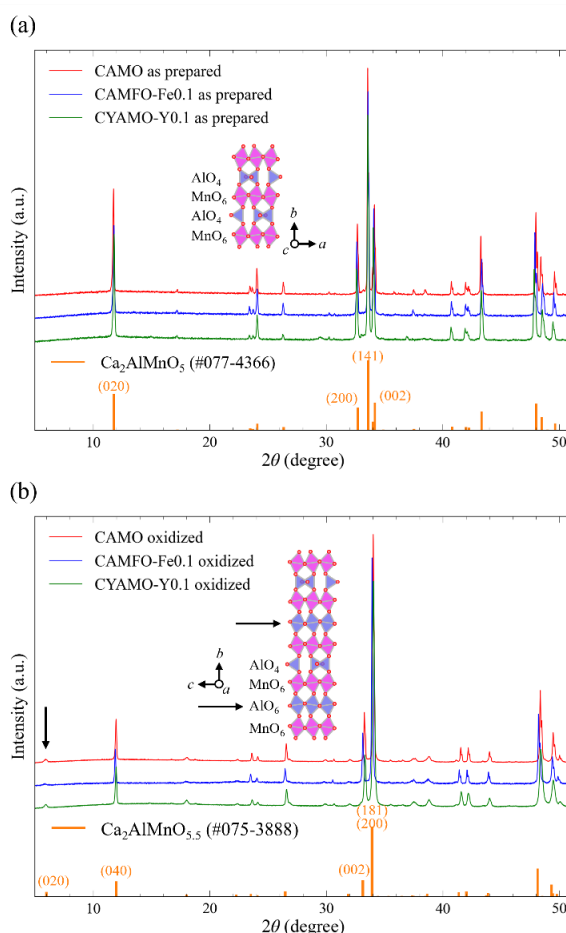


Figure 1: XRD patterns of CAMO, CAMFO-Fe0.1, and CYAMO-Y0.1 (a) as prepared and (b) oxidized. The insets of figures (a) and (b) are schematic diagrams of the crystal structures of the CAMO oxygen release phase and storage phase, respectively.

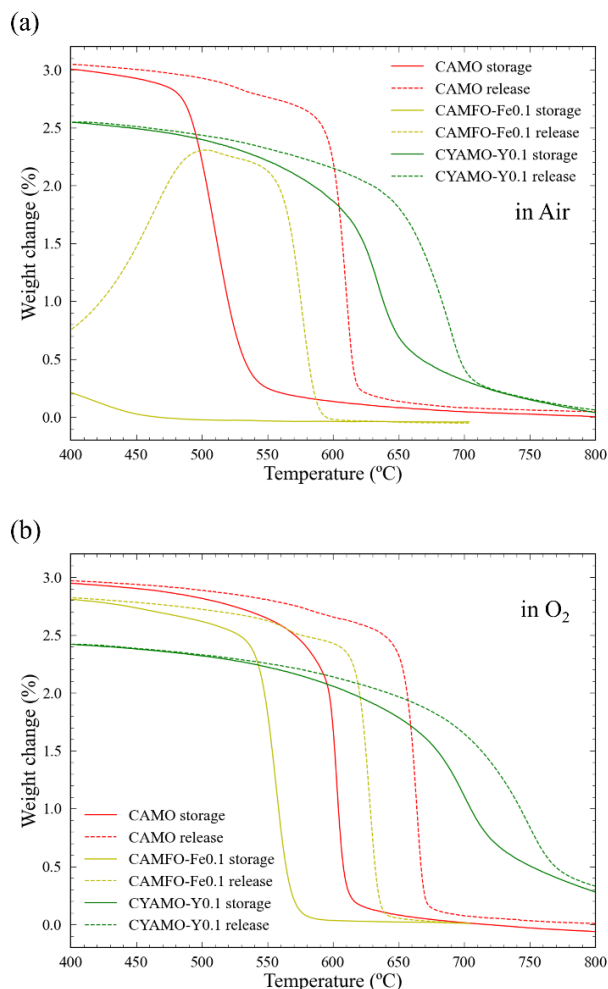
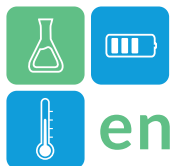


Figure 2: Thermogravimetry curves of CAMO, CAMFO-Fe0.1, and CYAMO-Y0.1 (a) in air and (b) in O₂.

Figure 2 shows the thermogravimetric curves of CAMO, CAMFO-Fe0.1, and CYAMO-Y0.1 (a) in air and (b) in O₂. In both air and O₂, the CAMO undergoes rapid reduction or oxidation reactions at certain temperatures. Furthermore, in both atmospheres, CAMO achieved a weight change rate of 3% owing to the temperature changes alone. This drastic reactivity and the amount of oxygen storage/release due to temperature changes that are independent of oxygen partial pressure clearly differentiate it from ABO_{3-δ} perovskites. This type of redox material is most effective in TCES when used in a temperature range slightly lower than the oxidation temperature and slightly higher than the reduction temperature. However, the relatively large hysteresis behavior causes the temperature of the released heat to be lower than that of the stored heat, resulting in energy loss.

Elemental doping changes the equilibrium temperature of the reaction. Fe-doping decreased the redox reaction temperature, whereas Y-doping increased it. This expands the usable temperature range of CAMO

systems. With CAMFO-Fe0.1 in air, sufficient oxidation did not occur during cooling. This was because a sufficient reaction rate could not be obtained owing to the decrease in the reaction temperature. Instead, additional oxidation reactions occur as the temperature increases. Comparing the curves of each sample in air and O₂, the redox reaction temperatures of all the samples increased in O₂.

Table 1: ΔH of the redox reactions for each sample

	ΔH_{ox} (kJ/mol-O ₂)	ΔH_{red} (kJ/mol-O ₂)
CAMO	-156.4	191.2
CAMFO-Fe0.1	-135.5	213.3
CYAMO-Y0.1	-188.3	199.8

Table 1 shows the enthalpy change (ΔH) of the redox reactions for CAMO, CAMFO-Fe0.1, and CYAMO-Y0.1. The absolute values of ΔH_{ox} in the oxidation reactions were smaller than those of ΔH_{red} in the reduction reactions. This difference appears to be related to the hysteresis. While the ΔH of SrFeO_{3-δ}, a well-studied perovskite system, is less than 100 kJ/mol-O₂ (Bulfin and *al.*, 2019), the CAMO system had a large ΔH , close to 200 kJ/mol-O₂.

Conclusions

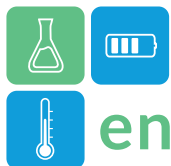
In this study, we synthesized CAMO and its Fe- and Y-doped counterparts and investigated their redox reactions. Unlike other perovskite oxides, CAMO and doped CAMO exhibit drastic redox reactivity with temperature changes alone. Furthermore, the reaction temperature could be controlled by varying the oxygen partial pressure and chemical doping. We plan to discuss the TCES performances on an event day.

Acknowledgment

The authors greatly appreciate the financial support from the JSPS KAKENHI, Grant Numbers 22H00306 and 23KJ003303.

References

- Bulfin, B. and *al.* (2019) Air separation and selective oxygen pumping via temperature and pressure swing oxygen adsorption using a redox cycle of SrFeO₃ perovskite. *Chemical Engineering Science*, doi.org/10.1016/j.ces.2019.03.057.
- Carrillo, A. J. and *al.* (2014) Thermochemical energy storage at high temperature via redox cycles of Mn and Co oxides: Pure oxides versus mixed ones. *Solar Energy Materials and Solar Cells*, doi.org/10.1016/j.solmat.2013.12.018.
- Carrillo, A. J. and *al.* (2019) Solar Energy on Demand: A Review on High Temperature Thermochemical Heat Storage Systems and Materials. *Chemical Reviews*, doi.org/10.1021/acs.chemrev.8b00315.



- Chen, X. and *al.* (2021) Investigation of Sr-based perovskites for redox-type thermochemical energy storage media at medium-high temperature. *Journal of Energy Storage*, doi.org/10.1016/j.est.2021.102501.
- Imponenti, L. and *al.* (2017) Thermochemical energy storage in strontium-doped calcium manganites for concentrating solar power applications. *Solar Energy*, doi.org/10.1016/j.solener.2017.05.010.
- M. D. Carvalho and *al.* (2008) Structure and magnetic properties of $\text{Ca}_2\text{Fe}_{1-x}\text{Mn}_x\text{AlO}_{5+\delta}$. *Journal of Solid State Chemistry*, doi.org/10.1016/j.jssc.2008.06.008.
- Mastronardo, E. and *al.* (2020) The favourable thermodynamic properties of Fe-doped CaMnO_3 for thermochemical heat storage. *Journal of Materials Chemistry A*, doi.org/10.1039/D0TA02031A.
- Motohashi, T. and *al.* (2013) Oxygen Storage Capability of Brownmillerite-type $\text{Ca}_2\text{AlMnO}_{5+\delta}$ and Its Application to Oxygen Enrichment. *Chemistry of Materials*, doi.org/10.1021/cm303156n.
- Saito, G. and *al.* (2017) Atomic and Local Electronic Structures of $\text{Ca}_2\text{AlMnO}_{5+\delta}$ as an Oxygen Storage Material. *Chemistry of Materials*, doi.org/10.1021/acs.chemmater.6b04099.
- Tanahashi, K. and *al.* (2021) Sr-Doped $\text{Ca}_2\text{AlMnO}_{5+\delta}$ for Energy-Saving Oxygen Separation Process. *ACS Sustainable Chemistry & Engineering*, doi.org/10.1021/acssuschemeng.1c02077.
- Wu, R. and *al.* (2023) Influence of CuO doping on cobalt oxide for thermochemical energy storage. *Solar Energy Materials and Solar Cells*, doi.org/10.1016/j.solmat.2023.112211.



Thermocline thermal storage material based on reclaimed and low-cost materials.

Charles Devise^{1*}, Yasmine Lalau¹, Nicolas Tessier-Doyen², Jean-Régis Martinent³, Guilhem Dejean³,
Doan Pham Minh¹

1 Université de Toulouse, IMT Mines Albi, CNRS UMR 5302, Centre RAPSODEE, Campus Jarlard,
81013 Albi CT CEDEX 09, France

2 University of Limoges, Institute of Research for Ceramics (IRCer), UMR 7315, European Ceramic
Center, 12 rue Atlantis, 87068, Limoges, France

3 ECO-TECH CERAM, Rue Edouard Belin, Rivesaltes, 66600, France

*Corresponding author e-mail: charles.devise@mines-albi.fr

Abstract

In response to the challenge raised by climate change, industries, and various sectors must transform to decarbonize their activities and facilitate the energy transition. To this end, thermal energy storage systems offer promising solutions. This study aims to explore the feasibility and performance of utilizing second-life materials as sensible thermal storage components integrated into high-temperature thermocline technologies, crucial for some industries facing this transition. The investigation ensures these materials possess the requisite energy density, operational stability, and cost-effectiveness. The materials were formulated by shaping reclaimed refractory fillers with low-cost clay-based binding matrices.

enerstock2024.sciencesconf.org.

Keywords: Sensible thermal energy storage, Formulation, Waste refractory ceramic, Thermocline, Design of experiments

Introduction

In 2021, France's industrial sector consumed 311.7 TWh (Sédillot, 2022), ranking third in energy usage, just behind transport and residential sectors. According to the ADEME (French Environment and Energy Management Agency), a third of this energy is lost through heat that could be used for other applications (La chaleur fatale, n.d.). However, this energy could be valorised if it were collected and stored (Récupération de chaleur fatale Etats des réalisations et évolution du gisement à fin 2020, 2022), reducing by the way raw energy consumption and greenhouse gas emissions.

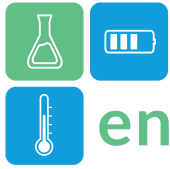
Such valorisation exists and the company Eco-Tech Ceram provides such a system with their Eco-Stock®, a sensible thermal energy storage system (STESS) (Lalau et al., 2022). Previous work showed that this system environmental performances could be improved by using Sensible Thermal Energy Storage Material (STESM) made from wastes or secondary raw materials (Jacob et al., 2022). Furthermore, a local and abundant supply is a strategic asset.

Our work focuses on the development of a new STESM composed of local, abundant, low-impact and low-cost materials. The STESM formulation is based on a clay matrix including second-life refractory ceramics. Their elaboration is optimized by a design of experiments (DOE) planning to meet the IEA recommendation on energetic density that should be above $2.6 \text{ MJ.m}^{-3}.\text{K}^{-1}$ (Meffre, 2013).

Methodology

Upon reception, the different clays and minerals fillers were prepared by passing through a jaw crusher (except the SD clay which was already fine) and reduced to centimetric dimensions.

The prepared materials were then dried at 105°C for a minimum of 24 hours before batch crushing in a mill grinder at a constant filling ratio. Post grind milling, the products passed through sieves; mineral fillers with a sieve diameter above $800 \mu\text{m}$ and clay above $200 \mu\text{m}$ remained in the mill, while the complementary fraction was added to maintain a constant grinding rate. Refractory fillers were



categorized as fine (passing through a 200 μm sieve), intermediate (passing through a 500 μm sieve), and coarse (below 800 μm).

Following material preparation, powder mixtures were prepared according our L₉ DOE, (detailed in Table 1). These mixtures, composed of fine clay and fillers of varying size distribution, were shaped using a uniaxial press at 48.8 MPa.

The resulting samples were fired in an electric kiln, with a temperature increase rate of 5°C/min and a step stage of 1 hour.

Table 1: Design of experiment

Sample	Clay	Particle size fraction of fillers	Mass ratio of filler / clay	Sintering temperature
T01	A	Fine	30/70	1050 °C
T02	B	Fine	70/30	1125 °C
T03	C	Fine	50/50	1200 °C
T04	A	Intermediate	50/50	1125 °C
T05	B	Intermediate	30/70	1200 °C
T06	C	Intermediate	70/30	1050 °C
T07	A	Coarse	70/30	1200 °C
T08	B	Coarse	50/50	1050 °C
T09	C	Coarse	30/70	1125 °C

Finally, the fired samples and powders underwent analysis. Powders were subjected to granulometry using laser diffraction analysis, X-ray Fluorescence (XRF) employing an Epsilon3-XL from Malvern Panalytical, and pycnometer, while sample density was measured following ISO 5017 standards.

The heat capacity of the samples was assessed through a mixture law (1) based on elements analyzed with XRF and the Shomate equation (2) using the NIST dataset (Linstrom, 1997). Differential scanning calorimetry (DSC) was conducted to confirm the heat capacity evaluation using a Labsys Evo.

$$C_{p_{sample}} = \sum_i w_i * M_i * C_{p_i} \quad \#(1)$$

$$C_{p_i} = A + B * t + C * t^2 + D * t^3 + \frac{E}{t^2} \quad \#(2)$$

$C_{p_{sample}}$: heat capacity of the sample ($\text{J.g}^{-1}.\text{K}^{-1}$)

C_{p_i} : heat capacity of i-element ($\text{J.mol}^{-1}.\text{K}^{-1}$)

w_i : weight percent of i-element

t : temperature (K/1000)

The energetic density U were defined as the products of the bulk density with the heat capacity of the sample

$$U = \rho_{bulk} * C_{p_{sample}} \quad \#(3)$$

U : energetic density of the sample (J.cm^{-3}).

Results and Discussion

XRF (Table 2) reveal the elemental composition of the raw material after calcination. The heat capacity of the sample is calculated for each sample as function of the temperature with equations (1) and (2) and compared to DSC measures (Table 3). The indices "e" and "m" in the data series T01e to T09e and T01m to T09m signify estimated and measured values, respectively.

Table 2: XRF Element analysis of clay and filler

Element	Clay 1	Clay 2	Clay 3	Filler
Na ₂ O	0	0	0	2.9
MgO	0	0.1	0.7	0
Al ₂ O ₃	23.1	24.1	18.5	94.3
SiO ₂	64.3	63.5	66.6	1.7
K ₂ O	1.4	3.6	4.1	0.4
CaO	0	0.3	0.3	0.2
TiO ₂	0.9	0.7	1.3	0
MnO ₂	0	0.1	0	0
Fe ₂ O ₃	9.8	7.2	8.1	0.9
I	0.5	0.4	0.4	0.3
ZrO ₂	0	0	0	0.2

The Table 3 illustrates the C_p increase with the temperature and shows a slightly superior value for the DSC measures (11 to 16% at high temperature). A slight drop is observed on estimated data near 600°C at 573°C due to the polymorphic transformation of α -quartz to β -quartz. This transformation does not appear on our measures but the heat capacity in this range of temperature varies little.

Table 3: Heat capacity of samples estimated and measured

Sample	C_p ($\text{J.g}^{-1}.\text{K}^{-1}$)		
	100 °C	400 °C	600 °C
T01e	0.87	1.11	1.15
T01m	1.06	1.30	1.36
T02e	0.90	1.13	1.18
T02m	1.17	1.32	1.34
T03e	0.89	1.12	1.17
T03m	1.12	1.30	1.34
T04e	0.89	1.12	1.17
T04m	1.08	1.30	1.35
T05e	0.88	1.11	1.15
T05m	1.20	1.35	1.36
T06e	0.90	1.13	1.18
T06m	1.13	1.30	1.34
T07e	0.90	1.13	1.18
T07m	1.11	1.29	1.34
T08e	0.89	1.12	1.17
T08m	1.18	1.33	1.35
T09e	0.88	1.12	1.15
T09m	1.10	1.31	1.35



Bulk and absolute densities of our samples were measured. Values varying from 2.10 ± 0.09 to $2.56 \pm 0.09 \text{ g.cm}^{-3}$ for the bulk density and from 2.85 to 3.27 g.cm^{-3} for the absolute density.

Further analysis, employing our L_9 design structure, reveals the average effects attributable to the different parameters studied (Figure 1). Clay type plays a crucial role, with the second and third clays demonstrating superior properties compared to the first. An X-ray Diffraction (XRD) analysis on the clays indicates higher content in illite and halloysite in clay 1 and 2. Additionally, unlike clay 2 and 3, clay 1 lacks a muscovite phase. These elements are believed to facilitate the densification of samples during sintering. Samples using an intermediate size fraction of mineral fillers and a higher proportion of filler exhibit increased density, facilitating shaping and densification. However, excessive filler amounts negatively impact shaping quality, hindering clay's binding role and resulting in reduced density and mechanical strength. The sintering temperature emerges as a critical parameter impacting density, revealing that a temperature of at least 1200°C is optimal for firing. Investigations into higher sintering temperatures demonstrated a decrease in bulk density after 1225°C due to increased closed porosity.

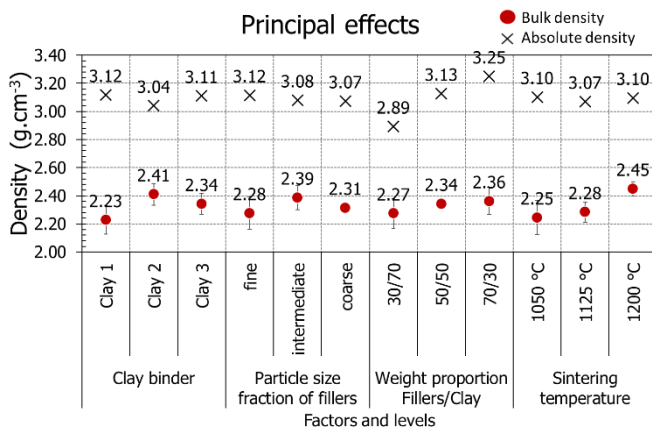


Figure 1 : Principal effect of the DOE parameters on density

Given the proximity of the sample's heat capacity, principal effects behave in the same way for the energetic density (3) (Figure 2) than for the bulk density. (Figure 1). The energetic density of all our samples (Table 4), with the exception of T01, surpasses the IEA recommendation of $2.6 \text{ J.cm}^{-3}.\text{K}^{-1}$ for temperatures above 200°C , corresponding to the operating zone of STESS.

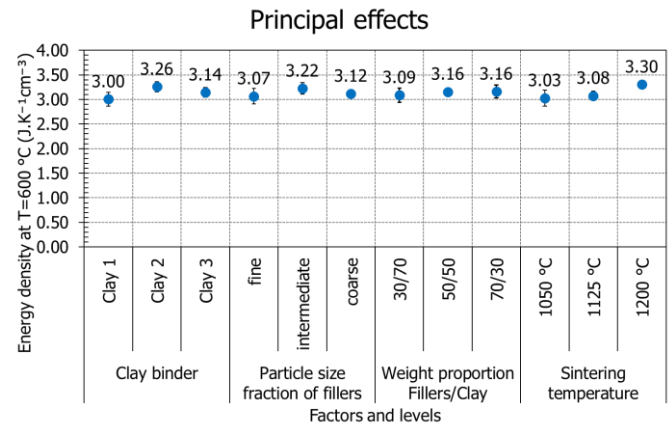


Figure 2: Principal effect of DOE parameters on energetic density

Table 4: Samples energetic density ($\pm 0.12 \text{ J.cm}^{-3}.\text{K}^{-1}$)

Sample	U (J.cm ⁻³ .K ⁻¹)		
	100 °C	400 °C	600 °C
T01m	2.16	2.66	2.78
T02m	2.75	3.10	3.15
T03m	2.71	3.17	3.26
T04m	2.45	2.94	3.05
T05m	3.05	3.44	3.47
T06m	2.66	3.06	3.15
T07m	2.63	3.07	3.18
T08m	2.76	3.11	3.15
T09m	2.47	2.92	3.02

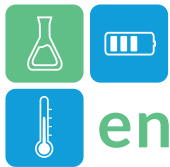
Conclusions

Our initial observations of clay and reclaimed refractory fillers reveal promising outcomes, indicating their suitability for integration into thermocline systems like the Eco-Stock®. The energy density exhibited by these materials aligns with the recommendations set forth by the IEA, positioning them as strong candidates for such applications while offering a way of recovering mineral waste.

Ongoing investigations using mixtures of clay and reclaimed refractory minerals are underway to identify an optimal composition that not only maintains a high energy density but also ensures a prolonged lifespan. This avenue of research seeks to enhance the performance and longevity of these materials, contributing to their efficacy in sustainable and efficient energy storage solutions.

Acknowledgement

This document has been prepared as part of the CHATO thesis programme supported by the Occitanie



region (France), IMT Mines Albi (France) and Eco-Tech Ceram (France).

References

Jacob R, Sergeev D, Müller M. Valorisation of waste materials for high temperature thermal storage: a review. *Journal of Energy Storage* 2022;47:103645. <https://doi.org/10.1016/j.est.2021.103645>.

La chaleur fatale. 2017th ed. L'Agence de l'Environnement et de la Maitrise de l'Énergie; n.d.

Lalau Y, Al Asmi I, Olives R, Dejean G, Meffre A, Py X. Energy analysis and life cycle assessment of a thermal energy storage unit involving conventional or recycled storage materials and devoted to

industrial waste heat valorisation. *Journal of Cleaner Production* 2022;330. <https://doi.org/10.1016/j.jclepro.2021.129950>.

Linstrom P. NIST Chemistry WebBook, NIST Standard Reference Database 69 1997. <https://doi.org/10.18434/T4D303>.

Meffre A. Matériaux de stockage thermique haute température issus de la valorisation de matières premières secondaires inorganiques. 2013.

Récupération de chaleur fatale États des réalisations et évolution du gisement à fin 2020. ADEME; 2022.

Sédillot B. Chiffres clés de l'énergie – Édition 2022 2022.

Thermochemical Energy Storage Unit for H₂ Based Systems

Inga Bürger^{1,*}, Alina Keller¹, Hanna Lösch¹, Marc Linder¹

¹ Institute for Engineering Thermodynamics, German Aerospace Center (DLR), 70569 Stuttgart, Germany

*Corresponding author e-mail: inga.buerger@dlr.de

Abstract

Thermochemical energy systems show high storage density, but also high system complexity due to the required gas management for the underlying gas solid reactions. Metal-hydride based systems can utilize synergies between hydrogen as energy carrier and hydrogen as reaction partner. In this case, the effort for gas management is clearly reduced as in this infrastructure the gaseous reaction partner is available at different pressure levels, and thus heat or cold can be provided in a flexible manner. Previously, a metal hydride based thermochemical unit has been developed, built using additive manufacturing, and demonstrated in TRL5. The first application of the unit has been as a preheating device releasing thermal energy at temperatures down to -20 °C. The current publication presents new results for the instantaneous release of heat at temperatures down to -40 °C. There is no significant reduction in performance and specific thermal power of 3 kW/kg_{MH} can be reached. Furthermore, the integration of the unit as bidirectional heating and cooling device for temperature control is introduced.

Keywords: Thermochemical Energy Storage, Metal Hydride, Thermal management

Introduction

Among different types of thermal energy storages, thermochemical storage based on reversible gas solid reactions show the advantage of high storage capacity. However, few systems are ready for applications, as the required gas management is usually quite complex and increases system weight.

In case of a thermochemical reaction based on metal hydrides, the system complexity can be significantly reduced, if the storage unit is integrated into the existing infrastructure of e.g. a fuel cell. Such an infrastructure not only provides and takes-up hydrogen, but it also offers the hydrogen supply and removal at different pressure levels, which is an additional feature (Kölbig, 2022).

Figure 1, shows an example of such a metal hydride based Thermochemical Unit (TCU) integrated as “open” system into the H₂ infrastructure of a fuel cell.

When thermal energy is required for the exothermal absorption reaction, H₂ can be provided to the TCU at high pressure. Whenever thermal energy needs to be removed, the system pressure is reduced and H₂ is released back to the fuel cell by the endothermal desorption reaction. In this manner, the TCU operates as thermal buffer and does not consume any hydrogen.

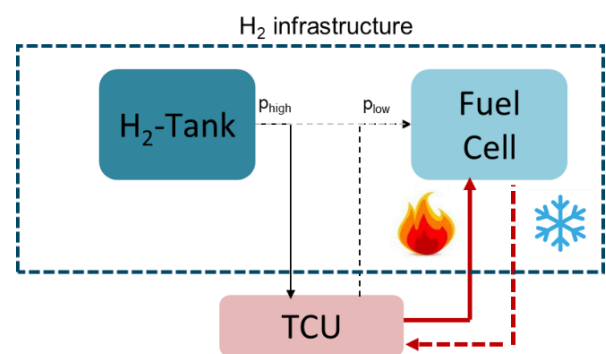


Figure 1: Integration of Thermochemical Unit (TCU) into H₂ infrastructure

One application of such a system, which has been previously studied, is the application as preheating module to support frost start of a fuel cell (Bürger, 2021). In this case, thermal energy is stored in the TCU at temperatures down to -20 °C. Whenever the fuel cell needs to be started, H₂ is provided at e.g. 5 bar, to the TCU. As a result, thermal energy is released and transferred to the fuel cell until it reaches +5 °C and can operate in a self-sufficient manner. As soon as the operation temperature of ~60 °C has been reached, the H₂ is released to the fuel cell again at few mbar above ambient and thereby the TCU is regenerated.

As frost start events at $-20\text{ }^{\circ}\text{C}$ can also be addressed by e.g., electrical heaters, this contribution will present results of the system, for temperatures as cold as $-40\text{ }^{\circ}\text{C}$. In this temperature range, batteries are not able to provide sufficient energy to an electric heater, thus the TCU based on metal hydrides can be a game changer for these events. However, as the metal hydride reaction system relies on a chemical reaction following Arrhenius Law, it must be proven that it is possible to provide thermal energy from a chemical reaction with technically relevant thermal power at these low temperatures.

Methodology

For the experiments presented in this contribution, a previously developed and published reactor design has been used. It has been manufactured by additive manufacturing using AlSi10 as base material and has proven the ability to transfer thermal powers of up to $3\text{ kW/kg}_{\text{MH}}$ with a ratio of reactor mass to metal hydride mass of less than one (Bürger, 2021). The reactor has been filled with 306 g of LaNi_5 material and has been activated at 8 bar H_2 .

The reactor has been integrated into a testing setup, where H_2 can be provided and removed at constant flow rates or constant pressures. Furthermore, the thermal energy, which is provided or released to the heat transfer fluid (a $\sim 50:50$ mixture of water and glycol), can be determined using a mass flow meter and thermocouples at the inlet and outlet of the reactor.

Results and Discussion

Figure 2 shows the specific thermal power versus time for the experiments performed between $+10$ and $-40\text{ }^{\circ}\text{C}$ at an H_2 pressure of 8 bar. The reaction was initiated at 10 s and it is obvious that 5 s later, the thermal energy released inside the metal hydride powder, is transferred the heat transfer fluid. Thus, the specific thermal power increases steeply. For all temperatures, the specific thermal power reaches a maximum of about $3.0\text{ kW/kg}_{\text{MH}}$ at $\sim 20\text{ s}$ after the reaction has been initiated. After 2 min, the reaction is completed. Thus, it has been proven that the chemical reaction between hydrogen and metal hydride is in the present setup not limited by temperatures as low as $-40\text{ }^{\circ}\text{C}$. Furthermore, on the right axis of Figure 2, the specific thermal energy is shown. In total, approx. 60 Wh could be stored per kg of MH. As a result, a C_{rate} for the reactor of as high as $\sim 50\text{ 1/h}$ can be calculated.

In the case of preheating, the application focuses on the absorption process, where a large temperature gradient is available.

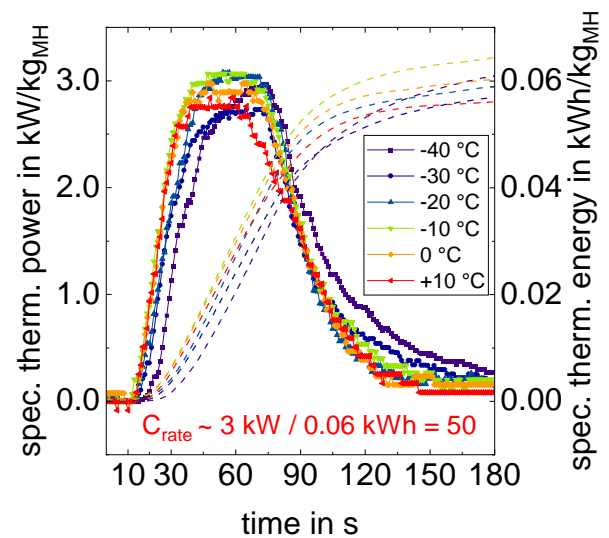


Figure 2: Specific thermal power and specific thermal energy measured in the heat transfer fluid for absorption reactions at -40 to $+10\text{ }^{\circ}\text{C}$ and 8 bar H_2 .

However, it is also possible to consider such an open metal hydride system for bidirectional temperature control. Thus, the reaction is used to release or absorb thermal energy as required and with high dynamics at low temperature differences.

Conclusions

A metal hydride based Thermochemical Unit can be flexibly integrated into a fuel cell infrastructure to provide the required gas management. The system has proven immediate release of thermal energy at temperatures down to $-40\text{ }^{\circ}\text{C}$ at $3\text{ kW/kg}_{\text{MH}}$. Furthermore, the unit can be used for bidirectional heating and cooling to provide active temperature control of e.g. a fuel cell.

Acknowledgment

Parts of this content has been part of FCCP (Fuel Cell Cargo Pedelec) project, which received funding from the interregNorthWestEurope under NWE596 in the program Priority Axis2 Low Carbon, specific objective SO4.

References

- Kölbig, M. et al. (2022) Review on thermal applications for metal hydrides in fuel cell vehicles: Operation modes, recent developments and crucial design aspects, Renewable and Sustainable Energy Reviews 162, doi.org/10.1016/j.rser.2022.112385.
- Bürger, I. et al. (2021) Lightweight reactor design by additive manufacturing for preheating applications using metal hydrides, Int. Journal of Hydrogen Energy, doi.org/10.1016/j.ijhydene.2021.06.091



Understanding and overcoming the challenges for the integration of large-scale Thermal Energy Storage

Alice Tosatto^{1,*}, Fabian Ochs¹, Christoph Muser²

1 Unit of Energy Efficient Building, Universität Innsbruck, Innsbruck, Tyrol, Austria

2 Ingenieurbüro ste.p ZT-GmbH, Vienna, Austria

*alice.tosatto@uibk.ac.at

Abstract

The path to reducing fossil fuels in district heating systems involves increasing the use of renewable energy sources. In this respect, the use of efficient thermal energy storage (TES) is an important solution to enable integration of renewable energies. However, the use of large-scale TES requires a suitable design that takes into account both the operation and the material properties of the storage envelope. This work discusses the challenges and solutions related to the construction and performance of large-scale TES with the aim of achieving economic feasibility considering the specific location and material performance. Different aspects are addressed from component level via the construction level to the environmental level; with a special focus on the thermal insulation.

The task of the TES envelope requires special attention, as it influences both the efficiency of the TES as well as the quality of the environment, in particular the avoidance of excess temperature in the case of groundwater must be taken into account. A good knowledge of the properties of the insulation material under the operational boundary conditions is a key element for the development of design solutions, such as moisture barriers or sinks and convection barriers in order to guarantee the insulation properties over the life-time of the TES.

Keywords: Thermal energy storage, Design and construction, Thermal Insulation, Natural convection

Introduction

District heating (DH) offers the opportunity to effectively exploit renewable and excess heat such as geothermal, industrial waste heat, biomass-based combined heat and power plants. However, the substitution of fossil-based energy sources with typically volatile RE is not a trivial question, due to their low specific energy, fluctuating availability and difficult storability and dispatchability. Large-scale thermal energy storage (TES) systems represent in this perspective a key element to ensure higher robustness in the energy system, allowing short as well as long term storage and later exploitation of energy that would be otherwise lost and enhancing the sector coupling.

The state-of-the-art of large-scale TES systems is represented by tank TES (TTES) and pit TES (PTES). Both solutions see a large number of systems already in operation, confirming the central role of these systems in the decarbonisation of DH networks. Despite the success of this technology, however, it is necessary to overcome major obstacles related to economic feasibility, area and location (often urban), geological and geotechnical characteristics (in the case of underground structures) of the ground, and the ability of the construction materials (liners, insulation, structural materials) to perform optimally.

In this work, the main challenges related to the large-scale TES construction and performance are presented and the solutions for their overcome are suggested. The focus will be mainly on the design and application of the thermal insulation, being one of the most critical and less investigated elements in existing TES systems.

In order to suggest an effective guideline for the construction and optimal design of a TES, it is possible to break down the planning into three main physical levels, which should be considered as mutually interpenetrated and should be approached as such:

- Structural, related to the chosen geometry (pit or tank) and the volume
- Environmental, related to the surrounding environment (i.e. the ground and eventually the groundwater) and to the interactions that can establish with it
- Component, related to the specific design characteristics of the TES envelope, namely material selection but also configuration.

It is important to remark that also operation and interaction with other DH elements (i.e. generation system, users) play a fundamental role in the choice of TES geometry and operation temperature, however, this work focuses on the following phase related to the construction planning and design.

Methods

New structural concepts for large-scale TES

In order to achieve the goal of developing concepts for large, cost-effective heat storage systems, efforts are needed in several areas. Within the *gigaTES* project (*GigaTES*, 2021) developments have been driven forward both in terms of the construction method, i.e. special civil engineering, the components and at the material level. A possible variant of a buried large-scale storage tank with a diaphragm wall, stainless steel gasket, an external insulating bored pile wall and a floating cover is shown in Figure 1. Backfilling the excavated soil to form a dam increases the volume or improves the height/diameter ratio and reduces costs (reduced surface area and depth for the same volume, leading to reduced disposal costs). Depths of around 50 metres can be achieved with diaphragm walls. Up to a diameter of about 50 to 65 m, the diaphragm wall can be designed as a pressure ring.

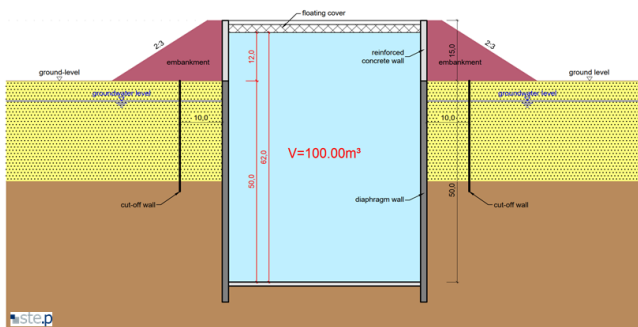


Figure 1 Sketch of the structure of a buried tank TES with diaphragm walls and embankment (Tosatto, Ochs, Dahash and Muser, 2022).

Figure 2 shows a diaphragm wall excavator and a diaphragm wall shaft as it could be used for the construction of underground cylindrical TTES. For larger diameters, anchors are required to hold the diaphragm wall against earth pressure.



Figure 2 Top view of a shaft with diaphragm walls.

Environmental protection

Storing water at temperatures higher than 90 °C over long periods of time can lead to considerable heat loss to the surrounding ground: this has the double effect of reducing the amount of energy actually available for

discharge and increasing the temperature of the surrounding groundwater (Dahash *et al.*, 2021). In order to prevent these undesired effects, two solutions are recommended: an impermeable cut-off wall, to block the groundwater from reaching the TES, and thermal insulation, to reduce the thermal losses from the storage side.

Component design and building physics challenges

As introduced in the previous section, thermal insulation is a key element for groundwater protection, but its costs and installation are a relevant aspect also in the definition of the TES construction solutions (Tosatto, Ochs, Dahash and Muser, 2022). The optimal design of insulation solutions cannot be separated from the specific application. It is therefore advisable to consider solutions for the side walls, the cover and the bottom of the storage unit separately, in order to take into account specific requirements (e.g. structural support, possibility of replacement or repair) and challenges (e.g. moisture infiltration, development of convective heat transport).

Moisture penetration

As investigated in (Ochs, 2009) and (Tosatto *et al.*, 2023), the presence of moisture in the insulation is not desirable, as it would lead to material degradation and increased thermal losses. The critical situations to be considered in preventing the moisture infiltrations are:

- during construction: failures or weaknesses in the liner welding, installation of already moist insulation (due to transport, storage, weather).
- during operation: diffusion driven by high temperatures from the TES through the liner, infiltration from the surroundings (ground, rainfall).

Often, the presence of moisture is not avoidable, therefore solution strategies to remove it should be implemented. These however must rely on a deep knowledge of the materials' properties (both liners and insulation itself).

Natural convection

Convection is another important source of thermal degradation that is likely to occur in TES insulation, because of the high temperature differences involved and the granular porous insulation materials commonly used in these structures (Ochs, 2009). Temperature gradients within the bulk determine local variations of the air density, thus establishing gravitational body forces proportional to the density of the air (Incropera *et al.*, 2017). The most critical TES elements are therefore the lateral walls and the cover, where the heat flux direction is horizontal and upwards respectively, thus allowing the risk of natural convection flows, as

the warmer and lighter air closer to the water domain will tend to migrate upwards.

In the planning of TES insulation, the first step is to assess whether natural convection can be an issue. The elements to be considered are heat flux direction, material characteristics (i.e., porosity), geometry and dimensions and operation conditions (i.e., temperatures). The calculation of the Rayleigh number for a specific material is a useful indicator for the possibility of formation of convective heat transfer. In case of porous materials, the Darcy-modified Rayleigh formulation is suggested (VDI-Wärmeatlas, 10th edn, 2006):

$$Ra = \frac{g \beta_a}{\nu_a} \cdot \frac{L K \Delta T}{a} \quad (1)$$

The single contributions on the development of convective heat flux depend on fluid characteristics (ν_a is the fluid, i.e. air, kinematic viscosity, [m²/s]), geometry and configuration (L is the characteristic length [m], ΔT is the temperature difference between the two sides of the insulation [K]), and material characteristics (a is the thermal diffusivity [m²/s], K the material permeability [m²]). Other factors are the gravitational acceleration (g , [m/s²]), the coefficient of thermal expansion (β_a , [1/K]). The thermal diffusivity is defined as

$$a = \frac{\lambda}{\rho_a \cdot c_{p,a}} \quad (2)$$

where λ is the bulk thermal conductivity (without convection) [W/(m·K)], ρ_a the air density [kg/m³] and $c_{p,a}$ the air specific heat capacity [J/(kg·K)]. From the Rayleigh number it is possible to define the Nusselt number, which expresses the ratio of convection to pure conduction (Incropera *et al.*, 2017) and can be used to define the effective thermal conductivity of the bulk as ($\lambda \cdot Nu$).

Insulating walls

The concept developed by the consortium of the “giga_TES” project consists in the construction of an insulating bore pile wall that can be drilled around the storage (Tosatto, Ochs, Dahash, Muser, *et al.*, 2022). This solution represents a step forward from the current use of concrete piles. The design concept of the insulating bore pile wall is shown in Figure 3 and consists of a sequence of primary and secondary drilled piles, filled with granular bulk insulation. While the use of granular insulation and a construction process (like drilled piles) already well established in geotechnical engineering are major advantages in reducing the construction costs, the actual thermal performance of

this solution can be strongly affected by the material behaviour. The insulating bore pile would be in direct contact with the concrete wall of the TES, meaning high temperatures could be observed on the internal side.

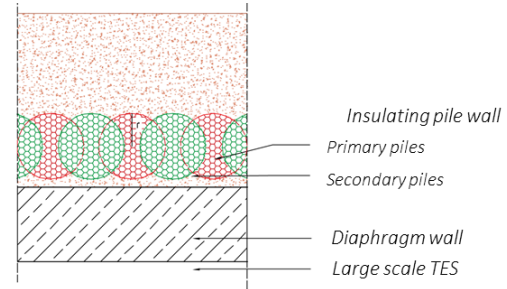


Figure 3 Horizontal section of a schematic representation of a TES envelope with insulating bore piles.

The vertical extension of the insulating pile can facilitate the formation of natural convection phenomena, which add to the conductive heat transport and thus increase the effective thermal conductivity of the insulating layer. This phenomenon was observed on a small scale on a 1 m high cylindrical mock-up filled with foam glass gravel (FGG), but the compaction of the material reduced the porosity sufficiently to block the development of convective plume. However, this may not be sufficient in practice, as observed in field tests, if the height of the piles (considered by the characteristic length in the Rayleigh number) is very high, as the space for the development of the convective plume is much larger.

Cover

Particularly in the case of underground PTES with a relatively shallow slope, the cover makes the greatest contribution both in terms of heat loss and investment costs. The functions of the cover are water- and vapour-tight separation of the storage medium (water) from the environment, thermal insulation and drainage of precipitation. If necessary, the cover must also compensate for the change in volume of the storage medium between fully charged and fully discharged.

In principle, covers can be self-supporting, supported or floating. Self-supporting covers are limited in size, supported covers appear to pose a technical and economic challenge and have only been investigated in a few research projects to date. For this reason, floating covers have so far established themselves as the predominant solution. However, the challenges here are also great and a technically mature solution is not clearly recognisable. The cover configuration, with the high temperature water layers on the bottom and the air on the upper side represents the most challenging element for the development of natural convection.

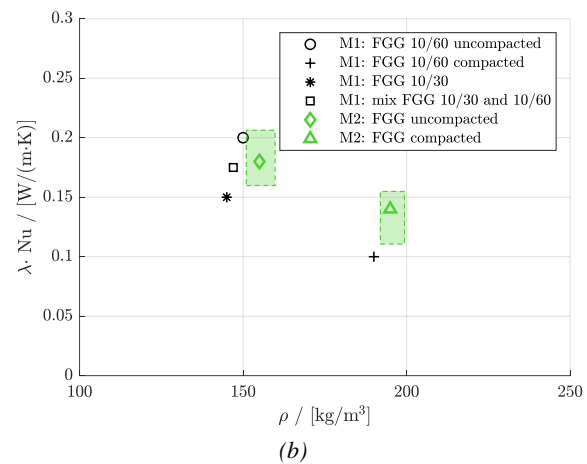
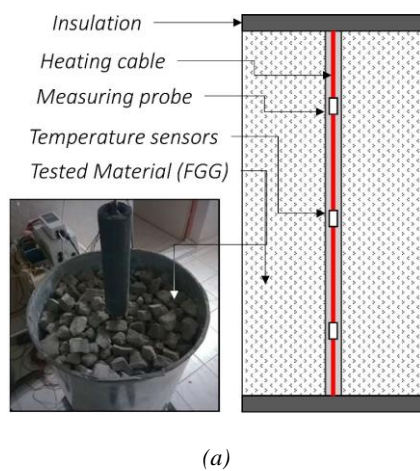


Figure 4 (a) Mock-up of a freestanding insulating bore pile (M1, 1 m high). (b) Thermal performance of the investigated insulating piles mock-ups. M1 is a 1 m high freestanding pile tested in lab conditions, M2 is a 6 m high drilled pile.

Results

Figure 4 presents a picture and an overview of the thermal performance (in terms of $\lambda \cdot Nu$) of the investigated insulating pile mock-ups.

Conclusions

The solutions to optimize TES construction are available from geotechnical engineering, but need to be appropriately adapted for the specific application of large-scale TES. The performance of thermal insulation is one of the critical challenges, but deep understanding of the building physics applied to the operation conditions allows developing solutions. In particular, in order to prevent convection, the following measures can be applied:

- Material compaction: this has proven to work in specific conditions, but may be not a sufficient measure.
- Mixing of granular insulation materials with different grain size, thus reducing the porosity and blocking the formation of the buoyant plume. Promising results in this field have been achieved by (Drück *et al.*, 2022), while test with other materials are currently ongoing within the new ‘ScaleUp4TESins’ project.
- Convection brakes.

Acknowledgment

This research was carried within the framework of IEA ECES Annex 39 and the Austrian flagship research project “Giga- Scale Thermal Energy Storage for Renewable Districts” (giga_TES, Project Nr.: 860949), financed by the Austrian “Klima- und Energiefonds”.

References

Dahash, A. *et al.* (2021) ‘Understanding the interaction

between groundwater and large-scale underground hot-water tanks and pits’, *Sustainable Cities and Society*, 71, p. 102928. doi: 10.1016/j.scs.2021.102928.

Drück, H. *et al.* (2022) ‘Erweiterung und Optimierung der solaren Nahwärmeversorgung Hirtenwiesen II in Crailsheim sowie Begleitforschung zu solarer Nahwärme und saisonaler Wärmespeicherung (CROW)’, pp. 1–130.

GigaTES (2021) Giga-scale thermal energy storage for renewable districts. Available at: <https://www.gigates.at/index.php/en/>.

Incropera, F. P. *et al.* (2017) *Incropera’s Principles of Heat and Mass Transfer*. Global Edi. Wiley.

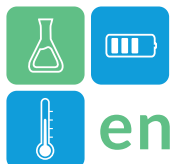
Ochs, F. (2009) *Modelling Large-Scale Thermal Energy Stores*. University of Stuttgart.

Tosatto, A., Ochs, F., Dahash, A., Muser, C., *et al.* (2022) ‘Insulating piles for the cost-effective construction of very large-scale high temperature thermal energy storage’, in *Proceedings of the International Renewable Energy Storage Conference 2021 (IRES 2021)*. Atlantis Press, pp. 67–77. doi: <https://doi.org/10.2991/ahe.k.220301.007>.

Tosatto, A., Ochs, F., Dahash, A. and Muser, C. (2022) ‘The Challenge of Planning and Constructing Large-Scale Hot Water TES for District Heating System: A Techno-Economic Analysis’, in *Proceedings of the International Renewable Energy Storage Conference 2021 (IRES 2021)*. Atlantis Press, pp. 52–66. doi: <https://doi.org/10.2991/ahe.k.220301.006>.

Tosatto, A. *et al.* (2023) ‘Influence of Heat and Mass Transfer on the Performance of Large-Scale Thermal Energy Storage Systems’, in *Proceedings of the International Renewable Energy Storage Conference (IRES 2022)*. Atlantis Press, pp. 470–488. doi: 10.2991/978-94-6463-156-2_30.

VDI-Wärmeatlas. 10th edn (2006) VDI-Wärmeatlas. Springer Verlag. doi: 10.1007/978-3-540-32218-4.



Unexplored synthetic approaches for CaCl₂ impregnation for sorption thermal energy storage

A. Fotia^{1,*}, E. Mastronardo¹, V. Brancato², A. Frazzica², L. Calabrese¹

¹ University of Messina, Department of Engineering, Contrada di Dio, 98165 Messina, Italy

² CNR - Istituto di Tecnologie Avanzate per l'Energia "Nicola Giordano", Via Salita S. Lucia sopra Contesse 5, 98126 Messina, Italy

*Corresponding author e-mail: antonio.fotia@unime.it

Encapsulation of inorganic salt hydrates for thermal energy storage has been extensively researched. The application of sorbent composites thermochemical materials has been investigated as a potential remedy for the shortcomings of inorganic salt hydrates, including their low thermal conductivity and unstable nature. Several studies have investigated the application of porous matrices impregnated with calcium chloride for various applications, such as desiccant rotary wheels in dehumidification systems or thermal energy storage. The objective of this study was to determine the morphological and thermogravimetric effects of the three distinct impregnation techniques used: dry, wet and airbrush. Water uptake is comparable among the three samples produced by the various impregnation techniques, according to the results. The wet method yields a sample with a slightly greater surface area compared to the other two, attributed to a better dispersion of the salt throughout the matrix. In conclusion, the sample produced via dry impregnation exhibits the best solution when applied to large-scale production.

Keywords: silica gel, salt hydrates, impregnation, thermal storage capacity, thermochemical storage

Introduction

The impregnation of silica gel with salt hydrates is a crucial process for various applications, particularly in thermal energy storage and sorption studies (Casey et al., 2014). This process consists in the segregation of a salt hydrate into the porous structure of silica gel (Zhang et al., 2023) to create a composite material, that offers several advantages, including increased thermal storage density and higher thermal stability (Huang et al., 2020). Furthermore, the impregnation of silica gel with salt hydrates has been shown to address challenges such as low viscosity and leakage problems associated with the pure salt hydrates, thereby enhancing their applicability in thermal energy storage systems (Rajagopalan et al., 2022). In this study, three different techniques of impregnation were considered: dry, wet, and airbrush, in order to evaluate the influence among the three methods.

Materials and Method

Silica gel in the shape of spheres (average grain size 0.779 mm) with a surface area of 366.30 m²/g and a pore volume of 1.049 cc/g, calcium chloride dihydrate and water for analysis were purchased from Sigma-Aldrich.

Firstly, the silica gel and the calcium chloride were dehydrated in oven at 120°C overnight. Following that, the salt was dissolved in varying volumes of

water, in accordance with the impregnation method that was employed.

Table 1 - Samples obtained.

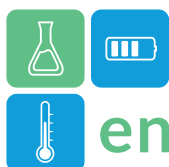
Sample Code	Approach	%CaCl ₂ (w/w)	H ₂ O/CaCl ₂ (w/w)
CaCl30SG_DRY	Dry	30.0	2.2
CaCl30SG_WET	Wet	30.0	3.6
CaCl30SG_AB	Airbrush	30.0	3.6

In the Table 1, the percentages of the different preparations are detailed.

Dry impregnation, wet impregnation, and airbrush impregnation were the three used approaches. In the dry method a lower amount of water was used to dissolve the salt than the wet one. In both cases, impregnation involved dropping the solution into the matrix while stirring.

For airbrush impregnation, the same volume of water was utilised as for the wet method. In this case, an airbrush pen, with a 0.2 mm diameter needle, was used. The pen was placed vertically and was connected to a compressor that supplied airflow at a pressure of 3 bar. The saline solution was nebulized into a beaker containing the silica gel.

All the obtained samples were left overnight in oven preheated at 120°C. Surface area, water sorption/desorption capacities, and thermal storage



capacity were analysed for each sample produced. The morphology of pure silica gel and impregnated materials was evaluated by an optical digital microscope.

Specific surface area and pore volume were measured using NOVA 1200e, Quantachrome Instruments. BET and BJH approaches were applied for the data analysis. The thermal storage capacity was measured through a customized thermogravimetric apparatus (Themys One, Setaram) with an evaporator and a vacuum system. Initially, the sample was dehydrated under vacuum (10^{-2} mbar) at a temperature of 120°C for 3 hours. The thermal storage capacity was evaluated under isobar conditions at 17 mbar (evaporation temperature of 15°C) within the cooling process from 120°C to 25°C with a scan rate of $5^{\circ}\text{C}/\text{min}$.

The evaluation of the composite materials hydration and dehydration capacities was carried out by DVS Vacuum, a thermo-gravimetric dynamic vapour system built by Surface Measurements Systems. The instrumental setup consists of a micro-balance (precision $0.1\ \mu\text{g}$) and a water vapor pressure flow control system inside the sample holder chamber.

Results and Discussion

With all the three impregnation methods, the calcium chloride was embedded within the pores of silica gel, as shown in Figure 1. Specifically, regarding airbrush impregnation, the salt has generated a shell that covers the matrix, resulting in a slight enlargement of its dimensions, which can be highlighted at higher degree of magnification with SEM pictures.

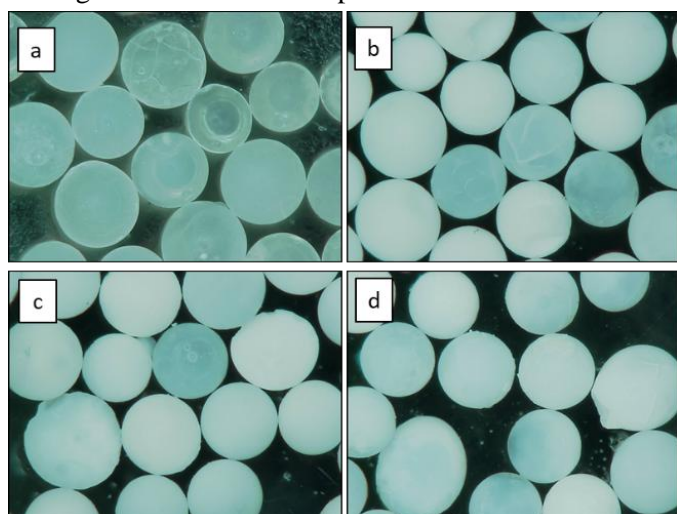


Figure 1 - Optical image of a) pure silica gel, b) $\text{CaCl}_30\text{SG_DRY}$, c) $\text{CaCl}_30\text{SG_WET}$ and d) $\text{CaCl}_30\text{SG_AB}$.

Furthermore, it is evident that all the synthetic approaches do not damage the matrix.

Table 2 shows the values of surface area compared to the silica gel. The materials obtained via dry and airbrush methods have a similar surface area, while that prepared with wet impregnation is slightly higher. This could be associated with the variation in water quantities used for the different impregnation techniques. The higher the salt solution, the higher is the capillary effect. Nevertheless, despite employing an equivalent volume of water, in both the wet and airbrush techniques, the nebulization doesn't permit full permeation into silica gel.

Table 2- Surface area results.

Sample Code	Surface area (m^2/g)
Silica Gel	386.30
$\text{CaCl}_30\text{SG_DRY}$	186.34
$\text{CaCl}_30\text{SG_WET}$	197.88
$\text{CaCl}_30\text{SG_AB}$	183.88

Based on the thermogravimetric analysis of the data displayed in Figure 2, it is evident that the mass of the silica gel impregnated using the dry, wet, and airbrush methods varies by 44.07%, 47%, and 46.10%, respectively, as a result of water vapour adsorption, confirming that the amount of impregnated salt is comparable for the three samples. Dry impregnation was observed to have a higher thermal storage capacity compared to the other two methods, which exhibited minimal differences.

The curves obtained from the DVS analysis (isobars at 17 mbar, 23 mbar and 31 mbar) confirm the trend of the thermogravimetric analysis, where the $\text{CaCl}_30\text{SG_WET}$ sample appears to absorb a greater quantity of water than the other two samples.

Furthermore, a slight local hysteresis cycle was observed on all the samples made at a temperature of 50°C and 75°C (Figure 3). This behavior is clearly associated with the change in the hydration level of calcium chloride (Van Essen et al., 2009).

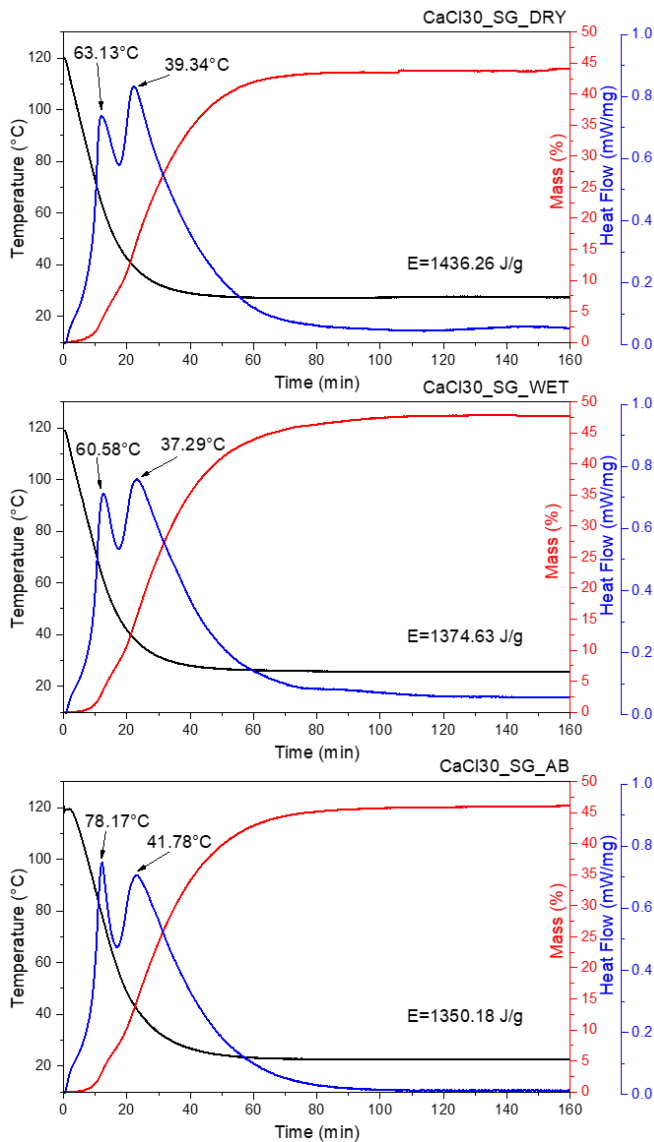
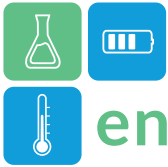


Figure 2 – Results of thermogravimetric analysis

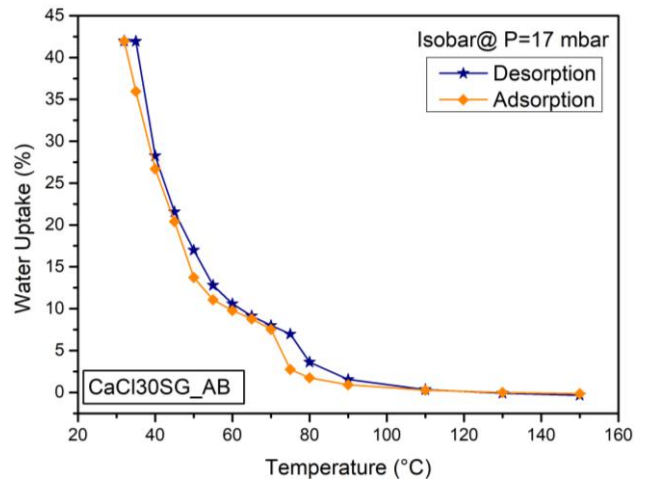


Figure 3 - Isotherm (P=17 mbar) of CaCl₃₀SG_AB

Conclusion

In this study we investigated how the performance of composite materials for thermal storage varies, using three different impregnation methodologies (dry, wet and airbrush). In terms of water uptake, the three samples present similar performances. However, the sample obtained with the wet approach shows a slightly higher surface area than the other two, due to a better dispersion of the salt within the matrix. The isobars obtained from the DVS analysis reveal a minor hysteresis between the absorption and desorption curves for all three samples. In conclusion, based on these preliminary data, the sample produced by dry impregnation appears to be the most effective for large scale production, thanks to the higher storage density and the optimal use of the prepared solution.

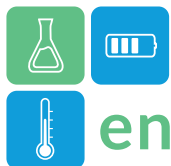
Acknowledgment

This project has received funding from ThumbsUp (Thermal energy storage solUtions to optimally Manage BuildingS and Unlock their grid balancing and

flexibility Potential).ThumbsUP is a Horizon Europe Project supported by the European Commission under contract No. 101096921.

References

- Casey, S. P. and al. (2014). Salt impregnated desiccant matrices for “open” thermochemical energy storage - Selection, synthesis and characterisation of candidate materials. Energy and Buildings. <https://doi.org/10.1016/j.enbuild.2014.08.028>



enerstock

ENERSTOCK 2024

The 16th IEA ES TCP International Conference on Energy Storage

June 5–7, 2024

Lyon, France

- Huang, K. and al. (2020). Effect of Graphene Oxide on Phase Change Materials Based on Disodium Hydrogen Phosphate Dodecahydrate for Thermal Storage. *ACS Omega*.
<https://doi.org/10.1021/acsomega.0c01184>
- Rajagopalan, K. K. and al (2022). Strong, thermo-reversible salogels with boronate ester bonds as thermal energy storage materials. *Journal of Materials Chemistry A*.
<https://doi.org/10.1039/d2ta06183j>
- Van Essen, V. and al. (2009). Characterization of Salt Hydrates for Compact Seasonal Thermochemical Storage. Proceedings of the ASME 2009 3rd International Conference on Energy Sustainability Collocated with the Heat Transfer and InterPACK09 Conferences. ASME 2009 3rd International Conference on Energy Sustainability. <https://doi.org/10.1115/ES2009-90289>.
- Zhang, Y. and al. (2023). Performance analysis of a lab-scale adsorption desalination system using silica gel/LiCl composite. *Desalination*.
<https://doi.org/10.1016/j.desal.2022.116278>



Unlocking feasibility: Role of insulation distribution in large-scale seasonal thermal energy storage applications

Abdulrahman Dahash^{1,*}

1 AIT Austrian Institute of Technology GmbH, Center for Energy, Giefinggasse 2, 1210 Vienna, Austria

*Corresponding author e-mail: Abdulrahman.dahash@ait.ac.at

Abstract

Large-scale thermal energy storage (TES) plays a crucial role in the expansion of renewables-based district heating (R-DH) effectively bridging the gap in the seasonal mismatch between heating demand and renewable energy availability. This study establishes a techno-economic analysis framework incorporating key performance indicators such as energy and exergy efficiency. Economic feasibility is assessed through TES-specific investment costs, recommending the use of levelized cost of stored heat (LCOS) as a practical measure for techno-economic analysis. Validated numerical simulation models are utilized for investigation. The outcomes highlight the advantage of pyramid-shaped insulation distribution over conventional methods within the TES envelope. Furthermore, the study emphasizes the necessity of expanding the analysis to encompass the impact of district heating (DH) temperature and TES volume for comprehensive insights.

Keywords: Seasonal thermal energy storage; large-scale TES; pit; techno-economic analysis; insulation.

Introduction

Large-scale seasonal thermal energy storage (STES) has gained prominence for its potential to address the seasonal mismatch between heat supply and demand, with a focus on utilizing solar heat surplus during summer to meet winter heating demands. These storage systems, often referred to as underground thermal energy storage (UTES), encompass various categories, including closed-loop systems like tank thermal energy storage (TTES) and pit thermal energy storage (PTES), as well as open-loop systems like aquifer thermal energy storage (ATES) and borehole thermal energy storage (BTES). UTES types are employed for different district heating (DH) applications based on temperature requirements.

Planning large-scale STES systems is a complex task, involving the evaluation of multiple interconnected variables. Numerical simulations play a vital role in assessing the impact of various boundary conditions on the planning process. Previous research has explored the effects of insulation and insulation distribution within STES envelopes. Insulation thickness and distribution significantly influence STES performance and cost. Furthermore, studies have examined the interaction between insulation levels and system operation, highlighting the importance of optimizing insulation distribution.

This study focuses on examining the influence of insulation distribution and thickness within STES

envelopes on both technical and economic aspects of large-scale STES systems. A validated numerical model will be used to assess the impact of insulation configurations, with a particular focus on large-scale hot-water tanks and pits, common choices for district-level applications (Mahon, H. et al., 2022).

On the other hand, the open-loop TES systems exploit the nearby available water sources and employ them as heat carriers, while storage medium is the soil or rock whereby the boreholes or aquifers are installed.

This work contributes to the planning challenges for the TTES and PTES types, whereas other types are not further considered in the work. This is due to fact that the TTES and PTES are capable to achieve high temperatures in the stores together with high flowrates enabling the DH operator to charge and/or discharge high energy rates. The ATES and BTES systems are employed for low temperature DH applications and, thus, lower energy rates compared to their UTES counterparts (Ochs, F. et al., 2019).

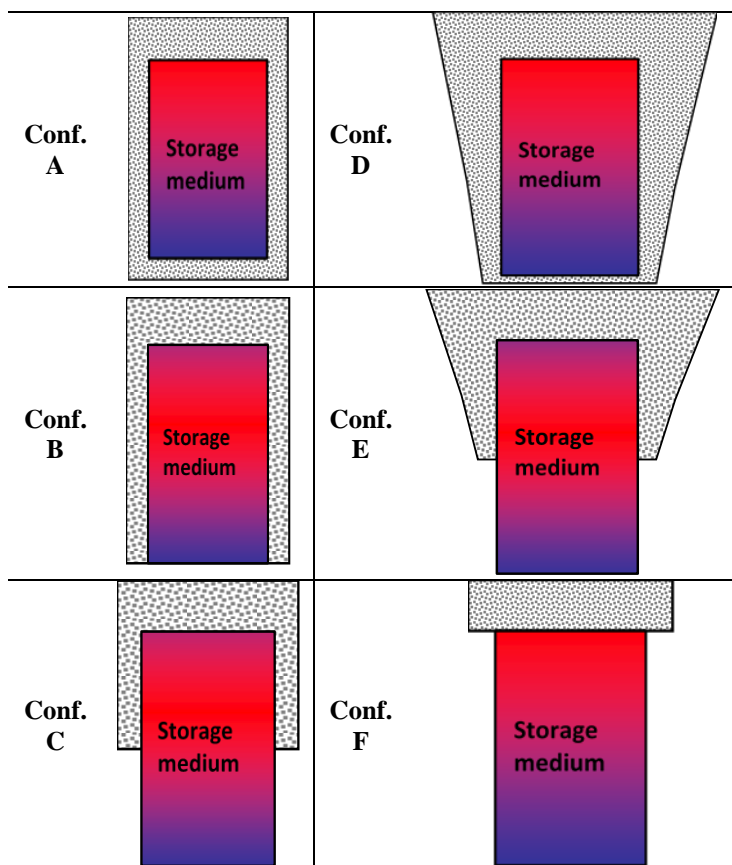
Literature review

Previous works considered tanks and pits that were insulated in a uniform manner (i.e. homogenous insulation distribution) as shown in Table 1(a). These storage systems however employ stratification as operation concept. Accordingly, hot water gathers at the top, while cold water is at bottom and, thus, TES has higher exergy at top than that at bottom.

Therefore, it is useful to enclose the TES envelope with inhomogeneous insulation thickness.

Table 1 compares various configurations for insulation distribution over the TES envelope. Option (a) presents a normal, homogenous distribution with a uniform thickness. Other options (b-f) show the possible configurations for insulation distribution. In this regard, (Huang, H. et al., 2020) investigated the interaction between the TES insulation level and the system operation. The work considered 5 insulation configurations as follows: full insulation (*option a*), no insulation, lid and sidewalls insulation (*option b*), upper half insulation (*option c*), and only lid insulation (*option f*).

Table 1: The insulation distribution variants considered in this work.



Compared to its counterparts, the configuration of insulating the upper half of TES (*option c*) showed a considerable increase in TES temperature and capacity. Yet, the work considered a tank with a volume of appx. 50 m³, which is far from the large-scale applications.

With the aid of CFD, (Kurşun, 2018) assessed the TES stratification improvement under several

insulation configurations. The work considered a residential hot water tank with a total volume of 33,6 L (0.0336 m³). The work suggested the use of an insulation in shape of truncated cone (*option b*) since it makes up to 131% stratification improvement compared to the insulation shown in Table 1(a). Yet, the TES scale is residential.

More recently, (Dolgun, G. et al., 2023) investigated the optimal insulation of an underground tank for seasonal applications. The work considered different levels of insulation and their impact on the cost savings. Yet, the work paid attention to spherical tanks that are formerly used as gas storage. Thus, it is crucial to expand such investigations to large-scale, long-term hot water tanks and pits.

This study aims to examine the influence of insulation distribution and thickness within the STES envelope on technical and economic levels for large-scale STES systems. To achieve this, a validated numerical model developed for large-scale, seasonal, underground TES systems will be utilized. The work will be focusing on large-scale hot-water tanks and pits as potential candidates for DH systems.

Methodology

Simulation model

Large-scale STES planning requires accurate thermo-hydraulic modeling, including multi-physical aspects (e.g., heat and mass transfer, flow dynamics, etc.) in numerical models. This work utilizes a COMSOL Multiphysics® TES model to represent diverse TES shapes (e.g., shallow pit, tank, cuboid).

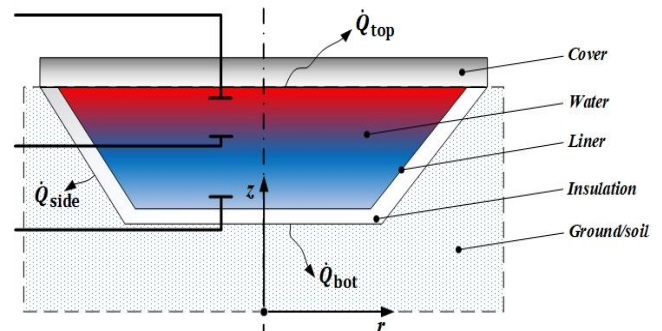
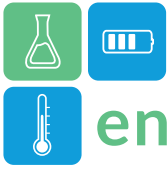


Figure 1: An exemplary 2-D representation of an underground shallow pit with the different required domains and surroundings.

Figure 1 exhibits a shallow pit with 3 diffusers, demonstrating multi-port simulation capability. This study does not detail the numerical model's development, extensively covered and validated in (Dahash, A. et al., 2020). The energy balance equation for each TES segment (*i*) involves heat transfer mechanisms expressed as a partial differential



equation; more specifics are available in (Dahash, A. et al., 2020).

Operation scenarios and boundary conditions

Seasonal TES operates in four phases, each spanning approximately 3-4 months to complete an annual cycle (Ochs, F. et al., 2019). The model simplifies the analysis by employing a standardized DH temperature profile: HT-DH supply and return temperatures at 90°C and 60°C, and LT-DH supply and return temperatures at 80°C and 30°C. Figure 2 and Figure 3 illustrate the periodic operating conditions for TES, while Table 2 lists essential thermo-physical properties and parameters for the simulations.

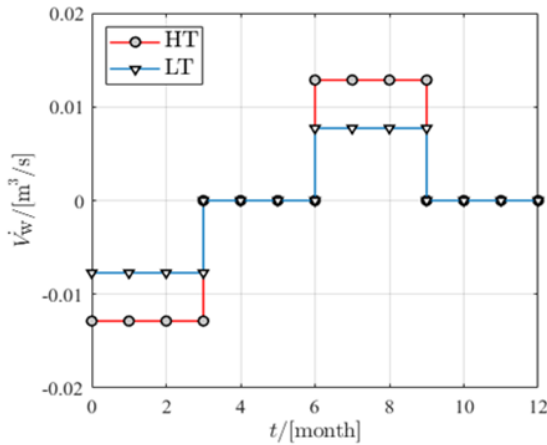


Figure 2: A year-round incoming/outgoing flowrate for a TES with a volume of 100,000 m³.

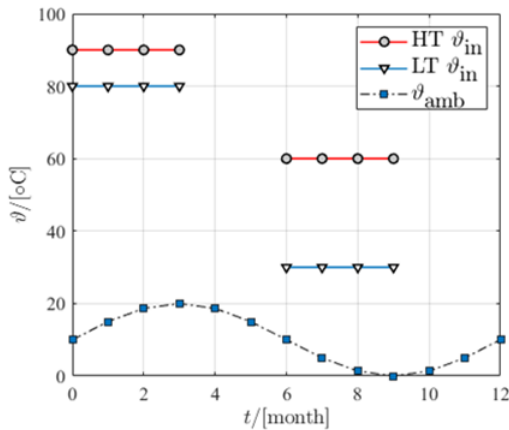


Figure 3: A year-round injection temperature into TES and ambient temperature an average of 10°C.

Table 2: Thermo-physical properties of the materials and heat transfer coefficients (HTC) of the different components in TES.

Parameter	Value
Water thermal conductivity, λ_w	0.6 W/(m.K)

Water density, ρ	1000 kg/m ³
Water specific heat capacity, c_p	4186 J/(kg.K)
Overall HTC of the top (cover), U_{top}	0.1 W/(m ² .K)
Overall HTC of the sidewalls, U_{side}	$f(\lambda_{ins}, x_{ins})$
Overall HTC of the bottom, U_{bot}	$f(\lambda_{ins}, x_{ins})$
Ground thermal conductivity, λ_g	1.5 W/(m.K)
Ground specific heat capacity, $c_{p,g}$	880 J/(kg.K)
Ground density, ρ_g	1000 kg/m ³

Key performance indicators

Table 3 reports a list of the key performance indicators used in this work and briefly documents the description of each metric considered. The reader is referred to (Dahash, A. et al., 2021) if further information on the key performance indicators is needed.

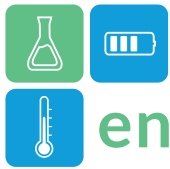
Table 3: List of KPIs used in the techno-economic analysis (Dahash, A. et al., 2021).

KPI	Equation	Description
Energy efficiency	$\eta_I = \frac{Q_{dis}}{Q_{ch}}$	Ratio of the heat discharged at useful temperature to the amount of heat charged.
Energy capacity efficiency	$\eta_{II} = 1 - \frac{Q_{loss}}{Q_{TES}}$	Ratio of the effective storage capacity to the maximum nominal capacity.
Exergy efficiency	$\psi = \frac{EX_{dis}}{EX_{ch}}$	Ratio of the exergy discharged to the amount of exergy charged.
LCOS	$LCOS = \frac{LCOS}{\sum_{i=0}^T Q_{dis}}$	Quotient of the annualized storage cost (i.e. capital and operational) to the discharged heat from TES.

Results and discussion

This section compares different insulation layouts for a fully buried, 50 m deep tank with 100,000 m³ used in DH. Configurations vary in insulating the upper 50% of the tank while leaving sidewalls uninsulated. Some configurations also lack bottom insulation due to lukewarm water accumulation. Figure 4 shows specific costs for each layout. Configuration D, with extensive insulation, has the highest cost, while F, without sidewall or bottom insulation, has the lowest. Configuration A has higher costs due to more insulation volume. Despite only insulating 50% of the storage volume, C and E exhibit slightly lower costs than A. Notably, all configurations share similar costs for excavation, geotechnics, cover, plant construction, and site facilities.

¹ In the x-axis, 0 refers to the month May at which the operational years starts.



This difference in insulation distribution and volume produces a notable impact on the TES performance. As the fully insulated TES (configuration A) has relatively lower thermal losses, this means more heat can be discharged into the DH grid. Yet, configuration D arises as a more promising insulation option as it reveals higher performance (i.e. energy efficiency and energy capacity efficiency) by 2.5% compared to its counterpart A as revealed in Figure 5. This is attributed to more insulation volume. Yet, the highest exergy efficiency goes for the configuration A as this indicates better stratification compared to all other options (Dahash, A. et al., 2021).

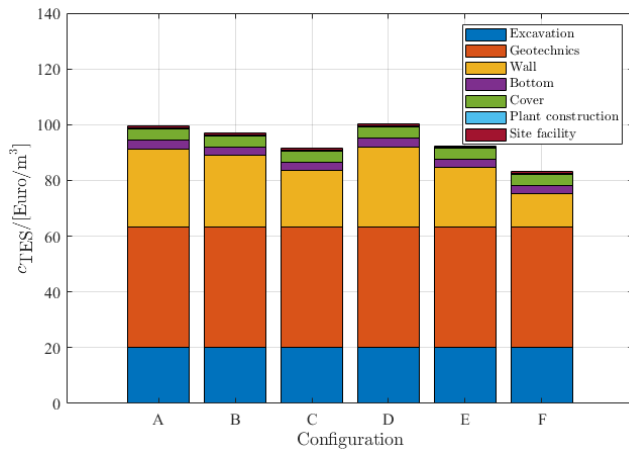


Figure 4: Breakdown of the specific investment cost for a 100,000 m³ fully buried tank installed in HT-DH with several insulation configurations according to the costs reported in (Dahash, A. et al., 2021). (Geotechnics cost item refers to diaphragm wall installation, wall cost item refers to insulation cost and liner installations and bottom refers to the installation and cost of insulation and liner).

In other words, it can be said that configuration A has higher energy quality for the heat discharged compared to others. Furthermore, it must be pointed out that the uninsulated TES (configuration F) has significantly lower performance (energetic and exergetic efficiency) compared to other counterparts.

Figure 6 depicts the levelized cost of stored heat (LCOS) for the several tank configurations in the foregoing discussion. Therein, it is revealed that the fully insulated tank has the highest LCOS despite its high efficiency (80%).

The tank in configuration D (gradient insulation), on the other hand, has comparably lower LCOS by 4 €/MWh, whereas the configurations C and E have comparably similar LCOS. Herein, it must be pointed out that only 50% of the buried tank volume is insulated but with different distribution for the options (C and E). Amongst the insulated options (A-E), the

tank with 50% insulation has the lowest LCOS and this stems from its low specific investment cost among the mentioned configurations.

It is held that the foregoing comparison and discussion might yield misleading planning findings as the insulation volume is not constant for all configurations and, thus, there is a difference in the specific investment cost, performance and LCOS. Therefore, future work will pay attention to the comparison of the configurations with a constant insulation volume of 3,616 m³ for all configuration except option F.

Conclusions

This study aimed to showcase the complexity in planning and construction of large-scale thermal energy storage systems through a techno-economic analysis. The work focused on establishing comprehensive planning guidelines. The work numerically examined the impact of insulation and its distribution within the TES envelope. Results showed that a pyramid-shaped insulation distribution (configuration D) was more energetically efficient compared to conventional distribution (configuration A). However, configuration D exhibited less exergetic efficiency. This later led to cheaper LCOS of 4 €/MWh, though both configurations reported similar specific costs. Future research will concentrate on maintaining a consistent insulation volume across configurations to deepen insights into the techno-economic impact.

Acknowledgments

This project is conducted within the framework of IEA ES Task 39 “Großwasserwärmespeicher für Fernwärmesysteme” (Task39; Project Nr.: 883015). Therefore, the author wishes to acknowledge the financial support for this work.

References

Dahash, A. et al. (2020). Toward Efficient Numerical Modeling and Analysis of Large-Scale Thermal Energy Storage for Renewable District Heating Systems. *Applied Energy*, 279. doi:DOI: 10.1016/j.apenergy.2020.115840

Dahash, A. et al. (2021). Techno-economic and exergy analysis of tank and pit thermal energy storage for renewables district heating systems. *Renewable Energy*, 180, 1358-1379. doi:10.1016/j.renene.2021.08.106

Dolgun, G. et al. (2023). Optimal insulation of underground spherical tanks for seasonal thermal energy storage applications. *Journal of Energy Storage*. doi:10.1016/j.est.2023.107865.

Huang, H. et al. (2020). Thermal characteristics of a seasonal solar assisted heat pump heating system with an underground tank. *Sustainable Cities and Society*, 53. doi:10.1016/j.scs.2019.101910

Kurşun, B. (2018). Thermal stratification enhancement in cylindrical and rectangular hot water tanks with truncated cone and

pyramid shaped insulation geometry. *Solar Energy*, 169, 512-525. doi:10.1016/j.solener.2018.05.019.

Mahon, H. et al. (2022). A review of thermal energy storage technologies for seasonal loops. *Energy*, 239, Part C. doi:10.1016/j.energy.2021.122207.

Ochs, F. et al. (2019). Techno-economic planning and construction of cost-effective large-scale hot water thermal energy storage for Renewable District heating systems. *Renewable Energy*, 150, 1165-1177. doi:doi.org/10.1016/j.renene.2019.11.017.

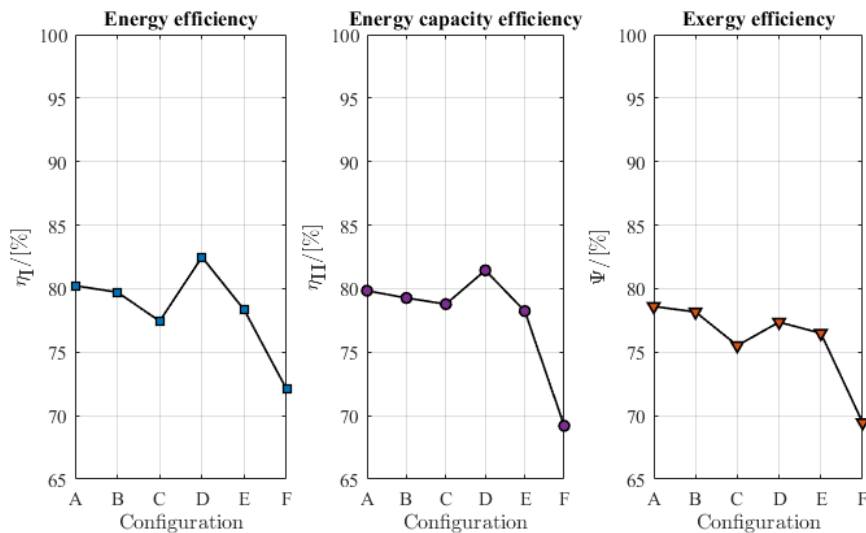


Figure 5: Energetic and exergetic efficiency for the different configurations considered for the insulation distribution for a 100,000 m³ fully buried tank installed in HT-DH.

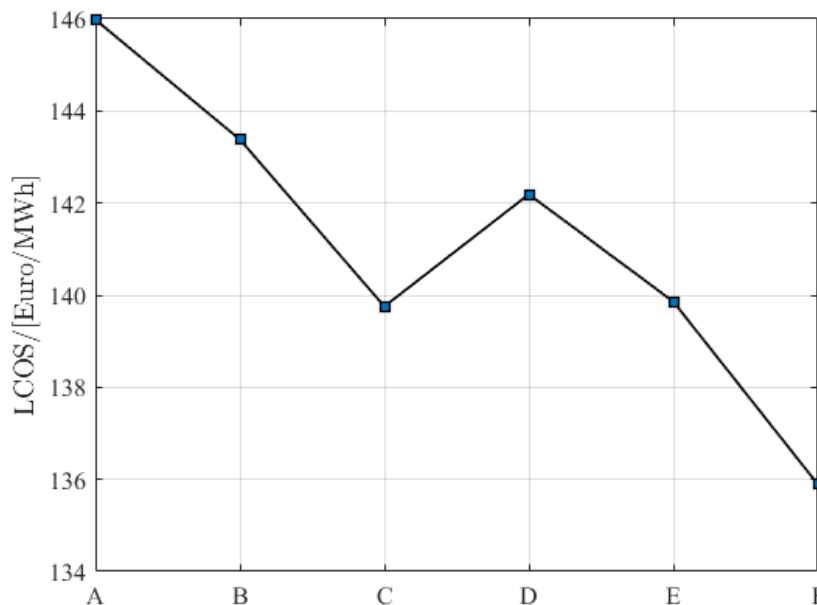


Figure 6: The levelized cost of stored heat for a 100,000 m³ fully buried tank with different insulation configurations.



Use of bibliometric analysis to evaluate the influence of cement and concrete on carbon capture, utilization, and storage over the years

Carolina Santini¹, Emiliano Borri², Claudia Fabiani^{1,3}, Anna Laura Pisello^{1,3}, Luisa F. Cabeza^{2,*}

¹EAPLAB at CIRIAF-Interuniversity Research Centre, University of Perugia, Via G. Duranti 63, 06125 Perugia, Italy

²GREiA Research Group, Universitat de Lleida, Pere de Cabrera s/n, Lleida, Spain

³Engineering Department, University of Perugia, Via G. Duranti 93, 06125 Perugia, Italy

*Corresponding author e-mail: luisaf.cabeza@udl.cat

Abstract

The cement industry is undeniably crucial to the global economy but causes large CO₂ emissions mainly due to its production process. Therefore, the technologies of CO₂ capture and storage have a strong connection with the evolution of the cement industry and with the optimization of its production and application procedures. This research aims to analyse the interaction between the cement and CCU (carbon capture, utilization, and storage) strategies in order to evaluate the fields in which research are moving on and the main results.

Keywords: cement; concrete; CCUS; carbon capture; carbon storage

Introduction

The concept of sustainability plays an important role in reducing global warming. Issues induced by climate change are increasing year by year. Eco-friendly practices to mitigate environmental impact are developing, focusing on the reduction of carbon into the atmosphere.

CO₂ emissions are strictly connected to cement industry. However, it is not enough to reduce emissions in this sector (Chaudhury *et al.*, 2023) to achieve carbon neutrality but it is necessary to adopt innovative technologies such as carbon capture, utilization, and storage (CCUS).

There are several capture technologies that are in the process of being further developed to a high degree of maturity. Industrial waste residues are ideal medium for CO₂ capture and storage (CCS), particularly those with abundant calcium and magnesium components. Residues such as fly ash, biochar, limestone, steel slag (SS), and waste concrete can be targeted for CCS and can partially replace geological storage.

CCUS in the cement-concrete sector can be achieved intervening on the cement carbonation process by capturing CO₂ emissions during cement production and after reusing the captured CO₂ for various applications. The purpose to be achieved is that of a carbon storage

safe and permanent to prevent its release into the atmosphere.

For this reason, the possibility of incorporating materials with carbon capture properties into the cement mix has recently been studied. In particular, biochar appears to have a good affinity with cementitious compounds (Akinoyemi and Adesina, 2020). The final product obtained maintains the mechanical characteristics of standard cement but allows the carbon contained in the biochar to be permanently storage.

This research intends to connect the cement and concrete with the CCUS to verify the evolution over the years and the strategies applied in this sector to make this material sustainable.

Materials and methods

A comprehensive and systematic search was conducted in the Scopus database to identify studies focusing on the development of cement and concrete in connection with CCUS. The search query encompassed all possible combinations of at least two terms: one term referring to cement materials or concrete, and the other term related to the carbon sequestration and storage.

Keyword combinations were carefully identified to cover all potentially relevant ones excluding irrelevant analyses that would be difficult to define within a large

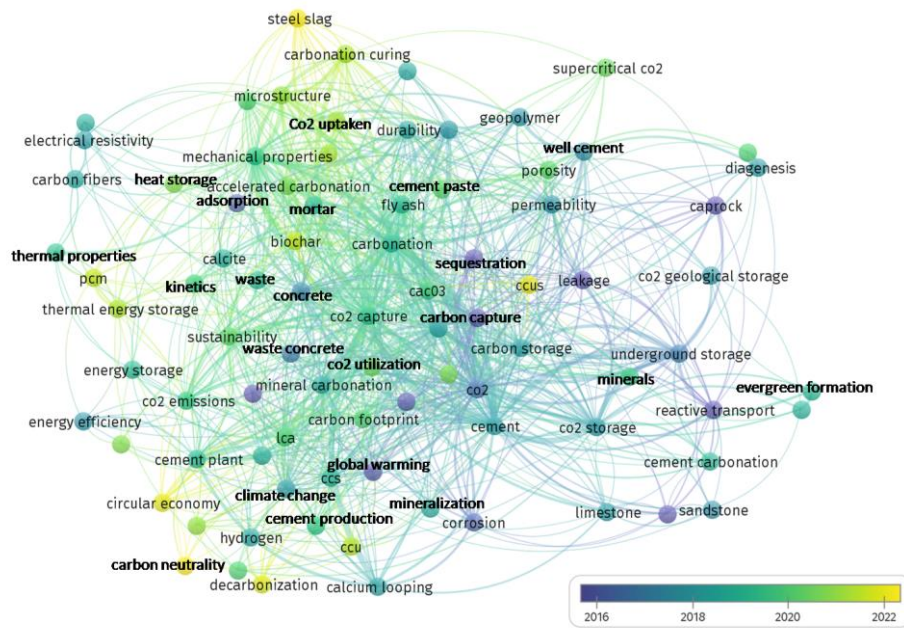


Figure 2. Overlay visualization

Conclusions

This work aims to connect the concept of CCUS (carbon capture, utilization, and storage) with the production and application of cement and concrete to verify how this connection has evolved. The query used takes these two major themes to set up a complete bibliometric analysis.

Results were processed via the software VOSviewer and highlighted how new technologies are evolving in the CCUS process following sustainability principles. Recently, cement and concrete have themselves been considered potential carbon sinks.

Acknowledgment

Funded by the European Union’s Horizon Europe Research and Innovation Programme under grant agreement No. 101086302 (CSTO2NE). Views and opinions expressed are however those of the author(s) only and do not necessarily reflect those of the European Union or REA. Neither the European Union nor the granting authority can be held responsible for them. The authors from University of Lleida would like to thank the Catalan Government for the quality accreditation given to their research group (2021 SGR 01615). GREiA is certified agent TECNIO in the category of technology developers from the Government of Catalonia. This work is partially supported by ICREA under the ICREA Academia programme.



enerstock

ENERSTOCK 2024
The 16th IEA ES TCP International Conference on Energy Storage
June 5–7, 2024
Lyon, France

References

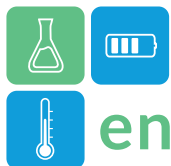
Akinyemi, B. A. and Adesina, A. (2020) ‘Journal of Building Engineering Recent advancements in the use of biochar for cementitious applications : A review’, *Journal of Building Engineering*, 32(May), p. 101705. doi: 10.1016/j.job.2020.101705.

Chaudhury, R. *et al.* (2023) ‘Low-CO₂ emission strategies to achieve net zero target in cement sector’, *Journal of Cleaner Production*, 417(April), p. 137466. doi: 10.1016/j.jclepro.2023.137466.

Van Eck, N. J. and Waltman, L. (2023) ‘VOSviewer Manual version 1-6-19’, *Leiden: Univeriteit Leiden*, (January), p. 54. Available at: http://www.vosviewer.com/documentation/Manual_VOSviewer_1.6.1.pdf.

Erdogmus, E. *et al.* (2023) ‘Thermal performance analysis of novel foam concrete composites with PCM for energy storage and environmental benefits in buildings’, *Energy and Buildings*, 296(July). doi: 10.1016/j.enbuild.2023.113413.

Roychand, R. *et al.* (2023) ‘Carbon sequestration from waste and carbon dioxide mineralisation in concrete – A stronger, sustainable and eco-friendly solution to support circular economy’, *Construction and Building Materials*, 379(April), p. 131221. doi: 10.1016/j.conbuildmat.2023.131221.



Use of plastic waste to formulate new microencapsulated phase change materials (MPCM) with thermal, mechanical and chemical resistance

Jessica Giro-Paloma^{1,*}, Leonard Wujec², David Vera Rivera¹, Anna Alfocea-Roig¹, Joan Formosa¹
¹ Department de Ciència de Materials i Química Física, Universitat de Barcelona, C/ Martí I Franquès, 1-11, 08028, Barcelona, Spain
² Gottfried Wilhelm Leibniz Universität Hannover, Welfengarten 1, Hanover, Germany
*Corresponding author e-mail: jessicagiro@ub.edu

Abstract

This study centres on science, technology, and innovation as crucial drivers to achieve the Sustainable Development Goals (SDGs) outlined in the 2030 agenda. It is focused on the development of Microencapsulated Phase Change Materials (MPCM) which must be resilient to the pH and temperatures variations, as well as possess enough mechanical strength to withstand the mixing process with construction materials. Hence, the investigation aims to use recycled polymers such as polystyrene (PS), polymethyl methacrylate (PMMA), and polyethylene terephthalate (PET) to create the outer shell of the MPCM, thereby helping to minimize the amount of microplastics entering the oceans. Then, the main objective of this findings is to develop polymeric materials from plastic waste to develop new MPCM shells, focusing on the chemical (pH), physical (T), and mechanical (σ) resistance.

Keywords: Microencapsulated phase change materials (MPCM), polymer, plastic, shell, waste

Introduction

Services including heating, ventilation and air conditioning, account for half of the energy used in buildings in developed countries. Furthermore, projections indicate a significant increase in energy consumption in the EU over the next 15 years, with an estimated growth of around 50%.^[1] In the last years, there has already been a significant increase in the rates of energy consumption for space heating and cooling, so to meet the SDGs, there is a need for a solution, whether using alternative and renewable energy sources, or by improving energy efficiency through more effective energy systems.^[2] One solution for improving energy efficiency is the use of energy storage systems (ESS), more specifically latent heat storage, which uses the phase transition of a phase change material (PCM) to absorb or release heat, providing cooling during the day and heating at night. To be used in building materials, the PCM needs to be protected and encapsulated as microencapsulated PCM (MPCM), with a shell made of a common polymer such as PET, acrylic polymers such as PMMA, or PS^[3]. In this study the shell is produced from recycled waste polymer addressing the problem of global plastic pollution.^[4]

Methodology and materials

Methodology

The encapsulation process is carried out using the solvent evaporation method provided by Shao et. Al., where an emulsion is formed between water/oil phases, and the shell material and the PCM are dissolved in a water-immiscible, volatile solvent that can be easily evaporated later. This allows the shell material to shrink around the PCM and cure. Figure 1 schematically illustrates the process and shows that the polymer begins to precipitate in the droplet of solvent as evaporation begins. For the subsequent migration of the polymer, the interfacial tensions between the polymer and the two phases are very important and can be influenced by the choice of solvent and surfactant.^[5] When all the solvent has evaporated, the polymer forms a stable shell around the PCM.

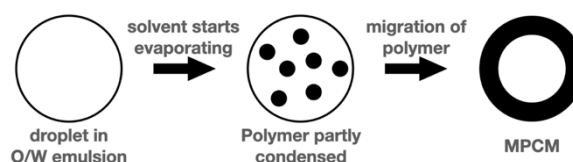


Figure 1: Schematic illustration of the encapsulation process.^[6]

Materials

The PS foam waste was from packaging material, the PMMA waste from acrylic glass, and the PET waste from drinking bottles. The used PCM was CRODATHERM 24W-LQ-(MV) purchased from

Croda Iberica SA and the sodium dodecyl sulfate (SDS, ultra-pure) was from MP Biomedicals, LLC.

Experimental procedure

For the encapsulation the polymer solution (PET and PS in DCM, PMMA in chloroform) was mixed with PCM to create the discontinuous phase and SDS was dissolved into distilled water to prepare the continuous phase. Then the discontinuous phase was slowly dripped into the water phase and stirred for 4 h to obtain an emulsion. Still under stirring the emulsion was heated to a) DCM: 45°C, b) chloroform: 75°C for 2.5 h more until all solvent was distilled from the system. The product was filtrated and washed with water to remove the surfactant. Then the remains were dried on air for 24 h.

To analyse the pH stability different basic and acidic solutions were made and 10 mg of MPCM was added to each solution and left for 24 h. After a filtration the samples were dried under ambient conditions.

For thermic stability measurements the sample was put in an oven for 24 h at different temperatures and the thermocyclic stability was tested with 200 thermocycles from 15°C to 35°C. After each experiment the samples were analysed in the SEM.

Results and Discussion

SEM analysis

Different results were obtained in the SEM for the various MPCM. For example, spherical capsules could be produced with PS-MPCM and PMMA-MPCM, whereas this was not possible with PET-MPCM (see Figure 2) and these are therefore not investigated further below.

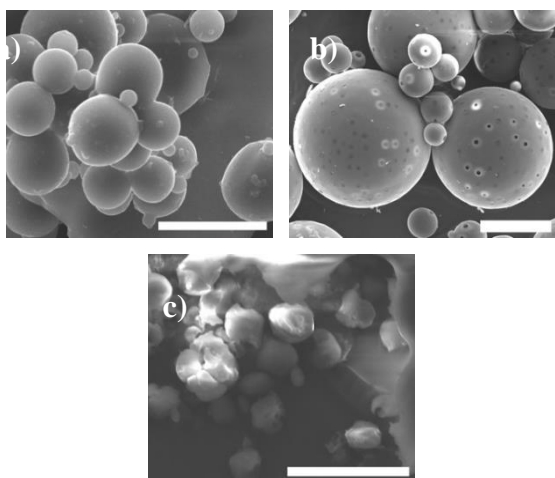


Figure 2: SEM of a) PS-MPCM, b) PMMA-MPCM and c) PET-MPCM (Scale: 25 μm).

Differences are also noticeable in the surface of the MPCM. PS-MPCM has a homogeneous surface, while

PMMA-MPCM has a partially porous surface. The extent to which this affects its suitability as an MPCM must be examined later.

In addition, with a PDI of 1.03, the PMMA-MPCM is more polydisperse than the PS-MPCM (PDI = 0.33) and with an average diameter of 26.95 μm it is significantly larger than the PS-MPCM ($\varnothing = 7.37 \mu\text{m}$).

FT-IR analysis

Obtained samples were analyzed by FT-IR and compared with pure polymer and PCM (see Figure 3). The spectrum of the latter shows the C-H stretching vibration at around 2950 cm^{-1} and the deformation vibration of the CH_3 groups in the region of 1400 cm^{-1} . The stretching vibrations of the CH_2 groups can be seen in the region around 2900 cm^{-1} and at about 1720 cm^{-1} there is a strong C=O stretching vibration, which shows that the PCM is an ester compound and correlates with the C-O stretching vibration of the ester group at about 1450 cm^{-1} . Finally, the C-C stretching vibration can be seen at around 720 cm^{-1} .^[7]

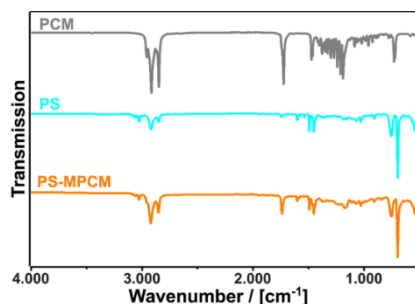


Figure 3: Infrared spectra comparison of PCM, PS and PS-MPCM.

In the spectrum of pure PS, the aromatic stretching vibrations occur in the region of about 3000 cm^{-1} and the stretching vibrations of the CH_2 groups just below, at around 2900 cm^{-1} . The peaks in the region of 1500 cm^{-1} can be assigned to the C=C stretching vibrations of the benzene ring and the peaks at about 750 cm^{-1} to the deformation vibrations of benzene.^[8] For the PS-MPCM, a mixture of the two spectra is expected and can indeed be found in Figure 3.

Looking at the pure PMMA (see Figure 4), the stretching vibrations of the CH_2 groups can be seen at around 2900 cm^{-1} . Below this, the C=O stretching vibration of the ester group occurs at around 1720 cm^{-1} and the corresponding C-O vibration of the ester group appears at around 1120 cm^{-1} . In addition, the C-H bending vibration can be seen at about 1450 cm^{-1} and the C-C stretching vibration at about 720 cm^{-1} .^[9]

For the PMMA-MPCM a mixture of PMMA and PCM spectra can be seen, particularly in the increased intensity ratio of the peaks around 2900 cm^{-1} to the peaks around 1700 cm^{-1} , so both samples showed the

presence of polymer and PCM, which indicates a successful MPCM synthesis.

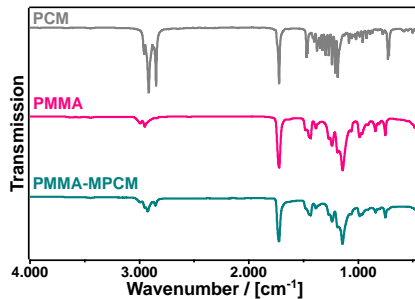


Figure 4: Infrared spectra comparison of PCM, PMMA and PMMA-MPCM.

DSC analysis

DSC measurements were performed over a temperature range of 5°C to 40°C with a ramp of 1°C/min in duplicate.

A phase change temperature of 25°C was chosen for the PCM, so that the typical minimum of the DSC curve for a melting process is expected to be at 25°C, as shown in Figure 5. It can also be seen that the melting range of the PCM from a solid to a fully molten state extends from approximately 17°C to 28°C. The plotted curves of PS-MPCM and PMMA-MPCM show a similar course, indicating the presence of PCM in the sample. However, the melting behaviour is influenced by encapsulation. In the case of PS-MPCM, the melting process initiates just above 20°C, resulting in a shorter melting range.

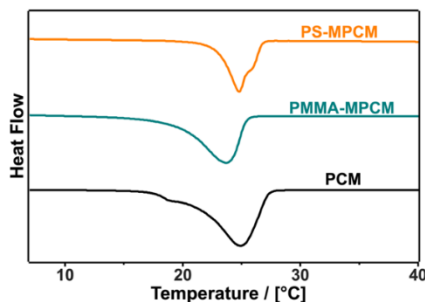


Figure 5: DSC curve of the PS-MPCM, the PMMA-MPCM and the pure PCM.

For PMMA-MPCM, the melting range is only slightly reduced, but the minimum of the melting process is shifted to lower temperatures (around 23°C), maybe because of the porous structure of the PMMA-MPCM. But there is no evidence of PCM leakage, even in the double version, as the DSC curve remains identical for both measurements.

The enthalpy of the melting process can be determined by integrating the whole peak, and for pure PCM, the melting enthalpy is 170.2 J/g, while for the MPCM it is lower, as expected, since a large part of the material

consists only of polymer. The amount of heat absorbed during the melting process can be determined to be 18.4 J/g for PS-MPCM and 35.8 J/g for PMMA-MPCM, so both samples can act as thermal heat stores.

TGA analysis

A temperature ramp of 5 °C/min up to a temperature of 550 °C was selected for the TGA measurements and Figure 6 shows the TGA results for the PS-MPCM.

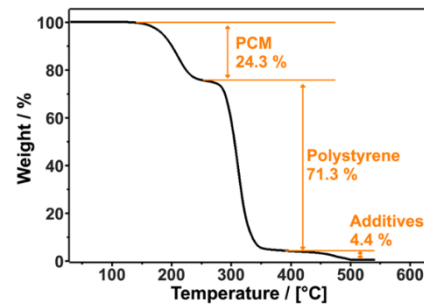


Figure 6: Thermogravimetric analysis of PS-MPCM.

The PCM decomposes in the range between 150°C and 250°C, followed by the decomposition of the polymer above 250°C up to about 400°C, which agrees with literature data for the decomposition point of PS.^[8] From approximately 450°C to 500°C, a lower mass loss of the sample is observed, which is presumably due to additives. Therefore, the two main components expected in the PS-MPCM can be identified in the TGA, and the ratio of polymer to PCM was found to be 3:1, which was the ratio used in the synthesis, so that the PCM and polymer participate in the encapsulation in the same way.

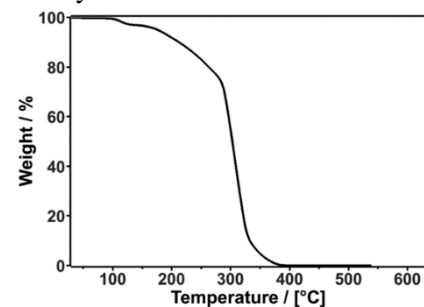
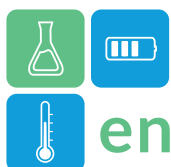


Figure 7: Thermogravimetric analysis of PMMA-MPCM.

The TGA of the PMMA-MPCM in Figure 7 shows a curve that is more difficult to interpret. Initially, at around 100°C to 150°C, there is a small loss of material, but this is due to aqueous residues or similar. Later, the loss of material from the PCM can be seen, but the decomposition of the PCM does not appear to be complete when the PMMA starts to decompose at around 275°C, so the decompositions overlap. Although the decomposition point of the PMMA is in good agreement with literature data, the delayed decomposition of the PCM makes it impossible to



determine the exact proportions of the MPCM, and it appears that the type of encapsulation in the partially porous network of PMMA-MPCM affects the decomposition of the PCM.^[10]

Stability tests

The pH stability of the MPCM was tested in the range of pH 4 - 14 and the SEM confirmed that no damage or similar occurred to the capsules. The same applies to the thermocyclic stability, where no change or damage to the MPCM was observed after 200 cycles.

However, there are differences when analyzing the thermal stability (see Figure 8). The PS-MPCM is already strongly agglomerated at 50°C, whereas the PMMA-MPCM shows only slight deformation at 105°C, which may be due to the higher T_g of PMMA.^{[11],[12]} In addition, the porous structure of the PMMA-MPCM can be clearly seen at one point in the figure.

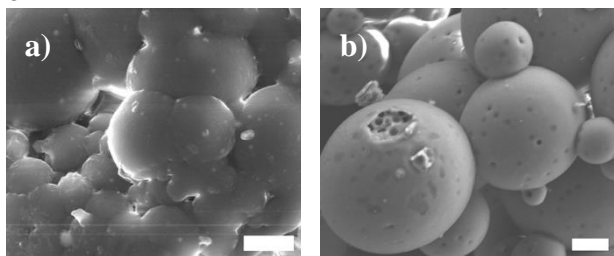


Figure 8: a) PS-MPCM after 24 h at 50°C b) PMMA-MPCM after 24 h at 105°C (Scale 10 μ m).

Conclusions

The synthesis with the different polymers is to be evaluated with different degrees of success. No capsules of sufficient quality could be obtained with PET, whereas the PS-MPCM and PMMA-MPCM syntheses could be considered successful, verified by several analytical methods, and it was found that the melting enthalpy, which is an important factor for applicability as a TES, was significantly higher for PMMA-MPCM than for PS-MPCM.

Regarding the stability both MPCM showed very high thermocyclic and pH stability, but there were differences in the thermal stability, with the PS-MPCM showing strong agglomeration of the capsules at 50°C, while the PMMA-MPCM still was mostly isolated capsules at 105°C.

A simple process for the preparation of stable MPCMs suitable for use as TES could be adapted to different polymers. Future studies need to explore the possibility

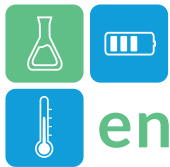
of mixing different polymers for encapsulation to reduce production costs and possibly reintroduce PET in smaller proportions. In addition, the optimization of the polymer to PCM ratio for maximum performance should be investigated.

Acknowledgments

This work is supported by the Spanish Government with the Grant CNS2022-135800, PID2021-123511OB-C32, and PID2021-125810OB-C21 funded by MCIN/AEI/10.13039/501100011033, “ERDF A way of making Europe”, and by the Catalan Government with the Grant 2021 SGR 00708. Furthermore, the Agència de Gestió d’Ajuts Universitaris i de Recerca (AGAUR) contributed through Ms. Anna Alcofea-Roig’s PhD grant (FI-DGR 2021). Dr. Jessica Giro-Paloma wants to thank the Serra Húnter Program. DIOPMA is a certified agent TECNIO in the category of technology developers from the Government of Catalonia.

References

- [1] Home - Eurostat. <https://ec.europa.eu/eurostat> (accessed Dec. 12, 2023).
- [2] Pérez-Lombard, L. et al. *Energy and Buildings* **2008**, 40, 394–398.
- [3] Giro-Paloma, J. et al. *Renewable and Sustainable Energy Reviews* **2016**, 53, 1059–1075.
- [4] Khare, R. et al. *Journal of the Indian Chemical Society* **2023**, 100, 100821.
- [5] Torza, S. et al. *Journal of Colloid and Interface Science* **1970**, 33, 67–83.
- [6] Shao, Y. et al. *Micro & Nano Letters* **2018**, 13, 998–1000.
- [7] Gao, X. et al. *Thermochimica Acta* **2018**, 659, 183–190.
- [8] Sami, S. et al. *Applied Thermal Engineering* **2018**, 130, 1416–1424.
- [9] Giro-Paloma, J. et al. *Energy Procedia* **2014**, 48, 347–354.
- [10] Korobeinichev, O. P. et al. *Thermochimica acta* **2019**, 671, 17–25.
- [11] Rieger, J. *Journal of Thermal Analysis* **1996**, 46, 965–972.
- [12] Soldera, A. *Macromolecular Symposia* **1998**, 133, 21–32.



Utilization of UTES with solar energy in de-icing and snow melting - IEA ES TASK 38

Bijan Adl-Zarrabi^{1*}, Signhild Gehlin²

¹ Chalmers University of Technology, Dpt. of Architecture and civil engineering, Gothenburg, Sweden

² The Swedish Geoenergy Centre, Lund, Sweden

*Corresponding author e-mail: bjan.adl-zarrabi@chalmers.se

Abstract

The international collaboration project Task 38 – Ground Source De-Icing and Snow Melting Systems for Infrastructure – initiated by the International Energy Agency (IEA) Energy Storage (ES) Technical Collaboration Project (TCP) is running from 2021 to 2024. Five countries are active in the project, with Sweden and Türkiye as lead countries. This paper gives an overview of the project and its outcomes so far.

Keywords: UTES, De-icing, Snow-melting, IEA ES Task 38

Introduction

Thermal de-icing and snow melting methods to control winter conditions on surfaces of transport infrastructure offer several advantages compared to conventional techniques. These include automated control of safe surface conditions, avoidance of chemicals and their environmental impact, and prolongation of the life of the infrastructure. According to a study by the Ministry of Transport, Energy and Regional Planning of the State of North Rhine-Westphalia (Würtele, 2005) in Germany, electricity in combination with electrical resistance heaters is the most common form of energy source for thermal de-icing. The remaining systems are operated by a hydraulic circuit that is heated with either gas, oil, or district heating. Using resistance heaters is a challenge for the electric grid since these systems have a huge power demand. Oil and gas are fossil energy sources that should be avoided, and district heating networks are mostly available in densely populated areas. The use of the ground as a heat source for thermal ice-prevention and de-icing is a renewable alternative to other heat sources. Ground source heat pumps (GSHP) and underground thermal energy storage (UTES) offer an additional possibility to use solar heat for de-icing of paved surfaces such as roads and bridge decks.

In June 2021, the International Energy Agency (IEA) technology collaboration program related to energy storage (ES), initiated an international collaboration project related to the utilization of ground thermal energy sources for de-icing of surfaces in transport

infrastructures. The full project name is IEA ES Task 38 - *Ground Source De-Icing and Snow Melting Systems for Infrastructure*. Sweden, Türkiye, Germany, Italy, and Belgium are active members of the collaboration project.

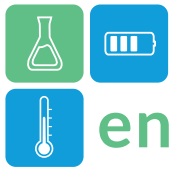
The overall goal of Task 38 is to contribute to the replacement of electrical resistance heater systems and expand the utilization of direct geothermal heating systems or ground source heat pumps in de-icing and snow melting of pavements in infrastructures. There are also other applications where ground source heated surfaces may be applied, e.g. sports arenas with artificial or natural turf. The Task 38 activities are divided into four subtasks:

- 1) Market potential and State-of-the-Art
- 2) Modelling of geothermal energy storage and de-icing systems
- 3) Development of system components for selected applications
- 4) Planning, construction, and monitoring.

More information about the workplan, objectives and activities of Task 38 can be found in the following link: <https://iea-es.org/annex-38/>.

The IEA ES Task 38 project closes at the end of 2024. National state-of-the-art reports for France, Germany, Belgium, Italy, Türkiye, Japan and Sweden (Andersson et al. 2023) are compiled within Task 38 and an overall state-of-the-art and market overview report is currently being prepared.

While snow melting and de-icing systems with hydronic heated pavements (HHP) are being used in



several countries, mostly utilizing heat sources such as district heating return flow or gas boilers, examples of geothermal energy sources for HHP systems are less common, with some examples in Japan, Europe and North America. There are two active test sites for geothermal de-icing and snow melting used within the Task 38 project. One is a test road surface in Östersund in Sweden (Johnsson 2019) and the other is a part of a foot and biking path in Antwerp in Belgium (Ghalandari 2021, 2023).

Hydronic heated pavement-solar energy

Solar thermal energy is a renewable energy source that is available in abundance. In 1994, a Hydronic heated Pavement (HHP) system that utilized solar energy was installed on a bridge near Därlingen in Switzerland (Eugster 2007; Lund 2000). This project, SERSO, proved the feasibility of such a system (Pahud 2007). They overcame the obvious problem associated with using solar energy in the winter by combining seasonal thermal energy storage with an HHP system. The working principle of the system used in the SERSO project can be divided into three parts: (I) During summer, the solar radiation heats the pavement and by the embedded pipe network, the heat is harvested and transferred to a seasonal thermal energy storage. (II) The system is dormant when no more heat can be gained from the surface of the pavement. (III) When there is a need for de-icing and friction control, the pumps are started and the stored heat is transferred to the pavement, thereby mitigating the slippery conditions.

The application of HHP is not limited to cold climates. In a warm climate, an HPP reduces the temperature of the pavement meanwhile harvesting energy. Reduction of the temperature prolongs the lifetime of the pavement.

Components of a HHP system

A HPP system consists of 1) a piping network embedded in the pavement, 2) a geothermal heating system (GSHP or seasonal thermal storage), and 3) a control system. In addition, a weather station may be included if optimization of energy demand is needed.

Piping: Integrating a pipe, into the pavement is a challenge since it introduces a new, unknown, feature from a structural point of view. However, the experience of ASC (Asphalt Solar Collector) and HHP is increasing. There are several studies and installations from which experience can be gathered e.g. (Ghalandari and al., 2021).

Integration of a pipe network in a pavement requires information about the buried depth of the pipe, the distance between pipes, the length of the pipe, and the thermo-mechanical material property of the pipes.

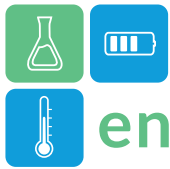
Diameter and length of the pipes is a function of acceptable pressure drop, the inlet temperature and the temperature drop along the pipe installation. A common diameter of the pipe is 25 mm. The most effective installation in roads seems to be obtained if the pipes are placed in parallel to the direction of the road. This might not be the most thermally effective installation, however, by using parallel pipes the number of bends is minimized. This puts a stress on the pipes and takes longer time to mount.



Figure 1. Installed heating pipes in Göteborgsbacken, Sweden, before installation of the binding layer. The figure also shows the connection of the heating pipes to the distribution system (Image source: NCC).

There are different materials available for producing the pipes necessary for the HHP. The selection should be based on the durability, workability, thermal characteristics, and cost of the material. The most common material used is plastics such as PEX pipes.

Seasonal thermal storage: Harvesting solar energy for de-icing and snow melting requires a seasonal thermal storage system. Depending on the application, location (rural or urban), and energy demand, different types of thermal storage can be used. Closed loop shallow geothermal energy e.g. borehole thermal energy storage (BTES), and tank thermal energy storage (TTES), are also suited for various applications used at several geotechnical conditions. From a drilling point of view, the depth limit of shallow geothermal systems is approximately 300 m, sometimes as deep as 500-600 m, with conventional drill rigs, depending on geological conditions and the type of drill rig. A heat pump is commonly used to increase the temperature of the ground source heat, i.e. to achieve the desired temperature level. The boreholes in the rock are fitted with a borehole heat exchanger (BHE), most commonly a plastic U-pipe.



Thermal energy is transported by circulating a fluid with an anti-freeze (e.g. water-ethanol) through the ground loop.

Control system: Optimization of the energy demand for de-icing requires information about the pavement surface. The condition of the pavement surface depends on the climate parameter such as temperature, moisture, wind, sky radiation etc. Thus, software-based simulation is needed for calculation of the surface condition. There are several software suitable for calculation of the surface conditions. A pre-study related to available software suitable for coupling the pavement and thermal storage, is on-going within Task 38 Subtask 2.

The input data for simulation of surface conditions could be gathered from a weather station at the location or by using the national metrological data for the area.

The charge and de-charge of the storage can be controlled by using the calculated surface temperature, e.g. de-charging (de-icing) starts when the temperature of the surface is about 4°C. Alternatively, charging of the storage is controlled by comparing the surface temperature in summertime with the temperature in the storage. When the surface temperature is below or equal to the storage temperature, the connection between the surface and storage (circulation of water) stops.

Field station in Östersund, Sweden

To test the technology of heating roads in an environmentally friendly and energy-efficient way, a test bed has been built in Östersund in a Nordic co-operation. Motivation for the choice of location was that the surface needed to be located far enough north to ensure access to snow during the limited measurement time, it must be possible to shut off the traffic, and the electricity grid must have sufficient capacity. The inauguration took place on March 22, 2018. A heated surface (concrete pavement) and a reference surface were constructed. Furthermore, HVAC containers, containing control and regulation equipment, pumps, and additional heat etc., boreholes for storage and extraction of geoenery and HVAC masts (climate masts) for measuring temperature, precipitation, relative humidity, and wind, etc. were installed. The test site is described in more detail by Johansson (2019).

In summer, the surface acts as a solar collector and heat are captured and stored in rock through

boreholes. In winter, the stored energy is used to heat the test surface.

The test surface of reinforced concrete is slightly over 20 m long and 3.5 m wide, and contains 20 mm PEX pipes with a centre-to-centre distance of 50 mm. A group of 10 pipes are distributed in 7 loops across the width of the test surface.

The depth of the pipe system below the surface and distance between pipes were designed to have an efficient function when using low temperature systems e.g., direct use of geoenery. This was judged to be a significantly more advanced case to investigate, but also a more sustainable system, compared to e.g., use higher temperature. The consequence of this is that the pipes are tight and shallow.

Results

Energy harvesting: To find out how much energy that could be harvested measurement were performed on the field station during the summer of 2018. The measurements started on the 14th of May and ended on the 31th of August. The summer of 2018 was exceptional warm, with a mean air temperature 2°C above average thereby increasing the amount of harvested energy. During the summer the accumulated energy from the pavement and the heat extraction rate were measured. The heat extraction rate reached peak values of 20 kW while the daily mean varies between 4kW and 10 kW. The total accumulated energy during the period was 17 200 kWh, equivalent to 245 kW h/m² while the total amount of incoming solar radiation was 614 kWh/m².

The calculated solar efficiency of the pavement during the summer of 2018, was found to be 42% which is higher than reported in other studies. The higher efficiency of the field station in Sweden can be explained by the close pipe distance of 5 cm, a high fluid flow rate and low supply temperature - all factors that increase the solar efficiency.

De-icing and snow melting: The HHP system was used for de-icing during the winter of 2018/2019. The experiments were conducted between the 15th of October 2018 and the 10th of April 2019. The energy source of the HHP system originates from two different sources, namely from the BTES and from the electric boiler. The energy supplied to the road reached 9175 kWh (132 kW h/m²) while the energy delivered from the storage was 4401 kWh (63 kW h/m²). The electric energy used during the winter was 4770 kWh (68kW h/m²). About 50% of the used



energy origins from electricity because of the need for higher supply temperatures to the pavement than the BTES could deliver.

Conclusions

Thermal de-icing with hydronic heated pavement using the ground as a heat source and seasonal storage medium is a promising although yet not widely used technology combination. Examples of such systems exist in Asia as well as in Europe and North America. Two test sites, in Sweden and in Belgium, have been used within the IEA ES Task 38 project. Conclusions from the study at the Östersund field stations were that the temperature level of the stored energy was not sufficient to fully provide de-icing and snow melting in the cold climate, so an additional energy source was necessary to increase the temperature to a sufficient level. Thus, control systems are important components for optimization of the de-icing system energy demand. The efficiency of energy harvesting with concrete pavement in the Östersund study was about 50%. Asphalt pavement with a higher absorption coefficient than concrete would increase the efficiency.

Acknowledgment

The work performed in the field station was founded by the Swedish Traffic Agency (TR) and Norwegian Public Road Administration (NPRA). Furthermore, thanks for all the support we have received by Östersund municipality and Jämtlands school. Finally, we thank Swedish Energy Agency for funding our involvement in IEA ES TCP TASK 38, Grant 51491-1.

References

- Andersson, O., Gehlin, S., Hellström, G., Adl-Zarrabi, B., Carlsson, A., Kalantar, A. (2023). State-of-the-Art: Sweden: Ground-Source De-Icing and Snow Melting Systems for Infrastructure. Final report. December 2023. IEA ES Task38 Report. http://media.geoenergicentrum.se/2024/01/Annex-38_SOTA-Sweden_Final-report-Dec-2023-Publ.pdf?_ga=2.254797134.718641499.1705419278-1472001483.1591185555
- Lund, John W. 2000. "Pavement Snow Melting." *Geo-Heat Center Quarterly Bulletin* 21(No. 2).
- Pahud, Daniel. 2007. *Serso, Stockage Saisonnier Solaire Pour Le Dégivrage d'un Pont*. Bern: Bundesamt für Energie BFE.
- Ghalandari, T. and al. (2021) A critical review on large-scale research prototypes and actual projects

- of hydronic asphalt pavement systems, *Renewable Energy*, Volume 177, Pages 1421-1437
- Ghalandari T, Kia A, DMG Taborda, Vuye C. (2023). Thermal performance optimisation of Pavement Solar Collectors using response surface methodology, *Renewable Energy*, 2023 – Elsevier.
- Johnsson, J. (2019). *Low Temperature Deicing of Road Infrastructure Using Renewable Energy*
- Würtele, M. and al. (2005) *Geothermie sorgt für Verkehrssicherheit, Studie im Auftrag des Ministeriums für Verkehr Energie und Landesplanung des Landes Nordrheinwestfalen, Düsseldorf 2005*

Author Index

- A. Leeke Gary, 381–384
Abohamzeh Elham, 231–234
Adl-Zarrabi Bijan, 504–507, 590–593
Adnan Ariba, 260–264
Agalit Hassan, 381–384
Ahmad Abdalqader, 338–341
Al-Saaidi Hussein Alawai Ibrahim, 163–166
Alahyari Arman, 29–36
Alberro Mikel, 429–431
Alfocea-Roig Anna, 586–589
Alma Fatma, 467–470
Almendros-Ibáñez José Antonio, 67–70, 175–178
Alonso-Martinez Mar, 25–28
Alvarez-Rodriguez Matias, 25–28
Ambardar Tridib, 228–230
Ambirajan Amrit, 138–142
Amini Sara, 319–322, 429–431
Ammann Sebastian, 6–8
Anagnostopoulos Argyrios, 338–341
Anastasija Jocić, 413–416
Andersson Olof, 330–333, 504–507
Andrea Frazzica, 573–576
Apostolopoulos - Kalkavouras Konstantinos, 87–91
Ardila Sergio, 551–553
Arnaud Bruch, 134–137
Ayaz Hamza, 326–329
Ayed Rabeb, 511–514

Bach Christian, 515–518
Badenes Borja, 239–242
Baik Young-Jin, 219–221
Balwani Apoorva, 228–230
Barot Hem, 99
Barreneche Camila, 79–83, 187–191, 342–344, 500–503, 547–550
Barz Tilman, 45–48
Baseri Gholamhossein Kahid, 265–268
Battaglia Matteo, 538–541
Bauer Dr. Thomas, 99
Bauer Thomas, 115–117, 307–310
Bayer Peter, 358–361, 526–529
Beaupere Noé, 554–558
Beceiro Jorge Salgado, 265–268, 326–329
Becke Walter, 374–376
Bejar Ramón, 366–369
Belinson Maxim, 269–272
Bentivoglio Fabrice, 377–380, 409–412, 542–546
Berberich Magdalena, 362–365
Bergamasco Luca, 224–227
Berlin Robin, 457–459
Betancor Lorena, 500–503
Beyne Wim, 277–280
Bilardo Matteo, 167–170
Biçer Göktepe Gizem, 467–470
Boeckmann Olaf, 222, 223
Boer Robert De, 247–250
Boit Baptiste, 377–380
Bonk Alexander, 307–310
Bonnin Salomé, 179–182
Borri Emiliano, 92–94, 224–227, 366–369, 453–456, 511–514, 534–537, 582–585
Bott Christoph, 358–361, 526–529
Bouadila Salwa, 511–514
Brancato Vincenza, 196–200
Brancato Vincenza, 573–576
Brand Tom, 362–365
Bregar Luka, 413–416
Bruch Arnaud, 377–380, 409–412
Brunelli Luca, 534–537
Bryden Thomas, 29–36
Byrne Ciara, 41–44
Bédécarrats Jean-Pierre, 265–268, 326–329
Bürger Inga, 567, 568
Bürger Inga, 519–521

Cabeza Luisa F., 92–94, 155–158, 171–174, 224–227, 281–284, 366–369, 453–456, 511–514, 534–537, 582–585
Cabeza Luisa F., 58–62
Cadia D'ottavi, 538–541
Cagnoli Mattia, 393–396
Calabrese Luigi, 196–200, 273–276
Calabrese Luigi, 573–576
Calderón Alejandro, 79–83, 187–191
Callaghan Ryan L., 269–272
Canales-Vázquez Jesús, 67–70

- Canela-Garayoa Ramon, 92–94
 Cardemil José Miguel, 478–481
 Casado Nerea, 432–436
 Centeno-Pedraza Ander, 508–510
 Cerutti-Cristaldo Leonel Mario, 67–70
 Cetkin Erdal, 474–477
 Chae Soowon, 389–392
 Champel Bénédicte, 409–412
 Chartier Thierry, 130–133
 Chate Akshay, 138–142
 Chiavazzo Eliodoro, 224–227
 Chiu Justin, 17–20, 213–215, 294–297
 Chiu Justin Ningwei, 45–48, 251–255, 421–424
 Choi Bongsu, 219–221
 Cogrel Landry, 45–48
 Coronado Juan, 273–276
 Correa Bernal Ana Maria, 45–48
 Corsaro Natale, 417–420, 538–541
 Couvreur Kenny, 277–280
 Crocomo Paola, 147–150, 260–264, 350–353
 Cyr Martin, 554–558
 Córcoles Juan Ignacio, 175–178
- D Widijatmoko Samuel, 381–384
 Da Col Amandine, 542–546
 Daehun Chung, 482–484
 Dahash Abdulrahman, 75–78, 577–581
 Daniel Bakker, 1–5
 Dash Susmita, 138–142
 Daubner Markus, 323–325
 Dauvergne Jean Luc, 260–264, 489–492
 Dauvergne Jean Luc, 432–436
 De Giorgi Paolo, 155–158
 De Paepe Michel, 277–280
 De Santiago Cristina, 239–242
 Dejean Guilhem, 563–566
 Delgado Mónica, 448–452
 Delise Tiziano, 538–541
 Demirkiran İsmail, 474–477
 Devise Charles, 563–566
 Dietz Larissa, 519–525
 Ding Dr. Wenjin, 99
 Ding Yulong, 192–195, 338–341
 Dominic Groulx, 269–272
 Dominkovic Dominik, 95–98
 Domínguez-Coy Pedro, 175–178
 Dong Haoyang, 421–424
 Dong Kaixin, 497–499
 Doppiu Stefania, 147–150, 260–264
 Dosta Sergi, 500–503
 Dragsted Janne, 95–98
 Dreißigacker Volker, 153, 154
- Duckjae Wei, 482–484
 Dutta Pradip, 138–142
 Díaz-Heras Minerva, 67–70
- Elahi Behrooz, 345–349
 Elarga Hagar, 111–114
 Emir Sedat, 13–16, 467–470
 Eneja Osterman, 413–416
 Englmaier Gerald, 95–98
 Erdocia Xabier, 319–322
 Escribà-Gelonch Marc, 92–94
- Fabiani Claudia, 582–585
 Fabrizio Enrico, 167–170
 Faigl Markus, 526–529
 Fan Jianhua, 401–404
 Fasano Matteo, 224–227
 Feine Julius, 243–246
 Fellmoser Frank, 323–325
 Fernández A Inés, 342–344
 Fernández Ana Inés, 79–83, 187–191, 478–481, 551–553
 Fernández Ángel G., 319–322, 429–431
 Feránadez A. Inés, 547–550
 Filonenko Konstantin, 95–98
 Fischer Ludger, 6–8
 Fiß Michael, 519–521
 Fluri Thomas, 205–208
 Font-Prieur Daylen Y., 92–94
 Formhals Julian, 75–78
 Formosa Joan, 586–589
 Forsyth Andrew, 29–36
 Fotia Antonio, 196–200
 Fotia Antonio, 573–576
 Fournier Nathan, 401–404
 Frazzica Andrea, 196–200
 Frey Georg, 231–234
 From Niels, 122–125
 Frédéric Kuznik, 134–137
 Fujii Kazuya, 530, 531
 Fujii Shoma, 213–215, 294–297, 463–466
 Funayama Shigehiko, 530, 531
 Furbo Simon, 401–404
- Gamisch Sebastian, 397–400
 Garcia Pierre, 401–404
 Garcia-Suarez Eduardo, 508–510
 Garcia-Suarez Eduardo, 432–436
 Gauthier Geoffroy, 75–78
 Gehlin Signhild, 504–507, 590–593
 Gengembre Edouard, 179–182
 Ginestet Stéphane, 554–558

- Giordano Fabrizia, 45–48
 Giro-Paloma Jessica, 586–589
 Giuseppe Vecchi, 393–396
 Gladwin Dan, 29–36
 Glomba Marcel, 45–48
 Goderis Maité, 277–280
 Gollsch Marie, 63, 64
 Golobič Amalija, 41–44
 Gonnelle Alexis, 401–404
 Grena Roberto, 393–396
 Gruber Peter, 374–376
 Grégory Largiller, 134–137
 Gschwander Stefan, 370–373, 397–400, 485–488
 Guedez Mata Rafael Eduardo, 87–91, 285–288
 Guillen-Lambea Silvia, 103–106
 Gunasekara Saman Nimali, 17–20, 45–48, 421–424
 Gupta Ankit, 205–208
 Gutierrez Andrea, 519–525
 Güngör Özge, 467–470

 Hafner Armin, 111–114
 Haghghat Fariborz, 21–24
 Han Gwangwoo, 159–162
 Harrison Stephen, 209–212
 Harrison Chris, 29–36
 Haussmann Thomas, 107–110
 He Fang, 183–186
 Heer Philipp, 126–129
 Hengel Franz, 37–40, 311–314
 Herder Gertjan, 247–250
 Hernández Fabio, 319–322
 Hewson Connor, 41–44
 Hiebler Stefan, 298–301, 425–428
 Hippler-Nettlau Janina, 334–337
 Hoffmann David, 526–529
 Hoffmann Ralf, 99
 Hong Sungkook, 216–218, 482–484
 Hooek Peter, 298–301
 Hoplamaz Filiz, 467–470
 Huebner Fanny, 205–208
 Huerta Ali, 260–264
 Humbert Gabriele, 126–129
 Hutchinson Andrew, 29–36
 Håkansson Niklas, 330–333

 Iacomi Paul, 41–44
 Ichikawa Hiroyuki, 289–293
 Ichitsubo Tetsu, 315–318
 Igor Rangel Correa Ferreira, 134–137
 Ikeda Shintaro, 289–293
 Ilbas Medine, 425–428

 Imaida Mio, 444–447
 Indranil Roy, 209–212
 Izaki Tsuyoshi, 530, 531

 Jain Kartik, 138–142
 Jeem Melbert, 151, 152, 460–462, 497–499, 559–562
 Jensen Adam R., 122–125
 Jensen Charlotte, 95–98
 Johannes Kevyn, 179–182
 Johnson Maiké, 522–525
 Junhyun Cho, 219–221

 Kanematsu Yuichiro, 294–297
 Kanghee Cho, 482–484
 Kardas Gulfeza, 13–16
 Kardaş Gülfeza, 84–86, 467–470
 Kargl Florian, 65, 66
 Karl Martin, 205–208
 Kato Takashi, 530, 531
 Kato Yukitaka, 530, 531
 KatourtZidis Anastasios, 243–246
 Kawaguchi Takahiro, 151, 152
 Kerschenbauer Roland, 37–40
 Kevyn Johannes, 134–137
 Kick Moritz, 370–373
 Kieseritzky Esther, 45–48
 Kieskamp Bram, 71–74
 Kikuchi Yasunori, 294–297, 463–466
 Kim Eui-Jong, 118–121
 Kim Jong-Kyu, 159–162
 Kim Min-Hwi, 159–162
 Kim Seong-Eun, 216–218
 Klasing Freerk, 115–117, 307–310
 Klockow Eva, 63, 64
 Klünder Franziska, 107–110
 Koirala Binod Prasad, 126–129
 Kolbe Matthias, 65, 66
 Komoda Hideharu, 444–447
 Kondo Minako, 497–499
 Kottarathil Aginmariya, 432–436
 Koçak Burcu, 84–86
 Kraft Werner, 65, 66
 Kraft Werner, 243–246
 Kuznik Frédéric, 179–182
 Kühl Viktor, 63, 64

 Labidi Jalel, 319–322
 Lalau Yasmine, 563–566
 Lampersberger Paul, 374–376
 Lanchi Michela, 393–396, 417–420
 Lara Cruz José, 265–268, 326–329

Largriller Grégory, 350–353, 471–473
 Lazaar Mariem, 511–514
 Lee Gilbong, 219–221
 Lee Hyunhee, 216–218
 Li Yongliang, 381–384
 Liberatore Raffaele, 417–420, 538–541
 Licoccia Silvia, 538–541
 Linder Marc, 63, 64
 Liu Hongzhi, 183–186
 Lopez-Morales Jorge L., 432–436
 Lopez-Roman Anton, 155–158, 354–357
 Luengo Cristina, 147–150, 260–264
 Lux Martin, 323–325
 Lyons Pdraig, 171–174
 Lázaro Ana, 448–452

 Magni Mara, 440–443
 Magraner Teresa, 239–242
 Mahkamov Khamid, 467–470
 Mahmoudi Amirhoushang, 71–74
 Majó Marc, 79–83, 187–191
 Makhkamova Irina, 467–470
 Malley-Ernewein Alexandre, 179–182, 554–558
 Mancin Simone, 385–388
 Mangold Dirk, 362–365
 Mani Kala Saranprabhu, 224–227
 Mani Kala Saranprabhu, 58–62
 Manosa Jofre, 342–344
 Mansi Emiliana, 538–541
 Marske Felix, 54–57
 Martinent Jean-Régis, 563–566
 Martinez Alcocer Franklin R., 453–456
 Martí Marta, 448–452
 Maskun Yelaman, 338–341
 Mastronardo Emanuela, 196–200, 273–276
 Mastronardo Emanuela, 573–576
 Mata-Marquez Fatima, 519–521
 Mateu Carles, 366–369, 534–537
 Mateu Carles, 58–62
 Matsuba Yu, 559–562
 Matsui Kazuki, 463–466
 Matthes Eric, 54–57
 Matthes Manuel, 9–12
 Mayr Martin, 374–376
 Mba Joshua Chidiebere, 497–499
 Mehraj Nadiya, 58–62
 Mehrali Mohammad, 49–53
 Milone Candida, 196–200, 273–276
 Mlakar Urška, 405–408
 Moghimi Pouria, 515–518
 Morciano Matteo, 224–227
 Mueller Ralf, 205–208
 Mukherjee Partha, 205–208
 Muser Christoph, 569–572
 Müller Simon, 526–529
 Müller-Trefzer Franziska, 323–325

 Na Sun Ik, 219–221
 Nagano Katsunori, 183–186
 Nahhas Tamar, 554–558
 Nakagaki Takao, 463–466
 Nakamura Tomokazu, 213–215, 251–255, 294–297, 497–499
 Nam Yujin, 389–392
 Naung Shine Win, 467–470
 Navarrete Nuria, 65, 66
 Navarrete Nuria, 243–246
 Navarro Helena, 338–341, 547–550
 Navarro Miguel, 448–452
 Nees Frank, 243–246
 Nefodov Dimitri, 457–459
 Nguyen Anh Kiet, 209–212
 Nicolini Andrea, 534–537
 Niederkofler Tobias, 302–306
 Niedermeier Klarissa, 323–325
 Nikulen Artem, 350–353
 Nishikawa Masaya, 493–496
 Nomura Takahiro, 151, 152, 213–215, 251–255, 294–297, 437–439, 460–462, 497–499, 559–562
 Noro Marco, 385–388

 O'donovan Keith, 311–314
 O'neill Poppy, 100–102, 425–428
 Ochs Fabian, 75–78, 440–443, 569–572
 Odenthal Christian, 307–310
 Oestreich Felix, 256–259
 Oh Bong Seong, 219–221
 Okamoto Norihiko L., 315–318
 Ooka Ryoza, 289–293
 Ott Thorsten, 153, 154

 Paksoy Halime, 13–16, 84–86, 467–470
 Pal Michel Van Der, 247–250
 Palacios Anabel, 6–8, 100–102, 425–428
 Palomo Del Barrio Elena, 147–150, 260–264, 350–353, 489–492, 508–510
 Palomo Del Barrio Elena, 432–436
 Parekh Parshva Atulbhai, 397–400
 Park Seung-Hoon, 118–121
 Patiño David, 171–174
 Patsios Charalampos, 29–36
 Pavón-Moreno M.carmen, 155–158, 354–357
 Peham Lukas, 143–146

- Perez-Arce Jonatan, 508–510
Perez-Arce Jonatan, 432–436
Perino Marco, 167–170
Pham Minh Doan, 563–566
Pietri Thomas, 471–473
Pisello Anna Laura, 534–537, 582–585
Pouvreau Jérôme, 201–204
Previti Emanuele, 273–276
Prieto Cristina, 171–174, 224–227, 281–284, 354–357, 453–456
Prieto Rios Cristina, 155–158, 163–166, 551–553
Pérez-Flores Juan Carlos, 67–70
- Ra Ho-Sang, 219–221
Rabbi Jawad, 265–268
Radcliffe Jonathan, 29–36
Ramos Adela, 239–242
Rathgeber Christoph, 100–102, 425–428
Rausendorf Jonathan, 9–12
Rawat Tanuj, 29–36
Reisenbichler-Sommerhofer Michael, 75–78, 311–314
Ribas Tugores Carles, 311–314
Ribezzo Alessandro, 224–227
Richter Markus, 9–12, 457–459
Risco Amigó Sara, 224–227
Risco Sara, 58–62
Ristić Alenka, 405–408
Rodríguez-García Dana, 25–28
Rogers Daniel J., 29–36
Rohringer Christoph, 374–376
Rojas Cala Edgar Felipe, 366–369
Rotan Magnus, 265–268, 326–329
Runk Finn, 334–337
Rydell Leif, 330–333
- S Prabakaran, 205–208
Saad Ali, 471–473
Saeki Hana, 530, 531
Safae Raman, 192–195
Saito Sogo, 463–466
Salehzadeh Delaram, 49–53
Salgado-Pizarro Rebeca, 342–344, 547–550
Samoteeva Oxana, 45–48
Samson Gabriel, 554–558
Sanclemente Lozano Mateo, 285–288
Santini Carolina, 582–585
Santos Humberto, 103–106
Santos-Moreno Sergio, 489–492
Sarkar Subrata, 205–208
Sato Yusuke, 213–215
Sau Salvatore, 417–420, 538–541
Sawalha Samer, 17–20, 45–48
Schaefer Micha, 222, 223
Schallenberg-Rodríguez Julieta, 171–174
Schedler Andreas, 222, 223
Schmidt Matthias, 63, 64
Schmidt Thomas, 75–78
Schmit Henri, 100–102, 298–301, 425–428
Schrag Tobias, 526–529
Sciacovelli Adriano, 192–195
Segovia Valentina, 478–481
Selvnes Håkon, 111–114
Seongeun Kim, 482–484
Serrano Ángel, 147–150, 260–264, 350–353, 508–510
Serrano Ángel, 432–436
Sevault Alexis, 111–114, 265–268, 326–329
Shahi Mina, 71–74
Shan Lianying, 213–215, 251–255
Sharma Shivangi, 338–341
Shimizu Yuto, 460–462, 497–499
Shin Hyungki, 219–221
Sifnaios Ioannis, 75–78, 122–125
Silva Silveira Maria Clara, 100–102
Siwon Yoon, 482–484
Slaviero Gianluca, 385–388
Sourmelis Venizelos, 63, 64
Spadoni Annarita, 417–420, 538–541
Spitler Jeffrey, 515–518
Stahl Veronika, 65, 66
Stahl Veronika, 243–246
Stamatiou Anastasia, 100–102
Stritih Uros, 405–408
Stritih Uros, 413–416
Strobel Rainer, 526–529
Stutz Benoit, 542–546
Suarez-Ramon Ines, 25–28
Sugiyama Tsukasa, 530, 531
Sun Ying, 21–24
Suswal Aditya Singh, 17–20
Svobodova Adela, 79–83, 187–191
Sy Awa, 377–380
Sylvie Rougé, 134–137
Sæterli Ragnhild, 265–268, 326–329
Sørensen Per Alex, 122–125
Sørensen Per Alex, 143–146
Südaş İbrahim, 467–470
- Taeño Maria, 147–150, 260–264
Tafelmeier Stefanie, 298–301
Tagle-Salazar Pablo, 171–174
Tagle-Salazar Pablo D., 281–284

Takahashi Ken, 289–293
 Takasu Hiroki, 530, 531
 Tamano Soichiro, 530, 531
 Tanahashi Keita, 559–562
 Tanaka Hideki, 444–447
 Tanaka Kazuya, 315–318
 Ten Elshof Johan E., 49–53
 Teodorescu Laura, 350–353
 Tessier-Doyen Nicolas, 563–566
 Tezcan Fatih, 13–16
 Theologou Konstantinos, 522–525
 Thornton Jeff, 75–78
 Tittlein Pierre, 130–133
 Tizzoni Anna Chiara, 417–420, 538–541
 Toifane Hachmi, 130–133
 Tombrink Jonas, 522–525
 Tomita Kenta, 530, 531
 Torre Francesco, 350–353
 Tosatto Alice, 75–78, 440–443, 569–572
 Tran Le Anh Dung, 130–133
 Traverso Dario, 385–388
 Traverso Franco, 385–388
 Trevisan Silvia, 87–91, 285–288
 Trinkl Christoph, 526–529

 Urbaneck Thorsten, 9–12, 256–259, 457–459
 Ushak Svetlana, 453–456

 Van Den Berg Helena, 239–242
 Van Der Wilk Steven, 75–78
 Van Zele Julie, 277–280
 Veca Elisabetta Maria, 538–541
 Vera Rivera David, 586–589
 Vesin Sébastien, 201–204
 Vielma Carlos A., 79–83
 Villada Carolina, 65, 66
 Villada Carolina, 243–246
 Vodlan Katja, 41–44
 Vullum-Bruer Frilde, 265–268, 326–329

 Wagner Waldemar, 37–40
 Wallner Gernot, 143–146
 Wang Haochen, 457–459
 Wang Xinfang, 532, 533
 Ward Phil, 192–195
 Weber Simon, 222, 223
 Wei Duck-Jae, 216–218
 Weick Clément, 471–473
 Weiss Julius, 205–208
 Wetzell Hendrik, 122–125
 Wetzell Thomas, 323–325
 Williamson Kyran, 350–353

 Witte Henk, 1–5, 235–238
 Wolfesberger David, 374–376
 Worlitschek Jörg, 6–8
 Wotawa Franz, 311–314
 Wujec Leonard, 586–589

 Yamanashi Haruki, 493–496
 Yan Hui, 29–36
 Yoon Si-Won, 216–218
 Yoshisako Hiroki, 315–318
 Yvernault Léa, 201–204

 Zabukovec Logar Nataša, 41–44
 Zalewski Laurent, 130–133
 Zanino Roberto, 393–396
 Zehnder Margaux, 323–325
 Zilio Claudio, 385–388
 Zondag Herbert, 247–250
 Zsembinszki Gabriel, 224–227, 534–537
 Zsembinszki Gabriel, 58–62
 Zunft Stefan, 153, 154

